Antares

ANTARES Collaboration

Published in:
Proceedings of the 46th Rencontres de Moriond - 2011 Electroweak Interactions and Unified Theories, EW 2011

2011

Electroweak Interactions and Unified Theories

Sponsored by

. CNRS (Centre National de la Recherche Scientifique)
. CEA (Commissariat à l'Énergie Atomique)
. IN2P3 (Institut National de Physique Nucléaire et de Physique des Particules)
. NSF (National Science Foundation)
. FNRS (Fond National de la Recherche Scientifique)
. BSP (Belgian Science Policy)

XLVIth Rencontres de Moriond

La Thuile, Aosta Valley, Italy – March 13-20, 2011

2011 Electroweak Interactions and Unified Theories

Proceedings of the XLVIth RENCONTRES DE MORIOND

Electroweak Interactions and Unified Theories

La Thuile, Aosta Valley Italy *March 13-20, 2011*

2011

Electroweak Interactions and Unified Theories

edited by

Etienne Augé,

Jacques Dumarchez,

and

Jean Trân Thanh Vân

The XLVIth Rencontres de Moriond

2011 Electroweak Interactions and Unified Theories

was organized by :

Etienne Augé (IN2P3, Paris)
Jacques Dumarchez (LPNHE, Paris)

with the active collaboration of :

A. Abada (LPT, Orsay),
J. Conrad (Columbia U)
S. Davidson (IPN Lyon),
P. Fayet (ENS, Paris),
J.-M. Frère (Brussels),
P. Hernandez (Valencia),
L. Iconomidou-Fayard (LAL, Orsay),
P. Janot (CERN),
M. Knecht (CPT, Marseille),
J. P. Lees (LAPP, Annecy),
S. Loucatos (IRFU-SPP, CEA, Saclay),
F. Montanet (LPSC, Grenoble),
J. Orloff (LPC, Clermont-Ferrand),
L. Okun (ITEP, Moscow),
A. Pich (Valencia),
S. Pokorski (Warsaw),
D. Wood (Northeastern Univ.,Boston)

2011 RENCONTRES DE MORIOND

The XLVIth Rencontres de Moriond were held in La Thuile, Valle d'Aosta, Italy.

The first meeting took place at Moriond in the French Alps in 1966. There, experimental as well as theoretical physicists not only shared their scientific preoccupations, but also the household chores. The participants in the first meeting were mainly french physicists interested in electromagnetic interactions. In subsequent years, a session on high energy strong interactions was added.

The main purpose of these meetings is to discuss recent developments in contemporary physics and also to promote effective collaboration between experimentalists and theorists in the field of elementary particle physics. By bringing together a relatively small number of participants, the meeting helps develop better human relations as well as more thorough and detailed discussion of the contributions.

Our wish to develop and to experiment with new channels of communication and dialogue, which was the driving force behind the original Moriond meetings, led us to organize a parallel meeting of biologists on Cell Differentiation (1980) and to create the Moriond Astrophysics Meeting (1981). In the same spirit, we started a new series on Condensed Matter physics in January 1994. Meetings between biologists, astrophysicists, condensed matter physicists and high energy physicists are organized to study how the progress in one field can lead to new developments in the others. We trust that these conferences and lively discussions will lead to new analytical methods and new mathematical languages.

The XLVIth Rencontres de Moriond in 2011 comprised four physics sessions:

- March 13 - 20: "Electroweak Interactions and Unified Theories"
- March 13 - 20: "Quantum Mesoscopic Physics"
- March 20 - 27: "QCD and High Energy Hadronic Interactions"
- March 20 - 27: "Gravitational Waves and Experimental Gravity"

We thank the organizers of the XLVIth Rencontres de Moriond:

- A. Abada, J. Conrad, S. Davidson, P. Fayet, J.-M. Frère, P. Hernandez, L. Iconomidou-Fayard, P. Janot, M. Knecht, J. P. Lees, S. Loucatos, F. Montanet, L. Okun, J. Orloff, A. Pich, S. Pokorski, D. Wood for the "Electroweak Interactions and Unified Theories" session,

- D. Averin, C. Beenakker, Y. Blanter, K. Ennslin, Jie Gao, L. Glazman, C. Glattli, Y. Imry, Young Kuk, T. Martin, G. Montambaux, V. Pellegrini, M. Sanquer, S. Tarucha for the "Quantum Mesoscopic Physics" session,

- E. Augé, E. Berger, S. Bethke, A. Capella, A. Czarnecki, D. Denegri, N. Glover, B. Klima, M. Krawczyk, L. McLerran, B. Pietrzyk, L. Schoeffel, Chung-I Tan, J. Trân Thanh Vân, U. Wiedemann for the "QCD and High Energy Hadronic Interactions" session,

- M.-Ch. Angonin, R. Ansari, M.-A. Bizouard, L. Blanchet, M. Cruise, J. Dumarchez, Y. Giraud-Héraud, S. Hoedl, Ch. Magneville, E. Rasel, S. Reynaud, F. Ricci, R. Schnabel, J.-Y. Vinet, P. Wolf for the "Gravitational Waves and Experimental Gravity" session, joint with the GPhyS Colloquium

and the conference secretariat and technical staff:

V. de Sá-Varanda and C. Bareille, I. Cossin, G. Dreneau, D. Fligiel, S. Hurtado, N. Ribet, S. Vydelingum.

We are also grateful to Andrea Righetto, Gioacchino Romani, Erik Agostini, Patrizia Rago, Matteo Tuzzi and the Planibel Hotel staff who contributed through their hospitality and cooperation to the well-being of the participants, enabling them to work in a relaxed atmosphere.

The Rencontres were sponsored by the Centre National de la Recherche Scientifique, the Institut National de Physique Nucléaire et de Physique des Particules (IN2P3-CNRS), the Fondation NanoSciences, the Commissariat à l'Energie Atomique (DSM and IRFU), the Centre National d'Etudes Spatiales, the European Space Agency, the Fonds de la Recherche Scientifique (FRS-FNRS), the Belgium Science Policy and the National Science Foundation. We would like to express our thanks for their encouraging support.

It is our sincere hope that a fruitful exchange and an efficient collaboration between the physicists and the astrophysicists will arise from these Rencontres as from previous ones.

E. Augé, J. Dumarchez and J. Trân Thanh Vân

Contents

6. Astroparticles

7. Dark Matter and Cosmology

8. Young Scientists Forum

1. Brout-Englert-Higgs Boson Searches

SEARCH FOR LOW MASS HIGGS BOSON AT THE TEVATRON

Pierluigi Totaro for the CDF and D0 Collaborations
Università di Padova, Dipartimento di Fisica, via Marzolo 8,
35131 Padova, Italy

We present the current status of searches for a low mass Standard Model Higgs boson (M_H below $\lesssim$ 135 GeV/c^2) using data collected from $p\bar{p}$ collisions at the Fermilab Tevatron collider at $\sqrt{s}$ = 1.96 TeV. A summary of the latest results from the CDF and D0 collaborations is reported in this paper, focusing in particular on ongoing efforts to increase overall search sensitivity through improvements to the analysis methods.

1 Introduction

The Higgs mechanism is introduced in the Standard Model (SM) to provide mass to fundamental particles, through the spontaneous breaking of the electroweak simmetry. This mechanism implies the existence of a yet experimentally unobserved scalar particle, the Higgs boson, whose search has represented one of the major goals of the high energy physics community over the last decade. The mass of the Higgs boson is a free parameter of the theory, but the strong coupling to massive particles allows to constrain its value: a global fit, which incorporates the measurements of the top quark and W boson masses, as well as additional precision electroweak data provided by LEP, SLD and Tevatron experiments [1], indicates that a light Higgs is preferred, M_H=89^{+35}_{-26} GeV/c^2, with a 95% Confidence Level (C.L.) upper limit of 158 GeV/c^2. On the other hand, results from direct searches at LEP [2] set a 95% lower limit of 114.4 GeV/c^2.

In the last few years CDF and D0 have steadily increased the efforts in extending the potential sensitivity of their searches: the most recent combined results [3] exclude the existence of the Higgs boson with a mass between 158 and 173 GeV/c^2. This interval is expected to further extend, as well as new data will be included. However, a substantial chance to make a signal observation or set an exclusion in the entire explored mass range (100$\div$200 GeV/c^2) will require several improvements in the analysis methods, beyond the increase of statistics provided by the end of Tevatron operations: a projection of the probability of seeing a 2σ excess, for an integrated luminosity of 10 fb^{-1} per experiment, calculated assuming 30$\div$40% of sensitivity increase in the analysis techniques with respect to Summer 2010 results, is reported in figure 1.

As of this paper, the observed upper limit at the reference mass of 115 GeV/c^2 is 1.58 times the predicted SM cross section (figure 2): this value refers to the CDF and D0's combined measurements with up to 5.7 fb^{-1} of data [4]. The plan of the two collaborations is to come out with a new more stringent combined limit in the low mass region by Summer 2011, when several search channels will almost double the analyzed integrated luminosity. A summary of the latest public results in the low mass Higgs boson searches is given in this paper, focusing on the most significant improvements which are being implemented and will allow to reach the best sensitivity in the next Tevatron combination.

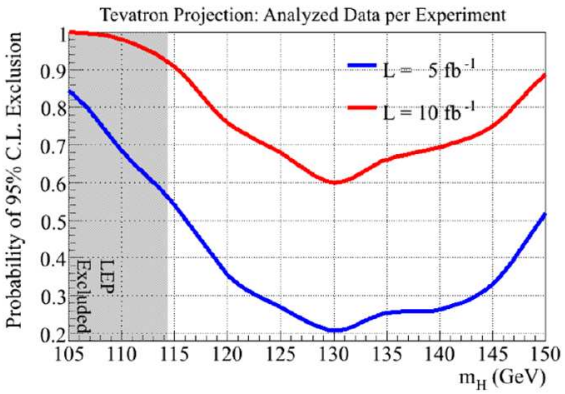

Figure 1: Tevatron probability projections of seeing a 2σ SM Higgs signal excess, for integrated luminosities of 5 fb^{-1} and 10 fb^{-1} per experiment, assuming improvements in the analysis techniques.

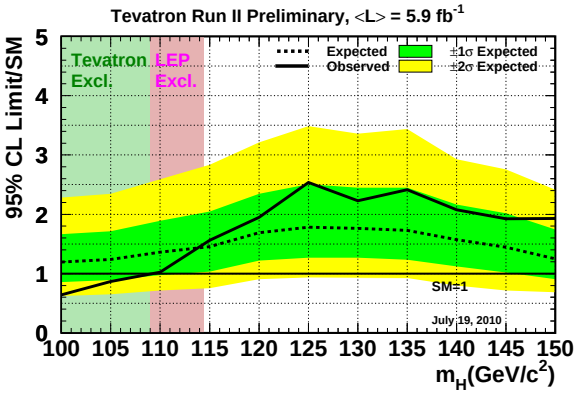

Figure 2: The observed and expected 95% C.L. upper limits on the Higgs production cross section, in units of the SM theoretical cross section, obtained by combining all CDF and D0 analyses with up to 5.7 fb^{-1} of data.

2 Experimental apparatus

A detailed description of the Tevatron collider and CDF and D0 detectors can be found elsewhere [5,6]. The accelerator provides $p\bar{p}$ collisions at $\sqrt{s} = 1.96$ TeV with stable and well performing operating conditions: as of May 2011 about 60 pb^{-1} are produced per week, with a typical instantaneous luminosity of 3×10^{32} cm^{-2}s^{-1}; since the beginning or Run II, over 10 fb^{-1} of data have been delivered at the two collision points, and more than 8 fb^{-1} were recorded and made available for the analyses by each experiment. Tevatron collisions are scheduled to stop in September 2011 and we expect that an additional 2 fb^{-1} of data will be delivered by that date.

3 Low Mass Higgs Boson at the Tevatron

At the Tevatron center of mass energy, the dominant Higgs production mode is represented by gluon-gluon fusion, gg→H, followed by the associated production with a W or a Z boson, $q\bar{q}$ →(W/Z)H, and the vector boson fusion, $qq \rightarrow qHq$. Depending on the mass, the inclusive predicted cross section in the 100÷200 GeV/c^2 interval ranges from about 2 to 0.7 pb: the achievable signal yield is therefore particularly small if compared to the main SM background processes, which are several orders of magnitude larger.

The Higgs search is particularly challenging for $M_H \lesssim 135$ GeV/c^2, where the decay mode into b quarks becomes dominant (∼73% at M_H=115 GeV/c^2), making difficult the investigation of the direct production: although being the most abundant, the gg→H→ $b\bar{b}$ process is indeed experimentally prohibitive because of the overwhelming non-resonant multijet background. It is then preferred to consider the associated production, whose cross section is smaller of one order of magnitude, but where the leptonic decays of the W and Z boson provide cleaner signatures, easy to trigger on and with a great reduction of the QCD background. The most sensitive channels are represented by WH→ $l\nu b\bar{b}$, ZH→ $\nu\bar{\nu}b\bar{b}$ and ZH→ $llb\bar{b}$, where the Higgs boson is detected through the reconstruction of the jets originating from the b quark hadronization.

Many other additional channels, although less powerful, are considered since they provide a sizeable contribution to the overall sensitivity: these include the all-hadronic associated production, where the W and Z bosons are searched in their hadronic decay, and the low branching ratio (B.R.) decay into a pair of tau leptons or a pair of photons.

No single channel provides by itself the sensitivity to discover the Higgs boson. The best

strategy is to perform dedicated analyses exploiting the specific topological features of the different final states and then combine the results into one single measurement. In order to maximize the sensitivity and optimize the analysis techniques, each channel can be further split into subcategories according to the lepton types or the jet multiplicity in the event selection.

4 Analysis strategies

4.1 Acceptance optimization

One of the main challenges in the Higgs searches is represented by the need to increase as much as possible the total signal acceptance: Tevatron experiments are pursuing this target by including new triggers in the online selection, by relaxing the kinematic cuts and by implementing additional lepton categories or more sophisticated identification algorithms in the event reconstruction. The larger explored phase space requires nevertheless an accurate understanding of the selected data sample, whose composition has to be well described by the background modelings.

An example of the potential gain provided by the increased event acceptance is given by the ongoing update of CDF's ZH$\rightarrow \mu\mu b\bar{b}$ search [7]: the preliminary results, obtained by employing a novel muon identification based on a neural network (NN) algorithm, as well as an extended kinematic selection, as described in figure 3, indicate a sensitivity improvement of the order of 30$\div$60% beyond the luminosity scaling, in the 100$\div$150 GeV/c^2 mass range.

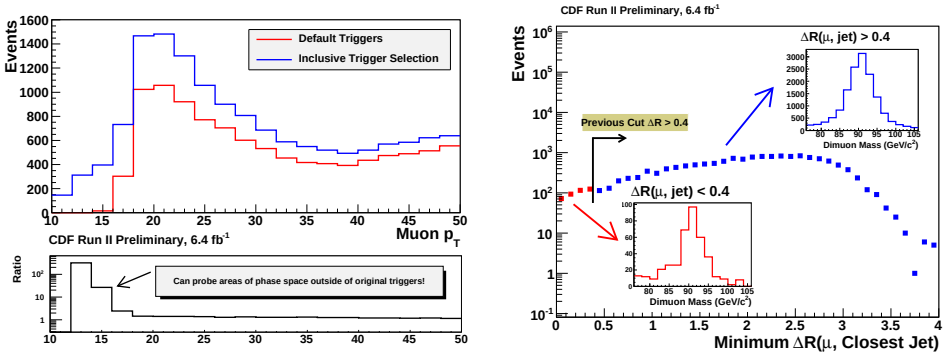

Figure 3: Acceptance increase in the CDF's ZH$\rightarrow \mu\bar{\mu}b\bar{b}$ search. Left: implementation of an inclusive trigger selection. Since no specific cuts on muon candidates are applied, a larger fraction of events is recored, compared to the standard high p$_T$ ($\geq$18 GeV/c) muon trigger. Right: removal of the spatial separation cut ($\Delta R=\sqrt{\Delta\eta^2+\Delta\varphi^2}$ >0.4) between the muon and the closest jet.

4.2 b-quark identification

When considering final states including b quarks, one fundamental ingredient is the capability of distinguishing jets originated from b quarks from those coming from gluons, light or c quarks.

Both CDF and D0 have developed specific "b-tagging" algorithms, which exploit the relatively long lifetime of b-hadrons and the high position resolution of the silicon detectors. Different approaches are followed: CDF's SecVtx [8] is based on the reconstruction of the b-hadron secondary vertex, obtained by fitting the tracks displaced from the interaction point; CDF's JetProb [9] uses the distribution of the track impact parameters, with respect to the primary vertex, to build a probability that a jet contains a b-hadron; More sophisticated algorithms adopted by both CDF and D0 are based on NNs [10,11] and Boosted Decision Trees (BDT) [15] and combine the information provided by different taggers, with the discriminating power of additional variables, including those related to the leptonic decay of b-hadrons inside the jet.

Table 1: Observed and expected upper limits at 95% C.L. on the Higgs boson production cross section, at the reference mass of 115 GeV/c^2, for the CDF and D0 experiments as of May 2011.

Channel	CDF			D0		
	$\mathcal{L}$ [fb^{-1}]	Exp.limit [σ/σ(SM)]	Obs.limit [σ/σ(SM)]	$\mathcal{L}$ [fb^{-1}]	Exp.limit [σ/σ(SM)]	Obs.limit [σ/σ(SM)]
WH$\rightarrow l\nu b\bar{b}$ [14]	5.7	3.5	3.6	5.3	4.8	4.1
ZH$\rightarrow ll b\bar{b}$ [7]	5.7	5.5	6.0	6.2	5.7	8.0
ZH$\rightarrow \nu\nu b\bar{b}$ [15]	5.7	4.0	2.3	6.2*	4.0	3.4
VH/VBF$\rightarrow b\bar{b}$+jets [16]	4.0	17.8	9.1	-	-	-
H$\rightarrow \tau\tau$+jets [17]	6.0*	15.2	14.7	4.3*	12.8	32.8
H$\rightarrow \gamma\gamma$ [18]	4.2	20.8	24.6	8.2*	11.0	19.9

These multivariate methods benefit of the correlations among the input variables, which help in increasing the signal to background separation; in addition, they have the advantage to provide continuos outputs instead of a simple binary one. This allows to easily modify the definition of a b-tagged jet, by changing the cut on the output distributions, and then alternatively maximize the sample purity or increase the signal acceptance of the analysis selection.

Typical b-tagging efficiencies are 40$\div$70%, with a corresponding light flavour jet mistag rate of 0.5$\div$3%.

4.3 Multivariate techniques

Given the small signal to background ratio, the analyses employ multivariate techniques in order to exploit all the event information, by collecting multiple distributions into a single and more powerful discriminating variable: the preferred methods are based on NNs, BDTs and matrix elements (ME). The search sensitivity usually increases by about 20% with respect to simply using one single kinematic distribution as discriminator.

The reliability of these techniques depends on the goodness of the background modeling for the input variables, which need to be carefully verified in dedicated control samples.

5 Results

In table 1 we summarize the expected and observed 95% C.L. upper limits for the different CDF and D0 search channels. More information can be found in the references and in the web pages of the two experiments [12,13]. The items marked with an asterisk refer to the analyses which were updated since Summer 2010 and for which a more detailed description is given here.

5.1 ZH$\rightarrow \nu\nu b\bar{b}$

The signature of this search is based on two b-jets plus an unbalance of transverse energy ($\not\!\!E_T$) due to the undetected neutrinos, coming from the Z boson invisible decay. The analysis is also sensitive to the WH$\rightarrow l\nu b\bar{b}$ channel, when the charged lepton from the W escapes the detection. CDF and D0 apply similar event selections and search strategies: they both require large $\not\!\!E_T$ and 2 or 3 jets, at least one of them b-tagged. NNs (CDF) and BDTs (D0) are implemented to reduce the main background process, represented by QCD multijet production, with $\not\!\!E_T$ coming from jet energy mismeasurements. A second discriminant is then used to separate the signal from the remaining sources of background.

The D0 latest search update has significantly increased the sensitivity thanks to the acceptance gain provided by loosening the b quark identification requirements, followed by a more

clever use of the b-tagger output information. The latter has been employed as additional input variable for the final multivariate algorithm, thus improving the separation between signal and background. This new approach results in a 14% improvement in the expected limit compared to the previous version of the analysis. The final distribution for events containing two b-tagged jets, and the corresponding observed and expected upper limits on the Higgs boson production cross section, as a function of the mass, are shown in figure 4.

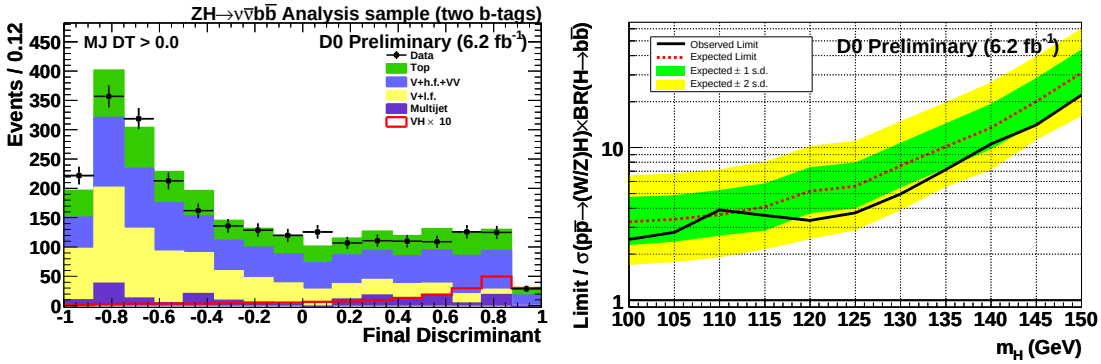

Figure 4: D0's ZH→ $\nu\bar{\nu}b\bar{b}$ search. Left: final discriminant distribution for the double b-tag channel, in the Higgs mass hypothesis of 115 GeV/c^2. Right: observed and expected upper limits on the Higgs boson production cross sections, as a function of the Higgs mass.

5.2 H→ ττ+jets

The B.R. of H→ $\tau\tau$ is one order of magnitude smaller than H→ $b\bar{b}$, but the contribution of this search is significant, since several production modes can be simultaneously investigated. In particular, the gluon fusion becomes accessible thanks to the selection of the leptonic decay of one of the two taus, which considerably reduces the multijet background. The requirement of jets in the final state further increases the signal to background ratio and optimizes the search for the vector boson fusion process and the associated production, where the W and Z are allowed to decay hadronically. However, the significance of this channel is affected by the similarity of the H→ $\tau\tau$ signal with the irreducible Z→ $\tau\tau$ background, both characterized by a resonant tau pair in the final state. One additional challenge is represented by the hard discrimination of real hadronically decaying taus from quark/gluon jets: CDF and D0 employ identification algorithms based on BDTs and NNs, respectively.

Both the experiments have recently presented an update of their searches, where the most relevant improvements are related to the refined multivariate techniques adopted to build the final discriminant. The best separation between signal and background is achieved by following a two stage procedure: first several independent BDTs are trained to distinguish the Higgs from the principal sources of background; the different outputs are then combined into one single distribution, chosen to maximize the sensitivity of the search. Figure 5 shows the CDF final discriminant for events containing 2 or more jets in the final state.

5.3 H→ γγ+X

The diphoton final state suffers from a very low B.R., but it is interesting because the photon identification efficiency and the energy resolution are much better then that of b-jets, and the narrow $M_{\gamma\gamma}$ mass peak can be exploited to reduce backgrounds. The selection is based on the requirement of two high E_T central photons. The dominant background is the direct SM diphoton production, followed by events with misidentified electrons and jets. CDF sets a limit

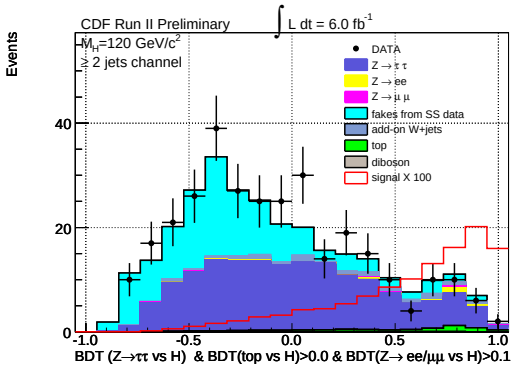

Figure 5: CDF's H→ $\tau\tau$+jets search: final discriminant distribution in the Higgs mass hypothesis of 120 GeV/c^2.

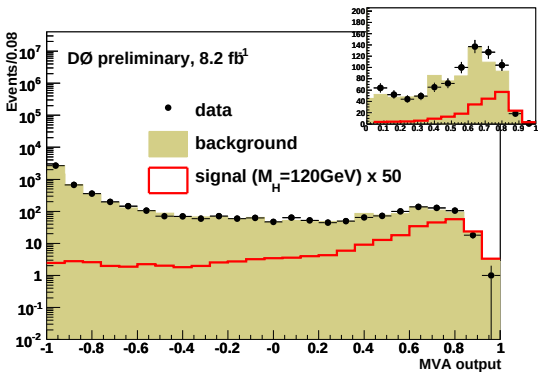

Figure 6: D0's H→ $\gamma\gamma$ search: final discriminant distribution in the Higgs mass hypothesis of 120 GeV/c^2.

by looking for a peak resonance in the $M_{\gamma\gamma}$ distribution; D0 has recently implemented a BDT which collects five kinematic variables, bringing an improvement of the sensitivity of about 20% with respect to the luminosity increase from the previous stage of the analysis.

6 Conclusions

We presented the latest results on the Tevatron searches for a low mass SM Higgs boson. The update of the CDF and D0's combination, currently in progress, will benefit from the ongoing efforts described in this paper to increase the performances beyond the luminosity scale: the projections shown in figure 1 suggest that, with the full data expected by the end of Run II, accompained by the suitable improvements in the analysis techniques, the Tevatron could reach the sensitivity to exclude the presence of the SM Higgs in the entire explored mass range below 150 GeV/c^2, with a sizeable chance to set a 3σ evidence of its existence.

References

1. ALEPH Collaboration et al., arxiv:1012.2367
2. R.Barate, *Phys. Lett.* B **565**, 61 (2003)
3. CDF and D0 Collaborations, arXiv:1103.3233
4. CDF and D0 Collaborations, arXiv:1007.4587
5. CDF Collaboration, D.Acosta et al., *Phys. Rev.* D **71**, 032001 (2005)
6. D0 Collaboration, V.M.Abazov et al., *Nucl. Instrum. Methods* A **565**, 463 (2006)
7. CDF Collaboration, Conf.Note 10235, D0 Collaboration, Conf.Note 6089
8. CDF Collaboration, D.Acosta et al., *Phys. Rev.* D **71**, 052003 (2005)
9. CDF Collaboration, A.Abulencia et al., *Phys. Rev.* D **74**, 072006 (2006)
10. CDF Collaboration, Conf.Note 10239
11. D0 Collaboration, V.M.Abazov et al., *Nucl. Instrum. Methods* A **620**, 400 (2010)
12. CDF Collaboration, `http://http://www-cdf.fnal.gov/physics/new/hdg/Results.html`
13. D0 Collaboration, `http://www-d0.fnal.gov/Run2Physics/WWW/results/higgs.htm`
14. CDF Collaboration, Conf.Notes 10217/10239, D0 Collaboration, Conf.Note 6092
15. CDF Collaboration, Conf.Note 10212, D0 Collaboration, Conf.Note 6170
16. CDF Collaboration, Conf.Note 10010
17. CDF Collaboration, Conf.Note 10439, D0 Collaboration, Conf.Note 6171
18. CDF Collaboration, Conf.Note 10065, D0 Collaboration, Conf.Note 6177

Searches for a High-Mass Standard Model Higgs Boson at the Tevatron

Konstantinos A. Petridis
on behalf of the CDF and D0 collaborations
The School of Physics and Astronomy, The University of Manchester, M13 9PL, UK

We present the results of searches for the Standard Model Higgs boson decaying predominantly to W^+W^- pairs, at a center-of-mass energy of $\sqrt{s}$ =1.96 TeV, using up to 8.1 fb^{-1} of data collected with the CDF and D0 detectors at the Fermilab Tevatron collider. The analysis techniques and the various channels considered are discussed. These searches result in the first single experiment exclusion across the Higgs mass ranges of [158,168] GeV and [163,168] GeV for CDF and D0 respectively.

1 Introduction

The search for the mechanism of electroweak symmetry breaking and a Standard Model (SM) Higgs boson has been a major goal of particle physics for many years. Within the Higgs sector of the SM, the mass of the Higgs boson (m_H) is a free parameter. Constraints on m_H come from direct searches at the LEP experiments [1] which conclude that m_H>114.4 GeV at 95% Confidence Level (CL), and indirect constraints using precision electroweak measurements which require m_H<185 GeV at 95% CL [2].

Higgs searches at the Tevatron collider are a subject of intense study. By combining CDF and D0 results, the SM Higgs mass range between 158 and 175 GeV was excluded at 95% CL using up to 6.7 fb^{-1} of data [3].

These proceedings present the status of the searches by CDF and D0 for a SM Higgs boson with $m_H \in$[130,200] GeV and using up to 8.1 fb^{-1} of data collected until the winter of 2010. All limits will be given at 95% CL

2 Higgs boson production and decays

At the Tevatron, the dominant production mode is via the gluon fusion process, $gg \rightarrow H$, with a cross section ranging between 840-190 fb for a Higgs mass between 130-200 GeV. The associated

production, $q\bar{q} \to VH$ ($V = W, Z$), and vector boson fusion, $q\bar{q} \to Hq\bar{q}$, processes with cross sections ranging between 180-32 fb and 57-22 fb respectively for the aforementioned Higgs mass range, are also considered in order to maximise the sensitivity of the searches.

For a Higgs mass m_H>135 GeV, the main decay mode is to a pair of W bosons while for m_H<135 GeV Higgs decays mainly to a pair of b-quarks. This distinction is what defines the high mass and low mass Higgs searches at the Tevatron.

3 Search channels

The high mass searches at CDF and D0 require at least one electron or a muon in the final state in order to suppress the QCD background. Given this requirement all possible decay modes are considered to maximise the signal acceptance. The di-lepton+missing transvere energy (E_T^{miss}) channel requires two electrons or muons (plus neutrinos) of opposite charge in the final state. This represents a small WW decay branching ratio, $\approx 6\%$ (including $\tau \to e, \mu$ decays), but a clean signature offering the highest sensitivity of all the high mass channels. Decays of one of the W bosons to a τ lepton and the other to an electron or muon, with a subsequent hadronic decay of the τ (τ_h) are also considered offering an additional branching ratio of $\approx 4\%$. The lepton+jets channel requires one W boson to decay hadronically and the other leptonically. This represents a signficant WW decay branching ratio, $\approx 30\%$, however suffers from a large W+jets background. Dedicated $q\bar{q} \to VH$ searches are also performed by looking for the SM suppressed signature of at least two leptons (electrons, muons) with one same charge pair originating from leptonic decays of the three vector bosons in the final state.

4 Search strategy

The high mass analyses are each split into categories based on the reconstructed lepton flavour, quality or jet multiplicity. This is done in order to take advantage of the differences in the detector response between the various lepton types, and between the kinematics of the signal production mechanisms and the background processes.

As the signal final states contain neutrinos, selections based on large E_T^{miss} are used, also accounting for energy mis-measurements. D0 employs Multivariate (MVA) techniques at this stage to reduce low E_T^{miss} backgrounds while maximising signal acceptance, by taking advantage of the different correlations for signal and backgrounds between the input variables. Selecting events with a high MVA response score, improves the sensitivity by up to 30% compared to conventional square selections. Figure 1 shows the E_T^{miss} distribution for di-electron+E_T^{miss} events and the response of the MVA trained against the large Z+jets background.

Even after all selections, the signal/background (S/B) ratio is still in the range of 0.1-1% for m_H=165 GeV. This requires the use of MVA discriminants, either boosted decision trees or artificial neural networks, to provide further discriminating power by using their response to derive limits on the Higgs boson yield for the cases where no signal-like excess is observed.

4.1 Di-lepton+E_T^{miss} channel

The signature of this channel is two high p_T oppositely charged isolated leptons and E_T^{miss}. A small angular separation, is also expected due to the spin-0 nature of the Higgs boson, which in turn gives rise to the spin-correlation between the final-state leptons. In contrast, leptons from the irreducible $Z \to WW$ background are predominantly back-to-back. Figure 2 shows the $\Delta R_{\ell\ell} = \sqrt{\Delta\phi_{\ell\ell}^2 + \Delta\eta_{\ell\ell}^2}$ distribution for a di-lepton+E_T^{miss} data sample with zero reconstructed jets. Full use of this topological distinction is made by using variables such as $\Delta R_{\ell\ell}$ and $\Delta\phi_{\ell\ell}$ as inputs to the MVA discriminants. CDF also makes use of likelihood ratios constructed from

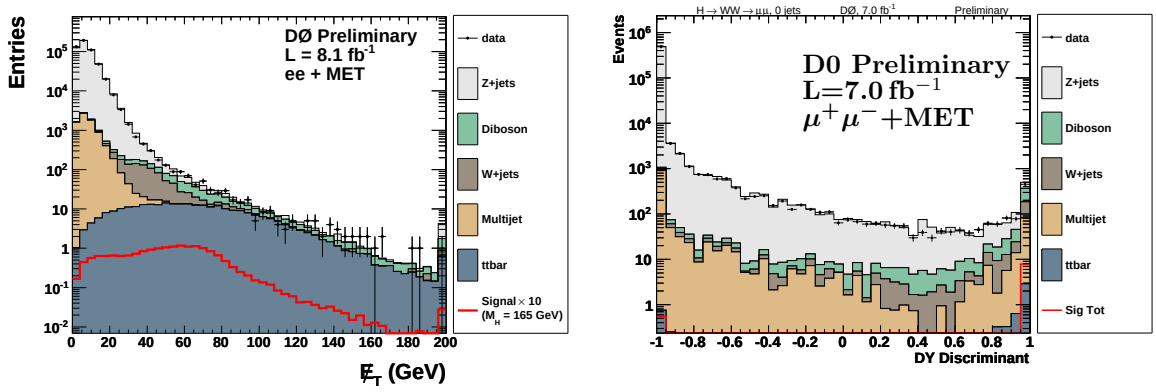

Figure 1: Left: Distribution of E_T^{miss} di-electron+E_T^{miss} events. Right: MVA discriminant trained to discriminate between signal and Z+jets in di-muon+E_T^{miss} events.

matrix-element probabilities as input variables to the MVA discriminants. Such a likelihood ratio is shown on the right plot of Figure 2.

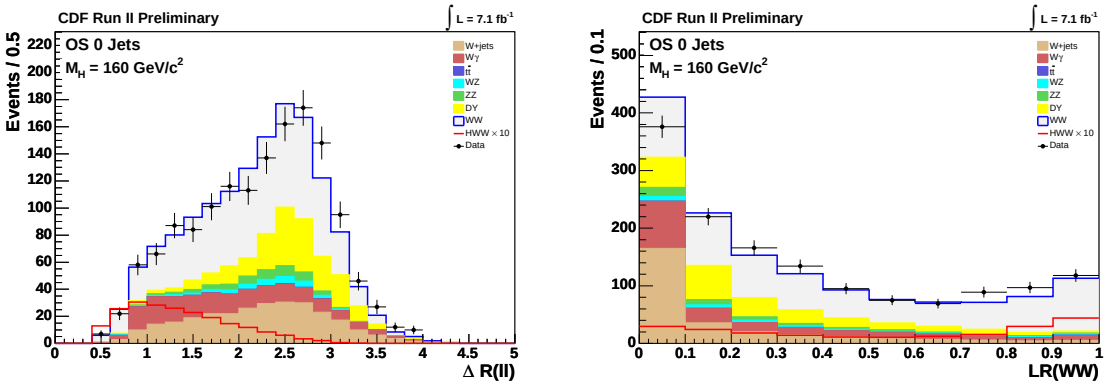

Figure 2: Left: $\Delta R_{\ell\ell}$ distribution in di-lepton+E_T^{miss} events. Right: Distribution of the matrix element likelihood ratio in di-lepton+E_T^{miss} events.

This channel is further split according to jet multiplicity into 0, 1 or more than 1 reconstructed jets in the final state. This enables the training of the MVA discriminant to focus on the different signal and background compositions in each of the jet multiplicity categories, such as WW for the 0 jet, Z + jets for the 1 jet and $t\bar{t}$ for the 2 jet where b-tagging information is used to suppress this background. The statistical analysis of the MVA final discriminant does not exhibit any excess with respect to the background expectations and limits are set. It is worth noting that the CDF limit was obtained including the same sign di-lepton and tri-lepton searches described in section 4.4 Using 7.1 and 8.1 fb^{-1} of CDF and D0 data respectively, the observed (expected) limits on the Higgs boson yield for m_H=165 GeV are for CDF σ_{95}/σ_{SM}=0.92(0.93) and D0 σ_{95}/σ_{SM}=0.91(0.97), excluding this mass hypothesis. It is worth noting that the CDF limit was obtained including the same sign di-lepton and tri-lepton searches and the di-lepton+E_T^{miss} with a τ_h as described in sections 4.2 and 4.4.

4.2 Di-lepton+E_T^{miss} channel with a τ_h

Additional signal acceptance can be obtained by considering hadronically decaying τ leptons from W decays. Muon(electron)+τ_h channels are a new addition to the D0 high mass program. In contrast to CDF, D0 splits these channels into $\leq$1 or >1 jets due to the different signal

production mechanisms and background compositions. The $\leq$1 jet category does not include an electron+τ_h final state due to the very large backgrounds and the >1 jet is also part of the low mass Higgs searches.

Both CDF and D0 see no excesses with respect to the background expectation in the statistical analysis of the respective MVA discriminants and therefore set limits. Using 7.1 fb^{-1} of data CDF obtains an observed (expected) limit for m_H=165 GeV of σ_{95}/σ_{SM}=28.4(13.1). For the muon+τ_h+E_T^{miss}+$\leq$1 jet and using 7.3 fb^{-1} D0 obtains a corresponding observed (expected) limit of σ_{95}/σ_{SM}=6.6(6.8). The lepton+τ+E_T^{miss}+> 1 jet uses 4.3 fb^{-1} of D0 data and obtains an observed (expected) limit for m_H=165 GeV of σ_{95}/σ_{SM}=12.4(12.3).

4.3 Lepton+jets channel

The signature of this channel is one isolated high p_T electron or muon, high E_T^{miss} and two high p_T jets[4]. For $m_H \geq 160$ GeV, the Higgs decays to two on-shell W bosons, thus offering the ability to reconstruct the kinematics of the full event including the longitudinal momentum of the neutrino, up to a two-fold ambiguity. Although this signature suffers from large W+jets backgrounds, the large branching ratio of hadronic W boson decays provide 52 expected signal events surviving all selections in 5.4 fb^{-1} of D0 data. The statistical analysis of the MVA discriminant does not exhibit any excess with respect to the background expectation and limits are set. Using 5.4 fb^{-1} of data, D0 obtains an observed (expected) limit for m_H=165 GeV of σ_{95}/σ_{SM}=5.2(5.1).

4.4 Same charge di-leptons and tri-leptons

In these channels, the defining characteristic is the presence of at least two isolated high p_T electrons or muons which can form a pair of the same charge, and high E_T^{miss}. Charge misidentification can lead to a significant migration of opposite sign charge backgrounds into the same sign region. Therefore high quality tracking criteria are also required to suppress this instrumental background. CDF also requires the presence of at least 1 jet in the same charge di-lepton final state, since the decay of the third boson will most likely result in the production of an additional jet.

In contrast to CDF, D0 does not include a dedicated tri-lepton search. Tri-lepton events can occur naturally in WH $\rightarrow$ WWW events with all Ws decaying leptonically, or in ZH $\rightarrow$ ZWW where the Z and one of the Ws decay leptonically and the other hadronically. This distinction allows the separation of tri-lepton events into cases where the same flavour opposite sign leptons, form an invariant mass compatible to the Z mass or not. If a mass compatible to the Z mass is found, the probability that one of the Ws decayed hadronically, allows this channel to be further split by requiring one or more than one reconstructed jets in the event. If more than one jets are found then the event is fully reconstructed and the mass of the Higgs can be determined. CDF ensures orthogonality between the same charge di-lepton and tri-lepton search by vetoing the presence of a third lepton in the di-lepton case. As D0 has no dedicated tri-lepton search, no such veto is required. Figure 3 shows the invariant mass distributions in same charge di-lepton and tri-lepton events after all selections.

No excess was observed in the statistical analysis of same charge di-lepton and tri-lepton MVA discriminants, with respect to the background expectation, and thus limits are set. The same charge di-lepton and tri-lepton limits of CDF are combined with the the di-lepton+E_T^{miss} searches of Section 4.1. The most sensitive channel is the same charge di-lepton + E_T^{miss}+> 1 jets which gives an observed (expected) limit for m_H=165 GeV of σ_{95}/σ_{SM}=7.7(4.5) for 7.1 fb^{-1} of CDF data. The observed (expected) limit of the same charge di-lepton channel of D0, using 5.4 fb^{-1} of data for m_H=165 GeV is σ_{95}/σ_{SM}=7.2(7.0).

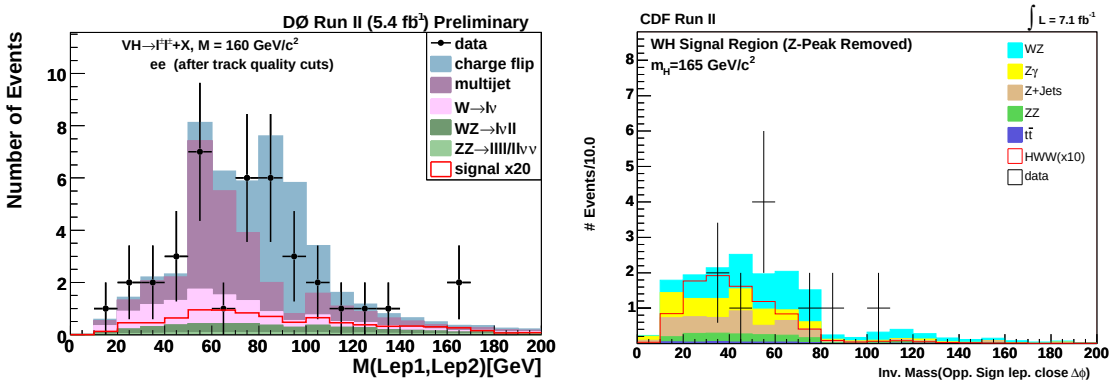

Figure 3: Left: invariant mass distributions between leptons in same charge di-lepton events. Right: Invariant mass of the opposite charge pair closest in ϕ in tri-lepton events with no compatible Z mass.

Table 1: Scale (μ_r,μ_f) and PDF uncertainties on $\sigma(gg \to H)$ for the three jet categories considered .

Uncertainty	0 jet	1 jet	>1 jet
Scale	7.0%	23.5%	33.3%
PDF	7.6%	13.8%	29.7%

5 Systematic uncertainties

The systematic uncertainties considered account for detector resolutions, reconstruction efficiencies, background normalizations and shapes both theoretical and data-driven. Where appropriate, these uncertainties are correlated between CDF and D0. Careful consideration has also been taken to account for the theoretical uncertainties related to the various Higgs production mechanisms and particularly for $gg \to H$, which is the main signal in the most sensitive di-lepton+E_T^{miss} channel.

The Higgs boson signal is normalized to the most recent highest-order calculations available for all production mechanisms considered. The gluon fusion cross section, $\sigma(gg \to H)$, is calculated to NNLO in QCD with soft gluon resummation to NNLL[56] and uses the MSTW 2008 NNLO PDF set as it is the only NNLO set which results from a global fit to all relevant data[7]. Since the di-lepton+E_T^{miss} analyses are split in categories depending on the number of reconstructed jets, the scale and PDF uncertainties on $\sigma(gg \to H)$ are estimated per jet category and correlated across these categories. These uncertainties are summarised in Table 1[8910].

6 Results

CDF and D0 set limits by combining all of the SM high mass channels with up to 8.1 fb^{-1} of integrated luminosity. Both experiments exclude a range of Higgs masses independently as shown in Figure 4. CDF excludes the range 158-168 GeV (160-167 GeV expected) and D0 excludes the range 163-168 GeV (160-168 GeV expected). This represents a significant milestone in Higgs searches and a testament to the comprehensive and aggressive search program of the Tevatron experiments. In order to further improve the sensitivity of these searches, CDF and D0 combined their individual high mass channels in the Tevatron high mass combination, which is discussed elsewhere in these proceedings[11].

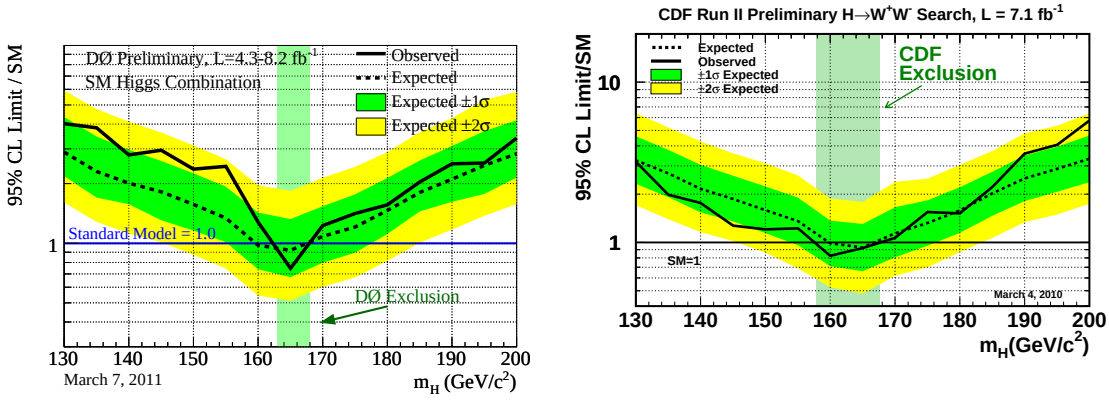

Figure 4: Combined limits using all of the SM high mass channels for D0 (left) and CDF (right). The CDF exclusion range is 158-168 GeV (160-167 GeV expected) at 95% CL and the D0 exclusion range is 163-168 GeV (160-168 GeV expected) at 95% CL

References

1. R. Barate et al. [LEP Working Group for Higgs boson searches], Search for the standard model Higgs boson at LEP, *Phys. Lett.* B **565**, 61 (2003).
2. J. Alcaraz, *Precision Electroweak Measurements and Constraints on the Standard Model*, arXiv:0911.2604 [hep-ex]
3. The TEVNPH Working Group, *Combined CDF and D0 Upper Limits on Standard Model Higgs-Boson Production with up to 6.7 fb^{-1} of Data*, arXiv:1007.4587v1 [hep-ex]
4. D0 Collaboration, V. Abazov et al., *Phys. Rev.* D **83**, 092002 (2011).
5. C. Anastasiou, R. Boughezal and F. Petriello, **JHEP** 0904, 003 (2009).
6. D. de Florian and M. Grazzini, *Phys. Lett.* B **674**, 291 (2009).
7. A. D. Martin, W. J. Stirling, R. S. Thorne and G. Watt, Eur. Phys. J. C **63**, 189 (2009).
8. S. Alekhin et al., (PDF4LHC Working Group), [arXiv:1101.0536v1 [hep-ph]];
   M. Botje et al., (PDF4LHC Working Group), [arXiv:1101.0538v1 [hep-ph]].
9. C. Anastasiou, G. Dissertori, M. Grazzini, F. Stöckli and B. R. Webber, JHEP **0908**, 099 (2009).
10. J. M. Campbell, R. K. Ellis, C. Williams, *Phys. Rev.* D **81**, 074023 (2010).
11. B. Jayatilaka, *Combination of Standard Model Higgs Boson searches at the Tevatron*, these proceedings.

Higgs Boson Searches with ATLAS based on 2010 Data

M. Schumacher on behalf of the ATLAS collaboration
Fakultät für Mathematik und Physik, Albert-Ludwigs Universität Freiburg, Hermann-Herder-Strasse 3, D-79104 Freiburg im Breisgau, Germany

The results of Higgs Boson searches with the ATLAS detector based on 2010 proton proton collision data corresponding to integrated luminosities of up to 39 pb^{-1} are presented. Searches for $H \to \gamma\gamma$, $H \to WW \to \ell^+\nu\ell^-\bar{\nu}$ and $H \to ZZ \to \ell^+\ell^-\nu\bar{\nu}/\ell^+\ell^-q\bar{q}$ in the context of the Standard Model (SM), for $H \to \tau\tau$ in the context of the Minimal Supersymmetric Extension of the Standard Model (MSSM) and for a generic scalar at low mass in the vicinity of the Υ resonance decaying to a pair of muons are discussed. All observations are in agreement with the expectations from the background-only hypothesis. Hence exclusion limits at 95% confidence level are derived.

1 Introduction

Unraveling the mechanism responsible for electroweak symmetry breaking and the generation of elementary particle masses is one of the great scientific quests of high energy physics today. The Standard Model (SM) and its supersymmetric extensions address this question by the Higgs-Englert-Brout-Gurnalik-Hagen-Kibble mechanism. The first manifestation of this mechanism is represented by the existence of at least one Higgs boson. This motivates the large experimental effort for the Higgs boson search in the past, presence and future. During the year 2010 the Large Hadron Collider (LHC) delivered proton proton collisions at a center of mass energy of 7 TeV corresponding to an integrated luminosity of 48 pb^{-1} to the ATLAS experiment [1]. These data have been used to search for Higgs bosons in the SM and its supersymmetric extensions in a variety of final states. For the signal rates, their central values and the estimation of the associated systematic uncertainties, which arise from variations in the renormalization and factorization scales, the choice of the value of the strong coupling constant and the choice of the parton distribution functions of the proton, the recommendations from the LHC Higgs cross-section working group have been used [2]. As no hints for the production of Higgs bosons are observed in data, exclusion limits at the 95% confidence level are derived. In order to do so

the profile likelihood method [3] is used as the test statistic, which allows systematic errors to be incorporated in the signal and background predictions as nuisance parameters. As the main result power constrained exclusion limits [4] to the signal+background hypothesis are derived (PCL_{S+B}). The power constraint requires that the confidence level for the background-only hypothesis is at least 16% ($CL_B > 0.16$). Hence, if the observed CL_{S+B} is smaller than the expected median CL_{S+B} minus one standard deviation, the observed limit quoted is replaced by $CL_{S+B}^{expected} - 1\sigma$. For comparisons with other experiments the exclusion limits obtained from $CL_S = CL_{S+B}/CL_B$ [5] are also given in [6,7,8,9,10], in which also details of the individual analyses discussed below can be found.

2 Searches for the Higgs Boson of the SM

2.1 $H \to \gamma\gamma$ with 38 pb^{-1}

In the mass range from 100 GeV to 140 GeV the decay of the SM Higgs boson into two photons provides a very good sensitivity to observe Higgs boson production. The signal topology is characterized by two isolated photons with large transverse momentum ($p_T^{1(2)} > 40(25)$ GeV). The reducible background arises from photon plus jet(s) and multijet production. These backgrounds are suppressed by the excellent capabilities of the ATLAS detector to discriminate photons from jets. The irreducible background stems from di-photon production which can be separated from the signal by excellent reconstruction of the invariant mass of the di-photon system. The contributions from the different background classes have been estimated from data using an iterative double sideband method by comparing event yields of loosely and tightly identified photon candidates which are isolated or non-isolated. The events yields extracted via this method are in good agreement with the prediction from simulations (see Fig. 1 (left)). The invariant di-photon mass spectrum after all selection cuts applied is shown in Fig. 1 (middle). No significant resonance structure is observed. The background is parametrized via an exponential shape with two nuisance parameters (normalization and slope) and no use is made of the MC prediction. The signal shape is described by the sum of a Crystal Ball function [11] plus a Gaussian with a full width at half maximum of 4.4 GeV. The uncertainties on the signal yield are dominated by the uncertainty on the inclusive signal cross-section (20%) and the one on the photon identification and isolation (10% each). The width of the hypothetical signal is known to a level of 13% from the energy scale and resolution uncertainties for photons. The expected limits are at the level of 20 times the SM predicted rate (Fig. 1 (right)), and the observed exclusion limits lie in the range between 8 and 38 times the SM cross-section in the mass range between 110 and 140 GeV.

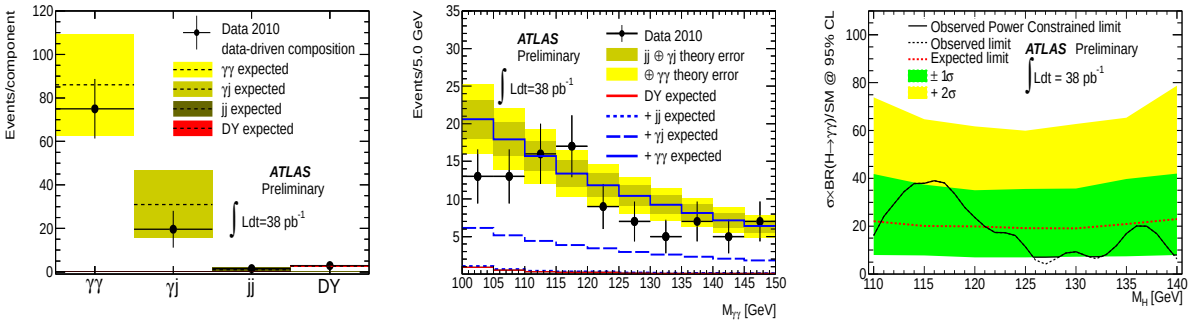

Figure 1: $H \to \gamma\gamma$: comparison of background prediction from simulation with the results from the data-driven technique (left), observed invariant di-photon mass spectrum with the one predicted from simulation (middle), and excluded signal cross-section with respect to the SM prediction (right).

2.2 $H \to WW \to \ell^+\nu\ell^-\bar{\nu}$ with 35 pb^{-1}

The decay of Higgs bosons into a pair of W bosons yields the highest sensitivity for an early discovery of a Higgs boson at the LHC especially in the mass range around 170 GeV. The decay of each W boson to an electron or muon and the corresponding neutrino, which is produced in gluon fusion or weak vector boson fusion, is considered. The preselection exploits the basic signature of two leptons, which due to spin correlations are close in phase space, and significant transverse missing energy (MET) arising from the two undetected neutrinos. In order to maximize the sensitivity the analysis is split into a zero, one and two jet selection, where different additional topological cuts are applied in each branch. The uncertainty on the fraction of signal events in each jet topology is determined by varying renormalization, factorization scales, parton density functions, and strong coupling constant in a NNLO+NNLL calculation for Higgs production in gluon fusion. Finally a cut on the transverse mass M_{T} derived from from the lepton momenta and the MET is applied, which depends on the Higgs boson mass hypothesis ($0.75{\cdot}M_H < M_{\mathrm{T}} < M_H$). The distribution of the transverse mass after all cuts for the zero and one jet analyses is shown in Fig. 2 (left and middle). The individual background contributions are derived from signal-free control regions in data, which are defined by inverting and omitting selection criteria or applying additional requirements to enhance a specific contribution. The extrapolation factors from control regions to signal regions as well from one control region to another control region are derived from MC simulated event samples. The extrapolation factors are subject to a variety of systematic uncertanties: experimental ones from lepton and MET energy scale and resolution uncertainties and theoretical ones from variation of QCD scales etc. (details can be found in [7]). As no deviatons from the background only hypothesis are observed, exclusion limits on the Higgs boson production cross-section are derived (see Fig. 2 (right)). Higgs boson production for a mass of 160 GeV with a rate larger than 1.2 times the SM rate can already be excluded.

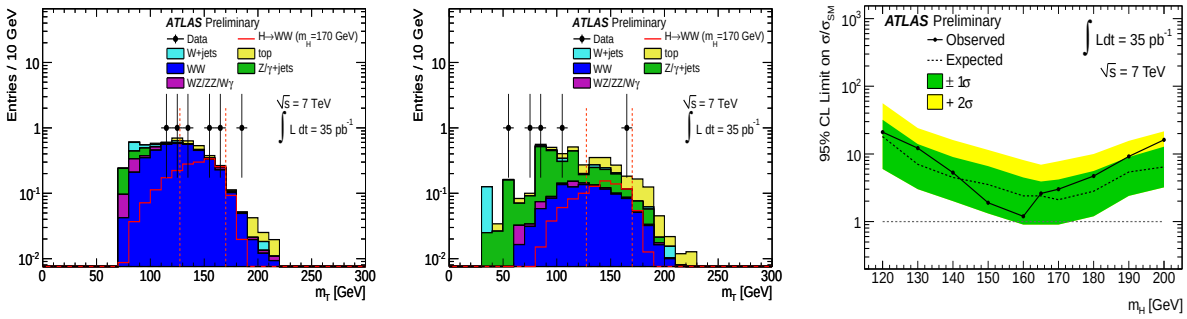

Figure 2: $H \to W^+W^-$: observed transverse mass spectrum compared to the background prediction for zero and one jet analyses (left and middle), and excluded signal cross-section with respect to the SM prediction (right).

2.3 $H \to ZZ \to \ell^+\ell^-\nu\bar{\nu}/\ell^+\ell^-q\bar{q}$ with 35 pb^{-1}

Higgs boson decays into $ZZ \to \ell^-\ell^+q\bar{q}$ and $ZZ \to \ell^+\ell^-\nu\bar{\nu}$ in the mass range between 200 and 600 GeV have been searched for. The signal is characterised by one pair of same flavour, oppositely charged leptons with invariant mass consistent with the Z boson and either a pair of jets whose invariant mass is also consistent with the Z boson mass or large MET due to the two neutrinos in the final state. Additional kinematical cuts are applied to suppress the backgrounds. The shape and normalisation of the expected backgrounds have been confirmed by comparing MC simulated event samples with the observed event yield in data e.g. in sideband regions of $M_{\ell^+\ell^-}$ and $M_{q\bar{q}}$ and other control regions. No deviation from the SM expectation without a Higgs boson are observed in the final mass distributions (shown in Fig. 3 (left) and (middle)) and hence exclusion limits with repect to the SM production rate are set. Those are

in the range of 3.5 to 39 times the SM prediction and are currently the most stringent exclusion limits for Higgs boson mass hypotheses beyond 300 GeV.

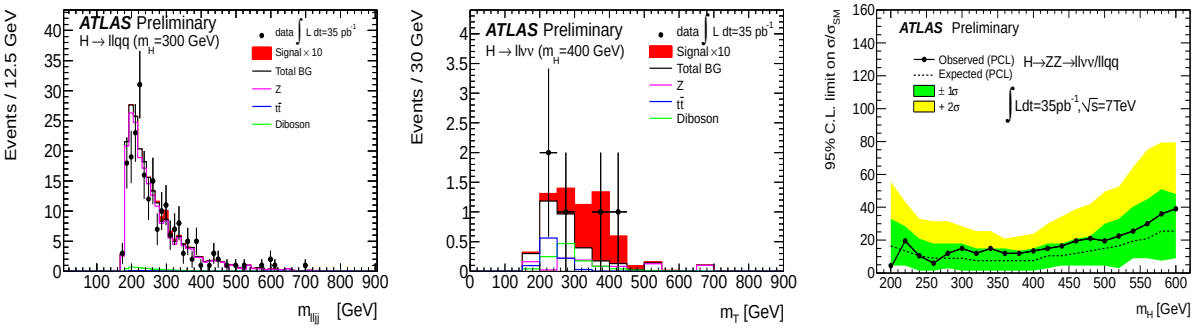

Figure 3: $H \to ZZ$: observed mass spectrum compared to the background prediction for the $\ell\ell qq$ final state (left), observed transverse mass spectrum compared to the background prediction for the $\ell\ell\nu\nu qq$ final state (middle), and excluded signal cross-section with respect to the SM prediction (right).

3 Search for $H \to \tau\tau$ in the MSSM with 36 pb^{-1}

The most promising channel for the observation of Higgs bosons in the context of the MSSM is the decay into a pair of tau leptons. Production in gluon fusion and in association with b-quarks have been considered. One tau lepton is assumed to decay hadronically, the other one leptonically. The inclusive selection exploits the signal characteristics by requiring one electron and muon, an oppositely charged hadronically decaying tau candidate and significant MET and applies an upper cut on the transverse mass of the lepton and MET system in order to suppress background from W boson production. The final discriminant is the invariant mass of the visible tau decay products. The prediction of the mass shape for the irreducible $Z \to \tau\tau$ background in MC simulated events has been confirmed in data, by selecting $Z \to \mu\mu$ collision events and replacing the muons by tau lepton decays from simulation with the same kinematic properties (see Fig. 4 (left)). The backgrounds with fake tau candidates dominated by $W + jet$ production has been estimated mostly from data by using the observed mass shape of signal free events with same charge sign of electron or muon and tau candidate and determining the ratio of same sign to opposite sign events for $W + jet$ and multijet production in control regions in data. The normalization of $Z \to \tau\tau$ background and the normalization and shape of other small backgrounds are obtained from MC simulated event samples. The dominant systematic uncertainties on shape and normalization of the $\tau\tau$ event yield from Z and H boson production arise from the uncertainty in the tau lepton energy scale and the jet energy scale its influence on the MET scale and to a lesser extent in the tau lepton identification efficiency. The final visible mass distribution (see Fig. 4 (middle)) with data-driven background predictions compared to the data shows no hint for Higgs boson production. Hence parameter regions in the M_A-vs.-tan β plane of the MHMAX benchmark scenario ($\mu > 0$) of the MSSM [12] can be excluded (see Fig. 4 (right)). At $M_A = 130$ GeV tan β values above 22 can be excluded. These findings extend those published previously by the LEP and Tevatron experiments [13,14].

4 Searches for $\phi \to \mu^+\mu^-$ at low mass with 39 pb^{-1}

In extensions of the MSSM either via additional singlets as in the NMSSM (see e.g. [15]) or via allowing for complex parameters in the MSSM, yielding additional sources of CP-violation, the existence of a low mass Higgs boson in the vicinity and below the masses of the Υ resonances is not completely excluded. A search for a generic scalar ϕ in the mass range from 6 to 9 and

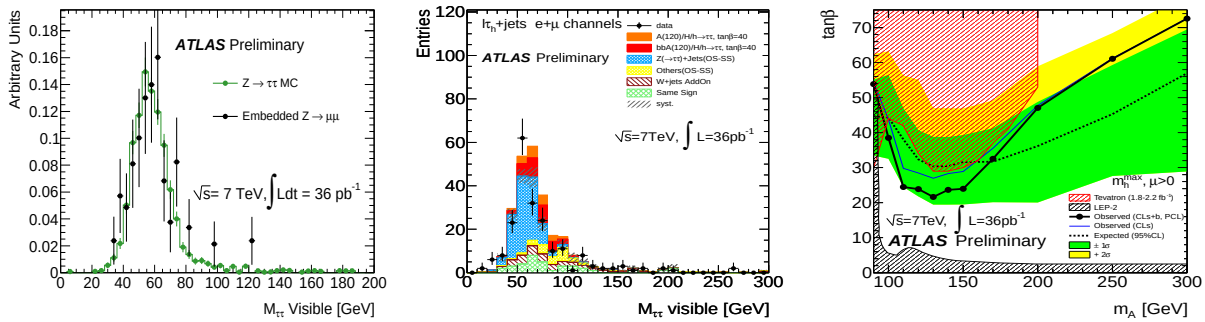

Figure 4: $H \to \tau\tau$: comparison of the visible mass shape of embedded $Z \to \mu\mu$ collision events with simulated $Z \to \tau\tau$ events (left), comparison of the visible mass distribution of event selected in data with the prediction for all background processes and a hypothetical signal (middle), and excluded parameter space in the MHMAX benchmark scenario of the MSSM (right).

11.0 to 12.5 decaying to a pair of muons produced in gluon fusion has been performed. After selecting events with two muons with a transverse momentum exceeding 4 GeV a likelihood ratio selection is applied. The probability density functions of the input variables for the signal and background hypothesis are derived from data itself by selecting events outside the search region: i.e. 9 to 11 GeV for the signal hypothesis, which has been confirmed to be kinematically identical to Υ production, and for the background hypothesis from events with $M_{\mu\mu}$ below 6 and above 11.5 GeV. The final mass distribution after applying a cut on the likehood ratio is shown in Fig. 5 (left). The uncertainty on the expected signal yield is estimated to be 70% for a signal mass of 6 GeV and 28% for a signal mass of 11 GeV, which is dominated by the uncertainty on the kinematical acceptance. The continuum background is parametrised by a forth order polynomial, where all parameters are nuisance parameters. The signal and the Υ resonances are modelled by a double Gaussian probability density function, where the masses are fixed to the hypothetical signal mass and the world averages for Υ masses, respectively. The width and fraction of the two Gaussians for the $\Upsilon(1S)$ resonance are nuisance parameters. For the other Υ resonances and the signal resonance the widths and fractions are obtained using a linear dependence of the mass resolution on the resonance mass. All normalisations are left floating in the fits. The cross-section times branching ratio limit is shown in Fig 5 (right). Production rates down to 200 pb can be excluded.

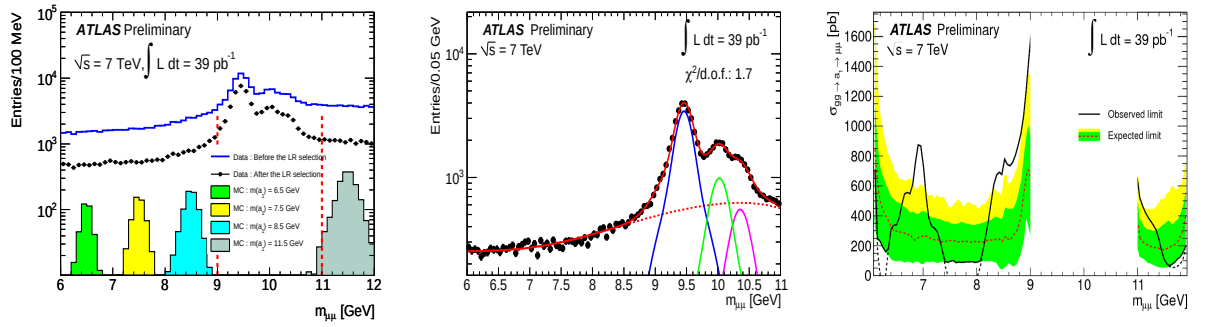

Figure 5: $\phi \to \mu\mu$: observed invariant di-muon mass spectrum (left), result of the background-only hypothesis fit to the invariant di-muon mass spectrum (middle), and cross-section times braching ratio limit(right).

5 Conclusions

LHC and ATLAS performed very well during their operation in 2010. However searches in a data sample corresponding to an integrated luminosity of up to 39 pb^{-1} have not revealed any hint for Higgs boson production at LHC yet. So far mostly simple cut based selections have been performed and the major backgrounds in most analyses have been estimated or at least being confirmed using data-driven methods. In the search for $H \to \gamma\gamma$ a sensitivity of 20 times the SM Higgs boson production rate has been achieved. The $H \to WW$ search allows to exclude already a production rate of 1.2 times the SM rate at a mass of 160 GeV. The search for $H \to ZZ$ decays yield the world's best limits for a Higgs boson mass above 300 GeV up to now. The sensitivity of the search for neutral Higgs bosons of the MSSM via decays to a pair of tau leptons already supercedes the findings obtained at the Tevatron. Collecting a data set corresponding to 4 fb^{-1} at LHC at a center of mass energy of 7 TeV will allow to exclude Higgs boson mass hypotheses in the SM down to the LEP limit of 114.4 GeV [16] assuming that no deviation from the background-only hypothesis is observed [17]. Higgs boson hunters in all experiments hope that a different scenario is realised in nature.

References

1. G. Aad *et al.* [ATLAS Collaboration], JINST **3** (2008) S08003.
2. LHC Higgs Cross-Section Working Group (S. Dittmaier *et al.*), *Handbook of LHC Higgs Cross-Sections: 1. Inclusive Observables*, CERN-2011-002, arXiv:1101.0593.
3. G. Cowan, K. Cranmer, E. Gross, O. Vitells, Eur. Phys. J. **C 71** (2011) 1554.
4. G. Cowan, K. Cranmer, E. Gross, O. Vitells, *Power-Constrained Limits*, arXiv:1105.3166.
5. A. L. Read, J. Phys. **G 28** (2002) 2693-2704; A. L. Read, CERN-OPEN-2000-205.
6. ATLAS Collaboration, *Search for the Higgs boson in the diphoton final state in 38 pb^{-1} of data recorded with the ATLAS detector at $\sqrt{s}$=7 TeV*, ATLAS-CONF-2011-025.
7. ATLAS Collaboration, *Higgs Boson Searches using the $H \to W^+W^- \to \ell^+\nu\ell^-\bar{\nu}$ Decay Mode with the ATLAS Detector at 7 TeV*, ATLAS-CONF-2011-005.
8. ATLAS Collaboration, *Search for a Standard Model Higgs Boson in the Mass Range 200-600 GeV in the Channels $H \to ZZ \to \ell^+\ell^-\nu\bar{\nu}$ and $H \to ZZ \to \ell^+\ell^-q\bar{q}$ with the ATLAS Detector*, ATLAS-CONF-2011-026.
9. ATLAS Collaboration, *Search for neutral MSSM Higgs bosons decaying to $\tau^+\tau^-$ pairs in proton-proton collisions at $\sqrt{s}$ =7 TeV with the ATLAS Experiment*, ATLAS-CONF-2011-024.
10. ATLAS Collaboration, *Search for NMSSM light CP-odd Higgs a1 with $\mu^+\mu^-$ final states with pp collisions at $\sqrt{s}$ =7 TeV in ATLAS*, ATLAS-CONF-2011-020.
11. M. J. Oreglia, *A Study of the Reactions $\Psi' \to \gamma\gamma\Psi$*, Ph.D. Thesis, SLAC-R-236 (1980).
12. M. S. Carena, S. Heinemeyer, C. E. M. Wagner, G. Weiglein, Eur. Phys. J. **C 26** (2003) 601.
13. S. Schael *et al.* [ALEPH, DELPHI, L3 and OPAL Collaborations and LEP Working Group for Higgs Boson Searches], Eur. Phys. J. **C 47** (2006) 547-587.
14. D. Benjamin *et al.* [Tevatron New Phenomena & Higgs Working Group, CDF and D0 Collaborations], *Combined CDF and D0 upper limits on MSSM Higgs boson production in tau-tau final states with up to 2.2 fb-1*, arXiv:1003.3363.
15. M. Maniatis, Int. J. Mod. Phys. **A25** (2010) 3505-3602.
16. R. Barate *et al.*[ALEPH and DELPHI and L3 and OPAL Collaborations and LEP Working Group for Higgs boson searches], Phys. Lett. **B565** (2003) 61-75.
17. ATLAS Collaboration, *Further investigations of ATLAS Sensitivity to Higgs Boson Production in different assumed LHC scenarios*, ATL-PHYS-PUB-2011-001.

Higgs and $Z \to \tau^+\tau^-$ in CMS

Christian Veelken
Department of Physics, University of California, Davis, USA

The production of oppositely–charged tau lepton pairs is studied at 7 TeV center–of–mass energy using 36 pb^{-1} of proton-proton collision data collected by the CMS experiment in 2010. Events are selected in a combination of different final states resulting from hadronic and leptonic tau decays. The $Z \to \tau^+\tau^-$ cross–section is measured. The tau–pair kinematics is fully reconstructed using a likelihood technique. The mass spectrum observed in data is used to derive upper bounds on the production cross section times branching ratio to tau–pairs as a function of the Higgs boson mass in the Minimal Supersymmetric extension of the Standard Model (MSSM).

1 Introduction

We report on the results of an analysis of oppositely charged tau lepton pairs, produced in pp collisions at $\sqrt{s} = 7$ TeV at the Large Hadron Collider (LHC). The analyzed dataset corresponds to an integrated luminosity of 36 pb^{-1} and has been recorded by the Compact Muon Solenoid (CMS) experiment in 2010.

Within the Standard Model (SM), the process $pp \to Z + X$, $Z \to \tau^+\tau^-$ constitutes the dominant source of tau lepton pairs considered in our study. $Z \to \tau^+\tau^-$ events are useful for measuring tau identification and trigger efficiencies. On the other hand, $Z \to \tau^+\tau^-$ events constitute an important irreducible background in searches for new physics. We measure the $Z \to \tau^+\tau^-$ production cross–section in a combination of four decay modes: $\tau^+\tau^- \to e\mu$, $\mu\mu$, $e\tau_{had}$ and $\mu\tau_{had}$, where we denote by τ_{had} a reconstructed hadronic decay of a tau.

We search for evidence for MSSM neutral Higgs bosons in the tau–pair mass spectrum observed in data. The tau lepton pair mass is reconstructed by a novel likelihood based algorithm.

2 CMS detector and coordinate system

The CMS detector is described in detail in[1].

CMS uses a right–handed coordinate system, with the origin at the nominal interaction point, the x axis pointing to the centre of the LHC, the y axis pointing up perpendicular to the LHC plane, and the z axis along the counterclockwise–beam direction. The polar angle θ is measured from the positive z axis and the azimuthal angle ϕ is measured in the xy plane. We will refer to the direction of particles also in terms of the pseudo–rapidity $\eta = -\ln\left(\tan\frac{\theta}{2}\right)$ and denote by p_T the component of particle momentum transverse to the beam direction.

3 Lepton reconstruction and identification

Electrons are reconstructed by combining energy deposits in the electromagnetic calorimeter with tracks in the silicon pixel and strip detectors[2]. Selection criteria are applied[3] to reduce the rates with which charged hadrons and neutral pions/photons are identified as electrons.

Muons are reconstructed in the tracking detectors and in dedicated muon chambers[4]. Quality cuts are applied[3] to ensure that muons are well reconstructed.

Electrons and muons are required to be isolated in the detector[5], in order to remove leptons originating from hadron decays, which are typically found within jets.

Tau lepton hadronic decays are reconstructed and identified by the Hadron plus Strips (HPS) algorithm[6]. The algorithm uses as input collections of particles reconstructed by the CMS particle flow (PF) algorithm[7,8]. π^0 meson candidates are build by clustering electrons and photons reconstructed by the PF algorithm in "strips" along the bending plane of the 4 T CMS magnetic field, taking into account the possible broadening of calorimeter signatures by photon conversions within the tracking detectors. From the list of charged hadrons plus π^0 candidates, different τ_{had} decay hypotheses are build, corresponding to specific hadronic tau decay modes. The HPS algorithm considers all possible combinations of charged hadrons and π^0 candidates and selects combinations which are consistent with specific hadronic tau decay modes. In case multiple hypotheses are consistent, the algorithm chooses the combination which is most isolated in terms of the presence of nearby reconstructed particles. Requirements on isolation variables define different working–points in the space of tau identification efficiency vs. jet–to–tau misidentification rate. We require that other than the τ_{had} constituents there be no charged hadrons of $p_T > 1.0$ GeV and no π^0 candidates of $p_T > 1.5$ GeV within a cone of size $\Delta R = 0.5$ around the tau direction.

Jets are build using the anti–k_T algorithm[9] from particles reconstructed by the PF algorithm not identified as electrons, muons or hadronic tau decays. Jet energy corrections are applied[10].

The missing transverse energy $E_T^{\rm miss}$ is measured using the collection of particles reconstructed by the PF algorithm.

4 Event selection

Events selected in the $e\mu$, $\mu\mu$ and $\mu\tau_{had}$ decay channels are triggered by single muon triggers. P_T thresholds of the muon triggers vary between 9–15 GeV, depending on instantaneous luminosity. $e\tau_{had}$ events are triggered by a combination of single electron triggers with P_T thresholds 8–12 GeV plus a dedicated $e\tau_{had}$ trigger. The $e\tau_{had}$ trigger runs a simplified version of the offline tau reconstruction algorithm with less stringent selection criteria and rejects events without hadronic tau decays. The requirement of a loosely identified τ_{had} reduces the trigger rate considerably and allows to keep the electron P_T threshold of the $e\tau_{had}$ trigger at 12 GeV.

The offline selection of $e\tau_{had}$ and $\mu\tau_{had}$ events requires the presence of an isolated electron or muon with $p_T > 15$ GeV and $|\eta| < 2.1$ and a τ_{had} of opposite charge with $p_T > 20$ GeV, $|\eta| < 2.3$. The transverse mass $M_T(\ell, E_T^{\rm miss}) = \sqrt{2p_T^{\ell} E_T^{\rm miss}\,(1-\cos\Delta\phi)}$, where $\Delta\phi$ is the difference in azimuth between the $E_T^{\rm miss}$ vector and either e or μ, is required to be below 40 GeV, in order to reduce W + jets background. Events with two isolated electrons or muons are rejected in order to remove Drell–Yan background.

Events in the $e\mu$ channel are selected by requiring an isolated muon within $|\eta| < 2.1$, plus an oppositely charged electron within $|\eta| < 2.4$, both with $p_T > 15$ GeV. W + jet and $t\bar{t}$ backgrounds are removed by requiring $M_T(e, E_T^{\rm miss}) < 50$ GeV and $M_T(\mu, E_T^{\rm miss}) < 50$ GeV.

Events in the $\mu\mu$ channel are required to have two muons of opposite charge with $|\eta| < 2.1$. The transverse momentum of the higher (lower) p_T muon is required to exceed 19 GeV (10 GeV). We further require $\Delta\phi_{\mu\mu} < 2.0$ for the azimuthal angle between the two muons, to remove QCD

background events in which muons result from quarkonia decays or from decay chains of heavy–flavored hadrons. W + jet and $t\bar{t}$ backgrounds are removed by requiring $E_T^{\rm miss} < 50$ GeV. Drell–Yan dimuon background is removed by a multivariate likelihood technique[5].

5 Background estimation

The main backgrounds are QCD multi–jet, W + jet and Drell–Yan events. Small additional background contributions are due to $t\bar{t}$ and diboson (WW, WZ, ZZ) events. Background contributions are estimated from data.

Two complementary data–driven methods are used to estimate background contributions in the $e\tau_{had}$ and $\mu\tau_{had}$ channels: The first method is based on the charge of μ plus τ_{had} and the extrapolation of background contributions measured in a high M_T sideband. The QCD background is estimated by measuring the ratio of same–sign (SS) to opposite–sign (OS) events in a control region defined by inverting the isolation criteria for electrons and muons. The measured OS/SS ratio is used to extrapolate the QCD event yield measured in another control region, identical to the signal region except that e and τ_{had} (μ and τ_{had}) are required to be of the same charge, into the signal region. A correction is applied to account for W + jet and other backgrounds, for which the OS/SS ratio may be different. The contribution of W + jet background in the control region and in the signal region is estimated by extrapolating the event yields measured in $M_T(\ell, E_T^{\rm miss}) > 60$ GeV sidebands into $M_T(\ell, E_T^{\rm miss}) < 40$ GeV regions. The second method is based on measuring jet–to–tau misidentification rates in event samples dominated by QCD and W + jet backgrounds, relaxing the τ_{had} identification criteria in the $Z \to \tau^+\tau^-$ event selection and applying the measured misidentification rates as weights to events which pass all event selection requirements except τ_{had} identification criteria.

In the $\mu\mu$ channel the dominant Drell–Yan background is estimated by selecting events with a reduced likelihood from which one of the input variables is excluded and fitting with signal and background templates the distribution of the excluded variable obtained after cutting on the reduced likelihood and applying all other event selection requirements. Contributions of other backgrounds to the $\mu\mu$ channel as well as background contributions to the $e\mu$ channel are small. Further details of estimating background contributions can be found in[5].

	$e\mu$	$\mu\mu$ ($M_{\mu\mu} < 70$ GeV)	$e\tau_{had}$	$\mu\tau_{had}$
$Z \to \ell^+\ell^-$, jet misidentified as τ	-		15.0 ± 6.2	6.4 ± 2.4
$Z \to \ell^+\ell^-$, lepton misidentified as τ	2.4 ± 0.3	20.1 ± 1.3	109 ± 28	12.9 ± 3.5
$t\bar{t}$	7.1 ± 1.3	0.15 ± 0.03	2.6 ± 1.3	6.0 ± 3.0
$W \to \ell\nu$	1.5 ± 0.5	2.5 ± 2.5	30.6 ± 3.1	54.9 ± 4.8
$W \to \tau\nu$			7.0 ± 0.7	14.7 ± 1.3
QCD multi–jet			181 ± 23	132 ± 14
$WW/WZ/ZZ$	3.0 ± 0.4	-	0.8 ± 0.4	1.6 ± 0.8
Total background	14.0 ± 1.8	22.8 ± 2.8	346 ± 37	228 ± 16
Total data	101	58	540	517

Table 1: Number of events expected in the $e\mu$, $\mu\mu$, $e\tau_{had}$ and $\mu\tau_{had}$ decay channels from different background processes. The uncertainties quoted in the table represent combined statistical plus systematic uncertainties on the background estimates. The number of events observed in each decay channel is given in the bottom row.

The background estimates obtained for all four channels are given in Tab. 1. The number of events expected in each decay channel is compared to the number of events observed in data. The difference between the number of events observed in data and the expected background total represents the signal.

6 Systematic uncertainties

Electron and muon reconstruction, identification, isolation and trigger efficiencies are measured in data, using the "tag–and–probe" method[3]. The resulting uncertainty on the signal efficiency varies between less than 1% and 3%, depending on decay channel.

In the $e\tau_{had}$ and $\mu\tau_{had}$ decay channels the by far dominant systematic uncertainty in the efficiency with which hadronic tau decays are reconstructed and identified. The τ_{had} efficiency is measured in data. At present the measurement is statistically limited and has an uncertainty of 23%.

The effect of energy scale uncertainties on the signal efficiency as well as on the shape of mass spectra is estimated by varying the energy and momentum of reconstructed objects within their respective uncertainties, recomputing all kinematic quantities and repeating the event selection. The energy scale uncertainty amounts to 2% for electrons, 1% for muons and 3% for τ_{had} decays. The uncertainty on the energy of jets with $p_T > 10$ GeV amounts to 3%. The energy of particles neither identified as e, μ or τ_{had} nor contained within a jet of $p_T > 10$ GeV is varied by 10%.

7 $Z \to \tau^+\tau^-$ cross–section measurement

The Z production cross–section times branching ratio for the decay into tau–pairs is extracted via the relation:

$$\sigma\left(pp \to Z + X\right) \times BR\left(Z \to \tau^+\tau^-\right) = \frac{N}{A \cdot \varepsilon \cdot B' \cdot L}.$$

N denotes the number of signal events, B' the branching fraction of the decay mode considered[11], and L the integrated luminosity of the analyzed dataset. The signal acceptance A represents the probability of the visible tau decay products to pass p_T and η cuts. The efficiency for signal events to pass all other event selection criteria is denoted by ε.

The number of signal events is determined by fitting the $e\mu$, $\mu\mu$, $e\tau_{had}$ and $\mu\tau_{had}$ visible mass distributions observed in data by shape templates for signal and background processes. Shape templates for QCD and Drell–Yan backgrounds are obtained from data. Templates for other background processes and for the $Z \to \tau^+\tau^-$ signal are taken from the Monte Carlo simulation[a]. All shape templates taken from the simulation are parametrized as function of e, μ and τ_{had} energy scales. The energy scales are allowed to vary during the fit, within their uncertainties. The background estimates obtained from data and shown in Tab. 1 enter the fit as constraints, with uncertainties given in the table.

The results of the fits are illustrated in Fig. 1, which compares the visible mass distributions observed in data to the sum of signal and background templates scaled by the yields obtained by the four individual fits. Good agreement is observed in all channels.

Final state	$\sigma\left(pp \to Z + X\right) \times BR\left(Z \to \tau^+\tau^-\right)$	stat.	syst.	lumi.	τ_{had}–ID eff.
$e\mu$	0.99	0.12	0.06	0.04	-
$\mu\mu$	1.14	0.27	0.04	0.05	-
$e\tau_{had}$	0.94	0.11	0.03	0.04	0.22
$\mu\tau_{had}$	0.83	0.07	0.04	0.03	0.19

Table 2: Z production cross–section times branching fraction for decay $Z \to \tau^+\tau^-$, measured in the four decay channels $e\mu$, $\mu\mu$, $e\tau_{had}$ and $\mu\tau_{had}$. The uncertainty associated to the efficiency to reconstruct and identified τ_{had} decays is shown separately from other systematic uncertainties. All numbers given in the table are in units of nb.

[a] It has been verified in background dominated control regions that the visible mass distributions for background processes are well modeled by the Monte Carlo simulation.

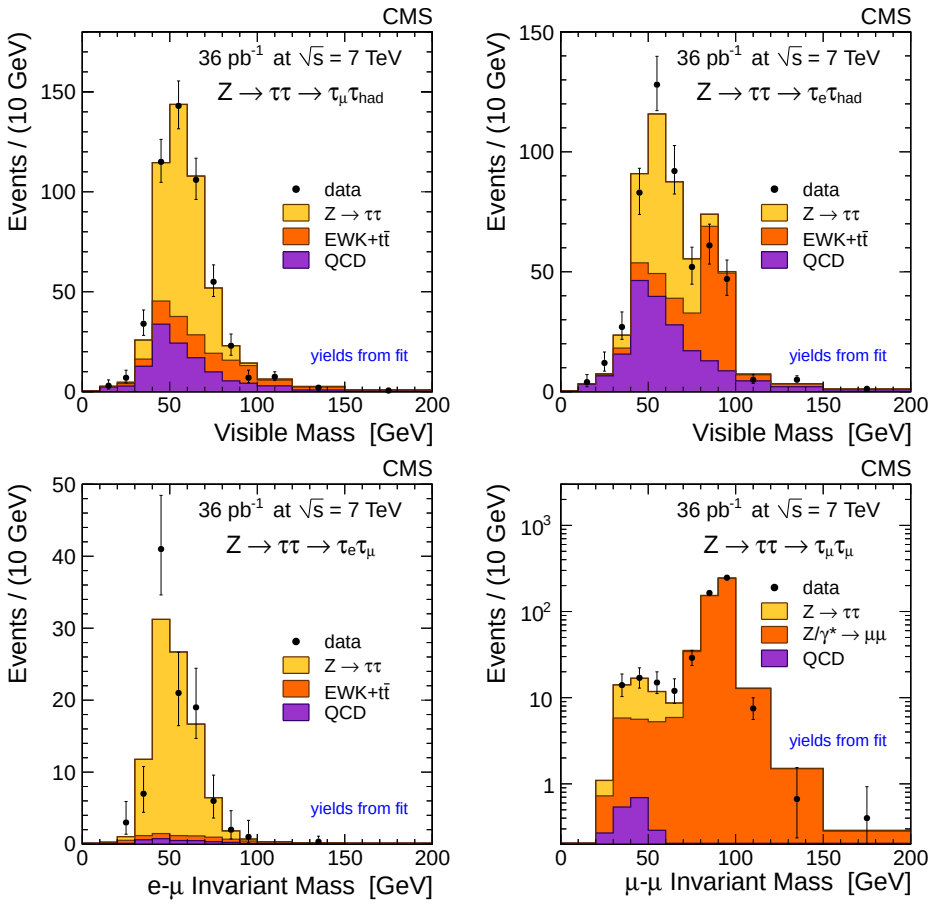

Figure 1: Visible mass spectra observed in data compared to shape templates of signal and background processes scaled by the yields obtained by fits of individual decay channels.

The $\sigma\,(pp \to Z + X) \times BR\,(Z \to \tau^+\tau^-)$ cross–section values extracted from the fits are given in Tab. 2. The cross–sections are quoted for $Z \to \tau^+\tau^-$ production within the mass window $60 < M_{\tau^+\tau^-} < 120$ GeV. Contributions from $Z/\gamma^* \to \tau^+\tau^-$ events outside the mass window are small (between $1-3\%$, depending on decay channel) and accounted for by correction factors.

Measured cross–sections are compatible with each other and in good agreement with the NNLO theoretical prediction[12] 0.972 ± 0.042 nb. The measured $Z \to \tau^+\tau^-$ cross–sections also agree well with the corresponding CMS measurement in $Z \to e^+e^-$ and $Z \to \mu^+\mu^-$ events[3]:

$$\sigma\,(pp \to Z + X) \times BR\left(Z \to e^+e^-, \mu^+\mu^-\right) = 0.931 \pm 0.026\ (\text{stat.}) \pm 0.023\ (\text{sys.}) \pm 0.102\ (\text{lumi.})\ \text{nb}.$$

In the $e\tau_{had}$ and $\mu\tau_{had}$ channels the precision of the cross–section measurement is limited by the uncertainty on the τ_{had} identification efficiency. A simultaneous fit of all four channels is performed in order to obtain $\sigma\,(pp \to Z + X) \times BR\,(Z \to \tau^+\tau^-)$ together with a scale–factor which represents the ratio of τ_{had}–ID efficiency in data to simulation. The result of the simultaneous fit is illustrated in Fig. 2 (left), showing the likelihood contours in the plane of cross–section versus scale–factor. The cross–section extracted from the simultaneous fit is:

$$\sigma\,(pp \to Z + X) \times BR\left(Z \to \tau^+\tau^-\right) = 1.00 \pm 0.05\ (\text{stat.}) \pm 0.08\ (\text{sys.}) \pm 0.04\ (\text{lumi.})\ \text{nb}.$$

The value of $\sigma\,(pp \to Z + X) \times BR\,(Z \to \tau^+\tau^-)$ obtained from the simultaneous fit is compared to the cross–sections measured individually for the four decay channels in Fig. 2 (right). The value of the τ_{had}–ID efficiency scale–factor obtained from the simultaneous fit is 0.93 ± 0.09.

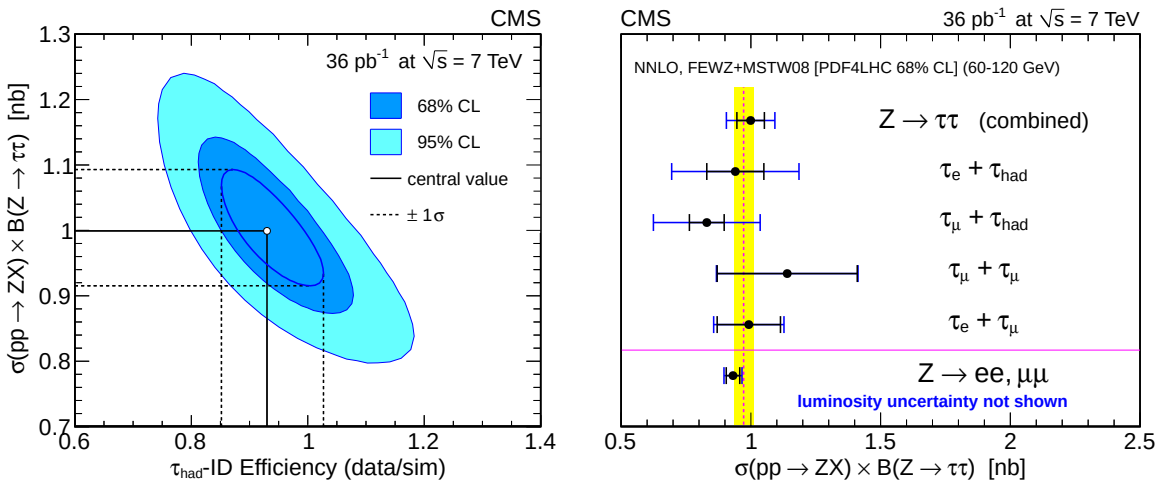

Figure 2: Left: Likelihood contours for the simultaneous fit of $e\mu$, $\mu\mu$, $e\tau_{had}$ and $\mu\tau_{had}$ decay channels. The inner (outer) ellipse indicates the region of 68% (95%) coverage in the $\sigma\left(pp \to Z + X\right) \times BR\left(Z \to \tau^{+}\tau^{-}\right)$ versus τ_{had}–ID efficiency scale–factor plane. The dashed lines indicate the one standard–deviation uncertainties on either one of the two parameters, obtained by marginalization of the second parameter. Right: Graphical representation of the cross–sections measured in individual decay channels compared to the result of the simultaneous fit. The shaded band represents the NNLO theoretical prediction and its uncertainty.

A more precise determination of the τ_{had}–ID efficiency is possible by relating the cross–section measured in the $Z \to \tau^{+}\tau^{-}$ channel to the cross–sections measured by CMS in the $Z \to e^{+}e^{-}$ and $Z \to \mu^{+}\mu^{-}$ channels, as systematic uncertainties partially cancel. The τ_{had}–ID efficiency obtained via this method is 0.96 ± 0.07 .

8 Search for neutral MSSM Higgs bosons

We search for evidence for neutral Higgs bosons in the tau–pair mass spectra observed in data. The results are interpreted in the minimal supersymmetric extension to the standard model (MSSM). In this model two Higgs doublets yield five massive Higgs bosons: a light neutral scalar (h), two charged scalars ($H^{\pm}$), a heavy neutral scalar (H) and a pseudo–scalar (A).

The Higgs boson signal is distinguished from backgrounds via the "full" mass, denoted by $M_{\tau^{+}\tau^{-}}$, of the tau–pair, reconstructed by a novel likelihood technique. The likelihood is build from three terms: the tau decay phase–space, the probability density in the tau transverse momentum, parametrized as a function of the tau pair mass, and the compatibility of the sum of neutrino momenta with the measured value of $E_T^{\rm miss}$. The product of the three terms is maximized with respect to the free parameters in the likelihood functions: the energies and directions of the neutrinos produced in the tau decays. The momenta of visible tau decay products are fixed to their measured values. The algorithm yields a tau pair mass solution for each event, with mean consistent with the true value and nearly Gaussian resolution. For a Higgs of mass 130 GeV a resolution of $\sim 21\%$ is attained. The data is in agreement with the expectation for background processes. No evidence for a Higgs signal is seen.

In the absence of evidence for a Higgs signal, we set limits on the product of Higgs boson production cross–section times branching fraction for the decay into tau pairs, which we denote by $\sigma_{\Phi}\cdot B_{\tau\tau}$. The limit is computed as function of m_A by fitting the $M_{\tau^{+}\tau^{-}}$ distribution observed in the $e\mu$, $e\tau_{had}$ and $\mu\tau_{had}$ decay channels with shape templates for different Higgs mass hypotheses, obtained from Monte Carlo simulation. We use a Bayesian approach with a uniform prior on $\sigma_{\Phi}\cdot B_{\tau\tau}$ to set the limit. Systematic uncertainties on fit parameters corresponding to background normalization, signal efficiencies and energy scales are represented by nuisance parameters and

removed by marginalization, assuming a log–normal prior for normalization parameters and signal efficiencies and Gaussian priors for energy scale parameters. The effect of energy scale parameters on the shape of $M_{\tau^+\tau^-}$ mass templates is modeled via a continuous alteration of the shape[13].

For a given mass hypothesis m_A the product of signal acceptance times efficiency is computed by weighting acceptances and efficiencies for h, H and A bosons according to cross–section. Higgs cross–sections entering the weighting procedure are computed for $\tan\beta = 30$. Acceptance times efficiency values are averaged over the two production processes $gg \to \Phi$ (gluon fusion through a b quark loop) and $b\bar{b} \to \Phi$ (direct $b\bar{b}$ annihilation from the b parton density in the beam protons). Differences between scalar and pseudo–scalar Higgs bosons and between the $gg \to \Phi$ and $b\bar{b} \to \Phi$ production mechanisms ($\lesssim 10\%$) are taken into account as systematic uncertainty.

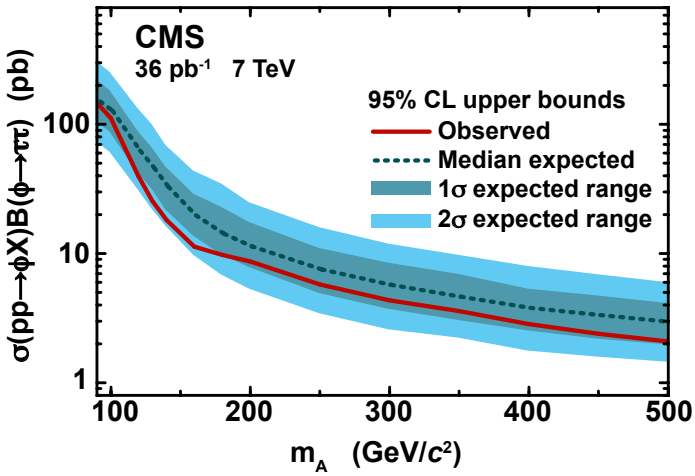

Figure 3: Observed 95% confidence level (CL) upper limit on $\sigma_\Phi \cdot B_{\tau\tau}$. The (dark) light shaded band indicates the one (two) standard–deviation range of experimental outcomes expected for background–only experiments, given the sensitivity of our analysis and 36 pb^{-1} of data.

The resulting limit on $\sigma_\Phi \cdot B_{\tau\tau}$ is shown in Fig. 3 (see[14] for tabulated values). The observed limit is within the range of experimental outcomes expected for background–only experiments.

We interpret the limit on $\sigma_\Phi \cdot B_{\tau\tau}$ in the m_h^{max} scenario of the MSSM and convert it into a corresponding limit on the MSSM parameters $\tan\beta$ versus m_A. Higgs boson cross–section values reported by the LHC Higgs Cross–section Working Group[15] are used for the conversion. For the $b\bar{b} \to \Phi$ cross–section we take the values computed in the 5–flavor scheme. The limits obtained on $\tan\beta$ versus m_A are shown in Fig. 4.

Our results exclude a region in $\tan\beta$ down to values smaller than those excluded by TeVatron experiments[16] for $m_A \lesssim 140$ GeV. For larger m_A our results significantly extend the previously excluded region. The region in $\tan\beta$ versus m_A parameter space excluded by LEP experiments[17] is also shown in the figure.

9 Summary

Tau lepton pair production has been analyzed in 36 pb^{-1} of pp collision data recorded by the CMS experiment in 2010. The measured Z production cross–section times branching fraction for the decay into tau pairs,

$\sigma\,(pp \to Z + X) \times BR\,(Z \to \tau^+\tau^-) = 1.00 \pm 0.05\ (\text{stat.}) \pm 0.08\ (\text{sys.}) \pm 0.04\ (\text{lumi.})$ nb,

is in agreement with NNLO theoretical predictions and with CMS measurements of the Z production cross–section in the $Z \to e^+e^-$ and $Z \to \mu^+\mu^-$ channels. The observed $Z \to \tau^+\tau^-$

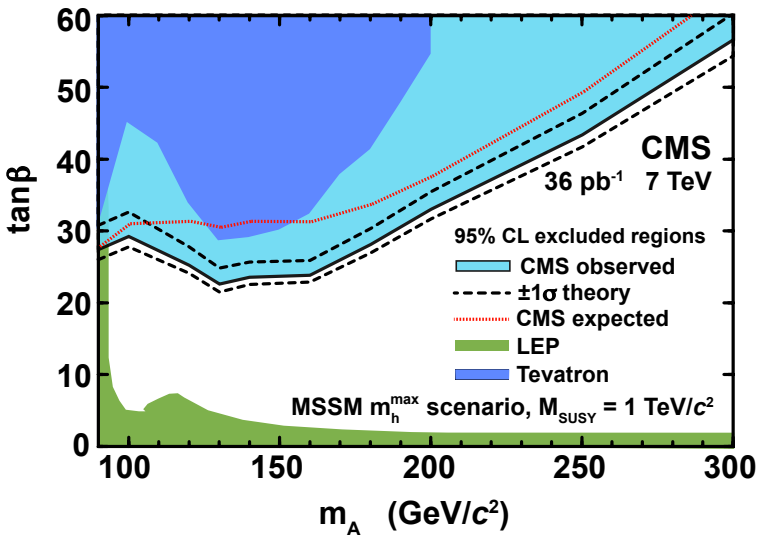

Figure 4: Region in tan β versus m_A parameter space excluded by CMS data at 95% CL. Theoretical uncertainties are represented by black dashed lines, enclosing the observed limit. Limits obtained by previous experiments at TeVatron and at LEP are indicated separately by shaded regions.

yield allows to determine the hadronic tau identification efficiency with an uncertainty of 7%.

No evidence for neutral MSSM Higgs boson production is observed in the distribution of the "full" tau lepton pair mass, reconstructed by a novel likelihood technique. A limit on Higgs boson cross-section times branching fraction for the decay into tau pairs is set. The observed limit excludes a significant region in the MSSM tan β versus m_A parameter space not previously explored by experiments at the TeVatron and at LEP.

References

1. R. Adolphi *et al*, *JINST* **0803**, S08004 (2008).
2. CMS Collaboration, CMS–PAS–EGM–10–004, http://cdsweb.cern.ch/record/1299116.
3. CMS Collaboration, *JHEP* **01**, 080 (2011).
4. CMS Collaboration, CMS–PAS–MUO–10–002, http://cdsweb.cern.ch/record/1279140.
5. CMS Collaboration, arXiv:1104.1617 [hep–ex], submitted to *JHEP.*
6. *CMS Collaboration, CMS–PAS–TAU–11–001, http://cdsweb.cern.ch/record/1337004.*
7. *CMS Collaboration, CMS–PAS–PFT–09–001, http://cdsweb.cern.ch/record/1194487.*
8. *CMS Collaboration, CMS–PAS–PFT–10–002, http://cdsweb.cern.ch/record/1279341.*
9. *M. Cacciari, G. P. Salam and G. Soyez,* JHEP **0804**, *063 (2008).*
10. *CMS Collaboration, CMS–PAS–JME–10–010, http://cdsweb.cern.ch/record/1308178.*
11. *K. Nakamura et al,* J. Phys. *G* **37**, *075021 (2010).*
12. *K. Melnikov and F. Petriello,* Phys. Rev. *D* **74**, *114017 (2006).*
13. *J. S. Conway, arXiv:1103.0354 [hep–ex], submitted to Proceedings of PhyStat 2011.*
14. *CMS Collaboration, arXiv:1104.1619 [hep–ex].*
15. *S. Dittmaier et al, arXiv:1101.0593 [hep–ph].*
16. *Tevatron New Physics and Higgs Working Group, arXiv:1003.3363 [hep–ex].*
17. *LEP Higgs Working Group, EPJC* **47**, *547 (2006).*

COMBINATION OF STANDARD MODEL HIGGS SEARCHES AT THE TEVATRON

BODHITHA JAYATILAKA
(on behalf of the CDF and DØ Collaborations)
Duke University, Department of Physics,
Durham, NC 27708, USA

We present a new combination of searches for a standard model Higgs Boson by the CDF and D0 experiments at the Fermilab Tevatron. This combination, covering possible Higgs boson masses between 130 GeV/c^2 and 200 GeV/c^2 and emphasizing the $H \to W^+W^-$ decay channel, utilizes up to 7.1 fb^{-1} of data collected at CDF and up to 8.2^{-1} of data collected at D0. We present 95% CL upper limits on standard model Higgs boson production in this mass range, including exclusion of the range $158 < m_H < 173$ GeV/c^2.

1 Introduction

In the standard model (SM) of particle physics, the observed spontaneous breaking of the electroweak symmetry can be explained via the Higgs mechanism. In addition to providing mass to fundamental particles, the Higgs mechanism would also manifest a physical particle, the Higgs boson. Finding experimental evidence of the Higgs boson or excluding its existence has been a high priority for the field of high-energy physics. A global fit of SM observables indicates a most likely Higgs boson mass $m_H = 89^{+35}_{-26}$ GeV/c^2 with 95% confidence level (CL) upper limit of 158 GeV/c^2, while direct searches at LEP have excluded $m_H < 114.4$ GeV/c^2 at 95% CL. The remaining likely region is within kinematic reach of the Fermilab Tevatron, a $\sqrt{s} = 1.96$ TeV $p\bar{p}$ collider. Thus, in the last few years, the CDF and D0 experiments have made substantial improvements in direct searches for the SM Higgs boson. Here, we present the most recent combination of direct search results from CDF and D0 in the range $130 < m_H < 200$ GeV/c^2.

2 Tevatron Higgs Search Channnels

Higgs boson production at the Tevatron is dominated by the process $gg \to H$ while its decay is dominated by $H \to b\bar{b}$ for $m_H < 130$ GeV/c^2, categorized as "low mass", and $H \to W^+W^-$ for $m_H > 130$ GeV/c^2, categorized as "high mass." The sensitivity of the high mass regime is dominated by searches for $gg \to H \to W^+W^-$. However, smaller channels are considered as well. Additionally, multivariate techniques such as artificial neural networks, boosted decision trees and matrix element calculations are utilized to enhance sensitivity to the small Higgs signal expected. A total of 12 mutually exclusive final states are considered by CDF (Table 1) and 35 by D0 (Table 2).

More details on the individual analyses can be found elsewhere[1]. For all processes considered, we normalize our Higgs boson signal prediction to the most recent highest-order calculations

Table 1: Luminosity, explored mass range and references for the different processes and final states ($\ell = e, \mu$) for the CDF analyses. A total of 12 mutually exclusive final states are considered.

Channel	Luminosity (fb^{-1})	m_H (GeV/c^2)
$H \to W^+W^-$ 2×(0,1 jets)+(≥2 jets)+(low-$m_{\ell\ell}$)+(e/μ-τ_{had})	7.1	130-200
$WH \to WW^+W^-$ (same-sign leptons ≥1 jets)+(tri-leptons)	7.1	130-200
$ZH \to ZW^+W^-$ (tri-lepton 1 jet)+(tri-lepton ≥2 jets)	7.1	130-200

Table 2: Luminosity, explored mass range and references for the different processes and final states ($\ell = e, \mu$) for the D0 analyses. A total of 35 mutually exclusive final states are considered.

Channel	Luminosity (fb^{-1})	m_H (GeV/c^2)
$H \to W^+W^- \to \ell^\pm\nu\ell^\mp\nu$ (0,1,2+ jets)	8.1	130-200
$H \to W^+W^- \to \mu\nu\tau_{had}\nu$	7.3	130-200
$H \to W^+W^- \to \ell\bar{\nu}jj$	5.4	130-200
$VH \to \ell^+\ell^- + X$	5.3	130-200
$H + X \to \ell^\pm\tau^\mp_{had}jj$	4.3	130-200
$H \to \gamma\gamma$	8.2	130-150

available.

3 Combination Procedure

In order to ensure that the combined result does not depend on the statistical method employed, the combination is performed using two methods: a Bayesian and Modified Frequentist method. At each m_H hypothesis considered, the result from the two methods is required to agree within 5% while the average over all masses agrees within 2%. Both methods utilize the distribution of final discriminants from each input analysis and utilize Poisson statistics.

3.1 Systematic Uncertainties

Systematic uncertainties are treated as nuisance parameters and both methods utilize the data to constrain these nuisance parameters. Two categories of systematic uncertainties are considered: rate systematics (such as tag uncertainty), which affect the overall normalization, and shape systematics (such as jet energy scale), which also affect the overall distributions.

Systematic uncertainties due to integrated luminosity and theoretical prediction of signal and background cross-sections are treated as correlated between CDF and D0 while other systematic uncertainties are treated as uncorrelated between experiments but correlated between analyses of a given experiment. Sources of these uncertainties include b-quark tagging efficiency, lepton selection, QCD radiation, jet energy scale, and other detector effects.

3.2 Validation with Data

In order to check the agreement between data and expectation, we can aggregate signal and background expectations in all analyses, bin them by signal-to-background ratio, s/b, and overlay the data binned in the same way, as shown in Figure 1 for $m_H = 165$ GeV/c^2. Additionally, we can subtract the expected background from the data distribution and compare to the expected Higgs signal. This comparison, again sorted by s/b, is shown in Figure 2 for $m_H = 165$ GeV/c^2. No significant excess is seen in high s/b bins.

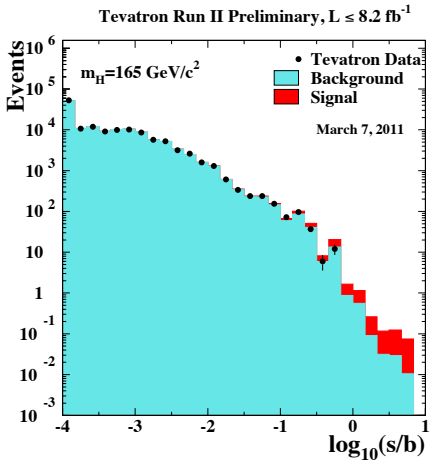

Figure 1: Distribution of $\log_{10}(s/b)$ from all contributing channels from CDF and D0 for $m_H = 165$ GeV/c^2.

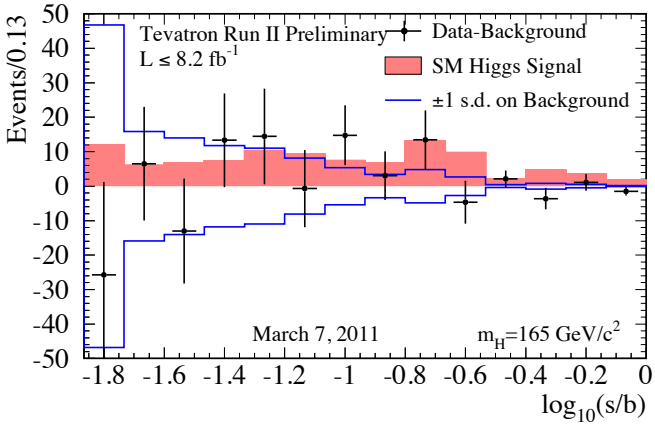

Figure 2: Background subtracted data distribution for discriminant histograms from all contributing channels from CDF and D0, for $m_H = 165$ GeV/c^2. Expected SM Higgs contribution is overlaid.

4 Results

Using the techniques outlined in Section 3, we combine SM Higgs boson searches from CDF and D0 in the mass range of $130 < m_H < 200$ GeV/c^2. We have decided, *a priori*, to quote results obtained from the Bayesian approach. Complete limits from both techniques can be found elsewhere [2]. Figure 3 shows the ratio of 95% CL expected and observed limits to the SM cross-section times branching ratio expected at the Tevatron after combining CDF and D0 results. We exclude at the 95% CL, the region $158 < m_H < 173$ GeV/c^2 with the expected exclusion being $153 < m_H < 179$ GeV/c^2. Observed exclusion at other confidence levels are shown in Figure 4, showing the Tevatron excluding SM Higgs production at 99.5% CL around $m_H = 165$ GeV/c^2.

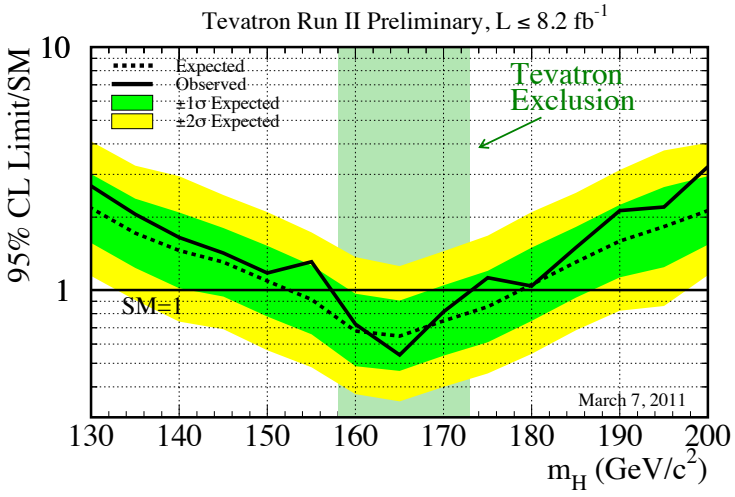

Figure 3: Observed and expected 95% CL upper limits on the ratios to the SM cross section, as a function of m_H. The 68% and 95% probability regions where the limit can fluctuate, in the absence of signal, are indicated by the green and yellow bands, respectively. The region excluded by Tevatron data is shown.

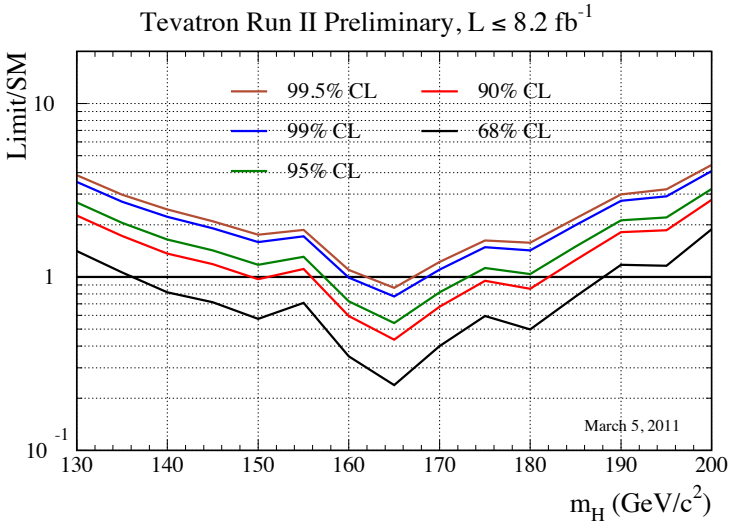

Figure 4: Observed limits on the ratio to the SM Higgs boson cross section at 68%, 90%, 95%, 99% and 99.5% CL.

5 Conclusions

We present the most recent combination of SM Higgs searches from the CDF and D0 experiments in the region $130 < m_H < 200$ GeV/c^2. In up to 8.2 fb^{-1} of data, the Tevatron has excluded the SM Higgs in the region $158 < m_H < 173$ GeV/c^2 at 95% CL. Additionally, the combined Tevatron SM Higgs searches in the mass range including $100 < m_H < 130$ GeV/c^2, presented elsewhere [3], exclude the region $100 < m_H < 109$ GeV/c^2 at 95% CL. With over 10 fb^{-1} of data expected by the end of the Tevatron run in September 2011 and further analysis improvements in progress, the region excluded is expected to grow.

Acknowledgments

The author would like to thank the organizers of XLVI Recontres de Moriond for the invitation to speak at a scientifically rewarding and well-organized conference. The author would also like to thank the dedicated teams at the CDF and D0 collaborations for the results presented, as well as the many funding agencies worldwide that make the Tevatron research program possible.

References

1. Totaro, P. "Search for Low Mass Higgs Boson at the Tevatron," this proceeding.
   Petridis, K. "High mass SM Higgs," this proceeding.
2. The CDF and D0 Collaborations and the TEVNPHWG Working Group, arXiv:1103.3233 [hep-ex] (2011)
3. The CDF and D0 Collaborations and the TEVNPHWG Working Group, arXiv:1007.4587 [hep-ex] (2010)

2.
The Standard Model and Beyond

Standard Model Measurements

Philip C. Harris on behalf of the CMS collaboration
Laboratory of Nuclear Science,Massachusetts Institute of Technology,Cambrdige,Ma, USA

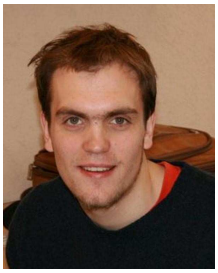

We present several measurements in the domain of electroweak and top physics in proton-proton collisions at the LHC using a centre-of-mass energy of 7 TeV. Data was collected with the CMS experiment during the year 2010, amounting to a total integrated luminosity of 36 pb^{-1}. All measurements are compared with theory and found to be consistent with standard model predictions.

1 Introduction

In 2010 CMS[1] running, a total of 47 pb^{-1} integrated luminosity was delivered and 43 pb^{-1} of that was recorded to tape. This yields 36 pb^{-1} of certified good data at $\sqrt{s} = 7$ TeV. This data resulted in a prodigious amount of W, Z, and top based measurements. These measurements consist of processes with cross sections ranging over three orders of magnitude from ≈ 10 nb to ≈ 10 pb. The precision of these measurements ranged inversely from 1% for processes with a large cross section upwards to 30% for processes with a small cross section.

Standard model measurements serve as a foundation to understanding new physics. Moreover, due to their large cross sections, W and Z boson related measurements are a powerful tool to constrain QCD calculations at 7 TeV and further improve understanding of quark and gluon parton distribution functions. Top quark pair production is the highest energy standard model resonant process. Thus measurements of top quark properties provide a tool to study high energy measurements at the LHC.

In most cases, the measurements presented here are the first measurements of its kind at 7 TeV. In the case of the top quark, this is the first time the top quark has been studied outside of the Tevatron.

In the following document, the CMS results of the 2010 LHC data concerning electroweak and top measurements are presented. These consist of: the W and Z total and differential cross sections, various diboson observations, the top pair production and single production cross sections, and additional studies of the top quark.

2 Selection and Calibration of the CMS detector

In order to perform all of the presented measurements, each event was required to have at least one isolated high p_T electron or muon in the final state. With the exception of the di-lepton $t\bar{t}$ analysis, the leptons in all of these events were required to fire the lowest energy unprescaled single electron or single muon trigger. For muon analyses, this requirement allowed for a single muon with $p_T > 15$ GeV/c. For the electron, the trigger requirements evolved with increasing luminosity, starting with a 10 GeV photon trigger and ending at an electron trigger with $E_T > 22$ GeV/c and loose electron shower shape requirements. The di-lepton $t\bar{t}$ cross section analyses additionally allowed events which had passed a di-electron trigger.

Following the trigger requirement, leptons were required to pass identification cuts yielding a well reconstructed lepton originating from the primary vertex. In order to avoid selection of leptons from hadronic decays, leptons were additionally required to be isolated by removing events with large energy deposits within a cone in η and ϕ along the path of the lepton.

The efficiency of the triggers, identification and isolation cuts on leptons utilize the "tag and probe" method on Z boson leptonic decays. In this method, a Z boson event is "tagged" by requiring a well reconstructed, isolated lepton along with a component of the second lepton(*i.e. track in the tracker*), which when combined have a mass compatible with the Z boson. The tagged event is then used to "probe" for an additional component of the second lepton (*i.e. track in the muon chambers*). This efficiency measurement in data is compared with that of Monte-Carlo simulation to determine a set of correction factors that translate efficiency measurements to other kinematic regimes.

The lepton energy resolution, and missing transverse energy ($\not\!\!E_T$) modelling are also quantified by utilizing Z events. In the case of the $\not\!\!E_T$, which is defined as the negative vector sum of all of the deposits in the detector, calibration was performed by comparing the lepton measured Z boson p_T with the measured Z boson p_T from the rest of the detector. The lepton energy resolution is determined by fitting the Z mass as a function of the two leptons' (η, ϕ) coordinates.

In some analyses, additional selections on a jet or a b-tagged jet are performed. To calibrate the reconstructed jet energy and resolution, jets originating in di-jet and γ+jet events are balanced with its opposite component. This balance is further compared with simulation yielding a set of uncertainties and corrections on the simulated jets. B-tagged jets are studied by tagging semileptonic b-decays in jet events and looking at the performance of the b-tag identification.

3 Electroweak Analyses

3.1 W/Z Inclusive cross section

The W/Z and inclusive sections have been previously measured with 2.7 pb^{-1} or data [2], in this conference an updated result with the full 2010 dataset is presented [3]. The inclusive Z cross section measurement is performed by requiring two well isolated leptons with a combined mass $m_{\ell\ell}$ given by $60 < m_{\ell\ell} < 120$ GeV/c^2. The cross section is then determined by fitting the data with a simulated template of the Z mass lineshape where energy scale and, resolution corrections have been applied. The W boson inclusive cross section is determined by requiring single isolated leptons and fitting the $\not\!\!E_T$ with a $\not\!\!E_T$ template correct to reflect the W boson $\not\!\!E_T$ in data.

The results of the cross section measurements and the cross section ratios are shown in table 1. The final results are, in most cases, strongly limited by the theoretical and luminosity uncertainties. These put a set of tight constraints on theoretical predictions.

Table 1: W and Z boson cross section and ratios

Measurement	Value$\pm(stat) \pm (sys) \pm (theory) \pm (lumi)$	Theory[3]
$\sigma(W) \times BF(W \to \ell\nu)$ pb	$10.31 \pm 0.02 \pm 0.09 \pm 0.10 \pm 0.41$	10.44 ± 0.52
$\sigma(W^+) \times BF(W^+ \to \ell^+\nu)$ pb	$6.04 \pm 0.02 \pm 0.06 \pm 0.08 \pm 0.24$	6.15 ± 0.29
$\sigma(W^-) \times BF(W^- \to \ell^-\nu)$ pb	$4.26 \pm 0.01 \pm 0.04 \pm 0.07 \pm 0.17$	4.29 ± 0.23
$\sigma(Z) \times BF(Z \to \ell^+\ell^-)$ pb	$0.975 \pm 0.007 \pm 0.007 \pm 0.018 \pm 0.039$	0.97 ± 0.04
$\sigma(W) \times BF/\sigma(Z) \times BF$	$10.54 \pm 0.07 \pm 0.08 \pm 0.16$	10.74 ± 0.04
$\sigma(W^+)/\sigma(W^-)$	$1.421 \pm 0.006 \pm 0.014 \pm 0.030$	1.43 ± 0.04

3.2 W Polarization measurement

In a proton-proton collider, W bosons produced at a transverse momentum > 50 GeV/c are typically produced with a gluon jet, which may induce a polarization in the W boson. Due to the CP asymmetry of the initial state, production of a left handed W boson is favored at high p_T. This effect is only true for proton-proton colliders where the CP conjugate is not present [4].

To measure the W polarization, a fit is performed to the transverse projection of the lepton boson direction for Ws with $p_T > 50$ GeV. The variable that is fit, is known as the LP variable and is defined to be

$$LP = \frac{\vec{p_T}(\ell) \cdot p_T(\vec{W})}{|p_T(W)|^2} \tag{1}$$

Where in this case $\vec{p_T}(\ell)$ and $\vec{p_T}(W)$ are the transverse momentum of the lepton and the W boson respectively. The fit yields both the left-right asymmetry and the longitudinal polarization of the W^+ and W^-. The measured left right asymmetry of $0.300 \pm 0.031(stat) \pm 0.034(sys)$ for W^+ and $0.226 \pm 0.031 \pm 0.050$ for W^- bosons confirms left-handed W polarization in proton-proton colliders. The longitudinal polarization is found to be $0.162 \pm 0.078(stat) \pm 0.136(sys)$ for W^- bosons and $0.192 \pm 0.075(stat) \pm 0.089(sys)$ for W^+ bosons.

3.3 Di-Lepton differential cross sections

In addition to the inclusive Z production cross section, differential production for the Z boson y,p_T [5], and mass($m_{\ell\ell}$) distributions [6] are also measured. In all of these distributions, the background subtracted, per-bin yield is calculated and then the distribution is unfolded to the differential distribution before final state radiation (FSR) correction .

The differential distributions are shown in figure 1. The y and p_T distributions are measured for di-lepton events within a mass window of $60 < m_{\ell\ell} < 120$ GeV/c^2. The resulting rapidity distribution goes out to a rapidity of $|y| < 3.5$. The rapidity measurement beyond $|y| > 2.4$ is performed with the electron reconstruction in the forward calorimeter (reconstruction out to $|\eta| < 4$). The measured distribution is sensitive to the the quark parton distributions. Following figure 1, the data favors well the prediction obtained with the CTEQ10 pdf set. The p_T distribution is sensitive to both higher order matrix element corrections and resummation. At low p_T the best matching calculation results from the Pythia Pro Q20 tune [7]. At high p_T the NLO calculation is sufficient to describe the data up to a region of 200 GeV/c. The mass differential distribution $m_{\ell\ell}$ matches the NNLO calculation as performed by FEWZ [8].

3.4 W+Jets and Z+Jets cross sections

The W and Z jet multiplicity and its trend from small jet multiplicities to large jet multiplicities are powerful tests of standard model QCD calculations. The measurement is performed by

Figure 1: Di-Lepton differential distributions for $m_{\ell\ell}$ in muons (top left),p_T for electrons and muons combined where p_T < 30 GeV/c (top right) and where p_T > 20 GeV/c (bottom right), and y for electrons and muons combined(bottom left)

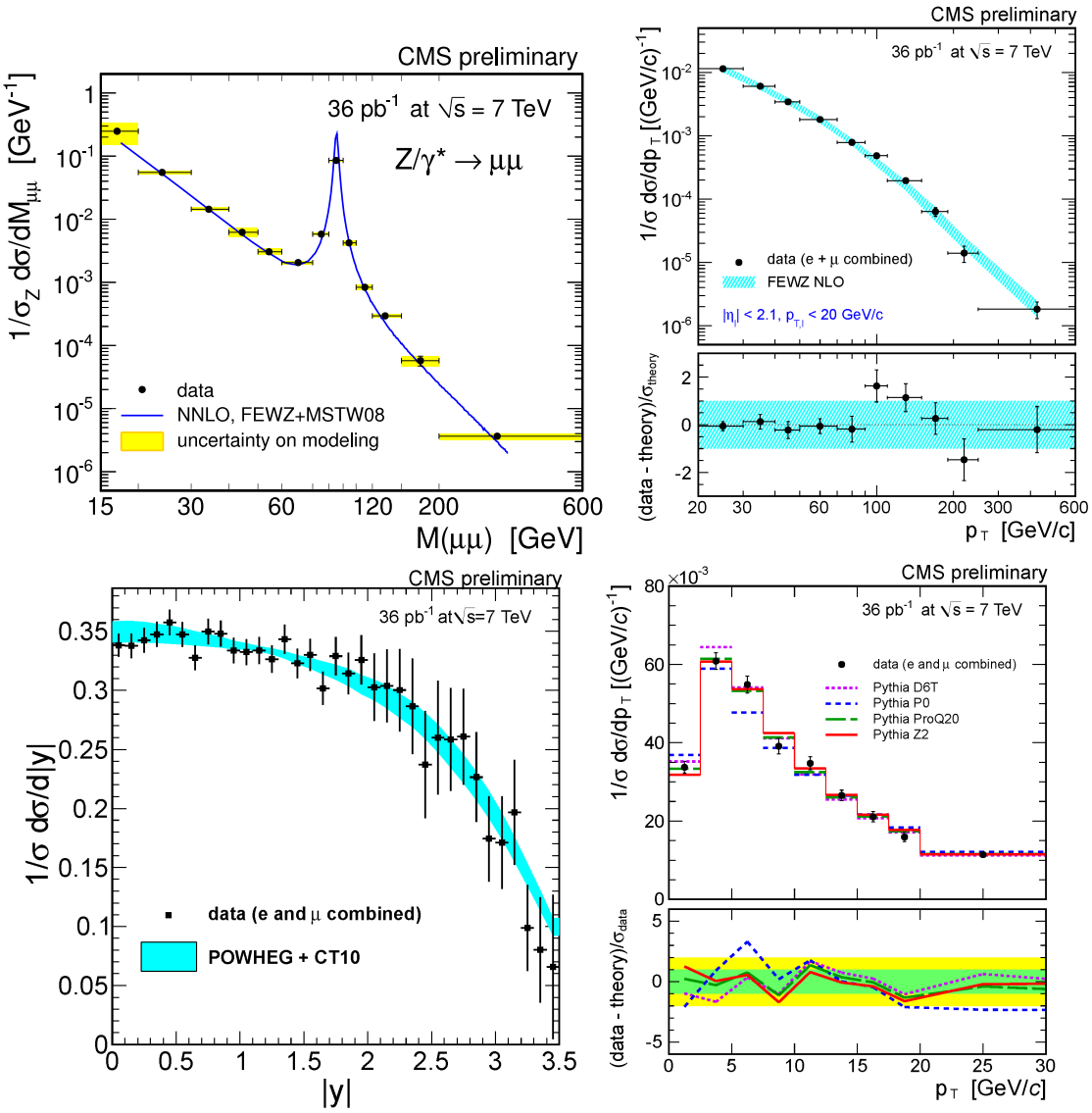

counting jets with an E_T > 30 GeV/c for a single and double lepton selection [9]. At high jet multiplicity, the single lepton + $\not\!\!E_T$ selection has large contributions from both $t\bar{t}$ and W boson events. Consequently, the W boson cross section for the specified jet multiplicity bin is extracted from a 2-dimensional fit in the variables transverse mass and number of b-tags. The final jet multiplicity is unfolded to the particle level incorporating energy scale and mis-modelling uncertainties.

The W and Z jet multiplicities are shown in figure 2. The resulting W and Z jet multiplicities demonstrate the effectiveness of MLM Monte-Carlo simulation [10]. This is indicated by the data simulation agreement in jet multiplicity of Madgraph and not Pythia. The per-jet cross section follows a trend given by (for n-jets)

$$\frac{\sigma_{n+1}}{\sigma_n} = \alpha + \beta n \tag{2}$$

This trend, known as the Berends-Giele scaling [11] can be fit for to obtain an overall prediction

of jet production. The resulting values for α and β are shown in table 2. The values for α in W production are smaller than the predicted standard model value indicating a slightly larger cross section in the high jet multiplicity bins.

Figure 2: W and Z Jet multiplicity measurements for W bosons (top), and Z bosons(bottom) separated out by muons(left), and electrons(right)

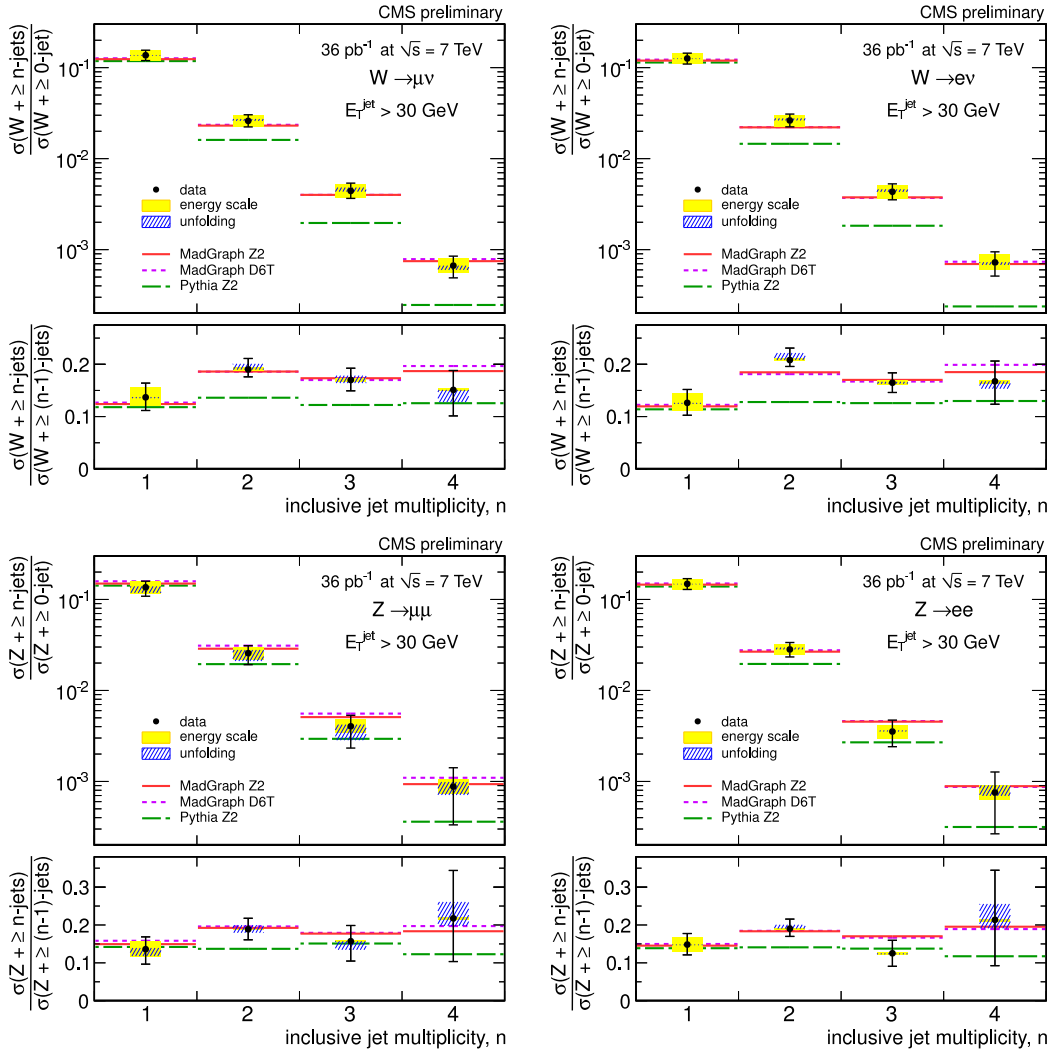

3.5 Z+b Jet production

In addition to Z+Jet measurements, a measurement of the b-jet production was performed in CMS by requiring Z events with 1 jet having a $p_T > 25$GeV/c and a high purity b-tag on the jet [12]. The results presented in table 2 are in close agreement with NLO theory predictions.

3.6 Z+γ production

In addition to single boson measurements, several di-boson measurements have been performed on the first 36 pb^{-1} of data. One such measurement is the measurement of a photon with $p_T > 10$ GeV/c in association with a Z boson [13]. In order to separate out photon production from radiative photons from the lepton final state radiation, the photon is required to be a distance $\Delta R = \sqrt{\Delta\eta^2 + \Delta\phi^2} > 0.7$ from any lepton in the $Z + \gamma$ event. The resulting events

Table 2: Properties of Z + jets and W + jets

Measurement	Value($\pm(stat) \pm (sys)$)	Theory(Madgraph)
$\alpha(Z \to \mu^+\mu^-)$	$5.8 \pm 1.2 \pm 0.6$	4.8 ± 0.1
$\beta(Z \to \mu^+\mu^-)$	$-0.2 \pm 1.0 \pm 0.3$	0.4 ± 0.1
$\alpha(Z \to e^+e^-)$	$5.0 \pm 1.0 \pm 0.1$	5.0 ± 0.1
$\beta(Z \to e^+e^-)$	$0.7 \pm 0.8^{+0.3}_{-0.6}$	0.5 ± 0.1
$\alpha(W \to \mu\nu)$	$4.3 \pm 0.3 \pm 0.3$	5.2 ± 0.1
$\beta(W \to \mu\nu)$	$0.7 \pm 0.3 \pm 0.5$	0.2 ± 0.1
$\alpha(W \to e\nu)$	$4.6 \pm 0.4^{+0.2}_{-0.0}$	5.2 ± 0.1
$\beta(W \to e\nu)$	$0.5 \pm 0.4^{+0.2}_{-0.4}$	0.4 ± 0.1
$\sigma(Z \to \mu^+\mu^- + b)/\sigma(Z \to \mu^+\mu^- + j)$	$0.054 \pm 0.010 \pm 0.012$	0.043 ± 0.005
$\sigma(Z \to e^+e^- + b)/\sigma(Z \to e^+e^- + j)$	$0.046 \pm 0.008 \pm 0.011$	0.047 ± 0.005

yield a cross section measurement of $9.4 \pm 1.0(sys) \pm 0.6(stat) \pm 0.4(lumi)$ pb in accordance with the standard model prediction of 9.6 ± 0.4 pb.

4 Top Analyses

In this section we present all measurements performed with a top quark in the final state. Top quarks decay into a W boson and bottom quark. For $t\bar{t}$ production, identification of one of the W bosons is performed with an isolated lepton. The second W boson is measured through either its hadronic or leptonic decay. The presence of b-tagged jets further improves the purity of the selected dataset.

4.1 $t\bar{t}$ Cross Section In The Di-Lepton channel

The di-lepton cross section measurement is performed by requiring two isolated leptons and the presence of large $\not\!\!E_T$ [14]. To maximize separation with background the analysis is performed in jet multiplicity bins, where in each jet bin a separate $\not\!\!E_T$ selection and background estimation from Drell-Yan and QCD contributions is performed. Uncertainties result from the lepton reconstruction and resolution, as well as the b-tag efficiency and modelling of the signal shape. The result of this method can be found in figure 3. The result compares well with the NLO and partial NNLO prediction.

4.2 $t\bar{t}$ Cross Section In The Lepton+Jets Channel

The single lepton top quark cross section is performed through two methods by requiring a single high p_T lepton and either ≥ 3 jets [15] or the presence of a b-tag [16]. In the instance where there is a b-tag, the yield is determined by fitting in three dimensions the vertex mass distribution of the b-tagged jet, the jet multiplicity and the number of b-tagged jets. The fit simultaneously floats the jet energy scale,the b-tag efficiency, and the W+jets Q^2 scale so as to reduce the systematic uncertainty. The choice of fitting the three variables separtely disentangles the signal along with the individual backgrounds coming from W+light quark flavor, W+ heavy quark flavor production, and QCD. This method is additionally performed simultaneously in lepton flavor(e and μ).

The method where 3 or more jets are utilized is performed by simultaneously fitting the $\not\!\!E_T$ and the mass of the 3 jets. The fit is performed in both the electron and muon plus jets channel while separately floating the single top,W,Z,electron QCD and muon QCD contributions. The measurement parallels the cross section measurement where a b-tag is applied. Deviations in

this lepton+jets cross section measurement with the b-tagged measurement may indicate new physics.

The resulting combined cross section[17] from the two different channels (excluding the non b-tagged cross section) is $\sigma = 158 \pm 10(stat) \pm 15(sys) \pm 6(lumi)$pb. This value is within the uncertainty band of the NLO cross section, with an uncertainty comparable to that of the uncertainty on the partial NNLO cross section prediction. A comparison of the three cross section measurements is shown in figure 3, all three measurements are in close agreement amongst themselves and the predicted measurement.

Figure 3: Summary of various inclusive $t\bar{t}$ production cross sections. The inner error bars of the data points correspond to the statistical uncertainty. The thin error bars incorporate the systematic uncertainties and the brackets incorporate the luminosity uncertainty

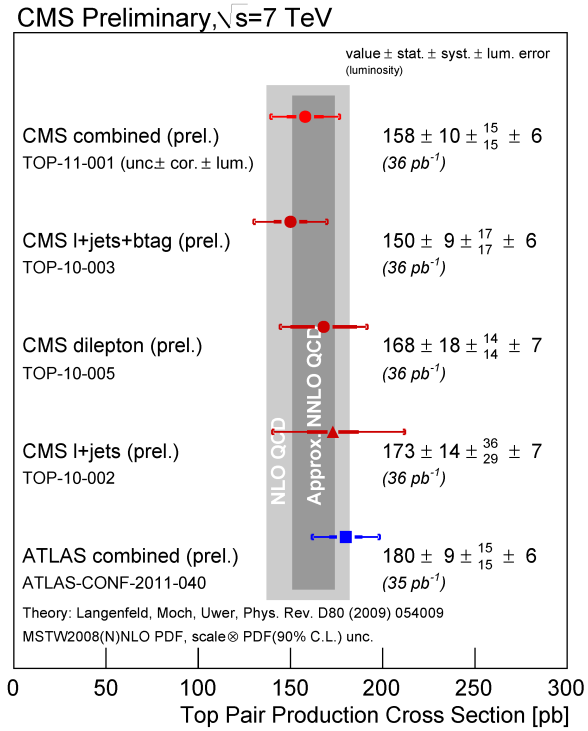

4.3 Top Quark Mass Measurement

The top quark mass measurement is performed in the di-lepton channel with two different techniques [18]. One technique relies on an assumption on the momentum distribution of the $t\bar{t}$ system along the beam axis. The other technique scans over the mass assumptions choosing the most likely mass assumption in accordance with lepton p_T distributions.

The resulting mass distributions from each technique are used to determine the top quark mass, which is found to be $m_t = 175.5 \pm 4.6(stat) \pm 4.6(sys)$ GeV/c^2. This measurement is in excellent agreement with both CDF and D0 measurements of the top quark mass.

4.4 Single Top Cross Section Measurement

The single top cross section measurement in the t-channel was performed using both a multivariate and a fitting technique [19]. In each case, a selection requiring an isolated lepton, at least one b-tag, and an additional jet is applied. In the fitting method, a selection explicitly requiring no more than one b-tag is additionally applied. The fitting method was performed by fitting

in two dimensions, the observable $cos\,(\theta_{\ell j})$, where $\theta_{\ell j}$ is the angle between the lepton and the non-b-tagged jet, and the pseudorapidity of the non b-tagged jet η_j. The multivariate analysis incorporated a boosted decision tree of 37 observables. The resulting output variable was fitted with templates.

The results are combined taking in the correlations. The final cross section measurement, $83.6 \pm 29.8(stat + sys) \pm 3.3(lumi)$, is consistent with the standard model prediction of $\sigma_{th} = 62.3^{+2.3}_{-2.4}$ pb. This is the first time the single top cross section measurement was performed without a multivariate analysis.

4.5 Top Charge Asymmetry Measurement

In light of the most recent measurements from the Tevatron reporting an excess in the top quark forward-backward asymmetry[20]($A_{FB} = 0.193 \pm 0.065(stat) \pm 0.024(sys)$), a measurement of the top quark charge asymmetry was performed by measuring the charge asymmetry of the top η observable, $\rho = |\eta_t| - |\eta_{\bar{t}}|$ [21]. The asymmetry is defined through the formula.

$$A_C = \frac{\rho_+ - \rho_-}{\rho_+ + \rho_-} \tag{3}$$

where ρ_+ designates the sign of the ρ variable. The measurement was performed on the same selection as used in the non b-tagged lepton+jets $t\bar{t}$ cross section analysis and then unfolded to the particle level. The measured value is found to be $A_C = 0.060 \pm 0.134(stat)^{+0.028}_{-0.025}(sys)$, which consistent with the standard model prediction $A_C = 0.011$.

5 Conclusions

In 2010, CMS has completed a large number of standard model measurements, which incorporate either electroweak bosons or top quarks. These measurements have all been found to be consistent with the standard model and in some cases these measurements have provided new constraints on standard model calculations, such as parton distribution functions, standard model couplings and NNLO differential calculations. In the course of these measurements a number of new techniques were developed, these techniques and further measurements will play a crucial role in the following years of LHC running.

References

1. CMS Collaboration, "The CMS experiment at the CERN LHC", JINST 3:S08004,2008.
2. CMS Collaboration, "Measurements of Inclusive W and Z Cross Sections in pp Collisions at $\sqrt{s}$ =7 TeV", JHEP 01(2011)080
3. CMS Collaboration, "Study of W and Z boson Production at $\sqrt{s}$ = 7 TeV", *CMS PAS* **EWK-10-005** (2011)
4. CMS Collaboration, "First Measurement of the Polarization of W Bosons with Large Transverse Momentum in W +Jets Events at a pp Collider", *CMS PAS* **EWK-10-014** (2011)
5. CMS Collaboration, "Differential Cross Section of Z boson", *CMS PAS* **EWK-10-010** (2011)
6. CMS Collaboration, "Measurement of the Drell-Yan cross section ($d\sigma/dM$)", *CMS PAS* **EWK-10-007** (2011)
7. A. Buckley, H. Hoeth, H. Lacker et al. "Systematic event generator tuning for the LHC", Eur. Phys. J. C65 (2010) 331-357
8. K. Melnikov and F. Petriello, "The W boson production cross section at the LHC through $O(\alpha_s^2)$", Phys. Rev. Lett. 96 (2006) 231803

9. CMS Collaboration, "Rates of Jets Produced in Association with W and Z Bosons", *CMS PAS* **EWK-10-012** (2011)
10. F. Maltoni and T. Stelzer, "MadEvent: Automatic event generation with MadGraph", JHEP 02 (2003) 027
11. F. A. Berends,W. T. Giele, H. Kuijf et al., "Multi-jet production in W, Z events at p anti-p colliders", Phys. Lett. B224 (1989) 237.
12. CMS Collaboration, "Observation of Z+b, Z→ee,$\mu\mu$ with CMS at $\sqrt{s}$ = 7 TeV", *CMS PAS* **EWK-10-015** (2011)
13. CMS Collaboration, "Measurement of Wγ and Zγ production in pp collisions at $\sqrt{s} = 7$ TeV", *CMS PAS* **EWK-10-008** (2011)
14. CMS Collaboration, "Measurement of the top-quark pair-production cross section in the dilepton channel at 7 TeV at $\sqrt{s} = 7$ TeV", *CMS PAS* **TOP-10-005** (2011)
15. CMS Collaboration, "Measurement of the $t\bar{t}$ Pair Production Cross Section at $\sqrt{s} = 7$ TeV using the Kinematic Properities of Lepton + Jet Events",*CMS PAS* **TOP-10-002** (2011)
16. CMS Collaboration, "Measurement of the $t\bar{t}$ Pair Production Cross Section at $\sqrt{s} = 7$ TeV using b-quark Jet Identification Techniques in Lepton + Jet Events", *CMS PAS* **TOP-10-003** (2011)
17. CMS Collaboration, "Combination of top pair production cross sections in pp collisions at $\sqrt{s} = 7$ TeV and comparisons with theory", *CMS PAS* **TOP-11-001** (2011)
18. CMS Collaboration, "First measurement of the the top-quark mass in the dilepton channel in pp collisions at $\sqrt{s} = 7$ TeV", *CMS PAS* **TOP-10-006** (2011)
19. CMS Collaboration, "Measurement of single top t-channel cross section in pp collisions at $\sqrt{s} = 7$ TeV", *CMS PAS* **TOP-10-008** (2011)
20. CDF Collaboration, "Measurement of the Forward-Backward Asymmetry in Top Pair Production in 3.2/fb of ppbar collisions at $\sqrt{s} = 1.96$ TeV", Conf. Note 9724 (March 2009)
21. CMS Collaboration, "Measurement of the charge asymmetry in top quark pair production with the CMS experiment", *CMS PAS* **TOP-10-010** (2011)

Single W and Z boson production properties and asymmetries

Mika Vesterinen
The School of Physics and Astronomy, The University of Manchester, Oxford Road, Manchester, M13 9PL, England.

Recent analyses of single W and Z boson production properties and asymmetries from the CDF and DØ experiments at the Fermilab Tevatron are reported. For W boson production, measurements of the production and lepton charge asymmetries are presented. For Z/γ^* production, the following measurements are presented: $d\sigma/dy$, $(1/\sigma)(d\sigma/dp_T)$, $(1/\sigma)(d\sigma/d\phi^*_\eta)$, lepton angular coefficients, and A_{FB} with extraction of $\sin^2\theta_W$ and the light quark couplings to the Z. Most of these measurements are in good agreement with QCD predictions.

1 Introduction

Production of electroweak vector bosons at hadron colliders provides a rich testing ground for predictions of the Standard Model. The production cross sections and distributions are sensitive to higher order QCD corrections, and to the parton distribution functions (PDFs). Leptonic (involving electrons and muons rather than taus) final states are experimentally convenient, due to the relatively low background rates and straightforward triggering on single (or pairs of) high transverse momentum, p_T, leptons.

2 W boson charge asymmetry

The production of W bosons at the Tevatron is mostly via the annihilation of valence light quarks; for example the annihilation of a u from a proton with a $\bar{d}$ from an antiproton to produce a W^+. It is well known that $u(\bar{u})$ quarks tend to carry a larger fraction (x) of the $p(\bar{p})$ momentum than $d(\bar{d})$ quarks. For the process $p\bar{p} \to W$, this implies a preferred boost of W^+s along the *proton* direction, and along the *antiproton* direction for W^-s. The W boson production asymmetry is defined as

$$A(y_W) = \frac{N^+(y_W) - N^-(y_W)}{N^+(y_W) + N^-(y_W)}$$

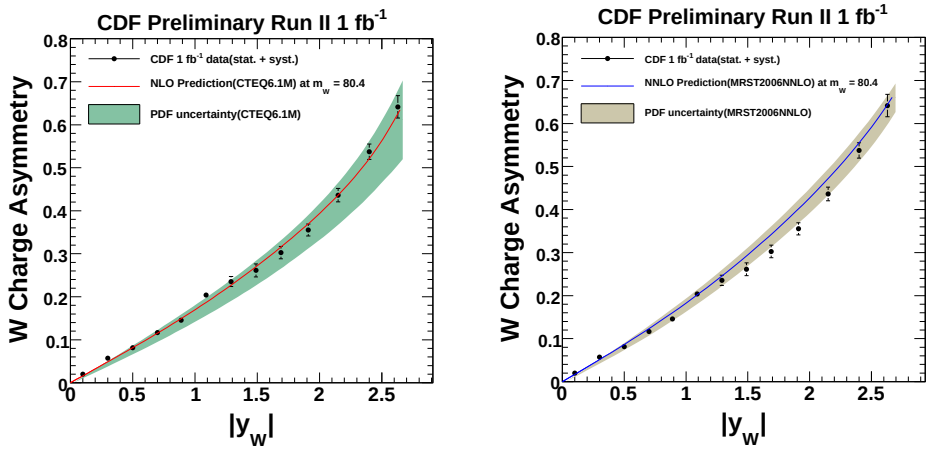

Figure 1: Comparison of the measured W boson charge asymmetry from CDF with (left) a NLO QCD prediction with CTEQ 6.6 PDFs, and (right) a NNLO QCD prediction with MRST2008 PDFs.

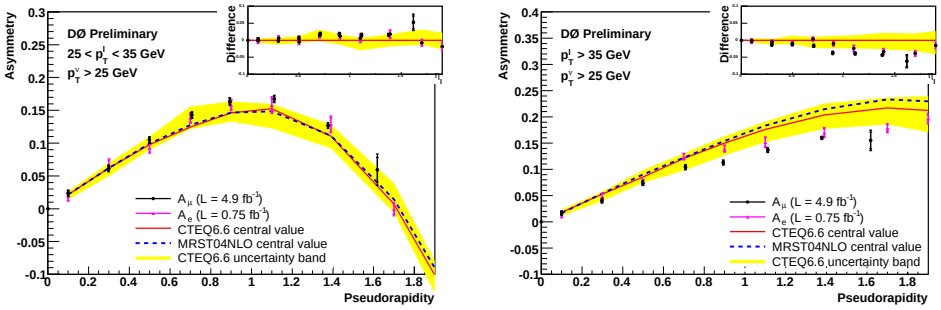

Figure 2: Comparison of the measured muon charge asymmetry from DØ with NLO QCD predictions for (left) $20 > p_T > 35$ GeV, and (right) $p_T > 35$ GeV.

where y_W is the boson rapidity, and is primarily sensitive to the slope of the ratio of u and d quark PDFs as a function of x. Unfortunately, y_W is unobservable due to the unknown momentum of the neutrino along the beam direction. A novel solution suggested by Bodek *et al* [1] involves constraining the invariant mass of the charged lepton and neutrino to the known W boson mass, leaving two solutions for y_W. Each of these is assigned a weight assuming the known $V-A$ structure of the weak decay vertex. This method was employed in a measurement by CDF in the $W \to e\nu_e$ channel using 1 fb^{-1} of data [2]. Figure 2 shows that the measured $A(y_W)$ agrees well with QCD predictions at both NLO and NNLO accuracies.

An alternative approach is to measure the asymmetry as a function of the *observable* lepton pseudorapidity, η_l. Unfortunately, the lepton charge asymmetry, $A(\eta_l)$, is less sensitive to the production asymmetry and thus also the PDFs. The $V-A$ structure of the decay vertex implies that the charged lepton tends to head backwards in the W boson rest frame, i.e. cancelling the production asymmetry; particularly at low lepton p_T and/or large lepton η. Nevertheless, the two approaches provide complementary information. The DØ Collaboration recently measured $A(\eta_l)$ using 4.9 fb^{-1} of data in the $W \to \mu\nu_\mu$ channel [3], and compared to NLO QCD predictions as shown in figure 2. The measurement is performed in two bins of muon p_T which partially disentangles the production and decay asymmetries. Interestingly, this measurement does not agree so well with the QCD predictions, particularly at larger muon p_T and pseudorapidity.

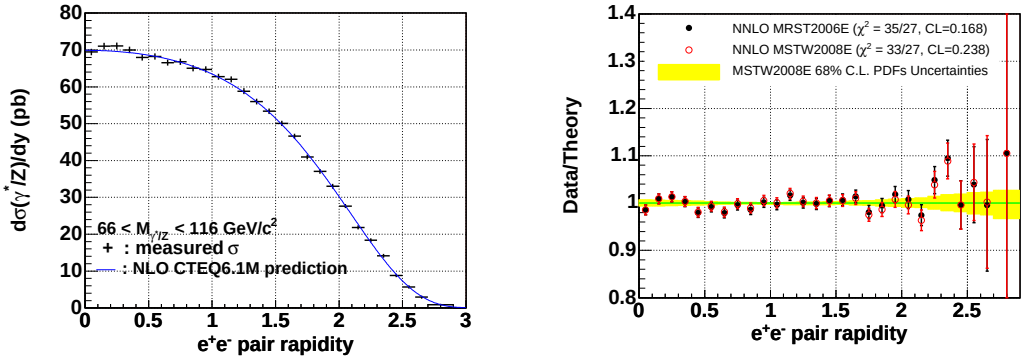

Figure 3: Left: measured $d\sigma/dy$ from CDF compared to a NLO QCD prediction. Right: ratio of the data to NNLO QCD predictions, where the yellow band represents the uncertainty on the prediction due to the PDFs.

3 Z/γ^* rapidity distribution

The rapidity, y, of the dilepton system in Z/γ^* decays is directly related to the x of the two partons: $x_{1,2} = (M_{ll}/\sqrt{s})e^{\pm y}$, where M_{ll} is the dilepton invariant mass, and $\sqrt{s}$ is the centre of mass energy of the collider. Events with large rapidity correspond to the annihilation of a low-x parton and a high-x parton. Thus, a measurement of $d\sigma/dy$ provides additional information on the PDFs that is complementary to the W charge asymmetry. CDF has measured $d\sigma/dy$ in the e^+e^- decay channel using 1 fb^{-1} of data [4]. Figure 3 shows that the data are in good agreement with NLO/NNLO QCD predictions, over the full range of probed rapidities. The Z/γ^* production cross section is measured as 257 ± 16 pb, also in agreement with NLO/NNLO QCD predictions.

4 Z/γ^* transverse momentum distribution

At lowest order in Z/γ^* production, the dilepton system has zero momentum transverse to the beam direction, p_T. Higher order QCD corrections include radiation of gluons from the one or both of the annihilating quarks. Alternatively, one or both of the annihilating quarks can result from a gluon splitting into a pair of quarks. In addition, the partons may carry some intrinsic transverse momentum within the colliding hadrons. A good understanding of these effects is paramount for many physics analyses at hadron colliders; for example the W boson mass measurement, which relies on a precise prediction of the lepton kinematics for different mass hypotheses.

The DØ Collaboration has recently measured the shape of the p_T distribution in the $\mu^+\mu^-$ final state using 1.0 fb^{-1} of data [5]. For $p_T > 10$ GeV, NLO QCD is able to describe the data reasonably well, whilst resummation is needed at lower p_T, as implemented at approximate leading-log (LL) in various Monte Carlo event generators, and at next-to-LL in the ResBos program [6]. Compared to the data, ResBos underestimates the cross section for larger p_T ($p_T >$ 50 GeV), and varying levels of agreement are observed for the different event generators.

This and other recent measurements of the Z/γ^* p_T distribution have been dominated by uncertainties in correcting for detector resolution and efficiency. An alternative approach is to measure the distribution of a variable that is less sensitive to these effects, such as a_T [7], or more recently ϕ^* [8] defined as $\phi^*_\eta = \tan[(\pi - \Delta\phi)/2] \sin\theta^*$, where $\Delta\phi$ is the azimuthal opening angle between the two leptons, and $\cos\theta^* = \tanh[(\eta^{(-)} - \eta^{(+)})/2]$, with $\eta^{(-)}$ being the pseudorapidity of the negatively charged lepton. The variable ϕ^*_η is sensitive to the same physics as the p_T, but is determined exclusively from lepton angles resulting in far better experimental resolution. Furthermore, ϕ^*_η is less correlated than the p_T, with efficiencies of typical Z/γ^* event selection

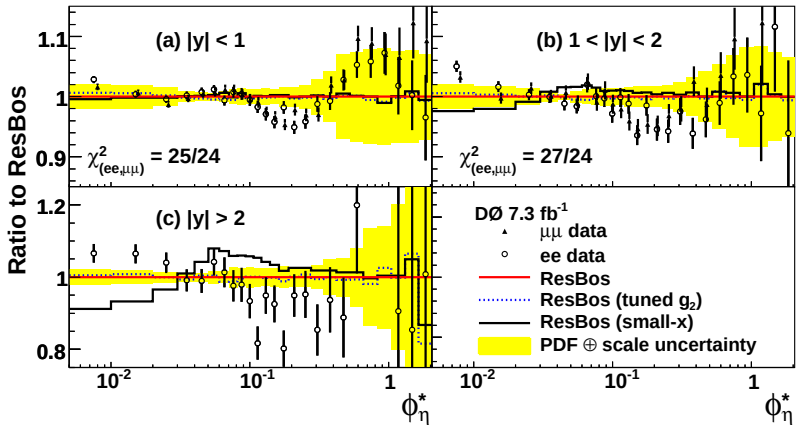

Figure 4: Ratio of measured $(1/\sigma)(d\sigma/d\phi^*_\eta)$, and alternative ResBos predictions, to the nominal ResBos prediction. The yellow band around the ResBos prediction represents the uncertainty due to renormalisation and factorisation scale variation added in quadrature with PDF parameter variations.

requirements; e.g. on lepton isolation.

The DØ Collaboration recently measured $(1/\sigma)$ $(d\sigma/d\phi^*_\eta)$ using 7.3 fb^{-1} of data, in the e^+e^- and $\mu^+\mu^-$ decay channels, and in three bins of dilepton rapidity [9]. The measured distributions are compared to predictions from the ResBos program in figure 4, with a modest level of agreement.

ResBos includes a non-perturbative form factor which has been tuned to simultaneously describe low-Q^2 Drell-Yan data, and Tevatron Run I Z/γ^* data [10]. Floating the g_2 parameter, which controls the width of the form factor, does not substantially improve the agreement, as represented by the blue line in figure 4. Recently, the x-dependence of the non perturbative form factor has received some attention, and an additional "small-x broadening" was suggested to describe SIDIS data from HERA [11], which would have significant effects at the LHC [12]. The $|y| > 2$ data clearly disfavour the small-x modification, which is represented by the black line in figure 4.

5 Z/γ^* lepton angular distributions and forward-backward asymmetry

The angular distributions of the leptons from Z/γ^* decays are often considered in the Collins-Soper frame [13], and are predicted by perturbative QCD [14] to take the following form:

$$\begin{aligned}\frac{d\sigma}{d\cos\theta d\phi} \quad &\propto \quad (1+\cos^2\theta) \\ &+ \quad \tfrac{1}{2}A_0(1-3\cos^2\theta) + A_1\sin 2\theta\cos\phi \\ &+ \quad \tfrac{1}{2}A_2\sin^2\theta\cos 2\phi + A_3\sin\theta\cos\phi \\ &+ \quad A_4\cos\theta + A_5\sin^2\theta\sin 2\phi \\ &+ \quad A_6\sin 2\theta\sin\phi + A_7\sin\theta\sin\phi\end{aligned}$$

where θ and ϕ are the polar and azimuthal angles respectively [13]. The coefficients, A_i, are dependent on the kinematics of the dilepton system; in particular the p_T. The A_5, A_6, A_7 parameters are calculated to be negligible [14]. The $A_4(\cos\theta)$ term generates an asymmetry in the $\cos\theta$ distribution, and is due to the different couplings of the Z boson to left- and right-handed fermions, whose relative strength is determined by the value of $\sin^2\theta_W$.

The forward-backward asymmetry is defined as $A_{FB} = (\sigma_F - \sigma_B)/(\sigma_F + \sigma_B)$, where σ_F and σ_B are the cross sections for forward ($\theta > 0$) and backward ($\theta < 0$) events respectively. Interference between the Z and the γ^* diagrams leads to an enhanced asymmetry for masses away from the Z pole. At higher invariant masses, A_{FB} is sensitive to the presence of additional

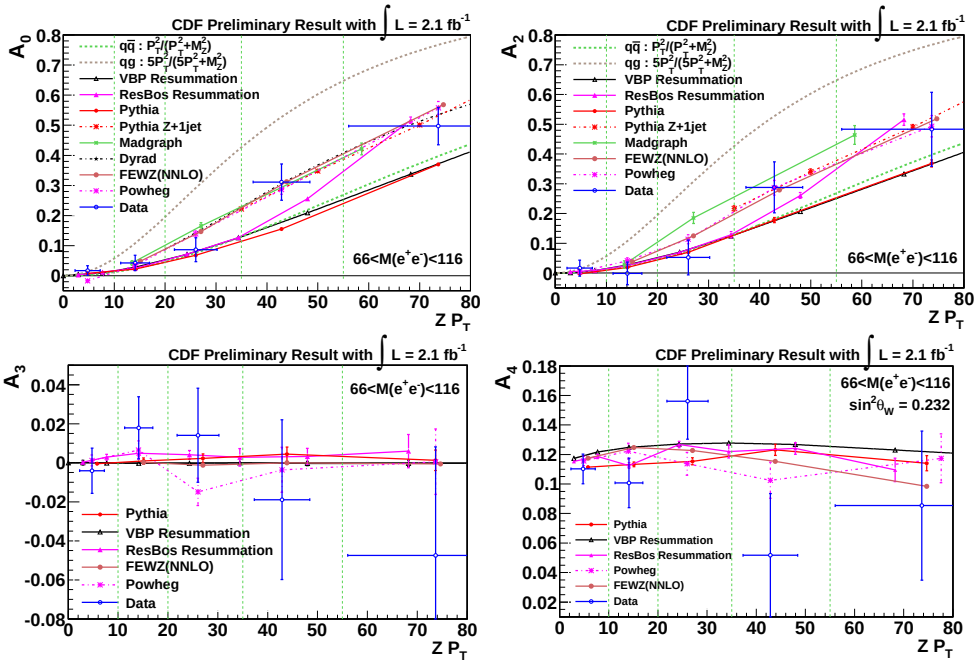

Figure 5: Measured angular coefficients as a function of dilepton p_T, compared to various QCD predictions.

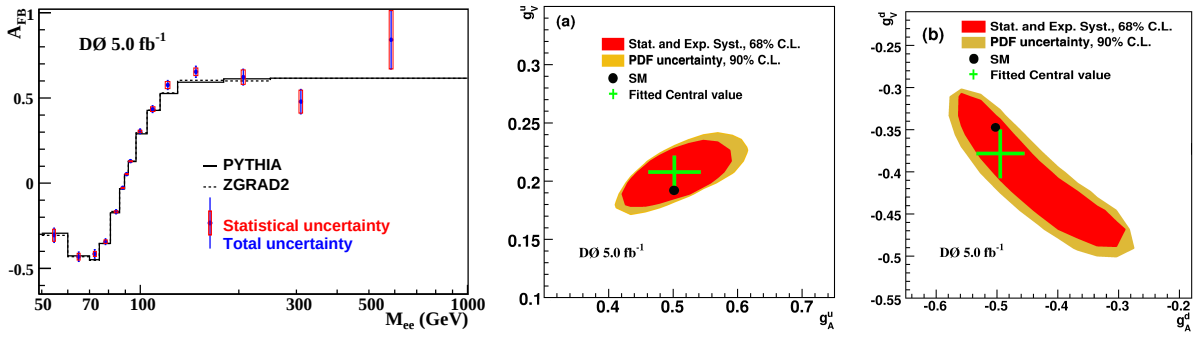

Figure 6: Left: measured A_{FB} compared to Standard Model predictions. Middle and right: measured u and d quark couplings to the Z.

gauge bosons. A_{FB} is sensitive to the couplings of the light quarks to the Z, which are relatively poorly constrained by measurements at LEP.

The CDF collaboration have measured A_0, A_2, A_3 and A_4 as a function of the dilepton p_T, using 2.1 fb^{-1} of data in the e^+e^- decay channel [15]. The data are compared to various QCD predictions in figure 5. The A_4 parameter (multiplying the $\cos\theta$ term) is directly related to the A_{FB}, and thus also the value of $\sin^2\theta_W$. The A_4 measurement is translated into a measurement of $\sin^2\theta_W = 0.2329 \pm 0.0008^{+0.001}_{-0.0009}$, where the first uncertainty is experimental and the second is theoretical.

The DØ Collaboration has recently measured A_{FB} as a function of the dilepton invariant mass, using 6.1 fb^{-1} of data, in the e^+e^- channel [16]. Figure 6 shows that the measurement is in reasonable agreement with Standard Model predictions. In addition, the couplings of the u and d quarks to the Z are extracted as shown in figure 6. A value of $\sin^2\theta_W$ is extracted as 0.2309 $\pm$ 0.001, in good agreement with the world average.

6 Conclusions

Recent analyses of single W and Z boson production properties and asymmetries from the CDF and DØ experiments at the Fermilab Tevatron are presented. A measurement of the W boson production asymmetry in $W \to e\nu_e$ events from CDF is in good agreement with QCD predictions. Conversely, a measurement of the muon charge asymmetry in $W \to \mu\nu_\mu$ events from DØ is in modest agreement with QCD predictions. The Z/γ^* production cross section, and rapidity distribution is measured in the e^+e^- decay channel by CDF, and agrees well with QCD predictions. The shape of the Z/γ^* transverse momentum distribution is measured using 1 fb^{-1} of data in the $\mu^+\mu^-$ decay channel by DØ, in reasonable agreement with various QCD predictions. The ϕ^*_η variable was recently proposed as an alternative variable for studying the transverse momentum. A measurement of the shape of the ϕ^*_η distribution from DØ using 7.3 fb^{-1} of data, in the e^+e^- and $\mu^+\mu^-$ decay channels is in modest agreement with a state-of-the-art QCD prediction. Four coefficients describing the angular distributions of the decay leptons from Z/γ^* decays are studied in the e^+e^- channel by CDF using 2.1 fb^{-1} of data. DØ measures A_{FB} as a function of the dilepton invariant mass, using 5 fb$^-$1 of data in the e^+e^- decay channel, in agreement with a QCD prediction. This measurement is used to extract $\sin^2\theta_W = 0.2309 \pm 0.001$, and the most precise determination of the Z boson couplings to u and d quarks.

References

1. A. Bodek, Y. Chung, B.-Y. Han, K. McFarland, E. Halkiadakis, *Phys. Rev.* D **77**, 111301(R) (2008).
2. CDF Collaboration, T. Aaltonen *et al*, *Phys. Rev. Lett.* **102**, 181801 (2009).
3. DØ Collaboration, V. M. Abazov *et al*, 5976-CONF (2009).
4. CDF Collaboration, T. Aaltonen *et al*, *Phys. Lett.* B **692**, 232 (2010).
5. DØ Collaboration, V. M. Abazov *et al*, *Phys. Lett.* B **693**, 522 (2010).
6. C. Balazs, C.-P. Yuan, *Phys. Rev.* D **56**, 5558-5583 (1997).
7. M. Vesterinen, T. R. Wyatt, *Nucl. Instrum. Methods* A **602**, 432-437 (2009).
8. A. Banfi, S. Redford, M. Vesterinen, P. Waller, T. R. Wyatt, *Eur. Phys. Jour.* C **71**, 1600 (2011).
9. DØ Collaboration, V. M. Abazov *et al*, *Phys. Rev. Lett.* **106**, 122001 (2011).
10. F. Landry *et al*, *Phys. Rev.* D **67**, 073016 (2003).
11. P. Nadolsky, D. R.Stump, C.-P. Yuan, *Phys. Rev.* D **64**, 114011 (2011).
12. S. Berge, P. Nadolsky, F. Olness, C.-P. Yuan, *Phys. Rev.* D **72**, 033015 (2005).
13. J. C. Collins and D. E. Soper, *Phys. Rev.* D **16**, 2219 (1977).
14. E. Mirkes and J. Ohnemus, *Phys. Rev.* D **50**, 5692 (1994); *Phys. Rev.* D **51**, 4891 (1995).
15. CDF Collaboration, T. Aaltonen *et al*, arXiv:1103.5699v3 (2011).
16. DØ Collaboration, V. M. Abazov *et al*, arXiv:1104.4590 (2011).

MEASUREMENTS OF STANDARD MODEL PROCESSES AT ATLAS

J. ALISON [a]
Department of Physics, University of Pennsylvania
209 South 33rd st. Philadelphia Pa., United States

With over 45 pb^{-1} of 7 TeV pp collisions recorded, the ATLAS Standard Model physics program is well under way. These proceedings survey the latest tests of the Standard Model at this unprecedented energy scale. An overview of recent ATLAS results is given. Measurements of the W boson charge asymmetry, di–boson production, and single top–quark production are highlighted.

1 Introduction

Measurements of Standard Model (SM) processes have been the flagship of the ATLAS [1] physics program in 2010. These measurements cover a wide range of topics from soft QCD measurements of particle multiplicities and the total pp inelastic cross section, through QCD measurements of inclusive jet production, photon production, and top-quark pair production, to electro-weak measurements of vector–boson properties, di–boson production, and single top–quark production.

In addition to being a rich source of physics, Standard Model processes serve as standard candles from which the detector performance can be understood. The expected SM signals can be used to commission the detector and refine analysis techniques in preparation for the unexpected. The physics objects used in SM measurements - charged leptons, missing transverse energy, photons, and jets - are critical for all physics analyses. The understanding of these objects, gained initially through SM measurements, is of wide–ranging importance for all the physics done at ATLAS.

These proceedings will focus on recent electro–weak measurements. The measurement of the W boson charge asymmetry is presented in Section 2, followed by the measurement of the $W\gamma$ and $Z\gamma$ cross sections in Section 3. Section 4 presents the measurement of the WW production cross section and results on single top–quark production are given in Section 5. As can be seen in Figure 1, the electro–weak measurements presented in these proceedings span several orders of magnitude in production cross section. The varying amounts of signal and sources of background across this broad spectrum pose unique challenges to the different analyses presented here.

2 W boson Charge Asymmetry

The W boson charge asymmetry is particularly interesting because it is sensitive to the parton distributions functions, PDFs, of the proton. A precision measurement of the asymmetry can

[a] on behalf of the ATLAS Collaboration

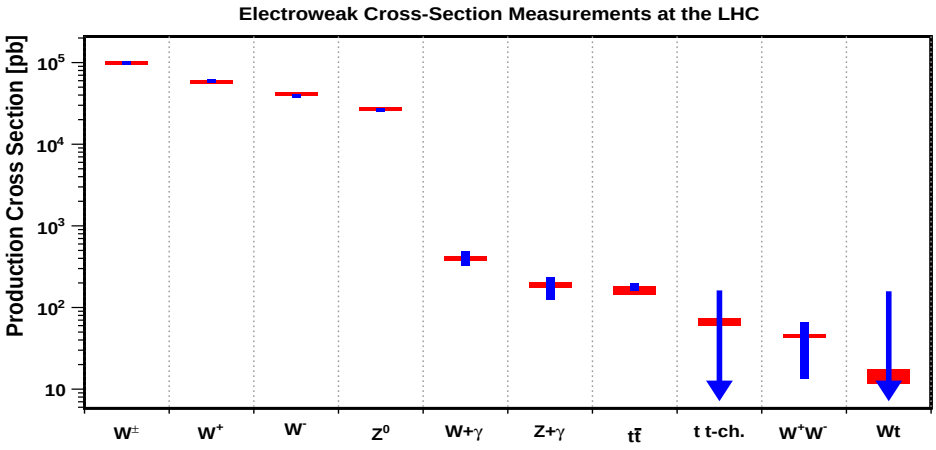

Figure 1: Electro–weak production cross sections at the LHC. Theoretical predictions are shown in red, the corresponding ATLAS measurements are given in blue. See references [2-6] for cross section measurements.

be used to constrain the PDFs of the valance quarks in the $10^{-3} - 10^{-4}$ region of momentum fraction. [7]

The W boson charge asymmetry has been measured by ATLAS in the muon decay channel as a function of the muon pseudo–rapidity, η_μ. [7] The asymmetry, defined as

$$A_\mu = \frac{\frac{\mathrm{d}\sigma_{W_\mu^+}}{\mathrm{d}\eta_\mu} - \frac{\mathrm{d}\sigma_{W_\mu^-}}{\mathrm{d}\eta_\mu}}{\frac{\mathrm{d}\sigma_{W_\mu^+}}{\mathrm{d}\eta_\mu} + \frac{\mathrm{d}\sigma_{W_\mu^-}}{\mathrm{d}\eta_\mu}}, \tag{1}$$

consists of the ratio of production cross sections, which has the advantage that many of the experimental uncertainties cancel. The measurement was performed by selecting events containing reconstructed muons with transverse momentum, p_T, above 20 GeV, and missing transverse energy, E_T^{miss}, above 25 GeV. The events were additionally required to contain a reconstructed W boson candidate with a transverse mass, m_T of more than 40 GeV. This selection led to 1.3×10^5 W boson candidates, with an estimated background of seven percent predominantly from background from other electro–weak processes.

The measured W boson asymmetry is shown as a function muon pseudo–rapidity in Figure 2(a). The asymmetry rises with η_μ, as predicted by theory, with statistical and systematic uncertainties that are comparable in each η_μ-bin. The limiting systematic uncertainties come from uncertainties on the trigger and muon identification efficiencies, which vary across η_μ from 1–7%. These systematics are currently limited by statistics in control regions and will decrease with further data taking.

The predicted W boson asymmetry from several global fits to the proton PDF are also shown in Figure 2(a). The current experimental uncertainty of the ATLAS measurement is already comparable to those of the global fits. Future measurements of the W boson asymmetry will constrain the proton PDFs.

3 $W\gamma$ and $Z\gamma$ Cross Sections

ATLAS has performed the measurement of the $W\gamma$ and $Z\gamma$ cross sections in the leptonic decay channels of the W and Z bosons [3] [b]. The measurement of these $W\gamma$ and $Z\gamma$ processes provides

[b] Here, and in the rest of these proceedings, the leptonic decay channels only refer to the decays of W or Z bosons to electrons or muons, including the decays to electrons and muons through τs. Decays to hadronicaly decaying τs have been neglected.

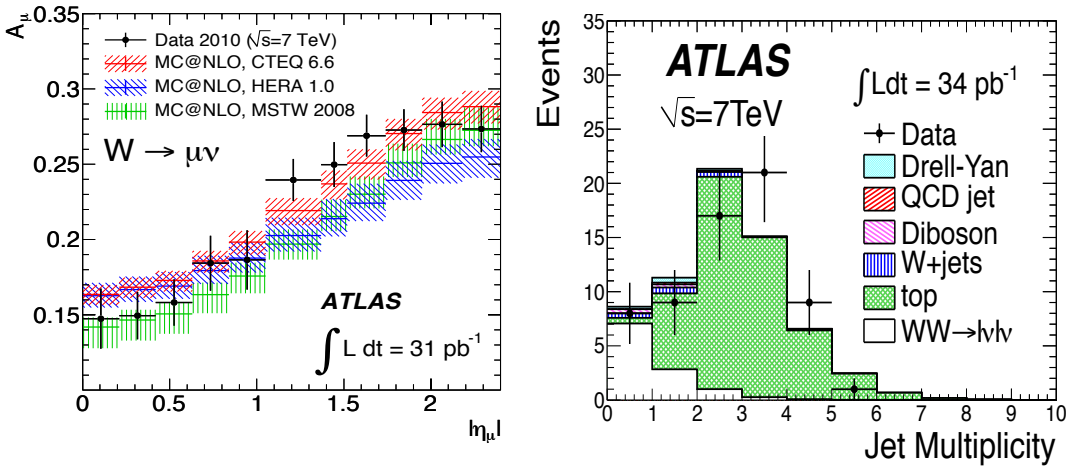

(a) (b)

Figure 2: (a) The W boson asymmetry as a function of muon pseudo–rapidity.[7] The measurement is shown in black along with theoretical predictions from several parametrizations of the parton distribution function. (b) The jet multiplicity distribution for events satisfying the di–lepton plus E_T^{miss} selection in the WW cross section analysis.[6] The zero–jet bin is used for the signal extraction.

a test of the electro–weak model. A photon can be produced in association with a W boson or a Z boson through the initial state radiation (ISR) of a photon off of an incoming quark, or by the final state radiation (FSR) of a photon off of the W boson or Z boson decay products. The $W\gamma$ process can also be produced through an additional diagram in which the photon is directly radiated from the W boson. This diagram is sensitive to the triple gauge coupling (TGC) predicted by the Standard Model.

Events were selected containing a W or Z boson candidate and an isolated reconstructed photon with transverse energy, E_T, greater than 15 GeV. The W boson candidates were required to have an electron or muon with E_T greater than 20 GeV, E_T^{miss} greater than 25 GeV, and m_T above 40 GeV. Z boson candidates were required to have two electrons or muons, each with E_T greater than 20 GeV, and having an invariant mass above 40 GeV. The reconstructed photons were required to be well isolated and to be separated from the reconstructed lepton by more than 0.7 in ΔR.[c] The event yields and estimated backgrounds are given in Tables 1 and 2. The W+jet background in the $W\gamma$ analysis is derived from control regions in the data.

$W\gamma$	electron-channel	muon-channel
Event Yield	95	97
W boson + jet Bkg	16.9 ± 5.3 ± 7.3	16.9 ± 5.3 ± 7.4
EW Bkg	10.3 ± 0.9 ± 0.7	11.9 ± 0.8 ± 0.8

Table 1: $W\gamma$ yields and background estimates. The W+jet background is derived from control regions in the data, whereas the remaining electro–weak background is taken from simulation.

The results of the $W\gamma$ and $Z\gamma$ cross section measurements are presented in Tables 3 and 4. The limiting systematic uncertainties are from uncertainties associated to the photon reconstruction and identification, uncertainties on the background predictions, and uncertainties associated with the signal acceptance. The measured cross sections are in good agreement with the NLO SM prediction. Future measurements of the $W\gamma$ and $Z\gamma$ processes will constrain new physics in

[c] ΔR^2 is defined as $\Delta R^2 = \Delta\phi^2 + \Delta\eta^2$, where $\Delta\phi(\Delta\eta)$ is the difference in $\phi(\eta)$ between the photon and the lepton.

$Z\gamma$	electron-channel	muon-channel
Event Yield	25	23
Background	3.7 ± 3.7	3.3 ± 3.3

Table 2: $Z\gamma$ yields and background estimates. The background estimates are taken from simulation.

anomalous TGCs.

$W\gamma$	Cross Section [pb]
e-channel	48.9 ± 6.6 (stat) ± 8.3 (sys) ± 1.7 (lumi)
μ-channel	38.7 ± 5.3 (stat) ± 6.4 (sys) ± 1.3 (lumi)
SM NLO Prediction	42.1 ± 2.7 (sys)

Table 3: The measured $W\gamma$ cross sections in electron and muon channel compared to the SM NLO predictions. The cross sections are reported for $E_T^\gamma > 15$ GeV and $\Delta R(l,\gamma) > 0.7$.

$Z\gamma$	Cross Section [pb]
e-channel	9.0 ± 2.5 (stat) ± 2.1 (sys) ± 0.3 (lumi)
μ-channel	5.6 ± 1.4 (stat) ± 1.2 (sys) ± 0.2 (lumi)
SM NLO Prediction	6.9 ± 0.5 (sys)

Table 4: The measured $Z\gamma$ cross sections in electron and muon channel compared to the SM NLO predictions. The cross sections are reported for $E_T^\gamma > 15$ GeV and $\Delta R(l,\gamma) > 0.7$.

4 *WW* Cross Section

Similar to the $W\gamma$ and $Z\gamma$ processes, another process which tests the electro–weak model is WW di–boson production. The WW final state is produced primarily through quark annihilation at the LHC, and includes a diagram sensitive to the WWZ TGC predicted by the SM. In addition to being sensitive to new physics through anomalous TGCs, the WW process is also important because it is the dominant background to searches for the Higgs boson in which the Higgs decays to pairs of W bosons.

ATLAS has performed the WW cross section measurement in the fully leptonic decay channels of the W's .[6] The event signature is two high–p_T isolated leptons with large missing energy. The jet multiplicity distribution of events satisfying the di–lepton plus E_T^{miss} selection[d] is shown in Figure 2(b).

The large remaining background from top–quark production is reduced by requiring that the event contain no reconstructed high p_T jets within the ATLAS acceptance. Eight signal candidates pass the full selection, one in the ee-channel, two in the $\mu\mu$-channel, and five in the $e\mu$-channel. The background estimation is provided in Table 5. The W+jet estimate is made from control regions in the data, whereas the remaining electro–weak backgrounds are taken from simulation and cross checked with data–driven procedures.

The measured WW cross section is $41^{+20}_{-16}(stat.) \pm 5(syst.) \pm 1(lumi.)$ pb, which is to be compared to the SM NLO prediction of 44 ± 3 pb. The dominant uncertainty on the cross section measurement is the statistical uncertainty on the number signal events, 44%. The

[d]The E_T^{miss} requirement is on the E_T^{miss} relative to the nearest lepton, $E_T^{miss,Rel}$. $E_T^{miss,Rel}$ is defined as $E_T^{miss,Rel} = sin(\phi) \times E_T^{miss}$, if $\phi < \frac{\pi}{2}$, otherwise $E_T^{miss,Rel} = E_T^{miss}$. ϕ is the angle between the missing energy and the nearest lepton. Events are required to have greater than 40 GeV relative E_T^{miss} in the ee and $\mu\mu$ channels, and greater than 25 GeV in the $e\mu$ channel.

Background	Events
Drell-Yan	0.23 ± 0.15 (stat) ± 0.17 (sys)
Top Quark	0.53 ± 0.12 (stat) ± 0.28 (sys)
W+jet	0.54 ± 0.32 (stat) ± 0.21 (sys)
Other Di-boson	0.38 ± 0.04 (stat) ± 0.04 (sys)
Total Bkg.	1.68 ± 0.37 (stat) ± 0.42 (sys)

Table 5: The estimated background for the WW cross section measurement. The background from W+jet was estimated from control regions in data, whereas the other background as estimated from simulation and cross checked by data-driven methods.

systematic uncertainty is 16%, and is dominated by uncertainties on the background modeling and signal acceptance. Further studies of the WW process will constrain new physics through measurements of anomalous TGCs and will be critical for understanding the background in the search for the Higgs boson.

5 Single Top-Quark Production

Single top-quark production is a direct probe of the CKM element V_{tb}. A precise measurement of the single top-quark cross section will provide a determination of V_{tb} without relying on unitarity constraints. Single top-quark production proceeds through three modes, each with a distinct experimental signature. The t-channel production has the largest expected contribution, ∼65 pb, and leads to a top quark and either a u or d-quark in the final state. Wt-production is expected to have the second largest contribution, ∼15 pb, and has a top-quark and a W boson in the final state. The s-channel is the smallest expected single top-quark contribution at the LHC, ∼4 pb, and produces a top quark and bottom quark in the final state. Each of the individual single top-quark production modes is sensitive to different forms of new physics. [8] With the 2010 data set, ATLAS has performed searches for the single top-quark in both the t-channel and Wt-production modes. [5]

The t-channel single top-quark analysis has been performed in the leptonic decay mode of the top-quark. Events were selected with one high-p_T electron or muon, large E_T^{miss}, and two jets, one of which was identified as a b-quark. The m_T of the lepton and E_T^{miss} system was required to be consistent with coming from a W boson and the reconstructed top-quark mass was required to be between 130 and 210 GeV. To enhance sensitivity, the analysis was performed separately in the positive and negative lepton channels. The event yield and background estimation of the t-channel analysis is given in Table 6. The background prediction was made using a combination of data-driven and simulation based estimates.

	l^+ channel	l^- channel
t-channel Expectation	10.3 ± 1.8	4.4 ± 0.8
Background Prediction	12.4 ± 3.3	8.8 ± 1.8
Event Yield	21	11

Table 6: Event yield and background estimation for the t-channel single top-quark analysis.

The result of the t-channel analysis is a signal significance of 1.6 σ. An excess over background that is consistent with t-channel production was seen. An upper limit of 162 pb was placed on the cross section at the 95% confidence level. The systematic uncertainties in the t-channel analysis are limited by uncertainties on the jet energy scale, b-quark identification, and background modeling. Many of these systematic uncertainties are limited by statistical uncertainties in control regions and are expected to improve with the addition of more data.

Single top-quark production in the Wt-channel gives rise to two W bosons in the final state: one directly produced with the top quark and the other the result of the top-quark decay. ATLAS has searched for Wt production in both the single and di-lepton final states. The single lepton Wt analysis is similar to the t-channel analysis with the additional requirement of extra jets in the event. The di-lepton analysis requires two high p_T leptons, large E_T^{miss}, and exactly one reconstructed jet in the final state. The event yields and background estimations for the Wt-channel analysis are given in Table 7. The background prediction was made using a combination of data-driven and simulation–based estimates.

	single lepton channel	di-lepton channel
Wt Expectation	12.6 ± 0.9	2.8 ± 0.5
Background Prediction	262.0 ± 22.8	12.7 ± 2.8
Event Yield	294	15

Table 7: Event yield and background estimation for the Wt single top-quark analysis.

The analysis of the Wt channel placed a combined upper limit of 158 pb on the Wt single top-quark cross section. As in the t-channel analysis the current systematic uncertainty is limited by uncertainties on the jet energy scale, b-quark identification, and background modeling, which are expected to improve with the addition of more data.

6 Conclusion

These proceedings have presented electro-weak measurements made by the ATLAS experiment with the 45 pb^{-1} of integrated luminosity collected during the 2010 data taking. These initial Standard Model measurements have allowed ATLAS to understand its detector performance and have provided the first electro-weak physics results at 7 TeV.

References

1. ATLAS Collaboration, The ATLAS Experiment at the CERN Large Hadron Collider, JINST 3 S08003. 2008.
2. ATLAS Collaboration, A measurement of the total W$^{\pm}$ and Z/γ^* cross sections in the e and μ decay channels and of their ratios in pp collisions at $\sqrt{s} = 7$ TeV with the ATLAS detector, ATLAS-CONF-2011-041, March, 2011.
3. ATLAS Collaboration, Measurement of Wγ and Zγ production in proton-proton collisions at sqrt(s) = 7 TeV with the ATLAS Detector, Submitted to Physics Letters B, June, 2011.
4. ATLAS, Collaboration, A combined measurement of the top quark pair production cross-section using dilepton and single-lepton final states, ATLAS-CONF-2011-040, March, 2011.
5. ATLAS Collaboration, Searches for Single Top-Quark Production with the ATLAS Detector in pp Collisions at sqrt(s) = 7TeV, ATLAS-CONF-2011-027, March 2011.
6. ATLAS Collaboration, Measurement of the W^+W^- cross section in $\sqrt{s} = 7$ TeV pp collisions with ATLAS. arXiv:1104.5225. Submitted to PRL. April, 2011.
7. ATLAS Collaboration, Measurement of the Muon Charge Asymmetry from W Bosons Produced in pp Collisions at $\sqrt{s} = 7$ TeV with the ATLAS detector, arXiv:1103.2929. Accepted by PLB. March, 2011.
8. T. Tait and C.P. Yuan, Single top quark production as a window to physics beyond the standard model, Phys. Rev. D 63 014018, arXiv:hep-ph/0007298, 2000.

Diboson measurements at the Tevatron

Martina Hurwitz for the CDF and D0 collaborations
Lawrence Berkeley National Laboratory, 1 Cyclotron Road, Mail Stop 50B-6222, Berkeley, CA, 94720, USA

Recent measurements of diboson production from the CDF and D0 experiments at the Tevatron are presented. Agreement with Standard Model predictions is observed in all measurements, and some are used to set limits on new physics. Searches in high-background topologies are also briefly described.

1 Introduction

Measurements of diboson production cross sections and other properties of diboson events are probes of the electroweak sector of the Standard Model (SM). Several models of new physics predict enhancements in the production rates of diboson events via anomalous triple gauge boson interactions [1] or from new resonances decaying to pairs of bosons. Diboson events are also relevant to the search for the Higgs boson at the Tevatron, as several sensitive channels in the Higgs search have topologies similar to those in diboson events. Therefore diboson events present a good place to test strategies employed in the Higgs search.

The cross sections of diboson ($Z\gamma$, $W\gamma$, WW, WZ, and ZZ) as well as other electroweak processes have been measured at the Tevatron by both the CDF and D0 experiments, and are summarized in Fig 1. The measurements, spanning orders of magnitude in production rates, agree both between the two experiments and with theoretical predictions. Recent work uses large data samples, sophisticated analysis techniques, and new decay topologies to improve the statistical and systematic precision of the measurements.

The measurements presented in these proceedings are performed based on data collected by the CDF [2] and D0 [3] experiments in $p\bar{p}$ collisions at $\sqrt{s} = 1.96$ TeV at the Tevatron. The integrated luminosity used in the measurements ranges up to 7.0 fb^{-1}.

2 Measurements of the ZZ production cross section

The production of ZZ events at the Tevatron is rare, with a predicted cross section of $\sigma(p\bar{p} \to ZZ) = 1.4 \pm 0.1$ pb at next-to-leading order [4]. In events where both Z bosons decay to charged leptons ($ZZ \to l^+l^-l^+l^-$), there is a very clean final state signature with two pairs of opposite-charge, same-flavor leptons. The backgrounds to this signal are negligible. Because of the low branching fraction for $Z \to l^+l^-$ and limited detector acceptance, the rate of detection of these events is extremely low. As a result, a large part of the experimental work in measurement of $ZZ \to l^+l^-l^+l^-$ consists of improving the lepton detection efficiency.

The D0 collaboration has analyzed 6.4 fb^{-1} of integrated luminosity, finding 10 events consistent with $ZZ \to l^+l^-l^+l^-$ where 9 signal events and 0.4 background events were expected [5].

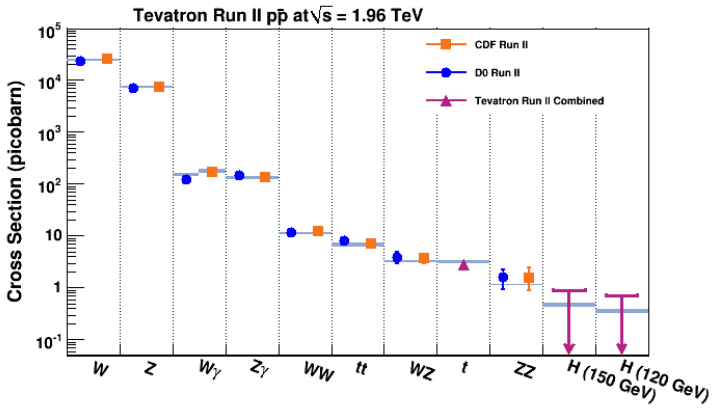

Figure 1: Measured and predicted production cross sections for several processes at the Tevatron.

Figure 2 (left) shows that the invariant mass of the two lepton pairs in the events is consistent with the decays of two Z bosons. The cross section for ZZ production was measured to be $1.33^{+0.50}_{-0.40}$(stat)$\pm$0.12(syst)$\pm$0.09(lumi) pb.

The CDF collaboration measured the ZZ cross section in $ZZ \to l^+l^-l^+l^-$ events using a data sample corresponding to 4.8 fb^{-1} of integrated luminosity [6]. Five events were observed, while 4.7 signal and < 0.1 background events were expected. The measured cross section was $1.56^{+0.80}_{-0.63}$(stat.)$\pm$0.25(syst) pb. Figure 2 (right) shows the correlation between the dilepton masses, with the signal region marked by the blue line.

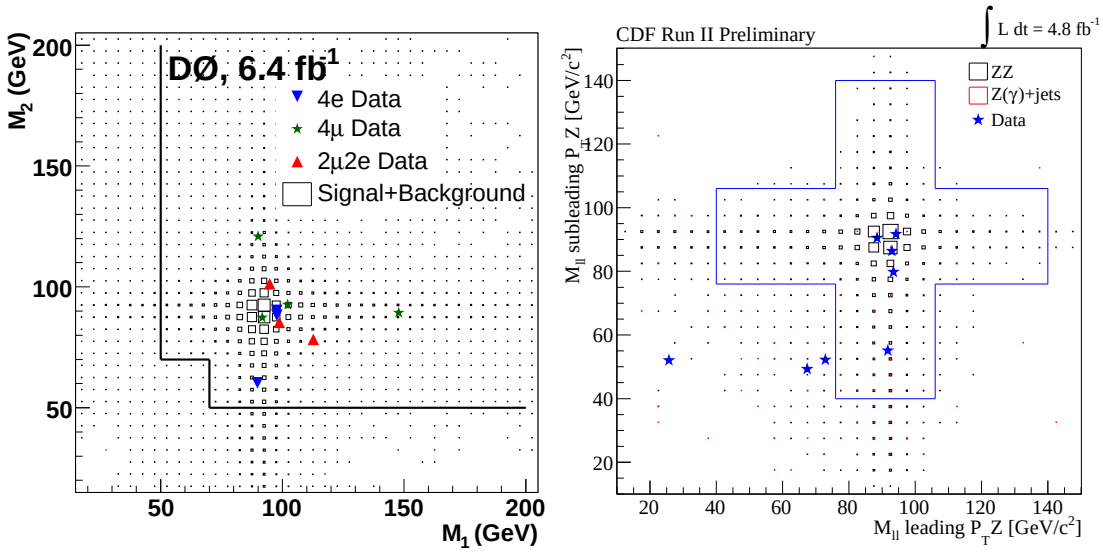

Figure 2: Scatter plots of the invariant mass distribution of two-lepton pairs in $ZZ \to l^+l^-l^+l^-$ candidate events at D0 (left) and CDF (right).

The CDF collaboration also recently presented a result for $ZZ \to l^+l^-\nu\nu$, detected in events with two opposite-charge leptons and large missing transverse energy ($\not\!\!E_T$) [7]. This final state topology suffers from a large background due to Drell-Yan production where an imbalance in the measurement leads to $\not\!\!E_T$. A requirement that the $\not\!\!E_T$ is nearly back-to-back with the Z boson in the transverse plane reduces the Drell-Yan background while retaining most of the signal. Even with this technique used to reduce the backgrounds, about 1100 background events and 50 signal events were expected in 5.9 fb^{-1}. A neural network, relying on variables like the

$\not\!\!E_T$ significance, is used to build a discriminant to separate signal from background. The neural network output for backgrounds and signal, with data superimposed, is shown in Figure 3. Using a fit to the neural network discriminant, the ZZ production cross section is measured to be $1.45^{+0.45}_{-0.42}(\text{stat.})^{+0.41}_{-0.30}(\text{syst.})$ pb. This result agrees with theoretical prediction as well as with the measured cross section in $ZZ \to llll$.

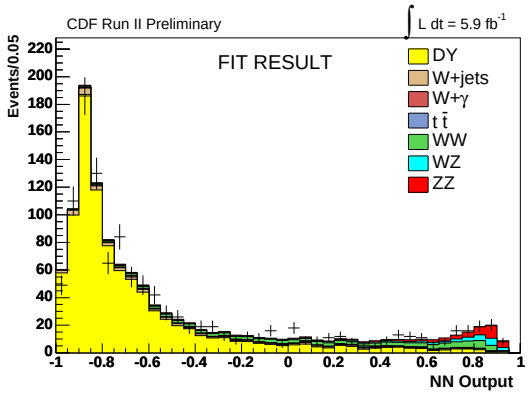

Figure 3: Fit to neural network output discriminant to determine the ZZ cross section in events with two charged leptons and large missing transverse energy.

3 $WZ \to l\nu ll$

The D0 collaboration measured the WZ production cross section with 4.1 fb^{-1} of integrated luminosity [8]. The measurement is based on the decay $WZ \to l\nu ll$, characterized by three high-p_T isolated leptons and missing transverse energy. The charged leptons from the Z boson decay are identified by finding the pair of opposite-charge, same-flavor leptons with an invariant mass closest to the mass of the Z boson. The backgrounds to WZ production in this final state topology are fairly small: six background and 23 signal events are expected. 34 candidate events are observed, leading to a measured cross section of $3.90^{+1.06}_{-0.90}$ pb. Anomalous WWZ couplings would enhance this cross section and lead to more W and Z bosons at high p_T. The distribution of the p_T of the Z boson matches the SM prediction well, as shown in Fig. 4(left), allowing stringent limits to be set on the WWZ coupling.

CDF also recently performed a measurement of the WZ production cross section in events with three charged leptons and $\not\!\!E_T$. The measurement was performed with 6 fb^{-1} and improved charged lepton acceptance with respect to previous measurements [9]. Figure 4 (right) shows the transverse mass of the W boson candidate formed from the non-Z lepton and the $\not\!\!E_T$. The shape is consistent with W decays in WZ events as described by simulation. The cross section is measured both with respect to the inclusive Z boson production cross section: $\sigma(p\bar{p} \to WZ)/\sigma(p\bar{p} \to Z) = (5.5 \pm 0.9) \times 10^{-4}$ and as an absolute number: $\sigma(p\bar{p} \to WZ) = 4.1 \pm 0.7$ pb. Both of these results are in good agreement with theoretical predictions. The systematic uncertainty on the WZ cross section is reduced when it is measured with respect to the inclusive Z production cross section.

4 $W\gamma \to \mu\nu\gamma$

The D0 collaboration used events with a muon, a photon, and large $\not\!\!E_T$ to study $W\gamma$ production [10]. The cross section for events with $p_T^\gamma > 8$ GeV/c and $\Delta R_{\mu\gamma} > 0.7$ was measured to be $15.2 \pm 0.4(\text{stat}) \pm 1.6(\text{syst})$ pb, in agreement with the SM prediction of 16.0 ± 0.4 pb. In addition, the SM prediction of a radiation amplitude zero (RAZ) resulting from interference between

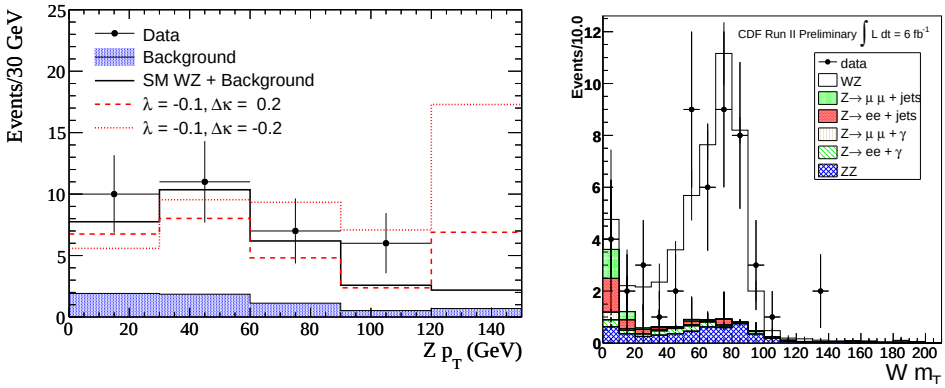

Figure 4: Distribution of transverse mass of the W boson in $WZ \to l\nu ll$ events at CDF (left). Distribution of the Z p_T in $WZ \to l\nu ll$ at D0.

production diagrams was tested by considering the distribution of $Q_\mu \times (\eta_\gamma - \eta_\mu)$, as shown in Fig. 5 (left). The distribution of the data matched the expected shape due to the RAZ. Finally, a limit on anomalous $WW\gamma$ couplings was placed by analyzing the distribution of the p_T of the photon, shown in Fig. 5 (right). The resulting limits on the anomalous coupling parameters are $-0.14 < \Delta\kappa_\gamma < 0.15$ and $-0.02 < \lambda_\gamma < 0.02$. These limits are the best limits on the $WW\gamma$ coupling achieved at a hadron collider and have similar sensitivity to that achieved at LEP.

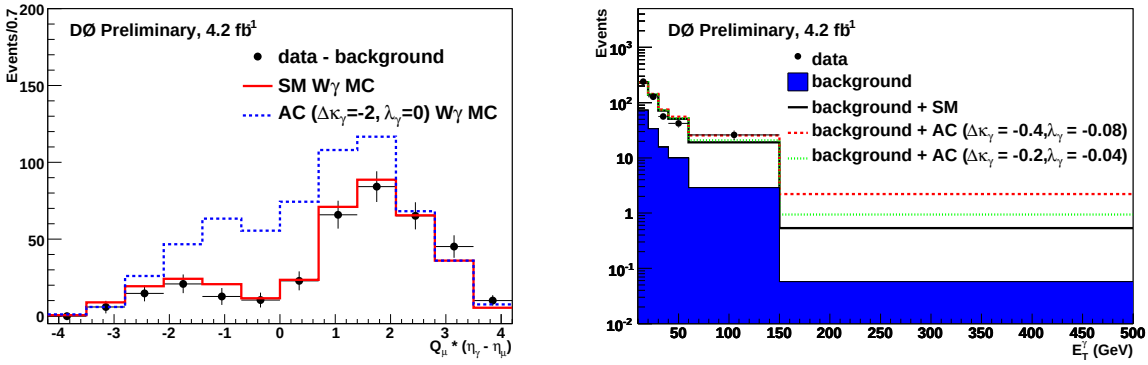

Figure 5: Distribution of the photon p_T in $W\gamma$ events at D0.

5 Measurements with hadronic decays

Diboson events where one boson decays to quarks are difficult to detect at a hadronic collider because of the large backgrounds from W/Z+jet production. Diboson events with a hadronic decay are topologically similar to events with associated Higgs boson production (WH and ZH) in the mass range where the Higgs boson decays primarily to two b quarks. The sophisticated analysis techniques applied in the Higgs searches, which optimize the separation between signal Higgs events and backgrounds from W/Z+jets, can thus be tested and improved in the context of measuring diboson production in events with a hadronic decay.

The D0 collaboration found strong evidence for $WW + WZ \to l\nu jj$ in events with a charged lepton, two jets, and $\not\!\!E_T$ [11]. The CDF collaboration subsequently observed and measured the cross section of $WW + WZ$ in events with the same final state signature, both using a matrix element technique and fitting the dijet invariant mass [12].

CDF also observed $WW+WZ+ZZ$ production in events with large $\not\!\!E_T$ nad two jets with 3.5 fb^{-1} [13]. Using the same techniques, a more recent measurement searches for the rarer process $WZ + ZZ \rightarrow \not\!\!E_T + b\bar{b}$ [14]. This search requires two jets and $\not\!\!E_T > 50$ GeV, resulting in large backgrounds from multi-jet events and from W/Z+jets events. Data-driven techniques are used to understand these backgrounds and reduce the systematic uncertainty on their normalization and shape. A neural network tagger is used to identify jets from b quark decays. Using a fit to the invariant mass of the two jets, the signal is extracted with a significance of 2σ with respect to a hypothesis with no $WZ + ZZ$ production. The measured cross section is $\sigma(WZ + ZZ) = 5.0^{+3.6}_{-2.6}$ pb, consistent with SM predictions.

6 Conclusions

The CDF and D0 experiments at the Tevatron collider have performed a wide variety of measurements of diboson processes. They are tests of the electroweak sector of the SM, and have thus far demonstrated excellent agreement with predictions. The properties of diboson events are also used to set some of the world's best limits on anomalous triple gauge boson couplings, providing constraints on models of new physics.

Sophisticated experimental techniques have been developed and used in the diboson measurements in order to increase the acceptance for the low-rate signal processes and to improve the discrimination from higher-rate background processes. The measurements are done and compared in a variety of decay channels. In all cases, agreement between different methods of measurement and between the two experiments are observed. This demonstrates the good understanding that CDF and D0 have of their detectors and of the physics modeling at the Tevatron, and builds confidence in the tools used in the search for the Higgs boson.

The larger data samples available to both experiments will lead to further improvement in the precision of the measurements. In addition, combinations between experiments and channels promises to reduce uncertainties and further strengthen the limits set on new physics.

References

1. K. Hagiwara, S. Ishihara, R. Szalapski, and D. Zeppenfeld, PRD **48**, 2182 (1993).
2. D. Acosta *et al.* (CDF Collaboration), *Phys. Rev.* D **71**, 032001 (2005).
3. V. M. Abazov *et al.* (D0 collaboration), *Nucl. Instrum. Methods* A **565**, 463 (2006).
4. J. M. Campbell and R. K. Ellis, *Phys. Rev.* D **60**, 113006 (1999).
5. V. Abazov *et al.* (D0 Collaboration), arXiv:hep-ex/1104.3078
6. CDF Collaboration, `http://www-cdf.fnal.gov/physics/ewk/2009/ZZllll/ZZWeb/index.html`.
7. CDF collaboration, `http://www-cdf.fnal.gov/physics/ewk/2010/ZZ/ZZllvv_web/ZZllvv.html`.
8. V. Abazov *et al.* (D0 Collaboration), *Phys. Lett.* B **695**, 23 (2011).
9. CDF collaboration, `http://www-cdf.fnal.gov/physics/ewk/2010/WZ_ZZ/`.
10. D0 collaboration, `http://www-d0.fnal.gov/Run2Physics/WWW/results/prelim/EW/E36/`.
11. V. Abazon *et al.* (D0 Collaboration), *Phys. Rev. Lett.* **102**, 092002 (2009)
12. T. Aaltonen *et al.* (CDF collaboration), *Phys. Rev. Lett.* **104**, 101801 (2010).
13. T. Aaltonen*et al.* (CDF collaborationn), *Phys. Rev. Lett.* **103**, 091803 (2009).
14. CDF collaboration, `http://www-cdf.fnal.gov/physics/new/hdg//Results_files/results/wzzz_sep10/METBB_dibosons/Dibosons_METJJ_2.html`.

Electroweak Symmetry Breaking in Warped Extra Dimensions

Gero von Gersdorff
CPhT, Ecole Polytechnique,
91128 Palaiseau CEDEX, France

We review Electroweak breaking in warped Extra Dimensions and show how it is constrained by Electroweak precision tests. We then proceed to describe a model which is based on a bulk Higgs field and a metric that is deformed from the usual five dimensional Anti de Sitter space near the Infrared (IR) boundary. It allows to softly decouple the Higgs field from the Kaluza Klein excitations near the IR and thus reduces their contribution to the precision observables.

1 The RS model and its variants

Following the influential work of Randall and Sundrum,[1] in the last decade a lot of effort has been put into constructing realistic warped models of Electroweak Symmetry breaking (EWSB) which obey all experimental constraints obtained in precision measurements of electroweak and flavour observables. In the Randall-Sundrum (RS) setup, a five dimensional (5D) bulk is endowed with an Anti de Sitter (AdS) metric that in proper coordinates is given by

$$ds^2 = e^{-2ky}\,\eta_{\mu\nu}\,dx^\mu dx^\nu + dy^2\,, \tag{1}$$

with the Minkowski metric $\eta_{\mu\nu}$ with signature $(-+++)$. The constant k of dimension mass is the inverse AdS curvature radius and is considered to be of the order of the Planck scale. The presence of the warp factor e^{-ky} introduces a scale dependence along the extra dimension and causes all mass scales to be redshifted when moving along increasing y. The space is bounded by two "branes", located at $y = 0$ (UV brane) and $y = y_1$ (IR brane).

In the simplest setup, the Higgs field is localized at the IR boundary:

$$\mathcal{L}_{\text{brane}-\text{Higgs}} = \sqrt{g}\,\left(-g^{\mu\nu}\,D_\mu H^\dagger D_\nu H - m_h^2|H|^2\right)|_{y=y_1} = -e^{-2ky_1}\,|D_\mu H|^2 - e^{-4ky_1}\,m_h^2|H|^2\,. \tag{2}$$

Canonically normalizing this Lagrangian, the – originally Planck size – Higgs mass m_h is "warped down" to the Electroweak (EW) scale

$$m_h \to e^{-ky_1}\,m_h \tag{3}$$

provided the volume (in units of k) is about $ky_1 = \log 10^{16} \sim 35$. This is a moderately large number that can be easily achieved dynamically by an appropriate stabilization mechanism. [2] The stabilization mechanism is also needed in order to give mass to the radion, the particle related to the fluctuations of the interbrane distance. Typically, the mass of the radion turns out to be about an order of magnitude lighter than the first KK excitations, although heavier masses are possible. [9]

The smoking gun signature of the RS model is the presence of strongly coupled KK resonances of the graviton. By considering fluctuations around the metric Eq. (1) it is found that the graviton KK spectrum is quantized with TeV spacing, the lowest excitations being

$$m_{\rm KK}^{\rm grav} = 3.8\, k\, e^{-ky_1}\,. \tag{4}$$

Moreover, its coupling is not Planck suppressed but rather set by the IR scale. It is thus a universal prediction of all variants of the RS model to produce spin–2 resonances at LHC or other future particle colliders. The wave functions of the KK modes are localized towards the IR boundary.

There exists a plethora of variations of this simplest setup, where the SM gauge and matter fields as well as the Higgs field are propagating in the bulk. [3] In this case, zero modes for the matter and Higgs fields typically feature nontrivial wave functions that depend on the bulk mass parameter. For instance, the Higgs boson zero mode has a profile

$$h(y) \sim e^{ak(y-y_1)}\,, \tag{5}$$

where the real parameter a is related to the bulk Higgs mass term $M_h^2\,|H^2|$ as $M_h^2 = k^2 a(a-4)$. Inserting this profile back into the 5D Higgs Lagrangian,

$$\mathcal{L}_{\rm bulk-Higgs} = \int_0^{y_1} dy\,\sqrt{g}\left(-g^{MN}\,D_M H^\dagger D_N H - \left[M_h^2 + M_0\,\delta(y) - M_1\,\delta(y-y_1)\right]\,|H|^2\right)\,, \tag{6}$$

one finds the physical Higgs mass

$$m_h^2 = \frac{2(a-1)}{e^{2(a-1)ky_1}-1}\,\left((M_0-ak)k - (M_1-ak)ke^{2(a-2)ky_1}\right)\,. \tag{7}$$

For $a<1$ this mass is $\mathcal{O}(k)$ unless one fine tunes $M_0 = ka$. This is the original hierarchy problem. In fact, in this range the Higgs can be considered near-UV localized in the sense that its kinetic term is multiplied by $e^{2(a-1)ky}$. For $1<a<2$, the hierarchy problem still partially persists, although the "natural " Higgs mass is now of the order $m_h \sim k\,e^{-(a-1)ky_1}$. Finally, for $a>2$, the Higgs mass is of the order $m_h \sim ke^{-ky_1}$ and the hierarchy problem is fully solved. For the pure AdS background metric, the Higgs mass is thus constrained by $a>2$ in order to fully address the hierarchy problem. There is a simple alternative interpretation of this result by invoking the AdS-CFT correspondence: The parameter a is related to the dimension of the strongly coupled Higgs condensate via $\dim\mathcal{O}_H = a$. The condition $a>2$ thus renders the mass operator $|O_H|^2$ irrelevant, which is precisely what is needed in order to solve the hierarchy problem. It has also been shown that under certain conditions, gauge coupling unification can be achieved at a scale $M_{\rm GUT}\sim 10^{15}$ GeV with a precision comparable to that of the MSSM. [4]

We should mention two more possibilities for the Higgs sector, which have been employed in the context of warped extra dimensions. The first one goes by the name of gauge-Higgs unification, or under its dual alias "composite pseudo Nambu-Goldstone Higgs". [5] Instead of a fundamental Higgs field, one introduces an extended gauge group G in the bulk, which by the IR boundary conditions is broken down to a subgroup H containing the Standard Model gauge group. At the UV brane, only the SM survives the boundary conditions. By appropriately choosing [a] G and H, the coset G/H contains scalars with the quantum numbers of the Higgs boson in the A_5 sector of the theory (the fifth component of the gauge boson). At tree level, its potential is flat due to the underlying 5D local gauge symmetry. However, at one loop a potential is generated [6] due to a Wilson line needed to make all bulk propagators gauge covariant. The potential is nonlocal and finite. These models have the advantage that the Higgs mass can be

[a] In the minimal model [5] $G = SO(5)\times U(1)$, $H = SU(2)_L\times SU(2)_R\times U(1)\supset SU(2)_L\times U(1)_Y$.

Table 1: The properties of the global currents, depending on the boundary conditions imposed on them at the two branes.

	Neumann	Dirichlet
UV brane	gauged	ungauged
IR brane	exact	spontaneously broken

naturally light due to the vanishing tree level contribution. In the holographic dual version of the theory the Higgs is identified as the (pseudo-) Nambu Goldstone bosons of the breaking of the *global* symmetry $G \to H$. Recall that according to the AdS-CFT dictionary, 5D gauge symmetries correspond to global currents in the 4D dual. The fate of the current depends on the imposed boundary condition according to table 1. We see that the global symmetry G is spontaneously broken to H producing Goldstone bosons in the coset G/H. The SM, a subgroup of H, is gauged and further spontaneously broken by a VEV of the pseudo-Goldstone Higgs. The second alternative, the "Higgsless model",[7] is an extreme version of the previous one, in which the coset G/H only contains the Goldstone bosons and no radial, "Higgslike" excitations. This can be achieved, for instance, by choosing $G = SU(2)_L \times SU(2)_R$ and $H = SU(2)_V \supset U(1)_{EM}$. Holographically these models thus bear some similarities to large-N_c Technicolor models.

Besides the aforementioned KK graviton modes which are universally present in any variant of the RS model, there are more model dependent resonances such as KK modes of the gauge bosons or even of the matter fields. These resonances can contribute to higher dimensional operators when integrated out at tree level and beyond, and hence precision measurements from LEP and flavour experiments tightly constrain the parameters of the model. Before turning to details of these constraints, let us pause and figure out the parameteric dependence of the coupling of SM zero modes to heavy KK resonances. The wave functions of the latter can be obtained by solving the 5D equations of motion (EOM) in the AdS background. It turns out that the wave functions of the first heavy KK resonances are mostly constant throughout the bulk and concentrated near the IR brane, see Fig. 1. The normalized wave function parametrically behaves as

$$f_n(0) \sim (ky_1)^{-1}\,, \qquad f_n(y_1) \sim 1\,. \tag{8}$$

The SM fields couple to the KK resonances of the gauge fields as

$$\mathcal{L}_{\rm SM-KK} = g_n\, J^\mu_{\rm SM}(x) \cdot A^n_\mu(x)\,, \tag{9}$$

where $J^\mu_{\rm SM}$ are the usual SM matter and Higgs currents. However, due to the non-flatness of the gauge-KK wave functions, the couplings can be highly nonuniversal, depending on the profile of the matter zero modes. Schematically,

$$g_n = g_5 \int f_n(y)\psi(y)^2 \sim \begin{cases} g_4\,(ky_1)^{-\frac{1}{2}} & \text{for mostly UV localized fields,} \\ g_4\,(ky_1)^{+\frac{1}{2}} & \text{for mostly IR localized fields,} \end{cases} \tag{10}$$

where $\psi(y)$ are the zero mode wave functions normalized as $\int \psi(y)^2 = 1$, and the 5D and 4D gauge couplings are related as $g_5 = g_4\sqrt{y_1}$.

2 Electroweak precision tests for RS

Any theory aiming to explain EWSB has to confront the precise measurements from LEP. In general, new physics beyond the SM will generate higher dimensional operators which are suppressed with inverse powers of the masses of the new states. In a completely model independent

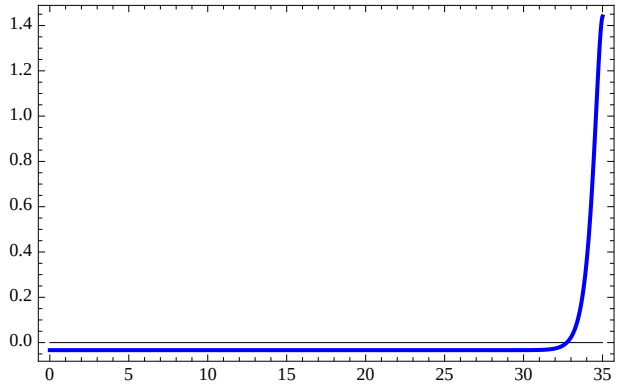

Figure 1: The normalized wave function of the first gauge boson KK mode as a function of the coordinate y.

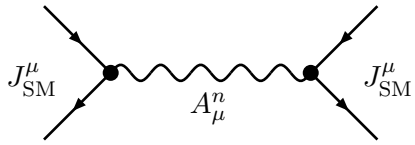

Figure 2: Diagram contributing to the effective Lagrangian.

approach, one would like to classify these new operators, compute their contribution to the LEP observables and perform a global fit to their coefficients. It turns out that in a large class of models, including most versions of RS, there is only a certain subset of operators which are relevant. These are the so-called oblique corrections, and they are defined as follows

$$\mathcal{L}_{\rm oblique} = \frac{1}{2\,m_W^2}\left(g^2\,\hat{T}\;|H^\dagger D_\mu H|^2 + gg'\,\hat{S}\;[H^\dagger\,W_{\mu\nu}HB^{\mu\nu}] + W\;[D_\rho W_{\mu\nu}]^2 + Y\;[\partial_\rho B_{\mu\nu}]^2\right)\,. \tag{11}$$

In the following, we will restrict ourselves to this subset.[b] Note that the slightly more commonly used T and S parameters are related by $\hat{T} = \alpha T$ and $4s_w^2\,\hat{S} = \alpha S$.

The tree level contributions to these coefficients from integrating out the gauge KK modes of the W and Z bosons can be computed from the vertex Eq. (8) according to the diagram in Fig. 2. This leads to operators consisting of products of two currents (fermionic ones as well as Higgs). The resulting effective Lagrangian contains the first operator in Eq. (11), but not the other three. Let us assume that the fermion fields are all localized in the UV region of the bulk. Then their coupling to the KK modes is to a large degree universal, and one can use the SM EOM to eliminate the fermion currents (For details see [9,10])

$$J^\mu_{\rm fermion} = -D_\nu F^{\nu\mu} - J^\mu_{\rm Higgs} \tag{12}$$

Now the only operators are those appearing in Eq. (11), and this basis of fields is referred to as the oblique basis. It is not hard to convince oneself that

$$\begin{aligned} J_{\rm Higgs}\cdot J_{\rm Higgs} \quad &\text{contributes to} \quad T\,, \\ J_{\rm Higgs}\cdot J_{\rm fermion} \quad &\text{contributes to} \quad S,\ T\,, \\ J_{\rm fermion}\cdot J_{\rm fermion} \quad &\text{contributes to} \quad S,\ T,\ Y,\ W\,. \end{aligned} \tag{13}$$

According to our assumtions that the Higgs is near-IR and the fermions are near-UV localized,

[b] Strictly speaking for RS models one should add one more operator related to the modified $Zb\bar{b}$ coupling. We will comment on this operator below.

one thus finds the following parametric dependence from Eq. (10).

$$\begin{aligned} T &\sim (ky_1)\,\epsilon^2\,, \\ S &\sim \epsilon^2\,, \\ W, Y &\sim (ky_1)^{-1}\epsilon^2\,, \end{aligned} \tag{14}$$

where $\epsilon = m_W/m_{\rm KK}$ is the little hierarchy. One thus expects that the T parameter provides the strongest contraints on ϵ. Indeed, for a strictly IR localized Higgs ($a = \infty$), one finds[8] $m_{\rm KK} \gtrsim 12$ TeV. Delocalizing the Higgs into the bulk reduces the coupling to the KK modes slightly. Recall that the lowest value of a still consistent with the RS solution to the hierarchy problem is $a = 2$. This reduces T by a factor of 3 and hence one still needs $m_{\rm KK} \gtrsim 7$ TeV.[9] These bounds refer to a light Higgs boson of $m_h \sim 115$ GeV. Recently it has been pointed out that with a heavy Higgs boson these bounds can be further reduced, due to a partial cancellation of the radiative Higgs contribution to T with the KK tree level contribution. For instance, for $m_h = 450$ GeV, the bound for a localized[12] (bulk[13]) Higgs field is $m_{\rm KK} \gtrsim 8$ TeV (4.6 TeV)

In any event, multi-TeV KK masses generate a serious little hierarchy problem and render the theory less natural. The rather large contribution to T is a consequence of the fact that in the simplest model with just the SM gauge group in the bulk, the gauge-KK sector breaks the custodial symmetry of the SM at tree level. Recall that in the SM, in the limit of vanishing hypercharge and Yukawa couplings, the Higgs sector enjoys a global "custodial" $SU(2)_R$ symmetry[c] which forbids the first operator in Eq. (11). Since hypercharge does not commute with $SU(2)_R$, the T parameter is generated at one-loop in the SM and its extensions. However, in the RS model there are also KK modes of the hypercharge gauge boson, and they are the culprits that generate the T parameter when integrated out at tree level.[d] There are at least two ways to remedy this situation. The first[14] is to enlarge the 5D bulk gauge symmetry according to $U(1)_Y \hookrightarrow SU(2)_R$.[e] This embeds the hypercharge KK modes into full $SU(2)_R$ multiplets and kills any tree level contributions to T. In order to achieve just the SM in the zero mode sector, one projects out the extra gauge bosons by giving them Dirichlet boundary conditions at the UV brane. Let us briefly comment on the CFT-dual interpretation of this idea. According to table 1 we have an exact global symmetry $SU(2)_L \times SU(2)_R$, of which the SM subgroup is gauged. The Higgs boson is now chosen to be a bulk or brane field transforming in the bifundamental and spontaneously breaks the global symmetry to the diagonal $SU(2)_V$. The bounds are dominated by the S parameter and one can roughly achieve $m_{\rm KK} \gtrsim 3$ TeV. The second possibility is to slightly decouple the dangerous hypercharge KK modes from the Higgs field.[9] We will describe such a model in the next section. For yet another idea, see[15].

So far we have assumed that all fermions are near UV localized. This is a good approximation for all the light fermions of the standard model, but not so for the heavy quarks of the third generation. In order to generate a top Yukawa coupling of order unity one needs to have the left handed quark doublet to be near IR localized in order to maximize the overlap with the Higgs wave function. One thus expects a volume enhanced correction $\delta g_{Zb\bar{b}} \sim (ky_1)\,\epsilon^2$ which contributes in particular to the partial width of the Z boson. For some ideas how to deal with this see[11].

---

[c] Sometimes the term "custodial symmetry" is reserved for the surviving global symmetry $SU(2)_V \subset SU(2)_L \times SU(2)_R$ in the broken phase. Since we are writing effective dimension-six operators at the scale $m_{\rm KK} \gg m_W$, it makes more sense to work in the symmetric phase and we will hence refer to $SU(2)_R$ as the custodial symmetry.

[d] In fact, it is a simple exercise to verify that only the hypercharge currents but not the $SU(2)_L$ currents contribute to T in Eq. (13).

[e] An extra $U(1)$ symmetry is needed to correctly assign hypercharge to the fermions if the latter propagate in the bulk.

3 Warped Electroweak breaking without custodial symmetry.

We would like to suppress the KK contribution to the T parameter by decreasing their coupling to the Higgs boson. Let us therefore consider the effective Higgs Lagrangian

$$\mathcal{L}_{Higgs} = -|D_\mu H|^2 + \mu^2 - \lambda |H|^4 + g_n J^\mu_{\rm Higgs} \cdot A^n_\mu \tag{15}$$

We will generalize the metric according to the replacement

$$e^{ky} \to e^{A(y)}\,, \tag{16}$$

and impose $A(0) = 0$, $A(y_1) = 35$ in order to generate the Planck-Weak hierarchy. We will give an explicit form for $A(y)$ below, but what we have in mind is a deformation of the form

$$A(y) = ky + (\text{correction near } y = y_1)\,, \tag{17}$$

such that the space is asymptotically AdS near the UV brane. By carefully integrating over the 5D Lagrangian with the Higgs zero mode profile $h(y)$ we obtain the parametric behaviour

$$\begin{aligned} \mu^2 &\sim Z^{-1}\rho^2\,, \\ \lambda &\sim Z^{-2}\,, \\ g_n &\sim Z^{-1}\sqrt{ky_1}\,. \end{aligned} \tag{18}$$

where we have suppressed only $\mathcal{O}(1)$ quantities and defined

$$\rho = ke^{-ky_1}\,, \qquad Z = k\int_0^{y_1}\left(\frac{h(y)\,e^{-A(y)}}{h(y_1)\,e^{-A(y_1)}}\right)^2\,. \tag{19}$$

This integral arises as a wave function renormalization in the effective theory when integrating over the 5D Higgs kinetic-term. The reason we have kept it here explicitly is that under certain circumstances it can become large and suppress the coupling g_n. Including the Z factor in the coupling g_n, one can see that Eq. (14) is replaced by

$$\begin{aligned} T &\sim (ky_1)\,Z^{-2}\,\epsilon^2\,, \\ S &\sim Z^{-1}\,\epsilon^2\,, \\ W, Y &\sim (ky_1)^{-1}\epsilon^2\,. \end{aligned} \tag{20}$$

In fact, it is easy to see that in pure RS Z it is given by (for $a > 1$)

$$Z = \frac{1}{2(a-1)}\,. \tag{21}$$

As expected, one can gradually decouple the Higgs from the KK modes by decreasing a, but one is at the same time required to keep $a > 2$ in order to maintain the RS solution to the hierarchy problem. One thus finds $Z_{\rm RS} < \frac{1}{2}$ which is not particularly large.

Next we will consider an explicit metric deformation of AdS in the IR region. It contains a stabilizing field ϕ which leads to the metric [16]

$$A(y) = ky - \frac{1}{\nu^2}\log\left(1 - y/y_s\right)\,, \tag{22}$$

where ν is a real parameter. The metric has a spurious singularity located at $y_s = y_1 + \Delta$, outside the physical interval. It was originally studied in the absence of an IR brane in which case the singularity is a physical one and certain constraints apply to the parameter ν in order

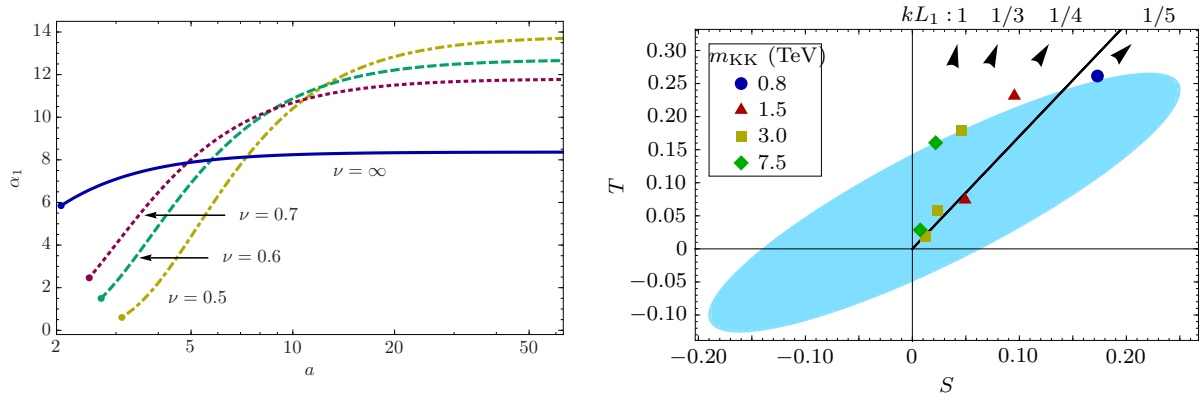

Figure 3: Left panel: Plot of the coupling $\alpha_1 = g_1/g$ as a function of a for $\nu = 0.5, 0.6, 0.7$ and ∞ (RS). Lines end at $a = a_0$. Right panel: 95% CL regions in the (S, T) plane for different deformations. The arrows indicate decreasing KK mass.

to have a sensible theory and generate a mass gap. [16] Here the singularity is shielded and ν remains arbitrary. In the limit of $\nu \to \infty$ one recovers the pure AdS metric. In order to solve the hierarchy problem we fix $A_1 = A(y_1) \sim 35$, which determines implicitely $ky_1 < A_1$ in terms of the other parameters.

One can choose a suitable (ϕ dependent) bulk mass to achieve again $h(y) \sim e^{ak(y-y_1)}$. The analogue of the condition $a > 2$ in RS becomes $a > a_0$ where $a_0 = 2A_1/(ky_1) > 2$. The fact that $a_0 > 2$ can be understood in the 4D dual interpretation. The dimension of the Higgs condensate corresponding to the solution $h(y) \sim e^{aky}$ depends on y. Since the renormalization group (RG) scale is given by the warp factor we have

$$\dim(\mathcal{O}_H) = \frac{h'}{h\,A'} = \frac{a}{1 + \frac{1}{k(y_s - y)\nu^2}}\,. \tag{23}$$

Starting in the UV with $\dim(\mathcal{O}_H) > 2$ the mass operator $|\mathcal{O}_H|^2$ has dimension [f] $\dim(|\mathcal{O}_H|^2) = 2\dim(|\mathcal{O}_H|) > 4$ which, being an irrelevant operator, will become more and more suppressed along the RG flow. However following the RG flow further the theory departs from the conformal fixed point, $\dim(\mathcal{O}_H)$ decreases and there will be a critical RG scale μ_c at which $\dim(\mathcal{O}_H) < 2$. As a consequence $|\mathcal{O}_H|^2$ will become a relevant operator and will start increasing again. As long as this happens far enough in the IR there is no concern as, at the scale μ_c, the mass term is really small and there is simply not enough RG time for it to become large enough before EWSB occurs. One thus has to choose $a_0 \approx \dim \mathcal{O}_H|_{UV}$ to be sufficiently greater than 2 such that the coefficient of $|\mathcal{O}_H|^2$ stays small all the way to the EW scale. The hierarchy problem is thus solved despite the fact that at the EW scale the Higgs condensate has a small dimension.

It is clear by looking at Eq. (19) that in general Z will increase for decreasing a. In Fig. 3 we plot the exact coupling of the first KK mode for different strengths of the deformation as a function of the parameter a, computed by numerically evaluating the wave function overlap in Eq. (10). One sees that, even though one has to stop at $a_0 > 2$, the coupling to the KK modes can be significantly reduced wrt. RS (the line with $\nu = \infty$). This is indeed due to the increasing Z factors. Accordingly, the bounds are largely affected by the deformation. [g] This is shown in the right panel of Fig. 3, where we have parametrized the deformation by the ratio of curvature radii in the UV ($L_0 = k^{-1}$) and IR (L_1). [9] The rightmost ray corresponds to roughly the parameters $k\Delta = 1$, $\nu = 0.5$, i.e. the endpoint of the yellow dashed-dotted line in the left

[f] We use the fact that in the large N_c limit operator products become trivial.

[g] It has been noted previously that, in models with custodial symmetry, the bounds from the S parameter can be reduced with an IR-modified metric. [17]

panel of the figure. One concludes that allowing for moderate deformations from the AdS metric in the IR, the bounds on the KK scale can be reduced to ~ 1 TeV, opening up the possibility of discovering KK resonances of the SM gauge bosons at the LHC.

A last word is in order regarding the other precision observables, in particular the W and Y parameters constrained by LEP-2 data, as well as the $Zb\bar{b}$ vertex. The former two multiply operators in Eq. (11) that do not involve the Higgs and hence will be unaffected by the reduced coupling. We have verified a posteriori that they are indeed inside their experimental errors at least in the parameter range displayed in Fig. 3. In contrast the $Zb\bar{b}$ vertex is affected by electroweak breaking and it is expected to scale as

$$\delta g_{Zb\bar{b}} \sim (ky_1)\, Z^{-1}\epsilon^2 \,. \tag{24}$$

Clearly one can expect some suppression due to the reduced Higgs coupling to the KK modes. However, it is more model dependent as the precise profile of the b quark has to be specified and one has to pay attention to the constraint that a large enough top Yukawa must be generated. Very recently it has been reported that in the described model one can achieve $m_{\rm KK} \sim 1-3$ TeV in some scenarios of fermion localization. [18]

Acknowledgments

I would like to thank the organizers of the Moriond Electroweak meeting 2011 for organizing a great conference and for inviting me to give this talk. This work is supported by the ERC Advanced Grant 226371, the ITN programme PITN- GA-2009-237920 and the IFCPAR CEFIPRA programme 4104-2.

References

1. L. Randall, R. Sundrum, Phys. Rev. Lett. **83** (1999) 3370-3373.
2. W. D. Goldberger, M. B. Wise, Phys. Rev. Lett. **83** (1999) 4922-4925.
3. T. Gherghetta, A. Pomarol, Nucl. Phys. **B586** (2000) 141-162.
4. K. Agashe, R. Contino, R. Sundrum, Phys. Rev. Lett. **95** (2005) 171804; M. Frigerio, J. Serra, A. Varagnolo, JHEP **1106** (2011) 029.
5. K. Agashe, R. Contino, A. Pomarol, Nucl. Phys. **B719** (2005) 165-187.
6. Y. Hosotani, Phys. Lett. **B126** (1983) 309; Annals Phys. **190** (1989) 233.
7. C. Csaki, C. Grojean, L. Pilo, J. Terning, Phys. Rev. Lett. **92** (2004) 101802.
8. S. J. Huber, Q. Shafi, Phys. Rev. **D63** (2001) 045010.
9. J. A. Cabrer, G. von Gersdorff, M. Quiros, Phys. Lett. **B697** (2011) 208-214; JHEP **1105** (2011) 083; [arXiv:1104.5253 [hep-ph]].
10. H. Davoudiasl, S. Gopalakrishna, E. Ponton, J. Santiago, New J. Phys. **12** (2010) 075011.
11. K. Agashe, R. Contino, L. Da Rold and A. Pomarol, Phys. Lett. B **641** (2006) 62; A. Djouadi, G. Moreau, F. Richard, Nucl. Phys. **B773** (2007) 43-64.
12. S. Casagrande, F. Goertz, U. Haisch, M. Neubert, T. Pfoh, JHEP **0810** (2008) 094.
13. J. A. Cabrer, G. von Gersdorff, M. Quiros, [arXiv:1104.3149 [hep-ph]].
14. K. Agashe, A. Delgado, M. J. May, R. Sundrum, JHEP **0308** (2003) 050.
15. H. Davoudiasl, J. L. Hewett, T. G. Rizzo, Phys. Rev. **D68** (2003) 045002; M. S. Carena, E. Ponton, T. M. P. Tait, C. E. MWagner, Phys. Rev. **D67** (2003) 096006.
16. J. A. Cabrer, G. von Gersdorff, M. Quiros, New J. Phys. **12** (2010) 075012; G. von Gersdorff, Phys. Rev. **D82** (2010) 086010.
17. A. Falkowski, M. Perez-Victoria, JHEP **0812** (2008) 107.
18. A. Carmona, E. Ponton and J. Santiago, arXiv:1107.1500 [hep-ph].

Beyond the Standard Model Higgs Boson Searches at the Tevatron

Tim Scanlon on behalf of the D0 and CDF Collaborations
Imperial College London, Physics Department,
Prince Consort Road, London SW7 2AZ, United Kingdom.

Results are presented for beyond the Standard Model Higgs boson searches using up to 8.2 fb^{-1} of data from Run II at the Tevatron. No significant excess is observed in any of the channels so 95% confidence level limits are presented.

1 Introduction

The search for the Higgs boson is one of the main goals in High Energy Physics and one of the highest priorities at Run II of the Tevatron. There are many alternative Higgs boson models beyond the SM, including Supersymmetry (SUSY) [1], Hidden Valley (HV) [2,3] and Fermiophobic Higgs bosons [4], which can actively be probed at the Tevatron, and in the absence of an excess constrained. The latest limits for several SUSY Higgs boson searches are presented in Section 2, for HV Higgs boson searches in Section 3 and for Fermiophobic Higgs boson searches in Section 4. More information on all these searches, along with the latest results, can be found on the CDF and D0 public results webpages [5,6].

2 Minimal Supersymmetric Standard Model Higgs Boson Searches

The Minimal Supersymmetric extension of the SM (MSSM) [1] introduces two Higgs doublets which results in five physical Higgs bosons after electroweak symmetry breaking. Three of the Higgs bosons are neutral, the CP-odd scalar, A, and the CP-even scalars, h and H (h is the lighter and SM like), and two are charged, $H^{\pm}$.

At tree level only two free parameters are needed for all couplings and masses to be calculated. These are chosen as the mass of the CP-odd pseudoscalar (m_A) and $\tan\beta$, the ratio of the two vacuum expectation values of the Higgs doublets.

The Higgs boson production cross section in the MSSM is proportional to the square of $\tan\beta$. Large values of $\tan\beta$ thus result in significantly increased production cross sections compared to the SM. Moreover, one of the CP-even scalars and the CP-odd scalar are degenerate in mass, leading to a further approximate doubling of the cross section.

The main production mechanisms for the neutral Higgs bosons are the $gg, b\bar{b} \rightarrow \phi$ and $gg, q\bar{q} \rightarrow \phi + b\bar{b}$ processes, where $\phi = h, H, A$. The branching ratio of $\phi \rightarrow b\bar{b}$ is around 90% and $\phi \rightarrow \tau^+\tau^-$ is around 10%. This results in three channels of interest: $\phi \rightarrow \tau^+\tau^-$, $\phi b \rightarrow b\bar{b}b$ and $\phi b \rightarrow \tau^+\tau^- b$. The overall experimental sensitivity of the three channels is similar due to the lower background from the more unique signature of the τ decays.

2.1 *Higgs* $\rightarrow \tau^+\tau^-$

D0's most recent search is in the $\tau_\mu\tau_{had}$ final state using 1.2 fb^{-1} of Run II data, where τ_{had} refers to a hadronic decay and τ_μ to a leptonic decay (to a μ) of the τ. This result is an extension to, and combined with, the published 1 fb^{-1} result which also included the $\tau_\mu\tau_e$, and $\tau_e\tau_{had}$ channels [7]. CDF have published a search combining the $\tau_\mu\tau_e$, $\tau_\mu\tau_{had}$ and $\tau_e\tau_{had}$ final states using 1.8 fb^{-1} of RunII data [8].

Both searches require events to have an isolated μ (e), separated from an opposite signed τ_{had} (or e for the $\tau_\mu\tau_e$ channel). Hadronic τ candidates are identified at D0 by neural networks designed to distinguish τ_{had} from multi-jet events and at CDF by using a variable size isolation cone. To minimise the W+jets background events are removed which have a large W transverse mass (D0) or by placing a cut on the relative direction of the visible τ decay products and the missing E_T (CDF).

In both analyses the $Z/\gamma \rightarrow \tau\tau$ and W+jets backgrounds are modelled using PYTHIA [9], with the W+jets normalisation and the multi-jet contribution modelled using data. Limits are set using the visible mass distribution (m_{vis}), which is the invariant mass of the visible τ products and the missing E_T. The CDF model independent 95% CL upper limit on the branching ratio multiplied by cross section is shown in Fig. 1.

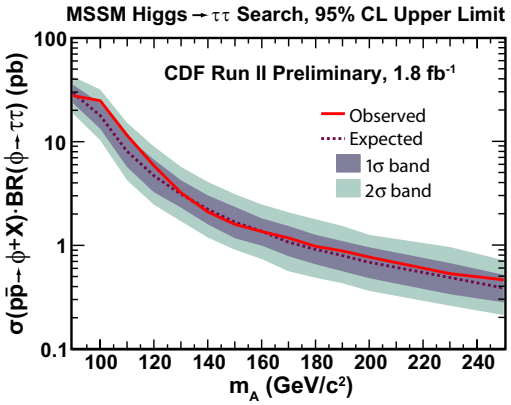

Figure 1: Model independent 95% CL upper limit on the branching ratio multiplied by cross section from the 1.8 fb^{-1} CDF publication. The dark (light) grey bands show the 1 (2) standard deviation bands around the expected limit.

2.2 *Higgs* + $b \rightarrow b\bar{b}b$

This channel has a signature of at least three b jets, with the background consequentially dominated by heavy flavour multi-jet events. D0 have recently published a search in this channel using 5.2 fb^{-1} of data [10] and CDF have a preliminary result using 2.2 fb^{-1} of data.

Both searches require three b-tagged jets, D0 uses its standard neural network b-tagging algorithm [11] and CDF uses its standard secondary vertex algorithm. Due to the difficultly of simulating the heavy flavour multi-jet background both analyses use data driven approaches. D0 uses a fit to data over several different b-tagging criteria whereas CDF uses fits to dijet invariant and secondary vertex mass templates to determine the heavy flavour sample composition.

To increase the sensitivity of the analysis, D0 splits it into exclusive three and four-jet channels, training a likelihood to distinguish the signal from background in each. Limits are set by both CDF and D0 on the Higgs boson production cross section times branching ratio using the dijet invariant mass as the discriminating variable. The D0 model independent 95% CL upper limit on the branching ratio multiplied by cross section is shown in Fig. 2.

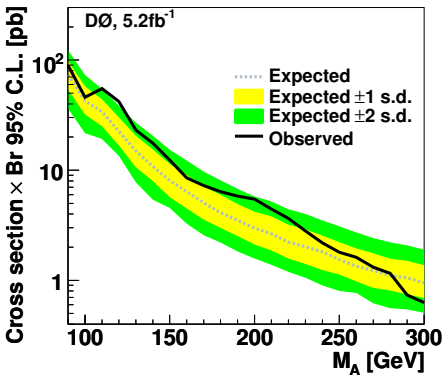

Figure 2: Model independent 95% CL upper limit on the branching ratio multiplied by cross section from the 5.2 fb^{-1} D0 publication. The yellow (green) bands show the 1 (2) standard deviation bands around the expected limit.

2.3 Higgs + b → $\tau^+\tau^-b$

D0 has performed a search for both the $\tau_\mu\tau_{had}$ and $\tau_e\tau_{had}$ signatures using 4.3 fb^{-1} and 3.7 fb^{-1} of Run II data respectively. Events are selected by requiring an isolated muon or electron separated from an opposite sign τ_{had} candidate, along with a b-tagged jet. The τ_{had} decays are identified using the standard D0 neural networks and b jets using the neural network b-tagging algorithm. The dominant backgrounds are $t\bar{t}$, W+jets, multi-jet and Z+jet events. The multi-jet and W+jets backgrounds are estimated from data with $t\bar{t}$ modelled using ALPGEN [12] interfaced with PYTHIA.

To improve the sensitivity of the analysis discriminants are trained which differentiate the signal from the $t\bar{t}$, multi-jet and Z+light parton (muon channel only) events respectively. The discriminants are combined to form a final discriminant which is used to set limits. Figure 3 shows the model independent 95% CL upper limit for the D0 $\tau_\mu\tau_{had}$ channel.

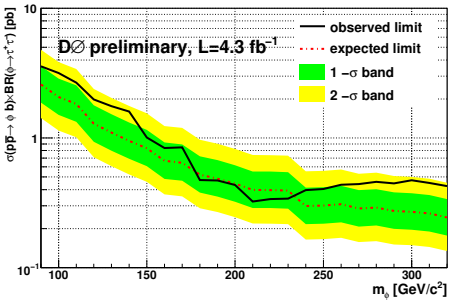

Figure 3: Model independent 95% CL upper limit on the branching ratio multiplied by cross section from the 4.2 fb^{-1} D0 $\tau_\mu\tau_{had}$ channel. The green (yellow) bands show the 1 (2) standard deviation bands around the expected limit.

2.4 Combined Limits

The channels described in Sections 2.1–2.3 are complementary and can be combined to increase the reach of the MSSM Higgs boson searches at the Tevatron. D0 has combined its three neutral Higgs boson channels (using an earlier version of the $\tau^+\tau^-b$ analysis based on only 1.2 fb^{-1} of RunII data and not including the $\tau_e\tau_{had}$ channel) and interpreted the limits in the standard MSSM scenarios [13]. A combined Tevatron limit on the MSSM Higgs sector has also been

produced from D0 and CDF's Higgs $\rightarrow \tau^+\tau^-$ channels. The combined Higgs $\rightarrow \tau^+\tau^-$ result has been interpreted in a quasi-model independent limit, as well as in the standard scenarios. Both the D0 and Tevatron combined 95% CL limits for one of the scenarios are shown in Fig. 4 along with the limit from LEP [14].

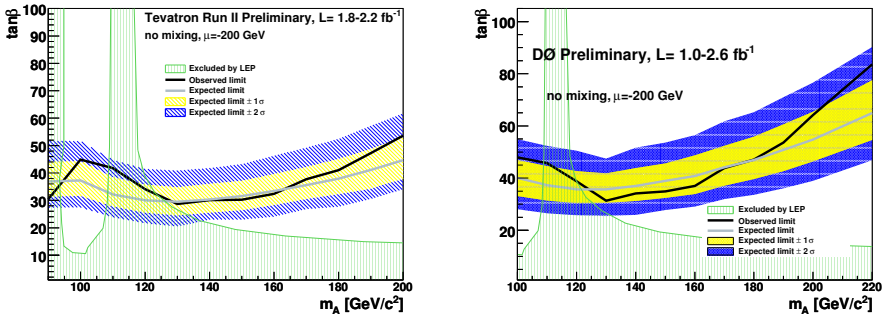

Figure 4: The combined D0 (left) and Tevatron (right) 95% CL limits on tanβ versus m$_a$ for the $\mu < 0$, no mixing scenario. The green area is the region excluded by LEP.

2.5 Next-to-MSSM Higgs Bosons Searches

In the next-to-MSSM (nMSSM) [15] the branching ratio of Higgs$\rightarrow b\bar{b}$ is greatly reduced. Instead the Higgs boson predominantly decays to a pair of lighter neutral pseudoscalor Higgs bosons, a. The nMSSM scheme is interesting as it allows the LEP limit on the h boson to be naturally lowered to the general Higgs boson search limit from LEP of $M_h > 82$ GeV [16].

CDF has conducted a search for a light nMSSM Higgs boson using 2.7 fb^{-1} of data in top quark decays, where $t \rightarrow W^{\pm(*)}ab$ and $a \rightarrow \tau\tau$. The τ particles are identified by the presence of additional isolated tracks in the event due to their low p_T. The dominant background is from soft parton interactions and is modelled using data. Upper limits are set at the 95% CL on the branching ratio of a top quark decaying to a charged Higgs boson from a fit to the p_T spectrum of the lead isolated track and are shown in Fig. 5.

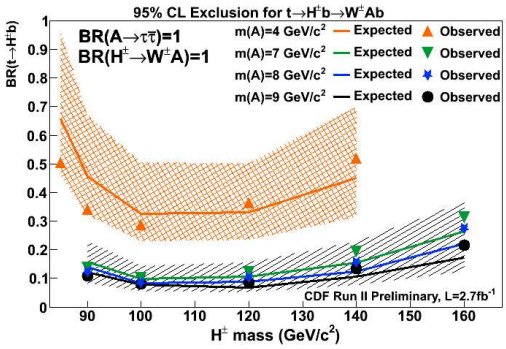

Figure 5: The 95% CL upper limits on branching ratio of top decaying to H^+b for various Higgs bosons masses.

3 Hidden Valley Higgs

CDF has conducted Higgs boson searches in Hidden Valley (HV) models, which contain long-lived particles which travel a macroscopic distance before decaying into two jets. The signature of this search is a Higgs boson decaying to two HV particles, which travel for $\sim$ 1 cm before decaying to two b-quarks. Although there are four b-jets present in the decay, to increase

the efficiency only three are required, two of which must be b-tagged and not back-to-back in the detector. A specially adapted version of CDF's secondary vertex b-tagging tool is used to reconstruct the displaced secondary vertices and the reconstructed HV decay points are required to have a large decay length.

Due to the difficulty of usinge Monte Carlo to model background events with large decay lengths, a data driven approach is used. The predicted number of background events is compared to the number seen in data and in the absence of a significant excess, limits are set on the production cross section times branching ratio on the benchmark HV model. Figure 6 shows the 95% CL upper limit for a Higgs mass of 130 GeV and a HV particle mass of 40 GeV as a function of the HV particle lifetime.

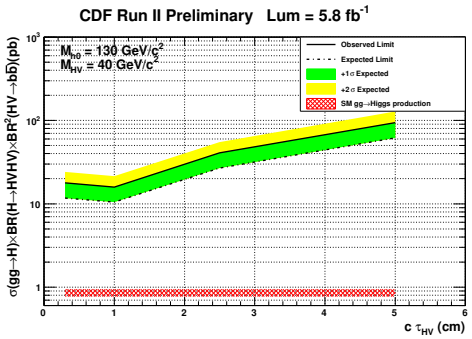

Figure 6: The 95% CL upper limit on $\sigma \times BR$ as a function of the Hidden Valley particle's lifetime.

4 Fermiophobic Higgs Boson Searches

The Standard Model Higgs boson branching ratio to a pair of photons is small. There are however several models where the decay of the Higgs boson to fermions is suppressed. In these models the decay of the Higgs boson to photons is greatly enhanced. Both D0 and CDF [18] have carried out searches for the Fermiophobic Higgs boson using 8.2 and 4.2 fb^{-1} respectively.

D0 requires two photon candidates in the central calorimeter, with jets misidentified as photons rejected by use of a neutral network. Electrons are suppressed by requiring that the photon candidates are not matched to activity in the tracking detectors. A decision tree is trained using five variables to distinguish signal from background events. The three main background sources are estimated separately: the jet and diphoton backgrounds are estimated from data and the Drell-Yan contribution is estimated using PYTHIA.

CDF's search also requires two photons, with only one of them required to be in the central region of the calorimeter. This looser photon requirement approximately doubles the acceptance compared to requiring both photons in the central region. In addition a cut is placed on the transverse momentum of the two photons which significantly reduces the background, which is estimated using a purely data-based approach.

Upper limits are set on the Higgs boson production cross section times branching ratio using the decision tree output (D0) or diphoton mass (CDF) as the discriminating variable. The 95% CL upper limit are shown in Fig. 7 for the D0 search.

5 Conclusions

CDF and D0 have a wide variety of beyond the Standard Model Higgs boson searches, presented here using up to 8.2 fb^{-1} of data. These searches are already powerful, and have set some of the best limits in the world. No signal has been observed yet, but with their rapidly improving

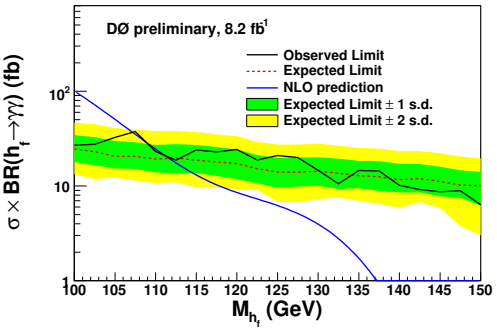

Figure 7: The 95% CL upper limit on $\sigma \times BR$ as a function of the Fermiophobic Higgs boson mass for D0.

sensitivity, due to both improved analysis techniques and the addition of between 2–5 times more data (which has already been recorded), these analyses will continue to probe extremely interesting regions of parameter space, promising many exciting results in the near future.

Acknowledgments

I would like to thank all the staff at Fermilab, the Tevatron accelerator division along with the CDF and the D0 Collaborations.

References

1. S. Dimopoulos, H. Georgi, *Nucl. Phys.* B **193**, 150 (1981).
2. M. Strassler, K. Zurek, *Phys. Lett.* B **651**, 374 (2007).
3. M. Strassler, K. Zurek, *Phys. Lett.* B **661**, 263 (2008).
4. H. E. Haber, G. L. Kane, T. Sterling, *Nucl. Phys.* B **161**, 493 (1979).
5. `http://www-cdf.fnal.gov`
6. `http://www-d0.fnal.gov`
7. V.M. Abazov *et al.* (D0 Collaboration), *Phys. Rev. Lett.* **101**, 071804 (2008).
8. T. Aaltonen *et al.* (CDF Collaboration,) *Phys. Rev. Lett.* **103**, 201801 (2009).
9. Sjöstrand T, Lönnblad L, Mrenna S and Skands P, *J. High Energy Phys.* **05**, 026 (2006).
10. V.M. Abazov *et al.* (D0 Collaboration), *Phys. Lett.* B **698**, 97 (2011).
11. V.M. Abazov *et al.* (D0 Collaboration), *Nucl. Instrum. Methods* A **620**, 490 (2010).
12. M. L. Mangano, M. Moretti, F. Piccinini, R. Pittau, A. D. Polosa, *J. High Energy Phys.* **307**, 001 (2003).
13. M. Carena, S. Heinemeyer, C. E. M. Wagner and G. Weiglein, *Eur. Phys. J.* C **45**, 797 (2006).
14. Schael S *et al.*, *Eur. Phys. J.* C **47**, 547-587 (2006).
15. U. Ellwanger, M. Rausch de Traubenberg, C. A. Savoy, *Nucl. Phys.* B **492**, 21 (1997).
16. G. Abbiendi et al. (OPAL Collaboration), *Eur. Phys. J.* C **27**, 311 (2003).
17. V.M. Abazov *et al.* (D0 Collaboration), *Phys. Rev. Lett.* **103**, 061801 (2009).
18. T. Aaltonen *et al.* (CDF Collaboration), *Phys. Rev. Lett.* **103**, 061803 (2009).

The Next-to-Minimal Supersymmetric Standard Model: an overview

Ana M. Teixeira
Laboratoire de Physique Corpusculaire, CNRS/IN2P3 – UMR 6533,
Campus des Cézeaux, 24 Av. des Landais, F-63171 Aubière Cedex, France

We review the most important aspects of the NMSSM, discussing the impact of the NMSSM on low-energy observables, for dark matter, as well as NMSSM specific signatures at colliders. We also briefly consider constrained realisations of the NMSSM.

1 Supersymmetric extensions of the Standard Model

Among the many extensions of the Standard Model (SM) which aim at solving or easing its observational and theoretical shortcomings, supersymmetry (SUSY) is one of the most appealing possibilities. SUSY extensions of the SM offer a potential solution to the hierarchy problem, allow for radiative spontaneous electroweak (EW) symmetry breaking, and provide a possible link between the EW scale and the scale of soft-supersymmetry breaking ($M_{\rm SUSY}$). SUSY models are further motivated by an automatic unification of the running gauge coupling constants under simple SU(5) or SO(10) grand unified (GUT) models, at a scale 10^{16} GeV $\lesssim M_{\rm GUT} \lesssim 10^{17}$ GeV. If R-parity is conserved, the lightest SUSY particle (LSP) is stable; if neutral and colourless, it can be a candidate to explain the observed dark matter (DM) relic density of the Universe.

The minimal supersymmetric extension of the SM (MSSM) is defined by the following superpotential and supersymmetry soft-breaking Lagrangian

$$\mathcal{W} = Y_u\,\hat{H}_u\,\hat{Q}\,\hat{u} + Y_d\,\hat{H}_d\,\hat{Q}\,\hat{d} + Y_e\,\hat{H}_d\,\hat{L}\,\hat{e} + \mu\,\hat{H}_u\hat{H}_d\,, \tag{1}$$

$$-\mathcal{L}_{\rm soft} = m^2_{H_u}\,H^*_u H_u + m^2_{H_d} H^*_d H_d + (M_i\psi_i\psi_i + A_F Y_F H_i \tilde{F}\tilde{F}^* + B\mu H_u H_d + \text{H.c.}) + ... \tag{2}$$

Other than squarks, sleptons and gluinos, the spectrum contains 2 charginos and 4 neutralinos, arising from the mixing of electroweak gauginos with the charged and neutral fermion components of the two Higgs superfields, $\hat{H}_d$ and $\hat{H}_u$. The Higgs sector is composed of 2 neutral scalars (H_i), one pseudoscalar A, and a pair of charged states $H^\pm$.

Despite its many appealing features, the MSSM suffers from phenomenological problems; among them, and deeply related to the Higgs sector, is the so-called "μ-problem" [1]. The latter arises from the presence of a non-vanishing dimensionful term in the MSSM superpotential of Eq. (1), for which there are only two "natural" values: either 0, or then the typical scale at which the model is defined ($\sim M_{\rm GUT,\,Planck}$). However, and as we briefly discuss, neither possibility is viable. The non-observation of charginos at LEP puts a limit on their mass ($m_{\chi_1^\pm} \gtrsim 103$ GeV), and hence a lower bound on the SUSY conserving mass term, $\mu\tilde{h}_u\tilde{h}_d$, $|\mu| \gtrsim 100$ GeV. In any case, in order to ensure that the neutral components of both Higgs scalars develop non-vanishing vacuum expectation values (VEVs), $\mu \neq 0$. Moreover, a correct EW symmetry breaking implies

that the SUSY conserving μ term cannot be excessively large: the μ-induced mass squared for H_u and H_d (always positive) must not dominate over the negative soft breaking masses, which further precludes $\mu \sim M_{\rm GUT,\,Planck}$. Everything taken into account, μ must be of order of the soft SUSY breaking scale, $|\mu| \sim \mathcal{O}(M_{\rm SUSY})$, which is a very unnatural scenario.

An elegant and yet simple way to solve this problem consists in the addition of a superfield to the MSSM content, and in taking a scale-invariant superpotential where only trilinear dimensionless couplings are present. The required non-vanishing bilinear mass term for the Higgs can then be effectively generated from the VEV of the new scalar field (necessarily a singlet since the μ-parameter is gauge invariant): $\mu^{\rm eff} = \lambda\langle S\rangle$. This is the so-called Next-to-Minimal supersymmetric standard model (for a recent review, see [2]).

2 The Next-to-Minimal Supersymmetric Standard Model

In its simplest form, the Next-to-Minimal supersymmetric standard model (NMSSM) is described by the superpotential

$$\mathcal{W}^{\rm NMSSM} = Y_u\,\hat{H}_u\,\hat{Q}\,\hat{u} + Y_d\,\hat{H}_d\,\hat{Q}\,\hat{d} + Y_e\,\hat{H}_d\,\hat{L}\,\hat{e} + \lambda\,\hat{S}\,\hat{H}_u\hat{H}_d + \frac{1}{3}\kappa\,\hat{S}^3\,. \tag{3}$$

In the soft breaking Lagrangian, the $B\mu$ term is replaced by trilinear couplings, A_λ and A_κ, and there is an additional soft breaking mass for the scalar, m_S^2. Phenomenologically viable values of $\mu_{\rm eff}$ can be easily obtained with negative soft SUSY breaking mass squared (and trilinear couplings) for the singlet. It is also important to stress that in this case, all the fermions belonging to a chiral superfield will have a supersymmetry conserving mass term in the Lagrangian arising from a trilinear (Yukawa) coupling. In particular, for the case of the higgsinos, one finds $\lambda\tilde{h}_u\tilde{h}_d S$. Since it allows for a scale invariant superpotential, as can be seen from Eq. (3), the NMSSM is in fact the simplest supersymmetric generalization of the SM in which the SUSY breaking scale is the only scale in the Lagrangian (notice that the EW scale originates exclusively from the SUSY breaking scale).

The scalar components of the singlet superfield mix with the neutral scalar components of $\hat{H}_u$ and $\hat{H}_d$, leading to an enlarged Higgs sector, which now comprises three scalars, h_i^0, and two pseudoscalars, a_i^0. Likewise, the fermionic component of $\hat{S}$ (the singlino, χ_S^0) mixes with the neutral higgsinos and gauginos, so that now one has five neutralinos. Depending on the regime considered, the new states can either decouple from the rest of the spectrum (an "effective"-MSSM scenario), be mixed with the MSSM states, or even be the lightest Higgs and neutralino. One can thus have a richer and more complex phenomenology, with a potential impact for low energy physics (e.g. flavour physics), dark matter scenarios and searches at colliders.

3 Higgs phenomenology in the NMSSM

When compared to the MSSM, the additional states and the new couplings of the NMSSM can significantly alter the phenomenology of scalar and pseudoscalar Higgs: in the NMSSM, both h_1^0 and a_1^0 can be very light, and still comply with all collider and low-energy bounds. Firstly, if the lightest scalar has a dominant singlet component, its reduced couplings to the Z boson ($\xi^Z \equiv g_{h_1ZZ}/g_{HZZ}^{\rm SM}$) can be much smaller than in the MSSM [3]. As can be seen from the left panel of Fig. 1, depending on the value of ξ^Z ($\xi = \xi^Z$), extremely light Higgs can still be in agreement with the combined results from the four experiments at LEP II.

Higgs-to-Higgs decays are an extremely interesting and peculiar feature of the NMSSM: in particular, in the presence of a light (singlet-dominated) pseudoscalar, a SM-like h_1^0 ($\xi^Z = 1$) can have dominant decays into a pair of light a_1^0 (thus reducing the $h_i^0 \to b\bar{b}$, $\tau^+\tau^-$ branching ratios). Should this be the case, then one can have $m_{h_1^0} \lesssim 114$ GeV, still in agreement with

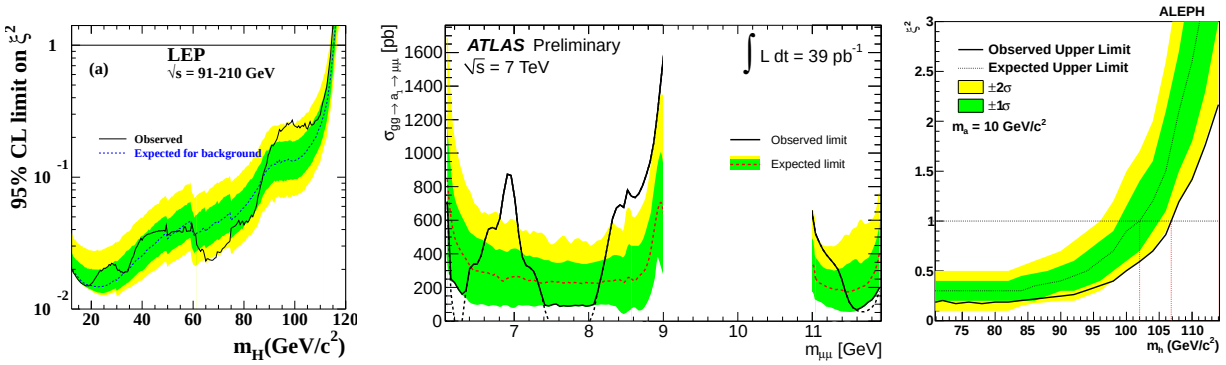

Figure 1: From left to right: upper bound on ξ^2 ($= \xi^{Z\,2}$) as a function of the scalar Higgs mass; upper limits on $\sigma(gg \to a_1 \to \mu\mu)$ as a function of the dimuon invariant mass; upper bound on ξ^2 ($= \xi^{A\,2}$) as a function of m_H, for $m_a = 10$ GeV.

LEP data [4,5]. Depending on the mass of a_1^0, it can decay to $b\bar{b}$, or into a pair of charged leptons. There are presently strong constraints on a light pseudoscalar, which we briefly summarise: for $m_{a_1^0} \gtrsim 2m_B$, LEP searches for $h_1^0 \to a_1^0 a_1^0 \to 4b$ strongly constrain $m_{h_1^0} \lesssim 100$ GeV; below the $b\bar{b}$ threshold, the most important constraints arise from B and Υ phenomenology, with KLEO and BABAR severely constraining the regimes leading to $m_{a_1^0} \lesssim 9$ GeV (the actual bounds depending on $X_d = \cos\theta_A \tan\beta$, where $\cos\theta_A$ denotes the doublet-like component of a_1^0) [6]. This has been reinforced by recent ATLAS searches for a light pseudoscalar decaying into $\mu\mu$ pairs [7], as shown on the centre plot of Fig. 1. An NMSSM pseudoscalar with a mass 9 GeV $\lesssim m_{a_1^0} \lesssim 10.1$ GeV satisfies all available constraints and, if such a light state mixes with the η_b meson, it could also explain the observed $\Upsilon(1s) - \eta_b(1s)$ hyperfine splitting [8]. On the right hand-side of Fig. 1 we display the ALEPH bounds, under the assumption that a light pseudoscalar, $m_{a_1^0} \sim 10$ GeV, is present (in this case, $\xi^{A\,2} = \frac{\sigma(e^+e^- \to Zh)}{\sigma(e^+e^- \to Zh)_{\rm SM}} \times {\rm BR}(h \to aa) \times {\rm BR}(a \to \tau^+\tau^-)^2$).

As pointed out in [9], for $m_{a_1^0} \sim 10$ GeV, and if ${\rm BR}(a_1^0 \to \tau^+\tau^-) \sim 80\%$ (i.e., $\xi^{A\,2} \lesssim 0.5 - 0.6$), LEP data allows a SM-like CP-even Higgs with $m_{h_1^0} \sim 100$ GeV. This interesting NMSSM regime offers the possibility to reconcile LEP Higgs searches with EW precision measurements, the latter strongly favouring $m_H \sim 100$ GeV.

Finally, it is interesting to remark that the NMSSM also offers two possible explanations for the slight excess of events ($\sim 2.3\,\sigma$) observed at LEP for $m_H \sim 95 - 100$ GeV: either the lightest Higgs has a non-vanishing singlet component [10] (leading to $\xi^Z \sim 0.4$, as can be infered from the left panel of Fig. 1), or it is indeed SM-like, but dominantly decays into a pair of light pseudoscalars [9], as discussed above.

On the theoretical side, it is also relevant to notice that in the NMSSM the mass of the SM-like Higgs can be larger than in the MSSM [11]: for large values of λ (but $\lambda \lesssim 0.7$ to avoid a Landau pole below $M_{\rm GUT}$) and in the low $\tan\beta$ regime, one can have $m_{h_1^0} \sim 140$ GeV, where h_1^0 has SM-like couplings to fermions and gauge bosons ($h_1^0 \sim H^{\rm SM}$). In the limit where the lightest Higgs is singlet-like ($\xi^Z \to 0$), h_2^0 behaves as $H^{\rm SM}$, its mass being no larger than the above mentioned bound. However, in scenarios of maximal mixing between doublet and singlet-like states, one can have $m_{h_1^0} \gtrsim 110$ GeV and $m_{h_2^0} \lesssim 162$ GeV, stil in agreement with LEP data. Moreover, should h_1^0 be singlet-like and decay unconventionally (e.g. $h_1^0 \to a_1^0 a_1^0 \to 4b$), then the upper bound on the mass of the SM-like h_2^0 can be even further relaxed. For these regimes, Tevatron exclusion results [12] already apply to part of the NMSSM parameter space (contrary to the MSSM case).

By relaxing the upper bound on the lightest Higgs boson, and allowing for regimes where

a light SM-like Higgs is still in agreement with LEP bounds, the NMSSM also renders less severe the so-called "Higgs little fine tuning problem" of the MSSM, which is related to the non-observation of a light Higgs state at LEP. In the MSSM, the mass of the lightest Higgs state is bounded from above: at tree level $m_{h_1^0} \lesssim M_Z |\cos 2\beta|$, and while the inclusion of radiative corrections allows to relax this bound, one still has $m_{h_1^0} \lesssim 130-135$ GeV (the limits being model dependent, and for a sparticle spectrum no heavier than a few TeV). The allowed interval for the mass of the lightest MSSM Higgs scalar is thus considerably narrower than in the NMSSM.

4 LHC search strategies

Having an extended and more complex Higgs sector[a] does not imply that detection of an NMSSM Higgs boson will be easier at the LHC. In the previous section we have seen that NMSSM Higgs might have escaped LEP detection, either due to non-standard couplings to SM fermions and gauge bosons, or in the presence of Higgs-to-Higgs decays. NMSSM searches at the LHC must strongly build upon LEP's lessons: the new, distinctive features of the NMSSM, especially concerning the Higgs sector, must be taken into account in devising strategies, for instance for ATLAS and CMS. The different production processes, new intermediate states in cascade decays, and unusual final-state configurations might require dedicated studies and simulations.

If Higgs-to-Higgs decays are kinematically forbidden (or marginally allowed, but with tiny branching ratios), then NMSSM Higgs searches can be carried out as in the MSSM [13]. Different couplings and new (loop) corrections should be taken into account in a (re)-evaluation of the expected production cross sections and decay rates. For some regimes, the Higgs sector can be more visible than in the MSSM (e.g., as shown in [14], up to 3 Higgs - $h^0_{1,2}$ and a^0_1 - can be observed, from the decays into 2 photons). Recently, it was noticed that light NMSSM Higgs, with a mass 80-100 GeV (in agreement with LEP constraints due to a large singlet component) may have a BR$(h^0_1 \to \gamma\gamma)$ considerably larger than a SM-like Higgs of similar mass, $\sigma(gg \to h^0_1 \to \gamma\gamma) \sim 6 \times \sigma(gg \to H^{\rm SM} \to \gamma\gamma)$, due to a reduced coupling to b quarks [15].

In recent years, many efforts have been put forward to generalise the "No-lose" theorem of the MSSM to the NMSSM: under the assumption that Higgs-to-Higgs decays are kinematically forbidden, it has been established that at least one of the NMSSM Higgs bosons can be detected at the LHC with 600 fb^{-1} of integrated luminosity [16].

However, not only Higgs-to-Higgs decays can occur in large regions of the NMSSM parameter space, but they also constitute one of the most interesting features of this model. If these decays are indeed present, Higgs searches at the LHC (and at the Tevatron) can be considerably more complicated, and many new channels have been considered, for the different $m_{a_1^0}$ regimes. Here we briefly comment on some dedicated strategies for regions in parameter space where the dominant decays of (light) Higgs are $h^0_1 \to a^0_1 a^0_1$, and $a^0_1 \to \tau\tau$. (For $m_{a_1^0}$ above the $b\bar{b}$ threshold, see for instance [17].) In general, it can be quite challenging to identify the four leptons in these decay modes, and final states containing as much as 8 neutrinos imply signatures of large missing energy. SM backgrounds will also be important (heavy flavour jets, vector boson and light jets, Υ production, etc.).

The $h^0_1 \to a^0_1 a^0_1 \to 4\tau$ channel, with the taus decaying into muons and jets, has been analysed in [18], resorting to both Higgs-strahlung (triggering on leptonic decays of $W^\pm$), and vector boson fusion (triggering on two same sign non-isolated muons). While the latter may yield a larger number of events, the former can lead to very clean, almost background free signals, so that in both cases there is a significant potential for discovery. In regions where $a^0_1 \to \mu\mu$, the 2μ (4μ) invariant mass allows a direct estimation of $m_{a_1^0}$ ($m_{h_1^0}$); furthermore, the extremely

[a] We will not discuss here the impact of an extended neutralino sector for sparticle production and decay at colliders.

small background allows to rely on direct gg and $b\bar{b}$ fusion for Higgs production (instead of the subdominant vector boson fusion) [19]. If the lightest Higgs is produced via central exclusive production, $pp \to h_1^0 \to p + h_1^0 + p$ (with $h_1^0 \to a_1^0 a_1^0 \to 4\tau$), the prospects for observing such an NMSSM Higgs at the LHC are good, and one could determine $m_{h_1^0}$ and $m_{a_1^0}$ on an event-to-event basis. However, this would require installing forward detectors to measure the final state protons [20]. Finally, for regimes of very low $\tan\beta$ ($\tan\beta \lesssim 2$), most of LHC (and Tevatron) discovery prospects must be reconsidered: in such regimes for $\tan\beta$, BR($a_1^0 \to \tau^+\tau^-$) becomes increasingly reduced (accompanied by an increase of BR($a_1^0 \to gg + c\bar{c}$)), so that the light pseudoscalar easily evades both ALEPH and meson physics constraints (due to small ξ^{A^2} and X_d). However, this also implies that searches using the $a_1^0 \to \tau\tau$ and $a_1^0 \to \mu\mu$ modes will be more difficult. Nevertheless, dedicated searches at the LHC and Tevatron include direct detection of a_1^0 in $gg \to a_1^0 \to \mu\mu$ channel (as wel as in the other channels mentioned before) [9].

Light singlet-like Higgs are very difficult to detect (due to the smallness of their couplings). It has been noticed that in this case the process $pp \to h_1^0 +$ resolved jet $\to \tau^+\tau^-+$ jet (via gluon fusion) could allow for LHC detection with $\sqrt{s} = 14$ TeV [21].

In NMSSM scenarios with a light doublet-like CP-odd Higgs boson, the charged Higgs can be lighter than the top quark, dominantly decaying as $h^\pm \to a_1^0 W^\pm$. The search for subleading a_1^0 decay modes (into a pair of muons) could provide evidence for the charged Higgs, or even a discovery, with early LHC data [22]. Other channels, which are absent in the MSSM, and that deserve further investigation are, for example, $gg \to a_2^0 \to h^\pm W^\mp$ (where the a_2^0 has an important singlet component) [23].

It is important to re-emphasise that the discovery of MSSM-like Higgs and neutralinos does not necessarily establish that the MSSM is indeed at work: disentangling the NMSSM from the MSSM might be challenging, especially in regimes where the new states decouple and/or in the absence of a singlino LSP. In this case additional studies might be required, and unravelling the nature of the SUSY model will strongly depend on the precision of the experimental data.

5 Implications for Dark Matter

Due to the differences in the neutralino and Higgs sectors of the NMSSM, one can have dark matter scenarios that are very distinct from the MSSM. Depending on the regions of the parameter space, the LSP can be singlino-like (or have an important singlino component). The additional scalar and pseudoscalar Higgs bosons can have in impact on the processes leading to LSP annihilation, so that the correct relic density can be obtained in large regions of the parameter space [24]: the extra states can offer rapid annihilation via new s-channel resonances, and if light, new final states can be kinemmatically open (e.g. annihilation into Zh_1^0, $h_1^0 h_1^0$, $h_1^0 a_1^0$ and $a_1^0 a_1^0$). For instance, nearly pure binos can efficiently annihilate via h_1^0 resonances into a pair of light $a_1^0 a_1^0$. Provided there is a small higgsino component, a singlino LSP can also rapidly annihilate via the latter process and co-annihilations with heavier neutralinos, or with a nearly degenerate NLSP, are also possible. A singlino LSP can also be instrumental in recovering MSSM scenarios with a charged LSP (e.g., the lightest stau for $m_0 \ll M_{1/2}$ in the constrained MSSM).

Dark matter detection prospects can also be significantly different [b]. As discussed in [25] light NMSSM neutralinos (with a mass below the MSSM lower bound) may have an elastic scattering cross section on nucleons allowing to explain recent direct detection results (DAMA/LIBRA, CoGeNT or CDMS), provided that the spectrum contains light scalar and pseudoscalar Higgs.

[b] This topic was also addressed in the talks of A. Goudelis and T. Delahaye.

6 A simple and predictive model: the constrained NMSSM

Assuming that supersymmetry is spontaneously broken in a hidden sector, and that the mediation of SUSY breaking to the observable sector occurs via flavour blind interactions (as is the case of minimal supergravity models), all soft SUSY breaking terms will be universal at some very large scale (e.g., $M_{\rm GUT}$). The scale invariant NMSSM with universal soft breaking terms is denoted the fully constrained NMSSM (cNMSSM) [26], and is one of the most appealing SUSY extensions of the SM, both for its simplicity and predictivity.

Other than the gauge and quark/lepton Yukawa couplings, the Lagrangian of the cNMSSM depends on five parameters - m_0^2, $M_{1/2}$, A_0, λ and κ -, the correct EW symmetry breaking reducing the parameter space from five to four degrees of freedom. However, phenomenological arguments strongly constrain the parameter space, as we proceed to briefly explain.

In order to generate a non-vanishing singlet VEV (as required by the lower bound on the effective μ-term ($|\mu| \gtrsim 100$ GeV), the singlet soft breaking mass m_S^2 must not be too large. Since m_S is hardly renormalised between the GUT and the EW scales, its value at $M_{\rm GUT}$, given by m_0, must also be small (compatible with $m_0 \sim 0$). While in the cMSSM a regime where $m_0 \lesssim 1/5\, M_{1/2}$ would lead to a charged LSP (the lightest stau), in the cNMSSM the additional singlino-like neutralino can be lighter than $\tilde{\tau}_1$, so that a viable dark matter candidate can be recovered for very small or even vanishing values of m_0. An efficient reduction of the LSP abundance can only be achieved via co-annihilations with the stau NLSP, requiring nearly degenerate LSP and NLSP ($m_{\tilde{\tau}_1} - m_{\chi_S^0} \sim$ few GeV), which implies that $A_0 \sim -1/4\, M_{1/2}$ (and furthermore $m_0 \leq 1/10\, M_{1/2}$). Under such a regime for the soft breaking parameters, LEP constraints on the Higgs sector imply that λ must be also very small, $\lambda \lesssim 0.02$. Provided λ is not excessively small ($\lambda \gtrsim 10^{-5}$, to allow for co-annihilation), the resulting phenomenology is largely independent of its exact value. Thus, as depicted on the left panel of Fig. 2, the parameter space of the fully constrained NMSSM is essentially determined by $M_{1/2}$ ($\tan\beta$, no longer a free parameter, is quite large, $\tan\beta > 25$). Collider constraints lead to $M_{1/2} \gtrsim 500$ GeV, while the requirement that SUSY contributions account for the discrepancy of the measured muon anomalous magnetic moment with respect to the SM prediction favours $M_{1/2} \lesssim 1$ TeV [27].

Concerning the Higgs sector of the cNMSSM, and for increasing values of $M_{1/2}$, the lightest state can be singlet-like, a doublet-singlet mixture and, for large $M_{1/2}$, SM-like (the actual cross-over range depending on the value of m_0). The lightest pseudoscalar (always heavier than $h^0_{1,2}$) is singlet-like, while h^0_3, a^0_2 and $h^\pm$ are significantly heavier and nearly degenerate. Interestingly, just below the singlet-doublet cross-over for $h^0_{1,2}$, the cNMSSM can actually account for the two LEP "excesses", with a singlet-like h^0_1 with mass around 100 GeV and a SM-like h^0_2 around 117 GeV. The cNMSSM strongly interacting sparticle spectrum, displayed on the right hand-side of Fig. 2, is quite heavy (typically $m_{\tilde{g},\tilde{q}} \gtrsim 1$ TeV), with the gluino always heavier than all squarks (and sleptons). As seen from Fig. 2, the measurement of one sparticle mass (or mass difference) would allow to predict quite accurately the remaining sparticle spectrum.

Having a singlino LSP, nearly degenerate with the NLSP, leaves a striking imprint on cNMSSM decay chains: due to the weakly coupled singlino-like LSP, all sparticle branching ratios into χ_S^0 are tiny, and thus sparticles first decay into the stau NLSP. As an example, the simplest squark cascades typically are $\tilde{q} \to q\chi_2^0 \to q\tilde{\tau}_1\tau \to q\tau\tau\chi_S^0$. Hence, practically all cascade decays will go via $\tilde{\tau}_1$, leading to two τ's per decaying squark. For very small λ, or a very small NLSP-LSP mass difference, the stau lifetime can be so large that its decay vertices are visibly displaced, $\mathcal{O}$(mm - cm), a "smoking-gun" for the cNMSSM. All the above features should in principle allow to discriminate the cNMSSM from most realisations of the MSSM.

Another very appealing feature of the cNMSSM is that it can be easily ruled out. Detection of a singlino LSP relies on its non-singlet component, which is $\mathcal{O}(\lambda)$; hence direct detection (LSP-nucleon) cross sections are extremely small, and indirect detection of the products of

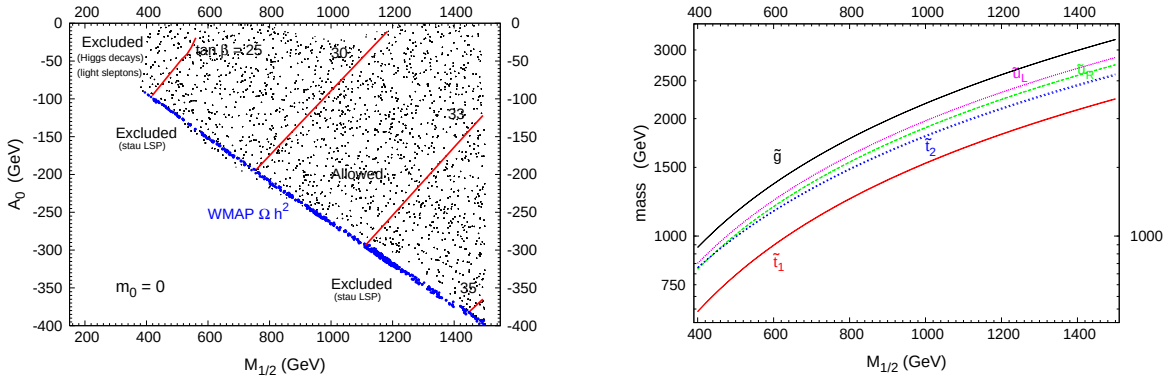

Figure 2: On the left, cNMSSM parameter space: experimentally allowed regions (scatter points) and imposing the correct DM relic density (blue). On the right, cNMSSM gluino and squark spectrum as a function of $M_{1/2}$.

LSP annihilation also appears impossible. Thus, the direct or indirect detection of a weakly interacting massive particle allows to exclude the cNMSSM.

The prospects for cNMSSM discovery at the LHC have been discussed in [28]. The dominant sparticle production modes are squark-gluino and squark pair production. Regarding the SM-like Higgs $h^0_{1,2}$, the most relevant production processes will be gluon-gluon and vector boson fusion, $gg \to$ Higgs and $qq \to qq$+Higgs, with the Higgs decaying into two photons (possibly $\tau^+\tau^-$ in the vector boson fusion process). The heavier non-singlet Higgs can be observed in associated production with $b\bar{b}$ pairs while, apart from the "cross-over" region, the singlet-like Higgs states are generally inaccessible. Dedicated cNMSSM cuts suggest that for the LHC operating at $\sqrt{s} = 14$ TeV, and for an integrated luminosity of 1 fb^{-1}, the signal-to-background ratio already allows for the discovery of the cNMSSM in the lower $M_{1/2}$ regime, while more luminosity will be required in the case of a heavier spectrum. Furthermore, the cNMSSM can be distinguished from the MSSM in the stau co-annihilation region.

7 Outlook

The NMSSM is a very interesting SUSY extension of the SM, solving in an elegant way the "μ-problem" of the MSSM, and rendering its "Higgs little fine tuning problem" less severe. Since it allows for a scale invariant superpotential, the NMSSM is the simplest supersymmetric model in which the SUSY breaking scale is the only scale in the Lagrangian.

The extended Higgs and neutralino sectors of the NMSSM have an impact regarding low-energy observables (such as B physics), dark matter prospects and collider phenomenology. Concerning the latter, the NMSSM allows to accommodate LEP constraints easier than the MSSM. In particular, the upper bound on the mass of the SM-like Higgs boson is relaxed, and the lightest Higgs scalar and pseudoscalar can be quite light (either due to an important singlet component, or to unconventional decays, such as $h \to aa$). Unconventional Higgs decay scenarios require dedicated studies and simulations. At present many studies are under way to ensure that at least one NMSSM Higgs will be observed at the LHC. The absence of a "No-lose" theorem should be kept in mind: a non-discovery of a Higgs boson at the LHC (potentially excluding scenarios as the cMSSM) could be a signal of the NMSSM.

The cNMSSM is perhaps one of the most simple and yet most predictive supersymmetric extensions of the SM since, in addition to all the appealing features of the NMSSM, its phenomenology is essentially described by one parameter, $M_{1/2}$. The cNMSSM predicts a heavy sparticle spectrum, with a $\tilde{\tau}_1$ appearing in all cascades, leading to a singlino-like LSP. The model can be discovered at the LHC, and be easilly ruled out by dark matter detection.

Acknowledgments

The author is grateful to the Organisers for the invitation to participate in the EW session of the *XLVI Rencontres de Moriond*, and for the scientifically rich and exciting atmosphere of the meeting, which allowed for many fruitful exchanges and discussions.

References

1. J. E. Kim and H. P. Nilles, Phys. Lett. B **138** (1984) 150.
2. U. Ellwanger, C. Hugonie and A. M. Teixeira, Phys. Rept. **496** (2010) 1 [arXiv:0910.1785 [hep-ph]].
3. U. Ellwanger, M. Rausch de Traubenberg and C. A. Savoy, Z. Phys. C **67** (1995) 665 [arXiv:hep-ph/9502206].
4. R. Dermisek and J. F. Gunion, Phys. Rev. Lett. **95** (2005) 041801 [arXiv:hep-ph/0502105]; U. Ellwanger, J. F. Gunion and C. Hugonie, JHEP **0507** (2005) 041 [arXiv:hep-ph/0503203].
5. R. Dermisek and J. F. Gunion, Phys. Rev. D **73** (2006) 111701 [arXiv:hep-ph/0510322].
6. See, e.g., G. Hiller, Phys. Rev. D **70** (2004) 034018 [arXiv:hep-ph/0404220]; F. Domingo and U. Ellwanger, JHEP **0712** (2007) 090 [arXiv:0710.3714 [hep-ph]]; F. Domingo *et al.*, JHEP **0901** (2009) 061 [arXiv:0810.4736 [hep-ph]].
7. M. Schumacher [ATLAS Collaboration], presented at Moriond 2011, EW session.
8. F. Domingo, U. Ellwanger and M. A. Sanchis-Lozano, Phys. Rev. Lett. **103** (2009) 111802 [arXiv:0907.0348 [hep-ph]].
9. R. Dermisek, J. F. Gunion, Phys. Rev. **D81** (2010) 075003 [arXiv:1002.1971 [hep-ph]].
10. R. Dermisek and J. F. Gunion, Phys. Rev. D **75** (2007) 075019 [arXiv:hep-ph/0611142]; Phys. Rev. D **76** (2007) 095006 [arXiv:0705.4387 [hep-ph]].
11. U. Ellwanger and C. Hugonie, Mod. Phys. Lett. A **22** (2007) 1581 [arXiv:hep-ph/0612133].
12. B. Jayatilaka [TEVATRON Collaboration], presented at Moriond 2011, EW session.
13. See, e.g., A. Djouadi, Phys. Rept. **459** (2008) 1 [arXiv:hep-ph/0503173].
14. S. Moretti, S. Munir, Eur. Phys. J. **C47** (2006) 791-803. [hep-ph/0603085].
15. U. Ellwanger, Phys. Lett. **B698** (2011) 293-296. [arXiv:1012.1201 [hep-ph]].
16. U. Ellwanger, J. F. Gunion and C. Hugonie, arXiv:hep-ph/0111179.
17. U. Ellwanger *et al.*, arXiv:hep-ph/0401228; S. Moretti *et al.*, Phys. Lett. B **644** (2007) 241 [arXiv:hep-ph/0608233]; M. Carena *et al.*, JHEP **0804** (2008) 092 [arXiv:0712.2466 [hep-ph]]; A. Djouadi *et al.*, JHEP **0807** (2008) 002 [arXiv:0801.4321 [hep-ph]].
18. A. Belyaev *et al.*, [arXiv:0805.3505 [hep-ph]].
19. A. Belyaev *et al.*, Phys. Rev. **D81** (2010) 075021 [arXiv:1002.1956 [hep-ph]].
20. J. R. Forshaw *et al.*, JHEP **0804** (2008) 090 [arXiv:0712.3510 [hep-ph]].
21. A. Belyaev *et al.*, PoS **DIS2010** (2010) 207 [arXiv:1006.0144 [hep-ph]].
22. R. Dermisek, [arXiv:1012.3487 [hep-ph]].
23. F. Mahmoudi *et al.*, Eur. Phys. J. **C71** (2011) 1608 [arXiv:1012.4490 [hep-ph]].
24. G. Belanger *et al.*, JCAP **0509** (2005) 001 [arXiv:hep-ph/0505142]; C. Hugonie, G. Belanger and A. Pukhov, JCAP **0711** (2007) 009 [arXiv:0707.0628 [hep-ph]].
25. D. Das and U. Ellwanger, JHEP **1009** (2010) 085 [arXiv:1007.1151 [hep-ph]]; D. A. Vasquez *et al.*, Phys. Rev. D **82** (2010) 115027 [arXiv:1009.4380 [hep-ph]].
26. A. Djouadi, U. Ellwanger and A. M. Teixeira, Phys. Rev. Lett. **101** (2008) 101802 [arXiv:0803.0253 [hep-ph]]; JHEP **0904** (2009) 031 [arXiv:0811.2699 [hep-ph]].
27. F. Domingo and U. Ellwanger, JHEP **0807** (2008) 079 [arXiv:0806.0733 [hep-ph]].
28. U. Ellwanger, A. Florent and D. Zerwas, JHEP **1101** (2011) 103 [arXiv:1011.0931 [hep-ph]].

Searches for Supersymmetry at CMS using the 2010 Data

C. Bernet, on behalf of the CMS collaboration
CERN, Geneva.

Searches for supersymmetry were conducted using the 35 pb^{-1} of data collected by the CMS experiment at the LHC in 2010, at a centre-of-mass energy of 7 TeV. A wide variety of final states featuring jets and missing transverse energy, possibly with leptons, were investigated. The data, consistent with the standard-model hypothesis, allow us to set limits on the existence of new physics, extending those previously obtained at the Tevatron and LEP.

1 Introduction

The standard model (SM) of particle physics has been enormously successful in describing all phenomena at the highest attainable energies thus far. Yet, it is widely believed to be only an effective description of a more complete theory which is valid at the highest energy scales. Of particular theoretical interest is supersymmetry (SUSY) [1,2,3,4,5] which solves the hierarchy problem [6,7] of the SM by compensating for each of the fermionic and bosonic degrees of freedom in the SM with a supersymmetric bosonic and fermionic degree of freedom, respectively. The resulting superfields have the same quantum numbers as their SM counterparts, except for spin. Since no SUSY particle has been observed so far, they must have higher masses than their SM partners, implying that SUSY is a broken symmetry.

At the Large Hadron Collider (LHC) at CERN, supersymmetric particles, if they exist, are predicted to be produced dominantly via QCD, through the fusion of two gluons into a pair of gluinos, a pair of squarks, or a gluino and a squark. The production cross-section for massive squarks or gluinos falls as a power law with the squark or gluino mass, following the available energy $\sqrt{\hat{s}}$ in the partonic centre-of-mass frame. The LHC, with a proton-proton centre-of-mass energy $\sqrt{s}$ of 7 TeV, is a copious source of high-energy partons which allows to probe squark and gluino masses beyond the limits previously set at LEP and at the Tevatron. Squarks and gluinos initiate a decay cascade in which quarks are produced, until the lightest supersymmetric particle (LSP) is created. The dynamics of the cascade depends on the SUSY model under consideration, and in particular on the masses of the supersymmetric particles. If R-parity is conserved, the LSP is unable to decay into SM particles and is therefore stable. If, in addition, the LSP is a neutralino, it is weakly interacting and thus escapes detection, hence missing transverse energy ($E_{\text{T}}^{\text{miss}}$) in the final state. Typical hadronic decay modes for gluinos ($\tilde{g}$) and squarks ($\tilde{q}$) are $\tilde{q} \to q\chi_1^0$ and $\tilde{g} \to qq\chi_1^0$. In these examples, the squark and the gluino directly decay to the lightest neutralino χ_1^0, the gluino doing so via an off-shell squark. As a result, squark pair production usually gives rise to more than two jets, and gluino pair production to more than four jets. The transverse momenta of the jets are driven by the difference in mass between the squark or gluino and the neutralino. Leptons can appear in the final state, for example if heavy neutralinos ($\tilde{\chi}_2^0 \to l^{\pm}\tilde{l}^{\mp} \to l^{\pm}l^{\mp}\chi_1^0$) or charginos ($\tilde{\chi}_1^{\pm} \to \chi_1^0 W^{\pm}$) are created in

the decays cascades of the squark or gluino.

The CMS detector [8] is used to investigate many final states that could arise from the strong production of squarks and gluinos. An effort is made to make these final states independent, so that all analyses can ultimately be easily combined. Because the presence of leptons is not guaranteed, investigating hadronic final states with jets and high missing transverse energy is the most efficient way to look for SUSY. Dealing with the huge QCD background is however a challenge. In CMS, three complementary approaches are followed. The α_T analysis, presented elsewhere [9] makes use of the α_T variable to completely remove the QCD background from the search region, leaving solely electroweak backgrounds, namely $t\bar{t} + jets$, W+jets and Z $\rightarrow \nu\nu$+jets. The jets + $H_{\mathrm{T}}^{\mathrm{miss}}$ analysis, summarized in Section 2.1, consists of looking for an excess of multi-jet events at high $H_{\mathrm{T}}^{\mathrm{miss}}$, an approximation of the $E_{\mathrm{T}}^{\mathrm{miss}}$ computed as the opposite of the vector sum of the jet transverse momenta. This approach is the most efficient of the three, but requires the QCD background to be accurately controlled. The so-called razor analysis, presented in Section 2.2 relies on novel variables to reduce the QCD background to a negligible level in the search region, and to predict the background contribution. The final search sample of this analysis has about 30% of events in common with the jets+$H_{\mathrm{T}}^{\mathrm{miss}}$ analysis. While the razor analysis is less efficient than the jets+$H_{\mathrm{T}}^{\mathrm{miss}}$ analysis, it is less sensitive to the effects of initial state radiation. Requiring leptons in the final state in addition to jets and missing transverse energy strongly reduce the standard-model background. With one isolated lepton, the QCD and Z $\rightarrow \nu\nu$+jets backgrounds get suppressed. With two opposite-sign leptons [10], the W+jets background becomes negligible, and several handles can be used for an accurate estimation of the remaining $t\bar{t}$ background from the data. Asking for two same-sign leptons, or for three or more leptons, dramatically suppresses the standard-model background, for a very clean search of physics beyond the standard model, like the production of squarks and gluinos which can naturally lead to such final states.

In these proceedings, the emphasis is put on the most recent fully hadronic analyses, and several leptonic analyses are briefly summarized. Other important search fields are also being covered by CMS but could not be presented here. For example, in the context of the general gauge-mediated SUSY breaking with the lightest neutralino as the next-to-lightest supersymmetric particle and the gravitino as the lightest, a natural signature for squark or gluino production is the presence of two photons and $E_{\mathrm{T}}^{\mathrm{miss}}$ in the final state [11].

2 Fully hadronic searches

2.1 Jets + H_{T}^{miss} analysis

The data used in this analysis [12] are collected using triggers requiring a minimal jet activity $H_{\mathrm{T}}^{\mathrm{trig}}$, measured as the scalar sum of the transverse momentum of the calorimeter jets reconstructed at trigger level. The rapid increase in instantaneous luminosity during the 2010 data taking resulted in the threshold on $H_{\mathrm{T}}^{\mathrm{trig}}$ being raised from 100 to 140 and finally 150 GeV. The particle flow algorithm [13,14] identifies and reconstructs all particles produced in the collision, namely charged hadrons, photons, neutral hadrons, muons, and electrons. The resulting list of particles is then used to reconstruct particle jets, compute the $E_{\mathrm{T}}^{\mathrm{miss}}$, and quantify the lepton isolation.

The event selection starts from a loose validation region. On top of this baseline selection, tighter selection criteria are applied to define the search regions. The baseline selection requirements after trigger boil down to selecting events with (i) at least three jets with $p_{\mathrm{T}} > 50\,\mathrm{GeV}/c$ and $|\eta| < 2.5$; (ii) $H_{\mathrm{T}} > 300\,\mathrm{GeV}$, where H_{T} is defined as the scalar sum of the transverse momenta of all the jets having $p_{\mathrm{T}} > 50\,\mathrm{GeV}/c$ and $|\eta| < 2.5$; (iii) $H_{\mathrm{T}}^{\mathrm{miss}} > 150\,\mathrm{GeV}$, where $H_{\mathrm{T}}^{\mathrm{miss}}$ is defined as the magnitude of the vectorial sum of the p_{T} of the jets having, in this case, $p_{\mathrm{T}} > 30\,\mathrm{GeV}/c$ and $|\eta| < 5$; (iii) no isolated electron nor muon with $p_{\mathrm{T}} > 10$ GeV/c. Additionally,

the $H_{\mathrm{T}}^{\mathrm{miss}}$ vector is required not to be aligned with one of the three leading jets, to reject QCD multi-jet events in which a single mis-measured jet yields high $H_{\mathrm{T}}^{\mathrm{miss}}$.

Two search regions were defined in this inclusive jets-plus-missing-momentum search. The first search selection, defining the "high-$H_{\mathrm{T}}^{\mathrm{miss}}$ search region", tightens the baseline cuts with an $H_{\mathrm{T}}^{\mathrm{miss}} > 250\,\mathrm{GeV}$ requirement, to search for a generic invisible particle in a low background environment. The second selection adds a $H_{\mathrm{T}} > 500\,\mathrm{GeV}$ cut to the baseline selection, yielding the "high-H_{T} search region", sensitive to cascade decays of high-mass new-physics particles where more energy is transferred to visible particles and less to the dark-matter candidate. The main background contributions in the two search regions are estimated using data-driven techniques. Due to its huge cross-section, QCD multi-jet production can give rise to high $H_{\mathrm{T}}^{\mathrm{miss}}$ because of the finite jet energy resolution, or of rare but dramatic mis-measurements of the jet energy induced by various instrumental effects. The most important instrumental effects were identified in the simulation to be related to missing channels in the ECAL, and to jet punch-through giving rise to multi-TeV fake muons in the particle jets. The simulation was used to design dedicated event filters to remove such events.

The QCD background was estimated using the so-called "rebalance+smear" technique. An inclusive multi-jet sample of events is selected. The energy of each jet is first rescaled to obtain a null $H_{\mathrm{T}}^{\mathrm{miss}}$ using a maximum-likelihood fit taking into account the jet energy resolution in the process. This rescaling produces a seed event from which all sources of $H_{\mathrm{T}}^{\mathrm{miss}}$, possibly genuine, have been removed. The jets are then smeared by a simulated jet energy response distribution. The simulated distribution is corrected for differences between the data and the simulation by factors obtained from di-jet asymmetry measurements. The other standard-model background events contributing to the search regions feature at least one neutrino in the final state, hence true $H_{\mathrm{T}}^{\mathrm{miss}}$. W+jets events, where the W possibly comes from a top and decays to a lepton and a neutrino, end up in the search region in case the lepton from the W decay is not identified in the analysis, either because it is a τ decaying hadronically, or an electron or muon that is lost (not identified by the lepton veto). The contribution of this source of background is estimated by selecting from the data a control sample of events with an isolated muon and jets. To predict the number of events with a lost lepton in the search region, the number of events in this control sample is corrected for lepton reconstruction and identification efficiency by factors measured using Z events in the data, and by acceptance factors from the simulation. To estimate the number of events in which a tau decays hadronically, the muon in the control sample is replaced by a jet representing the hadronically decaying tau, which is taken into account when applying the search selections. The uncertainty on the W+jets background estimation (including $t\bar{t}$) is dominated by the statistical error on the number of events in the control sample. The last source of background, especially important because it dominates at high $H_{\mathrm{T}}^{\mathrm{miss}}$, is $\mathrm{Z} \to \nu\nu$+jets. As no $\mathrm{Z} \to ee$ nor $\mathrm{Z} \to \mu\mu$ events are observed in the search regions, these processes cannot be used to predict the $\mathrm{Z} \to \nu\nu$+jets background contribution. This contribution is instead estimated using a control sample of isolated γ+jets events, in which the photon is ignored when applying the search selections. This strategy exploits the fact that at high boson p_{T}, the Z and γ behave in a similar way, apart from electroweak coupling differences, and small residual mass effects. The number of events in the control sample is corrected by a Z/γ cross-section correction factor obtained from the simulation. Several other effects, such as the contamination of the control sample by multi-jet QCD events, or the photon reconstruction and identification efficiencies, are taken into account. The error on this background prediction comes from the statistical error on the number of events in the control sample, and from systematic errors mostly related to the available number of events in the simulated samples and to the estimation of the contamination of the control sample by multi-jet events. Table 1 summarizes the results of the analysis, and shows that no excess of events is found in the data. The limit set on the number of signal events is interpreted in the context of various SUSY models in Section 2.3.

Table 1: Predicted and observed event yields for the baseline selection, and for the high-$H_{\mathrm{T}}^{\mathrm{miss}}$ and high-H_{T} search selections. The last line reports the 95% CL limit on the number of signal events given the observed number of events, and the total predicted background.

Background	Baseline selection		High-$H_{\mathrm{T}}^{\mathrm{miss}}$ selection		High-H_{T} selection	
$\mathrm{Z} \to \nu\nu + jets$ (γ+jets method)	26.3	$\pm$4.8	7.1	$\pm$2.2	8.4	$\pm$2.3
$W/t\bar{t} \to e, \mu$+X	33.0	$\pm$8.1	4.8	$\pm$1.9	10.9	$\pm$3.4
$W/t\bar{t} \to \tau_{\mathrm{had}}$+X	22.3	$\pm$4.6	6.7	$\pm$2.1	8.5	$\pm$2.5
QCD	29.7	$\pm$15.2	0.16	$\pm$0.10	16.0	$\pm$7.9
Total background estimated from data	111.3	$\pm$18.5	18.8	$\pm$3.5	43.8	$\pm$9.2
Observed in 36 pb^{-1} of data	111		15		40	
95% C.L. limit on signal events	40.4		9.6		19.6	

2.2 Razor analysis

This analysis relies on the novel "razor" variables [15] to define search regions and predict the background contribution in a data-driven way. For the pair-production of two heavy particles of mass $M_{\tilde{q}}$ decaying into a visible part and an invisible part of mass M_{χ}, the variable M_R provides an approximation of the quantity $M_{\Delta} \equiv (M_{\tilde{q}}^2 - M_{\tilde{\chi}}^2)/M_{\tilde{q}}$. The search consists of looking for a signal peak in the M_R distribution, on top of a steeply falling standard-model background distribution. Cutting on the dimensionless R variable strongly reduces the standard-model background, and to give its M_R distribution an easy-to-control exponential shape.

The razor analysis [16] defines a set of physics objects, namely jets, isolated electrons, and isolated muons. All of these objects are used in the computation of R and M_R, which proceeds in the following way. The objects are first grouped into two "mega-jets" using an hemisphere algorithm. Each mega-jet ideally corresponds to the visible part of the decay products of one of the pair-produced heavy particles. The R and M_R variables are then computed using the 4-momenta of the two mega-jets, and the $E_{\mathrm{T}}^{\mathrm{miss}}$ vector. Depending on the presence of an isolated electron or muon in the final states, the events are classified in three independent "boxes", the electron box, the muon box, and the hadronic box. The high R, high M_R region of each box constitutes an independent search region. The razor analysis is thus both a fully hadronic and a single lepton analysis. In these proceedings however, the focus is put on the more efficient fully hadronic sector, for which the low-M_R region of the leptonic boxes is used as a control sample

The event sample was collected using triggers based on the presence of a single electron, a single muon, and on H_T^{trig}. The jets are required to have $p_{\mathrm{T}} > 30$ GeV/c and $|\eta| < 3$, electrons to have $p_{\mathrm{T}} > 20$ GeV/c and $|\eta| < 2.5$, and muons to have $p_{\mathrm{T}} > 20$ GeV/c and $|\eta| < 2.1$. The difference in azimuth between the two mega-jets is required to be smaller than 2.8 rad, to reject di-jet QCD events. The M_R distribution for the data in the hadronic box, together with the full background prediction, is shown in Fig. 1, for $R > 0.5$.

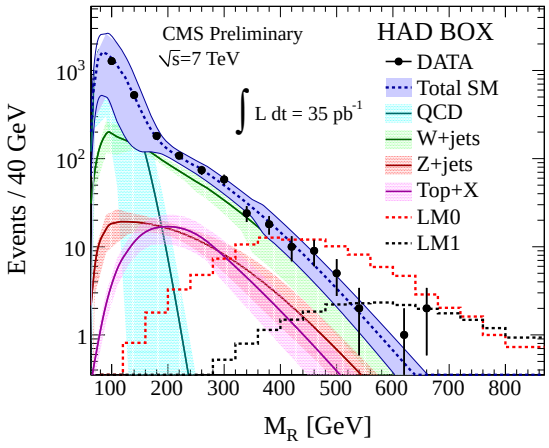

Figure 1: Distribution of M_R in the data, and background prediction for the "razor" analysis, with $R > 0.5$. The search region is defined by the additional requirement $M_R > 500$ GeV/c^2.

The background prediction is based on the observation that above a given

value of M_R, all background distributions drop following an exponential function. At low M_R, the background shape is mostly driven by the efficiency of the $H_{\rm T}$ trigger, and by the mass scales of the standard-model processes. For instance, M_R peaks around the mass of the top quark for $t\bar{t}$ events.

For the $t\bar{t}$, Z $\rightarrow \nu\nu$+jets, and W+jets backgrounds, the parameters of the exponential function driving the evolution of the M_R distribution at high M_R are taken from the simulation. In the simulation, and also in Fig. 1, these parameters appear to be roughly equal, indicating a similar behaviour of these background processes in terms of R and M_R. These parameters are then corrected by factors compatible with one, extracted from a comparison between data and simulation for W+jets events in the muon box. The relative normalization of these three sources of background is set according to the inclusive W, Z, and $t\bar{t}$ cross-sections measured by CMS [17,18]. The normalization of the overall background distribution to the data is performed by measuring lepton boxes event yields, which are then corrected for lepton reconstruction and identification efficiency. A fit is finally performed in the $80 < M_R < 400$ GeV/c^2 region, to obtain the parameters of the $H_{\rm T}$ trigger turn-on shape and the overall normalization of the QCD background. The shape of the QCD background was obtained using a low-bias, prescaled trigger. The background is predicted by extrapolating the resulting background distribution to the search region, defined as $M_R > 500$ GeV/c^2. In this region, 7 events are observed in the data, and 5.5 ± 1.4 are expected from the background. As no excess is observed, a model-independent upper limit is set on the number of signal events, $s < 8.4$. This limit is interpreted in the context of various SUSY models in Section 2.3.

2.3 Model dependent interpretation

The results of the fully hadronic (Sections 2.1 and 2.2) analyses were interpreted in the context of the constrained MSSM (cMSSM), a truncation of the full parameter space of the MSSM motivated by the minimal supergravity framework for spontaneous soft breaking of supersymmetry. In the cMSSM, the soft breaking parameters are reduced to five: three mass parameters, m_0, $m_{1/2}$ and A_0 being respectively the universal scalar mass, the universal gaugino mass, and the universal trilinear scalar coupling, as well as tanβ, the ratio of the up-type and down-type Higgs vacuum expectation values, and the sign of the supersymmetric Higgs mass parameter μ. Scanning over this parameter space yields models which, while not entirely representative of the complete MSSM, vary widely in their supersymmetric mass spectra and thus in the dominant production channels and decay chains.

After fixing A_0, tanβ and the sign of μ, the model independent upper limit s^* on the number of signal events s from each analysis is projected on the $(m_0, m_{1/2})$ plane by excluding the model if $s(m_0, m_{1/2}) > s^*$. The various sources of uncertainty on the signal yield and the signal contamination of the control samples are taken into account. Figures 2(a) and (b) present the limits set by the jets+$H_{\rm T}^{\rm miss}$ and razor analyses. The expected limits are obtained by taking the median of the background test statistics as the result of the experiment, and the $\pm 1\sigma$ band by taking the median $\pm 1\sigma$.

The results of the fully hadronic analyses were also interpreted in the context of two benchmark simplified models [19]: gluino-LSP production (left) and squark-LSP production (right). The former refers to pair-produced gluinos, where each gluino directly decays to two light quarks and the LSP resulting in a four jet plus missing transverse energy final state. The latter refers to pair-produced squarks, where each squark decays to one jet and the LSP resulting in a two jet plus missing transverse energy final state. Figures 2(c) and (d) show the upper limit on the cross-section as a function of the physical masses of the particles involved in each model. In each bin, the upper limits obtained in the α_T, the jets+$H_{\rm T}^{\rm miss}$ and the razor analyses are considered, and the minimum one is shown. Theoretical uncertainties are not included.

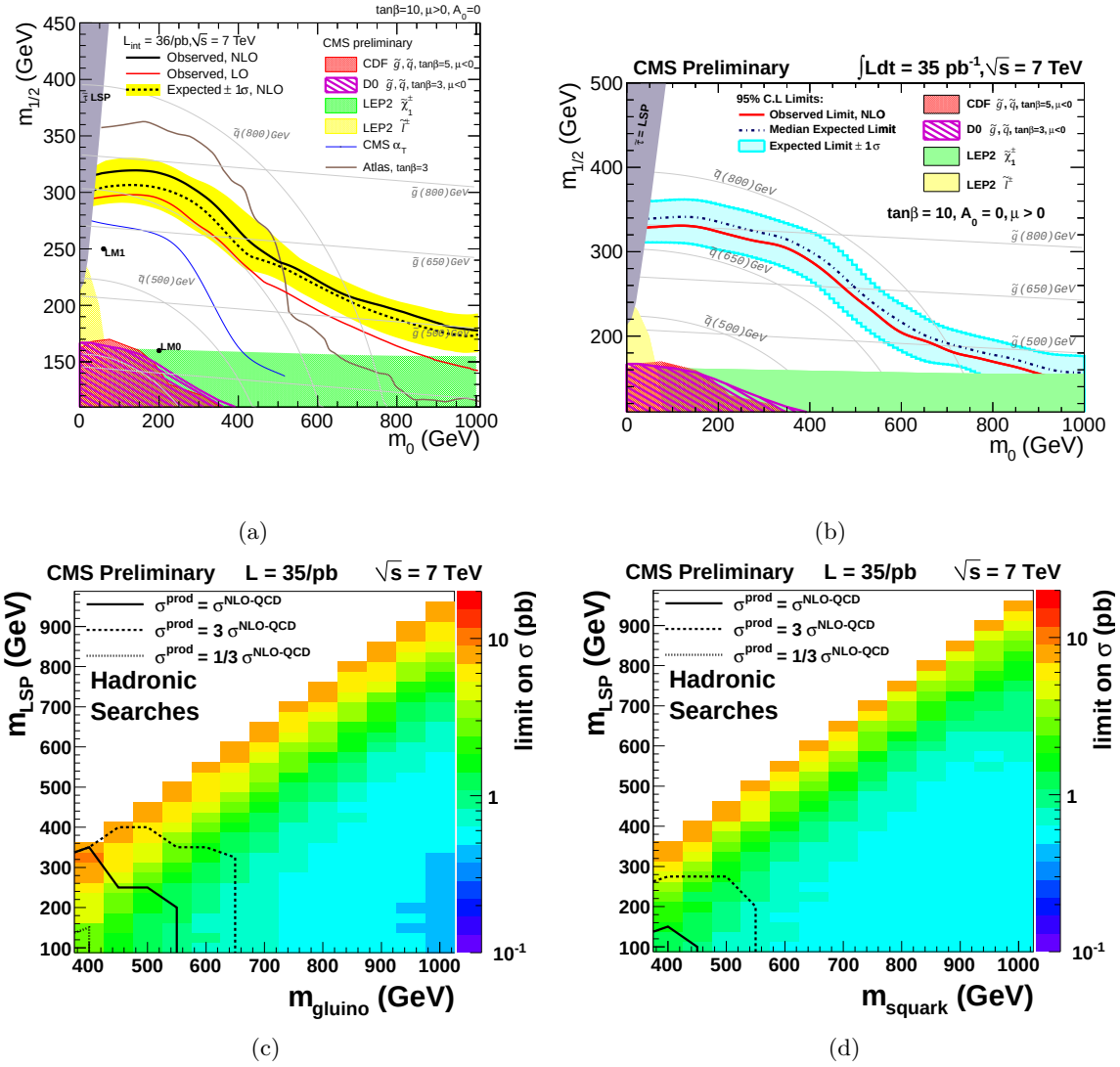

Figure 2: Expected and observed 95% C.L. limits in the cMSSM $(m_0, m_{1/2})$ parameter plane for (a) the jets+$H_{\mathrm{T}}^{\mathrm{miss}}$ analysis and (b) the razor analysis. Limits on the di-gluino (c) and di-squark (d) cross-sections in simplified models, obtained by combining the three fully hadronic analyses, namely α_T, jets+$H_{\mathrm{T}}^{\mathrm{miss}}$ and razor.

3 Leptonic searches

The single lepton analysis [20] selects events featuring jets, $E_{\mathrm{T}}^{\mathrm{miss}}$, and a single lepton in the final state. The presence of the lepton strongly reduces the contribution of the QCD multi-jet and $\mathrm{Z} \to \nu\nu$+jets backgrounds, and provides several handles to build a data-driven prediction of the remaining background contribution from QCD, $t\bar{t}$, and W+jets. Events containing an additional lepton are vetoed, and handled by the di-lepton and multi-lepton analyses. The event sample was collected using triggers based on the presence of a single electron or a single muon. The requirement of an H_{T} trigger was added when the peak luminosity increased beyond 2×10^{32} cm$^{-2}s^{-1}$. The trigger selection is fully efficient with respect to the baseline selection applied offline, which consists of requiring (i) four jets with $p_{\mathrm{T}} > 30$ GeV/c and $|\eta| < 2.4$ with $H_{\mathrm{T}} > 500$ GeV; (ii) an isolated lepton, which can be either a muon with $p_{\mathrm{T}} > 20$ GeV/c and $|\eta| < 2.1$, or an electron with $p_{\mathrm{T}} > 20$ GeV/c and $|\eta| < 2.4$. The search region is defined by an additional cut on the missing transverse energy, $E_{\mathrm{T}}^{\mathrm{miss}} > 250$ GeV. The contribution of the

main background processes to the search region, $t\bar{t}$ and W+jets, is estimated using the lepton spectrum method. The foundation of this method is that, when the lepton and neutrino are produced together in a W decay (either in $t\bar{t}$ or in W+jets events), the lepton p_{T} spectrum is directly related to the neutrino p_{T} spectrum. The lepton spectrum is used to predict the $E_{\mathrm{T}}^{\mathrm{miss}}$ distribution, after suitable corrections related to the effect of the W polarisation on the lepton and neutrino p_{T} spectra, and to the lepton acceptance and reconstruction efficiency. Combining the electron and muon channels, 2 events are observed in the search region, while 3.6 ± 2.9 are expected. A 95% model independent upper limit of 4.1 signal events is calculated. In the cMSSM, for $\tan\beta = 10$, $A_0 = 0$, and $\mu > 0$, gluino and squark masses larger than about 550 GeV/c^2 are excluded.

The same-sign di-lepton analysis requires, in addition to jets and $E_{\mathrm{T}}^{\mathrm{miss}}$, exactly two isolated leptons of the same sign which can be electrons, muons or taus decaying hadronically. The event sample was collected using di-lepton and single-lepton triggers, but also H_{T} triggers, which provide sensitivity to events with low p_{T} electrons and muons. The search selection and the data-driven background estimation techniques employed where chosen according to the trigger in use (lepton or hadron), and the channel ($l_i l_j$ where $l_{i,j} = e, \mu, \tau$). In all search regions, the predicted number of background events is compatible with zero, and no excess is observed. The analysis and the results are described in details in Ref [21], which also provides lepton efficiency maps that can be used to test a variety of models.

The multi-lepton analysis [22] selects events with three isolated leptons or more, acquired using single-lepton and di-lepton triggers. The events are sorted in 54 independent samples according to the relative charge of the leptons and their flavour, which can be e, μ, and τ. The three-lepton requirement strongly reduces the standard-model background, and the largest remaining background process is Z+jets, including Drell-Yan. The remaining background is further suppressed by requiring $H_{\mathrm{T}} > 30$ GeV, $E_{\mathrm{T}}^{\mathrm{miss}} > 50$ GeV or a Z veto, depending on the considered final state. No excess is found with respect to the predicted background in search region, and limits are set in a variety of models. In particular, in the so-called co-NLSPs scenario (see Ref [23] and references therein), squark and gluino masses lower than 830 GeV/c^2 and 1040 GeV/c^2 are excluded.

4 Conclusion

Complementary searches for Supersymmetry and other new physics leading to similar final states were conducted at CMS using the 35 pb^{-1} of data collected in 2010, in a wide variety of final states. No excess has been observed so far with respect to the expectations from the standard model, and stringent limits were set in various SUSY models. Data-driven background estimation techniques have been used wherever possible, paving the way towards the analysis of high-luminosity 2011 data.

5 Acknowledgements

I would like to thank the members of the CMS collaboration for the excellent performance of the detector and of all the steps culminating in these results, as well as the members of the CERN accelerator departments for the smooth operation of the LHC machine.

1. J. Wess and B. Zumino. Supergauge transformations in four dimensions. *Nucl. Phys.*, B70:39, 1974.
2. H.P.Nilles. Supersymmetry, supergravity and particle physics. *Phys. Reports*, 110:1, 1984.
3. H. E. Haber and G. L. Kane. The search for supersymmetry: Probing physics beyond the standard model. *Phys. Reports*, 117:75, 1987.

4. S. Ferrara R. Barbieri and C. A. Savoy. Gauge models with spontaneously broken local supersymmetry. *Phys. Lett.*, B 119:343, 1982.
5. E. Eichten S. Dawson and C. Quigg. Search for supersymmetric particles in hadron-hadron collisions. *Phys. Rev.*, D31:1581, 1985.
6. E.Witten. Dynamical breaking of supersymmetry. *Nucl. Phys.*, B 188:513, 1981.
7. S.Dimopoulos and H.Georgi. Softly broken supersymmetry and SU(5). *Nucl. Phys.*, B 193:150, 1981.
8. The CMS experiment at the CERN LHC. *JINST*, 0803:S08004, 2008.
9. The CMS collaboration. Search for supersymmetry in pp collisions at 7 TeV in events with jets and missing transverse energy. oai:cds.cern.ch:1320934. 2011.
10. The CMS collaboration. Search for physics beyond the standard model in opposite-sign dilepton events in pp collisions at $\sqrt{s} = 7$ TeV. oai:cds.cern.ch:1333985. 2011.
11. The CMS collaboration. Search for supersymmetry in pp collisions at $\sqrt{s} = 7$ TeV in events with two photons and missing transverse energy. *To appear*, 2011.
12. The CMS collaboration. Search for new physics at CMS with jets and missing momentum. *CMS PAS*, SUS-10-005, 2011.
13. The CMS collaboration. Particle-flow event reconstruction in CMS and performance for jets, taus, and missing E_{T}. *CMS PAS*, PFT-09-001, 2009.
14. The CMS collaboration. Commissioning of the particle-flow reconstruction in minimum-bias and jet events from pp collisions at 7 TeV. *CMS PAS*, PFT-10-002, 2010.
15. C. Rogan. Kinematics for new dynamics at the LHC. arxiv:1006.2727v2 [hep-ph]. *CALT 68-2790*, 2010.
16. The CMS collaboration. Inclusive search for squarks and gluinos at $\sqrt{s} = 7$ TeV. *CMS PAS*, SUS-10-009, 2011.
17. Measurements of inclusive w and z cross sections in pp collisions at 7 TeV. *CMS PAS*, EWK-10-002, 2010.
18. The CMS collaboration. Selection of top-like events in the dilepton and lepton-plus-jets channels in early 7 TeV data. *CMS PAS*, TOP-10-004, 2010.
19. Johan Alwall, Philip Schuster, and Natalia Toro. Simplified models for a first characterization of new physics at the LHC. *Phys.Rev.*, D79:075020, 2009.
20. The CMS collaboration. Search for supersymmetry in proton-proton collisions at $\sqrt{s} =$ 7 TeV in events with a single lepton, jets, and missing transverse momentum. *CMS PAS*, SUS-10-006, 2011.
21. The CMS collaboration. Search for new physics with same-sign isolated dilepton events with jets and missing transverse energy at the LHC. ai:cds.cern.ch:1345080. 2011.
22. The CMS collaboration. Search for physics beyond the standard model using multilepton signatures in $\sqrt{s} = 7$ TeV pp collisions with the CMS detector at the LHC. *To appear*, 2011.
23. Joshua T. Ruderman and David Shih. Slepton co-NLSPs at the Tevatron. arxiv:1009.1665 [hep-ph]. 2010.

Z' Bosons and Friends

Manuel Pérez-Victoria
Departamento de Física Teórica y del Cosmos and CAFPE,
Universidad de Granada, E-18071 Granada, Spain

The invariance of extensions of the Standard Model under the full $SU(3)_C \otimes SU(2)_L \otimes U(1)_Y$ gauge group can be used to classify general vector bosons and to write their interactions in a model-independent fashion. This description is useful for both direct and indirect searches. We comment on electroweak precision limits and show some simple applications to Higgs and top physics.

1 General extra vector bosons and gauge invariance

New vector bosons are a common occurrence in theories beyond the Standard Model (SM). They appear whenever the gauge group of the SM is extended, as the gauge bosons of the extra (broken) symmetries. This is the case of Grand Unified Theories (GUT), including string constructions, or Little Higgs models. They also occur in theories in extra dimensions, when the gauge bosons propagate through the bulk. Strongly-interacting theories, such as technicolor, often give rise to spin 1 resonances. This can be related to the previous possibilities via hidden gauge symmetry or holography. Extra vector bosons are also receiving a lot of attention these days because they are among the best candidates for an early discovery at the LHC.

It is possible to classify vector bosons according to their electric charge: neutral vector bosons, called Z', charge ± 1 vector bosons, called W' and vectors with other integer or fractional charges. On the other hand, the complete theory including the new vectors must be invariant under the full $SU(3)_C \otimes SU(2)_L \otimes U(1)_Y$ gauge group. This imposes additional restrictions on the allowed couplings to the SM fields, and also implies that certain vectors must appear simultaneously and have similar masses. Of course, electroweak symmetry breaking can give rise, in some cases, to splittings in the masses of the different components of a given multiplet. These splittings are of the order of the Higgs vacuum expectation value.

In Ref.[1], Francisco del Aguila, Jorge de Blas and the author have made use of this information to classify the new vectors into irreducible representations of the full SM gauge group, and to

Table 1: Vector bosons contributing to the dimension-six effective Lagrangian. The quantum numbers $(R_c, R_L)_Y$ denote the representation R_c under $SU(3)_c$, the representation R_L under $SU(2)_L$ and the hypercharge Y.

Vector	$\mathcal{B}_\mu$	$\mathcal{B}^1_\mu$	$\mathcal{W}_\mu$	$\mathcal{W}^1_\mu$	$\mathcal{G}_\mu$	$\mathcal{G}^1_\mu$	$\mathcal{H}_\mu$	$\mathcal{L}_\mu$
Irrep	$(1,1)_0$	$(1,1)_1$	$(1,\mathrm{Adj})_0$	$(1,\mathrm{Adj})_1$	$(\mathrm{Adj},1)_0$	$(\mathrm{Adj},1)_1$	$(\mathrm{Adj},\mathrm{Adj})_0$	$(1,2)_{-\frac{3}{2}}$

Vector	$\mathcal{U}^2_\mu$	$\mathcal{U}^5_\mu$	$\mathcal{Q}^1_\mu$	$\mathcal{Q}^5_\mu$	$\mathcal{X}_\mu$	$\mathcal{Y}^1_\mu$	$\mathcal{Y}^5_\mu$
Irrep	$(3,1)_{\frac{2}{3}}$	$(3,1)_{\frac{5}{3}}$	$(3,2)_{\frac{1}{6}}$	$(3,2)_{-\frac{5}{6}}$	$(3,\mathrm{Adj})_{\frac{2}{3}}$	$(\bar{6},2)_{\frac{1}{6}}$	$(\bar{6},2)_{-\frac{5}{6}}$

study the most general gauge-invariant Lagrangian of this class of SM extensions. Here, we will briefly describe this formalism and show some applications.

The extra vector bosons that have been most extensively studied are neutral singlets, usually associated to an extra abelian gauge symmetry (see, for instance, the review in Ref. [2]). We will go far beyond this particular case, and consider all the representations that could be potentially observable by their indirect effects on precision data or their direct effects at colliders. Our main assumption is that single production of the new vector bosons is possible, so that they have good chances or being observed at large colliders. This requires interactions that couple SM operators to the extra vector fields and are linear in the latter. Since all the leading contributions to electroweak precision data (EWPD) arise from tree-level exchanges of just one heavy vector boson, they are included in this analysis. The only other assumption we make is that the interactions of these extra fields should be renormalizable by power counting, to avoid extra suppressions. From the point of view of a low-energy effective theory, these couplings produce dimension-six operators, while interactions with more than one new vector field in the same operator—and nonrenormalizable interactions—give rise to operators of higher scaling dimension.

The requirement of linear renormalizable couplings, together with Lorentz symmetry and invariance under the full SM gauge group, constrain the possible quantum numbers of the new vectors. In Table 1, we give the quantum numbers for the 15 irreducible representations of vector fields that can have linear and renormalizable interactions. This table also introduces the notation for each class of vector boson, which is partly inspired by the usual notation for SM fields. Note that the representations with nonvanishing hypercharge are complex.

These representations contain Z′ and W′ vectors, gluon-like bosons, diquarks, leptoquarks, and other possibilities. All new vector bosons in arbitrary models are contained in this table, as long as they can be singly produced. Note that this excludes models with R, T or KK parity. For phenomenological purposes, it is not important whether the new vector bosons are the gauge bosons of a broken extended gauge group or not. Nevertheless, it is interesting to note that all the types of vector bosons in Table 1 can in principle be obtained as the gauge bosons of an extended gauge group broken down to the SM.

To illustrate the power of the complete SM gauge invariance, as opposed to simple conservation of electric charge, let us study briefly two examples that are often included in electroweak fits and direct searches. First, consider a pair of charged vector bosons, and assume that they have sizable couplings to both leptons and quarks and moreover that there are no light right-handed neutrinos. It turns out that there is only one possible vector irreducible representation with these properties: $\mathcal{W}_\mu$. It couples only to the left-handed SM fermions, just as the SM $SU(2)_L$ gauge boson. Thus, the charged components of this multiplet form a sequential W′. But these fields necessarily come together with the neutral component of the triplet, a Z′ boson. This simple fact is usually not taken into account in collider searches, even if it is a model-independent consequence of the $SU(2)_L$ gauge invariance of SM extensions.

As a second example, consider the case of a sequential Z′ boson, with couplings proportional

to the ones of the SM Z boson. This vector has different couplings to the two components of the $SU(2)_L$ doublets, so it cannot be a singlet under the SM group. Nevertheless, it can arise after electroweak symmetry breaking as a mixture of a singlet vector and the third component of a vector in the adjoint of $SU(2)_L$. This is the case of models with a replica of the SM gauge group, or in extra dimensions, but the mechanism is more general. Gauge invariance implies that the sequential Z$'$ boson necessarily comes together with a pair of charged vectors W$'$ and another neutral vector γ', which couples just like the photon. All these new fields have similar masses. Clearly, these extra vectors have the very same structure as the SM gauge bosons.

Once the field content of the theory has been established, we can proceed to construct the most general renormalizable theory invariant under $SU(3)_C \otimes SU(2)_L \otimes U(1)_Y$. The Lagrangian has the form

$$\mathcal{L} = \mathcal{L}_{\rm SM} + \mathcal{L}_V + \mathcal{L}_{V-{\rm SM}} + \text{ nonlinear}, \tag{1}$$

where $\mathcal{L}_{\rm SM}$ is the SM Lagrangian, $\mathcal{L}_V$ contains the quadratic terms for the heavy vector bosons (with kinetic terms covariantized with respect to the SM group) and $\mathcal{L}_{V-{\rm SM}}$ contains the possible interaction or kinetic terms formed as products of SM fields and a single vector field. Mass mixing terms of SM and new vectors are forbidden by gauge invariance.[a] Finally, "nonlinear" in Eq. (1) refers to interaction terms that are nonlinear in the heavy vector fields. As we have argued above, those terms can be safely neglected.

The quadratic terms for the new vector bosons are given by

$$\mathcal{L}_V = -\sum_V \eta_V \left(\frac{1}{2} D_\mu V_\nu^\dagger D^\mu V^\nu - \frac{1}{2} D_\mu V_\nu^\dagger D^\nu V^\mu + \frac{1}{2} M_V^2 V_\mu^\dagger V^\mu \right), \tag{2}$$

The sum is over all new vectors V, which can be classified into the different irreducible representations of Table 1. We set $\eta_V = 1$ (2) when V is in a real (complex) representation, in order to use the usual normalization. Note that we have written explicit mass terms for the new vectors. The masses can arise, in particular, from vacuum expectation values of extra scalar fields. In writing Eq. (2), we have chosen a basis with diagonal, canonically normalized kinetic terms and diagonal masses. The couplings of the new vectors to the SM are described by

$$\mathcal{L}_{V-{\rm SM}} = -\sum_V \frac{\eta_V}{2} \left(V^{\mu\dagger} J_\mu^V + \text{h.c.} \right). \tag{3}$$

The vector currents J_μ^V above have the form

$$J_\mu^V = \sum_k g_V^k j_\mu^{Vk}, \tag{4}$$

where $g_V^k$is a coupling constant and j_μ^{Vk} is a vector operator of scaling dimension 3 in the same representation as V. Actually, the different currents that can be built with the SM fields determine the possible representations of the extra vectors. We can distinguish three kinds of SM currents:

- *With two fermions*. Schematically, $j_\mu^{V\psi_1\psi_2} = [\overline{\psi_1} \otimes \gamma_\mu \psi_2]_{R_V}$, with ψ_1, ψ_2 (different in principle) fermion multiplets, R_V the representation of V and $\otimes$ a product of representations.

- *With two scalars and a covariant derivative*: $j_\mu^{V\phi} = [\Phi^\dagger \otimes D_\mu \phi]_{R_V}$, where Φ denotes either the scalar doublet ϕ or its form $\tilde{\phi}$.

- *With a gauge boson and two covariant derivatives*: $j_\mu^{\mathcal{A}} = D^\nu A_{\nu\mu}$.

[a] There are, nevertheless, interactions with the Higgs doublet that give rise to mass mixing of the Z and W bosons with the new vectors when the electroweak symmetry is broken.

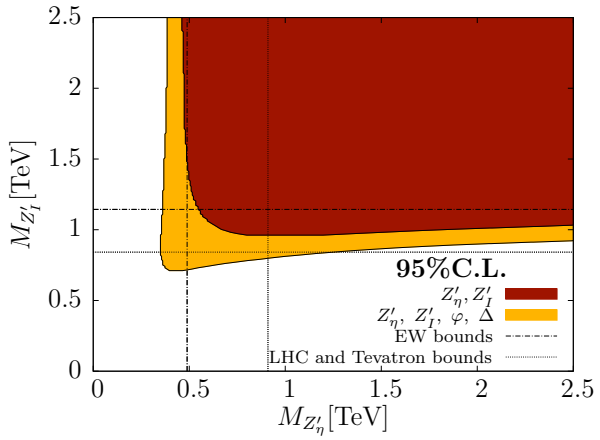

Figure 1: 95% C.L. regions in the $M_{Z'_I} - M_{Z'_\eta}$ plane for a two-Z′ global fit with and without extra scalars ϕ (singlet) and Δ (isotriplet).

The couplings to currents of the third type induce a kinetic mixing of the SM gauge bosons A with the heavy vectors $\mathcal{A}$. It turns out that the corresponding terms in $\mathcal{L}_{\mathrm{V-SM}}$ are redundant and can be eliminated by field redefinitions.

The currents J^V for all possible vectors V and the most general couplings have been given in Ref. [1]. Let us write, as an example, the current for the vector boson $\mathcal{B}^1_\mu$:

$$J^{\mathcal{B}^1}_\mu = \left(g^{du}_{\mathcal{B}^1}\right)_{ij} \overline{d^i_R}\gamma_\mu u^j_R + g^{\phi}_{\mathcal{B}^1} i D_\mu \phi^T i\sigma_2 \phi. \tag{5}$$

We see that in this case, up to flavour indices, there are just two independent couplings: the first one induces right-handed charged currents, while the second one gives rise to a mixing with the SM W$^\pm$ boson, which modifies the ρ parameter.

The model-independent limits from EWPD on all the extra vectors have been presented in Ref.[1]. On the other hand, Tevatron and LHC are placing better and better bounds on many of the vector bosons, especially those that have sizable couplings to both quarks and leptons. Here we shall just point out that the indirect limits can be relaxed in some cases with additional new particles, as has been systematically discussed in Ref. [3]. As an example of this, let us show the constraints on models with two kinds of Z′ bosons that appear in E_6 GUT, a Z'_I and a Z'_η (see [2]), plus optional extra scalar singlets ϕ and triplets Δ. In Fig. 1 we plot the 95% C.L. regions, together with the electroweak and direct limits for the cases of just one Z′. We see that the interplay of the different particles weakens the limits for individual Z′, and enlarges the parameter space available for discovery at the LHC.

2 A few consequences of extra vector bosons

We start by discussing the implications of new vector bosons on the value of the mass of the Higgs boson. Some of the new vectors modify the ρ parameter at tree level. In particular, the $\mathcal{B}_\mu$ and $\mathcal{W}^1_\mu$ representations can produce a shift that counteracts the effect of loops with a heavy Higgs (relative to the ones with a light Higgs). In Fig. 2 we plot the value of the χ^2 of a global fit in three scenarios: the SM, an extension with a singlet $\mathcal{B}_\mu$ and an extension with a hypercharged triplet $\mathcal{W}^1_\mu$. The fit includes EWPD, LEP 2 data and information from direct searches of the Higgs boson at Tevatron. The value of χ^2 over the number of degrees of freedom is comparable in all three scenarios for a light Higgs, $M_H \sim 125\,\mathrm{GeV}$. However, it is clear from the figure that for a heavy Higgs both extensions with extra vector bosons are clearly favored over the

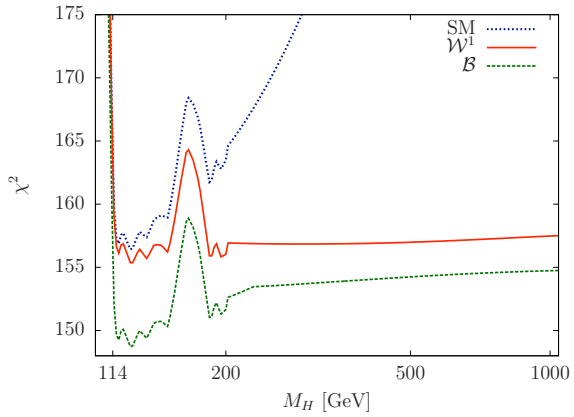

Figure 2: χ^2 of best fit as a function of the Higgs mass M_H for the SM and extensions with $\mathcal{B}_\mu$ and $\mathcal{W}^1_\mu$ vectors.

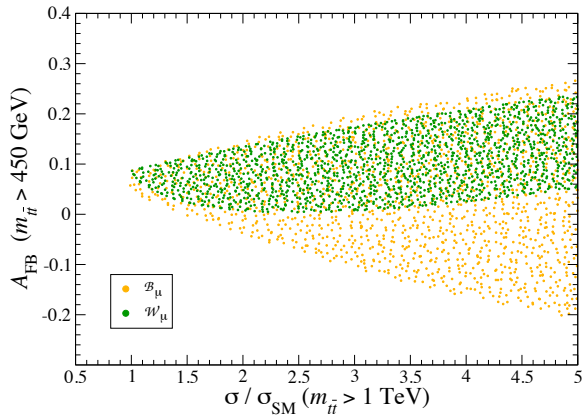

Figure 3: Allowed regions for the Tevatron $t\bar{t}$ asymmetry and the $t\bar{t}$ tail at LHC for heavy $\mathcal{B}_\mu$ and $\mathcal{W}_\mu$ bosons.

SM hypothesis. In other words, if a heavy Higgs boson were found at the LHC, it would be an indication of physics beyond the SM, possibly in the form of new vector bosons $\mathcal{B}_\mu$ or $\mathcal{W}^1_\mu$.

Let us now move to the possible impact of extra vector bosons in top physics. Tevatron and the LHC are studying in great detail the pair production of top quarks. Interestingly, the CDF collaboration has measured a value of the $t\bar{t}$ forward backward asymmetry A_{FB} (at high invariant mass) that is more than three sigmas away from the SM prediction [4]. Having a look at Table 1 and at the couplings in Ref. [1], it is easy to see that the vector bosons contributing to top pair production are:

- $\mathcal{B}_\mu$, $\mathcal{W}_\mu$, $\mathcal{G}_\mu$ and $\mathcal{H}_\mu$, in the s and/or t channels;
- $\mathcal{B}^1_\mu$, $\mathcal{G}^1_\mu$, in the t channel;
- $\mathcal{Q}^1_\mu$, $\mathcal{Q}^5_\mu$, $\mathcal{Y}^1_\mu$ and $\mathcal{Y}^5_\mu$, in the u channel.

All of these vector bosons, except $\mathcal{Y}^1_\mu$ and $\mathcal{Y}^1_\mu$, could give rise to the observed excess. However, this is not that simple, as there are important constraints as well. The more robust ones arise from $t\bar{t}$ production itself: the total cross section and its distribution as a function of the invariant mass. In Ref. [5], Juan Antonio Aguilar-Saavedra and the author have studied the effect of these vector bosons (and also of general scalars) over the tail in $t\bar{t}$ production at high invariant masses at the LHC. The result is that, with the exception of very light particles or particular couplings in the case of a gluon-like vector $\mathcal{G}$, these explanations of the excess in A_{FB} can be ruled out by

LHC data with the luminosity already collected. In Fig. 3 we show, for example, the relation between the predictions for A_{FB} and the LHC tail for the case of heavy $\mathcal{B}_\mu$ and $\mathcal{W}_\mu$ vector bosons. The different points scan all the allowed values of the couplings of these vector bosons to the t, u and d quarks.

3 Conclusions

Many beautiful models incorporating new physics have been constructed in the last thirty years, guided by different theoretical problems of the SM. We do not know which, if any, of these theories is realized in our Universe. Therefore, now that the LHC is running—and performing extremely well!—it seems wise not to trust particular models, but carry out model independent analyses of new physics. These studies can guide the experimental searches and give shape to the constraints. The most general model-independent formalism, effective Lagrangians, is not valid when the new particles can be produced. We advocate instead a scan over all possible particles that can give observable effects, allowing for completely general couplings. This is not an impossible mission once the possibilities are strongly restricted by the principles of gauge invariance and power counting. The result is a natural and convenient parameterization from both the theoretical and experimental points of view. In this talk, we have illustrated this program for the case of extra spin 1 particles.

Acknowledgments

It is a pleasure to thank Paco del Aguila, Juan Antonio Aguilar-Saavedra, Jorge de Blas and Paul Langacker for a fruitful collaboration, and the organizers of the Rencontres de Moriond for a very enjoyable meeting. This work has been partially supported by projects FPA 2010-17915 (MICINN), FQM 101 and FQM 437 (Junta de Andalucía).

1. F. del Aguila, J. de Blas and M. Pérez-Victoria, JHEP **1009**, 033 (2010).
2. P. Langacker, Rev. Mod. Phys. **81**, 1199 (2008).
3. F. del Aguila, J. de Blas, P. Langacker and M. Pérez-Victoria, arXiv:1104.5512 [hep-ph].
4. T. Aaltonen *et al.* [CDF Collaboration], arXiv:1101.0034 [hep-ex].
5. J.A. Aguilar-Saavedra and M. Pérez-Victoria, JHEP **1105**, 034 (2011).

SEARCHES FOR NEW PHYSICS AT THE TEVATRON

M. Jaffré
on behalf of the CDF and D0 collaborations
LAL, Université Paris-Sud, CNRS/IN2P3,
91898 Orsay Cedex, France

The Tevatron collider has provided the CDF and D0 experiences with large datasets as input to a rich program of searches for physics beyond the standard model. The results presented here are a partial survey of recent searches conducted by the two collaborations using up to 6 fb^{-1} of data.

1 Introduction

The standard model (SM) of particles, despite its remarkable description of experimental data at the elementary particle level, has some deficiencies to explain what is observed in the universe : lack of anti-matter, existence of dark matter,... Working at the energy frontier, as was the case at the Tevatron for so many years, gives experimentalists the hope to discover new non-SM particles which would indicate some direction to follow at explaining these SM deficiencies.

Over the years, the CDF and D0 experiments have gained experience in the detector responses to all particle types. It allows to look at a large number of different final states searching for deviations from the SM expectations. As the knowlegde of detector particle responses becomes more accurate, the complexity of final states can increase.

For a given final state signature, the non-observation of deviations from the SM prediction allows to constrain several models at once.

2 Dielectron, dimuon or diphoton resonance searches

Experimentally, in a hadronic environment, dielectron, dimuon or diphoton final states are easy to identify. A lot of extensions to the SM predicts the existence of new particles which could be observed as narrow resonances decaying into a pair of leptons or photons. Among those are new spin-1 gauge boson [1] or spin-2 Randall-Sundrum (RS) graviton [2].

The observed dilepton mass distributions observed in large datasets (around 5 fb^{-1} or more) by CDF [3,4] and D0 [5] are in agreement with the SM expectations. The largest invariant dielectron mass observed by CDF is 960 GeV(Fig. 1). No new resonance is observed above the Z gauge boson mass. This allows both experiments to set 95% C.L. cross section limits which can be compared to model predictions; as an example, the benchmark SM-like Z' is now excluded for masses below 1 TeV.

The same spectra can be used to extract limits for the graviton G mass; higher limits can be achieved with the diphoton spectra [6] as the G branching fraction into two photons is twice that into a lepton pair. But, the best limits are obtained by combining dielectron and diphoton

analyses[7,3]. Fig. 2 shows the excluded domain, obtained by CDF, in the two parameter space of the RS model, $k/\overline{M}_{Pl}$, the ratio of curvature of the extra dimension to reduced Planck scale, and the G mass.

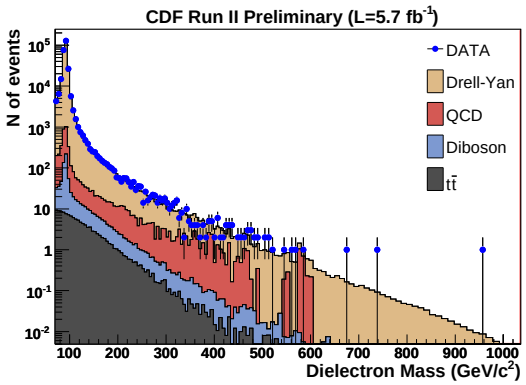

Figure 1: Invariant dielectron mass distribution compared to the expected backgrounds in CDF data.

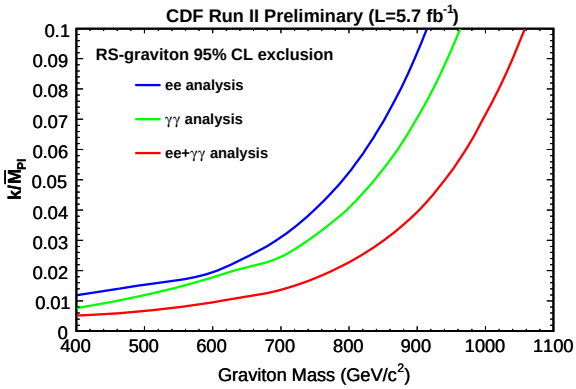

Figure 2: Excluded domains in the RS parameter space ($k/\overline{M}_{Pl}$, graviton mass) obtained in the dielectron analysis, the diphoton analysis and their combination

3 Diboson resonance search

Production of pairs of gauge vector bosons has been observed by CDF and D0 at the level predicted by the SM. This sector is however not well constrained due to the smallness of the cross sections. There is still room for an extra source of dibosons from the decay of massive charged or neutral particle as new gauge boson W' or RS graviton G. This has been looked at by CDF [8], and recently by D0 [9] using 5.4 fb^{-1} of data. One of the bosons is allowed to decay leptonically and the other hadronically leading to two event signatures (ll + jets, l + jets + $\not\!\!E_T$) where the lepton l is either an electron or a muon and $\not\!\!E_T$ is the missing transverse energy carried away by the neutrino. The two leptons or the lepton and $\not\!\!E_T$ are first combined to form a Z or W candidate. Since for a very high massive resonance, the two bosons would be highly boosted, the two hadronic showers from the decay of the second boson may be reconstructed as a single massive jet. So, D0 has increased its signal sensitivity by first trying to assign the $W(Z)$ hypothesis to a jet with a mass larger than 60(70) GeV before any two jet combination. Figure 3 shows for the data and the expected backgrounds the distributions of the reconstructed resonance and transverse masses in the dilepton and single lepton channels, respectively. The predicted distributions of a 600 GeV W' or G are also shown. Cross section limits are extracted from the absence of any significant excess of events in data from which one deduces lower bounds for W' and G masses of 690 and 754 GeV respectively.

4 Search for vectorlike quarks

Vectorlike quarks (VQ) share many characteristics of the SM quarks with the distinctive exception that their left and right components transform in the same way under $SU(3)\times SU(2)\times U(1)$. They can be singly produced via the electroweak interaction and may decay into a W or Z boson and a SM quark. D0 [10] has separated the analysis in two independant channels according to the leptonic decay of the vector boson (ll + jet, l +jet + $\not\!\!E_T$). The event's leading jet in transverse momentum is assumed to come from the VQ decay. Figure 4 shows, for the data and the expected backgrounds, the distributions of the reconstructed resonance and transverse masses in the dilepton and single lepton channels, respectively. The absence of any statistically

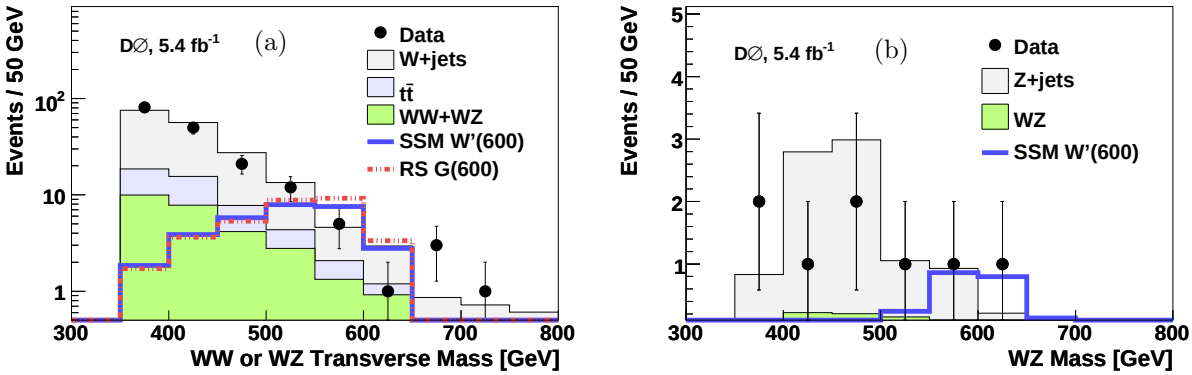

Figure 3: Distributions of the reconstructed WW or WZ transverse mass (left) and WZ mass (right) for data (dots), estimated backgrounds, and the estimated contributions of a 600 GeV SSM W' and a 600 GeV G.

significant excess in data allows to derive cross section limits which are compared to VQ production in two scenarios. VQ not coupled to down-quarks and decaying exclusively to Wq are excluded for masses below 693 GeV; if decaying to Zq the lower bound of the mass is 551 GeV. In the alternate scenario, i.e. no coupling to up-quarks, the mass limits are 403 GeV (Wq) and 430 GeV (Zq).

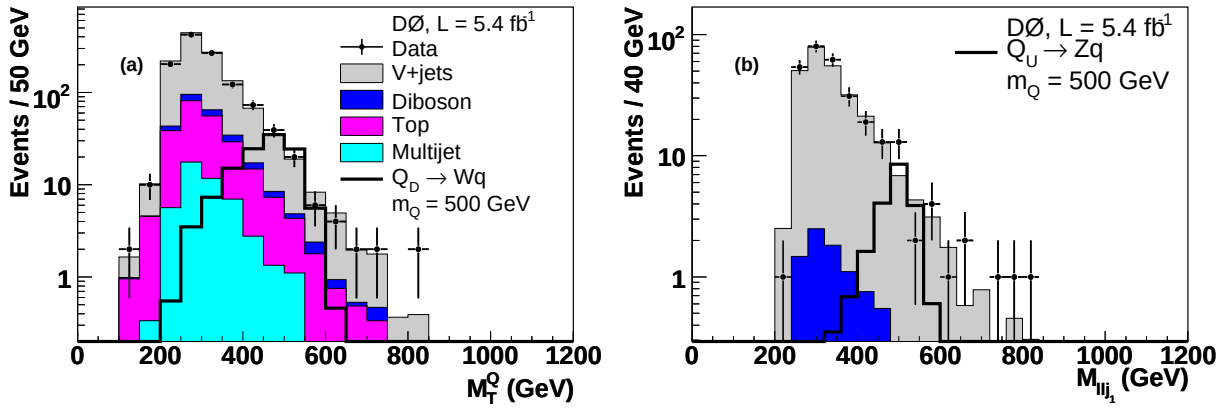

Figure 4: (a) Vector-like quark transverse mass and (b) vector-like quark mass for the single lepton and dilepton channels, respectively. Expected distributions for 500 GeV signals decaying as $Q_D \to Wq$ and $Q_U \to Zq$.

5 Search for new fermions ("Quirks")

A minimal extension of the standard model is obtained by the addition of a new unbroken SU(N) gauge group. Such a group is characterized by the mass of the new fermions (quirks),Q, and the strength of the gauge coupling, Λ. D0 [11] has considered the case where the quirks are charged, and $\Lambda << M_Q$, and $M_Q = 0.1 - 1$ TeV. The breaking of the infra color is thus suppressed and a $Q\bar{Q}$ pair produced in $p\bar{p}$ collisions will not hadronize. The quirks in the pair will stay connected, as with a rubber band, the two tracks will not be resolved by the tracking system and they will be reconstructed as a single straight highly ionizing track. This is the first search of this kind. Event selection requires an isolated track and a very high transverse momentum jet back to back. Such events are triggered by requiring jets and substantial $\not\!\!E_T$. Analysing 2.4 fb^{-1} of data, no excess of events at large ionization loss is observed over the expected background determined from isolated tracks in an orthogonal data sample. From the cross section limits on the quirk production, D0 extract limits on the quirk mass depending on N, the number of colors in the new gauge group, of 107, 119 and 133 GeV for N=2, 3 and 5 respectively.

6 Search for leptonic jets

Hidden Valley (HV) scenarios [12] contain a hidden sector which is weakly coupled to SM particles. They become popular as they provide convincing interpretation of observed astrophysical anomalies and discrepancies in dark matter search. New low mass particles are introduced in the hidden sector, and the dark photon, which is the force carrier, would have a mass around one GeV or less and would decay into a fermion or pion pair. The case of decays to lepton pair (electron or muon) is particularly attractive. SUSY is often included in HV models, one could have a situation where the lightest neutralino will decay to a dark photon and $\tilde{X}$, the lightest SUSY particle of the hidden sector, which will escape detection, leading to large $\not\!\!E_T$. As the dark photon is light, it will be highly boosted in the neutralino decay, and the two leptons will be close to each other. Experimentally, one has to change the isolation criteria usually applied to identify leptons. The presence of a track of opposite charge close to the lepton candidate will sign the so-called leptonic jet (l-jet). Using 5.8 fb^{-1} of data, D0 [13] has searched for pair production of l-jets in three configurations : ee, $\mu\mu$ and $e\mu$. No evidence of l-jets is observed in the distributions of the electron and muon pair masses (Fig. 5). Limits on the production cross section, around 100 fb for a 1 GeV dark photon, are obtained.

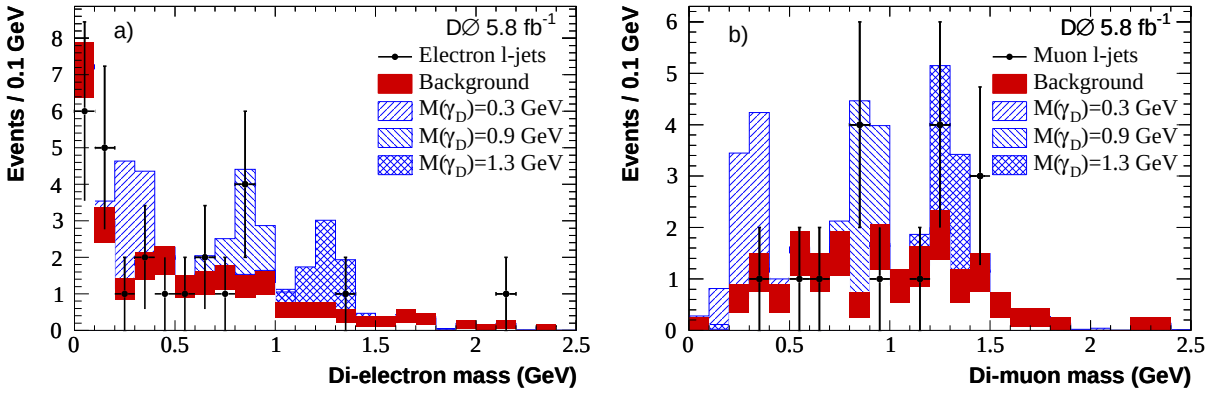

Figure 5: Invariant mass of dark photon candidates with two isolated l-jets and $\not\!\!E_T$ > 30 GeV, for (a) electron l-jets and (b) muon l-jets (two entries per event, the $e\mu$ events contribute to both plots). The red band shows the shape of the mass distribution for events with $\not\!\!E_T$ < 20 GeV. The shaded blue histograms show the shapes of 8 MC signal events added to backgrounds, for three masses of the dark photon.

7 Search for a fourth generation down-type quark

CDF [14] has searched for a fourth generation bottom-like quark (b'). Current limits push b' to be heavier than the sum of the t quark and the charged gauge boson W masses. The analysis is realised using 4.8 fb^{-1} of data assuming b' to decay exclusively to t and W. The b' pair produced in $p\bar{p}$ interactions will decay into two b quarks and four W's. One of the W decays leptonically and the others hadronically. The final state is then characterised by an isolated lepton (electron or muon), $\not\!\!E_T$ and many jets; one of the jets is required to be tagged as a b-jet. All the quark jets will not be reconstructed either because they fall below the transverse momentum cut or because their hadronic showers are overlapping and they are merged in a single jet. The analysis is performed in three jet multiplicity bins : 5, 6 and 7 jets or more. The other variable which helps fighting the SM backgrounds, mainly $t\bar{t}$ and W + jets production, is H_T, the scalar sum of the transverse momentum of the lepton, jets and $\not\!\!E_T$. Signal is expected to appear in the last multiplicity bin and for high H_T values. The H_T distributions for the three multiplicity bins are shown in a single plot (Fig.6) using the variable $Jet - H_T$ equal to H_T, H_T + 1000 GeV or H_T + 2000 GeV for events with 5, 6, and 7 jets or more respectively. In the absence of

any significant excess of events, cross section limits are set as a function of the b' mass. When compared to the NLO b' cross section [15], one gets a lower bound for its mass of 372 GeV (Fig. 7).

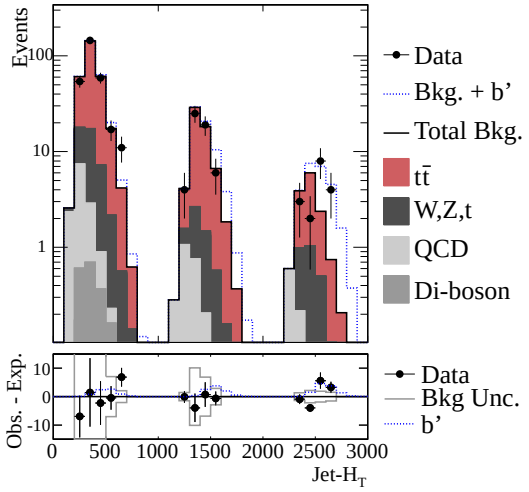

Figure 6: Distribution of the variable Jet-H_T for data and expected backgrounds. Contributions from a 350 GeV b' signal on top of the expected backgrounds are also shown. The bottom pane shows the difference between the expected and observed number of events, as well as the total uncertainty on the expected number of events.

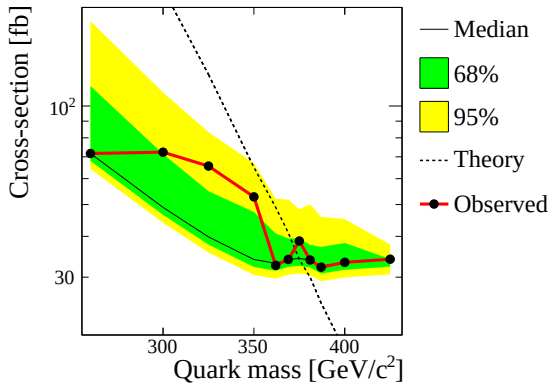

Figure 7: 95% C. L. observed upper limits on b' production cross section (red line) compared to the expected median limit (black line) in simulated experiments without b' signal. Green and yellow bands represent 68% and 95% of simulated experiments, respectively; the dashed line is the NLO b' production cross section [15].

8 Search for dark matter

CDF [16] has searched for dark matter through the production of an exotic fourth generation t' quark decaying to a t quark and a dark matter particle X. The decay of the t' to a b quark and a charged gauge boson W is not allowed. The signal is searched for in the following event topology: an isolated lepton (electron or muon), four jets or more, and very large $\not\!\!E_T$ due to the invisible particle X. The minimum value of $\not\!\!E_T$ is optimised for each point in the (t' mass, X mass) plane. The larger the mass difference, the higher the cut. The main SM backgrounds are $t\bar{t}$ pair and W + jets production. There are W bosons in the main backgrounds which are prominently visible in the transverse mass distribution of the lepton and $\not\!\!E_T$ pair in the signal depleted domains i.e. at low $\not\!\!E_T$ or low jet multiplicity as seen in Fig. 8a and 8b. In the signal region, no significant excess of events is observed (Fig. 8c). Cross section limits are obtained which allow to exclude a t' mass below 360 GeV for a X mass below 100 GeV.

9 Conclusions

The performance of the Tevatron has brought limits on BSM physics beyond one could have expected. LHC experiments will take over, but CDF and D0 have still assets with their large datasets; their analysis will be oriented towards complex final states. Further details on physics results can be obtained from :

CDF http://www-cdf.fnal.gov/physics/physics.html

D0 http://www-d0.fnal.gov/Run2Physics/WWW/results.htm

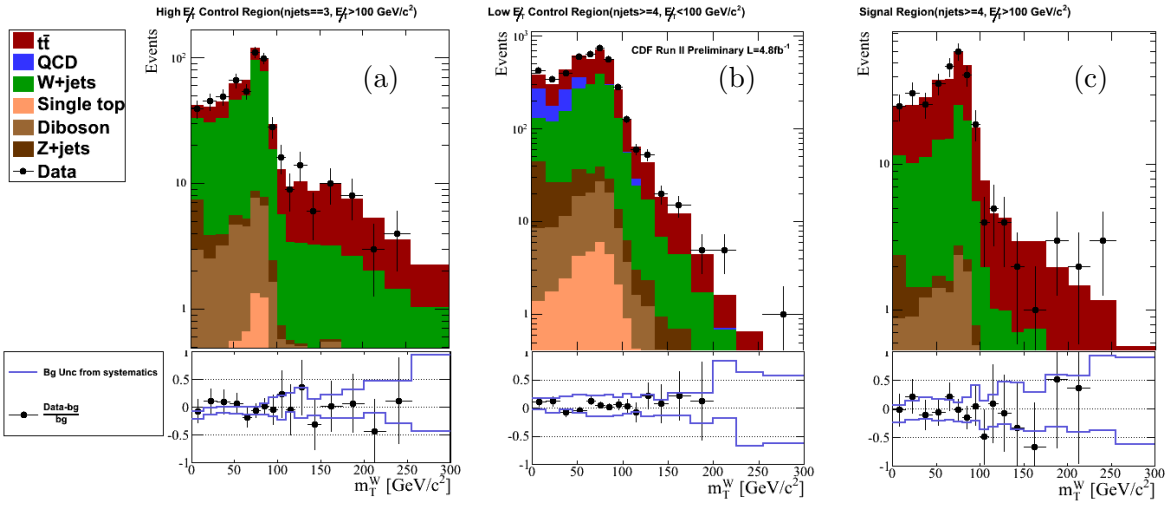

Figure 8: Transverse mass distributions of the lepton and $\not\!\!E_T$ for data and the expected backgrounds in control regions where signal is negligible (a and b) and where the W is visible and the region where it should appear (c). The bottom panes show the difference between expected background and observed events, as well as the total uncertainty on the expected background events.

Acknowledgments

The author would like to thank the CDF and D0 working groups for providing the material for this talk, and the organizers of the *Rencontres* for a very enjoyable conference and the excellent organization.

References

1. P. Langacker, *Rev. Mod. Phys.* **81**, 1199 (2008).
2. L. Randall and R. Sundrum, *Phys. Rev. Lett.* **83**, 3370 (1999); **83**, 4690 (1999).
3. CDF Collaboration, Public note CDF 10405 (unpublished).
4. T. Aaltonen *et al* (CDF Collaboration), *Phys. Rev. Lett.* **106**, 121801 (2011).
5. V.M. Abazov *et al* (D0 Collaboration), *Phys. Lett.* B **695**, 88 (2011).
6. T. Aaltonen *et al* (CDF Collaboration), *Phys. Rev.* D **83**, 011102(R) (2011).
7. V.M. Abazov *et al* (D0 Collaboration), *Phys. Rev. Lett.* **104**, 241802 (2010).
8. T. Aaltonen *et al* (CDF Collaboration), *Phys. Rev. Lett.* **104**, 241801 (2010).
9. W.M. Abazov *et al* (D0 Collaboration), *Phys. Rev. Lett.* **104**, 061801 (2010); arXiv:hep-ex/1011.6278, accepted by Phys. Rev. Lett.
10. V.M. Abazov *et al* (D0 Collaboration), *Phys. Rev. Lett.* **106**, 081801 (2011).
11. V.M. Abazov *et al* (D0 Collaboration), *Phys. Rev. Lett.* **105**, 211803 (2010).
12. T. Han et al., *J. High Energy Phys.* **07**, 008 (2008) 008; M. Strassler and K. Zurek, *Phys. Lett.* B **651**, 374 (2007).
13. V.M. Abazov *et al* (D0 Collaboration), *Phys. Rev. Lett.* **105**, 211802 (2010).
14. T. Aaltonen *et al* (CDF Collaboration), *Phys. Rev. Lett.* **106**, 141803 (2011).
15. R. Bonciani *et al*, *Nucl. Phys.* B **529**, 424 (1998); M. Cacciari *et al*, *J. High Energy Phys.* **04**, 068 (2004).
16. CDF Collaboration, Public note CDF 10374 (unpublished).

Implications of first LHC results

Alessandro Strumia
Dipartimento di Fisica dell'Università di Pisa and INFN, Italia
National Institute of Chemical Physics and Biophysics, Ravala 10, Tallin, Estonia

We discuss implications of first LHC results for models motivated by the hierarchy problem: large extra dimensions and supersymmetry. We present bounds, global fits and implications for naturalness.

1 Introduction

The main goal of the LHC is telling us why the weak scale is much below the Planck scale: this hierarchy problem was adopted in the past 30 years as guideline of many theoretical works. Maybe LHC will tell which CMSSM parameters are right. Or maybe LHC will tell which SUSY model is right. Or maybe LHC will tell which solution to the hierarchy problem is right. Or maybe LHC will tell that the hierarchy problem is not a good guideline.

The way to make progress is searching for the signals predicted by tentative solutions. We here discuss implications of first LHC results on two of these proposals: supersymmetry and large extra dimensions.

2 Large extra dimensions

The hierarchy problem can be solved assuming that the quantum gravity scale M_D is around the weak scale, and that the larger Planck scale arises because gravitons live in δ extra dimensions[1]. The following unavoidable collider signals of this scenario have been proposed:

1. Graviton emission (accompanied by a jet to tag the event).

2. Virtual graviton exchange, which gives the dimension 8 operator $\mathcal{L}_{\rm eff} = \mathcal{L}_{\rm SM} + 8\mathcal{T}/M_{\mathcal{T}}^4$, $M_{\mathcal{T}}$ is expected to be comparable to M_D, $\mathcal{T} = T_{\mu\nu}^2/2$, and $T_{\mu\nu}$ is the SM energy-momentum tensor.

3. Virtual graviton exchange at one loop level, which gives the dimension 6 operator $\Upsilon = (\sum_f \bar{f}\gamma_\mu\gamma_5 f)^2/2$.

4. The previous signals are computable at low energy, $E \ll M_D$. Other computable signals (such as black-hole production) arise in the opposite limit $E \gg M_D$, which is presumably not relevant for LHC.

In view of the high dimensionality of the operator $\mathcal{T}$, its effect grows fast with energy such that LHC (thanks to its increased energy) is more sensitive than all previous colliders, already with

Experiment	Process	+	−
LEP	$e^+e^- \to \gamma\gamma$	0.93 TeV	1.01 TeV
LEP	$e^+e^- \to e^+e^-$	1.18 TeV	1.17 TeV
CDF	$p\bar{p} \to e^+e^-, \gamma\gamma$	0.99 TeV	0.96 TeV
DØ	$p\bar{p} \to e^+e^-, \gamma\gamma$	1.28 TeV	1.14 TeV
DØ	$p\bar{p} \to jj$	1.48 TeV	1.48 TeV
CMS at 7 TeV with 34/pb	$pp \to \gamma\gamma$	1.72 TeV	1.70 TeV
CMS at 7 TeV with 40/pb	$pp \to \mu^-\mu^+$	1.6 TeV	1.6 TeV
ATLAS at 7 TeV with 36/pb	$pp \to jj$	4.2 TeV	3.2 TeV
ATLAS at 7 TeV with 3.1/pb	$pp \to jj$	2.2 TeV	2.1 TeV
CMS at 7 TeV with 36/pb	$pp \to jj$	4.2 TeV	3.4 TeV

Table 1: Limits on virtual graviton exchange for positive and negative interference with the SM amplitude.

integrated luminosity much lower than previous colliders. The operator $\mathcal{T}$ contributes to various cross sections:

$$\sigma = \left(\frac{2\,\text{TeV}}{M_{\mathcal{T}}}\right)^8 \times \begin{cases} 12.5\,\text{pb} & \text{for } pp \to jj \\ 10.4\,\text{fb} & \text{for } pp \to \mu^+\mu^- \\ 21.3\,\text{fb} & \text{for } pp \to \gamma\gamma \end{cases}$$

The $pp \to jj$ channel [2] was ignored because jets have more background than leptons or photons; but it has a much larger cross-section, and this is the most important aspect at LHC startup, with poor integrated luminosity. As summarized in table 1, already with 3/pb LHC data about $pp \to jj$ provided the dominant constraint [3].

Since quantum corrections to the higgs mass are made finite by unknown aspects of quantum gravity, we cannot tell if the LHC bound $M_{\mathcal{T}} > 3.4\,\text{TeV}$ got so strong that large extra dimensions no longer are a good solution to the hierarchy problem.

3 Supersymmetry

In supersymmetry quantum corrections to the higgs mass are made finite by sparticle loops. Thereby there is neat connection between sparticle masses and the weak scale:

$$M_Z^2 \approx 0.2m_0^2 + 0.7M_3^2 - 2\mu^2 = (91\,\text{GeV})^2 \times 80(\frac{M_3}{1\,\text{TeV}})^2 + \cdots \tag{1}$$

where we assumed the CMSSM (Constrained Minimal Supersymmetric Standard Model) and fixed $\tan\beta = 3$, $A_0 = 0$, like in the experimental analyses that presented first LHC bounds on such supersymmetric model [4].

The order one coefficient of M_3^2 arises due to RGE running from the GUT scale down to the weak scale, and thereby is generic of models where SUSY breaking is present at such high scale.

As a consequence of the LHC bound on the gluino mass M_3, its contribution to M_Z^2 is almost 100 times too large, and needs to be canceled by other terms giving rise to a fine-tuning problem. Within the CMSSM, supersymmetry allows to reduce the SM higgs mass fine tuning from $\sim 10^{30}$ down to ~ 100 only: no longer down to ~ 1, casting doubts on the ideology according to which the hierarchy problem is solved identifying the weak scale with the SUSY-breaking scale.

To be more precise, eq. (1) can be used to eliminate one parameter, such that the CMSSM model has two free parameters. Instead of the usual choice, m_0 and $M_{1/2} \approx M_3/2.6$, we choose any two adimensional ratios, such that the overall scale of supersymmetry is fixed by eq. (1), rather than by hand. Only in the part of the parameter space where cancellations happen, sparticles are heavier than M_Z (their natural scale according to eq. (1)) and compatible with

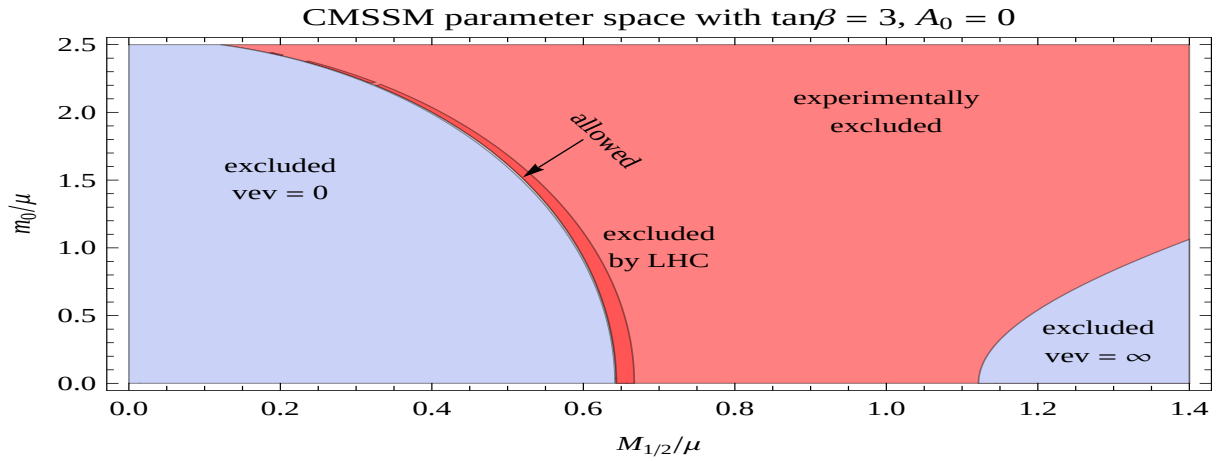

Figure 1: An example of the parameter space of the CMSSM model. The white region is allowed. The dashed line around the boundary of the allowed region is the prediction of the BS model.

experimental bounds. The result is shown in fig. 1 from [7] (here updated at the light of the latest ATLAS data with 165/pb [5]).

- The light-gray regions are theoretically excluded because the minimum of the potential is not the physical one.
- The red region in the middle is theoretically allowed, but it has now been experimentally excluded. The darker red shows the new region excluded by LHC with respect to the previous LEP bounds.
- The white region is allowed, but is now so small that enlarging the picture is needed to see it. It is close to the boundary where $M_Z = 0$ and thereby has $M_Z \ll m_0, M_{1/2}, \mu$.

So far we fixed $A_0 = 0$ and $\tan\beta = 3$, but the situation within this slice of parameter space is representative of the situation present in the full CMSSM parameter space. To explore it we scan all its adimensional parameters, and compute the allowed "fraction of parameters space", which generalized the "size of the allowed region" in fig. 1. We find that only about 0.7% of the CMSSM parameter space remains allowed. Furthermore non-minimal Higgs models invented to ameliorate the analogous issue already present after LEP no longer work, just because the LHC bound has nothing to do with the higgs (see table 2).

LEP excluded sparticles around the Z mass. LHC now excludes heavier sparticles, and reaches the next milestone: sparticles a loop factor above M_Z. Indeed the dashed line in fig. 1 is the prediction of a model where the usual relation, eq. (1), gets supplemented by a relation that demands sparticle to be a loop factor above M_Z: $m_{\tilde{t}} \approx 4\pi M_Z/\sqrt{12}$ [6].

Ignoring the naturalness issue, first data from LHC also affect CMSSM global fits [8], where the scale of supersymmetry is now fixed by i) fitting the anomaly in the $g-2$ of the muon

experimental bound	fraction of surviving CMSSM parameter space		
	any m_h	$m_h > 100\,\text{GeV}$	$m_h > 110\,\text{GeV}$
LEP	10%	3%	1%
LHC	2.2%	1.2%	0.7%

Table 2: Fraction of the CMSSM parameter space that survives to the various bounds.

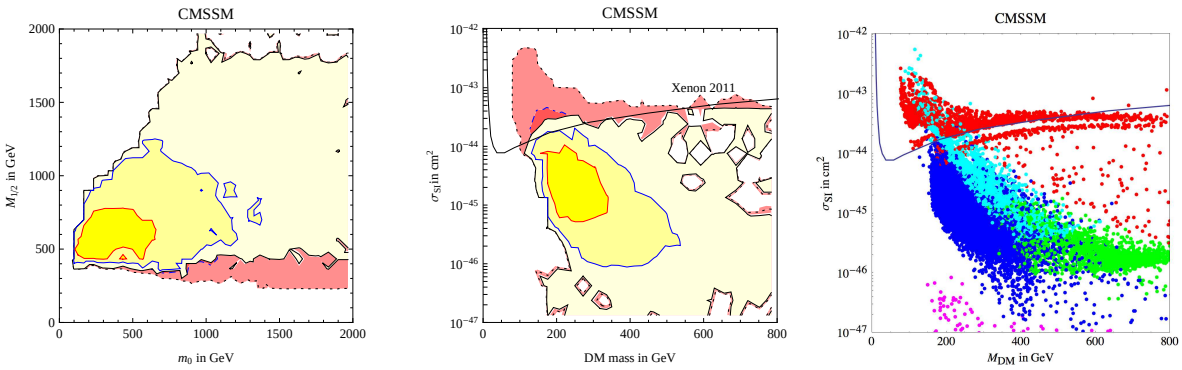

Figure 2: Global CMSSM fit updated to 165/pb of ATLAS data.

compatibly with other indirect data; ii) demanding that the thermal abundance of the lightest neutralino equals the Dark Matter abundance.

Fig. 2a shows the results: LHC has a minor impact, eliminating the part of the best-fit parameter space with lighter sparticles. Furthermore the recent Xenon-100 search for direct detection of Dark Matter [9] disfavors the region in pink in fig. 2a and b. To understand what is this region now disfavored, fig. 2c shows that the best CMSSM fit is made of a few qualitatively different corners of the CMSSM parameter space, corresponding to different ad hoc mechanisms that allow to reproduce the DM abundance:

- The now disfavored red dots correspond to the "well tempered bino-higgsino" mechanism i.e. $M_1 \sim |\mu|$, that in the CMSSM is possible for large m_0.
- The most natural DM annihilation mechanism (neutralino annihilations into sleptons) has been excluded because light enough sleptons are no longer allowed within the CMSSM.
- The "higgs-resonance" mechanism for enhanced DM annihilation, i.e. light $M_{\rm DM} \approx m_h/2$ and consequently a relatively light gluino, was allowed in the previous global fit [8]. It has now been excluded by the new ATLAS CMSSM bounds [5].
- The remaining allowed mechanisms are: slepton co-annihilations (blue dots), H or A resonance (green dots), h, H, A mediation at large $\tan\beta$ (cyan dots), stop co-annihilations (magenta dots).

References

1. N. Arkani-Hamed, S. Dimopoulos and G. R. Dvali, Phys. Lett. B 429 (1998) 263.
2. ATLAS collaboration, Phys. Lett. B694 (2011) 327 [arXiv:1009.5069]. CMS collaboration, Phys. Rev. Lett. 105 (2010) 262001 [arXiv:1010.0203].
3. R. Franceschini et al., arXiv:1101.4919.
4. CMS collaboration, arXiv:1101.1628. ATLAS collaboration, arXiv:1102.5290.
5. ATLAS collaboration, arXiv:1102.2357. ATLAS collaboration, note ATLAS-CONF-2011-086 (6 june 2011).
6. R. Barbieri, A. Strumia, Phys. Lett. B490 (2000) 247 [arXiv:hep-ph/0005203].
7. A. Strumia, arXiv:1101.2195.
8. M. Farina et al., arXiv:1104.3572. See references therein for other global CMSSM fits.
9. XENON100 collaboration, arXiv:1104.2549.

SUSY searches at ATLAS

Sascha Caron for the ATLAS collaboration
Physikalisches Institut, University of Freiburg Hermann-Herder Str.3 , Freiburg, Germany

First ATLAS searches for signals of Supersymmetry in proton-proton collisions at the LHC are presented. These searches are performed in various channels containing different lepton and jet multiplicities in the final states; the full data sample recorded in the 2010 LHC run, corresponding to an integrated luminosity of 35 pb^{-1}, has been analysed. The limits on squarks and gluinos are the most stringent to date.

1 Introduction

Supersymmetry (SUSY) is one of the most favoured candidates for new physics, predicting a new symmetry between fermions and bosons and therefore a large number of new particles [1]. There are various reasons why these new SUSY particles are expected to be not too heavy, but accessible with TeV scale energies. SUSY would reduce the so-called *fine-tuning problem* of the Standard Model (SM) and it indicates that the three forces of the Standard Model are unified at very high energies. On the other hand SUSY particles have not been discovered so far and thus need to be heavier than their SM counterparts. In addition a new multiplicative quantum number called R-parity is introduced to forbid strong lepton and baryon number violating terms in the SUSY Lagrangian leading to too rapid proton decay. If the R-parity quantum number is conserved and SUSY particles are heavier than their SM partners, then SUSY predicts a large amount of Dark Matter in the universe. These reasons make the search for SUSY particles a major and important part of the LHC physics program. New SUSY particles could be discovered or if nothing is found at the LHC the SUSY solution to the SM shortcomings will become very unlikely.

At the LHC new SUSY particles are produced in pairs (if R-parity is conserved) and each decays usually via several intermediate steps (cascade decay) to the lightest SUSY particle (LSP). The LSP is only weakly interacting due to cosmological arguments and leads to the most characteristic feature of these SUSY events, which is missing transverse momentum. Since the SUSY breaking mechanism is unknown the mass pattern of the SUSY particles cannot be predicted. The search strategy needs therefore to be quite generic or SUSY model parameter independent. A generic search strategy for R-parity conserving SUSY signatures would include the selection of events with large missing transverse energy and reconstructed particles with large transverse momentum. At the LHC these objects are predominantly jets since the coupling strength of the strong force would cause an abundance of squarks and gluinos if these particles are not too heavy. Squarks or gluinos will cascade decay to jets, several leptons or photons depending on the SUSY parameters and missing transverse momentum caused by the LSPs. The searches for SUSY signatures with R-parity conservation are performed by searching for more events than expected in a number of different channels. These channels explore a large variety of possible

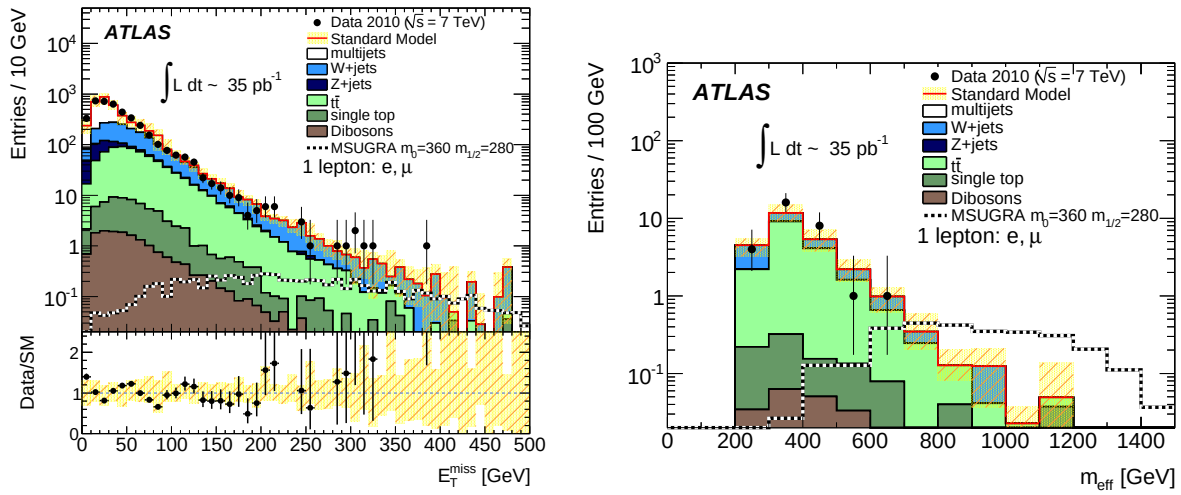

Figure 1: E_T^{miss} distribution after lepton and jet selection (left figure). Effective mass distribution after final selection criteria except for the cut on the effective mass itself (right figure). The plots are made for the electron and muon channel combined. Yellow bands indicate the uncertainty on the Monte Carlo prediction from finite Monte Carlo statistics and from the jet energy scale uncertainty.

signals, e.g. ATLAS studies various different jet (2,3,4) and lepton (0,1,2,3) multiplicities. The main challenge in these searches (and most of the work) is to reliably control the Standard Model background expectations. In the following we assume mostly the 5-parameter mSUGRA as a "general" model for R-parity conserving SUSY. Model-independent limits on an *effective* cross section for new processes in the signal region, including the effects of experimental acceptance and efficiency have also been derived. They can be used to exclude any model of new physics leading to a larger *effective* cross section.

All data presented in this summary are taken in the year 2010 at the ATLAS experiment [2] in LHC proton-proton collisions at 7 TeV centre-of-mass energy, using a data-set corresponding to an integrated luminosity of about 35pb^{-1}.

2 Searches with Jets, a Lepton and Missing Transverse Momentum (1 lepton channel)

The search in a channel with jets, exactly one muon or electron and significant missing transverse momentum $E_{\text{T}}^{\text{miss}}$constitutes the first ATLAS SUSY result [3]. This channel could be studied first due to the large reduction of the potentially dangerous QCD multijet background. Requiring one muon or electron reduces this background by several orders of magnitude. The left plot of Figure 1 shows the missing transverse momentum distributions after requiring three jets and one muon or electron. The data is compared to the prediction from Monte Carlo. Only the QCD prediction from PYTHIA was scaled with a k-factor depending on the muon or electron selection. The figure shows that at high $E_{\text{T}}^{\text{miss}}$ the main background comes from W+jets events and events from top pair production. The data is in agreement with the expectations. The signal region is defined by cuts on $E_{\text{T}}^{\text{miss}} > 125$ GeV, $E_{\text{T}}^{\text{miss}} > 0.25 m_{\text{eff}}$ and $m_{\text{eff}} > 500$ GeV. The effective mass m_{eff} is the sum of the p_T of the leading three jets, the p_T of the lepton and $E_{\text{T}}^{\text{miss}}$. The cut on $E_{\text{T}}^{\text{miss}}$ thus scales with the total transverse momentum in the event. The smallest of the azimuthal separations between the jets and missing transverse energy vectors $\Delta\phi(\text{jet}, \vec{P}_{\text{T}}^{\text{miss}})_{\text{min}}$ was required to be > 0.2 in order to remove QCD events caused by mismeasurements or heavy flavour decays. Finally, the transverse mass M_T, calculated with the lepton and the missing transverse momentum 2-vector $\vec{P}_{\text{T}}^{\text{miss}}$, is required to be > 100 GeV in order to reduce the

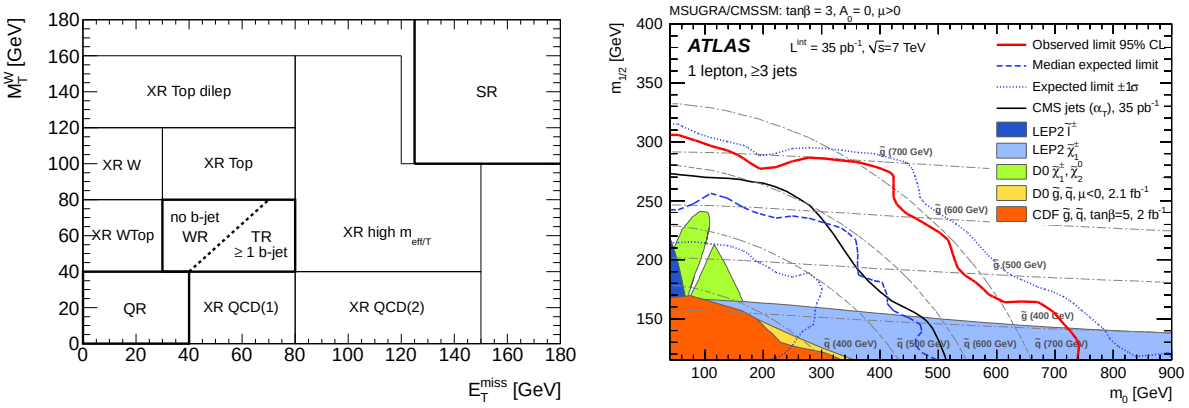

Figure 2: The left figure shows the position of the signal region (SR) and the main control regions (CR) in the (E_T^{miss}, M_T) plane. The top enriched control region (TR) and the W+jets enriched control region (WR) are separated by the existence of a b-tagged jet candidate among the three leading jets. The XR regions correspond to extra validation regions. The right plot shows the observed and expected 95% CL exclusion limits, as well as the $\pm 1\sigma$ variation on the expected limit, in the combined electron and muon channels. Also shown are the published limits from CMS, CDF, D0, and the results from the LEP experiments.

background from W bosons.

In order to determine the background predictions for the signal region, ATLAS has defined several control selections. The W and top control regions e.g. are defined by keeping the jet and lepton selection criteria as for the signal region, but requiring $30 < E_T^{miss} < 80$ GeV and $40 < M_T < 80$ GeV to enhance events with W bosons. In order to determine the amount of W+jets and top pair events separately a b-tagged jet is required for the top control region, and a b-veto is done for the W control region. The positions of the signal region (SR) and the main control regions (CR) in the (E_T^{miss}, M_T) plane are shown in Figure 2. The transfer of the top and W normalisation factors measured in the control region to the signal region is done by Monte Carlo and the uncertainty is carefully studied, including a validation in additional regions (see also Figure 2).

In the electron selection 1.81 ± 0.75 events are expected and one event is found in the data. For the muon selection 2.25 ± 0.94 events are expected and again only one event is found in the data. The small deficit results in an observed limit which is better than the expected limit. The limits are then derived from the profile likelihood ratio. A model independent 95% CL upper limit on the effective cross section for new processes in the signal region, including the effects of experimental acceptance and efficiency, of 0.065 pb for the electron channel and 0.073 pb for the muon channel is derived. Limits are also set on the parameters of the minimal supergravity framework, extending the limits set by the Tevatron experiment by far. The observed and expected upper limits are shown in Figure 2. For $A_0 = 0$ GeV, $\tan\beta = 3$, $\mu > 0$ and for equal squark and gluino masses, gluino masses below 700 GeV are excluded at 95% confidence level.

3 Searches with Jets and Missing Transverse Momentum (0 lepton channel)

The second analysis released by ATLAS only a few weeks later was the search in channels with jets and missing transverse momentum [4].

In order to achieve a maximal reach over the $(m_{\tilde{g}}, m_{\tilde{q}})$-plane, several signal regions are defined. When production of squark pairs $\tilde{q}\tilde{q}$ is dominant, only a small number of jets (one per squark from $\tilde{q} \to q\chi_1^0$) is expected. When production involves gluinos, extra jets are expected from $\tilde{g} \to qq\chi_1^0$. In these regions, requiring at least three jets yields better sensitivity. For each of the four signal regions (two dijet and two three-jet selections) E_T^{miss} is required to be > 100 GeV.

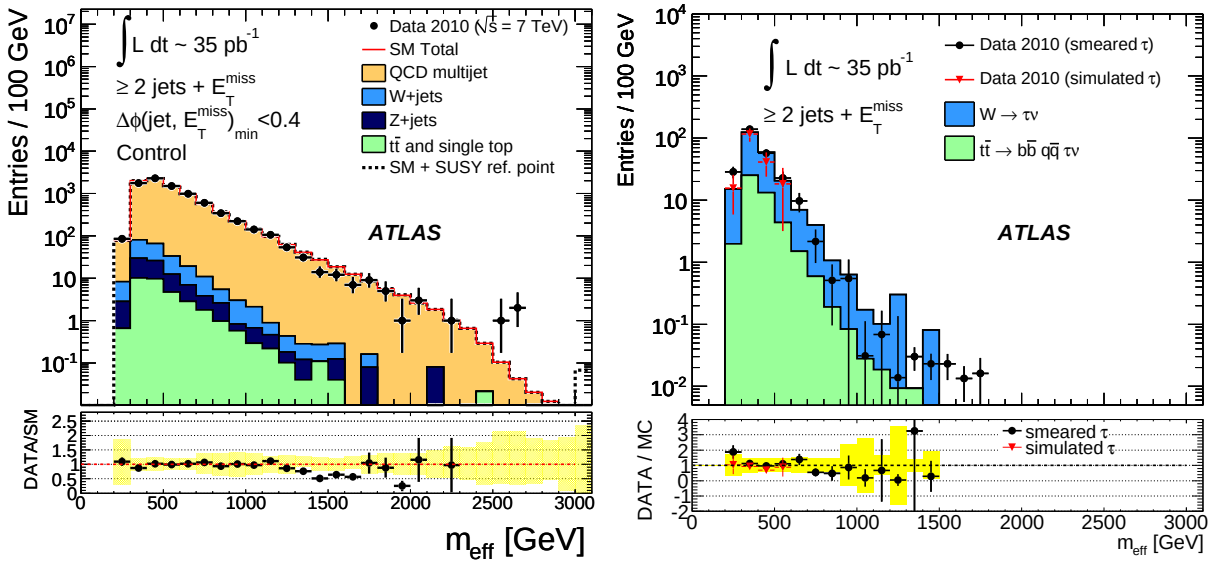

Figure 3: Left plot: Distribution of $m_{\rm eff}$ after the 2-jet and missing transverse momentum selection in the control region defined by the reverse cut on $\Delta\phi$. Right plot: Distribution of $m_{\rm eff}$ for the tau-related background after the full 2-jet selection, except the cut on $M_{\rm eff}$. Two data-driven background estimates are shown, both derived from selected $W \to \mu\nu$ events. The muon is removed from the event and replaced by a Monte Carlo tau lepton decay, which is either smeared using resolution functions to emulate the detector response (smeared tau) or processed using the full detector simulation (simulated tau).

The signal region aiming for high mass dijet events has a selection criteria on $m_{\rm T2}>$ 300 GeV. The quantity $m_{\rm T2}$ is a generalisation of the transverse mass for two particles decaying to a jet and missing transverse momentum [4]. The other three signal regions are defined with cuts on the effective mass, which is here a sum over the leading two or three jets (depending on the channel) and the missing transverse momentum.

The dominant SM background sources are W+jets, Z+jets, top pair, QCD multijet and single top production. The determination of a solid prediction for these backgrounds in the signal regions is the main challenge in these searches. ATLAS has carried out about $2-4$ control measurements per signal region and background. One method to derive the QCD prediction was a normalisation of the QCD MC samples by a scaling designed to achieve a match to data in control regions obtained by reversing the $\Delta\phi$ requirements. The $m_{\rm eff}$ distribution in the control region is shown in Figure 3. This result was found to be consistent with an other data-driven estimate in which high $E_{\rm T}^{\rm miss}$ events were generated from data by smearing low $E_{\rm T}^{\rm miss}$ events on a jet-by-jet basis with measured jet energy resolution functions. This latter technique has no MC dependencies; it provides a completely independent determination of the QCD multijet background using only quantities measured from the data. Additional control regions having reversed $E_{\rm T}^{\rm miss}/m_{\rm eff}$ requirements were used as further checks on the normalisation.

The Z+jets background originates from the irreducible component in which $Z \to \nu\bar{\nu}$ generates large $E_{\rm T}^{\rm miss}$. This background is measured in control regions were the Z decays to muons or electrons and is also modelled with a W+jets control sample. The W+jets background is determined via the same window in the $(M_T, E_{\rm T}^{\rm miss})$ plane as in the 1-lepton channel, but applying the jet cuts of this analysis. Hadronic τ decays in $t\bar{t} \to b\bar{b}\tau\nu qq$ can generate large $E_{\rm T}^{\rm miss}$ and pass the jet and lepton requirements at a non-negligible rate. The MC estimate for these events was checked to be consistent with a data-driven cross-check based on replacement of reconstructed muons in the corresponding single lepton channels with simulated hadronic τ decays. The resulting $m_{\rm eff}$ distribution is shown in Figure 3. Agreement was also found after reweighting the $t\bar{t}$ MC according to experimentally measured b-tag weights.

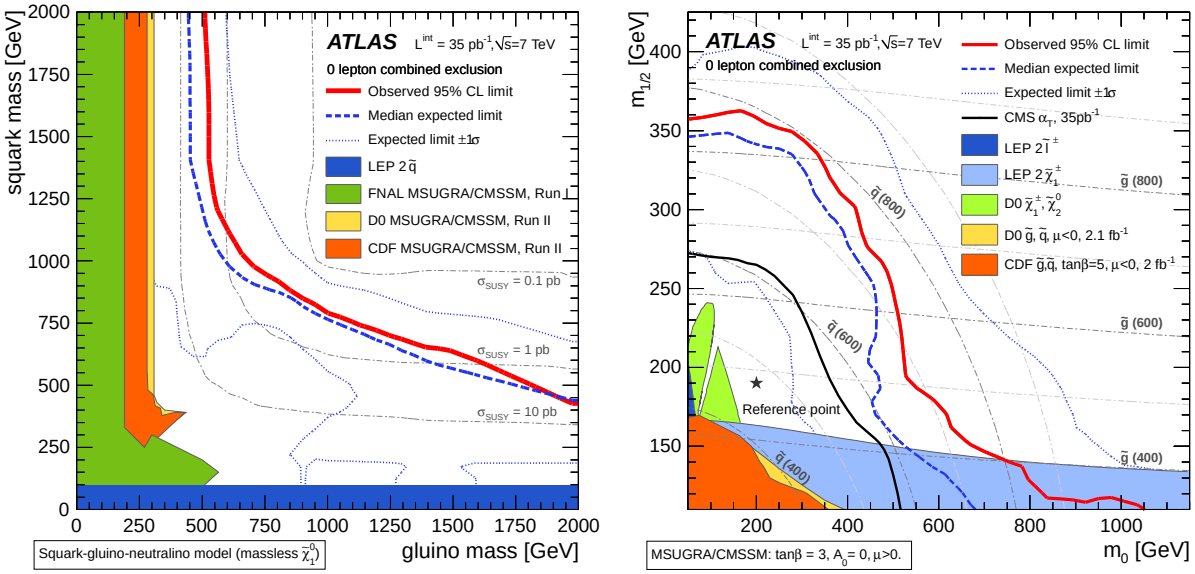

Figure 4: Left plot: 95% C.L. exclusion limits in the (gluino, squark) mass plane together with existing limits for a simplified MSSM model with a massless neutralino. Comparison with existing limits is illustrative only as some are derived in the context of MSUGRA/CMSSM or may not assume a massless neutralino. Right plot: 95% C.L. exclusion limits in the $\tan(\beta) = 3$, $A_0 = 0$ and $mu > 0$ slice of MSUGRA/CMSSM, together with existing limits with the different model assumptions given in the legend.

The number of observed data events and the number of SM events expected to enter each of the signal regions were found to be consistent in all four signal regions. The signal regions exclude again non-SM effective cross sections within acceptance. The results are interpreted in both a simplified model containing only squarks of the first two generations, a gluino octet and a massless neutralino, as well as in MSUGRA/CMSSM models with $\tan\beta = 3$, $A_0 = 0$ and $\mu > 0$. In the simplified model, gluino masses below 500 GeV are excluded at the 95% confidence level with the limit increasing to 870 GeV for equal mass squarks and gluinos. In the MSUGRA/CMSSM models equal mass squarks and gluinos below 775 GeV are excluded. Both exclusion plots are shown in Figure 4.

4 Searches with b-jets and missing transverse momentum

Events with jets, one or no lepton and missing transverse momentum are also studied with a b-tag requirement in order to enhance the sensitivity to the third generation, i.e. stops and sbottom squarks [5].

The 0-lepton b-jet selection uses slightly modified selection criteria compared to what was described above and is optimised for signals like sbottom production (either direct production or via gluino decay to sbottom and bottom) and the subsequent decay $\tilde{b} \to b\chi_1^0$. The 1-lepton b-jet selection aims for signals of stop production where the stop decays to a sbottom and chargino and finally the chargino could decay leptonically to a neutralino, a lepton and a neutrino. The signature would therefore be b-jets, leptons and missing transverse momentum. In both channels at least one jet is required to be b-tagged. The dominant background source is then top pair production due to this extra b-jet requirement. Again data-driven techniques have been employed to determine the QCD, W+jets and top backgrounds. No significant excess is observed with respect to the prediction for Standard Model processes. For R-parity conserving models in which sbottoms (stops) are the only squarks to appear in the gluino decay cascade, gluino masses below 590 GeV (520 GeV) are excluded at the 95% C.L. The results are also interpreted in an MSUGRA/CMSSM supersymmetry breaking scenario with $\tan(\beta) = 40$ and in an $SO(10)$

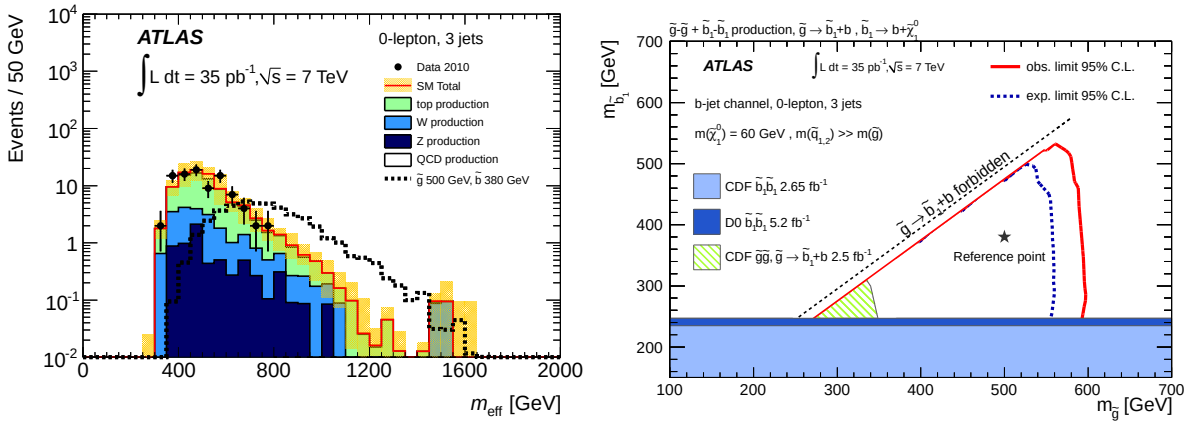

Figure 5: Left plot: Distributions of the effective mass for data and for the expectations from Standard Model processes after the baseline selections in the zero-lepton b-jet channel . Right plot: Observed and expected 95% C.L. exclusion limits, as obtained with the zero-lepton b-jet channel, in the $(m_{\tilde{g}}, m_{\tilde{b}1})$ plane. The neutralino mass is assumed to be 60 GeV. The result is compared to previous results from CDF and D0.

model framework. The $m_{\rm eff}$ distribution for the zero-lepton selection and the resulting limit are shown in Figure 5.

5 Searches with Dilepton events

A very clean potential signal for SUSY particles could come from dilepton events. In addition the shapes and endpoints of the dilepton mass distributions are a potentially perfect source to provide mass information for SUSY particles.

ATLAS has searched for the production of supersymmetric particles decaying into final states with missing transverse momentum and exactly two isolated leptons. The search strategies included events with lepton pairs with identical sign and events with opposite sign electric charges [6]. The signal region for the same sign analysis is defined by $E_{\rm T}^{\rm miss} > 100$ GeV, the signal region for the opposite sign analysis requires $E_{\rm T}^{\rm miss} > 150$ GeV. The main background of the same sign analysis arises from SM processes generating events containing at least one fake or non-isolated lepton. For the opposite sign analysis the main background arises from SM top pair production. The fake background is estimated by solving linear equations to get the fake probability for a "tight" lepton selections via a "loose" lepton selection. Dedicated control selections are developed to estimate the background from top events. Depending on the flavour of the two leptons $(ee, \mu\mu, \mu e)$ and the electric charge in total 6 signal regions are used for the search. Again no significant excesses are observed. Based on specific benchmark models, limits are placed on the squark mass between 450 and 690 GeV for squarks approximately degenerate in mass with gluinos, depending on the SUSY mass hierarchy considered (see Figure 6). The important (free) parameters of the MSSM model are the three gaugino masses and the squark and slepton masses [6]. The slepton is light in order to enhance the lepton decay.

Dilepton events are also studied with the so called "flavour subtraction" method [7]. Flavour uncorrelated backgrounds are subtracted using a sample of opposite flavour lepton pair events. The dominant background from top pair production can be subtracted via this method. In SUSY events the production of the two leptons can be correlated, if lepton flavor is conserved in the decays of e.g. a heavy neutralino to a slepton and a lepton and subsequently to $ll\chi_1^0$. The search for high missing transverse momentum events containing opposite charge identical flavour lepton pairs yields no significant excess. Here limits are set on the model-independent quantity S , which measures the mean excess from new physics taking into account flavour-dependent

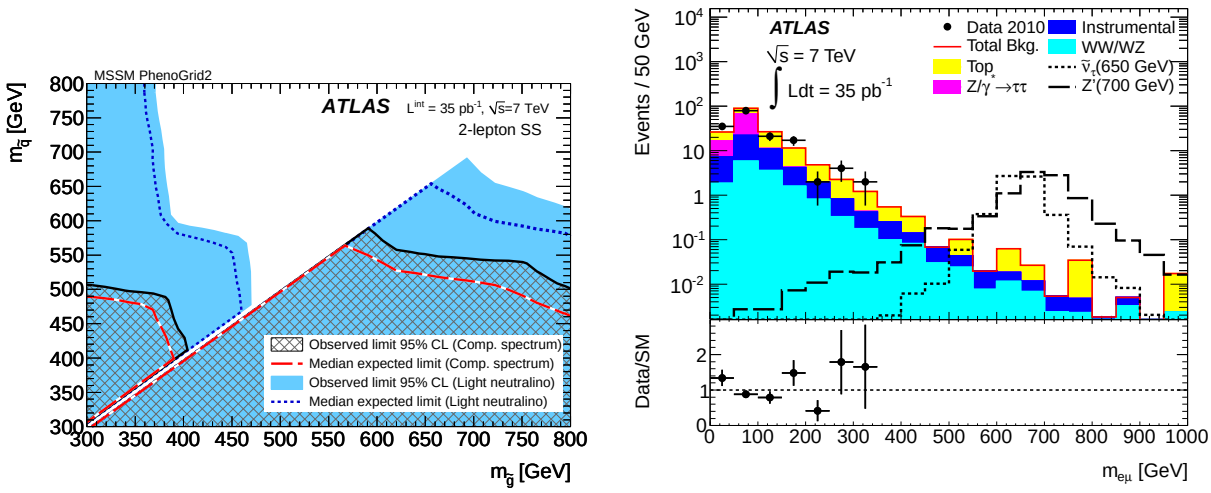

Figure 6: Left plot: Expected and observed 95% C.L. exclusion limits in the $(m_{\tilde{g}}, m_{\tilde{q}})$ plane for a MSSM models for the same sign dilepton analysis. Right plot: Observed and predicted electron-muon invariant mass distributions. The signal simulations are shown for tau-sneutrino with a mass of 650 GeV and a Z' with a mass of 700 GeV.

acceptances and effiencies.

A third generic search is performed for heavy particles decaying into an electron-muon final state [8]. Again the fake backgrounds are carefully determined via data-driven techniques. No excess above the Standard Model background expectation is observed (see Figure 6). Exclusions at 95% confidence level are placed on two representative models. In an R-parity violating supersymmetric model, tau sneutrinos with a mass below 0.75 TeV are excluded, assuming single coupling dominance and the R-parity violating couplings to be $\lambda'_{311} = 0.11$, $\lambda_{312} = 0.07$ (in order to compare with previous Tevatron studies). The ATLAS results extend to higher mass then previously studied at the Tevatron.

6 Searches for new slow-moving massive particles

ATLAS has also pursued a search for slow-moving charged particles (SMPs) [9]. Such particles are expected in some new physics models where the new (SUSY) particles are not allowed to decay, e.g. because the decay goes via highly virtual particles or because the couplings are very small. If these long lived particles are squarks or gluinos they will hadronize and form so called R-hadrons. The signal of such heavy particles will be a slowly moving heavy hadron.

The ATLAS detector contains a number of subsystems which provide information which can be used to distinguish SMPs from particles moving at velocities close to the speed of light. Two complementary subsystems used in this work are the pixel detector, which measures ionisation energy loss (dE/dx), and the tile calorimeter, which measures the time-of-fight from the interaction point for particles which traverse it.

The events are triggered by a $E_{\mathrm{T}}^{\mathrm{miss}}$ and track requirement. For each event, the mass is estimated by dividing its momentum by $\beta\gamma$, determined either from pixel detector ionisation or from the tile calorimeter. Rather than relying on simulations to predict the tails of the Pixel and Tile beta distributions, a data-driven method is used to estimate the background. Estimates for the background distributions are obtained by combining random momentum values (after the kinematic cuts) with random measurements of the Pixel and Tile β. This works since no correlation was observed in these three measurements.

Using data combined from these independent measurements, there are no events containing a candidate with mass greater than 100 GeV. This result is interpreted in a framework of

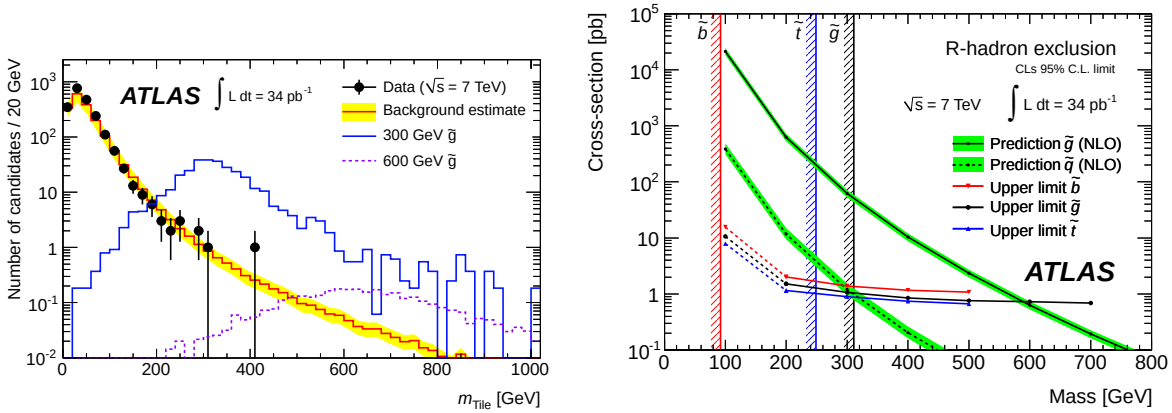

Figure 7: Left plot: The reconstructed mass of the R-hadron candidate and the background estimates for the tile calorimeter. Signal samples are superimposed on the background estimate. Right plot: Cross-section limits at 95% CL as a function of sparticle mass. The mass limits quoted in the text are inferred by comparing the cross-section limits with the model predictions. Previous mass limits are indicated by shaded vertical lines for sbottom (ALEPH), stop (CDF) and gluino (CMS).

supersymmetry models with R-hadrons and 95% CL limits are set on the production cross-sections of squarks and gluinos. The influence of R-hadron interactions in matter was studied using a number of different models, and lower mass limits for stable sbottoms and stops are found to be 294 and 309 GeV respectively (see Figure 7). The lower mass limit for a stable gluino lies in the range from 562 to 586 GeV depending on the model assumed. Each of these constraints is the most stringent to date.

7 Summary and Conclusion

The ATLAS experiment has started to search for signals of Supersymmetry. Due to the large cross sections for squarks and gluinos the sensitivity of the 2010 LHC data exceeds by far that of all previous collider experiments. The search is performed in a variety of different final states. ATLAS has presented the most stringent limits to date in many scenarios and no signal has been observed yet. The next years will likely allow a conclusive answer about the fate of low mass Supersymmetry.

Acknowledgments

The author acknowledges the support by the Landesstiftung Baden Württemberg and the BMBF.

References

1. S. P. Martin, arXiv:hep-ph/9709356.
2. ATLAS Collaboration, JINST **3** (2008) S08003.
3. ATLAS Collaboration, PRL 106, 131802 (2011), arXiv:1102.2357 [hep-ex].
4. ATLAS Collaboration, accepted by PLB, arXiv:1102.5290 [hep-ex].
5. ATLAS Collaboration, submitted to PLB, arXiv:1103.4344 [hep-ex].
6. ATLAS Collaboration, submitted to EPJC letters, arXiv:1103.6214 [hep-ex].
7. ATLAS Collaboration, accepted by EPJC letters, arXiv:1103.6208 [hep-ex].
8. ATLAS Collaboration, accepted by PRL, arXiv:1103.5559 [hep-ex].
9. ATLAS Collaboration, accepted by PLB, arXiv:1103.1984 [hep-ex].

A FOURTH CHIRAL GENERATION AND SUSY BREAKING

A. WINGERTER
Laboratoire de Physique Subatomique et de Cosmologie
UJF Grenoble 1, CNRS/IN2P3, INPG
53 Avenue des Martyrs, F-38026 Grenoble, France

We revisit four generations within the context of supersymmetry. We compute the perturbativity limits for the fourth generation Yukawa couplings and show that if the masses of the fourth generation lie within reasonable limits of their present experimental lower bounds, it is possible to have perturbativity only up to scales around 1000 TeV, i.e. the current experimental bounds and perturbative unification are mutually exclusive. Such low scales are ideally suited to incorporate gauge mediated supersymmetry breaking, where the mediation scale can be as low as 10-20 TeV. The minimal messenger model, however, is highly constrained. Lack of electroweak symmetry breaking rules out a large part of the parameter space, and in the remaining part, the fourth generation stau is tachyonic. Contribution to the proceedings of *Les Rencontres de Moriond EW 2011* based on ref. [1].

1 Is There Room For a Fourth Generation?

It was long believed to be common lore that an extra chiral generation of fermions was excluded by electroweak precision measurements [2]. Recently, however, the interest in a fourth sequential generation of fermions was revived after realizing that the constraints are by far not as stringent as they were thought to be. We start out by reviewing what we know about the fourth generation couplings to Standard Model quarks and leptons, and then revisit the various constraints from experiment and theory.

1.1 Determination of $|V_{tb}|$

Until recently the CKM matrix element $|V_{tb}|$ was determined indirectly from the ratio [3]

$$R = \frac{\mathcal{B}(t \to Wb)}{\mathcal{B}(t \to Wq)} = \frac{|V_{tb}|^2}{|V_{td}|^2 + |V_{ts}|^2 + |V_{tb}|^2} = 1.03^{+0.19}_{-0.17} \tag{1}$$

by assuming that $|V_{td}|^2 + |V_{ts}|^2 + |V_{tb}|^2 = 1$, or in other words, that the 3×3 CKM matrix is unitary. A value $R \neq 1$ would either imply non-standard-model-like interactions of the top quark or the existence of extra quarks [2]. From $R = 1$, however, we cannot infer that a fourth generation is ruled out [4]. The first direct measurement from observing single-top production [5, 6] gave $|V_{tb}| > 0.78$ which is consistent with $|V_{tb}| = 1$, but leaves enough room e.g. for a fourth generation replica of the top quark, t', to couple to the b quark.

1.2 *Do Electroweak Precision Observables Really Forbid a Fourth Generation?*

In Fig. (1) we show the constraints on new physics from the electroweak precision data. The contribution of a fourth chiral generation to the S and T parameters can be arranged to stay inside the *solid* confidence level ellipses by carefully adjusting the fermion masses so that ΔS and ΔT are positive, roughly equal and not too large, and assuming a *larger Higgs mass* [7]. The constraints coming from electroweak precision data can thus be circumvented.

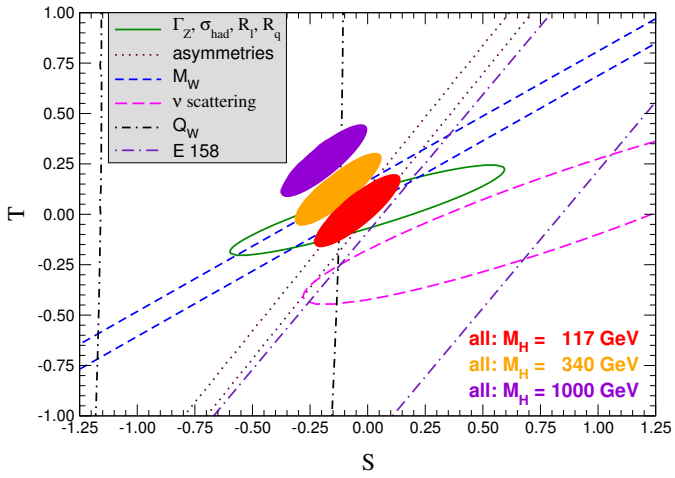

Figure 1: The 90% C.L. contours in the S and T plane for different Higgs masses (by J. Erler and P. Langacker, see ref. [2]). If the new physics contribution is such that $\Delta S \simeq \Delta T > 0$ is not too large, we have a fair chance of staying inside the confidence level ellipses, but we have to assume a larger Higgs mass.

1.3 *What About the Other Constraints?*

Constraints from FCNCs and $b \to s\gamma$ [8] are typically weaker than those from electroweak precision tests [9]. From the invisible decay width of the Z boson we know that there are exactly three neutrinos that couple to the Z and are lighter than $M_Z/2$, so for the fourth generation neutrino we have to assume $m_{\nu 4} \geq M_Z/2$. The limit from cosmology $\sum m_\nu \lesssim 1$ eV does not hold for heavy neutrinos [10].

1.4 *Our Theoretical Prejudice*

From a theoretical point of view it certainly looks odd that the fourth generation neutrino should be so much heavier than those from the first three generations. In absence of a complete and convincing neutrino mass generation mechanism, however, we cannot simply dismiss the idea on theoretical grounds.

Asymptotic freedom of QCD restricts the number of generations to be ≤ 8, but there is no really good reason why it should be exactly three. There are e.g. models in string theory that relate the number of generations to topological invariants of the compactification manifold, but these models usually fail to describe the details of the low-energy theory in a predictive way.

From direct searches at colliders we know that the fourth generation fermion masses are much larger as compared to their third generation counterparts, and one may be worried about the Yukawa couplings becoming non-perturbative. Loss of perturbativity simply means that our calculations become more cumbersome and has no bearing on the validity of the theory. In that case, the fourth generation fermions may form a condensate, see e.g. [11].

2 Why Is A Fourth Generation Interesting?

As already mentioned in Section 1.2, the effect of a fourth generation with a judicious choice of masses can be such that the electroweak precision observables would prefer a larger Higgs mass (see Fig. 1). This is very welcome, since a certain tension has built up between the best-fit value of the Higgs mass $m_H = 80^{+30}_{-23}$ GeV [12] as obtained from electroweak precision data and the direct exclusion limit of $m_H > 114.4$ GeV from LEP.

If the CKM matrix is extended to a 4-by-4 matrix, there are 2 additional phases, and this extra CP violation may be large enough to make electroweak baryogenesis viable. In the Standard Model, the first order phase transition is not strong enough to preserve the generated baryon asymmetry from being washed out, but the presence of extra scalars in the MSSM may solve this problem [13, 14]. There have been speculations [15] that this may work even without SUSY, but this has been contradicted by ref. [14].

3 Four Generations and Supersymmetry

The generalization of the MSSM to four generations (MSSM4) is straightforward, since the fourth generation is an exact replica of the third one except for the larger masses. In the following, we will denote the fourth generation quarks and leptons by t', b', τ', and ν'_τ. In the graphs, we may use the alternate notation t_4, b_4, τ_4, and $\nu_{\tau 4}$ for the sake of better readability.

To reduce the large number of soft parameters that are introduced into the Lagrangian for supersymmetry breaking, we will look at two unifying frameworks, namely the constrained MSSM and minimal gauge mediation. Before we do that, however, we need to discuss the regime of perturbativity for the MSSM4.

3.1 Perturbativity of the Yukawa Couplings

The top Yukawa coupling is already dangerously close to the non-perturbative regime so that we have to worry about perturbation theory breaking down for not-too-large values of the fourth generation fermion masses. The left panel of Fig. 2 shows the values of $m_{t'}$ and $m_{b'}$ for which the t' Yukawa coupling becomes non-perturbative (black area) before reaching the assumed unification scale of $M_X = 2.3 \times 10^{16}$ GeV for constant $m_{\tau'} = 100.8$ GeV which is the lower experimental bound (see Eq. (2)). For $m_{t'} \gtrsim 150$ GeV perturbativity is lost for relatively small values of $m_{b'}$.

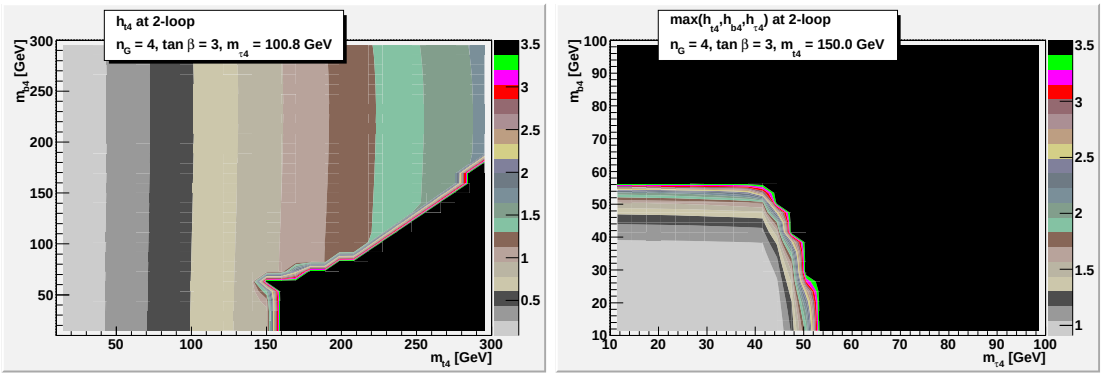

(a) Values of $m_{t'}$, $m_{b'}$ where $h_{t'}$ becomes non-perturbative for $m_{\tau'} = 100.8$ GeV.

(b) Values of $m_{\tau'}$, $m_{b'}$ where $h_{t'}$, $h_{b'}$ or $h_{\tau'}$ becomes non-perturbative for $m_{t'} = 150$ GeV.

Figure 2: The black area shows the region in parameter space where the theory becomes non-perturbative.

We now fix $m_{t'} = 150$ GeV and show in the right panel of Fig. 2 the values of $m_{\tau'}$ and $m_{b'}$ for which either of the fourth generation Yukawa couplings becomes non-perturbative. The result is that $m_{\tau'}$ and $m_{b'}$ cannot be larger than roughly 50 GeV. This is in conflict with the experimental bounds [2]

$$m_{t'} > 256 \text{ GeV}, \quad m_{b'} > 128 \text{ GeV}, \quad m_{\tau'} > 100.8 \text{ GeV},. \tag{2}$$

Reversing the logic, we fix the fourth generation fermion masses at their experimental lower bounds and ask at what scale the theory becomes non-perturbative. The left panel of Fig. 3 shows that the highest scale that we can reach before perturbation theory breaks down is $M_X \simeq 15$ TeV for $\tan\beta \simeq 2$.

We can have a larger domain of perturbativity for lower fourth generation fermion masses. To that end, we recall that the limits quoted in Eq. (2) are at 95% C.L. and can be relaxed by assuming a higher level of confidence. Furthermore, the exclusion limits denote the pole masses, whereas in our calculations, we are using the running masses. We will account for these differences by taking 25% off the masses in Eq. (2). Additionally, in order to satisfy the T-parameter constraint which measures the mass splitting in the SU(2) multiplet, we impose $|m_{t'} - m_{b'}| = 75$ GeV:

$$m_{t'} = 192 \text{ GeV}, \quad m_{b'} = 117 \text{ GeV}, \quad m_{\tau'} = 75 \text{ GeV} \tag{3}$$

Even with all these assumptions, we can maintain perturbativity only up to $M_X \simeq 900$ TeV. As an aside, we remark that assuming the extra generation to be vectorlike largely avoids problems with perturbativity; we are not considering this option here, because we are interested in a *sequential* extra generation that is an exact replica of the third one except for the larger masses.

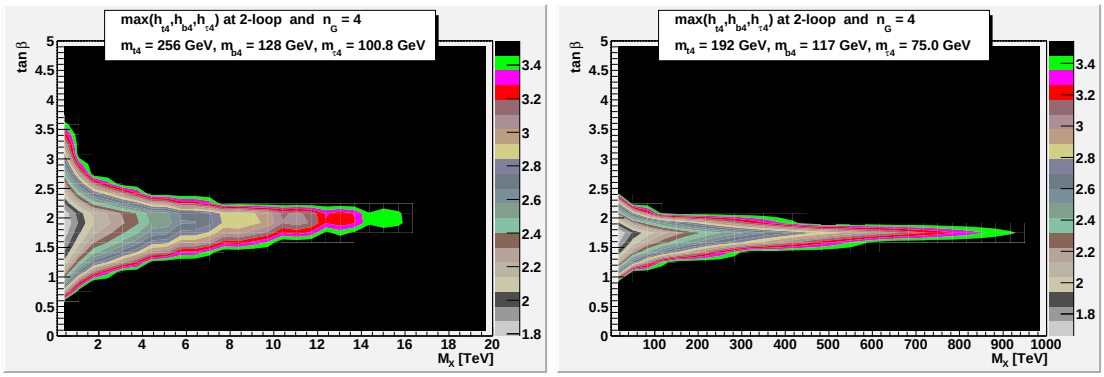

Figure 3: Perturbativity limits for the masses given in Eq. (2) (left panel) and Eq. (3) (right panel), respectively.

3.2 The Constrained MSSM

The results from the previous section clearly show that the existence of a fourth generation and the idea of perturbative unification are mutually exclusive. Yet, to illustrate how things change in the presence of an extra generation, we present a *toy model* where we take all fourth generation fermion masses to be equal to their third generation counterparts.

In the left and right panels of Fig. 4 we show the running of m_0, $m_{1/2}$ and $\sqrt{\mu^2 + m_0^2}$ in the MSSM with three and four generations, respectively. We notice that in the case of four generations (i) the unification scale has increased to $M_{\rm GUT} = 8.82 \times 10^{16}$ GeV, (ii) $|\mu|$ is larger and leads to a heavier Higgs, (iii) the squark and gluino masses grow slower (reading the graph from right to left).

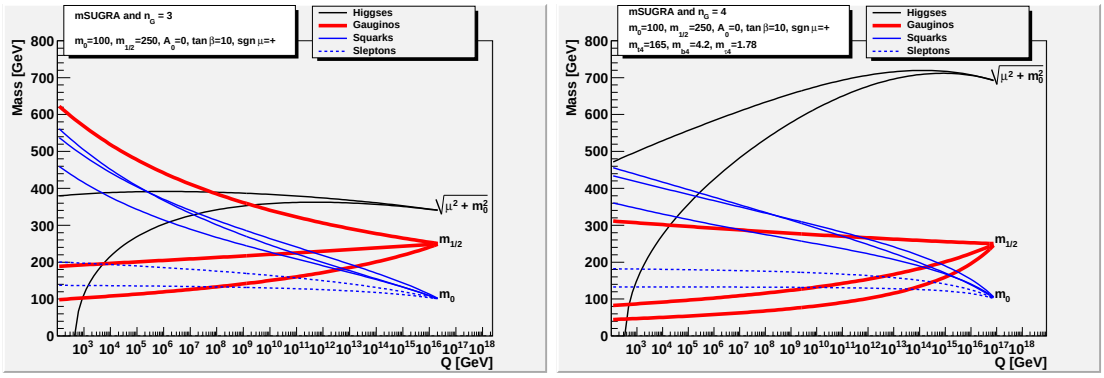

(a) Three generations. (b) Four generations.

Figure 4: The running of the various soft masses in the MSSM3 (left panel) and MSSM4 (right panel). The unification scale is $M_{\rm GUT} = 2.40 \times 10^{16}$ GeV and $M_{\rm GUT} = 8.82 \times 10^{16}$ GeV, respectively.

These qualitative features (except the jump in $|\mu|$ in Fig. 4) can be easily understood by looking at the changes to the renormalization group equations in going from three to four generations. Comparing the spectra (see ref. [1]) of the MSSM3 and MSSM4 with the same mSUGRA boundary conditions, we see that the mass of the lightest CP even Higgs boson h^0 has indeed increased as was anticipated (the exclusion limit [12] for a neutral MSSM Higgs boson is $m_{h^0} > 92.8$ GeV). The squarks, sleptons and gluinos are lighter and the CP odd and charged Higgses are heavier.

3.3 Minimal Gauge Mediation

Minimal gauge mediation is especially suited for constraining the soft SUSY breaking parameters of the MSSM4, because it does not require the perturbativity of the theory to hold all the way up to the GUT scale. In particular, the mediation scale can be as low as 10-20 TeV.

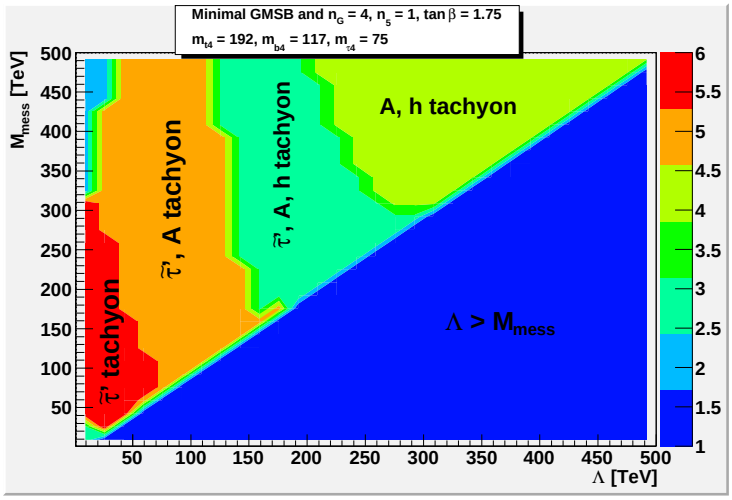

Figure 5: Regions in mGMSB parameter space Λ–$M_{\rm mess}$ for fixed $n_5 = 1$, $\tan\beta = 1.75$, $\mathrm{sgn}\,\mu$=+. The fourth generation masses are $m_{t'} = 192$ GeV, $m_{b'} = 117$ GeV, $m_{\tau'} = 75$ GeV. The lower-diagonal part is ruled out as $\Lambda > M_{\rm mess}$. In the upper-diagonal part, most of the parameter space does not have consistent radiative electroweak symmetry breaking as indicated by the tachyonic Higgses.

In Fig. 5 we show a slice of the parameter space of minimal gauge mediation where we have fixed three of the five parameters ($n_5 = 1$, $\tan\beta = 1.75$, $\mathrm{sgn}\,\mu{=}+$) and varied the messenger scale M_{mess} and the parameter $\Lambda = \langle F_S\rangle/\langle S\rangle$. Here, F_S and S denote the auxiliary and scalar components of the gauge singlet field that is responsible for SUSY breaking.

Unfortunately, the full parameter space of minimal gauge mediation is ruled out for any of the fourth generation masses that are compatible with experiment. The small region where only the lightest $\widetilde{\tau}'$ is tachyonic (colored red in Fig. 5) can possibly be tractable in the sense that additional model building assumptions may lift the mass into the positive regime. This, however, would necessarily depart from the elegant and simple picture of minimal gauge mediation.

4 Conclusions

A fourth chiral generation is not favored by experiment, but it is not ruled out either. As an obvious extension of the Standard Model, it should be considered as a possibility for new physics to be discovered at the LHC. In the Standard Model, the presence of the fourth generation fermions with appropriately chosen masses may ease the tension between the lower experimental bound on the Higgs mass and its best-fit value from electroweak precision data. In the context of SUSY breaking, however, a fourth generation is problematic: Two of the most popular mechanisms for SUSY breaking do not work, and the main problem is the loss of perturbativity at scales.

Acknowledgments

I thank the organizers of *Les Rencontres de Moriond EW 2011* for providing an inspiring and hospitable atmosphere, Rohini M. Godbole and Sudhir K. Vempati for their collaboration, and Tomáš Ježo for comments.

References

1. R. M. Godbole, S. K. Vempati, A. Wingerter, JHEP **1003** (2010) 023. [arXiv:0911.1882 [hep-ph]].
2. C. Amsler *et al.* [Particle Data Group Collaboration], Phys. Lett. **B667** (2008) 1-1340.
3. V. M. Abazov *et al.* [D0 Collaboration], Phys. Lett. **B639** (2006) 616-622. [hep-ex/0603002].
4. J. Alwall, R. Frederix, J. -M. Gerard, A. Giammanco, M. Herquet, S. Kalinin, E. Kou, V. Lemaitre *et al.*, Eur. Phys. J. **C49** (2007) 791-801. [hep-ph/0607115].
5. V. M. Abazov *et al.* [D0 Collaboration], Phys. Rev. Lett. **103** (2009) 092001 [arXiv:0903.0850 [hep-ex]].
6. T. Aaltonen *et al.* [CDF Collaboration], Phys. Rev. Lett. **103** (2009) 092002. [arXiv:0903.0885 [hep-ex]].
7. G. D. Kribs, T. Plehn, M. Spannowsky and T. M. P. Tait, Phys. Rev. D **76** (2007) 075016 [arXiv:0706.3718 [hep-ph]].
8. M. Bobrowski, A. Lenz, J. Riedl and J. Rohrwild, Phys. Rev. D **79** (2009) 113006 [arXiv:0902.4883 [hep-ph]].
9. M. S. Chanowitz, Phys. Rev. D **79** (2009) 113008 [arXiv:0904.3570 [hep-ph]].
10. A. D. Dolgov, Phys. Rept. **370** (2002) 333 [arXiv:hep-ph/0202122].
11. A. Soni, Talk presented at *Les Rencontres de Moriond EW 2011*
12. K. Nakamura *et al.* [Particle Data Group Collaboration], J. Phys. G **G37** (2010) 075021.
13. S. W. Ham, S. K. Oh, D. Son, Phys. Rev. **D71** (2005) 015001. [hep-ph/0411012].
14. R. Fok and G. D. Kribs, Phys. Rev. D **78** (2008) 075023 [arXiv:0803.4207 [hep-ph]].
15. W. S. Hou, Chin. J. Phys. **47** (2009) 134 [arXiv:0803.1234 [hep-ph]].

EXOTICA SEARCHES AT THE CMS EXPERIMENT

F. SANTANASTASIO
(ON BEHALF OF THE CMS COLLABORATION)
University of Maryland, Department of Physics - John S. Toll Physics Building, College Park, MD 20742-4111, United States of America

This paper presents the results of searches for various new physics phenomena in proton-proton collisions at $\sqrt{s} = 7$ TeV delivered by the LHC and collected with the CMS detector in 2010. While the sensitivity of these early searches varies, in many cases they set the most stringent limits on these new physics phenomena. These results demonstrate good understanding of the detector and backgrounds in a variety of channels, which is a fundamental component of successful searches in view of the much larger data sample expected to be delivered by LHC in 2011 and beyond.

1 Introduction

This paper presents the results of searches for various new physics phenomena beyond the standard model (SM) [a] in proton-proton collisions at $\sqrt{s} = 7$ TeV delivered by the LHC and collected with the Compact Muon Solenoid (CMS) [1] detector in 2010. For the majority of these searches the full dataset has been used, corresponding to an integrated luminosity of almost 40 pb^{-1}.

2 New Heavy Resonances

2.1 Dilepton and Diphoton Resonances

Many models of new physics beyond the SM predict the existence of narrow resonances, possibly at the TeV mass scale, that decay to a pair of charged leptons (such as Z' bosons) or to lepton and neutrino (such as W' bosons). Also the Randall-Sundrum (RS) model of extra dimensions foresees the existence of Kaluza–Klein graviton excitations (G_{KK}) decaying to a pair of charged leptons or pair of photons. The CMS collaboration has searched for such narrow resonances in the invariant mass spectrum of dimuon/dielectron [2] and diphoton [3] final states, as well as in the transverse mass spectrum of electron+neutrino [4] and muon+neutrino [5] final states. The spectra are consistent with standard model expectations in both the bulk and the tails of the aforementioned distributions. Figure 1 shows the 95% confidence level (CL) upper limits on the cross section of $\text{Z}'/\text{G}_{\text{KK}}$ (W') production, obtained combining the dielectron (electron+neutrino) and dimuon (muon+neutrino) channels. A Z' (W') with SM-like coupling can be excluded below 1.14 (1.58) TeV. Model-independent lower limits on the Z' mass have also been reported in Ref. [2] as a function of the couplings of the Z' to fermions in the annihilation of charge 2/3 and charge

[a] Searches for Supersymmetry at CMS are not discussed in this paper. These results can be found in other proceedings of this conference.

-1/3 quarks. In the diphoton channel, limits are derived on the cross section for the production of RS gravitons, and hence on the parameters of the warped extra dimension model. For values of the coupling parameter ranging from 0.01 to 0.1, graviton masses below 371 to 945 GeV are excluded at the 95% CL.

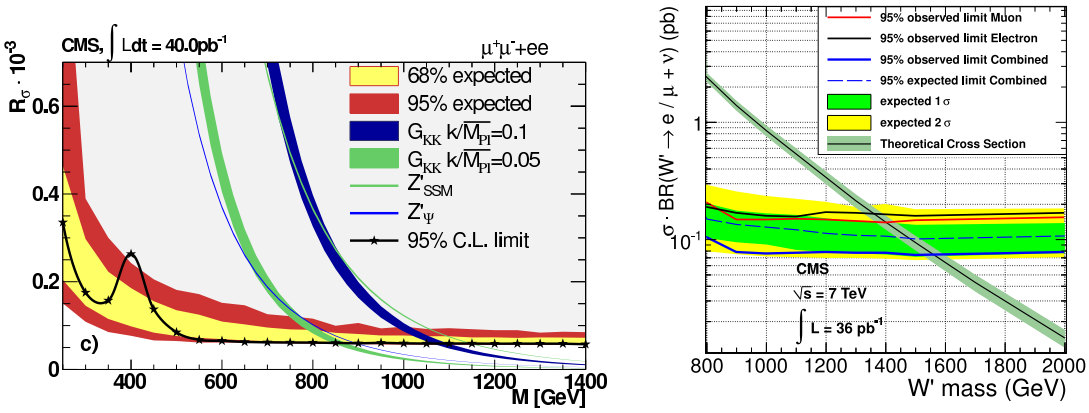

Figure 1: (Left) Upper limits as a function of resonance mass on the Z′ cross section relative to standard model Z boson production, obtained combining dielectron and dimuon final states. The distortion of the observed limits at ∼400 GeV is the result of a clustering of several dimuon and dielectron events around this mass. An excess of 1.1σ is quantified in the combined sample, after taking into account the "look-elsewhere" effect. (Right) Upper limits as a function of the resonance mass on the W′ cross section for the individual electron+neutrino and muon+neutrino channels, and their combination.

2.2 Leptoquarks

The standard model has an intriguing but ad hoc symmetry between quarks and leptons. In some theories beyond the SM, such as SU(5) gran unification, Pati–Salam SU(4), and others, the existence of a new symmetry relates the quarks and leptons in a fundamental way. These models predict the existence of new bosons, called leptoquarks. The leptoquark (LQ) is coloured, has fractional electric charge, and decays to a charged lepton and a quark with unknown branching fraction β, or a neutrino and a quark with branching fraction $(1-\beta)$. Constraints from experiments sensitive to flavour-changing neutral currents, lepton-family-number violation, and other rare processes favour LQs that couple to quarks and leptons within the same SM generation, for LQ masses accessible to current colliders. Searches for pair-production of first and second generation scalar LQs have been performed in the eejj [6], eνjj [7], and $\mu\mu$jj [8] channels. The dominant backgrounds for these searches arise from the SM production of Z/γ+jets, W+jets and $\mathrm{t\bar{t}}$ events. The reconstructed variable S_{T}, defined below [b], has a large signal-to-background discrimination power, and it is used to select LQ candidate events. Figure 2 (left) shows the exclusion limits at 95% CL on the first generation leptoquark hypothesis in the β versus LQ mass plane for the eejj and eνjj channels, and their combination. First generation scalar LQ masses below 384 GeV (340 GeV) are excluded at 95% CL for $\beta = 1$ ($\beta = 0.5$). In the $\mu\mu$jj channel, a 95% CL lower limit on the second generation scalar LQ mass is set at 394 GeV assuming $\beta = 1$.

2.3 Dijet Searches

In the standard model, point like parton-parton scatterings in high energy proton-proton collisions can give rise to final states with energetic jets. At large momentum transfers, events

[b] In the eejj and $\mu\mu$jj channels, S_{T} is defined as the scalar sum of the transverse momenta of the two leading (in p_{T}) charged leptons and jets. In the eνjj channel, S_{T} is defined as the scalar sum of the transverse momentum of the electron, the missing transverse energy, and the two leading jets.

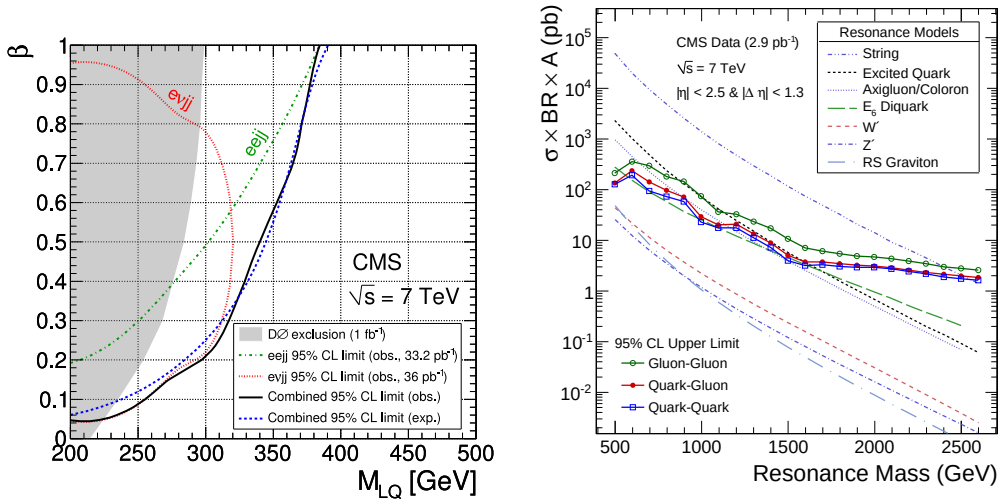

Figure 2: (Left) Exclusion limits at 95% CL on the first generation LQ hypothesis in the β versus LQ mass plane. The shaded region is excluded by the current D0 limits, which combine results of eejj, eνjj, and $\nu\nu$jj decay modes. (Right) 95% CL upper limits on signal cross section for dijet resonances of type gluon-gluon, quark-gluon, or quark-quark, versus dijet resonance mass, compared to theoretical predictions for various new physics models.

with at least two energetic jets (dijets) may be used to confront the predictions of perturbative Quantum Chromodynamics (QCD) and to search for signatures of new physics. The new physics could manifest itself via the direct production of a new massive particle that then decays into a dijet final state (quark-quark, quark-gluon, or gluon-gluon resonances), and/or the rate of dijet events could be enhanced through a new force that only manifests itself at very large CM energies (contact interactions). Complementary search strategies have been pursued by the CMS experiment in the dijet channel: search for narrow resonances in the dijet mass spectrum [9], search for narrow resonances and contact interactions using the dijet centrality ratio variable [10], and search for contact interactions using dijet angular distributions [11]. The first two analyses were performed with the early 3 pb^{-1} of proton-proton collisions at $\sqrt{s} = 7$ TeV, and they are now being updated with more data. Figure 2 (right) shows the 95% CL upper limits on signal cross section versus dijet resonance mass, compared to theoretical predictions for various new physics models. String resonances, with mass less than 2.50 TeV, excited quarks, with mass less than 1.58 TeV, and axigluons, colorons, and E_6 diquarks, in specific mass intervals, have been excluded at 95% CL. Using measurements of dijet angular distributions over a wide range of dijet invariant masses, a lower limit on the contact interaction scale for left-handed quarks of $\Lambda^+ = 5.6$ TeV ($\Lambda^- = 5.6$ TeV) for constructive (destructive) interference is obtained at the 95% CL.

2.4 Fourth Generation of Fermions and $\mathrm{t\bar{t}}$ *Resonances*

Recently, there has been renewed interest in extensions of the SM predicting a fourth generation of massive fermions. Theoretical studies have shown that indirect bounds on the Higgs boson mass can be relaxed, and an additional generation of quarks may possess enough intrinsic matter and anti-matter asymmetry to be relevant for the baryon asymmetry of the Universe. Driven by this motivation, a search for pair production of heavy bottom-like quarks (b') in trileptons and same-sign dilepton final states [12], arising from the decay chain $\mathrm{b}'\bar{\mathrm{b}}' \rightarrow \mathrm{tW}^-\bar{\mathrm{t}}\mathrm{W}^+ \rightarrow \mathrm{bW}^+\mathrm{W}^-\bar{\mathrm{b}}\mathrm{W}^-\mathrm{W}^+$, has been performed at CMS. The total branching ratio for these channels is 7.3% and the very small expected SM background comes mainly from $\mathrm{t\bar{t}}$ events. No events are found in the signal region defined in the analysis, and the b' mass range from 255 to 361 GeV

has been excluded at the 95% CL.

The CMS experiment has also performed a model-independent search for new massive neutral bosons (such as Z′) decaying via a top-antitop quark pair [13]. The event reconstruction and selection is optimized for the production of top quarks close to rest, with well separated decay products. The analysis focuses on decay channels of the $t\bar{t}$ system that include a single isolated electron or muon. No significant deviation from SM expectations is found in the $t\bar{t}$ mass spectra obtained from eight independent data samples, categorized by lepton type, multiplicity of jets and number of b-tagged jets. Upper limits on the production cross section times branching fraction, $\sigma_{Z'} \times \mathrm{BR}(Z' \to t\bar{t})$, of the order of 25, 7, and 4 pb^{-1} for invariant masses in the region $m_{Z'} = 0.5$, 1, and 1.5 TeV, respectively, are set. These results are competitive with the current limits from the Tevatron, particularly at high mass values.

3 Compositeness Models

A fundamental question in the standard model of particle physics is the source of the mass hierarchy of the quarks and leptons. A commonly proposed explanation for the three generations is a compositeness model in which the known leptons and quarks are bound states of either three fermions, or a fermion-boson pair. The underlying substructure of these new bound states implies a large spectrum of excited states. Novel strong contact interactions (CI) couple excited fermions (f^*) to ordinary quarks and leptons (f) and can be described with the effective lagrangian $\mathcal{L}_{\mathrm{CI}} \propto (\jmath^\mu \jmath_\mu)/\Lambda^2$, where Λ is the compositeness scale, and $\jmath_\mu$ is the fermion current.

3.1 Excited Leptons

A search for the associated production of a lepton (ℓ) and an oppositely charged excited lepton (ℓ^*) is performed [14]. The final state contains two leptons and a photon, $\ell\ell\gamma$, arising from the decay $\ell^* \to \ell\gamma$, where ℓ is either an electron or a muon. The SM backgrounds containing misidentified electrons or photons are estimated using data-driven methods. The maximum reconstructed invariant mass among the two possible lepton-photon combination, $\mathrm{M}_{\ell\gamma}^{\mathrm{max}}$, is used to discriminate between signal and SM backgrounds. No excess of events is found in the $\mathrm{M}_{\ell\gamma}^{\mathrm{max}}$ spectra above the SM expectation in the electron or muon channel. Figure 3 (left) shows the region excluded at 95% CL in the $\Lambda - \mathrm{M}_{\ell^*}$ parameter space for the $\mu\mu\gamma$ channel, where M_{ℓ^*} is the excited lepton mass. A similar exclusion is obtained in the eeγ channel.

3.2 Excited Quarks

The CMS experiment has performed a search for anomalous production of highly boosted Z bosons in the dimuon decay channel arising from the decays of new heavy particles [15]. The search is optimized for the detection of excited quark production and decay via $q^* \to qZ \to q\mu\mu$, with no explicit requirement on the jet recoiling against a high transverse momentum Z. Figure 3 shows the dimuon p_{T} spectrum from data compared to the simulation of excited quark signals. The results are consistent with background-only expectations. Limits are derived on excited quark production in the plane of compositeness scale Λ versus mass for two scenarios of production and decay: one assuming excited quark transitions via SM gauge bosons only, and one including also novel contact interaction transitions from new strong dynamics. The q^* mass limits at 95% CL with contact interactions are more sensitive than previous searches in scenarios where the coupling to gluons is suppressed relative to the electroweak gauge bosons, ruling out masses below 1.17 TeV in the extreme case when this coupling is zero.

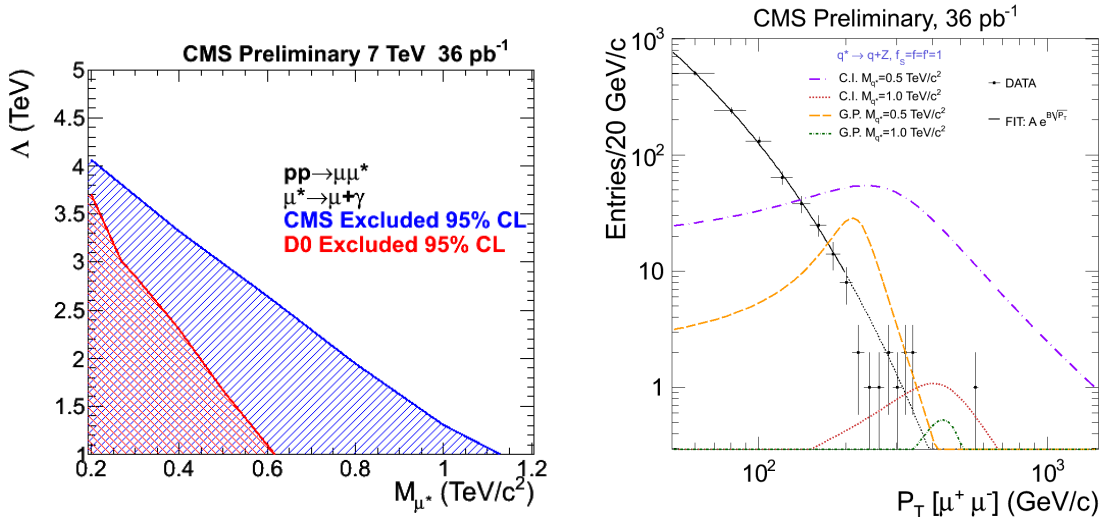

Figure 3: (Left) Exclusion at 95% CL in the $\Lambda - M_{\ell^*}$ parameter space for the $\mu\mu\gamma$ channel. (Right) The dimuon p_T spectrum distribution from data with a background parametrization overlaid. Various excited quark signals are shown, corresponding to different production mechanisms (gauge interaction and contact interaction) and different q^* masses.

4 Extra Dimensions

Compact large extra dimensions (ED) are an intriguing proposed solution to the hierarchy problem of the SM, which refers to the puzzling fact that the fundamental scale of gravity $M_{Planck} \sim 10^{19}$ GeV is so much higher than the electroweak symmetry breaking scale $\sim 10^3$ GeV. In the ADD model [c], the SM is constrained to the common 3+1 space-time dimensions, while gravity is free to propagate through the entire multidimensional space. The gravitational flux in 3+1 dimensions is effectively diluted by virtue of the multidimensional Gauss's Law. In this framework, the fundamental Planck scale can be lowered to the electroweak scale, thus making production of gravitons possible at the LHC. Some of the experimental signatures of the existence of such extra dimensions are discussed below.

4.1 Diphoton and Dimuon Channels

Searches for virtual-graviton contributions in the diphoton [16] and dimuon [17] final states have been performed. Figure 4 displays the diphoton (left) and dimuon (right) invariant mass distribution for the observed data, the backgrounds, and the ADD signal. The ADD signal, differently from the searches discussed in Section 2.1, would not appear as a narrow peak but as an overall excess of events at high values of invariant mass. In both $\gamma\gamma$ and $\mu\mu$ channels, the data is found to be consistent with SM expectations. Lower limits at the 95% CL are set on the fundamental Planck scale in the approximate range of 1.4–2.3 TeV, depending on the final state considered, the number of extra dimensions, and the theoretical conventions used to describe the virtual-graviton production.

4.2 Mono-jet Final State

A search for production of a real graviton G balanced by an energetic hadronic jet via the processes $q\bar{q} \rightarrow gG$, $qg \rightarrow qG$, and $gg \rightarrow gG$ has been performed [18]. Since gravitons are free

[c] The original proposal to use extra dimensions to solve the hierarchy problem was presented by Arkani-Hamed, Dimopoulos, and Dvali (ADD).

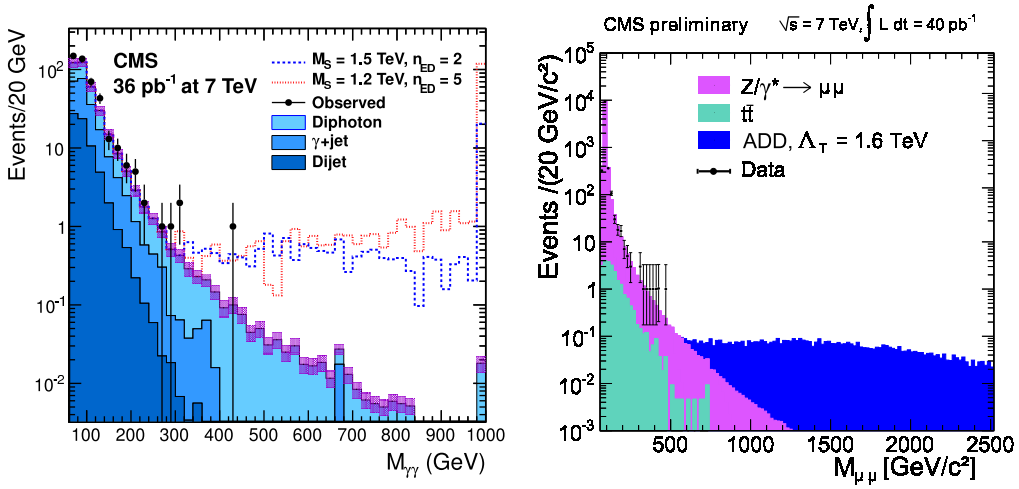

Figure 4: Diphoton (left) and dimuon (right) invariant mass spectra compared with the SM prediction and simulated ADD signals.

to propagate in the extra dimensions, they escape the detector and can only be inferred from the amount of missing transverse energy ($\not\!\!E_{\mathrm{T}}$). The offline event selection requires large $\not\!\!E_{\mathrm{T}}$, one high p_{T} jet, a veto on the presence of well-identified leptons and isolated tracks, and additional requirements to suppress the cosmics, beam halo, and instrumental backgrounds that can fake the mono-jet+$\not\!\!E_{\mathrm{T}}$ signature. Figure 5 (left) shows the p_{T} distribution of the leading jet after the full selection. A measurement of the electroweak background from $\mathrm{W} \to \mu\nu$ enriched data is used to derive a data-driven background estimate for the Z/γ+jets and W+jets contributions remaining in the signal region. The number of observed events in data is in good agreement with the SM prediction, and significant improvements are made to the current limits on the fundamental parameters of the model describing real-graviton emission.

4.3 Microscopic Black Holes

One of the exciting predictions of theoretical models with extra dimensions and low-scale quantum gravity is the possibility of copious production of microscopic black holes in particle collisions at the LHC. Events with large total transverse energy are analyzed for the presence of multiple high-energy jets, leptons, and photons, typical of a signal expected from a microscopic black hole [19]. Figure 5 (right) shows the distribution of the total transverse energy for data, background prediction and various signal samples. Good agreement with the standard model backgrounds, dominated by QCD multijet production, is observed for various final-state multiplicities and model-independent limits on new physics in these final states are set. Using simple semi-classical approximation, limits on the minimum black hole mass are derived as well, in the range 3.5–4.5 TeV.

5 Long-Lived Particles and Other Exotic Signatures

5.1 Massive Long-Lived Particles

Heavy stable (or quasi-stable) charged particles appear in various extensions of the SM. Heavy long-lived particles with hadronic nature, such as gluinos or stops, hadronize in flight, forming meta-stable bound states with quarks and gluons (so called R-Hadrons). If the lifetime of R-Hadrons produced at LHC is longer than a few nanoseconds, these particles will travel over distances that are comparable or larger than the size of a typical particle detector, and hence

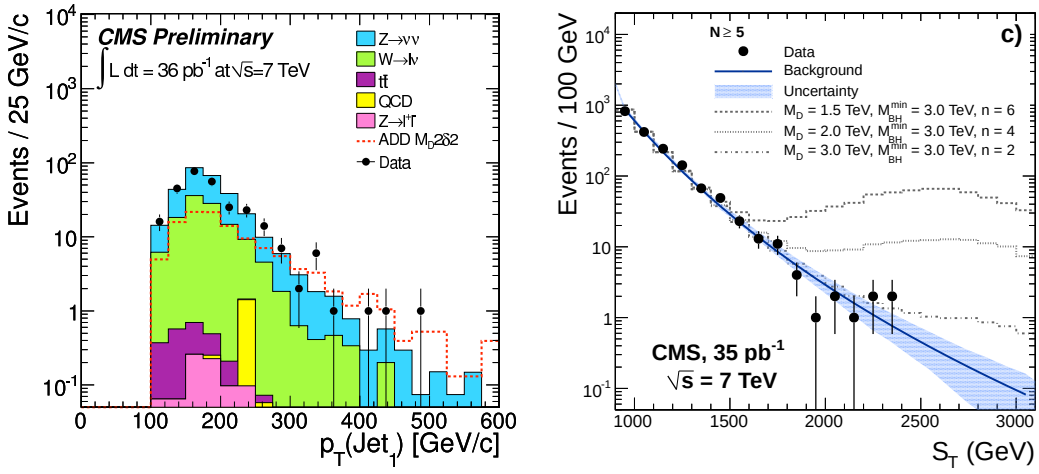

Figure 5: (Left) p_{T} distribution of the leading jet after the full mono-jet+$\not\!\!E_{\mathrm{T}}$ selection. The distribution for an ADD signal (shown in red) is overlaid. (Right) Total transverse energy (including the $\not\!\!E_{\mathrm{T}}$ in the sum) for events with more than 5 objects (jets, leptons, and photons) for data, background prediction, and black hole signals for three different parameter sets.

might be detected directly. The CMS experiment uses two complementary strategies to identify such long-lived particles.

A significant fraction of these massive particles (assuming masses greater than 100 GeV) will have a velocity $\beta = v/c$, smaller than 0.9. A search has been performed to identify R-Hadrons through the distinctive signature of a high momentum track with an anomalously large rate of energy loss through ionization in the silicon tracker, using the first 3 pb^{-1} of data collected in 2010 [20]. Lower limits at the 95% CL on the mass of a stable gluino are set i) at 398 GeV, using a conventional model of nuclear interactions that allows charged hadrons containing this particle to reach the muon detectors, ii) at 311 GeV, in a conservative scenario where any hadron containing this particle becomes neutral before reaching the muon detectors.

Searches have been also performed for very slow ($\beta \leq 0.4$) R-hadrons containing a gluino, for which the electromagnetic and nuclear energy loss is sufficient to bring a significant fraction of the produced particles to rest inside the CMS detector volume [21]. These stopped R-hadrons will decay into an hadronic jet and a neutralino only seconds, days, or weeks later (accordingly to their unknown lifetime), and out-of-time with respect to the LHC collisions. The online selection of events requires the firing of a single jet trigger with an explicit veto on the beam presence. In a dataset with a peak instantaneous luminosity of $1 \times 10^{32}\mathrm{cm}^{-2}\mathrm{s}^{-1}$, an integrated luminosity of 10 pb^{-1}, and a search interval corresponding to 62 hours of LHC operation, no significant excess above background (mainly instrumental noise) was observed. Limits at the 95% confidence level on gluino pair production over 13 orders of magnitude of gluino lifetime are set. For a mass difference $\mathrm{m}_{\tilde{\mathrm{g}}} - \mathrm{m}_{\tilde{\chi}^0_1} > 100$ GeV, and assuming $\mathrm{BR}(\tilde{\mathrm{g}} \to \mathrm{g}\tilde{\chi}^0_1) = 100\%$, $\mathrm{m}_{\tilde{\mathrm{g}}} < 370$ GeV are excluded for lifetimes from 10 μs to 1000 s.

5.2 New Light Resonances Decaying into Pairs of Muons

Recent astrophysical observations of an excess of high-energy positrons in the cosmic ray spectrum have motivated the rise of new physics scenarios suggesting that this excess may be associated with annihilation of dark matter particles in the galactic halo. One realization of such models assumes an extra U(1) gauge symmetry with weak coupling to the standard model. The U(1) symmetry is broken, leading to a light massive vector boson (m $\sim$ O(1GeV)), a "hidden sector" (or "dark") photon γ_{dark}, which decays into leptons and, if kinematically allowed,

hadrons. More complex models can lead to a whole hierarchy of the dark sector states or can have dark photons preferentially couple to leptons. Hidden sectors can be realized naturally in supersymmetric (SUSY) models where coupling of the dark sector to the SUSY sector can be enhanced. Depending on the complexity of the light dark sector, at the LHC one may expect either a single dark photon at the end of each SUSY cascade or a whole cascade of hidden state decays with emission of multiple dark photons. Subsequent decays of the new states into leptons leads to appearance of the energetic collimated groups of leptons (leptonic jets).

A signature-based search for groups of collimated muons has been performed at CMS [22]. The analysis searches for production of new low-mass states (m $\sim$ 0.5–5 GeV) decaying into pairs of muons and is designed to achieve high sensitivity to a broad range of models predicting leptonic jet signatures. With no excess observed in the data over the background expectation, model-independent upper limits on the production cross section times branching fraction times acceptance are derived for several event topologies, and range from 0.1 to 0.5 pb^{-1} at the 95% CL. In addition, the results are interpreted in several benchmark models in the context of supersymmetry with a new light dark sector exploring previously inaccessible parameter space.

Acknowledgments

The author wishes to thank the organizers of the "Rencontres de Moriond/EW" for the rich and interesting physics program, and the beautiful location of the conference.

References

1. The CMS Collaboration, *JINST* **03**, S08004 (2008).
2. The CMS Collaboration, *arXiv:1103.0981* (2011). Accepted by *JHEP* .
3. The CMS Collaboration, *CMS Physics Analysis Summary* **EXO-10-019** (2011).
4. The CMS Collaboration, *Phys. Lett.* B **698**, 21 (2011).
5. The CMS Collaboration, *arXiv:1103.0030* (2011). Accepted by *Phys. Lett.* B.
6. The CMS Collaboration, *Phys. Rev. Lett.* **106**, 201802 (2011).
7. The CMS Collaboration, *arXiv:1105.5237* (2011). Submitted to *Phys. Lett.* B.
8. The CMS Collaboration, *Phys. Rev. Lett.* **106**, 201803 (2011).
9. The CMS Collaboration, *Phys. Rev. Lett.* **105**, 211801 (2010).
10. The CMS Collaboration, *Phys. Rev. Lett.* **105**, 262001 (2010).
11. The CMS Collaboration, *Phys. Rev. Lett.* **106**, 201804 (2011).
12. The CMS Collaboration, *arXiv:1102.4746* (2011). Submitted to *Phys. Lett.* B.
13. The CMS Collaboration, *CMS Physics Analysis Summary* **TOP-10-007** (2011).
14. The CMS Collaboration, *CERN-PH-EP-2011-081* (2011). To be submitted to *Phys. Lett.* B.
15. The CMS Collaboration, *CMS Physics Analysis Summary* **EXO-10-025** (2011).
16. The CMS Collaboration, *JHEP* **05**, 085 (2011).
17. The CMS Collaboration, *CMS Physics Analysis Summary* **EXO-10-020** (2011).
18. The CMS Collaboration, *CERN-PH-EP-2011-070* (2011). To be submitted to *Phys. Rev. Lett.*.
19. The CMS Collaboration, *Phys. Lett.* B **697**, 434 (2011).
20. The CMS Collaboration, *JHEP* **03**, 024 (2011).
21. The CMS Collaboration, *Phys. Rev. Lett.* **106**, 011801 (2011).
22. The CMS Collaboration, *CERN-PH-EP-2011-064* (2011). To be submitted to *JHEP* .

EXOTIC SEARCHES AT ATLAS

D.M. GINGRICH
(on behalf of the ATLAS Collaboration)
Centre for Particle Physics, Department of Physics, University of Alberta, Edmonton, AB T6G 2G7 Canada &
TRIUMF, Vancouver, BC V6T 2A3 Canada

We present the first results of searches for new physics with the ATLAS detector using the 2010 Large Hadron Collider proton-proton collision data at a centre of mass energy of 7 TeV. After a few months of operation, these searches already go beyond the reach of previous experiments, and start to explore new territories.

1 Introduction

This paper presents five searches for new physics in proton-proton collisions using the ATLAS detector at the Large Hadron Collider. The data were collected in 2010 at a centre of mass energy of 7 TeV. The first two searches use 3.1 pb^{-1} of early data, while the later three searches use the full 2010 data set with a typical luminosity of 36 pb^{-1}.

2 Long-Lived Highly Ionising Particles

The ATLAS collaboration has performed a search for massive long-lived highly ionising particles (HIP).[1] Some examples that may give rise to highly ionising particle signatures are Q-balls, black hole remnants, magnetic monopoles, and dyons. We have performed a model independent search. Due to their large mass, HIPs are also characterised by their non-relativistic speeds, as well as, high electric charge. We expect large amounts of energy loss through ionisation for these states. In ATLAS, HIPs would leave tracks in the inner tracking detector, matched to narrow energy loss in the electromagnetic calorimeter.

ATLAS is not able to search for HIP of all charges, masses, and lifetimes. The accessible parameter space was determined as follows. A lower charge bound of $|q| \geq 6e$ was determined by the $E_{\text{T}} > 10$ GeV trigger threshold. The upper charge bound of $|q| \leq 17e$ was determined by delta electrons and electron recombination. An upper bound on the mass of 1 TeV was determined by trigger timing constraints. A lifetime greater than 100 ns was required to maintain narrow energy deposits. A data sample with a luminosity of 3.1 pb^{-1} was used.

HIPs were discriminated by the proportion of high-ionisation hits and the lateral extent of the energy deposition. Specifically, the fraction f_{HT} of transition radiation tracker (TRT) hits on the track which pass a high ionisation threshold was used. In addition, a requirement on the fraction of energy outside the three most energetic cells associated to a selected electromagnetic (EM) energy cluster, in the second EM calorimeter layer, w_2, was made. Figure 1 shows that the

data matches Standard Model (SM) expectations, and no HIPs were observed. The estimated background in the signal region was 0.019 ± 0.005 events. Limits for particles produced in the acceptance kinematic region and by Drell-Yan production are shown in Table 1. A Bayesian statistical approach with a uniform prior for the signal was used. HIP masses above 800 GeV are probed for the first time at particle colliders.

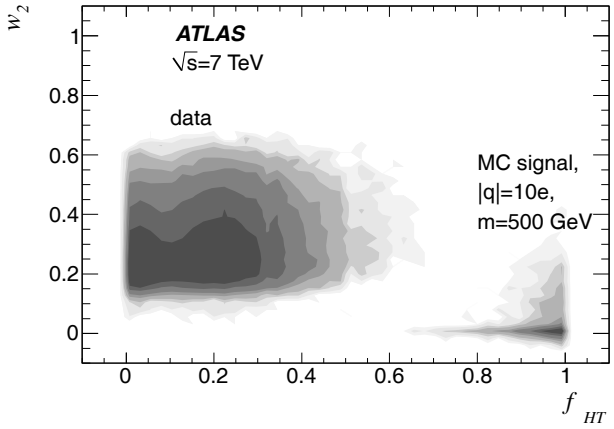

Figure 1: Contours of w_2 versus f_{HT} distributions showing the density of entries on a log scale. Data and a signal Monte Carlo simulated sample are shown.

Table 1: Inclusive and pair production cross section upper limits (95% C.L.) for long-lived massive particles with high electric charges $|q|$, produced in the search acceptance and assuming a Drell-Yan production mechanism.

Mass	Inclusive Search			Drell-Yan Mechanism		
	$\|q\| = 6e$	$\|q\| = 10e$	$\|q\| = 17e$	$\|q\| = 6e$	$\|q\| = 10e$	$\|q\| = 17e$
200 GeV	1.4 pb	1.2 pb	2.1 pb	11.5 pb	5.9 pb	9.1 pb
500 GeV	1.2 pb	1.2 pb	1.6 pb	7.2 pb	4.3 pb	5.3 pb
1000 GeV	2.2 pb	1.2 pb	1.5 pb	9.3 pb	3.4 pb	4.3 pb

3 Diphoton with Large Missing Energy

ATLAS has performed a search for events with diphotons ($\gamma\gamma$) and large missing transverse energy $E_{\mathrm{T}}^{\mathrm{miss}}$.[2] This signature has been interpreted in the context of Universal Extra Dimensions (UED). We considered a single TeV^{-1} sized UED with a compactification radius R. In this model, the lightest Kaluza-Klein (KK) particle (LKP) is the KK photon γ^*. The KK particles are produced as pairs of KK quarks and/or KK gluons in the strong interaction. These KK particles then decay down, via KK states, to the LKP. The LKP decays by $\gamma^* \to \gamma + G$. We interpreted the results of the search using a model in which $\Lambda R = 20$, where Λ is the UV cutoff and R is a free parameter

Figure 2 shows the $E_{\mathrm{T}}^{\mathrm{miss}}$ spectrum of events with diphotons. Events were required to have two photons each with $E_{\mathrm{T}} > 25$ GeV, and an event $E_{\mathrm{T}}^{\mathrm{miss}} > 75$ GeV. Zero signal events were observed and the estimated background was $0.32 \pm 0.16^{+0.37}_{-0.10}$ events. Figure 3 shows upper limits on the cross section. The upper limits were calculated using a Bayesian approach with a flat prior for the signal cross section. It was verified that the result is not very sensitive to the detailed form of the assumed prior. In context of the previously specified model, values of $1/R < 728$ GeV are excluded. This is the most sensitive limit on this model to date.

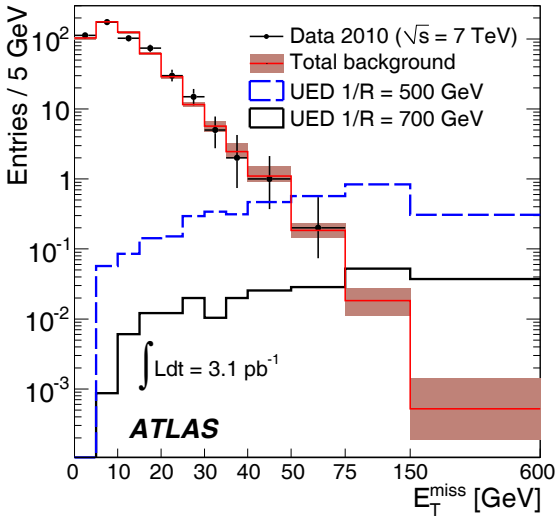

Figure 2: $E_{\mathrm{T}}^{\mathrm{miss}}$ spectra for $\gamma\gamma$ events, compared to the total SM background as estimated from data. Also shown are two hypothetical UED signals. The vertical error bars and shaded bands show the statistical errors.

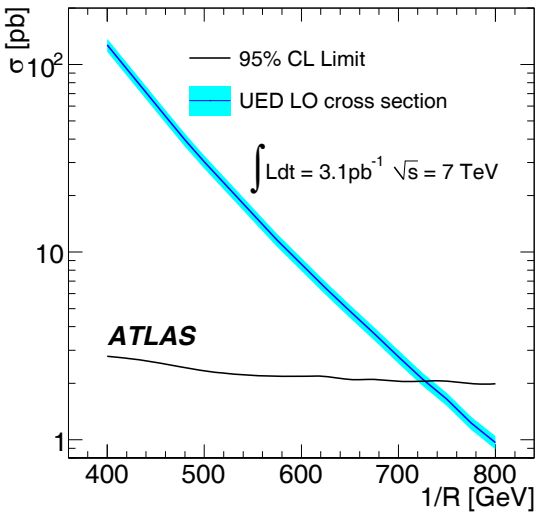

Figure 3: 95% C.L. upper limits on the UED production cross section, and the leading order (LO) theory cross section prediction, as a function of $1/R$. The shaded band shows the PDF uncertainty.

4 Search for New Physics in Dijets

ATLAS has performed a study of dijet events using both the invariant mass of the two jets and angular distributions of energetic jets up to 3.5 TeV. [3] For the invariant mass studies, we required $p_{\mathrm{T}}^{\mathrm{j1}} > 150$ GeV and $p_{\mathrm{T}}^{\mathrm{j2}} > 30$ GeV, as well as, $|\Delta\eta_{\mathrm{jj}}| > 1.3$. Figure 4 shows that the invariant mass distribution is smooth as expected for QCD jet production and agrees with the SM background parameterisation.

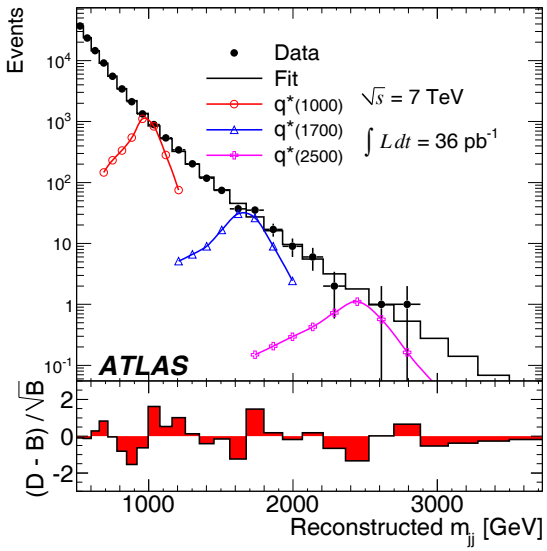

Figure 4: Observed (D) dijet mass distribution (solid dots) fitted using a binned QCD background (B) parameterisation (histogram). Predicted q* signals normalised to 36 pb^{-1} for masses of 1.0, 1.7, and 2.5 TeV are overlaid. The bin-by-bin significance of the data-background difference is shown in the lower panel.

For the angular distributions, we required $p_{\mathrm{T}}^{\mathrm{j1}} > 60$ GeV and $p_{\mathrm{T}}^{\mathrm{j2}} > 30$ GeV. The rapidities of the two leading jets per event are required to satisfy $y_B = 0.5(y_1 + y_2) < 1.10$ and $y^* = 0.5(y_1 - y_2) < 1.70$. Figure 5 shows the χ distributions, where $\chi = \exp(|y_1 - y_2|) = \exp(2|y^*|)$. Data are consistent with QCD. We also examined the dijet centrality, where $F_\chi(m_{\mathrm{jj}}) = N_{\mathrm{events}}(|y^*| < 0.6)/N_{\mathrm{events}}(|y^*| < 1.7)$. This distribution is shown in Fig. 6.

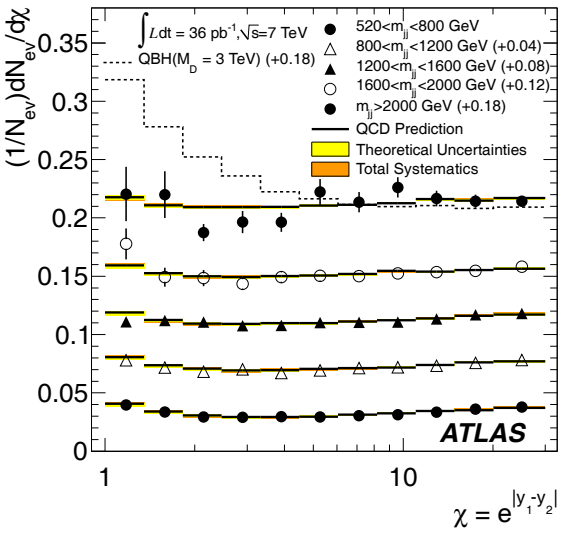

Figure 5: χ distributions for different m_{jj} bins. Shown are the QCD predictions with systematic uncertainties, and data points with statistical uncertainties. The dashed line is the prediction of a quantum black hole (QBH) signal in the highest mass bin. The distributions and QCD predictions have been offset.

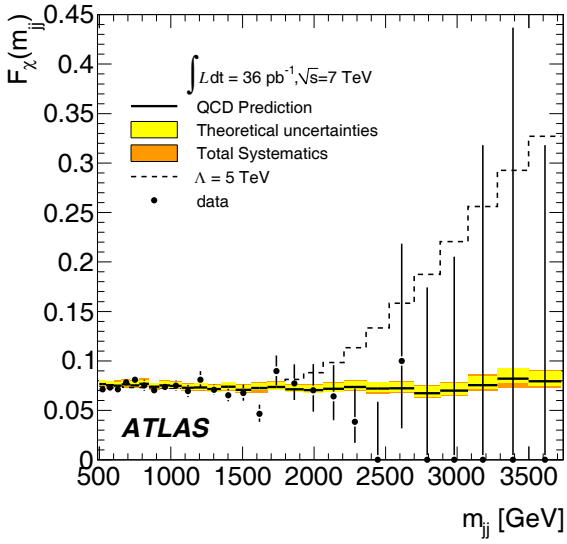

Figure 6: $F_\chi(m_{\mathrm{jj}})$ function versus m_{jj}. We show the QCD prediction with systematic uncertainties (band) and data (solid dots) with statistical uncertainties. The expected signal for QCD plus a quark contact interaction with $\Lambda = 0.5$ TeV is also shown.

We now interprete the results using several models, showing both the dijet mass and angular distribution results. For the resonance results, we set Bayesian credibility levels by defining a posterior probability density from the likelihood function for the observed mass spectrum, obtained by a fit to the background functional form and a signal shape derived from MC calculation. For the angular distribution results, likelihood ratios for comparing the different hypotheses and parameter estimators were used. Confidence level limits are set using the frequentist CLs+b approach.

Excited quarks can be produced in $\mathrm{qg} \to \mathrm{q}^*$ and decay by $\mathrm{q}^* \to \mathrm{qg}$, $\mathrm{qW/Z}/\gamma$. Figure 7 shows the results of the resonance search. Excited quarks are excluded in the mass range $0.60 < m < 2.15$ TeV, while axigluons are excluded in the range $0.60 < m < 2.10$ TeV. Shown in Fig. 8 is the Q distribution, where $Q = -2[\ln(F_\chi(m_{\mathrm{jj}})|H0) - \ln(F_\chi(m_{\mathrm{jj}})|H1)]$, and $H0$ is the null hypothesis (QCD only) and $H1$ is the hypothesis for new physics. From this analysis, excited quarks in the mass range $0.60 < m < 2.64$ TeV are excluded.

We searched for quantum black holes (QBH) decaying to dijets, where M_D is the higher-dimensional Planck scale and n is the number of extra dimensions. These states would be expected to produce a large mass threshold effect with long tails to higher masses. The results of the resonance search are show in Fig. 9. Planck scales in the range $0.75 < M_D < 3.67$ TeV are exclude. The results of the angular distributions analysis are shown in Fig. 10. From the $dN/d\chi$ distribution, Planck scales less than 3.69 TeV are excluded, while from the $F_\chi(m_{\mathrm{jj}})$ distribution Planck scales of less than 3.78 TeV are excluded.

Finally, limits are given for a generic signal with a Gaussian profile. Signal templates in the range $0.6 < m < 4.0$ with $3\% < \sigma < 15\%$ (5 different σ values) were generated. The results

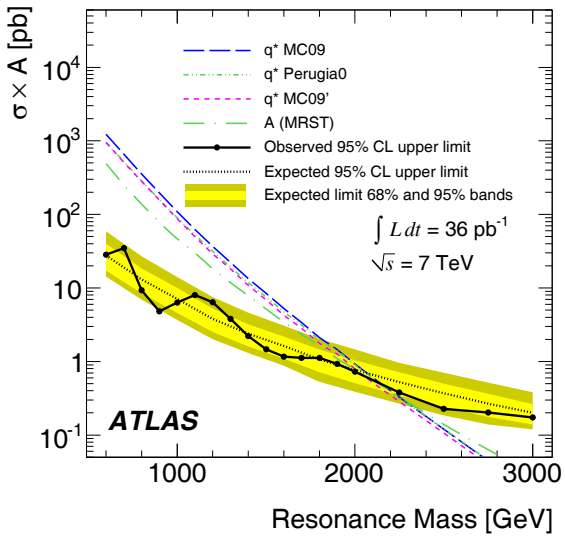

Figure 7: 95% C.L. upper limits on cross section times acceptance for a resonance decaying to dijets taking into account both statistical and systematic uncertainties (points and solid line) compared to an axigluon model and to a q* model with three alternative MC tunes.

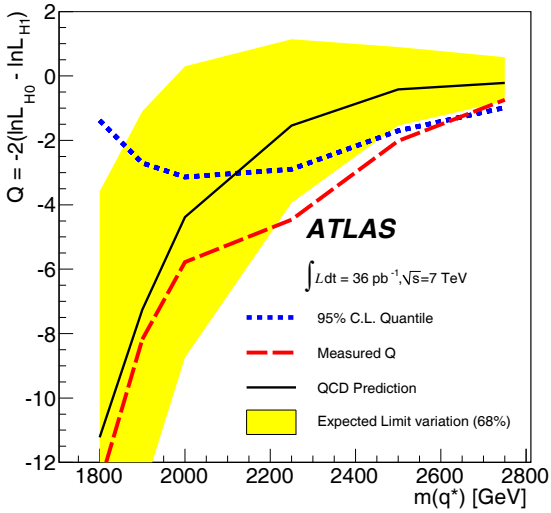

Figure 8: 95% C.L. limits on the excited quark model using the logarithm of the likelihood ratios obtained from the $F_\chi(m_{jj})$ distributions. The expected 68% interval for the expected limits are shown by the band.

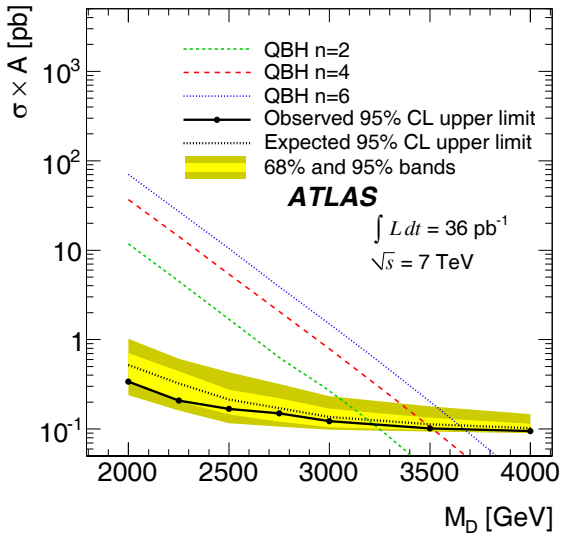

Figure 9: 95% C.L. limits on the cross section times acceptance versus the Planck scale for three quantum black hole (QBH) models, taking into account both statistical and systematic uncertainties.

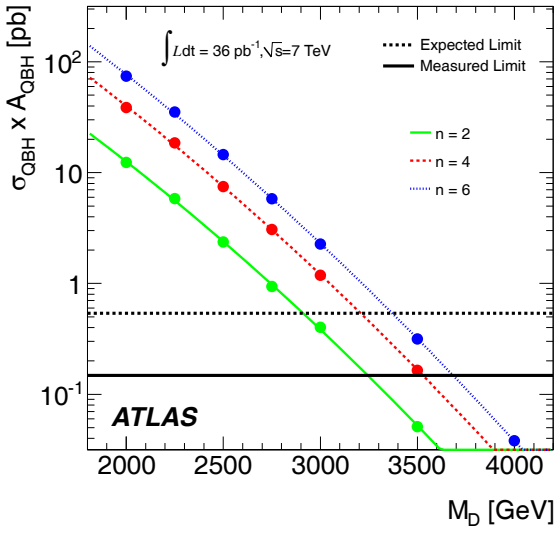

Figure 10: Cross section times acceptance for quantum black holes (QBH) as a function of M_D. The measured and expected limits are shown as the solid and dashed lines.

are shown in Fig. 11. These results can be used for different models by employing the following prescription: 1) Check the validity of the Gaussian signal approximation, and determine the peak and width of the signal; 2) Determine the model acceptance; 3) Calculate the event yield for the model cross section and luminosity of 36 pb^{-1}; 4) Compare this event yield with the limits in Fig. 11.

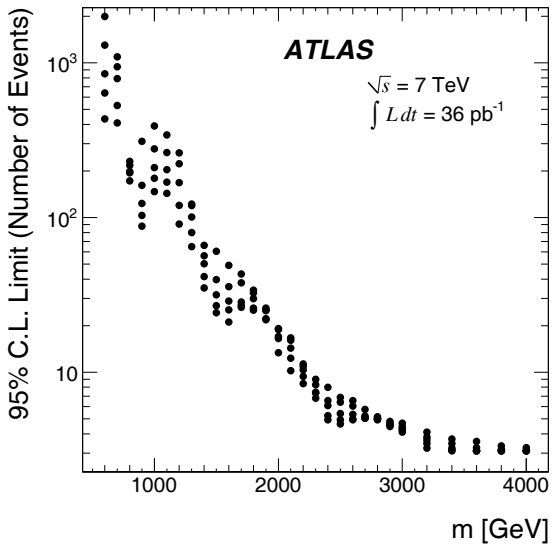

Figure 11: 95% C.L. upper limits for the number of observed events for Gaussians of width σ/m of 0.03, 0.05, 0.07, 0.10, 0.15, at each of various masses m.

5 Lepton plus Missing Transverse Energy

ATLAS has performed a search for high-mass states decaying to an electron or muon with missing energy: $\mathrm{W}'/\mathrm{W}^* \to (\mathrm{e}/\mu)\nu$. [4] The W' is a sequential SM boson with the same SM couplings as the W-boson. The W^* is a boson with anomalous magnetic moment type couplings. The search was performed in the transverse mass defined as $m_{\mathrm{T}} = \sqrt{2p_T E_{\mathrm{T}}^{\mathrm{miss}}(1-\cos\phi_{\ell\nu})}$. Events with electrons were chosen by requiring the electron to have $E_{\mathrm{T}} > 25$ GeV, and the event to have $E_{\mathrm{T}}^{\mathrm{miss}} > 25$ GeV and $E_{\mathrm{T}}^{\mathrm{miss}}/E_{\mathrm{T}} > 0.6$. Events with muons were chosen by requiring muons, in the barrel only, to have $p_{\mathrm{T}} > 25$ GeV, and the event to have $E_{\mathrm{T}}^{\mathrm{miss}} > 25$ GeV. Figure 12 shows the transverse mass distribution for the two channels.

The agreement between data and the expected backgrounds is good. Limits on σB for each W' and W^* mass and decay channel are set using a likelihood function as input to the estimate $\mathrm{CL}_s = \mathrm{CL}_{s+b}/\mathrm{CL}_s$. To set limits, we counted events with $m_{\mathrm{T}} > 0.5\, m_{\mathrm{W}'/\mathrm{W}^*}$. Figure 13 shows the limits on the cross section times branching ratio. A W' with mass below 1.49 TeV and W^* with mass below 1.47 TeV are excluded.

6 High Mass Dilepton Resonances

ATLAS has performed a search for high-mass neutral resonance states decaying to two leptons of the same generation. [5] Examples of such high-mass resonances are new heavy neutral gauge bosons (Z' and Z^*), the Randall-Sundrum spin-2 graviton, and a spin-1 techni-meson. The search looked for $\mathrm{Z}' \to \mathrm{e}^+\mathrm{e}^-$ or $\mu^+\mu^-$, where Z' is a high-mass sequential SM (SSM) gauge boson with SM couplings, or a Z' motivated by an E_6 model. Six different E_6 motivated gauge bosons were searched for with different mixing angles between the two $U(1)$ states. We assumed the

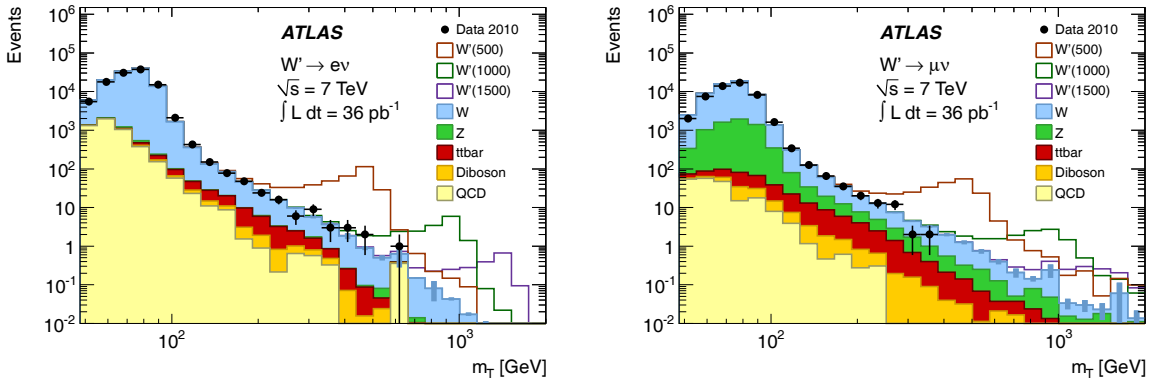

Figure 12: m_{T} spectra for electron (left) and muon (right) channels after final event selection. The points represent data and the filled histograms show the stacked backgrounds. Open histograms are W′ signals added to the background with masses indicated in parentheses in the legend. The signal and other background samples are normalised using the integrated luminosity of the data and the NNLO (near-NNLO for $t\bar{t}$) cross sections.

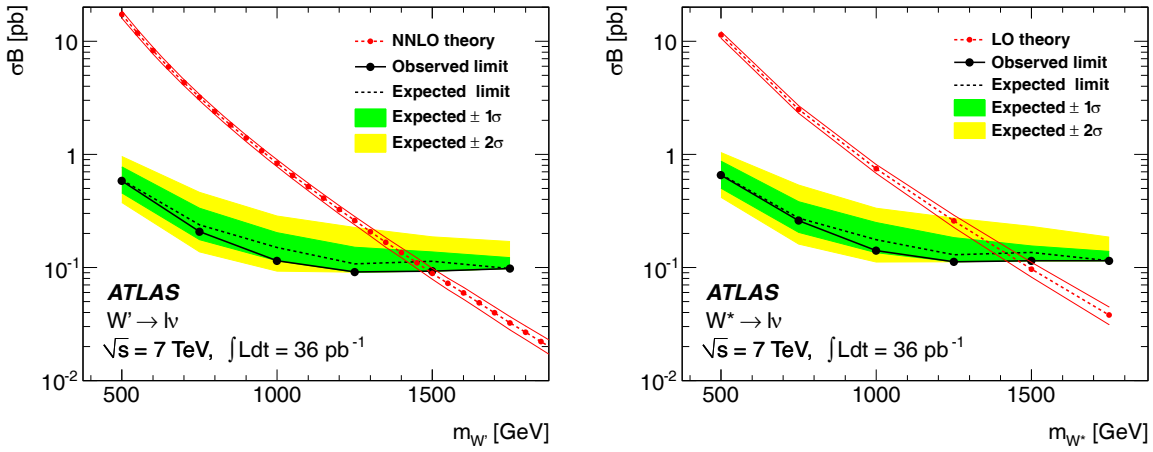

Figure 13: Limits at the 95% C.L. for W′ (left) and W* (right) production in the combination of decay channels. The solid lines show the observed limits with all uncertainties. The expected limit is indicated with dashed lines surrounded by 1σ and 2σ shaded bands. Dashed lines show the theory predictions (NNLO for W′, LO for W*) between solid lines indicating their uncertainties.

resonance has a narrow intrinsic width compared to the detector mass resolution, and required $E_{\mathrm{T}} > 25$ GeV for the electrons in the dielectron channel, and $p_{\mathrm{T}} > 25$ GeV for the muons in the dimuon channel. Figure 14 shows the invariant mass distributions for the two decay channels.

Given the absence of a signal, an upper limit on the number of Z′ events is determined using a Bayesian approach. For each Z′ pole mass, a uniform prior in the Z′ cross section was used. Figure 15 shows the limits on cross section times branching ratio for the combined decay channels. The measured and expected (shown in parenthesis) lower mass limits are 0.957 (0.964) TeV in the dielectron, 0.834 (0.895) TeV in the dimuon, and 1.048 (1.084) TeV in the combined decay channels. The lower mass limits on the E_6 gauge bosons range from 0.738 TeV (Z'_{ψ}) to 0.900 TeV (Z'_{χ}).

References

1. The ATLAS Collaboration, G. Aad *et al.*, "Search for Massive Long-lived Highly Ionising Particles with the ATLAS Detector at the LHC," accepted by Phys. Lett. B (2011),

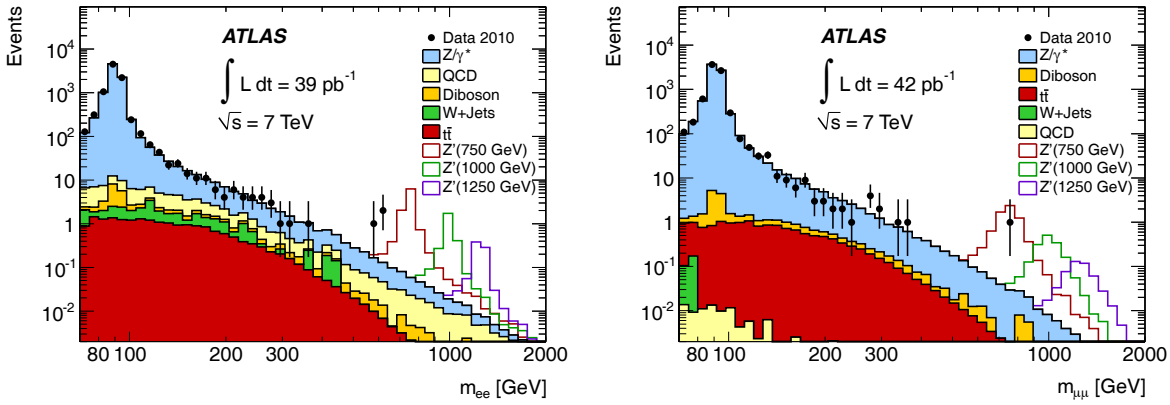

Figure 14: Dielectron (left) and dimuon (right) invariant mass distribution after final selection, compared to the stacked sum of all expected backgrounds, with three example Z'_{SSM} signals overlaid.

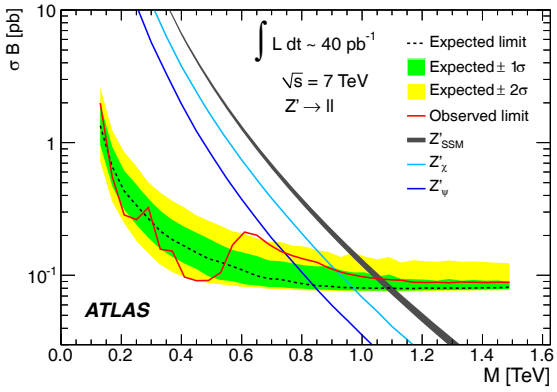

Figure 15: Expected and observed 95% C.L. limits on σB and expected σB for Z'_{SSM} production and two E_6 motivated Z′ models with lowest and highest σB for the combined electron and muon channels. The thickness of the SSM curve represents the theoretical uncertainty.

CERN-PH-EP-2011-010, arXiv:1102.0459 [hep-ex].

2. The ATLAS Collaboration, G. Aad *et al.*, "Search for Diphoton Events with Large Missing Transverse Energy in 7 TeV Proton-Proton Collisions with the ATLAS Detector," Phys. Rev. Lett. 121803 (2011).
3. The ATLAS Collaboration, G. Aad *et al.*, "Search for New Physics in Dijet Mass and Angular Distributions in *pp* Collisions at $\sqrt{s} = 7$ TeV Measured with the ATLAS Detector," accepted by the New Journal of Physics (2011); CERN-PH-EP-2011-030, arXiv:1103.3864 [hep-ex].
4. The ATLAS Collaboration, G. Aad *et al.*, "Search for high-mass states with one lepton plus missing transverse momentum in proton-proton collisions at $\sqrt{s} = 7$ TeV with the ATLAS detector," submitted to Phys. Lett. B; CERN-PH-EP-2011-023, arXiv:1103.1391 [hep-ex].
5. The ATLAS Collaboration, G. Aad *et al.*, "Search for high mass dilepton resonances in *pp* collisions at $\sqrt{s} = 7$ TeV with the ATLAS experiment," submitted to Phys. Lett. B; CERN-PH-EP-2011-037, arXiv:1103.6218 [hep-ex].

Present and possible future implications for mSUGRA of the non-discovery of SUSY at the LHC

P. Bechtle[a], K. Desch[b], H. Dreiner[b], M. Krämer[c], B. O'Leary[d], C. Robens[c], B. Sarrazin[a], P. Wienemann[b]

Both ATLAS and CMS have published results of SUSY searches putting limits on SUSY parameters and masses. A non-discovery of SUSY in the next two years would push these limits further. On the other hand, precision data of low energy measurements and the dark matter relic density favor a light scale of supersymmetry. Therefore we investigate if supersymmetry – more specifically the highly constraint model mSUGRA – does at all agree with precision data and LHC exclusions at the same time, and whether the first two years of LHC will be capable of excluding models of supersymmetry. We consider the current non observation of supersymmetry with 35 pb^{-1} as well as the possible non observation with 1, 2 and 7 fb^{-1} in a global fit using the framework Fittino.

1 Introduction

Supersymmetry[1] (SUSY) provides an elegant and renormalizable solution to several current problems of the Standard Model (SM) of elementary particles: Provided its parameters are chosen appropriately, it can explain electroweak symmetry breaking, solve the hierarchy problem of the Higgs sector of the SM, and provide the correct amount and structure of Dark Matter (DM) in the universe, together with agreement of its predictions with precision measurements at various experiments. However, all these are typically only fulfilled simultaneously for very specific parameter settings and breaking assumptions.

Many previous studies of the available data before the LHC[2,3,4,5,6,7] era indicate that a mass scale of the SUSY particles below around 1.6 GeV is required at the 2 σ level to bring a highly constrained model such as mSUGRA/CMSSM in agreement with all precision results. Strong constraints are placed on details of the mass spectrum and the couplings, e.g. corresponding to a co-annihilation process to control the DM content (see e.g.[6]).

Since SUSY is already highly constrained before including the present non-observation of new physics at LHC in the fit, it is a highly non-trivial question whether SUSY can be brought in agreement with both the LHC limits and the precision data, even though the upper mass bound on the colored particles from the previous fits is considerably higher than the present LHC limits (see e.g.[8,9]), at around 800 GeV, since the precision data also put constraints on details of the model, as described above.

The analysis presented here[10] is using the mSUGRA model to answer the question of the

[a]Deutsches Elektronen-Synchrotron DESY, Notkestraße 85, D-22607 Hamburg, Germany
[b]Physikalisches Institut der Universität Bonn, Nussallee 12, D-53115 Bonn, Germany
[c]Institute for Theoretical Particle Physics and Cosmology, RWTH Aachen, D-52056 Aachen, Germany
[d]Institute for Theoretical Physics and Astrophysics, Würzburg University, Am Hubland, D-97074 Würzburg, Germany

level of agreement for the following reason: if this highly constrained (but well-understood) model is in agreement with the data, then more general SUSY models will be in agreement, too. If not, other breaking scenarios and generalizations of mSUGRA with weaker high-scale assumptions will have to be tested.

At LHC, SUSY can be searched in different channels asking for varying numbers of hard jets, leptons and amounts of missing transverse energy. The strongest constraints are currently stemming from very inclusive analyses asking only for jets and leptons. In addition, such analyses have the advantage that their results do depend on only few mSUGRA parameters. Therefore, a study for inclusive searches at ATLAS[11] has been modeled as a prediction for the actual results of the experiments, since the fits presented here were performed in parallel to the presently public searches by ATLAS and CMS. For other recent contributions in the same field, see e.g. Ref.[12]

2 Model, Inputs to the Fit and Statistics

The mSUGRA model used in the fit are evaluated using a Markov Chain Monte Carlo technique. The theoretical predictions are calculated using SPheno[13] for the RGE running and the spectrum calculation, and programs compiled in the mastercode package for the prediction of the low energy precision observables and the Higgs boson masses, most notably FeynHiggs, micrOmegas and SuperISO[7]. SoftSUSY[14] is used for cross-checks.

2.1 Observables from the pre-LHC era

Following the Fittino[15] analysis in Ref.[6], the following set of low-energy observables and existing collider limits is used: *(i)* rare decays of B- and K-mesons; *(ii)* the anomalous magnetic moment of the muon, a_μ; *(iii)* electroweak precision measurements from LEP, SLC and the Tevatron and the Higgs boson mass limit from LEP; and *(iv)* the relic density of cold dark matter in the universe, Ω_χ. In contrast to Ref.[6], we employ the program HiggsBounds[16] and not a rigid Higgs mass limit. We refer to Ref.[6] for a detailed discussion of the low-energy inputs and the collider limits.

2.2 Modeling the ATLAS analysis

The most sensitive and at the same time rather model independent search channel for R-parity conserving SUSY at the LHC relies on jets and missing transverse energy $E_T^{\rm miss}$ for the selection. From the analyses presented in the ATLAS MC study[11], we consider the search channel with four jets, zero leptons and $E_T^{\rm miss}$. This channel drives the sensitivity, in particular for large $M_{1/2}$. For a detailed description of the selection cuts applied see Ref.[10]. As a final discriminating variable the effective mass is used. It is defined as the scalar sum of the transverse momenta of all main objects, *i.e.*

$$M_{\rm eff} = \sum_{i=1}^{N_{\rm jets}=4} p_T^{{\rm jet},i} + E_T^{\rm miss}. \tag{1}$$

The SM background processes have been described in detail in Ref.[11]. We use the background shape of $M_{\rm eff}$ from the ATLAS analysis directly in our fit. A systematic uncertainty of 20 %, derived from Ref.[11] has been used on the background, which is also in rough agreement with the present results based on data[8]. The signal cross section is dominated by squark and gluino pair production, $pp \to \tilde{q}\tilde{q}^*, \tilde{q}\tilde{q}, \tilde{q}\tilde{g}$ and $\tilde{g}\tilde{g}$, but all SUSY pair production processes are included in our numerical analysis. We use Herwig++[17] in combination with the parametrized fast detector simulation Delphes[18] to obtain the detector response and, in particular, the shape of the $M_{\rm eff}$ distribution for a given point in the supersymmetric parameter space. The simulation has been

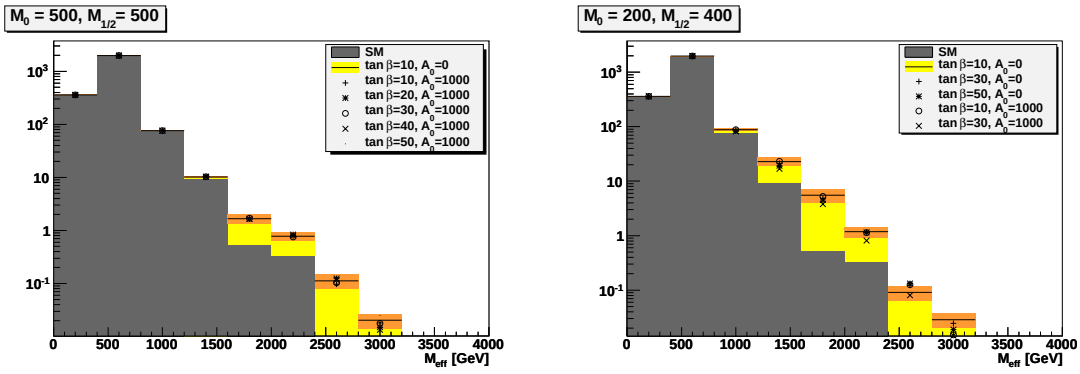

(a) (b)

Figure 1: *Systematic check of the dependence of the simulated SUSY M_{eff} spectrum on the parameters A_0 and $\tan\beta$ for two different parameter points in M_0 and $M_{1/2}$. In (a), a point with low dependence on the parameters fixed in the grid are shown, showing a small variation of the predicted SUSY M_{eff} spectrum well within systematics. In (b), a point with relatively large dependence is shown, which is still in agreement with the systematics. This shows the reliability of the application of the grid in $M_0, M_{1/2}$ in the fit.*

carefully modified to match the published measured resolutions and efficiencies of the ATLAS experiment, and the resulting M_{eff} has been compared to the public spectra at an mSUGRA benchmark point. The signal estimate is normalized to the NLO+NLL QCD prediction for the inclusive squark and gluino cross sections [19].

On the signal, we apply a systematic uncertainty of 30 %, covering both the uncertainty in the calculation of the cross section and the remaining model dependence. The fit presented in Section 3 uses a grid spanned in M_0 and $M_{1/2}$ for the model prediction of the M_{eff} spectrum. In between the model points, a bi-linear interpolation is used. The variation of the M_{eff} spectrum with the remaining parameters $\tan\beta$ and A_0 is shown in Fig. 1. The variations are clearly compatible with the systematic uncertainty shown as the orange band.

2.3 Statistics

We use a likelihood ratio technique to calculate an expected CL_{s+b} for the non-observation of a signal at LHC. This confidence level is then transferred into a contribution to the χ^2 of the frequentist fit. For a detailed description of the statistical method, see Ref.[10]

As shown in Fig. (a), this technique transfers the exact statistical power of the LHC search into a contribution to the χ^2. Thus, the global fit can find the exact minimum and the exact uncertainties arising from the interplay between the LHC contribution (orange) and the contribution from pre-LHC observables (red). It can be seen that naturally LHC prefers high SUSY mass scales, whereas the precision results prefer low scales, and that the LHC contribution does not provide a considerably steeper χ^2 profile than the other results. The blue line represents the combined χ^2.

Very good agreement is achieved between the results presented here and the official ATLAS study[11]. Also, the limit derived from our implementation agrees with the actual search result for $\mathcal{L}^{int} = 35\,\text{pb}^{-1}$ of data within a $1\,\sigma$ fluctuation of the background.

3 Results

The following results are obtained from global fits of the mSUGRA to the observables described in Sec. 2. $\text{sign}\mu = +1$ is assumed for all fits due to the observed value of $(g-2)_\mu$. For a more detailed analysis of the dependence of the pre-LHC-era fit on $\text{sign}\mu$, see Ref.[6]. For the LHC,

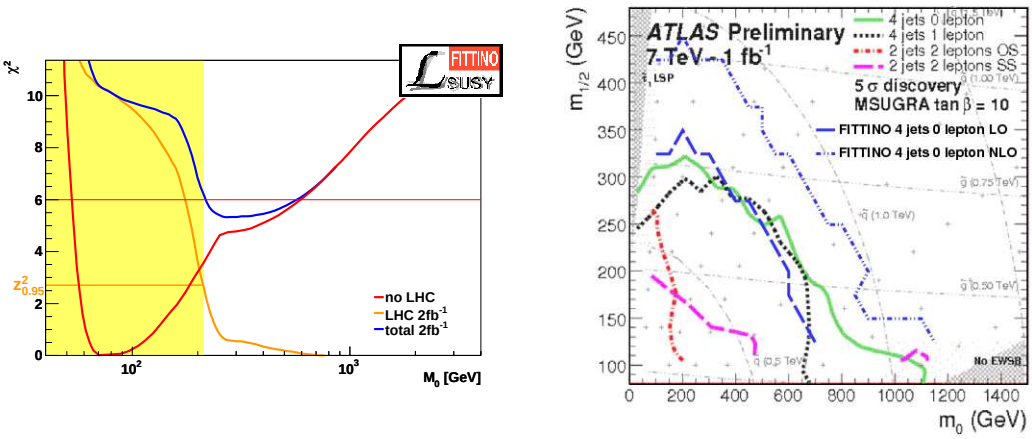

(a) (b)

Figure 2: *(a): Interplay between the LHC and the pre-LHC contribution to the global χ^2. (b): Comparison between the discovery potential based on the ATLAS MC study (green line) and the LO result based on our implementation of the simulation of the detector and the analysis (dashed blue line).*

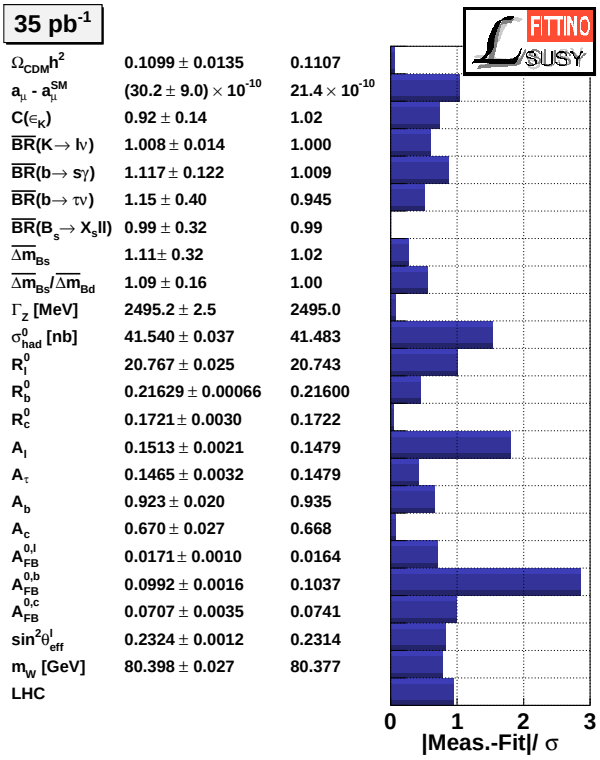

$\Omega_{CDM}h^2$	0.1099 ± 0.0135	0.1107
a_μ - a_μ^{SM}	(30.2 ± 9.0) × 10^{-10}	21.4 × 10^{-10}
$C(\epsilon_K)$	0.92 ± 0.14	1.02
$\overline{BR}(K\to l\nu)$	1.008 ± 0.014	1.000
$\overline{BR}(b\to s\gamma)$	1.117 ± 0.122	1.009
$\overline{BR}(b\to \tau\nu)$	1.15 ± 0.40	0.945
$\overline{BR}(B_s\to X_s ll)$	0.99 ± 0.32	0.99
$\overline{\Delta m}_{Bs}$	1.11± 0.32	1.02
$\overline{\Delta m}_{Bs}/\overline{\Delta m}_{Bd}$	1.09 ± 0.16	1.00
Γ_Z [MeV]	2495.2 ± 2.5	2495.0
σ^0_{had} [nb]	41.540 ± 0.037	41.483
R^0_l	20.767 ± 0.025	20.743
R^0_b	0.21629 ± 0.00066	0.21600
R^0_c	0.1721± 0.0030	0.1722
A_l	0.1513 ± 0.0021	0.1479
A_τ	0.1465 ± 0.0032	0.1479
A_b	0.923 ± 0.020	0.935
A_c	0.670 ± 0.027	0.668
$A^{0,l}_{FB}$	0.0171± 0.0010	0.0164
$A^{0,b}_{FB}$	0.0992 ± 0.0016	0.1037
$A^{0,c}_{FB}$	0.0707 ± 0.0035	0.0741
$\sin^2\theta^l_{eff}$	0.2324 ± 0.0012	0.2314
m_W [GeV]	80.398 ± 0.027	80.377
LHC		

Figure 3: *All observables in the global fit and their pulls are shown for $\mathcal{L}^{int} = 35\,\mathrm{pb}^{-1}$. Excellent agreement is observed.*

integrated luminosities $\mathcal{L}^{int} = 0.035, 1, 2, 7\,\mathrm{fb}^{-1}$ are assumed, the first of those corresponding to the presently published analyses, while the last corresponds to a reasonable expectation for the available data set in 2011/2012.

For fits without LHC and for $\mathcal{L}^{int} = 35\,\mathrm{pb}^{-1}$, excellent agreement between the data and the mSUGRA model is found. The pulls of the variables in the fit are shown in Fig. 3 for $\mathcal{L}^{int} = 35\,\mathrm{pb}^{-1}$. More importantly, there still is a significant agreement between the resulting parameter ranges from the two fits, as shown in Fig. 4(a). While the LHC just excludes the

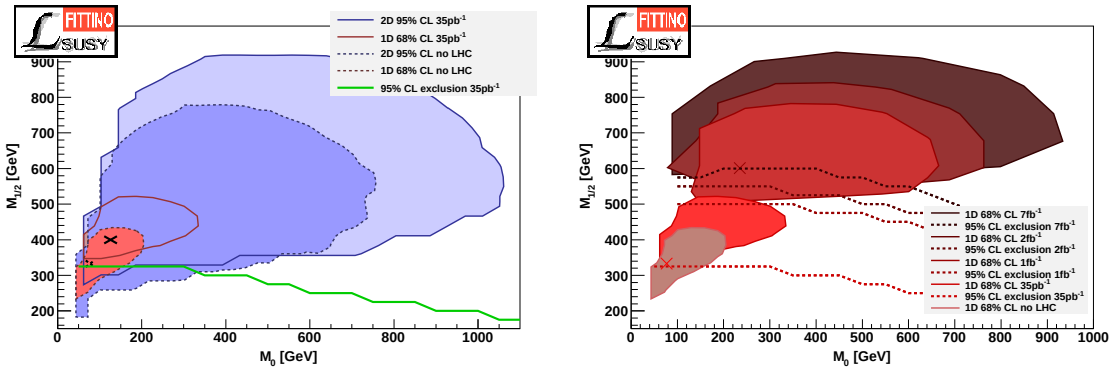

(a) (b)

Figure 4: *The allowed parameter range for the fits without LHC and for the fit with our implementation present luminosity is shown in (a). The tension between the two fits is observed to be very moderate. In (b), the evolution of the $\Delta\chi^2 = 1$ area with increasing luminosity is shown. As expected, it moves to higher values of M_0 and $M_{1/2}$, and in addition the uncertainties grow very significantly.*

Table 1: *Overview of the best fit points for all considered LHC luminosities. The values of χ^2/ndf underline that mSUGRA can not be excluded in the first 2 years of LHC.*

$\mathcal{L}^{int}/\text{fb}^{-1}$	M_0	$M_{1/2}$	$\tan\beta$	A_0	χ^2/ndf	$\mathcal{P}-Value$
0	77.1	332.8	12.8	426.2	18.9/20	53.1 %
0.035	125.9	399.8	17.3	742.3	20.4/21	49.8 %
1	235.1	601.0	31.1	626.8	23.7/21	30.9 %
2	254.1	647.1	30.2	770.7	24.2/21	28.3 %
7	402.7	744.1	43.1	780.7	25.0/21	24.6 %

best fit point for the fit without LHC data, the $\Delta\chi^2 = 1$ areas do still overlap significantly, and there is a large overlap in the $\Delta\chi^2 = 5.99$ area, corresponding to a 95 % CL in two dimensions.

The fact that the current LHC analyses put little pressure on SUSY is also evident from Tab. 1, which shows the best fit points of the five fits together with the observed χ^2/ndf values and the corresponding $\mathcal{P}$-values (the latter being only for completeness, since it is technically not proven that the expected fit results follow a χ^2 curve, due to significant non-linearities both in the LHC limits and in the relation between parameters and observables). In any case, the change in χ^2/ndf is very moderate when going from the fit without LHC to the fit with $\mathcal{L}^{int} = 35\,\text{pb}^{-1}$.

This observation contradicts the disappointment about the non-observation of SUSY at LHC with $\mathcal{L}^{int} = 35\,\text{pb}^{-1}$, which is mostly based on finetuning arguments or Bayesian discussions of the size of the available parameter space for arbitrary priors. Without those more subjective measures of the attractiveness of a theory, even the highly constrained mSUGRA is still in natural agreement with the data. To the contrary, squark masses of around 1 TeV or slightly higher are a welcome ingredient to lift the mass of the lightest, SM-like Higgs boson above the LEP limit.

For higher assumed LHC luminosities, still assuming no observation of new physics, the $\Delta\chi^2 = 1$ areas of the fits do start to deviate significantly from each other, as evident from Fig. 4(b). This corresponds to a building tension in the fit between mainly $(g-2)_\mu$ and Ω_χ, pushing mSUGRA to lower scales via the gaugino and slepton sector, and the LHC, pushing mSUGRA to higher scales via the more direct limit on the squark and gluino mass scale. This results in a degradation of χ^2/ndf, as evident from Tab. 1. However, even for $\mathcal{L}^{int} = 7\,\text{fb}^{-1}$, mSUGRA can not be excluded with the given observable set and SUSY searches alone. This tension is expected to be significantly weaker for more general SUSY models.

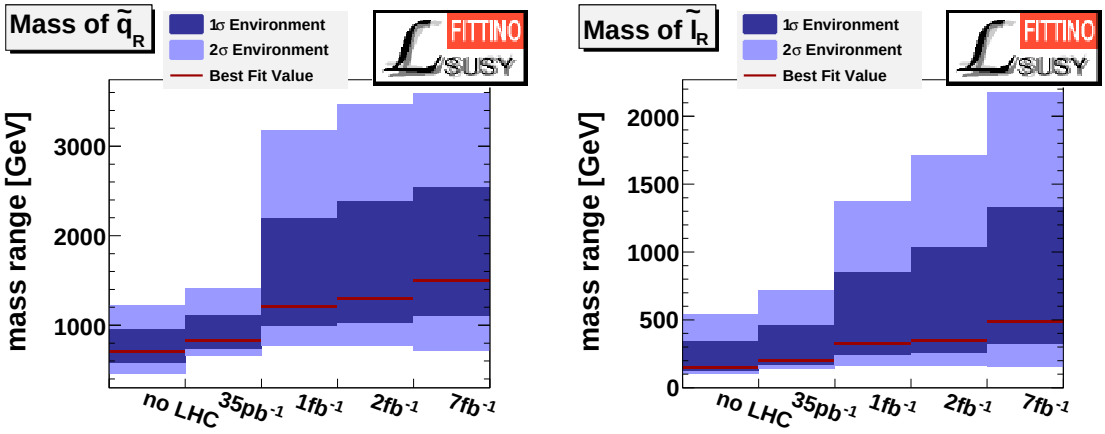

(a) (b)

Figure 5: *For the different LHC luminosities, this figure shows the allowed mass ranges of squarks in (a) and of sleptons in (b). While the former is quite model independent, the latter strongly depends on assumptions in the mSUGRA model.*

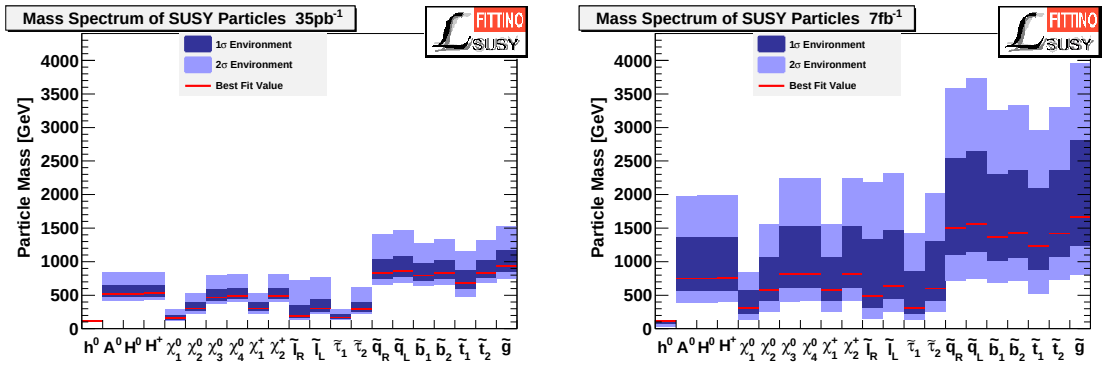

(a) (b)

Figure 6: *Comparison of the allowed mass ranges of all sparticles and Higgs bosons for the fits with* $\mathcal{L}^{int} = 35\,\mathrm{pb}^{-1}$ *in (a) and* $\mathcal{L}^{int} = 7\,\mathrm{fb}^{-1}$ *in (b).*

Even though the tension is rising, SUSY cannot be excluded at the LHC in the first two years of running. The interesting observation here is that the inclusion of the LHC exclusion to the fit only has a very moderate effect on the lower mass bound of the sparticles, as shown in Fig. 5. The by far non-trivial result from the fit, however, is the fact that the upper bound on the sparticle masses depends very strongly on including the LHC into the fit. The reason for this behavior can be seen in Fig. 2(a). The χ^2 surface is influenced by LHC only for $M_0 < 1.5$ GeV, it remains independent of the LHC luminosity above that value. However, there it is significantly more flat than close to the minimum of the fit without LHC. Including the LHC cuts away the low χ^2 values, shifting up the $\Delta\chi^2 = 4$ area significantly into shallower areas of the χ^2 profile. Therefore, non-trivially, the upper mass bounds on the sparticles increase very strongly, allowing mSUGRA to escape the LHC detection to higher mass regions.

Fig. 6 shows the same for all sparticles and Higgs bosons, but only for $\mathcal{L}^{int} = 35\,\mathrm{pb}^{-1}$ and $\mathcal{L}^{int} = 7\,\mathrm{fb}^{-1}$. The interesting observation is that the only particle of which the allowed mass range does not change is the SM-like Higgs boson h^0, which is bound in mSUGRA at $m_{h^0} < 135$ GeV. Therefore, the only chance for an exclusion of mSUGRA and many other SUSY breaking scenarios can be obtained via SM-like Higgs searches at the Tevatron and LHC.

One interesting observation is the fact that the LHC pushes the best fit point of $\tan\beta$ to

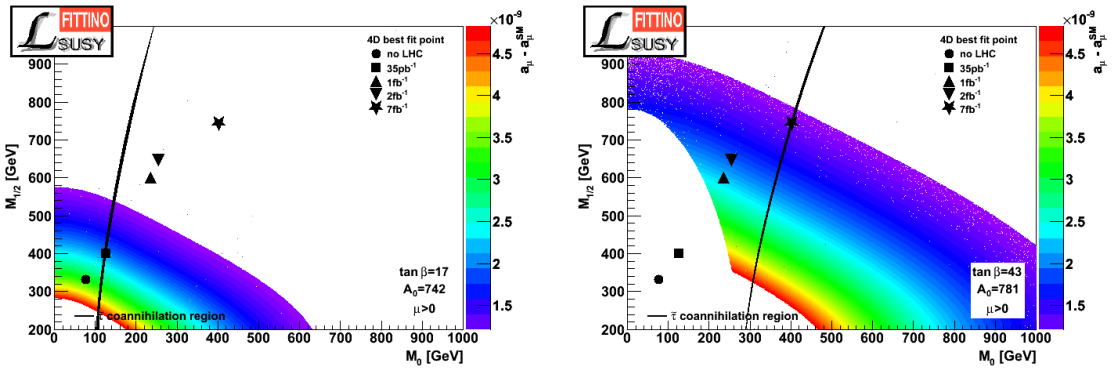

(a) (b)

Figure 7: *Explanation, of how the interplay of* $(g-2)_\mu$, Ω_χ *and the LHC moves the best fit point of* $\tan\beta$ *to significantly higher values for higher LHC luminosities. In (a), the situation for* $\tan\beta = 17$ *is shown, where* $(g-2)_\mu$ *and* Ω_χ *are in good agreement with the data for low* M_0 *and* $M_{1/2}$*. If LHC should exclude those low regions of* M_0 *and* $M_{1/2}$*, a higher value of* $\tan\beta$ *is necessary to reconcile* $(g-2)_\mu$ *and* Ω_χ *with the data, as shown in (b) for* $\tan\beta = 43$*.*

significantly higher values than observed for the fit without LHC. This is interesting since it is shown in Fig. 1 that the LHC limit in the chosen search channel does not depend significantly on $\tan\beta$. The increase however is an interesting showcase of an interplay between low-energy precision observables, cosmological observables and direct limits from the LHC. This is described in Fig. 7, showing the co-annihilation region which is mainly responsible for a good fit of Ω_χ (another region with some contribution from the Higgs funnel also is allowed at very large $\tan\beta$) and the predicted values of $(g-2)_\mu$ for M_0 and $M_{1/2}$. In Fig. 7(a), $\tan\beta = 17$ is used and the two observables agree with the measurements for low mass scales. In Fig. 7(b) and $\tan\beta = 43$, the low mass scales can be excluded by the LHC, retaining agreement with Ω_χ and $(g-2)_\mu$ at high mass scales. Thus, the exclusion of low mass scales pushes mSUGRA to higher values of $\tan\beta$, since only then the pre-LHC-era observables can be correctly described. This is an interesting observation, since also in the detailed study of theoretical uncertainties of mSUGRA models up to now the focus was on the low to intermediate $\tan\beta$ region. A further non-observation of SUSY at the LHC would highlight the importance of understanding SUSY precision calculations at high values of $\tan\beta$.

4 Conclusions

We have presented a global mSUGRA analysis of supersymmetric models which includes the current low-energy precision measurements, the dark matter relic density as well as potential LHC exclusion limits from direct SUSY searches in the zero-lepton plus jets and missing transverse energy channel.

We conclude that non-trivially it is possible to reconcile the supersymmetric description of low-energy observables and the dark matter relic density with a non-observation of supersymmetry in the first phase of the LHC with acceptable χ^2/ndf values, despite some tension building up in a combined fit within mSUGRA.

While our study is exploratory in the sense that it is based on one search channel only, and on a simplified description of the LHC detectors, it clearly demonstrates the potential of the first phase of LHC running at 7 TeV in 2011/12 to constrain supersymmetric models and the sparticle mass spectrum, or to discover such models.

However, the interesting fact that including LHC limits in the global fit significantly increases the upper bounds on the sparticle masses make it impossible to exclude mSUGRA in the first

two years at LHC based on SUSY searches. Excluding the model could however be possible using Higgs boson searches.

Acknowledgments

We thank Sascha Caron and Werner Porod for valuable discussions. This work has been supported in part by the Helmholtz Alliance "Physics at the Terascale", the DFG SFB/TR9 "Computational Particle Physics", the DFG SFB 676 "Particles, Strings and the Early Universe", the European Community's Marie-Curie Research Training Network under contract MRTN-CT-2006-035505 "Tools and Precision Calculations for Physics Discoveries at Colliders" and the Helmholtz Young Investigator Grant VH-NG-303. MK thanks the CERN TH unit for hospitality.

References

1. H. P. Nilles, Phys. Rept. **110** (1984) 1.
2. R. R. de Austri, R. Trotta, L. Roszkowski, JHEP **0605** (2006) 002.
3. B. C. Allanach, K. Cranmer, C. G. Lester *et al.*, JHEP **0708** (2007) 023.
4. R. Lafaye, T. Plehn, M. Rauch *et al.*, Eur. Phys. J. **C54** (2008) 617-644.
5. O. Buchmueller *et al.*, JHEP **0809** (2008) 117.
6. P. Bechtle, K. Desch, M. Uhlenbrock and P. Wienemann, Eur. Phys. J. C **66** (2010) 215.
7. O. Buchmueller, R. Cavanaugh, A. De Roeck, J. R. Ellis, H. Flacher, S. Heinemeyer, G. Isidori, K. A. Olive *et al.*, Eur. Phys. J. **C64** (2009) 391-415, [arXiv:0907.5568 [hep-ph]].
8. G. Aad *et al.* [Atlas Collaboration], [arXiv:1102.5290 [hep-ex]].
9. V. Khachatryan *et al.* [CMS Collaboration], Phys. Lett. **B698** (2011) 196-218. [arXiv:1101.1628 [hep-ex]].
10. P. Bechtle, K. Desch, H. K. Dreiner, M. Krämer, B. O'Leary, C. Robens, B. Sarrazin, P. Wienemann, [arXiv:1102.4693 [hep-ph]], 2011.
11. The ATLAS collaboration, "Prospects for Supersymmetry discovery based on inclusive searches at a 7 TeV centre-of-mass energy with the ATLAS detector," ATL-PHYS-PUB-2010-010.
12. B. C. Allanach, [arXiv:1102.3149 [hep-ph]], 2011;
    O. Buchmueller, R. Cavanaugh, D. Colling, A. De Roeck, M. J. Dolan, J. R. Ellis, H. Flacher, S. Heinemeyer *et al.*, [arXiv:1102.4585 [hep-ph]], 2011;
    A. Strumia, JHEP **1104** (2011) 073, [arXiv:1101.2195 [hep-ph]], 2011;
    S. Cassel, D. M. Ghilencea, S. Kraml, A. Lessa, G. G. Ross, [arXiv:1101.4664 [hep-ph]].
13. W. Porod, Comput. Phys. Commun. **153** (2003) 275-315, [hep-ph/0301101].
14. B. C. Allanach, Comput. Phys. Commun. **143** (2002) 305-331. [hep-ph/0104145].
15. P. Bechtle, K. Desch and P. Wienemann, Comput. Phys. Commun. **174** (2006) 47.
16. P. Bechtle, O. Brein, S. Heinemeyer, G. Weiglein and K. E. Williams, Comput. Phys. Commun. **181** (2010) 138.
    $\sqrt{s} = 10\,\text{TeV}$, ATL-PHYS-PUB-2009-085, 2009.
17. M. Bahr *et al.*, Eur. Phys. J. C **58** (2008) 639.
18. S. Ovyn, X. Rouby and V. Lemaitre, arXiv:0903.2225 [hep-ph].
19. W. Beenakker, R. Höpker, M. Spira *et al.*, Nucl. Phys. **B492** (1997) 51-103; W. Beenakker, M. Krämer, T. Plehn *et al.*, Nucl. Phys. **B515**, 3-14 (1998); A. Kulesza, L. Motyka, Phys. Rev. Lett. **102** (2009) 111802 and Phys. Rev. **D80** (2009) 095004; W. Beenakker, S. Brensing, M. Krämer *et al.*, JHEP **0912** (2009) 041 and JHEP **1008** (2010) 098.

3.
Flavour Physics

Flavour physics, supersymmetry and grand unification

Ulrich Nierste
Institut für Theoretische Teilchenphysik
Karlsruhe Institute of Technology, Universität Karlsruhe
Engesserstraße 7, 76128 Karlsruhe, Germany

A global fit to quark flavour-physics data disfavours the Standard Model with 3.6 standard deviations and points towards new CP-violating physics in meson-antimeson mixing amplitudes. Tevatron data call for a new $B_s-\overline{B}_s$ mixing phase and new physics in $B_d-\overline{B}_d$ mixing alleviates the tension on the unitarity triangle driven by $B(B \to \tau\nu)$. In supersymmetric GUT models the large atmospheric neutrino mixing angle can influence $b \to s$ transitions. I present the results of a recent analysis in an SO(10) GUT model which accomodates the large $B_s-\overline{B}_s$ mixing phase while simultaneously obeying all other experimental constraints.

1 Introduction

On May 17, 2010, *The New York Times* wrote:

> *Physicists at the Fermi National Accelerator Laboratory are reporting that they have discovered a new clue that could help unravel one of the biggest mysteries of cosmology: why the universe is composed of matter and not its evil-twin opposite, antimatter.*

This phrase was contained in an article featuring a measurement by the DØ collaboration presented three days earlier by Guennadi Borissov in the talk

Evidence for an anomalous like-sign dimuon charge asymmetry.

DØ has studied the decays of pair-produced hadrons into final states with muons [1]. If, for example, a $(b,\overline{b})$ pair hadronises into a Λ_b baryon, a B^+ meson, and several lighter hadrons, the semileptonic decays of Λ_b and B^+ will result in leptons of opposite charges. However, if the b or $\overline{b}$ quark ends up in a neutral B meson, $B-\overline{B}$ oscillations may lead to a "wrong-sign" muon charge: While a B meson contains a $\overline{b}$ quark decaying into a μ^+, $B-\overline{B}$ mixing permits the process $B \to \overline{B} \to X\mu^-\overline{\nu}_\mu$ resulting in a muon with negative charge. The data sample with like-sign dimuons is therefore enriched with events which involve a mixed neutral meson. By further comparing the numbers of (μ^-,μ^-) and (μ^+,μ^+) pairs in the final states DØ has quantified the CP violation in $B-\overline{B}$ mixing for a data sample composed of B_d and B_s mesons. The central value of the measured CP asymmetry exceeds the theory prediction [2] by a factor of 42 and the statistical significance of the discrepancy is 3.2 standard deviations.[a] A new-physics interpretation of the measurement requires a large effect in $B_s-\overline{B}_s$ mixing, because the precision measurements at the B factories limit the size of a possible new CP phase in $B_d-\overline{B}_d$ mixing.

The Standard-Model (SM) predictions for the $B-\overline{B}$ mixing amplitudes involve elements of the Cabibbo-Kobayashi-Maskawa (CKM) matrix, which are found from global fits to many observables of flavour physics. CP-violating quantities depend in a crucial way on the parameters $\overline{\rho}$ and $\overline{\eta}$, which define the apex of the CKM unitarity triangle (UT) (see Fig. 1). $\overline{\rho}$ and $\overline{\eta}$ also govern the sizes of $b \to u$ and $b \to d$ transitions. Among the quantities used in global fits to the UT are the precisely measured $B_d-\overline{B}_d$ mixing and $B_s-\overline{B}_s$ mixing oscillation frequencies, the CP phase in $B_d-\overline{B}_d$ mixing measured in the decay $B_d \to J/\psi K_S$, and ϵ_K, which quantifies CP violation in $K-\overline{K}$ mixing. Several authors have noticed a tension in the Standard-Model (SM) fit of the UT to data [4]. Meson-antimeson mixing amplitudes are $\Delta F = 2$ amplitudes, meaning that the flavour quantum number $F = B, S, \ldots$ changes by two units. In a wide class of models beyond the SM $\Delta F = 2$ transitions receive larger new-physics corrections than the $\Delta F = 1$ decay amplitudes. The relation of the measured quantities to the CKM elements will be altered if new physics affects the $\Delta F = 2$ amplitudes. A proper theoretical assessment of the quoted DØ measurement and of the tensions in the over-constrained CKM matrix therefore

[a] After this conference DØ has updated the analysis with a larger data sample and found a discrepancy of 3.9 standard deviations with respect to the SM prediction [3].

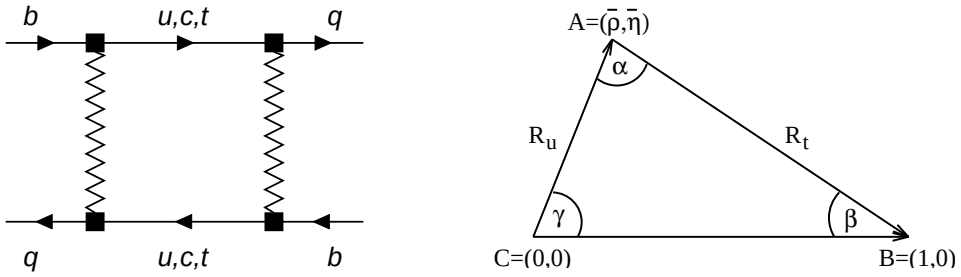

Figure 1: Left: SM box diagram describing $\mathrm{B_q}-\overline{\mathrm{B}}_\mathrm{q}$ mixing, with $q = d$ or s. Right: Standard unitarity triangle.

calls for a global analysis which fits the elements of the Cabibbo-Kobayashi-Maskawa (CKM) matrix simultaneously with complex parameters quantifying new physics in $\mathrm{K}-\overline{\mathrm{K}}$, $\mathrm{B_d}-\overline{\mathrm{B}}_\mathrm{d}$, and $\mathrm{B_s}-\overline{\mathrm{B}}_\mathrm{s}$ mixing. Such an analysis has been performed in Ref. [5]. In this talk I first summarise the results of this analysis in Sec. 2. Subsequently, in Sec. 3 I interpret the results within a supersymmetric grand unified theory (GUT). In Sec. 4 I conclude.

2 Anatomy of new physics in $\mathrm{B}-\overline{\mathrm{B}}$ mixing

In this section I present the essentials of the analysis in Ref. [5], which shows evidence for new physics (NP) in $\mathrm{B}-\overline{\mathrm{B}}$ mixing. While I use the numerical ranges for experimental and theoretical input quantities compiled in this reference, I use two simplifications in this talk: First, for clarity of the presentation my quoted errors contain statistical, systematic and theoretical errors added in quadrature. By contrast, the original analysis in Ref. [5] has used the more conservative Rfit procedure [6], which scans over systematic and theoretical uncertainties. Second, whenever possible I present simplified derivations of the tensions between experimental results and SM predictions. In this way the main sources of the quoted tensions become transparent.

Flavour-changing neutral current (FCNC) processes are known to be very sensitive to NP. Schematically, any contribution to an FCNC $\Delta F = 1$ decay amplitude is proportional to $\delta_{\mathrm{FCNC}}/M^2$, where δ_{FCNC} is a small flavour-violating parameter and M is some heavy mass scale. In a SM diagram, δ_{FCNC} is the product of two CKM elements and the relevant scale M is the W boson mass entering the FCNC loop diagrams. $\Delta F = 2$ amplitudes, however, scale like $\delta^2_{\mathrm{FCNC}}/M^2$, for instance the $\Delta B = 2$ box diagram of Fig. 1 is proportional to $(V_{tb}V^*_{tq})^2/M_W^2$. One realises that $\Delta F = 2$ amplitudes are more sensitive to NP than $\Delta F = 1$ transitions in a wide class of models: Whenever $|\delta^{\mathrm{NP}}_{\mathrm{FCNC}}| > |\delta^{\mathrm{SM}}_{\mathrm{FCNC}}|$, which must come with $M > M_W$ to keep the NP contribution smaller than the SM one, the relative impact of NP on a $\Delta F = 1$ transition is smaller by factor of $|\delta^{\mathrm{SM}}_{\mathrm{FCNC}}|/|\delta^{\mathrm{NP}}_{\mathrm{FCNC}}|$ with respect to the $\Delta F = 2$ case. In extensions of the SM with new sources of flavour violation the case $|\delta^{\mathrm{NP}}_{\mathrm{FCNC}}| > |\delta^{\mathrm{SM}}_{\mathrm{FCNC}}|$ is the default situation, because off-diagonal CKM elements are small. Moreover, $\Delta F = 1$ FCNC decays hardly enter the global fit determining the CKM elements. It is therefore well-motivated to fit these elements in scenarios in which the NP effects are confined to $\Delta F = 2$ processes [5].

2.1 The $|V_{ub}|$ puzzle

The CKM matrix

$$V_{\mathrm{CKM}} = \begin{pmatrix} V_{ud} & V_{us} & V_{ub} \\ V_{cd} & V_{cs} & V_{cb} \\ V_{td} & V_{ts} & V_{tb} \end{pmatrix}$$

is fixed by the measurements of

$$|V_{us}| = 0.2254 \pm 0.0013, \qquad |V_{cb}| = (40.9 \pm 0.7) \cdot 10^{-3}, \tag{1}$$

Figure 2: Measurements of $|V_{ub}|$. The fourth value is indirectly obtained from the side R_u of the UT.

and the values of $\overline{\rho}$ and $\overline{\eta}$, which define the apex of the unitarity triangle (UT) depicted in Fig. 1:

$$\overline{\rho} + i\overline{\eta} \;\equiv\; -\frac{V_{ub}^* V_{ud}}{V_{cb}^* V_{cd}} \;\equiv\; R_u e^{i\gamma} \tag{2}$$

Currently $|V_{ub}|$ is measured in three ways, from i) the exclusive decays $B \to \pi\ell\nu$, ii) the inclusive decays $B \to X\ell\nu$, and iii) the leptonic decay $B^+ \to \tau^+\nu_\tau$. $B(B^+ \to \tau^+\nu_\tau)$ has been measured by both the BaBar and Belle collaboration, each with two methods using either a leptonic or a hadronic tag [7], resulting in[b]

$$B^{\mathrm{exp}}(B^+ \to \tau^+\nu_\tau) \;=\; (1.68 \pm 0.31) \cdot 10^{-4}.$$

The theory prediction involves the B meson decay constant f_B, which is calculated with the help of lattice QCD:

$$B(B^+ \to \tau^+\nu_\tau) \;=\; 1.13 \cdot 10^{-4} \cdot \left(\frac{|V_{ub}|}{4{\cdot}10^{-3}}\right)^2 \left(\frac{f_B}{200\ \mathrm{MeV}}\right)^2$$

With $f_B = (191 \pm 13)$ MeV one finds

$$\begin{aligned} |V_{ub,B\to\tau\nu}| &= \left[5.10 \pm 0.47|_{\mathrm{exp}} \pm 0.35|_{\mathrm{f_B}}\right] \cdot 10^{-3} \\ &= [5.10 \pm 0.59] \cdot 10^{-3}. \end{aligned}$$

The measurement of $|V_{ub}|$ constrains the side R_u of the UT, because $|V_{ub}| \propto |V_{cb}| R_u$ (see Eq. (2)). However, in the global fit to the UT the dominant constraint on R_u stems from the precise measurement of the mixing-induced CP asymmetry $A_{\mathrm{CP}}^{\mathrm{mix}}(B_d \to J/\psi K_S)$. If the SM describes $\mathrm{B_d} - \overline{\mathrm{B}}_\mathrm{d}$ mixing correctly, this quantity determines the UT angle $\beta = 21.15^\circ \pm 0.89^\circ$. Using further $\alpha = 89^\circ{}^{+4.4^\circ}_{-4.2^\circ}$, we find $R_u = \sin\beta/\sin\alpha = 0.361 \pm 0.015$ with a negligible impact of the error in α. This value is in excellent agreement with the result of the full global fit to the UT. With our number for R_u we can determine $|V_{ub}|$ indirectly through Eq. (2):

$$|V_{ub}|_{\mathrm{ind}} \;=\; (3.41 \pm 0.15) \cdot 10^{-3}.$$

The four determinations of $|V_{ub}|$ are shown in Fig. 2. We observe no significant discrepancy between the individual direct measurements of $|V_{ub}|$. However, there is a 2.9 σ tension between $B^+ \to \tau^+\nu$ and the indirect determination of $|V_{ub}|$ driven by $A_{\mathrm{CP}}^{\mathrm{mix}}(B_d \to J/\psi K_S)$.

Several authors have studied NP contributions to $B^+ \to \tau^+\nu$ [9–11]. While a charged Higgs boson can contribute to $B^+ \to \tau^+\nu$, the contribution typically decreases the branching fraction and therefore cannot solve the $|V_{ub}|$ puzzle. (A control channel for charged-Higgs effects is $B \to D\tau\nu$ [12].) A more promising NP explanation of the $|V_{ub}|$ puzzle has been pointed out by Crivellin, who has observed that an effective right-handed W coupling $\overline{b}_R \gamma^\mu u_R W_\mu$ can simultaneously shift $|V_{ub,\mathrm{excl}}|$ upwards and $|V_{ub,B\to\tau\nu}|$ downwards [10]. The effect of a right-handed W coupling on $|V_{ub,\mathrm{ind}}|$ is model-dependent.

[b] After this conference the average $(1.64 \pm 0.34) \cdot 10^{-4}$ has been presented [8].

Since the direct determinations of $|V_{ub}|$ agree up to normal statistical fluctuations, I argue that the simplest solution to the $|V_{ub}|$ puzzle is NP in the $\mathrm{B_d}-\overline{\mathrm{B}}_\mathrm{d}$ mixing amplitude. In the presence of a new contribution ϕ_d^Δ to the $\mathrm{B_d}-\overline{\mathrm{B}}_\mathrm{d}$ mixing phase the well-measured $A_{\rm CP}^{\rm mix}(B_d \to J/\psi K_S)$ determines $\sin(2\beta+\phi_d^\Delta)$. With $\phi_d^\Delta < 0$ the true value of β will be larger than $\beta = 21.15^\circ \pm 0.89^\circ$ inferred from the SM analysis. Since β is also constrained by other measurements, a global fit is required [5].

2.2 New physics in $\mathrm{B}-\overline{\mathrm{B}}$ *mixing*

$\mathrm{B_q}-\overline{\mathrm{B}}_\mathrm{q}$ mixing involves two hermitian 2×2 matrices, the mass matrix M^q and the decay matrix Γ^q. The off-diagonal elements M_{12}^q and Γ_{12}^q are calculated from the dispersive and absorptive parts of the $\overline{B}_q \to B_q$ transition amplitude, respectively. In the SM M_{12}^q is dominated by the box diagram in Fig. 1 with internal top quarks, while Γ_{12}^q stems from box diagrams with only charm and up quarks on the internal lines. The SM expression for M_{12}^q including NLO QCD corrections has been calculated in Ref. [13]; the corresponding results for Γ_{12}^q have been obtained in Ref. [2, 14]. The numerical predictions in Ref. [2] have been recently updated with present-day values of CKM elements, quark masses and hadronic parameters in Refs. [5, 15]. As a consequence of $\mathrm{B_q}-\overline{\mathrm{B}}_\mathrm{q}$ mixing, the mass eigenstates B_q^H and B_q^L (with "H" and "L" denoting "heavy" and "light") found by diagonalising $M^q - i\Gamma^q/2$ are linear combinations of B_q and $\overline{B}_q$. The mass and width differences between B_q^H and B_q^L are given by

$$\Delta M_q \;=\; M_H^q - M_L^q \;\simeq\; 2|M_{12}^q|\,, \qquad\qquad \Delta\Gamma_q \;=\; \Gamma_L^q - \Gamma_H^q \;\simeq\; 2|\Gamma_{12}^q|\cos\phi_q\,.$$

The CP asymmetry in flavour-specific decays (such as $B_s \to X\ell^+\nu_\ell$) reads

$$a_{\rm fs}^q \;=\; \frac{|\Gamma_{12}^q|}{|M_{12}^q|}\sin\phi_q$$

with the CP-violating phase

$$\phi_q \;\equiv\; \arg\left(-\frac{M_{12}^q}{\Gamma_{12}^q}\right). \tag{3}$$

The DØ measurement of the like-sign dimuon asymmetry [1,3] involves a sample which is almost evenly composed of B_d and B_s mesons. The measured value is[c]

$$\begin{aligned} a_{\rm fs} &= (0.506\pm 0.043)a_{\rm fs}^d + (0.494\pm 0.043)a_{\rm fs}^s \\ &= (-9.57 \pm 2.51 \pm 1.46)\cdot 10^{-3} \end{aligned} \tag{4}$$

Averaging with an older CDF measurement yields

$$a_{\rm fs} = (-8.5\pm 2.8)\cdot 10^{-3}. \tag{5}$$

The numbers in Eqs. (4) and (5) are 3.2σ and 2.9σ away from the SM prediction $a_{\rm fs}^{\rm SM} = (-0.20\pm 0.03)\cdot 10^{-3}$ [15], respectively.

Γ_{12}^s originates from Cabibbo-favoured tree-level decays and is insensitive to new physics.[d] While Γ_{12}^d involves some Cabibbo suppression, it is nevertheless difficult to engineer a sizable new-physics contribution to Γ_{12}^d without running into conflict with the plethora of measured exclusive B decay branching fractions. It is therefore safe to assume that NP contributions to $\Gamma_{12}^{d,s}$ are irrelevant in view of today's experimental errors. In our analysis in Ref. [5] we

[c] The 2011 value is $a_{\rm fs} = (-7.87 \pm 1.72 \pm 0.93)\cdot 10^{-3}$ [3].

[d] Any NP competing with the tree-level $b \to s\overline{c}c$ decays constituting Γ_{12}^s will alter the $b \to s\overline{c}c$ decay rates of all b-flavoured hadrons in conflict with the precisely measured charm content n_c of B decay final states and/or the semileptonic branching fraction [5].

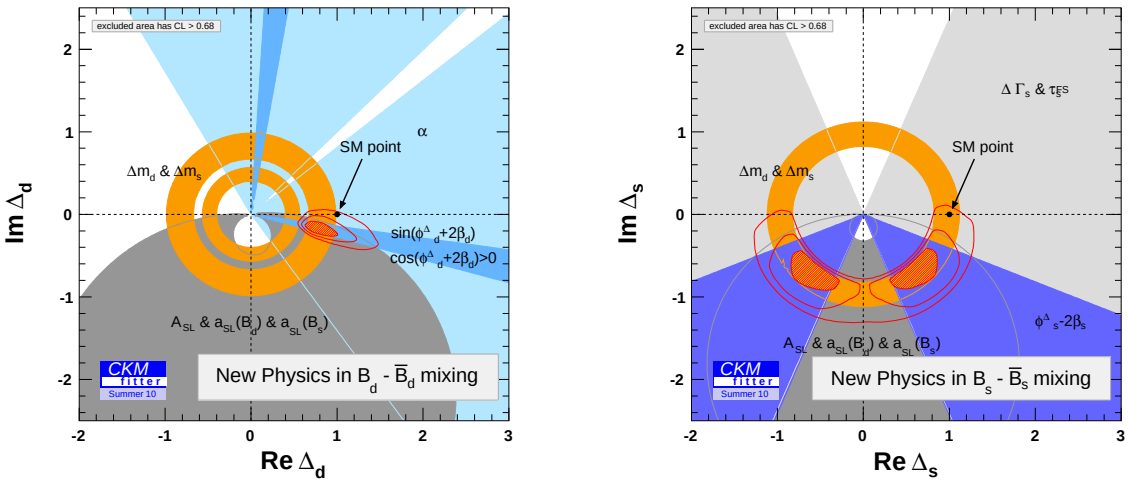

Figure 3: Allowed regions for Δ_d (left) and Δ_s (right) from the global fit [5].

have fitted the CKM elements together with complex quantities parametrising new physics in meson-antimeson mixing. For $B_q - \overline{B}_q$ mixing these parameters are defined as

$$\Delta_q \equiv \frac{M_{12}^q}{M_{12}^{q,\mathrm{SM}}}, \qquad \Delta_q \equiv |\Delta_q| e^{i\phi_q^\Delta}, \qquad \text{with } q = d \text{ or } s.$$

For $K - \overline{K}$ mixing one needs three such parameters. We have considered three scenarios, with i) new physics with arbitrary flavour structure, ii) minimally flavour-violating (MFV)[e] new physics with small bottom Yukawa coupling, and iii) MFV new physics with large bottom Yukawa coupling. These scenarios correspond to i) Δ_d, Δ_s complex and unrelated, ii) $\Delta \equiv \Delta_d = \Delta_s$ real, and iii) $\Delta \equiv \Delta_d = \Delta_s$ complex, respectively. In the first and third scenario the constraint from ϵ_K is simply absent, because $K - \overline{K}$ mixing is unrelated to $B - \overline{B}$ mixing, while in scenario ii) the $K - \overline{K}$ mixing NP parameters can be expressed in terms of Δ. In scenario i) we obtain an excellent fit, the preferred regions in the complex $\Delta_{d,s}$ planes are shown in Fig. 3. The point $\Delta_d = 1$ is disfavoured by 2.7σ, and this discrepancy is mainly driven by $B^+ \to \tau\nu$ as discussed in Sec. 2.1. ϵ_K plays a minor role in our analysis because of our conservative error estimate of the hadronic parameter B_K. For a discussion of this issue see Soni's talk at this conference [16]. Δ_s deviates from its SM value $\Delta_s = 1$ by 2.7σ as well, with a_{fs} as the main driver. Yet also the CDF and DØ measurements of the CP phase in $B_s - \overline{B}_s$ mixing through $B_s \to J/\psi\phi$ contribute here: Both measurements favour $\phi_s < 0$, in agreement with the conclusion drawn from a_{fs} in Eq. (5). The SM point $\Delta_d = \Delta_s = 1$ is disfavoured with 3.6 standard deviations, establishing evidence of new physics. Choosing a different statistical test, $\mathrm{Im}\,\Delta_d = \mathrm{Im}\,\Delta_s = 0$ is even disfavoured at a level of 3.8σ.

It is instructive to compare our best-fit result $\phi_s^\Delta = (-52^{+32}_{-25})^\circ$ at 95% CL with the 2010 Tevatron measurements. (I do not discuss the mirror solution $\phi_s^\Delta = (-130^{+28}_{-28})^\circ$ in the third quadrant of the complex Δ_s plane here.) The results of Ref. [17] read $\phi_s^\Delta = (-29^{+44}_{-49})^\circ$ (CDF) and $\phi_s^\Delta = (-44^{+59}_{-51})^\circ$ (DØ) at 95%CL . The naive average is $\phi_s^{\mathrm{avg}} = (-36 \pm 35)^\circ$ at 95% CL. While the Tevatron measurements of ϕ_s^Δ alone contain only weak hints to new physics, they perfectly agree with our best-fit value within normal statistical fluctuations. If one discards a_{fs} in Eq. (5) altogether and instead predicts it from the fit, one finds $a_{\mathrm{fs}} = \left(-4.2^{+2.9}_{-2.7}\right) \cdot 10^{-3}$ at

[e] In MFV models all quark flavour violation is governed by the same CKM elements as in the SM.

95%CL , which is just 1.5σ away from the DØ/CDF average in Eq. (5). In total a consistent picture of new physics in $\mathrm{B}-\overline{\mathrm{B}}$ mixing emerges, with a normal upward statistical fluctuation of $a_{\rm fs}$ and a mild downward fluctuation of the CDF value for ϕ_s^Δ from $B_s \to J/\psi\phi$.

Scenario iii) also gives a reasonable fit to the data, but scenario ii) is as bad as the SM. This is bad news for the popular Constrained Minimal Supersymmetric Standard Model (CMSSM) and its variant minimal supergravity (mSUGRA), which are realisations of scenario ii).

3 Supersymmetry and grand unification

The MSSM has many new sources of flavour violation, all of which reside in the supersymmetry-breaking sector. It is easy to get big effects in $\mathrm{B_s}$–$\overline{\mathrm{B}}_\mathrm{s}$ mixing, and the challenge is to suppress big effects elsewhere. MFV variants of the MSSM cannot produce large effects in $\mathrm{B_s}$–$\overline{\mathrm{B}}_\mathrm{s}$ mixing [18]. An attractive way to deviate from MFV in a controlled way (i.e. without producing too large FCNC in observables agreeing with the SM) emerges if one embeds the MSSM into a grand unified theory (GUT). In a GUT quarks and leptons reside in the same symmetry multiplets, which opens the possibility of quark-flavour transitions driven by the leptonic mixing matrix $U_{\rm PMNS}$ [19, 20]. Consider SU(5) multiplets:

$$\overline{\mathbf{5}}_\mathbf{1} = \begin{pmatrix} d_R^c \\ d_R^c \\ d_R^c \\ e_L \\ -\nu_e \end{pmatrix}, \qquad \overline{\mathbf{5}}_\mathbf{2} = \begin{pmatrix} s_R^c \\ s_R^c \\ s_R^c \\ \mu_L \\ -\nu_\mu \end{pmatrix}, \qquad \overline{\mathbf{5}}_\mathbf{3} = \begin{pmatrix} b_R^c \\ b_R^c \\ b_R^c \\ \tau_L \\ -\nu_\tau \end{pmatrix}.$$

If the observed large atmospheric neutrino mixing angle stems from a rotation of $\overline{\mathbf{5}}_\mathbf{2}$ and $\overline{\mathbf{5}}_\mathbf{3}$, it will also affect the b_R and s_R superfields. While rotations of quark fields in flavour space are unphysical, this is not the case for the corresponding squark fields $\widetilde{b}_R$ and $\widetilde{s}_R$ because of the supersymmetry-breaking terms. The key ingredients of the idea of Refs. [19, 20] is the following: In a weak basis with diagonal up-type Yukawa matrix the down-type Yukawa matrix Y_d is diagonalised as $\mathsf{Y}_d = V_{\rm CKM}^* \mathrm{diag}\,(y_d, y_s, y_b) U_{\rm PMNS}$. In this basis the right-handed down-squark mass matrix has the form $\mathsf{m}^2_{\tilde{d}} = \mathrm{diag}\,(m^2_{\tilde{d}}, m^2_{\tilde{d}}, m^2_{\tilde{d}} - \Delta_{\tilde{d}})$ with a calculable real parameter $\Delta_{\tilde{d}}$ generated by top-Yukawa renormalisation group effects. Rotating now Y_d to diagonal form puts the large atmospheric neutrino mixing angle into $\mathsf{m}^2_{\tilde{d}}$:

$$U_{\rm PMNS}^\dagger\, \mathsf{m}^2_{\tilde{d}}\, U_{\rm PMNS} = \begin{pmatrix} m^2_{\tilde{d}} & 0 & 0 \\ 0 & m^2_{\tilde{d}} - \frac{1}{2}\Delta_{\tilde{d}} & -\frac{1}{2}\Delta_{\tilde{d}}\, e^{i\xi} \\ 0 & -\frac{1}{2}\Delta_{\tilde{d}}\, e^{-i\xi} & m^2_{\tilde{d}} - \frac{1}{2}\Delta_{\tilde{d}} \end{pmatrix}$$

As a result we find large new transitions between right-handed $\widetilde{b}$ and $\widetilde{s}$ squarks while keeping all other quark FCNC transitions MFV-like. Moreover, the CP phase ξ affects $\mathrm{B_s}$–$\overline{\mathrm{B}}_\mathrm{s}$ mixing! The GUT boundary conditions further connect $b_R \to s_R$ with $\tau_L \to \mu_L$ transitions, so that $\mathrm{B_s}-\overline{\mathrm{B}}_\mathrm{s}$ mixing is correlated with $\tau \to \mu\gamma$. The CMM model realises this idea using the GUT symmetry breaking chain SO(10)$\to$ SU(5) $\to$ SU(3)$\times$SU(2)$_L\times$U(1)$_Y$. In Ref. [21] we have performed a global analysis of the CMM model, considering flavour physics data, vacuum stability bounds and the lower bounds on sparticle masses and the mass of the lightest Higgs boson. All MSSM parameters involved depend on just seven CMM-model parameters. We find that we can accommodate a large $\mathrm{B_s}-\overline{\mathrm{B}}_\mathrm{s}$ mixing phase while simultaneously obeying all other experimental constraints (see Fig. 4). In the CMM model eight of the twelve squark masses are essentially degenerate and are typically larger than 1 TeV, as can be seen from Fig. 4. Finally, corrections to the Yukawa couplings from dimension-5 terms can leak some of the CMM contribution in $\mathrm{B_s}-\overline{\mathrm{B}}_\mathrm{s}$ mixing to $\mathrm{B_d}-\overline{\mathrm{B}}_\mathrm{d}$ and $\mathrm{K}-\overline{\mathrm{K}}$ mixing and alleviate the tension in the fit to the UT [22].

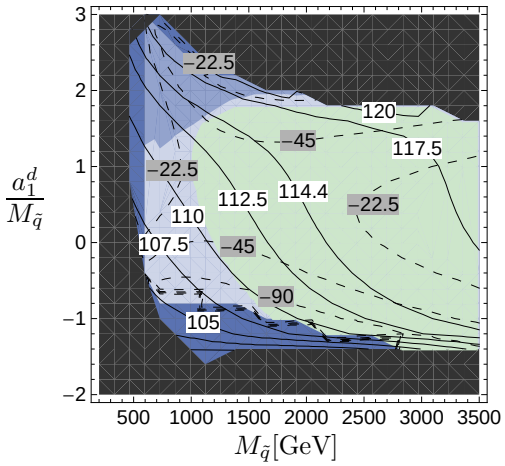

Black: unphysical soft masses
Light blue: excluded by $\tau \to \mu\gamma$
Medium blue: excluded by $b \to s\gamma$
Dark blue: excluded by $B_s - \overline{B}_s$ mixing
Green: allowed

Figure 4: Predictions of the CMM model for $m_{\tilde{g}_3} = 500$ GeV, $\tan\beta = 6$ and $\mu > 0$. $M_{\tilde{q}}$ is the (essentially degenerate) squark mass of the first two generations and a_1^d is the trilinear supersymmetry-breaking term of the down squarks. The dashed lines with grey labels show the value of $\phi_s \simeq \phi_s^\Delta$ in degrees, the solid lines with white labels show the mass of the lightest neutral Higgs boson. The black and blue regions are excluded.

4 Conclusions

Precision data of flavour physics put the Standard Model under pressure. The global analysis of Ref. [5] disfavours the SM at a level of 3.6σ and reveals a consistent picture of new CP-violating physics in meson-antimeson mixing. The data cannot be accommodated in the popular CMSSM and mSUGRA scenarios. However, the large CP phase in $B_s - \overline{B}_s$ mixing can naturally be explained in GUT models which link the large atmospheric neutrino mixing angle to novel $b \to s$ transitions [19, 20]. Our recent quantitative analysis, which relates FCNC observables, the Higgs mass and other theoretical and experimental constraints to just seven parameters, has found that this idea is indeed viable and permits large effects in $B_s - \overline{B}_s$ mixing [21].

Acknowledgements

I thank the organisers for inviting me to this conference. I appreciate the enjoyable collaborations with A. Lenz, J. Charles, S. Descotes-Genon, A. Jantsch, C. Kaufhold, H. Lacker, S. Monteil, V. Niess, S. T'Jampens, J. Girrbach, S. Jäger, M. Knopf, W. Martens, C. Scherrer and S. Wiesenfeldt on the presented results. I thank A. Crivellin for proofreading the manuscript. My work was supported by DFG through grant No. NI 1105/1-1, project C6 of the CRC–TR 9 and by BMBF through grant no. 05H09VKF.

References

1. Talk by G. Borissov at *Joint Experimental-Theoretical Physics Seminar*, Fermilab, Batavia, USA, May 14, 2010. V. M. Abazov *et al.* [D0 Collaboration], Phys. Rev. D **82** (2010) 032001. V. M. Abazov *et al.* [D0 Collaboration], Phys. Rev. Lett. **105** (2010) 081801.
2. A. Lenz and U. Nierste, JHEP **0706**, 072 (2007).
3. V.M. Abazov *et al.* [D0 Collaboration], *Measurement of the anomalous like-sign dimuon charge asymmetry with 9 fb^{-1} of $p\overline{p}$ collisions*, arXiv:1106.6308 [hep-ex].
4. E. Lunghi and A. Soni, Phys. Lett. B **666**, 162 (2008). Phys. Lett. B **697** (2011) 323. A. J. Buras and D. Guadagnoli, Phys. Rev. D **78**, 033005 (2008). A. J. Buras and D. Guadagnoli, Phys. Rev. D **79**, 2009 (053010).

5. A. Lenz, U. Nierste, and J. Charles, S. Descotes-Genon, A. Jantsch, C. Kaufhold, H. Lacker, S. Monteil, V. Niess, S. T'Jampens [CKMfitter Group]. Phys. Rev. D **83** (2011) 036004.
6. The CKMfitter Group (J. Charles *et al.*), Eur. Phys. J. C **41**, 1 (2005); updated at `http://ckmfitter.in2p3.fr/`.
7. B. Aubert *et al.* (BaBar collaboration), Phys. Rev. D **77**, 011107(R) (2008). I. Adachi *et al.* (Belle collaboration), arxiv:0809.3834 [hep-ex]. B. Aubert *et al.* (BaBar collaboration), Phys. Rev. D **81**, 051101 (2010). K. Hara *et al.* (Belle collaboration), arxiv:1006.4201 [hep-ex]. P. d. A. Sanchez *et al.* (BaBar collaboration), arxiv:1008.0104 [hep-ex].
8. B. Kowalewski (BaBar collaboration), talk at *Beauty 2011*, Amsterdam, The Netherlands, 4-8 Apr 2011.
9. W. S. Hou, Phys. Rev. D **48** (1993) 2342. A. G. Akeroyd and S. Recksiegel, J. Phys. G **29** (2003) 2311. H. Itoh, S. Komine and Y. Okada, Prog. Theor. Phys. **114** (2005) 179.
10. A. Crivellin, Phys. Rev. D **81** (2010) 031301. A. J. Buras, K. Gemmler and G. Isidori, Nucl. Phys. B **843** (2011) 107.
11. M. Bona *et al.* [UTfit Collaboration], Phys. Lett. B **687** (2010) 61. M. Bauer, S. Casagrande, U. Haisch and M. Neubert, JHEP **1009** (2010) 017.
12. K. Kiers and A. Soni, Phys. Rev. D **56** (1997) 5786. U. Nierste, S. Trine and S. Westhoff, Phys. Rev. D **78** (2008) 015006. M. Tanaka and R. Watanabe, Phys. Rev. D **82** (2010) 034027.
13. A. J. Buras, M. Jamin and P. H. Weisz, Nucl. Phys. B **347** (1990) 491.
14. M. Beneke, G. Buchalla, C. Greub, A. Lenz and U. Nierste, Phys. Lett. B **459**, 631 (1999). M. Ciuchini, E. Franco, V. Lubicz, F. Mescia and C. Tarantino, JHEP **0308**, 031 (2003). M. Beneke, G. Buchalla, A. Lenz and U. Nierste, Phys. Lett. B **576** (2003) 173.
15. A. Lenz and U. Nierste, arXiv:1102.4274 [hep-ph].
16. E. Lunghi and A. Soni, arXiv:1104.2117 [hep-ph].
17. T. Aaltonen *et al.*[CDF Collaboration], CDF public note 10206. V. M. Abazov *et al.*[D0 Collaboration], DØ Conference note 6098.
18. A. J. Buras, P. H. Chankowski, J. Rosiek and L. Slawianowska, Phys. Lett. B **546** (2002) 96. A. J. Buras, P. H. Chankowski, J. Rosiek and L. Slawianowska, Nucl. Phys. B **659** (2003) 3. M. Gorbahn, S. Jager, U. Nierste and S. Trine, arXiv:0901.2065 [hep-ph], to appear in Phys. Rev. D. L. Hofer, U. Nierste and D. Scherer, JHEP **0910** (2009) 081; PoS **EPS-HEP2009** (2009) 181 [arXiv:0909.4749 [hep-ph]].
19. T. Moroi, JHEP **0003** (2000) 019; Phys. Lett. B **493** (2000) 366.
20. D. Chang, A. Masiero and H. Murayama, Phys. Rev. D **67** (2003) 075013.
21. J. Girrbach, S. Jager, M. Knopf, W. Martens, U. Nierste, C. Scherrer and S. Wiesenfeldt, JHEP **1106**, 044 (2011). For early studies of B_s–$\overline{B}_s$ mixing in the CMM model see S. Jäger and U. Nierste, Eur. Phys. J. C **33** (2004) S256; arXiv:hep-ph/0410360, in: *Proceedings of 12th International Conference on Supersymmetry and Unification of Fundamental Interactions (SUSY2004), Tsukuba, Japan, June 17-23, 2004,* Eds. K. Hagiwara, J. Kanzaki, N. Okada. S. Jager, arXiv:hep-ph/0505243, in: *Proceedings of the XLth Rencontres de Moriond, Electroweak Interactions and Unified Theories, 5-12 March 2005, La Thuile, Italy,* Ed. J. Tran Thanh Van.
22. S. Trine, S. Westhoff and S. Wiesenfeldt, JHEP **0908** (2009) 002. For corresponding studies including the lepton sector see: P. Ko, J. h. Park and M. Yamaguchi, JHEP **0811** (2008) 051. F. Borzumati and T. Yamashita, Prog. Theor. Phys. **124**, 761 (2010). J. Girrbach, S. Mertens, U. Nierste and S. Wiesenfeldt, JHEP **1005** (2010) 026.

Top Quark Production at the Tevatron

Liang Li
Department of Physics and Astronomy, University of California, Riverside, CA 92521, USA

Top quark physics has been a rich testing ground for the standard model since the top quark discovery in 1995. The large mass of top quark suggests that it could play a special role in searches for new phenomena. In this paper I provide an overview of recent top quark production cross section measurements from both CDF and D0 collaborations and also some new physics searches done in the top quark sector.

1 Introduction

Top quarks are produced in pair via the strong interactions or singly via the electroweak interactions at hadron colliders. The top quark pair production gives a larger yield [1] and provides more discrimination against backgrounds compared to the single top quark production. This is the main reason why the former was first discovered in 1995 [2,3] and only after 14 years the later was observed at the Tevatron Collider [4,5]. Due to the large mass of the top quark, many models of physics beyond the standard model (BSM) predict observable effects in the top quark production rate. Measurements of top quark production cross section serve as tests of possible new physics processes and can place stringent limits on these models. In the standard model (SM), top quarks decay almost 100% of the time to a W boson and a bottom quark. The signature of top quark events is therefore defined by the decay products of the W boson. For $t\bar{t}$ events, if two W bosons decay leptonically and there are two leptons in the final state, it is defined as the "dilepton" channel of the $t\bar{t}$ production. Similarly, the "all-hadronic" channel is defined when both W bosons decay hadronically and the "lepton+jets" channel is defined when one W boson decays leptonically and the other decays hadronically. The all-hadronic channel has the largest branching ratio (BR) however also the lowest signal-to-background (S:B) ratio due to high multijets background. The dilepton channel has the highest S:B ratio however the signal statistics is limited by the lowest BR. Thus the most precise measurements on the top quark pair production rates are obtained in the lepton+jets channel. In the case of single top quark production, the cross section measurement is also done using the lepton+jets channel.

2 Top Quark Pair Production

2.1 Lepton+jets channel

In this channel, the $t\bar{t}$ events are identified using the decay of one W boson to quarks and the other to a lepton and a neutrino. Each event is required to have a single high-p_T electron or muon (for taus, only leptonically decaying taus are considered) and at least three reconstructed jets. To suppress the background processes, at least one identified b-jet is required using the

lifetime-based b-tagging algorithm [6]. The dominant background is the W+jet production and other backgrounds are Z+jet, diboson (WW, WZ, ZZ), single top quark and multijet processes.

The inclusive $t\bar{t}$ production cross section is measured by fitting the $t\bar{t}$ cross section to data using a binned maximum likelihood. The likelihood is formed from the data, the $t\bar{t}$ cross section and the predicted background for that cross section. The "b-tagging" method utilizes the event distributions after b-jet identification to calculate the likelihood while the "kinematics" method constructs a multivariant discriminant to distinguish $t\bar{t}$ signal from background and later uses the discriminant function to obtain the likelihood. The kinematics method exploits the kinematic differences between the signal and background before b-jet indentification and is therefore not sensitive to the large systematic uncertainty induced from the b-tagging. Using the b-tagging method with 4.3 fb^{-1} data, CDF experiment measures $\sigma_{t\bar{t}} = 7.22 \pm 0.35$ (stat) ± 0.56 (syst) $\pm$ 0.44 (lumi) pb [7]. Figure 1 (left) shows the the predicted number of events for each background process, along with the number of expected $t\bar{t}$ events at the measured cross section compared to data. D0 experiment's b-tagging and kinematics measurements of $t\bar{t}$ cross section are described in detail in Ref. [8]. D0 also uses a third method which is a combination of the first two methods: construct a multivariant discriminant (RF) for channels dominated by backgrounds, otherwise use b-tagging method. The combination takes advantage of the two methods and yields a more precise measurement of $\sigma_{t\bar{t}} = 7.78\ ^{+0.77}_{-0.64}$ (stat + syst + lumi) pb [8] using 5.3 fb^{-1} of integrated luminosity for a top quark mass of 172.5 GeV. The discriminant output distributions using the combination method for one channel (as an example) is shown in Fig. 1 (right). To reduce the large luminosity uncertainty on the $t\bar{t}$ cross section, CDF measures the $t\bar{t}$ to $Z/\gamma^* \to ll$ ratio in the same corresponding data sample and determine the $t\bar{t}$ cross section by multiplying the ratio by the theoretical $t\bar{t}$ to $Z/\gamma^* \to ll$ cross section given by the SM. The small uncertainties on the theoretical and measured $t\bar{t}$ to $Z/\gamma^* \to ll$ cross sections are propagated to the final $t\bar{t}$ cross section measurement. CDF uses a best linear unbiased estimate (BLUE) [9] method to combine the b-tagging measurement and kinematics measurement and finds $\sigma_{t\bar{t}} = 7.70 \pm 0.52$ pb [7] for $M_t = 172.5$ GeV.

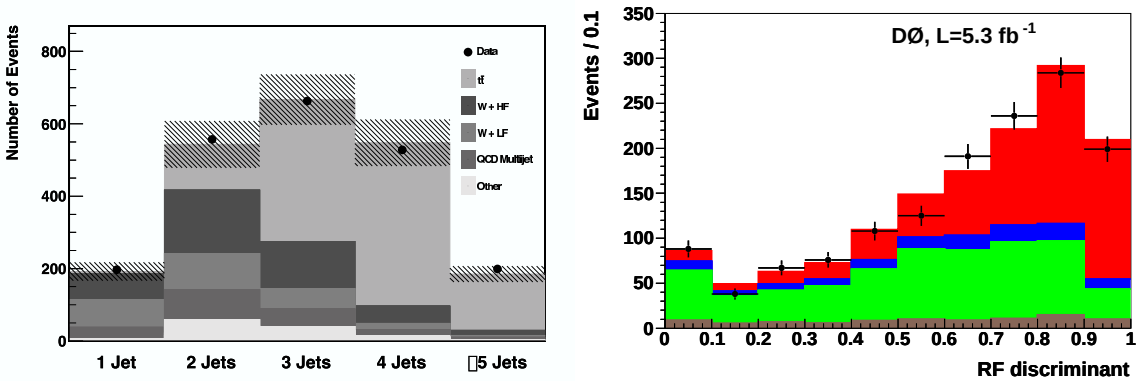

Figure 1: Left: Number of data and predicted background events as a function of jet multiplicity, with the number of $t\bar{t}$ t events at the measured cross section events normalized to the measured cross section. The hashed lines represent the uncertainty on the predicted number of events. Right: Output of the RF discriminant for events with three jets and one b-tagged jet for data, backgrounds and $t\bar{t}$ signal normalized to the measured cross section.

2.2 Dilepton channel

In this channel, we require two high-p_T leptons, high missing transverse energy ($\not\!\!E_T$) and at least two jets in the final state. It is independent and orthogonal to the lepton+jets channel and is the only channel which has a favorable S:B ratio. Two dominant backgrounds are $Z/\gamma^* \to ee/\mu\mu$ with fake $\not\!\!E_T$ and W+jets with fake leptons. They are modeled using the data-driven method [10].

After event selection, the final sample contains a high concentration of $t\bar{t}$ events, which allows us to perform a direct extraction of $t\bar{t}$ cross section by $\sigma_{t\bar{t}} = \frac{N_{obs}-N_{bkg}}{\Sigma_i \mathcal{A}_i \cdot \mathcal{L}_i}$. N_{obs} is the observed number of dilepton candidate events, N_{bkg} is the total background and $\mathcal{A}_i$ and $\mathcal{L}_i$ are the corrected acceptance and integrated luminosity for analysis channel i. CDF measures the $t\bar{t}$ cross section using 5.1 fb^{-1} of data for a top mass of 172.5 GeV. The measurement is done before and after applying the b-tagging requirement and the results are $\sigma_{t\bar{t}} = 7.40 \pm 0.58$ (stat) ± 0.63 (syst) $\pm$ 0.45 (lumi) pb and $\sigma_{t\bar{t}} = 7.25 \pm 0.66$ (stat) ± 0.47 (syst) ± 0.44 (lumi) pb correspondingly [10].

2.3 Tau+jets channel

Top quark is the heaviest quark and tau is the heaviest lepton, any non-SM mass- or flavor-dependent couplings could change the top quark decay rate into final states with taus. Therefore it is of interest to measure $\sigma(p\bar{p} \to t\bar{t} + X) \cdot \mathrm{BR}(t\bar{t} \to \tau + jets)$ (denoted by "$\sigma_{t\bar{t}} \cdot \mathrm{BR}_{\tau_h+j}$") and compare to the SM prediction. D0 performs the measurement using semi-hadronic tau decays (τ_h) since secondary electrons and muons from tau leptonic decays are difficult to distinguish from primary electrons and muons from W decays. The measurement also provides complementary information regarding $t\bar{t}$ production cross section compared to the more precise lepton+jets measurements. We select events to have at least four reconstructed jets and at least one one τ_h candidate. In addition, each event must have at least one b-jet using the b-tagging algorithm [6]. The main physics backgrounds are the W+jets and Z+jets contribution and the main instrumental background is the multijet production. We use a neural network (NN_{sb}) event discriminant to separate signal from background and then fit the entire NN_{sb} output distribution to data to extract the numbers of signal and background events. The measured $\sigma_{t\bar{t}} \cdot \mathrm{BR}_{\tau_h+j}$ value is $0.60\ ^{+0.23}_{-0.22}$ (stat) $^{+0.15}_{-0.14}$ (syst) ± 0.04 (lumi) pb for $M_t = 170$ GeV [11], which is consistent with the SM predicted value. We repeat the fit while fixing the $t\bar{t}$ BRs to their SM values and obtain the $t\bar{t}$ production cross section $\sigma_{t\bar{t}} = 6.9^{+1.5}_{-1.4}$ pb [11] for a top quark mass of 170 GeV.

2.4 New Physics Searches: 4^{th} generation quark t'

$t\bar{t}$ production measurements are also useful when searching for new physics, e.g. the 4^{th} generation quark t' search. CDF performs two types of searches for pair production of t' using $t\bar{t}$ event topology. One analysis is to search for t' decaying via $t' \to t + X$, where X is the dark matter particle and manifests itself as an excess of missing transverse energy in the detector. The analysis is done in the lepton+jets channel with an additional requirement of large $\not\!\!E_T$. Another kinematic variable besides $\not\!\!E_T$ which is sensitive to the signal and background discrimination is the transverse mass of the leptonically decaying W (mT_W). The signal cross section is extracted by fitting templates of the signal and background shapes in mT_W to the observed number of data events taking into account statistical and systematics uncertainties. We obtain the expected and observed upper limits on the signal using a Frequentist approach [12] done in the two-dimensional (2D) plane of (m'_T, m_X), where m'_T is the mass of the fourth generation quark, and m_X is the mass of the dark matter particle. The observed limits are consistent with what the SM predictions. The final 2D limit is shown in Fig. 2 (left) using 4.8 fb^{-1} of data.

Another search for t' is performed in the Wb final state assuming $t' \to W+b$. We assume that t' is produced strongly and has the same couplings as the three generations of the SM quarks. We use a similar event selection and background modeling as in the $t\bar{t}$ lepton+jets channel measurements. The dominant backgrounds are top pair production and W+jet production. The new quark is heavier than the top quark and the decay products are more energetic. This effect can be observed in the total transverse energy variable (H_T) [13]. It also decays in the same chain and allows us to reconstruct its mass in a similar way as in the top mass measurements. We reconstruct the mass of the t' quark (M_{reco}) and perform a two-dimensional fit of the observed

(H_T,M_{reco}) distribution to discriminate the new physics signal from Standard Model processes. We form a binned likelihood as a function of $t'\bar{t}'$ cross section and use a Bayesian approach [13] to set an upper limit. We generate pseudo-experiments assuming no t' signal and use that to gauge the sensitivity of the analysis. Fig. 2 (right) shows the ranges of the expected and observed upper limits at 95% C.L compared to the theoretical calculations. With 5.6 fb^{-1} of data, CDF excludes the hypothetical 4^{th} generation quark t' with mass below 358 GeV at 95% C.L. for $M_t = 172.5$ GeV.

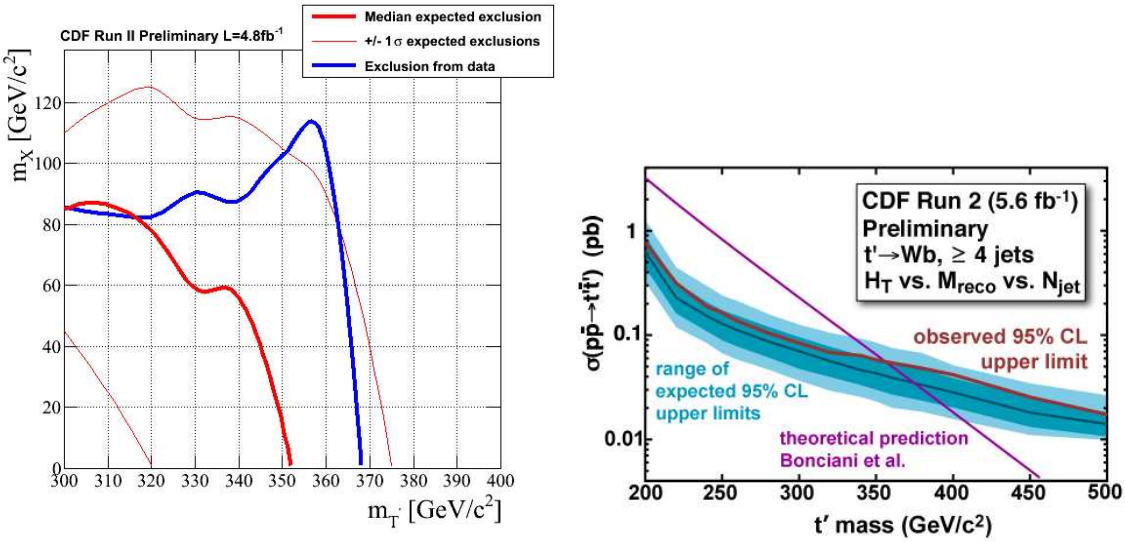

Figure 2: Left: Observed and expected exclusion area as a function of (m'_T, m_X). Right: Observed upper limit at 95% C.L. on the t' production rate as a function of t' mass (red curve). The purple curve is a theoretical cross section. The blue band represents ± 1 standard deviation expected limit (the light blue band corresponds to ± 2 standard deviation).

3 Single Top Quark Production

Single top quarks are produced via the decay of a time-like virtual W boson accompanied by a bottom quark in the s-channel (denoted by "tb") or via the exchange of a space-like virtual W boson between a light quark and a bottom quark in the t-channel (denoted by "tqb") process. Previous D0 and CDF publications [4,5] measured the total single top quark production cross section assuming the SM predicted ratio between the individual channel's cross sections. However several BSM models predict different values of this ratio compared to the SM. Therefore it is of interest to remove this assumption and measure $s-$channel and $t-$channel production cross section independently.

D0 extends its previous analyses [4,14,15,16] and performs a new measurement on the t-channel production rate using a larger dataset of 5.4 fb^{-1} and improved techniques [17]. We require events to have exactly one isolated high-p_T electron or muon, a large $\not\!\!E_T$ and two to four reconstructed jets (one or two of the jets are identified as $b-$jets [6]). The main backgrounds are $W+$jets, $t\bar{t}$ and multijet production. The largest uncertainties come from the jet energy resolution (JER), corrections to the b-tagging efficiency, and the corrections for the jet-flavor composition in $W+$jets events, with smaller contribution from jet energy scale (JES), MC statistics, integrated luminosity, and trigger uncertainties. The total systematic uncertainty on the background is 11%. We construct multivariant discriminants to improve discrimination between signal and background. We use three methods to train these discriminants: boosted decision trees (BDT), Bayesian neural networks (BNN) and neuroevolution of augmented topologies (NEAT). We later combine these methods using an additional BNN algorithm that takes to produces a single combined

output discriminant (BNNComb), which further improves the sensitivity and the precision of the cross section measurement. Each method is optimized to maximize the sensitivity to the $t-$channel signal by treating the $s-$channel process as a background component with normalization given by the SM cross section [18]. Figure 3 shows comparisons between the t-channel signal, the background model, and data for the combined discriminant,

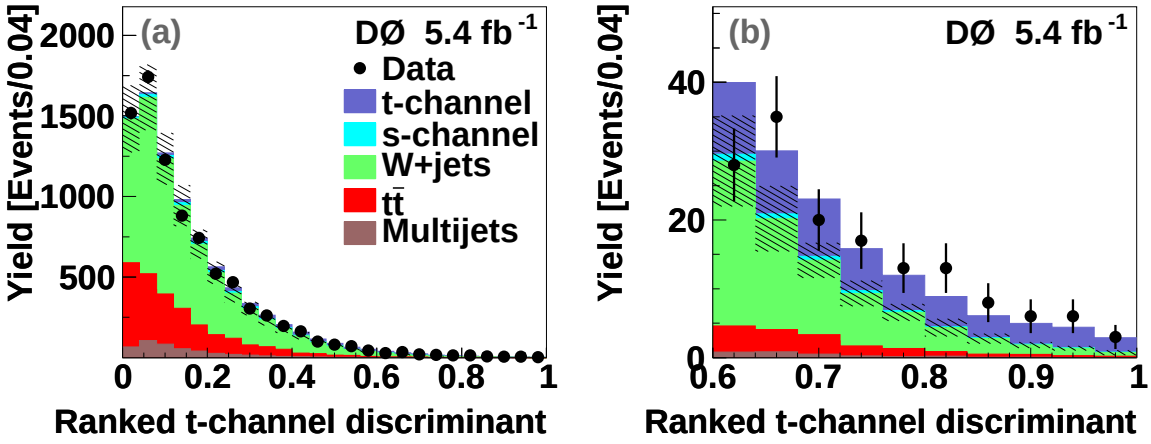

Figure 3: Comparison of the signal and background models to data for the combined t-channel discriminant for (a) the entire discriminant range and (b) the signal region. The bins have been ordered by their expected S:B. The single top quark contributions are normalized to the measured cross sections. The t-channel contribution is visible above the hatched bands that show the uncertainty on the background prediction.

The single top quark production cross section is measured using a Bayesian approach as in [14,15,4]. We follow the approach of [16] and construct a two-dimensional (2D) posterior probability density as a function of the cross sections for the s- and t-channel processes. A binned likelihood is formed using the output discriminants for the signals, backgrounds, and data, taking into account all systematic uncertainties and their correlations. We assume a Poisson distribution for the observed number of data events and nonnegative uniform prior probabilities for the two cross sections without any assumption on their ratio. The t-channel cross section is then extracted from a one-dimensional posterior probability density obtained from this 2D posterior by integrating over the s-channel axis, thus not making any assumptions about the value of the s-channel cross section. Similarly, the s-channel cross section is obtained by integrating over the t-channel axis. We generate ensembles of pseudo-experiments to validate the cross section extraction procedure. Figure 4 shows the 2D posterior probability density for the combined discriminant together with predictions from the SM [18] and various BSM scenarios [19,20,21].

We measure $\sigma(p\bar{p} \to tqb + X) = 2.90 \pm 0.59$ pb and $\sigma(p\bar{p} \to tb + X) = 0.98 \pm 0.63$ pb which are in good agreement with the SM predictions for a top quark mass of 172.5 GeV [18]. The significance of the t-channel cross section measurement is computed following a log-likelihood ratio approach [5,16] and is found to be 5.5 standard deviation (SD) using an asymptotic Gaussian approximation [22]. The measured cross section depends on the assumed mass of the top quark (M_t). The dependence is studied by repeating the analysis on MC samples generated at different values of M_t. Table 1 summarizes the measured cross sections for different top quark masses.

Acknowledgments

I thank the D0 and CDF collaborations and Fermilab staffs for producing such nice results on top quark physics. I also would like to thank the conference organizers for hosting a wonderful conference with a broad and exciting physics program. I acknowledge support from DOE (USA).

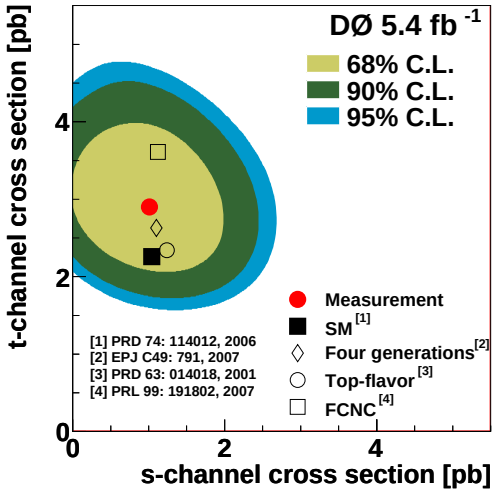

Figure 4: Posterior probability density for t-channel vs s-channel single top quark production in contours of equal probability density. The measured cross section and various theoretical predictions are also shown.

Table 1: Measured single top quark production cross sections for different top quark masses.

M_t	170 GeV	172.5 GeV	175 GeV
tqb	$2.80^{+0.57}_{-0.61}$	$2.90^{+0.59}_{-0.59}$	$2.53^{+0.58}_{-0.57}$
tb	$1.31^{+0.77}_{-0.74}$	$0.98^{+0.62}_{-0.63}$	$0.65^{+0.51}_{-0.50}$

References

1. S. Moch and P. Uwer, Phys. Rev. D **78**, 034003 (2008). At $m_t = 172.5$ GeV, $\sigma(p\bar{p} \to t\bar{t} + X) = 7.46$ pb.
2. F. Abe *et al.* (CDF Collaboration), Phys. Rev. Lett. **74**, 2626 (1995).
3. S. Abachi *et al.* (D0 Collaboration), Phys. Rev. Lett. **74**, 2632 (1995).
4. V. M. Abazov *et al.* (D0 Collaboration), Phys. Rev. Lett. **103**, 092001 (2009).
5. T. Aaltonen *et al.* (CDF Collaboration), Phys. Rev. Lett. **103**, 092002 (2009).
6. V. M. Abazov *et al.* (D0 Collaboration), Nucl. Instrum. Methods Phys. Res. A **620**, 490 (2010); T. Aaltonen *et al.* (CDF Collaboration), Phys. Rev. D **71**, 052003 (2005).
7. T. Aaltonen *et al.* (CDF Collaboration), Phys. Rev. Lett. **105**, 012001 (2010).
8. V. M. Abazov *et al.* (D0 Collaboration), arXiv:1101.0124
9. L. Lyons, D. Gibaut, and P. Clifford, Nucl. Instrum. Methods A **270**, 110 (1988);
10. T. Aaltonen *et al.* (CDF Collaboration), CDF Conference Note 10163.
11. V. M. Abazov *et al.* (D0 Collaboration), Phys. Rev. D **82**, 071102(R) (2010).
12. T. Aaltonen *et al.* (CDF Collaboration), CDF Conference Note 10374.
13. T. Aaltonen *et al.* (CDF Collaboration), CDF Conference Note 10395.
14. V. M. Abazov *et al.* (D0 Collaboration), Phys. Rev. Lett. **98**, 181802 (2007).
15. V. M. Abazov *et al.* (D0 Collaboration), Phys. Rev. D **78**, 012005 (2008).
16. V. M. Abazov *et al.* (D0 Collaboration), Phys. Lett. B **682**, 363 (2010).
17. V. M. Abazov *et al.* (D0 Collaboration), arXiv:1105.2788
18. N. Kidonakis, Phys. Rev. D **74**, 114012 (2006). The cross sections for the single top quark processes ($m_t = 172.5$ GeV) are 1.04 ± 0.04 pb (s-channel) and 2.26 ± 0.12 pb (t-channel).
19. J. Alwall *et al.*, Eur. Phys. J. **C** 49, 791 (2007).
20. T. Tait and C.-P. Yuan, Phys. Rev. D **63**, 014018 (2001).
21. V. M. Abazov *et al.* (D0 Collaboration), Phys. Rev. Lett. **99**, 191802 (2007).
22. G. Cowan, K. Cranmer, E. Gross and O. Vitells, Eur. Phys. J. C **71**, 1554 (2011).

Top, Polarization, LHC and New Physics

J.F. KAMENIK
J. Stefan Institute, Jamova 39, P. O. Box 3000, 1001 Ljubljana, Slovenia

Department of Physics, University of Ljubljana, Jadranska 19, 1000 Ljubljana, Slovenia

Polarization observables in top quark decays are sensitive probes of possible new physics contributions to the interactions of the heavy third generation quarks. Within an effective theory approach such new physics contributions can be classified in terms of several higher dimensional operators. We investigate the interplay between indirect constraints on such operators, coming mainly from rare B physics processes, and direct measurements of top polarization observables at the LHC.

1 Introduction

The extensive production of top quarks at the LHC and Tevatron colliders offers the possibility to study tWb interactions with high accuracy. Within the Standard Model (SM) the partial $t \to bW$ decay width and the branching fraction

$$\Gamma(t \to bW)^{\rm SM} \simeq \frac{\alpha |V_{tb}|^2}{16 s_W^2} \frac{m_t^3}{m_W^2}\,, \qquad \mathcal{B}(t \to bW)^{\rm SM} \simeq \frac{|V_{tb}^2|}{|V_{tb}^2| + |V_{ts}^2| + |V_{td}^2|}\,, \tag{1}$$

are sensitive to the value of the CKM matrix element V_{tb}, related to the top-bottom charged current.[1] However, present indirect constraints on V_{tb} within the SM employing CKM unitarity[2] are already much stronger compared to the present[3] and projected[4] experimental direct sensitivity.

Fortunately, helicity fractions of the final state W in this decay provide additional information on the structure of the tWb interaction. Considering leptonically decaying W's, one can define the angle between the charged lepton momentum in the W rest frame and the W momentum in the t-quark rest frame (θ_ℓ^*). Then the normalized differential decay rate for unpolarized top quarks can be written as

$$\frac{1}{\Gamma}\frac{d\Gamma}{d\cos\theta_\ell^*} = \frac{3}{8}(1+\cos\theta_\ell^*)^2 \mathcal{F}_+ + \frac{3}{8}(1-\cos\theta_\ell^*)^2 \mathcal{F}_- + \frac{3}{4}\sin^2\theta_\ell^* \mathcal{F}_L\,, \tag{2}$$

with $\mathcal{F}_i = \Gamma_i/\Gamma$ being the W-boson helicity fractions.[5,6 a] There has been a continuing interest in the measurement of $\mathcal{F}_i$ by the CDF and DØ collaborations at the Tevatron. Their most recent

[a] Note that by definition $\sum_i \mathcal{F}_i = 1$ so that only two of the helicity fractions represent independent observables.

analyses yield [7,8]

$$\begin{aligned} \mathcal{F}_L^{\rm CDF} &= 0.88(13)\,, & \mathcal{F}_L^{\rm D\O} &= 0.669(102)\,, \\ \mathcal{F}_+^{\rm CDF} &= -0.15(9)\,, & \mathcal{F}_+^{\rm D\O} &= 0.023(53)\,, \end{aligned} \tag{3}$$

where the statistical and systematic uncertainties have been combined in quadrature. Compared to these values, an order of magnitude improvement in precision is expected from the LHC experiments in the coming years. [5,9]

In the SM, simple helicity considerations show that $\mathcal{F}_+$ vanishes at the Born level in the $m_b = 0$ limit. A non-vanishing $\mathcal{F}_+$ could arise from i) $m_b \neq 0$ effects, ii) $\mathcal{O}(\alpha_s)$ radiative corrections due to gluon emission [b], or from iii) non-SM tWb interactions. The $\mathcal{O}(\alpha_s)$ and the $m_b \neq 0$ corrections to $\mathcal{F}_+$ have been shown to occur only at the per-mille level in the SM. [11] Specifically, they yield

$$\mathcal{F}_L^{\rm SM} = 0.687(5)\,, \qquad \mathcal{F}_+^{\rm SM} = 0.0017(1)\,. \tag{4}$$

One could therefore conclude that measured values of $\mathcal{F}_+$ exceeding 0.2% level, would signal the presence of new physics (NP) beyond the SM.

2 Effective theory analysis

The structure of NP contributions possibly affecting $t \to bW$ transitions can be analyzed using effective field theory methods – by introducing the effective Lagrangian

$$\mathcal{L} = \mathcal{L}_{\rm SM} + \frac{1}{\Lambda^2}\sum_i C_i \mathcal{Q}_i + \text{h.c.} + \mathcal{O}(1/\Lambda^3)\,, \tag{5}$$

where $\mathcal{L}_{\rm SM}$ is the SM part, Λ is the scale of NP and $\mathcal{Q}_i$ are dimension-six operators, invariant under SM gauge transformations and consisting of SM fields. In order to exhibit observable effects in the $t \to bW$ decays $\mathcal{Q}_i$ should also not mediate flavor changing neutral currents (FCNCs) in the down sector at the tree-level.[12] Since the SM electroweak symmetry breaking induces misalignment between the up and down quark mass eigenbases via the CKM mechanism, isolating NP effects in tWd_j interactions to a particular single flavor transition in the physical (mass) basis in general requires a large degree of fine-tuning in the flavor structure of the effective operators at the high scale, where they are generated. One possible solution is to require the operators to be flavor aligned with either the up or the down Yukawas of the SM resulting effectively in minimal flavor violating (MFV) scenarios.[13] A systematic analysis of all MFV allowed flavor structures even in the presence of large bottom Yukawa effects yields a total of seven dimension-six effective operators which can significantly affect the tWb interaction [14]

$$\begin{aligned} \mathcal{Q}_{LL} &= [\bar{Q}'_3\tau^a\gamma^\mu Q'_3]\big(\phi_d^\dagger\tau^a \mathrm{i}D_\mu\phi_d\big) - [\bar{Q}'_3\gamma^\mu Q'_3]\big(\phi_d^\dagger \mathrm{i}D_\mu\phi_d\big), \\ \mathcal{Q}_{LRt} &= [\bar{Q}'_3\sigma^{\mu\nu}\tau^a t_R]\phi_u W^a_{\mu\nu}\,, \\ \mathcal{Q}_{RR} &= V_{tb}[\bar{t}_R\gamma^\mu b_R]\big(\phi_u^\dagger \mathrm{i}D_\mu\phi_d\big)\,, \\ \mathcal{Q}_{LRb} &= [\bar{Q}_3\sigma^{\mu\nu}\tau^a b_R]\phi_d W^a_{\mu\nu}\,, \\ \mathcal{Q}'_{LL} &= [\bar{Q}_3\tau^a\gamma^\mu Q_3]\big(\phi_d^\dagger\tau^a \mathrm{i}D_\mu\phi_d\big) - [\bar{Q}_3\gamma^\mu Q_3]\big(\phi_d^\dagger \mathrm{i}D_\mu\phi_d\big), \\ \mathcal{Q}''_{LL} &= [\bar{Q}'_3\tau^a\gamma^\mu Q_3]\big(\phi_d^\dagger\tau^a \mathrm{i}D_\mu\phi_d\big) - [\bar{Q}'_3\gamma^\mu Q_3]\big(\phi_d^\dagger \mathrm{i}D_\mu\phi_d\big), \\ \mathcal{Q}'_{LRt} &= [\bar{Q}_3\sigma^{\mu\nu}\tau^a t_R]\phi_u W^a_{\mu\nu}\,, \end{aligned} \tag{6}$$

where we have introduced $Q_3 = (V^*_{kb}u_{Lk}, b_L)$, $Q'_3 = (t_L, V_{ti}d_{iL})$, $\sigma^{\mu\nu} = \mathrm{i}[\gamma^\mu,\gamma^\nu]/2$ and $W^a_{\mu\nu} = \partial_\mu W^a_\nu - \partial_\nu W^a_\mu - g\epsilon_{abc}W^b_\mu W^c_\nu$. Furthermore, $q_{L(R)} = P_{L(R)}q$ denote the left- and right-handed

[b] Electroweak corrections also contribute, but turn out to be much smaller. [10]

quark fields ($q = u_i, d_i$), where $P_{L(R)} = (1 \mp \gamma_5)/2$, while $\phi_{u,d}$ are the up- and down-type Higgs fields (in the SM $\phi_u = \mathrm{i}\tau^2\phi_d^*$) and g is the weak coupling constant. The first two operators in (6) appear already at zeroth order in the down-type Yukawa insertions, the following two would be linear in a bottom Yukawa expansion, while the remaining three necessarily require the insertion of at least two down-type Yukawa matrices.

In the mass basis all of these operators contribute to the four possible helicity structures of the tWb vertex

$$\mathcal{O}_{L(R)} = \frac{g}{\sqrt{2}} W^-_\mu \left[\bar{b}\gamma^\mu P_{L(R)} t\right] , \qquad \mathcal{O}_{LR(RL)} = \frac{g}{\sqrt{2}} W^-_{\mu\nu} \left[\bar{b}\sigma^{\mu\nu} P_{L(R)} t\right] . \tag{7}$$

However, at the same time they also enter FCNCs in the B meson sector at one-loop resulting in severe constraints from $B \to X_s\gamma$ branching ratio measurements[12] and $B_{s,d}$ meson oscillation observables.[14] Presently, the operator $\mathcal{O}_{LR}$ is least affected by these indirect constraints and thus has the potential to modify the $t \to bW$ decay characteristics in an observable way. However its contributions to $\mathcal{F}_+$ exhibit the same helicity suppression as the SM, mandating the evaluation of $t \to bW$ decay in presence of such NP contributions at next-to-leading order (NLO) in QCD.[15] After taking into account the existing indirect bounds on the operators in (7), contributions of $\mathcal{O}_{LR}$ indeed allow for largest enhancement in $\mathcal{F}_+$, but are still necessarily below 2‰. Turning to $\mathcal{F}_L$, observable effects due to most operators in (7) are again suppressed due to indirect constraints from B FCNCs, with the exception of $\mathcal{O}_{LR}$ where direct measurements at the Tevatron [7,8] are already providing competitive constraints (see figure 1).

3 Interplay with new CP violating contributions in $B_{d,s} - \bar{B}_{d,s}$ oscillations

Recently, possible NP effects in the $B_{d,s} - \bar{B}_{d,s}$, mixing amplitudes have received considerable attention. In particular within the SM, the $B^0 - \bar{B}^0$ mass difference and the time-dependent CP asymmetry in $B \to J/\psi K_s$ are strongly correlated with the branching ratio $\mathrm{Br}(B^+ \to \tau^+\nu)$.[17] The most recent global analyses point to a disagreement of this correlation with direct measurements at the level of 2.9 standard deviations.[16] Similarly in the B_s sector the recently measured CP-asymmetries by the Tevatron experiments, namely in $B_s \to J/\psi\phi$ [18] and in di-muonic inclusive decays [19] when combined, deviate from the SM prediction for the CP violating phase in $B_s - \bar{B}_s$ mixing by 3.3 standard deviations.[16]

Anomalous tWd_j interactions offer a possible solution of these anomalies via their contributions to $B_{d,s} - \bar{B}_{d,s}$ oscillation observables at the one-loop level. Within the MFV approach they contribute universally to B_d and B_s mixing amplitudes.[14] Such case has been analyzed in general [16,20] and found consistent with present data. Among the operators in (6), contributions of $\mathcal{Q}_{RR}$ and $\mathcal{Q}_{LRb}$ to $B_{s,d}$ oscillations are severely suppressed by constraints coming from the $B \to X_s\gamma$ decay.[12] On the other hand, contributions of operators $\mathcal{Q}_{LL}$ and $\mathcal{Q}_{LRt}$ cannot introduce new CP violating phases. Namely as shown recently,[21] a necessary condition for new flavor violating structures $\mathcal{Y}_x$ to introduce new sources of CP violation in quark transitions is that $\mathrm{Tr}(\mathcal{Y}_x[Y_u Y_u^\dagger, Y_d Y_d^\dagger]) \neq 0$, where $Y_{u,d}$ are the SM up- and down-quark Yukawa matrices. In MFV models (where $\mathcal{Y}_x$ is built out of Y_u and Y_d) this condition can only be met if $\mathcal{Y}_x$ contains products of both Y_u and Y_d. In (6) this is true for all operators except $\mathcal{Q}_{LL}$ and $\mathcal{Q}_{LRt}$. One can still use the present oscillation data to put bounds on contributions of these two operators. In particular, the resulting indirect constraint on the $\mathcal{O}_{LR}$ structure contributing to $t \to bW$ decay is comparable to both, the indirect $B \to X_s\gamma$ bound due to the same $\mathcal{Q}_{LRt}$ operator, as well the present direct $\mathcal{F}_L$ measurements as shown in figure 1. The remaining three operators in (6), $\mathcal{Q}'^{(\prime\prime)}_{LL}$ and $\mathcal{Q}'_{LRt}$ can contribute with new CP violating phases and are not overly constrained by the $B \to X_s\gamma$ decay rate measurement.[14] As such they can account for the recently observed anomalies in the CP violating observables related to $B_{s,d} - \bar{B}_{s,d}$ mixing.

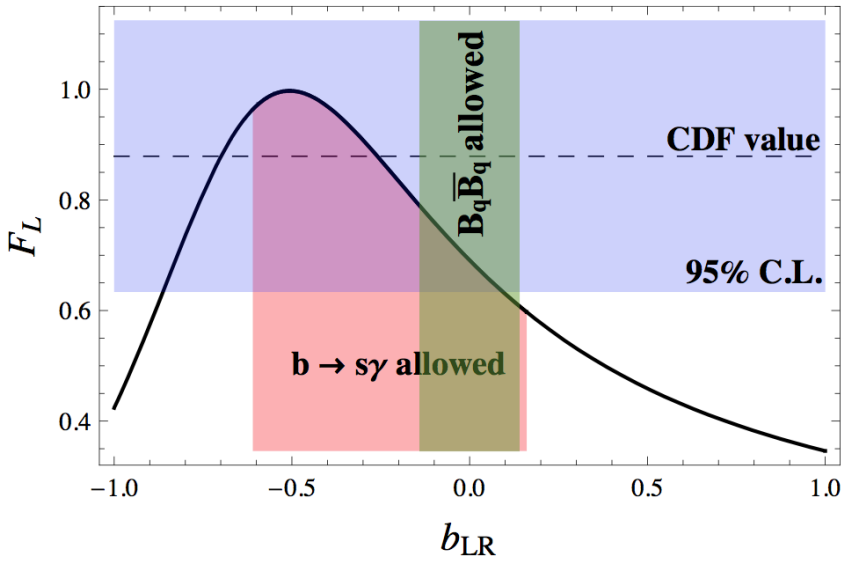

Figure 1: Prediction of $\mathcal{F}_L$ as a function of the normalized Wilson coefficient $b_{LR} = C_{LRt} v m_t/\Lambda^2$, where $v = 246$ GeV corresponding to the effective operator $\mathcal{Q}_{LRt}$ in (6) (other possible NP contributions being set to zero). Red band below the full curve shows the allowed interval for b_{LR} as given by the $B \to X_s\gamma$ analysis while the vertical green band denotes values allowed $B_{s,d}$ oscillation data, both at 95% C.L.. For comparison, we also show the recent CDF measurement of $\mathcal{F}_L$ given in eq. (3) (horizontal blue shaded region).

Finally, one can try to predict the effects of effective operators in (6) on the helicity fractions of the W boson in the $t \to bW$ decay channel, provided these same operators are responsible for new CP violating contributions in $B_{d,s}$ meson mixing. Both $\mathcal{Q}^{\prime(\prime\prime)}_{LL}$ have the same chiral structure as the SM contribution and thus cannot affect the helicity fractions. They only yield small corrections to the total $t \to bW$ decay rate. On the other hand $\mathcal{Q}'_{LRt}$ contributes to the helicity structure $\mathcal{O}_{LR}$. Under its influence, $\mathcal{F}_{L,+}$ can deviate by as much as 15% and 30% respectively compared to the SM predictions, although much smaller deviations are perfectly consistent with the ranges for the relevant Wilson coefficient of $\mathcal{Q}'_{LRt}$ preferred by the $B_{d,s}$ mixing analysis. A robust prediction that can be made however is that at least one of the two independent helicity fractions ($\mathcal{F}_{L,+}$) needs to deviate by at least 5% from the corresponding SM prediction. While this is clearly beyond the reach of the LHC experiments for the $\mathcal{F}_+$, it is comparable to the expected precision for $\mathcal{F}_L$.[9]

4 Conclusions

Polarization observables in $t \to bW$ decay as represented by the W helicity fractions $\mathcal{F}_i$ can probe the structure of the tWb vertex and are thus sensitive probes of possible new contributions to top quark interactions beyond the SM. Such effects can be analyzed using effective theory methods in terms of contributions of higher dimensional effective operators. Within the paradigm of MFV they can also be correlated with other observables, sensitive to new flavor violating contributions, in particular FCNC processes in the down sector. Then, indirect bounds from $B \to X_s\gamma$ disfavor significant deviations in the $\mathcal{F}_+$ helicity fraction for individual contributions of dimension-six effective operators, even after taking into account possible significant enhancements due to QCD corrections. On the other hand, the current measurements of $\mathcal{F}_L$ are already competitive with B physics observables in constraining the effective tWb dipole interactions.

Anomalous tWd_j interactions can also affect $B_{s,d} - \bar{B}_{s,d}$ mixing phenomenology at one loop.

The associated CP violating observables are particularly interesting to consider in light of recently reported anomalies in both $B_{s,d}$ sectors. Within MFV and up to $\mathcal{O}(m_s/m_b)$ suppressed effects, contributions induced via new tWd_j interactions to $B_{s,d}$ mixing amplitudes are universal. Upon single insertions of individual dimension-six effective operators contributing to tWb interactions, they yield constraints comparable in some cases to $B \to X_s\gamma$ and current direct measurements of $\mathcal{F}_i$. On the other hand, taking into account possible large bottom Yukawa effects, several of the MFV allowed effective operators can accommodate the CP violating anomalies and be consistent with constraints from $B \to X_s\gamma$ decay rate measurements. Unfortunately among these possibilities, only one operator predicts observable effects in $t \to bW$ decay. In particular, at least one of the two independent W helicity fractions $\mathcal{F}_{L,+}$ needs to deviate by at least 5% if this (dipole) operator is solely responsible for the new CP violating effects in $B_{s,d}$ oscillations. In the future, such CP violating contributions might nonetheless be probed more directly in decays of polarized top quarks, where it is possible to define sensitive CP violating helicity observables.[22] Such effects could possibly be measured in single top production at the LHC.

Acknowledgments

The author would like to thank the organizers of Moriond EW 2011 for the invitation to this exciting conference, as well as Jure Drobnak and Svjetlana Fajfer for a fruitful collaboration on the subject. This work is supported in part by the Slovenian Research Agency.

References

1. J. Alwall, R. Frederix, J. -M. Gerard, A. Giammanco, M. Herquet, S. Kalinin, E. Kou, V. Lemaitre *et al.*, *Eur. Phys. J.* C **49**, 791-801 (2007).
2. K. Nakamura *et al.* [Particle Data Group], *J. Phys.* G **37**, 075021 (2010).
3. T. E. W. Group [CDF and D0 Collaboration], [arXiv:0908.2171 [hep-ex]].
4. The ATLAS Collaboration, ATL-PHYS-PUB-2010-003, May 2010; The CMS Collaboration, CMS-PAS-TOP-09-005, 2009.
5. N. de Castro, CERN-THESIS-2008-083.
6. R. H. Dalitz and G. R. Goldstein, *Phys. Rev.* D **45**, 15311543 (1992) .
7. T. Aaltonen *et al.* [The CDF Collaboration], *Phys. Rev. Lett.* **105**, 042002 (2010),
8. V. M. Abazov *et al.* [D0 Collaboration], *Phys. Rev.* D **83**, 032009 (2011),
9. J. A. Aguilar-Saavedra, J. Carvalho, N. F. Castro, A. Onofre, F. Veloso, *Eur. Phys. J.* **C53**, 689-699 (2008).
10. H. S. Do, S. Groote, J. G. Korner, M. C. Mauser, *Phys. Rev.* D **67**, 091501 (2003),
11. M. Fischer, S. Groote, J. G. Korner, M. C. Mauser, *Phys. Rev.* D **63**, 031501 (2001),
12. B. Grzadkowski, M. Misiak, Phys. Rev. **D78** (2008) 077501.
13. R. S. Chivukula and H. Georgi, *Phys. Lett.* B **188**, 99 (1987); A. J. Buras, *et al. Phys. Lett.* B **500**, 161 (2001); G. D'Ambrosio, G. F. Giudice, G. Isidori and A. Strumia, *Nucl. Phys.* B **645**, 155 (2002)
14. J. Drobnak, S. Fajfer, J. F. Kamenik, [arXiv:1102.4347 [hep-ph]].
15. J. Drobnak, S. Fajfer, J. F. Kamenik, *Phys. Rev.* D **82**, 114008 (2010),
16. A. Lenz, U. Nierste, J. Charles *et al.*, [arXiv:1008.1593 [hep-ph]].
17. O. Deschamps, [arXiv:0810.3139 [hep-ph]].
18. V. M. Abazov *et al.* [D0 Collaboration], *Phys. Rev. Lett.* **101**, 241801 (2008) T. Aaltonen *et al.* [CDF Collaboration], CDF public note **9458**; G. Punzi, PoS **EPS-HEP2009** (2009) 022,
19. V. M. Abazov *et al.* [D0 Collaboration], *Phys. Rev. Lett.* **105**, 081801 (2010).

20. Z. Ligeti, M. Papucci, G. Perez, J. Zupan, *Phys. Rev. Lett.* **105**, 131601 (2010).
21. K. Blum, Y. Grossman, Y. Nir *et al.*, *Phys. Rev. Lett.* **102**, 211802 (2009).
22. J. A. Aguilar-Saavedra, J. Bernabeu, *Phys. Lett.* B **840**, 349-378 (2010).

Top quark properties at the Tevatron

Fabrizio Margaroli
Purdue University, Department of Physics, 525 Northwestern Avenue, West Lafayette, Indiana 47907, USA

The discovery of the top quark in 1995 opened a whole new sector of investigation of the Standard Model; today top quark physics remains a key priority of the Tevatron program. Some of the measurements of top quark properties, for example its mass, will be a long-standing legacy. The recent evidence of an anomalously large charge asymmetry in top quark events suggests that new physics could couple preferably with top quarks. I will summarize this long chapter of particle physics history and discuss the road the top quark is highlighting for the LHC program.

1 Introduction

The top quark is the last discovered quark, and by far the most massive particle in the Standard Model (SM) of particle interactions, its mass being approximately 30 times larger than the next-to-heaviest quark. The value close to $175\,\mathrm{GeV}c^2$ surprised the high energy community as it corresponds to a Yukawa coupling of the top quarks very close to one, suggesting a possible special role of the top quark in the electroweak symmetry breaking mechanism. Another very interesting consequence of its very large mass is the top quark lifetime being shorter than the hadronization time: $1/\Gamma_{top} < 1/\Lambda_{QCD}$: the top quark is the only quark that decays before hadronizing, and thus the only quark that can be studied naked. According to the SM, top quarks decay almost always to a W boson and a b quark. Top quarks can be produced singly through electroweak interactions, or more abundantly in pairs through QCD interactions. The pair production cross section is approximately 7.5 pb, more than a factor of two larger than the single top quark production cross section. More importantly, the larger energy scale of the pair production process and the striking $W^+W^-b\bar{b}$ decays allow for a much better background rejection than in the single top quark production, thus making the pair production the favored channel for top quark properties studies. The signature of $t\bar{t} \to WbWb$ events is completely characterized by the leptonic or hadronic decays of the two W bosons. It is tradition to call

"dileptonic decays" the events where both W bosons decay leptonically, "semileptonic" decays the ones where only one W boson decays leptonically, and "all-hadronic decays" the ones where both W bosons decay hadronically. The branching ratios (BR) are 10% 44% and 46% respectively. In the dilepton channel, the mere requirement of two leptons, missing transverse energy ($\not\!\!E_T$) as a signature of neutrinos, and jets gives a good signal-to-background (S/B) ratio. In the semileptonic channel, it is common to add to the lepton, $\not\!\!E_T$ and jets requirement, the additional requirement of at least one jet being identified as originating from a b quark (b-tagged jet) to achieve a good S/B ratio. In the all-hadronic channel, the requirement of at least one b-tagged jet and several high p_T jets in the final state is not sufficient to suppress the overwhelming QCD multijet background - additional kinematical and topological requirements are needed. The ideal balance between the branching ratio, S/B, and overall event reconstruction is achieved in the semileptonic channel, which is thus the best suited for most top quark properties measurements. Having collected more than $8.5\,\mathrm{fb}^{-1}$ of integrated luminosity at both experiments as of this conference, several top quark properties have been measured with increasing precision, while other properties have been investigated for the first time.

2 Intrinsic top quark properties

The CDF and D0 collaborations have measured the width of the top quark, excluded exotic values for its charge, and measured its mass. Among the intrinsic top quark parameters, the mass is the one that deserves most attention. In fact, the top quark mass is a free parameter in the SM, and indirect determination using constraints from precisely known electroweak parameters[1] can predict its value with limited precision. In turn, the precision on the top quark mass measurements is of crucial importance as the top quark mass is the single most sensitive parameter once using electroweak data to constrain the SM Higgs boson mass range[1,2]. The same experimental set of inputs, top quark mass included, is used to constrain a large number of new physics scenarios: extra dimensions, technicolor, fourth fermion generation, etc. From an experimental point of view, the precise knowledge of the top quark mass reflects in more precise predictions on the top quark production cross sections at colliders, and understanding of the production and decay kinematics. Thus the precise measurement of the top quark mass translates into refined measurements of all top quark properties.

As mention in the Introduction, the semileptonic channel is the one that provides the best sensitivity to top quark mass measurements. Still, different channels provide statistically independent results, and are affected by different systematics; it is thus of the utmost importance to measure the top quark mass in all available channels. The jet energy scale (JES) uncertainty is the largest systematic affecting top quark mass measurements, and it has been reduced sensibly by calibrating it *in situ* using events where at least one W boson decays hadronically. In this regard, the all-hadronic decays have the advantage of having two W bosons to calibrate the top quark mass. CDF updated a previously published measurement[3] using twice the data, totaling $5.8\,\mathrm{fb}^{-1}$. The event selections requires 6-to-8 jets in the final state, at least one $b-$tagged jet, low $\not\!\!E_T$, and utilizes a neural network to optimally suppress the QCD background while retaining large acceptance to the signal. The main challenge has been to cope with the increasing Tevatron instantaneous luminosity and the consequently increasingly larger backgrounds; CDF dealt with it by cutting to higher neural-network output value. CDF measures $M_{top} = 172.5 \pm 1.7(stat + JES) \pm 1.2(syst)\mathrm{GeV}/c^2$, where the first uncertainty contains the statistical part of the JES uncertainty as it is measured *in situ*. The distribution of the reconstructed top quark mass for the signal plus background can be seen in Figure 1.

Due to limitation in tracking and muon chamber pseudorapidity coverage, a relatively large fraction of forward electrons and muons are not identified at CDF. Also, the identification of hadronically decaying taus is especially difficult. A new CDF measurements measures the top

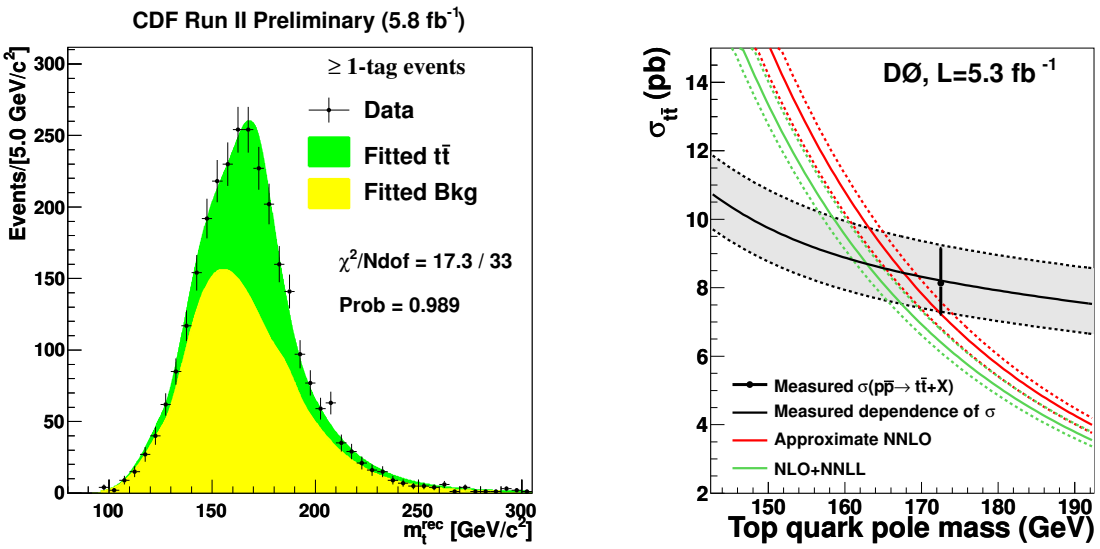

Figure 1: The left plot shows the reconstructed top quark invariant mass distribution in the all-hadronic decay mode, for events passing kinematical and topological cuts, and the requirement of at least one b-tagged jet. The green area represent the signal contribution as modeled with a Monte Carlo simulation of top quark mass equal to $172.5\,\mathrm{GeV}/c^2$. The right plot shows the top quark mass extracted from the D0 cross section measurement in the lepton+jets channel, in the hypothesis that the Monte Carlo encoded mass is the top quark pole mass.

quark mass in events selected with large $\not\!\!E_T$, at least four jets where at least one is b-tagged, and further applies topological and kinematical requirements through a neural network, to recover the semileptonic events where electrons/muons/taus are not identified. The sample composition has been understood in the context of an earlier measurement of $\sigma_{t\bar{t}}$ in the same dataset[5]. In these events, it is impossible to fully reconstruct the kinematics due to the undetected $W \to \ell\nu_\ell$. Still, the reconstruction of only one of the two top quarks is sufficient to extract an M_{top} measurement. Using $5.6\,\mathrm{fb}^{-1}$ of data, CDF measures[6] $M_{top} = 172.3 \pm 2.4(stat + JES) \pm 1.0(syst)\,\mathrm{GeV}/c^2$. To increase precision in the M_{top} determination, CDF combines the most precise measurement in each decay mode. The event selection for the several decay channels are devised to select independent datasets. The combination requires properly taking into account the correlation of the systematic uncertainties among all measurements. CDF uses the BLUE method[7] and obtains an average of $M_{top} = 172.7 \pm 0.6(stat) \pm 0.9(syst)\,\mathrm{GeV}/c^2$. The CDF average shown at this conference is as precise as the 2010 Tevatron average[9]. All the measurements that enter into the CDF, D0, and thus the Tevatron combination are calibrated to Monte Carlo simulations. Thus the "mass" measured is effectively the definition contained in the leading order (LO) Monte Carlo used; theorists agree that the Monte Carlo mass should be very close to the top quark pole mass[11]. Beyond LO quantum chromodynamics (QCD), the mass of the top quark is a convention-dependent parameter, the other dominant convention being the MS scheme. To probe further into this ambiguity, D0 compares the measured inclusive $t\bar{t}$ production cross section[10] with fully inclusive calculations at higher-order QCD that involve an unambiguous definition of M_{top}[12,13] and compares the results to MC[14]. The measurement favors the pole mass hypothesis over the $\bar{\mathrm{M}}$S hypothesis.

By the end of the Tevatron run, the CDF and D0 collaborations will analyze a dataset more than twice as large as the one shown at this conference. It is expected that the precision on M_{top} measurements will drop below $1\,\mathrm{GeV}/c^2$, and that the scheme interpretation would be better understood.

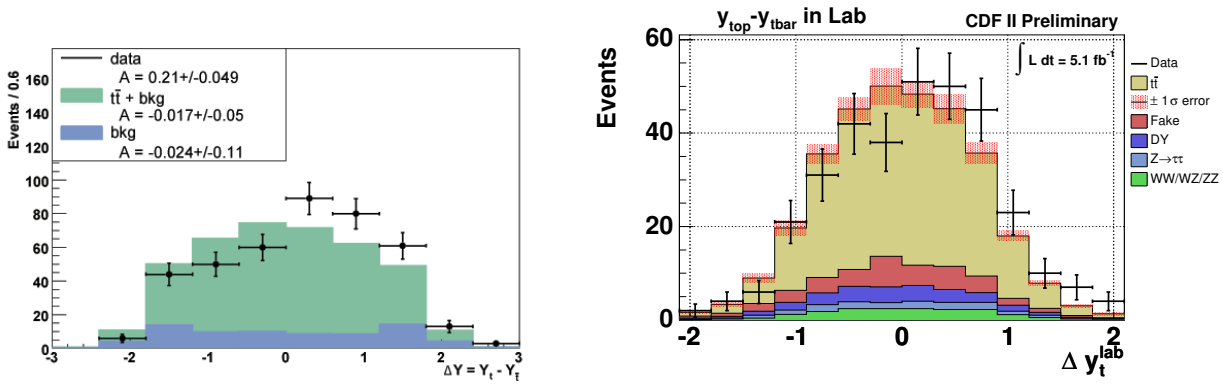

Figure 2: The left plot shows the distribution of Δy at high top-antitop invariant mass in the lepton+jets channel. The right plot shows the Δy distribution in the dilepton channel. No invariant mass cut is applied in the latter plot.

3 Top quark production properties

The top quark pair production cross section has been measured in all decay modes by the Tevatron (and in the semileptonic and dileptonic modes at the LHC collider). The most precise determination comes from CDF[15] and has a precision of 6.5% and is in excellent agreement with approximate NNLO[12] QCD computation and consistent with NLO+next-to-leading-log (NLL) computation[13]. While these results are impressive, there is still room for a contribution from new physics at top quark production level of the order of 0.5 - 1.0 pb. A sensitive probe of the SM nature of top quark production at the Tevatron $p\bar{p}$ collider is the measurement of the forward-backward asymmetry of top quarks production, where "forward" ("backward") stands for "along the proton (antiproton) direction". QCD predicts a positive asymmetry of about 5% originating from interference effects between LO and NLO diagrams[16]. Early CDF and D0[17] measurements in the semileptonic decay mode showed a positive deviation of approximately $2\,\sigma$ from the SM predictions. Several new physics scenarios predict this asymmetry to be enhanced due to $t\bar{t}$ creation through exotic mechanisms contributing to $s-$ or $t-$channel diagrams[a]. In most scenarios, the departure from SM prediction increases by looking at particular regions of the phase space. Using about $5\,\mathrm{fb}^{-1}$ of data, CDF investigated this asymmetry as a function of the rapidity difference among top and antitop quarks, and as a function of the top-antitop system invariant mass[19]. The asymmetry was found to be the largest for events with $M(t\bar{t}) > 450\,\mathrm{GeV}/c^2$, amounting to $48 \pm 11\%$, more than $3\,\sigma$ deviation from the SM predictions. An independent measurement performed in the dileptonic decay mode observes an inclusive asymmetry of $42 \pm 16\%$, corresponding to a $2.3\,\sigma$ deviation from the SM[20]. The rapidity difference between the top and antitop quarks in the semileptonic and dileptonic decay modes can be observed in Figure 2. The statistics in the dileptonic decay mode is not yet sufficient to establish a trend of the asymmetry as a function of the total invariant mass. In summary, the CDF and D0 collaborations observe a consistently larger-than-expected asymmetry. CDF notes that this asymmetry (and the deviation from the SM) grows with the invariant mass of the system. This latter result ignited the already present interest by theoreticians, and is currently being used to set constraints to new physics scenarios affecting top quark production. One particular model, the $t-$channel production through leptophobic Z' boson exchange, saw a surge in popularity after CDF published a study showing a possible new resonance decaying to two jets in the $\ell\nu jj$ data sample[21]. More studies are ongoing at both collaborations.

[a] One notable exception would be the possibility of a new process giving rise to top quarks and invisible particles that blends with the SM $t\bar{t}$ production[18].

At the Tevatron, the $p\bar{p}$ collision center-of-mass (COM) energy of 1.96 TeV is large enough for heavy particles to be produced occasionally with very large Lorentz boost. The identification of boosted heavy objects decaying to jets will be a very useful tool in the search for new physics at colliders with even larger COM such as the LHC, as it would provide large discrimination of interesting signals against the much more common QCD background. One notable example would be the search for the low mass Higgs boson in $\ell\nu b\bar{b}$ events, where with sufficient boost the $b\bar{b}$ system would appear as a single massive jet. Another example is the search for heavy resonances decaying to top quarks, as for example a leptophobic Z' or an axigluon of the kind that could explain the anomalously large forward backward asymmetry described in this Section. CDF performed the first search for SM $t\bar{t}$ production through the boosted top signature[22]. The SM predicts only a very small fraction of top quarks to be produced with $p_T^{top} > 400GeV$, corresponding to a cross section of approximately a few fb. In this momentum range, the top daughter decay particles would appear as highly collimated. In case of an hadronic top decay $t \to Wb \to qqb$ the signature would be that of a large jet with substructure. The decays of a boosted top with decays $t \to Wb \to \ell\nu b$ are more difficult as leptons are usually required to be isolated to suppress the fake rate. CDF looks at both the all-hadronic (semileptonic) final state, reconstructing jets using a clustering algorithm with the cone size parameter set to 1.0, significantly larger than the one used in top quark physics. The jets mass (and missing transverse energy significance) are used as discriminants against the vast background of QCD production of lighter quarks and gluons. In the case of boosted top quarks decaying hadronically, the jet mass is in fact close to the top quark mass itself, while it peaks at lower values in the case of QCD light quark/gluon production. For top quarks decaying to $\ell\nu b$, the requirement of large missing trasnverse energy alone is used to reject the QCD background. Analyzing $6\,\text{fb}^{-1}$ of data, CDF finds a modest excess of events: 58 candidate events with an estimated background of 44 ± 15 events. In absence of a signal, this analysis sets a 95% confidence level (C.L.) upper limit on the rate of top quark production for top quarks with $p_T > 400\,\text{GeV}/c$ of 40 fb. The same data is used to search for pair production of a massive object with masses comparable to that of the top quark, setting an upper limit on the pair production of 20 fb at 95% C.L..

4 Top quark decay properties

While top and anti-top quarks are pair produced unpolarized at hadron colliders, the orientations of their spins are correlated. Top quarks are the ideal laboratory for spin correlation studies as they decay before this correlation can be affected by the fragmentation process. Spin correlation is also a sensitive probe of beyond the standard model scenarios, as different model would predict different top polarizations. The charged leptons from the $t \to Wb \to \ell\nu b$ decays are the probes with the highest sensitivity to the direction of the top quark spin. In a recent paper[23] D0 measures the strength of the $t\bar{t}$ spin correlation C from a differential angular distribution involving the angles between the flight direction of the two decay leptons in the rest frames of their respective top quarks and the spin quantization axis. NLO QCD computation predicts this quantity to be $C = 0.78 \pm 0.03$. The measurement uses $5.4\,\text{fb}^{-1}$ of $p\bar{p}$ collision and finds $C = 0.10 \pm 0.45$, in reasonable agreement with the SM predictions.

The on-shell W bosons from top quark decays can have three possible helicity states. SM predicts that the top quark decays via the $V - A$ charged weak current interaction, which strongly suppresses the presence of right-handed W bosons. The fraction of $t\bar{t}$ events where the W bosons are produced longitudinally polarized, f_0, left-handed, f_- or right-handed, f_+ depend upon the masses of the top quark M_{top} and W boson (M_W). Using the current world average values for M_{top} and M_W, the expected SM values are[24]. $f_0 = 0.698$, $f_- = 0.301$, and $f_+ = 4.1 \times 10^{-4}$. A significant deviation from these predictions would provide strong evidence of physics beyond the SM, indicating either a departure from the expected $V - A$ structure of

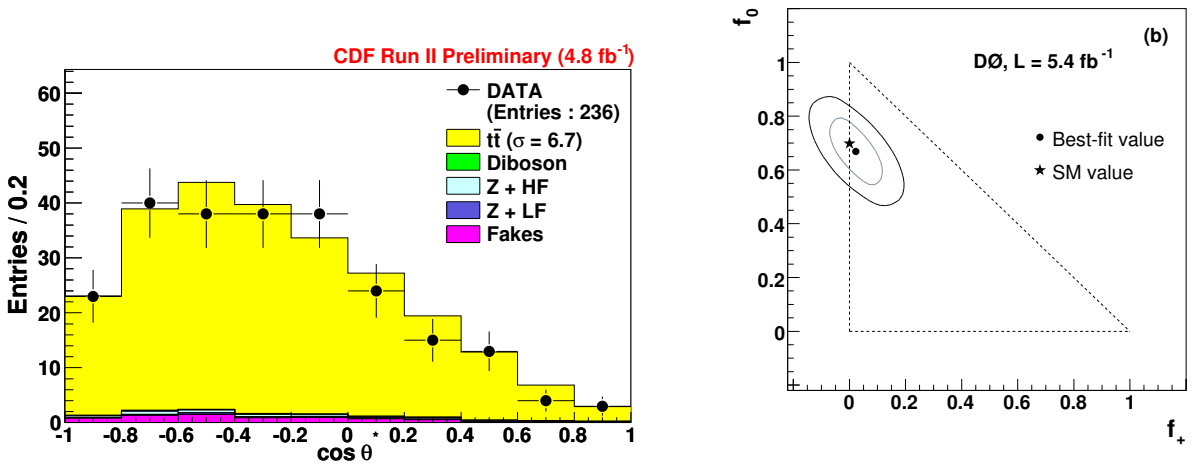

Figure 3: The left plot shows the $cos\theta^*$ distribution comparison between data and expected SM contributions in the CDF dilepton sample. The right plots shows the model-independent D0 measurement in the 2-dimensional plane of f_+ and f_0, along with the SM predictions.

the tWb vertex, or the presence of a non-SM component in the $t\bar{t}$ candidate sample. CDF and D0 measured simultaneously the fraction of longitudinal and right-handed W bosons from top quark decays in the semileptonic and dileptonic decay modes. The latest CDF measurement[25] analyzes $4.8\,\mathrm{fb}^{-1}$ of dileptonic events to measure the following fractions $f_+ = 0.12 \pm 0.12$ and $f_0 = 0.78 \pm 0.20$. In order to measure the W boson helicity fractions, the angle θ^* between the down-type decay product of the W boson in the rest frame of the latter, with respect to the W boson flight direction in the top quark rest frame is measured. The distribution of the cosine of this angle differs for the three possible helicity fractions, which is exploited in the measurement. The plot in Figure 3 shows the distribution for the observable sensitive to the W boson polarization and the agreement with SM expectations. D0 reports a measurement in the dileptonic and semileptonic final states using $5.4\,\mathrm{fb}^{-1}$ of collisions[26] of $f_+ = 0.02 \pm 0.05$ and $f_0 = 0.67 \pm 0.10$.

The knowledge of the color-connections between jets can serve as a powerful tool for separating processes that would otherwise appear similar. For example, in the decay of a Higgs (H) boson to a pair of b quarks, the two b quarks are color connected to each other, since the H is a color singlet,whereas in $g \to b\bar{b}$ background events, they are color-connected to beam remnants since the gluon is a color-octet. The technique involves measuring a vectorial quantity called jet pull, which represents the eccentricity of the jet in the $\eta - \phi$ plane and the direction of the major axis of the ellipse formed from the jet energy pattern. Jets tend to have their pull pointing towards their color-connected partner: in $H \to b\bar{b}$ events, the pulls of the two b-jets tend to point towards each other, whereas in $g \to b\bar{b}$ events, they point in opposite directions along the collision axis. D0 tests this technique looking at the light quark jets coming from the W boson decay in semileptonic events using $5.3\,\mathrm{fb}^{-1}$ of collisions [28]. The data are compared to both standard model $t\bar{t}$ Monte Carlo (with a color-singlet W boson) and an alternative model of $t\bar{t}$ with a hypothetical color-octet "W" boson decaying hadronically. D0 determines the fraction of events coming from color-singlet W boson decay ($f_{Singlet}$) to be $f_{Singlet} = 0.56 \pm 0.42$, in agreement with the expectation of $f_{Singlet} > 0.277$ at 95% C.L.

Searches for flavor changing neutral current (FCNC) are also sensitive probes to new physics. The top quark decays $t \to Zu(c)$ are heavily suppressed in the SM; still, extensions of the SM such as SUSY or quark compositeness would predict much larger values. D0 looks for the first time at the possible signature of $t\bar{t} \to ZqWb \to \ell^+\ell^- q\ell b$ and in the absence of signal, sets a limit

on the hypothetical branching ratio of top quarks to Zq: $B(t \to Zq) < 3.2\%$ at the 95% C.L. This result surpasses previous limits[30]. The result presented here translates into an observed limit on the FCNC coupling of $vtqZ < 0.19$ for $M_{top} = 172.5\,\mathrm{GeV}/c^2$.

5 Conclusions

Top quark physics has proceeded with giant's steps over the first results obtained with Tevatron Run I data. Analyzing a top quark sample 100 times larger than the one needed for its discovery, the CDF and D0 collaborations have been able to greatly expand the range of top quark properties measurements, increase precision to unprecedented levels, and to probe in a much finer detail the nature of this very peculiar quark. For 15 years, top quark physics remained a Tevatron prerogative. In 2011 the first statistically significant deviation from SM predictions appeared in the charge asymmetry of top quark pair production, immediately confirmed in an independent dataset. While the possibility of an underestimation of the SM predictions is still open, this result gave rise to en enormous interest in the theoretical community. Twice the current dataset will be available in a few months, and it is expected that its study will increase further the precision of measurements such as the top quark mass one, and shed a brighter light on subtler SM effects. Recently, the LHC collider produced the definitive confirmation of abundant top quark production in pp collisions; according to projections the LHC top sample by 2012 could be one order of magnitude larger than the Tevatron one. It is an exciting time for top quark physics, one where the top sector of the SM will be under serious stress.

Acknowledgments

The author wish to thank the CDF and D0 collaborations for their effort in advancing the understanding of top quark physics, and the conference organizers for the excellent organization and the beautiful settings that stimulated exchanges between the experimental and theoretical community. In this regard, I would like to thank in particular Andreas Weiler, Jernej Kamenik, Michele Papucci, Adam Falkowski, Manuel Perez-Victoria and Gero von Gersdorff for the interesting conversations.

1. H. Flacher, M. Goebel, J. Haller, A. Hocker, K. Monig and J. Stelzer, Eur. Phys. J. C **60** (2009) 543 arXiv:0811.0009.
2. See also Max Baak, these proceedings.
3. T. Aaltonen *et al.* [The CDF Collaboration], Phys. Rev. D **81**, 052011 (2010) arXiv:1002.0365.
4. T. Aaltonen *et al.* [CDF Collaboration] CDF Conference Note 10456.
5. T. Aaltonen *et al.* [CDF Collaboration], arXiv:1105.1806.
6. T. Aaltonen *et al.* [CDF Collaboration] CDF Conference Note 10433.
7. L. Lyons, D. Gibaut, and P. Clifford, Nucl. Instrum. Meth. **A270** (1988) 110.
8. T. Aaltonen *et al.* [CDF Collaboration] CDF Conference Note 10444.
9. Tevatron Electroweak Working Group, [CDF and D0 Collaborations], arXiv:1007.3178.
10. V. M. Abazov *et al.* [D0 Collaboration], arXiv:1101.0124.
11. D. Glenzinski, Nuovo Cim. B **123** (2008) 1085.
12. S. Moch and P. Uwer, Nucl. Phys. Proc. Suppl. **183**, 75 (2008).
13. V. Ahrens, A. Ferroglia, M. Neubert, B. D. Pecjak and L. L. Yang, JHEP **1009** 097 (2010).
14. V. M. Abazov *et al.* [D0 Collaboration], arXiv:1104.2887.
15. L.Li, these proceedings.
16. J. M. Campbell and R. K. Ellis, Nucl. Phys. Proc. Suppl. **205-206**, 10 (2010) arXiv:1007.3492.

17. V. M. Abazov *et al.* [D0 Collaboration], D0 Conference Note 6062.
18. G. Isidori and J. F. Kamenik, arXiv:1103.0016.
19. T. Aaltonen *et al.* [CDF Collaboration], arXiv:1101.0034.
20. T. Aaltonen *et al.* [CDF Collaboration] CDF Conference Note 10436.
21. T. Aaltonen *et al.* [CDF Collaboration], Phys. Rev. Lett. **106** (2011) 171801 arXiv:1104.0699.
22. T. Aaltonen *et al.* [CDF Collaboration] CDF Conference Note 10234.
23. V. M. Abazov *et al.* [D0 Collaboration], arXiv:1103.1871.
24. M. Fischer *et al.*, Phys. Rev. D **63**, 031501(R) (2001).
25. T. Aaltonen *et al.* [CDF Collaboration] CDF Conference Note 10333.
26. V. M. Abazov *et al.* [D0 Collaboration], Phys. Rev. D **83** (2011) 032009 arXiv:1011.6549.
27. T. Aaltonen *et al.* [The CDF Collaboration], Phys. Rev. Lett. **105** (2010) 042002 arXiv:1003.0224.
28. V. M. Abazov *et al.* [D0 Collaboration], Phys. Rev. D **83** (2011) 092002 arXiv:1101.0648.
29. V. M. Abazov *et al.* [D0 Collaboration], arXiv:1103.4574.
30. T. Aaltonen *et al.* [CDF Collaboration], Phys. Rev. Lett. **101** (2008) 192002 [arXiv:0805.2109 [hep-ex]].

TOP-QUARK FORWARD-BACKWARD SYMMETRY

SUSANNE WESTHOFF
Institut für Physik (THEP), Johannes Gutenberg-Universität
D-55099 Mainz, Germany

Top-quark pair production at the Tevatron is discussed within the Randall-Sundrum model of warped extra dimensions. Generically, the exchange of massive Kaluza-Klein gluons has the potential to generate a large forward-backward asymmetry. In models with an anarchic flavor structure, however, their coupling to the light quarks inside the proton is strongly suppressed. The consequent suppression of the asymmetry at tree level is lifted at next-to-leading order. Still, it is not possible to increase the forward-backward asymmetry with respect to the Standard-Model prediction in this framework.

1 Introduction

Since the discovery of the top quark in 1995, the experiments at the Tevatron have made remarkable achievements in measuring the properties of the heaviest fermion in the Standard Model (SM). The motivation behind this effort is evident: due to its particularly large mass, the top quark is supposed to play a key role in understanding the mechanism of electroweak symmetry breaking. Within the SM, all quarks possess the same gauge couplings, which prevents us from explaining their strong mass hierarchy by a fundamental interaction. Extensions of the SM addressing the origin of quark masses commonly imply new gauge interactions that distinguish the heavy top quark from the light quarks. We will concentrate on massive color-octet gauge bosons with strong couplings to top quarks, which occur in a wide class of models. Examples include colorons in topcolor models, axigluons from flavor non-universal chiral color, and Kaluza-Klein (KK) gluons in warped extra dimensions. They all share the feature to yield characteristic effects in top-quark observables, which serve as probes of the underlying theory. Our framework will be the Randall-Sundrum (RS) model, where the fermion mass hierarchy can be explained by the localization of fermion fields in the bulk of a warped extra dimension. These localizations manifest themselves in flavor- and chirality-specific couplings of quarks to KK excitations of the gluon. Since the coupling to top quarks in this setup is typically strong, the exchange of a massive KK gluon is expected to affect top-quark pair production.

Let us briefly summarize the status of measurements in top-antitop quark production at the Tevatron. In proton-antiproton collisions at a center-of-mass (CM) energy of $\sqrt{s} = 1.96\,\text{TeV}$, the production of $t\bar{t}$ pairs is dominated by the partonic process $q\bar{q} \to t\bar{t}$. The measured total cross section and its distribution with respect to the invariant mass of the top-antitop pair, [1,2]

$$\sigma_{t\bar{t}} = (7.50 \pm 0.48)\,\text{pb}\,, \qquad (d\sigma_{t\bar{t}}/dM_{t\bar{t}})^{M_{t\bar{t}}\in[0.8,1.4]\,\text{TeV}} = (0.068 \pm 0.034)\,\frac{\text{fb}}{\text{GeV}}\,, \tag{1}$$

are in good agreement with their SM predictions. In contrast, the forward-backward asymmetry of the top quark is in variance with the result in Quantum Chromodynamics (QCD): the

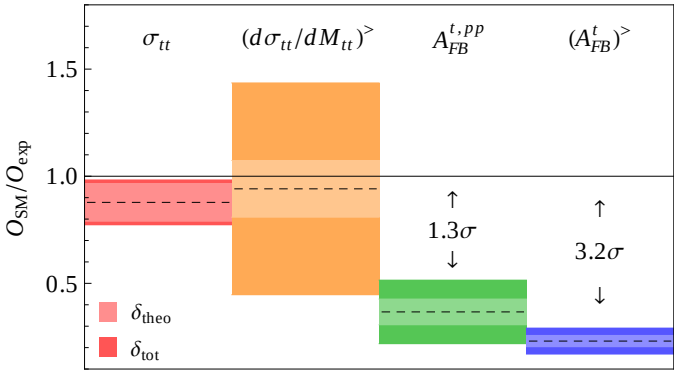

Figure 1: Top-quark pair production in the SM. The ratio $O_{\rm SM}/O_{\rm exp}$ is shown for the total cross section $\sigma_{t\bar{t}}$, the distribution for $M_{t\bar{t}} \in [0.8, 1.4]$ TeV, the inclusive asymmetry in the lab frame $A_{\rm FB}^{t,p\bar{p}}$ and for $M_{t\bar{t}} > 450\,\text{GeV}$. Central values are drawn as dashed lines.

measured total asymmetry in the laboratory frame and the result at $t\bar{t}$ invariant mass measured at CDF, [3]

$$(A_{\rm FB}^t)_{\rm exp}^{p\bar{p}} = (15.0 \pm 5.0_{\rm stat} \pm 2.4_{\rm syst})\%\,, \qquad (A_{\rm FB}^t)_{\rm exp}^{M_{t\bar{t}}>450\,\text{GeV}} = (47.5 \pm 11.2)\%\,, \tag{2}$$

exceed the SM predictions by about $1.3\,\sigma$ and $3.2\,\sigma$, respectively. [a] The situation is displayed in Figure 1, where we show the ratio of the SM prediction with respect to the CDF measurement for the four observables discussed above. The observed pattern suggests new physics (NP) with a large positive contribution to the asymmetry, but only little impact on the cross section.

In a theory with CP-conserving couplings, the forward-backward asymmetry is equivalent to a charge asymmetry,

$$A_{\rm FB}^t = \frac{\sigma_a}{\sigma_s}\,, \qquad \sigma_{a(s)} = \int_0^1 \cos\theta \left[\frac{d\sigma(p\bar{p}\to t\bar{t}X)}{d\cos\theta} - (+)\frac{d\sigma(p\bar{p}\to \bar{t}tX)}{d\cos\theta}\right]. \tag{3}$$

It requires a production amplitude that is antisymmetric under the interchange of t and $\bar{t}$ in the final state for a fixed top-quark scattering angle θ. In QCD, $t\bar{t}$ production is charge-symmetric at tree level. The asymmetry arises at next-to-leading order (NLO) from the interference of the tree-level gluon exchange with QCD box diagrams and from the interference of final- and initial-state radiation. Up-to-date QCD calculations predict a small value of the asymmetry in the laboratory frame, $(A_{\rm FB}^t)_{\rm SM}^{p\bar{p}} = (4 - 5.6)\%$ [6]. A large charge asymmetry is expected to be generated by the positive interference of new physics (NP) with the SM gluon exchange at tree level. Any new particle in the s channel of $t\bar{t}$ production ought to exhibit large axial-vector couplings to both light quarks, g_A^q, and top quarks, g_A^t, fulfilling $g_A^q\, g_A^t < 0$ for a mass of $\mathcal{O}(1\,\text{TeV})$. The product of vector couplings, $g_V^q\, g_V^t$, however, is restricted to be small in order to fit the measured charge-symmetric cross section $\sigma_{t\bar{t}}$ and the spectrum $d\sigma_{t\bar{t}}/dM_{t\bar{t}}$.

Within the RS model, KK gluons have axial-vector couplings to quarks, due to the different localizations of left- and right-handed quark fields in the extra dimension. We explore the possibility of a large top-quark forward-backward asymmetry from KK gluon exchange in the RS model with an anarchic flavor structure. It will turn out that within this setup axial-vector couplings of KK gluons to top quarks are large, but strongly suppressed for light quarks. The asymmetry at tree level is thus negligibly small. We will explain how the suppression is lifted at NLO, yielding the leading RS contributions to the asymmetric cross section σ_a. These effects, however, partially cancel with tree-level contributions to the symmetric cross section σ_s, which normalizes the forward-backward asymmetry. The observable $A_{\rm FB}^t$ thus cannot be increased with respect to its SM prediction within the flavor-anarchic RS model.

[a] This excess has also been observed in $t\bar{t}$ dilepton events at CDF [4] and by the D0 collaboration [5].

2 Randall-Sundrum model with flavor anarchy

The Randall-Sundrum model was originally designed to explain the large hierarchy between the electroweak and the Planck scales by gravitational red-shifting in a warped extra dimension [7]. If the SM fermions are allowed to propagate into the bulk of the fifth dimension, the RS model also offers a geometrical description of flavor. As anticipated, the fermion mass hierarchy is explained by different localizations in the extra dimension: the wave functions of light fermions are exponentially localized in the ultraviolet (UV), while the heavy fermions reside in the infrared (IR). The effective Yukawa couplings, resulting from wave-function overlap with the IR-localized Higgs boson, therefore exhibit an exponential hierarchy. Starting from flavor anarchy, i.e. arbitrary five-dimensional Yukawa couplings of $\mathcal{O}(1)$, one naturally obtains a strong hierarchy of fermion masses, quantified by the warp factor of the extra dimension, $\exp(L) = \Lambda_{\rm UV}/\Lambda_{\rm IR} \approx 10^{16}$. The actual localization of fermions is determined by bulk mass parameters c_f. For quarks, the measured masses and CKM mixings require $c_q < -1/2$ and $c_t > -1/2$, corresponding to UV and IR localization, respectively.

The pattern of localization of the quark fields has a crucial impact on their couplings to KK gluons. Since KK excitations of the SM particles are associated with a scale $M_{\rm KK} \gtrsim 1\,\text{TeV}$, virtual RS effects in top-quark pair production can be described in terms of dimension-six operators in the framework of an effective theory. The low-energy Lagrangian for the exchange of a KK gluon in the s channel of $q\bar{q} \to t\bar{t}$ is given by [b]

$$\mathcal{L}_{\rm eff} = \sum_q \sum_{A,B=L,R} C_{q\bar{q}}^{AB}\, Q_{q\bar{q}}^{AB}\,, \qquad Q_{q\bar{q}}^{AB} = (\bar{q}_A\,\gamma_\mu T^a\, q_A)(\bar{t}_B\,\gamma^\mu T^a\, t_B)\,, \tag{4}$$

where $A, B = L, R$ denote the quark chiralities and T^a are the generators of color $SU(3)$. For phenomenology, it is useful to consider the combinations of Wilson coefficients that correspond to vector and axial-vector structures,

$$C_{q\bar{q}}^V = \sum_{A,B=L,R} C_{q\bar{q}}^{AB}\,, \qquad C_{q\bar{q}}^A = \sum_{A\neq B} (C_{q\bar{q}}^{AA} - C_{q\bar{q}}^{AB})\,. \tag{5}$$

These effective couplings depend on the overlap of the quark wave functions with the IR-localized KK gluons. The size of the couplings is governed by the quark profiles, given to good approximation by [8]

$$F^2(c_t) \approx 1 + 2c_t\,, \qquad F^2(c_q) \approx (-1-2c_q)\, e^{L\,(2c_q+1)}\,. \tag{6}$$

For mass parameters $c_t > -1/2$ and $c_q < -1/2$, the profile function is of $\mathcal{O}(1)$ for top quarks, but exponentially suppressed for light quarks. In terms of these quark profiles, the Wilson coefficients for KK gluon exchange from Eq. (5) read [8,9]

$$C_{q\bar{q}}^V \;\approx\; -\frac{\pi\alpha_s}{M_{\rm KK}^2}\,\left[F^2(c_{t_R}) + F^2(c_{t_L})\right]\,, \tag{7}$$

$$C_{q\bar{q}}^A \;\approx\; -\frac{\pi\alpha_s}{M_{\rm KK}^2}\,L\,\left[F^2(c_{q_R}) - F^2(c_{q_L})\right]\left[F^2(c_{t_R}) - F^2(c_{t_L})\right]\,, \tag{8}$$

where α_s is the strong coupling constant of QCD. The vector coefficient $C_{q\bar{q}}^V$ is dominated by the top-quark profiles. Comparing with Eq. (6), one observes that it is large and positive due to the IR localization of the top quark. We define the dimensionless coefficient $\tilde{C}_{q\bar{q}}^V \equiv 1\,\text{TeV}^2\, C_{q\bar{q}}^V = \mathcal{O}(1)$. The axial-vector coefficient $C_{q\bar{q}}^A$ is enhanced by the warp factor $L \approx 37$. It is proportional to the difference between the profiles for left- and right-handed quarks. For top quarks, this

[b] Further contributions of KK gluons in the t channel, as well as of Z, γ, their KK excitations, and the Higgs boson, are numerically subleading and therefore neglected.

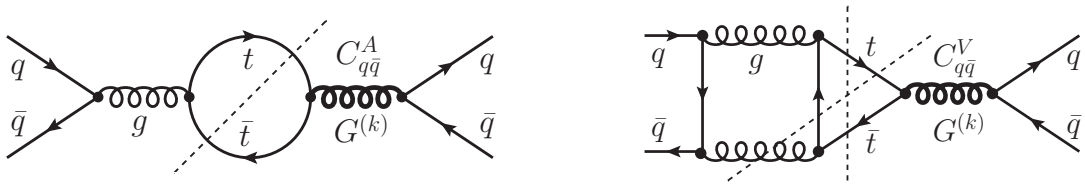

Figure 2: Charge-asymmetric contributions to $\sigma_a(p\bar{p} \to t\bar{t})$ via the exchange of Kaluza-Klein gluons $G^{(k)}$ at leading order (left) and next-to-leading order (right).

difference may be large, yielding a sizeable axial-vector coupling g_A^t to KK gluons. The axial-vector coupling of light quarks, however, is doubly suppressed: firstly, left- and right-handed light quarks' profiles ought to be largely identical, in order to accommodate the measured quark masses and mixings. Secondly, and even more severely, light quarks are localized in the UV and thereby exponentially suppressed, as stated below Eq. (6). The effective axial-vector coefficient is thus strongly suppressed, $\tilde{C}^A_{q\bar{q}} \equiv 1\,\text{TeV}^2\, C^A_{q\bar{q}} = \mathcal{O}(10^{-3})$.

3 Top-quark pair production

What are the resultant effects of KK gluons on the forward-backward asymmetry in top-quark pair production? The charge-asymmetric (-symmetric) cross section defined in Eq. (2) is given by

$$\sigma_{a(s)} = \frac{\alpha_s}{m_t^2} \sum_q \int_{4m_t^2}^s \frac{d\hat{s}}{s} \left[ff_{q\bar{q}}(\hat{s}/s, \mu_f) - (+) ff_{\bar{q}q}(\hat{s}/s, \mu_f) \right] A_{q\bar{q}}\,(S_{q\bar{q}})\,, \tag{9}$$

where $\hat{s}$ denotes the partonic CM energy, and the sum is taken over all quark flavors q inside the proton. The parton luminosities $ff_{q\bar{q}}(\hat{s}/s, \mu_f)$ as well as the hard-scattering kernels $A_{q\bar{q}}$ and $S_{q\bar{q}}$ in QCD are defined in [10]. RS contributions at leading order (LO) arise from the interference of the s-channel exchange of a KK gluon with the tree-level gluon diagram. For the charge-asymmetric contribution, this is shown on the left-hand side of Figure 2. The corresponding hard-scattering kernels for inclusive symmetric and asymmetric $t\bar{t}$ production are readily computed using the effective Lagrangian in Eq. (4),

$$S^{\text{LO}}_{q\bar{q}} = \frac{\hat{s}}{M^2_{\text{KK}}} \frac{\rho}{216} \sqrt{1-\rho}\,(2+\rho)\;\tilde{C}^V_{q\bar{q}}\,, \qquad A^{\text{LO}}_{q\bar{q}} = \frac{\hat{s}}{M^2_{\text{KK}}} \frac{\rho}{144}\,(1-\rho)\;\tilde{C}^A_{q\bar{q}}\,, \tag{10}$$

with $\rho = 4m_t^2/\hat{s}$ and M_{KK} in units of 1 TeV. Referring to our considerations in Section 2, we expect significant contributions of KK gluons to the cross section $\sigma_{t\bar{t}}$, which is sensitive to the vector coefficient $\tilde{C}^V_{q\bar{q}} = \mathcal{O}(1)$. Tree-level effects on the charge-asymmetric amplitude, however, are negligibly small due to the strongly suppressed axial-vector coefficient $\tilde{C}^A_{q\bar{q}} = \mathcal{O}(10^{-3})$. Thus there is no large forward-backward symmetry at tree level.

The suppression can be lifted by going to NLO, after paying the price of a loop factor $\alpha_s/(4\pi)$. The interference of a tree-level KK gluon exchange with a QCD box diagram, shown on the right-hand side of Figure 2, has the same topology as the leading contribution to the asymmetry in QCD. The charge-asymmetric amplitude thus involves the unsuppressed vector coefficient $C^V_{q\bar{q}}$. The asymmetric hard-scattering kernel at NLO is given by

$$A^{\text{NLO}}_{q\bar{q}} = \frac{\alpha_s}{4\pi} \frac{\hat{s}}{M^2_{\text{KK}}} \frac{\tilde{A}_{q\bar{q}}}{16\pi}\,\tilde{C}^V_{q\bar{q}}\,, \tag{11}$$

with the SM coefficient $\tilde{A}_{q\bar{q}} \equiv A^{(1)}_{q\bar{q}}/\alpha_s$ defined in [10]. Roughly, these NLO vector contributions are dominant if the condition $\alpha_s/(4\pi) \cdot (1 + c_{t_L} + c_{t_R}) \gtrsim L \exp[L(1 + c_{q_L} + c_{q_R})]$ is fulfilled by

the bulk mass parameters. For parameter sets that reproduce the quark masses and mixings, the NLO contributions to σ_a exceed the LO contributions by a factor of about 100.

4 Discussion and conclusions

After having assessed the size of vector and axial-vector RS contributions in top-quark pair production, we discuss the numerical effects on the observables. Using Eqs. (9), (10), and (11), and focussing on the dominant contributions from $u\bar{u}$ initial states, one obtains [c]

$$\begin{aligned}
(\sigma_{t\bar{t}})_{\rm RS} &= \left[1 + 0.053\,\tilde{C}^V_{u\bar{u}}\right]\left(6.73^{+0.52}_{-0.80}\right)\,{\rm pb}\,, \\
\left(\frac{d\sigma_{t\bar{t}}}{dM_{t\bar{t}}}\right)^{M_{t\bar{t}}\in[0.8,1.4]\,{\rm TeV}}_{\rm RS} &= \left[1 + 0.33\,\tilde{C}^V_{u\bar{u}}\right]\left(0.061^{+0.012}_{-0.006}\right)\frac{\rm fb}{\rm GeV}\,, \\
(A^t_{\rm FB})^{p\bar{p}}_{\rm RS} &= \left[\frac{1 + 0.22\,\tilde{C}^A_{u\bar{u}} + 0.034\,\tilde{C}^V_{u\bar{u}}}{1 + 0.053\,\tilde{C}^V_{u\bar{u}}}\right]\left(5.6^{+0.8}_{-1.0}\right)\%\,.
\end{aligned} \tag{12}$$

Discarding the axial-vector contributions, proportional to $\tilde{C}^A_{u\bar{u}} = \mathcal{O}(10^{-3})$, we inspect the interplay of NP effects mediated by the vector coefficient $\tilde{C}^V_{u\bar{u}}$. The corrections with respect to the SM prediction are at the percent level for all observables. Outstanding is the large correction to the cross section at high $M_{t\bar{t}}$ of about 30% for $\tilde{C}^V_{u\bar{u}} = \mathcal{O}(1)$, compared to a moderate 5% effect in the total cross section. This behavior is understood by noticing the increase of the NP contribution in the effective theory as $M^2_{t\bar{t}}/M^2_{\rm KK}$ at LO, cf. Eq. (10). The high-$M_{t\bar{t}}$ bin of the distribution $d\sigma_{t\bar{t}}/dM_{t\bar{t}}$ in Eq. (12) constrains the vector coefficient to $\tilde{C}^V_{u\bar{u}} \in [-3.4, 3.5]$ at 95% CL. From the total cross section $\sigma_{t\bar{t}}$, one obtains an allowed range of $\tilde{C}^V_{u\bar{u}} \in [-1.5, 7.4]$. These model-independent constraints limit the vector corrections to the charge-asymmetric cross section σ_a to $[-6, +8]\%$ and $[-10, +3]\%$ of the SM prediction, respectively. Notice that the NLO effects in the numerator of $(A^t_{\rm FB})^{p\bar{p}}_{\rm RS}$ are over-compensated by the charge-symmetric LO effects in the normalization. In the case of a positive vector coefficient $\tilde{C}^V_{u\bar{u}}$, the forward-backward asymmetry is thus always decreased with respect to its QCD value. The constraints on the effective couplings $C^V_{u\bar{u}}$ and $C^A_{u\bar{u}}$ are summarized in Figure 3, where we show a combined fit to the $t\bar{t}$ observables $\sigma_{t\bar{t}}$, $(d\sigma_{t\bar{t}}/dM_{t\bar{t}})^{>}$, and $A^{t,p\bar{p}}_{\rm FB}$. It is clearly visible that the forward-backward asymmetry (vertical dashed lines) cannot be increased beyond $A^{t,p\bar{p}}_{\rm FB} = 5.8\%$ (6.0%) at the 95% (99%) CL by vector contributions alone. To reach the best-fit point $(\tilde{C}^A_{u\bar{u}}, \tilde{C}^V_{u\bar{u}}) = (8.3, 1.4)$, large axial-vector contributions at tree level are required. [d] In the RS model with flavor anarchy, one typically has $\tilde{C}^V_{q\bar{q}} \approx +0.5$ in the regime of perturbative Yukawa couplings. The resulting absolute correction to the asymmetry amounts to $\delta(A^t_{\rm FB})^{p\bar{p}}_{\rm RS} = -0.05\%$, assuming a KK scale of $M_{\rm KK} = 1\,{\rm TeV}$. For this scale, the first KK excitation of the gluon exhibits a mass of around 2.5 TeV. Notice that for new particles with masses below about 2 TeV, the treatment in terms of an effective theory does not apply any longer and width effects have to be taken into account.

In summary, top-quark pair production in the RS model with flavor anarchy is essentially forward-backward symmetric: axial-vector contributions from KK gluons at tree level are strongly suppressed, because the light quarks are localized in the UV regime of the extra dimension. At NLO, a charge asymmetry arises from vector contributions, but these effects are over-compensated by the simultaneous LO contributions in the symmetric cross section, which normalizes the forward-backward asymmetry. On general grounds, it is therefore not possible to achieve a large forward-backward asymmetry from vector contributions alone. The asymmetry has to be generated at tree level either by NP with large axial-vector couplings in the s channel or flavor-changing couplings in the t channel. In the model at hand, the forward-backward

[c] For details on the inputs and the numerical calculation, please consult [10].

[d] To satisfy the measured asymmetry at high $M_{t\bar{t}}$, axial-vector contributions have to be even larger.

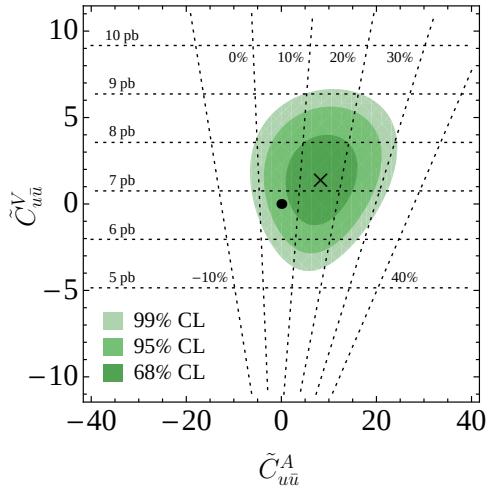

Figure 3: Constraints from combined fit to $\sigma_{t\bar{t}}$, $(d\sigma_{t\bar{t}}/dM_{t\bar{t}})^{>}$, and $A_{\rm FB}^{t,p\bar{p}}$ in the $\tilde{C}^A_{u\bar{u}} - \tilde{C}^V_{u\bar{u}}$ plane. The best fit point $(8.3, 1.4)$ is marked by a cross, the SM $(0, 0)$ by a black dot. The horizontal (vertical) lines correspond to the theoretical value of the total cross section $\sigma_{t\bar{t}}$ (of the forward-backward asymmetry $A_{\rm FB}^{t,p\bar{p}}$).

asymmetry is slightly decreased with respect to the SM value. A larger asymmetry in the RS framework can theoretically be obtained by moving the localization of the light quarks more towards the IR regime. The prize to pay is to give up the appealing feature of explaining the quark mass hierarchy exclusively by localization in the extra dimension. The LHC starts to probe charge-asymmetric top-quark pair production. However, KK gluons - if existing - will rather show up as resonances in the symmetric $t\bar{t}$ cross section. They naturally generate a large top-quark forward-backward *symmetry*.

Acknowledgments

It is a pleasure to thank the organizers of *Les Rencontres de Moriond 2011 EW* for an interesting and inspiring conference, as well as Martin Bauer, Florian Goertz, Uli Haisch, and Torsten Pfoh for an enjoyable collaboration on this subject. Many thanks to Paul Archer and Uli Haisch for proofreading the manuscript. This research is supported by the Helmholtz-Institut Mainz.

References

1. E. Thomson *et al.* [CDF Collaboration], Conference Note 9913, October 19, 2009.
2. T. Aaltonen *et al.* [CDF Collaboration], Phys. Rev. Lett. **102**, 222003 (2009), arXiv:0903.2850 [hep-ex].
3. T. Aaltonen *et al.* [CDF Collaboration], arXiv:1101.0034 [hep-ex].
4. CDF Collaboration, CDF Note 10398, March 10, 2011.
5. DØ Collaboration, Conference Note 6062-CONF, July 23, 2010.
6. V. Ahrens, A. Ferroglia, M. Neubert, B. Pecjak and L.L. Yang, arXiv:1103.0550 [hep-ph].
7. L. Randall and R. Sundrum, Phys. Rev. Lett. **83**, 3370 (1999), arXiv:hep-ph/9905221.
8. S. Casagrande, F. Goertz, U. Haisch, M. Neubert and T. Pfoh, JHEP **0810**, 094 (2008), arXiv:0807.4937 [hep-ph].
9. M. Bauer, S. Casagrande, U. Haisch and M. Neubert, JHEP **1009**, 017 (2010), arXiv:0912.1625 [hep-ph].
10. M. Bauer, F. Goertz, U. Haisch, T. Pfoh and S. Westhoff, JHEP **1011**, 039 (2010), arXiv:1008.0742 [hep-ph].

HEAVY FLAVOUR PHYSICS AT ATLAS

R.W.L. JONES [a]
Department of Physics, Lancaster University, Physics Avenue, Lancaster LA1 4YB, England

Early results on heavy flavours and onia from the ATLAS experiment are presented. The signals for various charms states have been identified. Charmonia have also been isolated, and both the prompt and non-prompt production cross-section determined for the J/ψ; allowing comparisons with various theoretical predictions in a kinematic regime not previously accessed. Exclusive B-meson states have been reconstructed, opening the prospect for an exciting programme of study.

1 The ATLAS Experiment

The ATLAS detector [1] has the familiar concentric cylindrical design common for collider experiments. For the studies in this paper, the most important elements are the Inner Detector, which provides precise tracking information, and the Muon Spectrometer, which provides muon identification and precise momentum measurements. The Inner Detector is composed of silicon pixels, silicon strips and a transition radiation tracker. It sits in a solenoidal magnetic field of 2 T, and provides tracking coverage out to a pseudorapidity, η, of 2.5. The nominal Inner Detector performance gives a relative uncertainty on p_T measurements in the barrel ($|\eta| < 1.5$) of $\sigma/p_T \sim 3.4 \cdot 10^{-4} p_T \oplus 0.015$. The Muon Spectrometer provides coverage out to $|\eta| < 2.7$, and sits in an a toroidal B-field with average strength ~ 0.5 T. It provides a fractional muon momentum uncertainty of 10% up to momenta of ~ 1 TeV.

Muons provide a clean signature and Muon triggers are key to most of the heavy flavour measurements. These provide a clean signature. In the early data taking, they could be run without prescaling and momentum thresholds, but as the luminosity increased the single muon triggers had to be prescaled for p_T below 6 GeV; to compensate, di-muon triggers were introduced.

2 Heavy Flavour Production

2.1 Charmonia and Υ states

Charmonia are of interest for several reasons. Firstly, they provide a standard candle for the commissioning and for studying the detector performance. Secondly, they provide important insight into the production mechanisms at play at these energies, and various theoretical predictions can be tested. Finally, they provide an essential building block to exclusive decay channels such as the $B_s \to J/\psi\phi$ and $B_d \to J/\psi K_s$, which are important for measurements of CP violation and the effects of SUSY and other new physics processes.

[a] On behalf of the ATLAS Collaboration

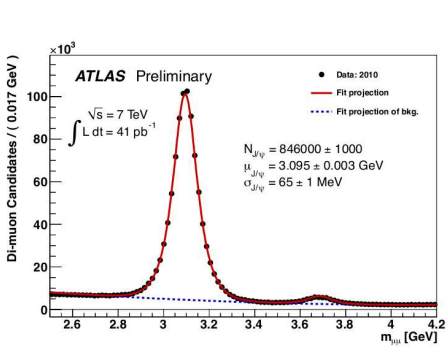

(a) The J/ψ mass region

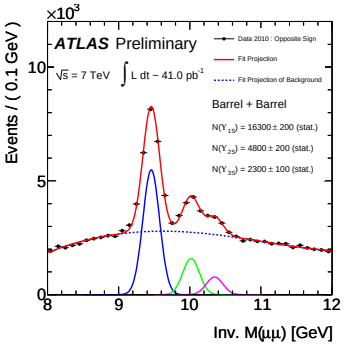

(b) The Υ mass region for candidates with both muons in the barrel of the detector

Figure 1: The charm and bottom onia spectra in dimuon events.

Figure 1 shows the dimuon spectrum using a suite of muon triggers recorded in 41pb^{-1} of 7 TeV data recorded in 2010 [2]. One muon is required to have $p_T > 4$ GeV and the other > 2.5 GeV. The J/ψ and ψ' resonances are clearly evident, with the mass peaks in excellent agreement with the PDG averages. Similar spectra are shown for the Υ mass region in the case where both muons are detected in the barrel region. The $\Upsilon(1S)$ is clearly seem, while the $\Upsilon(2S)$ and $\Upsilon(3S)$ can be distinguished separately. The resolution degrades as one or more of the muons is detected in the barrel end-caps, but a cross-section measurement is possible and underway

2.2 Open charm meson cross-sections

ATLAS has also observed open charm mesons [3,4]. The D_s^+ is reconstructed via the decay chain $D_s^+ \to \phi\pi \to (KK)\pi$, while the D^+ is reconstructed in the decay $D^+ \to K\pi\pi$. The D^{*+} is observed using the usual mass-difference technique, seeking the slow pion peak in the mass difference between D^0 candidates from $K\pi$ combinations and D* candidates from $K\pi\pi$ combinations. In all cases, the fitted mass peaks are in good agreement with PDG averages. These signals have now been used to derive single differential cross-sections for the $D^\pm$ and D^* in p_T and $|\eta|$. These have then been compared with QCD-based Monte Carlo predictions from MC@NLO [5], and from POWHEG [6] applied in PYTHIA [7] and HERWIG [8]. In all cases, the data fall towards the upper range of the predictions, as illustrated for the D^* in Figure 2, and for the $D^\pm$ in Figure 3.

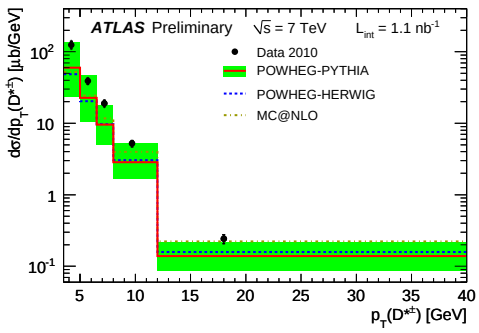

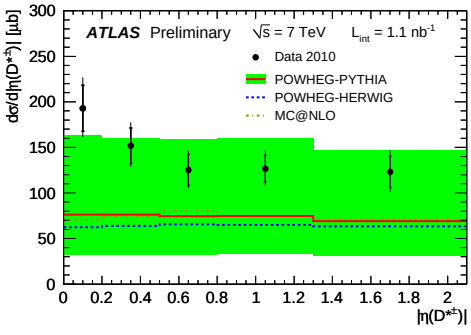

(a) The $D^{*\pm}$ cross-section with respect to p_T. (b) The $D^{*\pm}$ cross-section with respect to $|\eta|$.

Figure 2: The $D^{*\pm}$ production cross-section.

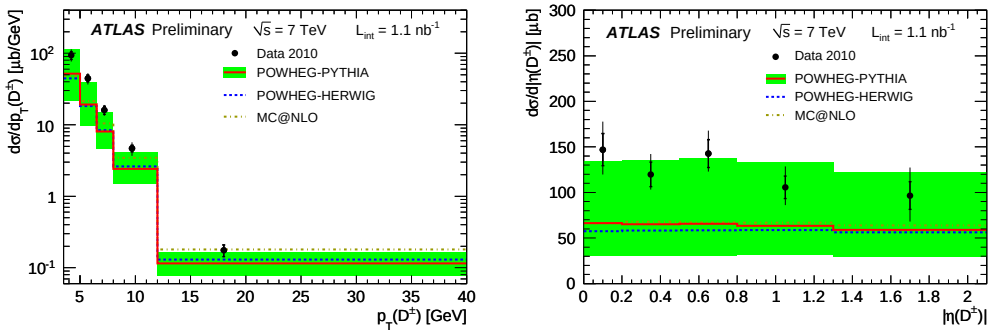

(a) The $D^{\pm}$ cross-section with respect to p_T. (b) The $D^{\pm}$ cross-section with respect to $|\eta|$.

Figure 3: The $D^{\pm}$ production cross-section.

3 The J/ψ differential cross-section

Using the signals identified earlier, ATLAS has derived doubly differential cross-sections for J/ψ production in bins of rapidity, y, and p_T [9]. The measurement requires an extremely well-understood and unbiased trigger selection. As a consequence, low luminosity data is employed and only single muon triggers; at higher luminosities, the pre-scaling would require dimuon triggers to obtain significant statistics, especially at lower p_T, and very many sets with different trigger conditions. The important inputs to the measurement are:

- The acceptance behaviour as a function of the spin-alignment. This is significant, and the true spin-alignment at the LHC is not yet measured. The full range of possibilities is considered in determining the associated systematic uncertainty.
- The muon reconstruction efficiencies. These are determined from the data, using a tag and probe technique.
- The muon trigger efficiencies. These are also obtained from the data; however, there are insufficient statistics to obtain the fine-binning required, so Monte Carlo predictions are used, which are then re-weighted to the measured values in larger bins.

A second measurement is made of the production fraction of non-prompt J/ψ, which are almost entirely produced from B-hadron decays, and often may be distinguished by the finite pseudo decay length. The remainder of the J/ψ are either produced directly or in the feed-down from higher-mass charmonia. The non-prompt fraction is defined as

$$f_B \equiv \frac{d\sigma(pp \to B + X \to J/\psi X')}{d\sigma(pp \to \text{ Inclusive } J/\psi X'')} \tag{1}$$

This observable has the advantage that many systematic effects cancel. This allows combinations of triggers to be employed, leading to increased statistics. For both measurements, the principle of the measurement is simple. The J/ψ yields are extracted from fits to the mass spectra in each p_T and y region. These are then translated into cross-sections by correcting for detector acceptance, reconstruction and trigger efficiencies and for the small effects of bin-to-bin migration. A per-candidate weighting procedure is used, with the weight defined as:

Here, the trigger efficiency is defined as:

$$w^{-1} \quad = \quad \mathcal{A} \cdot \mathcal{M} \cdot \mathcal{E}^2_{\text{trk}} \cdot \mathcal{E}^+{}_{\mu}(p_T^+, \eta^+) \cdot \mathcal{E}^-{}_{\mu}(p_T^-, \eta^-) \cdot \mathcal{E}_{\text{trig}} \tag{2}$$

where $\mathcal{A}$ is the kinematic acceptance, $\mathcal{M}$ is a correction factor for bin migrations due to finite detector resolution, $\mathcal{E}_{\rm trk}$ is the ID tracking efficiency and $\mathcal{E}_{\mu}$ is the single-muon offline reconstruction efficiency. Here $p_T^{\pm}$ and $\eta^{\pm}$ are the transverse momenta and pseudorapidities of the positive and negative muons from the J/ψ decay. The trigger efficiency $\mathcal{E}_{\rm trig}$ for a given J/ψ candidate is calculated from single-muon trigger efficiencies $\mathcal{E}^{\pm}_{\rm trig}(p_T^{\pm}, \eta^{\pm})$ as follows:

$$\mathcal{E}_{\rm trig} = 1 - \left(1 - \mathcal{E}^{+}_{\rm trig}(p_T^{+}, \eta^{+})\right) \cdot \left(1 - \mathcal{E}^{-}_{\rm trig}(p_T^{-}, \eta^{-})\right). \quad (3)$$

The spin-alignment can be characterised by two angles with associated amplitudes, and so the full range of possibilities is limited by the four extreme points and a fifth point where both amplitudes are zero (the flat hypothesis). For the presentation of the results, the flat hypothesis is chosen, with the maximum deviation due to spin-alignment taken as the systematic uncertainty. The inclusive cross-section is shown for two of the four rapidity regions studied in Figure 4 . Also shown are measurements from CMS [10]. As a consequence of the trigger strategies chosen, CMS extend to lower p_T, while ATLAS increases the p_T reach upwards. There is good agreement in the regions of overlap.

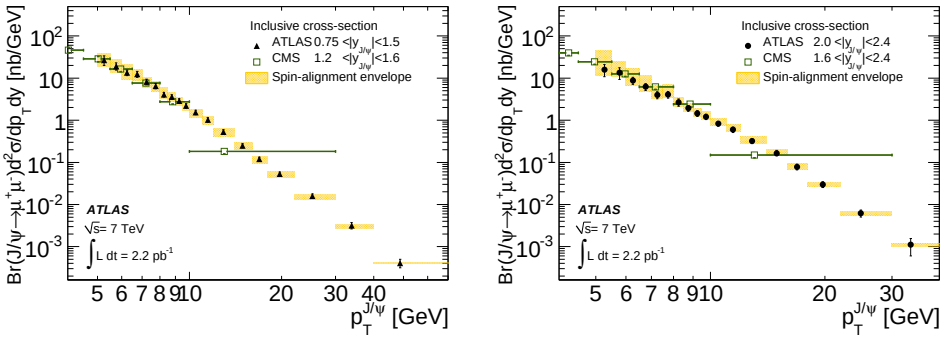

(a) The inclusive $J/'psi$ production cross-section with respect to p_T for one of the lowest of the four $|y|$ bins.

(b) TThe inclusive $J/'psi$ production cross-section with respect to p_T for one of the highest of the four $|y|$ bins.

Figure 4: Illustrative inclusive J/ψ production cross-sections .

The non-prompt fraction determination proceeds in a similar way, but uses the pseudo-proper lifetime and the mass of the candidates in the fits to extract the ratio in bins of p_T and $|y|$. Again, these are compared with CMS [10] and (despite the different centre of mass energy) CDF [11]. There is good agreement between the three experiments, with CDF providing the lowest p_T coverage and ATLAS the high-p_T information, as illustrated in Figure 5 for the lowest of the four rapidity regions studied. Agreement with the CDF point suggests indepdence of the ratio from the center of mass energy.

Combining the two results, the prompt and non-prompt cross-sections can be extracted, as illustrated in Figure 6 for another of the rapidity bins studied. The non-prompt cross-section is compared with the FONLL [12] prediction for $B \to J/\psi X$, and good agreement is found. The prompt cross-section may be compared with various models. Of those used, the previously popular colour evaporation model [13] performs best, but it over-estimates the cross-section at high p_T.

4 Exclusive B-meson decays

In preparation for future studies, various exclusive B-meson decay channels have been investigated. The decay $B^{\pm} \to J/\psi K^{\pm}$ has been reconstructed for both charged states. A clear signal

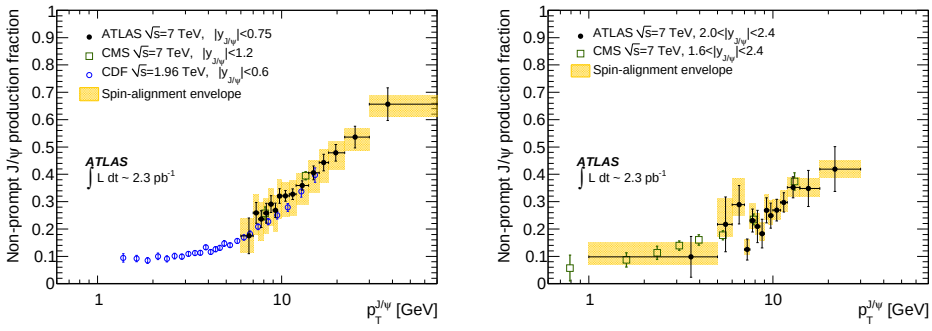

(a) The non-prompt $J/'psi$ production fraction with respect to p_T for the lowest of the four $|y|$ bins studied.

(b) The non-prompt J/ψ production fraction with respect to p_T for the highest of the four $|y|$ bins studied.

Figure 5: Illustrative J/ψ non-prompt production fractions.

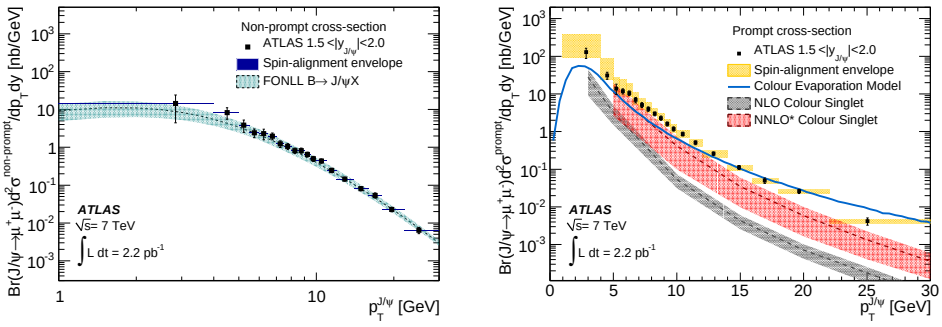

(a) The non-prompt $J/'psi$ production cross-section with respect to p_T for one of the four $|y|$ bins.

(b) The prompt J/ψ production cross-section with respect to p_T for one of the four $|y|$ bins.

Figure 6: Illustrative J/ψ production cross-sections .

is observed even without a cut on the lifetime properties of the candidates (which is important for lifetime-dependent studies), the signal is much purer if one is made, as illustrated in Figure 7. The mass observed is consistent with the PDF value for both selections and for both charged states. Similarly, the decays $B^0 \to J/\psi K^*(K\pi)$ and $B^\pm \to J/\psi\phi(KK)$ have been observed and their masses determined to be consistent with the PDF expectations. Lifetime measurements are underway. These results open the door to lifetime-difference and CP violating weak phase studies as statistics increase.

5 Conclusions

In the first year of 7 TeV data-taking, ATLAS has observed the charm- and bottom-onia states, and has reconstructed important B-meson exclusive decays. Various single-charm states have also been observed and their single-differential production cross-sections measured. Doubly-differential cross-section measurements have been made for the J/ψ, and the prompt fraction determined. Both results extend the previously available kinematic range, agreeing with previous measurements in the areas of overlap. The prompt and non-prompt cross-sections have been extracted and compared with theory. The non-prompt predictions fare well, while the prompt predictions do less well at high p_T. The immediate future includes lifetime measurements, early CP violation studies and as well as studies of the B_c. In the longer term, ATLAS will make

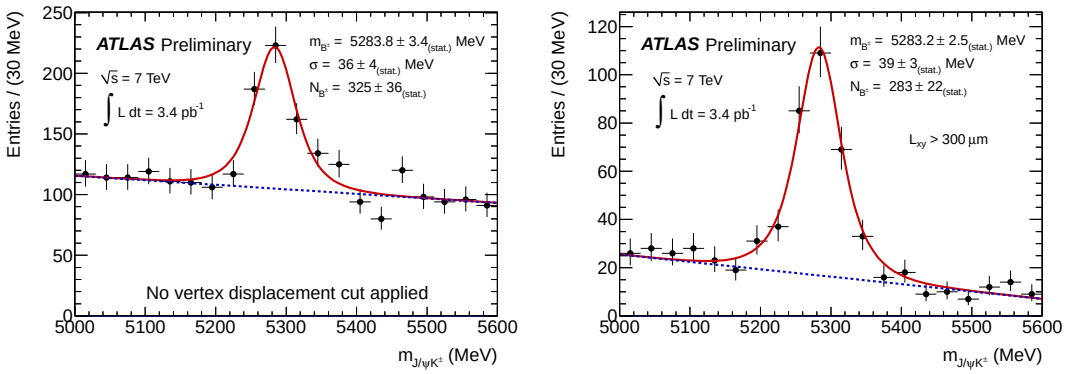

(a) Before lifetime cuts.

(b) After lifetime cuts.

Figure 7: The $B^{\pm}$ signal with and without lifetime cuts.

measurements of rare B-decays to muons.

References

1. ATLAS Collaboration, *JINST* **3**, S08003 (2008)
2. ATLAS Collaboration, ATLAS-CONF-2010-045, http://cdsweb.cern.ch/record/1277685.
3. ATLAS Collaboration, ATLAS-CONF-2010-034 http://cdsweb.cern.ch/record/1277669.
4. ATLAS Collaboration, ATLAS-CONF-2011-017, http://cdsweb.cern.ch/record/1336746.
5. S. Frixione, P. Nason and B. R. Webber, *JHEP* **0308**, 007 (2003) .
6. S. Frixione, P. Nason and G. Ridolfi, *JHEP* **0709**, 126 (2007).
7. T. Sjostrand, S. Mrenna, P. Skands, *JHEP* **05**, 026 (2006).
8. G. Corcella et al., *JHEP* **0101**, 010 (2001).
9. ATLAS Collaboration, G. Aad et al, arXiv:1104.3038 [hep-ex], accepted for publication *Nucl. Phys.* B.
10. CMS Collaboration, arXiv:1011.4193 [hep-ex]
11. CDF Collaboration, D. Acosta et al., *Phys. Rev.* D **71**, 032001 (2005).
12. M. Cacciari, M. Greco and P. Nason, *JHEP* **9805**, 007 (1998)
    M. Cacciari, M. Greco and P. Nason, *JHEP* **0103**, 006 (2001).
13. T. Ullrich, A. D. Frawley and R. Vogt, *Phys. Rep.* **462**, 125 (2008)
    V. D. Barger, W. Y. Keung and R. J. N. Phillips, *Phys. Lett.* B **91**, 253 (1980)
    V. D. Barger, W. Y. Keung and R. J. N. Phillips, *Z. Phys.* C **6**, 169 (2010).
14. ATLAS Collaboration, ATLAS-CONF-2010-098, http://cdsweb.cern.ch/record/1307530.

CP Violation in $D^0 - \bar{D}^0$ Mixing and Electric Dipole Moments in SUSY Alignment Models

W. ALTMANNSHOFER
Theoretical Physics Department,
Fermilab, P.O. Box 500, Batavia, IL 60510, USA

We report on a study of CP Violation in $D^0 - \bar{D}^0$ mixing and Electric Dipole Moments in the framework of supersymmetric alignment models. Both classes of observables are strongly suppressed in the Standard Model and highly sensitive to new sources of flavor and CP violation that can be present in models of New Physics. Supersymmetric alignment models generically predict large non-standard effects in $D^0 - \bar{D}^0$ mixing and we show that visible CP violation in $D^0 - \bar{D}^0$ mixing implies lower bounds for the EDMs of hadronic systems, like the neutron EDM and the mercury EDM, in the reach of future experimental sensitivities. We also give updated constraints on the mass insertions of the Minimal Supersymmetric Standard Model using the current data on $D^0 - \bar{D}^0$ mixing.

1 Introduction

Models of New Physics (NP) often contain new sources of flavor violation and are therefore strongly constrained by experimental data on Flavor Changing Neutral Current (FCNC) processes. This is in particular the case for Supersymmetric (SUSY) extensions of the Standard Model (SM) like the Minimal Supersymmetric Standard Model (MSSM), as long as the SUSY degrees of freedom are not far above the TeV scale [1,2]. This so-called SUSY flavor problem is for example addressed in SUSY alignment models [3,4] that align the down quark and down squark mass matrices such that down quark – down squark – gaugino couplings are flavor diagonal and FCNC processes in the down sector are under control. A characteristic prediction of these models are however sizable NP effects in up sector FCNCs, in particular in $D^0 - \bar{D}^0$ mixing [3]. On general grounds $D^0 - \bar{D}^0$ mixing observables are highly sensitive probes of the flavor sector of NP models [5]. Especially CP violation in $D^0 - \bar{D}^0$ mixing is strongly suppressed in the SM by $\mathrm{O}(V_{ub}V_{cb}/V_{us}V_{cs}) \sim 10^{-3}$ and experimental evidence for it considerably above the per mill level

would clearly point towards the presence of NP (see however [6]).

In the following we give updated bounds on the mass insertions of the MSSM using the latest experimental data on $D^0-\bar{D}^0$ mixing, we analyze the predictions of SUSY alignment models for CP violation in $D^0-\bar{D}^0$ mixing and show that sizable CP violating effects in $D^0-\bar{D}^0$ mixing imply lower bounds on the Electric Dipole Moments (EDMs) of hadronic systems within this class of SUSY models. The presentation is mainly based on [7].

2 Bounds on Mass Insertions from $D^0-\bar{D}^0$ Mixing

The neutral D meson mass eigenstates D_1 and D_2 are linear combinations of the strong interaction eigenstates, D^0 and $\bar{D}^0$

$$|D_{1,2}\rangle = p|D^0\rangle \pm q|\bar{D}^0\rangle \ , \quad \frac{q}{p} = \sqrt{\frac{M_{12}^* - \frac{i}{2}\Gamma_{12}^*}{M_{12} - \frac{i}{2}\Gamma_{12}}} \ , \tag{1}$$

where M_{12} is the dispersive part and Γ_{12} the absorptive part of the $D^0-\bar{D}^0$ mixing amplitude

$$\langle D^0|\mathcal{H}_{\rm eff}|\bar{D}^0\rangle = M_{12} - \frac{i}{2}\Gamma_{12} \ , \quad \langle \bar{D}^0|\mathcal{H}_{\rm eff}|D^0\rangle = M_{12}^* - \frac{i}{2}\Gamma_{12}^* \ . \tag{2}$$

The normalized mass and width differences in the $D^0-\bar{D}^0$ system, x and y, are given by

$$x = \frac{\Delta M_D}{\Gamma_D} = 2\tau_D {\rm Re}\left[\frac{q}{p}\left(M_{12} - \frac{i}{2}\Gamma_{12}\right)\right] \ , \quad y = \frac{\Delta\Gamma}{2\Gamma_D} = -2\tau_D {\rm Im}\left[\frac{q}{p}\left(M_{12} - \frac{i}{2}\Gamma_{12}\right)\right] \ , \tag{3}$$

with the lifetime of the neutral D mesons $\tau_D = 1/\Gamma_D = 0.41$ps.

Experimentally, $D^0-\bar{D}^0$ mixing is firmly established with the non-mixing hypothesis $x = y = 0$ excluded at 10.2σ [8]. Still, at the current level of sensitivity, there is no evidence for CP violation in $D^0-\bar{D}^0$ mixing. The experimental data on both $|q/p|$ and $\phi = {\rm Arg}(q/p)$ is compatible with CP conservation, i.e. $|q/p| = 1$ and $\phi = 0$. The most recent world averages as obtained by HFAG read [8]

$$x = (0.63^{+0.19}_{-0.20})\% \ , \quad y = (0.75 \pm 0.12)\% \ , \quad |q/p| = 0.91^{+0.18}_{-0.16} \ , \quad \phi = (-10.2^{+9.4}_{-8.9})^\circ \ . \tag{4}$$

These experimental results on $D^0-\bar{D}^0$ mixing lead to strong constraints on possible new sources of flavor violation in extensions of the Standard Model [9,10,1].

The MSSM contains many new sources of flavor violation. A convenient parametrization is given by so-called mass insertions δ that can be defined as the deviations of the up and down squark mass matrices from universality in the super-CKM basis

$$M_{\tilde{q}}^2 = \tilde{m}_Q^2(\mathbb{1} + \delta_q) \ , \quad \delta_q = \begin{pmatrix} \delta_q^{LL} & \delta_q^{LR} \\ \delta_q^{RL} & \delta_q^{RR} \end{pmatrix} \ , \quad q = u, d \ . \tag{5}$$

Complex flavor off-diagonal mass insertions lead to flavor and CP violating gluino – squark – quark interactions that typically lead to huge contributions to FCNC processes. Taking into account only gluino box contributions in the so-called mass insertion approximation, neglecting for simplicity renormalization group effects as well as setting the B-parameter to 1 in the evaluation of the hadronic matrix elements, one finds for the MSSM contributions to the $D^0-\bar{D}^0$ mixing amplitude the following approximate expression [a]

$$M_{12}^{\rm NP} \simeq \frac{\alpha_s^2}{\tilde{m}_Q^2} m_D f_D^2 \left[\left((\delta_u^{LL})_{12}^2 + (\delta_u^{RR})_{12}^2\right)\frac{g_1(x_g)}{3} + (\delta_u^{LL})_{12}(\delta_u^{RR})_{12}\,\frac{m_D^2}{m_c^2}\left(\frac{g_4(x_g)}{4} + \frac{g_5(x_g)}{12}\right)\right] \ , \tag{6}$$

[a] In our numerical analysis we implement the full set of 1 loop MSSM contributions that can be found e.g. in [11], we include 2 loop renormalization group running [12] and use the hadronic matrix elements given in [9].

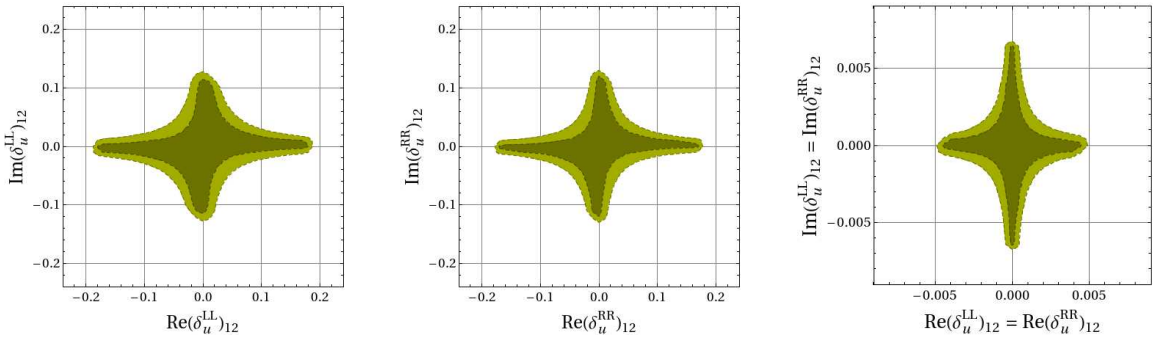

Figure 1: Updated constraints on the mass insertions $(\delta_u^{LL})_{12}$ and $(\delta_u^{RR})_{12}$ from $D^0 - \bar{D}^0$ mixing for a common squark and gluino mass of $\tilde{m}_Q = M_{\tilde{g}} = 1$ TeV.

where m_D is the mass and f_D the decay constant of the neutral D mesons. The loop functions g_1, g_4 and g_5 depend on the ratio $x_g = M_{\tilde{g}}^2/\tilde{m}_Q^2$ of the gluino and squark masses and their explicit expression can be found e.g. in [1]. In the limiting case of degenerate masses one has $g_1(1) = -\frac{1}{216}$, $g_4(1) = \frac{23}{180}$ and $g_5(1) = -\frac{7}{540}$. In (6) we neglected contributions from δ_u^{LR} and δ_u^{RL} mass insertions. They are given e.g. in [1].

In Fig. 1 we show the allowed regions for the mass insertions $(\delta_u^{LL})_{12}$ and $(\delta_u^{RR})_{12}$. As the SM contributions to M_{12} and Γ_{12} cannot be predicted in a reliable way, we allow them to vary in the range $-0.02\text{ps}^{-1} < M_{12}^{\rm SM} < 0.02\text{ps}^{-1}$ and $-0.04\text{ps}^{-1} < \Gamma_{12}^{\rm SM} < 0.04\text{ps}^{-1}$ and impose the constraints (4) at the 2σ level. The bounds on the mass insertions are obtained for a SUSY spectrum with a common squark and gluino mass of $\tilde{m}_Q = M_{\tilde{g}} = M_{\rm SUSY} = 1$TeV and switching on one mass insertion at a time. They scale as $\delta_u/M_{\rm SUSY}$ and hold barring accidental cancellations among the different contributions in (6).

The case where both LL and RR mass insertions are present simultaneously is particularly strong constrained (see right plot of Fig. 1). Even for the rather heavy SUSY spectrum that we consider, the mass insertions have to be smaller then about $5 \cdot 10^{-3}$. For maximal phases of the mass insertions, the bounds are stronger by approximately a factor of 3.

3 CP Violation in $D^0 - \bar{D}^0$ Mixing in SUSY Alignment Models

A popular class of SUSY models that generically predict large NP effects in $D^0 - \bar{D}^0$ mixing are SUSY alignment models [3]. The quark-squark alignment mechanism occurs naturally in models with abelian horizontal symmetries that reproduce the observed hierarchy in the SM Yukawa couplings. Interestingly, in the framework of alignment it is possible to predict for a broad class of abelian flavor models both lower and upper bounds for the mass insertions [13].

The most characteristic prediction of alignment models is the appearance of a large $(\delta_u^{LL})_{12}$ mass insertion that leads to large effects in $D^0 - \bar{D}^0$ mixing. Indeed, $SU(2)$ invariance implies a relation between the left-left mass insertions in the up and down sector

$$(\delta_u^{LL})_{12} = (V \delta_d^{LL} V^\dagger)_{12} \simeq (\delta_d^{LL})_{12} + \lambda \frac{m_{\tilde{c}_L}^2 - m_{\tilde{u}_L}^2}{\tilde{m}_Q^2} + O(\lambda^2) \ , \qquad (7)$$

where V is the CKM matrix, $\lambda \simeq 0.2$ is the Cabibbo angle and $m_{\tilde{u}_L}$ and $m_{\tilde{c}_L}$ are the left handed up and charm squark masses, respectively. As abelian flavor symmetries do not impose any restriction on the mass splittings between squarks of different generations, they are expected to be non-degenerate with natural order one mass splittings. Correspondingly, even for $(\delta_d^{LL})_{12} = 0$, which is approximately satisfied in alignment models to avoid the strong constraints from Kaon mixing, there is an irreducible flavor violating term of order λ leading to $c - u$ transitions. Note that this $(\delta_u^{LL})_{12}$ is real to a good approximation.

As shown in [13], the right-right mass insertion leading to $c-u$ transitions is predicted to be $\lambda^2 < |(\delta_u^{RR})|_{12} < \lambda^4$ in abelian flavor models with alignment. This mass insertion is naturally expected to be complex. Therefore, all CP violating phenomena in $D^0-\bar{D}^0$ mixing are dominantly generated by the following combination of mass insertions

$$\mathrm{Im}M_{12}^{\mathrm{NP}} \propto \mathrm{Im}[(\delta_u^{LL})_{12}(\delta_u^{RR})_{12}] \ . \tag{8}$$

In the following we focus on two observables sensitive to CP violation in $D^0-\bar{D}^0$ mixing: (i) the semileptonic asymmetry a_{SL} and (ii) the time dependent CP asymmetry in decays to CP eigenstates S_f.

The semileptonic asymmetry in the decay to "wrong sign" leptons is defined as

$$a_{\mathrm{SL}} = \frac{\Gamma(D^0 \to K^+\ell^-\nu) - \Gamma(\bar{D}^0 \to K^-\ell^+\nu)}{\Gamma(D^0 \to K^+\ell^-\nu) + \Gamma(\bar{D}^0 \to K^-\ell^+\nu)} = \frac{|q|^4-|p|^4}{|q|^4+|p|^4} \tag{9}$$

and is a direct measure of CP violation in the mixing. However, as the decay rates to the "wrong sign" leptons are strongly suppressed by x^2+y^2, measurements of this asymmetry are experimentally challenging.

Also the time dependent CP asymmetry S_f in decays to a common CP eigenstate f, aka lifetime CP asymmetry ΔY_f, is a sensitive probe of CP violation in $D^0-\bar{D}^0$ mixing [14,15]

$$S_f = 2\Delta Y_f = \frac{1}{\Gamma_D}\left(\hat{\Gamma}_{\bar{D}^0\to f} - \hat{\Gamma}_{D^0\to f}\right) \ , \tag{10}$$

$$\eta_f^{\mathrm{CP}} S_f = \eta_f^{\mathrm{CP}} 2\Delta Y_f = x\left(\left|\frac{q}{p}\right| + \left|\frac{p}{q}\right|\right)\sin\phi - y\left(\left|\frac{q}{p}\right| - \left|\frac{p}{q}\right|\right)\cos\phi \ . \tag{11}$$

Here η_f^{CP} is the CP parity of the final state f. While singly Cabibbo suppressed decay modes can in principle be affected by new weak phases in the decay [16], possible effects in the lifetime CP asymmetry are strongly constrained by existing data on time integrated CP asymmetries [17,18] and Eq. (11) still holds to an excellent approximation. I.e. $\eta_f^{\mathrm{CP}} S_f$ is universal for all final states and practically independent of direct CP violation in the decays. In fact, time dependent CP asymmetries are currently determined from the singly Cabibbo suppressed $D^0 \to K^+K^-$ and $D^0 \to \pi^+\pi^-$ modes and one has [8]

$$\eta_f^{\mathrm{CP}} S_f = (-0.246 \pm 0.496)\% \ . \tag{12}$$

Concerning Cabibbo favored decay modes, the most promising channel seems to be $D^0 \to K_S\phi$ [15].

In the left plot of Fig. 2 we show the model independent correlation between a_{SL} and S_f [19] in the context of SUSY alignment models. We assume a MSUGRA-like spectrum and scan the input parameter $m_0 < 2$TeV, $M_{1/2} < 1$TeV, $|A_0| < 3m_0$ and $5 < \tan\beta < 55$. At the GUT scale we fix $|(\delta_u^{RR})_{12}| = \lambda^3$ with an O(1) phase and set a mass splitting between the 1st and 2nd generation of squarks such that $m_{\tilde{u}_L} = 2m_{\tilde{c}_L} = 2m_0$. We find that in this setup the full range of values for a_{SL} and S_f that is compatible with the experimental constraints (4) can be reached.

4 A Lower Bound on Hadronic EDMs in SUSY Alignment Models

Electric Dipole Moments represent very clean probes of CP violation in extensions of the SM [20]. While the SM predicts EDMs far below the present experimental bounds [21]

$$d_{\mathrm{Tl}} \leq 9.4\times10^{-25}\ e\,\mathrm{cm} \quad @\ 90\%\ \mathrm{C.L.}\ , \tag{13}$$

$$d_{\mathrm{Hg}} \leq 3.1\times10^{-29}\ e\,\mathrm{cm} \quad @\ 95\%\ \mathrm{C.L.}\ , \tag{14}$$

$$d_{n} \leq 2.9\times10^{-26}\ e\,\mathrm{cm} \quad @\ 90\%\ \mathrm{C.L.}\ , \tag{15}$$

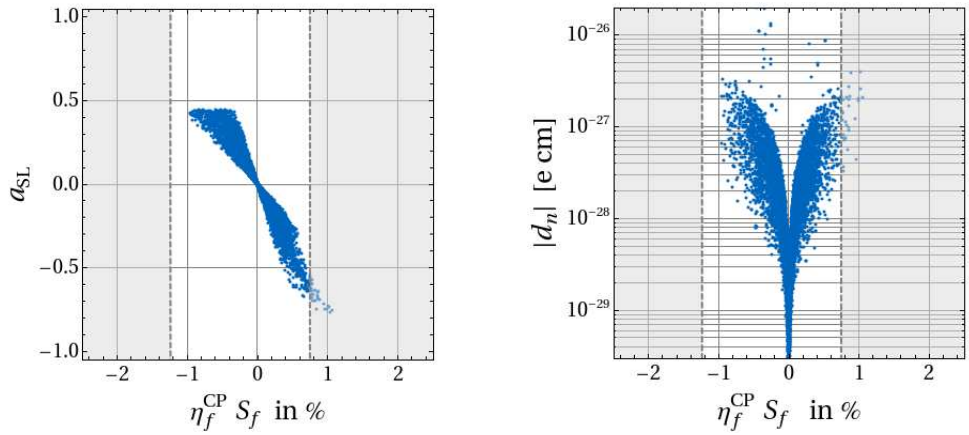

Figure 2: The semileptonic asymmetry a_{SL} (left) and the neutron EDM d_n (right) as a function of S_f in SUSY alignment models. The gray region is excluded by the present data on S_f.

New Physics models that introduce new sources of CP violation are often strongly constrained by these bounds. In particular in the MSSM with SUSY particles at the TeV scale, flavor diagonal CP violating phases of e.g. the gaugino masses, the higgsino mass or the trilinear couplings are strongly constrained [22] at the level of 10^{-2}.

In the MSSM with flavor violating soft terms, large NP effects for the hadronic EDMs can be naturally generated (see e.g. [23]). In particular, within SUSY alignment models, we find that the dominant SUSY contributions to the hadronic EDMs arise from "flavored" gluino – up squark contributions to the up quark (C)EDM. At the SUSY scale one has

$$\left\{\frac{d_u}{e},\ d_u^c\right\} \simeq -\frac{\alpha_s}{4\pi}\ m_c\ \frac{M_{\tilde g} A_c}{\tilde m_Q^4}\ \left\{f(x_g),\ f^c(x_g)\right\}\ {\rm Im}\left[(\delta_u^{LL})^*_{12}(\delta_u^{RR})_{12}\right]\ , \tag{16}$$

with the loop functions f and f^c given e.g. in [23]. Even though this contribution is suppressed by a double flavor flip, the corresponding up quark (C)EDM is sizable due to the chiral enhancement by the charm quark mass. As in alignment models $(\delta_u^{LL})_{12}$ is real to an excellent approximation, the up quark (C)EDM (16) and CP violation in $D^0 - \bar D^0$ mixing (8) is induced by the same combination of mass insertions. As also the charm trilinear coupling A_c that enters (16) is naturally of the order of the gluino and squark masses, CP violating contributions to $D^0 - \bar D^0$ mixing automatically also imply a non-zero up quark (C)EDM that in turn will induce EDMs of hadronic systems like the neutron EDM d_n or the mercury EDM $d_{\rm Hg}$, but not of the Thallium EDM $d_{\rm Tl}$.

In the right plot of Fig. 2 we show the correlation between the time dependent CP asymmetry S_f and the neutron EDM d_n in SUSY alignment models (we use the same setup as described at the end of Sec. 3). We observe that visible CP violating effects in $D^0 - \bar D^0$ mixing imply a lower bound on the neutron EDM. For $|S_f| > 0.1\%$ we find $d_n >$ few $\cdot 10^{-29}\, e\,$cm and simultaneously for the mercury EDM $d_{\rm Hg} >$ few $\cdot 10^{-31}\, e\,$cm which is an interesting level in view of future experimental sensitivities.

5 Conclusions

Electric Dipole Moments and CP violation in $D^0 - \bar D^0$ mixing are examples of low energy observables that are highly suppressed in the SM. Experimental evidence for them significantly above the tiny SM predictions would unambiguously signal the presence of NP.

Supersymmetric alignment models generically predict large non-standard effects in $D^0 - \bar D^0$ mixing [3]. In addition, as we demonstrated in [7], large CP violating effects in $D^0 - \bar D^0$ mixing in

SUSY alignment models, generically also imply lower bounds for the EDMs of hadronic systems, like the neutron EDM and the mercury EDM, within the future experimental sensitivities. Correspondingly, the simultaneous evidence of CP violation in the neutral D meson system together with non-vanishing hadronic EDMs would strongly support the idea of SUSY alignment models.

Acknowledgments

I would like to thank the organizers for the invitation to Moriond EW 2011, Andrzej Buras and Paride Paradisi for the interesting collaboration and Stefania Gori for a reading of the manuscript. Fermilab is operated by Fermi Research Alliance, LLC under Contract No. DE-AC02-07CH11359 with the United States Department of Energy.

References

1. W. Altmannshofer *et al.*, Nucl. Phys. B **830**, 17 (2010).
2. F. Gabbiani, E. Gabrielli, A. Masiero and L. Silvestrini, Nucl. Phys. B **477**, 321 (1996).
3. Y. Nir and N. Seiberg, Phys. Lett. B **309**, 337 (1993).
4. M. Leurer, Y. Nir and N. Seiberg, Nucl. Phys. B **420**, 468 (1994).
5. S. Bianco, F. L. Fabbri, D. Benson and I. Bigi, Riv. Nuovo Cim. **26N7**, 1 (2003).
6. M. Bobrowski, A. Lenz, J. Riedl, J. Rohrwild, JHEP **1003**, 009 (2010).
7. W. Altmannshofer, A. J. Buras and P. Paradisi, Phys. Lett. B **688**, 202 (2010).
8. D. Asner *et al.* [Heavy Flavor Averaging Group], arXiv:1010.1589 [hep-ex], and online update at `http://www.slac.stanford.edu/xorg/hfag` .
9. M. Ciuchini *et al.*, Phys. Lett. B **655**, 162 (2007).
10. E. Golowich, J. Hewett, S. Pakvasa and A. A. Petrov, Phys. Rev. D **76**, 095009 (2007); K. Blum, Y. Grossman, Y. Nir, G. Perez, Phys. Rev. Lett. **102**, 211802 (2009); O. Gedalia, Y. Grossman, Y. Nir and G. Perez, Phys. Rev. D **80**, 055024 (2009).
11. W. Altmannshofer, A. J. Buras and D. Guadagnoli, JHEP **0711**, 065 (2007).
12. M. Ciuchini *et al.*, Nucl. Phys. **B523**, 501-525 (1998); A. J. Buras, M. Misiak, J. Urban, Nucl. Phys. **B586**, 397-426 (2000).
13. Y. Nir and G. Raz, Phys. Rev. D **66**, 035007 (2002).
14. S. Bergmann *et al.*, Phys. Lett. B **486**, 418 (2000).
15. I. I. Bigi, M. Blanke, A. J. Buras and S. Recksiegel, JHEP **0907**, 097 (2009).
16. Y. Grossman, A. L. Kagan and Y. Nir, Phys. Rev. D **75**, 036008 (2007).
17. A. L. Kagan and M. D. Sokoloff, Phys. Rev. D **80**, 076008 (2009).
18. B. Aubert *et al.* [BaBar Collaboration], Phys. Rev. Lett. **100**, 061803 (2008); M. Staric *et al.* [Belle Collaboration], Phys. Lett. B **670**, 190 (2008); D. E. Acosta *et al.* [CDF Collaboration], Phys. Rev. Lett. **94**, 122001 (2005) and CDF Public Note 10296.
19. Y. Grossman, Y. Nir and G. Perez, Phys. Rev. Lett. **103**, 071602 (2009).
20. M. Pospelov and A. Ritz, Annals Phys. **318**, 119 (2005).
21. B. C. Regan *et al.*, Phys. Rev. Lett. **88**, 071805 (2002); C. A. Baker *et al.*, Phys. Rev. Lett. **97**, 131801 (2006); W. C. Griffith *et al.*, Phys. Rev. Lett. **102**, 101601 (2009).
22. S. Pokorski, J. Rosiek and C. A. Savoy, Nucl. Phys. B **570**, 81 (2000); J. R. Ellis, J. S. Lee and A. Pilaftsis, JHEP **0810**, 049 (2008); Y. Li, S. Profumo, M. Ramsey-Musolf, JHEP **1008** , 062 (2010).
23. J. Hisano, M. Nagai and P. Paradisi, Phys. Rev. D **80**, 095014 (2009).

HEAVY FLAVOR PHYSICS AT THE TEVATRON

JULIA THOM, FOR THE D0 AND CDF COLLABORATIONS
Cornell University, Department of Physics, 395 Physical Sciences Building, 142 Sciences Drive, Ithaca, NY 14853, USA

Recent heavy flavor results at a center of mass energy of 1.96 TeV are presented. The measurements and searches were performed by the D0 and CDF collaborations, using between 1-6 fb^{-1} of data, taken during Run II at the Tevatron.

1 B_s mixing phase from $B_s \to J/\Psi\Phi$ and A_{sl}

The B_s mixing phase is expected to be tiny in the Standard Model (SM):

$$\beta_s^{SM} = arg(-V_{ts}V_{tb}^*/V_{cs}V_{cb}^*) \approx 0.02, \tag{1}$$

and it is unconstrained by the 2006 measurements of the B_s mixing frequency. Large values, as those induced by New Physics (NP) have not been excluded. The values are accessed experimentally by studying the time evolution of flavor tagged $B_s \to J/\Psi\Phi$ decays or, inclusively, by measuring mixing rate differences between B_s and $\overline{B_s}$. The CDF and D0 collaborations have pursued both paths, and first measurements showed interesting indications of departure from SM predictions, calling for more studies.

1.1 Measurement of the di-muon charge asymmetry at D0

One of the results that has caused much excitement recently has been presented by the D0 collaboration, where the asymmetry of muon pairs produced in semileptonically decaying b hadrons is measured[1]. The asymmetry A_{sl}^b is defined as

$$A_{sl}^b = \frac{N_b^{++} - N_b^{--}}{N_b^{++} + N_b^{--}}, \tag{2}$$

where N_b^{++} and N_b^{--} are the numbers of events with two b hadrons decaying semileptonically to produce a same sign muon pair. One of the muons is from a $b \to \mu X$ decay, and the other muon from a semileptonic decay after mixing. The quantity A_{sl}^b is expected to be approximately zero within the SM. D0's analysis of 6.1 fb^{-1} of Run II data yields $A_{sl}^b = (-0.957 \pm 0.251(stat.) \pm 0.146(syst.))\%$, which differs from the SM prediction[2] of $A_{sl}^b(SM) = (-0.023^{+0.005}_{-0.006})\%$ at about 3.2σ, indicating an anomalously large B_s mixing phase. Fig.1 shows the asymmetry band in red, the SM prediction, and measurements of a_{sl}^s from D0 and a_{sl}^d from the B factories, for comparison.

The CDF collaboration is also working on an analysis of A_{sl}^b, using a different technique. In it, the muon impact parameter (IP) information is used to fit for the muon sample composition,

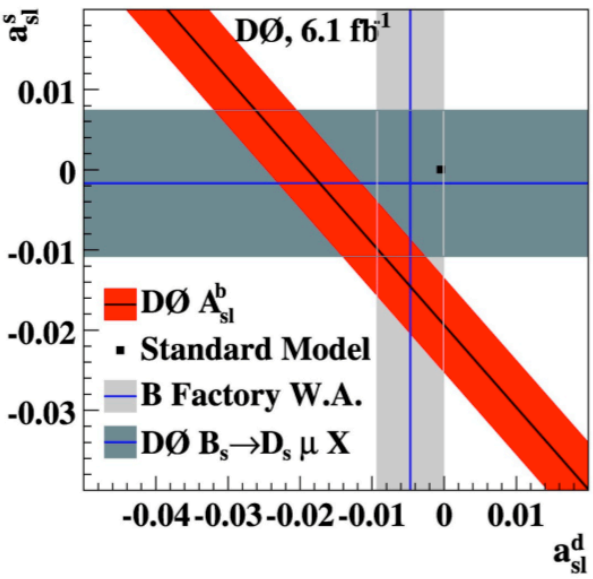

Figure 1: Di-muon charge asymmetry, measured at D0 with 6.1 fb^{-1} of Run II data.

ensuring that same sign di-muons originate from B decays. This technique has already been used and documented, for example in the CDF measurement of the correlated $B\overline{B}$ cross section[3]. As a first step, CDF has measured the time-integrated mixing probability $\overline{\chi}$, using the IP fit technique.

1.2 Measurement of the time-integrated mixing probability $\overline{\chi}$ at CDF

The time-integrated mixing probability $\overline{\chi}$ is defined as

$$\overline{\chi} = \frac{\Gamma(B^0_{d,s} \to \overline{B}^0_{d,s} \to l^+ X)}{\Gamma(B_{all} \to l^{\pm} X)} \tag{3}$$

defining an average mixing probability of semileptonically decaying B_d and B_s mesons. At CDF, the number of oppositely charged and same-sign muon pairs is measured and $\overline{\chi}$ is extracted from the ratio $R = [N(\mu^+\mu^+) + N(\mu^-\mu^-)]/N(\mu^+\mu^-)$. A 2004 measurement from CDF[4], showed a discrepancy with an earlier result from LEP. A new CDF result using 1.4 fb^{-1} of data now uses a much tighter muon selection, requiring at least one hit in the first layer of the Silicon Vertex Detector, thus improving the impact parameter measurement significantly. The result is

$$\overline{\chi} = 0.126 \pm 0.008, \tag{4}$$

in very good agreement with the LEP result of $\overline{\chi} = 0.126 \pm 0.004$, and it presents an encouraging first step toward CDF's future A_{sl} measurement.

2 The $B_s \to J/\Psi\Phi$ system

$B_s \to J/\Psi\Phi$ decays are still considered the best probe for new sources of CP violation in B_s decays, however the analysis is complicated by the fact that B_s mesons (spin 0) decay to J/Ψ (spin1) and Φ (spin 0), giving rise to s-wave as well as p-wave contributions. The analysis, documented extensively before, uses a simultaneous fit to mass, decay time, angles and production flavor distributions. Fig.2 documents the current results. The D0 measurement

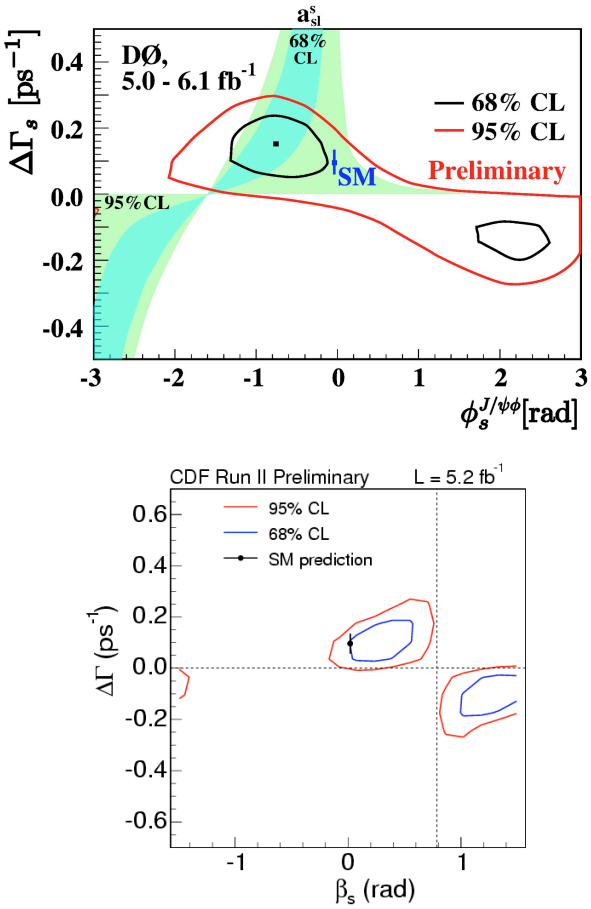

Figure 2: D0 and CDF results of fits to the B_s mixing phase in $B_s \to J/\Psi\Phi$ decays. In the top plot (D0), the information from the measurement of the di-muon charge asymmetry is overlaid in green.

uses 6.1 fb^{-1} and shows a mild disagreement between the SM value and the best fit value, and the CDF result, based on 5.2 fb^{-1}, shows good agreement. It is clear that more information is needed to settle the questions that arise.

An alternative way to access β_s is through the study of $B_s \to J/\Psi f0(980)$ decays. This suppressed decay is a CP=-1 eigenstate and will provide a clean measure of the CP violating parameter β_s, since no complex angular analysis is necessary. Here, the first step toward this goal is reported, which is the reconstruction of this signal and the measurement of the branching ratio in 3.8 fb^{-1} data taken with the CDF detector.

3 Measurement of $BR(B_s \to J/\Psi f0(980))$ at CDF

The search for $B_s \to J/\Psi f0(980)$ decays starts with a loose selection of $\mu\mu\pi\pi$ candidates, which is then improved using a Neural Network based on kinematic variables, track and vertex displacement, and isolation. The identical selection is used for the $B_s \to J/\Psi\Phi$ reference mode. A fit to the signal and normalization channels finally yields 571±37(stat.)±25(syst.) $B_s \to J/\Psi f0(980)$ candidates. For comparison, 2302±49 $B_s \to J/\Psi\Phi$ candidates are observed. Fig.3 shows the invariant mass of the $J/\Psi\pi\pi$ candidate events. The ratio between $BR(B_s \to J/\Psi f0(980), f0(980) \to \pi\pi)$ and $BR(B_s \to J/\Psi\Phi, \Phi \to KK)$ candidates is $0.292 \pm 0.020(stat.) \pm 0.017(syst.)$, resulting in a measurement of the branching ratio

$$BR(B_s \to j/\Psi f0(980), f0(980) \to \pi\pi = 1.85 \pm 0.13(stat.) \pm 0.11(syst.) \pm 0.57(PDG) \times 10^{-4}. \quad (5)$$

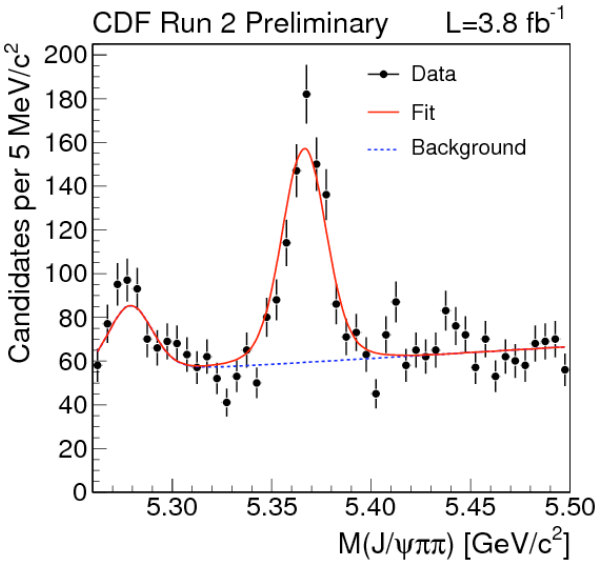

Figure 3: The invariant mass of selected $J\Psi\pi\pi$ candidate events, as measured at CDF with 3.8 fb^{-1} of data.

The significance of the observation is 17.9σ, and confirms earlier resuts from Belle and LHC-b with higher precision.

4 Search for CP Violation in $D \to \pi\pi$ and $D \to KK$ at CDF

CP violation in the charm sector has been an area of great interest, and recent studies[5] have pointed out that, similarly to D^0 oscillations, NP contributions could play a role in enhancing the size of CP violation in the charm sector. An asymmetry is defined as

$$A_{CP}(h^+h^-) = \frac{\Gamma(D^0 \to h^+h^-) - \Gamma(\overline{D^0} \to h^+h^-)}{\Gamma(D^0 \to h^+h^-) + \Gamma(\overline{D^0} \to h^+h^-)}. \tag{6}$$

At CDF, 5.94 fb^{-1} of data is used to analyze D^* tagged D^0 decays. The asymmetry in $\pi\pi$ and KK samples is measured and corrected for the instrumental asymmetry using $K\pi$ samples, with and without the D^* tag. The resulting limits are the world's most sensitive limits:

$$A_{CP}(D^0 \to \pi^+\pi^-) = [+0.22 \pm 0.24(stat.) \pm 0.11(syst.)]\% \tag{7}$$

$$A_{CP}(D^0 \to K^+K^-) = [-0.24 \pm 0.22(stat.) \pm 0.10(syst.)]\% \tag{8}$$

5 CP Asymmetry in $B^\pm \to D^0h^\pm$ at CDF

The branching fractions and searches for CP asymmetries in $B^\pm \to D^0h^\pm$ decays allow for a clean measurement of γ, the least well constrained angle of the CKM matrix. To this end, the ADS method has been proposed[6], making use of doubly Cabibbo suppressed (DCS) D^0 modes. CDF's new measurement of direct CP asymmetry for the DCS modes will be used in the future to extract γ. A DCS fraction and asymmetry is defined as follows:

$$R_{ADS}(K) = \frac{BR(B^- \to [K^+\pi^-]_D K^-) + BR(B^+ \to [K^-\pi^+]_D K^+)}{BR(B^- \to [K^-\pi^+]_D K^-) + BR(B^+ \to [K^+\pi^-]_D K^+)} \tag{9}$$

$$A_{ADS}(K) = \frac{BR(B^- \to [K^+\pi^-]_D K^-) - BR(B^+ \to [K^-\pi^+]_D K^+)}{BR(B^- \to [K^-\pi^+]_D K^-) + BR(B^+ \to [K^+\pi^-]_D K^+)} \tag{10}$$

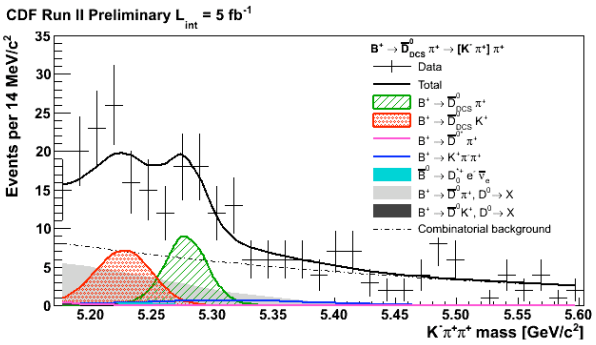

Figure 4: The invariant $K^+\pi^+\pi^-$ mass with data and various background and signal distributions, as measured at CDF with 5 fb^{-1}.

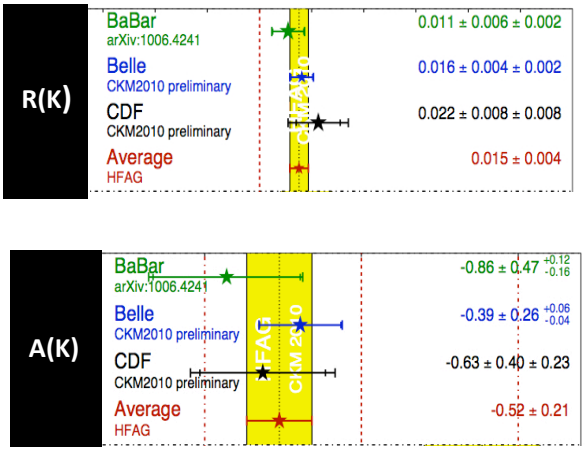

Figure 5: The results of measurements of DCS fractions and asymmetries for the Kaon mode, as measured at CDF with 5 fb^{-1}.

(11)

and similar for pions. The experimental challenge is to suppress combinatorial and physics backgrounds when extracting the highly suppressed DCS signal. Using 4 fb^{-1} of data taken with the CDF detector, a combined Likelihood fit is used to distinguish the signal modes from background. As an example, Fig.4 shows the invariant $K^+\pi^+\pi^-$ mass with data and various background and signal distributions. The results for the Kaon mode are shown in Fig.5, demonstrating good agreement with BaBar and Belle. It is the first application of the ADS method at a hadron machine.

6 Conclusion

The Tevatron is producing a steady flow of interesting Heavy Flavor results, and a few of them have been summarized in this article. For the analyses described here, only a fraction of the final Run II data has been used, and we look forward to challenging the SM predictions of Heavy Flavor Physics and constraining parameters of NP models in the months and years to come.

Acknowledgments

I would like to thank the CDF and D0 collaborations for their help in preparing this contribution. I would like to acknowledge support from the National Science Foundation (USA).

References

1. Abazov et al, *Phys. Rev. Lett.* **105**, 081801 (2010).
2. Lenz, Nierste, hep-ph/0612167.
3. CDF collaboration, *Phys. Rev.* D **77**, 072004 (2008).
4. CDF collaboration, *Phys. Rev.* D **69**, 012002 (2004).
5. Grossman, Kagan, Nir, *Phys. Rev.* D **75**, 036008 (2006).
6. Atwood, Dunietz, Soni, *Phys. Rev. Lett.* **78**, 3257 (1997) and *Phys. Rev.* D **63**, 036005 (2001).

THE PHENO-ANALYSIS OF $B \to K^{(*)}\mu^+\mu^-$ DECAYS IN 2011 PLUS

G.HILLER
Institut für Physik, Technische Universität Dortmund, D-44221 Dortmund, Germany

We report on recent developments in the phenomenology of exclusive $b \to s\mu^+\mu^-$ decays in testing the standard model and explore its borders: the benefits of the region of large dimuon invariant masses and the exploitation of the angular distributions. Consequences of model-independent analyses from current and future data are pointed out.

1 Introduction

There exists a strong and long-standing interest in $\Delta B = 1$ exclusive $b \to s\mu^+\mu^-$ processes because of their accessibility at hadron colliders, good theory control and sensitivity to short-distance physics within and beyond the standard model, see, for instance [1,2]. Many modes have been observed by now by several experiments with branching ratios at the level of $10^{-(6-7)}$, such as $B \to K^{(*)}\mu^+\mu^-$ by BaBar [3], Belle [4], CDF [5], and recently $B_s \to \Phi\mu^+\mu^-$ decays by CDF [5].

At present, each experiment has collected about order hundred events per mode. This already enables dedicated studies of spectra and asymmetries [6,7], which exhibit a much larger sensitivity to electroweak physics than the determination of the (un-binned integrated) branching ratios. The situation will further improve in the near future with the anticipated updates from the b-factories and the Tevatron, and with the ongoing run of the LHC. In fact, LHCb has reported 35 $B^+ \to K^+\mu^+\mu^-$ events in 37 pb^{-1}, and expects by the end of 2011 with 1 fb^{-1} order 10^3 $B \to K^*\mu^+\mu^-$ events [8].

2 $B \to K^*\mu^+\mu^-$ Theory and Recent Highlights

The kinematically available phase space in $B \to K^{(*)}\mu^+\mu^-$ decays is $4m_\mu^2 \le q^2 < (m_B - m_{K^{(*)}})^2$ for the dilepton invariant mass squared q^2. This region is fully covered experimentally with the exception of the J/Ψ and Ψ' resonances from $B \to K^{(*)}(\bar{c}c) \to K^{(*)}\mu^+\mu^-$, which are removed by cuts. A systematic theory treatment exists for the region of high $q^2 \sim \mathcal{O}(m_b^2)$ by means of an operator product expansion (OPE) put forward by Grinstein and Pirjol some time ago [9]. The latter approach has recently been phenomenologically developed and exploited [6,7]. We give a brief overview of the benefits of the high-q^2 region, corresponding to low hadronic recoil, in Section 2.1. In the region of low q^2, where the $K^{(*)}$ is energetic in the B restframe, the decays are eligible to QCD factorization methods [10]. The region between the J/Ψ and the Ψ' peaks is informative on charmonia physics [11].

Because of the different theory frameworks applicable to the low-q^2 and high-q^2 region, as well as the resonance veto, appropriately q^2-binned data are vital for precisely testing the standard model with exclusive semileptonic $b \to s\mu^+\mu^-$ modes. The current situation is exemplified in Figure 1 for the forward-backward asymmetry $A_{\rm FB}$ in $B \to K^*\mu^+\mu^-$ decays.

2.1 The High-q^2 Region

The OPE [9] in $1/Q$, $Q = \{m_b, \sqrt{q^2}\}$ is combined with the improved heavy quark form factor relations [12] between the dipole form factors $T_{1,2,3}$ and vector ones $V, A_{1,2}$. To leading order in $1/m_b$ and including radiative corrections

$$T_1(q^2) = \kappa V(q^2), \qquad T_2(q^2) = \kappa A_1(q^2), \qquad T_3(q^2) = \kappa A_2(q^2)\frac{m_B^2}{q^2}, \tag{1}$$

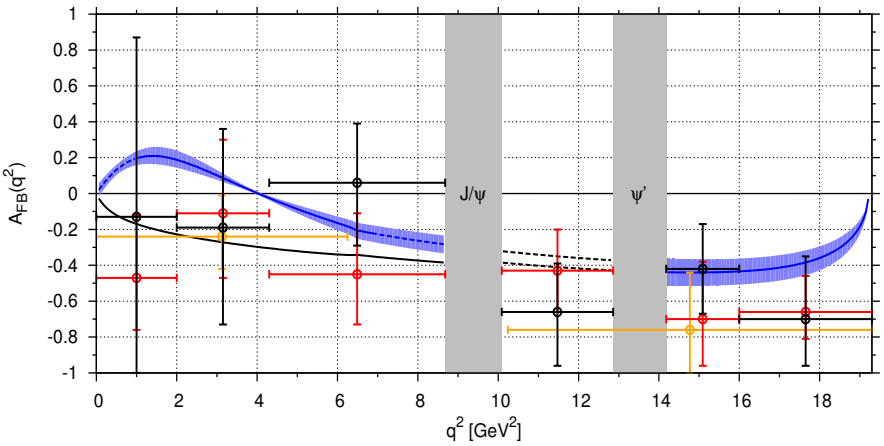

Figure 1: $A_{\rm FB}(B \to K^*\mu^+\mu^-)$ in the standard model (blue band) versus data: CDF '10 with 4.4fb^{-1} (black), BaBar '08 (gold) and Belle '09 (red). The black solid curve corresponds to $C_7 = -C_7^{\rm SM}$. Figure taken from [6].

where $\kappa = 1 - 2\alpha_s/3\pi \ln(\mu/m_b) \simeq 1$. The heavy quark-based OPE is powerful because it predicts a simple transversity structure for the $B \to K^*\mu^+\mu^-$ decay amplitudes: Each of the transversity amplitudes $A_i^{L/R}$, $i = 0, \perp, ||$ factorizes into universal short-distance $C^{L/R}$ and form factor coefficients f_i as [6] [a]

$$A_i^{L/R} \propto C^{L/R} \cdot f_i, \tag{2}$$

up to corrections of order $\alpha_s\Lambda/m_b$ and $(C_7/C_9)\Lambda/m_b$ that is, a few percent. This in turn allows to design high-q^2 observables which are [6] [7]

1. independent of the form factors ($H_T^{(2,3)}$, $a_{\rm CP}^{(i)}$); note that $H_T^{(3)}$ probes the same short-distance physics as $A_{\rm FB}$ while having a significantly smaller theoretical uncertainty.

2. independent of the short-distance coefficients (f_i/f_j) and test the form factors at low recoil, for instance, the ratio $V/A_1 \propto \sqrt{(2J_2^s + J_3)/(2J_2^s - J_3)}$. An extraction from data can be used to compare against theory predicitions from lattice [20] or other means.

3. independent of neither short-distance nor form factor coefficients and test the theoretical low recoil framework, such as

$$H_T^{(1)} = 1, \qquad J_7 = 0. \tag{3}$$

The new form factor-free high-q^2 observables $H_T^{(i)}$ are defined in terms of the transversity amplitudes as

$$H_T^{(1)}(q^2) = \frac{\mathrm{Re}(A_0^L A_\parallel^{L*} + A_0^{R*} A_\parallel^R)}{\sqrt{(|A_0^L|^2+|A_0^R|^2)(|A_\parallel^L|^2+|A_\parallel^R|^2)}} = \frac{\sqrt{2}J_4}{\sqrt{-J_2^c(2J_2^s - J_3)}}, \tag{4}$$

$$H_T^{(2)}(q^2) = \frac{\mathrm{Re}(A_0^L A_\perp^{L*} - A_0^{R*} A_\perp^R)}{\sqrt{(|A_0^L|^2+|A_0^R|^2)(|A_\perp^L|^2+|A_\perp^R|^2)}} = \frac{\beta_l J_5}{\sqrt{-2J_2^c(2J_2^s + J_3)}}, \tag{5}$$

$$H_T^{(3)}(q^2) = \frac{\mathrm{Re}(A_\parallel^L A_\perp^{L*} - A_\parallel^{R*} A_\perp^R)}{\sqrt{(|A_\parallel^L|^2+|A_\parallel^R|^2)(|A_\perp^L|^2+|A_\perp^R|^2)}} = \frac{\beta_l J_6}{2\sqrt{(2J_2^s)^2 - J_3^2}}, \tag{6}$$

or likewise the angular coefficients $J_i(q^2)$. Ways to extract the latter from single or double differential angular distributions in $B \to K^*(\to K\pi)\mu^+\mu^-$ decays have been given in [13].

[a] Assuming standard model-type operators commonly termed $\mathcal{O}_7, \mathcal{O}_9$ and $\mathcal{O}_{10}$.

Eq. (2) further limits the number of independent CP-asymmetries in $B \to K^* \mu^+ \mu^-$ decays to three, one related to the rate, $a_{\rm CP}^{(1)}$, one related to $A_{\rm FB}$, $a_{\rm CP}^{(2)}$, or with a more favorable normalization related to $H_T^{(2,3)}$, $a_{\rm CP}^{(3)}$, and one from meson mixing, $a_{\rm CP}^{mix}$ [7].

Beylich *et al.* [14] recently proposed a local expansion without engaging heavy quark effective theory. In their OPE, Eq. (2) is not manifest, hence the aforementioned symmetry-based high-q^2 predictions 1. – 3. are no longer explicit, however, the OPE itself has a simpler structure. It will become most useful once all $B \to K^*$ form factors are known with sufficient accuracy.

The treatment of the high-q^2 region is based on an OPE, whose performance can be tested by checking *e.g.*, Eq. (3). The OPE is supported by consistency between the constraints obtained from excluding and using only the high-q^2 region data [6], and by a recent model-study [14].

2.2 Angular Distributions

With high event rates at the horizon the angular analysis with an on-shell decaying $K^* \to K\pi$ [15] has received recently a lot of attention as a tool to maximize the extraction of physics from $B \to K^* \mu^+ \mu^-$ decays [6,7,13,16,17,18]. In a full angular analysis the quartic differential decay distribution $d^4\Gamma$ factorizes into q^2-dependent angular coefficients J_i and trigonometric functions of three angles: θ_l, the angle between the l^- and the $\bar{B}$ in the dilepton CMS, θ_{K^*}, the angle between the K and the $\bar{B}$ in the K^*-CMS and ϕ, the angle between the normals of the $K\pi$ and l^+l^- plane

$$d^4\Gamma = \frac{3}{8\pi} J(q^2, \theta_l, \theta_{K^*}, \phi) dq^2 d\cos\theta_l d\cos\theta_{K^*} d\phi, \tag{7}$$

where

$$\begin{aligned} J(q^2, \theta_l, \theta_{K^*}, \phi) &= J_1^s \sin^2\theta_{K^*} + J_1^c \cos^2\theta_{K^*} + (J_2^s \sin^2\theta_{K^*} + J_2^c \cos^2\theta_{K^*}) \cos 2\theta_l \\ &+ J_3 \sin^2\theta_{K^*} \sin^2\theta_l \cos 2\phi + J_4 \sin 2\theta_{K^*} \sin 2\theta_l \cos\phi + J_5 \sin 2\theta_{K^*} \sin\theta_l \cos\phi \\ &+ J_6 \sin^2\theta_{K^*} \cos\theta_l + J_7 \sin 2\theta_{K^*} \sin\theta_l \sin\phi \\ &+ J_8 \sin 2\theta_{K^*} \sin 2\theta_l \sin\phi + J_9 \sin^2\theta_{K^*} \sin^2\theta_l \sin 2\phi, \qquad J_i = J_i(q^2). \end{aligned} \tag{8}$$

The angular analysis offers opportunities for searches for beyond the standard model (BSM) CP-violation. The angular distribution $d^4\bar{\Gamma}$ of the CP-conjugate decays is obtained from $d^4\Gamma$ after flipping the sign of the CP phases and by replacing $J_{1,2,3,4,7} \to \bar{J}_{1,2,3,4,7}$ and $J_{5,6,8,9} \to -\bar{J}_{5,6,8,9}$. Several CP-asymmetries $A_i \propto J_i - \bar{J}_i$ can be obtained. Highlights include [7,13]: $A_{3,9}$ vanish in the standard model by helicity conservation, hence, they are sensitive to right-handed currents. $A_{3,9,(6)}$ can be extracted from a single-differential distribution in $\phi(\theta_l)$. $A_{7,8,9}$ are (naive) T-odd and not suppressed by small strong phases; they can be order one with order one BSM CP-phases. $A_{5,6,8,9}$ and $a_{\rm CP}^{(3)}$ are CP-odd and can be extracted without tagging from $\Gamma + \bar{\Gamma}$; this is advantageous for $B_s, \bar{B}_s \to (\Phi \to K^+K^-)\mu^+\mu^-$ decays which are not self-tagging; time-integrated measurements are possible as well. Note that in the standard model all $b \to s$ CP-asymmetries are doubly Cabibbo-suppressed and small. At high q^2, due to Eq. (2), $A_{7,8,9} = 0$. The angular distribution in $B \to K\mu^+\mu^-$ decays involves only one angle θ_l and is simpler [19].

3 BSM Implications

Measurements of $B \to K^* \mu^+ \mu^-$ observables place model-independent constraints on the Wilson coefficients of the four-fermi operators $\mathcal{O}_{9,10}$. Assuming real-valued coefficients C_9, C_{10} the constraints from branching ratio and $A_{\rm FB}$ spectra at high q^2 are illustrated in the left-handed plot of Figure 2. The high-q^2 constraints from $A_{\rm FB} \sim Re(C_{10}C_9^*)$ are orthogonal to the ones from the branching ratio $\sim |C_9|^2 + |C_{10}|^2$. The magnitude of C_7 is fixed by the measured $B \to X_s\gamma$ branching ratio to be near its standard model value.

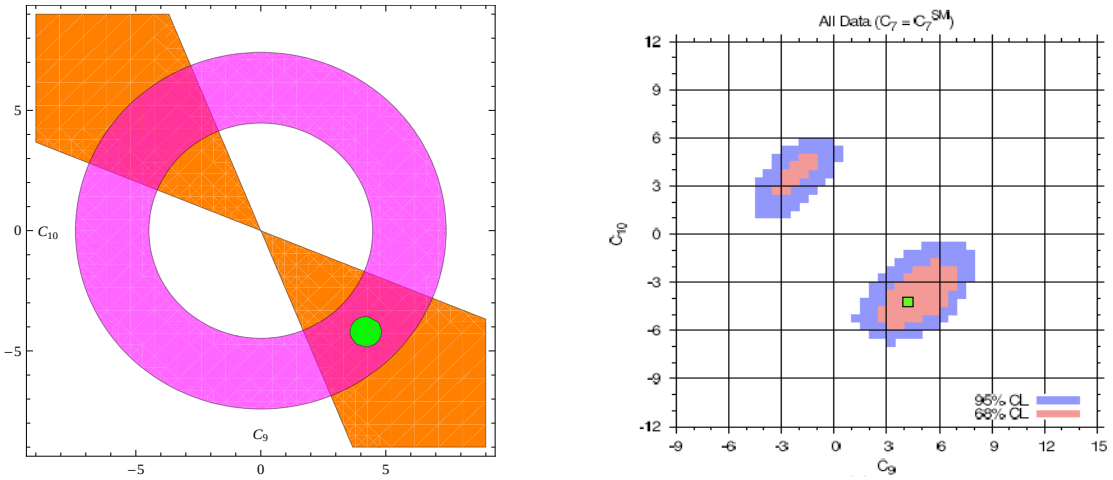

Figure 2: Todays model-independent bounds on real-valued C_9, C_{10} from $b \to s\mu^+\mu^-$ decays for $C_7 \simeq C_7^{\rm SM} < 0$. The left-handed plot is schematic only and illustrates the allowed regions from branching ratio measurements (magenta ring) and $A_{\rm FB}$ determinations at large q^2 (orange wedges). The green dot corresponds to $(C_9^{\rm SM}, C_{10}^{\rm SM})$. The right-handed plot with the allowed 68 and 95 % C.L. regions is taken from Ref. [6]. There are similar plots for $C_7 \simeq -C_7^{\rm SM} > 0$, hence in total four disconnected allowed regions in C_7, C_9 and C_{10}.

The outcome of a recent analysis using $B \to K^*\mu^+\mu^-$ data [3,4,5] as well as the constraints from $B \to X_s l^+ l^-$ decays is shown in the right-handed plot of Figure 2 [6]. The constraints from $A_{\rm FB}$ at high q^2 significantly improve the scan. They are manifest in the plane by selecting arcs from the area allowed by the various branching ratio measurements. Because of the $Re(C_7 C_9^*)$ interference term in $\mathcal{B}(B \to X_s l^+ l^-)$ the ambiguity in the disconnected allowed regions is mildly broken. The allowed regions include the standard model, but order one deviations in all three Wilson coefficients C_7, C_9 and C_{10} are allowed as well.

The experimental situation of $A_{\rm FB}$ at low q^2, unlike the one at high q^2, is currently not settled, see Figure 1. To find out whether there is a zero-crossing of the $A_{\rm FB}$ at low q^2 as predicted by the standard model $q_0^2|_{\rm SM} = 4.36^{+0.33}_{-0.31}\,{\rm GeV}^2$ (for $B^0 \to K^{*0}\mu^+\mu^-$), $q_0^2|_{\rm SM} = 4.15 \pm 0.27\,{\rm GeV}^2$ (for $B^+ \to K^{*+}\mu^+\mu^-$) [10] and likewise for $B \to X_s l^+ l^-$ decays $q_0^2|_{\rm SM} = (3.34 \ldots 3.40)^{+0.22}_{-0.25}\,{\rm GeV}^2$ [21] remains a central goal for next years b-physics programs.

A future analysis assuming the existence and determination of the $A_{\rm FB}$ zero at low q^2 is given in Figure 3. The establishment of the zero reduces the four-fold ambiguity to two. Resolving the last ambiguity requires precision studies sensitive to the contributions from four-quark operators which are commonly absorbed in the effective coefficients $C_i^{\rm eff}$. Assuming vanishing or very small CP phases a lower bound on the position of the $A_{\rm FB}(B \to K^*\mu^+\mu^-)$ zero can be derived from the respective upper bounds on $|C_9|$ [6]. Very roughly, $q_0^2 \simeq q_0^2|_{\rm SM} |C_9^{\rm SM}|/|C_9^{\rm max}| \gtrsim 2\,{\rm GeV}^2$.

Model-independent $\Delta B = 1$ BSM implications can be drawn using an effective theory[b]

$$\mathcal{H}_{\rm eff} = \sum_i \frac{\tilde{c}_i}{\Lambda_{\rm NP}^2} \widetilde{O}_i\,, \qquad \widetilde{O}_{10} = \bar{s}\gamma_\mu(1-\gamma_5) b\, \bar{\mu}\gamma^\mu\gamma_5\mu\,. \tag{9}$$

Assuming new physics at the scale $\Lambda_{\rm NP} = 1$ TeV the coefficient of the higher dimensional operator $\tilde{O}_{10}$ needs a (flavor) suppression as strong as $|\tilde{c}_{10}| < 2 \cdot 10^{-3}\,(5 \cdot 10^{-3})$. If one assumes no suppression at all, $|\tilde{c}_{10}| = 1$, the scale of new physics is pushed up to

$$\Lambda_{\rm NP} > 26\,{\rm TeV}\ (15\,{\rm TeV})\,. \tag{10}$$

The bounds are obtained at 95 % C.L. [6]. The first numbers correspond to $\max|C_{10} - C_{10}^{\rm SM}|$ from the nearby solution, that is, from the allowed region including the standard model whereas

[b] Thanks to Gilad Perez for suggesting this.

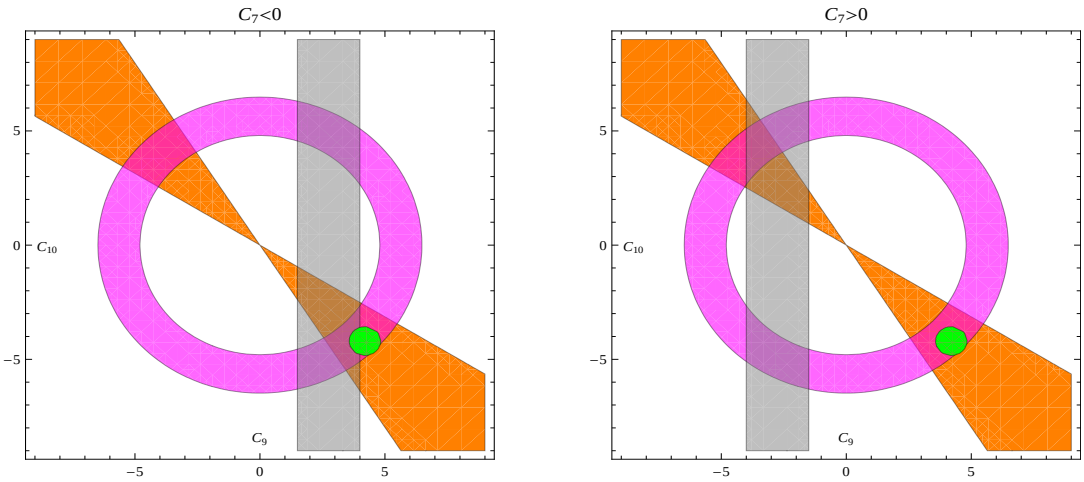

Figure 3: Future scenario of the model-independent bounds on real-valued C_9, C_{10} from $b \to s\mu^+\mu^-$ decays for $C_7 \simeq C_7^{\rm SM} < 0$ (left-handed plot) and $C_7 \simeq -C_7^{\rm SM} > 0$ (right-handed plot). The grey vertical bands denote the constraints arising if an $A_{\rm FB}$ zero at low q^2 could be established. There remain two allowed disconnected regions.

the weaker bounds in parentheses are obtained from the far away region, not connected to $(C_9^{\rm SM}, C_{10}^{\rm SM})$.

A recent complex-valued scan [22] in $C_{7,9,10}$ returns the allowed 68% C.L. (95% C.L.) ranges [7]

$$\begin{aligned} 0.8 \le |C_9| \le 6.8 \quad (0.0 \le |C_9| \le 7.8)\,, \\ 1.8 \le |C_{10}| \le 5.5 \quad (0.8 \le |C_{10}| \le 6.3)\,. \end{aligned} \tag{11}$$

with some of the lower bounds being sensitive to the discretization of the scan. The constraints on the CP phases are not very strong, approximately $\frac{\pi}{2} \lesssim \arg\,(C_9 C_{10}^*) \lesssim \frac{3\pi}{2}$ at 68% C.L. [7].

Eqs. (11) imply a maximal enhancement of the $\bar{B}_s \to \mu^+\mu^-$ branching ratio $\mathcal{B}(\bar{B}_s \to \mu^+\mu^-) \propto f_{B_s}^2 |C_{10}|^2$ with respect to its standard model value by a factor 2.3. The dominant uncertainty of the standard model prediction is stemming from the decay constant of the B_s meson. Using [23] [24] gives [7]

$$\begin{aligned} \mathcal{B}(\bar{B}_s \to \mu^+\mu^-)_{\rm SM} = (3.1 \pm 0.6) \times 10^{-9}, \quad f_{Bs} = 231(15)(4)\,{\rm MeV} \quad \text{(Gamiz et al '09)}, \\ \mathcal{B}(\bar{B}_s \to \mu^+\mu^-)_{\rm SM} = (3.8 \pm 0.4) \times 10^{-9}, \quad f_{Bs} = 256(6)(6)\,{\rm MeV} \quad \text{(Simone et al '10)}. \end{aligned} \tag{12}$$

It follows the upper limit (at 95 % C.L.) [7]

$$\mathcal{B}(\bar{B}_s \to \mu^+\mu^-) < 10 \times 10^{-9}\,, \tag{13}$$

which could be invalidated by sizable contributions from scalar and pseudo-scalar operators not considered here. Experimentally, $\mathcal{B}(\bar{B}_s \to \mu^+\mu^-) < 43 \times 10^{-9}$ at 95 % C.L. from CDF [25].

4 Outlook

At this stage first results for basic decay distributions and asymmetries of exclusive $b \to s l^+ l^-$ modes have become available. With more data soon and shrinking error bars the constraints from the $\Delta B = 1$ analysis will tighten. Steep progress in the BSM reach is expected from additional and complementary observables which could remove – or verify – currently allowed solutions far away from the standard model. A useful nearer term observable in this regard is $A_{\rm FB}$ at low recoil, perhaps also combined with improved constraints from the $B \to X_s l^+ l^-$ branching ratio. Further observables designed with good theory properties are accessible by angular analysis, which is promising for higher statistics searches.

BSM models often induce operators beyond those of the standard model. These include right-handed currents, enhanced scalar and pseudo-scalar couplings or lepton-flavor non-universal effects, and can *e.g.* be searched for with, respectively, transverse asymmetries [16], $\bar{B}_s \to \mu^+\mu^-$ or by comparing $l = e$ to μ modes [19]. $\mathcal{O}(1)$ BSM CP phases can show up as $\mathcal{O}(1)$ T-odd CP asymmetries $A_{7,8,9}$ [13]. Angular analysis becomes most powerful and essential here.

Dimuons provide great opportunities for LHC(b) and the Tevatron. They could also be studied at future super flavor e^+e^- factories, which moreover have good capabilities to investigate dielectron and inclusive modes, and missing energy searches covering $l = \nu$ or possibly $l = \tau$.

Acknowledgments

GH is happy to thank her collaborators from the EOS team and the organizers of the 2011 Moriond Electroweak session for the invitation to the meeting. The works presented here are supported in part by the Bundesministerium für Bildung und Forschung (BMBF).

1. A. Ali, P. Ball, L. T. Handoko and G. Hiller, Phys. Rev. D **61**, 074024 (2000), [arXiv:hep-ph/9910221].
2. C. Bobeth, G. Hiller and G. Piranishvili, PoS **BEAUTY2009**, 047 (2009) [arXiv:0911.4054 [hep-ph]].
3. B. Aubert *et al.* [BABAR Collaboration], Phys. Rev. Lett. **102**, 091803 (2009), [arXiv:0807.4119 [hep-ex]].
4. J. T. Wei *et al.* [BELLE Collaboration], Phys. Rev. Lett. **103**, 171801 (2009), [arXiv:0904.0770 [hep-ex]].
5. T. Aaltonen *et al.* [CDF Collaboration], arXiv:1101.1028 [hep-ex].
6. C. Bobeth, G. Hiller and D. van Dyk, JHEP **1007**, 098 (2010), [arXiv:1006.5013 [hep-ph]].
7. C. Bobeth, G. Hiller and D. van Dyk, arXiv:1105.0376 [hep-ph].
8. A. Golutvin for the LHCb collaboration; Talk given at La Thuile 2011.
9. B. Grinstein and D. Pirjol, Phys. Rev. D **70**, 114005 (2004), [arXiv:hep-ph/0404250].
10. M. Beneke, T. Feldmann, D. Seidel, Eur. Phys. J. **C41**, 173-188 (2005), [hep-ph/0412400].
11. A. Khodjamirian, T. Mannel, A.A. Pivovarov and Y.M. Wang, JHEP **1009** (2010) 089, [arXiv:1006.4945 [hep-ph]].
12. B. Grinstein and D. Pirjol, Phys. Lett. B **533**, 8 (2002), [arXiv:hep-ph/0201298].
13. C. Bobeth, G. Hiller and G. Piranishvili, JHEP **0807**, 106 (2008), [arXiv:0805.2525 [hep-ph]].
14. M. Beylich, G. Buchalla and T. Feldmann, arXiv:1101.5118 [hep-ph].
15. F. Kruger, L. M. Sehgal, N. Sinha and R. Sinha, Phys. Rev. D **61**, 114028 (2000) [Erratum-ibid. D **63**, 019901 (2001)], [arXiv:hep-ph/9907386].
16. U. Egede *et al.*, JHEP **0811**, 032 (2008), [arXiv:0807.2589 [hep-ph]].
17. W. Altmannshofer *et al.*, JHEP **0901**, 019 (2009), [arXiv:0811.1214 [hep-ph]].
18. U. Egede, T. Hurth, J. Matias *et al.*, JHEP **1010**, 056 (2010), [arXiv:1005.0571 [hep-ph]].
19. C. Bobeth, G. Hiller and G. Piranishvili, JHEP **0712** (2007) 040, [arXiv:0709.4174 [hep-ph]].
20. Z. Liu *et al.*, arXiv:1101.2726 [hep-ph].
21. G. Bell, M. Beneke, T. Huber, X. -Q. Li, Nucl. Phys. **B843**, 143-176 (2011), [arXiv:1007.3758 [hep-ph]].
22. D. van Dyk *et al.*, http://project.het.physik.tu-dortmund.de/source/eos.
23. E. Gamiz, C. T. H. Davies, G. P. Lepage, J. Shigemitsu and M. Wingate [HPQCD Collaboration], Phys. Rev. D **80** (2009) 014503, [arXiv:0902.1815 [hep-lat]].
24. J. Simone *et al.* [Fermilab Lattice and MILC Collaborations], PoS **LATTICE2010** (2010) 317.
25. CDF Public Note 9892; with $3.7\,\mathrm{fb}^{-1}$.

.

Demise of CKM & its aftermath [a]

Enrico Lunghi[†] and Amarjiit Soni[††b]
[†] *Physics Department, Indiana University, Bloomington, IN 47405, USA*
[††] *Department of Physics, Brookhaven National Laboratory,Upton, NY 11973, USA*


Using firmly established experimental inputs such as ϵ_K, ΔM_d, ΔM_s, Br$(B \to \tau\nu)$, γ, V_{cb} along with corresponding lattice matrix elements which have been well studied and are in full QCD such as B_K, SU3 breaking ratio ξ, B_{B_s} and in particular without using V_{ub} or the pseudoscalar decay constants f_{B_d} or f_{B_s} from the lattice, we show that the CKM-paradigm now appears to be in serious conflict with the data. Specifically the SM predicted value of $\sin 2\beta$ seems too high compared to direct experimental measured value by over 3σ. Furthermore, our study shows that new physics predominantly effects B-mixings and $B_d \to \psi K_s$, and not primarily in kaon-mixing or in $B \to \tau\nu$. Model independent operator analysis suggests the scale of underlying new physics, accompanied by a BSM CP-odd phase, responsible for breaking of the SM is less than a few TeV, possibly as low as a few hundred GeV. Two possible BSM scenarios, namely warped extra-dimensions and SM with a 4th generation, are briefly discussed. Generic predictions of warped flavor models are briefly discussed. While SM with 4th generation (SM4) is a very simple way to account for the observed anomalies, SM4 is also well motivated due to its potential role in dynamical electroweak symmetry breaking via condensation of heavy quarks and in baryogenesis.

1 Introduction

The next big step in our understanding of particle physics will be the uncovering of the electroweak symmetry breaking (EWSB) mechanism. The present and upcoming collider experiments

[a] Invited talk at the EW Moriond 2010
[b] Speaker

(Fermilab and LHC) will be able to test the Standard Model (SM) Higgs mechanism. New physics is widely expected at around the TeV scale if the Higgs mass is not to receive large radiative corrections and require severe fine-tuning. A stringent constraint on the SM mechanism of EWSB is the tight structure of flavor changing (FC) interactions: tree–level FC neutral currents are forbidden and charged currents are controlled by the Cabibbo–Kobayashi–Maskawa (CKM) [1] mixing matrix

$$V = \begin{pmatrix} 1-\frac{\lambda^2}{2} & \lambda & A\lambda^3(\rho - i\eta) \\ -\lambda & 1-\frac{\lambda^2}{2} & A\lambda^2 \\ A\lambda^3(1-\rho-i\eta) & -A\lambda^2 & 1 \end{pmatrix}. \tag{1}$$

Within the SM, the CKM matrix is the only source of FC interactions and of CP violation. There is no reason, in general, to expect that new physics (needed to stabilize the Higgs mass) at the TeV scale will be in the basis wherein the quark mass matrix is diagonal. This reasoning gives rise to another fundamental problem in particle physics, namely the flavor puzzle i.e. unless the scale of new physics is larger than 10^3 TeV it causes large FCNC especially for the $K - \bar{K}$ system. Thus flavor physics provides constraints on models of new physics up to scales that are much much larger than what is accessible to direct searches at colliders such as the Tevatron or the LHC. Flavor physics is therefore expected to continue to provide crucial information for the interpretation of any physics that LHC may find.

In the past decade significant progress was made in our understanding of flavor physics, thanks in large part to the spectacular performance of the two asymmetric B-factories. For the first time it was experimentally established that the CKM-paradigm [1] of the Standard Model (SM) provides a quantitative description of the observed CP violation, simultaneously in the B-system as well as in the K-system with a single CP-odd phase, to an accuracy of about 20% [2]. While this success of the CKM picture is very impressive, the flip side is that an accuracy of $O(20\%)$ leaves open the possibility of quite sizable new physics contributions. In this context it is important to recall that the indirect CP violation parameter, $\varepsilon_K \sim 2 \times 10^{-3}$ [3] is an asymmetry of $O(10^{-3})$ and an important reminder that if searches had been abandoned even at $O(1\%)$ the history of Particle Physics would have been completely different. Indeed, in the past few years as better data and better theoretical calculations became available some rather serious tensions have emerged [4–9].

Recently [10], we showed that the use of the latest experimental inputs along with a careful use of the latest lattice results leads to a rather strong case for a sizable contribution due to beyond the Standard Model sources of CP violation that in $\sin 2\beta$ could be around 15-25%. Clearly if this result stands further scrutiny it would have widespread and significant repercussions for experiments at the intensity as well as the high energy frontier. We also were able to isolate the presence of new physics primarily in the time dependent CP measurements via the "gold-plated" ψK_s mode which intimately involves B-mixing amplitude and the decay $B \to \psi K_s$. Our analysis does not exclude possible sub-dominant effect in kaon-mixing and/or in $B \to \tau\nu$. In particular, our analysis [10] indicates that the data does not seem to provide a consistent interpretation for the presence of large new physics contribution to the tree amplitude for $B \to \tau\nu$.

2 Choice of lattice inputs

Key inputs from experiment and from the lattice needed for our analysis are shown in Table 1. Below we briefly remark on a few of the items here that deserve special mention:

• With regard to lattice inputs we want to emphasize that quantities used here have been carefully chosen and are extensively studied on the lattice for many years. Results that we use

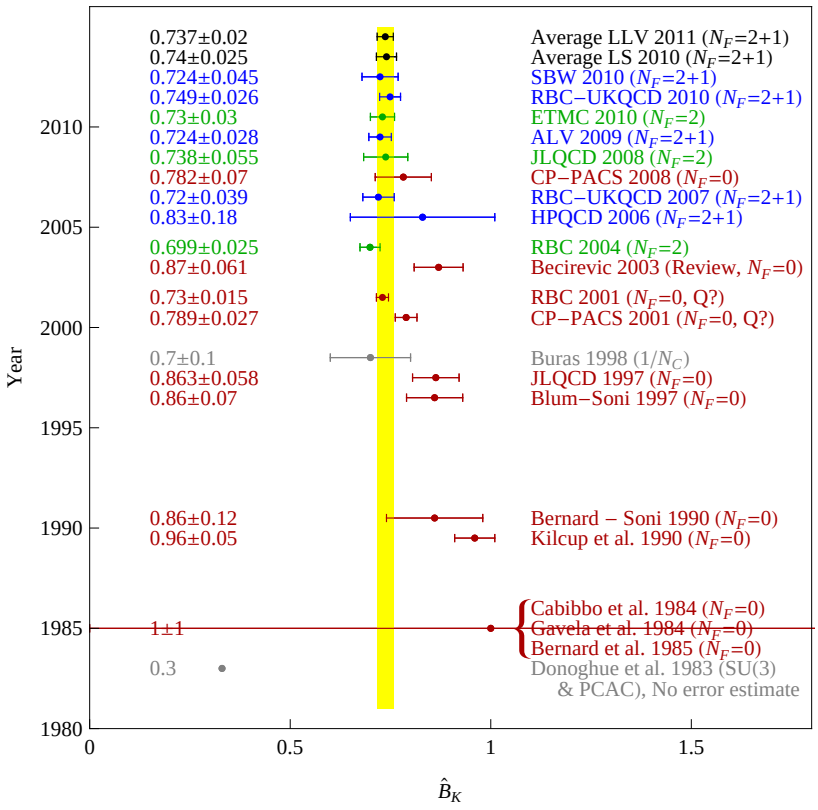

Figure 1: A quarter century of lattice–QCD efforts to improve the determination of B_K. As a representative of continuum methods, the results of Refs. [20, 21] using lowest order ChPT and $SU(3)$ flavor symmetry with no estimate of errors and of Ref. [22,23] using large N_C are shown in gray. Several quenched lattice results are shown in red. In particular, three earliest attempts on the lattice around 1984-85 (marked as Cabibbo *et al.*, Gavela *et al.* and Bernard *et al.*) [24–26]. Amongst these early attempts are also [27] using Wilson Fermions and of [28] using staggered quarks. First large scale staggered result, marked as JLQCD is of [29]. Blum and Soni [30] marks the first simulation of B_K using quenched domain-wall quarks followed by large scale studies of that approach by CP-PACS 2001 [31], RBC 2001 [32] and CP-PACS 2008 [33]. Review of all quenched results prior to 2003 is marked as Becirevic [34]. Unquenched 2 flavors calculations are shown in green including RBC 2004 [35]; JLQCD 2008 [17] and ETMC 2009 [36, 37]. Unquenched 2+1 flavors calculations are shown in Blue: HPQCD 2006 [12] with staggered; RBC-UKQCD 2007 [38] with domain wall and ALV [14] using mixed action. Also RBC-UKQCD 2010 [19] using domain-wall quarks and SBW [16] using staggered. In black [LS] is the average used in the analysis of Ref. [10] and the recent average[LLV] obtained in Refs. [39, 40].

are obtained in full QCD with $N_F = 2 + 1$ simulations, are in the continuum limit, are fairly robust and emerge from the works of more than one collaboration and in most cases by many collaborations.

• Regarding calculations of $\hat{B}_K$ [11] on the lattice, it is useful to note that in the past 3 years a dramatic reduction in errors has been achieved and by now a number of independent calculations with errors $\lesssim 5\%$ and with consistent central values have been obtained using $N_f = 2 + 1$ [12–16] as well as $N_f = 2$ [17] dynamical simulations (see Ref. [18] for a review). Again, to be conservative, we only use weighted average of two results that are both in full QCD, use different fermion discretizations (domain-wall and staggered) and that also use completely different gauge configurations and completely different procedures for operator renormalization [16, 19].

Given the important role lattice calculations of weak matrix element are playing in the evaluation of some of the important non-perturbative quantities that are critical to constraining fundamental parameters in flavor physics, we now take this opportunity to briefly comment on how the calculation of B_K evolved over the past ∼25 years. This example should serve to

illustrate developments in many such calculations; the history of B_K is summarized in Fig. 1 [41].

Recall that before the advent of the lattice approach to B_K, an interesting first attempt [20, 21], using charged kaon lifetime, lowest order chiral perturbation theory and flavor SU(3) symmetry, estimated $B_K \approx 0.33$. But of course an estimate such as this represents an uncontrollable approximation, with no reliable error estimate or understanding of scale dependence. If one were to use such a value of B_K, in conjunction with experimentally measured value of ϵ_K, to deduce the Wolfenstein parameter η, that uniquely controls CP violation in the CKM picture, we would get a central value about a factor of two higher than modern numbers, but even more noticeably the error on η could easily be O(100%) rather than $\sim 10\%$ [7] that we now have.

One of the primary purpose for the construction of the two asymmetric B-factories in the 1990's was that they would allow us to extract directly from experiment the weak CP-odd phase via $B \to \psi K_S$. They accomplished this task beautifully, providing us with a rather precise value, $\sin 2\beta = 0.668 \pm 0.023$, *i.e.* with an accuracy of about 3.4%. But for this accurate determination, attained at a significant expense and effort, to be useful in testing the Standard Model, and in particular to test that the CP-odd phase in the CKM paradigm is quantitatively responsible for the observed CP violation in K_L decays as well as in B-decays, a value for B_K with commensurate precision is essential. If the accuracy on B_K had stayed at the level of O(100%) then the B-factory measurement would have failed to have an impact on the fundamental theory.

The very first attempts [24–26] in the 80's on calculating B_K all started with Wilson fermions in the quenched approximation and of course had huge errors with a value of B_K consistent with 0 or 1.

Amongst the continuum methods, perhaps the most interesting result was that of [22], $\hat{B}_K = 0.70 \pm 0.10$ [23], obtained by using the large N approximation: this result corresponds to lattice results obtained in the quenched approximation. Remarkably, this calculation has been consistent with all older lattice results obtained over the years in the quenched approximation, and in fact its claimed accuracy is higher, since, following [42] many, if not most, lattice calculations done in the quenched approximation were quoting a (conservative) guess-estimate for the systematic error due to the quenched approximation of $\approx 15\%$ [43], though with hindsight we now see that the quenching error on B_K was less than 5%.

In the quenched approximation, the result, $\hat{B}_K = 0.863 \pm 0.058$ (where the stated error does not include quenching error) of [29], obtained by using staggered quarks, and perturbative renormalization, stood as the most precise lattice result for a long time. With the advent of domain-wall quarks [30, 44, 45] and with large scale (quenched) simulations with domain wall quarks [31, 32] it was found that domain wall quarks consistently tended to give about 8 to 15% smaller B_K (implying a larger CP-odd phase, η) compared to the staggered result of [29].

With dynamical 2+1 simulations there is no longer any need for estimating quenching errors and 3-4 years ago RBC–UKQCD [13] obtained the first result in full QCD using DWQ, with an estimated total error of about 5.5%, finally managing to by-pass the stated accuracy of [23]. Furthermore, by 2010 quite a few lattice calculations using full QCD (and with different discretizations [18]) have managed to reduce the error even less than that to about 4%. Furthermore, the latest RBC-UKQCD calculation [19] made significant improvements in renormalization and in chiral extrapolation to reduce the error further to 3.6%.

As mentioned previously, in our study we are using a weighted average of this latest domain-wall result [19] and that of Ref. [16] obtained by using staggered quarks.

• Given the large disparity between the exclusive and inclusive determinations of V_{ub} at the level of 3.3σ, see Table 1, it is very difficult to draw reliable conclusions by using this quantity; therefore, since 2008 [5] we have been advocating not using V_{ub} for testing or constraining the UT. Consequently in this work also we will make very limited and peripheral use of V_{ub} only. We should also stress that this is one of the key differences between other groups [6, 9] work

$\|V_{cb}\|_{\rm excl} = (39.5 \pm 1.0) \times 10^{-3}$	$\eta_1 = 1.51 \pm 0.24$ [49]
$\|V_{cb}\|_{\rm incl} = (41.68 \pm 0.44 \pm 0.09 \pm 0.58) \times 10^{-3}$ [50]	$\eta_2 = 0.5765 \pm 0.0065$ [51]
$\|V_{cb}\|_{\rm avg} = (40.9 \pm 1.0) \times 10^{-3}$	$\eta_3 = 0.494 \pm 0.046$ [52,53]
$\|V_{ub}\|_{\rm excl} = (31.2 \pm 2.6) \times 10^{-4}$	$\eta_B = 0.551 \pm 0.007$ [54]
$\|V_{ub}\|_{\rm incl} = (43.4 \pm 1.6^{+1.5}_{-2.2}) \times 10^{-4}$ [50]	$\xi = 1.23 \pm 0.04$
$\|V_{ub}\|_{\rm tot} = (33.7 \pm 4.9) 10^{-4}$	$\lambda = 0.2253 \pm 0.0009$ [55]
$\Delta m_{B_d} = (0.507 \pm 0.005)$ ps^{-1}	$\alpha = (89.5 \pm 4.3)^{\rm o}$
$\Delta m_{B_s} = (17.77 \pm 0.12)$ ps^{-1}	$\kappa_\varepsilon = 0.94 \pm 0.02$ [39,56,57]
$\varepsilon_K = (2.229 \pm 0.012) 10^{-3}$	$\hat{B}_d = 1.26 \pm 0.11$
$m_{t,pole} = (172.4 \pm 1.2)$ GeV	$f_{B_d} = (208 \pm 8)$ MeV [48]
$m_c(m_c) = (1.268 \pm 0.009)$ GeV	$f_K = (155.8 \pm 1.7)$ MeV
$S_{\psi K_S} = 0.668 \pm 0.023$ [58]	$\hat{B}_K = 0.742 \pm 0.023$
$f_{B_s}\sqrt{\hat{B}_{B_s}} = (291 \pm 16)$ MeV	$\gamma = (78 \pm 12)^{\rm o}$ [59,60]
${\rm BR}_{B\to\tau\nu} = (1.68 \pm 0.31) \times 10^{-4}$ [61–63]	

Table 1: Lattice QCD and other inputs to the unitarity triangle analysis. The determination of α is obtained from a combined isospin analysis of $B \to (\pi\pi,\ \rho\rho,\ \rho\pi)$ branching ratios and CP asymmetries [50]. Statistical and systematic errors are combined in quadrature; for the error on V_{ub} see [64]. We adopt the averages of Ref. [39,40] (updates at `www.latticeaverages.org`) for all quantities with the exception of ξ, $f_{B_s}\hat{B}_s^{1/2}$, $\hat{B}_K$ and f_{B_d} (see text).

on UT fits and us. Another difference from those works is that we use $\xi = f_{B_s}\hat{B}_s^{1/2}/f_{B_d}\hat{B}_d^{1/2}$, $f_{B_s}\hat{B}_s^{1/2}$ and $\hat{B}_d$ to describe B_q mixing and $B \to \tau\nu$ (as opposed to f_{B_s}/f_{B_d}, $\hat{B}_s/\hat{B}_d$, $\hat{B}_s$ and f_{B_s}). Moreover, we fit f_{B_d} in conjunction with particular hypotheses and use the determined value of f_{B_d} as a diagnostic tool. Another difference between our work and Ref. [9] is that, in the latter, the authors include in the fit the D0 dimuon asymmetry [46,47], a^s_{SL}, in semileptonic B_s and $\bar{B}_s$ decays; while we agree that this is a very interesting result, we believe that it needs confirmation and therefore are not using it in our fit.

• The complete set of lattice inputs that we use is presented in Table 1. All inputs, are taken from Refs. [39, 40] (see `http://www.latticeaverages.org` for updates) with the exception of $\hat{B}_K$ (see discussion above), ξ (since the statistical errors of the HPQCD and Fermilab/MILC results are 100% correlated, we decided to increase the statistical error of the HPQCD result to bring it in line with the with the more conservative Fermilab/MILC estimate), f_{B_d} (we update the HPQCD determination of f_{B_d} [48]) and $f_{B_s}\hat{B}_s^{1/2}$ (we update the HPQCD determination of f_{B_s} [48] and combine it with the Fermilab/MILC result; we then combine the f_{B_s} average with the HPQCD determination of $\hat{B}_s$ adding *linearly* the uncertainties.).

3 Some results of the fit.

We first draw attention to the results of the fit shown in the upper panel of Fig. 2. Here we use as inputs from experiments, ϵ_K, ΔM_d, ΔM_s, γ and BR($B \to \tau\nu$) [65] and from the lattice, $\hat{B}_K$, ξ, $f_{B_s}\hat{B}^1_s/2$ and $\hat{B}_d$ (but not f_{B_d}) and we extract the fitted value of $\sin 2\beta$ and of f_{B_d}. We obtain:

$$\sin(2\beta)^{\rm fit} = 0.867 \pm 0.050\ , \tag{2}$$

which is about 3.2 σ away from the experimentally measured value of 0.668 ± 0.023. We believe this result provides a strong indication that the CKM description of the observed CP violation is breaking down [66].

For the fitted value of f_{B_d} along with the predicted value of $\sin(2\beta)$ given above, we find:

$$f_{B_d}^{\rm fit} = (201.5 \pm 9.4)\ {\rm MeV}\ . \tag{3}$$

This "predicted" value is in very good agreement with the one obtained by direct lattice calculation, $f_{B_d} = (208 \pm 8)$ MeV. This is a useful consistency check signifying that the SM description of the inputs used, especially of $B \to \tau\nu$, is working fairly well and that it is unlikely that the $B \to \tau\nu$ tree amplitude is receiving large contributions from new physics; most likely the dominant effect of new physics is in fact in $\sin(2\beta)$. Later we will reexamine this from an entirely different perspective and show in fact there is additional independent support to these interpretations.

In order to further scrutinize the tentative conclusion reached above, we next present an alternate scenario depicted in the bottom panel of Fig. 2. Here, we make one important change in the inputs used. Instead of using the measured value of ${\rm BR}(B \to \tau\nu)$ we now use as input the measured value of $\sin(2\beta)$ from the "gold-plated" $B_d \to \psi K_s$ mode. Again, this fit yields two important predictions:

$${\rm BR}(B \to \tau\nu)^{\rm fit} = (0.768 \pm 0.099) \times 10^{-4}\ , \tag{4}$$

$$f_{B_d}^{\rm fit} = (185.6 \pm 9.1)\ {\rm MeV}\ . \tag{5}$$

Eq. (4) deviates by 2.7σ from the experimental measurement, as can also be gleaned from an inspection of the bottom panel of Fig. 2. It is particularly interesting that also the fit prediction for f_{B_d} now deviates by about 1.8σ from the direct lattice determination given in Table 1. We believe this provides additional support that the measured value of $\sin(2\beta)$ being used here as a key input is not consistent with the SM and in fact is receiving appreciable contributions from new physics.

This leads us to conclude that while the presence of some sub-dominant contribution of new physics in $B \to \tau\nu$ is possible, a large contribution of new physics in there is not able to explain, in a consistent fashion, the tension we are observing in the unitarity triangle fit.

This conclusion receives corroboration by the observation that even without using $B \to \tau\nu$ at all, and using as input only ϵ_K, $\Delta M_{B_s}/\Delta M_{B_d}$ and $|V_{cb}|$ (see Fig. 5), the predicted value of $\sin(2\beta)$ deviates by 1.8σ from its measurement (in this case we find $\sin(2\beta)^{\rm fit} = 0.814 \pm 0.081$). Thus, possible new physics in $B \to \tau\nu$ can alleviate but not remove completely the tension in the fit.

We recall that the fit above is actually the simple fit we had reported some time ago (now with updated lattice inputs) with its resulting $\approx 2\ \sigma$ deviation [5]. This fit is somewhat special as primarily one is only using $\Delta F = 2$ box graphs from ϵ_K and $\Delta M_{B_s}/\Delta M_{B_d}$ in conjunction with lattice inputs for B_K and the SU(3) breaking ratio ξ. The experimental input from box graphs is clearly short-distance dominated and for the lattice these two inputs are particularly simple to calculate as the relevant 4-quark operators have no mixing with lower dimensional operators and also require no momentum injection. The prospects for further improvements in these calculations are high and the method should continue to provide an accurate and clean "prediction" for $\sin(2\beta)$ in the SM. So even if the current tensions get resolved, this type of fit should remain a viable way to test the SM as lattice calculations and experimental inputs continue to improve.

3.1 Roles of V_{cb}, ε_K, V_{ub} and of hadronic uncertainties.

The fit described above does use V_{cb} where again the inclusive and exclusive methods differ mildly (about 1.7σ). Of greater concern here is that ϵ_K scales as $|V_{cb}|^4$ and therefore is very sensitive to the error on V_{cb}. We address this in two ways. First in the upper panel of Fig. 3 we

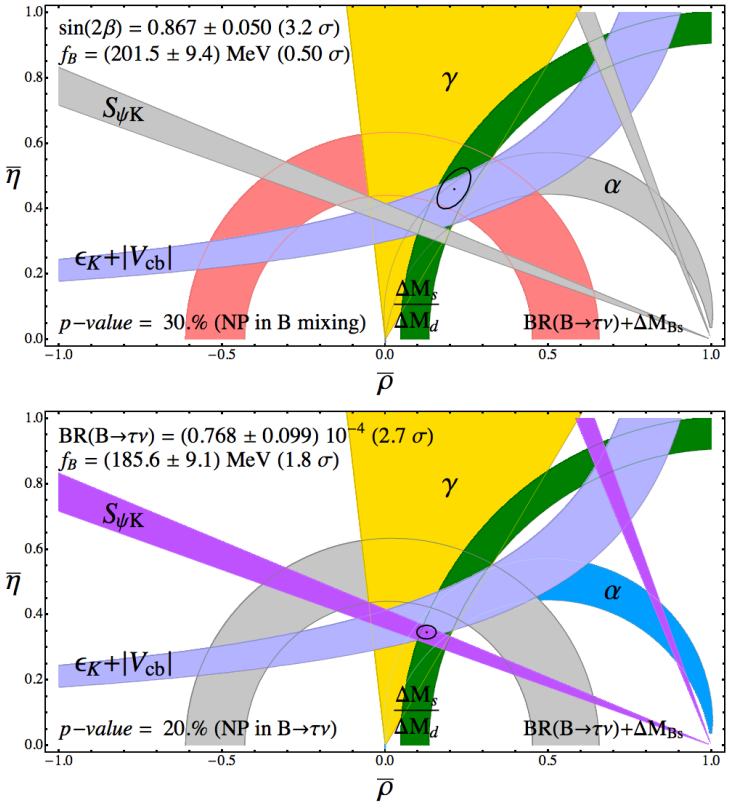

Figure 2: Unitarity triangle fit. In each plot inputs that are grayed out are *not* used to obtain the black contour (which represents the SM allowed 1σ region), the p–value and the fit predictions presented in the upper left corners. The deviations of the fit predictions for $\sin(2\beta)$ and $\mathrm{BR}(B \to \tau\nu)$ from the respective measurements are obtained using the actual chi-square distribution for these quantities. The p-value of the complete SM fit (i.e. including all the inputs) is $p_{\rm SM} = 1.7\%$. In the upper panel, we consider a scenario with a new phase in B_d mixing, thereby removing the $\sin(2\beta)$ and α inputs. In the lower panel we consider a scenario with new physics in $B \to \tau\nu$, thereby removing the $\mathrm{BR}(B \to \tau\nu)$ input.

study a fit wherein no semi-leptonic input from $b \to c$ or $b \to u$ is being used. Instead, in this fit $\mathrm{BR}(B \to \tau\nu)$ and ΔM_{B_s} along with ϵ_K, $\Delta M_{B_s}/\Delta M_{B_d}$ and γ are used. Interestingly this fit gives

$$\sin(2\beta)^{\rm fit} = 0.905 \pm 0.047 \,, \tag{6}$$

$$f_{B_d}^{\rm fit} = (202.9 \pm 9.3)\ \mathrm{MeV} \tag{7}$$

Thus, once again, $\sin(2\beta)$ is off by 3.1σ whereas f_{B_d} is in very good agreement with directly measured value which we again take to mean that the *bulk* of the discrepancy is in $\sin(2\beta)$ rather than in $B \to \tau\nu$ or in V_{cb}.

Next we investigate the role of ϵ_K. In the bottom panel of Fig. 3 we show a fit where only input from B-physics, namely $\Delta M_{B_s}/\Delta M_{B_d}$, ΔM_{B_s}, γ, $|V_{cb}|$ and $\mathrm{BR}(B \to \tau\nu)$ are used. This fit yields,

$$\sin(2\beta)^{\rm fit} = 0.889 \pm 0.055 \,, \tag{8}$$

$$f_{B_d}^{\rm fit} = (200.7 \pm 11)\ \mathrm{MeV} \tag{9}$$

Thus, $\sin(2\beta)^{\rm fit}$ is off by $\approx 2.4\sigma$ and again $f_{B_d}^{\rm fit}$ is in good agreement with its direct determination. We are, therefore, led to conclude that the role of ϵ_K in the discrepancy is subdominant and that the bulk of the new physics contribution is likely to be in B–physics. As before, the fact that

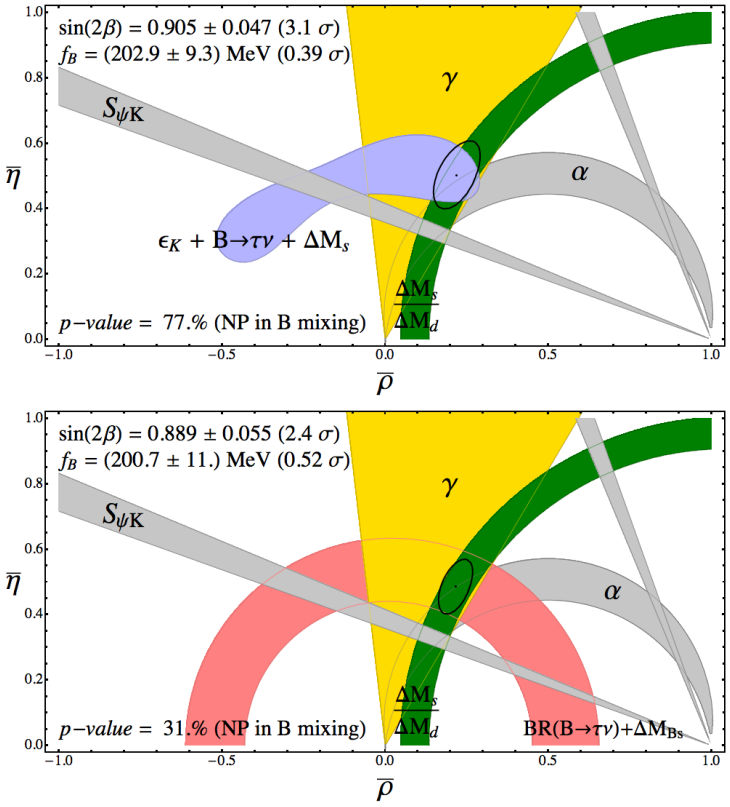

Figure 3: Unitarity triangle fit without semileptonic decays (upper panel) and without use of K mixing (lower panel). See the caption in Fig. 2.

the fitted value of f_{B_d} is in good agreement with its direct determination seems to suggest that the input BR($B \to \tau\nu$) is most likely not in any large conflict with the SM, though, obviously we cannot rule out the possibility of it receiving a sub-dominant contribution from new physics.

For completeness, we present in Fig. 4 the results we obtain when including V_{ub} in the fit. Note that inclusive and exclusive determinations of $|V_{ub}|$ differ at 3.3σ (see Table 1) and, for this reason, are presented separately in the plot. Before taking the average, we add a 10% model uncertainty to the inclusive determination. This reduces the discrepancy to 2.1σ. We finally rescale the error on the average by the square root of the reduced chi-square (following the PDG recipe). In Table 1 we report the result we obtain and that we use in the fit.

A compilation of all the eleven fits that we studied for $\sin 2\beta$ are shown in Fig. 5. Notice that there is only one case in here (8th from the top) where the discrepancy in $\sin 2\beta$ is only $O(1\sigma)$. We believe this is primarily a reflection of the large ($\approx 14.4\%$) uncertainty with our combined V_{ub} fit originating from the large disparity between inclusive and exclusive determinations. This is again a reminder of the fact that till this discrepancy gets removed, we cannot use V_{ub} to draw any reliable conclusion.

4 $B \to \tau\nu$ and new physics

Now with regard to $B \to \tau\nu$, Fig. 6 shows a summary of predictions versus the measured BR. Notice that whenever the measured value of $\sin(2\beta)$ is used as an input, the predicted BR is $\approx 2.7\sigma$ from the measured one. In the preceding discussion we have emphasized that this seems to us to be a consequence of new physics largely in B mixings and/or in $B_d \to \psi K_s$ decay. This

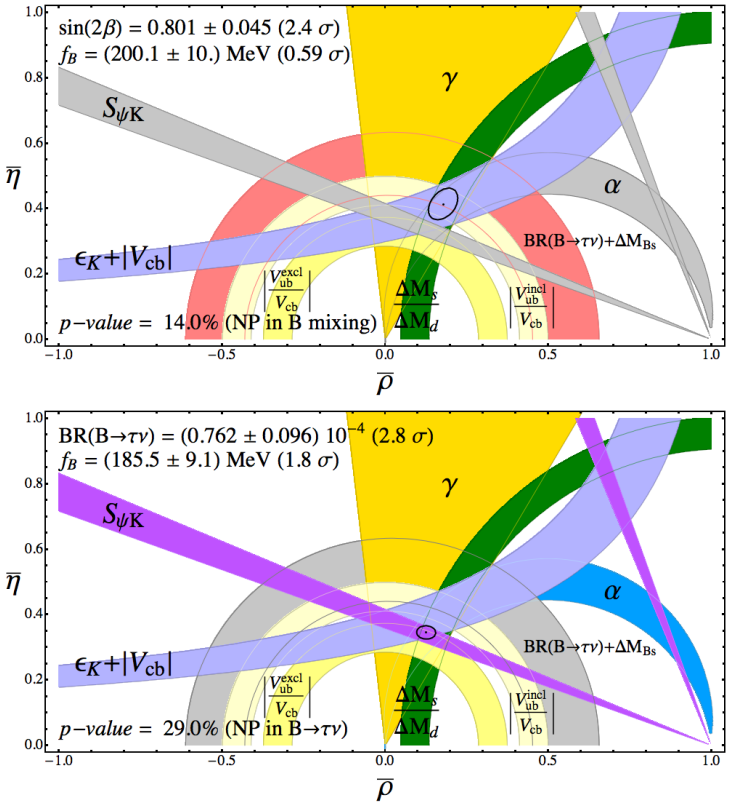

Figure 4: Unitarity triangle fit with V_{ub}. We plot separately the constraints from inclusive and exclusive semileptonic B decays. The contour, p-value and fit predictions are obtained using the $|V_{ub}|_{\rm tot}$. See the caption in Fig. 2.

conclusion receives further strong support when we try determine the $B \to \tau\nu$ branching ratio without using $\sin 2\beta$. Indeed as shown in Fig. 6 when we use ϵ_K, ΔM_{B_q}, V_{cb} and γ only, the fitted value of BR($B \to \tau\nu$) is in very good agreement with the measured value.

In principle, of course, the prediction for BR($B \to \tau\nu$) only needs the values of f_{B_d} and of V_{ub}. Fixing now $f_{B_d} = 208 \pm 8$ MeV as directly determined on the lattice (see Table 1) we show the corresponding two predictions for the BR using separately the values of V_{ub} determined in inclusive and in exclusive decays. It is clear that the inclusive determination yields results that are within one σ of experiment (see also Fig. 2); however with V_{ub} from exclusive modes (that makes use of the semileptonic form factor as determined on the lattice), the BR deviates by $\approx 2.8\sigma$ from experiment. This may be a hint that lattice based exclusive methods have some intrinsic difficulty or that the exclusive modes are sensitive to some new physics that the inclusive modes are insensitive to, *e.g.* right-handed currents [67, 68]. In either case, this reasoning suggests that we try using the value of V_{ub} given by inclusive methods only in our fit for determining $\sin 2\beta$. This line of reasoning is also supported by the analysis presented in Ref. [69] in which the discrepancy between the experimental determination and the SM prediction of ratio $R_{s/l} = {\rm BR}(B \to \pi\ell\nu)/{\rm BR}(B \to \tau\nu)$ is considered. Note that the authors of Ref. [69] find that the experimental value of this ratio is about a factor of 2 smaller than the SM prediction and that this discrepancy is independent of whether lattice QCD or Light-Cone QCD Sum Rules are used to determine the $B \to \pi$ form factor and the B decay constant. This result can be seen as a solid consistency check of the lattice QCD calculation of the $B \to \pi$ form factor. Within the SM this ratio is independent of short distance physics (the $|V_{ub}|^2$ factors cancel out) and measures the ratio of the $B \to \pi$ form factor to the B decay constant. New physics in right–handed currents affects differently the $B \to \pi\ell\nu$ and $B \to \tau\nu$ transitions and might be responsible for

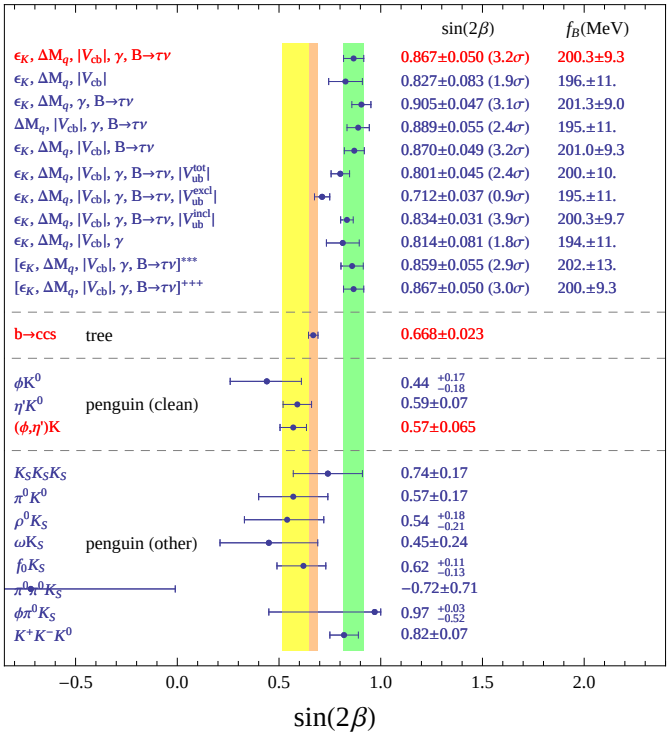

Figure 5: Summary of $\sin(2\beta)$ determinations. The entry marked *** (tenth from the top) is obtained with lattice errors increased by 50% over those given in Table 1 for each of the input quantities that we use and the entry marked +++ (eleventh from the top) corresponds to adding an hadronic uncertainty $\delta\Delta S_{\psi K} = 0.021$ to the relation between $\sin(2\beta)$ and $S_{\psi K}$. See the text for further explanations.

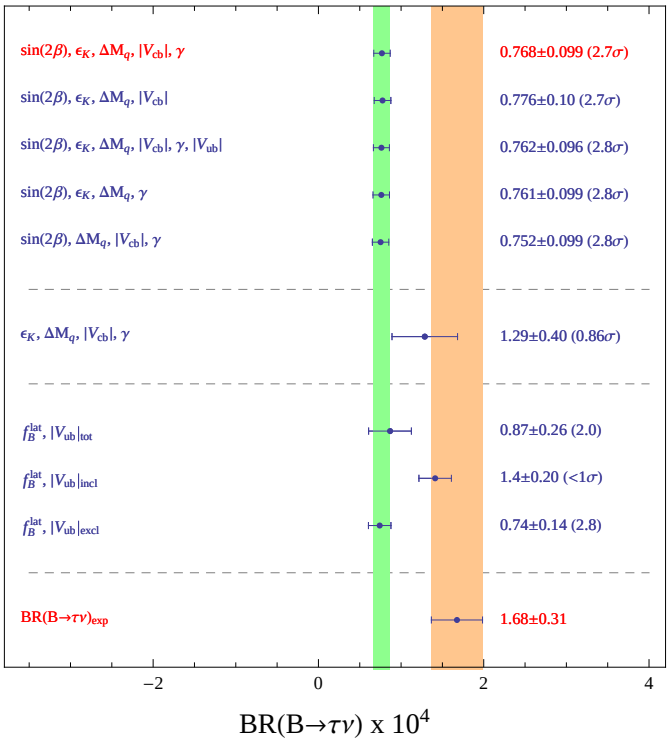

Figure 6: Summary of $\mathrm{BR}(B \to \tau\nu)$ determinations.

the observed discrepancy.

5 Summary of fits, perspective & outlook.

The result of our analysis strongly suggests that the SM predicted value of $\sin(2\beta)$ is around 0.85 whereas the value measured experimentally via the gold plated ψK_s mode is around 0.66 constituting a deviation of about 3σ from the SM (see Fig. 5). To put this result in a broader perspective let us now recall that in fact in the SM $\sin(2\beta)$ can also be measured via the penguin dominated modes (see Fig. 5) [70–73]. Unfortunately several of these modes suffer from a potentially large tree pollution, though there are good reasons to believe that the $\eta' K_s$, ϕK_s and 3 K_s modes are rather clean [74–76] wherein the deviations from $\sin 2\beta$ are expected to be only O(few %). The striking aspect of these three clean modes as well as many others penguin dominated modes (see Fig. 5) is that the central values of almost all of them tend to be even smaller than the value (0.66), measured in ψK_s, and consequently tend to exhibit even a larger deviation from the SM prediction of around 0.85. Thus, seen in the light of our analysis, the deviation in these penguin modes suggests the presence of new CP-violating physics not just in B-mixing but also in $b \to s$ penguin transitions.

Moreover, the large difference ($\approx (14.4 \pm 2.9)\%$) [3] in the direct CP asymmetry measured in $B^0 \to K^+\pi^-$ versus that in $B^+ \to K^+\pi^0$ provides another hint that $b \to s$ penguin transitions may be receiving the contribution from a beyond the SM source of CP-violation (for alternate explanation see Refs. [77–79]). To briefly recapitulate, in the SM one naively expects this difference to be vanishingly small and careful estimates based on QCD factorization ideas suggest that it is very difficult to get a difference much larger than $(2.2 \pm 2.4)\%$ [7].

Of course, if $b \to s$ penguin transitions ($\Delta Flavor = 1$) are receiving contributions from new physics, then it is quite unnatural for B_s mixing amplitudes ($\Delta Flavor = 2$) to remain unaffected. Therefore, this reasoning suggests that we should expect non-vanishing CP asymmetries in $B_s \to \psi\phi$ as well as a non-vanishing di-lepton asymmetry in $B_s \to X_s l\nu$. As is well known, at Fermilab, in the past couple of years CDF and D0 experiments have been studying CP asymmetry in $B_s \to \psi\phi$. The latest result with about 6 fb^{-1} from each experiment seems to reveal a reduction from $\sim 1.8\sigma$ tension to $\sim 1\sigma$ from the SM [50, 80, 81]. Thus, findings in $B_s \to \psi\phi$ from Fermilab and from LHCb are eagerly awaited.

Another interesting and potentially very important development with regard to non-standard CP in B_s is that last year D0 announced the observation of a large dimuon asymmetry in B-decays amounting to a deviation of ($\approx 3.2\sigma$) from the minuscule asymmetry predicted in the SM [46,47]. They attribute this largely to originate from B_s mixing. While this is a very exciting development, their experimental analysis is extremely challenging and a confirmation is highly desirable before their findings can be safely assumed. Note, though, HFAG [50] has combined CDF and D0 results on $B_s \to \psi\phi$ and on the dimuon asymmetry, A^s_{sl} and finds the deviation from the SM to be around 2.7σ.

Be that as it may, we reiterate that our analysis suggests that the deviation from the SM in $\sin(2\beta)$ is difficult to reconcile with errors in the inputs from the lattice that we use, and strongly suggests the presence of a non-standard source of CP violation largely in B/B_s mixings, thereby predicting that non-standard signals of CP violation in $S(B_d \to \eta' K_s, \phi K_s, 3K_s etc.)$ as well as in $S(B_s \to \psi\phi)$, and the semileptonic and di-lepton asymmetries in B_s, and possibly also in B_d, decays will persist and survive further scrutiny in experiments at the intensity frontiers such as Fermilab (CDF, D0), LHCb and the Super-B factories. Lastly, the fact that our analysis rules out the possibility that new physics exclusively in kaon mixing is responsible for the deviations in $\sin(2\beta)$, has the very important repercussions for the mass scale of the underlying new physics contributing to these deviations: model independent analysis then imply that the relevant mass scale of the new physics is necessarily relatively low, *i.e.* below O(2 TeV) [7, 82]. Thus, collider

experiments at the high energy frontier at LHC and possibly even at Fermilab should see direct signals of the underlying degrees of freedom appearing in any relevant beyond the Standard Model scenario.

6 Aftermath: BSM possibilities

Let us next discuss a model independent point of view as to the possible underlying cause for these anomalies and then two specific models that may be relevant.

6.1 Brief Summary of the model independent analysis

One of the important issue is how these B-CP anomalies will impact search for New Physics at the LHC wherein a knowledge of underlying scale of NP would be very useful. With this in mind we [7] write down dimension-6 operators under the general assumptions of NP in $\Delta Flavor = 2$ effective Hamiltonian for K, B_d or B_s mixing or for the case of $\Delta Flavor = 1$ Hamiltonian that may be relevant for $b \to s$ penguin transitions [7]. Our model independent analysis shows that the scale of CP violating NP is only a few hundred GeV if it originates from $b \to s$, $\Delta Flavor = 1$ penguin Hamiltonian. It rises to about a few TeV if it originates from B_d and/or B_s mixing. From the perspective of LHC the scenario that is the most pessimistic, with NP scale in the range of a few tens of TeVs, is when all of the NP resides only in the dimension-6 LR-operator relevant for the $K - \bar{K}$ mixing [83]. However, in the preceding sections we have shown that bulk of the deviation from the SM does not originate in ϵ_K or $K - \bar{K}$ mixing. This, therefore, has the important consequence that taken seriously these discrepancies with the CKM hint at scale of new physics that is quite likely to be less than a few TeV, possibly even a few hundred GeV. Note also that in our 08-09 work [7] we were unable to rule out the possibility that dominantly NP resides in K–mixing; this only became possible in our 2010 analysis [10].

6.2 Warped Flavordynamics & duality

Perhaps the most interesting and even compelling BSM scenario is that of warped extra dimensional models [84] as it offers a simultaneous resolution to EW-Planck hierarchy as well as flavor puzzle [85,86]. While explicit flavor models are still evolving, potentially this class of models has many interesting features; for example, in general one expects several new BSM CP-odd phases (presumably O(1)) [87] that can have important repercussions for flavor physics. Indeed in the simplest scenario it was *predicted* [88] that there should be smallish (*i.e.* O(20%)) deviations from the SM in B_d decays to penguin-dominated final states such as ϕK_s, $\eta' K_s$ etc as well as the possibility of a largish CP-odd phase in B_s mixing which then of course has manifestations in *e.g.* $B_s \to \psi\phi$, time-dependent asymmetries in $B_d \to (\rho, K^*)\gamma$, etc [87, 88]. In fact there was also a mild CP problem in that very simple rough estimates suggest neutron-EDM should be bigger than current bounds [89] by about an order of magnitude.

Note though that in this original study, for simplicity, it was assumed that B_d mixing was essentially described by the SM. More recently there have been two extensive studies of the possibility of warped models being the origin of the several hints in B, B_s decays mentioned above [90–92].

A common feature of these warped models is that they also imply the existence of various Kaluza-Klein states, excited counterparts of the gluon, weak gauge bosons and of the graviton with masses heavier than about 3 TeV [93]. Note also that unless the masses of these particles are less than about 3 TeV their direct detection at LHC will be very difficult [94–102].

Since viable explicit models are still being developed, it is useful to emphasize generic predictions of warped flavor models. Top quark should exhibit large flavor violations via *e.g.* $t \to c(u)Z$ [102], largish D^0 mixing with possibly enhanced CP violations, beyond the SM CP

asymmetries are also possible in B_d, B_s physics, also polarized top quarks endowed with some forward-backward asymmetry [103] should be expected. Furthermore, KK particles such as the KK-glue, graviton, Z' should have large BR to top quark pairs and in fact the tops should be boosted since the decaying resonances are expected to have TeV-scale masses [94–97, 99].

An extremely interesting subtlety about these 5-dimensional warped models is that they are supposed to be dual to some 4-dimensional models with strong dynamics [104–110]. This serves as motivation to search for effective 4-dimensional models that provide a good description of the data.

6.3 Extension of SM to four generations: SM4

SM with four generations provides a rather simple and an interesting extension to address the B-CP anomalies [111–118]. Actually,for several reasons, SM4 is of considerable interest irrespective of these anomalies:

• The heavier quarks could form condensates and thereby play an important role in dynamical electroweak symmetry breaking [119–122].

• Two new CP -odd phases and the heavier quark masses also significantly alleviate one of the key difficulty that SM3 has for baryogenesis [123].

• SM4 can open new avenues for addressing the dark matter issue [124, 125].

• Besides, since we have already seen three families, it is natural to ask why not the fourth?

Note also that while practically all BSM scenarios have difficult time accounting for the (almost) absence of FCNC (in processes such as BR($B \to X_s\gamma$)), SM4 explains this readily. First of all in SM4 (as in SM) FCNC are loop suppressed via the GIM [126] mechanism. Furthermore, as you extend the 3×3 matrix to 4×4 and impose unitarity, the hierarchical structure of CKM matrix extended to 4×4 automatically allows only small residual CP-conserving effects in quantities such as BR($B \to X_s\gamma$); on the other hand, there can be dramatic difference in CP violating observables where in the SM null results are predicted [127].

In contrast to CP-conserving FCNC, since there are now two new CP-odd phases, they can cause large (O(1)) CP -asymmetries in channels that the CKM phase has negligible effect in the SM [127]. This is expected to be the case *e.g.* in Bs mixing, causing S($B_s \to \psi\phi$) and the semileptonic asymmetry, a^s_{sl}, in $B_s \to X_s\ell\nu$ to be non-vanishing. Similarly there may be non-vanishing CP-asymmetries in $b \to s\gamma$, $b \to sll$, $B_d \to \eta' K_s$, $B_d \to \phi K_s$ wherein the SM one expects negligible effects. Moreover, we should also expect the effects due to an additional phase in B_d mixing beyond what's there in the SM. This manifests itself say as a deviation in *e.g* $\sin 2\beta$ from the SM predicted value and also can cause the semi-leptonic asymmetry, a^d_{sl} to differ from the SM predicted value (that is negligibly small).

It may be useful also to note that seen from the perspectives of SM4 the hierarchy puzzle may just be a historical accident.

Natural mass scale for a Higgs particle in SM4, where the heavy quarks are geared towards EW symmetry breaking, is around $2m_{b'}$. Such a heavy Higgs would of course have very clean decays to $H \to ZZ$.

Electroweak precision tests do not rule out the existence of a 4th generation though they restrict the mass splitting between the 4th generation doublet (t', b') of quarks to be less than around 75 GeV [128, 129]. This requires some 10% degeneracy in their masses. One cautionary

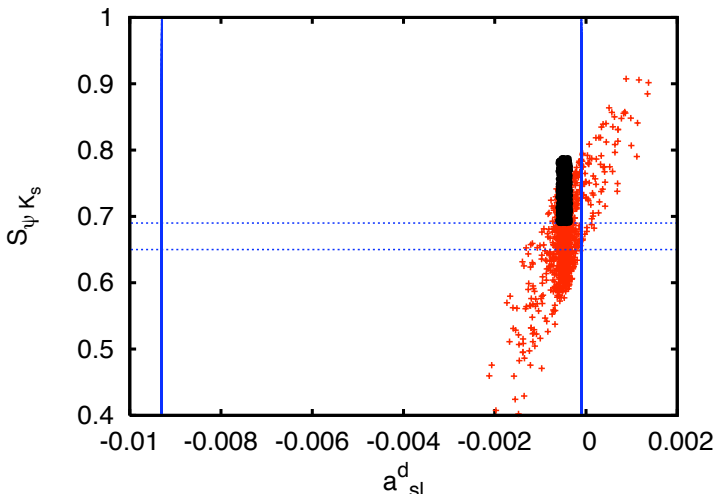

Figure 7: Correlation between $S\psi K_S$ and the semi-leptonic asymmetry, a^d_{sl} in SM4 is shown for $m_{t'}$ varying between 375 and 575 GeV. The experimentally allowed region as well as the SM3 bounds are also shown. See Ref. [113] for details.

remark is that such heavy quark masses means large Yukawa couplings, therefore many perturbative calculations, including those relevant for EW precision tests may receive large corrections.

Furthermore LEP experiments require that the 4th generation neutral lepton has to be rather heavy $\gtrsim m_Z/2$; this begs the question as to why there should be such a huge disparity with the three almost massless neutrinos of the conventional SM3 [124, 125]. Issues such as these are interesting and require further investigations.

We will briefly now summarize the possible relevance of SM4 to alleviating the discrepancies in the CKM picture that has been our primary focus here. In particular, the tension in $\mathrm{S}(\psi K_s)$ that we emphasized has been examined in [113]. Fig 7 from Ref. [113] shows a study of the correlation between the predicted value of $\sin 2\beta$ and a^d_{sl}, which is the semi-leptonic asymmetry in $B_d \to X_d l\nu$. In this study all known experimental constraints such as ϵ_K, $Br(K^+ \to \pi^+ \nu\bar{\nu})$, ΔM_d, ΔM_s, constraints on the unitarity angle γ etc have all been incorporated. As is evident from the figure, while the SM4 can accommodate the measured value of $\mathrm{S}(\psi K_s)$ it also requires simultaneously that $a^d_{sl} \gtrsim -0.001$, which is only about a factor of a few different from the SM3. This underscores another attractive aspect of SM4: it is rather predictive, highly constrained extension of the SM and can be ruled out with relative ease. In this specific illustration it requires improved determination of a^d_{sl} as well as $S_{\psi K_s}$ both theoretically and experimentally. Improved bound from the B factories, who need to update their several years old result [50] on a^d_{sl} would be very useful.

Another interesting example is the semi-leptonic asymmetry in B_s, a^s_{sl} and its correlation with $\mathrm{S}(B_s \to \psi\phi)$, see Fig. 8 from [113]. It is interesting to note here that while SM4 allows a much larger semi-leptonic asymmetry as shown, it is still not large enough to explain the central value of the asymmetry reported by the recent D0 result [47]. Thus, if improved experimental results uphold near the central value of the D0 experiment, then SM4 may also be ruled out.

Finally, let us also briefly mention that experimental searches for quarks (t', b') of the 4th generation have already been underway at Fermilab leading to a lower bound of around 350 GeV [130]. We should expect intensified searches at LHC especially since this is something that can be achieved even in the early 7 GeV run [131]. It is expected that after several years of efforts, LHC should be able to find these quarks or put a bound close to a TeV [132].

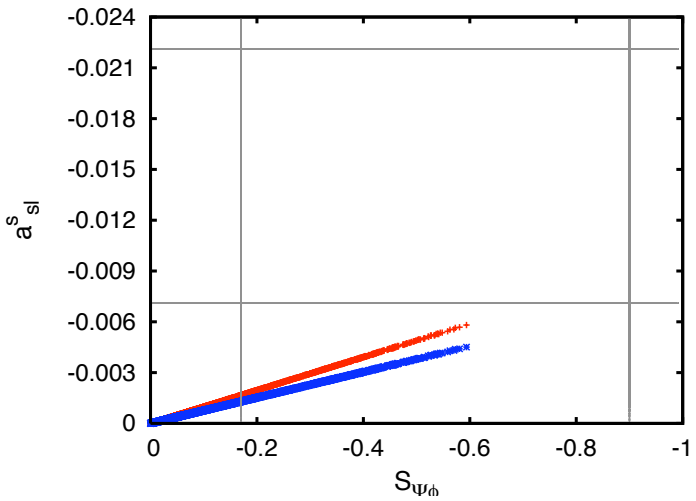

Figure 8: Correlation between $S\psi K_S$ and the semi-leptonic asymmetry, a^d_{sl} in SM4 is shown for $m_{t'}$ varying between 375 and 575 GeV. The experimentally allowed region (1σ) is shown. See Ref. [113] for details.

Acknowledgments

We want to thank Jean-Marie Frere, Maurizio Pierini, Yuval Grossman, Uli Haisch and Alexander Khodjamirian for discussions and suggestions. This research was supported in part by the U.S. DOE contract No.DE-AC02-98CH10886(BNL).

1. N. Cabibbo, Phys. Rev. Lett., **10**, 531 (1963); M. Kobayashi and T. Maskawa, Prog. Theor. Phys., **49** 652 (1973).
2. Y. Nir, Nucl. Phys. Proc. Suppl. **117**, 111 (2003).
3. K. Nakamura et al. (Particle Data Group), J. Phys. G 37, 075021 (2010)
4. E. Lunghi and A. Soni, JHEP **09**, 053 (2007).
5. E. Lunghi and A. Soni, Phys. Lett. **B666** 162 (2008).
6. M. Bona *et al.*, Phys. Lett. B **687**, 61 (2010).
7. E. Lunghi and A. Soni, JHEP **0908**, 051 (2009).
8. E. Lunghi and A. Soni, Phys. Rev. Lett. **104**, 251802 (2010).
9. A. Lenz *et al.*, arXiv:1008.1593 [hep-ph].
10. E. Lunghi and A. Soni, arXiv:1010.6069 [hep-ph].
11. Recall $B_K \equiv < K^0|[\bar{s}\gamma_\mu Ld]^2|\bar{K}^0 > /[(8/3)f_K^2 m_K^2]$ where m_K and f_K are the mass and the pseudoscalar decay constant of the kaon, in the convention that experimentally $f_K \approx 160 MeV$.
12. E. Gamiz *et al.* [HPQCD and UKQCD Collaborations], Phys. Rev. **D73**, 114502 (2006).
13. D. J. Antonio *et al.* [RBC and UKQCD Collaborations], Phys. Rev. Lett. **100**, 032001 (2008); See also, C. Kelly, talk at Lattice 2010, June 14-19 2010, Sardinia, Italy, http://www.infn.it/Lattice2010.
14. C. Aubin, J. Laiho and R. S. Van de Water, Phys. Rev. D **81**, 014507 (2010).
15. H. J. Kim *et al.*, PoS **LAT2009**, 262 (2009).
16. T. Bae, Y. -C. Jang, C. Jung *et al.*, Phys. Rev. **D82**, 114509 (2010).
17. S. Aoki *et al.* [JLQCD Coll.], Phys. Rev. D **77**, 094503 (2008).
18. See the review talk by J. Laiho at Lattice 2010, June 14-19 2010, Sardinia, Italy, http://www.infn.it/Lattice2010.
19. Y. Aoki, R. Arthur, T. Blum *et al.* [RBC and UKQCD Collaborations], arXiv:1012.4178 [hep-lat].

20. J. F. Donoghue, E. Golowich, B. R. Holstein, Phys. Lett. **B119**, 412 (1982).
21. P. H. Ginsparg and M. B. Wise, Phys. Lett. B **127**, 265 (1983).
22. W. A. Bardeen, A. J. Buras, J. M. Gerard, Phys. Lett. **B211**, 343 (1988).
23. A. J. Buras, arXiv:hep-ph/9806471.
24. N. Cabibbo, G. Martinelli, R. Petronzio, Nucl. Phys. **B244**, 381-391 (1984).
25. R. C. Brower, G. Maturana, M. Belen Gavela and R. Gupta, Phys. Rev. Lett. **53** (1984) 1318.
26. C. W. Bernard, T. Draper, G. Hockney, A. M. Rushton and A. Soni, Phys. Rev. Lett. **55** (1985) 2770.
27. C. W. Bernard, A. Soni, Nucl. Phys. Proc. Suppl. **17**, 495-498 (1990).
28. G. W. Kilcup, S. R. Sharpe, R. Gupta and A. Patel, Phys. Rev. Lett. **64**, 25 (1990).
29. S. Aoki *et al.* [JLQCD Collaboration], Phys. Rev. Lett. **80**, 5271-5274 (1998).
30. T. Blum, A. Soni, Phys. Rev. Lett. **79**, 3595 (1997).
31. A. Ali Khan *et al.* [CP-PACS Collaboration], Phys. Rev. **D64**, 114506 (2001).
32. T. Blum *et al.* [RBC Collaboration], Phys. Rev. **D68**, 114506 (2003).
33. Y. Nakamura *et al.* [CP-PACS Collaboration], Phys. Rev. **D78**, 034502 (2008).
34. For a review see, D. Becirevic, talk at Lattice 2003, July 15-19 2003, Tsukuba, Ibaraki, Japan; http://www.rccp.tsukuba.ac.jp/lat03/
35. C. Dawson [RBC Collaboration], Nucl. Phys. Proc. Suppl. **140**, 356-358 (2005).
36. V. Bertone *et al.* [ETM Collaboration], PoS **LAT2009**, 258 (2009).
37. M. Constantinou *et al.* [ETM Collaboration], Phys. Rev. **D83**, 014505 (2011).
38. S. D. Cohen *et al.* [RBC and UKQCD Collaboration], PoS **LAT2007**, 347 (2007).
39. J. Laiho, E. Lunghi and R. S. Van de Water, Phys. Rev. D **81**, 034503 (2010).
40. J. Laiho, E. Lunghi and R. Van De Water, arXiv:1102.3917 [hep-ph].
41. We want to thank Taku Izubuchi for help with this figure.
42. S. R. Sharpe, Nucl. Phys. Proc. Suppl. **53**, 181 (1997).
43. D. Becirevic, Nucl. Phys. Proc. Suppl. **129**, 34 (2004).
44. V. Furman and Y. Shamir, Nucl. Phys. B **439**, 54 (1995).
45. T. Blum and A. Soni, Phys. Rev. D **56**, 174 (1997).
46. V. M. Abazov *et al.* [D0 Coll.], Phys. Rev. D **82**, 032001 (2010).
47. V. M. Abazov *et al.* [D0 Coll.], Phys. Rev. Lett. **105**, 081801 (2010).
48. Our value of f_{B_d} differs from the average presented in Ref. [40] because it reflects the change in the overall scale (r_1) recently adopted by HPQCD collaboration [133, 134].
49. S. Herrlich and U. Nierste, Nucl. Phys. B **419**, 292 (1994).
50. D. Asner *et al.*, HFAG Collab., arXiv:1010.1589
51. A. J. Buras, M. Jamin and P. H. Weisz, Nucl. Phys. B **347**, 491 (1990).
52. S. Herrlich and U. Nierste, Phys. Rev. D **52**, 6505 (1995).
53. J. Brod and M. Gorbahn, Phys. Rev. D **82**, 094026 (2010).
54. G. Buchalla, A. J. Buras and M. E. Lautenbacher, Rev. Mod. Phys. **68**, 1125 (1996).
55. M. Antonelli *et al.*, Eur. Phys. J. **C69**, 399-424 (2010).
56. A. J. Buras and D. Guadagnoli, Phys. Rev. D **78**, 033005 (2008).
57. A. J. Buras, D. Guadagnoli and G. Isidori, Phys. Lett. B **688**, 309 (2010).
58. M. Kreps, arXiv:1008.0247 and references therein.
59. M. Bona *et al.* [UTfit Collaboration], JHEP **0507**, 028 (2005).
60. M. Bona *et al.* [UTfit Collaboration], JHEP **0610**, 081 (2006).
61. K. Ikado *et al.* [Belle Coll.], Phys. Rev. Lett. **97**, 251802 (2006).
62. P. d. A. Sanchez *et al.* [BaBar Coll.], arXiv:1008.0104.
63. K. Hara *et al.* [Belle collaboration], Phys. Rev. D **82**, 071101 (2010).
64. The inclusive and exclusive determinations of $|V_{ub}|$ differ at the 1.8σ level even after including an additional 10% model uncertainty to the former. We first calculate the standard

weighted average of these two determinations and then, following the PDG prescription, we rescale the resulting uncertainty by the square root of the reduced chi-square.
65. In contrast to γ, α is not used as an input since it receives appreciable contribution from penguin amplitudes which are sensitive to new physics.
66. Note that when γ is not used as an input and only ϵ_K, $\Delta M_s/\Delta M_d$ and BR($B \to \tau\nu$) are used, the deviation of the fitted $\sin(2\beta)$ from the measured one stays unchanged at 3.2σ, see Fig. 5.
67. A. Crivellin, Phys. Rev. D **81**, 031301 (2010).
68. A. J. Buras, K. Gemmler and G. Isidori, Nucl. Phys. B **843**, 107 (2011).
69. A. Khodjamirian, T. .Mannel, N. Offen, Y. M. Wang, arXiv:1103.2655.
70. Y. Grossman and M. P. Worah, Phys. Lett. B **395**, 241 (1997).
71. R. Fleischer, Int. J. Mod. Phys. A **12**, 2459 (1997).
72. Y. Grossman, G. Isidori and M. P. Worah, Phys. Rev. D **58**, 057504 (1998).
73. D. London and A. Soni, Phys. Lett. B **407**, 61 (1997).
74. H. Y. Cheng, C. K. Chua and A. Soni, Phys. Rev. D **72**, 014006 (2005).
75. H. Y. Cheng, C. K. Chua and A. Soni, Phys. Rev. D **72**, 094003 (2005).
76. M. Beneke, Phys. Lett. B **620**, 143 (2005).
77. S. Mishima, arXiv:1101.1501 [hep-ph].
78. M. Gronau, J. L. Rosner, Phys. Lett. **B644**, 237-240 (2007).
79. H. -Y. Cheng, C. -K. Chua, Phys. Rev. **D80**, 114008 (2009).
80. R. Van Kooten, talk at ICHEP 2010, July 22-28 2010, Paris, France, http://www.ichep2010.fr.
81. D. Tonelli, talk at Brookhaven Forum 2010, May 26-28, BNL, http://www.bnl.gov/bf2010.
82. The reason that the presence of new physics in kaon mixings can shift the relevant scale to much larger energies (O(20TeV)) is the possible presence of left-right 4-quark operators whose matrix elements for kaon mixing and RG running are significantly enhanced as emphasized in Ref. [83] (See also, Refs. [7, 135]).
83. G. Beall, M. Bander and A. Soni, Phys. Rev. Lett. **48**, 848 (1982).
84. L. Randall and R. Sundrum, Phys. Rev. Lett. **83**, 3370 (1999).
85. Y. Grossman and M. Neubert, Phys. Lett. B **474**, 361 (2000).
86. T. Gherghetta and A. Pomarol, Nucl. Phys. B **586** (2000) 14.
87. K. Agashe, G. Perez and A. Soni, Phys. Rev. Lett. **93**, 201804 (2004).
88. K. Agashe, G. Perez and A. Soni, Phys. Rev. D **71**, 016002 (2005).
89. C. A. Baker *et al.*, Phys. Rev. Lett. **97** (2006) 131801.
90. M. Blanke, A. J. Buras, B. Duling, S. Gori and A. Weiler, JHEP **0903**, 001 (2009).
91. M. Blanke, A. J. Buras, B. Duling, K. Gemmler and S. Gori, JHEP **0903**, 108 (2009).
92. M. Bauer, S. Casagrande, U. Haisch, M. Neubert, JHEP **1009**, 017 (2010).
93. K. Agashe, A. Delgado, M. May. R. Sundrum, JHEP **0308**, 050, (2003).
94. K. Agashe, A. Belyaev, T. Krupovnickas, G. Perez and J. Virzi, Phys. Rev. D **77**, 015003 (2008).
95. B. Lillie, L. Randall and L. T. Wang, JHEP **0709**, 074 (2007).
96. K. Agashe *et al*, Phys. Rev. D **76**, 115015 (2007).
97. K. Agashe, S. Gopalakrishna, T. Han, G. Y. Huang and A. Soni, Phys. Rev. D **80**, 075007 (2009).
98. A. Fitzpatrick, J. Kaplan and L. Randall, JHEP **0709**, 013, (2007).
99. K. Agashe, H. Davoudiasl, G. Perez and A. Soni, Phys. Rev. D **76**, 036006 (2007).
100. O. Antipin, D. Atwood and A. Soni, Phys. Lett. **B666**, 151, 2008.
101. O. Antipin and A. Soni, JHEP **0810**, 018 (2008).
102. K. Agashe, G. Perez and A. Soni, Phys. Rev. D **75**, 015002, (2007).
103. M. Bauer *et. al*, arXiv:1008.0742.

104. J. M. Maldacena, Adv. Theor. Math. Phys. **2**, 231 (1998) [Int. J. Theor. Phys. **38**, 1113 (1999)]
105. S. S. Gubser, I. R. Klebanov and A. M. Polyakov, Phys. Lett. B **428**, 105 (1998).
106. E. Witten, Adv. Theor. Math. Phys. **2**, 253 (1998).
107. N. Arkani-Hamed, M. Porrati and L. Randall, JHEP **0108**, 017 (2001).
108. R. Rattazzi and A. Zaffaroni, JHEP **0104**, 021 (2001).
109. R. Contino, Y. Nomura and A. Pomarol, Nucl. Phys. B **671**, 148 (2003).
110. K. Agashe, R. Contino and A. Pomarol, Nucl. Phys. B **719**, 165 (2005).
111. A. Soni, A. K. Alok, A. Giri, R. Mohanta and S. Nandi, Phys. Lett. B **683**, 302 (2010)
112. A. Soni, A. K. Alok, A. Giri, R. Mohanta and S. Nandi, Phys. Rev. D **82**, 033009 (2010).
113. S. Nandi and A. Soni, arXiv:1011.6091 [hep-ph].
114. A. J. Buras, B. Duling, T. Feldmann, T. Heidsieck, C. Promberger and S. Recksiegel, JHEP **1009**, 106 (2010).
115. A. J. Buras, B. Duling, T. Feldmann, T. Heidsieck, C. Promberger and S. Recksiegel, JHEP **1007**, 094 (2010).
116. W. S. Hou and C. Y. Ma, Phys. Rev. D **82**, 036002 (2010).
117. See also,M. Bobrowski, A. Lenz, J. Riedl and J. Rohrwild, Phys. Rev. D **79**, 113006 (2009).
118. O. Eberhardt, A. Lenz and J. Rohrwild, Phys. Rev. D **82**, 095006 (2010).
119. P. Q. Hung and C. Xiong, Phys. Lett. B **694**, 430 (2011) [arXiv:0911.3892 [hep-ph]].
120. M. Hashimoto and V. A. Miransky, Phys. Rev. D **81**, 055014 (2010).
121. B. Holdom, JHEP **0608**, 076, (2006); W. A. Bardeen, C. T. Hill and M. Lindner, Phys. Rev. D **41**, 1647 (1990); C. T. Hill, M. A. Luty and E. A. Paschos, Phys. Rev. D **43**, 3011 (1991); P. Q. Hung and G. Isidori, Phys. Lett. B **402**, 122 (1997); J. Carpenter, R. Norton, S. Siegemund-Broka, A. Soni, Phys. Rev. Lett. **65**, 153-156 (1990).
122. G. Burdman and L. D. Rold, JHEP **0712**, 086, (2007).
123. G. W. S. Hou, arXiv:0810.3396 [hep-ph]; see also [136]
124. G. E. Volovik, Pisma Zh. Eksp. Teor. Fiz. **78**, 1203 (2003) [JETP Lett. **78**, 691 (2003)].
125. H. S. Lee, Z. Liu and A. Soni, arXiv:1105.3490 [hep-ph].
126. S. L. Glashow, J. Iliopoulos, L. Maiani, Phys. Rev. **D2**, 1285-1292 (1970).
127. T. Gershon and A. Soni, J. Phys. G **33**, 479 (2007).
128. G. D. Kribs, T. Plehn, M. Spannowsky and T. M. P. Tait, Phys. Rev. D **76**, 075016 (2007)
129. J. Erler and P. Langacker, arXiv:1003.3211 [hep-ph]; see also [137–140]
130. See the talk by P. Murat on "Searches Beyond the Standard Model" at the Fermilab Tevatron at the ICEHEP 2010 (Paris); See the talk by John Conway at the Brookaven Forum 2010; T. Aaltonen *et al*, CDF Collab, Phys. Rev. Lett. 104, 0911801, 2010.
131. D. Atwood, S. K. Gupta and A. Soni, arXiv:1104.3874 [hep-ph].
132. See the talk by Daniel Whiteson at the NTU workshop, Jan 2010.
133. E. Gamiz *et al.*, Phys. Rev. D **80**, 014503 (2009).
134. E. Gamiz, private communication.
135. M. Bona *et al.* [UTfit Coll.], JHEP **0803**, 049 (2008).
136. For earlier related works see,C. Jarlskog and R. Stora, Phys. Lett. B **208**, 268 (1988); F. del Aguila and J. A. Aguilar-Saavedra, Phys. Lett. B **386**, 241 (1996); F. del Aguila and J. A. Aguilar-Saavedra and G. C. Branco, Nucl. Phys. **B510**,39,1998.
137. M. S. Chanowitz, Phys. Rev. D **79**, 113008 (2009).
138. M. S. Chanowitz, Phys. Rev. D , 035018 (2010).
139. H. J. He, N. Polonsky and S. f. Su, Phys. Rev. D **64**, 053004 (2001).
140. V. A. Novikov, L. B. Okun, A. N. Rozanov and M. I. Vysotsky, Phys. Lett. B **529**, 111 (2002).

CP VIOLATION STUDIES IN B DECAYS WITH LHCB

YUEHONG XIE (on behalf of the LHCb Collaboration)
School of Physics and Astronomy, University of Edinburgh, Edinburgh EH9 3JZ, UK

Search for new physics beyond the Standard Model through study of CP violation (CPV) using B meson decays is one of the major physics goals of the LHCb experiment. In this contribution, first results of CPV studies using data collected in the 2010 LHC run are presented. Results, status and prospects of the analysis of the golden decay channel $B_s \to J/\psi\phi$ are discussed in detail. Also presented are the first observations of the $B_s \to J/\psi f_0$ and $B_s \to K^{*0}\bar{K}^{*0}$ decays, both of which will be used to probe CP violating new physics at LHCb. Future prospects of CPV studies in B decays at LHCb are discussed.

1 Why Study CP Violation at LHCb

The major physics objective of the LHCb experiment is to search for effects of new physics (NP) beyond the Standard Model (SM) in loop-mediated processes. The study of CP violation (CPV) is a powerful tool to search for NP. In the SM, CPV originates from a complex phase in the CKM matrix. Any departure of a CPV measurement from its SM prediction is a signal of NP. Particularly interesting places to search for NP are loop processes, where NP contribution could significantly modify the SM predictions. LHCb aims to perform high precision studies of CPV using many different decay processes of B mesons, particularly B_s mesons. [1] For instance, $B_s \to J/\psi\phi$ and $B_s \to J/\psi f_0$ decays can be used to probe NP contributions to B_s mixing via box diagrams; $B_s \to K^{*0}\bar{K}^{*0}$, $B_s \to \phi\phi$ and $B_s \to K^+K^-$ decays can be used to probe NP contributions in decay processes via loop diagrams.

2 The LHCb Detector and 2010 Data Sample

The LHCb detector is a single arm forward spectrometer, described in detail elsewhere. [2] The features essential for CPV study include: precise vertexing and tracking; good particle identification; efficient and flexible trigger. The data sample used to obtain the reported results corresponds to an integrated luminosity of about 36 pb^{-1} and was collected at an centre-of-mass energy of $\sqrt{s} = 7$ TeV in the 2010 LHC run.

3 Analysis of $B_s \to J/\psi\phi$ and related channels

$B_s \to J/\psi\phi$ is a golden decay channel for CPV study. In the SM, the weak phase difference between the amplitudes of direct decay and decay via mixing is clearly predicted to be $\phi_s = -2\beta_s$, where $\beta_s = \arg\left(-V_{ts}V_{tb}^*/V_{cs}V_{cb}^*\right)$. An indirect determination via global fits to experimental data gives $2\beta_s = (0.0363 \pm 0.0017)$ rad. [3] However, NP contributions to B_s mixing can significantly alter this expectation. Besides the weak phase, the difference between the decay width of the light and heavy mass eigenstates of the B_s system, $\Delta\Gamma_s$, is also of theoretical interest.

The measurement of ϕ_s and $\Delta\Gamma_s$ in $B_s \to J/\psi\phi$ requires a complicated flavour-tagged time-dependent angular analysis. This section discusses the analysis of not only $B_s \to J/\psi\phi$, but also some related channels used to validate the analysis procedure and demonstrate our good understanding of the detector effects such as background, resolution, acceptance and wrong tag probability.

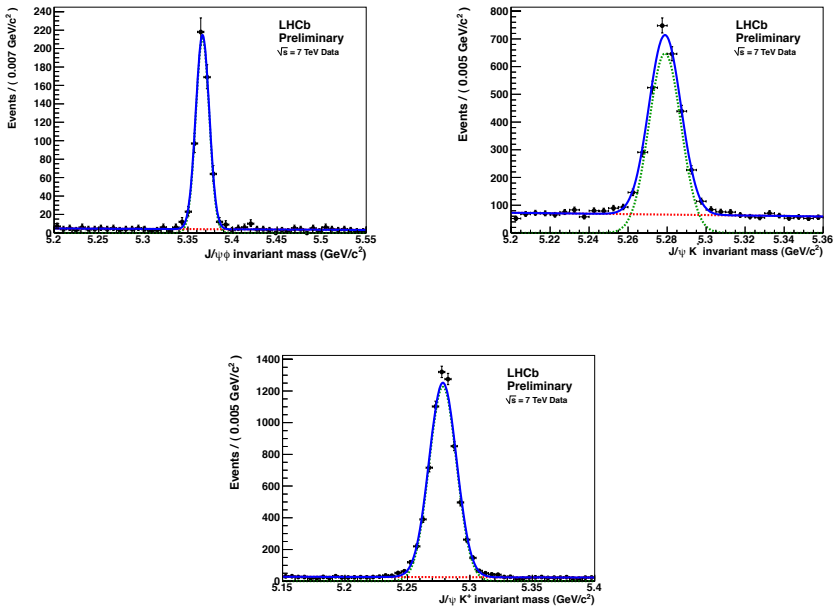

Figure 1: $B_s \to J/\psi\phi$ (top left), $B^0 \to J/\psi K^*$ (top right) and $B^+ \to J/\psi K^+$ (bottom) mass distributions with $t > 0.3$ ps. Superimposed are the total fit (solid blud), signal projection modeled by a single Gaussian (dashed green) and background projection modeled by a linear function (dashed red).

3.1 Selection of $b \to J/\psi X$ Channels

Five $b \to J/\psi X$ channels ($B_s \to J/\psi\phi$, $B^0 \to J/\psi K^{*0}$, $B^+ \to J/\psi K^+$, $B^0 \to J/\psi K^0_S$ and $\lambda_b \to J/\psi\Lambda$) are triggered and selected using similar criteria wherever possible. The baseline selection minimizes the distortion of proper time distributions in order to reduce the systematic uncertainties for time-dependent analysis. This selection retains the prompt background events with proper time $t \sim 0$, from which the proper time resolution is estimated to be $\sigma_t \approx 50$ fs. The reconstructed B mass resolution is excellent, ranging from 6 to 11 MeV for the various modes. The background level is found to be very low for $t > 0.3$ ps, as shown in Figure 1.

3.2 Lifetime Measurements in $b \to J/\psi X$ Channels

A maximum likelihood fit is performed to the proper time distribution of fully reconstructed candidates in the range $t \in [0.3, 14]$ ps in each decay mode. In the fit the theoretical proper time distribution of the signal events is modeled by a single exponential function. This ignores the non-zero decay-width difference of the B_s system. The extracted lifetimes and signal yields are given in Table 1. Details can be found in the reference [4].

Table 1: Signal event yields and lifetimes extracted from the likelihood fits to the candidate time distributions.

Channel	Lifetime (ps)	Yield
$B^+ \to J/\psi K^+$	1.689 ± 0.022 (stat.) ± 0.047 (syst.)	6741 ± 85
$B^0 \to J/\psi K^{*0}$	1.512 ± 0.032 (stat.) ± 0.042 (syst.)	2668 ± 58
$B^0 \to J/\psi K_S$	1.558 ± 0.056 (stat.) ± 0.022 (syst.)	838 ± 31
$B_s \to J/\psi\phi$	1.447 ± 0.064 (stat.) ± 0.056 (syst.)	570 ± 24
$\Lambda_b \to J/\psi\Lambda$	1.353 ± 0.108 (stat.) ± 0.035 (syst.)	187 ± 16

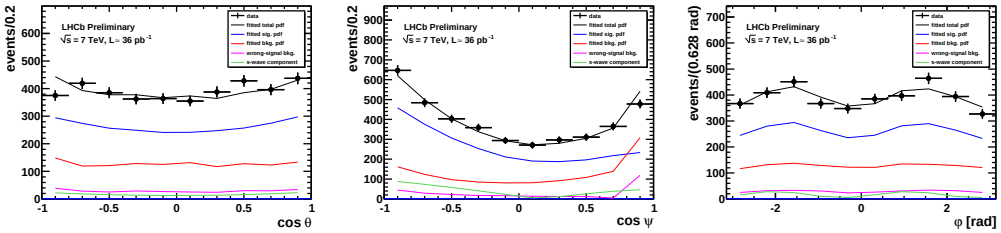

Figure 2: The transversity angle distributions for the selected $B^0 \to J/\psi K^*$ candidates, compared to the total fit (black solid), the projections for signal (blue), S-wave (green), total background (red) and wrong-signal (purple).

3.3 Angular Analysis of $B^0 \to J/\psi K^{*0}$

Both $B_s \to J/\psi\phi$ and $B^0 \to J/\psi K^*$ are decays of a pseudo-scalar meson into two vector mesons. A maximum likelihood fit to the angular distribution is needed to extract the polarization amplitudes and strong phases. A detailed description of the fit technique is in the reference [5]. The results extracted from a fit to the $B^0 \to J/\psi K^*$ decays are given in Table 2. The fit includes an S-wave contribution. The distributions of the transversity angular variables, which are defined in the reference [5], are shown in Figure 2.

Table 2: Results of a fit to the selected $B^0 \to J/\psi K^{*0}$ events, and comparison with Babar results. The first and second errors are statistical and systematic, respectively.

Parameter	LHCb results	Babar results [6]
$\|A_{\|\|}\|^2$	0.252 ± 0.020 ± 0.016	0.211 ± 0.010 ± 0.006
$\|A_\perp\|^2$	0.178 ± 0.020 ± 0.016	0.233 ± 0.010 ± 0.005
$\delta_{\|\|}$ (rad)	-2.87 ± 0.11 ± 0.010	-2.93 ± 0.08 ± 0.004
$\delta_\perp$ (rad)	3.02 ± 0.010 ± 0.07	2.91 ± 0.05 ± 0.003

3.4 Untagged Time-dependent Angular Analysis of $B_s \to J/\psi\phi$

A maximum likelihood fit is performed to the 4-dimensional time and angular distribution. In addition to the polarization magnitudes and strong phases, the probability density function involves also the weak phase ϕ_s, the B_s average decay width Γ_s and the decay width difference $\Delta\Gamma_s$. Since no tagging information is used in this analysis, the data has very little power to constrain ϕ_s. The fit results when fixing $\phi_s = 0$ is given in Table 3. Fits without fixing ϕ_s are also performed. The confidence contours in the ($\Delta\Gamma_s$, ϕ_s) plane derived using the Feldman-Cousins method [8] is shown in Figure 3. Details can be found in the reference [5].

Table 3: Results of a fit to the selected $B_s \to J/\psi\phi$ candidates with $\phi_s = 0$ fixed in the fit. The first and second errors are statistical and systematic, respectively.

Parameter	LHCb results	CDF results [7]
Γ_s	0.679 ± 0.036 ± 0.027	0.653 ± 0.011± 0.005
$\Delta\Gamma_s$	0.077 ± 0.119 ± 0.021	0.075 ± 0.035 ± 0.010
$\|A_0\|^2$	0.528 ± 0.040 ± 0.028	0.524 ± 0.013 ± 0.015
$\|A_\perp\|^2$	0.263 ± 0.056 ± 0.014	/
$\delta_{\|\|}$ (rad)	3.14 ± 0.52 ± 0.013	/

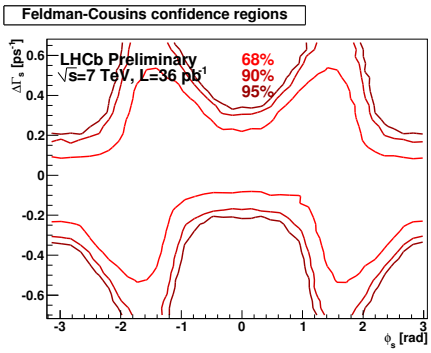

Figure 3: The confidence contours in the ($\Delta\Gamma_s$, ϕ_s) plane from untagged fits to $B_s \to J/\psi\phi$ candidates.

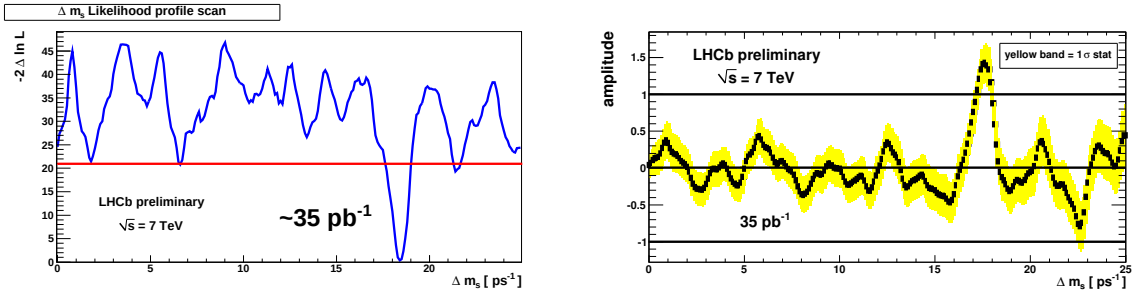

Figure 4: Left: likelihood scan for Δm_s; Right: fitted amplitude as a function of Δm_s.

3.5 Flavour Tagging and Measurements of Δm_s and Δm_d

The initial flavour of a B particle can be inferred from the products of the other B particle (called "opposite side tagging"), or from the fragmentation particles associated to the production of the signal B particle (called "same side tagging"). Currently the same side tagging is still under development. The opposite side tagging software is optimized and calibrated using control channels $B^0 \to D^{*-}\mu^+\nu_\mu$, $B^+ \to J/\psi K^+$ and $B^0 \to J/\psi K^{*0}$. More details about flavour tagging performance are given in the reference [9]. The flavour tagging software is validated in the measurements of Δm_s and Δm_d.

About 1350 B_s signals are reconstructed in the $B_s \to D_s^-(3)\pi$ decays. Using opposite side tagging information a 4.6 σ significant mixing signal is observed and the mixing frequency is measured to be $\Delta m_s = 17.63 \pm 0.11$ (stat.) $\pm$ 0.04 (syst.) ps^{-1}, [10] in very good agreement with the CDF measurement [11] $\Delta m_s = 17.77 \pm 0.10$ (stat.) $\pm$ 0.07 (syst.) ps^{-1}. The likelihood scan and amplitude scan for Δm_s are shown in Figure 4.

The B_d mixing frequency is measured to be $\Delta m_d = 0.499 \pm 0.032$ (stat.) $\pm$ 0.003 (syst.) ps^{-1} using $B_d \to D^-\pi^+$ decays, [12] consistent with the PDG [13] average value $\Delta m_d = 0.507 \pm 0.005$ ps^{-1}.

3.6 Tagged Analysis of $B_s \to J/\psi\phi$ and Prospect

While completing these proceedings, the LHCb Collaboration has reported the first preliminary results on ϕ_s from a tagged analysis of 836 ± 60 $B_s \to J/\psi\phi$ signals. No point estimate of ϕ_s is possible with this amount of data, and the results are presented as 2-dimensional confidence regions in the ($\Delta\Gamma_s$, ϕ_s) plane, which show a 1.2σ deviation from the SM expectation. The tagged analysis benefits from an excellent proper time resolution of around 50 fs. So far the analysis only uses opposite side tagging, which has an effective tagging power $\epsilon_{eff}^{OS} = (2.2 \pm 0.5)\%$. The

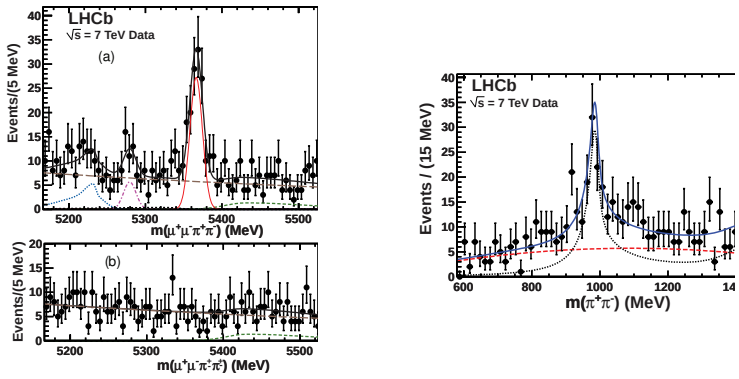

Figure 5: Left: (a) the $J/\psi\pi^+\pi^-$ mass distribution for selected candidates. Superimposed curves are the total fit (solid black), the signal (solid red), combinatorial background (long dashed brown), $B^+ \to J/\psi K^+(\pi^+)$ background (dashed green) and $B^+ \to J/\psi K^+$ background (dotted blue); (b) the same as above but for like-sign di-pion combinations. Right: the mass distribution of the $\pi^+\pi^-$ combinations. Superimposed curves are the total fit (solid blue), the interfering resonances $f_0(980)$ and $f_0(1370)$ (dotted black) and background (dashed red).

work to optimize and calibrate the same side kaon tagging is ongoing. The LHCb experiment will soon become competitive with the Tevatron experiments in measuring ϕ_s, once it collects 200 pb^{-1} of data in 2011 and include the same kaon tagging, which is expected to double the effective tagging power. LHCb aims to make the world's best measurement of ϕ_s using about 1 fb^{-1} of data due to be collected in 2011.

4 First Observation of the Decay $B_s \to J/\psi f_0(980)$

LHCb made the first observation of a new CP-odd decay $B_s \to J/\psi f_0(980)$ with about 13 standard deviations of significance, using $f_0 \to \pi^+\pi^-$. [15] Figure 5 shows the mass distributions of the $J/\psi\pi^+\pi^-$ and $\pi^+\pi^-$ combinations. The ratio to $J/\psi\phi$ production is measured as $R_{f_0/\phi} \equiv \frac{\Gamma(B_s\to J/\psi f_0, f_0\to\pi^+\pi^-)}{\Gamma(B_s\to J/\psi\phi,\phi\to K^+K^-)} = 0.252^{\pm 0.046\pm 0.027}_{-0.032-0.033}$, consistent with the theoretical expectation. [16] The $B_s \to J/\psi f_0(\pi^+\pi^-)$ mode will be very useful for measuring the weak phase ϕ_s since it does not require any angular analysis. If the branching ratio of $f_0 \to K^+K^-$ is not too small, the interference of the $f_0(980)$ and $\phi(1020)$ contributions in $B_s \to J/\psi K^+K^-$ allows to resolve a two-fold ambiguity in the measurement of ϕ_s. [17]

5 First Observation of the Decay $B_s \to K^{*0}\bar{K}^{*0}$

LHCb made the first observation of the decay $B_s \to K^{*0}\bar{K}^{*0}$ with a 7σ significance. [18] The fit to the $K^+\pi^-K^-\pi^+$ mass distribution is shown in Figure 6. 34.0 ± 7.4 signals are found in the mass interval ± 50 MeV around the B_s mass. A preliminary measurement of the branching ratio is $BR(B_s \to K^{*0}\bar{K}^{*0}) = (1.95 \pm 0.47(stat.) \pm 0.51(syst.) \pm 0.29(f_d/f_s))\%$. This decay mode can be used to probe NP contributions in decay processes via loop diagrams. [19]

6 Conclusions and Prospects

The LHCb experiment collected about 36 pb^{-1} of data in the 2010 LHC run. Using this data sample, the experiment fully tested the mechanism for CP violation study with B decays, and produced some interesting results, including measurements of b-hadron lifetimes, measurements

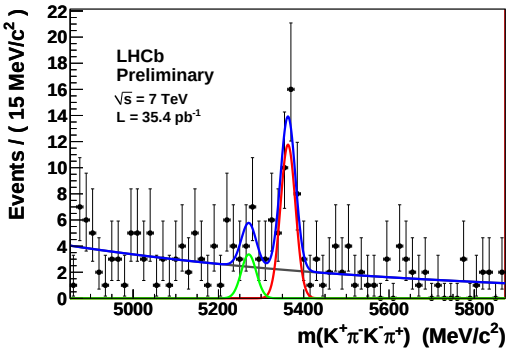

Figure 6: The $K^+\pi^-K^-\pi^+$ mass distribution for selected candidates. Superimposed curves are: the total fit (blue), Gaussian components for decays of B_s (red) and B_d (green), and an exponential component for the combinatorial background (black).

of polarization parameters in $B^0 \to J/\psi K^{*0}$ and $B_s \to J/\psi\phi$ decays, measurement of Δm_s, optimization and calibration of flavour tagging software, first observations of the decays $B_s \to J/\psi f_0(980)$ and $B_s \to K^{*0}\bar{K}^{*0}$. The LHCb experiment is ready to produce high precision results from flavour-tagged time-dependent analysis of the golden decay channel $B_s \to J/\psi\phi$ and other important channels such as $B_s \to J/\psi f_0(980)$ and $B \to hh$, using the 1 fb^{-1} of data that will be collected in 2011.

References

1. The LHCb Collaboration, LHCB-PUB-2009-029, arXiv:0912.4179.
2. The LHCb Collaboration, *Journal of Instrumentation* **3**, S08005 (2008).
3. J. Charles *et al.* (CKMfitter group), *Eur. Phys. J.* C **41**, 1 (2005).
4. The LHCb Collaboration, LHCB-CONF-2011-001.
5. The LHCb Collaboration, LHCB-CONF-2011-002.
6. The Babar Collaboration, *Phys. Rev.* D **76**, 031102 (2007).
7. The CDF Collaboration, CDF note 10206.
8. Gary J. Feldman and Robert D. Cousins, *Phys. Rev.* D **57**, 3873 (1998).
9. The LHCb Collaboration, LHCB-CONF-2011-003.
10. The LHCb Collaboration, LHCB-CONF-2011-005.
11. The CDF Collaboration, *Phys. Rev. Lett.* **97**, 242003 (2006).
12. The LHCb Collaboration, LHCB-CONF-2011-010.
13. K. Nakamura, *J. Phys.* G **37**, 075021 (2010).
14. The LHCb Collaboration, LHCB-CONF-2011-006.
15. The LHCb Collaboration, *Phys. Lett.* B **698**, 115 (2011).
16. S. Stone and L. Zhang, *Phys. Rev.* D **79**, 074024 (2009).
17. Y. Xie *et al.*, *Journal of High Energy Physics* **0909**, 074 (2009).
18. The LHCb Collaboration, LHCB-CONF-2011-019.
19. M. Ciuchini, M. Pierini, L. Silvestrini *Phys. Rev. Lett.* **100**, 031802 (2008).

Lattice QCD flavour physics results for phenomenologists

Andreas Jüttner
CERN, Physics Department, TH Unit, CH-1211 Geneva 23, Switzerland

Lattice QCD results relevant for flavour phenomenology and recent efforts that are aimed at facilitating access to lattice results for the non-specialist are reviewed.

1 Introduction

Strong claims have recently been made based on lattice QCD results:

- "We find a (2-3)σ tension in the unitarity triangle" [1]
- "... confirming CKM unitarity at the permille level" [2]
- "... we find evidence of new physics in both B_d and B_s systems" [3]
- "Possible evidence for the breakdown of the CKM-paradigm of CP-violation" [4].

The underlying Standard Model (SM) tests are based on comparisons of experimental measurements (e.g. decay rate) with theoretical predictions which factorise into a perturbative and a non-perturbative contribution. While the former can be treated in perturbation theory, several methods exist that approximate the non-perturbative physics (sum-rules, potential models) but only lattice QCD is systematically improvable and from first principles. A precise assessment of the lattice computation entering such SM analyses is mandatory.

Physical observables in QCD can be expressed in terms of the discretised Euclidean QCD path integral. In lattice QCD one solves this integral by means of a Monte-Carlo integration. Being a computationally extremely demanding exercise typical project time-scales are of the order of years even on the fastest high-performance computers available. While the simulations are benefiting from the availability of ever faster computing resources, it is in particular the improved analytical understanding of QCD and its effective theories (chiral effective theory [5,6] and heavy quark effective theory [7,8,9]) hand in hand with progress in algorithm development [10,11,12,13] that are driving the field. In principle, once the parameters of QCD, the quark masses and the gauge coupling have been fixed, model independent predictions for baryon spectra and matrix elements of QCD are possible. However, in many aspects lattice simulations do not simulate the *real world*: Current lattice computations simulate either a degenerate pair of light quarks ($N_f = 2$), in addition the strange quark ($N_f = 2 + 1$) or in addition both the strange and the charm quark ($N_f = 2 + 1 + 1$); see figure 1. Apart from the flavour content, systematic uncertainties arise from:

- **discretisation effects:** Simulations with lattice spacings down to 0.05fm are standard nowadays (see figure 1). However, it was recently found that the simulation algorithms slow down severely in the approach to the continuum limit [14,15,16,17], indicating a lack

Figure 1: Some properties of the simulations currently carried out by major collaborations: flavour content N_f, lattice spacings a vs. pion mass $m_{\rm PS}$. Thanks to Gregorio Herdoiza for providing this plot.

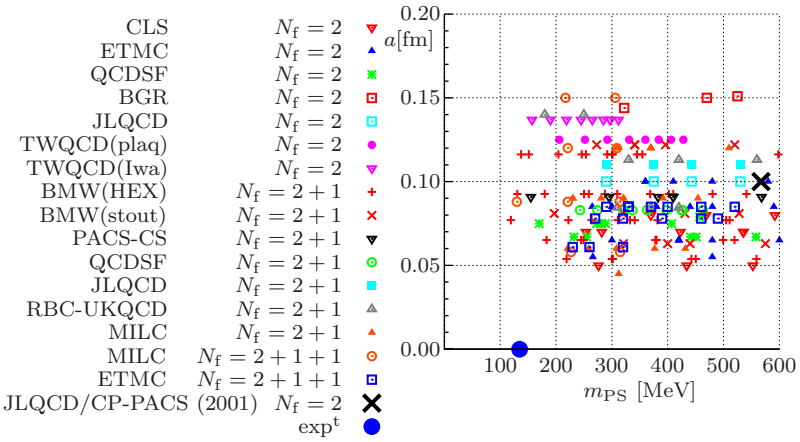

of ergodicity. A potential fix to the problem has just been proposed [18]. In particular in view of quoted uncertainties at the level of per cent this issue has to be taken seriously by every lattice collaboration presenting data in the continuum limit.

- **quark mass:** First collaborations [19,20] have presented results for physical quark masses. Until recently this seemed like a far-away goal and indeed the majority of lattice collaborations still need to extrapolate their lattice data to the physical values of the quark masses (cf. figure 1) using ansätze motivated by chiral perturbation theory.
- **renormalisation:** Matrix elements are renormalised in a lattice renormalisation scheme in a first step and then contact to a continuum scheme has to be made (e.g. $\overline{MS}$). Both steps can in principle be done entirely independently of perturbation theory (RI/MOM [21] and Schrödinger Functional [22] and non-perturbative running, e.g. [23]) thereby removing any perturbative uncertainty on the lattice side. Some lattice collaborations however still prefer to rely on perturbation theory and systematic effects then have to be estimated by power counting arguments.
- **finite size effects:** These can be subtracted by means of effective theory computations or directly by extrapolating to the infinite volume in cases where lattices with several volumes have been simulated.

There are other issues like the choice of lattice discretisation which deserve consideration (see for example discussion in [2]). Admittedly the above sources of systematic uncertainty are rather technical in nature. With the aim of facilitating a judgement of the quality of a given lattice computation for the non-expert two groups are now offering their quality assessment of lattice data relevant for SM phenomenology:

- Flavia Net Lattice Averaging Group (FLAG) [2]: A colour code for various quality criteria illustrates FLAG's results: ★ for satisfactory, ● for should be improved, ■ for unsatisfactory attempt to satisfy systematics. The criteria set up by FLAG are subject to change as the quality of available lattice QCD results evolve. The set of quantities considered currently comprises $N_f = 2, 2+1$ and $N_f = 2+1+1$, pion and kaon leptonic decay constants and semi-leptonic decay form factors, light quark masses, low-energy constants and the neutral kaon bag-parameter.
- Laiho, Lunghi, van de Water [1]: provide a CKM-triangle analysis and a detailed discussion of the lattice input they are using (in contrast to FLAG they consider $N_f = 2+1$ flavour simulations only); the set of quantities covered comprises light as well as heavy-light meson form factors and mixing parameters.

Figure 2: Scatter plots by FLAG[2] of the lattice data on the ratio of leptonic decay constants f_K/f_π and the semi-leptonic $K \to \pi$ vector form factor at vanishing momentum transfer, $f_+(0)$. Green symbols identify results that are free of *red tags* according to FLAG's assessment. The vertical bands correspond to FLAG's average/recommended range for $N_f = 2$ and $N_f = 2+1$, respectively.

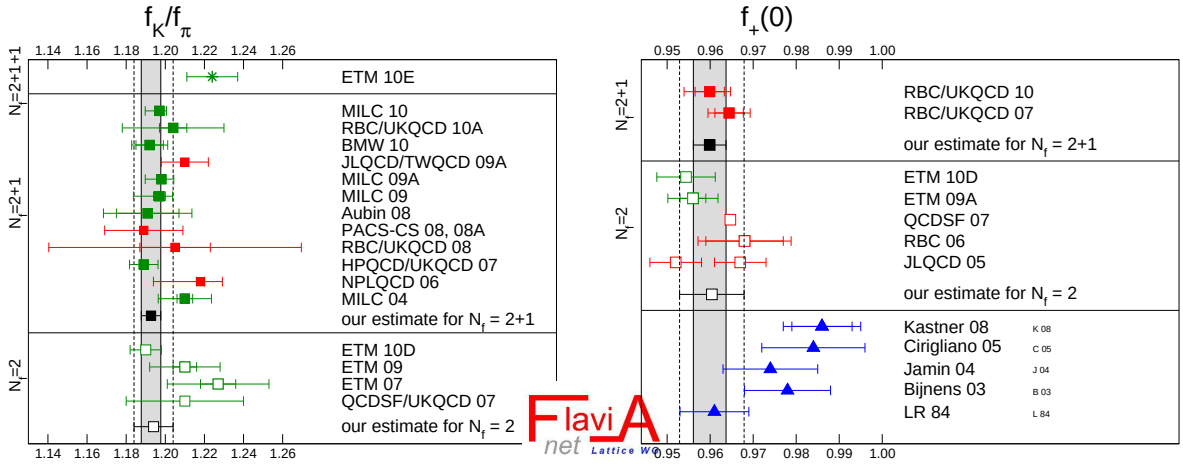

2 Recent lattice results relevant for flavour physics

In this section recent progress on a number of lattice predictions for observables relevant for flavour physics are presented.

2.1 CKM first-row unitarity - $|V_{us}|$

The determination of $|V_{us}|$ proceeds as follows: On the one hand, one experimentally measures the rate of a flavour changing process $s \to u$, where s is the strange quark and u the up quark. On the other hand one computes the SM prediction for the same process whose amplitude is proportional to the CKM-matrix element $|V_{us}|$ and which receives contributions from the electromagnetic, the weak and the strong interactions. While the former two can be treated conveniently in perturbation theory for the processes considered here, the contribution from the latter needs to be computed in lattice QCD. Eventually, $|V_{us}|$ is determined by equating the experimental result with the SM-prediction.

For kaon/pion leptonic decays the relation between experiment and theory in the SM was computed by Marciano [24] and using the latest analysis of experimental results [25] it yields the correlation

$$\left|\frac{V_{us} f_K}{V_{ud} f_\pi}\right| = 0.2758(5)\,. \tag{1}$$

Since lattice QCD can provide f_K/f_π one obtains a prediction for $|V_{us}/V_{ud}|$. For semi-leptonic kaon decays the latest summary of experimental results together with SM-contributions yields[25]

$$|V_{us}| f_+(0) = 0.2163(5)\,, \tag{2}$$

and $|V_{us}|$ is readily extracted provided the prediction of $f_+(0)$.

Figure 2 exemplifies FLAG's compilation of results showing all currently available lattice data with 2, 2+1 and 2+1+1 flavours of dynamical fermions for both $f_+(0)$ and f_K/f_π. Representative error budgets by BMW for f_K/f_π and by RBC+UKQCD for $f_+(0)$ are provided in the table in figure 3.

The results for f_K/f_π and for $f_+(0)$ for $N_f = 2$, $N_f = 2+1$ and $N_f = 2+1+1$, respectively, are all mutually compatible. The observation that the simulation and analysis techniques that lead to all these results differ significantly amongst the quoted collaborations causes confidence

Figure 3: Left: Error budgets for state-of-the art lattice computations for f_K/f_π (BMW [20]) and for $f_+(0)$ (RBC+UKQCD[26,27]); Right: FLAG's illustration of lattice results in the $|V_{us}|$-$|V_{ud}|$-plane[2]. The ellipse represent the combined unitarity analysis for $N_f = 2+1$ flavours (solid red) and $N_f = 2$ flavours (dashed blue) while the black dashed line represents SM-unitarity. According to this analysis all results are compatible with first row unitarity.

source	$\delta(f_K/f_\pi)$
statistics	0.6%
chiral extrapolation	
- functional form	0.3%
- pion mass range	0.3%
cont. extrapolation	0.3%
exited states	0.2%
scale setting	0.1%
finite volume	0.1%
total	0.8%

source	$\delta f_+(0)$
statistical	0.3%
chiral extrapolation	0.4%
cont. extrapolation	0.1%
total	0.5%

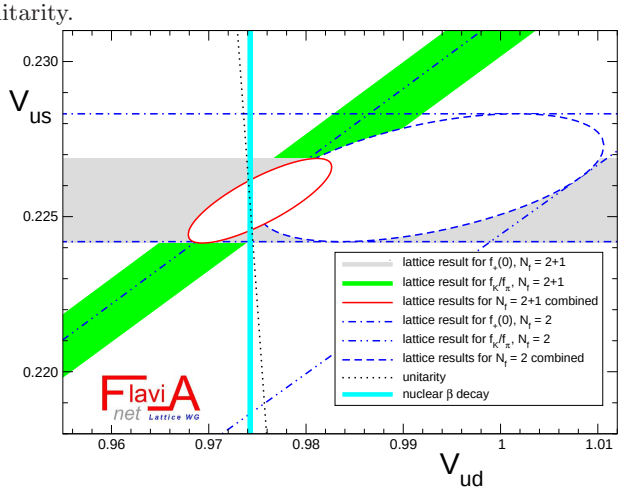

in the approach. The effect of adding the dynamical strange quark (and the charm quark) does not lead to any visible effects beyond the current level of precision.

An in-depth review of current lattice results for f_K/f_π and $f_+(0)$ is provided in [2] and the following averages/recommended values are taken from this reference: $f_K/f_\pi|_{N_f=2+1} = 1.193(5)$ (average over BMW, MILC and HPQCD/UKQCD), $f_K/f_\pi|_{N_f=2} = 1.210(18)$ (ETM) and, $f_+(0)|_{N_f=2+1} = 0.959(5)$ (RBC+UKQCD) and $f_+(0)|_{N_f=2} = 0.956(8)$ (ETM).

On the one hand these results can be used for making predictions for $|V_{ud}|$, $|V_{us}|$, $f_+(0)$ and f_K/f_π based on the experimental results (1) and (2) and on the assumption of CKM first row unitarity $|V_{ud}|^2 + |V_{us}|^2 + |V_{ub}|^2 = 1$ (at the current level of precision $|V_{ub}|$ is too small to play any significant role). On the other hand, when using only the experimental result as input the first row unitarity can be tested. This is summarised in the plot in figure 3.

Given that KLOE-2 is aiming at reducing the uncertainty in their experimental determination for $|V_{us}|f_+(0)$ by a factor of about two in the next three years [28,29] it is fair to ask about prospects on the theory side. Recent progress for $f_+(0)$ [30,26,27] has allowed to remove one of the two most dominant uncertainties (momentum resolution in lattice simulations). The remaining dominant uncertainty is the one due to the chiral extrapolation which will disappear once results appear for physical pion masses. Cut-off effects in this observable will remain a sub-dominant uncertainty for a while: flavour symmetry implies that if the average light quark mass m_q is set equal to the strange quark mass m_s, the lattice data yield $f_+(0) = 1$, irrespective of the lattice spacing or the size of the box and for any value of m_s. Cut-off effects can therefore only affect the difference $1 - f_+(0)$, which turns out to be about 0.04. For f_K/f_π the error due to the chiral extrapolation will also disappear once all collaborations simulate directly at the physical point. The statistical error can be reduced by simulating longer (naively it reduces with $1/\sqrt{N}$ where N is proportional to the Monte Carlo time). Once the abovementioned algorithmic problems with the approach to the continuum limit are solved this uncertainty will also be further reduced. In particular $f_+(0)$, where lattice artefacts are a sub-dominant effect, is expected to see a considerable improvement in the near future.

2.2 Input for the CKM unitarity triangle analysis: $\hat{B}_K$, $f_{B_{(s)}}$ and $B_{B_{(s)}}$

Lattice QCD can provide predictions for the quantities

Figure 4: For $\hat{B}_K$ the uncertainty by e.g. RBC/UKQCD 10B is $\delta(\hat{B}_K) \approx 4\%$. Only the compilation on $\hat{B}_K$ is by FLAG where the vertical band corresponds to FLAG's average. Lattice results for CKM-unitarity triangle analysis. Uncertainties: e.g. HPQCD $\delta(f_{B_s}\sqrt{\hat{B}_{B_s}}) \approx 7\%$, $\delta(\xi) \approx 3\%$, $\delta(f_{B_s}/f_B) \approx 2\%$, $\delta(f_{B_s}) \approx 6\%$.

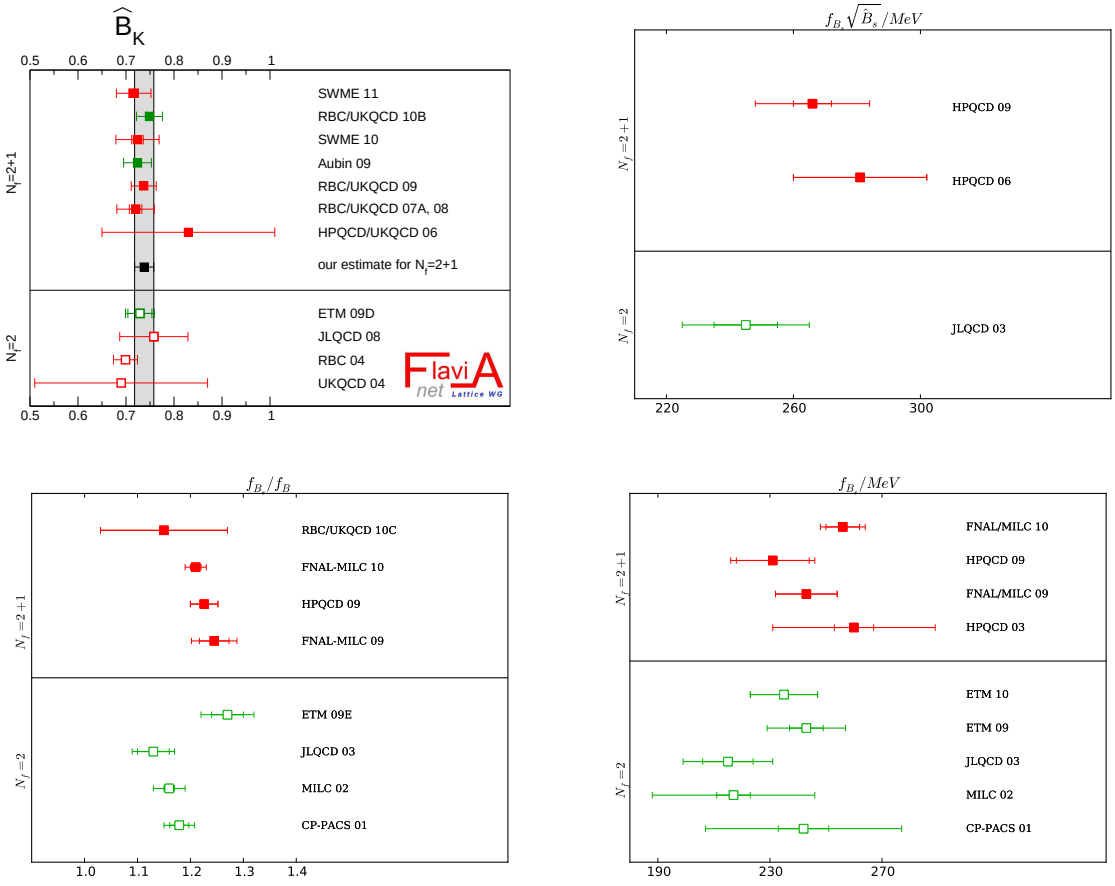

lattice		experiment	
$\hat{B}_K$	$\propto$	ϵ_K	K-mixing
$f_{B_d}^2 B_{B_d}$	$\propto$	ΔM_d	B-mixing
$f_{B_s}^2 B_{B_s}$	$\propto$	ΔM_s	
$(f_{B_d} B_{B_d})^2$	$\propto$	$\Delta\Gamma_d$	
$(f_{B_s} B_{B_s})^2$	$\propto$	$\Delta\Gamma_s$	

The plot in figure 4 shows the status of lattice computations for $\hat{B}_K$. There has been tremendous progress over the last, say, five years. In particular the utilisation of chirally symmetric lattice fermion formulations [31,32] has allowed to circumvent the problem of operator mixing of the 4-fermion operator. This reduces systematic effects considerably. From the figure one sees that all results are mutually compatible. This is a very nice observation given that most collaborations present data from entirely uncorrelated simulations.

B-physics observables like the decay constants $f_{B_{(s)}}$ and the mixing parameters $B_{B_{(s)}}$ are conceptionally harder to study in lattice simulations - this is also reflected in the fact that fewer results are available in comparison to the light meson results of the previous section (see plots in figure 3 and 4). The reason is the multi-scale problem posed by $m_{u(s)} << \Lambda_{\rm QCD} << a^{-1} \lesssim m_b$, where a^{-1} is the inverse lattice spacing. While the properties of hadrons containing an up, down and/or a strange quark can nowadays be studied rather straightforwardly, in most simulations

the cut-off is lower than the b-quark mass and naively lattice-artefacts are out of control. Yet, lattice-based predictions of b-observables are possible through the use of effective field theory methods (Heavy Quark Effective Theory [7,8,9], relativistic heavy quark action [48], ...). Given it's potentially huge impact and the fact that b-physics observables are less straight forward to compute on the lattice in particular $f_{B_{(s)}}$ and $B_{B_{(s)}}$ urgently need independent confirmation by groups, ideally with different choice of discretisation and with fully non-perturbative renormalisation and parameter determination [49,50].

2.3 $K \to \pi\pi$

Large scale simulations towards an understanding of the $\Delta I = 3/2$ and $\Delta I = 1/2$ hadronic kaon decays were first carried out about 10 years ago [51,52]. The results back then were not fully conclusive, partly due to the use of the quenched approximation but also due to the use of chiral perturbation theory in a regime where it is very likely not applicable. In a computation that relies less on chiral perturbation theory (*direct computation*) the main problem consists in mimicking the correct kinematic situation of the physical process in the finite volume lattice box [53,54,55]. To this end a number of techniques have been developed which are now being applied and it seems very feasible to make reliable predictions in the $\Delta I = 3/2$ channel [56,57]. Progress has also been made in the $\Delta I = 1/2$ channel where the necessary effort for reliable predictions is much larger [58,59].

3 Conclusions

In this talk a selection of activities in lattice QCD with relevance for flavour physics was presented. Important quantities can now be computed with per cent level precision. But it cannot be emphasised enough that systematic uncertainties contribute a significant, often dominant part to the total error budget. Ongoing work on algorithms and improvements in our understanding of QCD itself is mandatory and will allow to better control and improve the understanding of systematic effects uncertainties.

Acknowledgement: Many thanks to the organisers for the invitation, for putting together this stimulating programme and for creating this inspiring atmosphere!

Bibliography:

1. J. Laiho, E. Lunghi, and Ruth S. Van de Water. Lattice QCD inputs to the CKM unitarity triangle analysis. *Phys.Rev.*, D81:034503, 2010.
2. G. Colangelo, S. Dürr, A. Jüttner, L. Lellouch, H. Leutwyler, et al. Review of lattice results concerning low energy particle physics. 2010. arXiv:1011.4408.
3. A. Lenz, U. Nierste, J. Charles, S. Descotes-Genon, A. Jantsch, et al. Anatomy of New Physics in $B - \bar{B}$ mixing. *Phys.Rev.*, D83:036004, 2011.
4. E. Lunghi and Amarjit Soni. Possible evidence for the breakdown of the CKM-paradigm of CP-violation. *Phys.Lett.*, B697:323–328, 2011.
5. J. Gasser and H. Leutwyler. Chiral Perturbation Theory to One Loop. *Annals Phys.*, 158:142, 1984.
6. J. Gasser and H. Leutwyler. Chiral Perturbation Theory: Expansions in the Mass of the Strange Quark. *Nucl.Phys.*, B250:465, 1985.
7. B. Grinstein. The static quark effective theory. *Nucl.Phys.*, B339:253–268, 1990.
8. H. Georgi. An effective field theory for heavy quarks at low energies. *Phys.Lett.*, B240:447–450, 1990.
9. A. F. Falk, H. Georgi, B. Grinstein, and M. B. Wise. Heavy meson form factors from QCD. *Nucl.Phys.*, B343:1–13, 1990.

10. M. Hasenbusch. Speeding up the hybrid Monte Carlo algorithm for dynamical fermions. *Phys.Lett.*, B519:177–182, 2001.
11. M. Lüscher. Schwarz-preconditioned HMC algorithm for two-flavour lattice QCD. *Comput. Phys. Commun.*, 165:199–220, 2005.
12. C. Urbach, K. Jansen, A. Shindler, and U. Wenger. HMC algorithm with multiple time scale integration and mass preconditioning. *Comput. Phys. Commun.*, 174:87–98, 2006.
13. M. A. Clark and A. D. Kennedy. Accelerating Dynamical Fermion Computations using the Rational Hybrid Monte Carlo (RHMC) Algorithm with Multiple Pseudofermion Fields. *Phys. Rev. Lett.*, 98:051601, 2007.
14. D. J. Antonio et al. Localization and chiral symmetry in three flavor domain wall QCD. *Phys.Rev.*, D77:014509, 2008.
15. A. Bazavov et al. Topological susceptibility with the asqtad action. *Phys.Rev.*, D81:114501, 2010.
16. S. Schaefer, R. Sommer, and F. Virotta. Critical slowing down and error analysis in lattice QCD simulations. *Nucl.Phys.*, B845:93–119, 2011.
17. M. Lüscher. Topology, the Wilson flow and the HMC algorithm. 2010. arXiv:1009.5877.
18. M. Lüscher and S. Schaefer. Lattice QCD without topology barriers. 2011. arXiv:1105.4749.
19. [PACS-CS 09], S. Aoki, et al. Physical point simulation in 2+1 flavor lattice QCD. *Phys. Rev.*, D81:074503, 2010.
20. [BMW 10], S. Dürr, et al. The ratio F_K/F_π in QCD. *Phys. Rev.*, D81:054507, 2010.
21. G. Martinelli, C. Pittori, C. T. Sachrajda, M. Testa, and A. Vladikas. A general method for nonperturbative renormalization of lattice operators. *Nucl. Phys.*, B445:81–108, 1995.
22. M. Lüscher, R. Narayanan, P. Weisz, and U. Wolff. The Schrödinger functional: a renormalizable probe for non-Abelian gauge theories. *Nucl. Phys.*, B384:168–228, 1992.
23. M. Della Morte et al. Non-perturbative quark mass renormalization in two-flavor QCD. *Nucl. Phys.*, B729:117–134, 2005.
24. W. J. Marciano. Precise determination of $|V_{us}|$ from lattice calculations of pseudoscalar decay constants. *Phys. Rev. Lett.*, 93:231803, 2004.
25. M. Antonelli et al. An evaluation of $|V_{us}|$ and precise tests of the Standard Model from world data on leptonic and semileptonic kaon decays. *Eur. Phys. J.*, C69:399–424, 2010.
26. [RBC/UKQCD 07], P. A. Boyle, et al. K_{l3} semileptonic form factor from 2+1 flavour lattice QCD. *Phys. Rev. Lett.*, 100:141601, 2008.
27. [RBC/UKQCD 10], P. A. Boyle, et al. $K \to \pi$ form factors with reduced model dependence. *Eur. Phys. J.*, C69:159–167, 2010.
28. D. Babusci, C. Bini, F. Bossi, G. Isidori, D. Moricciani, et al. Proposal for taking data with the KLOE-2 detector at the DAΦNE collider upgraded in energy. 2010. arXiv:1007.5219.
29. E. De Lucia. Determination of Vus at the KLOE experiment: present results and future perspectives. 2010. Talk at CKM2010 - 6th International Workshop on the CKM Unitarity Triangle, Warwick, UK.
30. P.A. Boyle, J.M. Flynn, A. Jüttner, C.T. Sachrajda, and J.M. Zanotti. Hadronic form factors in Lattice QCD at small and vanishing momentum transfer. *JHEP*, 0705:016, 2007.
31. [Aubin 09], C. Aubin, J. Laiho, and R. S. Van de Water. The neutral kaon mixing parameter B_K from unquenched mixed-action lattice QCD. *Phys. Rev.*, D81:014507, 2010.
32. [RBC/UKQCD 10B], Y. Aoki, et al. Continuum Limit of B_K from 2+1 Flavor Domain Wall QCD. 2010.
33. [SWME 11], J. Kim, C. Jung, H.-J. Kim, W. Lee, and S. R. Sharpe. Finite volume effects in B_K with improved staggered fermions. 2011. arXiv:1101.2685.

34. [SWME 10], T. Bae, et al. B_K using HYP-smeared staggered fermions in $N_f = 2 + 1$ unquenched QCD. *Phys. Rev.*, D82:114509, 2010.
35. [RBC/UKQCD 09], C. Kelly, P. A. Boyle, and C. T. Sachrajda. Continuum results for light hadrons from 2+1 flavor DWF ensembles. *PoS*, LAT2009:087, 2009.
36. [RBC/UKQCD 07A], D. J. Antonio, et al. Neutral kaon mixing from 2+1 flavor domain wall QCD. *Phys. Rev. Lett.*, 100:032001, 2008.
37. [RBC/UKQCD 08], C. Allton, et al. Physical results from 2+1 flavor domain wall QCD and SU(2) chiral perturbation theory. *Phys. Rev.*, D78:114509, 2008.
38. [HPQCD/UKQCD 06], Elvira Gamiz, et al. Unquenched determination of the kaon parameter B_K from improved staggered fermions. *Phys. Rev.*, D73:114502, 2006.
39. [ETM 09D], V. Bertone, et al. Kaon oscillations in the Standard Model and beyond using $N_f = 2$ dynamical quarks. *PoS*, LAT2009:258, 2009.
40. [JLQCD 08], S. Aoki, et al. B_K with two flavors of dynamical overlap fermions. *Phys. Rev.*, D77:094503, 2008.
41. [RBC 04], Y. Aoki, et al. Lattice QCD with two dynamical flavors of domain wall fermions. *Phys. Rev.*, D72:114505, 2005.
42. [UKQCD 04], J. M. Flynn, F. Mescia, and A. Shams B. Tariq. Sea quark effects in B_K from $N_f = 2$ clover-improved Wilson fermions. *JHEP*, 11:049, 2004.
43. [ETM 09], B. Blossier, et al.
44. [JLQCD 03], S. Aoki, et al. $B_0 - \bar{B}_0$ mixing in unquenched lattice QCD. *Phys.Rev.Lett.*, 91:212001, 2003.
45. [MILC 02], C. Bernard, et al. Lattice calculation of heavy light decay constants with two flavors of dynamical quarks. *Phys.Rev.*, D66:094501, 2002.
46. [CP-PACS 01], A. Ali Khan, et al. B meson decay constant from two flavor lattice QCD with nonrelativistic heavy quarks. *Phys.Rev.*, D64:054504, 2001.
47. [HPQCD 06], E. Dalgic, A. Gray, E. Gamiz, C. T.H. Davies, G.P. Lepage, et al. $B_s^0 - \bar{B}_s^0$ mixing parameters from unquenched lattice QCD. *Phys.Rev.*, D76:011501, 2007.
48. A. X. El-Khadra, A. S. Kronfeld, and P. B. Mackenzie. Massive fermions in lattice gauge theory. *Phys.Rev.*, D55:3933–3957, 1997.
49. H.-W. Lin and N. Christ. Non-perturbatively Determined Relativistic Heavy Quark Action. *Phys.Rev.*, D76:074506, 2007.
50. B. Blossier, M. della Morte, N. Garron, and R. Sommer. HQET at order $1/m$: I. Non-perturbative parameters in the quenched approximation. *JHEP*, 1006:002, 2010.
51. J.I. Noaki et al. Calculation of nonleptonic kaon decay amplitudes from $K \to \pi$ matrix elements in quenched domain wall QCD. *Phys.Rev.*, D68:014501, 2003.
52. T. Blum et al. Kaon matrix elements and CP violation from quenched lattice QCD: 1. The three flavor case. *Phys.Rev.*, D68:114506, 2003.
53. M. Lüscher. Volume Dependence of the Energy Spectrum in Massive Quantum Field Theories. 2. Scattering States. *Commun.Math.Phys.*, 105:153–188, 1986.
54. M. Lüscher. Two particle states on a torus and their relation to the scattering matrix. *Nucl.Phys.*, B354:531–578, 1991.
55. M. Lüscher. Signatures of unstable particles in finite volume. *Nucl.Phys.*, B364:237–254, 1991.
56. C.H. Kim and C.T. Sachrajda. $K \to (\pi\pi)_{I=2}$ decays and twisted boundary conditions. *Phys.Rev.*, D81:114506, 2010.
57. Elaine J. Goode and Matthew Lightman. $\Delta I = 3/2, Kto\pi\pi$ Decays with a Nearly Physical Pion Mass. *PoS*, LATTICE2010:313, 2010.
58. N. H. Christ. Theoretical strategies for epsilon'/epsilon. *PoS*, KAON09:027, 2009.
59. Q. Liu. Preliminary results of $\Delta I = 1/2$ and $3/2$, K to $\pi\pi$ Decay Amplitudes from Lattice QCD. *PoS*, LATTICE2010:314, 2010.

Search for the FCNC's $B_s^0 \to \mu^+\mu^-$ and $B^0 \to \mu^+\mu^-$ with the LHCb spectrometer

D. Martínez Santos
on behalf of the LHCb Collaboration
European Organization for Nuclear Research (CERN), Geneva, Switzerland

Abstract

A search for the decays $B_s^0 \to \mu^+\mu^-$ and $B^0 \to \mu^+\mu^-$ is performed with about 37 pb^{-1} of pp collisions at $\sqrt{s} = 7$ TeV collected by the LHCb experiment at the Large Hadron Collider at CERN. The observed numbers of events are consistent with the background expectations. The resulting upper limits on the branching ratios are BR($B_s^0 \to \mu^+\mu^-$) $< 5.6 \times 10^{-8}$ and BR($B^0 \to \mu^+\mu^-$)$< 1.5 \times 10^{-8}$ at 95% confidence level.

1 Introduction

Precision observables at low energy allow access to information at higher energy scales, constraining possible New Physics (NP) scenarios. The branching ratios (BR) $BR(B^0_{(s)} \to \mu^+\mu^-)$ have been identified as a very interesting potential constraint on the parameter space of NP models.

The SM prediction for the BR of the decays $B_s^0 \to \mu^+\mu^-$ and $B^0 \to \mu^+\mu^-$ have been computed [1] to be $BR(B_s^0 \to \mu^+\mu^-) = (3.2 \pm 0.2) \times 10^{-9}$ and $BR(B^0 \to \mu^+\mu^-) = (0.10 \pm 0.01) \times 10^{-9}$.

However NP contributions can significantly modify these values. For example, within Minimal Supersymmetric extensions of the SM (MSSM), the $BR(B_s \to \mu^+\mu^-)$ has contributions proportional to $\sim \tan^6\beta$ [2], where $\tan\beta$ is the ratio of vacuum expectation values of the two neutral CP-even Higgs fields.

The current published 95% upper limits were obtained using 6.1 fb^{-1} by the D0 collaboration [3], BR($B_s^0 \to \mu^+\mu^-$) $< 5.1 \times 10^{-8}$ and using 2 fb^{-1} by the CDF collaboration [4], BR($B_s^0 \to \mu^+\mu^-$) $< 5.8 \times 10^{-8}$ and BR($B^0 \to \mu^+\mu^-$)$< 1.8 \times 10^{-8}$. The CDF collaboration has also presented preliminary results [5] with 3.7 fb^{-1} that lower the limits to BR($B_s^0 \to \mu^+\mu^-$)$< 4.3 \times 10^{-8}$ and BR($B^0 \to \mu^+\mu^-$)$< 0.76 \times 10^{-8}$.

The LHCb experiment is well suited for such searches due to the high $b\bar{b}$ cross section at LHC, the good invariant mass resolution, vertex resolution, muon identification and trigger efficiency.

The measurements presented in this document use about 37 pb^{-1} of integrated luminosity collected by LHCb between July and October 2010 at $\sqrt{s} = 7$ TeV. Assuming the SM branching ratio, about 0.7 (0.08) $B^0_{(s)} \to \mu^+\mu^-$ ($B^0 \to \mu^+\mu^-$) are expected to be reconstructed within LHCb acceptance.

2 The LHCb detector

The LHCb detector [6] is a single-arm forward spectrometer with an angular coverage from approximately 10 mrad to 300 (250) mrad in the bending (non-bending) plane.

The detector consists of a vertex locator, a warm dipole magnet with a bending power of $\int Bdl = 4$ T m, a tracking system, two RICH detectors, a calorimeter system and a muon system.

Track momenta are measured with a precision between $\delta p/p = 0.35\%$ at 5 GeV/c and $\delta p/p = 0.5\%$ at 100 GeV/c. The RICH system provides charged hadron identification in a momentum range 2–100 GeV/c. Typically kaon identification efficiencies of over 90% can be attained for a $\pi \to K$ fake rate below 10%. The calorimeter system consists of a preshower, a scintillating pad detector, an electromagnetic calorimeter and a hadronic calorimeter. It identifies high transverse energy ($E_{\rm T}$) hadron, electron and photon candidates and provides

information for the trigger. Five muon stations provide fast information for the trigger and muon identification capability: a muon identification efficiency of $\sim 95\%$ is obtained for a misidentification rate of about 1–2 % for momenta above 10 GeV/c.

LHCb has a two-level flexible and efficient trigger system both for leptonic and purely hadronic B decays. It exploits the finite lifetime and relatively large mass of charm and beauty hadrons to distinguish heavy flavour decays from the dominant light quark processes. The first trigger level (L0) is implemented in hardware and reduces the rate to a maximum of 1 MHz, the read-out rate of the whole detector. The second trigger level (High Level Trigger, HLT) is implemented in software running on an event filter CPU farm. The forward geometry allows the LHCb first level trigger to collect events with one or two muons with p_T values as low as 1.4 GeV/c for single muon and $p_{\rm T}(\mu_1) > 0.48$ GeV/c and $p_{\rm T}(\mu_2) > 0.56$ GeV/c for dimuon triggers. During 2010 data taking, the $E_{\rm T}$ threshold for the hadron trigger varied in the range 2.6 to 3.6 GeV.

The dimuon trigger line requires muon pairs of opposite charge forming a common vertex and an invariant mass $M_{\mu\mu} > 4.7$ GeV/c^2. A second trigger line, primarily to select $J/\psi \to \mu\mu$ events, requires $2.97 < M_{\mu\mu} < 3.21$ GeV/c^2. The remaining region of the dimuon invariant mass is also covered by trigger lines that in addition require the dimuon secondary vertex to be well separated from the primary vertex. Other HLT trigger lines select generic displaced vertices, providing a high efficiency for purely hadronic decays.

3 Analysis Strategy

The analysis for the $B^0_{(s)} \to \mu^+\mu^-$ search at LHCb is described in detail in [7]. It is done in two steps: first a set of selection cuts removes the biggest amount of the background while keeping $\sim 60\%$ of the reconstructed signal decays. Then each event is given a probability to be signal or background in a two-dimensional probability space defined by the dimuon invariant mass and a multivariate analysis discriminant likelihood, the *Geometrical Likelihood* (GL) [10,11]. The compatibility of the observed distribution of events in the GL *vs* invariant mass plane with a given branching ratio hypothesis is computed using the $\rm CL_s$ method [8].

The number of expected signal events is evaluated by normalizing with channels of known branching ratios: $B^+ \to J/\psi(\to \mu^+\mu^-)K^+$, $B^0_s \to J/\psi(\to \mu^+\mu^-)\phi(\to K^+K^-)$ and $B^0 \to K^+\pi^-$. This normalization ensures that knowledge of the absolute integrated luminosity and $b\bar{b}$ production cross-section are not needed, and that systematic uncertainties related to the efficiency cancel out in the ratio.

3.1 Event selection

The event selection is designed to reduce the amount of data to analyze, and the real discrimination between signal and background is done by the likelihoods. The selection consists of loose requirements on track separation from the interaction point, decay vertex quality and compatibility of the reconstructed origin of the B meson with the interaction point. The selection cuts were defined in simulation before starting data taking. Events passing the selection are considered $B^0_{(s)} \to \mu^+\mu^-$ candidates if their invariant mass lies within $60\,\rm MeV/c^2$ of the nominal $B^0_{(s)}$ mass. Assuming the SM branching ratio, There are 343 (342) $B^0_{(s)} \to \mu^+\mu^-$ candidates selected from data in the $B^0_s(B^0)$ mass window. A similar selection is applied to the normalization channels, in order to minimize systematic errors in the ratio of efficiencies.

The dominant background after the $B^0_{(s)} \to \mu^+\mu^-$ selection is expected to be $b\bar{b} \to \mu\mu X$ [9]. This is confirmed by comparing expected yield and the kinematical distributions of the sideband data with a $b\bar{b} \to \mu\mu X$ MC sample.

The muon misidentification probability as a function of momentum obtained from data using $K^0_S \to \pi^+\pi^-$, $\Lambda \to p\pi^-$ and $\phi \to K^+K^-$ decays is in good agreement with MC expectations. It is found that the background from misidentified $B^0_{s,d} \to h^+h'^-$ is negligible for the amount of data used in this analysis.

3.2 Signal and background likelihoods

After the selection the signal purity is still about 10^{-3} for $B^0_s \to \mu^+\mu^-$ and 10^{-4} for $B^0 \to \mu^+\mu^-$ assuming the SM branching ratios. Further discrimination is achieved through the combination of two independent variables: the multivariate analysis discriminant likelihood, GL, and the invariant mass. The GL combines information related with the topology and kinematics of the event as the $B^0_{(s)}$ lifetime, the minimum impact parameter of the two muons, the distance of closest approach of the two tracks, the $B^0_{(s)}$ impact parameter and p_T and the isolation of the muons with respect to the other tracks of the event. These variables are combined using the method described in [10,11]. The expected GL distribution for signal events is flat, while for background events it falls exponentially.

The analysis is performed in two-dimensional bins of invariant mass and GL. The invariant mass in the signal regions (± 60 MeV/c^2 around the B^0_s and the B^0 masses) is divided into six bins of equal width, and the GL into four bins of equal width distributed between zero and one. A probability to be signal or background is assigned to events falling in each bin.

The GL variable is defined using MC events but calibrated with data using $B^0_{s,d} \to h^+h'^-$ selected as the signal events and triggered independently on the signal in order to avoid the bias introduced by the hadronic trigger lines.

The number of $B^0_{s,d} \to h^+h'^-$ events in each GL bin is obtained from a fit to the inclusive mass distribution.

Two methods have been used to estimate the $B^0_{(s)} \to \mu^+\mu^-$ mass resolution from data. The first method uses an interpolation between the measured resolutions for $c\bar{c}$ resonances (J/ψ, ψ(2S)) and $b\bar{b}$ resonances ($\Upsilon(1S)$, $\Upsilon(2S)$, $\Upsilon(3S)$) decaying into two muons. Interpolating linearly between the five fitted resolutions to $M_{B^0_s}$ an invariant mass resolution of $\sigma = 26.83 \pm 1.0$ MeV/c^2 was estimated.

The second method that was used to estimate the invariant mass resolution from data is to use the inclusive $B^0_{s,d} \to h^+h'^-$ sample. The result of the fit for the mass resolution, $\sigma = 25.8 \pm 2.5$ MeV/c^2, is consistent with the value obtained from the interpolation method.

The weighted average of the two methods, $\sigma = 26.7 \pm 0.9$ MeV/c^2, is taken as the invariant mass resolution and considered to be the same for B^0 and B^0_s decays.

The prediction of the number of background events in the signal regions is obtained by fitting with an exponential function the $\mu\mu$ mass sidebands independently in each GL bin. The mass sidebands are defined in the range between $M_{B^0_{(s)}} \pm 600$ (1200) MeV/c^2 for the lower (upper) two GL bins, excluding the two search windows ($M_{B^0_{(s)}} \pm 60$ MeV/c^2).

4 Normalization factors

The number of expected signal events is evaluated by normalizing with channels of known branching ratios, $B^+ \to J/\psi K^+$, $B^0_s \to J/\psi\phi$ and $B^0 \to K^+\pi^-$, as shown in Table 1, first column.

The first two decays have similar trigger and muon identification efficiency to the signal but a different number of particles in the final state, while the third channel has the same two-body topology but cannot be efficiently selected with the muon triggers. The branching ratio of the $B^0_s \to J/\psi\phi$ decay is not known precisely ($\sim 25\%$) but has the advantage that the normalization

Table 1: Summary of the factors and their uncertainties needed to calculate the normalization factors ($\alpha_{B^0_{(s)}\to\mu^+\mu^-}$) for the three normalization channels considered. The branching ratios are taken from Refs. [12,14] and includes also the BR($J/\psi \to \mu^+\mu^-$) and BR($\phi \to K^+K^-$). The trigger efficiency and number of $B^0 \to K^+\pi^-$ candidates correspond to only TIS events, as described in the text.

	BR ($\times 10^{-5}$)	$\frac{\epsilon^{\rm REC}_{\rm norm}\epsilon^{\rm SEL|REC}_{\rm norm}}{\epsilon^{\rm REC}_{\rm sig}\epsilon^{\rm SEL|REC}_{\rm sig}}$	$\frac{\epsilon^{\rm TRIG|SEL}_{\rm norm}}{\epsilon^{\rm TRIG|SEL}_{\rm sig}}$	$N_{\rm norm}$	$\alpha_{B^0_{(s)}\to\mu^+\mu^-}$ ($\times 10^{-9}$)	$\alpha_{B^0\to\mu^+\mu^-}$ ($\times 10^{-9}$)
$B^+ \to J/\psi K^+$	5.98 ± 0.22	0.49 ± 0.02	0.96 ± 0.05	$12,366 \pm 403$	8.4 ± 1.3	2.27 ± 0.18
$B^0_s \to J/\psi\phi$	3.4 ± 0.9	0.25 ± 0.02	0.96 ± 0.05	760 ± 71	10.5 ± 2.9	2.83 ± 0.86
$B^0 \to K^+\pi^-$	1.94 ± 0.06	0.82 ± 0.06	0.072 ± 0.010	578 ± 74	7.3 ± 1.8	1.99 ± 0.40

of $B^0_{(s)} \to \mu\mu$ with a B^0_s decay does not require the knowledge of the ratio of fragmentation fractions, which has an uncertainty of $\sim 13\%$ [13].

Using each of these normalization channels, BR($B^0_{(s)} \to \mu\mu$) can be calculated as:

$$\begin{aligned} BR(B^0_{(s)} \to \mu\mu) &= BR_{\rm norm} \times \frac{\epsilon^{\rm REC}_{\rm norm}\epsilon^{\rm SEL|REC}_{\rm norm}\epsilon^{\rm TRIG|SEL}_{\rm norm}}{\epsilon^{\rm REC}_{\rm sig}\epsilon^{\rm SEL|REC}_{\rm sig}\epsilon^{\rm TRIG|SEL}_{\rm sig}} \times \frac{f_{\rm norm}}{f_{B^0_{(s)}}} \times \frac{N_{B^0_{(s)}\to\mu\mu}}{N_{\rm norm}} \\ &= \alpha_{B^0_{(s)}\to\mu\mu} \times N_{B^0_{(s)}\to\mu\mu}\,, \end{aligned} \quad (1)$$

where $\alpha_{B^0_{(s)}\to\mu\mu}$ denotes the normalization factor, $f_{B^0_{(s)}}$ denotes the probability that a b-quark fragments into a $B^0_{(s)}$ and $f_{\rm norm}$ denotes the probability that a b-quark fragments into the b-hadron relevant for the chosen normalization channel with branching fraction $\rm BR_{norm}$. The reconstruction efficiency ($\epsilon^{\rm REC}$) includes the acceptance and particle identification, while $\epsilon^{\rm SEL|REC}$ denotes the selection efficiency on reconstructed events. The trigger efficiency on selected events is denoted by $\epsilon^{\rm TRIG|SEL}$.

The ratios of reconstruction and selection efficiencies are estimated from the simulation using different levels of smearing on the track parameters and checked with data, while the ratios of trigger efficiencies on selected events are determined from data [15].

The yields needed to evaluate the normalization factor are shown in Table 1, where the uncertainty is dominated by the differences observed using different models in fitting the invariant mass lineshape.

As can be seen in Table 1, the normalization factors calculated using the three complementary channels give compatible results. The final normalization factor is a weighted average which takes, with the result:

$$\alpha_{B^0_{(s)}\to\mu\mu} = (8.6 \pm 1.1) \times 10^{-9}\,,$$
$$\alpha_{B^0\to\mu\mu} = (2.24 \pm 0.16) \times 10^{-9}\,.$$

5 Results

For each of the 24 bins (4 bins in GL and 6 bins in mass) the expected number of background events is computed from the fits to the invariant mass sidebands described in Sect. 3.2. The expected numbers of signal events are computed using the normalization factors from Sect. 4,

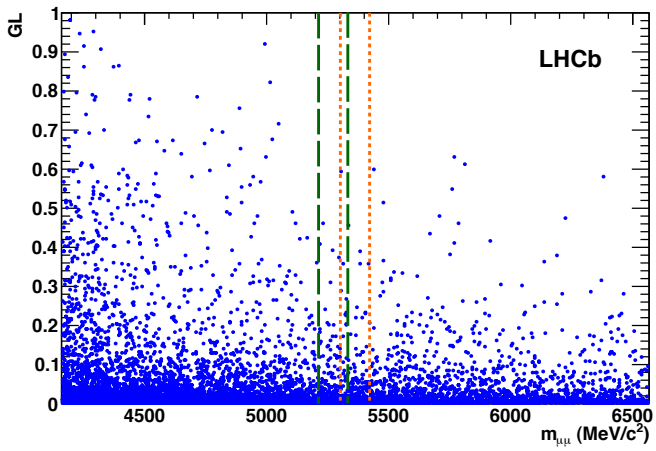

Figure 1: Observed distribution of selected dimuon events in the GL *vs* invariant mass plane. The orange short-dashed (green long-dashed) lines indicate the ± 60 MeV/c^2 search window around the $B_s^0(B^0)$.

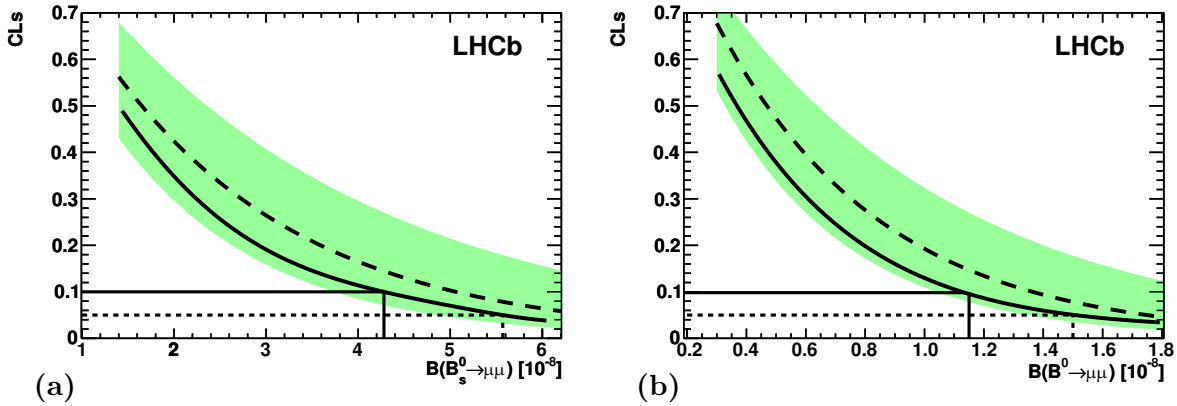

Figure 2: (a) Observed (solid curve) and expected (dashed curve) CL_s values as a function of $BR(B_s^0 \to \mu^+\mu^-)$. The green shaded area contains the $\pm 1\sigma$ interval of possible results compatible with the expected value when only background is observed. The 90 % (95 %) CL observed value is identified by the solid (dashed) line. (b) the same for $BR(B^0 \to \mu^+\mu^-)$.

and the signal likelihoods computed in Section 3.2. The distribution of observed events in the GL *vs* invariant mass plane can be seen in Fig. 1.

The compatibility of the observed distribution of events in the GL *vs* invariant mass plane with a given branching ratio hypothesis is evaluated using the CL_s method [8]. The observed distribution of CL_s as a function of the assumed branching ratio can be seen in Fig. 2.

The expected distributions of possible values of CL_s assuming the background-only hypothesis are also shown in the same figure as a green shaded area that covers the region of $\pm 1\sigma$ of background compatible observations. The uncertainties in the signal and background likelihoods and normalization factors are used to compute the uncertainties in the background and signal predictions.

The upper limits are computed using the CL_s distributions in Fig. 2 with the results:

$$\begin{aligned} BR(B_s^0 \to \mu^+\mu^-) &< 4.3\ (5.6) \times 10^{-8} \text{ at } 90\,\%\ (95\,\%) \text{ C.L.}, \\ BR(B^0 \to \mu^+\mu^-) &< 1.2\ (1.5) \times 10^{-8} \text{ at } 90\,\%\ (95\,\%) \text{ C.L.}, \end{aligned}$$

while the expected values of the limits are $BR(B_s^0 \to \mu^+\mu^-) < 5.1\ (6.5) \times 10^{-8}$ and $BR(B^0 \to \mu^+\mu^-) < 1.4\ (1.8) \times 10^{-8}$ at 90 % (95 %) CL. The limits observed are similar to the best published

limits [3] for the decay $B_s^0 \to \mu^+\mu^-$ and more restrictive for the decay $B^0 \to \mu^+\mu^-$ [4].

References

1. A.J. Buras, "Minimal flavour violation and beyond: Towards a flavour code for short distance dynamics", arXiv:1012.1447;
   E. Gamiz *et al*, "Neutral B meson mixing in unquenched lattice QCD", *Phys. Rev.* D**80** (2009) 014503;
   A.J. Buras, "Relations between $\Delta M_{s,d}$ and $B_{s,d} \to \mu^+\mu^-$ in models with Minimal Flavour Violation", *Phys. Lett.* B**566** (2003) 115.
2. L. J. Hall, R. Rattazzi and U. Sarid, "The top quark mass in supersymmetric SO(10) unification" *Phys. Rev.* D**50** (1994) 7048;
   C. Hamzaoui, M. Pospelov and M. Toharia, "Higgs-mediated FCNC in supersymmetric models with large $\tan\beta$", *Phys. Rev.* D**59** (1999) 095005;
   K.S. Babu and C.F. Kolda, "Higgs-mediated $B_{s,d} \to \mu^+\mu^-$ in minimal supersymmetry", *Phys. Rev. Lett.***84** (2000) 228.
3. V. Abazov *et al.* [D0 Collaboration], "Search for the rare decay $B_s^0 \to \mu^+\mu^-$", *Phys. Lett.* B**693** (2010) 539.
4. T. Aaltonen *et al.* [CDF Collaboration], "Search for $B_s^0 \to \mu^+\mu^-$ and $B_d^0 \to \mu^+\mu^-$ decays with 2 fb^{-1} of $p\bar{p}$ Collisions", *Phys. Rev. Lett.***100** (2008) 101802.
5. T. Aaltonen *et al.* [CDF Collaboration], "Search for $B_s^0 \to \mu^+\mu^-$ and $B^0 \to \mu^+\mu^-$ decays in 3.7 fb^{-1} of $p\bar{p}$ collisions with CDF II", CDF Public Note 9892.
6. A.A. Alves *et al.* [LHCb Collaboration], "The LHCb detector at the LHC", *JINST***3** (2008) S08005, and references therein.
7. R. Aaji *et al.* [LHCb Collaboration], "Search for the rare decays $B_s^0 \to \mu^+\mu^-$ and $B^0 \to \mu^+\mu^-$", *Phys. Lett.* B699 (2011), 330-340.
8. A.L. Read, "Presentation of search results: the CL_s technique", *J. Phys.* G**28** (2002) 2693;
   T. Junk, "Confidence level computation for combining searches with small statistics", *Nucl. Instrum. Methods* A**434** (1999) 435.
9. B. Adeva *et al.* [LHCb Collaboration], "Roadmap for selected key measurements of LHCb", v:0912.4179v2.
10. D. Karlen, "Using projections and correlations to approximate probability distributions", Comp. Phys. **12** (1998) 380.
11. D. Martinez Santos, "Study of the very rare decay $B_s^0 \to \mu^+\mu^-$ in LHCb", CERN-THESIS-2010-068.
12. K. Nakamura *et al.* [Particle Data Group], "Review of particle physics", *J. Phys.* G**37** (2010) 075021.
13. D. Asner *et al.* [Heavy Flavour Averaging Group], "Averages of b-hadron, c-hadron, and τ-lepton properties", arXiv:1010.1589. Updated values for f_d/f_s available at http://www.slac.stanford.edu/xorg/hfag/osc/end_2009/ have been used for this document, as they include also pre-summer 2010 results which are not contained in [12].
14. R. Louvot, "Υ(5S) Results at BELLE", arXiv:0905.4345v2.
15. E. Lopez Asamar et al., "Measurement of trigger efficiencies and biases", LHCb-PUB-2007-073.

4. Lepton Flavour and Leptogenesis

LHC AND LEPTON FLAVOUR VIOLATION PHENOMENOLOGY IN SEESAW MODELS

J. C. ROMÃO
Departamento de Física & CFTP, Instituto Superior Técnico, Technical University of Lisbon
A. Rovisco Pais 1, 1049-001 Lisboa, Portugal

We review Lepton Flavour Violation (LFV) in the supersymmetric version of the seesaw mechanism (type I, II, III) and in Left-Right models. The LFV needed to explain neutrino masses and mixings is the only source of LFV and has experimental implications both in low-energy experiments where we search for the radiative decays of leptons, and at the LHC where we look at its imprint on the LFV decays of the sparticles and on slepton mass splittings. We discuss how this confrontation between high- and low-energy LFV observables may provide information about the underlying mechanism of LFV.

1 Introduction

The experimental observation of non-vanishing neutrino masses and mixings,[1] constitutes clear evidence for physics beyond the Standard Model (SM). As neutrino oscillations indisputably signal lepton flavour violation (LFV) in the neutral sector, it is only natural to expect that charged lepton flavour will also be violated in extensions of the SM where ν oscillations can be naturally accommodated. The search for manifestations of charged LFV constitutes the goal of several experiments,[2] exclusively dedicated to look for signals of processes such as rare radiative as well as three-body decays and lepton conversion in muonic nuclei.

In parallel to these low-energy searches, if the high-energy Large Hadron Collider (LHC) finds signatures of supersymmetry (SUSY), it is then extremely appealing to consider SUSY models that can also accommodate neutrino oscillations. One of the most economical and elegant possibilities is perhaps to embed a seesaw mechanism in this framework, the so-called SUSY seesaw.

If the seesaw is indeed the source of both neutrino masses and leptonic mixings and accounts for low-energy LFV observables within future sensitivity reach, we show that interesting phenomena are expected to be observed at the LHC: in addition to measurable slepton mass splittings, the most striking effect will be the possible appearance of new edges in di-lepton mass distributions.

2 Models

2.1 Seesaw type I,II, III & Left-Right Model

At GUT scale the SU(5) invariant superpotentials for type I, II and III SUSY seesaw are[3]

$$W_{\rm RHN} = \mathbf{Y}^{\rm I}_N \; N^c \; \overline{5} \cdot 5_H + \frac{1}{2} \; M_R \; N^c N^c \; , \tag{1}$$

$$W_{15\mathrm{H}} = \frac{1}{\sqrt{2}}\mathbf{Y}_N^{\mathrm{II}}\ \bar{5}\cdot 15\cdot\bar{5} + \frac{1}{\sqrt{2}}\lambda_1\bar{5}_H\cdot 15\cdot\bar{5}_H + \frac{1}{\sqrt{2}}\lambda_2 5_H\cdot\overline{15}\cdot 5_H + \mathbf{Y}_5 10\cdot\bar{5}\cdot\bar{5}_H + \mathbf{Y}_{10}10\cdot 10\cdot 5_H + M_{15}15\cdot\overline{15} + M_5\bar{5}_H\cdot 5_H\ , \tag{2}$$

$$W_{24\mathrm{H}} = \sqrt{2}\,\bar{5}_M Y^5 10_M\bar{5}_H - \frac{1}{4}10_M Y^{10}10_M 5_H + 5_H 24_M Y_N^{III}\bar{5}_M + \frac{1}{2}24_M M_{24}24_M\ . \tag{3}$$

The exchange of the singlet N^c in type I, of the scalar triplet T in type II and of both the

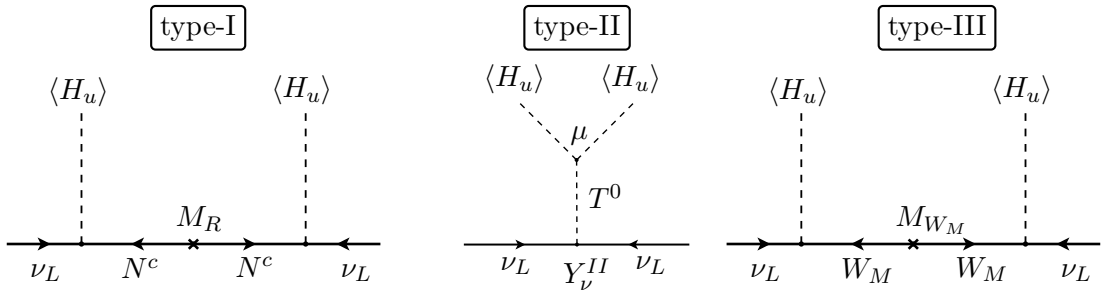

Figure 1: Seesaw types

fermionic triplet W_M and fermionic singlet B_M in type III lead, through the diagrams of Fig. 1 to the well known effective neutrino mass matrix formulas,

$$m_{\mathrm{eff}}^{\mathrm{I}} = -(vY_\nu)M_R^{-1}(vY_\nu)^T,\quad m_{\mathrm{eff}}^{\mathrm{II}} = \frac{v^2\mu Y_\nu^{\mathrm{II}}}{M_T^2},\quad m_{\mathrm{eff}}^{\mathrm{III}} = -(vY_\nu^{\mathrm{III}})M_{W_M}^{-1}(vY_\nu^{\mathrm{III}})^T\ . \tag{4}$$

We have also studied [4] a SUSY seesaw in which the breaking from $SU(5)$ to the SM gauge group is done in two steps, first to a Left-Right (LR) symmetric model, $SU(3)_c\times SU(2)_L\times SU(2)_R\times U(1)_{B-L}$ at scale v_R, and then with the $B-L$ broken at a lower scale v_{B-L}. For neutrino physics, as well as for the LFV, the relevant part of the superpotential is,

$$\mathcal{W}^{LR} = Y_L L\Phi L^c - f_c L^c\Delta^c L^c + \cdots\ , \tag{5}$$

where Y_L and f_c complex 3×3 matrices. After the $B-L$ breaking we have,

$$\mathcal{L} = H_u\,\overline{\nu_L}\,Y_\nu^{\mathrm{I}}\,\nu_R - \frac{1}{2}\nu_R^T\,C^{-1}\,(f_c v_{BL})\,\nu_R + \cdots\ , \tag{6}$$

leading to an effective neutrino mass matrix of the type I form,

$$m_{\mathrm{eff}}^{\mathrm{LR}} = -(vY_\nu)(f_c v_{BL})^{-1}(vY_\nu)^T\ . \tag{7}$$

The important point here is that, as we have two complex matrices, we can have different types of neutrino fits. We studied two limiting situations, the so-called Y_ν fit where $f_c = \mathbb{1}$ (Y_ν arbitrary), and the f fit where $Y_\nu = \mathbb{1}$ (f_c arbitrary). These will leave different imprints on the LFV through their RGE running.

2.2 LFV in the Models

Starting with universal minimal supergravity inspired (mSUGRA) boundary conditions at M_{GUT}, the off-diagonal entries in Y^ν will induce the LFV on the slepton mass matrices through RGE effects. For type I, II and III we have

$$\Delta m_{L,ij}^2 \simeq -\frac{a_k}{8\pi^2}\left(3m_0^2 + A_0^2\right)\left(Y_N^{k,\dagger}LY_N^k\right)_{ij},\quad L = \ln(\frac{M_{\mathrm{GUT}}}{M_{\mathrm{N}}}) \tag{8}$$

$$\Delta m^2_{E,ij} \simeq 0 \qquad\qquad a_{\rm I} = 1\ ,\ a_{\rm II} = 6 \text{ and } a_{\rm III} = \frac{9}{5}\ , \tag{9}$$

while for the LR model we have two situations. From $M_{\rm GUT}$ to v_R,

$$\Delta m^2_L \simeq -\frac{1}{4\pi^2}\left(3ff^\dagger + Y_L^{(k)}Y_L^{(k)\,\dagger}\right)(3m_0^2 + A_0^2)\ln\left(\frac{M_{\rm GUT}}{v_R}\right) \tag{10}$$

$$\Delta m^2_E \simeq -\frac{1}{4\pi^2}\left(3f^\dagger f + Y_L^{(k)\,\dagger}Y_L^{(k)}\right)(3m_0^2 + A_0^2)\ln\left(\frac{M_{\rm GUT}}{v_R}\right)\ , \tag{11}$$

while from v_R to v_{BL},

$$\Delta m^2_L \simeq -\frac{1}{8\pi^2}Y_\nu Y_\nu^\dagger\left(m_L^2|_{v_R} + A_e^2|_{v_R}\right)\ln\left(\frac{v_R}{v_{BL}}\right), \quad \Delta m^2_E \simeq 0\ . \tag{12}$$

Therefore, the choice of the different neutrino fits will have implications on the lepton flavour violation observables. The low energy LFV processes are described by an effective Lagrangian,

$$\mathcal{L}_{eff} = e\frac{m_{l_i}}{2}\ \bar{l}_i\sigma_{\mu\nu}F^{\mu\nu}(A_L^{ij}P_L + A_R^{ij}P_R)l_j + h.c. \tag{13}$$

For seesaw models,

$$A_L^{ij} \sim \frac{(\Delta m^2_L)_{ij}}{m^4_{\rm SUSY}}, \quad A_R^{ij} \sim \frac{(\Delta m^2_E)_{ij}}{m^4_{\rm SUSY}}\ . \tag{14}$$

This implies that for type I, II and II we have only $A_L \neq 0$, while for the LR model we can have both, A_L and A_R. This implies that if MEG [2] finds evidence for the decay $\mu^+ \to e^+\gamma$, then we can distinguish among the models by looking at the positron polarization asymmetry,

$$\mathcal{A}(\mu^+ \to e^+\gamma) = \frac{|A_L|^2 - |A_R|^2}{|A_L|^2 + |A_R|^2}\ \begin{cases} = 1 & \text{type-I-II-III} \\ \neq 1 & \text{LR} \end{cases}\ . \tag{15}$$

3 Results

For all the models we have studied [3,4,5] the different low- and high-energy LFV observables. The numerical analysis was done using the public code SPheno, [6] that includes the 2-loop RGEs calculated with the public code SARAH. [7]

3.1 Low-Energy Observables

The present bounds on low-energy LFV observables and dark matter abundance already constrain the parameter space of the models. As an example we give in Fig. 2 the type II case. On the left panel we show the allowed regions for dark matter abundance (within 3σ of the WMAP [8] observation). A scan was performed in the $M_{1/2} - m_0$ plane, the other cMSSM parameters being taken as $A_0 = 0$, $\tan\beta = 10$, $\mu > 0$. The seesaw scale was fixed at $M_T = 5 \times 10^{13}$ GeV. Superimposed are the contours for BR($\mu \to e\gamma$). We see that for these input parameters only a small part of the parameter space remains viable after imposing the LFV and dark matter constrains. Once MEG gets to the sensitivity of 10^{-13}, most of the parameter space will be excluded if no signal is found. On the right panel of Fig. 2 we show a similar plot, now in the so-called Higgs funnel region obtained for $\tan\beta = 52$, the other parameters as before. The variation with the top mass is shown: $m_{top} = 169.1$ GeV (blue), 171.2 GeV (red), 173.3 GeV (green).

As another example we consider the e^+ asymmetry defined in Eq. (15) in the LR model [4]. On the left panel of Fig. 3 we show the contours for $\mathcal{A}$ in the $M_{1/2} - m_0$ plane. The cMSSM parameters were taken as those of the SPS3 point, $m_0 = 90$ GeV, $M_{1/2} = 400$ GeV, $A_0 = 0$ GeV, $\tan\beta = 10$ and $\mu > 0$. We take $M_{\rm Seesaw} = 10^{12}$ GeV, while the LR breaking scales were $v_{BL} = 10^{15}$ GeV, $v_R \in [10^{14}, 10^{15}]$ GeV and Y_ν fit was chosen. On the right panel we show, for the same parameters, the correlation between the asymmetry and the breaking scales. If MEG measures $\mathcal{A} < 1$, we can have an handle on the scales v_R, v_{BL} and test the LR model.

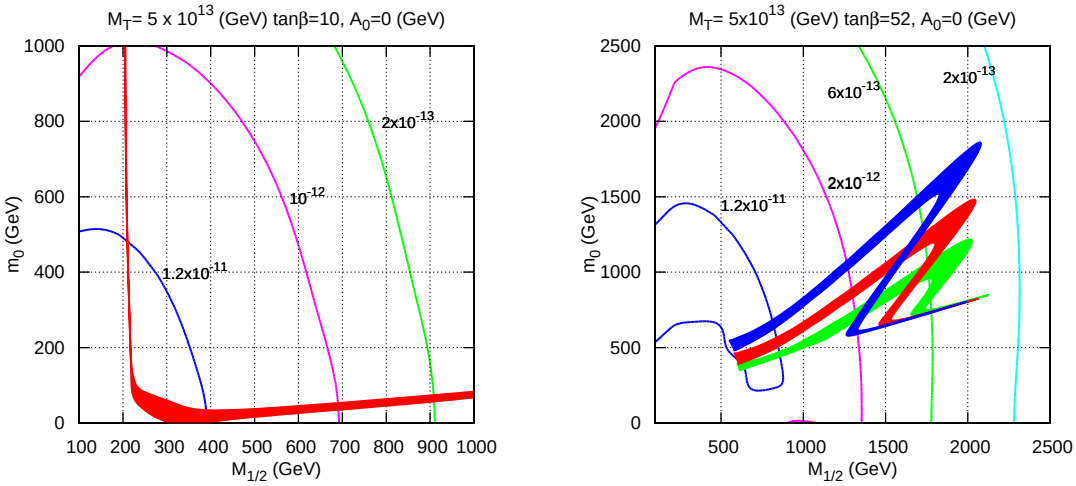

Figure 2: Dark matter allowed regions and BR($\mu \to e\gamma$) contours for type II,

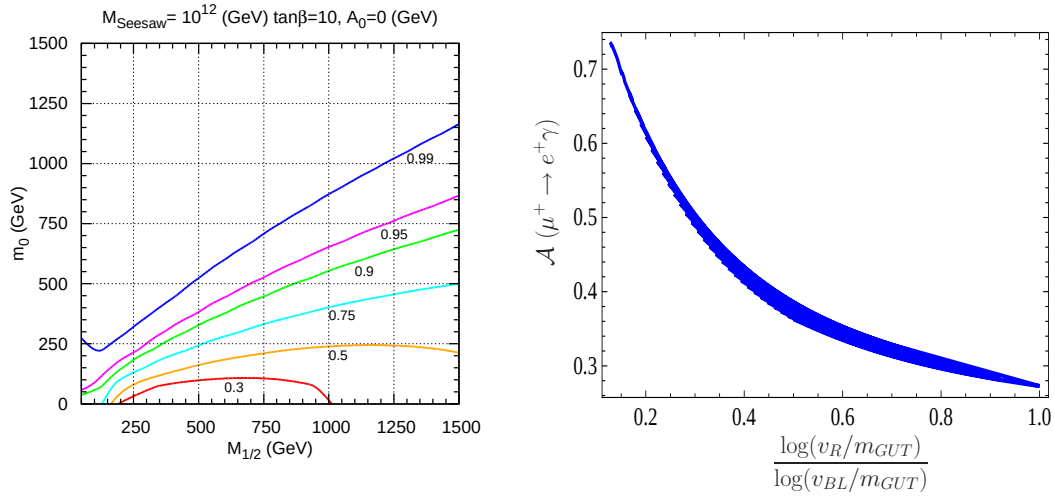

Figure 3: Positron asymmetry in the Left-Right model.

3.2 LHC Observables

At LHC we look at di-lepton invariant mass distributions from $\chi_2^0 \to \tilde{\ell}^i_{L,R}\ell_{\to}\chi_1^0\ell\ell$ decays, that can be measured with a precision of 0.1%, [9] for on-shell sleptons and isolated leptons with large $p_T > 10$ GeV. From this we can infer the slepton mass splittings,

$$\frac{\Delta m_{\tilde{\ell}}}{m_{\tilde{\ell}}}(\tilde{\ell}_i, \tilde{\ell}_j) \;=\; \frac{|m_{\tilde{\ell}_i} - m_{\tilde{\ell}_j}|}{< m_{\tilde{\ell}_{i,j}} >} \quad \text{@LHC}: \quad \begin{array}{l} \Delta m/m_{\tilde{\ell}}(\tilde{e}_L, \tilde{\mu}_L) \sim \mathcal{O}(0.1\%) \\ \Delta m/m_{\tilde{\ell}}(\tilde{\mu}_L, \tilde{\tau}_L) \sim \mathcal{O}(1\%)\ . \end{array} \tag{16}$$

We start our analysis by identifying what we call a *standard window*. This is defined by the requirement of having on-shell sleptons decaying with isolated leptons with large $p_T > 10$ GeV. We also require large χ_2^0 production, a sizable BR($\chi_2^0 \to \chi_1^0\ell\ell$) and, if possible, the correct abundance of dark matter, Ωh^2. This is shown on the left panel of Fig. 4, where the white region fulfills all the requirements (the correct dark matter abundance corresponds to the black line inside the region). To carry out our analysis we chose the cMSSM study points shown in the right panel of Fig. 4 and then varied the seesaw parameters. In the cMSSM we get double-triangular distributions corresponding to intermediate $\tilde{\mu}_L$ and $\tilde{\mu}_R$ in $\chi_2^0 \to \chi_1^0\mu\mu$, with superimposed $\tilde{\ell}_{L,R}$ edges for $m_{\mu\mu}$ and m_{ee} because of "degenerate" $\tilde{\mu}, \tilde{e}$. In Fig. 5 we show the di-muon invariant distribution, and number of expected events, for the case of SUSY type I seesaw, for the following choice of seesaw parameters: M_N=$\{10^{10}, 5 \times 10^{10}, 5 \times 10^{13}\}$ GeV

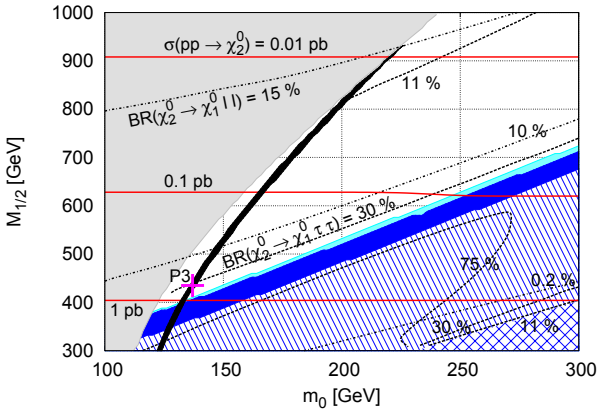

Point	m_0 (GeV)	$M_{1/2}$ (GeV)	A_0 (TeV)	$\tan\beta$
P1	110	528	0	10
P2	110	471	1	10
P3	137	435	-1	10
P4	490	1161	0	40
P5-HM1	180	850	0	10
P6-SU1	70	350	0	10

Figure 4: Standard window (see text) and benchmark points used in the analysis.

(P2′, P3′) and M_N=$\{10^{10}, 5\times10^{12}, 10^{15}\}$ GeV (P1‴, SU1‴), always with $\theta_{13} = 0.1°$. We get

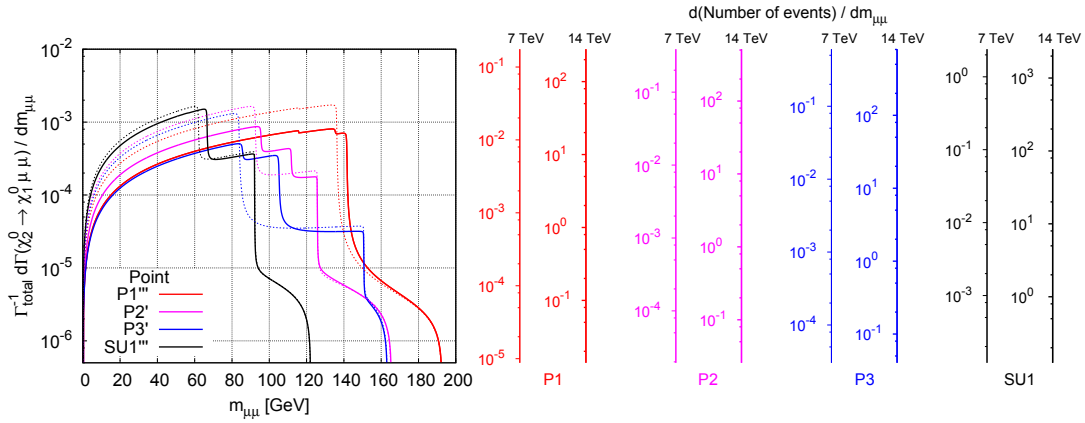

Figure 5: Di-muon invariant mass distribution for the SUSY seesaw for the benchmark points defined in Fig. 4.

displaced $m_{\mu\mu}$ and m_{ee} edges (ℓ_L) which give sizable mass splittings $\frac{\Delta m_{\tilde{\ell}}}{m_{\tilde{\ell}}}(\tilde{e}_L, \tilde{\mu}_L)$. We also find the appearance of a new edge in $m_{\mu\mu}$ corresponding to an intermediate $\tilde{\tau}_2$. These mass splittings are correlated with the low-energy observables as we show in Fig. 6. On the left panel we show the correlation for BR($\mu \to e\gamma$) for the CMS benchmark point HM1 ($m_0 = 180$ GeV, $M_{1/2} = 800$ GeV, $A_0 = 0$ GeV, $\tan\beta = 10$ and $\mu > 0$) while on the right panel we show the correlation for BR($\tau \to \mu\gamma$) for the ATLAS benchmark point SU1 ($m_0 = 70$ GeV, $M_{1/2} = 350$ GeV, $A_0 = 0$ GeV, $\tan\beta = 10$ and $\mu > 0$). In these plots we performed a scan over the SUSY seesaw parameters, with $M_{N_3} = 10^{12,13,14}$ GeV, $\theta_{13} = 0.1°$.

We conclude that if SUSY is discovered with a spectrum similar to HM1 or SU1 and a type-I seesaw is at work, then the LFV observables will be within experimental reach at LHC, while BR($\mu \to e\gamma$) and BR($\tau \to e\gamma$) will be within the reach of MEG and SuperB, respectively.

4 Conclusions

In SUSY seesaw models the neutrino Yukawa couplings, Y_ν, acts as the only source of LFV, implying a correlation between low- and high-energy LFV observables. We have performed a study of these correlations in the so-called SUSY seesaws type I, II and III, as well as in a seesaw model that is Left-Right symmetric below the GUT scale.

If SUSY seesaw is to account for neutrino masses and mixings then we will have slepton mass

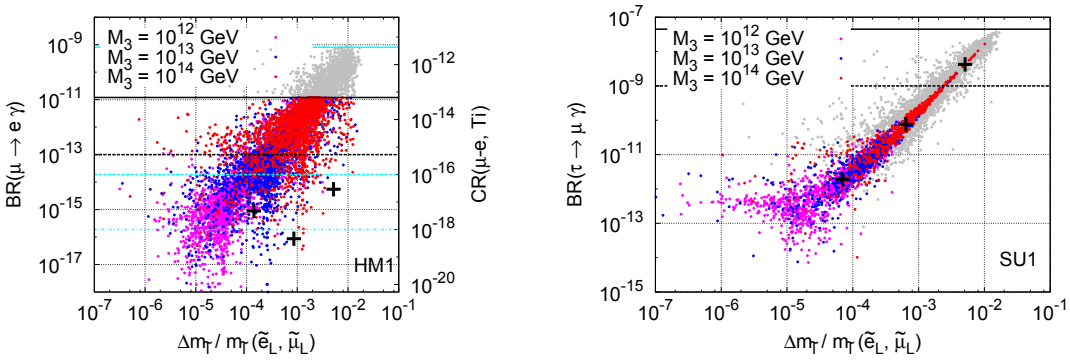

Figure 6: Correlation between low-energy and LHC observables for the benchmark points HM1 and SU1.

splittings within LHC sensitivity, with the possible observation of new edges in the di-lepton invariant mass distributions. In most cases a clear correlation can be established between low- and high-energy LFV observables (e.g. BR vs $\Delta m_{\tilde{\ell}}$) due to their unique source.

The experimental data that will be available soon, both from the high- and low-energy experiments, will either substantiate the seesaw hypothesis, or disfavour the SUSY seesaw as the (only) source of flavour violation.

Acknowledgments

This work has been done partly under the EU Network grant UNILHC PITN-GA-2009-237920 and from *Fundação para a Ciência e a Tecnologia* grants CFTP-FCT UNIT 777, PTDC/-FIS/102120/2008, CERN/FP/109305/2009.

References

1. For a recent review see T. Schwetz, M. Tortola, J. W. F. Valle, [arXiv:1103.0734 [hep-ph]].
2. For a comprehensive list see Ref. [5].
3. M. Hirsch, J. W. F. Valle, W. Porod, J. C. Romao and A. Villanova del Moral, Phys. Rev. D **78** (2008) 013006; J. N. Esteves, J. C. Romao, A. Villanova del Moral, M. Hirsch, J. W. F. Valle and W. Porod, JHEP **0905**, 003 (2009); J. N. Esteves, J. C. Romao, M. Hirsch, F. Staub and W. Porod, Phys. Rev. D **83** (2011) 013003.
4. J. N. Esteves, J. C. Romao, M. Hirsch, A. Vicente, W. Porod, F. Staub, JHEP **1012** (2010) 077.
5. A. Abada, A. J. R. Figueiredo, J. C. Romao and A. M. Teixeira, JHEP **1010 (2010)** 104; *ibidem* [arXiv:1104.3962 [hep-ph]].
6. W. Porod, Comput. Phys. Commun. **153**, (2003) 275.
7. F. Staub, Comput. Phys. Commun. 181 (2010) 1077-1086.
8. D. Larson *et al.*, Astrophys. J. Suppl. **192** (2011) 16.
9. F. E. Paige, "Determining SUSY particle masses at LHC", arXiv:hep-ph/9609373; I. Hinchliffe, F. E. Paige, M. D. Shapiro, J. Soderqvist and W. Yao, Phys. Rev. D **55** (1997) 5520; H. Bachacou, I. Hinchliffe and F. E. Paige, Phys. Rev. D **62** (2000) 015009.

SEARCHES FOR LEPTON FLAVOUR AND LEPTON NUMBER VIOLATION IN KAON DECAYS

Evgueni Goudzovski
Centre for Cosmology, Particle Physics and Phenomenology,
Catholic University of Louvain, B-1348 Louvain-la-Neuve, Belgium
and
School of Physics and Astronomy, University of Birmingham,
Edgbaston, Birmingham, B15 2TT, United Kingdom

Searches for lepton flavour and lepton number violation in kaon decays by the NA48/2 and NA62 experiments at CERN are presented. A new measurement of the helicity suppressed ratio of charged kaon leptonic decay rates $R_K = \Gamma(K_{e2})/\Gamma(K_{\mu 2})$ to sub-percent relative precision is discussed. An improved upper limit on the lepton number violating $K^\pm \to \pi^\mp \mu^\pm \mu^\pm$ decay rate is also presented.

1 Introduction

In the Standard Model (SM) the decays of pseudoscalar mesons to light leptons are helicity suppressed. In particular, the SM width of $P^\pm \to \ell^\pm \nu$ decays with $P = \pi, K, D, B$ (denoted $P_{\ell 2}$ in the following) is

$$\Gamma^{\rm SM}(P^\pm \to \ell^\pm \nu) = \frac{G_F^2 M_P M_\ell^2}{8\pi}\left(1 - \frac{M_\ell^2}{M_P^2}\right)^2 f_P^2 |V_{qq'}|^2, \tag{1}$$

where G_F is the Fermi constant, M_P and M_ℓ are meson and lepton masses, f_P is the decay constant, and $V_{qq'}$ is the corresponding Cabibbo-Kobayashi-Maskawa matrix element. Although the SM predictions for the $P_{\ell 2}$ decay rates are limited by hadronic uncertainties, their specific ratios do not depend on f_P and can be computed very precisely. In particular, the SM prediction for the ratio $R_K = \Gamma(K_{e2})/\Gamma(K_{\mu 2})$ of kaon leptonic decay widths inclusive of internal bremsstrahlung (IB) radiation is [1]

$$R_K^{\rm SM} = \left(\frac{M_e}{M_\mu}\right)^2 \left(\frac{M_K^2 - M_e^2}{M_K^2 - M_\mu^2}\right)^2 (1 + \delta R_{\rm QED}) = (2.477 \pm 0.001) \times 10^{-5}, \tag{2}$$

where $\delta R_{\rm QED} = (-3.79 \pm 0.04)\%$ is an electromagnetic correction due to the IB and structure-dependent effects.

Within certain two Higgs doublet models (2HDM of type II), including the minimal supersymmetric model (MSSM), R_K is sensitive to lepton flavour violating (LFV) effects appearing at the one-loop level via the charged Higgs boson ($H^\pm$) exchange [2,3], representing a unique probe into mixing in the right-handed slepton sector [4]. The dominant contribution due to the LFV

coupling of the $H^{\pm}$ is

$$R_K^{\rm LFV} \simeq R_K^{\rm SM}\left[1+\left(\frac{M_K}{M_H}\right)^4\left(\frac{M_\tau}{M_e}\right)^2|\Delta_R^{31}|^2\tan^6\beta\right], \quad (3)$$

where $\tan\beta$ is the ratio of the two Higgs vacuum expectation values, and $|\Delta_R^{31}|$ is the mixing parameter between the superpartners of the right-handed leptons, which can reach $\sim 10^{-3}$. This can enhance R_K by $\mathcal{O}(1\%)$ without contradicting any experimental constraints known at present, including upper bounds on the LFV decays $\tau \to eX$ with $X = \eta, \gamma, \mu\bar{\mu}$. On the other hand, R_K is sensitive to the neutrino mixing parameters within the SM extension involving a fourth generation [5].

The first measurements of R_K were performed in the 1970s [6,7,8], while the current PDG world average [9] is based on a more precise recent result [10] $R_K = (2.493 \pm 0.031) \times 10^{-5}$. A new measurement of R_K based on a part of a dedicated data sample collected by the NA62 experiment at CERN in 2007 is reported here: the analyzed K_{e2} sample is ~ 4 times larger than the total world sample, allowing the first measurement of R_K with a relative precision below 1%.

The decay $K^{\pm} \to \pi^{\mp}\mu^{\pm}\mu^{\pm}$ violating lepton number by two units can proceed via a neutrino exchange if the neutrino is a Majorana particle, consequently the experimental limits on this decay provide constraints on the effective Majorana neutrino mass $\langle m_{\mu\mu}\rangle$ [11]. This decay has also been studied in the context of supersymmetric models with R-parity violation [12]. The best previous upper limit on the decay rate was based on a special data set collected by the BNL E865 experiment in 1997 [13]. The sample of $\pi\mu\mu$ triggers collected by the NA48/2 experiment at CERN during the 2003–04 data taking is about 8 times larger than the E865 one, which allows improving the upper limit significantly.

2 Beam and detector

The NA48/2 and NA62 (phase I) experiments at CERN took data in 2003–04 and 2007–08, respectively, using the same kaon beamline and experimental setup [14]. The trigger logic was optimized to detect direct CP violating charge asymmetries in $K^{\pm}$ decays in 2003–04 [15], and for the $K_{e2}/K_{\mu 2}$ ratio measurement in 2007–08. The beam line is capable of delivering simultaneous unseparated K^+ and K^- beams derived from the 400 GeV/c primary proton beam extracted from the CERN SPS. Central values of kaon momentum of 60 GeV/c (both K^+ and K^- beams) and 74 GeV/c (K^+ beam only), with a narrow momentum band, were used for collection of the main data samples by the NA48/2 and NA62 experiments, correspondingly.

The fiducial decay region is contained in a 114 m long cylindrical vacuum tank. With $\sim 10^{12}$ primary protons incident on the target per SPS pulse of 4.8 s duration, the typical secondary beam flux at the entrance to the decay volume is 10^7 to 10^8 particles per pulse, of which about 5% are kaons, while pions constitute the dominant component. The transverse size of the beams within the decay volume is below 1 cm (rms), and their angular divergence is negligible.

Among the subdetectors located downstream the decay volume, a magnetic spectrometer, a plastic scintillator hodoscope (HOD), a liquid krypton electromagnetic calorimeter (LKr) and a muon veto counter (MUV) are principal for the present measurements. The spectrometer, used to detect charged products of kaon decays, is composed of four drift chambers (DCHs) and a dipole magnet. The HOD producing fast trigger signals consists of two planes of strip-shaped counters. The LKr, used for particle identification and as a veto, is an almost homogeneous ionization chamber, $27X_0$ deep, segmented transversally into 13,248 cells (2×2 cm^2 each), and with no longitudinal segmentation. The MUV is composed of three planes of plastic scintillator strips read out by photomultipliers at both ends. A beam pipe traversing the centres of the

detectors allows undecayed beam particles and muons from decays of beam pions to continue their path in vacuum.

3 Search for lepton flavour violation

The precision measurement of $R_K = \Gamma(K_{e2})/\Gamma(K_{\mu 2})$ is based on the NA62 2007 data sample. The measurement method is based on counting the numbers of reconstructed K_{e2} and $K_{\mu 2}$ candidates collected concurrently. Consequently the result does not rely on kaon flux measurement, and several systematic effects (e.g. due to reconstruction and trigger efficiencies, time-dependent effects) cancel to first order. To take into account the significant dependence of signal acceptance and background level on lepton momentum, the measurement is performed independently in bins of this observable: 10 bins covering a lepton momentum range of $(13; 65)$ GeV/c are used. The ratio R_K in each bin is computed as

$$R_K = \frac{1}{D} \cdot \frac{N(K_{e2}) - N_{\rm B}(K_{e2})}{N(K_{\mu 2}) - N_{\rm B}(K_{\mu 2})} \cdot \frac{A(K_{\mu 2})}{A(K_{e2})} \cdot \frac{f_\mu \times \epsilon(K_{\mu 2})}{f_e \times \epsilon(K_{e2})} \cdot \frac{1}{f_{\rm LKr}}, \tag{4}$$

where $N(K_{\ell 2})$ are the numbers of selected $K_{\ell 2}$ candidates ($\ell = e, \mu$), $N_{\rm B}(K_{\ell 2})$ are numbers of background events, $A(K_{\mu 2})/A(K_{e2})$ is the geometric acceptance correction, f_ℓ are efficiencies of e/μ identification, $\epsilon(K_{\ell 2})$ are trigger efficiencies, $f_{\rm LKr}$ is the global efficiency of the LKr readout, and $D = 150$ is the downscaling factor of the $K_{\mu 2}$ trigger.

A detailed Monte Carlo (MC) simulation including beam line optics, full detector geometry and material description, stray magnetic fields, local inefficiencies of DCH wires, and time variations of the above throughout the running period, is used to evaluate the acceptance correction $A(K_{\mu 2})/A(K_{e2})$ and the geometric parts of the acceptances for background processes entering the computation of $N_B(K_{\ell 2})$. Simulations are used to a limited extent only: particle identification, trigger and readout efficiencies are measured directly.

Due to the topological similarity of K_{e2} and $K_{\mu 2}$ decays, a large part of the selection conditions is common for both decays: (1) exactly one reconstructed positively charged particle compatible with originating from a beam K decay; (2) its momentum 13 GeV/c $< p <$ 65 GeV/c (the lower limit is due to the 10 GeV LKr energy deposit trigger requirement); (3) extrapolated track impact points in subdetectors are within their geometrical acceptances; (4) no LKr energy deposition clusters with energy $E > 2$ GeV not associated to the track, to suppress background from other kaon decays; (5) distance between the charged track and the nominal kaon beam axis CDA < 3 cm, and decay vertex longitudinal position within the nominal decay volume.

The following two principal selection criteria are different for the K_{e2} and $K_{\mu 2}$ decays. $K_{\ell 2}$ kinematic identification is based on the reconstructed squared missing mass assuming the track to be a positron or a muon: $M^2_{\rm miss}(\ell) = (P_K - P_\ell)^2$, where P_K and P_ℓ ($\ell = e, \mu$) are the four-momenta of the kaon (average beam momentum assumed) and the lepton (positron or muon mass assumed). A selection condition $-M_1^2 < M^2_{\rm miss}(\ell) < M_2^2$ is applied to select $K_{\ell 2}$ candidates, where M_1^2 varies between 0.013 and 0.016 (GeV/c^2)^2 and M_2^2 between 0.010 and 0.013 (GeV/c^2)^2 across the lepton momentum bins, depending on $M^2_{\rm miss}(\ell)$ resolution. Particle identification is based on the ratio E/p of track energy deposit in the LKr calorimeter to its momentum measured by the spectrometer. Particles with $0.95 < E/p < 1.1$ ($E/p < 0.85$) are identified as positrons (muons).

Kinematic separation of K_{e2} from $K_{\mu 2}$ decays is achievable at low lepton momentum only ($p < 35$ GeV/c). At high lepton momentum, the $K_{\mu 2}$ decay with a mis-identified muon ($E/p > 0.95$) is the largest background source. The dominant process leading to mis-identification of the muon as a positron is 'catastrophic' bremsstrahlung in or in front of the LKr leading to significant energy deposit in the LKr. Mis-identification due to accidental LKr clusters associated with

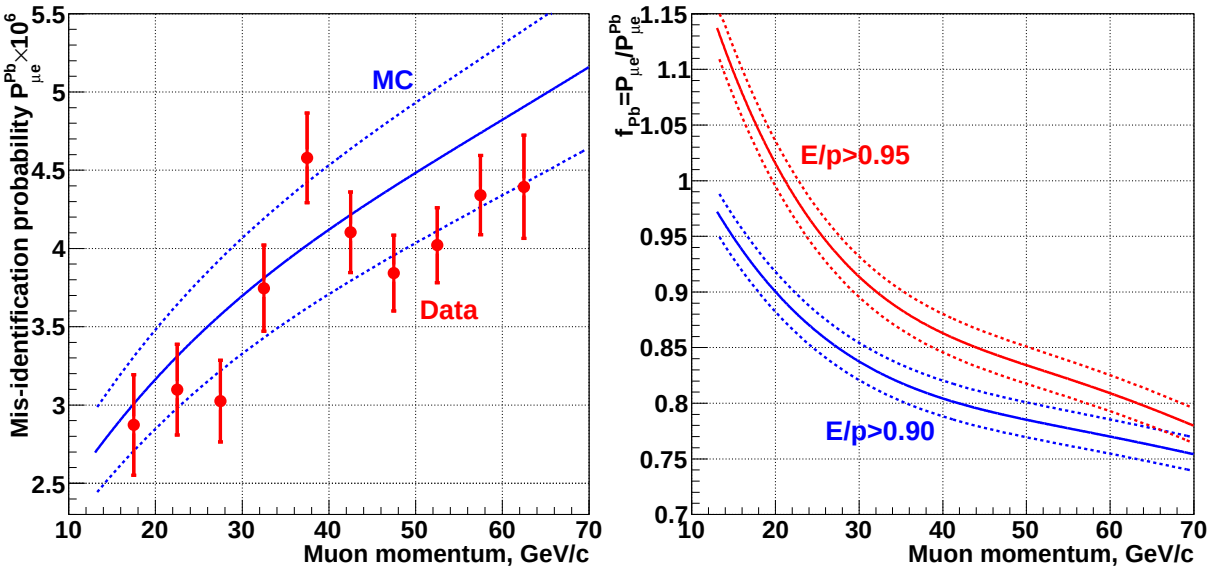

Figure 1: Left: Mis-identification probability for muons traversing the lead wall, $P^{\rm Pb}_{\mu e}$, for $(E/p)_{\rm min} = 0.95$ as a function of momentum: measurement (solid circles with error bars) and simulation (solid line). Right: Correction factors $f_{\rm Pb} = P_{\mu e}/P^{\rm Pb}_{\mu e}$ for the considered values of $(E/p)_{\rm min}$, as evaluated with simulation. Dotted lines in both plots indicate the estimated systematic uncertainties of the simulation.

the muon track is negligible, as concluded from a study of the sidebands of track-cluster time difference and distance distributions.

The muon mis-identification probability $P_{\mu e}$ has been measured as a function of momentum. To collect a muon sample free from the typical $\sim 10^{-4}$ positron contamination due to $\mu \to e$ decays, a $9.2X_0$ thick lead (Pb) wall covering $\sim 20\%$ of the geometric acceptance was installed approximately 1.2 m in front of the LKr calorimeter (between the two HOD planes) during a period of data taking. The component from positrons which traverse the Pb wall and are mis-identified as muons from $K_{\mu 2}$ decay with $p > 30$ GeV/c and $E/p > 0.95$ is suppressed down to a negligible level ($\sim 10^{-8}$) by energy losses in the Pb.

However, muon passage through the Pb wall affects the measured $P^{\rm Pb}_{\mu e}$ via two principal effects: 1) ionization energy loss in Pb decreases $P_{\mu e}$ and dominates at low momentum; 2) bremsstrahlung in Pb increases $P_{\mu e}$ and dominates at high momentum. To evaluate the correction factor $f_{\rm Pb} = P_{\mu e}/P^{\rm Pb}_{\mu e}$, a dedicated MC simulation based on Geant4 (version 9.2) has been developed to describe the propagation of muons downstream from the last DCH, involving all electromagnetic processes including muon bremsstrahlung [16].

The measurements of $P^{\rm Pb}_{\mu e}$ in momentum bins compared with the results of the MC simulation and the correction factors $f_{\rm Pb}$ obtained from simulation, along with the estimated systematic uncertainties of the simulated values, are shown in Fig. 1. The relative systematic uncertainties on $P_{\mu e}$ and $P^{\rm Pb}_{\mu e}$ obtained by simulation have been estimated to be 10%, and are mainly due to the simulation of cluster reconstruction and energy calibration. However the error of the ratio $f_{\rm Pb} = P_{\mu e}/P^{\rm Pb}_{\mu e}$ is significantly smaller ($\delta f_{\rm Pb}/f_{\rm Pb} = 2\%$) due to cancellation of the main systematic effects. The measured $P^{\rm Pb}_{\mu e}$ is in agreement with the simulation within their uncertainties.

The $K_{\mu 2}$ background contamination integrated over lepton momentum has been computed to be $(6.11 \pm 0.22)\%$ using the measured $P^{\rm Pb}_{\mu e}$ corrected by $f_{\rm Pb}$. The quoted error is due to the limited size of the data sample used to measure $P^{\rm Pb}_{\mu e}$ (0.16%), the uncertainty $\delta f_{\rm Pb}$ (0.12%), and the model-dependence of the correction for the $M^2_{\rm miss}(e)$ vs E/p correlation (0.08%).

R_K is defined to be fully inclusive of internal bremsstrahlung (IB) radiation [1]. The structure-dependent (SD) $K^+ \to e^+\nu\gamma$ process [17,18] may lead to a K_{e2} signature if the positron is energetic and the photon is undetected. In particular, the $\rm SD^+$ component with positive photon helicity

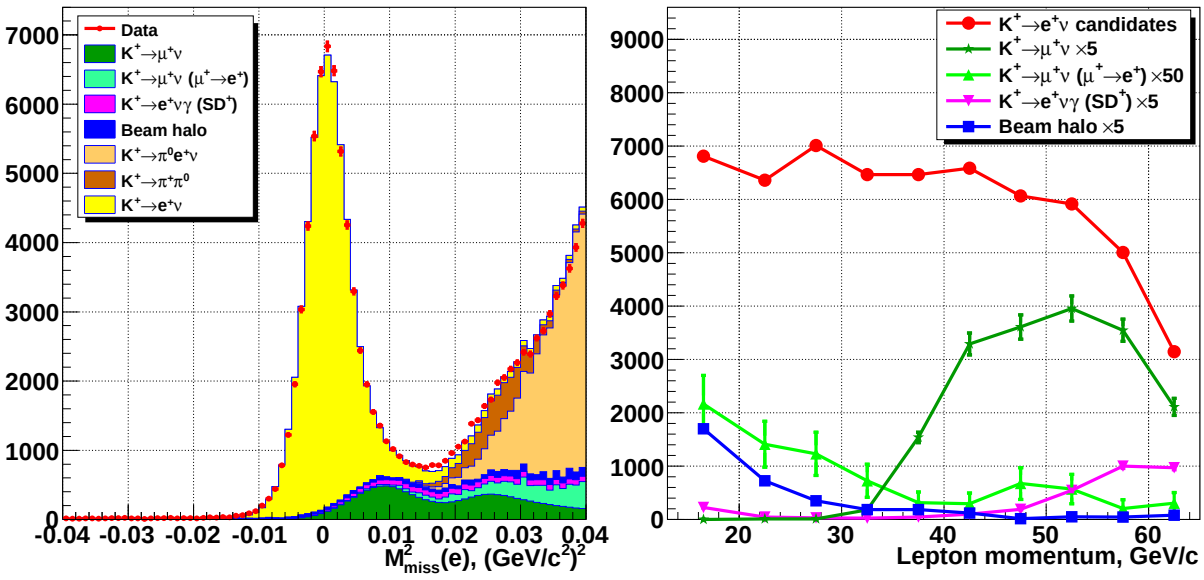

Figure 2: Left: Reconstructed squared missing mass $M^2_{\rm miss}(e)$ distribution of the K_{e2} candidates compared with the sum of normalised estimated signal and background components. Right: Lepton momentum distributions of the K_{e2} candidates and the dominant backgrounds; the backgrounds are scaled for visibility.

Table 1: Summary of backgrounds in the K_{e2} sample.

Source	$N_B/N(K_{e2})$
$K_{\mu 2}$	$(6.11 \pm 0.22)\%$
$K_{\mu 2}(\mu \to e)$	$(0.27 \pm 0.04)\%$
$K^+ \to e^+\nu\gamma$ (SD$^+$)	$(1.07 \pm 0.05)\%$
$K^+ \to \pi^0 e^+\nu$	$(0.05 \pm 0.03)\%$
$K^+ \to \pi^+\pi^0$	$(0.05 \pm 0.03)\%$
Beam halo	$(1.16 \pm 0.06)\%$
Total	$(8.71 \pm 0.24)\%$

peaks at high positron momentum in the K^+ rest frame ($E^*_e \approx M_K/2$) and has a similar branching ratio to K_{e2}. The background due to $K^+ \to e^+\nu\gamma$ (SD$^-$) decay with negative photon helicity peaking at $E^*_e \approx M_K/4$ and the interference between the IB and SD processes are negligible. The SD$^+$ background contribution has been estimated by MC simulation as $(1.07 \pm 0.05)\%$, using a recent measurement of the $K^+ \to e^+\nu\gamma$ (SD$^+$) differential decay rate [10]. The quoted uncertainty is due to the limited precision on the form factors and decay rate, and is therefore correlated between lepton momentum bins.

The beam halo background in the K_{e2} sample induced by halo muons (undergoing $\mu \to e$ decay in flight or mis-identified) is measured using a data-driven method, by reconstructing K^+_{e2} candidates from a control K^- data sample collected with the K^+ beam dumped, to be $(1.16 \pm 0.06)\%$. Background rate and kinematical distribution are qualitatively reproduced by a halo simulation. The uncertainty is due to the limited size of the control sample. The beam halo is the only significant background source in the $K_{\mu 2}$ sample. Its contribution is mainly at low muon momentum, and has been measured to be $(0.38 \pm 0.01)\%$ using the same technique as for the K_{e2} sample.

The numbers of selected K_{e2} and $K_{\mu 2}$ candidates are 59813 and 1.803×10^7, respectively (the latter samples has been pre-scaled by a factor of 150 at the trigger level). Backgrounds in the K_{e2} sample integrated over lepton momentum are summarised in Table 1: the total background contamination is $(8.71 \pm 0.24)\%$, and its uncertainty is smaller than the relative statistical

Table 2: Summary of the uncertainties on R_K.

Source	$\delta R_K \times 10^5$
Statistical	0.011
$K_{\mu 2}$ background	0.005
$K^+ \to e^+\nu\gamma$ (SD^+) background	0.001
$K^+ \to \pi^0 e^+\nu$, $K^+ \to \pi^+\pi^0$ backgrounds	0.001
Beam halo background	0.001
Helium purity	0.003
Acceptance correction	0.002
Spectrometer alignment	0.001
Positron identification efficiency	0.001
1-track trigger efficiency	0.002
LKr readout inefficiency	0.001
Total systematic	0.007
Total	0.013

uncertainty of 0.43%. The $M^2_{\mathrm{miss}}(e)$ and lepton momentum distributions of K_{e2} candidates and backgrounds are shown in Fig. 2.

The ratio of geometric acceptances $A(K_{\mu 2})/A(K_{e2})$ in each lepton momentum bin has been evaluated with MC simulation. The radiative $K^+ \to e^+\nu\gamma$ (IB) process, which is responsible for the loss of about 5% of the K_{e2} acceptance by increasing the reconstructed $M^2_{\mathrm{miss}}(e)$, is taken into account following [17], with higher order corrections according to [19,20].

The acceptance correction is strongly influenced by bremsstrahlung suffered by the positron in the material upstream of the spectrometer magnet (Kevlar window, helium, DCHs). This results in an almost momentum-independent loss of K_{e2} acceptance of about 6%, mainly by increasing the reconstructed $M^2_{\mathrm{miss}}(e)$. The relevant material thickness has been measured by studying the spectra and rates of bremsstrahlung photons produced by low intensity 25 GeV/c and 40 GeV/c electron and positron beams steered into the DCH acceptance, using special data samples collected in the same setup by the NA48/2 experiment in 2004 and 2006. The material thickness during the 2007 run has been estimated to be $(1.56 \pm 0.03)\% X_0$, where the quoted uncertainty is dominated by the limited knowledge of helium purity in the spectrometer tank.

A χ^2 fit to the measurements of R_K in the 10 lepton momentum bins has been performed, taking into account the bin-to-bin correlations between the systematic errors. The uncertainties of the combined result are summarized in Table 2. To validate the assigned systematic uncertainties, extensive stability checks have been performed in bins of kinematic variables and by varying selection criteria and analysis procedures. The fit result is [21]

$$R_K = (2.487 \pm 0.011_{\mathrm{stat.}} \pm 0.007_{\mathrm{syst.}}) \times 10^{-5} = (2.487 \pm 0.013) \times 10^{-5}, \qquad (5)$$

with $\chi^2/\mathrm{ndf} = 3.6/9$. The individual measurements with their statistical and total uncertainties, the combined NA62 result, and the new world average are presented in Fig. 3.

4 Search for lepton number violation

The $K^\pm \to \pi^\mp\mu^\pm\mu^\pm$ decay has been searched for using the NA48/2 2003–04 data sample, normalizing to the abundant $K^\pm \to \pi^\pm\pi^+\pi^-$ normalization channel (denoted $K_{3\pi}$ below). Three-track vertices (compatible with either $K^\pm \to \pi\mu\mu$ or $K_{3\pi}$ decay topology) are reconstructed by extrapolation of track segments from the spectrometer upstream into the decay volume, taking into account the measured Earth's magnetic field, stray fields due to magnetization of the

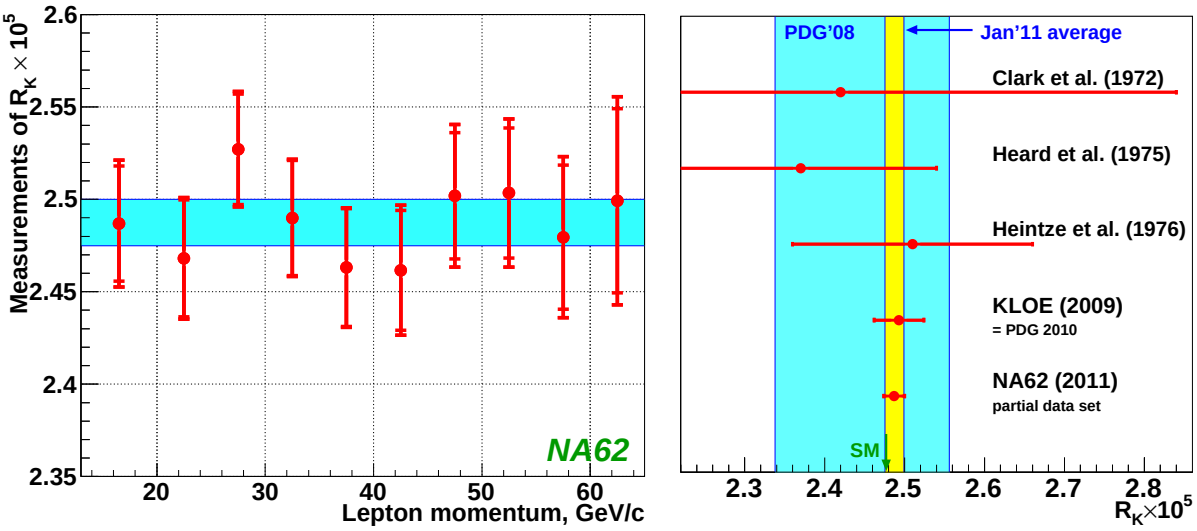

Figure 3: Left: Measurements of R_K in lepton momentum bins with their uncorrelated statistical uncertainties and the partially correlated total uncertainties; the average R_K and its total uncertainty are indicated by a band. Right: The new world average including the present result.

vacuum tank, and multiple scattering. The vertex is required to have no significant missing momentum, and to be composed of one $\pi^\pm$ candidate (with the ratio of energy deposition in the LKr calorimeter to momentum measured by the spectrometer $E/p < 0.95$, which suppresses electrons, and no in-time associated hits in the MUV), and a pair of $\mu^\pm$ candidates (with $E/p < 0.2$ and associated signal in the MUV). The muon identification efficiency has been measured to be above 98% for $p > 10$ GeV/c, and above 99% for $p > 15$ GeV/c.

The invariant mass spectra of the reconstructed $\pi^\pm\mu^\pm\mu^\mp$ and $\pi^\mp\mu^\pm\mu^\pm$ candidates are presented in Fig. 4. The observed flavour changing neutral current $K^\pm \to \pi^\pm\mu^\pm\mu^\mp$ decay (3120 candidates with a background of 3.3%) has been studied separately [22]. In the mass spectrum with same sign muons, corresponding to the lepton number violating signature, 52 events are observed in the signal region $|M_{\pi\mu\mu} - M_K| < 8$ MeV/c^2. The background comes from the $K_{3\pi}$ decay, and has been estimated by MC simulation to be (52.6 ± 19.8) events. The quoted uncertainty is systematic due to the limited precision of MC description of the high-mass region, and has been estimated from the level of data/MC agreement in the control mass region of (465; 485) MeV/c^2. This background estimate has been cross-checked by fitting the mass spectrum in the region between 460 and 520 MeV/c^2, excluding the signal region between 485 and 502 MeV/c^2, with an empirical function similar to that used in the E865 analysis [13] using the maximum likelihood estimator and assuming a Poisson probability density in each mass bin.

The Feldman-Cousins method [23] is employed for confidence interval evaluation; the systematic uncertainty of the background estimate is taken into account. Conservatively assuming the expected background to be $52.6 - 19.8 = 32.8$ events to take into account its uncertainty, this translates into an upper limit of 32.2 signal events at 90% CL. The geometrical acceptance is conservatively assumed to be the smallest of those averaged over the $K^\pm \to \pi^\pm\mu^\pm\mu^\mp$ and $K_{3\pi}$ samples ($A_{\pi\mu\mu} = 15.4\%$ and $A_{3\pi} = 22.2\%$). This leads to an upper limit [22] of $\mathrm{BR}(K^\pm \to \pi^\mp\mu^\pm\mu^\pm) < 1.1 \times 10^{-9}$ at 90% CL, which improves the best previous limit [13] by almost a factor of 3.

5 Conclusions

The most precise measurement of lepton flavour violation parameter R_K has been performed: $R_K = (2.487 \pm 0.013) \times 10^{-5}$ is consistent with the SM expectation, and can be used to constrain

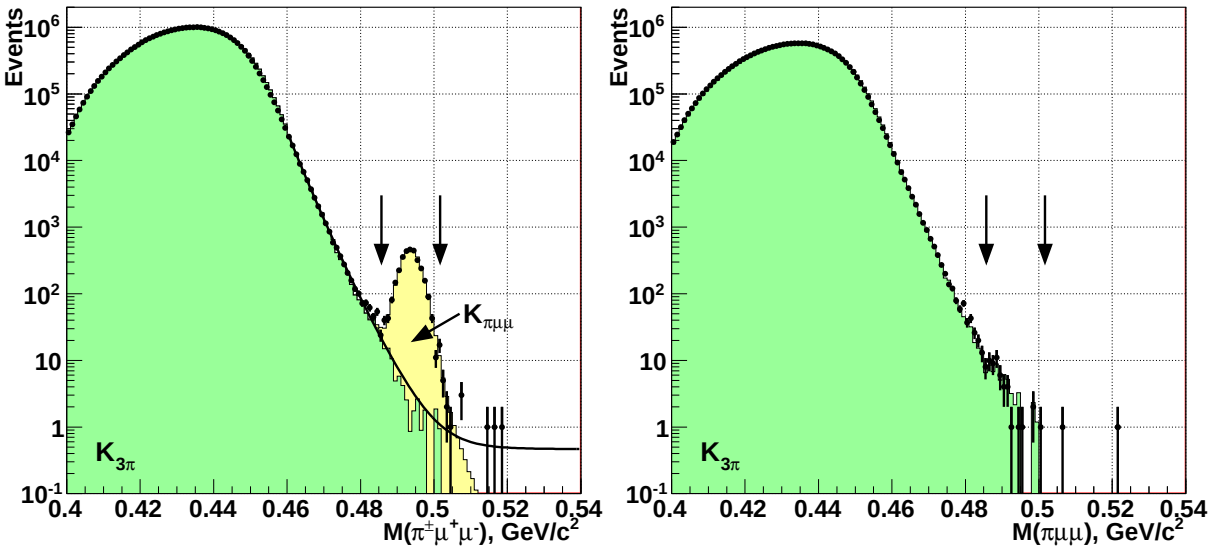

Figure 4: Reconstructed $M_{\pi\mu\mu}$ spectra for candidates with different (left) and same sign (right) muons: data (dots), $K_{3\pi}$ and $K_{\pi\mu\mu}$ MC simulations (filled areas); fit to background using the empirical parameterization as explained in the text (solid line). The signal region is indicated with arrows.

multi-Higgs [2] and fourth generation [5] new physics scenarios. An improved upper limit of 1.1×10^{-9} for the branching fraction of the lepton number violating $K^{\pm} \to \pi^{\mp}\mu^{\pm}\mu^{\pm}$ decay has been established.

References

1. V. Cirigliano and I. Rosell, *Phys. Rev. Lett.* **99**, 231801 (2007).
2. A. Masiero, P. Paradisi and R. Petronzio, *Phys. Rev.* D **74**, 011701 (2006).
3. A. Masiero, P. Paradisi and R. Petronzio, *JHEP* **0811**, 042 (2008).
4. J. Ellis, S. Lola and M. Raidal, *Nucl. Phys.* B **812**, 128 (2009).
5. H. Lacker and A. Menzel, *JHEP* **1007**, 006 (2010).
6. A.G. Clark *et al*, *Phys. Rev. Lett.* **29**, 1274 (1972).
7. K.S. Heard *et al*, *Phys. Lett.* B **55**, 327 (1975).
8. J. Heintze *et al*, *Phys. Lett.* B **60**, 302 (1976).
9. K. Nakamura *et al* (PDG), *J. Phys.* G **37**, 075021 (2010).
10. F. Ambrosino *et al*, *Eur. Phys. J.* C **64**, 627 (2009); ibid. C **65**, 703 (2010).
11. K. Zuber, *Phys. Lett.* B **479**, 33 (2000).
12. L.S. Littenberg and R. Shrock, *Phys. Lett.* B **491**, 285 (2000).
13. R. Appel *et al*, *Phys. Rev. Lett.* **85**, 2877 (2000).
14. V. Fanti *et al*, *Nucl. Instrum. Methods* A **574**, 433 (2007).
15. J.R. Batley *et al*, *Eur. Phys. J.* C **52**, 875 (2007).
16. S.R. Kelner, R.P. Kokoulin and A.A. Petrukhin, *Phys. Atom. Nucl.* **60**, 576 (1997).
17. J. Bijnens, G. Ecker and J. Gasser, *Nucl. Phys.* B **396**, 81 (1993).
18. C.H. Chen, C.Q. Geng and C.C. Lih, *Phys. Rev.* D **77**, 014004 (2008).
19. S. Weinberg, *Phys. Rev.* **140**, B516 (1965).
20. C. Gatti, *Eur. Phys. J.* C **45**, 417 (2006).
21. C. Lazzeroni *et al*, *Phys. Lett.* B **698**, 105 (2011).
22. J.R. Batley *et al*, *Phys. Lett.* B **697**, 107 (2011).
23. G.J. Feldman and R.D. Cousins, *Rhys. Rev.* D **57**, 3873 (1998).

RECONCILING SUPERSYMMETRY AND THERMAL LEPTOGENESIS BY ENTROPY PRODUCTION

J. KERSTEN
II. Institute for Theoretical Physics, University of Hamburg,
Luruper Chaussee 149, 22761 Hamburg, Germany

The entropy produced in the decays of super-weakly interacting particles may help to reconcile thermal leptogenesis and Big Bang Nucleosynthesis (BBN) in scenarios with gravitino dark matter, which is usually difficult due to late decays of the next-to-lightest supersymmetric particle (NLSP) spoiling BBN. We study this possibility for a general neutralino NLSP. We discuss the constraints on the entropy-producing particle, considering as an example the saxion from the axion multiplet. We show that, in addition to enabling a solution of the strong CP problem, it can indeed produce a suitable amount of entropy.

1 The Gravitino Problem

The tiny but non-zero neutrino masses, which constitute the first solid evidence for physics beyond the Standard Model (SM), find a natural explanation in the see-saw mechanism.[1,2,3,4,5] In this setup the SM is extended by gauge-singlet neutrinos with very large masses. The C- and CP-violating decay of these heavy neutrinos in the early universe can provide the observed baryon asymmetry via leptogenesis [6] as an almost free by-product. The CP asymmetry of the decays

$$\epsilon = \frac{\Gamma(\nu_{\rm R} \to \ell H) - \Gamma(\nu_{\rm R} \to \overline{\ell}\,\overline{H})}{\Gamma(\nu_{\rm R} \to \ell H) + \Gamma(\nu_{\rm R} \to \overline{\ell}\,\overline{H})} \tag{1}$$

creates a lepton asymmetry, which is afterwards converted into a baryon asymmetry $\eta_{\rm B} = \frac{n_{\rm B}}{n_\gamma} \propto |\epsilon|$ by sphaleron processes.[7] We denote the lightest of the heavy neutrinos by $\nu_{\rm R}$ and its mass by $M_{\rm R}$. For hierarchical heavy neutrino masses and no fine-tuning, the CP asymmetry is limited by [8]

$$|\epsilon| < \frac{3}{16\pi} \frac{M_{\rm R}\sqrt{\Delta m^2_{\rm atm}}}{v^2} \ . \tag{2}$$

Using the mass squared difference $\Delta m^2_{\rm atm}$ measured in atmospheric neutrino oscillations, the Higgs vacuum expectation value v, the observed baryon asymmetry $\eta_{\rm B} \simeq 6 \cdot 10^{-10}$, and other known quantities then leads to the lower limit $M_{\rm R} \gtrsim 2 \cdot 10^9$ GeV.[9]

The only price to pay for all the baryons is a mechanism producing the heavy neutrinos in the first place. In the simplest scenario, thermal leptogenesis, the temperature is larger than $M_{\rm R}$, so the heavy neutrinos are abundantly produced, since they are in contact with the thermal bath via their Yukawa couplings. Consequently, thermal leptogenesis requires a sufficiently high reheating temperature after inflation,

$$T_{\rm R} \gtrsim M_{\rm R} \gtrsim 2 \cdot 10^9 \text{ GeV} \ . \tag{3}$$

This scenario does not address the biggest theoretical problem of the SM, the hierarchy problem. This problem is elegantly solved by supersymmetry (SUSY), which in turn offers a natural way to include gravity in the form of supergravity. Within this theory, the large temperature in the early universe also leads to a thermal production of gravitinos, the superpartners of the graviton. Their relic density is approximately [10,11]

$$\Omega_{3/2}^{\mathrm{tp}} h^2 \simeq 0.11 \left(\frac{T_{\mathrm{R}}}{2 \cdot 10^9 \,\mathrm{GeV}}\right) \left(\frac{67 \,\mathrm{GeV}}{m_{3/2}}\right) \left(\frac{M_{\tilde{g}}}{10^3 \,\mathrm{GeV}}\right)^2 . \tag{4}$$

Thus, the observed dark matter abundance $\Omega_{\mathrm{DM}} h^2 \simeq 0.11$ is compatible with the reheating temperature required by thermal leptogenesis both for a gravitino lightest superparticle (LSP) with a sufficiently large mass $m_{3/2} \gtrsim 60 \,\mathrm{GeV}$ and for a heavier non-LSP gravitino.

However, as it interacts only via gravity, a non-LSP gravitino has a long lifetime between, very roughly, $10^{-2}\,\mathrm{s}$ and several years. Consequently, it decays during or after Big Bang Nucleosynthesis (BBN), releasing energetic decay products that destroy the light nuclei produced by BBN.[12,13] The observed primordial element abundances limit the gravitino density and thus the reheating temperature. The result is $T_{\mathrm{R}} \ll 10^8 \,\mathrm{GeV}$, unless $m_{3/2} \gg 1 \,\mathrm{TeV}$.[14] So thermal leptogenesis is not possible for an unstable gravitino with a mass similar to the other superparticle masses, as expected in most scenarios of SUSY breaking.

Let us therefore concentrate on the case of a gravitino LSP with a mass around 100 GeV. For conserved R parity, the gravitino is now stable and does not cause any problems. However, the next-to-LSP (NLSP) can only decay to the gravitino via gravity. Thus, it is long-lived and its decay products threaten the success of BBN. If the NLSP relic density is determined by the standard freeze-out mechanism, the resulting changes of the primordial abundances are incompatible with observations in the Minimal Supersymmetric Standard Model (MSSM) with TeV-scale SUSY, with the exception of very small corners of the parameter space. Consequently, the gravitino problem survives in the form of the NLSP decay problem.

2 Entropy Production

We consider one of the many approaches to solve the gravitino problem, the possibility that a large amount of entropy is produced after the freeze-out of the NLSP, diluting its density by a factor Δ.[15,16,17,18] This reduces the impact of the NLSP decays on BBN, possibly making it compatible with observations.

The entropy can stem from the decay of a non-relativistic particle ϕ. The energy density of such a particle only decreases as $\rho_\phi \propto R^{-3}$, where R is the scale factor of the universe, while the energy density of radiation decreases faster, $\rho_{\mathrm{rad}} \propto R^{-4}$. Consequently, if ϕ is sufficiently long-lived, ρ_ϕ will equal ρ_{rad} at some temperature $T_\phi^=$, and it will dominate the energy density of the universe afterwards. Eventually, the particle decays into radiation at a temperature T_ϕ^{dec}, increasing the entropy per comoving volume by a factor [19,20]

$$\Delta \simeq 0.75 \, \frac{T_\phi^=}{T_\phi^{\mathrm{dec}}} \tag{5}$$

and thus diluting all previously produced relic abundances by the same factor.

We require radiation domination at the time of NLSP freeze-out, so that the standard computation of its thermal relic density is valid. This means that $T_\phi^= < T_{\mathrm{NLSP}}^{\mathrm{fo}} \sim \frac{m_{\mathrm{NLSP}}}{25}$. The decay of ϕ has to happen before BBN to avoid changing the primordial abundances, $T_\phi^{\mathrm{dec}} > T_{\mathrm{BBN}} \sim 4 \,\mathrm{MeV}$. This leads to the upper bound

$$\Delta \lesssim 0.75 \cdot 10^3 \left(\frac{m_{\mathrm{NLSP}}}{100 \,\mathrm{GeV}}\right) . \tag{6}$$

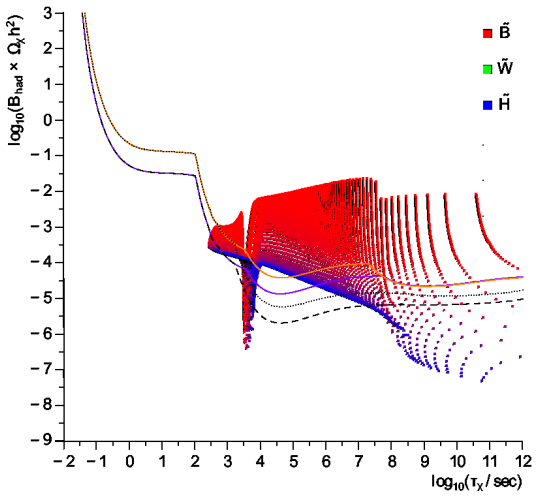

Figure 1: Lifetime versus hadronic energy release of a bino-higgsino neutralino compared with the hadronic BBN constraints [23] for the case of a 100 GeV gravitino mass and a dilution factor $\Delta = 10^3$. All points above the uppermost line are excluded, while those between the curves should not be considered as strictly excluded. The neutralino mass increases from right to left. Its composition varies from bino at the top to higgsino at the bottom, with the colors giving the dominant component (from [18]).

The amount of entropy production is also limited by leptogenesis, since it dilutes the baryon asymmetry by a factor Δ, too. According to Eq. 2, this has to be compensated by increasing $M_{\rm R}$ by the same factor. However, for very large values of $M_{\rm R}$ the baryon asymmetry is strongly reduced by washout processes.[21] This places an upper limit on $M_{\rm R}$ and thus on Δ. We estimate $\Delta \lesssim 10^3 \ldots 10^4$, which roughly coincides with the bound in Eq. 6 for NLSP masses around the electroweak scale. Note that the increase of $M_{\rm R}$ raises the lower limit on the reheating temperature by a factor Δ as well. Assuming $T_{\rm R} \sim M_{\rm R}$, this exactly compensates the dilution of the gravitino density, so we still obtain the correct dark matter density.

As a concrete example, let us consider the constraints from BBN on a neutralino NLSP for a gravitino LSP mass of 100 GeV and a dilution factor $\Delta = 10^3$. Performing a scan over the low-energy gaugino and higgsino mass parameters allowed by LEP and corresponding to neutralino masses up to 2 TeV, we arrive at the points shown in Fig. 1 for the case of a neutralino whose main components are the bino and the higgsinos. The horizontal axis of the plot is the neutralino lifetime. The vertical axis is its relic density multiplied by the hadronic branching ratio and thus determines the energy released in the form of hadrons. See [22] for details of the calculation of these quantities. The curves in the figure are the bounds from BBN on hadronic energy release.[23] All points above the uppermost line are definitely excluded, while those between this line and the dashed line may be allowed. Everything below the dashed line is definitely compatible with current observations.

We see that even with considerable entropy production a large part of the parameter space remains excluded. In particular, a neutralino with dominant bino component is only possible for quite small lifetimes correponding to masses above 1 TeV. However, unlike in the case without entropy production, we do find allowed regions now. There are states with comparable bino and higgsino components and $m_{\rm NLSP} \simeq 230$ GeV violating only the less conservative BBN bound. Neutralinos that are mainly higgsino satisfy even these constraints, if they are lighter than 250 GeV. They can be almost as light as the gravitino. Thus, we have arrived at a scenario where thermal leptogenesis is possible and the gravitino or NLSP decay problem is solved.

A change of Δ shifts all points vertically by a corresponding factor. Therefore, it is straightforward to infer the constraints for arbitrary Δ from the results shown here. In [18] other possible neutralino compositions and also the BBN constraints from electromagnetic energy release have

been discussed in detail. In particular, it turned out that a neutralino with a large wino component is also possible.

3 Candidates for the Entropy Producer

Let us next discuss candidates for the field ϕ producing the entropy. A list of general requirements is shown in Tab. 1. Most of them are already clear from the discussion in the previous section. Requirement vii is that the presence of ϕ be compatible with gravitino dark matter. This would be violated, for example, if the gravitino could decay into ϕ with a lifetime shorter than the age of the universe t_0. The last requirement concerns other particles that have to be introduced together with ϕ, such as its superpartners. They must not violate ii or vii, must not produce many NLSPs or gravitinos in their decays (v, vi) and must not introduce new problems on their own.

In fact, the requirements in the table either have to be fulfilled or are generically fulfilled in any scenario containing long-lived particles. As a consequence, the solution of the generic problems of long-lived particles may automatically lead to the desired entropy production.

One potential candidate for the entropy producer exists if the strong CP problem is solved by the Peccei-Quinn mechanism.[24,25] This mechanism involves the axion supermultiplet containing two real scalars, the axion and the saxion ϕ_{sax}, as well as their superpartner, the axino $\widetilde{a}$. Their interactions with the MSSM particles are suppressed by the Peccei-Quinn scale $f_a \gtrsim 6 \cdot 10^8\,\text{GeV}$, which makes them long-lived.

In particular, the saxion is a suitable candidate to produce entropy, since it has even R parity and therefore can decay into SM particles without producing superparticles. If its dominant decay mode is into a pair of gluons, the decay temperature is [26]

$$T_{\text{sax}}^{\text{dec}} \simeq 53\,\text{MeV} \left(\frac{10^{12}\,\text{GeV}}{f_a}\right) \left(\frac{m_{\text{sax}}}{1\,\text{TeV}}\right)^{\frac{3}{2}}. \tag{7}$$

Thus, a decay shortly before BBN is possible.

If the saxion is produced in thermal equilibrium, its density starts to dominate at

$$T_{\text{sax}}^{=} \simeq 1.6\,\text{GeV} \left(\frac{m_{\text{sax}}}{1\,\text{TeV}}\right). \tag{8}$$

Together with Eq. 5, this yields

$$\Delta \lesssim 55 \left(\frac{f_a}{10^{12}\,\text{GeV}}\right)^{\frac{2}{3}}. \tag{9}$$

Table 1: List of requirements for our scenario of entropy produced by ϕ to dilute the NLSP (from [18]).

No.	Requirement	Reason or Comment
i	$T_\phi^{\text{dec}} < T_{\text{NLSP}}^{\text{fo}}$	dilute Ω_{NLSP}
ii	$T_\phi^{\text{dec}} > T_{\text{BBN}}$	do not spoil BBN
iii	$\frac{\rho_\phi}{\rho_{\text{rad}}}(T_\phi^{\text{dec}}) > 1$	needed for $\Delta \gg 1$
iv	$\frac{\rho_\phi}{\rho_{\text{rad}}}(T_{\text{NLSP}}^{\text{fo}}) < 1$	for standard NLSP freeze-out
v	$\text{Br}(\phi \to \text{NLSP}) \simeq 0$	avoid NLSP decay problem
vi	$\text{Br}(\phi \to \text{gravitino}) \simeq 0$	avoid gravitino overproduction
vii	e.g., $\tau_{3/2} \gg t_0$	compatibility with gravitino dark matter
viii	ii and v–vii	for by-products; no new problems

This dilution factor is much smaller than the value $\Delta = 10^3$ considered previously and in fact inconsistent with gravitino dark matter, since saxions enter thermal equilibrium only if $T_\mathrm{R} \gtrsim f_a$. Besides, the decays of axinos would produce a disastrous amount of NLPSs for $f_a \gtrsim 10^{10}\,\mathrm{GeV}$.

We have to conclude that the thermally produced saxion is not suited to produce a sufficient amount of entropy. While it satisfies all the requirements of Tab. 1 (if we choose $f_a \lesssim 10^{10}\,\mathrm{GeV}$ to fulfill viii), the resulting dilution factor is simply too small. This can be traced back to two conflicting requirements: on the one hand sufficient saxion production requires sufficiently strong couplings (small f_a), while on the other hand sufficiently late decay requires weak couplings (large f_a), where later decay corresponds to more entropy production. In the considered case, the allowed parameter ranges fail to overlap. Using simple estimates we can generalize this negative conclusion to a generic thermally produced particle.[18]

Fortunately, we do not have to rely on thermal production of saxions. It can be abundantly produced in coherent oscillations about its potential minimum, if the saxion field is displaced from this minimum during inflation. In this case, Eq. 8 changes to [27]

$$T_\mathrm{sax}^{=} \simeq 6.4\,\mathrm{GeV} \left(\frac{m_\mathrm{sax}}{1\,\mathrm{TeV}}\right)^{\frac{1}{2}} \left(\frac{f_a}{10^{14}\,\mathrm{GeV}}\right)^2 \left(\frac{\phi_\mathrm{sax}^\mathrm{i}}{f_a}\right)^2, \tag{10}$$

where $\phi_\mathrm{sax}^\mathrm{i}$ denotes the initial amplitude of the oscillations. Now production and decay are decoupled, so we are able to choose parameter values that yield a large dilution factor saturating the upper bound of Eq. 6. For example, this is the case for $m_\mathrm{sax} \sim 10\,\mathrm{GeV}$, $m_{\widetilde{a}} \sim 1\,\mathrm{TeV}$, $f_a \sim 10^{10}\,\mathrm{GeV}$, and $\phi_\mathrm{sax}^\mathrm{i} \sim 10^4 f_a$.

4 Conclusions

We have considered the early universe in a scenario where a relatively heavy gravitino is the LSP and forms the dark matter, enabling a reheating temperature large enough for thermal leptogenesis. In order to prevent late NLSP decays from ruining the success of BBN, we have required a dilution of the NLSP relic density by a factor $\Delta \sim 10^3$. This dilution can be caused by the entropy from the decay of a long-lived non-relativistic particle. A diluted neutralino NLSP can be compatible with BBN, if it has a large higgsino or wino component.

We have discussed the general requirements for the entropy-producing particle. Afterwards, we have studied the saxion from the axion supermultiplet as a specific example. We have found that the saxion will not have the desired effects if it is produced only thermally. However, non-thermal production in coherent oscillations overcomes this problem and allows the saxion to produce a large amount of entropy.

Thus, we may conclude that we have arrived at a scenario with a completely consistent cosmology. Thermal leptogenesis produces the correct baryon asymmetry, the density of the gravitino dark matter is compatible with the observed value, and BBN works as successfully as in the Standard Model. In addition, the strong CP problem is solved by the Peccei-Quinn mechanism.

Acknowledgments

I'd like to thank Jasper Hasenkamp for the collaboration on [18], on which this talk was based, as well as the organizers of the Rencontres de Moriond for financial support. This work was also supported by the German Science Foundation (DFG) via the Junior Research Group "SUSY Phenomenology" within the Collaborative Research Centre 676 "Particles, Strings and the Early Universe".

References

1. P. Minkowski, Phys. Lett. **B67**, 421 (1977).
2. T. Yanagida in *Proceedings of the Workshop on the Unified Theory and the Baryon Number in the Universe*, eds. O. Sawada and A. Sugamoto (KEK, Tsukuba, 1979).
3. S. L. Glashow in *Proceedings of the 1979 Cargèse Summer Institute on Quarks and Leptons*, eds. M. Lévy et al. (Plenum Press, New York, 1980).
4. M. Gell-Mann, P. Ramond, and R. Slansky in *Supergravity*, eds. P. van Nieuwenhuizen and D. Z. Freedman (North Holland, Amsterdam, 1979).
5. R. N. Mohapatra and G. Senjanović, Phys. Rev. Lett. **44**, 912 (1980).
6. M. Fukugita and T. Yanagida, Phys. Lett. **B174**, 45 (1986).
7. V. A. Kuzmin, V. A. Rubakov, and M. E. Shaposhnikov, Phys. Lett. **B155**, 36 (1985).
8. S. Davidson and A. Ibarra, Phys. Lett. **B535**, 25 (2002), `hep-ph/0202239`.
9. W. Buchmüller, P. Di Bari, and M. Plümacher, Nucl. Phys. **B643**, 367 (2002), `hep-ph/0205349`.
10. M. Bolz, A. Brandenburg, and W. Buchmüller, Nucl. Phys. **B606**, 518 (2001), `hep-ph/0012052`.
11. J. Pradler and F. D. Steffen, Phys. Rev. **D75**, 023509 (2007), `hep-ph/0608344`.
12. I. V. Falomkin et al., Nuovo Cim. **A79**, 193 (1984) [Yad. Fiz. **39**, 990 (1984)].
13. J. R. Ellis, J. E. Kim, and D. V. Nanopoulos, Phys. Lett. **B145**, 181 (1984).
14. M. Kawasaki, K. Kohri, and T. Moroi, Phys. Rev. **D71**, 083502 (2005), `astro-ph/0408426`.
15. W. Buchmüller, K. Hamaguchi, M. Ibe, and T. T. Yanagida, Phys. Lett. **B643**, 124 (2006), `hep-ph/0605164`.
16. J. Pradler and F. D. Steffen, Phys. Lett. **B648**, 224 (2007), `hep-ph/0612291`.
17. S. Kasuya and F. Takahashi, JCAP **0711**, 019 (2007), `0709.2634 [hep-ph]`.
18. J. Hasenkamp and J. Kersten, Phys.Rev. **D82**, 115029 (2010), `1008.1740 [hep-ph]`.
19. R. J. Scherrer and M. S. Turner, Phys. Rev. **D31**, 681 (1985).
20. E. W. Kolb and M. S. Turner, Front. Phys. **69** (1990).
21. W. Buchmüller, P. Di Bari, and M. Plümacher, Ann. Phys. **315**, 305 (2005), `hep-ph/0401240`.
22. L. Covi, J. Hasenkamp, S. Pokorski, and J. Roberts, JHEP **11**, 003 (2009), `0908.3399 [hep-ph]`.
23. K. Jedamzik, Phys. Rev. **D74**, 103509 (2006), `hep-ph/0604251`.
24. R. D. Peccei and H. R. Quinn, Phys. Rev. Lett. **38**, 1440 (1977).
25. R. D. Peccei and H. R. Quinn, Phys. Rev. **D16**, 1791 (1977).
26. D. H. Lyth, Phys. Rev. **D48**, 4523 (1993), `hep-ph/9306293`.
27. M. Kawasaki, K. Nakayama, and M. Senami, JCAP **0803**, 009 (2008), `0711.3083 [hep-ph]`.

5.
Neutrinos

First Oscillation Results for the T2K Experiment

M. Hartz, for the T2K Collaboration
Department of Physics, University of Toronto, 60 St. George St., Toronto, M4V 2B8, Canada

T2K is a long baseline high intensity neutrino oscillation experiment employing an off-axis design to search for the as yet unobserved appearance of ν_e neutrinos in a ν_μ beam. The neutrino beam originates at the J-PARC facility in Tokai, Japan and the Super-Kamiokande (SK) detector, located 295 km away, measures the composition of the oscillated beam. The SK data are searched for an excess of ν_e, constraining the allowed parameter space of $sin^2(2\theta_{13})$, the parameter governing the amplitude of oscillations from ν_μ to ν_e. This amplitude is of particular interest since it also modulates the amplitude of CP violating terms in the lepton mixing matrix. This paper presents results from the first T2K physics run in 2010 with 3.23×10^{19} protons on target.

1 Introduction

In the three flavor oscillation model, neutrino mixing is parameterized by three mixing angles, θ_{12}, θ_{23} and θ_{13} and a CP violating phase δ_{CP}. Additionally the oscillation probabilities depend on the mass squared differences between the neutrino mass eigenstates, Δm^2_{12} and Δm^2_{23}. The mixing through θ_{12} has been well constrained by solar [1] and reactor [2] experiments, while mixing through θ_{23} has been constrained by atmospheric [3] and accelerator based [4] [5] experiments. Searches for oscillations depending on θ_{13} have so far been inconclusive, but measurements by the CHOOZ [6] and MINOS [7] experiments place upper limits on its value, $\sin^2(\theta_{13}) < 0.12 - 0.15$ at 90% C.L..

The T2K (Tokai to Kamioka) experiment is a long baseline experiment designed with the primary goal of searching for the appearance of electron neutrinos in a muon neutrino beam to measure the mixing angle θ_{13}. To leading order, the oscillation probability is:

$$P(\nu_\mu \rightarrow \nu_e) \approx sin^2(\theta_{23}) sin^2(2\theta_{13}) sin^2(\frac{\Delta m^2_{23} L}{4E_\nu}) \quad (1)$$

If the mixing angle θ_{13} is found to be non-zero, then the observation of CP violation in neutrino mixing will be possible, and T2K will play an important role in searching for it. This paper describes the first search for ν_e appearance at T2K.

2 The T2K experiment

The T2K experiment is described in detail elsewhere. [8] A brief description of the experiment follows. The T2K muon neutrino beam is produced when 30 GeV protons from the J-PARC accelerator facility collide with a 90 cm graphite target. Positively charged particles (predominantly pions) produced in the collisions are focused by three magnetic horns and allowed to

decay in a 96 m long decay volume. The decay of the π^+ hadrons produces a beam of ν_μ. Decays of muons and kaons contaminate the beam with ν_e at the level of 1%.

T2K employs two near detectors located 280 m from the graphite target to measure the properties of the un-oscillated beam, and a far detector, the Super-Kamiokande (SK) detector, located 295 km away to measure the oscillated beam. SK sits 2.5° from the axis of the neutrino beam. This off-axis angle takes advantage of the decay kinematics of pions to produce a narrow band beam at the off-axis detector that peaks at the energy where neutrino oscillations are expected. [9]

The INGRID near detector consists of 16 modules, 14 of which are arranged in a cross configuration, centered on the beam axis. These modules consist of iron and scintillator layers and measure the neutrino rate and profile on the beam axis direction. The ND280 off-axis near detector is located off the beam axis in the same direction as SK and is used to measure the properties of the un-oscillated off-axis beam. ND280 consists of a number of sub-detectors, but for the analysis presented here, the Fine Grained Detectors (FGDs) and Time Projection Chambers (TPCs) are used. The two FGDs consist of scintillator bars, with the second also including water targets. Their 2.2 tons of mass provide the target material for neutrino interactions, and the scintillation light is read out to reconstruct particle tracks near the interaction vertices. The three TPCs measure the momentum of charged particles in ND280's 0.2 T magnetic field to better than 10% at 1 GeV/c. They also provide dE/dx measurements with $< 10\%$ resolution for particle identification.

The SK detector is a 50 kton water Cherenkov detector that consists of an inner (ID) and outer (OD) detector. The OD is used to veto events that enter or exit the ID. Neutrino interactions taking place in the 22.5 kton fiducial volume of the ID are detected by the Cherenkov light from charged interaction products produced above threshold. Photo-multiplier tubes instrumenting the walls of the ID image the Cherenkov light rings and the properties of the rings are used to reconstruct the particle type, energy and vertex position.

The primary neutrino interaction mode that is of interest for T2K is the charged-current quasi-elastic (CCQE) interaction, where a charged lepton and recoil nucleons are the only final state particles. This interaction mode is significant at T2K energies and allows for the approximate reconstruction of the neutrino energy if the charged lepton kinematics and neutrino beam direction are known. An important background interaction mode for T2K is the neutral-current π^0 (NCπ^0) mode. Here the final state includes the undetected neutrino, a π^0 and recoil nucleons. The π^0 decays to two photons that can be misidentified as a single electron in the SK detector.

The measurement described in this paper uses data accumulated with 3.23×10^{19} protons on target from January through June of 2010.

3 Electron neutrino appearance analysis

To measure θ_{13}, T2K searches for an excess of ν_e candidate events observed at SK that can be interpreted as $\nu_\mu \to \nu_e$ oscillations. There are two major sources of background ν_e candidates at SK that must be accounted for: intrinsic ν_e contamination of the beam from muon and kaon decays and non ν_e interactions that are reconstructed as ν_e, in large part consisting of NCπ^0 interactions. The background and oscillation signal predictions are produced using model and data based simulations of the neutrino flux and interactions, as well as the constraint from an inclusive ν_μ measurement made using the ND280 detector. The data over simulation rate measured at ND280 is used to renormalise the SK prediction:

$$N_{SK}^{exp} = N_{ND280}^{data} / N_{ND280}^{MC} \times N_{SK}^{MC} \tag{2}$$

By doing this, the neutrino rate prediction is constrained by the near detector data, and significant cancellations in the neutrino flux uncertainties are realized. The SK ν_e selection is applied

to the simulation as well as the data, and the measured number of events compared to the prediction provides a constraint on θ_{13}.

3.1 SK ν_e selection

The selection criteria for ν_e candidates at SK was finalized before looking at the data to avoid bias. Cuts were optimized for the relatively small expected sample size of T2K's initial data sets. The selection looks for events with a single electron like ring that will be produced by the final state electron in CCQE interaction of ν_e.

The selection of SK ν_e candidates begins with the sample of neutrino interaction candidates that are fully contained in the ID with vertices in the fiducial volume. A > 100 MeV visible energy cut is applied to reduce the backgrounds from neutral current interactions or electrons from muon decays. The candidates are required to have a single ring, and the ring must be identified as an electron like ring. Electron rings are identified by their "fuzzy" edges compared to muon rings due to the electromagnetic scattering of the electron in the water. No delayed activity can be observed in the detector as this is interpreted as electrons from muon decays. For each event, a π^0 mass is reconstructed under the two ring hypothesis, and if $m_{\pi^0} > 105$ MeV/c^2 the event is rejected. This cut removes background due to photons from π^0 decays. Finally, the reconstructed energy of the ν_e candidate is required to be < 1250 MeV since the oscillation probability peaks below 1000 MeV. This selection has an efficiency of 66% for signal events with efficiency uncertainties of 7.6% and 15.8% for signal and background respectively.

3.2 Flux prediction

The flux prediction is made from the simulation of protons interacting in the T2K target and the subsequent propagation of secondary particles through the magnetic horns and decay volume until they decay to produce neutrinos. T2K proton beam monitor measurements are used to set the initial conditions for the protons in the simulation. The production of pions by proton interactions inside the target are modeled with data from the NA61 experiment [10], while other in-target interactions are modeled with FLUKA. [11] [12] Propagation of particles outside the target is carried out with GEANT3 [13] and hadron interactions are modeled with the GCALOR [14] package. Fig. 1 shows the expected ν_μ and ν_e neutrino fluxes seen by SK, broken down by the parent particle that produces the neutrino. The ν_μ produced in the < 1 GeV region of interest are predominantly from pion decays, while the ν_e contamination is predominantly from muon decays. The dominant sources of uncertainty in the neutrino flux come from the production of pions and kaons in the interactions of protons, and the total flux uncertainty contributes a 9.2% uncertainty to ν_e background candidate prediction.

3.3 Neutrino interaction modeling

The interactions of neutrinos are modeled with the NEUT [15] neutrino interaction generator, while the GENIE [16] neutrino interaction generator is used for cross-checks. The uncertainties on the neutrino interaction models are evaluated in three ways:

- Comparisons between models
- Variations of parameters within models
- Comparisons to data from the MiniBooNE [17] and SciBooNE [18] [19] experiments, as well as the SK atmospheric data set

The uncertainty on the SK ν_e candidate sample size from background sources due to neutrino interaction uncertainties is 14.2%. The dominant sources of uncertainties are final state interactions of pions, and the NCπ^0 cross section.

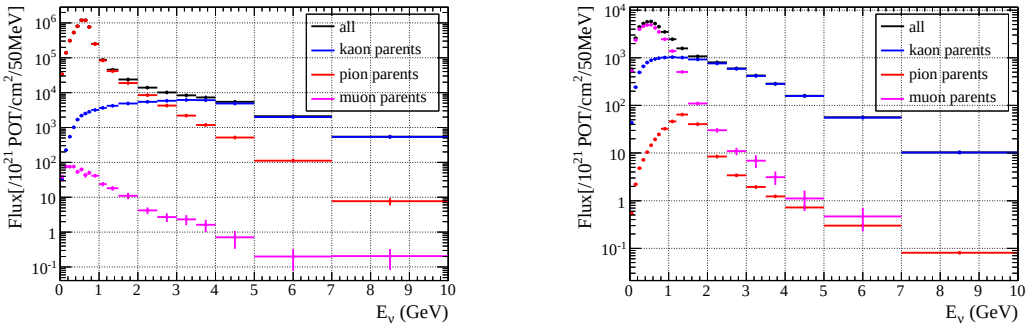

Figure 1: Predicted ν_μ (left) and ν_e (right) fluxes at SK based on simulation. Error bars represent the statistical uncertainty of the simulated flux.

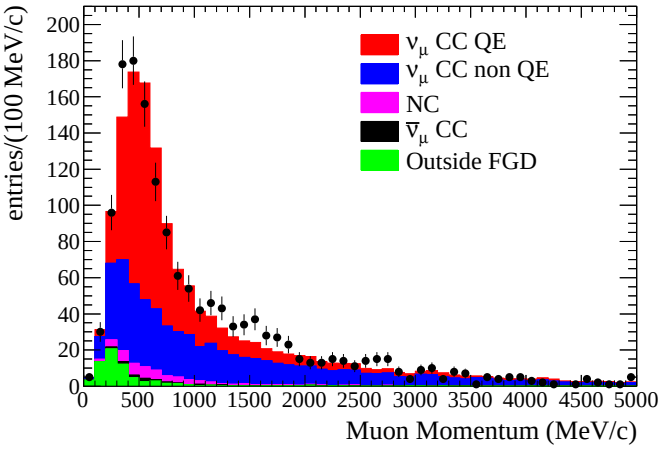

Figure 2: Muon momentum from the inclusive ν_μ interaction data measured at ND280. Error bars represent the statistical uncertainty of the data points.

3.4 ND280 inclusive ν_μ measurement

The rate of ν_μ charged current interactions is measured by ND280 using a sample of events where a negative track originates in one of the two FGDs and is tracked by the downstream TPC. The TPC dE/dx measurement is used to select muons and reject electrons, resulting in a sample that is 90% ν_μ charged current interactions, and 50% CCQE. Fig. 2 shows the predicted distribution of reconstructed muon momentum compared to the measured distribution. The ratio of data over the prediction for the full sample is:

$$N^{data}_{ND280}/N^{MC}_{ND280} = 1.061 \pm 0.028(stat.)^{+0.044}_{-0.038}(syst.) \pm 0.039(phys.model) \quad (3)$$

This ratio is used to renormalise the SK event rate predictions, and the uncertainties on this ratio are propagated into uncertainty on the predicted SK samples.

3.5 SK ν_e prediction

Using the flux prediction, neutrino interaction models and near detector measurement, the background and signal expectations for ν_e candidates at SK are calculated. Table 3.5 shows the predictions for 3.23×10^{19} p.o.t. and $\sin^2(2\theta_{13}) = 0.1$. The background prediction is

Table 1: SK ν_e candidate predictions for 3.23×10^{19} p.o.t. and $\sin^2(2\theta_{13}) = 0.1$.

Source	Events	Systematic Error
Background	0.30	23.9%
Beam ν_e (85% CCQE)	0.16	
ν_μ (95% NC)	0.13	
$\bar{\nu}_\mu$	0.01	
Signal ν_e	1.20	19.5%

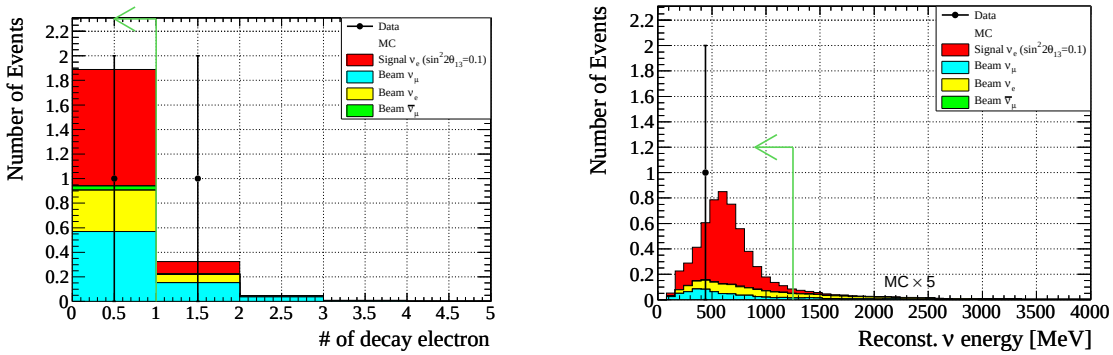

Figure 3: Data and predicted ν_e candidate samples at the decay electron (left) and reconstructed neutrino energy (right) cuts.

$0.30 \pm 0.07(syst.)$ events. The dominant sources of uncertainty come from the flux prediction, neutrino interaction modeling and SK ring counting, particle ID and π^0 mass cuts.

3.6 SK data sample and interpretation

The ν_e selection cuts are applied to the SK data and the resulting number of events is used to place a constraint on θ_{13}. Fig. 3 shows the effect of the decay electron and reconstructed neutrino energy cuts on the data and predicted distributions. After all cuts are applied, one candidate event remains. With this single event and the background and signal predictions, limits on $sin^2(2\theta_{13})$ are calculated using the Feldman-Cousins [20] method. The resulting 90% C.L. limit for varying δ_{CP} are shown in Fig. 4. For $\delta_{CP} = 0$, $\Delta m^2_{23} = 2.4 \times 10^{-3}\ eV^2$ and $sin^2(2\theta_{23}) = 1.0$ the 90% C.L. upper limit is found to be 0.5.

4 Conclusion

T2K has carried out a search for ν_e appearance in a ν_μ beam with data produced from 3.23×10^{19} protons on target. In these data, T2K observes one ν_e candidate event at the SK detector when $0.30 \pm 0.07(syst.)$ events are expected from background sources. T2K sets the upper limit $sin^2(2\theta_{13}) < 0.5$ at 90% C.L. (for $\Delta m^2_{23} = 2.4 \times 10^{-3}\ eV^2$ and $sin^2(2\theta_{23}) = 1.0$). Although this first measurement from T2K does not yet challenge the sensitivity of previous experiments' measurements, future T2K measurements will follow, with four times the data set already available, promising interesting results in the near future.

References

1. B. Aharmim *et al.* [SNO Collaboration], Phys. Rev. C **72**, 055502 (2005)

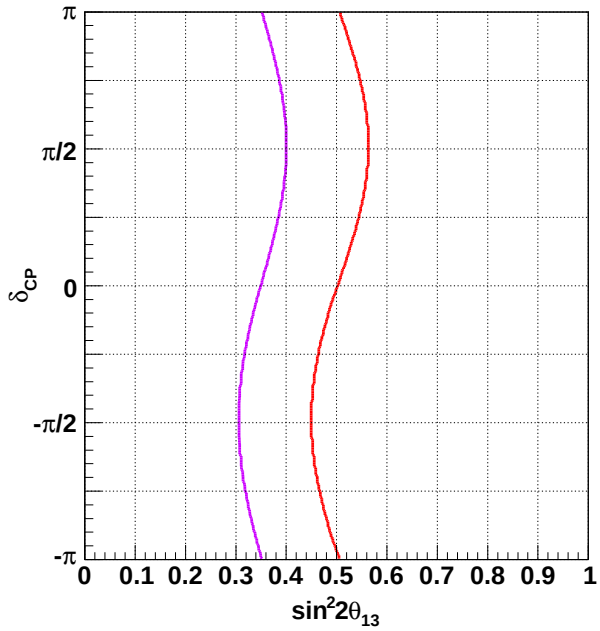

Figure 4: The 90% C.L. upper limit (red) and sensitivity (magenta) for the T2K data set with $\Delta m^2_{23}(> 0) = 2.4 \times 10^{-3}\ eV^2$ and $sin^2(2\theta_{23}) = 1.0$.

2. S. Abe *et al.* [KamLAND Collaboration], Phys. Rev. Lett. **100**, 221803 (2008)
3. Y. Ashie *et al.* [Super-Kamiokande Collaboration], Phys. Rev. D **71**, 112005 (2005)
4. M. H. Ahn *et al.* [K2K Collaboration], Phys. Rev. D **74**, 072003 (2006)
5. D. G. Michael *et al.* [MINOS Collaboration], Phys. Rev. Lett. **97**, 191801 (2006)
6. M. Apollonio *et al.* [CHOOZ Collaboration], Phys. Lett. B **466**, 415 (1999)
7. P. Adamson *et al.* [MINOS Collaboration], Phys. Rev. Lett. **103**, 261802 (2009)
8. K. Abe *et al.* [T2K Collaboration],
9. D. Beavis *et al.* [E889 Collaboration], Physics Design Report **BNL 52459** (1995)
10. N. Abgrall *et al.* [NA61 Collaboration], CERN-SPSC-2010-025; SPSC-SR-066, (2010).
11. G. Battistoni *et al.*, AIP Conf. Proc. **896**, 31 (2007).
12. A. Ferrari, P. R. Sala, A. Fasso and J. Ranft, CERN-2005-010, SLAC-R-773, INFN-TC-05-11
13. GEANT – Detector Description and Simulation Tool, Application Software Group, Computing and Networks Division, CERN, Geneva (1993).
14. C. Zeitnitz and T. Gabriel, Proc. of International Conference on Calorimetry in High Energy Physics, Tallahasse, FL, USA, February, 1993.
15. Y. Hayato, Nucl. Phys. (Proc. Suppl.) **B112**, 171 (2002).
16. C. Andreopoulos *et al.* , Nucl. Instrum. Meth. **A614**, 87 (2010).
17. A. A. Aguilar-Arevalo *et al.* [MiniBooNE Collaboration], Phys. Rev. D **81**, 092005 (2010)
18. Y. Kurimoto *et al.* [SciBooNE Collaboration], Phys. Rev. D **81**, 033004 (2010) [arXiv:0910.5768 [hep-ex]].
19. Y. Nakajima *et al.* [SciBooNE Collaboration], Phys. Rev. D **83**, 012005 (2011)
20. G. J. Feldman and R. D. Cousins, Phys. Rev. D **57**, 3873 (1998)

Recent results of the OPERA experiment

M. Pozzato on behalf of the OPERA collaboration
Bologna University - INFN Bologna, 6/2 V.le Berti Pichat, Bologna, Italy

OPERA is a long baseline hybrid experiment located in the Gran Sasso underground laboratory designed to study the $\nu_\mu \longrightarrow \nu_\tau$ neutrino oscillations. OPERA is the first experiment searching for ν_τ appearance from a pure high energy ν_μ beam (CNGS) produced at CERN and travelling a distance of 730 km to the OPERA detector. Tau leptons produced in charged current interactions are identified from their decay topology using the technique of nuclear emulsions. After a brief introduction on the physics motivation, on the OPERA hybrid electronic-emulsion detector and the description of the principle of tau detection, the recent results are presented including a topological and kinematical description of the first candidate event.

1 The OPERA experiment

Neutrino physics, and in particular neutrino oscillations, is one of the most challenging and important topics in particle physics. There is a convincing evidence for neutrino oscillations provided by many experiments which studied solar and atmospheric neutrinos. The ν oscillation in the atmospheric sector was first established in disappearance mode by Super-Kamiokande [1] and then confirmed by K2K [2] and MINOS [3]. The final proof for neutrino oscillation should be the detection of a ν_τ in a terrestrial (almost) pure ν_μ beam. The OPERA experiment aims at the direct observation of $\nu_\mu \longrightarrow \nu_\tau$ oscillation in the CNGS (CERN Neutrinos to Gran Sasso) neutrino beam produced at CERN.

The OPERA detector is located in the Hall C in the underground laboratories at LNGS and it is a hybrid detector made of two identical Super Modules (SM): each SM is formed by a target section (composed by a large amount of nuclear emulsions and lead piled up into a modular structure called brick), electronic detectors and a muon spectrometer. The electronic detectors select the brick in which the interactions took place and identify the muon determining also its momentum and charge; nuclear emulsions are used to study in detail the neutrino interactions and to identify the daughter particles produced.

1.1 The CNGS beam

The CNGS beam [4] is a high energy beam ($\langle E_{\nu_\mu} \rangle \approx 17$ GeV) and it was designed and optimized for the appearance study of ν_τ starting from a pure beam of ν_μ. At the CNGS energies the average τ decay length is submillimetric, so OPERA uses nuclear emulsion films as high precision tracking device in order to be able to detect such short decays. The contamination (in terms of interations

in the target) of τ from D_s decay is negligible and the contamination due to $\overline{\nu}_\mu$ is about 2.0%. ν_e ($\overline{\nu}_e$) contamination is low and allows to investigate the sub-dominant oscillation channel.

1.2 The Veto

Following the beam line, the first OPERA detector component is the Veto designed to reduce wrong triggers due to particles produced by neutrino interactions in the rock, in the mechanical structures and in the Borexino detector. Veto is also used to monitor CNGS beam counting muons which pass through it.

1.3 The Target

The target has an overall mass of about 625 ton per Supermodule and it has a modular structure whose basic cell is made of a sheet of lead (1 mm thick) and a thin nuclear emulsion. Each emulsion film is made of two layers (each with a nominal thickness 44 μm) separated-out by a plastic base (nominal thickness of 200 μm). An OPERA brick is obtained piling up 56 cells and adding an extra-emulsion film called Changeable Sheet (CS). Brick transversal dimensions are 12.7 x 10.2 cm^2, while the total thickness is about 7.5 cm (that means 10 X_0): one brick has a weight of 8.3 kg. Bricks are assembled into walls.

1.4 Target Tracker

Target trackers located after each brick wall, are used to select the brick in which neutrino interactions took place. Plastic scintillator strips equipped with Wave Length Shifting (WLS) fibers coupled to multi-anode PM tubes are chosen to perform this task; they are used to sample hadronic showers energy and contribute to identify and reconstruct high penetrating tracks. Each brick-wall is followed by two orthogonal planes of electronic trackers ($\sim$ 6.7 x 6.7 m^2), each of them contains 256 scintillating strips.

1.5 The Muon Spectrometer

The OPERA spectrometers allow determining the momentum and charge of penetrating charged particles identified as muons by measuring their deflection in the 1.55 T magnetic field of a dipolar magnet instrumented with planes of RPC. Three stations of drift tubes placed in front, behind and in between the two magnet walls provide the high precision measurement of the trajectories [5].

2 Neutrino event analysis

The selection of neutrino events is done discarding the events occurring in the materials surrounding the target; this operation is done by an offline algorithm that classifies in-target events into CC and NC interactions. The next step is to build a probability map for bricks to contain the selected event and to extract from the target the brick with the highest probability. The CS films are detached from the bricks, developed and analysed with high-speed automatic optical microscopes [9], [10] looking for neutrino-related charged tracks compatible with the ED data. If such tracks are found, the brick is then unpacked and the emulsion films are developed.
All the CS tracks are searched for in the most downstream films of the brick and, if found, are followed back film by film until they disappears because of a primary or a secondary vertex. In order to study the located vertices and reconstruct the events, a volume of about 2 cm^3 surrounding the vertex point is analyzed. The next phase of the analysis is called decay search procedure and is applied to vertices to detect decay topologies,secondary interactions and gamma-ray conversions.

If a secondary vertex is found in the event, a kinematical analysis is performed using particle angles and momenta measured in the emulsion films and in the electronic detectors. For charged particles up to 6 GeV/c, the momentum is estimated using the angular deviations generated by multiple Coulomb scattering of tracks in the lead plates [11] with a resolution better than 22% while for higher momentum particles the measurement is based on position deviations with a resolution better than 33% up to 12 GeV/c. The momentum of muons reaching the spectrometer is measured with a resolution better than 20% up to 30 GeV/c and the sign of their charge is also measured [5]. The gamma-ray energy is estimated by a Neural Network algorithm. Due to the position and angle resolution provided by the emulsion, the impact parameter (defined as the minimum distance between one track and the reconstructed vertex) of tracks attached to the primary vertex is below 10 μm excluding low momentum tracks. The detection of decay topologies is based on the observation of tracks with impact parameter greater than this value. The decay search was applied to a subsample of 1088 neutrino events (187 NC), corresponding to about 35% of the 2008 and 2009 data sample in the analysis of a first data sample [6].

Since charmed particles have lifetimes similar to the τ lepton and decay topologies in common, the study of the production of charmed particles in the OPERA experiment is useful to validate the procedures used for the selection and identification of ν_τ interaction candidates. Charmed particles are produced in about 4% of Charged Current neutrino interactions at the CNGS energy. In the analysed CC interactions of the cited sample, a total of 20 charm decay candidates passing all selection cuts have been observed. This number is well compatible with the expectations coming from the Monte Carlo simulation (16.0 $\pm$ 2.9), and demonstrates that the efficiency of the search for short-lived decay topologies is understood. The background in this charm event sample is about 2 events.

3 Candidate event topological and kinematical analysis

The decay search procedure applied to the data sample reported in [6] yielded one event passing the selection criteria defined for the ν_τ interaction search with the τ lepton decaying into one charged hadron. The cuts used in the analysis are described in details in the experiment proposal [7] and in its addendum [8].

Since the neutrino interaction occurred is well inside the target it is possible to perform a very deep study on this event. Tracks belonging to the primary vertex are followed down through several bricks (until they stop) to assess the muon-less nature of the event (with a confidence level of $\sim$ 99%) and a datailed analysis looking for secondary interactions and electromagnetic shower is performed.

Seven charged tracks are associated with the primary vertex. Two electromagnetic showers induced by gamma rays associated to the event have been located: the event-display of the reconstructed interaction is shown in Fig. 1. Track 4 travels over a distance of 1335 $\pm$ 35 μm before showing a kink topology (kink angle = 41 $\pm$ 2 mrad) satisfying the selection criteria. The daughter track (labelled 8) has an impact parameter with respect to the primary vertex of 55 $\pm$ 4 μm and a momentum of 12^{+6}_{-3} GeV/c well above the selection criterion.

The energy and the pointing probability has been measured. The energy of tgamma ray 1 is 5.6 $\pm$ 1.0 (stat.) $\pm$ 1.7 (syst.) GeV and its converting point is 2.2 mm downstream of the secondary vertex to which the shower points with a probability of $\sim$ 32 %) whereas the probabilty to be attached at the primary is less than 10^{-3}.
The energy of gamma ray 2 is 1.2 $\pm$ 0.4 (stat.) $\pm$ 0.4(syst.) GeV. It is compatible with pointing to both vertexes, with a significantly larger probability ($\sim$ 82%) at the secondary vertex, compared to ($\sim$ 10 %) at the primary vertex. Its longitudinal distance to both vertices is about 13 mm.

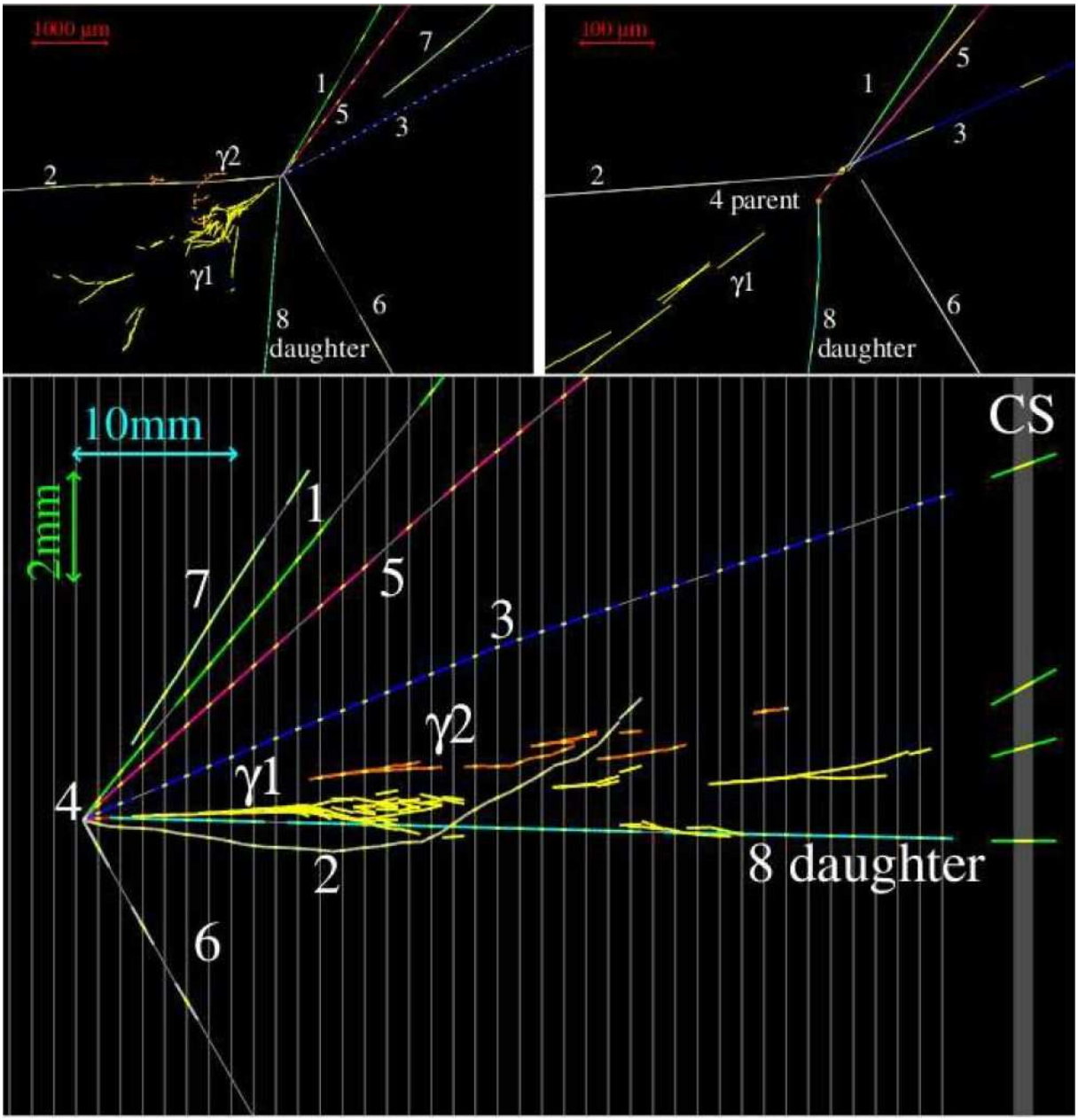

Figure 1: Display of the ν_τ candidate event. Top left: view transverse to the neutrino direction. Top right: same view zoomed on the vertices. Bottom: longitudinal view.

In the most probable hypothesis both gamma rays are emitted at the secondary vertex. The total transverse momentum of the daughter particles with respect to the parent track is $0.47^{+0.24}_{-0.12}$ GeV/c (over the selection cut, 0.3 GeV).

The missing transverse momentum at the primary vertex is $0.57\ ^{+0.32}_{-0.17}$ GeV/c, which is lower than the the upper cut at 1 GeV/c. The angle ϕ in the transverse plane between the parent track and the momentum of hadronic shower is equal to 3.01 ± 0.03 rad, well above the lower selection cut-off fixed at $\pi/2$. The invariant mass estimation of the two-gammas system is compatible with the π^0 mass (120 ± 20 (stat.) $\pm$ 35 (syst.) MeV/c^2). Similarly, the invariant mass of the charged decay daughter assumed to be a π^- plus the two gamma rays is $640\ ^{+125}_{-80}$ (stat.) $^{+100}_{-90}$ (syst.) MeV/c^2, compatible with the $\rho(770)$ mass. The branching ratio of the decay mode $\tau \to \rho\nu_\tau$ is about 25%.

4 Background estimation

The secondary vertex is compatible with the decay of a τ into $\rho\nu_\tau$. In this channel the main background sources are

- the decays to a single charged hadron of charged charmed particles produced in ν_μ CC interactions where the primary muon is notidenti?ed as well as the c $\bar{c}$ pair production in ν_μ NC interactions when one charm particle is not identi?ed and the other decays to a one-prong hadron channel;
- the one prong inelastic interactions of primary hadrons produced in ν_μ CC interactions where the primary muon is not identified or in ν_μ NC interactions and in which no nuclear fragment can be associated with the secondary interaction.

The charm background in the analysed sample amounts to 0.007 ± 0.004 (syst.) events [6]. The estimation of the charm background is conservative since it is evaluated assuming a single-brick based scanning strategy, and they do not include the additional reduction obtained by following all tracks up to their end points as it was done for this event.

An additional search for hadronic activity looking for nuclear fragments pointing to the secondary vertex was performed and no track is observed.

The probability for a hadronic reinteraction to satisfy the selection criteria of the kink decay topology and its kinematics is (3.8 ± 0.2) x 10^{-5} per NC event, leading to a total of 0.011 ± 0.006 (syst.) background events when adding the misclassification of CC events into NC. By considering the one-prong hadron channel only the probability to observe one event due to a background fluctuation is ~ 1.8 % for a statistical significance of 2.36 σ. Since all the τ decay modes are included in the search, this probability increases to 4.5 % corrisponding to a significance of 2.01 σ.

At $\Delta m^2 = 2.5$ x 10^{-3} eV^2 and full mixing, the expected number of observed ν_τ events with the reported event statistics is 0.54 ± 0.13 (syst.), of which 0.16 ± 0.04 (syst.) in the one-prong hadron channel in agreement with the observation of one event.

5 Conclusions

The OPERA experiment has been designed to perform the first detection of neutrino oscillations in direct appearance mode in the muon to tau neutrino channel where the oscillated nu-tau is unambiguously identified through the identification of the tau lepton produced in its CC interaction. OPERA is a large scale hybrid apparatus equipped with electronic detectors and a highly segmented target section made of Emulsion Cloud Chamber (ECC) units. The analysis of a sample of events corresponding to 1.89 x 10^{19} p.o.t. in the CERN CNGS ν_μ beam yielded the observation of a first candidate ν_τ CC interaction.

This event is compatible with the production of a τ lepton and the subsequent decay into $\rho\nu_\tau \rightarrow \pi^-\pi^0\nu_\tau$ and more generally to $h^-(n\pi^0)\nu_\tau$ and passes the selection criteria. The observation of a tau candidate in this decay channel has a significance of 2.36 σ of not being a background fluctuation, which becomes 2.01 σ when all decay modes are considered.

References

1. Y. Fukuda, et al., *Phys. Rev. Lett.* **81**, 1562 (1998).
2. M.H. Ahn, et al., *Phys. Rev.* D **74**, 074003 (2006).
3. D.G. Michael, et al., *Phys. Rev. Lett.* **101**, 131802 (2009).
4. CNGS project, http://proj-cngs.web.cern.ch/proj-cngs/.
5. N. Agafonova, *New Journal of Physics* **13**, 053051 (2011).
6. OPERA Collaboration, *Phys. Lett.* B **691**, 138-145 (2010).
7. OPERA Collaboration, M. Guler et al., "An appearance experiment to search for $\nu_\mu \rightarrow \nu_\tau$ oscillations in the CNGS beam: experimantal proposal.", CERN-SPSC-2000-029, LNGS P25/2000.
8. OPERA Collaboration, M. Guler et al., "Status report on the OPERA experiment.", CERN-SPSC-2001-025, LNGS-EXP 30/2001 Add. 1/01.
9. N. Armenise et al., *Nucl. Instrum. Methods* A **551**, 261 (2005); M. De Serio et al., *Nucl. Instrum. Methods* A **554**, 247 (2005); L. Arrabito et al., *Nucl. Instrum. Methods* A **568**, 578 (2006).
10. K. Moroshima and T. Nakano, JINST (2010) 5 P04011.
11. M. De Serio et al., *Nucl. Instrum. Methods* **512**, 539 (2003); M. Besnier, PhD thesis (2008) Universit de Savoie, LAPP-T-2008-02.

Status Update for the MINERνA Experiment

Gabriel Perdue [a]
Fermilab, PO Box 500, MS 220
Batavia, IL 60510, USA

MINERνA (Main INjEctoR ν-A) is a few-GeV neutrino cross section experiment that began taking data in the FNAL NuMI beam-line in the fall of 2009. MINERνA employs a fine-grained detector capable of complete kinematic characterization of neutrino interactions. The detector consists of an approximately 6.5 ton active target region composed of plastic scintillator with additional carbon, iron, and lead targets upstream of the active region. The experiment will provide important inputs for neutrino oscillation searches and a pure weak probe of nuclear structure. Here we offer a set of initial kinematic distributions of interest and provide a general status update.

1 Brief Introduction to the MINERνA Experiment

MINERνA is a dedicated on-axis neutrino-nucleus scattering experiment running at Fermilab in the NuMI (Neutrinos at the Main Injector) beamline. The primary motivation of MINERνA is to accurately measure scattering cross-sections and event kinematics in exclusive and inclusive final states. By including a variety of high and low atomic number (A) targets in the same detector and beam, MINERνA will contribute to untangling nuclear effects and determining nuclear parton distribution functions (PDF's).

1.1 The Era of Precision Neutrino Oscillation Experiments

MINERνA results will be important for present and future neutrino oscillation experiments, where cross-sections, final state details, and nuclear effects are all important in calculating incoming neutrino energy and in separating backgrounds from the oscillation signal. Recall that oscillation probability depends on E_ν, the neutrino energy. For example, in a ν_μ disappearance experiment, the two-flavor disappearance relation is show in Eq. 1:

$$P\left(\nu_\mu \rightarrow \nu_\mu\right) = 1 - \sin^2\left(2\theta_{23}\right)\sin^2\left(\frac{1.27\Delta m^2_{23}(eV^2)L(km)}{E_\nu(GeV)}\right) \quad (1)$$

[a] On Behalf of the MINERνA Collaboration.

Table 1: MINERνA Nuclear Target Masses in the Winter 2011 Run. Note the tracker mass includes the full longitudinal span. For most analyses, the effective mass will be closer to five tons.

Target	Fiducial Mass (90 cm radius cut)
Scintillator Tracker (CH)	6.43 tons
Carbon (Graphite)	0.17 tons
Iron	0.97 tons
Lead	0.98 tons

However, experiments measure the visible energy of the interaction. Visible energy is a function of flux, cross-section, and detector response. Because the neutrino interacts in dense nuclear matter, final state interactions (FSI) play a significant role in the observed final state particles. Near to Far-Detector ratios cannot handle all of the associated uncertainties because the Near / Far energy spectra are different due to beam, oscillation, matter, and possibly nuclear effects.

1.2 Nuclear Effects

As weak force only probes of the nucleus, neutrinos are complementary to charged lepton scattering measurements. There are many quantities of interest with large uncertainties: axial form factors as a function A and momentum transfer (Q^2), quark-hadron duality, x-dependent nuclear effects, etc. Additionally, MINERνA will study nuclear effects in order to understand how interaction probabilities with heavy nuclei differ from those with free nucleons and how to characterize FSI.

2 The MINERνA Detector

MINERνA is a horizontal stack of roughly identical modules weighing on average about two tons each. Modules contain an inner detector (ID) region composed of triangular plastic scintillator strips and an outer detector (OD) steel frame and support structure also instrumented with plastic scintillator bars. Most modules feature an ID composed of two planes of scintillator, but some in the targets and calorimetric regions of the detector give up one or both scintillator planes for target or absorber materials. The total nuclear target masses installed as of the end of Winter 2011 are listed in Table 1.

See Fig. 1 for an illustration of the triangular strips used in the ID. We utilize charge sharing to improve position resolution and are able to achieve tracking residuals of just over 3 mm. Fig. 2 shows the arrangement of planes, along with a photograph from module construction.

Planes are composed of strips oriented along the X, U, or V axes. The typical arrangement is a module containing two planes, one with strips in the U or V direction and one with strips in the X direction. The stack alternates through the detector, UX, VX, UX, etc. Combination of the X, U, and V views allows three-dimensional reconstruction. Figure 3 shows a schematic of the detector layout.

3 Data Collection

MINERvA began taking neutrino data in March, 2010, with the NuMI beam line in the forward horn current (FHC) mode, focusing π^+ mesons ("neutrino mode"). Reverse horn current (RHC) mode data, focusing π^- mesons ("anti-neutrinos mode"), was taken prior to March, 2010. Table 2 shows raw MC event generator estimates for the event rates in these data samples. Our MC

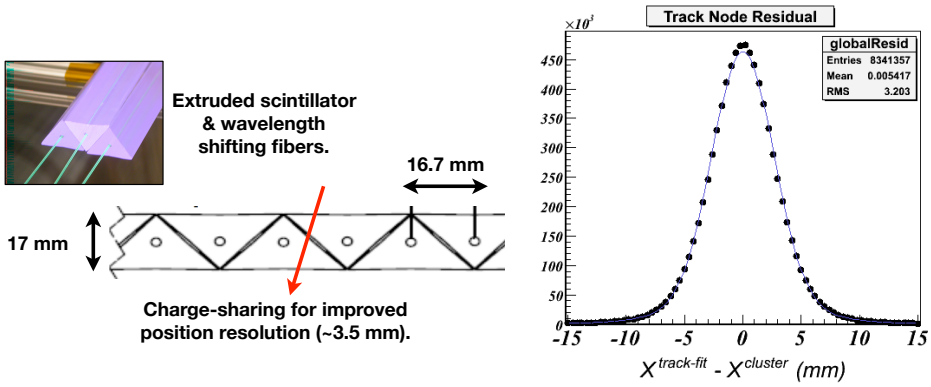

Figure 1: Shown here is an illustration of the triangular scintillator strip arrangement. Groups of 127 strips are bundled into "planes." Also shown are tracking residuals between a fitted position along a track the charge-weighted hit in that plane for a sample of through-going muons.

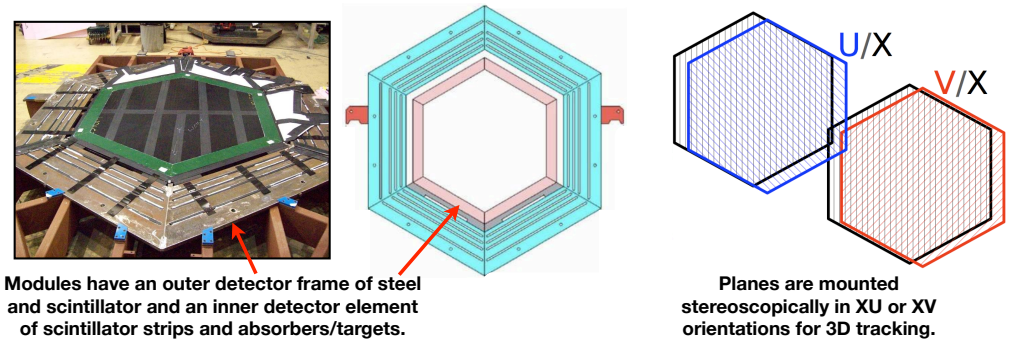

Figure 2: Plane structure illustrated in a photograph from module construction and an engineering diagram. There are three basic orientations for strips in scintillator planes: "U" , where the strips are oriented perpendicular to $-\left(60^0\right)$, "X" (strips oriented vertically), and "V", where the strips are oriented perpendicular to $\left(60^0\right)$.

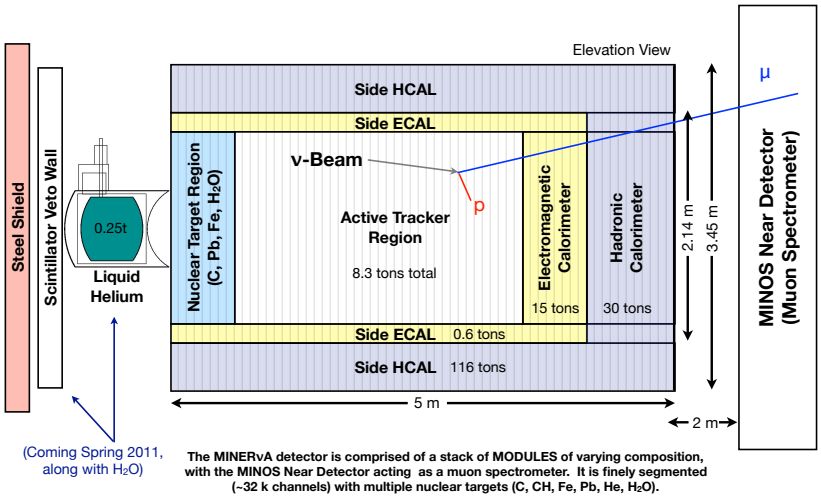

Figure 3: Schematic of the MINERνA detector as of winter 2011. The figure is only roughly to scale.

Table 2: Charged-current inclusive event rates in the current data sample. (GENIE 2.6.2 Generator raw events, not acceptance corrected.)

Material	1.2×10^{20} P.O.T. LE ν Mode	1.2×10^{20} P.O.T. LE $\bar{\nu}$ Mode
Carbon Target	10,800	3,400
Iron Target	64,500	19,200
Lead Target	68,400	10,800
Scintillator (CH) Tracker	409,000	134,000

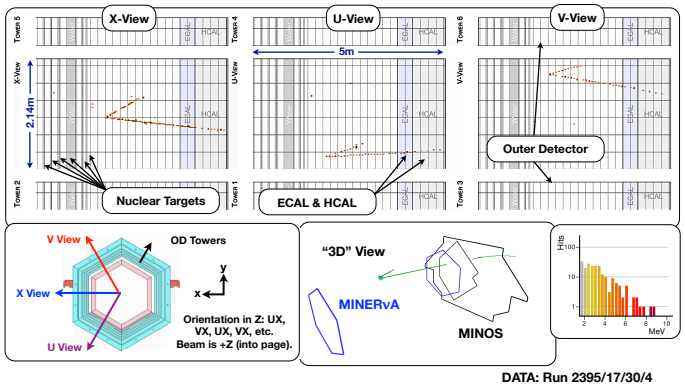

Figure 4: A charged-current interaction candidate event display from data.

event generator is GENIE 2.6.2 [1]. Figure 4 shows a typical charged-current (CC) neutrino event candidate from our FHC data set.

4 Flux Estimate

MINERνA uses the FNAL NuMI beam-line. One of the key features of the beam-line is the ability to move the target relative to the meson focusing horns and change the current in the horns. This allows experiments to tune the energy spectra of the beam.

The largest uncertainty when estimating the neutrino flux is the hadron production spectra at the target. By utilizing the variable spectra at the NuMI beam-line, it is possible to fit for the various hadron production parameters in the MC. We do this by varying the focusing horn current (to focus pions of different P_T) and by varying the position of the target (to focus pions of different $x_F = P_Z/P_T$). See Fig. 5 for an illustration of the impact of changing the horn current amplitude and position of the target on the pion focusing performance.

5 Antineutrino Analysis

The charged current (CC) signature is a muon from W exchange ($\bar{\nu} + p \rightarrow \mu^+ + X$). We examine only muon candidates originating in the fiducial tracker volume, and analyze momentum and sign in the MINOS Near Detector (we do not yet consider muons that stop inside MINERνA).

5.1 Antineutrino Charged Current Quasi-elastic Events

The charged current quasi-elastic (CCQE) channel ($\bar{\nu} + p \rightarrow \mu^+ + n$) is both clean and possesses a relatively large cross-section at the energies of the NuMI Low Energy (LE) configuration. The final state neutron is often invisible and the muon is relatively easy to identify and measure.

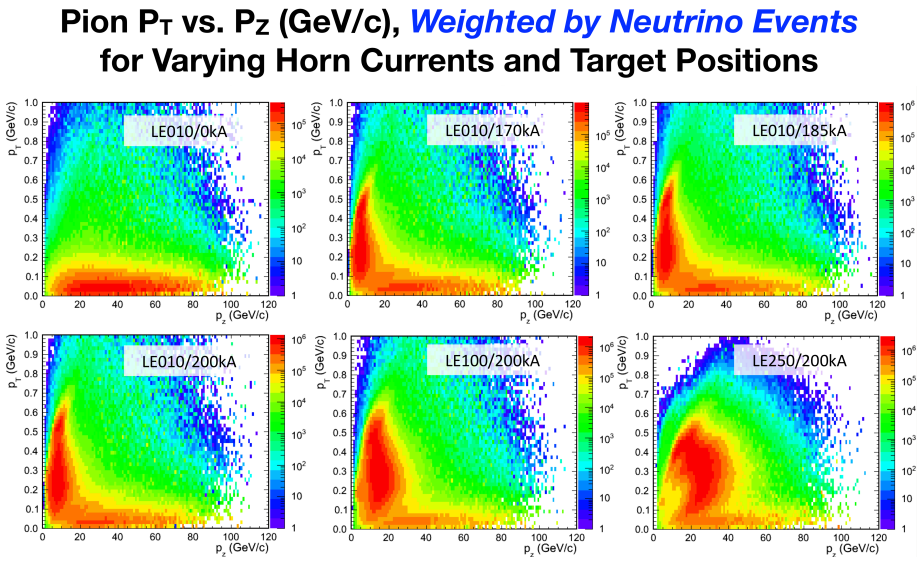

Figure 5: Shown here are pion P_T vs. P_Z distributions from hadrons produced on the primary target for a variety of horn currents and target positions. Events are weighted by neutrino events observed in the detector. 0kA, 170kA, etc. label the horn current. Higher currents focus higher P_Ts. LE010, LE100, etc. label the target position. Moving the target back (LE100 > LE010) focuses higher energy pions.

Presented here is a preliminary analysis conducted with 4×10^{19} protons on target (POT) in the RHC LE beam configuration during detector construction, before starting our official physics run. The fiducial mass in the active tracker region used for this analysis was 2.86 tons of plastic scintillator.

The selection criterion is a μ^+ originating in the fiducial MINERνA tracker volume well-reconstructed in the MINOS Near-Detector. In addition, very small "recoil energy," or extra energy is required; where that energy was defined as all the energy outside a 5 cm radial cylinder around the track with a very tight (100 ns) time window. Figure 6 shows a candidate event display and the extra energy distribution comparison between our data and MC (GENIE 2.6.2 with a GEANT4 detector simulation and custom optical model).

Under the QE hypothesis, we can reconstruct the neutrino energy and four-momentum transfer with only the muon information. Equation 2 is for the neutrino energy; flip the nucleon masses for the antineutrino formula:

$$E_\nu^{rec} = \frac{m_p^2 - (m_n - E_B)^2 - m_\mu^2 + 2\,(m_n - E_B)\,E_\mu}{2\,(m_n - E_B - E_\mu + p_\mu \cos\theta_\mu)}, \tag{2}$$

and with the neutrino energy in hand, we can calculate the four-momentum transfer, Q^2, using Eq. 3:

$$Q^2_{rec} = 2\,E_\nu^{rec}\,(E_\mu - p_\mu \cos\theta_\mu) - m_\mu^2. \tag{3}$$

By cutting on the extra-energy vs Q^2, we can produce a purified sample of CCQE candidates from our CC inclusive sample. Our cut is defined in Fig. 7.

Finally, in Fig. 8 we show the reconstructed neutrino energy and Q^2 compared to our current MC prediction, where absolute predictions are provided by our flux simulation. Note that the event deficit is flat in Q^2, but not neutrino energy.

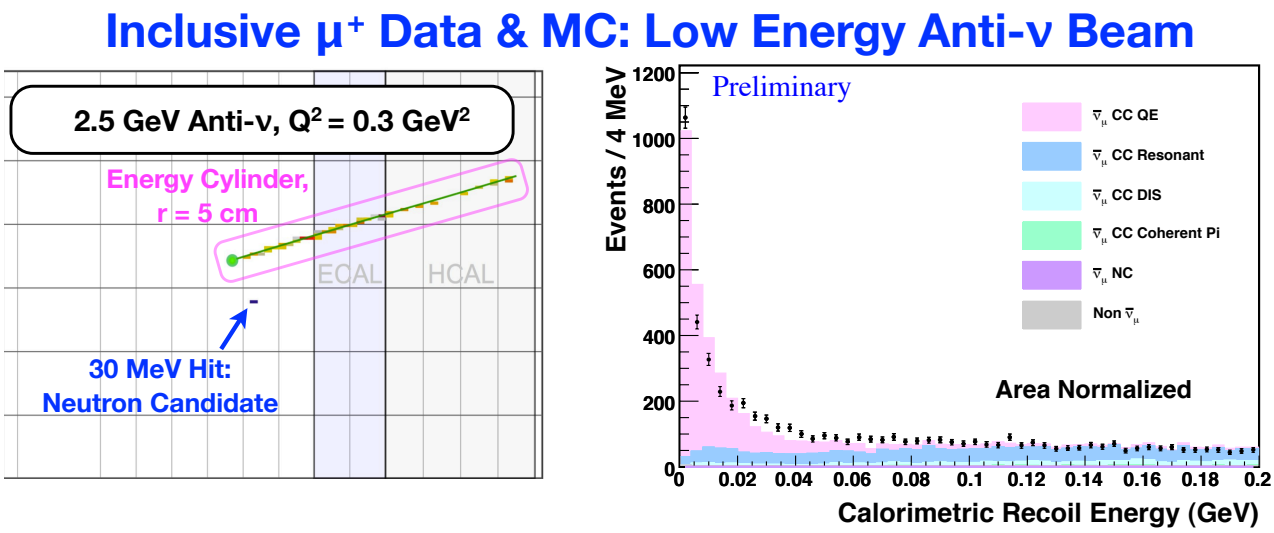

Figure 6: $\bar{\nu}$ charged-current "extra-energy" (recoil energy) data / simulation.

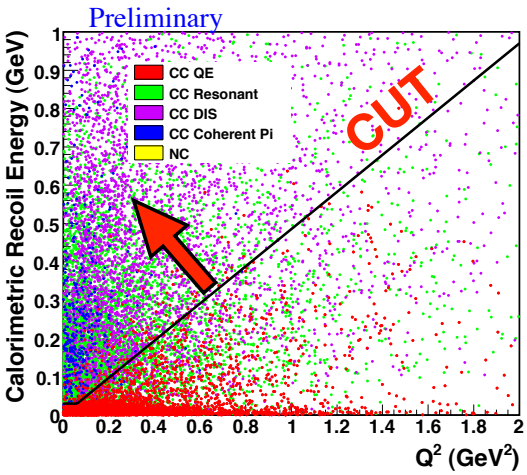

Figure 7: $\bar{\nu}$ charged-current "extra-energy" (recoil energy) versus Q^2 in simulation.

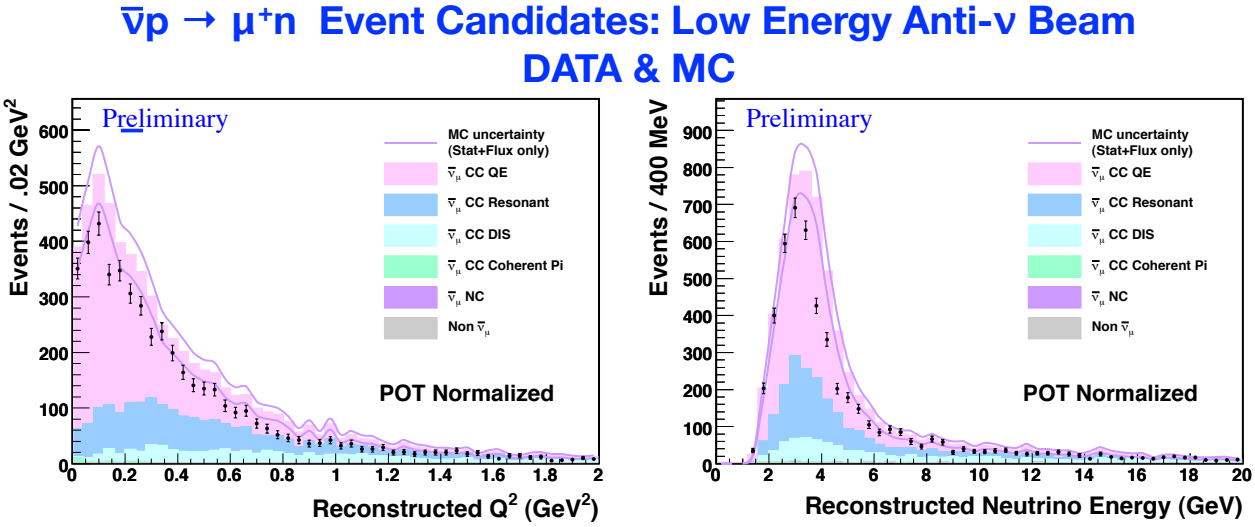

Figure 8: $\bar{\nu}$ data / simulation comparisons of energy and Q^2 reconstructed under the charged-current quasi-elastic hypothesis.

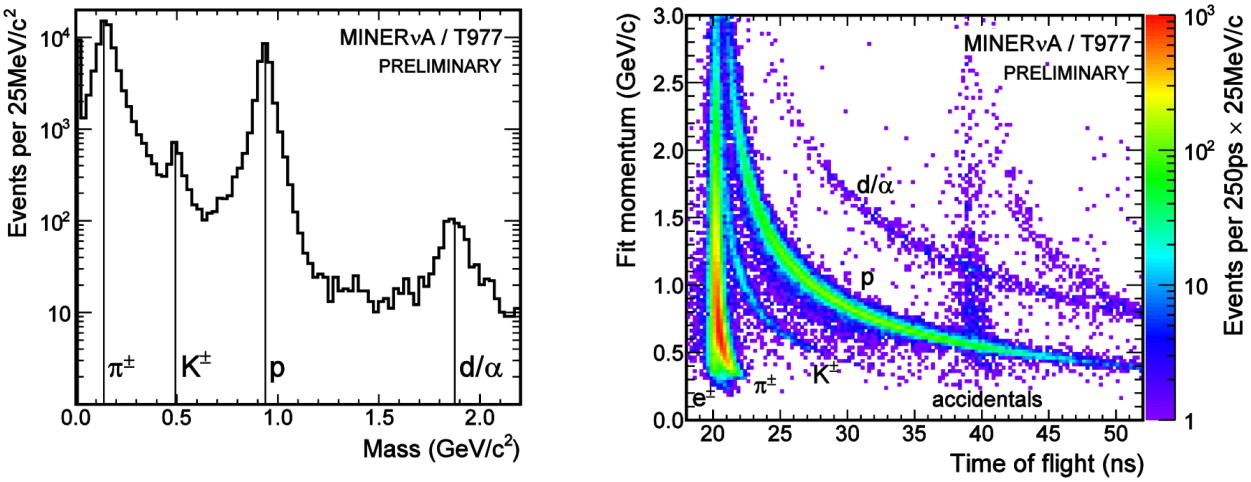

Figure 9: MINERνA Test Beam particle identification.

Table 3: MINERνA Sample sizes from the Test Beam Experiment

Configuration	Total Events	Passing All Beamline Selections
20 ECAL - 20 HCAL π^-	79,562	24,988
20 ECAL - 20 HCAL π^+	77,639	32,935
20 Tracker - 20 ECAL π^-	15,657	4,861
20 Tracker - 20 ECAL π^+	93,667	43,587

6 Calibration: The MINERνA Test Beam

In order to calibrate the detector response of MINERνA, we conducted a Test Beam Experiment (TBE) at the FNAL Test Beam Facility (FTBF). The goal is to provide a hadronic response calibration, normalized to muon response, in a small-sized replica of the MINERνA detector. The TBE detector was composed of roughly quarter-sized MINERνA planes that in every other aspect were as similar to the main MINERνA planes as possible. The TBE detector was read-out with photomultiplier tubes from the same set used to instrument the main detector, and all of the electronics and DAQ system were identical as well.

The TBE ran in two different detector configurations - one with 20 MINERνA Tracker planes and 20 ECAL planes, and another with 20 ECAL planes and 20 HCAL planes. We took roughly equal amounts of data in these two configurations, further dividing the data sets by magnet polarity (focusing either negative or positive pions in the tertiary beamline). Figure 9 shows some particle ID distributions from the entire TBE data set. See Table 3 for a table of the data sample sizes.

Acknowledgments

This work was supported by DOE Grant No. DE-FG02-91ER40685.

References

1. GENIE, http://www.genie-mc.org 2011.
2. MINOS, http://www-numi.fnal.gov 2011.

DOUBLE CHOOZ: SEARCHING FOR θ_{13} WITH REACTOR NEUTRINOS

P. NOVELLA
CIEMAT, Av. Complutense 22,
Madrid 28040, Spain

The discovery of neutrino oscillations is a direct indication of physics beyond the Standard Model. The so-called atmospheric and solar sectors have been explored by several experiments, meanwhile the mixing angle θ_{13} connecting both sectors remains unknown. In contrast to accelerator experiments, reactor neutrinos arise as a clean probe to search for this angle. The Double Chooz experiment is meant to search for θ_{13} taking advantage of the neutrinos generated at the nuclear power plant of Chooz. Double Chooz relies on neutrino flux measurements at two different locations, the so-called far an near detectors, although the first phase runs only with the far detector. The relative comparison of the fluxes at both sites will reduce the systematic uncertainties down to 0.6%. The commissioning of the far detector took place between January 2011 and March 2011, when physics data taking started. First results are expected by the summer 2011. These results will improve the current limit to θ_{13} in case the oscillation signal is not observed. The final sensitivity to $\sin^2(2\theta_{13})$ is exepcted to be 0.03 at 90% C.L. after 5 years of data taking.

1 One step beyond in neutrino oscillation physics

Neutrino oscillation data can be described within a three neutrino mixing scheme, in which the flavor states ν_α (e, ν, μ) are connected to the mass states ν_i (i=1,2,3) through the PMNS mixing matrix U_{PMNS} [1]. This matrix can be expressed as the product of three matrices where the mixing parameters remain decoupled: $U_{PMNS} = U_{atm} \cdot U_{inter} \cdot U_{sol}$. The terms U_{atm} and U_{sol} describe the mixing in the so-called atmospheric and solar sectors, which are driven by the mixing angles θ_{23} and θ_{12}, respectively. The U_{inter} matrix stands for the interference sector which connects the previous two, according to the mixing angle θ_{13} and the phase δ responsible for the CP violation in the leptonic sector. Finally, the oscillation probability between two neutrino species becomes a function of the above oscillation parameters and the two independent mass squared differences $\Delta m^2_{ij} = m^2_i - m^2_j$.

The KamLAND experiment [2] has explored the oscillation in the solar sector and provided allowed and best fit values for θ_{12} and Δm^2_{21}, showing consistency with solar experiments data. In the same way, the MINOS experiment [3] has published results for atmospheric sector (θ_{23} and $|\Delta m^2_{31}|$), being consistent with atmospheric neutrino data. However, the subdominant oscillation corresponding to the interference sector has not been observed yet. Results from CHOOZ experiment [4] show at 90% C.L. that $\sin^2(2\theta_{13}) < 0.15$ for $|\Delta m^2_{31}| = 2.5 \times 10^{-3}\text{eV}^2$. Provided that δ appears in U_{inter} only in combination with $\sin^2(2\theta_{13})$, the CP-violating phase also remains unknown. As a direct consequence, the search for the third mixing angle stands as one of the major open issues in neutrino oscillation physics.

2 Reactor neutrinos in the quest for θ_{13}

Nuclear reactors produce nearly pure $\bar{\nu}_e$ fluxes coming from β decay of fission fragments. A typical core delivers about 2×10^{20} $\bar{\nu}_e$ per second and GW_{th} of thermal power. Such high isotropic fluxes compensate for the small neutrino cross-section and allow for an arbitrary location of neutrino detectors, scaling the flux with $1/L^2$ where L is the distance between the core and the detector. Any oscillation effect in the $\bar{\nu}_e$ survival is governed by the following equation:

$$P(\bar{\nu}_e \to \bar{\nu}_e) \cong 1 - \sin^2 2\theta_{13} \sin^2(\frac{\Delta m^2_{31} L}{4E_\nu}) - \cos^4 \theta_{13} \sin^2 2\theta_{12} \sin^2(\frac{\Delta m^2_{21} L}{4E_\nu}) \quad (1)$$

where E_ν is the neutrino energy. The second and third terms of Eq. 1 describe the oscillation driven by θ_{13} and θ_{12} (solar regime), respectively. The value of θ_{13} can be derived directly by measuring $P(\bar{\nu}_e \to \bar{\nu}_e)$. Notice that in contrast to accelerator neutrino experiments, this measurement does not suffer from the $\delta - \theta_{13}$ degeneracy.

2.1 Detecting reactor neutrinos

The most common way of detecting reactor neutrinos is via the inverse beta decay (IBD) $\bar{\nu}_e + p \to n + e^+$. When this reaction takes place in liquid scintillator doped with Gadolinium, it produces two signals separated by about ~ 30 μs: the first one due to the e^+ and its annihilation (prompt signal), and the second one due to the n capture in a Gd nucleus (delayed signal). This characteristic signature yields a very efficient background rejection. The e^+ energy spectrum peaks at $\sim$ 3MeV and can be related to E_ν. The mean energy of the $\bar{\nu}_e$ spectrum in a detector filled by such a scintillator is around 4 MeV, as shown in left panel of Fig. 1. According to Eq. 1, for this energy the oscillation effect due to θ_{13} starts to show up at $L \sim 0.5$ km, where the effect of θ_{12} is still negligible. Therefore, neutrino reactor experiments with short baselines become a clean laboratory to search for θ_{13}.

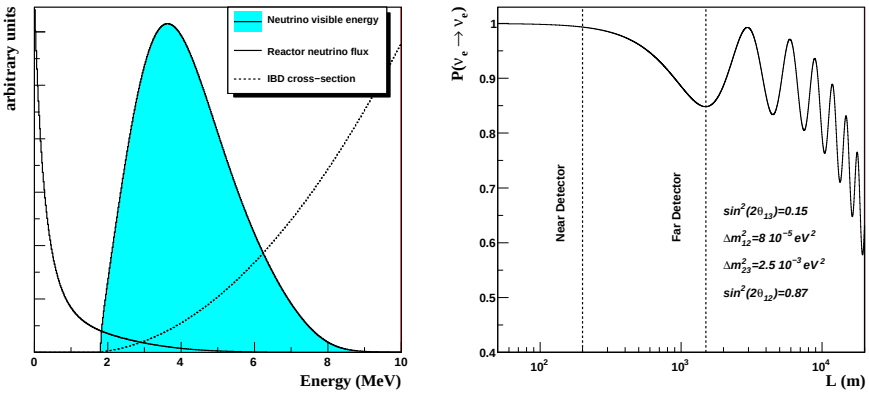

Figure 1: Left: $\bar{\nu}_e$ visible spectrum as a result of the flux shape and IBD cross-section. Right: $\bar{\nu}_e$ survival probability for $E_\nu = 3$ MeV, as a function of the distance L.

In spite of its characteristic signature, the IBD signal can be mimicked by the so-called accidental and correlated backgrounds. The accidental background is defined as the coincidence of a positron-like signal coming from natural radioactivity, and the capture in the detector of a neutron created by cosmic muon spallation in the surrounding rock. The correlated background consists of events which may mimic both the prompt and the delayed signals of the IBD. Fast neutrons and cosmogenic isotopes, both generated in muon interactions, are the main sources of this background. Fast neutrons are produced by muons in the surrounding rock and enter

the detector leading to proton recoils, thus faking a prompt signal, before being captured by a Gd nucleus. Muons also produce inside the detector long-lived β-n decay isotopes, like ^{9}Li and ^{8}He. As the half-life of such cosmogenic isotopes is $\sim$100 ms, their decay cannot be related to the muon interaction.

3 Getting the most from reactor experiments

The sensitivity to the θ_{13}-driven oscillation is optimized by detecting a deficit in the expected neutrino events around 1 km away from the nuclear power plant, as shown in right panel of Fig. 1. However, some of the largest systematics in reactor experiments arise from the uncertainties in the original $\bar{\nu}_e$ fluxes. In order to reduce them, a relative comparison between two or more identical detectors located at different distances from the reactors becomes critical. In particular, a detector placed a few hundred meters away can measure the fluxes before any oscillation takes place, as demonstrated in right panel of Fig. 1. The comparison between the so-called far and near detectors leads to a breakthrough in the sensitivity to θ_{13}, as all the fully correlated systematics cancel out. Further steps in the sensitivity optimization relay on reducing the relative normalization and the relative energy scale uncertainties of the detectors, as well as on minimizing the backgrounds.

4 The Double Chooz approach

The Double Chooz experiment [5], located at the nuclear power plant of Chooz (France), aims at improving the CHOOZ experience by means of a long-term stability multi-detector setup. The comparison between un-oscillated reactor neutrino flux at a near site and the oscillated flux at a far site allows for the cancellation of the reactor-related correlated errors. The detector-related systematics are kept under control by constructing two identical detectors providing accurate energy reconstruction and high signal-to-noise ratios. The Double Chooz collaboration involves institutes from Brazil, France, Germany, Japan, Russia, Spain, UK and USA.

The Chooz nuclear plant consists of two cores yielding a total thermal power of 8.54 GW_{th}. The Double Chooz far detector is placed 1050 m away from the cores, in the same underground laboratory used by the CHOOZ experiment. The laboratory is located close to the maximal oscillation distance and provides enough shielding (300 m.w.e.) against cosmic rays. A second identical detector (near detector) will be installed 400 m away from the reactor cores, in a new laboratory (115 m.w.e) whose construction started in April 2011.

4.1 The Double Chooz detectors

The Double Chooz detectors design is optimized to reduce backgrounds. The detectors, shown in Fig. 2, consist of a set of concentric cylinders and an outer plastic scintillator muon veto (*outer veto*) on the top. The innermost volume (*target*) contains about 10 tons of Gd-loaded (0.1%) liquid scintillator inside a transparent acrylic vessel, where the neutrinos interact via the IBD process. This volume is surrounded by another acrylic vessel filled with unloaded scintillator (*gamma-catcher*). This second volume is meant to fully contain the energy deposition of gamma rays from the neutron capture on Gd and the positron annihilation in the target region. The gamma-catcher is in turn contained within a third volume (*buffer tank*) made of stainless steel and filled with mineral oil. As the wall and the lids of the buffer are covered with an array of 390 10" photomultiplier tubes (PMTs), meant to detect the scintillation light (13% photocathode coverage), the oil shields the target and the gamma-catcher against the radioactivity of the PMT components. The target, gamma-catcher and buffer tank define the *inner detector*. Finally, the outer volume containing the inner detector is a stainless steel vessel covered with 78 8" PMTs

and filled with scintillator. This volume plays the role of the *inner muon veto*. To protect the Double Chooz detector from the radioactivity of the surrounding rock, a 15 cm layer of iron is used.

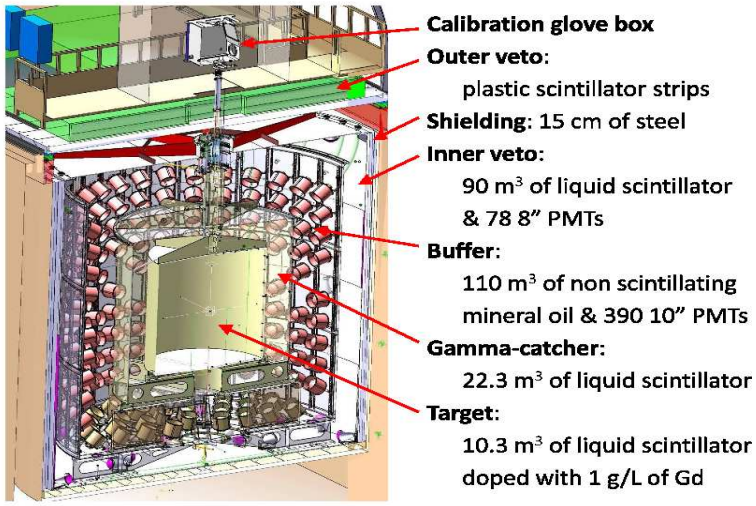

Figure 2: The Double Chooz detector design.

The detector performance is analyzed by means of a redundant set of calibration systems. Apart from the natural calibration sources (neutron captures in H, Gd and C), radioactive sources can be introduced in the different volumes of the detector, via a glove box. The goal is to achieve a relative error on the neutrino detection efficiency of 0.5% with both detectors, and an energy scale uncertainty of 0.5%. In addition, a set of LEDs embedded in the PMTs structure is used to measure the PMTs gains and timing, as well as to monitor the stability of the detector.

4.2 Improving the CHOOZ experience

The Double Chooz experiment aims at improving the CHOOZ result by means of an increase of the exposure and a reduction of the systematics. In order to reduce the statistical error down to 0.5% (was 2.8% in CHOOZ), a long-term stability scintillator has been developed, which will allow for a total data taking time of 5 years. Besides, a larger target volume (10.3 mm^3) is used. The relative comparison of the fluxes between the far and the near detector will allow for the reduction of the systematics error down to 0.6% (was 2.7% in CHOOZ), as shown in Tab. 1. Backgrounds are also expected to be reduced with respect to CHOOZ due to the selection of radiopure materials used in the detector, the two independent muon vetoes, and the buffer volume which isolates the PMTs from the active part of the detector.

Table 1: Main systematic uncertainties in CHOOZ and Double Chooz reactor experiments.

	CHOOZ	**Double Chooz**
Reactor fuel cross section	1.9%	–
Reactor power	0.7%	–
Energy per fission	0.6%	–
Number of protons	0.8%	0.2%
Detection efficiency	1.5%	0.5%
TOTAL	2.7%	0.6%

5 The newborn detector

The integration phase of the far detector of Double Chooz started in May 2008 with the integration of the external shield, followed by the assembly of the inner veto tank. The buffer vessel was completed in summer 2009, and the 330 10" PMTs were successfully mounted by fall 2009. Finally, the acrylic gamma-catcher and target vessels were installed inside the buffer, as shown in Fig. 3, and the detector was closed. First signals from the PMTs were observed in summer 2010 as the DAQ and electronics systems became ready. The filling of the detector started in October 2010 and was completed by the end of 2010.

Figure 3: View of the acrylic vessels and the PMTs covering the the buffer tank walls.

The commissioning period took place between January 2011 and March 2011. First analysis of the detector response was carried out, assuring the good performance of both the inner detector and the inner veto. First events in the filled detector were observed in January 2011. As an example, the display of a muon crossing both detectors is shown in Fig. 4.

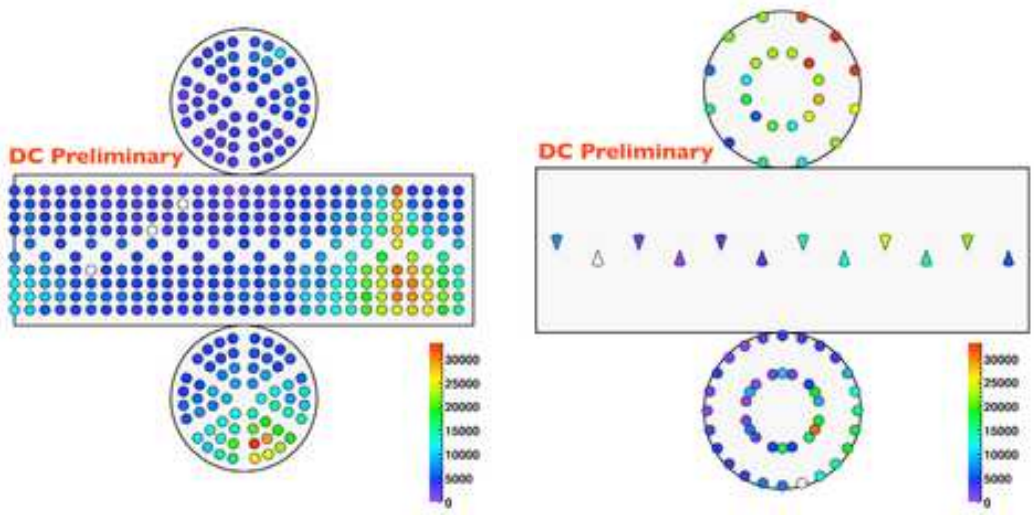

Figure 4: Display of a crossing muon event in both inner detector (left) and inner veto (right). Colors show the charge (digital units) collected at each PMT.

6 Getting the most from Double Chooz

The Double Chooz experiment is developed in two phases. Phase I started in March 2011 once the commissioning of the far detector was completed. Even operating only one detector, this phase will be able to improve the current θ_{13} limit in a few months of data taking. A sensitivity of $\sin^2(2\theta_{13}) \sim 0.6$ is expected after 1.5 years of data taking. The oscillation analysis in phase I will be limited by the uncertainties in reactor fluxes, being the total systematics around 2.8%. Ultimate systematics reduction, down to 0.6%, will be achieved in Phase II (2012) when the second detector (near site) starts taking data. Dominant errors in this phase will be the relative detector normalization and energy scale and the event selection cuts. After 4 months of data taking, Phase II will improve the results of Phase I. After 3 years of data taking, a sensitivity to $\sin^2(2\theta_{13})$ of 0.03 (90% C.L.) will be achieved. A 3σ measurement will be feasible if $\sin^2(2\theta_{13}) > 0.05$. A summary of the sensitivity of both phases is shown in Fig. 5.

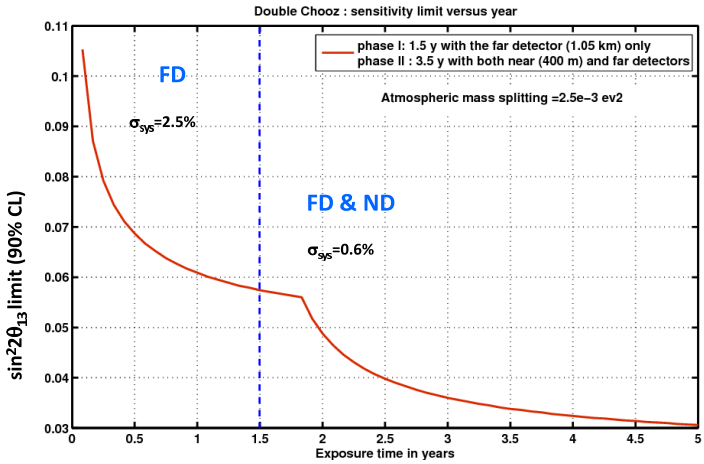

Figure 5: Double Chooz expected sensitivity limit (90% C.L.) to $\sin^2(2\theta_{13})$ as a function of time for $\Delta m^2_{31} = 2.5 \times 10^{-3}$ eV^2. Near detector is assumed to be ready 1.5 years after the start of the far detector operation.

References

1. M. C. Gonzalez-Garcia and M. Maltoni, Phys. Rept. **460** (2008)
2. S. Abe *et al.* [KamLAND Collaboration], Phys. Rev. Lett. **100** (2008)
3. P. Adamson *et al.* [MINOS Collaboration], Phys. Rev. Lett. **101** (2008)
4. M. Apollonio *et al.* [CHOOZ Collaboration], Eur. Phys. J. C **27** (2003)
5. F. Ardellier *et al.*, arXiv:hep-ex/0606025.

THE RECENT RESULTS OF THE SOLAR NEUTRINO MEASUREMENT IN BOREXINO

Y.KOSHIO on behalf of Borexino Collaboration :
G. Bellini, J. Benziger, D. Bick, S. Bonetti, M. Buizza Avanzini,
B. Caccianiga, L. Cadonati, F. Calaprice, C. Carraro, P. Cavalcante,
A. Chavarria, D. DAngelo, S. Davini, A. Derbin, A.Etenko,
F. von Feilitzsch, K. Fomenko, D. Franco, C. Galbiati, C. Ghiano,
M. Giammarchi, M. Goger-Neff, A. Goretti, L. Grandi, E. Guardincerri,
S. Hardy, Aldo Ianni, Andrea Ianni, V. Kobychev, D. Korablev, G. Korga,
Y. Koshio, D. Kryn, T. Lewke, B. Loer, F. Lombardi, L. Ludhova, I. Machulin,
W. Maneschg, G. Manuzio, Q. Meindl, E. Meroni, L. Miramonti, M. Misiaszek,
D. Montanari, P. Mosteiro, V. Muratova, L. Oberauer, M. Obolensky,
M. Pallavicini, L. Papp, L. Perasso, S. Perasso, A. Pocar, R.S. Raghavan,
G. Ranucci, A.Razeto, A. Re, A. Romani, A. Sabelnikov, R. Saldanha,
C. Salvo, S. Schonert, H. Simgen, M. Skorokhvatov, O. Smirnov,
A. Sotnikov, S. Sukhotin, Y. Suvorov, R. Tartaglia, G.Testera,
D. Vignaud, R.B. Vogelaar, J. Winter, M. Wojcik, A. Wright, M. Wurm, J. Xu,
O.Zaimidoroga, S. Zavatarelli, and G. Zuzel
Laboratori Nazionali del Gran Sasso, INFN,
S.S. 17 BIS km. 18.910, 67010 Assergi L'Aquila, Italy
koshio@lngs.infn.it

The recent released results of 153.62 ton·year exposure of solar neutrino data in Borexino are here discussed. Borexino is a multi-purpose detector with large volume liquid scintillator, located in the underground halls of the Laboratori Nazionali del Gran Sasso in Italy. The experiment is running since 2007. The first realtime ^{7}Be solar neutrino measurement has been released in 2008. Thanks to the precise detector calibration in 2009, the ^{7}Be flux measurement has been reached with an accuracy better than 5%. The result related to the day/night effect in the ^{7}Be energy region is also discussed. These results validate the MSW-LMA model for solar neutrino oscillation.

1 Introduction

The next nuclear fusion reaction in main sequence stars like the Sun is the following:

$$4p \rightarrow \alpha + 2e^+ + 2\nu_e + 26.73\text{MeV}. \quad (1)$$

Neutrinos, generated in the Sun core reach the surface of the Sun almost immediately (∼2sec) unlike other particles. Therefore, the solar neutrino measurements directly bring information about the current status of the center of the Sun. The neutrino generation is realized through the pp-chains and CNO cycle. The model of the Sun including these reactions is called the 'Standard Solar Model' (SSM) [1], and predicts the solar neutrino flux and spectra good accuracy. Fig. 1 shows the predicted spectra and observable energy region for several experiments. The

advantage of Borexino is the capability to measure Solar neutrinos in elastic scattering, from $\sim$ 0.2 to $\sim$20 MeV. The wide energy range allowed to measure in real-time both ^{8}B and ^{7}Be neutrinos, and pep, CNO and pp neutrinos are also future targets.

The physics motivation of research in solar neutrinos is twofold. In the neutrino oscillation field, even though the discovery of MSW-LMA scenario for the last decades, [2] [3] [4] the survival probability in ν_e was very poor constraint before Borexino. In solar physics, Borexino can help in solving the metallicity controversy between the new solar composition calculation and helioseismology. The present goals of Borexino are the measurements of the precise ^{7}Be flux, its day-night asymmetry, and finally CNO and pp neutrino observation in future. Other purposes of Borexino are geo-neutrinos [5] and SuperNova neutrinos.

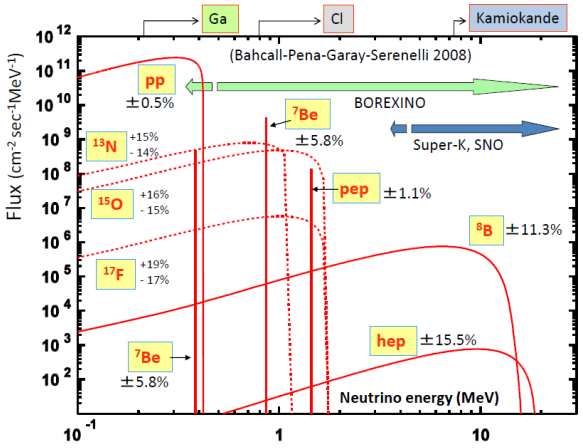

Figure 1: Solar neutrino spectra with sensitive energy region in each experiment.

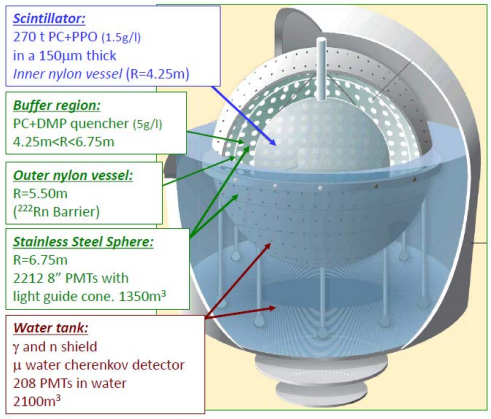

Figure 2: Borexino detector

2 Borexino detector

The Borexino is an ultra-high radiopure large volume liquid scintillator detector, located underground (3500m water equivalent) in Gran Sasso in Italy. The detector is shown in Fig. 2. The inner core scintillator is a target for neutrino detection, and consists of 270 tons of pseudocumene as a solvent doped with 1.5 g/l of PPO as a solute. It is contained in a 4.25m radius of spherical nylon vessel. The scintillation light are detected by 2212 8-inch photomultiplier tubes (PMTs) mounted on a stainless steel sphere (SSS). In order to reduce external γ and neutron backgrounds from PMTs and the rock, the inner scintillator is shielded by 1000 tons of pseudocumene doped with 5.0 g/l of dimethylphthalate (DMP) as a quencher in buffer region, and 2000 tons of pure water outside of SSS. The external water tank is also used to detect the residual cosmic muons crossing the detector by Cherenkov light.

Solar neutrinos are detected via elastic scattering on electrons in liquid scintillator. The advantages of this measurement are high light yield ($\sim$500 photo electrons/MeV), which realizes low energy threshold ($\sim$250keV) and good energy energy resolution ($\sim 5\%/\sqrt{E/(1MeV)}$), and a pulse shape discrimination between α and β is also possible. However, there is no way to distinguish neutrino signal and β like events due to radioactivity, therefore, an extreme radiopurity is required. Thanks to the liquid scintillator purification system the contamination of ^{238}U and ^{232}Th has been removed, reaching a purification level better than the designed value of 10^{-16} g/g, enough to measure not only ^{7}Be solar neutrino, but also 8B and potentially pep and CNO. More details are reported in [6].

The trigger condition for an event is 25 hit PMTs within 99 ns time window. When the

detector is triggered, hit time and charge information in a 16μs gate are recorded. Event position is reconstructed by comparing the hit time after the time-of-flight subtraction, with a reference *pdf* curve. Energy is determined by number of hit PMTs or summed their photoelectrons. These qualities were confirmed by several detector calibrations discussed in the next section.

3 Detector calibration

Several internal sources of calibration were inserted in the detector in 2009, aimed to reduce systematic uncertainties, and to tune the reconstruction algorithm and Monte Carlo simulation. In the previous result [7], energy and position calibrations relied on internal contaminants such as ^{14}C, ^{222}Rn. The correspondent systematic error on the ^{7}Be solar neutrino flux was at the level of 6% for both the fiducial volume and the energy scale. The calibration strategy is based on several sources, alphas, betas, gammas, and neutrons, at different energies, and in hundreds of insertion positions. In order to avoid additional background contaminations into the detector, the source vials were carefully developed. We use a one inch diameter of quartz sphere for filling radioactive source such as ^{222}Rn loaded scintillator or γ emitters in aqueous solution. This quartz sphere was attached to a set of stainless steel bars with a movable arm which could locate the source in various positions inside the detector. The nominal position of the source was determined independently by a system of 7 CCD cameras, whose precision was less than 2cm.

For studying the position reconstruction, α and β events from ^{222}Rn were used. Comparing the reconstructed position with nominal position in 184 points of data, the inaccuracy on the position is less than 3cm level, which is equivalent to a systematic error of 1.3% for the overall fiducial volume in ^{7}Be solar neutrino energy region. The energy response was studied with 8 γ sources and Am-Be neutron source, (2.2MeV γ is generated when thermal neutron is captured by proton.) Fig. 3 shows the comparison between calibration data and Monte Carlo at several energies within the energy region in solar neutrino analysis. Thanks to this study, the energy scale uncertainty was determined to be less than 1.5%. The PMT hit timing in Monte Carlo was tuned by α and β events from ^{222}Rn calibration data. After this tuning, the particle identification has good agreement between data and Monte Carlo both α and β.

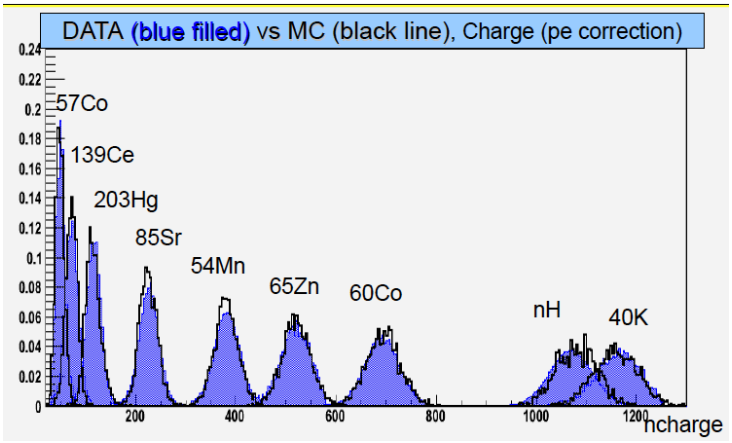

Figure 3: Total photo electron distribution of various γ sources between calibration data and Monte Carlo.

4 Results and implications

4.1 Data analysis

The analyzed data set is 740.66 days taken in the period from May 16, 2007 to May 8, 2010. The following selections have been applied;

1. Muons and their daughters are rejected. The selection of muons is the combination of the inner and outer detector information. The daughters are defined as all events within 300 ms after each muon.

2. A fiducial volume cut was applied to reject the external background events. The reconstructed position must be within a spherical volume of 3m, and also the event position in vertical coordinate must be within ±1.7m to remove background near the poles of the nylon vessel.

Finally, the fiducial exposure in this analysis is equivalent to 153.62 ton·year. The left in Fig. 4 shows the spectrum after the above reduction. The remaining peak around 450 keV comes from α events from ^{210}Po. For extraction of the ^{7}Be solar neutrino signal, the spectral fit was applied assuming all the intrinsic background components such as ^{85}Kr, ^{210}Bi, ^{14}C, ^{11}C. As for the peak related to ^{210}Po events, both fits with and without alpha subtraction were performed.

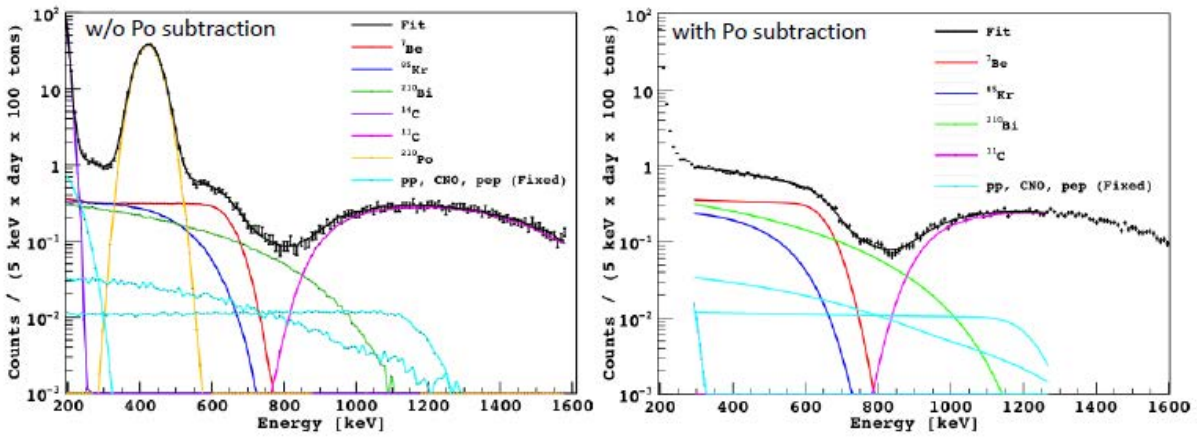

Figure 4: Spectrum after analysis cuts, before(left) and after(right) statistically subtraction of αs from ^{210}Po.

4.2 ^{7}Be solar neutrino rate

The ^{7}Be solar neutrino rate was evaluated with the spectral fit in $46.0 \pm 1.5(stat.) \pm 1.3(sys.)$ counts/day/100ton. Total uncertainty including systematic uncertainty is 4.3%, (the component of systematic error is 2.7%) which is lower than in the previous result: ∼12% [7].

Table 1 shows the expected rate with several assumptions both for neutrino oscillation and solar metallicity. Comparing the result to the expected, no oscillation can be rejected in any metallicity hypothesis. Fig. 5 shows the electron neutrino survival probability for the ^{7}Be and ^{8}B [8] solar neutrino from the Borexino data. This is the first measurement probing both in the vacuum and in the matter enhanced regimes combined to ^{8}B solar neutrino flux measurement from the single detector, and the result is good agreement with MSW-LMA scenario.

Oscillation	Metal	Rate
No	High	74±4
No	Low	67±4
MSW-LMA	High	48±4
MSW-LMA	Low	44±4

Table 1: Expected event rate in Borexino (count/day/100ton) from several hypothesis.

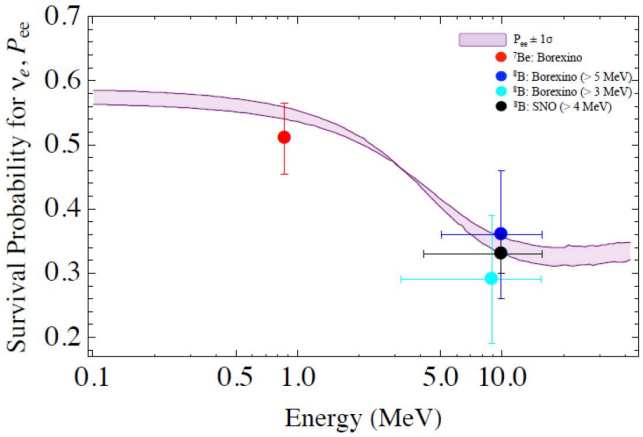

Figure 5: Electron neutrino survival probability of expected under the assumption of MSW-LMA scenario and experimental results.

4.3 Day/Night asymmetry

In the ^{7}Be solar neutrino energy region, the day-night flux difference is sensitive to distinguish between MSW-LMA and MSW-LOW model, because about 20% difference should appear in MSW-LOW region while no effect in MSW-LMA region. Fig. 6 show the spectrum both for day-time(D) and night-time(N), and the energy dependence of its asymmetry which is defined by (N-D)/((N+D)/2). No significant day-night effect was found, and the overall asymmetry is 0.7%. Detailed analysis is now in progress.

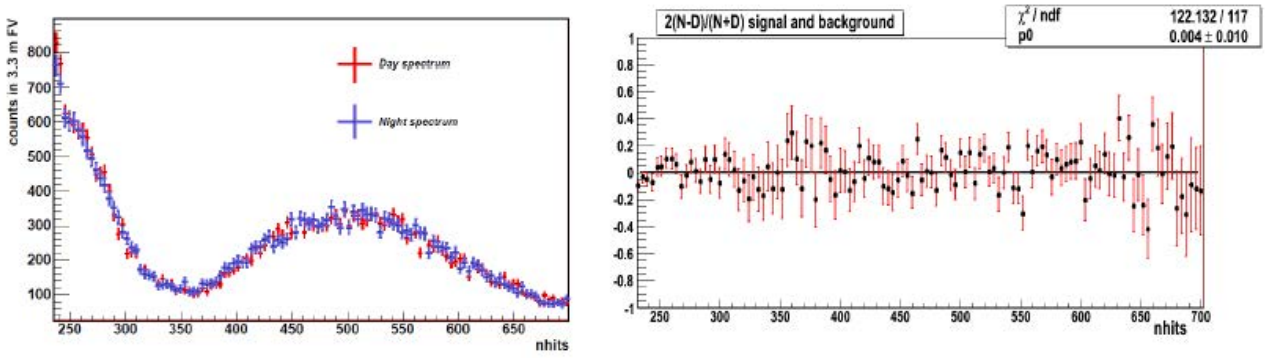

Figure 6: (left) Spectrum in day-time and night-time. (right) Day-night asymmetry as a function of energy.

5 Conclusion and perspective

The Borexino is running since 2007. The calibration with radioactive source was performed in 2009. Increased statistics and calibration lead to a drastic reduction of the overall error. The results of ^{7}Be solar neutrino, its rate and day-night asymmetry, and probing both in the vacuum and in the matter enhanced regimes combined to ^{8}B solar neutrino flux measurement, strongly support an MSW-LMA scenario.

In order to reduce the internal background and observe pep and CNO solar neutrinos in near future, the purification with water extraction is in progress. This measurement will be crucial to distinguish between high and low metallicity in the solar model. The measurement of pp solar neutrinos, which is more than 99% ratio, is also one of important goal for Borexino, since

it promises a complete understanding the solar interior.

References

1. C.Pena-Garay and A.M.Serenelli, arXiv:0811.2424 (2008).
2. J.Hosaka *et al*, Phys.Rev.D73, 112001 (2006).
3. Q.R.Ahmad *et al*, Phys.Rev.Lett., 89, 011301 (2002).
4. S.Abe *et al*, *Phys. Rev. Lett.* **100**, 221803 (2008).
5. C.Arpesella *et al*, *Phys. Lett.* B **687**, 299 (2010).
6. G.Alimonti *et al*, *Nucl. Instrum. Methods* A **609**, 58 (2009).
7. G.Bellini *et al*, *Phys. Rev. Lett.* **101**, 091302 (2008).
8. G.Bellini *et al*, *Phys. Rev.* D **82**, 033006 (2010).

The Reactor Antineutrino Anomaly

G. Mention
CEA, Irfu, SPP, Centre de Saclay, F-91191 Gif-sur-Yvette, France

Recently, new reactor antineutrino spectra have been provided for ^{235}U, ^{239}Pu, ^{241}Pu, and ^{238}U, increasing the mean flux by about 3 percent. To a good approximation, this reevaluation applies to all reactor neutrino experiments. The synthesis of published experiments at reactor-detector distances below 100 m leads to a ratio of observed event rate to predicted rate of 0.976 ± 0.024. With our new flux evaluation, this ratio shifts to 0.943 ± 0.023, leading to a deviation from unity at 98.6% C.L. which we call the reactor antineutrino anomaly. The compatibility of our results with the existence of a fourth non-standard neutrino state driving neutrino oscillations at short distances is discussed. The combined analysis of reactor data, gallium solar neutrino calibration experiments, and MiniBooNE-ν data disfavors the no-oscillation hypothesis at 99.8% C.L. The oscillation parameters are such that $|\Delta m^2_{\rm new}| > 1.5$ eV^2 (95%) and $\sin^2(2\theta_{\rm new}) = 0.14 \pm 0.08$ (95%).

1 Introduction

Neutrino oscillation experiments over the last twenty years have established a picture of neutrino mixing and masses that explains the results of solar, atmospheric and reactor neutrino experiments.[3] These experiments are consistent with the mixing of ν_e, ν_μ and ν_τ with three mass eigenstates, ν_1, ν_2 and ν_3. In particular, the squared mass differences are required to be $|\Delta m^2_{31}| \simeq 2.4\,10^{-3}$ eV^2 and $\Delta m^2_{21}/|\Delta m^2_{31}| \simeq 0.032$.

Reactor experiments at distances below 100 m from the reactor core (ILL-Grenoble, Goesgen, Rovno, Krasnoyarsk, Savannah River and Bugey[4–7]) have played an important role in the establishment of this pattern. The measured rate of $\bar{\nu}_e$ was found to be in reasonable agreement with that predicted from the reactor antineutrino spectra, though slightly lower than expected, with the measured/expected ratio at 0.976 ± 0.024, including recent revisions of the neutron mean lifetime[3] ($\tau_n = 885.7$ s). The cross section of the detection reaction of $\bar{\nu}_e$ on free protons $\bar{\nu}_e + p \rightarrow e^+ + n$ is inversely proportionnal to the neutron lifetime, whose uncertainty is the dominant source of systematic for the cross section. The new world average should evolve and settle to 881.4(1.4) s in 2011 (Ref.[11,12] and private communication from K. Schreckenbach) increasing the cross section by 0.5% compared to the value used in this work.

In preparation for the Double Chooz reactor experiment, we have re-evaluated the specific reactor antineutrino flux (ν/fission), improving the electron to antineutrino data conversion.[1] The method relies on detailed knowledge of the decays of thousands of fission products, while the previous conversion procedure used a phenomenological model based on 30 effective beta branches. Both methods are constrained by the well-measured ILL spectrum of fission induced electrons that accompanies the antineutrinos.[8]

2 New Predicted Cross Section per Fission

Fission reactors release about $10^{20}\,\bar{\nu}_e$ GW^{-1}s^{-1}, which mainly come from the beta decays of the fission products of ^{235}U, ^{238}U, ^{239}Pu, and ^{241}Pu. The emitted antineutrino spectrum is then given by: $S_{\rm tot}(E_\nu) = \sum_k f_k S_k(E_\nu)$ where f_k refers to the contribution of the main fissile nuclei to the total number of fissions of the k$^{\rm th}$ branch, and S_k to their corresponding neutrino spectrum per fission.

For the last 25 years the $\bar{\nu}_e$ spectra have been estimated from measurements of the total electron spectra associated with the beta decays of all fission products of ^{235}U, ^{239}Pu, and ^{241}Pu. Thin target foils of these isotopes were irradiated with thermal neutrons at the ILL reactor.[8] The measured spectra then had to be converted from electron to antineutrino spectra invoking a set of 30 effective beta-branches, adjusted to reproduce the total electron spectrum.[14]

Recently we revisited the conversion procedure with a novel mixed-approach combining the accurate reference of the ILL electron spectra with the physical distribution of beta branches of all fission products provided by the nuclear databases.[1] This new approach provided a better handle on the systematic errors of the conversion. Although it did not reduce the final error budget, it led to a systematic shift of about 3% in the normalization of ^{235}U, ^{239}Pu, and ^{241}Pu antineutrino fluxes, respectively. This normalization shift has been attributed to two main systematic effects in the original conversion of the ILL electron data. At low energy ($E_\nu < 4$ MeV) the implementation of Coulomb and weak magnetism corrections to the Fermi theory in the new approach turned out to deviate from the effective linear correction ($0.65 \times (E_\nu - 4$ MeV) in %) used in the previous work. At high energy ($E_\nu > 4$ MeV), the converted antineutrino spectra become very sensitive to the knowledge of the charge Z of the nuclei contributing to the total spectrum. In the previous approach, only the mean dependence of Z versus the end-point of the effective beta-branches had been used while in the new conversion we had access to the complete distribution, nucleus by nucleus. These two effects could be numerically studied and confirmed on various independent sets of beta-branches. Because ^{238}U nuclei undergo fission with fast neutrons, the associated electron spectrum could not be measured in the thermal neutron flux of the ILL reactor. Therefore the *ab initio* summation of the $\bar{\nu}_e$ from all possible beta decays of fission products was performed to predict the neutrino spectrum.[9] In Ref.[1] we provided a new prediction with an estimated relative uncertainty of the order of 15% in the 2-8 MeV range. This uncertainty of *ab initio* calculations is still too large to be generalized to all isotopes but it is sufficiently accurate in the case of ^{238}U, which contributes to less than 10% of the total fission rate for all reactors considered in this work. An ongoing measurement at the FRM II reactor in Garching will soon provide experimental constraints.[10]

Experiments at baselines below 100 m reported either the ratios (R) of the measured to predicted cross section per fission, or the observed event rate to the predicted rate. The prediction of the cross section per fission is defined as:

$$\sigma_f^{\rm pred} = \int_0^\infty S_{\rm tot}(E_\nu)\sigma_{\rm V-A}(E_\nu)dE_\nu = \sum_k f_k \sigma_{f,k}^{\rm pred}, \qquad (1)$$

where the $\sigma_{f,k}^{\rm pred}$ are the predicted cross sections for each fissile isotope, $S_{\rm tot}$ is the model dependent reactor neutrino spectrum for a given average fuel composition (f_k) and $\sigma_{\rm V-A}$ is the theoretical cross section of reaction $\bar{\nu}_e + p \rightarrow e^+ + n$:

$$\sigma_{\rm V-A}(E_e)[{\rm cm}^2] = \frac{846.7\,10^{-43}}{\tau_n[{\rm s}]}\, p_e[{\rm MeV}]\, E_e[{\rm MeV}]\, (1 + \delta_{\rm rec} + \delta_{\rm wm} + \delta_{\rm rad}), \qquad (2)$$

where $\delta_{\rm rec}$, $\delta_{\rm wm}$ and $\delta_{\rm rad}$ are respectively the nucleon recoil, weak magnetism and radiative corretions to the cross section (see[1,2] for details).

Accounting for new reactor antineutrino spectra[1] the normalization of predicted antineutrino rates, $\sigma_{f,k}^{\rm pred}$, is shifted by +2.5%, +3.1%, +3.7%, +9.8% for k=^{235}U, ^{239}Pu, ^{241}Pu, and ^{238}U respectively. In the case of ^{238}U the completeness of nuclear databases over the years largely explains the +9.8% shift from the reference computations.[9] The new predicted cross section for any fuel composition can be computed from Eq. (1). By default our new computation takes into account the so-called off-equilibrium correction[1] of the antineutrino fluxes (increase in fluxes caused by the decay of long-lived fission products).

3 Impact on past experimental results

In the eighties and nineties, experiments were performed at a few tens of meters from nuclear reactor cores at ILL, Goesgen, Rovno, Krasnoyarsk, Bugey (so called 3 and 4) and Savannah River.[4–7] We only consider here experiments with baselines below 100 m to get rid of a possible (θ_{13}, Δm^2_{31}) driven oscillation effect at Palo Verde or CHOOZ.

The ratios of observed event rates to predicted event rates (or cross section per fission), $R = N_{\rm obs}/N_{\rm pred}$, are summarized in Table 1. The observed event rates and their associated errors are unchanged with respect to the publications, the predicted rates are reevaluated separately in each experimental case. We observe a general systematic shift more or less significantly below unity. These reevaluations unveil a new *reactor antineutrino anomaly*,[2] clearly illustrated in Fig. 1. In order to quantify the statistical significance of the anomaly we can compute the weighted average of the ratios of expected over predicted rates, for all short baseline reactor neutrino experiments (including their possible correlations).

Table 1: $N_{\rm obs}/N_{\rm pred}$ ratios based on old and new spectra. Off-equilibrium corrections have been applied when justified. The err column is the total error published by the collaborations including the error on $S_{\rm tot}$, the corr column is the part of the error correlated among experiments (multiple-baseline or same detector).

#	result	Det. type	τ_n (s)	^{235}U	^{239}Pu	^{238}U	^{241}Pu	old	new	err(%)	corr(%)	L(m)
1	Bugey-4	^{3}He+H_2O	888.7	0.538	0.328	0.078	0.056	0.987	0.942	3.0	3.0	15
2	ROVNO91	^{3}He+H_2O	888.6	0.614	0.274	0.074	0.038	0.985	0.940	3.9	3.0	18
3	Bugey-3-I	^{6}Li-LS	889	0.538	0.328	0.078	0.056	0.988	0.946	4.8	4.8	15
4	Bugey-3-II	^{6}Li-LS	889	0.538	0.328	0.078	0.056	0.994	0.952	4.9	4.8	40
5	Bugey-3-III	^{6}Li-LS	889	0.538	0.328	0.078	0.056	0.915	0.876	14.1	4.8	95
6	Goesgen-I	^{3}He+LS	897	0.620	0.274	0.074	0.042	1.018	0.966	6.5	6.0	38
7	Goesgen-II	^{3}He+LS	897	0.584	0.298	0.068	0.050	1.045	0.992	6.5	6.0	45
8	Goesgen-II	^{3}He+LS	897	0.543	0.329	0.070	0.058	0.975	0.925	7.6	6.0	65
9	ILL	^{3}He+LS	889	$\simeq 1$	—	—	—	0.832	0.802	9.5	6.0	9
10	Krasn. I	^{3}He+PE	899	$\simeq 1$	—	—	—	1.013	0.936	5.8	4.9	33
11	Krasn. II	^{3}He+PE	899	$\simeq 1$	—	—	—	1.031	0.953	20.3	4.9	92
12	Krasn. III	^{3}He+PE	899	$\simeq 1$	—	—	—	0.989	0.947	4.9	4.9	57
13	SRP I	Gd-LS	887	$\simeq 1$	—	—	—	0.987	0.952	3.7	3.7	18
14	SRP II	Gd-LS	887	$\simeq 1$	—	—	—	1.055	1.018	3.8	3.7	24
15	ROVNO88-1I	^{3}He+PE	898.8	0.607	0.277	0.074	0.042	0.969	0.917	6.9	6.9	18
16	ROVNO88-2I	^{3}He+PE	898.8	0.603	0.276	0.076	0.045	1.001	0.948	6.9	6.9	18
17	ROVNO88-1S	Gd-LS	898.8	0.606	0.277	0.074	0.043	1.026	0.972	7.8	7.2	18
18	ROVNO88-2S	Gd-LS	898.8	0.557	0.313	0.076	0.054	1.013	0.959	7.8	7.2	25
19	ROVNO88-3S	Gd-LS	898.8	0.606	0.274	0.074	0.046	0.990	0.938	7.2	7.2	18

We consider the following experimental rate information: Bugey-4 and Rovno91, the three Bugey-3 experiments, the three Goesgen experiments and the ILL experiment, the three Krasnoyarsk experiments, the two Savannah River results (SRP), and the five Rovno88 experiments. $\overrightarrow{\rm R}$ is the corresponding vector of 19 ratios of observed to predicted event rates. We assume a 2.0% systematic uncertainty fully correlated among all 19 ratios in result of the common normalization uncertainty of the beta-spectra measured in.[8] In order to account for the potential experimental correlations, we fully correlated the experimental errors of Bugey-4 and Rovno91, of the three Goesgen and the ILL experiments, the three Krasnoyarsk experiments, the five Rovno88 experiments, and the two SRP results. We also fully correlated the Rovno88 (1I and 2I) results with Rovno91, and we added an arbitrary 50% correlation between the Rovno88 (1I and 2I) and the

Bugey-4 measurement. We motivated these latest correlations by the use of similar or identical integral detectors.

In order to account for the non-gaussianity of the ratios R we developed a Monte Carlo simulation to check this point and found that the ratios distribution is almost Gaussian, but with slightly longer tails, which we decided to take into account in our calculations (in contours that appear later we enlarged the error bars). With the old antineutrino spectra the mean ratio is μ=0.976±0.024, and the fraction of simple Monte-Carlo experiments with $r \geq 1$ is 17.1% ($-0.95\,\sigma$ from expectation). With the new antineutrino spectra, we obtain μ=0.943±0.023, and the fraction of simple Monte-Carlo experiments with $r \geq 1$ is 1.3%, corresponding to a $-2.2\,\sigma$ effect (while a simple calculation assuming normality would lead to $-2.4\,\sigma$). Clearly the new spectra induce a statistically significant deviation from the expectation. In the following we define an experimental cross section $\sigma_f^{\rm ano} = 0.943 \times \sigma_f^{\rm pred,new}$ 10^{-43} cm^2/fission. With the new antineutrino spectra, we observe that for the data sample the minimum χ^2 is $\chi^2_{\rm min,data} = 19.6$. The fraction of simple Monte-Carlo experiments with $\chi^2_{\rm min} < \chi^2_{\rm min,data}$ is 25%, showing that the distribution of experimental ratios in $\overrightarrow{\rm R}$ around the mean value is representative given the correlations.

Assuming the correctness of $\sigma_f^{\rm pred,new}$ the anomaly could be explained by a common bias in all reactor neutrino experiments. The measurements used different detection techniques (scintillator counters and integral detectors). Neutrons were tagged either by their capture in metal-loaded scintillator, or in proportional counters, thus leading to two distinct systematics. As far as the neutron detection efficiency calibration is concerned, we note that different types of radioactive sources emitting MeV or sub-MeV neutrons were used (Am-Be, ^{252}Cf, Sb-Pu, Pu-Be). It should be mentioned that the Krasnoyarsk, ILL, and SRP experiments operated with nuclear fuel such that the difference between the real antineutrino spectrum and that of pure ^{235}U was less than 1.5%. They reported similar deficits to those observed at other reactors operating with a mixed fuel. Hence the anomaly cannot be associated with a single fissile isotope neither with a single detection technique. All these elements argue against a trivial bias in the experiments, but a detailed analysis of the most sensitive of them, involving experts, would certainly improve the quantification of the anomaly. Theother possible explanation of the anomaly is based on a real physical effect and is detailed in Section 5.

We used shape information from the Bugey-3 and ILL published data[4,5] for our combined analysis described in Section 5. From the analysis of the shape of their energy spectra at different source-detector distances,[5,6] the Goesgen and Bugey-3 measurements exclude oscillations such that $0.06 < \Delta m^2 < 1$ eV^2 for $\sin^2(2\theta) > 0.05$. We used Bugey-3's 40 m/15 m ratio data from[5] as it provides the best limit. As already noted in Ref.[13] the data from ILL showed a spectral deformation compatible with an oscillation pattern in their measured over predicted events ratio. It should be mentioned that the parameters best fitting the data reported by the authors of Ref.[13] were $\Delta m^2 = 2.2$ eV^2 and $\sin^2(2\theta) = 0.3$. We reanalyzed the data of Ref.[13] in order to include the ILL shape-only information in our analysis of the reactor antineutrino anomaly. We reproduced the contour in Fig. 14 of Ref.,[4] for the shape-only analysis (while we reproduced that of Ref.[13] which excludes the no-oscillation hypothesis at 2σ for the rate-only analysis in the previous section). The shape-only information of the data is compatible with the no-oscillation hypothesis at 1σ.

4 Other experimental results considered here

We considered the previously quoted anomalies affecting other short baseline electron neutrino experiments Gallex, Sage and MiniBooNE, reviewed in Ref.[15] Our goal is to quantify the compatibility with those anomalies. We first reanalyzed the Gallex and Sage calibration runs

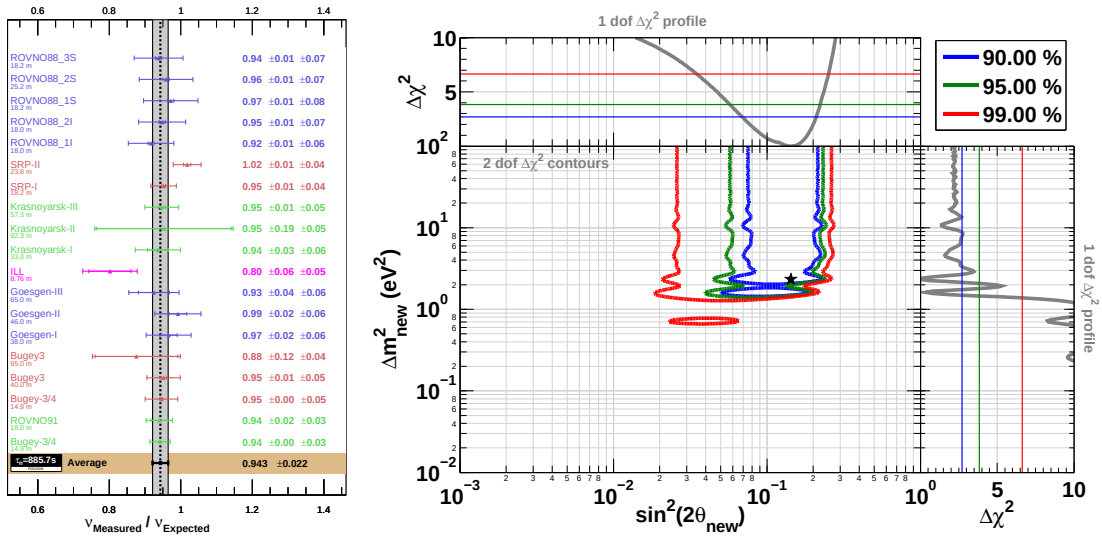

Figure 1: Left: weighted average (with correlations) of 19 measurements of reactor neutrino experiments operating at short baselines. A summary of experiment details is given in Table 1. Right: Allowed regions in the $\sin^2(2\theta_{\rm new}) - \Delta m^2_{\rm new}$ plane from the combination of reactor neutrino experiments, Gallex and Sage calibration sources experiments, MiniBooNE reanalysis, and the ILL and Bugey-3-energy spectra. The data are well fitted by the 3+1 neutrino hypothesis, while the no-oscillation hypothesis is disfavored at 99.8% C.L.

with ^{51}Cr and ^{37}Ar radioactive sources emitting ~ 1 MeV electron neutrinos.,[16] following the methodology developed in Ref.[15,17] However we decided to include possible correlations between these four measurements in this present work. Details are given in.[2] This has the effect of being slightly more conservative, with the no-oscillation hypothesis disfavored at 97.7% C.L., instead of 98% C.L. in Ref.[15] Gallex and Sage observed an average deficit of $R_G = 0.86 \pm 0.06\,(1\sigma)$.

We also reanalyzed the MiniBooNE electron neutrino excess assuming the very short baseline neutrino oscillation explanation of Ref.[15] Details of our reproduction of the latter analysis are provided in.[2]

5 The fourth neutrino hypothesis

The reactor antineutrino anomaly could be explained through the existence of a fourth non-standard neutrino, corresponding in the flavor basis to a sterile neutrino ν_s (see[3] and references therein) with a large $\Delta m^2_{\rm new}$ value. For simplicity we restrict our analysis to the 3+1 four-neutrino scheme in which there is a group of three active neutrino masses separated from an isolated neutrino mass, such that $|\Delta m^2_{\rm new}| \gg 10^{-2}$ eV^2. The latter would be responsible for very short baseline reactor neutrino oscillations. For energies above the inverse beta decay threshold and baselines below 100 m, we adopt the approximated oscillation formula:

$$P_{ee} = 1 - \sin^2(2\theta_{\rm new}) \sin^2\left(\frac{\Delta m^2_{\rm new} L}{4E_{\bar{\nu}_e}}\right) \qquad (3)$$

where active neutrino oscillation effects are negligible at these short baselines.

The ILL experiment may have seen a hint of oscillation in their measured positron energy spectrum ,[4,13] but Bugey-3's results do not point to any significant spectral distortion more than 15 m away from the antineutrino source. Hence, in a first approximation, hypothetical oscillations could be seen as an energy-independent suppression of the $\bar{\nu}_e$ rate by a factor of $\frac{1}{2}\sin^2(2\theta_{\rm new,R})$, thus leading to $\Delta m^2_{\rm new,R} \gtrsim 1$ eV^2 and accounting for Bugey-3 and Goesgen shape analyses.[5,6] Considering the weighted averaged of all reactor experiments we get an estimate of the mixing angle, $\sin^2(2\theta_{\rm new,R}) \sim 0.115$. The ILL positron spectrum is thus in agreement

with the oscillation parameters found independently in our re-analyses, mainly based on rate information. Because of the differences in the systematic effects in the rate and shape analyses, this coincidence is in favor of a true physical effect rather than an experimental anomaly. Including the finite spatial extension of the nuclear reactors and the ILL and Bugey-3 detectors, we found that the small dimensions of the ILL nuclear core lead to small corrections of the oscillation pattern imprinted on the positron spectrum. However the large extension of the Bugey nuclear core is sufficient to wash out most of the oscillation pattern at 15 m. This explains the absence of shape distortion in the Bugey-3 experiment.

The no-oscillation hypothesis is disfavored at 99.8% C.L. The significance is dominated by the gallium and reactor data. Allowed regions in the $\sin^2(2\theta_{\rm new}) - \Delta m^2_{\rm new}$ plane are displayed in Fig. 1, together with the marginal $\Delta\chi^2$ profiles for $|\Delta m^2_{\rm new}|$ and $\sin^2(2\theta_{\rm new})$. The combined fit leads to the following constraints on oscillation parameters: $|\Delta m^2_{\rm new}| > 1.5$ eV^2 (95% C.L.) and $\sin^2(2\theta_{\rm new}) = 0.14 \pm 0.08$ (95% C.L.).

References

1. Th. A. Mueller, *et al.*, *arXiv:***1101.2663**; *Phys. Rev.* **C83**, 054615, (2011). Th. A. Mueller, PhD Thesis, Paris-Sud XI University (2010).
2. G. Mention, *et al.*, *arXiv:***1101.2755**; *Phys. Rev.* **D83**, 073006, (2011).
3. K. Nakamura *et al.*, (Particle Data Group), *J. Phys.* **G37**, 075021 (2010).
4. H. Kwon *et al.*, *Phys. Rev.* **D24**, 1097, (1981).
5. B. Achkar *et al.*, *Nucl. Phys.* **B434**, 503, (1995).
6. G. Zacek *et al.*, *Phys. Rev.* **D34**, 2621, (1986).
7. Y. Déclais *et al.*, *Phys. Lett.* **B 338**, 383, (1994); A.I. Afonin *et al.*, *JETP***94**, 1-17, (1988); V. Kuvshinnikov *et al.*, *JETP***54 N5**, 259, (1991); G.S. Vidyakin *et al.*, *JETP***93**, 424-431, (1987); G.S. Vidyakin *et al.*, *JETP***59**, 390, (1994); Z.D. Greenwood *et al.*, *Phys. Rev.* **D53**, 11, (1996).
8. K. Schreckenbach *et al.*, *Phys. Lett.* **B 99**, 251, (1981); K. Schreckenbach *et al.*, *Phys. Lett.* **B 160**, 325, (1985); F. von Feilitzsch, A. A. Hahn and K. Schreckenbach, *Phys. Lett.* **B 118**, 162, (1982); A. A. Hahn *et al.*, *Phys. Lett.* **B 218**, 365, (1989).
9. B. R. Davis *et al.*, *Phys. Rev.* **C19**, 2259, (1979). P. Vogel *et al.*, *Phys. Rev.* **C24**, 1543, (1981).
10. N. H. Haag, Bestimmung des Antineutrinospektrums der Spaltprodukte von ^{238}U, Diplomarbeit, Technische Universität München.
11. A. P. Serebrov and A. K. Fomin, *Phys. Rev.* **C82**, 035501, (2010).
12. A. Pilchmaier *et al.*, *Phys. Lett.* **B 693**, 221-226, (2010).
13. A. Hoummada *et al.*, Appl. Rad. Isot. Vol. **46**, No. 6/7, pp. 449-450, (1995).
14. P. Vogel, *Phys. Rev.* **D29**, 1918, (1984).
15. C. Giunti, M. Laveder, *Phys. Rev.* **D82**, 053005, (2010).
16. P. Anselmann *et al.* (GALLEX), *Phys. Lett.* **B 342**, 440, (1995); W. Hampel *et al.* (GALLEX), *Phys. Lett.* **B 420**, 114, (1998); F. Kaether *et al.*, *Phys. Lett.* **B 685**, 47, (2010); J. N. Abdurashitov *et al.* (SAGE), *Phys. Rev. Lett.* **77**, 4708, (1996); J. N. Abdurashitov *et al.* (SAGE), *Phys. Rev.* **C59**, 2246, (1999); J. N. Abdurashitov *et al.*, *Phys. Rev.* **C73**, 045805, (2006); J. N. Abdurashitov *et al.* (SAGE), *Phys. Rev.* **C80**, 015807, (2009).
17. C. Giunti, M. Laveder, *arXiv:***1006.3244v2**.
18. A. A. Aguilar-Arevalo *et al.*, *Phys. Rev. Lett.* **98**, 231801, (2007); A. A. Aguilar-Arevalo *et al.*, *Phys. Rev. Lett.* **102**, 101802, (2009). Data release available at www-boone.fnal.gov.

GERDA commissioning results and summary of double beta decay projects

F. Cossavella for the GERDA collaboration
Max-Planck-Institut für Physik, Föhringer Ring 6,
80805 München, Germany

The Germanium Detector Array (GERDA) experiment searches for neutrinoless double beta decay of ^{76}Ge to test if neutrinos are Majorana particles, identical to their own antiparticles, or Dirac particles with distinct antiparticles. Neutrinoless double beta decay experiments can also place a limit on the effective neutrino mass and probe the neutrino mass hierarchy. Acting as both source and detector, germanium crystals enriched in ^{76}Ge will be submerged in an ultrapure cryogenic liquid that serves as a cooling medium and a shield against radiation. Together with a careful selection of radiopure construction materials and backround recognition techniques, GERDA can suppress background signals up to two orders of magnitude better than earlier experiments. This contribution presents the status of the GERDA experiment, installed in the underground laboratory of LNGS (INFN, Italy). The expected performance is compared to other neutrinoless double beta decay searches that start commissioning in the near future.

1 Neutrino properties

Several experiments have observed the oscillation of neutrino species, which requires nonzero neutrino masses, and measured their squared-mass differences.[1] However, there are still unknowns: the neutrino absolute mass scale, the mass hierarchy, and whether the neutrinos are their own antiparticles, that is whether the neutrino is a Majorana particle or the neutrino and the antineutrino are distinc Dirac particles.

The best known method to directly test the Majorana nature of the neutrino is the observation of neutrinoless double beta ($0\nu\beta\beta$) decay. Neutrino-accompanied double beta ($2\nu\beta\beta$) decay has been observed in several even-even nuclei,[2] for which the single beta decay is energetically forbidden. In these cases the final state consists of the residual nucleus, the two $\overline{\nu}_e$ and two electrons; and so the spectrum of the combined electron energies is continuous. Since the neutrino is massive, if it is its own antiparticle, then the $0\nu\beta\beta$ decay is allowed.[3] Since all the energy released by the nuclear decay is carried by detectable particles, the characteristic signature is a sharp peak in the combined-electron-energy spectrum at the Q value of the decay, known experimentally to within a fraction of a keV.

The $0\nu\beta\beta$ decay half life $T_{1/2}$ is inversely proportional to the square of the effective Majorana neutrino mass ($\langle m_{ee}\rangle$) according to the following relation:

$$\frac{1}{T_{1/2}} = F(Q,Z)\cdot|M_{\rm nucl}|^2\cdot\langle m_{ee}\rangle^2 \quad (1)$$

$$\langle m_{ee}\rangle = \left|\sum_{i=1}^{3}|U_{e_i}|^2\, e^{i\beta_i}\, m_i\right|, \quad (2)$$

Table 1: Selective list of past $0\nu\beta\beta$ decay experiments and their 90%-C.L. half life lower limits.

Experiment	Underground lab	Isotope	Technology	$T_{1/2}[10^{24}\,\mathrm{y}]$	Ref.
Heidelberg-Moscow	LNGS (Italy)	^{76}Ge	HPGe	>19	5
claim:				$22.3^{+4.4}_{-3.1}$	6
IGEX	LSC (Spain)	^{76}Ge	HPGe	>16	7
NEMO-III	LSM (France)	^{82}Se	Foils btw.	>0.36	2
		^{100}Mo	tracker	>1.1	2
$CdWO_4$	Solotvina (Ukrain)	^{116}Cd	Scintillator	>0.17	8
CUORICINO	LNGS (Italy)	^{130}Te	Bolometry	>2.8	9

where the U_{e_i} are the electron-neutrino elements from the mixing matrix, $e^{i\beta_i}$ are their phase factors, m_i are the neutrino mass eigenvalues, $F(Q,Z)$ is the phase-space factor of the decay of a nucleus with atomic number Z and Q values Q, and $|M_{\mathrm{nucl}}|^2$ is the decay nuclear matrix element. Measurement of the $0\nu\beta\beta$ decay half life also gives information on the absolute mass scale of the neutrino, assuming the neutrino exchange is the dominant mechanism of the process. The overall uncertainty in the derived effective Majorana neutrino mass will be dominated by the uncertainties in the nuclear matrix element calculations.[4]

2 Results from former experiments

There are approximately thirty isotopes for which double beta decay is the primary decay channel. The sensitivity on the half-life $T_{1/2}$ for an experiment with nonvanishing background rate can be expressed as

$$\text{sensitivity on } T_{1/2} \propto \epsilon \cdot A \cdot \sqrt{\frac{M \cdot T}{b \cdot \Delta E}}, \tag{3}$$

where ϵ is the detection efficiency, A is the double beta decay active mass fraction, M the target mass, T the measuring time, b the background rate, and ΔE is the energy resolution of the detector.

Increasing the exposure $M \cdot T$ is not sufficient to improve the sensitivity, if it is not accompanied by a reduction of the background level. Additionally, the sensitivity can be increased by an improvement of the energy resolution and by using source isotopes with a high natural abundance. We reduce the background rates by carefully selecting radiopure construction materials for any apparati in close proximity to the detectors and by shielding against external radiation. Employing high-resolution spectroscopy, we define a small energy window around the Q value in which to search for the $0\nu\beta\beta$ decay peak. By using a detector that is constructed from the source material, we obtain a detection efficiency of ≈100%.

Table 1 shows the results of some of the experiments performed so far. A variety of technologies and isotopes have been used in these experiments. They have measured lower limits on the half life of the decay. The best limits are set by the Heidelberg-Moscow (HdM)[5] and IGEX[7] collaborations, together with the most recent results of CUORICINO.[9] The corresponding upper limits on $\langle m_{ee} \rangle$, which are affected by the uncertainties in the calculation of the nuclear matrix elements, are in the sub-eV range. A subgroup of the Heidelberg-Moscow experiment claims evidence[6] for neutrinoless double beta decay with a half life of $22.3^{+4.4}_{-3.1} \cdot 10^{24}\,\mathrm{y}$, which gives[9] an effective Majorana neutrino mass of 0.18 eV–0.70 eV.

3 The GERDA experiment

The Germanium Detector Array (GERDA) experiment,[10] located at the Laboratori Nazionali del Gran Sasso of the INFN, Italy, uses germanium detectors enriched in the isotope ^{76}Ge to search for neutrinoless double beta decay. Although the ^{76}Ge natural abundance is only of 7.6%, it is possible to enrich germanium material to an abundance of more than 85%. This material can be used to produce high-purity germanium detectors that have good energy resolutions ($\Delta E = 3\,\mathrm{keV}$ at 2039 keV). Due to the uncertainties on the nuclear matrix elements, the claim[6] reported by part of the Heidelberg-Moscow collaboration can only be directly checked using the same isotope (^{76}Ge). GERDA is currently the only experiment able to do this.

The experiment is foreseen to proceed in two phases. In the first phase, enriched-Ge detectors which were previously operated by the Heidelberg-Moscow and IGEX collaborations will be redeployed, for a total mass of approximately 18 kg. With a background rate of 10^{-2} cts/(keV kg y), GERDA will be able to check the HdM claim within one year.[11] In the second phase, about 20 kg of new high-purity ^{76}Ge detectors will be produced with the goal of reaching an exposure of about 100 kg·y. GERDA Phase II aims at probing $0\nu\beta\beta$ decay of ^{76}Ge with a sensitivity of $T^{0\nu}_{1/2} > 1.5 \cdot 10^{26}$ y, corresponding to an upper limit on the effective Majorana neutrino mass in the range from 90 meV to 150 meV.[4] To reach this goal the background rate has to be further reduced to 10^{-3} cts/(keV kg y). For this purpose, GERDA will use Broad Energy Germanium (BEGe) detectors with a special electrode configuration, allowing for event-topology reconstruction by pulse-shape analysis and thus identification of background-like events.[12] A performance test of segmented germanium detectors[13,14] is also under discussion.

The detector array has to be shielded against external radiation. To reduce material in the proximity of the detectors, they are operated with minimal support and cabling in liquid argon, which acts as both a cooling medium and a shield. The cryostat is constructed from radiopure stainless steel with a low-background copper inset. It has a diameter of 4 m and a height of 8.9 m, and it is surrounded by a 10-m-diameter tank (8.5 m in height) containing ultrapure water that serves as a neutron moderator. This tank is equipped with photomultiplier tubes to detect the Čerenkhov light emitted by charged particles crossing the water medium; this allows it to also function as an active muon veto. A clean room with a lock system is placed on top of the cryostat. It allows for the clean access to the detectors and their submersion into the cooling medium. The setup is schematically depicted in Figure 1a.

3.1 Commissioning results

In June 2010 GERDA deployed the first string of natural Ge detector in the cryostat. A resolution of approximately 4 keV at 2.6 MeV was achieved in all three of the detectors on the string.

Since then, GERDA has been measuring the background spectrum and has seen a prominent line at 1524.7 keV from the decay of ^{42}K, a daughter of ^{42}Ar, expected to be a rare contaminant in atmospheric argon from a measured upper limit[15] and from numerical estimations.[16] ^{42}Ar is a β^- emitter with $T_{1/2} = 32.9$ y and a Q value of 599 keV.[17] The daughter of this reaction, ^{42}K, is also a β^- emitter ($T_{1/2} = 12.36$ h), which decays to the ground state of the stable isotope ^{42}Ca with a branching ratio of 82% and $Q_\beta = 3525.3$ keV. With 18% probability it decays to an excited level of ^{42}Ca that decays to the ground state by emission of a 1524.7 keV γ-ray, as has been observed in the background spectrum of GERDA. Since the endpoint energy of the ^{42}K decay is higher than that of ^{76}Ge, it can contribute to the GERDA background in the region of the ^{76}Ge Q value.

The decay of ^{42}Ar produces positively-charged ions that in the presence of an electrical field may drift long distances in liquid argon. Since the detectors have voltage-biased surfaces,

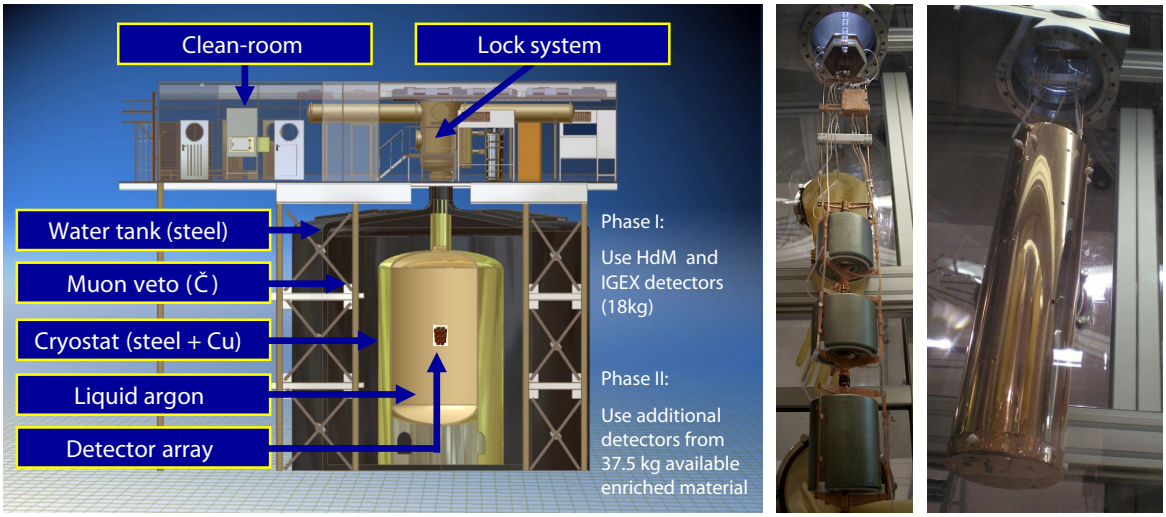

(a) (b) (c)

Figure 1: (a) Sketch of the GERDA experiment. The diameter of the cryostat is of 4 [m] for a height of 8.9 m and it is inserted into a water tank with a diameter of 10 m and height of 8.5 m)(b) First string deployed in June 2010 (c) Mini-shroud surrounding the string of detectors.

potassium ions drift to the detector surface before they neutralize, where they can contribute to the observed background above 1600 keV.

To close the electrical field lines from the germanium detectors and prevent the drifting of the ions onto the detector surface, the detector string has been surrounded by a thin copper layer (mini-shroud, Figure 1c). The mini-shroud was used for data taking runs 10 and 11; we compare the results to those from run 1–3, in which the mini-shroud was not present. Figure 2a shows that the count rate under the 1524.7 keV peak drops approximately by a factor of four when the mini-shroud is used. The integral count rate above this peak (between 1550 keV and 3000 keV) is also considerably reduced. In runs 1–3 a count rate of 0.17 cts/(keV kg y) was measured, with a 68% credibility interval from 0.16 cts/(keV kg y) to 0.19 cts/(keV kg y). In runs 10 and 11, with the introduction of the mini-shroud, the count rate in the same energy interval has been reduced to 0.074 cts/(keV kg y), with a 68% credibility interval of 0.066 cts/(keV kg y)–0.084 cts/(keV kg y) (see Figure. 2b).

From June 2010 to March 2011 a total of twelve runs with different detectors, electric field configurations and read out schemes were performed. To evaluate the background rate we take into account the total count rate in the region of interest, an energy window 400 keV-wide centered at $Q_{\beta\beta}$. The calculation is performed according to a Bayesian analysis, under the assumption that the spectrum in the energy window is flat. Using the framework Bayesian Analysis Toolkit (BAT),[18] the lowest measured background rate is 0.055 cts/(keV kg y) with a 68% credibility interval ranging from 0.041 cts/(keV kg y) to 0.072 cts/(keV kg y) (see fig. 3).

The measured background rate is a factor of two better than the past experiments,[5,7] although still a factor of five higher than the goal of GERDA Phase I. It has to be noticed that no pulse-shape analysis to discriminate background-like from signal-like events has been applied so far and that the measurement was performed with ^{nat}Ge detectors, whose cosmogenic-activation history is not as well known as that of the enriched Ge detectors. The origin of the background counts observed at $Q_{\beta\beta}$ is currently under investigation, in particular the contribution of the Compton continuum from natural chains (^{226}Ra, ^{228}Th) and from ^{42}K decays.

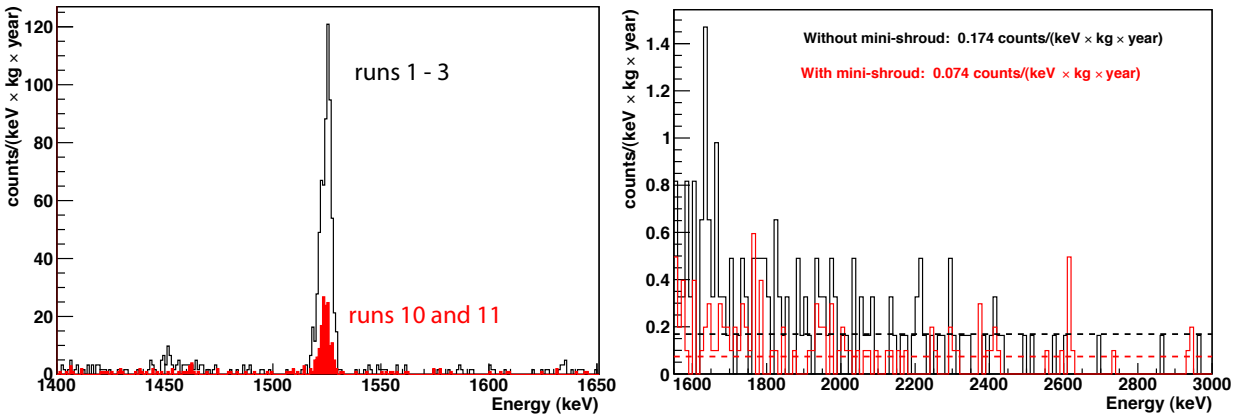

(a) (b)

Figure 2: (a) Measured spectrum in an energy range centered at 1524.7 keV. In black are events from runs 1–3, without the mini-shroud; and in red are data collected in runs 10 and 11, with the mini-shroud. (b) Measured spectrum above 1550 keV for runs 1–3 (black) and runs 10 and 11 (red).

4 Status of other $0\nu\beta\beta$ decay experiments

In the coming years, a few other experiments will be able to test the Heidelberg-Moscow results. Some of them are summarized in Table 2 and discussed in this contribution.

4.1 Majorana demonstrator

The Majorana demonstrator[19] is located at the Sanford laboratories, USA. The design uses high-purity ^{76}Ge-enriched BEGe detectors, which will be operated inside conventional low-background copper cryostats electro-formed underground. Like in GERDA Phase II, BEGe detectors with their very good pulse-shape analysis capabilities will allow for a better recognition of the background events. Majorana is currently in the construction phase. Commissioning of a prototype cryostat is foreseen in 2012. The first run with three strings of $^{\mathrm{enr}}$Ge detectors and four strings of $^{\mathrm{nat}}$Ge detector, with a total mass of about 20 kg, is planned for 2013. In 2014, an additional module with 20 kg detectors enriched in ^{76}Ge will be included, increasing the total target mass to 40 kg. The aim is to reach a background rate of 0.001 cts/(keV kg y) and a sensitivity on the neutrino Majorana mass better than 140 meV within three years of measurements.[20]

4.2 CUORE

The CUORE experiment[21] is currently being built at the Laboratori Nazionali del Gran Sasso. CUORE will use the ^{130}Te isotope in the form of TeO_2 crystals. The crystals, cooled down to mK temperatures, will be operated as bolometers, the energy deposits being measured by the induced temperature increase in the crystal. ^{130}Te has a natural isotopic abundance of 33.8%, so no enrichment is required. CUORE will also run in two phases. CUORE-0 will deploy into the cryostat of the CUORICINO experiment a detector tower with 52 crystals with improved radiopurity, for a total ^{130}Te mass of 11 kg. The background in this first phase is limited by an irreducible contribution from the CUORICINO cryostat to approximately 0.06 cts/(keV y) per kg of TeO_2. Together with the measured surface background contributions, the total background rate in the region of interest is estimated[22] to be approximately 0.12 cts/(keV y) per kg of TeO_2, which scales to approximately 0.4 cts/(keV y) per kg of ^{130}Te. With this assumption a sensitivity

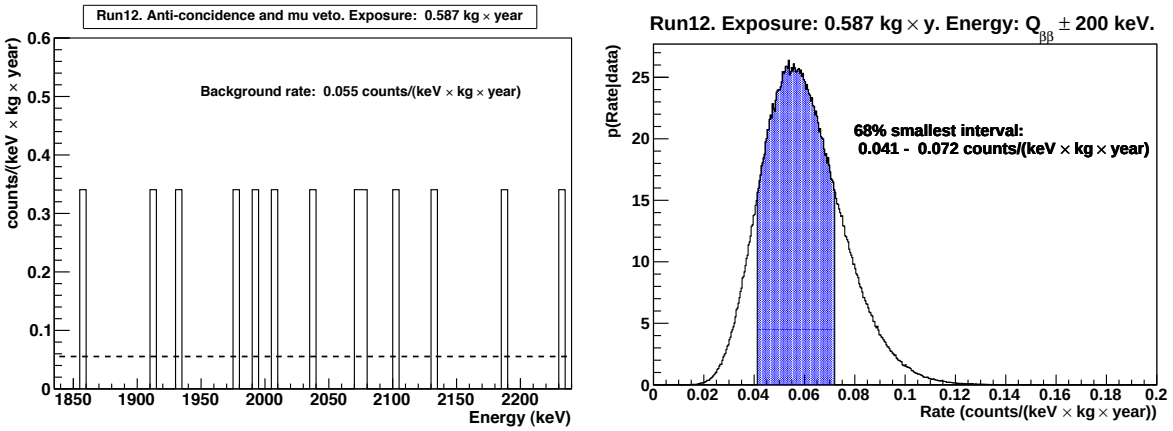

(a) (b)

Figure 3: (a) Measured spectrum in a 400-keV-wide window around $Q_{\beta\beta} = 2039\,\mathrm{keV}$ for run 12. (b) posterior pdf for the background rate given the observed counts in the window. The smallest 68% interval is highlighted.

Table 2: Selective list of $0\nu\beta\beta$ decay experiments that are commissioned now or in the near future and will be able to test the HdM claim. Measured or estimated background rates and sensitivities on the effective Majorana neutrino mass are quoted (references in the text). The latter depend on the nuclear matrix element calculations used.

Experiment	Isotope	mass [kg]	FWHM %	BI [cts/(keV kg y)]	Sens. on $\langle m_{ee}\rangle$[meV]	Planned
GERDA I	^{76}Ge	18	0.2	0.05 (0.01)	230-390	2011
GERDA II		40		0.001	90-150	2013
Majorana	^{76}Ge	~ 20	0.2	0.001	<140	2013
demonstrator		40				2014
CUORE-0	^{130}Te	~ 10	0.25	~ 0.4	~ 300	2011
CUORE		200		<0.04	35-82	2014
EXO-200	^{136}Xe	200	3.7	~ 0.002	109-135	2011

to a half life of $8 \cdot 10^{24}$ y could be reached within two years of measurement, corresponding to a limit on $\langle m_{ee}\rangle$ of the order of 300 meV. Commissioning of the complete CUORE experiment is foreseen for 2014. In its final configuration CUORE will operate 988 TeO_2 crystals, with a total active mass of ^{130}Te of 200 kg. Most of the effort is directed to the reduction of the background rate to less than 0.04 cts/(keV kg y).[23,24] Given a resolution of 0.25% FWHM and the expected background rate, CUORE will be sensitive[22] to masses in the 35 meV[a] to 82 meV[b] range.

4.3 EXO-200

EXO[28] is a multiphase program to search for neutrinoless double beta decay of ^{136}Xe, the ultimate aim being a ton-scale experiment with a sensitivity to the Majorana neutrino mass of about 10 meV.

EXO-200 is a 200-kg prototype experiment using a time projection chamber (TPC), filled

[a] Nuclear matrix element from the RQRPA model[25]

[b] Nuclear matrix elements from the ISM model[26]

with liquid xenon enriched to 80% in ^{136}Xe. The experiment will detect scintillation light of liquid Xenon using avalanche photodiodes, and ionization electrons with grid wires. This technique is easy to scale to big masses, however a resolution of only 3.7% FWHM has been reported so far. Currently a TPC containing 200 kg of cryogenic liquid is being commissioned. In fall 2010 the TPC was filled with 200 kg $^{\mathrm{nat}}$Xe and results from engineering runs are being analyzed. For 2011 a refill of the system followed by low-background measurements is scheduled. With a nominal background rate of 0.002 cts/(keV kg y), EXO-200[29] will probe the Majorana neutrino mass down to 109 meV[c] – 135 meV[d].

5 Conclusions

The observation of $0\nu\beta\beta$ decay is the only practical way to test the charge-conjugation nature of the neutrino. Past experiments set upper limits on the effective Majorana neutrino mass in the sub-eV range. A claim of evidence has been reported by a subgroup of the Heidelberg-Moscow experiment and it must be tested by a new generation of experiments based not only on ^{76}Ge, but also on different isotopes.

The GERDA infrastructure has been completed in 2010, and the first background measurements have been performed, resulting in a background rate of approximately 0.05 cts/(keV kg y). The first detectors from enriched Ge will be deployed in summer 2011. Majorana, CUORE, and EXO-200, the latter two based on different isotopes, are also commissioning and expected to start taking data in the next few years.

References

1. S.N. Ahmed et al. SNO Collaboration, *Phys. Rev. Lett.* **92**, 181301 (2004)
2. A.S. Barabash, *Phys. Atom. Nucl.* **74**, 603-613 (2011)
3. J. Schechter and J. W. F. Valle, *Phys. Rev.* D **25**, 295 (1982)
4. A. Smolnikov, P. Grabmayr, *Phys. Rev.* C **81**, 028502 (2010) and references therein
5. H.V. Klapdor-Kleingrothaus et al., *Eur. Phys. J.* A **12**, 147-154 (2001)
6. H.V. Klapdor-Kleingrothaus, I.V. Krivosheina, *Mod. Phys. Lett.* A **21**, 1547-1566 (2006)
7. C.E. AAlseth et al., *Phys. Rev.* D **65**, 092007 (2002)
8. F.A. Danevich et al., *Phys. Rev.* C **68**, 035501 (2003)
9. E. Andreotti et al., *Astropart. Phys.* **34**, 822-831 (2011) and references therein
10. S. Schönert et al., *Nucl. Phys. Proc. Suppl.* **145**, 242 (2005)
11. A. Caldwell, K. Kröninger, *Phys. Rev.* D **74**, 092003 (2006)
12. M. Barnabe-Heider et al., *JINST* **5**, P10007 (2010)
13. I. Abt et al., *Nucl. Instrum. Methods* A **577**, 574 (2007)
14. I. Abt et al., *J. Instrum.* **4**, p11008 (2009)
15. V.D. Ashitkov et al., [arXiv:nucl-ex/0309001]
16. P. Cennini et al., *Nucl. Instrum. Methods* A **356**, 526-529 (1995)
17. R.B. Firestone, Table of Isotopes, Eight Edition, John Wiley and Sons, Incorp., N.Y. (1998)
18. A. Caldwell, D. Kollar, K. Kröninger, *Computer Physics Communications* **180**, 2197-2209 (2009)
19. The Majorana Collaboration, arXiv:nucl-ex/0311013
20. G.K. Giovanetti, talk at International Student Workshop on Neutrinoless Double Beta Decay, November 11-13 2010, LNGS
21. CUORE proposal, R. Ardito et al., arXiv:hep-ex/0501010

[c] nuclear matrix element from RQRPA model[27]

[d] nuclear matrix element from NSM model[26]

22. E. Previtali, talk at WIN'11 (Cape Town, South Africa, January 31- February 5, 2011), proceeding to be published by World Scientific
23. J.J. Gómez-Cadena et al., arXiv:1010.5112v4
24. A. Giuliani, talk at International Student Workshop on Neutrinoless Double Beta Decay, November 11-13 2010, LNGS
25. F. Šimkovic et al., *Phys. Rev.* C **77**, 045503 (2008)
26. F. Menéndez et al., *Nucl. Phys.* A **818**, 139-151 (2009)
27. F. Šimkovic et al., *Phys. Rev.* C **79**, 055501 (2009)
28. M. Dabilov et al., *Phys. Lett.* B **480**, 12 (2000)
29. M. Dolinski, talk at Neutrino 2010 (Athens, Greece, June 14-19, 2010), proceeding to be published in *Nucl. Phys. B. Proceedings Supplements*

New approach to anti-neutrino from muon decay at rest

Sanjib Kumar Agarwalla [a]
Instituto de Física Corpuscular, CSIC-Universitat de València,
Apartado de Correos 22085, E-46071 Valencia, Spain

Neutrino physics is going through a very exciting phase. In last one and half years, crucial informations have been provided by both short and long baseline neutrino oscillation experiments. At short-baseline, recent neutrino oscillation studies seem to point towards the existence of active-sterile mixing. On the other hand at long-basline, recent T2K and MINOS data are in favor of non-zero θ_{13} opening up the possibility of observing CP-violation in the lepton sector. A stopped pion source provides neutrino beams with energy of a few tens of MeV from pion and muon decay-at-rest. A rich physics program can be accomplished with such a neutrino source. We discuss the role of such a neutrino facility to test short-baseline anomalies and to study CP violation in active neutrinos.

1 Introduction

Neutrino physics is now all set to move into the precision regime, with the emphasis now shifting to detailed knowledge of the structure of the neutrino mass matrix, accurate reconstruction of which would unravel the underlying new physics that gives rise to neutrino mass and mixing. In last couple of years, we are blessed with fantastic data which have been provided by both short and long baseline neutrino oscillation experiments.

Recent results from short-baseline (SBL) neutrino oscillation studies seem to point towards the existence of active-sterile mixing. The MiniBooNE experiment has reported an apparent excess of $\bar{\nu}_e$ events in a beam of $\bar{\nu}_\mu$ above 475 MeV [1] which is consistent with two-neutrino $\bar{\nu}_\mu \to \bar{\nu}_e$ oscillations at 99.4% confidence level. This result supports the claim of the LSND experiment [2;3], which has reported a $3.8\,\sigma$ excess of $\bar{\nu}_e$ events in a beam of $\bar{\nu}_\mu$. If one interprets these results with neutrino oscillation the relevant parameter is the ratio of the distance L to the neutrino energy E, the so called L/E. The L/E ratio is indeed very similar between LSND and MiniBooNE. The oscillation interpretation of LSND and MiniBooNE points to a mass squared

[a] Invited talk in the Electroweak session of the Rencontres de Moriond, 2011, La Thuile, Italy.

difference of the order $0.1 - 10\,\mathrm{eV}^2$ and hence requires a sterile neutrino. More motivation has been provoked from a recent reanalysis of the expected $\bar{\nu}_e$ flux emitted from nuclear reactors[4] that leads to an observed deficit of $\bar{\nu}_e$ at 98.6% C.L.. The overall reduction in predicted flux compared to the existing data from SBL neutrino experiments can be interpreted as oscillations at baselines of order 10–100 m[5] consistent with the LSND and MiniBooNE anti-neutrino results.

In the month of June, 2011, new exciting results have been announced by the T2K and MINOS long-baseline (LBL) accelerator neutrino oscillation experiments which are sensitive to θ_{13} driven $\nu_\mu \to \nu_e$ appearance channel. The T2K experiment in Japan has reported an indication of electron neutrino appearance from an accelerator-produced off-axis muon neutrino beam of energy about 0.6 GeV produced at J-PARC[6]. They have observed six electron-like events with an estimated background of 1.5 events in the Super-Kamiokande detector at a distance of 295 km from the J-PARC which indicates towards a non-zero value of θ_{13} at $2.5\,\sigma$ significance. Within a couple of weeks of the T2K results, the MINOS collaboration has announced the observation of 62 electron-like events with an estimated background of 49 events[7]. This favors a non-zero θ_{13} at $1.5\,\sigma$. A latest global fit of all the available neutrino oscillation data[8] indicates non-zero θ_{13} at more than $3\,\sigma$ C.L.. The results on θ_{13} from these experiments are going to play a crucial role in exploring CP violation in future large scale experimental program of long-baseline neutrino experiments[9].

The pion decay-at-rest (DAR) chain leads to a beam dominated by neutrinos between 20 and 52.8 MeV, with a well-defined flavor content of ν_e, ν_μ and $\bar{\nu}_\mu$. The source may be provided by a low energy proton accelerator with a beam impinging on a target/dump. Potentially, this can be the cyclotrons planned for the DAEδALUS CP-violation search[10–12]. In view of the recent SBL anomalies, we discuss in the first half of my talk to repeat the original LSND experiment using Super-Kamiokande, doped with Gadolinium, as detector which can be coupled with a modest-power DAR neutrino source[13] positioned within 20 m of the detector. Then in the second half of my talk, we present the possibility to replace the anti-neutrino run of a long-baseline neutrino oscillation experiment, with anti-neutrinos from muon decay at rest. The low energy of these neutrinos allows the use of inverse beta decay for detection in a Gadolinium-doped water Cerenkov detector. We show that this approach[11] yields a factor of five times larger anti-neutrino event sample. The resulting discovery reaches in θ_{13}, mass hierarchy and leptonic CP violation are compared with those from a conventional superbeam experiment with combined neutrino and anti-neutrino running.

2 The Neutrino Source and Decay-at-rest Flux

In a stopped pion source a proton beam of ~ 1 GeV energy interacts in a low-A target producing π^+ and, at a low level, π^- mesons. The pions then are brought to rest in a high-A beam stop. The π^- will be captured. The π^+ will produce the following cascade of decays

$$\begin{aligned} \pi^+ \quad &\to \quad \mu^+ + \nu_\mu \\ &\qquad \hookrightarrow \; e^+ + \nu_e + \bar{\nu}_\mu \end{aligned}$$

resulting in ν_μ, $\bar{\nu}_\mu$ and ν_e, but no $\bar{\nu}_e$. The resulting flux is isotropic. As a model of a DAR source, we use the DAEδALUS design[12]. The DAEδALUS accelerators are cyclotrons[14–16], an ideal low-cost source for low energy (800 MeV) protons. A detailed description of the neutrino source and DAR flux can be found in[17].

3 Final Verdict on LSND and MiniBooNE

We suggest to perform a modern version of LSND, *i.e.* use $\bar{\nu}_\mu$ from a stopped pion source and inverse beta decay to detect the appearance of $\bar{\nu}_e$. The main difference with respect to the

Δm^2 [eV^2]	0.1	1	10	100
signal	29	1605	1232	1314

Table 1: Number of signal events after one year for $\sin^2 2\theta = 10^{-3}$ including efficiency and energy resolution.

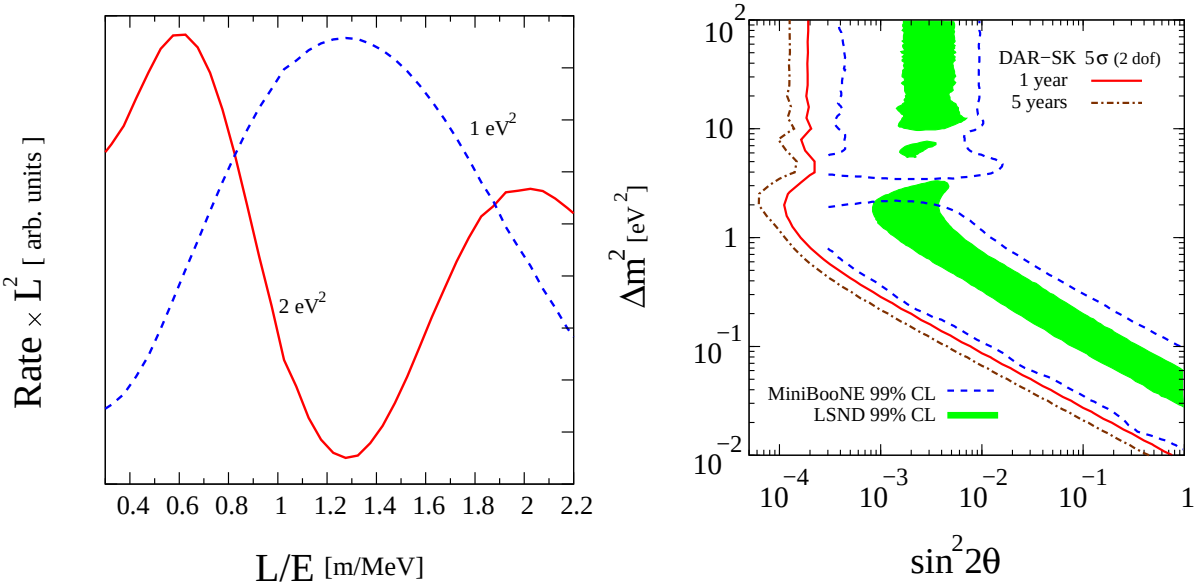

Figure 1: Left panel shows the signal event rate after one year weighted with L^2 as a function of the reconstructed L/E. The oscillation signal is computed for $\sin^2 2\theta = 10^{-3}$ and $\Delta m^2 = 2\,\mathrm{eV}^2$ (soild red line) and $1\,\mathrm{eV}^2$ (dashed blue line). Right panel depicts sensitivity limit of DAR-SK setup to sterile neutrino oscillation in the (3+1) model at $5\,\sigma$ CL (2 dof) using appearance mode. The solid red line corresponds to one year run of a 100 kW machine which can deliver 4×10^{21} $\bar{\nu}_\mu$. The dash-dotted brown line is for five years running of a 100 kW machine. The green/gray shaded region is the LSND allowed region at 99% confidence level, whereas the dashed blue line is the MiniBooNE anti-neutrino run allowed region at 99% confidence level[1].

original LSND experiment is that we suggest to use Super-Kamiokande doped with Gadolinium as detector[18] instead of a liquid scintillator detector. Super-Kamiokande has a fiducial mass of 22.5 kt compared to around 120 t in LSND. Gadolinium doping allows to efficiently detect the capture of the neutron which is produced in inverse beta decay with an efficiency of 67%[19;20]. Furthermore, we use an energy resolution as given in reference[21] and an energy threshold of 20 MeV. We consider a 100 kW average power proton cyclotron which provides 4×10^{21} $\bar{\nu}_\mu$ per year at the source. The contamination with $\bar{\nu}_e$ from π^- decays is very small and we take a value of 4×10^{-4}. The neutrino source will be located on the axis of the cylinder which describes the fiducial volume and will be 20 m away from the first cylinder surface. The resulting signal event rates for one year of operation are shown in table 1 and the background event rate due to beam contamination is 765.

The large rock overburden of approximately 2,700 mwe at Super-Kamiokande, compared to 120 mwe in LSND, reduces cosmic ray induced backgrounds to negligible levels[10;12]. Also, atmospheric neutrino backgrounds are small compared to the beam induced backgrounds. The large dimensions of the Super-Kamiokande fiducial volume, a cylinder of 14 m radius with a height of 36 m allows to observe the characteristic baseline dependence of oscillation with great accuracy. The size of the copper beam stop used in LSND was about 50 cm[22] and the position resolution for electrons (or positrons) in Super-Kamiokande at energies above 10 MeV has been measured to be better than 75 cm[23]. Adding these two sources of baseline uncertainty in quadrature we obtain about 0.9 m. In our analysis we account for this uncertainty by using a baseline resolution width of 1 m. Thus, with a source detector distance of 20 m and an energy range from

	$\bar{\nu}_\mu \to \bar{\nu}_e$	Background	$\nu_\mu \to \nu_e$	Background
DAR+HFN	1194	217	1532	428
HFA+HFN	231	158	766	214

Table 2: Comparison of the signal and background event rates of 6 years running of DAR+HFN and HFA+HFN. Note, that for DAR+HFN this is 6 years of simultaneous running of ν and $\bar{\nu}$, whereas for HFA+HFN this is 3 years each, run consecutively. Oscillation parameters are $\sin^2 2\theta_{13} = 0.1$ and $\delta_{\rm CP} = 0$ and normal hierarchy.

$20 - 52.8\,\mathrm{MeV}$ the oscillation pattern can be observed for an L/E range of $0.4 - 2.8\,\mathrm{m\,MeV}^{-1}$. This is illustrated in the left panel of figure 1, where we show the signal rates weighted with L^2 as a function of reconstructed L/E. The oscillation signal is computed for two different values of Δm^2 using the usual 2 flavor expression with $\sin^2 2\theta = 10^{-3}$. The ability to study the L/E dependence in detail is crucial if a signal is observed, since it will allow to establish or refute oscillation as the underlying physical mechanism. In the right panel of figure 1 we show sensitivity for the L/E binning analysis at $5\,\sigma$ confidence level (2 degrees of freedom) as well as the 99% confidence level allowed regions obtained from LSND and the MiniBooNE anti-neutrino run[1].

4 An Ultimate Probe for Leptonic CP violation

Here the main idea is to combine a horn focused high energy ν_μ beam (HFN) with $\bar{\nu}_\mu$ from a DAR setup to study θ_{13}, the mass hierarchy and leptonic CP violation. We will denote this new technique as DAR+HFN. To illustrate the strength of DAR+HFN, we will study a specific setup, which closely resembles the Fermilab DUSEL concept for a long baseline experiment, currently known as LBNE. This setup has a total running time of 6 years and a 300 kt water Cerenkov detector. The entire HFN part is very similar to the setup described in detail in[24], specifically we take the source detector distance to be 1300 km and use the same detector performance. The beam delivers 6.2×10^{20} protons on target per year, which for 120 GeV protons corresponds roughly to 700 kW of beam power. For DAR setup, we consider proton cyclotrons of 1 MW beam power which can deliver 4×10^{22} of ν_e, ν_μ and $\bar{\nu}_\mu$ per flavor per year per cyclotron. We use 4 of these cyclotrons with a source detector distance of 20 km. In the context of superbeam experiments, a CP violation measurement requires data from both $\nu_\mu \to \nu_e$ *and* $\bar{\nu}_\mu \to \bar{\nu}_e$. However, the horn focused high energy $\bar{\nu}_\mu$ beam (HFA) poses a number of specific challenges: the production rate for π^-, the parent of $\bar{\nu}_\mu$, is lower than for π^+, the anti-neutrino charged current cross section is lower, the background levels are higher[b], and the systematic errors are expected to be larger. Overall, the event rate for anti-neutrinos is suppressed by a factor of 2-5, depending on the anti-neutrino energy, which is illustrated by table 2.

In figure 2, we compare the results from DAR+HFN with HFA+HFN. The reaches are given as a fraction of $\delta_{\rm CP}$ and as a function of the true value of $\sin^2 2\theta_{13}$. In panel (a), we show the results for the discovery of the θ_{13} and find that DAR+HFN outperforms the superbeam experiment HFA+HFN for all CP phases and both hierarchies by roughly a factor two. The discovery reach for the mass hierarchy is shown in panel (b) and here, we see that for some values of the CP phase, in particular for inverted mass hierarchy, the reach is somewhat smaller for DAR+HFN. If at the end of the DAR+HFN run, the mass hierarchy has not been discovered adding a HFA run may be required. Finally, in panel (c) the discovery reach for CP violation is shown. For $\sin^2 2\theta_{13} = 0.05$, DAR+HFN has 75% CP coverage while HFA+HFN has 62%.

[b] This is due to the larger contamination from wrong sign pions.

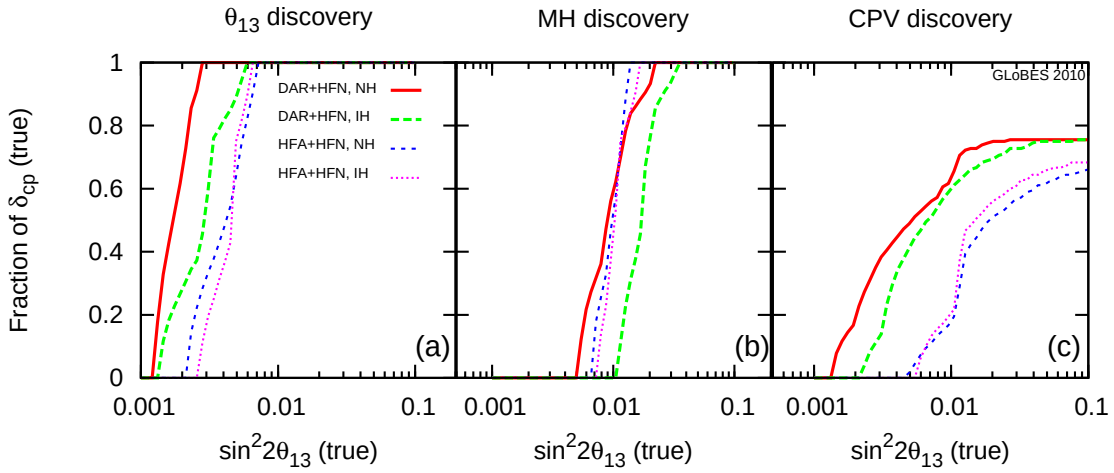

Figure 2: CP fractions for which a discovery at $3\,\sigma$ confidence level is possible as function of $\sin^2 2\theta_{13}$. From left to right for θ_{13}, mass hierarchy and CP violation. The different lines are for normal (NH) and inverted (IH) true mass hierarchies and for DAR+HFN and HFA+HFN, respectively.

5 Conclusions

In this talk, we present the physics prospects of DAR neutrino sources in testing the short-baseline anomalies and to study CP violation in active neutrinos. We have shown that Gd doped Super-Kamiokande detector combined with high intensity 100 kW cyclotron DAR neutrino source can test the LSND and MiniBooNE claims for SBL $\bar{\nu}_\mu \to \bar{\nu}_e$ oscillations with more than $5\,\sigma$ significance within one year of running time. Also, we have demonstrated that a combination of low energy $\bar{\nu}_\mu$ from muon decay at rest with high energy ν_μ from a superbeam aimed at the same Gadolinium-doped water Cerenkov detector yields a moderately improved reach for θ_{13} and a significantly improved discovery reach for CP violation while only marginally affecting the mass hierarchy sensitivity. These improvements are a direct result of combining an optimized neutrino with an optimized anti-neutrino run.

Acknowledgments

I am grateful to the conference organizers for the invitation. I would like to thank J.M. Conrad, Patrick Huber, Jonathan M. Link, Debabrata Mohapatra and M.H. Shaevitz for their collaboration. I acknowledge the support from the European Union under the European Commission Framework Programme 07 Design Study EUROnu, Project 212372 and the project Consolider-Ingenio CUP.

References

[1] A. Aguilar-Arevalo *et al.* (The MiniBooNE Collaboration), Phys.Rev.Lett. **105**, 181801 (2010), 1007.1150.

[2] C. Athanassopoulos *et al.* (LSND Collaboration), Phys.Rev.Lett. **75**, 2650 (1995), nucl-ex/9504002.

[3] A. Aguilar *et al.* (LSND Collaboration), Phys.Rev. **D64**, 112007 (2001), hep-ex/0104049.

[4] T. Mueller, D. Lhuillier, M. Fallot, A. Letourneau, S. Cormon, *et al.*, Phys.Rev.C (2011), 1101.2663.

[5] G. Mention, M. Fechner, T. Lasserre, T. Mueller, D. Lhuillier, *et al.* (2011), 1101.2755.

[6] K. Abe *et al.* (T2K Collaboration) (2011), * Temporary entry *, 1106.2822.

[7] L. Whitehead [MINOS Collaboration], Recent results from MINOS, Joint Experimental-Theoretical Seminar (24th June 2011, Fermilab, USA). Websites : theory.fnal.gov/jetp, http://www-numi.fnal.gov/pr plots/.

[8] G. Fogli, E. Lisi, A. Marrone, A. Palazzo, and A. Rotunno (2011), * Temporary entry *, 1106.6028.

[9] A. Bandyopadhyay *et al.* (ISS Physics Working Group), Rept.Prog.Phys. **72**, 106201 (2009), 0710.4947.

[10] J. M. Conrad and M. H. Shaevitz, Phys. Rev. Lett. **104**, 141802 (2010), 0912.4079.

[11] S. K. Agarwalla, P. Huber, J. M. Link, and D. Mohapatra, JHEP **1104**, 099 (2011), 1005.4055.

[12] J. Alonso *et al.* (2010), 1006.0260.

[13] S. K. Agarwalla and P. Huber, Phys. Lett. **B696**, 359 (2011), 1007.3228.

[14] J. R. Alonso (DAEdeltaALUS Collaboration) (2010), 1010.0971.

[15] L. Calabretta, M. Maggiore, L. A. C. Piazza, D. Rifuggiato, and A. Calanna (2010), 1010.1493.

[16] A. Calanna, L. Calabretta, M. Maggiore, L. A. C. Piazza, and D. Rifuggiato (2011), 1104.4985.

[17] S. K. Agarwalla, J. Conrad, and M. Shaevitz (2011), * Temporary entry *, 1105.4984.

[18] J. F. Beacom and M. R. Vagins, Phys.Rev.Lett. **93**, 171101 (2004), hep-ph/0309300.

[19] H. Watanabe *et al.* (Super-Kamiokande Collaboration) (2008), 0811.0735.

[20] S. Dazeley, A. Bernstein, N. Bowden, and R. Svoboda, Nucl.Instrum.Meth. **A607**, 616 (2009), 0808.0219.

[21] J. Cravens *et al.* (Super-Kamiokande Collaboration), Phys.Rev. **D78**, 032002 (2008), 0803.4312.

[22] C. Athanassopoulos *et al.* (LSND Collaboration), Nucl.Instrum.Meth. **A388**, 149 (1997), nucl-ex/9605002.

[23] M. Nakahata *et al.* (Super-Kamiokande Collaboration), Nucl.Instrum.Meth. **A421**, 113 (1999), hep-ex/9807027.

[24] V. Barger, M. Dierckxsens, M. Diwan, P. Huber, C. Lewis, *et al.*, Phys.Rev. **D74**, 073004 (2006), hep-ph/0607177.

DO SOLAR NEUTRINOS MIX WITH NEW STERILE SPECIES?

A. PALAZZO [a]
Cluster of Excellence, Origin and Structure of the Universe, Technische Universität München, Boltzmannstraße 2, D-85748, Garching, Germany

Several indications in favor of new light sterile neutrinos have recently emerged. Here, we discuss the constraints attainable from the solar sector data (solar and KamLAND) on the possible admixture of the electron neutrino with the new putative sterile species.

1 Introduction

The emergence of new anomalies in very-short baseline (VSBL) setups [1,2,3] and in cosmological data analyses [4,5,6,7] has given renewed interest to the theoretical and experimental study of light sterile neutrinos.

The new neutrino species must be introduced without spoiling the basic success of the standard 3-flavor paradigm. This can be realized in the so-called $3 + s$ schemes, where the s new mass eigenstates are assumed to be separated from the three standard ones by large splittings. With the additional assumption of small admixtures of the new sterile species with the three standard "active" neutrinos, such frameworks realize a genuine perturbation of the leading 3-flavor scenario.

The size of such a perturbation can be constrained by all the existing phenomenology and, in particular, the solar sector data (Solar and KamLAND) offer a sensitive probe of the admixture of the new sterile species with the electron neutrino. The role of new sterile species on the phenomenology of the solar neutrino sector has been investigated in several works. However, all the existing analyses have been performed in the simple framework developed in [8] of pure (ν_1-ν_2)-driven oscillations, which neglects the possible mixing of the electron neutrino with the third standard mass eigenstate ($U_{e3} = 0$) and with a new fourth one ($U_{e4} = 0$). In [9] we have recently extended the treatment of the MSW transitions to the most general case (see aslo [10]), also providing the first quantitative constraints on the amplitude of the matrix element U_{e4}. Here we show only the basic results of the numerical analysis, referring the reader to the original work [9] for the complete theoretical details.

2 Parameterization of the lepton mixing matrix

In the presence of a fourth sterile neutrino ν_s, the flavor (ν_α, $\alpha = e, \mu, \tau, s$) and the mass eigenstates ($\nu_i, i = 1, 2, 3, 4$), are connected through a 4×4 unitary mixing matrix U, which depends on six complex parameters [11]. Such a matrix can thus be expressed as the product of six complex elementary rotations, which define six real mixing angles and six CP-violating

[a] Email: antonio.palazzo@tum.de

phases. Of the six phases three are of the Majorana type and are unobservable in oscillation processes, while the three remaining ones are of the Dirac type. For simplicity, we set to zero all the Dirac phases referring the reader to [9] for comments on the potential sensitivity of the solar data to them.

For the treatment of the solar MSW transitions under study, it is convenient to parameterize the mixing matrix as

$$U = R_{23} R_{24} R_{34} R_{14} R_{13} R_{12} \tag{1}$$

where R_{ij} represents a real 4×4 rotation in the (i, j) plane. In such a parameterization, the elements involving the electron neutrino take the explicit expressions

$$U_{e1} = \; c_{14} c_{13} c_{12} \,, \tag{2}$$
$$U_{e2} = \; c_{14} c_{13} s_{12} \,, \tag{3}$$
$$U_{e3} = \; c_{14} s_{13} \,, \tag{4}$$
$$U_{e4} = \; s_{14} \,, \tag{5}$$

where $c_{ij} \equiv \cos\theta_{ij}, s_{ij} \equiv \sin\theta_{ij}$. In the numerical analysis we are going to present, we shall limit ourselves to the simple case $\theta_{24} = \theta_{34} = 0$. In this case, the following simple expressions hold for the mixing elements involving the sterile flavor

$$U_{s1} = \; -s_{14} c_{13} c_{12} \,, \tag{6}$$
$$U_{s2} = \; -s_{14} c_{13} s_{12} \,, \tag{7}$$
$$U_{s3} = \; -s_{14} s_{13} \,, \tag{8}$$
$$U_{s4} = \; c_{14} \,. \tag{9}$$

Therefore, for small values of θ_{13}, the new mixing angle θ_{14} induces a non-zero admixture U_{e4} of the electron neutrino with the fourth state and a non-null sterile content of the (ν_1, ν_2) "doublet", leaving the flavor composition of ν_3 almost unaltered respect to the standard case ($U_{s3} \sim 0$).

3 Numerical results

In our analysis we have included all the available solar data [12,13,14,15,16,17,18,19,20,21,22,23] with the exception of the SNO Low Energy Threshold Analysis [24], which can be used only under the assumption of unitary conversion among the active neutrino species ($P_{ee} + P_{e\mu} + P_{e\tau} = 1$), not valid in the presence of transitions into new sterile states. Concerning KamLAND, we have included in our analysis the latest data released in [25]. For definiteness, we have adopted the new improved reactor flux determinations [26]. In all numerical computations we have set $\theta_{24} = \theta_{34} = 0$. Therefore, the parameter space spanned by our analysis involves the solar mass-spliting Δm^2_{12} and the three mixing angles $(\theta_{12}, \theta_{13}, \theta_{14})$.

We start our numerical study considering the familiar three-flavor case ($\theta_{13} \neq 0, \theta_{14} = 0$), in which the results of the analysis depend on the three parameters $(\Delta m^2_{12}, \theta_{12}, \theta_{13})$. In the left panel of Fig. 1 we show the region allowed by solar (S) and KamLAND (K) in the plane spanned by the two mixing angles, having marginalized away the solar mass splitting in the region determined by KamLAND. Respect to previous analyses [27,28,29,30,31,25], the KamLAND data *taken alone* now tend to prefer values of $\theta_{13} > 0$ (see also [1,32]). This behavior can be traced to our adoption of the new (higher) reactor fluxes [26]. In fact, a larger value of θ_{13} is now required to suppress the bigger total rate induced by the new higher fluxes. Furthermore, similarly to previous analyses [27,28,29,30,31,25], for $\theta_{13} > 0$ the values of the mixing angle θ_{12} identified by the solar and KamLAND experiments are in better agreement due to the opposite-leaning correlations exhibited by their respective contours, giving rise to an enhanced preference

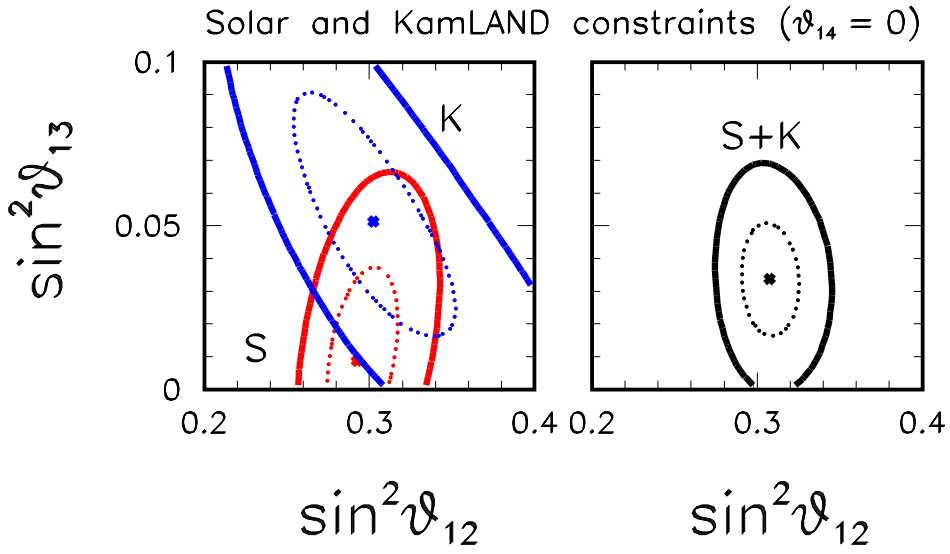

Figure 1: Region allowed in the $[\sin^2\theta_{12}, \sin^2\theta_{13}]$ plane for $\theta_{14} = 0$, after marginalization of Δm^2_{12} as constrained by KamLAND, separately (left panel) by solar (S) and KamLAND (K) data and by their combination (right panel). In both panels it has been set $\theta_{24} = \theta_{34} = 0$. The contours refer to $\Delta\chi^2 = 1$ (dotted line) and $\Delta\chi^2 = 4$ (solid line).

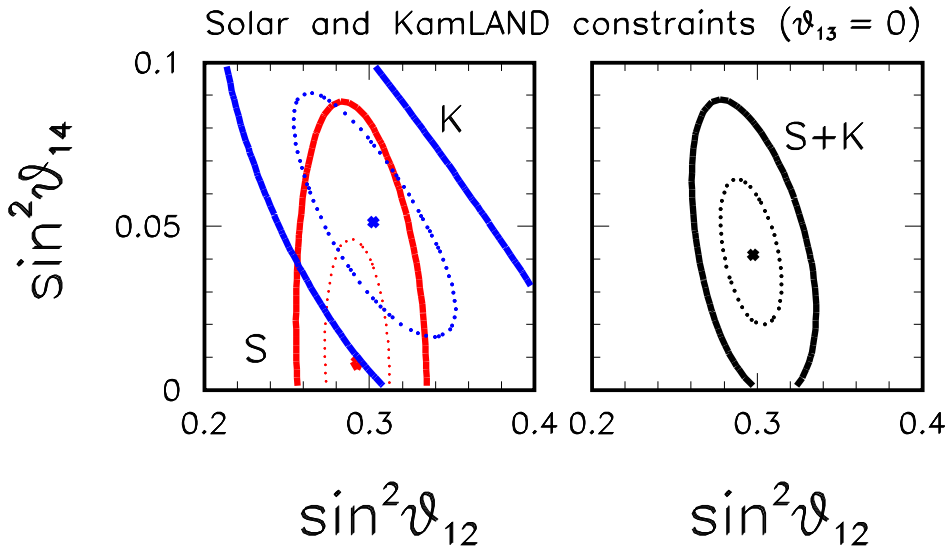

Figure 2: Region allowed in the $[\sin^2\theta_{12}, \sin^2\theta_{14}]$ plane for $\theta_{13} = 0$, after marginalization of Δm^2_{12} as constrained by KamLAND, separately (left panel) by solar (S) and KamLAND (K) data and by their combination (right panel). In both panels it has been set $\theta_{24} = \theta_{34} = 0$. The contours refer to $\Delta\chi^2 = 1$ (dotted line) and $\Delta\chi^2 = 4$ (solid line).

for non-zero θ_{13} in their combination (right panel). We find that the 2-flavor case ($\theta_{13} = 0$) is disfavored at the 1.8 σ level (which is reduced to 1.3 σ using the old reactor fluxes).

As as second step we switch on only the mixing angle θ_{14}, setting $\theta_{13} = 0$. In this case, the results of the analysis depend on the three parameters $(\Delta m^2_{12}, \theta_{12}, \theta_{14})$, whose allowed regions are displayed in Fig. 2. KamLAND cannot distinguish θ_{13} from θ_{14} and, as a result, the region

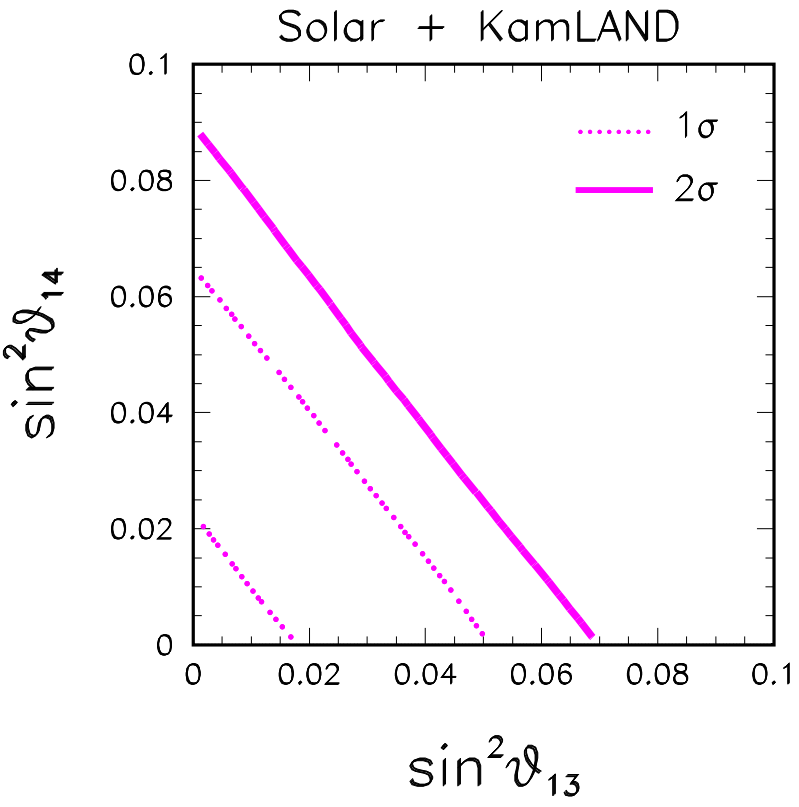

Figure 3: Region allowed, after marginalization of Δm^2_{12} and θ_{12}, by the combination of solar and KamLAND data (for $\theta_{24} = \theta_{34} = 0$). The contours refer to $\Delta\chi^2 = 1$ (dotted line) and $\Delta\chi^2 = 4$ (solid line).

identified by such an experiment is identical to that found in the 3-flavor case. In contrast, the region determined by the solar data is slightly different from the corresponding one identified in the 3-flavor case. In particular, we see that the correlation in the $[s^2_{12}, s^2_{14}]$ plane is different from that exhibited in the $[s^2_{12}, s^2_{13}]$ plane.

Furthermore, the following small differences appear between the two cases in the global combination: I) A weaker upper bound on θ_{14} ($s^2_{14} < 0.089$ at the 2σ level) with respect to that obtained for θ_{13} ($s^2_{13} < 0.070$ at the 2σ level); II) A slightly bigger best fit value for θ_{14} ($s^2_{14} = 0.041$) with respect to that obtained for θ_{13} ($s^2_{13} = 0.033$). It is interesting to note that the best fit value obtained for θ_{14} practically coincides with that indicated by the VSBL reactor and Gallium calibration anomalies taken in combination [1]. Therefore, combining the solar sector results with such data would reinforce their preference for non-zero θ_{14}, providing an overall indication, which we roughly estimate to be around the $\sim 4\sigma$ level.

As a third step, we have switched on both mixing angles ($\theta_{13} \neq 0, \theta_{14} \neq 0$). In Fig. 3 we show the region allowed by the combination of solar and KamLAND in the plane spanned by such two parameters, having marginalized away both the mass splitting Δm^2_{12} and the mixing angle θ_{12}. From this plot we see that there is a complete degeneracy among the two parameters. In practice, this dataset is basically sensitive to the combination $U^2_{e3} + U^2_{e4}$, the small deviations from this behavior being induced by the SNO neutral current measurement (see [9]). Therefore, the solar sector data, while indicating a weak preference for non-zero admixture of the electron neutrino with the "far" mass eigenstates ν_3 and ν_4, cannot distinguish between them.

4 Conclusions

Working in a CPT-conserving 3+1 scheme, we have considered the constraints attainable on the admixture of the electron neutrino with a fourth sterile neutrino specie. Our quantitative analysis shows that the present data posses a sensitivity to the amplitude of the lepton mixing matrix element U_{e4}, which is comparable to that achieved on the standard matrix element U_{e3}. In addition, our analysis evidences that, in a 4-flavor framework, the current preference for $|U_{e3}| \neq 0$ is indistinguishable from that for $|U_{e4}| \neq 0$, having both a similar statistical significance, which is $\sim 1.3\sigma$ adopting the old reactor fluxes determinations, and $\sim 1.8\sigma$ using their new estimates.

5 Acknowledgments

Our work is supported by the DFG Cluster of Excellence on the "Origin and Structure of the Universe".

References

1. G. Mention *et al.*, [arXiv:1101.2755 [hep-ex]].
2. J. N. Abdurashitov *et al.*, Phys. Rev. C **73**, 045805 (2006) [arXiv:nucl-ex/0512041].
3. C. Giunti, M. Laveder, [arXiv:1006.3244 [hep-ph]].
4. J. Hamann, S. Hannestad, G. G. Raffelt, I. Tamborra and Y. Y. Y. Wong, Phys. Rev. Lett. **105**, 181301 (2010) [arXiv:1006.5276 [hep-ph]].
5. E. Giusarma *et al.*, [arXiv:1102.4774 [astro-ph.CO]].
6. Y. I. Izotov, T. X. Thuan, Astrophys. J. **710**, L67-L71 (2010) [arXiv:1001.4440 [astro-ph.CO]].
7. G. Mangano and P. D. Serpico, arXiv:1103.1261 [astro-ph.CO].
8. D. Dooling, C. Giunti, K. Kang, C. W. Kim, Phys. Rev. D **61**, 073011 (2000) [hep-ph/9908513].
9. A. Palazzo, [arXiv:1105.1705 [hep-ph]], accepted for publication in Phys. Rev. D.
10. C. Giunti and Y. F. Li, Phys. Rev. D **80**, 113007 (2009) [arXiv:0910.5856 [hep-ph]].
11. J. Schechter, J. W. F. Valle, Phys. Rev. D **22**, 2227 (1980).
12. B. T. Cleveland *et al.*, Astrophys. J. **496**, 505 (1998).
13. J. N. Abdurashitov *et al.* (SAGE Collaboration), J. Exp. Theor. Phys. **95**, 181 (2002).
14. W. Hampel *et al.* (GALLEX Collaboration), Phys. Lett. B **447**, 127 (1999).
15. M. Altmann *et al.* (GNO Collaboration), Phys. Lett. B **616**, 174 (2005).
16. T. Kirsten, J. Phys. Conf. Ser **120**, 052013 (2008).
17. S. Fukuda *et al.* (Super-Kamiokande Collaboration), Phys. Rev. Lett. **86**, 5651 (2001); **86**, 5656 (2001); Phys. Lett. B **539**, 179 (2002).
18. Q. R. Ahmad *et al.* (SNO Collaboration), Phys. Rev. Lett. **87**, 071301 (2001); **89**, 011301 (2002); **89**, 011302 (2002).
19. S. N. Ahmed *et al.* (SNO Collaboration), Phys. Rev. Lett. **92**, 181301 (2004).
20. B. Aharmim *et al.* (SNO Collaboration), Phys. Rev. C **72**, 055502 (2005).
21. B. Aharmim *et al.* (SNO Collaboration), Phys. Rev. Lett. **101**, 111301 (2008).
22. G. Bellini *et al.* (Borexino Collaboration), [arXiv:1104.1816 [hep-ex]].
23. G. Bellini *et al.* (Borexino Collaboration), Phys. Rev. D **82**, 033006 (2010).
24. B. Aharmim *et al.* (SNO Collaboration), Phys. Rev. C **81**, 055504 (2010).
25. A. Gando *et al.* (KamLAND Collaboration), Phys. Rev. D **83**, 052002 (2011) [arXiv:1009.4771 [hep-ex]].
26. T. A. Mueller *et al.*, [arXiv:1101.2663 [hep-ex]].

27. G. L. Fogli, E. Lisi, A. Marrone, A. Palazzo and A. M. Rotunno, Phys. Rev. Lett. **101**, 141801 (2008) [arXiv:0806.2649 [hep-ph]].
28. A. B. Balantekin and D. Yilmaz, J. Phys. G **35**, 075007 (2008).
29. T. Schwetz, M. Tortola and J. W. F. Valle, New J. Phys. **10**, 113011 (2008).
30. H. L. Ge, C. Giunti and Q. Y. Liu, Phys. Rev. D **80**, 053009 (2009).
31. M. C. Gonzalez-Garcia, M. Maltoni and J. Salvado, JHEP **1004**, 056 (2010) [arXiv:1001.4524 [hep-ph]].
32. T. Schwetz, M. Tortola, J. W. F. Valle, [arXiv:1103.0734 [hep-ph]].

Flavour puzzle or Why neutrinos are different?

M. Libanov[a] and F.-S. Ling[b]
[a] *Institute for Nuclear Research of the Russian Academy of Sciences, 60th October Anniversary Prospect, 7a, 117312 Moscow, Russia*
[b] *Institute of Theoretical Physics, Chinese University of Hong Kong*

We present a short review of a 6-dimensional model where a flavour puzzle of the Standard Model fermions finds an elegant solution. The mechanism is based on an idea that the three fermionic generations originate from a single 6D family. The model explains in a natural way both charged fermions mass hierarchy and small mixings in the quark sector, and tiny neutrino masses and large neutrino mixings. We also discuss some phenomenological aspects of the model which can distinguish this class of the models from another one and can help to look for manifestations of new physics at colliders and other experiments.

1 Introduction

One of the most intriguing issues of the Standard Model (SM) is a flavour puzzle which can be formulated as the following three problems:

- *Problem of families replication and mass hierarchy:* Why are there three families of fermions in the SM? In particular, why are these generations differing only by masses and why is this difference so large ($m_{\rm top}/m_{\rm up} \sim 10^4$)? Why are mixings in the quark sector relatively small and why is the mixing between first and third generations suppressed compare to the mixings between adjacent generations?

- *Neutrino mass problem:* Why do neutrinos have tiny masses and large mixings? Why neutrinos are so different from charged fermions?

- *Flavour-changing neutral currents (FCNC) problem:* Why we do not observe "horizontal" inter-generation transitions?

This paper is a short review of existing works.[1–9] In these papers in the frameworks of "large extra dimensions" (LED) (see Ref.[10] for a review) an elegant solution to the flavour puzzle has been suggested. The basic idea is an assumption that *three* generations of SM fermions appear as three zero modes of *single* multi-dimensional vector-like (with respect to SM gauge group) family. In the current review we concentrate on main points and basic ideas of the model at the cost of loss of mathematical rigor. For more complete and more advanced details the Reader is directed to the original works.

Fields		Profiles	Charges		Representations	
			$U_g(1)$	$U_Y(1)$	$SU_W(2)$	$SU_C(3)$
scalar	Φ	$F(\theta)\mathrm{e}^{i\varphi}$ $F(0)=0,\ F(\pi)\simeq v$	$+1$	0	**1**	**1**
vector	A_φ	$A(\theta)/e$ $A(0)=0,\ A(\pi)=1$	0	0	**0**	**0**
scalar	X	$X(\theta)$ $X(0)=v_X,\ X(\pi)=0$	$+1$	0	**1**	**1**
scalar	H	$H(\theta)$ $H_i(0)=\delta_{2i}v_H,\ H_i(\pi)=0$	-1	$+1/2$	**2**	**1**
fermion	Q	3 L zero modes	axial $(3,0)$	$+1/6$	**2**	**3**
fermion	U	3 R zero modes	axial $(0,3)$	$+2/3$	**1**	**3**
fermion	D	3 R zero modes	axial $(0,3)$	$-1/3$	**1**	**3**
fermion	L	3 L zero modes	axial $(3,0)$	$-1/2$	**2**	**1**
fermion	E	3 R zero modes	axial $(0,3)$	-1	**1**	**1**
fermion	N	Kaluza-Klein spectrum, no zero mode	0	0	**1**	**1**
SM gauge bosons	γ, G $Z, W^\pm$	Kaluza-Klein spectrum starting from zero	0	–	–	–

Table 1: Field content of the model. For convenience, we describe here also the fields profiles in extra dimensions. θ and φ are the polar and the azimuthal angles on the sphere, respectively. The vortex is localized at $\theta = 0$.

2 The Setup

Suppose one has single fermionic generation in a multi-dimensional theory. Let us consider a topological defect whose core corresponds to our four-dimensional world. Chiral fermionic zero modes may be trapped in the core due to specific interaction with the fields which build up the defect. In some cases, the index theorem guarantees that the number of chiral zero modes is determined by the topological number of the defect and by the charge of the fermion with respect to the symmetry group of the fields forming the defect. We use this property to obtain three fermionic generations localized on a defect while having only one generation in the bulk. If the Brout-Englert-Higgs scalar couples to the defect, it can also be trapped in the core. Hierarchy between masses of three fermionic modes arises due to their different profiles in extra dimensions.[1] [2] [3]

To be specific, let us assume that there are two large additional dimensions.[a] The topological defect is an gauge vortex. A principal issue of models with LED is the localization of the SM gauge fields. One of possible ways to avoid this problem is to consider the transverse extra dimensional space as a compact manifold and to allow gauge fields to propagate freely in the extra dimensions. In what follows we assume that the extra dimensions form a two dimensional sphere with radius R.[4] Though gravity is not included in the consideration, it should be stressed that the choice of the manifold is not important for our principal conclusions.[5] The extra dimensions can even be infinitely large. In this case, the role of the radius R of the sphere is taken by a typical size of the localized gauge zero modes but *not* by a size of the extra dimensions.

The matter field content of the model is summarized in Table 1 and the profiles of the relevant fields are sketched in Fig 1. The scalar field Φ, together with $U(1)_g$ gauge field, forms a vortex, while two other scalars, X and H, develop profiles localized on the vortex. There is *one* fermionic generation which consists of five six-dimensional fermions Q, U, D, L, and E.

[a] The number of extra dimensions may be larger than two. What we in fact assume is that the size of another additional dimensions much smaller than the size of the two dimensions under consideration.

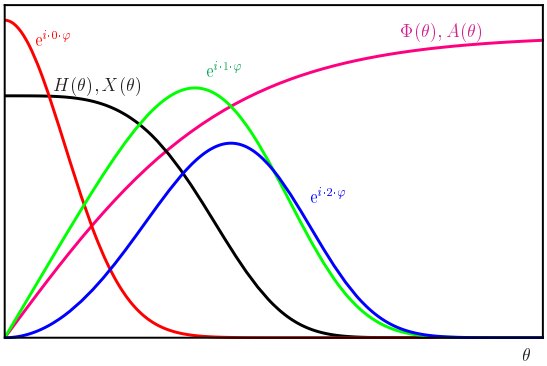

Figure 1: Sketch of the relevant background fields profiles (black and pink) and the fermionic zero modes (red, green and blue). The latter are labeled by their φ-dependencies.

Each of the fermions develops, in the vortex background, three chiral zero modes localized in the core of the vortex, which correspond to three generations of the SM fermions. There is an additional fermion N which is neutral both under $U(1)_g$ and SM gauge group. This fermion is not localized and its Kaluza-Klein (KK) modes play a role of sterile neutrinos.

The spinor-scalar couplings, responsible for the localization of the fermionic zero modes, are[b]

$$\begin{aligned}
&\sum_{\Psi=Q,L} g_\Psi \Phi^3 \bar{\Psi} \frac{1-\Gamma_7}{2} \Psi + \text{h.c.} \quad \longrightarrow \quad \text{3 left handed zero modes} \\
&\sum_{\Psi=U,D,E} g_\Psi \Phi^3 \bar{\Psi} \frac{1+\Gamma_7}{2} \Psi + \text{h.c.} \quad \longrightarrow \quad \text{3 right handed zero modes}
\end{aligned} \tag{1}$$

This coupling may look surprising, as it is obviously non-renormalisable in 4 dimensions. We are not considering renormalisability of the theory here, as the 6-dimensional context is most likely an effective model, but even in this case it might be suitable that the 4-dimensional reduction be renormalisable.

What is important here is that three fermionic zero modes localized in the vortex background have different generalized (supplemented by $U(1)_g$ global rotations) angular momentum[4] and, as a result, have different φ and θ-dependencies. Typically, one has

$$\Psi_n(\theta,\varphi) \sim f_n(\theta) e^{i(3-n)\varphi} , \qquad n = 1,2,3 , \tag{2}$$

with the θ-dependent wave functions $f_n(\theta)$ behaving near the origin as:

$$f_n(\theta) \sim \theta^{3-n} , \qquad \theta \to 0 . \tag{3}$$

3 Mass hierarchy and mixings

The couplings (1) are responsible only for the localization of the fermionic zero modes. From the 4-dimensional point of view these modes describe localized *massless* chiral fermions with the usual quantum numbers under SM gauge group. Now comes the time to generate the "usual" fermion masses, and to break the $SU(3) \times SU(2) \times U(1)$ symmetry. This is done in the usual way, through the Brout-Englert-Higgs mechanism, at the price of introducing a scalar doublet, which we name H. In fact, for the purpose of separating the various quantum numbers, we write (e.g., for the "down" quarks), instead of the usual coupling:

$$\mathcal{L}_{\text{Yukawa}} = Y_d H X \bar{Q} \frac{1-\Gamma_7}{2} D + \varepsilon_d Y_d H \Phi \bar{Q} \frac{1-\Gamma_7}{2} D + \text{h.c.} , \tag{4}$$

[b] We use the chiral representation for the six-dimensional Dirac Γ-matrices (see Ref.[1] for notations). In particular, $\Gamma_7 = \text{diag}(\mathbf{1}, -\mathbf{1})$ is a six-dimensional analog of the four-dimensional γ_5.

where Y_d and $\varepsilon_d Y_d$ are coupling constants, the vortex scalar Φ has winding number 1 (see Table 1), while X and H have non-vanishing values at $\theta = 0$ and zero winding number.

The reduction to 4 dimensions involves integration over φ and θ and generates the mass terms. The first term in (4) yields

$$m^{(1)}_{D,nm} \propto \int\limits_0^\pi d\theta \sin\theta \int\limits_0^{2\pi} d\varphi f^\dagger_{Q,n} f_{D,m} X(\theta) H(\theta) \mathrm{e}^{i(n-m)\varphi} \ . \tag{5}$$

Clearly, the integration over φ guarantees that only diagonal entries occur. The integral over θ is saturated near the origin, more precisely, in the region where the fields H and X are non-zero. This region coincides, as it is shown in Fig. 1, with the region $[0, \theta_\Phi]$ where Φ is appreciably different from its VEV.[3,6] In this region one can safely use Eq. (3) for the fermionic wave functions and finds[4]

$$m^{(1)}_{D,nm} \sim \delta_{nm} \sigma^{2(3-n)} \ , \tag{6}$$

where $\sigma = \theta_\Phi / \theta_A$ and $\theta_A \sim 1$ is the typical size of the gauge field of the vortex.

Due to the non-trivial φ-dependence of Φ the second term in (4) results in non-diagonal elements of the mass matrix:

$$m^{(2)}_{D,nm} \sim \varepsilon_d \delta_{n+1,m} \sigma^{2(3-n)-1} \tag{7}$$

The mass eigenstates are obtained by diagonalization (6), (7) and the power-like hierarchical mass pattern

$$m_{33} : m_{22} : m_{11} = 1 : \sigma^2 : \sigma^4$$

arises at $\sigma \simeq 0.1$. The CKM-matrix has the form

$$U^{\mathrm{CKM}} \sim \begin{pmatrix} 1 & \sigma & \sigma^4 \\ \sigma & 1 & \sigma \\ \sigma^2 & \sigma & 1 \end{pmatrix}$$

and reproduces observed mixings in the quark sector of the SM.

4 Neutrinos masses. Why are they different?

Now we want to consider whether the scheme can be extended to accommodate mass and mixing data in the neutrino sector. An obvious possibility to generate neutrino masses would be to treat them exactly like the charged fermions, with a Dirac mass obtained at the cost of introducing a 6D field N, bound to the vortex, and from which the three families of 4D right-handed neutrinos emerge. However, this possibility does not offer a natural explanation for the smallness of the neutrino masses, which in this case require tiny coefficients in the Lagrangian.

It is therefore tempting to consider other solutions, namely the case where the "right hande" neutrino field is *NOT* bound to the vortex. In the context of models with LED, tiny neutrino masses are often the result of a dilution effect: the field that provides right hande neutrinos, being singlet under the SM gauge group, can be non-localized, and therefore have a small overlap with the wave function of SM fields. A first attempt using a non-localized field N was made in Ref.[7] However, that approach predicts a neutrino mixing pattern that differs significantly from the observed one.

Here we consider another possibility.[9] We assume that spinor N is a gauge singlet both under SM and $U(1)_g$ gauge group. It means first of all, that it can freely propagate in the extra dimensions. Secondly, one can (and, in general, have to) write a Majorana-like mass term in 6D for it:

$$\frac{M}{2}(\bar{N}^c N + \bar{N} N^c).$$

From 4-dimensional point of view one has KK tower of fermions possessing 4D Majorana mass M and different Dirac masses starting from $1/R$.[c]

Thirdly, the gauge invariance allows one to introduce the following couplings ($\tilde{H} = i\sigma_2 H^*$)

$$\sum_{S_+} Y^+_{\nu,S_+} \tilde{H} S_+ \bar{L} \frac{1+\Gamma_7}{2} N + \sum_{S_-} Y^-_{\nu,S_-} \tilde{H} S_- \bar{L} \frac{1-\Gamma_7}{2} N + \text{h.c.} \quad ,$$

where S_+ and S_- have $U(1)_g$ gauge charges 1 and -2, respectively, and can be[d]

$$\begin{aligned} S_+ &= X^*,\ \Phi^*,\ X^{*2}\Phi,\ \ldots \\ S_- &= X^2,\ X\Phi,\ \Phi^2,\ \ldots \end{aligned} \tag{8}$$

In 4D these couplings give rise to mixings between heavy modes of N and zero modes of active SM neutrinos. Together with the Majorana mass of modes of N it winds up a "see-saw" mechanism yielding tiny Majorana masses of the active neutrinos. The resulting neutrino mass matrix can be schematically written in the form:

$$m^\nu_{mn} \sim \int_0^\pi d\theta \int_0^{2\pi} d\varphi F(\theta,\varphi) \bar{L}^c_n L_m \ , \tag{9}$$

where $F(\theta,\varphi)$ is determined by $S_\pm$ as well as by wave functions of N. The main point and the main difference from the quark sector (see Eq. (5)) is the presence *charge conjugated* spinor in the integrand: $\bar{L}^c \sim L^T$. This leads to completely different from (6), (7) selection rules. For instance, if we restricted ourselves by φ-independent $S_\pm$ (the first structures in (8)) then F does not depend on φ, and one has

$$m^\nu_{mn} \sim \int_0^{2\pi} d\varphi \mathrm{e}^{i(4-n-m)\varphi} \sim \delta_{n,4-m} \sim \begin{pmatrix} \cdot & \cdot & 1 \\ \cdot & \sigma^2 & \cdot \\ 1 & \cdot & \cdot \end{pmatrix} \tag{10}$$

The inclusion of the φ-dependent structures in (8) gives rise to non-zero off secondary diagonal elements which have at least an order of σ.

What are consequences of the mass pattern (10)? The neutrino mass matrix (10) is diagonalized by a matrix with the structure

$$U_\nu \sim \begin{pmatrix} 1/\sqrt{2} & 1/\sqrt{2} & \sigma \\ \sigma & \sigma & 1 \\ -1/\sqrt{2} & 1/\sqrt{2} & \sigma \end{pmatrix} + \mathcal{O}(\sigma^2) \ .$$

Let us emphasize that the large mixing angle in the 1–3 block is maximal up to σ^2 corrections. When the charged lepton mass matrix contains a large mixing angle in the 2–3 block, this model predicts two large mixing angles, as observed. The remaining small mixing angle U_{e3}, which corresponds to the weight of the lightest mass eigenstate in the electronic neutrino, is predicted to be of order $\sigma \sim 0.1$.

The diagonalized neutrino mass matrix has the inverted hierarchy pattern diag$(m+\mathcal{O}(\sigma^2), -m+\mathcal{O}(\sigma^2), m\sigma^2)$. Therefore, this model naturally predicts a hierarchy in the mass squared splittings relevant in neutrino oscillation experiments $\Delta m^2_{12}/\Delta m^2_{13} \sim \sigma^2 \sim 0.01$, in good agreement with the observed data $\Delta m^2_{12}/\Delta m^2_{13} \simeq 3.2\%$. Moreover, m_1 and m_2 form a "pseudo-Dirac" pair as $m_1 + m_2 \sim \sigma^2 m$. It leads to a partial cancellation in the effective Majorana mass, $|\langle m_{\beta\beta}\rangle| = |\sum_i m_i U^2_{ei}| \simeq 1/3\sqrt{\Delta m^2_{13}}$, defining the amplitude for neutrinoless double-beta decay.

[c] It is worth noting that a possible 6D Dirac mass term does not play any role and translates to a shift of 4D Dirac mass spectrum. This is the reason why we do not consider it.

[d] In the quark sector (Sec. 3) we restricted ourselves to considering $S_+ = \Phi^*, X^*$ only. The reason is that an inclusion of more composite structures (e.g., S_-) does not play any significant role.

5 FCNC

From the 4D point of view the presented model completely reproduces all properties of SM if one considers zero modes only (including zero modes of the SM gauge fields). In particular, all FCNC processes are strongly suppressed as it occurs in SM. However, from the 6D point of view we have only a single generation and there is no difference, say, between μ and e. That is, heavy (non-zero) modes of the neutral SM gauge bosons can (and have to) violate flavour and/or lepton numbers. Nevertheless, without account of inter-generation mixings, the generalized angular momentum or, what is the same, the generation number G is exactly conserved. This forbids all processes with nonzero change of G; the probabilities of the latters in the full theory are thus suppressed by powers of the mass-matrix mixing parameter, $(\varepsilon\sigma)^{2\Delta G}$. However, the amplitudes of processes with $\Delta G = 0$ but lepton and quark flavours violated separately are suppressed only by the mass squared of the KK modes of the SM gauge bosons.

In Ref.[5] the following specific flavour violating processes have been studied:

- $\Delta G = 0$: $K_L^{0\to} \to \mu e$, $K^+ \to \pi^+ e^- \mu^+$;
- $\Delta G = 1$: $\mu \to e\gamma$, $\mu \to 3e$, $\mu \to e$-conversion;
- $\Delta G = 2$: $K_L - K_S$ mass difference and CP violation in kaons.

These processes are known to give the strongest constraints on masses and couplings of new vector bosons. It was found that indeed the pattern of flavour violation is distinctive: contrary to other models, processes with change of the generation number G by one or two units are strongly suppressed compared to other rare processes. The strongest constraint on the model arises from non-observation of the decay $K^0 \to \mu e$; it requires that the size of the sphere (size of the gauge-boson localization) R satisfies $\varkappa/R \gtrsim 64$ TeV, where $\varkappa$ is a dimensionless parameter depending on specific model: details of the geometry, mechanism of the localization of the vector fields, and so on. A clear signature of the model would be an observation of $K^0 \to \mu e$ decay without observation of $\mu \to 3e$, $\mu \to e\gamma$ and μe-conversion at the same precision level.

For the spherical model under discussion $\varkappa = 1$. However, in general one can expect that $\varkappa$ can differ from unit and can be small enough ($\varkappa \sim 0.01$). In the latter case the masses of the first non-zero excitations of the SM gauge bosons $M' \simeq 1/R$ can be of order of few TeV and vector bosons can, in principle, be observed at colliders. In general, there are two possibilities. First of all, one can try to search for "usual" heavy vector bosons, that is the heavy KK modes which do not change generation number. The second possibility is to look for heavy KK vector bosons due to the flavour-changing decay modes into (μe) or $(\mu\tau)$ pairs. The flavour-changing decays of this kind have a distinctive signature: antimuon and electron (or their antiparticles) with equal and large transverse momenta in the final state.

The latter possibility has been investigated in Ref.[8] In particular, it was found for the expected LHC value of 100fb^{-1} for luminosity and $\sqrt{s} = 14$TeV that the number of $pp \to \mu^+ e^-$ events varies from 1 to 10 per year for $M' \simeq 3 \div 1$TeV. The probability of the production $(\mu^- e^+)$ pairs is approximately ten times smaller due to the former process can use valence u and d-quarks in the proton, while the second only involves partons from the sea. The same numbers are representative also for the $(\mu\tau)$ channels.

There are also other signatures of FCNC effects, in particular, with hadronic final states, when $(\bar{t}, c)$ or $(\bar{b}, s)$ jets are produced. The dominant contribution to these processes arises from the interactions with higher KK modes of gluons, which have large coupling constant. For the mass of $M' = 1$TeV the number of events has been estimated as $N = 1.2 \cdot 10^3$. But potentially large SM backgrounds should be carefully considered for such channels.

6 Conclusions

To conclude, we presented a possible elegant solution to the flavour puzzle. The mechanism is based on an assumptions that the *three* SM generations originate from a *single* family in a higher-dimensional theory. The generation number is none other than angular momentum and, therefore, has an geometrical origin.

We explained why neutrinos are different from the sector of the charged fermions. A light neutrino mass matrix where one mixing angle is automatically maximal and where the eigenvalues obey an inverted hierarchy with a pseudo-Dirac pattern for the heavier states $m_1 \simeq -m_2 \gg m_3$ is a result of a mixing between active neutrinos and a single heavy sterile 6D fermion with *Majorana-like* mass.

The 6D Lagrangian with one generation contains much less parameters than the effective one. All masses and mixings of the SM fermions are governed by a few parameters of order one. This fact allows for specific phenomenological predictions. In particular, the KK modes of the vector bosons mediate flavour-violating processes. The pattern of flavour violation is distinctive: contrary to other models, processes with change of the generation number by one or two units are strongly suppressed compared to other rare processes. The strongest constraint on the model arises from non-observation of the decay $K \to \mu e$; it requires that the size of the extra-dimensional sphere (size of the gauge-boson localization) satisfies $1/R \gtrsim 64$ TeV. The KK modes of vector bosons have larger masses, but for large enough R, could be detected by precision measurements at colliders.

One more point which we did not discuss in this review is a Brout-Englert-Higgs boson properties. The model predicts that its mass can not be much larger then 100 GeV.[6]

Acknowledgments

Many thanks to the conference organizers for the invitation. We wish to thank very warmly our colleagues J.-M. Frere, E. Nugaev and S. Troitsky for our ongoing collaboration. The work of M.L. has been supported in part by the Federal Agency for Science and Innovations under state contract 02.740.11.0244, by the grant of the President of the Russian Federation NS-5525.2010.2, by the RFBR grants 11-02-08018 and 11-02-92108, and by the Dynasty Foundation.

References

1. M. V. Libanov and S. V. Troitsky, Nucl. Phys. B **599**, 319 (2001).
2. J. M. Frere, M. V. Libanov and S. V. Troitsky, Phys. Lett. B **512**, 169 (2001).
3. M. V. Libanov and E. Y. Nougaev, JHEP **0204**, 055 (2002); Surveys High Energ. Phys. **17** (2002) 165.
4. J. M. Frere, M. V. Libanov, E. Y. Nugaev and S. V. Troitsky, JHEP **0306**, 009 (2003).
5. J. M. Frere, M. V. Libanov, E. Y. Nugaev and S. V. Troitsky, JHEP **0403**, 001 (2004).
6. M. V. Libanov and E. Y. Nugaev, Phys. Atom. Nucl. **70**, 864 (2007) [Yad. Fiz. **70**, 898 (2007)] [arXiv:hep-ph/0512223].
7. J. M. Frere, M. V. Libanov and S. V. Troitsky, JHEP **0111**, 025 (2001).
8. J. M. Frere, M. V. Libanov, E. Y. Nugaev and S. V. Troitsky, JETP Lett. **79**, 598 (2004) [Pisma Zh. Eksp. Teor. Fiz. **79**, 734 (2004)] [arXiv:hep-ph/0404139].
9. J. M. Frere, M. Libanov and F. S. Ling, JHEP **1009**, 081 (2010).
10. V. A. Rubakov, Phys. Usp. **44**, 871 (2001) [Usp. Fiz. Nauk **171**, 913 (2001)] [arXiv:hep-ph/0104152].

TRANSITION RADIATION BY STANDARD MODEL NEUTRINOS AT AN INTERFACE

A. N. IOANNISIAN[a,b,c], D. A. IOANNISIAN[c,d], N. A. KAZARIAN[c],
[a] *Yerevan Physics Institute, Alikhanian Br. 2, 375036 Yerevan, Armenia*
[b] *CERN, Theory Division, CH-1211 Geneva 23, Switzerland*
[c] *Institute for Theoretical Physics and Modeling, 375036, Yerevan, Armenia*
[d] *Physics Department, Yerevan State Univesrity, 1 Alex Manoogian, Armenia*

We discuss the transition radiation process $\nu \to \nu\gamma$ at an interface of two media. The medium fulfills the dual purpose of inducing an effective neutrino-photon vertex and of modifying the photon dispersion relation. The transition radiation occurs when at least one of those quantities have different values in different media. We present a result for the probability of the transition radiation which is both accurate and analytic. For $E_\nu = 1$MeV neutrino crossing polyethylene-vacuum interface the transition radiation probability is about 10^{-39} and the energy intensity (deposition) is about 10^{-34}eV. At the surface of the neutron stars the transition radiation probability may be $\sim 10^{-20}$. Our result on three orders of magnitude is larger than the results of previous calculations.

1 Introduction

In many astrophysical environments the absorption, emission, or scattering of neutrinos occurs in media, in the presence of magnetic fields [1] or at the interface of two media.

In the presence of a media, neutrinos acquire an effective coupling to photons by virtue of intermediate charged particles. The violation of the translational invariance at the direction from one media into another leads to the non conservation of the momentum at the same direction so that transition radiation becomes kinematically allowed.

The theory of the transition radiation by charged particle has been developed in [2,3]. It those articles authors used classical theory of electrodynamics. In [4] the quantum field theory was used for describing the phenomenon. The neutrinos have very tiny masses. Therefore one has to use the quantum field theory approach in order to study transition radiation by neutrinos.

The presence of a magnetic field induces an effective ν-γ-coupling. The Cherenkov decay in a magnetic field was calculated in [5].

At the interface of two media with different refractive indices the transition radiation $\nu \to \nu\gamma$ was studied in [6] with an assumption of existence of large (neutrino) magnetic dipole moment.

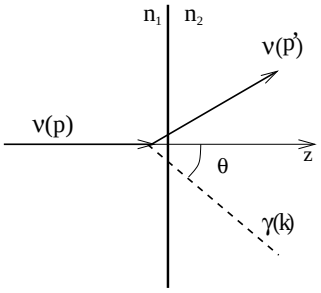

Figure 1: Transition radiation by neutrino at an interface of two media with refractive indexes n_1 and n_2.

We presently extend previous studies of the transition radiation to neutrinos with only standard-model couplings. The media changes the photon dispersion relation. In addition, the media causes an effective ν-γ-vertex by standard-model neutrino couplings to the background electrons. We neglect neutrino masses and medium-induced modifications of their dispersion relation due to their negligible role. Therefore, we study the transition radiation entirely within the particle-physics standard model.

A detailed literature search reveals that neutrino transition radiation has been studied earlier in [7]. They used vacuum induced ν-γ vertex ("neutrino toroid dipole moment") for the $\nu \to \nu\gamma$ matrix element. We do not agree with their treatment of the process. The media itself induces ν-γ vertex. The vacuum induced vertex can be treated as a radiation correction to the medium induced one. We found that the result of [7] for the transition radiation rate is more than three orders of magnitude, $(\frac{8\alpha}{\pi})^2$, smaller than our result.

2 Transition Radiation

Let us consider a neutrino crossing the interface of two media with refraction indices n_1 and n_2 (see Fig. 1). In terms of the matrix element $\mathcal{M}$ the transition radiation probability of the process $\nu \to \nu\gamma$ is

$$W = \frac{1}{(2\pi)^3}\frac{1}{2E\beta_z}\int \frac{d^3\mathbf{p}'}{2E'}\frac{d^3\mathbf{k}}{2\omega}\sum_{pols}\left|\int_{-\infty}^{\infty} dz e^{i(p_z - p'_z - k_z)z}\mathcal{M}\right|^2 \delta(E - E' - \omega)\delta(p'_x + k_x)\delta(p'_y + k_y)\ . \quad (1)$$

Here, $p = (E, \mathbf{p})$, $p' = (E', \mathbf{p}')$, and $k = (\omega, \mathbf{k})$ are the four momenta of the incoming neutrino, outgoing neutrino, and photon, respectively and $\beta_z = p_z/E$. The sum is over photon polarizations.

We shall neglect the neutrino masses and the deformation of its dispersion relations due to the forward scattering. Thus we assume that the neutrino dispersion relation is precisely light-like so that $p^2 = 0$ and $E = |\mathbf{p}|$.

The formation zone length of the medium is

$$|p_z - p'_z - k_z|^{-1}. \quad (2)$$

The integral over z in eq. (1) oscillates beyond the length of the formation zone. Therefore the contributions to the process from the depths over the formation zone length may be neglected.

The z momentum $(p_z - p'_z - k_z)$ transfers to the media from the neutrino. Since photons propagation in the media suffers from the attenuation(absorption) the formation zone length must be limited by the attenuation length of the photons in the media when the later is shorter than the formation zone length.

After integration of (1) over $\mathbf{p'}$ and z we find

$$W = \frac{1}{(2\pi)^3}\frac{1}{8E\beta_z}\int \frac{|\mathbf{k}|^2 d|\mathbf{k}|}{\omega E'\beta'_z}\ \sin\theta\ d\theta\ d\varphi \sum_{pols}\left|\frac{\mathcal{M}^{(1)}}{p_z - p_z'^{(1)} - k_z^{(1)}} - \frac{\mathcal{M}^{(2)}}{p_z - p_z'^{(2)} - k_z^{(2)}}\right|^2, \qquad (3)$$

where $\beta'_z = p'_z/E'$, θ is the angle between the emitted photon and incoming neutrino. $\mathcal{M}^{(1,2)}$ are matrix elements of the $\nu \to \nu\gamma$ in each media. $k_z^{(i)}$ and $p_z'^{(i)}$ are z components of momenta of the photon and of the outgoing neutrino in each media.

As it will be shown below main contribution to the process comes from large formation zone lengths and ,thus, small angle θ. Therefore the rate of the process does not depend on the angle between the momenta of the incoming neutrino and the boundary surface of two media (if that angle is not close to zero). The integration over φ drops out and we may replace $d\varphi \to 2\pi$. $k_z^{(i)}$ and $p_z'^{(i)}$ have the forms

$$k_z^{(i)} = n^{(i)}\omega\cos\theta, \quad p_z'^{(i)} = \sqrt{(E-\omega)^2 - {n^{(i)}}^2\omega^2\sin^2\theta}\ , \qquad (4)$$

here we have used $n^{(1,2)} = |\mathbf{k}|^{(1,2)}/\omega$.

If the medium is isotropic and homogeneous the polarization tensor, $\pi^{\mu\nu}$, is uniquely characterized by a pair of two polarization functions which are often chosen to be the longitudinal and transverse polarization functions. They can be projected from the full polarization matrix. In this paper we are interested in transverse photons, since they may propagate in the vacuum as well. The transverse polarization function is

$$\pi_t = \frac{1}{2}T_{\mu\nu}\pi^{\mu\nu},\ T^{\mu\nu} = -g^{\mu i}(\delta_{ij} - \frac{\mathbf{k}_i\mathbf{k}_j}{\mathbf{k}^2})g^{j\nu}. \qquad (5)$$

The dispersion relation for the photon in the media is the location of its pole in the effective propagator (which is gauge independent)

$$\frac{1}{\omega^2 - \mathbf{k}^2 - \pi_t} \qquad (6)$$

3 Neutrino-photon vertex

In a media, photons couple to neutrinos via interactions to electrons by the amplitudes shown in Fig 2. One may take into account similar graphs with nuclei as well, but their contribution are usually negligible. When photon energy is below weak scale ($E \ll M_W$) one may use four-fermion interactions and the matrix element for the ν-γ vertex can be written in the form

$$M = -\frac{G_F}{\sqrt{2}e}Z\epsilon_\mu\bar{u}(p')\gamma_\nu(1-\gamma_5)u(p)\ (g_V\pi_t^{\mu\nu} - g_A\pi_5^{\mu\nu}) \qquad (7)$$

$$= \frac{G_F}{\sqrt{2}e}Z\epsilon_\mu\bar{u}(p')\gamma_\nu(1-\gamma_5)u(p)\ g^{\mu i}\left(g_V\pi_t(\delta_{ij} - \frac{\mathbf{k}_i\mathbf{k}_j}{\mathbf{k}^2}) - ig_A\pi_5\epsilon_{ijl}\frac{\mathbf{k}_l}{|\mathbf{k}|}\right)g^{j\nu}, \qquad (8)$$

here

$$g_V = \{\ \begin{array}{l} 2\sin^2\theta_W + \frac{1}{2}\ \text{for}\ \nu_e \\ 2\sin^2\theta_W - \frac{1}{2}\ \text{for}\ \nu_\mu, \nu_\tau \end{array}\ ,\quad g_A = \{\ \begin{array}{l} +\frac{1}{2}\ \text{for}\ \nu_e \\ -\frac{1}{2}\ \text{for}\ \nu_\mu, \nu_\tau \end{array}\ . \qquad (9)$$

$\pi_t^{\mu\nu}$ is the polarization tensor for transverse photons, while $\pi_5^{\mu\nu}$ is the axialvecor-vector tensor [8].

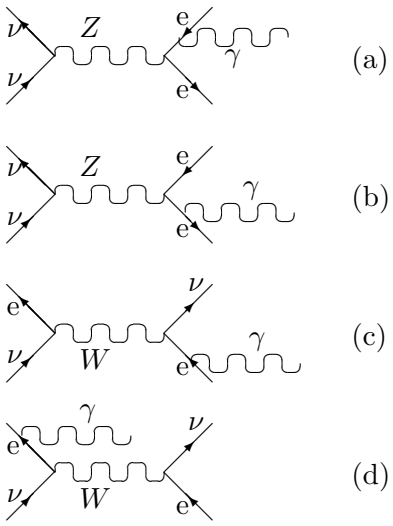

Figure 2: Neutrino-photon coupling in electrons background. (a,b) Z-γ-mixing. (c,d) "Penguin" diagrams (only for ν_e).

4 Transition radiation probability

Armed with these results we may now turn to an evaluation of the $\nu \to \nu\gamma$ rate at the interface of the media and the vacuum. We find that the transition probability is

$$W = \frac{G_F^2}{16\pi^3\alpha}\int \frac{\omega\ d\omega\ \sin\theta d\theta}{(E-p'_z-n\omega\cos\theta)^2} \tag{10}$$

$$\times\Big[(g_V^2\pi_t^2+g_A^2\pi_5^2)(1-\frac{\cos^2\theta}{E-\omega}(p'_z-n\omega\frac{\sin^2\theta}{\cos\theta}))-2g_Vg_A\pi_t\pi_5\cos\theta(1-\frac{p'_z-n\omega\frac{\sin^2\theta}{\cos\theta}}{E-\omega})\Big], \tag{11}$$

here

$$p'_z=\sqrt{(E-\omega)^2-n^2\omega^2\sin^2\theta}\ . \tag{12}$$

Now we expand underintegral expressions on small angle, since only in that case the denominator is small (and the formation zone length is large). Thus we write the transition probability in the form

$$W\simeq\frac{G_F^2}{16\pi^3\alpha}\int\frac{d\omega\ \theta^2 d\theta^2}{\omega\ [\ \theta^2+(1-n^2)(1-\frac{\omega}{E})\ ]^2}\Big[(g_V^2\pi_t^2+g_A^2\pi_5^2)(2-2\frac{\omega}{E}+\frac{\omega^2}{E^2})-2g_Vg_A\pi_t\pi_5\frac{\omega}{E}(2-\frac{\omega}{E})\Big]\ . \tag{13}$$

Eq.(13) tells us that the radiation is forward peaked within an angle of order $\theta\sim\sqrt{1-n^2}$.

After integration over angle θ we get

$$W \simeq \frac{G_F^2}{16\pi^3\alpha}\int\frac{d\omega}{\omega}\Big[-\ln[(1-n^2)(1-\frac{\omega}{E})]+\ln[(1-n^2)(1-\frac{\omega}{E})+\theta_{max}^2]-1\Big] \tag{14}$$

$$\times\Big[(g_V^2\pi_t^2+g_A^2\pi_5^2)(2-2\frac{\omega}{E}+\frac{\omega^2}{E^2})-2g_Vg_A\pi_t\pi_5\frac{\omega}{E}(2-\frac{\omega}{E})\Big]. \tag{15}$$

Numerically eq. (15) does not depend much on θ_{max}.

Usually the axialvector polarization function is much less than the vector one. For instance in nonrelativistic and nondegenerate plasma these functions are [8]

$$\pi_t=\omega_p^2\ \text{ and }\ \pi_5=\frac{|\mathbf{k}|}{2m_e}\frac{\omega_p^4}{\omega^2}, \tag{16}$$

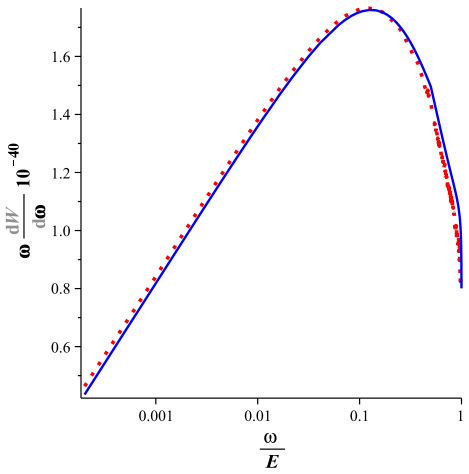

Figure 3: Energy spectrum of the transition radiation by electron neutrinos at an interface of media with plasma frequency $\omega_p = 20$eV and vacuum. The energy of the incoming neutrino is $E = 1$ MeV. The dot line is numerical and the solid line is semi-analytical integration over angle between photon and incoming neutrino momenta.

where $\omega_p^2 = \frac{4\pi\alpha N_e}{m_e}$ is the plasma frequency. Therefore we may ignore the term proportional to π_5.

Since we are interested in the forward radiation in the gamma ray region, we assume that the index of refraction of the photon is

$$n^2 = 1 - \frac{\omega_p^2}{\omega^2} \tag{17}$$

and the photons from the medium to the vacuum propagate without any reflection or/and refraction.

In Fig.3 we plot the energy spectrum of the photons from the transition radiation by electron neutrinos with energy $E = 1$MeV.

After integration over photon energy we find the neutrino transition radiation probability as

$$W = \int_{\omega_{min}}^{E} dW \simeq \frac{g_V^2 G_F^2 \omega_p^4}{16\pi^3\alpha}\left(2\ \ln^2\frac{E}{\omega_p} - 5\ln\frac{E}{\omega_p} + \delta\right) \tag{18}$$

here $\delta \simeq 5$ for $\omega_{min} = \omega_p$, $\delta \simeq -1$ for $\omega_{min} = 10\omega_p$.

The energy deposition of the neutrino in the media due to the transition radiation

$$\int_{\omega_p}^{E} \omega\ dW_{\nu\to\nu\gamma} \simeq \frac{g_V^2 G_F^2 \omega_p^4}{16\pi^3\alpha} E\Big[\frac{8}{3}\ln\frac{E}{\omega_p} - 4.9 + 9\frac{\omega_p}{E} + O(\frac{\omega_p^2}{E^2})\Big] \tag{19}$$

The eqs.(15),(18) and (19) are main results.

For MeV electronic neutrinos the transition radiation probability is about $W \sim 10^{-39}$ and the energy deposit is about $1.4\cdot 10^{-34}$ eV when they cross the interface of the media with $\omega_p = 20$ eV to vacuum.

Unfortunately the transition radiation probability is extremely small and cannot be observed at the Earth.

On the other hand at the surface of the neutron stars electron layer may exist with density $\sim m_e^3$, due to the fact that the electrons not being bound by the strong interactions are displaced to the outside of the neutron star [9]. Therefore MeV energy neutrinos emited by the neutron stars during its cooling processes will have transition radiation with the probability of $\sim 10^{-20}$ and energy spectrum given in Eq. (15).

5 Summary and Conclusion

We have calculated the neutrino transition radiation at the interface of two media. The charged particles of the media provide an effective ν-γ vertex, and they modify the photon dispersion relation. We got analytical expressions for the energy spectrum of the transition radiation, its probability and the energy deposition at the process. The radiation is forward peaked within an angle of order $\frac{\omega_p}{\omega}$. The photons energy spectrum is falling almost linearly over photon energy.

Acknowledgments

We are grateful to K. Ispirian for bringing our attention to [7] and for discussions. The research was supported by the Schwinger Foundation and by the RGS Armenia. IA would like to thank the organizers for very interesting and enjoyable conference.

References

1. G. G. Raffelt, *Chicago, USA: Univ. Pr. (1996) 664 p*
2. V. L. Ginzburg and I. M. Frank, J. Phys. (USSR) **9** (1945) 353 [Zh. Eksp. Teor. Fiz. **16** (1946) 15].
3. G. M. Garibyan, J. Exp. Theor. Phys. **37** (1959) 527 [Sov. Phys. JETP **10** (1960) 372]; see also [10]
4. G. M. Garibyan, J. Exp. Theor. Phys. **39** (1960) 1630 [Sov. Phys. JETP **12** (1961) 1138]]; see also [11]
5. A. N. Ioannisian and G. G. Raffelt, Phys. Rev. D **55** (1997) 7038.
6. M. Sakuda and Y. Kurihara, Phys. Rev. Lett. **74**, 1284 (1995); W. Grimus and H. Neufeld, Phys. Lett. B **344**, 252 (1995).
7. E. N. Bukina, V. M. Dubovik and V. E. Kuznetsov, Phys. Lett. B **435**, 134 (1998).
8. E. Braaten and D. Segel, Phys. Rev. D **48**, 1478 (1993).
9. R. Picanco Negreiros, I. N. Mishustin, S. Schramm and F. Weber, Phys. Rev. D **82**, 103010 (2010); and references therein.
10. M.L. Ter-Mikaelian. High-energy electromagnetic processes in condensed media. *Wiley-Interscience, New York* (1972)
11. L. L. . DeRaad, W. y. . Tsai and T. Erber, Phys. Rev. D **18**, 2152 (1978).

6.
Astroparticles

ICECUBE AS A DISCOVERY OBSERVATORY FOR PHYSICS BEYOND THE STANDARD MODEL

K. Helbing, for the IceCube Collaboration[a]

Department of Physics, University of Wuppertal,
D-42119 Wuppertal, Germany

Construction of the cubic-kilometer neutrino detector IceCube at the South Pole has been completed in December 2010. It forms a lattice of 5160 photomultiplier tubes monitoring a gigaton of the deep Antarctic ice for particle induced photons. The telescope is primarily designed to detect neutrinos with energies greater than 100 GeV from astrophysical sources. Beyond this astrophysical motivation IceCube is also a discovery instrument for the search for physics beyond the Standard Model. Owing to subfreezing ice temperatures, the photomultiplier dark noise rates are particularly low which opens up tantalizing possibilities for particle detection. This includes the indirect detection of weakly interacting dark matter, direct detection of SUSY particles, monopoles and extremely-high energy phenomena.

1 Introduction

The physics questions that can be addressed with neutrino telescopes are manifold. They cover the internal mechanisms of cosmic accelerators, the cosmological evolution of sources, particle physics at center of mass energies far beyond the TeV scale and the search for new particles and physics beyond the Standard Model.

1.1 The detector

The IceCube Neutrino Observatory at the geographic South Pole has been completed in December 2010. The detector comprises 5160 digital optical modules (DOMs) deployed in a three-dimensional array approximately one cubic-kilometer in size and centered 2 km deep in the clear Antarctic ice (Fig. 1). Each DOM consists of a photo-multiplier tube and electronics for digitization of waveforms and communication with neighboring DOMs and the

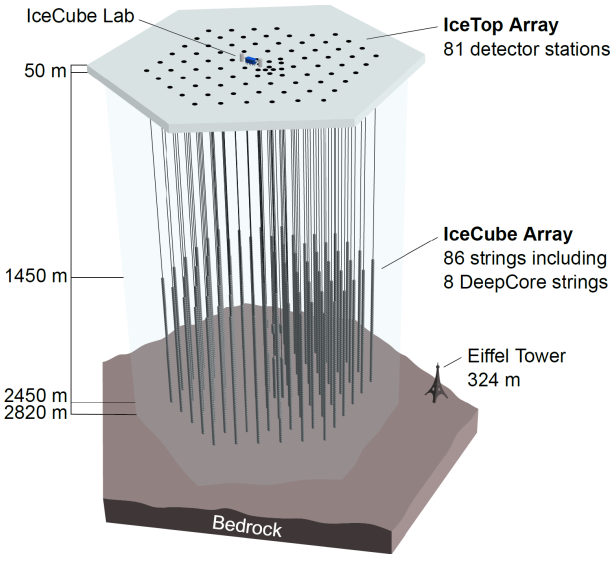

Figure 1: The IceCube observatory.

[a]Complete author list at http://www.icecube.wisc.edu/collaboration/authorlists/2011/5.html

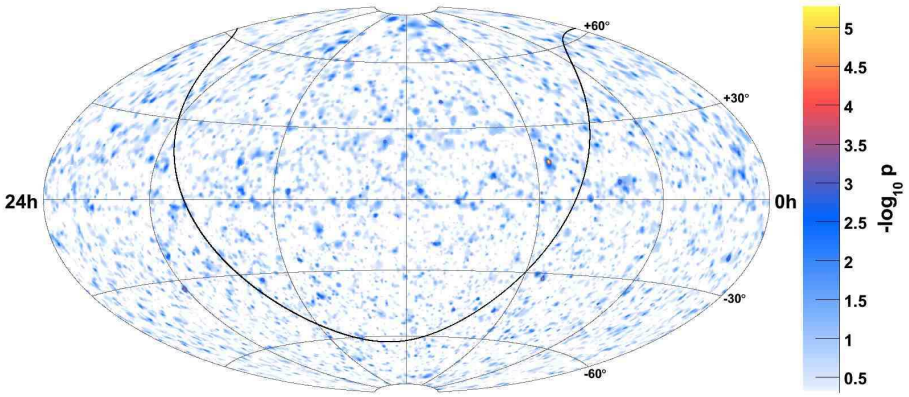

Figure 2: Equatorial skymap (J2000) of pre-trial significances (p-value) of the all-sky point source scan. The galactic plane is shown as the solid black curve.

surface. Cherenkov light from the passage of a relativistic charged particle through the ice creates a pattern of "hit" DOMs in the array, and the position and timing of the hits is used to reconstruct the path of the particle.

The vast majority of these particles are muons, arriving from cosmic ray air showers occurring in the atmosphere above the site. IceTop, the surface component above IceCube, is an air shower array with an area of 1 km^2 at a height of 2830 m above sea level. It consists of 162 ice Cherenkov tanks, grouped in 81 stations. IceTop is primarily designed to study the mass composition of primary cosmic rays in the energy range from about 10^{14} eV to 10^{18} eV by exploiting the correlation between the shower energy measured in IceTop and the energy deposited by muons in the deep ice.

2 Astronomy

2.1 Neutrino sky

IceCube's principal mission is to detect high energy neutrinos from astrophysical sources. Ultra-high energy cosmic ray (UHECR) experiments have shown that particles with energies up to a few times 10^{20} eV arrive at Earth. Since the cosmic rays are hadrons also ultra-high energy (UHE) neutrinos should be produced at these cosmic accelerators. These neutrinos propagate undeflected through galactic and inter-galactic magnetic fields and their measurement allows to point back to the source. Due to the low predicted neutrino fluxes, target masses of cubic kilometers of water or ice need to be instrumented with photomultiplier tubes for detection of these neutrinos.

The detection principle for high energy neutrinos is the measurement of the Cherenkov light in transparent media which is emitted by charged leptons produced in neutrino interactions in and around the detector. The most promising detection channel is muons since muons can propagate up to several kilometers through the medium. The results of an all-sky scan [1] performed with the half-completed IceCube detector (IC40) are shown in the map of the pre-trial p-values in Fig. 2. The most significant deviation from background is located at 113.75° r.a., 15.15° dec. The best-fit parameters are 11.0 signal events above background, with spectral index $\gamma = 2.1$. The pre-trial estimated p-value of the maximum log likelihood ratio at this location is $5.2 \cdot 10^{-6}$. In trials using data sets scrambled in right ascension the resulting post-trial p-value was found to be 18% – consequently, the excess is not claimed. While no TeV neutrinos from astrophysical sources have been identified yet unambiguously, the partially completed IceCube detector has

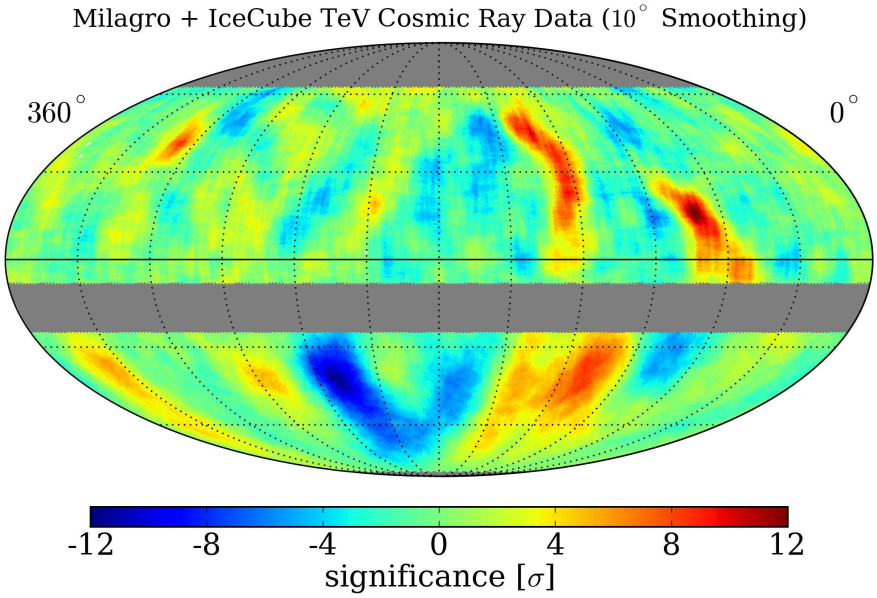

Figure 3: Combined map of significances in the cosmic ray arrival direction distribution observed by Milagro in the northern hemisphere and IceCube in the southern hemisphere.

set the most stringent upper limits to date.

2.2 Cosmic rays

Between May 2009 and May 2010, the IceCube neutrino detector consisted of 59 data taking strings recording 32 billion muons. The muons are generated in air showers produced by cosmic rays with a median energy of 20 TeV. With this data the southern sky was probed for per-mille anisotropies in the arrival direction distribution of cosmic rays. The arrival direction distribution is not isotropic, but shows significant structure on several angular scales [3]. In addition to a large-scale structure in the form of a strong dipole and quadrupole, the data show small-scale structures. Fig. 3 shows the combined skymap of significances in the cosmic ray arrival direction distribution observed by Milagro in the northern hemisphere [2] and IceCube in the southern hemisphere on scales between 15° and 30°. It exhibits several localized regions of significant excess and deficit in cosmic ray intensity. The most significant excess is localized at right ascension 122.4° and declination −47.4° and has a post-trials significance of 5.3σ. The origin of this anisotropy is unknown.

3 Searches for non Standard Model particles

Supersymmetry (SUSY) is currently the most extensively studied amongst theories beyond the Standard Model (SM). The most direct constraints on SUSY particle masses have been obtained at LEP and the Tevatron. While cryogenic dark matter detectors presently have the best sensitivity for spin independent WIMP-nucleon scattering, indirect searches with IceCube constrain the spin-dependent cross-sections for neutralino-proton scattering.

Direct detection channels for SUSY particles are only now being investigated with the parameter space being largely complementary to that covered by LHC experiments and WIMP searches – especially in scenarios where the gravitino is the lightest SUSY particle. Also, studies of high light yield exotic signatures from particles like magnetic monopoles have been performed.

3.1 Indirect WIMP searches

A search for muon neutrinos from neutralino annihilations in the Sun has been performed with the combined data set of AMANDA and IC22. No excess over the expected atmospheric background has been observed. Upper limits have been obtained on the annihilation rate of captured neutralinos in the Sun and converted to limits on the WIMP-proton cross-sections. These results are the most stringent limits to date on neutralino annihilation in the Sun. In Fig. 4 the limits on the spin-dependent WIMP-proton cross-section are compared with direct search experiments [5,6,7] and Super-K [8]. Soft WIMP models (annihilation into $b\bar{b}$) are indicated by the dashed lines, whereas hard models (W^+W^-) are shown in solid lines. Our limits also present the most stringent limits on the spin-dependent WIMP-proton cross-section for neutralino masses above 100 GeV. The full IceCube detector with the densely instrumented DeepCore extension is expected to test viable MSSM models down to 50 GeV. IceCube is also able to constrain the dark matter self-annihilation cross section by searching for a neutrino signal from the Galactic halo [9].

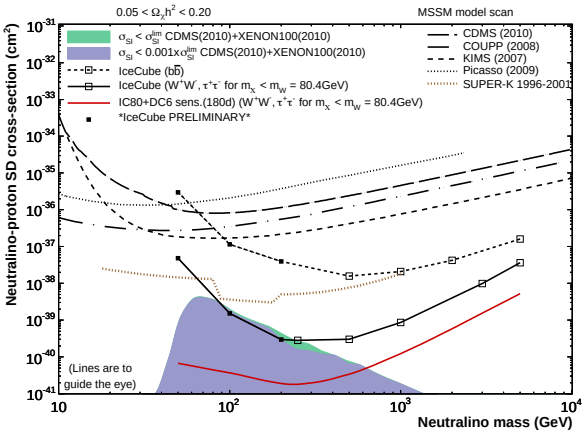

Figure 4: Limits on the spin-dependent WIMP-proton cross-section.

3.2 Direct SUSY searches

The main phenomenological features of SUSY models arise from the choice of the symmetry breaking mechanism. Within the minimal supersymmetric extension of the Standard Model (MSSM) the most extensively studied mechanisms are gravity mediated supersymmetry breaking and gauge mediated supersymmetry breaking. In both scenarios the gravitino may be the lightest supersymmetric particle (LSP). This scenario however, has not been widely addressed at collider experiments (except in terms of future concepts) and also WIMP searches usually assume the neutralino to be the LSP. In that respect a direct search for SUSY with the gravitino being the LSP is complementary to both ongoing collider experiments and also to indirect searches.

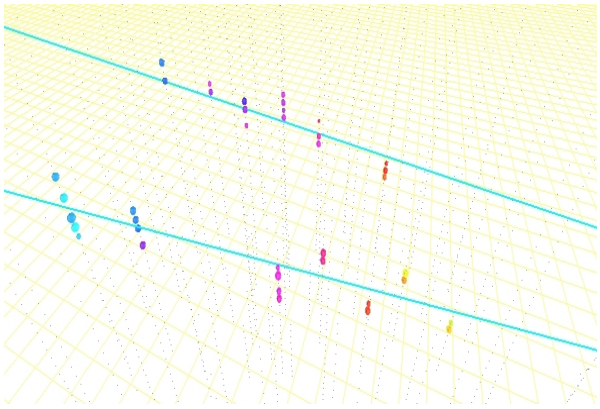

Figure 5: Two faint tracks in IceCube from a simulation of parallel staus

In models where the lightest supersymmetric particle (LSP) is the gravitino, typically the next to lightest SUSY particle (NLSP) is a long lived meta stable slepton (typically a stau). Being charged the stau is detected by its Cherenkov radiation in the neutrino telescope. Staus have a small cross section for interactions with "normal" matter. In interactions in the Earth of cosmic neutrinos of typically PeV energies and above SUSY particles can be produced which eventually decay into a pair of staus. This pair of staus of a few hundred GeV mass can propagate through the whole Earth [10], leaving the very distinct signature of two parallel, up-going tracks separated by several hundred meters when they pass a neutrino telescope (see Fig. 5).

This detection signature is quasi background free: Because of the down-going nature of air shower events, the up-going double stau tracks are distinguishable e.g. from the high-p_T muon events. Upgoing muon pairs can be created in neutrino-nucleon interactions in the earth involving charm production and decay [11]: $\nu N \rightarrow \mu H_c \rightarrow 2\mu\nu_\mu H_x$. The track length of these muons is however much shorter than that of staus. Hence their track separation is smaller as they need to be produced closer to the detector. Algorithms to identify such stau signatures are currently being developed for IceCube based e.g. on the track separation and the low brightness.

3.3 Magnetic monopoles

Generally, cosmic rays and the big bang are the most likely sources of massive monopoles, since accelerator energies are likely insufficient to produce them. The predictions for the mass and charge of monopoles depend strongly on the choice of the unified group and its symmetry breaking pattern in the early Universe. The non-observation of the partner to electric charges may be explained by inflation diluting the primordial monopole abundance.

Monopole detectors have predominantly used either induction or ionization and Cherenkov radiation. Ionization experiments rely on a magnetic charge producing more ionization than an electrical charge with the same velocity. The MACRO and Ohya experiments are examples for the ionization technique [12,13].

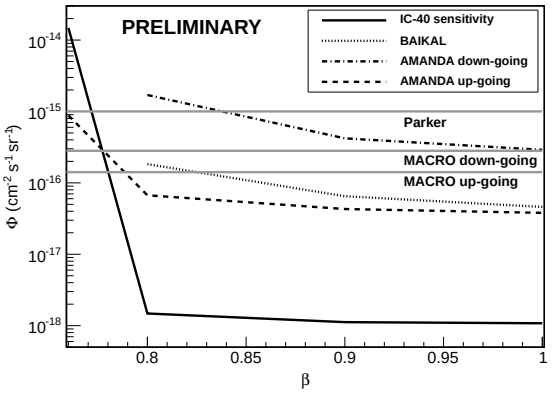

Figure 6: Monopole limits and the expected sensitivity of the half completed IceCube.

Large scale Cherenkov telescopes deployed in naturally occurring transparent media like sea water or glacial ice can detect magnetic monopoles with both the ionization and Cherenkov radiation from magnetic monopoles: For relativistic monopoles moving at a speed above the Cherenkov threshold the light yield is excessive (several thousand times more) compared to Standard Model particles. But even at velocities below the Cherenkov threshold monopoles are observable through delta rays and ionization, again exceeding the light yield of other particles of the same velocity. Moreover, some GUT theories predict that monopoles catalyze the decay of nucleons which would be observed by a series of light bursts produced along the monopole trajectory.

Searches for relativistic monopoles with Cherenkov neutrino telescopes have already been performed with the AMANDA and BAIKAL detector and are being investigated with the IceCube detector [14,15]. Fig. 6 shows that sensitivities well below the so called Parker bound [16,17] have been reached for relativistic monopoles. Parker pointed out that the abundance of magnetic monopoles cannot be as high as to deplete galactic magnetic fields. Strategies to identify non-relativistic monopoles in IceCube are currently being developed. In conclusion, IceCube is entering the interesting region of sensitivities for monopole searches spanning a wide range of relativistic and sub-relativistic velocities.

4 Extremely-high energy neutrinos

Cosmogenic neutrinos may give a unique picture of the Universe in the highest energy regime. With the Greisen-Zatsepin-Kuzmin (GZK) process the highest energy cosmic-rays interact with the cosmic microwave background producing these neutrinos [19,20]. Hence, cosmogenic neutrinos

carry information about the sources of the highest energy cosmic-rays, such as their location, cosmological evolution, and cosmic-ray spectra at the sources.

On the other hand, tiny departures from Lorentz invariance have effects that increase rapidly with energy and can kinematically prevent cosmic-ray nucleons from undergoing inelastic collisions with CMB photons. With charged cosmic-rays alone it is impossible to differentiate between a true GZK cutoff or the fading spectrum of cosmological accelerators.

Underground neutrino telescopes, such as IceCube, can detect EHE neutrino interactions through the strong Cherenkov radiation emitted by the charged secondary particles. In a neutrino telescope, an EHE neutrino interaction is identified by the extremely high number of Cherenkov photons deposited in the detector. Fig. 7 shows the search for neutrinos with energies above 10^{15} eV using data collected with the half-completed IceCube detector in 2008−2009 [18]. Our limits are competitive up 10^{19} eV.

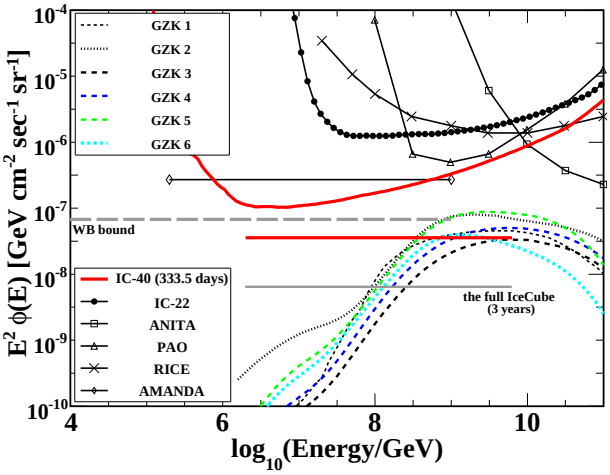

Figure 7: Quasi-differential model-independent 90% CL limit normalized by energy decade and E^{-2} spectrum integrated limit on all flavor neutrino fluxes from the 2008-2009 IceCube EHE analysis (red solid lines). The systematic errors are included. Various model predictions (assuming primary protons) are shown for comparison.

4.1 Extensions of IceCube

Besides the GZK process, neutrinos at ultra-high energies are also a valuable tool to study the neutrino-nucleon cross section at high center of mass energies. For energies above 10^{16} eV the Standard Model cross section rises roughly with a power law $\sigma_{SM} \propto E_\nu^{0.36}$ in the energy of the neutrino [23]. Naively, the cross section for black hole creation scales with the Schwarzschild radius $\sigma_{BH} \propto r_S^2 \propto E_{cm}^2 \propto E_\nu$ eventually exceeding the Standard Model processes. For a more refined discussions also addressing extra dimensions see for example [24].

The detection of the small neutrino flux predicted at the highest energies (E $> 10^{17}$ eV) requires detector target masses of the order of 100 gigatons, corresponding to 100 km^3 of water or ice. The optical Cherenkov neutrino detection technique is not easily scalable from the 1 km^3-scale telescopes to such large volumes. Several techniques have been studied to realize such huge detection volumes. Radio Cherenkov neutrino detectors search for radio Askaryan pulses in a dielectric medium as the EHE neutrino signature [21]. Acoustic detection is based on the thermo-acoustic sound emission from a particle cascade depositing its energy in a very localized volume causing a sudden expansion that propagates as a shock wave perpendicular to the cascade [22].

Within IceCube the properties of the South Pole ice for acoustic [25,26,27] and radio [28] detection have been studied with respect to signal attenuation, refraction and the noise environment . The results turn out to be very favorable promising longer signal attenuation lengths than for the optical detection, allowing for a sparse instrumentation of the Antarctic ice. Consequently, the installation of a 80 km^2 radio array dubbed ARA has commenced [30]. Studies to augment the radio detection with acoustic sensors show that it may be possible to bootstrap detection strategies for the large effective volumes by building a hybrid detector [29]. A signal seen in coincidence between any two of the three methods (radio, acoustic, optical) would be unequivocal. The information from multiple methods can also be combined for hybrid reconstruction, yielding improved angular and energy resolution.

Another addition pursued is the RASTA detector which will complement the IceTop air-

shower detector with an extended surface array of radio antennas [31]. Besides the additional capabilities for cosmic-ray composition studies, this combination also enhances IceCube's optical high-energy neutrino sensitivity by vetoing the air-shower background.

Acknowledgments

KH acknowledges the support from German Ministry for Education and Research (BMBF).

1. R. Abbasi *et al.* [IceCube Collaboration], *Astrophys. J.* **732**, 18 (2011)
2. A. A. Abdo *et al.*, *Phys. Rev. Lett.* **101**, 221101 (2008), A. A. Abdo *et al.*, *Astrophys. J.* **698**, 2121 (2009).
3. R. Abbasi *et al.* [IceCube Collaboration], accepted by *Astrophys. J.*, arXiv:1105.2326.
4. R. Abbasi *et al.* [ICECUBE Collaboration], *Phys. Rev. Lett.* **102**, 201302 (2009).
5. Z. Ahmed *et al.* [CDMS Collaboration], *Phys. Rev. Lett.* **102**, 011301 (2009).
6. E. Behnke *et al.*, Science **319**, 933 (2008).
7. H.S. Lee *et al.*, *Phys. Rev. Lett.* **99**, 091301 (2007).
8. S. Desai *et al.*, *Phys. Rev.* D **70**, 083523 (2004).
9. R. Abbasi *et al.* [IceCube Collaboration], arXiv:1101.3349 [astro-ph.HE].
10. I. Albuquerque, G. Burdman and Z. Chacko, *Phys. Rev. Lett.* **92**, 221802 (2004).
11. I. F. M. Albuquerque, G. Burdman and Z. Chacko, *Phys. Rev.* D **75**, 035006 (2007); I.F.M. Albuquerque and S.R. Klein, *Phys. Rev.* D **80**, 015015 (2009).
12. M. Ambrosio *et al.* [MACRO Collaboration], *Eur. Phys. J.* C **25**, 511 (2002).
13. S. Orito *et al.*, *Phys. Rev. Lett.* **66**, 1951 (1991).
14. K. Antipin *et al.* [BAIKAL Collaboration], *Astropart. Phys.* **29**, 366 (2008).
15. R. Abbasi *et al.* [IceCube Collaboration], *Eur. Phys. J.* C **69**, 361 (2010).
16. E.N. Parker, *Astrophys. J.* **160**, 383 (1970).
17. M.S. Turner, E.N. Parker and T.J. Bogdan, *Phys. Rev.* D **26**, 1296 (1982).
18. R. Abbasi *et al.* [IceCube Collaboration], *Phys. Rev.* D **83**, 092003 (2011).
19. K. Greisen, *Phys. Rev. Lett.* **16**, 748 (1966); G. T. Zatsepin and V. A. Kuzmin, *Pisma Zh. Eksp. Teor. Fiz.* **4**, 114 (1966) [*JETP. Lett.* **4**, 78 (1966)].
20. V. S. Berezinsky and G. T. Zatsepin, *Phys. Lett.* B **28**, 423 (1969).
21. G. A. Askaryan, *Sov. Phys. JETP* **14 (2)** 441–443 (1962).
22. G. A. Askaryan, B. A. Dolgoshein, A. N. Kalinovsky, N. V. Mokhov, *Nucl. Instrum. Methods* A **164**, 267 (1979).
23. R. Gandhi, C. Quigg, M.H. Reno and I. Sarcevic, *Phys. Rev.* D **58**, 093009 (1998).
24. L.A. Anchordoqui, J.L. Feng, H. Goldberg and A. D. Shapere, *Phys. Rev.* D **68**, 104025 (2003).
25. R. Abbasi *et al.* [IceCube Collaboration], *Astropart. Phys.* **33**, 277 (2010).
26. R. Abbasi *et al.* [IceCube Collaboration], arXiv:1103.1216 [astro-ph.IM].
27. R. Abbasi *et al.* [IceCube Collaboration], *Astropart. Phys.* **34**, 382 (2011).
28. H. Landsman for the IceCube Collaboration, arXiv:1010.3949 [astro-ph.IM].
29. D. Besson, R. Nahnhauer, P.B. Price, D. Tosi, J.A. Vandenbroucke and B. Voigt, *Nucl. Instrum. Methods* A **604**, 179 (2009).
30. P. Allison *et al.*, arXiv:1105.2854 [astro-ph.IM].
31. S. Böser for the IceCube Collaboration, arXiv:1010.1737 [astro-ph.HE].

ANTARES: Status, first results and multi-messenger astronomy

Manuela Vecchi for the ANTARES Collaboration
Université Aix-Marseille II and CPPM,
163, avenue de Luminy - Case 902 - 13288
Marseille cedex 09 France

The ANTARES Collaboration has completed in 2008 the deployment of what is currently the largest high energy neutrino detector in the Northern hemisphere, covering a volume of about 0.01 km^3. The search for cosmic neutrinos in the energy range between tens of GeV and tens of PeV is performed by means of a three dimensional array of photomultiplier tubes (PMTs), arranged on 12 vertical structures (strings) located in the Mediterranean Sea at a depth of about 2500 meters. The detection principle relies on the identification of the Cherenkov light produced as ultra-relativistic muons propagate in water. The main goal of the detector is the search for point-like sources of cosmic neutrinos from both Galactic and extra-Galactic sources. Besides the search for point sources, other analysis topics are strongly pursued and will be described in the following.

1 Introduction

Cosmic rays (CRs) were discovered a century ago, but it is still uncertain where or how they are accelerated: multi-messenger astronomy [1] could solve this *puzzle*, combining the information coming from γ-rays, cosmic rays, neutrinos and gravitational waves. Charged particles, whose paths are deflected by magnetic fields, cannot carry the information on the arrival direction up to ultra high energies, so that a close look at production and acceleration sites of cosmic rays is only possible with neutral particles. Neutrinos are thought to be produced by the interaction of accelerated particles (protons and nuclei) with matter and radiation surrounding the sources. In these interactions a massive production of hadrons with short lifetime (mostly pions and kaons, both charged and neutral) is expected to take place, high energy neutrinos being their decay products. Neutral hadrons, produced along with the charged particles generating neutrinos, are expected to decay into couples of high energy γ-rays, so that simultaneous emitters of neutrinos and γ-rays are very likely to exist.

2 Operation of the ANTARES Neutrino Telescope

Cosmic neutrinos can be detected via the identification of the charged particles, in particular muons, that are produced as a consequence of charged current interactions of neutrinos with the target matter. Relativistic muons propagating in a transparent medium, can induce the Cherenkov effect, i. e. the emission of coherent electromagnetic radiation along the surface of a cone, whose aperture is a function of the refraction index of the medium itself (about 42° for deep sea water). The detection technique relies on the observation of Cherenkov radiation in the visible range, by means of a tridimensional array of photomultiplier tubes (PMTs).

The ANTARES Collaboration has completed the deployment of a neutrino telescope[2] that is located about 2500 meters deep, offshore Toulon, France. The PMTs are arranged on 12 detection lines, each comprising up to 25 triplets of PMTs (floors), regularly distributed on 350 m, the lowest floor being located at 100 m above the sea bed. Each line is connected to a junction box, which is itself connected to the shore station by a 40 km long electro-optical cable. The data collected on shore are then processed by a PC farm running several trigger algorithms looking for signals compatible with the ones produced by charged particles propagating through the detector. The counting rate of the detector, of the order of 100 kHz, is dominated by light emitted by bioluminescent bacteria and by the Cherenkov light that is emitted by electrons created as a decay product of radioactive elements present in sea water, such as ^{40}K. Environmental background hits are mostly uncorrelated, and can be easily rejected by the trigger algorithm, which selects about 20 Hz of data.
The search for HE neutrinos is affected by a particle background, coming from the interactions of CRs with the upper layers of the atmosphere, producing both neutrinos and muons, showing the same experimental signature of cosmic neutrinos. Atmospheric muons, providing the most abun-

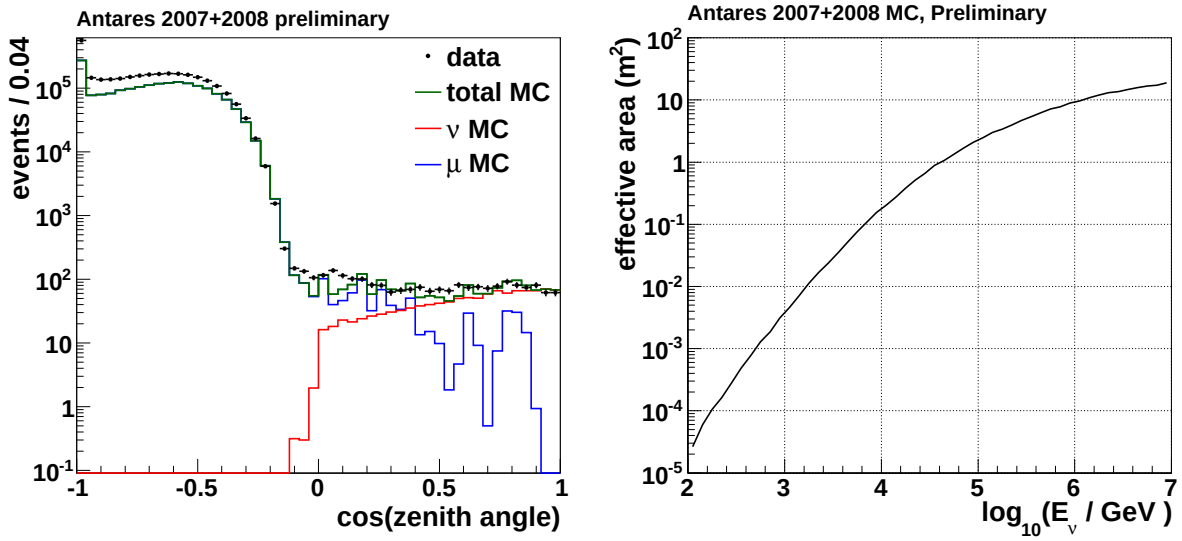

Figure 1: *Left*: Reconstructed arrival directions of the events detected with the ANTARES detector between 2007 and 2008. Events with $\cos\theta < 0$ are reconstructed as down-going, while events with $\cos\theta > 0$ are reconstructed as up-going. *Right*: Effective area of the ANTARES detector as a function of the neutrino energy, for an analysis optimized for point-like sources search.

dant flux, propagate downward through the detector, while atmospheric neutrinos contribute providing an isotropic flux that is several orders of magnitude less abundant, as can be seen in figure 1-*Left*, showing the distribution of reconstructed arrival directions of the events detected with the ANTARES detector between 2007 and 2008, together with background expectations from simulations.

3 Search for neutrinos from point-like sources

A cosmic neutrino point-like source would manifest itself as a localized excess of events on top of the background.
To ensure a high signal-to-noise ratio, the event reconstruction[3] and selection are optimized to provide tracks with good angular resolution, in a wide energy range: the detector effective area

is shown in figure 1-*Right*. Using data collected between 2007 and 2008, a search for point-like sources has been performed. The integrated live-time of the data sample is 295 days, after data quality selection and rejection of the periods of high bioluminescence and high sea current. Upgoing events, induced by muon neutrinos, are selected by imposing track quality criteria. The event selection was optimized to achieve the best discovery potential for an assumed power-law signal with energy spectrum with spectral index $\gamma = 2$. Figure 2-*Left* shows the preliminary sample of selected events: 2040 neutrino candidates have been identified. Simulations indicate that this sample is contaminated by a 40% of misreconstructed atmospheric muons. Based on these events, a dedicated search for candidate sources, already known as HE gamma-rays emitters, was performed. This search was also completed by a full scan of the Southern sky. Preliminary results find GX 339 as the most likely candidate source, where two events have

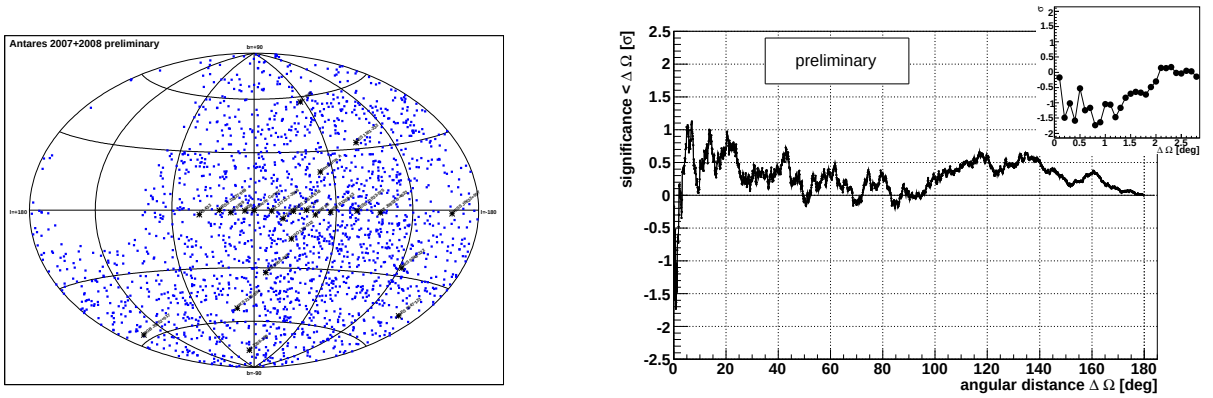

Figure 2: *Left*: Skymap of the 2040 neutrino candidates selected for the point source search. Stars indicate the 24 sources of the candidate list. *Right*: Autocorrelation significance as a function of the cumulative angular scale. A maximum significance of 1.13 sigma is found for angular scales smaller than 7 degrees.

been found within 1 degree of its position. The probability to observe this or a larger excess due to a statistical fluctuation of the background is 7%. It can be concluded therefore that all observed excesses are compatible with the background hypothesis, and 90% C.L. upper limits on the neutrino flux from the considered sources have been set. Figure 3 shows ANTARES upper limits as function of the declination, together with the expected sensitivity for 1 year of data taking. Results from both previous and current experiments are shown for comparison. The ANTARES experiment is currently providing the more stringent upper limits on the Southern sky sources, moreover these limits are in good agreement with the expected sensitivity.
In a complementary analysis, the two point autocorrelation of the selected dataset has been studied. The applied method is independent on MonteCarlo simulations and it is sensitive to a larger variety of source morphologies. The reference autocorrelation distribution is determined by scrambling the data itself, so that randomized sky maps are obtained. The final comparison between the data and the reference distributions yields the significance of the differences, as a function of the cumulative angular scale, as shown in figure 2-*Right*. The maximum significance is of 1.3 sigma, and it corresponds to angular bins smaller than 7 degrees.

4 Search for diffuse neutrino flux

The search for a diffuse neutrino flux, i.e. unresolved (neither in time nor in space) neutrino sources, is based on the search for an excess of high energy (TeV ÷ PeV) events above the irreducible background of atmospheric neutrinos, whose flux is described by a power law with

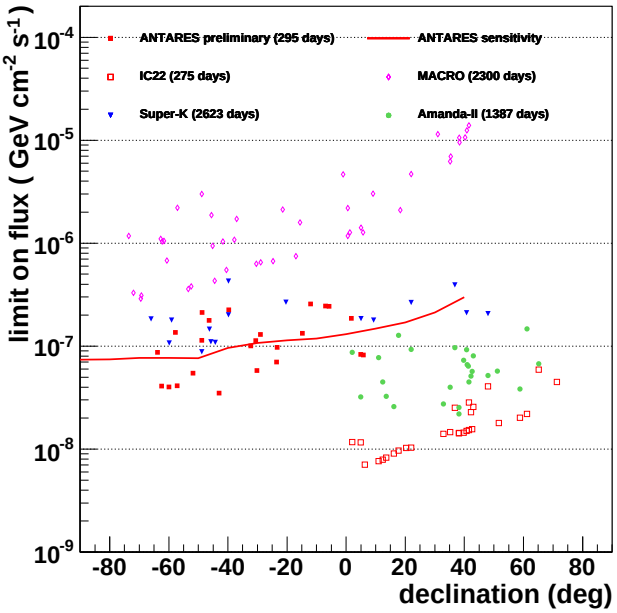

Figure 3: Upper limits on the flux of HE neutrinos, assuming an E^{-2} spectrum, for selected sources. The expected sensitivity of the ANTARES detector for a full year of data taking is also shown for comparison. Limits set by MACRO, AMANDA II, Super-K and IC22 [4] are superposed.

a spectral index $\alpha \sim -3.5$, while several theoretical models have foreseen an E^{-2} spectrum for astrophysical neutrinos. Atmospheric and astrophysical neutrinos can be therefore distinguished statistically on the basis of the particle energy. The energy estimator, called R, is based on hit repetitions on the PMTs, due to the different arrival time of Cherenkov photons produced directly by the muon, and by delayed Cherenkov photons from secondary electrons and positrons dressing up the HE muon tracks. The average number of hit repetitions in the event is defined as the number of hits in the same PMT, within 500 ns from the earliest hit selected by the reconstruction algorithm. A complete analysis has been performed on data collected from December 2007 to December 2009 for a total live-time of 334 days [5]. Figure 4-*Left* shows the distribution of the R parameter for the 134 candidate neutrino events found in the data sample, together with simulation for both background and signal neutrino events. The number of selected events was found to be compatible with the expected background, so that the 90% C.L. upper limit on the diffuse ν_μ flux with a E^{-2} spectrum is set at $E^2\Phi_{90\%} = 5.3 \times 10^{-8}$ GeV cm^{-2} s^{-1} sr^{-1} for the energy range between 20 TeV and 5 PeV, where the energy estimator is approximately linear with log E_μ. This result is shown in figure 4-*Right*: the upper limit is competitive with upper limits set by other neutrino telescopes of comparable size and is compared to theoretical predictions [6].

5 ANTARES as an observatory for physics beyond the Standard Model

Neutrino telescopes could also probe physics beyond the Standard Model, by detecting neutrinos from the annihilation of Dark Matter (DM) particles, or exotic particles [7] such as magnetic monopoles (MM) and slow nuclearites.

Neutrinos with energies of the order of tens of GeV could be produced in the annihilation of Weakly Interacting Massive Particles, e.g. neutralinos, which become gravitationally trapped in celestial bodies, like the Galactic Center or the Sun. The existence of magnetic monopoles

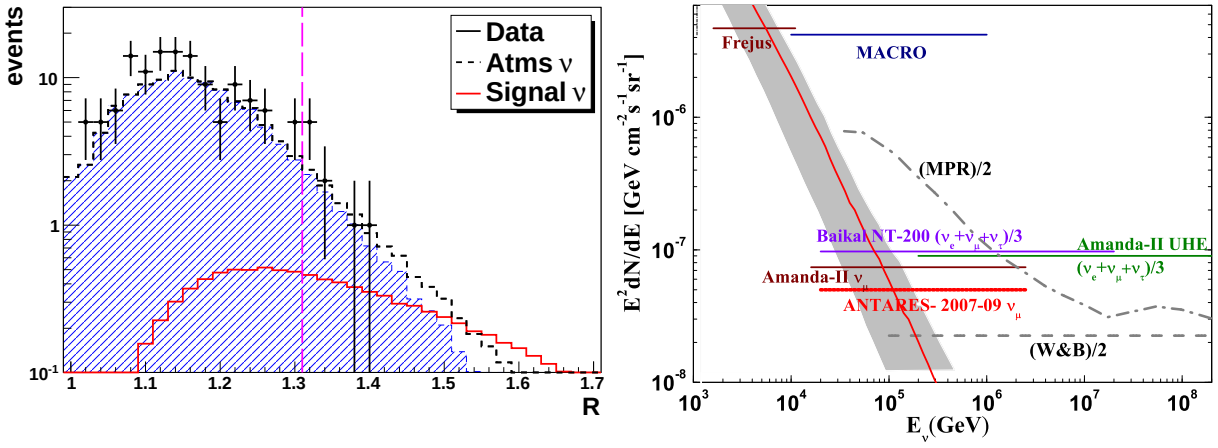

Figure 4: *Left*: Distribution of the energy estimator R for the 134 candidate neutrino events found in the 2007-2009 ANTARES data [5], together with MonteCarlo predictions. Points represent data, the filled histogram and the dashed line represents simulated atmospheric neutrinos. The signal, normalized at the upper limit, is shown as a full line. The optimized value $R = 1.31$, that is used to discriminate between signal and background event, is indicated as a vertical line. *Right*: Upper limit on the diffuse neutrino flux of HE neutrinos obtained from the 2007-2009 ANTARES data [5], compared to theoretical predictions [6] and to limits set by other neutrino telescopes. See the paper for more references.

has been initially predicted by P. Dirac in 1931. Up-going magnetic monopoles with masses

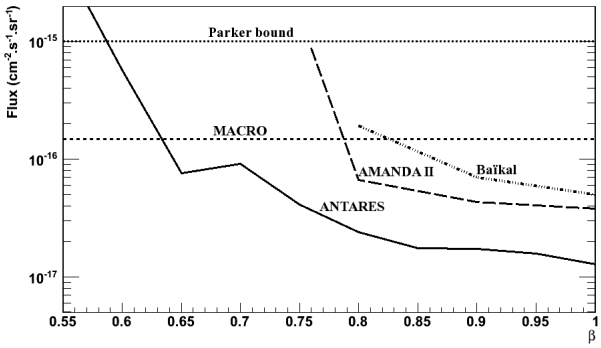

Figure 5: Upper limits at 90% C.L. on the flux of fast magnetic monopoles, as a function of the monopoles speed: solid line indicates the preliminary result from the ANTARES Collaboration.

between 10^{10} and 10^{14} GeV could be detected with the ANTARES detector, given their typical experimental signature: a very bright muon-like track, providing an amount of photons that is estimated to be more than 8000 times higher than that of a muon.
The solid line in figure 5 shows the preliminary limit set on the flux of MM by the ANTARES Collaboration, for $\beta > 0.55$. This limit is currently competitive with those previously established [8], that are also shown for comparison.

6 Multi-messenger approach within the ANTARES Collaboration

The search for neutrino emission from transient sources, like for example Micro-quasars, Gamma Ray Bursts (GRBs) [9] or core collapse supernovae (ccSNe) [10], is well suited for the multi-messenger strategy. Given the expected small difference in the arrival time and position between photons

and neutrinos, a very efficient rejection of the associated background can be achieved. Due to the very low background rate, even the detection of a small number of neutrinos correlated with a transient source could lead to a discovery.
Two different detection methods have been implemented within the ANTARES Collaboration. The first one is the triggered search method, based on the search for neutrino candidates in conjunction with an accurate timing and positional information provided by an external source. The second one is the rolling search method, based on the search for high energy events or multiplets of neutrino events coming from the same position within a given time window,
GRBs are detected by gamma-ray satellites, which deliver in real time an alert to the Gamma-ray bursts Coordinates Network (GCN). The characteristics of this alert, mainly the direction and the time of the detection, are then distributed to the other observatories. Most gamma-ray, X-ray and optical observatories are capable of observing only a small fraction of the sky, for example Swift has a 1.4 sr field of view, while neutrino telescopes monitor essentially a full hemisphere. To avoid dependence on external triggers as well as to cover a larger region of the sky, events detected with the ANTARES telescope can be used to trigger optical follow-up observations [11], using a Target-of-Opportunity (ToO) program. This method is sensitive to all transient sources producing high energy neutrinos.
The ANTARES Collaboration has developed an alert system [12] that triggers the observation with a network of optical telescopes. The key ingredients are the use of a fast and robust reconstruction algorithm [13] and the connection with a network of robotic telescopes with large field of view (approximately $2^\circ \times 2^\circ$), with slewing times of the order of tens of seconds. This is important since a GRB afterglow requires a very fast observation strategy, in contrary to a core collapse supernovae, for which the optical signal will appear several days after the neutrino signal. To be sensitive to all these astrophysical sources, the observational strategy is composed of a real time observation, followed by several observations during the following month. The system is operational since 2009 and, since then, more than 30 alerts have been sent to optical telescopes. The analysis of the optical images is under way.

References

1. J. K. Becker, Physics Reports, 458(4-5):173-246, 2008.
2. M. Ageron *et al*, submitted to N.I.M. A, arXiv:1104.1607
3. A. Heijboer, Track reconstruction and point source searches with ANTARES, PhD thesis, Universiteit van Amsterdam, 2004, http://antares.in2p3.fr/Publications.
4. M. Ambrosio *et al.*, Astrophys. J. **546**, 1038 (2001), R. Abbasi *et al.*, Phys. Rev. D **79**, 062001 (2009), E. Thrane *et al.*, Astrophys. J. **704**, 503 (2009), R. Abbasi *et al.*, Astrophys. J. **701**, L47 (2009)
5. J. Aguilar *et al.*, *Phys. Rev.* B **696**, 1622 (2011)
6. E. Waxman and J. N. Bahcall, Phys. Rev. D **59** (1999) 023002, J. N. Bahcall and E. Waxman, Phys. Rev. D **64**, 023002 (2001), K. Mannheim, R. J. Protheroe and J. P. Rachen, Phys. Rev. D **63**, 023003 (2001)
7. G. Pavalas, N. P. Clemente, Proceedings of the 31^{st} ICRC, arXiv:0908.0860
8. M. Ambrosio *et al.* Eur. Phys. J. C **25**, 511 (2002), R. Abbasi *et al.*, Eur. Phys. J. C **69**, 361 (2010), V. Aynutdinov *et al.*, arXiv:astro-ph/0507713.
9. S. Razzaque, P. Meszaros, E. Waxman, Phys. Rev. Lett. 90 (2003) 241103
10. S. Ando and J. Beacom, Phys.Rev.Lett. 95 (2005) 061103
11. M. Kowalski and A. Mohr, Astropart. Phys., 27 (2007) 533-538
12. M. Ageron *et al*, submitted to Astropart. Phys., arXiv:1103.4477
13. J. Aguilar *et al*, Astropart. Phys. **34 I9**, 652-662 (2011)

Lower limit on the extragalactic magnetic field

M. Kachelrieß
Institutt for fysikk, NTNU Trondheim, Norway

High energy photons from blazars can initiate electromagnetic pair cascades interacting with the extragalactic photon background. The charged component of such cascades is deflected and delayed by extragalactic magnetic fields (EGMF), reducing thereby the observed point-like flux and leading potentially to multi degree images in the GeV energy range. Therefore the non-observation of GeV extensions around TeV blazars implies lower limits on the strength and the filling factor of the EGMF: Magnetic fields stronger than $\mathcal{O}(10^{-17})$ G fill at least 60% of space. This requires that EGMFs were generated in a space filling manner, e.g. primordially in phase transitions or inflation.

1 Introduction

While magnetic fields are known to play a prominent role for the dynamics and in the energy budget of astrophysical systems on galactic and smaller scales, their role on larger scales is still elusive[1]. Extragalactic magnetic fields (EGMF) are notoriously difficult to measure and the data are incomplete. So far only in a few galaxy clusters observational constraints have been obtained, either by observing their synchrotron radiation halos or by performing Faraday rotation measurements (RMs). Within galaxy clusters the inferred magnetic fields are between 0.1 and 1.0 μG on scales as large as 1 Mpc, and can be as strong as 30 μG localised inside cluster cool cores. However, as both observational methods need a prerequisite to measure magnetic fields (high thermal density for RMs and presence of relativistic particles for radio emission), they have been successfully applied only to high density regions of collapsed objects as galaxies and galaxy clusters. Fields significantly below μG level are barely detectable with these methods. Also other constraints, for instance the absence of distortions in the spectrum and the polarisation properties of the cosmic microwave background radiation implies only a fairly large, global upper limit on the EGMF at the level of 10^{-9} G.

The observed magnetic fields in galaxies and galaxy clusters are assumed to result from the amplification of much weaker seed fields. Such seeds could be created in the early universe, e.g. during phase transitions or inflation, and then amplified by plasma processes. Alternatively, an early population of starburst galaxies or AGN could have generated the seeds of the EGMFs at redshift before six, i.e. before galaxy clusters formed as gravitationally bound systems. While a large fraction of the material collapsing to today's visible structures could be seeded by such fields, it is doubtful if a significant fraction of the volume of the universe could be filled in the latter case.

An alternative approach to obtain information about the EGMFs is to use its effect on the radiation from TeV gamma-ray sources. The multi-TeV γ-ray flux from distant blazars is strongly attenuated by pair production on the infrared/optical extragalactic background light

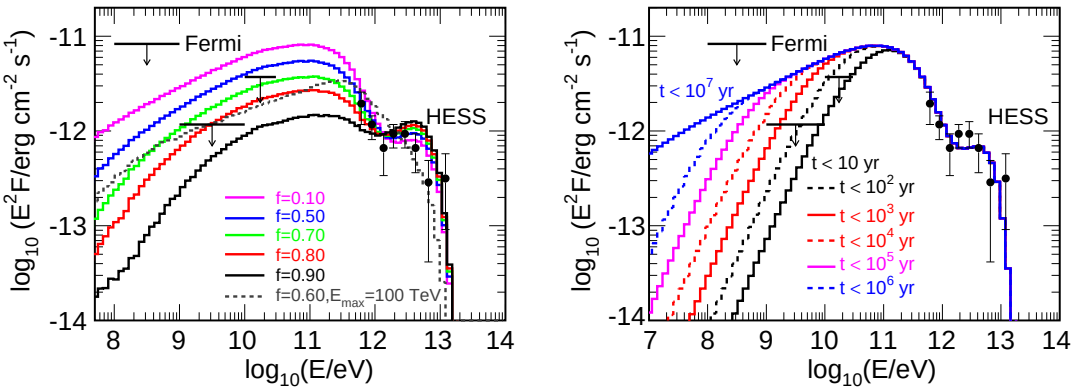

Figure 1: Fluence as function of energy contained inside the 95% confidence contour of the PSF of Fermi-LAT, left for a EGMF with top-hat profile and filling factor f varying from $f = 0.1$ to $f = 0.9$ with $E_{\rm max} = 20\,$TeV (solid) and 100 TeV (dashed), right for $B = 10^{-17}\,$G as function of the time-delay.

(EBL), initiating electromagnetic cascades in the intergalactic space. The charged component of these cascades is deflected by the EGMF. Potentially observable effects of such electromagnetic cascades in the EGMF include the delayed "echoes" of multi-TeV γ-ray flares or gamma-ray bursts [2,3,4,5] and the appearance of extended emission around initially point-like γ-ray sources [6,7,8,9,10].

An additional way to derive lower limits on the EGMF has been pointed out recently [11,12]: Since the deflection of the cascade flux into an extended halo weakens the point-like image, the non-observation of TeV blazars in the GeV range by Fermi-LAT can been used to derive a lower limit on the EGMF. Particular suitable candidates are blazars with a very hard TeV spectrum like 1ES 0229+200 that show a low intrinsic GeV emission. In the following, we will review briefly this approach and its results, and finally comment on consequences for particle physics models aiming at explanation of EGMF seed fields.

2 Limits on the EGMF from TeV blazars

We describe the procedure used to derive limits on the EGMF using the publicly available code `ELMAG` [13]. As first step, one chooses as suitable candidate sources blazars with a very hard TeV spectrum together with low intrinsic GeV emission, as 1ES 0229+200. The injection spectrum of TeV photons is fixed fitting observations from imaging atmospheric Cherenkov telescopes together with data from lower energies as e.g. from SWIFT [14]. Then the Monte Carlo code `ELMAG` follows electromagnetic cascades initiated by these high energy photons on the EBL background. As final result, the simulation procedure provides the energy, the observation angle, and the time delay of secondary cascade particles at the present epoch.

In Fig. 1 we show some results [15] for the fluence contained inside the 95% confidence contour of the PSF of Fermi-LAT. Additionally, these figures contain the HESS observations [16] as black dots with error bars and the Fermi-LAT upper limits derived by [12]. The fluences have been normalised fitting them to the HESS data. Note that a turbulent field with correlation length $L_{\rm cr}$ much larger than the mean free path $l_{\rm IC}$ of electrons in the Thomson regime, $L_{\rm cr} \gg l_{\rm IC} \sim 100\,$kpc, is well approximated by a uniform field. For smaller correlation lengths, $L_{\rm cr} \ll l_{\rm IC}$, the electron diffuses in the small-angle deflection regime, requiring larger magnetic fields for the same deflection angle. Demanding that the cascade flux is below the upper limits of Fermi-LAT leads to a lower limit on the magnetic field strength of $\sim 10^{-14}\,$G for a stationary source. Note that for small $E_{\rm max}$ the transition from the direct component, i.e. photons arriving at the detector without cascading, to the cascade contribution leads to a break at $\sim$TeV in the spectrum, as suggested by the HESS data.

Since the EGMF is strongly structured, one may wonder how a non-uniform field modifies this limit. In particular, we want to address the question whether the presence of relatively strong fields concentrated inside cosmic structures like filaments could mimic the effect of an EGMF present also in voids. As simplest possible test, we use first a top-hat profile for the structure of the EGMF: We set the field strength to zero in a fraction $1-f$ of space and use a value which in general is assumed to be representative for filaments, $B = 10^{-10}\,\mathrm{G}$, in the remaining part. For the separation of the peaks we use $D = 10\,\mathrm{Mpc}$ motivated by the typical distances between cosmological structures, although the exact value of D plays no role as long as $(1-f)D \ll l_\gamma$, with l_γ as mean free path of photons. The dependence of the fluence contained inside the PSF of Fermi-LAT on the filling factor f is shown in the left panel of Fig. 1. To be consistent with the Fermi upper limits, sufficiently strong magnetic fields should fill $\gtrsim 80\%$ of space. The derived limit on the filling factor is practically independent of the source life time τ and B, as long as the field is stronger than $\gtrsim 5\times10^{-15}\,\mathrm{G}$. As in the previous case, by assuming a higher injected $E_{\max}$ the required filling factor is slightly reduced to 60% .

The failure of strong fields filling only a small fraction of the universe to suppress sufficiently the point-like cascade flux can be understood as follows: The HESS observations of 1ES 0229+200 cover the energy range 0.5–11 TeV. In the same energy range, the mean free path l_γ of VHE γ-rays through the EBL varies between 1000 and 50 Mpc and is thus always much larger than the typical extension of regions with large fields, $(1-f)D$. For the energies considered, the cascade consists typically of only three steps, $\gamma \to e^{\pm} \to \gamma$. Since the mean free path l_{IC} of electrons in the Thomson regime is very small, $l_{\mathrm{IC}} \sim 1\,\mathrm{kpc}$, all cascades with electrons created outside the strong-field regions are undeflected. Thus it is not possible to trade smaller values of f against larger values of B: Increasing the field strength beyond $\sim 10^{-13}\,\mathrm{G}$ leads only to an increase of the deflection, while the fraction of cascades deflected outside the Fermi PSF remains constant.

We discuss next the consequence of time delays induced by the EGMF. For $B = 10^{-17}\,\mathrm{G}$, we show in the right panel of Fig. 1 the observed fluence as function of energy integrated up to different maximal time-delays t. If the source was switched on less than 10 years ago, most of the cascade photons are sufficiently delayed and will arrive only in the future. Since the typical time-scale τ of AGN activity is of the order $10^6\,\mathrm{yr}$, the observations of several sources restricts the unlikely case that the start of AGN activity coincides precisely with the begin of Fermi-LAT observations.

3 Generation and evolution of primordial magnetic fields

The turbulent magnetic field generated in the early universe is mathematically described by a Gaussian field with two-point correlation function given by

$$\langle B_i(k) B_j^*(k')\rangle = \delta(k-k')\left[\left(\delta_{ij} - \hat{k}_i\hat{k}_j\right) S(k) + i\varepsilon_{ijl}k^l H(k)\right] . \tag{1}$$

Such a random field can be characterised by its coherence length L_c and the field-strength B_λ averaged over the scale λ. The two-point function consists of two parts, one being proportional to the energy density $4\pi\int_0^\infty k^2 S(k)$ and one to the helicity density $4\pi\int_0^\infty kH(k)$. Helicity is closely analogous to vorticity in fluid dynamics and to the Chern-Simon number in field theory, counting the number of links and twists of field-lines.

In any causal generation mechanism, the coherence length has to be smaller than the Hubble horizon, $L_c(t_*) \lesssim H(t_*)^{-1}$ at the time of generation t_*. Therefore $\langle B_i(x)B_j(y)\rangle$ has compact support and its Fourier transform is an analytic function. Combining analyticity and the requirement of finite ρ gives then $B_\lambda \sim B_0(L_c/\lambda)^{5/2}$ instead of $B_\lambda \sim B_0(L_c/\lambda)^{3/2}$ naively expected in a random-walk picture. Therefore field modes on sufficiently large scales to be of interest today are strongly suppressed at generation.

In order to answer the question if the EGMF can be generated successfully in the early universe by phase transitions or during inflation one has to address the following two rather separated key problems: First one has to derive the coherence length L_c and the field-strength B_λ with which the field is generated at t_* within a specific particle physics model. Secondly, one has to understand the evolution of the field modes afterwards, especially those with wave-number smaller than the horizon scale. Since magnetohydrodynamics (MHD) is a non-linear theory, this question is highly non-trivial.

3.1 Generation mechanisms

Magnetogenesis at the weak scale has several aspects common with baryogenesis. Both mechanisms require a first (or second) order phase transition. Moreover, the generation of helicity is closely related to the generation of baryon asymmetry. Thus successful magnetogenesis requires as baryogenesis an extension of the standard model, to ensure a first order transition and facilitate the generation of helicity.

As an alternative may serve inflation as a "acausal" generation mechanism , i.e. one where $L_c \gg H_0^{-1}$ is possible. In such a scenario, it is possible to generate fields coherently on arbitrarily large scales, simply requiring enough e-foldings inflation during the magnetic field generation. On the other hand, the inflationary generation mechanisms is much less predictive than electroweak magnetogenesis.

3.2 Evolution of the field

The evolution of primordial magnetic fields is driven by three basic effects: i) cosmological dilution, ii) cascading of magnetic turbulence and iii) damping. Cosmological dilution caused by the expansion of the universe, $B \propto 1/a^2$, where a is the scale-factor of the universe, arises simply because for an ideal conductor the magnetic flux $\Phi = \int \mathrm{d}A\, B$ is conserved. The latter condition is for the the plasma in the early universe—except for the phase between recombination and reionisation—an excellent approximation.

Numerical MHD simulations show a transfer of magnetic energy from small to large magnetic configurations, a phenomenon known in hydrodynamics as an inverse cascade. Such cascade processes are connected to the conservation of magnetic helicity.

Damping of MHD perturbations was studied by Jedamzik, Katalini and Olinto who first determined the damping rates of fast and slow magnetosonic waves as well as of Alfven waves. As a spatially tangled magnetic field produces Lorentz forces which accelerate the plasma and set up oscillations, Alfven waves are excited. In the absence of dissipation, this process would continue until for all scales shorter than the Hubble time an approximate equipartition between magnetic and kinetic energies is obtained. If the fluid is non-ideal, however, shear viscosity will induce dissipation of kinetic energy, hence also of magnetic energy, into heat. In this case dissipation will end only when the magnetic field reaches a force-free state.

The question how damping, inverse cascades, and the coupling to hydrodynamic turbulence with $\rho_\lambda \sim \rho_0 (L_c/\lambda)^{3/2}$ affects the important large-scale magnetic field fluctuations requires in the future more detailed studies, before one can either exclude or validate either phase transitions or inflation as generation mechanism of the observed EGMF.

4 Summary

I discussed how the non-observation of GeV extensions around TeV blazars can be used to derive lower limits on the strength and the filling factor of the EGMF: Since the electron cooling length is much smaller than the mean free path of the TeV photons, a sufficient suppression of the point-like flux requires that the EGMF fills a large fraction along the line-of-sight towards

TeV blazars, $f \gtrsim 0.6$. This requires that EGMFs were generated in a space filling manner, e.g. primordially in phase transitions or inflation.

Acknowledgements I am grateful to all my co-authors for fruitful collaborations and discussions.

1. L. M. Widrow, Rev. Mod. Phys. **74**, 775 (2002); D. Grasso and H. R. Rubinstein, Phys. Rept. **348** (2001) 163 R. M. Kulsrud and E. G. Zweibel Rept. Prog. Phys. **71**, 0046901 (2008).
2. R. Plaga, Nature **374**, 430 (1995).
3. Takahashi, K. et al. 2008, ApJL 687, L5
4. Murase, K. et al. 2008, ApJ, 686, L67
5. Murase, K. et al. 2009, Phys. Rev. Lett. **103**, 081102
6. Aharonian, F. A., Coppi, P. S. and Völk, H. J. 1994, ApJ, 423, L5
7. A. Neronov and D. V. Semikoz 2007, JETP Lett., 85, 473
8. Dolag, K., Kachelrieß, M., Ostapchenko, S. and Tomàs, R. 2009, ApJ, 703, 1078
9. Elyiv, A., Neronov, A. and Semikoz, D. V. 2009, Phys. Rev. D **80**, 023010
10. Neronov, A. et al. 2010a, ApJ 719, L130
11. Neronov, A. and Vovk, I. 2010, Science, 328, 73
12. Tavecchio, F. *et al.* 2010a, MNRAS **406**, L70 (2010)
13. M. Kachelrieß, S. Ostapchenko, R. Tomàs, [arXiv:1106.5508 [astro-ph.HE]], the program is available from `http://elmag.sourceforge.net/`.
14. Burrows, D. et al. 2005, Space Sci. Rev. 120, 165, 2005
15. K. Dolag, M. Kachelrieß, S. Ostapchenko and R. Tomàs, Astrophys. J. **727**, L4 (2011). [arXiv:1009.1782 [astro-ph.HE]].
16. Aharonian, F. *et al.* 2007, A & A, 475, L9

RECENT RESULTS FROM THE PIERRE AUGER OBSERVATORY

I. LHENRY-YVON[1], for the PIERRE AUGER COLLABORATION[2]
1 Institut de Physique Nucléaire d'Orsay, CNRS/IN2P3,
Université Paris-Sud 11 , 91 406 Orsay cedex, France
2 Observatorio Pierre Auger, Av. San Martin Norte 304, 5613 Malarge, Argentina full author list at http: // www. auger. org/ archive/ authors_2011_3. html

The Pierre Auger Observatory is measuring the ultra-high energy cosmic ray air showers with unprecedented sensitivity. Recent results will be reported, including measurements of the spectrum and anisotropy studies at the highest energies. These results will be discussed together with the latest composition estimations from the measurement of the depth of shower maximum by the fluorescence detector.

1 Introduction

The Pierre Auger Observatory is the largest aperture cosmic ray observatory at present, built to reach large statistics for the low flux of Ultra High Energy Cosmic Rays (UHECR). Constructed in the province of Mendoza, Argentina, the observatory is the first hybrid air shower experiment combining two independent observation techniques [1]. Indeed, it consists of a 3,000 km^2 array of 1660 water Cherenkov stations with 1.5 km spacing on a triangular grid (the surface detector, SD), overlooked by 24 fluorescence telescopes housed in four buildings (fluorescence detector, FD). These two detectors measure in a complementary way the extensive air showers initiated by primary cosmic rays. The longitudinal development of air showers in the atmosphere is measured directly with the FD. It has better energy resolution and well understood energy systematics, while the SD has greater statistics and a well defined aperture. In addition, the depth of maximum development of the showers is measured with the FD. This observable encodes information about the composition of the primaries and about the properties of the first hadronic interactions.

The Pierre Auger Observatory started data taking in January 2004 with only 100 water Cherenkov detectors and one fluorescence telescope and is operating continuously since then. The construction of the Observatory was completed in mid 2008.

2 The Pierre Auger Observatory

Each of the 1660 SD stations is a 10 m^2 area tank containing a depth of 1.2 m of ultra-pure water. Cherenkov light produced in the water by shower particles is collected by three photomultiplier tubes and signals are digitized in 25 ns bins and time-stamped using a local GPS receiver. Trigger and signal information is transmitted to a central data acquisition system via technology based on mobile telephony [1]. The surface array operates with a close to 100% duty cycle, and the acceptance for events above 3.10^{18}eV is nearly 100% [3]. The 4 sites of the fluorescence

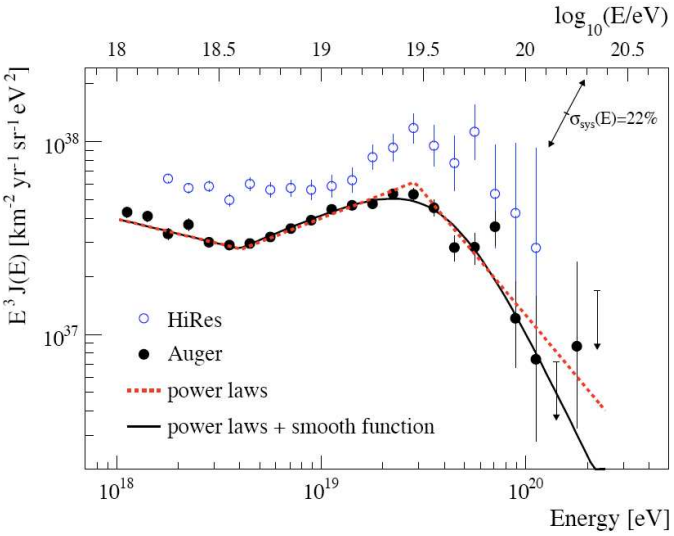

Figure 1: The combined hybrid and SD spectra from the Pierre Auger Collaboration [5] compared with the stereo spectrum from the HiRes experiment [9].

detectors are located on the edge of the SD array [2]. Each site contains 6 telescopes covering 180° of azimuth and 30° of elevation. A telescope consists of a 11m^2 spherical mirror with a 2.2 m diameter entrance aperture containing a corrector ring for improved image quality, and an optical filter (300-400 nm) tuned for the nitrogen fluorescence signal. Images are formed on a 440-pixel photomultiplier camera, and signals are digitized with 100 ns resolution, providing a time profile of the shower as it develops in the atmosphere. The FD can be operated only when the sky is dark and clear, and has a duty cycle of 10-15%. In contrast to the SD, the acceptance of FD events depends strongly on energy [4] and extends down to about 10^{18} eV.

A subset of showers is observed simultaneously by the SD and FD. These hybrid events are very precisely measured and provide an invaluable calibration tool. Hybrid events allow the cross-checks of SD arrival direction assignments by the fluorescence detectors as well as SD cross-checks of the FD triggering efficiency, important in the calculation of the exposure for the hybrid spectrum. In addition, the FD allows a roughly calorimetric measurement of the shower energy since the amount of fluorescence light generated is proportional to the energy deposited along the shower path; in contrast, extracting the shower energy via analysis of particle densities at the ground relies on predictions from hadronic interaction models describing physics at energies beyond those accessible to current experiments. Hybrid events can therefore be exploited to set a model-independent energy scale for the SD array, which in turn has access to a greater data sample than the FD due to the greater live time.

The hybrid nature of the Pierre Auger Observatory allows unprecedented analysis where key scientific outputs are produced avoiding when possible the heavy use of simulation. Even if the interpretation of results like the elongation rate may require comparison with air shower simulations, the production of the experimental result is largely free of simulation input.

3 Spectrum

A key observable in the study of UHECRs is their energy spectrum measured on Earth. Figure 1 presents the energy spectra calculated using data from the Pierre Auger Observatory[5].

This spectrum was obtained by combining the spectra derived from SD events and from hybrid events, using a maximum likelihood method. This analysis used SD events acquired between January 2004 and December 2008 and hybrid events acquired between November 2005

and May 2008. The exposure for SD events is 12,790 km^{2}sr yr. The calculation of the energy-dependent hybrid exposure is challenging, and requires a detailed simulation that takes into account measured atmospheric and detector conditions [6]. Quality and anti-bias cuts are applied to the events to minimize the influence of mass composition on the expected exposure.

As is traditional, the flux axis is multiplied by E^3 to emphasise features of the rapidly falling spectrum. The spectrum can be described by a broken power-law, E^{-s}, with spectral index $s \sim 3.3$ below the break (called the ankle) around $10^{18.6}$ eV, and $s \sim 2.6$, followed by a flux suppression above $10^{19.5}$ eV. Compared with an extrapolation of the power law spectrum above $10^{18.6}$ eV, the flux drops to 50% of the expectation at $10^{19.6}$ eV. The significance of the deficit is 20σ and confirms (with superior statistical power) the result reported by the HiRes Collaboration [7]. The vertical error bars represent statistical uncertainties. A systematic error in energy will shift a spectrum diagonally on such a plot. The reported systematic uncertainties of the energy measurement of the Pierre Auger Observatory (22%, indicated on plot) and HiRes (17%) suggest that the two spectra are consistent.

The spectral suppression (GZK "feature" [?]) at the highest energies is frequently attributed to photopion production by protons against the cosmic microwave background, but heavy nuclei experience similar energy losses via interactions with cosmic photons. In particular, iron suffers photo-erosion interactions with CMB photons, giving an energy loss length for the leading particle ($E/\frac{dE}{dX}$) which drops below 100 Mpc at energies beyond $10^{19.5}$ eV, quite similar to the energy loss length of protons due to the GZK interaction[10]. Alternative interpretation attribute the flux decrease to a limitation of acceleration mechanisms in sources.

A full astrophysical interpretations of the energy spectrum requires information on the mass composition of the flux and input from anisotropy analysis.

4 Anisotropies of the highest energy events

Our searches for cosmic ray anisotropy include point source correlations with the highest energy particles. They are motivated by the fact that cosmic rays trajectories in galactic and extra-galactic magnetic fields become straighter as the energy increases. This gives the hope that cosmic ray astronomy may become feasible at ultra-high energies. Moreover, the GZK effect, if observed, would limit the horizon from which UHECR can be observed to less than about 100 Mpc. This would imply that only sources within a relatively close-by neighborhood can contribute to the fluxes observed at Earth.

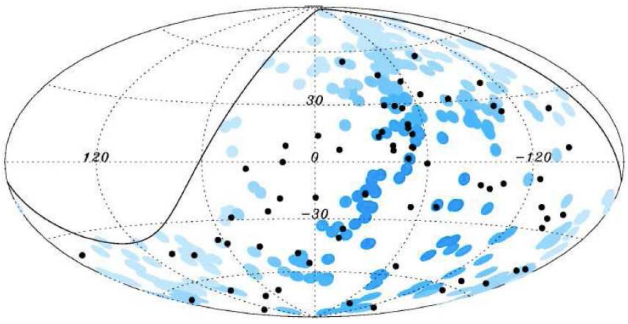

Figure 2: Sky map of 69 events (E>5.5 10^{19} eV) detected by the Auger Observatory up to 31 December 2009, including 14 events from the data set used to define the prescription [12]. The blue circles have radius 3.1° and define the 318 AGNs from the Véron-Cetty ans Véron catalog that are within the field of view of the observatory and have z≤ 0.018. Darker blue indicates higher relative exposure.

An analysis performed by the Auger Collaboration indeed established a correlation with the

Active Galaxy Nuclei (AGN) in the Véron Cetty and Véron (VCV) catalog [11]. This correlation (9/13 i.e. 69%) was most significant for events above 55 EeV and angular separations of less than 3.1° from AGN closer than 75 Mpc.

An update on this correlation has recently been published [12], and the sky map is shown in Figure 2. The fraction of events correlating is now 21/55 or 0.38, compared to the expectation for an isotropic distribution of arrival directions of 0.21, as illustrated in Figure 3. While this degree of correlation is lower than was expected given the earlier publication, the arrival directions are still anisotropic at the following level: there is a 0.3% chance of finding 21 or more correlating events from an isotropic distribution of arrival directions.

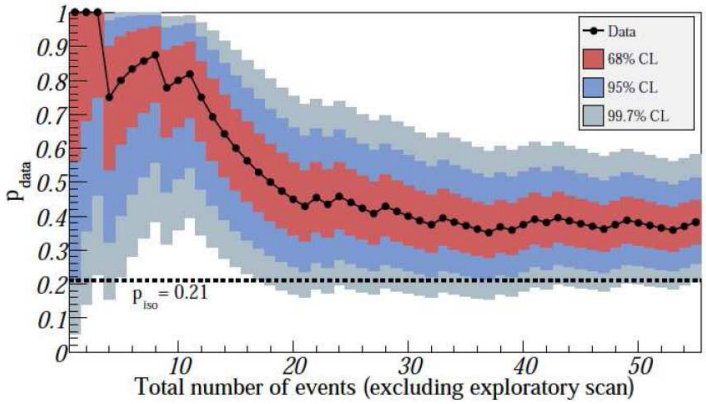

Figure 3: The most likely degree of correlation $pdata = \frac{k}{N}$ as a function of the total number of time ordered events, N (excluding the events in the exploratory scan). k is the number of correlating events. The 68%, 95% and 99.7% confidence level intervals around the most likely value are shaded. The horizontal dashed line shows the isotropic expectation of 0.21. From reference [12].

Our recent publication also explores some interesting correlations of the high energy arrival directions with astronomical objects. All of these studies are made a posteriori, and therefore cannot be used to estimate a confidence level for anisotropy. We find that there exists a cluster of events with E $< 5.5\ 10^{19}$ eV around the direction of the local active galaxy Centaurus A, which is of particular interest since it lies at only ~ 4 Mpc from us. The degree of clustering is maximised for a radius of 18° centred on the object, where we observe 13 events while only 3.2 are expected from the hypothesis of isotropy. Whether these events come from Cen A or from other sources, such as from the Centaurus cluster lying behind (at 45 Mpc) is still unclear, but this is certainly a region that looks especially promising for future anisotropy searches.

The correlation of our largest energy events (E $> 5.5\ 10^{19}$ eV) with two other astronomical catalogs are investigated. The correlation with 22,000 normal galaxies within 200 Mpc from the 2MRS catalog of galaxy redshifts (a subset of the 2MASS galaxy catalog), and the 373 x-ray galaxies closer than 200 Mpc from the Swift-BAT catalog, is also studied by calculating the number of pairs (a cosmic ray arrival direction + a galaxy direction) within angles ranging from 1 to 90. We find that the number of correlating pairs is above expectation for both catalogs over a broad range of correlating angles, but the significance cannot be evaluated in such a posteriori study.

5 Mass Composition

Knowledge of the mass composition is another key component in understanding the origin of UHECR. For instance, the variation of composition with energy may shed light on what mechanism is responsible for the ankle, and help to clarify whether the flux suppression is the GZK effect or a limitation of acceleration mechanisms [13]. Information about the mass and type of

a primary particle can be inferred from various observational features of extensive air showers, most importantly from the electron/muon ratio of particles at ground and from measurements of the depth of maximum development of the shower in the atmosphere. For example, a primary proton of given energy will penetrate much deeper into the atmosphere than an Fe nucleus of the same total energy and will lead to much larger fluctuations on shower-by-shower basis.

The two related observables accessible to fluorescence telescopes are X_{max} and its fluctuations. The measurement of X_{max} by the FD is straightforward in that the depth of maximum is directly viewed for many EAS. However, care must be taken in order not to introduce bias in the event selection nor in reconstruction that would result in X_{max} distributions inconsistent with reality. The most serious potential bias results from the limited elevation range of the FD field of view (FOV). The FOV of each telescope covers approximately 2° to 30° in elevation. For showers landing close to an FD station, the limited FOV may result in shallow developing showers (smaller X_{max}) not being properly viewed, and an X_{max} distribution being biased towards deeper showers. For distant high-energy showers, there is some danger of a bias in the other direction, since near-vertical deeply developing showers will hit ground level (or exit the FD FOV) before X_{max} is reached. To avoid these biases, fiducial volume cuts are applied to the data based on the shower geometry and energy. A minimum range of viewable atmospheric depths is demanded, such that X_{max} would be detected and measured with good resolution no matter the nature of the primary particle. A procedure for defining the viewable depth ranges using the data themselves is described in [14]. With these cuts, we have verified that the analysis is free of bias using simulations of the detection and reconstruction of proton and iron primary particles, and a 50:50 mixture of each; the mean input depths of maximum, and their fluctuations, are well reproduced by the analysis.

The typical X_{max} measurement uncertainty is estimated using simulations, but importantly the calculation is verified by the data themselves. At sufficiently high energies, above 10^{19} eV, a large fraction of showers are seen by two or more fluorescence detectors, and X_{max} can be independently measured in each. Comparing those depths of maximum, we find that the typical measurement resolution at 10^{19} eV is 20 ± 2 g/cm^2, in excellent agreement with the simulation result of 19 ± 0.1 g/cm^2 [15]. This provides confidence in the simulation which must be relied upon to estimate the depth of maximum resolution at lower energies.

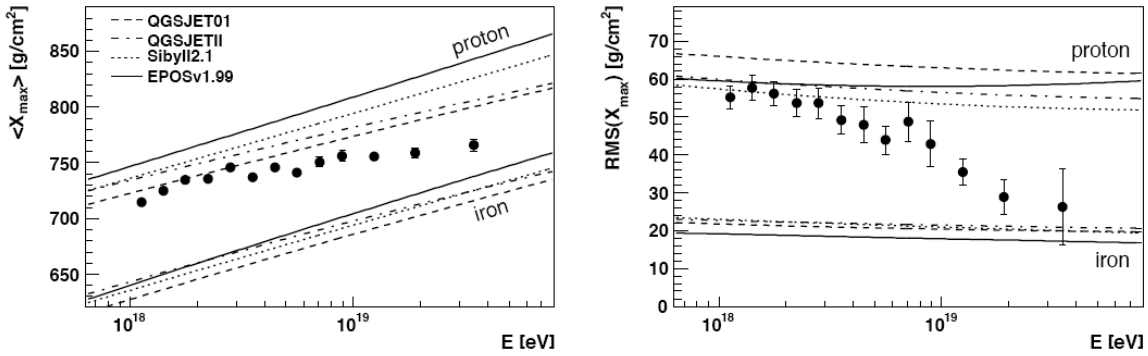

Figure 4: Mean and RMS of the Xmax distribution as a function of energy from [15]. Data are compared with expectations for proton and iron primary particles assuming four representative hadronic interaction models.

The results of such measurements are presented in Figure 4 together with predictions for proton and Fe primaries using different hadronic interaction models [15]. These models are based on extrapolation of features of hadronic interactions well beyond the cms-energies accessible at

man-made accelerators. Their uncertainties are correspondingly large and the wide distribution of predictions in the figure demonstrates that the systematic uncertainties in this analysis can be significant.

With this caveat kept in mind, a transition from a light composition up to the ankle approaching the expectations for heavier nuclei up to 40 EeV is inferred from both the X_{max} values and from its RMS values. Unfortunately, FD data statistics do not yet allow the extension of these X_{max} measurements into the GZK domain, where the onset of directional correlations is observed. An Fe dominated composition to beyond 55 EeV would indeed be challenging to understand in combination with the reported observations of directional correlations with AGN. One needs to note here that an increase of the p-nucleus inelastic cross-section beyond what is adopted in the interaction models could mimic the expectations for heavier nuclei, but simultaneous description of X_{max} and its RMS would be difficult to reach. Thus, LHC data in the forward region will be of great importance to improve the reliability of the interaction models. This, together with increased statistics, particularly of composition observables and anisotropy measurements at higher energies will help to unravel the puzzles of cosmic rays at the highest energies.

6 Conclusion

Our future plans include continuing to accumulate over 7000 km^2sr of exposure every year with the current observatory in Argentina.We are developing new analysis techniques (e.g.mass composition indicators from SD data) and exploring new detection techniques (f.i. using radio-detection) while extending our energy reach downwards. Unexpected results, like the tension between a possible heavy composition and anisotropy at the highest energies, adds to the interest and excitement in the field. The results of the Auger Observatory have shown that a large collection area is mandatory for collecting good arrival direction statistics, but that good mass and energy resolutions are crucial for the solution to this long-standing puzzle.

References

1. J. Abraham et al. [Pierre Auger Coll.], *Nucl. Instrum. Methods* **A523**, 50 (2003)
2. J. Abraham et al. [Pierre Auger Coll.], *Nucl. Instrum. Methods* **A613**, 29 (2010)
3. J. Abraham et al. [Pierre Auger Coll.], *Nucl. Instrum. Methods* **A620**, 227 (2010)
4. J. Abraham et al. [Pierre Auger Coll.], *Astroparticle Physics* **35**, 368 (2011)
5. J. Abraham et al. [Pierre Auger Coll.], *Phys. Lett.* B **685**, 239 (2010)
6. P. Abreu et al. [Pierre Auger Coll.], *Astroparticle Physics* **34**, 368 (2011)
7. R. U. Abbasi et al.,*Phys. Rev. Lett.* **100**, 101101 (2008)
8. K. Greisen, *Phys. Rev. Lett.* **16**, 748 (1966); G.T. Zatsepin and V.A. Kuzmin, *Pisma Zh. Eksp. Teor. Fiz* **4**, 114 (1966)
9. R. U. Abbasi et al., HiRes Coll. *Astroparticle Physics* **32**, 53 (2009)
10. D. Allard, *Proc. Rencontres de Moriond 2009*, arXiv:0906.3156.
11. Abraham et al. [Pierre Auger Collaboration], *Science* **318**, 939 (2007) ,*Astroparticle Physics* **29**, 188 (2008)
12. P. Abreu et al. [Pierre Auger Collaboration], *Astroparticle Physics* **34**, 314 (2010)
13. D. Allard, N. G. Busca, G. Decerprit et al., *JCAP* **810**, 33 (2008)
14. M. Unger [Pierre Auger Collaboration], *Nucl. Phys.* B **190**, 240 (2009)
15. J. Abraham et al. [Pierre Auger Collaboration], *Phys. Rev. Lett.* **104**, 091101 (2010)

Observation of Ultra High Energy Cosmic Ray at Telescope Array Experiment

T.Nonaka
for Telescope Array Collaboration
Institute for Cosmic Ray Research
University of Tokyo 5-1-5 Kashiwanoha Kashiwa Chiba
277-8582 JAPAN

The Telescope Array(TA) experiment, located in the western desert of Utah, USA, at 39.3° north and 112.9° west, is designed for observation of air showers from ultra high energy cosmic rays. The experiment has a Surface Detector (SD) array surrounded by three Fluorescence Detectors (FD) to enable simultaneous detection of shower particles at ground level and fluorescence photons along the shower track. The SD array consists of 507 scintillation detectors (each consisting of 2 layers of scintillator of area $3m^2$) deployed with 1.2km of separation. Total coverage of the array is $\sim 700km^2$. Full hybrid observation was started using the entire array in March,2008. Detailed monitoring of the detector has been dedicated to confirm the stability of detector response and system operation. The variation of detector response due to outdoor environment needs to be monitored carefully. Here the observation status and result are presented.

1 Introduction

The main aim of the Telescope Array (TA) experiment [1] is to explore cosmic ray origin of the extremely high energy cosmic rays (EHECR) using their energy spectrum, composition and anisotropy. There exist two major methods of observation for detecting cosmic rays in this energy region. One is the method which was taken at the High Resolution Fly's Eye (HiRes) [5] experiment that detects air fluorescence light along air shower track using fluorescence detector. The other is the method adopted by the AGASA experiment that detects air shower particles at ground level using surface detectors deployed in wide area ($\sim 100km^2$).
The AGASA experiment reported that there are 11 events beyond the GZK cutoff [2,3] in the energy spectrum [4]. However, the High Resolution Fly's Eye (HiRes) experiment reported the existence of the GZK cutoff [5].
The Pierre Auger experiment confirmed a suppression on the cosmic ray flux at energy above 4×10^{19}eV [6]. But still the contradiction between results from fluorescence detectors and surface arrays remains to be investigated by having independent energy scale by both techniques.

2 Telescope Array experiment

The TA site is located in the desert at about 1400 m above sea level at the position (39.3° N, 112.9° W) as the center of the site in Millard County, about 200 km southwest of Salt Lake City in the state of Utah in the United States. An observatory to support construction and

operation of the TA instruments is in Delta city located near the northeast side of the array. The experiment is aimed for observation of the cascade shower induced by cosmic rays above 10^{19}eV. The altitude of the experimental site between 1300 and 1500 m above sea level is required for optimal condition to observe particles at nearly maximum development of the cascade. For hybrid observation the site is located in the semi-desert area with less town lights also. The climate enables us to keep higher duty cycle of FD-SD hybrid exposure. It is about 7 % of real time. Fig.1 shows layout of experimental setup. Fig.2 shows telescope and one of the deployed surface detector.

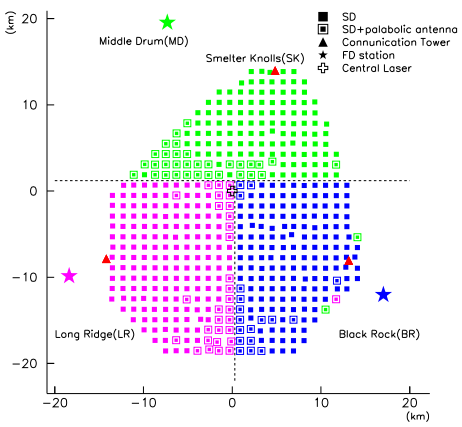

Figure 1: Layout of the Telescope Array in Utah, USA. there are three FD stations,three Commnunication Towers and 507 SD detectors)

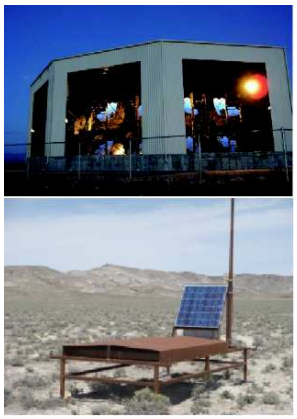

Figure 2: Top: Telescope array Fluorecence Detector (LR,BR)Bottom: Surface Detector deployed in the field.

2.1 Fluorescence Detector

The three FD stations which is surrounding SD array is observing sky above SD. The FD locates at the North west of site is known as the Middle Drum (MD) station [9]. The FDs locates at West and East of site is known as Long Ridge(LR) and Black Rock (BR) respectively. The MD station is instrumented with 14 refurbished telescopes from the HiRes-I site. The telescopes have a field of view that is 3-31° above horizon and 114° in azimuth centered to Central Laser Facility [10] which locates at center of TA observation site. The electronics system also shifted to MD site from HiRes experiment. The other two station LR and BR sites are each instrumented with 12 new telescopes and have a field of view which is 3-33° above horizon and 108° in azimuth. Three FD sites started standard data collection in Nov.2007.

2.2 Fluorecence Detector calibrations

New constructed FD detector(LR and BR telescope) consist of a spherical mirror,a PMT camera, and readout electronics [22,23]. The mirror has 3m of aperture. It is consist of 18 segment of hexagonal mirror. Each telescope has one camera at the prime focus of the mirror. The camera consist of 16x16 PMTs that has hexagonal shape (HAMAMATSU R9501) and UV transparent filter cut light $\lambda \geq 400$nm on its surface. The corresponding field of view is 15° × 18° (elevation×azimuth).

There are several steps of calibration to monitor absolute gain of PMTs. For several number of PMTs,the quantum efficiency (QE) and collection efficiency (CE) are measured by production company. To obtain non uniformity of each PMT, uniformity of photo cathode have been measured by using LEDs on XY scanner [25]. Three PMTs for each camera are calibrated its

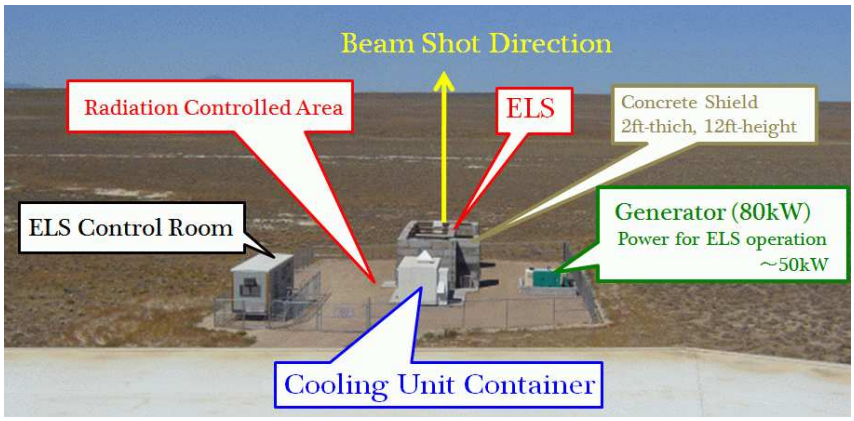

Figure 3: Set Up of ELS facility

absolute gain in Laboratory using Rayleigh scattering light from nitrogen [26]. The gain of those standard PMT are monitored using tiny light source called YAP pulser on its surface. The YAP pulser is an scintillator($YAIO_3$:Ce) contain 50Bq alpha-ray source (Am^{241}). The temperature dependence of the YAP also checked [30]. The relative gain of PMTs in a camera is measured and every hour by using Xe light source. The Xe light source consists of an Xe lanp and a 4mm thick Teflon diffuser is mounted at the center of each telescope.The detailed uniformity of light on the camera surface and its evaluation is summarized in a paper [25]. Since the mirrors are exposed to out side while observation the reflectivity of mirror are monitored. The precise measurement of reflectivity are done regularly with the photometer. It enable us monitor time variations and degradations of mirror reflectance. The reflectance change is ~3% per half year at a mirror mounted lowest place and less than 1% per half year at a mirror highest place. The mirror is washed periodically the washing make the reflectivity to be recovered. For more the detail of instrument and evaluation of spectral reflectivity,it is summarized in a paper [24].

2.3 Electron light source

To do an end to end calibration ,electron light source [13] also have started operation. The Electron Light Source (ELS) is an electron linear accelerator. The output beam energy is 40 MeV and the typical out put is 10^9 electrons in 1μsec pulse width. It locates 100m away forward of center of BR telescopes. The light amount observed at FD station is compared with the expectation obtained from calculations based on electron transportation , ray trace and fluorescence yield model using measured out put beam energy and measured current. Currently The instrument also have started it's operation since September of 2010. [11] The system was constructed and assembled in KEK [?] in Japan and shipped to Utah.

2.4 Surface Detector

Fig.2 shows one of the SDs which have deployed at one of the communication towers placed at hill called Smelter Knolls(SK). The SD communication antenna is mounted at the 3m of iron pole and the height is adjustable. There a 1m×1m square solar panel is seen. Front end electronics and a battery are contained in the box made of 1.2mm of thick stainless steel under the solar panel. Each surface detector consists of two layers of plastic scintillators. Each layer of scintillator has $3m^2$ of area and 1.2cm thick. Scintillation light is collected through 104 of 5m long Wave-Length Shifting fibers (WLSfiber Y-11 Kuraray make) those are laid for each layer. Both ends of the fiber are bundled and connected to a PMT (Electron tubes : 9124SA) to obtain uniform responce. The SD array is divided into three sub-arrays of 207,190 and 110

SDs. The sub-arrays are named Long Ridge(LR) array , Black Rock(BR) array and Smelter Knolls(SK) array respectively. The LR array covers west side of the entire array.The SK and BR covers north and east side,respectively. Each sub-array is controlled from its trigger judgment electronics installed at communication tower. At energy of $\sim 10^{18.7} eV$, the trigger efficiency of SD array reaches 100%. [16] The more detail of trigger system and calibrations is summarized in paper [17,18,19]

3 Current observation result

In the analysis, we determine total energy of primary cosmic ray , arrival direction and depth of maximum development. Here the depth of maximum development is called Xmax.

In case of event reconstruction using SD data, arrival direction and charge density at 800m from shower core is extracted as S(800) from observed arrival timing and lateral distribution of shower particles.

Here the S(800) is known as a parameter which well represent primary energy as shown in fig4. The 800m is optimized distance under TA detector configuration and altitude. The details of employed Lateral Distribution Function and shower disk structure are based on the lateral distribution [28] and arrival time distribution [27] respectively. And those LDF are made to fit well with the one obtained air shower Monte Carlo simulation (CORSIKA +QGSJETII) [31]. This method gives 1.2° of resolution in arrival direction and 20% of energy resolution at E≥ $10^{19.0} eV$. Using the relation between observed S(800),zenith angle and primary energy obtained from MC, first estimation of primary energy is obtained. The detailed procedure for reconstructing shower in SD observation is described at [29].

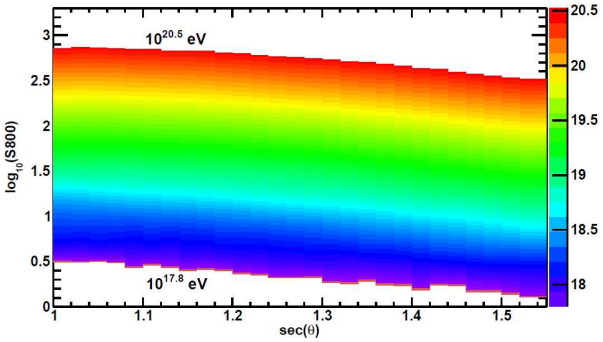

Figure 4: S(800) and primary particle energy at different zenith angale.

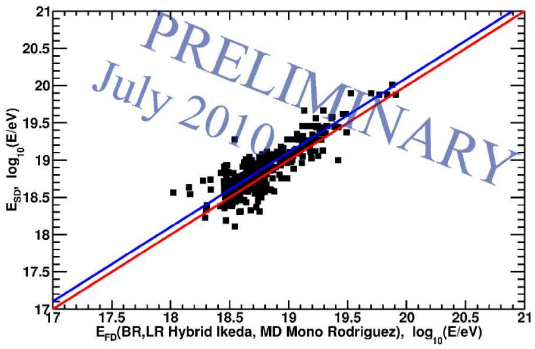

Figure 5: Energy calibration betwenn SD and FD using hybrid event

In case of FD event reconstruction, there are two way of reconstruction of shower geometry. One is using shower track and timing recorded in one FD and timing in SD. Another is using shower track recorded in two FDs. The former is called Hybrid reconstruction, latter is called stereo reconstruction. In case of hybrid reconstruction,the angular resolution is typically 1.1°[32]. In case of stereo reconstruction ,the angular resolution is more precise.

The primary energy and Xmax depth is determined from observed shower development after deter ming shower axis. The observed photon is basically proportional to energy deposition of shower particles and Cerenkov photons directed to telescope. The shower development fit with Gaisser-Hillas (GH) function. Here a method called Inverse Monte Carlo are employed. It determines the longitudinal shower development by comparison with the observed charge of each PMT between data and MC generated by using GH function. In the MC we consider Cherenkov and non-uniformity of detector response with applying calibration factor. Currently the fluorescence yield used in this analysis consists of differential spectrum taken from FLASH

model[33] and total yield from Kakimoto model[34]. Missing energy which is a energy taken by neutral particles in shower is also considered by comparing standard air shower Monte Carlo codes. The estimated amount of missing energy is about 8%. The more detail of calculation is described in [32]. Fig5 shows correlation of reconstructed energy reconstructed with SD and FD(Hybrid analysis).

3.1 Energy spectrum

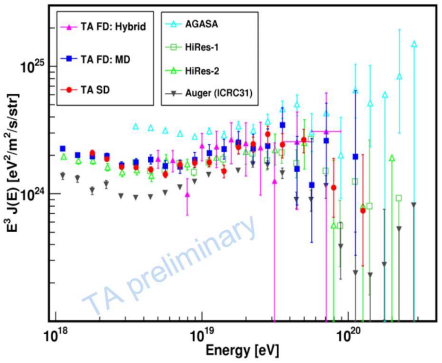

Figure 6: Observed energy spectrum at TA with different method.

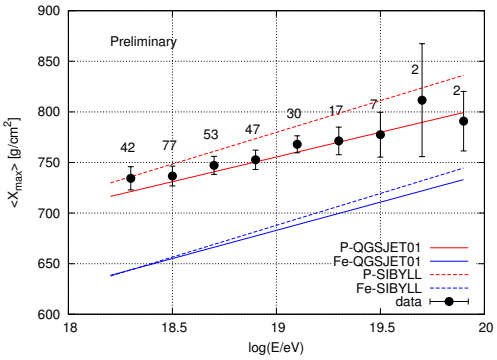

Figure 7: Observed Xmax elongation compared with the one expected from Proton and Iron primary.

Spectrum from MD station from data collected over a three year period December 2007-September 2010 shows very good agree ment with HiRes spectra. The detail of the analysis of the MD telescope is described in [35]. At Hybrid event reconstruction performed using LR and BR FD. The effective aperture after the quality cuts in obtained using Monte Carlo simulation code COSMOS [36]. Systematic uncertainty in the fluorescence yield(12%), atmospheric attenuation (11%) and the absolute detector calibration (10%). Total systematics are ∼19% in energy measurement from Hybrid observation. The Hybrid spectrum was obtained data set from May 2008 to Septamber 2009. There was 1978 of hybrid event. After reconstruction , 124 event remain above $10^{18.65}$eV. The quality cut applied is mainly consist of Xmax is ovserved and zenith angle is less than 45°. The energy resolution is 8%. The preliminary spectrum is shown in fig.6, together with MD FD and SD spectrum [29] calibrated using FD Hybrid energy scale. The SD spectrum shown in Fig.6 is obtained from data from May 2008 to February 2010. Its energy is calibrated using the hybrid event. The exposure at SD observation is approximately 1500 km^2 sr yr. Which is equivalent the total exposure of the AGASA experiment. The spectrum from SD shows feature that there is two breaks at logE of 19.75 and 18.71 which is correspond to the GZK suppression and the ankle respectively. Observed event above $10^{19.75}$eV are five event. Expected number of event from continuous spectrum is 18.4 event. The suppression of flux is seen with significance of about 3.5σ.

3.2 Chemical composition

In case of hevier nuclei primary,air shower cascade develop shallower depth. Since the cascade develop until energy is distributed to electro-magnetic component which have energy of critical energy, primary cosmic ray which have higher mass number give shallower Xmax as compared to proton which have same total energy. As an indicator of the primary chemical composition, the Xmax was measured by using data set from November 2007 to September 2010. There stereo reconstruction method is employed to obtain accurate geometry reconstruction and the obtained Xmax distribution are compared with the one obtained from events generated from

CORSIKA code using two interaction model QGSJET-01 and SIBYLL. In this analysis method, the resolution of Energy is ∼8% and the one of Xmax is 23g/cm^2 at energy of $10^{19.0}eV$.

Since there is a bias due to a limited elevation range of field of view, the observed Xmax distribution is compared with MC event analyzed in same way with real data. The result shown in fig.7 is the observed Xmax average including observation bias. The result is in good agreement with pure proton predicted using the QGSJET-01 model under same bias effect with real data. Comparison of observed Xmax distribution at several energy bins with Monte Carlo also performed and result is surmised in [37].

3.3 Arrival direction anisotropy

Since the exposure observed by SD array is largest in northern hemisphere and quite uniform along right ascension due to stable operation of array. It is an advantage to see anisotropy of arrival direction .Fig.8 is a skymap from observed events has energy of 4×10^{19}eV. The deflection in our galaxy become smaller int this energy range. If a strong cosmic ray source exist, there is possibility to see such object as a clustering of the observed arrival direction [38,39].

Fig.9 shows number of pair of event per solid angle observed as a function of opening angle between two event. From data set May.2008 to September 2010,Total 42 events are observed

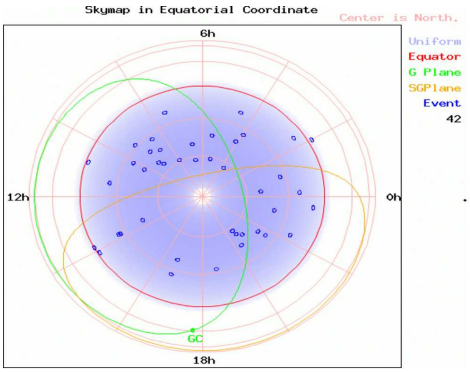

Figure 8: Distribution of arrival direction in equetrial coordinate.

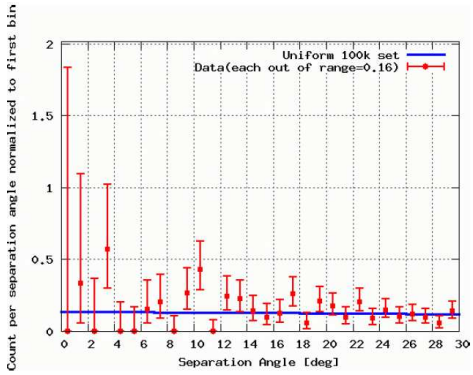

Figure 9: Comparison of number of pair events in unit solid angle with the expected uniform event distribution.

above 4×10^{19}eV. From observed number of event, 0.84 of cluser are expected from uniform distribution in 2.5° of angle distance. Observed number of cluster is 1. Till now there no significant excess of clustering is seen. The detailed analysis method is summarized in a paper [40].

4 Discussion and Summary

We presented current status of observation of Telescope Array experiment. The exposure for UHECR will reach equivarant to AGASA experiment. The spectrum from MD detector obtained monocular observation is consistent with previous observation (HiRes) experiment. The spectrum from Hybrid (BR,LR+SDs) also consistent with MD and HiRes experiment. The spectrum from SD is showing 3.5σ level of flux cutoff at the energy which is consistent with GZK cutoff and HiRes spectrum. The Xmax distribution is compatible with proton in this energy range. Now more detailed study for anisotropy using SD data and more analysis of the recorded data is on going.

Acknowledgments

The Telescope Array experiment is supported by the Ministry of Education, Culture, Sports, Science and Technology-Japan through Kakenhi grants on priority area (431) "Highest Energy Cosmic Rays", basic research awards 18204020(A), 18403004(B) and 20340057(B); by the U.S. National Science Foundation awards PHY-0307098, PHY-0601915, PHY-0703893, PHY-0758342, and PHY-0848320 (Utah) and PHY-0649681 (Rutgers); by the Korea Research Foundation (KRF-2007-341-C00020); by the Korean Science and Engineering Foundation (KOSEF, R01-2007-000-21088-0); by the Russian Academy of Sciences, RFBR grants 07-02-00820a and 09-07-00388a (INR), the FNRS contract 1.5.335.08, IISN and Belgian Science Policy under IUAP VI/11 (ULB). The foundations of Dr. Ezekiel R. and Edna Wattis Dumke, Willard L. Eccles and the George S. and Dolores Dore Eccles all helped with generous donations. The State of Utah supported the project through its Economic Development Board, and the University of Utah through the Office of the Vice President for Research. The experimental site became available through the cooperation of the Utah School and Institutional Trust Lands Administration (SITLA), U.S. Bureau of Land Management and the U.S. Air Force. We also wish to thank the people and the officials of Millard County, Utah, for their steadfast and warm supports. We gratefully acknowledge the contributions from the technical staffs of our home institutions and the University of Utah Center for High Performance Computing (CHPC).

References

1. H.Kawai *et.al J.Phys.Soc.Jpn Suppl,A 79 (2009) 108*
2. K. Greisen, *Phys. Rev. Lett. 16, (1966) 748.*
3. T. Zatsepin and V.A.Kuzmin, *JETP Lett 4 (1966) 178.*
4. M. Takeda *et.al.*, *Phys. Rev. Lett. 81 (1998) 1163.*
5. T. Abu-Zayyad *et.al.*, *Phys. Rev. Lett. 92 (2004) 151101.*
6. J. Abraham *et.al.*, *Phys.Rev.Lett.101 (2008) 061101.*
7. N. Hayashida *et.al*, *Astroparticle Physics 10 (1999) 3031311.*
8. H. Wahlberg *et.al*, *Proceedings of the 31th ICRC in Łódź ID ???,(2009)*
9. J.N. Matthews *et al.*, Telescope Array Collaboration, 30th ICRC, Merida (2007).
10. S. Udo *et. al.*, *Proceedings of the 30th ICRC in Merida Vol.5 (2007) 1021.*
11. T. Shibata *et al.*, Telescope Array Collaboration, 30th ICRC, Merida (2007).
12. http://www.kek.jp/intra-e/
13. T. Shibata *et al.*, *Nucl.Instr.and Meth. A 597 (2008) 61.*
14. S. Yoshida *et.al.*, *Proceedings of the 29th ICRC in Pune 8 (2005) 2411.*
15. S. Kawakami *et.al.*, *Proceedings of the 29th ICRC in Pune 8 (2005) 161.*
16. N. Sakurai *et.al.*, *Proceedings of the 30th ICRC in Merida, Vol.5 (2007) 1159.*
17. T. Nonaka *et.al.*, *Proceedings of the 30th ICRC in Merida,Vol 5 (2007) 1005.*
18. T. Nonaka *et.al.*, *Proceedings of the 31th ICRC in in Łódź (2009) ID974*
19. A. Taketa *et.al.*, *Proceedings of the 31th ICRC in Łódź (2009) ID855*
20. S. Iwamoto *University of Yamanashi Master thesis (2009).*
21. H. Sagawa *Proceedings of UHECR2010 in Nagoya (2011) O-10a3.*
22. Y. Tameda *et.al Nucl.Instr and Method A 609 (2009) 227.*
23. A. Taketa *et.al Nucl.Instr and Method A in prep.*
24. D. Ikeda *et.al Proceedings of the 31th ICRC in Łódź (2009) ID858*
25. H. Tokuno *Nucl.Instr and Method A 601 (2009) 364*
26. S. Kawana *et.al Proeedings of 31th ICRC in Łódź (2009) ID846*
27. Linsley,J *et.al J.Phys.G Nucl phys, 12,51-57 (1986)*
28. S.Yoshida *et.al J.Phys.G:Nucl.Phys 20,651-664 (1994)*

29. B.Stokes, D.Ivanov *et.al Proceedings of UHECR2010 in Nagoya (2011).O-12a3*
30. S.Ogio *et.al Proceedings of the 31th ICRC in Łódź (2009) ID811*
31. Heck D. *et al , Report FZKA (1998) 6019.*
32. D. Ikeda *et.al PhD.thesis, University of Tokyo (2010);Proceedings of UHECR2010 in Nagoya (2011) O-10P7*
33. Abbash.R.U *et.al*, *J.Astropart phys 2007.11.010, (2007)*
34. F.Kakimoto *et.al Nucl.Instr and Method A 372,527-533, (1996)*
35. D. Rodriguez, *PhD.thesis, University of Utah (2011).*
36. K.Kasahara *et.al Proceedings of the 30th ICRC in Merida (2007)*
37. Y. Tameda *et.al PhD.thesis, Tokyo Institute of Technology (2010);Proceedings of UHECR2010 in Nagoya (2011) O-11p5.*
38. N. Hayashida *et.al Phys. Rev. Lett 77 (1996)78*
39. M.Takeda *et.al J.Phys.Soc.Jpn (Suppl) B 70 (2001)*
40. T.Okuda *PhD.thesis, Osaka City University (2011).Proceedings of UHECR2010 in Nagoya (2011).P-110*

7.
Dark Matter and Cosmology

DARK MATTER CANDIDATES: AXINO AND GRAVITINO

L. Covi
Institute for Theoretical Physics, Georg-August University Göttingen,
Friedrich-Hund-Platz 1, D-37077 Göttingen, Germany

We review the scenarios of axino and gravitino Cold Dark Matter, highlighting recent theoretical developments and discussing possible signatures in the SUSY searches at the LHC and in indirect Dark Matter detection experiments.

1 Introduction

Axino and gravitino are particles that are found in models extending the Standard Model of particle physics to include supersymmetry and either the Peccei-Quinn (PQ) symmetry [1] or gravity. These extensions of the SM have a strong theoretical motivation for completely independent reasons compared to providing a DM candidate: Supersymmetry [2] solves the hierarchy problem connected to the Higgs mass and allows for gauge coupling unification. It is also the largest possible extension of the Poincaré symmetry. Gravity of course does not need any justification, since it is the first force observed in nature and should in any case be taken into account in any model discussing cosmology. The PQ symmetry instead has at the moment no phenomenological motivation, but is the most promising solution of the strong CP problem and offers also without supersymmetry another viable DM candidate, the axion [3]. So in both cases the additional particles are not introduced just to explain the Dark Matter conundrum, but arise from the assumed symmetries and their properties are determined by no or very few free parameters.

Moreover it is easy to see that axino and gravitino do indeed have the right characteristics to be Dark Matter [4]: they do not carry charge nor baryonic number, they are massive since supersymmetry has to be broken and can be sufficiently heavy to become cold DM. Moreover, if they are the lightest supersymmetric particle, they can be stable or sufficiently long-lived to be still present today.

They are Dark Matter candidates of the type called "SuperWIMPs" [5] or "E-WIMPs" [6], since their interactions with the SM and themselves are non-renormalizable and suppressed, in one case by the Planck mass and in the other by the Peccei-Quinn scale f_a. They are therefore usually non-thermal relics and not WIMPs. In fact if they did reach thermal equilibrium in the early universe, they decoupled when still relativistic with a large number density, such that they must have mass in the keV range and can only be Hot or Warm DM [7].

The fact that they interact so weakly means also that they are very elusive particles to study and measure at a collider. Only if they are DM and played a substantial role in the evolution of the Universe we may hope to gain information on their properties, like mass and couplings. While the SuperWIMPs scenario may seem therefore far away from collider phenomenology or even DM detection, we will see that this is not the case and that a "SuperWIMP connection"

can arise, analogously as for the WIMP case, giving signals at LHC and, if R-parity is broken and the axino or gravitino DM is unstable, in indirect DM detection.

1.1 The axino

The Peccei-Quinn symmetry is an anomalous global $U(1)$ symmetry, broken at a high scale $f_a \sim 10^{11}$ GeV. After the breaking, the only surviving field in a non-supersymmetric model is the pseudo-goldstone boson of the symmetry, the axion. Due to the anomalous nature of the symmetry, the axion couples with the gluon field as [3]

$$\mathcal{L}_{PQ} = \frac{\alpha_s}{8\pi f_a} a F^a_{\mu\nu} \tilde{F}^{\mu\nu}_a \ . \tag{1}$$

This coupling has the same form as the QCD θ term and therefore a non-vanishing θ can be reabsorbed into a and becomes a dynamical field. At the chiral QCD phase transition the axion acquires a mass and a potential via instanton effects and relaxes to the minimum with zero effective θ solving the strong CP problem. This is the PQ mechanism in a nutshell.

The axino is the superpartner of the axion [8] and its couplings can be obtained by supersymmetrising the axion ones as [9]

$$W_{PQ} = \frac{\alpha_s}{4\sqrt{2}\pi f_a} A W^\alpha W_\alpha \ . \tag{2}$$

where A is the axion chiral multiplet and W^α the vector multiplet containing the gluino λ^α and the gluon. In some models also couplings with the other SM gauge groups can arise and are of the same type. There are different axion models, depending on the PQ charges of the SM fields and on the presence of additional states: the KVSZ models [10] assume the existence of heavy colored states charged under the PQ symmetry, while the DFSZ models [11] mix the axion with the Higgs fields and give PQ charge also to SM fields. In the latter models also the superpotential couplings between the axino and Higgs/Higgsino can become important [12,13]. For a recent discussion on the axino couplings in all its subtleties, including momentum dependence, see [14,13].

1.2 The gravitino

The gravitino is the superpartner of the graviton and belongs to the gravity multiplet in local supersymmetry (supergravity). Since the graviton has spin 2, the gravitino has spin 3/2 and its interactions are completely determined by the gravitational interaction and SUSY breaking [2]. In fact after SUSY breaking, thanks to the SuperHiggs mechanism, the gravitino absorbs the Goldstino state and becomes massive, similarly to what happens for the EW gauge fields with the Higgs Goldstone modes. If the gravitino is the lightest supersymmetric particle, the Goldstino component dominates the interactions and its couplings are just fixed by the Planck scale and the supersymmetry breaking masses. Singling out the Goldstino component as $\psi_\mu \sim i\sqrt{\frac{2}{3}}\frac{\partial_\mu \psi}{m_{\tilde{G}}}$ one obtaines the effective Goldstino lagrangian as [15]:

$$\mathcal{L}_{eff,\tilde{G}} = -\frac{m_\lambda}{4\sqrt{6} M_P m_{\tilde{G}}} \bar{\psi}\sigma^{\nu\rho}\lambda^a F^a_{\nu\rho} + i\frac{(m^2_\phi - m^2_\chi)}{\sqrt{3} M_P m_{\tilde{G}}} \bar{\psi} P_R \chi \phi^* + h.c. \tag{3}$$

where M_P is the Planck mass, $m_{\tilde{G}}, m_\lambda, m_\phi, m_\chi$ are the gravitino, gaugino, scalar and chiral fermion masses respectively. Here $\lambda, F_{\nu\rho}$ belong to the same vector multiplet, while ϕ, χ are the scalar and fermion in a chiral multiplet.

We see from the above expression that the (light) gravitino couplings are completely fixed by the particle spectrum and the Planck scale. This is a consequence of the fact that the Goldstino couples to the supercurrent. Note that the lighter the gravitino is, the stronger it couples for

the same superpartner masses. Since at the end all the SUSY breaking masses are proportional to the gravitino mass, the strength of the gravitino coupling is a signal of the SUSY breaking mediation model.

2 Thermal production and BBN constraints

Below the temperature at which the axino or gravitino are in thermal equilibrium, they are still produced by 2-to-2 body scatterings in the thermal bath. In considering these processes one can usually disregard back-reaction and obtains a thermal yield proportional to the highest temperature in the thermal bath, which we will call T_R. The interactions of axino and gravitino with the QCD gauge multiplet are very similar and the computations can be done with analogous techniques. One of the sources of uncertainties is the treatment of the IR divergence in the gluon t-channel, which has to be regulated by a gluon thermal mass. The gravitino abundance obtains substantial contributions from all SM gauge sectors, while on the other hand, the interaction with the EW and hypercharge groups is different and model-dependent for the axino case.

The gravitino yield reads [16]

$$\Omega_{\tilde{G}} h^2 = 0.3 \left(\frac{1\ \text{GeV}}{m_{\tilde{G}}}\right) \left(\frac{T_R}{10^{10}\ \text{GeV}}\right) \sum_i c_i \left(\frac{m_{\lambda_i}}{100\ \text{GeV}}\right) \tag{4}$$

where m_{λ_i} are the 3 gaugino masses and $c_i \sim \mathcal{O}(1)$.

So in general there is always a bound on the reheat temperature and such temperature has to take a specific value in order to match the DM density. Note that the smaller $m_{\tilde{G}}$, the smaller the temperature has to be. Also given a specific temperature, the gaugino masses must satisfy an upper bound to avoid overclosure [17], so that one cannot push the whole SUSY spectrum to a high scale and still have gravitino DM.

The axino yield instead is given as [18]

$$\Omega_{\tilde{a}} h^2 \sim 0.3 \left(\frac{m_{\tilde{a}}}{0.01\ \text{GeV}}\right) \left(\frac{T_R}{10^4\ \text{GeV}}\right) \left(\frac{10^{11}\ \text{GeV}}{f_a}\right)^2 \tag{5}$$

where $m_{\tilde{a}}$ is the axino mass. This computation has been recently revisited in [13], where also subleading terms in the gluon thermal mass have been included ending in a slightly larger yield than given in Eq. 5. In any case the axino DM case points at a pretty low reheat temperature [a].

For both axino and gravitino, also the yield coming from the decay of superpartners instead of scatterings can be substantial and even dominate the production. On one hand, the decay of particles still in thermal equilibrium has recently attracted renewed attention [19] since it results in a yield independent on the reheat temperature, but so it corresponds to the DM abundance only for a particular value of the DM mass. On the other hand, the decay of the NLSP out of equilibrium [20,5] may also generate the correct DM number density independently of the temperature, but it can also endanger Big Bang Nucleosynthesis (BBN) predictions [21]. In fact the decays produce not only axino/gravitino but also energetic SM particles, that may change the abundance of light elements and spoil the agreement of BBN with the observations. The key parameter to check how dangerous the decay can be for BBN is the NLSP lifetime, which is very different for axino or gravitino LSP. For a Bino NLSP we have

$$\tau_{\tilde{B}} = 0.25\ s \left(\frac{m_{\tilde{B}}}{100\ \text{GeV}}\right)^{-3} \left(\frac{f_a}{10^{11}\ \text{GeV}}\right)^2 \tag{6}$$

$$\tau_{\tilde{B}} = 5.7 \times 10^4\ s \left(\frac{m_{\tilde{B}}}{100\ \text{GeV}}\right)^{-5} \left(\frac{m_{\tilde{G}}}{1\ \text{GeV}}\right)^2 \tag{7}$$

[a] Note, though, that very recently [14] finds a suppressed yield for axion models with light PQ charged fermionic states.

for axino and gravitino LSP respectively. So we see immediately that the BBN constraints are much more stringent for gravitino DM than for the axino case, since for the axino case the NLSP often decays before BBN starts. For this reason, BBN constraints play an important role in the axino LSP scenario only for large values of f_a as obtained in [22] [23].

Different mechanisms have been proposed to ease these troubles with Nucleosynthesis, e.g. NLSP dilution by entropy production [24], or tuning of the NLSP to have harmless decay channels, etc.. Here we will consider only two possibilities: reducing the NLSP number density by coannihilation with the gluino or shortening of the NLSP lifetime via R-parity breaking.

3 NLSP coannihilation and degenerate gaugino spectrum

Considering a light degenerate gaugino spectrum has two clear advantages: on one side it allows for larger T_R since the gravitino abundance is reduced by small gaugino masses [25] and on the other it allows to reduce substantially the NLSP number density at freeze-out via coannihilation [26]. We proposed this scenario in particular in order to reach reheat temperatures compatible with thermal leptogenesis [27]. We found that the most efficient coannihilation is between gluinos and Bino neutralinos and that it suppresses the Bino abundance up to four order of magnitude for a mass degeneracy below 5%. The coannihilation of Wino neutralino with the gluino is instead much less strong and does not improve much the situation; nevertheless, even without a degenerate gluino, the Wino neutralino coannihilates with the charginos and this effect allows to avoid the BBN constraints in a small window for light Wino around 100 GeV [28]. For Higgsino neutralino, the strong annihilation via Higgs resonance is more efficient in reducing the abundance than the coannihilation with the gluino.

We are therefore lead to a scenario with Bino-gluino coannihilation and in such case the BBN constraints can be evaded for light NLSP masses below 300 GeV and gravitino masses of the order of 1-10 GeV. The scalar supersymmetric spectrum was chosen heavy in our model, with sleptons above 600 GeV and squarks above 1 TeV.

3.1 Collider signatures and constraints

Such a low gluino and Bino mass may seem to be already excluded by colliders. Unfortunately (or fortunately for us) it is not, and this is due to the fact that the gluino decays mainly into Bino and gluon with a very soft jet, most of the cases with tranverse momentum below the experimental cuts. The signal from two light gluinos remains then only missing energy with very soft radiation and it is not easily triggered on.

More promising is instead the associate production of a squark and a gluino. Then an energetic jet arises from the much heavier squark decaying into gluino and quark and the resulting signal is a mono-jet and missing energy, similarly to what happens for WIMP DM with ISR [29] or graviton production in extra-dimensional models like ADD. The gluino-squark production rate depends strongly on the squark mass and we estimated last year that the first phase of LHC measurements, with 1 fb^{-1} of data, should be able to exclude a 300 GeV gluino NNLSP up to squark masses as large as 1.8 TeV. Preliminary results on the monojet signature have been presented in this conference [30] by the CMS collaboration for 36 pb^{-1}. Recently at the Europhysics Conference on High-Energy Physics 2011, new results were presented using 1 fb^{-1} of data by the ATLAS collaboration, which correspond to a model-independent constrain on the cross-section times acceptance for a monojet to lie below 0.11 pb at 95% CL [?]. While a detailed analysis of the acceptance for our scenario is missing, assuming it to be larger than 90%, this exclusion reaches approximately our expectation.

4 R-parity breaking

One easy way to avoid any clash with BBN predictions is to assume that the NLSP decays fast enough, i.e. with a lifetime below 0.1 s. This may happen for conserved R-parity if the gravitino is lighter than 0.01 GeV or so (see Eq. 7 for the dependence on the NLSP mass), but the decay is usually much faster if R-parity is violated, since it can proceed via a renormalisable interaction. In general the R-parity violating superpotential is given by

$$W_{R\not{p}} = \mu_i L_i H_u + \lambda_{ijk} L_i L_j E^c_k + \lambda'_{ijk} L_i Q_j D^c_k + \lambda''_{ijk} U^c_i D^c_j D^c_k \tag{8}$$

where capital letters denote MSSM chiral multiplets. The couplings μ_i, λ, λ' violate not only R-parity, but also lepton number conservation, while λ'' violates the baryon number conservation. If all these couplings are non-vanishing, the proton decays much too quickly, but for suppressing proton decay to acceptable level it is sufficient to require λ'' to be zero or very very small. The other couplings then can be large enough to allow for the decay of the NLSP directly to SM particles before BBN. Note that in this case there is no gravitino/axino in the final state and therefore no yield from NLSP decay.

The lifetime of a Bino NLSP can be estimated to be of the order

$$\tau_{\tilde{B}} \sim 10^{-10}\ s \left(\frac{|\zeta|}{10^{-7}}\right)^{-2} \left(\frac{m_{\tilde{B}}}{100\ \mathrm{GeV}}\right)^{-1} \tag{9}$$

where ζ denotes the dominant R-parity violating coupling $\sim \frac{\mu_i}{\mu}, \lambda, \lambda'$ and the superpartners are assumed to have $m \sim m_{\tilde{B}}$. It is clear therefore that even R-parity violating couplings as small as 10^{-12} can still lead to NLSP decay before Nucleosynthesis. On the other hand, the R-parity and lepton violating couplings do have to be sufficiently small to avoid wash-out of the baryon number via sphaleron processes and this gives an upper bound around 10^{-7}. We have then a window of couplings between $10^{-7} - 10^{-12}$ that gives consistency between cosmology and gravitino DM [32]. For the case of axino DM, we have seen that the BBN constraints are much weaker and R-parity violation is probably not necessary, but still possible [9].

4.1 Axino and gravitino decay

If R-parity is broken, then the LSP is not stable any more and we could be in danger of losing our DM candidate. We can see that this does not happen, since the decay rates are very small due to the non-renormalizable couplings and the smallness of the R-parity violation. The lifetimes for axino and gravitino for the case of bilinear R-parity violation read [33,9]

$$\tau_{\tilde{a}} = 10^{27}\ s \left(\frac{|\zeta|}{10^{-10}}\right)^{-2} \left(\frac{m_{\tilde{B}}}{100\ \mathrm{GeV}}\right)^{2} \left(\frac{m_{\tilde{a}}}{10\ \mathrm{GeV}}\right)^{-3} \left(\frac{f_a}{10^{11}\ \mathrm{GeV}}\right)^{2} \tag{10}$$

$$\tau_{\tilde{G}} = 10^{27}\ s \left(\frac{|\zeta|}{10^{-7}}\right)^{-2} \left(\frac{m_{\tilde{B}}}{100\ \mathrm{GeV}}\right)^{2} \left(\frac{m_{\tilde{G}}}{10\ \mathrm{GeV}}\right)^{-3} \tag{11}$$

and can therefore be much longer than the age of the Universe. Similar lifetimes can be expected for trilinear R-parity violation, studied in the case of the gravitino in [34,35], but the decay channels are different. For gravitino masses just below the W/Z threshold 3-body decays are important though also for the case of bilinear R-parity breaking [36].

This lifetime may appear to be too large to give any observable signal, but note that it is smaller than the bounds on the proton lifetime. In fact the smallness of the decay rate is compensated by the number of DM particles in our halo and we can therefore predict signals from DM decay in all possible cosmic ray channels, i.e. gamma-rays [37], neutrinos [38] and gamma-rays and charged particles together[39]. For the case of bilinear parity violation, the most stringent

bounds arise from the recent FERMI search for γ-lines [40], which can be translated into a bound on the decaying particle lifetime of the order of 6×10^{28} s [41,42]. This already excludes part of the interesting parameter space for gravitino Dark Matter [41,42], requiring $\zeta < 10^{-8}$, and is even stronger for the axino case, for which the R-parity violation couplings have already to be less than 10^{-11}.

4.2 Signals at colliders

Both in the case of R-parity conservation or not, the NLSP may appear stable at colliders and just escape with either missing energy for a neutralino NLSP or a charged track, for e.g. a stau NLSP. For the axino case, the NLSP can have a large range of lifetimes, but it always decays outside the detector, both for conserved R-parity, due to $f_a > 5 \times 10^9$ GeV, see Eq. 6, and for broken R-parity, due to the smallness of ζ, as discussed in the previous section. In this case, probably the most promising signal is a metastable stau NLSP leaving a highly ionizing track in the LHC detectors.

For gravitino LSP instead, different signals are possible, also depending on the NLSP. For the R-parity violation scenario with neutralino NLSP, the constraints from the FERMI Gamma-ray telescope push the decay length to be of order 100 m [42], but still a fraction of NLSPs could decay inside the detectors and be observed at the LHC [41]. In the same scenario with stau NLSP instead, the relation between the FERMI constraints and the stau decay length is more model-dependent [41] and also shorter decay lenghts may still be allowed.

Instead if R-parity is conserved, the NLSP decays inside the detectors only if the gravitino is light [43], with mass smaller than 1 MeV. Then even kinks in stau tracks may be observable [44]. For larger masses the NLSP will escape the detector as in the axino case and it will be difficult to distinguish between the different LSPs. In principle if the NLSP is charged and can be stopped, its decay may allow to disentangle the two cases [45].

5 Conclusions

The axino and the gravitino are good DM candidates, with similar properties. For both cases the reheat temperature in the Early Universe is bounded from above and Big Bang Nucleosynthesis gives constraints on the lifetime and density of the NLSP. These bounds are usually severe for the gravitino, but can be relaxed in specific scenarios. Here we have presented the case of a neutralino NLSP with a degenerate gaugino spectrum, which allows to avoid the constraints and gives quite special signatures at the LHC.

We have also shown that axino and gravitinos can survive as DM even for broken R-parity, but the breaking has to be suppressed. Indirect DM searches already set limits on the R-parity breaking couplings on the order 10^{-11} and 10^{-8} for the axino and the gravitino respectively. In the case of the axino LSP, R-parity breaking does not bring substantial advantages with respect to Nucleosynthesis constraints, apart for the case of very large f_a.

Different signals are expected at the LHC for axino or gravitino LSP compared to the usual supersymmetric scenarios with neutralino LSP: displaced vertices are still possible for the light gravitino case or for R-parity breaking parameters not far from the present bounds. Otherwise also just missing energy due to a long-lived neutralino NLSP or a metastable charged NLSP could appear as a signal. In the last case, it will be more difficult to identify the nature of the LSP.

Acknowledgments

It is a pleasure to thank G. Bertone, A. Brandenburg, W. Buchmüller, K.Y. Choi, , M. Grefe, J. Hasenkamp, K. Hamaguchi, A. Ibarra, H. B. Kim, J. E. Kim, M. Olechowski, S. Pokorski, J. Roberts, L. Roszkowski, F. D. Steffen, D. Tran, K. Turzynski, J. D. Wells and T. Yanagida for the fruitful collaborations. The author would like also to thank the organizers of Rencontres de Moriond EW 2011 for the chance to present this talk, the very lively and enjoyable atmosphere during the meeting and their patience in waiting for these Proceedings.

References

1. R.D. Peccei, H. R. Quinn, *Phys. Rev. Lett.* **38**, 1440 (1977).
2. J. Wess and J. Bagger, *Supersymmetry and supergravity*, (University Press, Princeton, 1992).
3. For recent reviews, see, J. E. Kim and G. Carosi, Rev. Mod. Phys. **82**, 557 (2010) and P. Sikivie, *Int. J. Mod. Phys.* A **25**, 554 (2010).
4. G. Bertone, D. Hooper and J. Silk, *Phys. Rept.* **405** 279 (2005).
5. J. L. Feng, A. Rajaraman and F. Takayama, *Phys. Rev. Lett.* **91**, 011302 (2003); J. L. Feng, A. Rajaraman and F. Takayama, *Phys. Rev.* D **68**, 063504 (2003); J. L. Feng, *Annals Phys.* **315**, 2 (2005).
6. K. Y. Choi and L. Roszkowski, *AIP Conf. Proc.* **805**, 30 (2006).
7. H. Pagels and J. R. Primack, *Phys. Rev. Lett.* **48**, 223 (1982); K. Rajagopal, M.S. Turner and F. Wilczek, *Nucl. Phys.* B **358**, 1991 (447).
8. H. P. Nilles and S. Raby, *Nucl. Phys.* B **198**, 102 (1982); K. Tamvakis and D. Wyler, *Phys. Lett.* B **112**, 451 (1982); J. M. Frere and J. M. Gerard, Lett. Nuovo Cim. **37**, 135 (1983); J. E. Kim, *Phys. Lett.* B **136**, 78 (1984).
9. L. Covi and J. E. Kim, *New J. of Phys.* **11** (2009) 105003
10. J. E. Kim, *Phys. Rev. Lett.* **43**, 103 (1979); M. A. Shifman, V. I. Vainstein, V. I. Zakharov, *Nucl. Phys.* B **166**, 4933 (1980).
11. M. Dine, W. Fischler and M. Srednicki, *Phys. Lett.* B **104**, 199 (1981); A. P. Zhitnitskii, Sov. J. Nucl. Phys. **31**, 260 (1980).
12. E. J. Chun, arXiv:1104.2219 [hep-ph].
13. K.Y. Choi, L. Covi, J. E. Kim and L. Roszkowski, to appear soon.
14. K. J. Bae, K. Choi and S. H. Im, arXiv:1106.2452 [hep-ph].
15. T. Lee and G. H. Wu, *Phys. Lett.* B **447**, 83 (1999).
16. M. Bolz, A. Brandenburg and W. Buchmüller, *Nucl. Phys.* B **606**, 518 (2001) [Erratum-ibid. **790**, 336 (2008)]; J. Pradler and F. D. Steffen, *Phys. Rev.* D **75**, 023509 (2007); V. S. Rychkov and A. Strumia, *Phys. Rev.* D **75**, 075011 (2007).
17. M. Fujii, M. Ibe and T. Yanagida, *Phys. Lett.* B **579**, 6 (2004).
18. L. Covi, H. B. Kim, J. E. Kim and L. Roszkowski, JHEP **0105**, 033 (2001); A. Brandenburg and F. D. Steffen, JCAP **0408**, 008 (2004); A. Strumia, JHEP **1006**, 036 (2010).
19. L. Covi, L. Roszkowski and M. Small, JHEP **0207**, 2002 (023); C. Cheung, G. Elor and L. Hall, arXiv:1103.4394 [hep-ph]; C. Cheung, G. Elor and L. J. Hall, arXiv:1104.0692 [hep-ph].
20. L. Covi, J. E. Kim and L. Roszkowski, *Phys. Rev. Lett.* **82**, 4180 (1999)
21. For a recent review see K. Jedamzik and M. Pospelov, *New J. Phys.* **11**, 105028 (2009).
22. A. Freitas, F. D. Steffen, N. Tajuddin, and D. Wyler, *Phys. Lett.* B **679**, 270 (2009); A. Freitas, F. D. Steffen, N. Tajuddin, and D. Wyler, *Phys. Lett.* B **682**, 193 (2009); A. Freitas, F. D. Steffen, N. Tajuddin and D. Wyler, arXiv:1105.1113 [hep-ph].
23. H. Baer, S. Kraml, A. Lessa, S. Sekmen, JCAP **1011** 040 (2010); H. Baer, S. Kraml,

A. Lessa, S. Sekmen, JCAP **1104** 039 (2011).
24. J. Kersten, Reconciling Supersymmetry and Thermal Leptogenesis, These Proceedings; J. Hasenkamp and J. Kersten, *Phys. Rev.* D **82**, 115029 (2010).
25. M. Olechowski, S. Pokorski, K. Turzynski and J. D. Wells, JHEP **0912** 026 (2009).
26. L. Covi, M. Olechowski, S. Pokorski, K. Turzynski and J. D. Wells, JHEP **1101**, 033 (2011).
27. For a recent report, see S. Davidson, E. Nardi and Y. Nir, *Phys. Rept.* **466** 105 (2008).
28. L. Covi, J. Hasenkamp, S. Pokorski and J. Roberts, JHEP **0911** 003 (2009).
29. J. Kopp, *Collider Limits on Dark Matter*, These Proceedings.
30. F. Santanastasio, *Exotica Searches at CMS*, These Proceedings.
31. A. Baroncelli, *Exotics Searches in Jet Final States with the ATLAS detector*, Talk at the Europhysics Conference on High-Energy Physics 2011.
32. W. Buchmüller, L. Covi, K. Hamaguchi, A. Ibarra, and T. Yanagida, JHEP 03 037 (2007).
33. F. Takayama and M. Yamaguchi, *Phys. Lett.* B **485**, 388 (2000).
34. S. Lola, P. Osland and A. R. Raklev, *Phys. Lett.* B **656**, 83 (2007).
35. B. Bajc, T. Enkhbat, D. K. Ghosh, G. Senjanovic and Y. Zhang, JHEP **1005**, 048 (2010).
36. K. Y. Choi and C. E. Yaguna, *Phys. Rev.* D **82**, 015008 (2010).
37. G. Bertone, W. Buchmüller, L. Covi and A. Ibarra, JCAP **0711**, 003 (2007); A. Ibarra and D. Tran, *Phys. Rev. Lett.* **100**, 061301 (2008).
38. L. Covi, M. Grefe, A. Ibarra and D. Tran, JCAP **0901**, 029 (2009).
39. A. Ibarra and D. Tran, JCAP **0807**, 002 (2008) K. Ishiwata, S. Matsumoto and T. Moroi, *Phys. Rev.* D **78**, 063505 (2008); W. Buchmüller, A. Ibarra, T. Shindou, F. Takayama and D. Tran, JCAP **0909**, 021 (2009); N. E. Bomark, S. Lola, P. Osland and A. R. Raklev, *Phys. Lett.* B **686**, 152 (2010).
40. A. A. Abdo *et al.*, *Phys. Rev. Lett.* **104**, 091302 (2010).
41. S. Bobrovskyi, W. Buchmüller, J. Hajer and J. Schmidt, JHEP **1010**, 061 (2010); S. Bobrovskyi, W. Buchmüller, J. Hajer and J. Schmidt, arXiv:1107.0926 [hep-ph].
42. G. Vertongen and C. Weniger, JCAP **1105**, 027 (2011).
43. K. Ishiwata, T. Ito and T. Moroi, *Phys. Lett.* B **669**, 28 (2008); P. Meade, M. Reece and D. Shih, JHEP **1010**, 067 (2010); J. L. Feng, M. Kamionkowski and S. K. Lee, *Phys. Rev.* D **82**, 015012 (2010).
44. S. Asai, Y. Azuma, M. Endo, K. Hamaguchi and S. Iwamoto, arXiv:1103.1881 [hep-ph].
45. A. Brandenburg, L. Covi, K. Hamaguchi, L. Roszkowski and F. D. Steffen, *Phys. Lett.* B **617**, 99 (2005).

Neutralino dark matter with a Light Higgs

Andreas Goudelis
Deutsches Elektronen-Synchrotron (DESY), Notkestrasse 85,
D-22603 Hamburg, Germany

We examine the neutralino dark matter (DM) phenomenology in supersymmetric scenarios with nonuniversal Higgs masses (NUHM) at the gauge coupling unification scale that can acommodate a light Higgs boson, where the correct relic density is obtained mostly through the annihilation into a pseudoscalar A. Our analysis shows that most part of the A pole region can produce detectable gamma-ray and antiproton signals. We further focus on uncertainties influencing the results in indirect and mainly direct detection.

1 Introduction

1.1 The model

One of the major experimental constraints on the constrained-MSSM parameter space comes from the LEP-2 limits on the lightest higgs boson mass. In particular, LEP-2 set a lower bound of 114.4 GeV for this mass [1], excluding the largest part of the model's viable parameter space. However, strictly speaking, this bound only applies to the SM. It comes mostly from searches in the Higgsstrahlung channel, which in the case of the MSSM is actually not identical to the SM one. In particular, $\sigma_{\rm MSSM}(e^+e^- \to hZ) = \sin^2(\beta-\alpha)\sigma_{\rm SM}(e^+e^- \to hZ)$ [2,3]. Hence, the LEP2 bound $m_h \gtrsim 114$ GeV applies to the MSSM only if $\sin^2(\beta-\alpha) = \mathcal{O}(1)$. This is the case in cMSSM/mSUGRA scenarios.

This limit can actually be partially circumvented once some of the cMSSM constraints are relaxed. In particular, it has been pointed out [4,5,6] that relaxing the requirement for higgs mass universality at the GUT scale can effectively reduce the $\sin^2(\beta-\alpha)$ factor, leading to a smaller cross-section and thus to weaker bounds on the lightest higgs mass.
Our particular model [7] is characterised by the following parameters

$$m_{1/2},\ A_0,\ \mathrm{sign}(\mu),\ \tan\beta,\ m_0,\ m^2_{H_u},\ m^2_{H_d} \tag{1}$$

where the GUT-scale common scalar mass m_0 concerns all scalars but the two Higgs bosons.

We examined the neutralino dark matter - related phenomenology of this model, notably the behavior of the relic density over some region of the parameter space, the prospects for indirect detection as well as the constraints coming from direct DM detection experiments. Viable parameter space points have to satisfy a number of constraints:
- Higgs boson mass limit: In the *non decoupling* region where the A boson becomes very light the lower limit of m_h goes down to 93 GeV or even lower. We consider that the parameter space with $\sin^2(\beta-\alpha) < 0.3$ (or, $\sin(\beta-\alpha) \lesssim 0.6$), and $93 < m_h < 114$ is in agreement with the LEP2 limit [1]. Consequently, the coupling of the heavier Higgs boson to the Z boson

($g_{ZZH} \propto \cos(\beta - \alpha)$) becomes dominant and this makes the heavier Higgs boson SM - like, so the LEP-2 114 GeV limit starts applying for the heavier CP-even higgs boson. On the other hand, in the decoupling region $\sin(\beta - \alpha) \sim 1$, which means that the 114 GeV limit applies to the lightest higgs. Given the fact that there exists an uncertainty of about 3 GeV in computing the mass of the light Higgs boson [8], we accept a lower limit of 111 GeV.
- $Br(b \to s\gamma)$ **constraint:** We demand [9,10] $2.77 \times 10^{-4} < Br(b \to s\gamma) < 4.33 \times 10^{-4}$.
- $Br(B_s \to \mu^+\mu^-)$ **constraint:** We further impose the important $Br(B_s \to \mu^+\mu^-)$ constraint coming from CDF, [11] $\mathrm{Br}(B_s \to \mu^+\mu^-) < 5.8 \times 10^{-8}$ (at 95 % C.L.), which has recently been improved to $< 4.3 \times 10^{-8}$ at 95% C.L [12].
- **WMAP constraint :** In computing the relic density constraint, we consider the 3σ limit of the WMAP data [13] $0.091 < \Omega_{CDM}h^2 < 0.128$. Here $\Omega_{CDM}h^2$ is the dark matter relic density in units of the critical density and $h = 0.71 \pm 0.026$ is the Hubble constant in units of 100 Km s^{-1} Mpc^{-1}. We use the code micrOMEGAS [14] to compute the neutralino relic density.

1.2 Dark matter detection

There exist two main modes of dark matter detection, usually referred to as "indirect" and "direct". Indirect detection is based on the principle that if DM can annihilate (or decay), in the early universe in order to give the measured relic density, this process should also occur today throughout the galaxy (and beyond), so we could hope to detect its annihilation products: gamma-rays, positrons, antiprotons and neutrinos. Direct detection of DM relies on the fact that WIMPs may interact with (scatter on) ordinary matter. This scattering is an in principle measurable effect and indeed a huge effort is currently being developped worldwide to measure potential signals coming from DM scatterings upon large underground detectors.

Concerning indirect detecion, in this work we compute the gamma-ray signals at intermediate galactic latitudes [15] in the spirit of elliminating as much as possible uncertainties coming from the DM "halo profile" (i.e. its distribution in the galaxy) as well as background contributions to the spectrum. These gamma-rays can be detected by the Fermi satelite [16]. For the case of antiprotons, we compute the prospects for detection in the AMS-02 mission [17]. We adopt a semi-analytical treatment of the diffusion equation [18,19,20], presenting results for the so-called MAX propagation model.

Finally, we compare the neutralino-nucleon spin-independent scattering cross-section to some of the tightest bounds available in the literature [21,22,23]. As it has been pointed out, uncertainties are not absent in direct detection as well. These can be of a twofold nature: First of all, when giving exclusion bounds on the $(m_\chi, \sigma_{\chi(p,n)})$ plane, a set of astrophysical assumptions (as well as some assumptions on the passage from the nuclear to the nucleonic level) have already been made. These assumptions are thought to have a small impact on the results, the mangitude of which depends, among other factors, on the considered mass range [24,25,26,27,28]. Secondly, there are often uncertainties in the cross-section computations performed by theorists in specific models. In our case, what is of relevance is one of the parameters entering the passage from the partonic to the the WIMP-nucleon scattering cross-section, denoted by f_{T_s}. This parameter is actually related to the strange quark content of the nucleon. Its value can be either measured or estimated through lattice QCD methods. The DarkSUSY [29] code, which was used to compute the cross-section, adopts a default value of $f_{T_s} = 0.14$. However, recent lattice simulations [30,31] point towards much lower values, of the order of 0.02, being even compatible with zero. The effect of this uncertainty has been quantified [32] and is known to range from negligible to very large, depending on the specific mechanism driving the scattering cross-section. In what follows we shall quantify the effect of this uncertainty showing that it is really crucial in assessing the viability of our models.

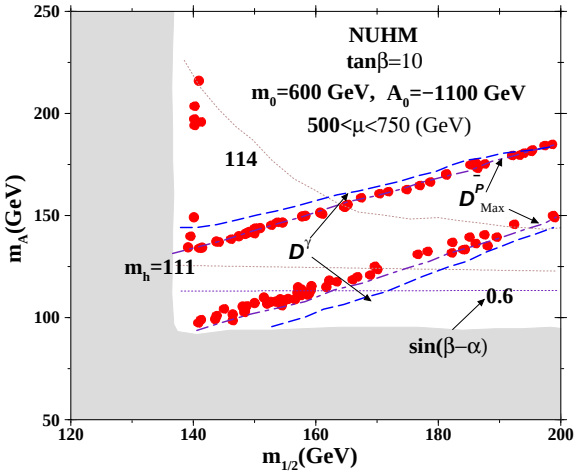

Figure 1: Viable points in the $m_{1/2} - m_A$ plane. Neutralino masses of $\sim 55 - 65$ GeV correspond to the *Light Higgs Boson* region. Detectability of the photon and anti-proton signals are represented by D^{γ} and $D^{\bar{p}}_{Max}$ lines.

2 Results

2.1 Indirect detection

We performed [7] two scans in the model's parameter space:
- In the first one, we fix $\tan\beta(= 10)$, $m_0 = 600$ GeV, $A_0 = -1100$ GeV, $\text{sign}(\mu) > 0$. Then, we vary the mass parameters m_{h_u} $(0 < m_{h_u} < m_0^2)$ and m_{h_d} $(-1.5m_0^2 < m_{h_d} < -0.5m_0^2)$ to obtain light neutralino dark matter consistent with light Higgs masses $(m_{H,A} \leq 250$ GeV) at the electroweak scale. μ and m_A are derived quantities. We note that the high μ parameter values obtained in this scenario correspond to an essentially pure bino LSP.
- In our second scan, we fix m_0 at the very similar value $m_0 = 600$ GeV, while $A_0 = -1000$ GeV is chosen to make $b \to s\gamma$ less restrictive. We set m_{h_u} $(= 2.4m_0^2)$ and vary m_{h_d} $(-0.3m_0^2 < m_{h_d} < 0.1)$ with $m_{1/2}$ to obtain the WMAP-compatible regions for neutralinos. Our scan renders very small μ values $(150 < \mu < 300)$, consequently the LSP can have large Higgsino components.
In both cases, we look for points satisfying the relic abundance requirement while passing all constraints previously mentioned. The viable points are then scattered on the $m_{1/2} - m_A$ plane as red dots.

Our results can be seen in figures 1 and 2. Appart from the WMAP-compliant points, we demonstrate in the same plots regions excluded by other constraints (gray regions), higgs mass isocontours, as well the parameter space regions that can be probed during a 3-year data acquisition period for Fermi and AMS-02: all points lying inside the two parallel lines in the case of fig.1 and on the left or below the lines in fig.2 can -in principle- be probed.

In the first set of scenarios, there are mainly two mechanisms that can generate the correct relic density: quasi-resonnant annihilation through a A or H pole, extending along the direction of the line where $2m_{\chi_1^0} \approx m_A, m_H$, or the light Higgs pole at low $m_{1/2}$ and along the m_A direction.

In the second set of scenarios the neutralino self-annihilation cross-section is enhanced kinematically as before (i.e. we are once again sitting near the A pole), but moreover the neutralino acquires a non-negligible higgsino component which enhances its couplings to the higgs bosons.

In both scenarios, we see that the detection prospects are quite good. Significant portions of the viable parameter space can be probed.

In the first case, perspectives are actually good along the A-pole. On the contrary, we see that the light higgs pole seems to be completely invisible in both channels. This is due to

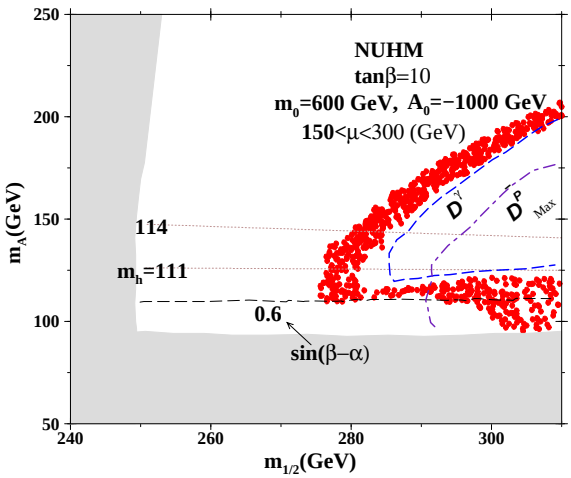

Figure 2: Same as Fig.1, except that the *light Higgs boson* zone is shifted to larger neutralino mass values.

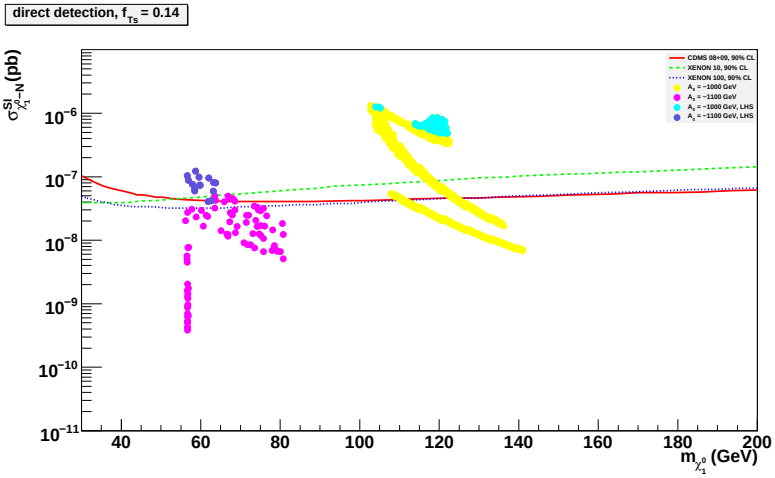

Figure 3: $(m_{\chi_1^0}, \sigma^{SI}_{\chi_1^0-N})$ combinations along with the relevant exclusion limits from direct detection experiments for $f_{Ts}^{(p,(n))} = 0.14$. Points lying above the lines are excluded according to the published limits. The light blue and the dark blue points represent the *light Higgs boson* regime for the two scenarios at stake.

the fact that whereas resonnant annihilation is an efficient mechanism in the early universe, the cross-section for this process tends to zero as the neutralino velocity does so [33,34]. This is actually the case at present times, which are of relevance for indirect detection. On the other hand, annihilation through a pseudoscalar is not that sensitive to changes in the WIMP velocity [33], so the cross-section remains relatively high even at present times.

In the second set of scenarios, the prospects are actually even better. On the one hand, any interference of CP-even higgs bosons is negligible. Moreover, the fact that in this case the neutralino has a significant higgsino component enhances its couplings to the higgs sector, an effect which is practically insensitive to velocity changes. So, the cross-section remains quite stable at present times.

2.2 Direct detection and associated uncertainties

As a final step, we computed the spin-independent neutralino-nucleon scattering cross-section. The results can be seen if figures 3 and 4, for two different values of the f_{T_s} parameter, namely the default DarkSUSY value of 0.14 and a reduced value of 0.02 respectively.

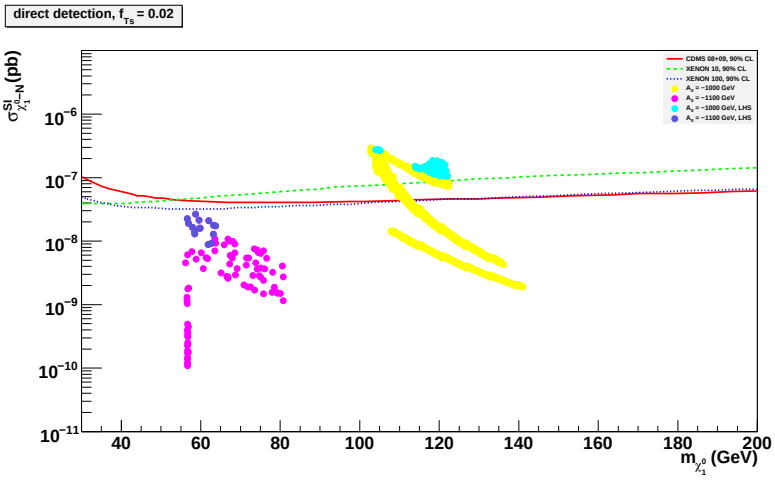

Figure 4: As in fig.3 but for $f_{Ts}^{(p,(n))} = 0.02$.

From fig.3 we see that our NUHM model seems to be hopelessly excluded, especially when it comes to the Light Higgs Scenarios. The situation seems to be however quite different once we look at fig.4.

A comparison of the two figures demonstrates the importance of the uncertainty in the value of f_{T_s}. We see that once we reduce its value from the default one towards lower values the cross-section is reduced by something like an order of magnitude. We further remind that f_{T_s} estimates are even compatible with zero. Moreover, once a set of astrophysical or nuclear uncertainties is taken into account (local density, velocity distribution, nuclear form factors), the experimental limits may be considered to bare an additional uncertainty of a factor $3-4$. We thus see that stating whether a model is excluded by direct detection data or not may be a tricky issue. All potential sources of uncertainty should be examined before definitively ruling out a model. Fortunately, a large effort is being devoted by several groups in quantifying these uncertainties and incorporating them in a systematic manner, both in the limits published by experimental collaborations and in the calculations performed by theorists.

Acknowledgments

The work of A.G. is supported in part by the Landes-Exzellenzinitiative Hamburg. A.G. would further like to thank the organisers of the Rencontres de Moriond 2011 for their warm hospitality.

References

1. R. Barate *et al.* [LEP Working Group for Higgs boson searches], Phys. Lett. B **565**, 61 (2003) [arXiv:hep-ex/0306033].
2. J. F. Gunion and H. E. Haber, Nucl. Phys. B **272**, 1 (1986) [Erratum-ibid. B **402**, 567 (1993)]; M. Carena and H.E. Haber, Prog. Part. Nucl. Phys. **50**(2003) 63.
3. A. Djouadi, Phys. Rept. **459**, 1 (2008) [arXiv:hep-ph/0503173].
4. R. Rattazzi, U. Sarid and L. J. Hall, arXiv:hep-ph/9405313; N. Polonsky and A. Pomarol, Phys. Rev. Lett. **73**, 2292 (1994) [arXiv:hep-ph/9406224]; D. Matalliotakis and H. P. Nilles, Nucl. Phys. B **435**, 115 (1995) [arXiv:hep-ph/9407251]; N. Polonsky and A. Pomarol, Phys. Rev. D **51**, 6532 (1995) [arXiv:hep-ph/9410231].
5. P. Nath and R. L. Arnowitt, Phys. Rev. D **56**, 2820 (1997) [arXiv:hep-ph/9701301]; J. R. Ellis, T. Falk, K. A. Olive and Y. Santoso, Nucl. Phys. B **652**, 259 (2003) [arXiv:hep-ph/0210205]; J. R. Ellis, K. A. Olive, Y. Santoso and V. C. Spanos, Phys. Lett. B **603**, 51

(2004); H. Baer, A. Mustafayev, S. Profumo, A. Belyaev and X. Tata, JHEP **0507**, 065 (2005); H. Baer, A. Mustafayev, S. Profumo, A. Belyaev and X. Tata, Phys. Rev. D **71**, 095008 (2005); J. R. Ellis, K. A. Olive and P. Sandick, Phys. Rev. D **78**, 075012 (2008); J. Ellis, K. A. Olive and P. Sandick, New J. Phys. **11**, 105015 (2009).
6. U. Chattopadhyay and D. Das, Phys. Rev. D **79**, 035007 (2009) [arXiv:0809.4065 [hep-ph]]; S. Bhattacharya, U. Chattopadhyay, D. Choudhury, D. Das and B. Mukhopadhyaya, Phys. Rev. D **81**, 075009 (2010) [arXiv:0907.3428 [hep-ph]].
7. D. Das, A. Goudelis and Y. Mambrini, JCAP **1012**, 018 (2010) [arXiv:1007.4812 [hep-ph]].
8. G. Degrassi, S. Heinemeyer, W. Hollik, P. Slavich and G. Weiglein, Eur. Phys. J. C **28**, 133 (2003); B. C. Allanach, A. Djouadi, J. L. Kneur, W. Porod and P. Slavich, JHEP **0409**, 044 (2004); S. Heinemeyer, W. Hollik and G. Weiglein, Phys. Rept. **425**, 265 (2006) [arXiv:hep-ph/0412214]; S. Heinemeyer, hep-ph/0408340; S. Heinemeyer, Int. J. Mod. Phys. A **21**, 2659 (2006).
9. S. G. Kim, N. Maekawa, A. Matsuzaki, K. Sakurai, A. I. Sanda and T. Yoshikawa, Phys. Rev. D **74**, 115016 (2006) [arXiv:hep-ph/0609076].
10. P. Koppenburg *et al.* [Belle Collaboration], Phys. Rev. Lett. **93**, 061803 (2004) B. Aubert, et al., BaBar Collaboration, hep-ex/0207076; E. Barberio *et al.* [Heavy Flavor Averaging Group (HFAG)], arXiv:hep-ex/0603003.
11. T. Aaltonen *et al.* [CDF Collaboration], Phys. Rev. Lett. **100**, 101802 (2008).
12. M. J. Morello [CDF Collaboration and D0 Collaboration], arXiv:0912.2446 [hep-ex].
13. E. Komatsu *et al.* [WMAP Collaboration], Astrophys. J. Suppl. **180**, 330 (2009), arXiv:0803.0547 [astro-ph].
14. G. Belanger, F. Boudjema, A. Pukhov and A. Semenov, Comput. Phys. Commun. **176**, 367 (2007) [arXiv:hep-ph/0607059].
15. F. Stoehr, S. D. M. White, V. Springel, G. Tormen and N. Yoshida, Mon. Not. Roy. Astron. Soc. **345**, 1313 (2003) [arXiv:astro-ph/0307026].
16. A. A. Abdo *et al.* [The Fermi-LAT collaboration], Phys. Rev. Lett. **104**, 101101 (2010) [arXiv:1002.3603 [astro-ph.HE]].
17. C. Goy [AMS Collaboration], J. Phys. Conf. Ser. **39**, 185 (2006).
18. D. Maurin, R. Taillet and C. Combet, arXiv:astro-ph/0609522.
19. D. Maurin, R. Taillet and C. Combet, arXiv:astro-ph/0612714.
20. J. Lavalle, Q. Yuan, D. Maurin and X. J. Bi, Astron. Astrophys. **479**, 427 (2008) [arXiv:0709.3634 [astro-ph]].
21. Z. Ahmed *et al.* [The CDMS-II Collaboration], arXiv:0912.3592 [astro-ph.CO].
22. E. Aprile *et al.* [XENON100 Collaboration], arXiv:1005.0380 [astro-ph.CO].
23. J. Kopp, T. Schwetz and J. Zupan, JCAP **1002**, 014 (2010) [arXiv:0912.4264 [hep-ph]].
24. C. McCabe, arXiv:1005.0579 [hep-ph].
25. A. M. Green, arXiv:1004.2383 [astro-ph.CO].
26. M. Weber and W. de Boer, arXiv:0910.4272 [astro-ph.CO].
27. P. Salucci, F. Nesti, G. Gentile and C. F. Martins, arXiv:1003.3101 [astro-ph.GA].
28. M. Vogelsberger *et al.*, arXiv:0812.0362 [astro-ph].
29. P. Gondolo, J. Edsjo, P. Ullio, L. Bergstrom, M. Schelke and E. A. Baltz, JCAP **0407**, 008 (2004).
30. J. Cao, K. i. Hikasa, W. Wang, J. M. Yang and L. X. Yu, arXiv:1006.4811 [hep-ph].
31. H. Ohki *et al.*, Phys. Rev. D **78**, 054502 (2008) [arXiv:0806.4744 [hep-lat]].
32. J. R. Ellis, K. A. Olive and C. Savage, Phys. Rev. D **77**, 065026 (2008) [arXiv:0801.3656 [hep-ph]].
33. G. Jungman, M. Kamionkowski and K. Greist, Phys. Rep. **267**, 195 (1995); G. Bertone, D. Hooper and J. Silk, Phys. Rept. **405**, 279 (2005).
34. N. Bernal and A. Goudelis, JCAP **1003**, 007 (2010) [arXiv:0912.3905 [hep-ph]].

TOKYO AXION HELIOSCOPE EXPERIMENT

Y. INOUE[1,4,a], Y. AKIMOTO[2,b], R. OHTA[2], T. MIZUMOTO[2,c], T. HORIE[2], A. YAMAMOTO[3,4], M. MINOWA[1,4]
(Sumico collaboration)
[1] *International Center for Elementary Particle Physics, The University of Tokyo, 7-3-1 Hongo, Bunkyo-ku, Tokyo 113-0033, Japan*

[2] *Department of Physics, School of Science, The University of Tokyo, 7-3-1 Hongo, Bunkyo-ku, Tokyo 113-0033, Japan*

[3] *High Energy Accelerator Research Organization (KEK), 1-1 Oho, Tsukuba, Ibaraki 305-0801, Japan*

[4] *Research Center for the Early Universe (RESCEU), School of Science, The University of Tokyo, 7-3-1 Hongo, Bunkyo-ku, Tokyo 113-0033, Japan*

The Tokyo axion helioscope experiment aims to detect the solar axions which can be produced in the solar core and are arriving to the Earth. It is equipped with a 2.3m-long 4T superconducting magnet to convert axions into photons, a gas container to hold dispersion-matching medium, a PIN-photodiode-array X-ray detector, and a telescope mount mechanism to track the Sun. In the latest measurement, the axion mass range $m_a = 0.84$–$1.00\,\mathrm{eV}$ was scanned. Analysis set a new limit on the axion-photon coupling constant to be $g_{a\gamma} < 5.6$–$13.4 \times 10^{-10}\mathrm{GeV}^{-1}$ at 95% CL. The latest result and the recent status of this experiment are presented.

1 Introduction

1.1 Axion model

The axion is a hypothetical elementary particle which was introduced to solve the "strong-CP problem" in quantum chromodynamics (QCD).[1] The effective Lagrangian contains a P- and CP violating term originating from the nonperturbative effects of QCD, whose strength is proportional to θ, an angular constant of the vacuum. This term is known to be physical and contributing to the electric dipole moment (EDM) of neutron. Moreover, the phase of the quark mass matrix affects it additively as $\bar{\theta} = \theta + \arg\det\mathcal{M}_q$. Thus, the apparent vanishing of the neutron EDM [2] implies the miraculous cancellation of the two independent physical constants.

Peccei and Quinn proposed a solution which involves the spontaneous breaking of a new global U(1) quasisymmetry, by which $\bar{\theta}$ changes dynamically. Although the postulated symmetry, $\mathrm{U}(1)_{\mathrm{PQ}}$, is a symmetry at the Lagrangian level, it must be explicitly broken by the nonperturbative effects of QCD. When it is spontaneously broken, the associated Nambu-Goldstone

[a] Speaker.
[b] Present address: Graduate School of Medicine, The University of Tokyo
[c] Present address: Cosmic-Ray Group, Department of Physics, Graduate School of Science, Kyoto University

boson field should relax to the potential minimum, where $\bar{\theta} = 0$, i.e., CP is conserved. The excitation about this minimum is called the axion and its mass m_a is related to the symmetry-breaking scale f_a by $m_a = \frac{\sqrt{z}}{1+z}\frac{f_\pi m_\pi}{f_a} = 6 \times 10^{15}[\mathrm{eV}^2]/f_a$. As far as the solution to the strong CP problem is concerned, there are no *a priori* values for f_a or m_a.

One of the universal properties of the axion is its coupling to two photons: [3]

$$\mathcal{L}_{a\gamma\gamma} = -\frac{1}{4} g_{a\gamma} a F^{\mu\nu} \tilde{F}_{\mu\nu} = g_{a\gamma} a \vec{E} \cdot \vec{B}, \tag{1}$$

where $\vec{E}$, $\vec{B}$ and a are the electric, magnetic and axion fields. The axion-photon coupling constant $g_{a\gamma}$ is proportional to m_a as

$$g_{a\gamma} = \frac{\alpha}{2\pi f_a}\left[\frac{E}{N} - \frac{2(4+z)}{3(1+z)}\right] = 1.9 \times 10^{-10}\left(\frac{m_a}{1\,\mathrm{eV}}\right)[E/N - 1.92][\mathrm{GeV}^{-1}], \tag{2}$$

where E/N is a parameter dependent on the specific axion model, eg., $E/N = 0$ in the standard KSVZ model, or $E/N = 8/3$ in the GUT-inspired DFSZ model.

1.2 Experimental searches for axions

Axion phenomenology depends primarily on the unknown m_a. If $m_a \sim 10^{-6}$–$10^{-3}\,\mathrm{eV}$, relic axions from the early universe can be attractive candidates for the cold dark matter (CDM). An elegant technique for detecting axions constituting the dark halo of the Milky Way was developed by Sikivie,[4] by which axions resonantly convert to microwave photons in a tunable high-Q cavity permeated by a strong magnetic field. The Axion Dark Matter Experiment (ADMX) [5] and the CARRACK experiment [6] are presently ongoing along this line.

If m_a is at around 1 eV, the Sun can be a powerful source of axions. The technique for detecting solar axions called "the axion helioscope" was also developed by Sikivie.[4] A pioneering experiment based on this idea was performed by Lazarus *et al.*[7] using a fixed dipole magnet, which was followed by the Tokyo axion helioscope (Sumico) [8,9,10] with a solar tracking superconducting magnet, and later by the CERN Axion Solar Telescope (CAST) [11] using a large decommissioned magnet of the LHC. This technique is described in detail in the next section.

Some other solar axion searches, SOLAX,[12] COSME,[13] DAMA,[14] and CDMS,[15] were making use of crystalline detectors such as germanium or NaI(Tl), where the axion Bragg scattering,[16] or the coherent Primakoff conversion in the periodic lattice of crystals, were exploited.

1.3 Axion helioscope

The detection principle of the axion helioscope is illustrated in Fig. 1. Axions are expected to be produced in the solar core through the Primakoff process. The average energy of the solar axions is 4.2 keV and their differential flux expected at the Earth is approximated by [17,18]

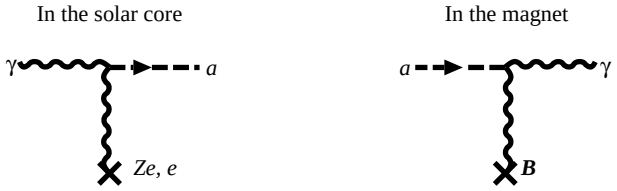

Figure 1: The solar axions produced via the Primakoff process in the solar core are, then, converted into X-rays via the inverse process in the magnet.

$$\begin{aligned} \mathrm{d}\Phi_a/\mathrm{d}E &= 6.020 \times 10^{10}[\mathrm{cm}^{-2}\mathrm{s}^{-1}\mathrm{keV}^{-1}] \\ &\quad \times \left(\frac{g_{a\gamma}}{10^{-10}\mathrm{GeV}^{-1}}\right)^2 \left(\frac{E}{1\,\mathrm{keV}}\right)^{2.481} \exp\left(-\frac{E}{1.205\,\mathrm{keV}}\right), \end{aligned} \tag{3}$$

where E is the energy of the axions. They would be converted into X-ray photons through the inverse process in a strong magnetic field at a laboratory. The conversion rate is given by

$$P_{a\to\gamma} = \frac{g_{a\gamma}^2}{4} \exp\left[-\int_0^L \mathrm{d}z\,\Gamma\right] \times \left|\int_0^L \mathrm{d}z\, B_\perp \exp\left[i\int_0^z \mathrm{d}z'\left(q - \frac{i\Gamma}{2}\right)\right]\right|^2, \tag{4}$$

where z and z' are the coordinate along the incident solar axion, $B_\perp$ is the strength of the transverse magnetic field, L is the length of the field along z-axis, Γ is the X-ray absorption coefficient of the filling medium, $q = k_\gamma - k_a \approx (m_\gamma^2 - m_a^2)/2E$ is the momentum transfer by the virtual photon, and m_γ is the effective mass of the photon in medium.

In vacuum, $m_\gamma = 0$ limiting the sensitive mass range below $m_a \lesssim O(\sqrt{\pi E/L})$ due to the loss of coherence by non-zero q. In a buffer gas, however, coherence can be restored for heavier axions if m_γ could be adjusted to m_a. In light gas such as hydrogen or helium, m_γ is well approximated by $m_\gamma = \sqrt{4\pi\alpha N_e/m_e}$, where α is the fine structure constant, m_e is the electron mass, and N_e is the number density of electrons.

1.4 The Tokyo axion helioscope experiment

The Tokyo axion helioscope or Sumico is an axion helioscope using a dedicated superconducting magnet mounted on a precision solar tracking system. In 1997, Phase 1 measurement [8] was performed without the gas container. From the absence of the expected signals from axions, a limit on axion-photon coupling constant was set to be $g_{a\gamma} < 6.0 \times 10^{-10}\mathrm{GeV}^{-1}$ at 95% CL. The sensitive mass range was limited below $m_a < 0.03\,\mathrm{eV}$ because of the vacuum conversion region. In Phase 2,[9] the apparatus was upgraded to introduce low density ^{4}He gas to the conversion region. The maximum allowed density corresponded to helium gas of 1 atm at the room temperature so that a clogging of the helium pipeline by solid air or moisture would not destroy the cryogenic part of the gas system. The measurement in 2000, together with the Phase 1 result, yielded an upper limit of $g_{a\gamma} < 6.0$–$10.5 \times 10^{-10}\mathrm{GeV}^{-1}$ at 95% CL for $m_a < 0.27\,\mathrm{eV}$. In Phase 3, we are developing an automated, precise, and safe control of higher density cold ^{4}He gas aiming to extend the sensitive mass range up to $m_a \lesssim 2\,\mathrm{eV}$. In the latest measurement in 2007–2008, the mass region $0.84 < m_a < 1.00\,\mathrm{eV}$ was explored. In the following sections, the hardware of the Sumico experiment, result of the latest measurement, and the current status of the experiment are described.

2 Experimental apparatus

The axion helioscope consists of a superconducting magnet, an X-ray detector, a gas container, and an altazimuth mounting to track the Sun. The schematic figure is shown in Fig. 2.

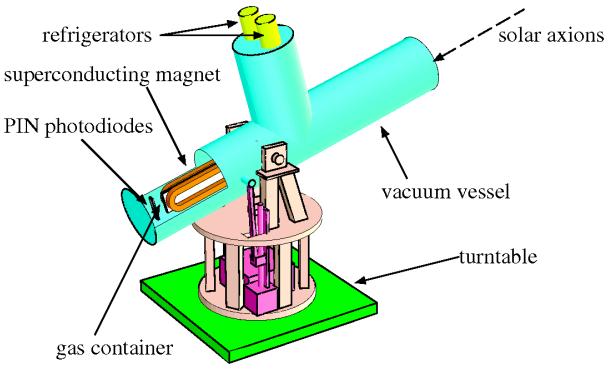

Figure 2: The schematic view of the axion helioscope called the Sumico V detector.

The superconducting magnet [19] consists of two 2.3-m long race-track shaped coils running parallel with a 20-mm wide gap between them. The magnetic field in the gap is 4 T perpendicular to the helioscope axis. The coils are kept at 5–6 K during operation. The magnet is made cryogen-free by two Gifford-McMahon refrigerators cooling directly by conduction, and is equipped with a persistent current switch.

The container to hold buffer gas is inserted in the gap of the magnet. We adopted ^{4}He as the buffer gas, which was kept at $T \lesssim 6\,\mathrm{K}$, just above the critical temperature of ^{4}He, $T_c = 5.2\,\mathrm{K}$. It is worth noting that axions as heavy as a few eV can be reached with helium gas of only about 1 atm and ^{4}He will not liquefy at any pressure at this temperature. The container body is made of four stainless-steel square pipes welded side by side to each other, and is wrapped with 5N high purity aluminium sheet to achieve high uniformity of temperature. The measured thermal conductance between the both ends was $1 \times 10^{-2}\mathrm{W/K}$ at 6 K. The uniformity of the temperature

guarantees the homogeneous density along the length of the container. The detector side of the container is ended with an X-ray window (METOREX C10 custom) which is transparent to X-ray above 2 keV and can withstand up to 0.3 MPa. The container is fixed to the magnet at this side through a temperature-stabilized thermal linkage. The opposite end toward the Sun is blind-ended and is suspended by three Kevlar cords, so that thermal flow through this end is highly suppressed.

To have automatic sequential pressure settings, a gas handling system is built with piezo valves (HORIBASTEC PV1101, PV1302) and a precision pressure gauge (YOKOGAWA MU101-AH1N). For emergency exhaust of the gas in case of rapid temperature increase due to a magnet quenching, a cryogenic rupture disk, which is designed to break at 0.248 MPa, is also introduced into the gas handling system to avoid destruction of the X-ray window by the over pressure.

An array of sixteen PIN photodiodes, Hamamatsu Photonics S3590-06-SPL, is used as the X-ray detector.[20] In the latest measurement, however, twelve of them are used for the analysis because four went defective through thermal stresses. The chip size of a photodiode is $11 \times 11 \times 0.5\,\mathrm{mm}^3$, and the effective area is larger than $9 \times 9\,\mathrm{mm}^2$. It has an inactive surface layer of $\lesssim 0.35\,\mu$m.[21] The output from each photodiode is fed to a charge sensitive preamplifier and waveforms of the preamplifier outputs are digitized using FADCs. We applied off-line pulse shaping to the recorded waveforms.[9] Each photodiode was calibrated by 5.9-keV manganese X-rays from a ^{55}Fe source which is manipulated from the outside and is completely retracted out of the sight of the X-ray detector during the observations.

The entire axion detector is constructed in a vacuum vessel which is mounted on a computer-controlled altazimuth mount. Its trackable altitude ranges from $-28°$ to $+28°$ and its trackable azimuthal range is almost 360°. This range corresponds to an exposure time of about a half of the day in observing the Sun, while background is measured during the rest of the day.

3 Sumico Phase 3 — Measurement, analysis and current status

From December 21 2007 through April 21 2008, a new measurement was performed for 34 gas-density settings with about three days of running time per setting. This time, the azimuthal range was restricted to about 60° because a cable handling system for its unmanned operation is not completed yet. Accordingly, the exposure time was reduced to about a quarter of a day. The scanned mass range was 0.84–1 eV. Since we had not completed the gas relief system, the highest density was determined so that the gas pressure would not exceed the breakage pressure

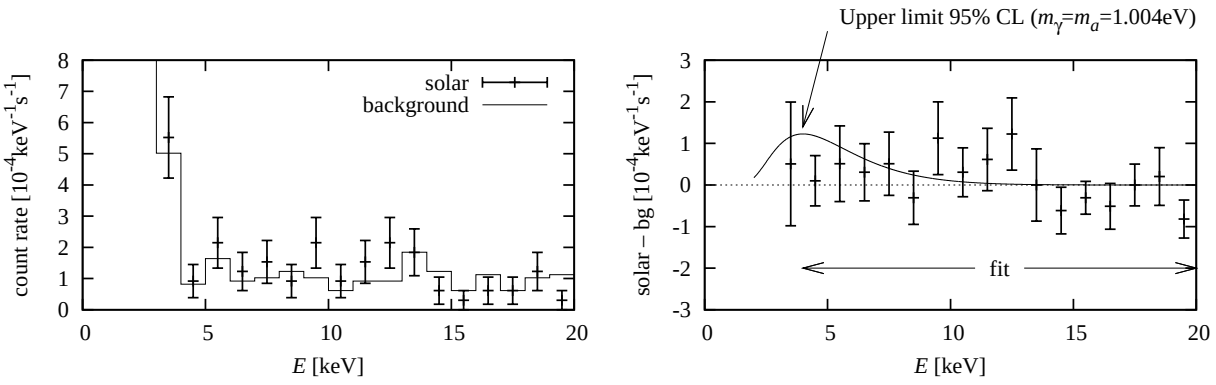

Figure 3: The left figure shows the energy spectrum of the solar observation (error bars) and the background spectrum (solid line) for the effective PIN photodiode area of 371 mm^2 when the gas density was tuned to $m_\gamma = 1.004\,$eV. The right figure shows the net energy spectrum of the left where the background is subtracted from the solar observation. The solid curve shows the expected solar axion energy spectrum corresponding to the 95% CL upper limit.

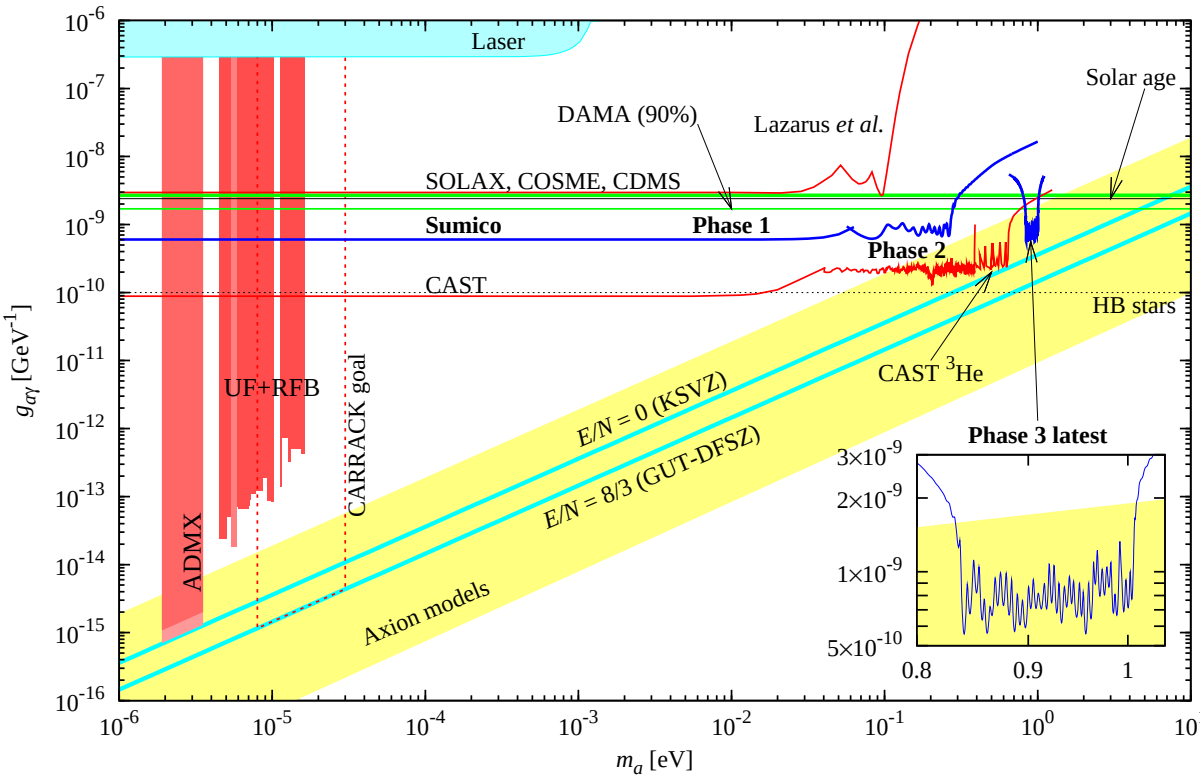

Figure 4: Exclusion plot for $g_{a\gamma}$ as a function of m_a. The yellow band indicates the preferred axion models,[22] in which two slopes (cyan) correspond to two popular models. The new limit [10] by Sumico and the previous ones [8,9] are plotted in blue curves. Other helioscope limits: Lazarus *et al.*[7] and CAST [11] are shown in red curves, axion Bragg scattering experiments: SOLAX,[12] COSME,[13] DAMA,[14] and CDMS [15] are shown in green horizontal lines, two pioneering microwave cavity experiments and ADMX [5] are shown in red area, the newCARRACK prospect is shown in red dashed lines, and Laser based experiments are shown in sky blue area. Two astrophysical bounds considering the solar- (solid black) and HB stars' (dotted black) ages are also shown.

of the rupture disk even during a magnet quenching.

Energy spectra for the solar observation and the background are obtained for each density settings based on the measured direction of the helioscope. Event reduction process was applied in the same way as Phase 2 analysis.[9] In Fig. 3, the energy spectrum of the solar observation with the gas density for $m_\gamma = 1.004\,\mathrm{eV}$ is shown together with the background spectrum as an example. We searched for expected axion signals which scale with $g_{a\gamma}^4$ and vary with m_a in these spectra by applying a series of least-χ^2 fittings. Data from the 34 different gas density settings were combined by using the summed χ^2 of the 34. The energy region of 4–20 keV was used for fitting. No significant excess was seen for any m_a, and thus an upper limit on $g_{a\gamma}$ at 95% CL was given. The smooth curve in Fig. 3 represents an example for the expected axion signal where $m_a = m_\gamma = 1.004\,\mathrm{eV}$ and $g_{a\gamma} = 7.7 \times 10^{-10}\mathrm{GeV}^{-1}$, which corresponds to the upper limit for $m_a = 1.004\,\mathrm{eV}$. Fig. 4 shows the limit plotted as a function of m_a. The previous limits [8,9] and some other bounds (see caption) are also plotted in the same figure.

Currently, upgrades are being continued to deal with cold ^{4}He gas of higher densities. Gas of higher densities requires a higher level of safety against the magnet quenching. The helium pipelines were made thicker for quicker evacuation and the relief valve at the room temperature was replaced based on a new estimation of the maximum flow. A blind-end bellows was attached to the room temperature section of the gas system to prevent the thermoacoustic oscillations which occurred at higher densities. Current effort is being focused on a yet unidentified density-dependent heat influx into the buffer gas.

4 Conclusion

Experimental searches for axions are currently active in two mass regions, where the sensitivities of the experiments have reached the model band. One is at around $m_a \sim 1$–$10\,\mu$eV reached by the cavity dark matter searches. The other is at around $m_a \sim 0.1$–$1\,$eV by the axion helioscopes. Sumico has opened up a new area in the $g_{a\gamma}$-m_a parameter space: $g_{a\gamma} < 6.0$–$10.5 \times 10^{-10}\mathrm{GeV}^{-1}$ (95% CL) for $m_a < 0.27\,$eV and $g_{a\gamma} < 5.6$–$13.4 \times 10^{-10}\mathrm{GeV}^{-1}$ (95% CL) for $m_a = 0.84$–$1.00\,$eV. The latter was the first published helioscope result which scanned in the model band. Although CAST is now leading in terms of the sensitivity owing to its one order of magnitude larger BL value, Sumico is still continuing its development to explore higher masses up to $m_a \lesssim 2\,$eV and is expecting a new measurement this year.

Acknowledgments

The authors thank the former director general of KEK, Professor H. Sugawara, for his support in the beginning of the helioscope experiment. This research was partially supported by the Japanese Ministry of Education, Science, Sports and Culture, Grant-in-Aid for COE Research and Grant-in-Aid for Scientific Research (B), and also by the Matsuo Foundation.

References

1. R. D. Peccei, H. R. Quinn, *Phys. Rev. Lett.* **38**, 1440 (1977); S. Weinberg, *ibid.* **40**, 223 (1978); F. Wilczek, *ibid.* **40**, 279 (1978).
2. C. A. Baker *et al.*, *Phys. Rev. Lett.* **97**, 131801 (2006).
3. D. B. Kaplan, *Nucl. Phys. B* **260**, 215 (1985); M. Srednicki, *ibid.* **260**, 689 (1985).
4. P. Sikivie, *Phys. Rev. Lett.* **51**, 1415 (1983); *ibid.* **52**, 695 (1984) (erratum).
5. S. J. Asztalos *et al.*, *Phys. Rev. Lett.* **104**, 041301 (2010).
6. M. Tada *et al.*, *Nucl. Phys. B (Proc. Suppl.)* **72**, 164 (1999).
7. D. M. Lazarus *et al.*, *Phys. Rev. Lett.* **69**, 2333 (1992).
8. S. Moriyama *et al.*, *Phys. Lett. B* **434**, 147 (1998) [arXiv:hep-ex/9805026].
9. Y. Inoue *et al.*, *Phys. Lett. B* **536**, 18 (2002) [arXiv:astro-ph/0204388].
10. Y. Inoue, *et al.*, *Phys. Lett. B* **668**, 93 (2008) [arXiv:0806.2230].
11. K. Zioutas *et al.*, *Phys. Rev. Lett.* **94**, 121301 (2005); J. Galan, Ph. D thesis, [arXiv:1102.1406].
12. A. O. Gattone *et al.*, *Nucl. Phys. B (Proc. Suppl.)* **70**, 59 (1999).
13. A. Morales *et al.*, *Astropart. Phys.* **16**, 325 (2002).
14. R. Bernabei *et al.*, *Phys. Lett. B* **515**, 6 (2001).
15. Z. Ahmed *et al.*, *Phys. Rev. Lett.* **103**, 141802 (2009).
16. E. A. Paschos, K. Zioutas, *Phys. Lett. B* **323**, 367 (1994).
17. J. N. Bahcall and M. H. Pinsonneault, *Phys. Rev. Lett.* **92**, 121301 (2004).
18. G. G. Raffelt, contribution to *XI International Workshop on "Neutrino Telescope"*, Venice, Italy, 2005.
19. Y. Sato *et al.*, *Development of a Cryogen-free Superconducting Dipole Magnet*, in proceedings of *the 15th International Conference on Magnet Technology (MT-15)*, Science Press, Beijing, 1998, pp. 262–265; KEK-Preprint-97-202 (November, 1997).
20. T. Namba *et al.*, *Nucl. Instr. Meth. A* **489**, 224 (2002) [arXiv:astro-ph/0109041].
21. Y. Akimoto *et al.*, *Nucl. Instr. Meth. A* **557**, 684 (2006) [arXiv:physics/0504147].
22. S. L. Cheng, C. Q. Geng, W.-T. Ni, *Phys. Rev. D* **52**, 3132 (1995).

Cosmic ray constraints on singlino-like dark matter candidates

Timur DELAHAYE [a], David CERDEÑO & Julien LAVALLE
Instituto de Física Teórica UAM/CSIC
Universidad Autónoma de Madrid Cantoblanco, 28049 Madrid, Spain

Recent results from direct detection experiments (Dama, CoGeNT), though subject to debate, seem to point toward a low mass (few GeV) dark matter (DM) particle. However, low mass DM candidates are not easily achieved in the MSSM nor NMSSM. As shown by some authors, singlet extensions of the MSSM can lead to GeV mass neutralinos and satisfy relic abundance constraints. We propose here to extract indirect detection constraints on these models in a generic way from cosmic-ray anti-proton measurements (PAMELA data)

Recent results from dark matter direct detection experiments DAMA [1] and CoGeNT [2] have risen a lot of interest for light dark matter (masses between 3 an 20 GeV, roughly). Though these results are in tension with those of the Xenon100 [3] experiment (in the case of a pure spin-independent scattering), the light dark matter hypothesis is an interesting one to explore.

As it has been shown by Julien Lavalle [4], interpreting the results from DAMA [1] and CoGeNT [2] in terms of dark matter may be in tension with anti-proton cosmic rays constraints. Indeed a dark matter candidate that has such a large coupling to quarks (as suggested by the CoGeNT results) may imply a strong annihilation into quark pairs which, may produce more cosmic ray anti-protons in the Galactic halo than what has been observed by PAMELA [5]. It has been shown [6] that some part of phase of the MSMM may survive the cosmic-ray constraints, however only if the astrophysical parameters are very favourable.

Following the idea of other works [7, 8, 9, 10], we have investigated the possibility that rather than having a dark matter particle annihilating into lepton pairs, it would annihilate into scalar and pseudo-scalar particles which, in turn would decay into Standard Model fermions. There still would be a cosmic anti-proton production, however, which a much less sharp spectrum, and, in some cases, compatible with the PAMELA measurements. The Next-to-Minimal SuperSymetric Model (NMSSM) may have such a particle content (in the case where the dark matter particle is mainly singlino it can be made very light and annihilate into the scalar and the pseudo-scalar Higgses). However NMSSM is not a requirement and any particle physics model with a similar particle content would give comparable results.

1 Particle content and cross sections

The phenomenology of singlino-like dark matter scenarios is mostly set by the couplings between the neutralino, a Majorana fermion, and the light scalar and pseudo-scalar particles of the Higgs sector. Denoting χ the neutralino field and ϕ_i the scalar or pseudo-scalar fields, the effective Lagrangian that we consider reads:

[a] presenting author

$$\mathcal{L}_{\rm eff} = -\frac{1}{2}\sum_i \chi\,\mathcal{C}_{\chi i}\,\chi\,\phi_i - \frac{1}{2}\sum_{i\le j\le k}\lambda_{ijk}\,\phi_i\,\phi_j\,\phi_k\ ,$$

where we $\lambda_{i,j,k}$ is a dimensional coupling taken either fully real or fully imaginary, and where

$$\begin{aligned}\mathcal{C}_{\chi i} &\equiv c_{\chi\chi i} + \tilde{c}_{\chi\chi i}\gamma_5\\ \bar{\mathcal{C}}_{\chi i} &\equiv c_{\chi\chi i} - \tilde{c}_{\chi\chi i}\gamma_5\end{aligned}$$

features both the couplings of the scalar and pseudo-scalar fields ϕ_i to the dark matter fermionic field χ. With this parametrisation, considering the diagrams of Figure 1, the annihilation cross-section can be computed analytically (see details in[11]).

All we have to do is hence to restrict the parameter space of masses and coupling that is compatible with the CoGeNT region and collider constraints.

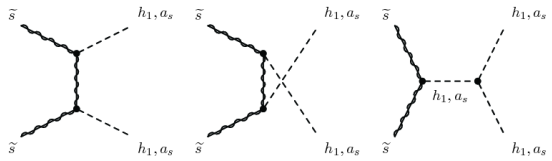

Figure 1: Dark matter annihilation channels considered.

2 Relic Density

In the standard Λ-Cold Dark Matter model (ΛCDM), the dark matter we consider here is thermally produced during the first times of the universe. Initially in chemical and thermal equilibrium with the plasma, its abundance obeys standard quantum statistical equilibrium. When the temperature drops below their mass, dark matter particles still annihilate and experience Boltzmann suppression until the expansion rate of the universe, controlled by the effective degrees of freedom $g_\star$, gets larger than the annihilation rate (see e.g. [12]). At that time ($T \sim \frac{m_\chi}{20}$), dark matter freezes out, and its relic comoving density is fixed. The present abundance is $\Omega h^2 \propto \frac{1}{g_\star^{1/2}\langle\sigma v\rangle}$. It is important to note that when considering low mass dark matter, the decoupling from the thermal bath occurs at a temperature close to the one of the QCD phase transition which strongly affects the value of $g_\star$.

As one can see from Figure 2, for a dark matter particle of 10 GeV, the relic density may vary by 60% depending on the QCD phase transition, which is much more than the observational uncertainty. This consideration is not new at all, however, as it is more usual to consider higher dark matter masses, it is worth recalling.

Because of the high accuracy of WMAP7 data [13], the relic density is extremely constraining and as one can see from Figure 4, it reduces considerably the number of possible values of the couplings of our model. With this reduced parameter space it is now possible to test the cosmic anti-proton flux.

3 The pbar spectrum

Before estimating the anti-proton flux at the Earth, one needs to know the anti-proton spectrum before propagation, that is the one after the dark matter annihilation into scalar h and pseudo-scalar a, their subsequent decay into quark pairs and their hadronization. The first step is easy: it is two body annihilation so all the 4-momenta are set by kinematics. In the approximation

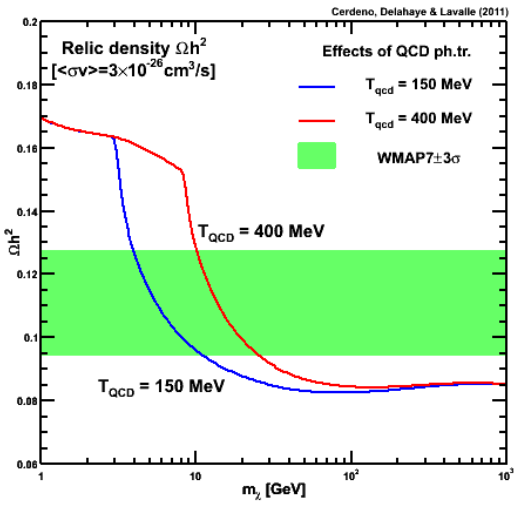

Figure 2: Dark matter relic density as a function of dark matter particle mass. The green band corresponds to WMAP7 data [13]. The red and blue lines are the results when considering a first order QCD phase transition happening at 400 MeV and 150 MeV respectively.

that the dark matter particles annihilate at rest in the halo frame the energy of particle 1 (either h or a), is

$$E_1 = \frac{4m_\chi^2 + m_1^2 - m_2^2}{4m_\chi}$$

and the norm of its momentum is :

$$k = \frac{\sqrt{\lambda\left(4m_\chi^2, m_1^2, m_2^2\right)}}{4m_\chi}$$

which are enough to change from the halo frame to the rest frame of particle 1: (γ, β)=$(E_1/m_1, k/E_1)$. In the rest frame of particle 1, the quarks it decays into have energy $E_q^* = m_1/2$ and momentum $|k_q^*| = \sqrt{m_1^2/4 - m_q^2}$. One finally gets the energy of the quarks in the halo frame:

$$E_q = \frac{E_1}{2} - \cos(\theta)\frac{\sqrt{\lambda\left(4m_\chi^2, m_1^2, m_2^2\right)}}{8m_\chi}\sqrt{1 - \frac{4m_q^2}{m_1}} = \frac{E_1}{2} - \cos(\theta)\mathcal{E}.$$

So the energies of the quarks and anti-quarks coming from the decay of particle 1 are evenly distributed between $\frac{E_1}{2} - \mathcal{E}$ and $\frac{E_1}{2} + \mathcal{E}$. Finally one gets the probability of having an anti-proton of energy $E_{\overline{p}}$ from a quark of energy E_q $f(E_q, E_{\overline{p}})$ thanks to the PYTHIA[b] package [14]. So finally the anti-proton spectrum after the dark matter annihilation is:

$$\mathcal{F}(E_{\overline{p}}) = \sum_{i=1,2}\sum_q BR_{i,q}\int_{\frac{E_i}{2}-\mathcal{E}}^{\frac{E_i}{2}+\mathcal{E}} \frac{f(E_q, E_{\overline{p}}) + f(E_{\overline{q}}, E_{\overline{p}})}{2\mathcal{E}} dE_q,$$

where the first sum is done over the annihilation products (1,2)=(h, a), and the second sum is over all the quark flavours for which $2m_q \leqslant m_i$ is satisfied. The branching ratios $BR_{i,q}$ depend on the particle physics model considered.

[b] For this work we made use of version 6.4.24 with CDF tune A

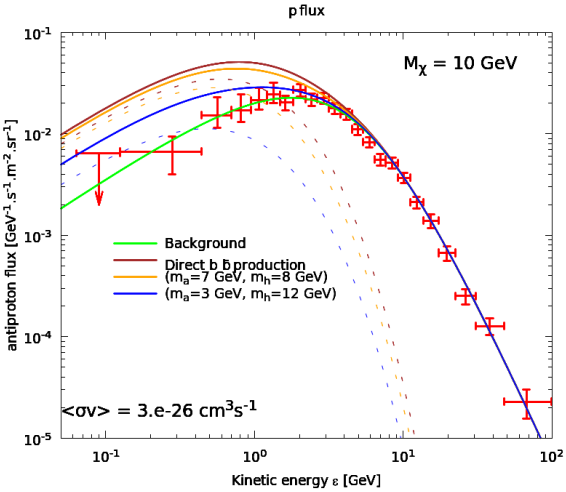

Figure 3: Anti-proton flux at the Earth as a function of particle kinetic energy. Data are from PAMELA [5]. Green line: background estimation. Brown, yellow and blue correspond to direct annihilation into $b\bar{b}$, annihilation into a scalar and a pseudo-scalar of masses of 7 and 8 GeV or 3 and 12 GeV, respectively. Dashed are signal only, lines are signal plus background.

Finally, one has to propagate the anti-proton from the annihilation place to the Earth. The model used here to describe this propagation has been detailed at length in many other papers [15, 16, 17]. In this model, the charged cosmic rays diffuse off the inhomogeneities of the Galactic magnetic field, they interact with the interstellar gas when they cross the disk and finally reach the Earth. This model has been shown to be extremely accurate in describing many cosmic ray species and, in particular, describes very well the anti-proton astrophysical background. This background is due to the spallation of cosmic ray protons and α on the interstellar hydrogen and helium (secondary cosmic rays). Moreover, when considering anti-protons it is important to also take into account tertiary cosmic rays from inelastic scattering of cosmic ray anti-protons. The prediction is in very good agreement with present data (as one can see from Figure 3) and suffers very little from the uncertainties affecting the propagation parameters.

In order to determine whether or not a point in our parameter space is in agreement with anti-proton constraints, we simply summed the astrophysical prediction and the dark matter component and checked if the total was flux was higher than the PAMELA data.

4 Results and conclusions

As one can see from Figure 4, the parameter space which gives a signal in the CoGeNT region, gives the correct relic density and in the same time does not give a too high cosmic ray anti-proton flux is quite small. This is not the place for a thorough study of the parameter space (see more details in [11]), however some features can be stressed thanks to Figure 4.

Large masses of the scalar particle h are forbidden by cosmic ray constraints. Indeed, when m_h is too large, the quark spectrum is not very much boosted (the quark pairs are almost produced at rest) so the anti-proton spectrum is peaked and easily exceed the observation, as if the dark matter particles were annihilating directly into quark pairs. Conversely, very low scalar masses cannot be constrained as they cannot decay into $b\bar{b}$ pairs. From the right panel of Figure 4, it appears that, quite naturally, high annihilation cross sections at zero velocity ($< \sigma v_0 > \gtrsim 10^{-27}$ cm^3.s^{-1}) are excluded but not very low ones. The large discrepancy that can occur between annihilation cross sections at rest and at time of decoupling shows that the

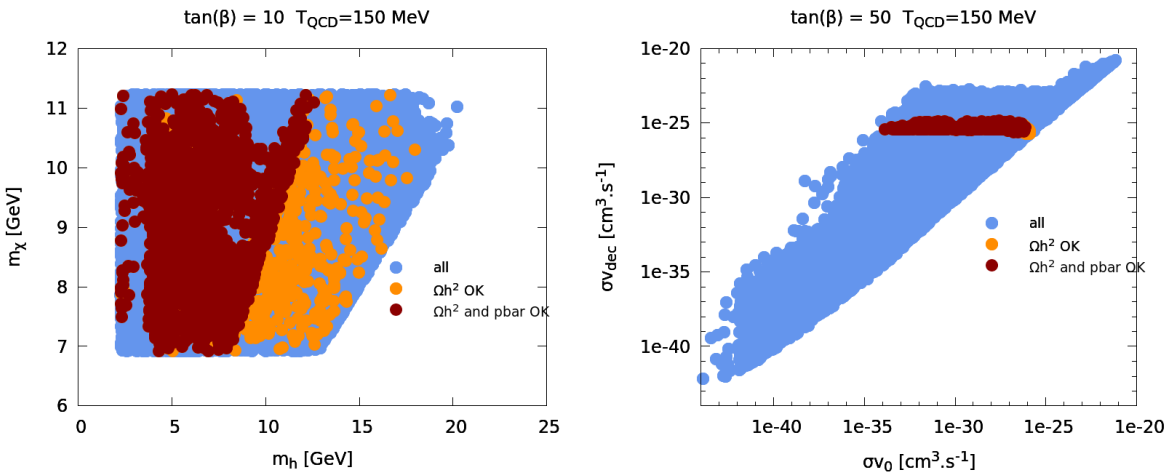

Figure 4: Probing the parameter space. Left: scalar and singlino masses. Right : annihilation cross-section at time of decoupling and in the halo. Blue, points in the CoGeNT region, orange: correct relic density but excessive anti-proton production, brown, correct relic density and correct anti-proton flux.

relic density can sometimes been set by the t-channel annihilation rather than by the s-channel, alleviating the constraints from anti-proton data.

Of course, one needs to repeat this work for the different possible dark matter halo profiles (here we made use of the profile proposed by [18]) and for different propagation parameter sets. However one can already conclude that interpreting the recent direct detection experiments results in term of dark matter is quite challenging. The compatible parameter space, even when the dark matter annihilation does not directly goes into quark pairs, is extremely reduced. If the CoGeNT, DAMA/Libra result were to be confirmed by CDMS, Xenon and Edelweiss, it is interesting to stress that the absence of signal in the cosmic anti-proton channel is very enlightening from the point of view of the nature of dark matter as it would put very strict constraints on masses and couplings which could be challenging for LHC.

Acknowledgments

This work was supported by the Spanish MICINNs Consolider-Ingenio 2010 Programme under grants CPAN CSD2007-00042 and MultiDark CSD2009-00064. We also acknowledge the support of the MICINN under grant FPA2009-08958, the Community of Madrid under grant HEPHACOS S2009/ESP-1473, and the European Union under the Marie Curie-ITN program PITN-GA-2009-237920.

References

[1] R. Bernabei et al. New results from DAMA/LIBRA. *Eur. Phys. J.*, C67:39–49, 2010.

[2] C. E. Aalseth et al. Results from a Search for Light-Mass Dark Matter with a p-Type Point Contact Germanium Detector. *Physical Review Letters*, 106(13):131301–+, April 2011.

[3] E. Aprile *et al.* for the XENON100 Collaboration. First Dark Matter Results from the XENON100 Experiment. *Physical Review Letters*, 105(13):131302–+, September 2010.

[4] J. Lavalle. 10 GeV dark matter candidates and cosmic-ray antiprotons. Phys. Rev. D, 82(8):081302–+, October 2010.

[5] O. Adriani *et al.* for the PAMELA Collaboration. PAMELA Results on the Cosmic-Ray Antiproton Flux from 60 MeV to 180 GeV in Kinetic Energy. *Physical Review Letters*, 105(12):121101–+, September 2010.

[6] N. Fornengo, S. Scopel, and A. Bottino. Discussing direct search of dark matter particles in the minimal supersymmetric extension of the standard model with light neutralinos. Phys. Rev. D, 83(1):015001–+, January 2011.

[7] R. Kappl, M. Ratz, and M. W. Winkler. Light dark matter in the singlet-extended MSSM. *Physics Letters B*, 695:169–173, January 2011.

[8] R. Kappl and M. W. Winkler. New Limits on Dark Matter from Super-Kamiokande. *ArXiv e-prints 1104.0679*, April 2011.

[9] J. F. Gunion, A. V. ˜Belikov, and D. Hooper. CoGeNT, DAMA, and Neutralino Dark Matter in the Next-To-Minimal Supersymmetric Standard Model. *ArXiv e-prints 1009.2555*, September 2010.

[10] P. Draper, T. Liu, C. E. M. Wagner, L.-T. Wang, and H. Zhang. Dark Light-Higgs Bosons. *Physical Review Letters*, 106(12):121805–+, March 2011.

[11] D. Cerdeño, T. Delahaye, and J. Lavalle. Cosmic ray constraints on singlino-like dark matter candidates. *in preparation*, 2011.

[12] P. Gondolo and G. Gelmini. Cosmic abundances of stable particles: improved analysis. *Nuclear Physics B*, 360:145–179, August 1991.

[13] E. Komatsu et al. Seven-year Wilkinson Microwave Anisotropy Probe (WMAP) Observations: Cosmological Interpretation. ApJS, 192:18–+, February 2011.

[14] T. Sjöstrand, S. Mrenna, and P. Skands. PYTHIA 6.4 physics and manual. *Journal of High Energy Physics*, 5:26–+, May 2006.

[15] D. Maurin, R. Taillet, and C. Combet. Transport of exotic anti-nuclei: I- Fast formulae for antiproton fluxes. *ArXiv Astrophysics e-prints astro-ph/0609522*, September 2006.

[16] D. Maurin, R. Taillet, and C. Combet. Transport of exotic anti-nuclei: II- Antiproton and Antideuteron astrophysical uncertainties. *ArXiv Astrophysics e-prints astro-ph/0612714*, December 2006.

[17] F. Donato, D. Maurin, P. Brun, T. Delahaye, and P. Salati. Constraints on WIMP Dark Matter from the High Energy PAMELA $\bar{p}/p$ Data. *Physical Review Letters*, 102(7):071301–+, February 2009.

[18] R. Catena and P. Ullio. A novel determination of the local dark matter density. J. Cosmology Astropart. Phys., 8:4–+, August 2010.

Diffuse γ-ray emission constraints on light WIMPs

Michel H.G. Tytgat
Service de Physique Théorique, CP225
Université Libre de Bruxelles
Bld du Triomphe, 1050 Brussels, Belgium
E-mail: mtytgat@ulb.ac.be

In these proceedings I report on a study of the contribution of light WIMPs to the isotropic gamma-ray diffuse emission. Specifically, I confront a singlet scalar candidate interacting through the Higgs portal to the Fermi-LAT data and the (unmodulated) signal from CoGeNT, a neat illustration of the complementarity between direct and indirect searches for dark matter.

We still have no clue of the nature of dark matter, but recently some interest has been taken in Light WIMPs, that is particles with picobarn scale annihilation cross-sections, but which are substantially lighter than the usual suspects, say the neutralino [1]. This is of course motivated by the DAMA/LIBRA [2] and CoGeNT [3] signals. Now, after Xenon100 [4] or CDMS-II [5], to speak of light WIMPs may sound like beating a dead horse – for sure this is what it felt like this Winter. However the current exclusion limits on light WIMPs are, apparently, not yet bullet proof.[6] Of course the new development is the modulation observed by CoGeNT.[7] Although of low statistical significance, the rough agreement with DAMA is more than intriguing.[8,9,10,11,12,13]

It is a very interesting coincidence that, while we are being puzzled by direct detection data, at the very same moment indirect searches experiments are reaching the sensitivity required to probe Light WIMP candidates. This is for sure well-known and appreciated but yet is not enough advocated in my humble opinion. Baring threshold effects, that indirect searches are relatively more sensitive to relatively lighter WIMPs is just because of the dark matter mass dependence of the flux of, say gamma-rays,

$$\phi_\gamma \propto \langle \sigma v \rangle \times \frac{dN_\gamma}{dE} \times \int_{los} dl \frac{\rho^2_{\rm dm}(l)}{M^2_{\rm dm}}. \tag{1}$$

For fixed annihilation cross-section, say $\langle \sigma v \rangle \approx 3 \cdot 10^{-26}$ cm^2·s^{-1}, there is a decrease of the number of gamma-rays produced by a lighter WIMPs, but this is more than compensated by their increasing number density. Interesting constraints on light WIMPs may be get based on solar neutrinos limits [14,15,16,17], anti-protons in cosmic rays [18,19], gamma-rays from the galactic centre [20] and from dwarf spheroidal galaxies [21,22,23] and synchrotron radiation [24,25].

Here I briefly report on an analysis [26] of the isotropic diffuse gamma-ray emission, based on the data released by the Fermi-LAT collaboration [27]. Our work is complementary (and concords) with the other works on the same topic[28,29], but our analysis extends to slightly lighter candidates, and as shown in the figure, conservatively obtained by requiring that the signal from a putative Light WIMPs does not exceed the signal inferred by the Fermi-LAT

collaboration, puts interesting constraints on Light WIMPs candidates. Here this is illustrated by a scalar singlet interacting through the Higgs portal[22], but which also apply to other portals, like a Z' [30].

The basic quantity is the spectral flux,

$$\frac{d\Phi_\gamma}{dE} = \frac{1}{4\pi}\frac{\langle\sigma v\rangle}{2M_{DM}^2}\int_0^\infty dz' \frac{1}{H(z')(1+z')^4}\frac{dN_\gamma}{dE'}\mathcal{B}^2(z')\mathrm{e}^{-\tau(E',0,z')}\,. \tag{2}$$

which in general depends critically on two astrophysical factors, a boost factor $\mathcal{B}^2(z')$ which depends on the distribution of halos of dark matter of all size and at all redshift z, and an absorption factor which depends on the optical depth $\tau(E,z)$ of a photon of energy E emitted at redshift z. Absorption of a gamma-ray may be due to various processes (Compton scattering on background photons, etc) but interestingly the universe is optically thin for a light WIMP, say with $M_{\rm dm} \leq 20$ GeV.[26] Hence, at the end of the day, the largest uncertainty comes from the boost factor.

The boost factor may be evaluated using different approaches, and our analysis is based on the standard Press-Schechter formalism[31], like many works in the field.[32,33] The Press-Schechter formula depends in turn on various cosmological and astrophysical parameters. For instance we have adopted a NFW profile for early DM halos, clearly a more shallow profile would give less stringent constraints, but all in all the most critical parameter is the mass of the lightest halo that may form in the Early Universe. This depends on the temperature of kinetic decoupling of the DM candidate (see *e.g.* [34]). The kinetic decoupling temperature is generically much lower than the freeze-out temperature. The latter is typically $\mathcal{O}(100$ MeV) for a Light WIMP, hence around the temperature of the QCD phase transition, while the former depends on the coupling to the thermal bath, which is composed of Standard Model particles. For the case of a Light WIMP interacting through the Higgs portal, and thus through Yukawa couplings, the couplings to the lighest Standard e^+e^- and neutrinos is completely negligible, and kinetic decoupling occurs close to the chemical freeze-out, $T \sim 150$ MeV. For the sake of comparison, typical neutralino candidates decouple close to $T \sim 1$ MeV. This in turn implies that quite light (and thus dense) dark matter halos may form in the early universe, so that the constraints are comparatively stronger.[26] To conclude we should emphasize that, as time goes by, the Fermi-LAT will resolve more extra-galactic astrophysical sources, and that the foreseen improvement in the analysis of the isotropic diffuse gamma-ray emission is likely to give stronger constraints on Light WIMPs, possibly by a factor of a few on the annihilation cross section, and thus, as emphasized here, on the spin independent cross section.[35]

Acknowledgments

This talk is a summary of results obtained in works done in collaboration with S. Andreas, C. Arina, Th. Hambye and F.S. Ling. My work is supported by the FNRS-FRS, the IISN and the Belgian Science Policy (IAP VI-11).

References

1. Graciela B. Gelmini. Direct Dark Matter Searches: Fits to WIMP Candidates. 2011.
2. R. Bernabei et al. First results from DAMA/LIBRA and the combined results with DAMA/NaI. *Eur. Phys. J.*, C56:333–355, 2008.
3. C.E. Aalseth et al. Results from a Search for Light-Mass Dark Matter with a P-type Point Contact Germanium Detector. *Phys.Rev.Lett.*, 106:131301, 2011.
4. E. Aprile et al. Dark Matter Results from 100 Live Days of XENON100 Data. *Phys.Rev.Lett.*, 2011.

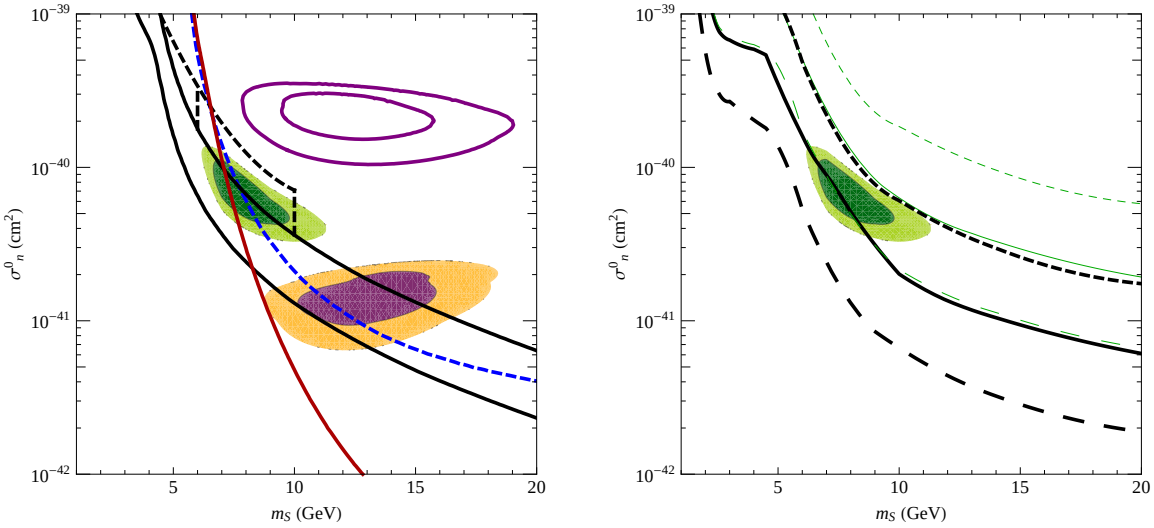

Figure 1: Left panel: SI cross-section (σ_n^0) *vs* scalar singlet mass (M_S) with the CoGeNT umodulated (middle, in green), and DAMA (in purple, above without channelling, below with channelling). The contours are given for 90 and 99.9 % C.L. The single continuous line (red) is the exclusion limit from Xenon10 (95 % C.L.). The dashed (blue) line corresponds to the CDMS-Si limit. The region between the two continuous black line correspond to S candidates with WMAP relic abundance. Right panel: only the CoGeNT region, together with 95 % C.L. exclusion limits from isotropic diffuse gamma-ray emission observation by *Fermi*-LAT. The lines correspond to distinct astrophysical assumptions. The region between the two continuous (black and green) lines may be considered to give conservative (range of) exclusions limits.

5. Z. Ahmed et al. Results from a Low-Energy Analysis of the CDMS II Germanium Data. *Phys.Rev.Lett.*, 106:131302, 2011.
6. J.I. Collar. A Realistic Assessment of the Sensitivity of XENON10 and XENON100 to Light-Mass WIMPs. 2011.
7. C.E. Aalseth, P.S. Barbeau, J. Colaresi, J.I. Collar, J.Diaz Leon, et al. Search for an Annual Modulation in a P-type Point Contact Germanium Dark Matter Detector. 2011.
8. P. Belli, R. Bernabei, A. Bottino, F. Cappella, R. Cerulli, et al. Observations of annual modulation in direct detection of relic particles and light neutralinos. 2011.
9. Dan Hooper and Chris Kelso. Implications of CoGeNT's New Results For Dark Matter. 2011.
10. Marco Farina, Duccio Pappadopulo, Alessandro Strumia, and Tomer Volansky. Can CoGeNT and DAMA Modulations Be Due to Dark Matter? 2011.
11. Thomas Schwetz and Jure Zupan. Dark Matter attempts for CoGeNT and DAMA. 2011.
12. Patrick J. Fox, Joachim Kopp, Mariangela Lisanti, and Neal Weiner. A CoGeNT Modulation Analysis. 2011.
13. Christopher McCabe. DAMA and CoGeNT without astrophysical uncertainties. 2011.
14. Dan Hooper, Frank Petriello, Kathryn M. Zurek, and Marc Kamionkowski. The New DAMA Dark-Matter Window and Energetic-Neutrino Searches. *Phys.Rev.*, D79:015010, 2009.
15. Jonathan L. Feng, Jason Kumar, John Learned, and Louis E. Strigari. Testing the Dark Matter Interpretation of the DAMA/LIBRA Result with Super-Kamiokande. *JCAP*, 0901:032, 2009.
16. Rolf Kappl and Martin Wolfgang Winkler. New Limits on Dark Matter from Super-Kamiokande. *Nucl.Phys.*, B850:505–521, 2011.
17. Sarah Andreas, Michel H. G. Tytgat, and Quentin Swillens. Neutrinos from Inert Doublet Dark Matter. *JCAP*, 0904:004, 2009.
18. Emmanuel Nezri, Michel H. G. Tytgat, and Gilles Vertongen. Positrons and antiprotons

from inert doublet model dark matter. *JCAP*, 0904:014, 2009.
19. Julien Lavalle. 10 GeV dark matter candidates and cosmic-ray antiprotons. *Phys. Rev.*, D82:081302, 2010.
20. Dan Hooper and Lisa Goodenough. Dark Matter Annihilation in The Galactic Center As Seen by the Fermi Gamma Ray Space Telescope. *Phys.Lett.*, B697:412–428, 2011.
21. A.Liam Fitzpatrick, Dan Hooper, and Kathryn M. Zurek. Implications of CoGeNT and DAMA for Light WIMP Dark Matter. *Phys.Rev.*, D81:115005, 2010.
22. Sarah Andreas, Chiara Arina, Thomas Hambye, Fu-Sin Ling, and Michel H. G. Tytgat. A light scalar WIMP through the Higgs portal and CoGeNT. *Phys. Rev.*, D82:043522, 2010.
23. Maja Llena Garde. Constraining dark matter signal from a combined analysis of Milky Way satellites using the Fermi-LAT. 2011.
24. Celine Boehm, Joseph Silk, and Torsten Ensslin. Radio observations of the Galactic Centre and the Coma cluster as a probe of light dark matter self-annihilations and decay. 2010.
25. Dan Hooper and Tim Linden. Gamma Rays From The Galactic Center and the WMAP Haze. 2010.
26. Chiara Arina and Michel H.G. Tytgat. Constraints on a Light WIMP from the Isotropic Diffuse Gamma-Ray Emission. 2010.
27. A. A. Abdo et al. The Spectrum of the Isotropic Diffuse Gamma-Ray Emission Derived From First-Year Fermi Large Area Telescope Data. *Phys. Rev. Lett.*, 104:101101, 2010.
28. A. A. Abdo et al. Constraints on Cosmological Dark Matter Annihilation from the Fermi-LAT Isotropic Diffuse Gamma-Ray Measurement. *JCAP*, 1004:014, 2010.
29. Kevork N. Abazajian, Prateek Agrawal, Zackaria Chacko, and Can Kilic. Conservative Constraints on Dark Matter from the Fermi-LAT Isotropic Diffuse Gamma-Ray Background Spectrum. 2010.
30. Yann Mambrini. The kinetic dark-mixing in the light of CoGENT and XENON100. *JCAP*, 1009:022, 2010.
31. William H. Press and Paul Schechter. Formation of galaxies and clusters of galaxies by selfsimilar gravitational condensation. *Astrophys. J.*, 187:425–438, 1974.
32. Aravind Natarajan and Dominik J. Schwarz. The effect of early dark matter halos on reionization. *Phys. Rev.*, D78:103524, 2008.
33. Marco Cirelli, Fabio Iocco, and Paolo Panci. Constraints on Dark Matter annihilations from reionization and heating of the intergalactic gas. *JCAP*, 0910:009, 2009.
34. Torsten Bringmann. Particle Models and the Small-Scale Structure of Dark Matter. *New J. Phys.*, 11:105027, 2009.
35. Kevork N. Abazajian, Steve Blanchet, and J. Patrick Harding. Enhanced Dark Matter Sensitivity from Fermi-LAT Resolution of the Diffuse Gamma-Ray Background. 2010.

COLLIDER LIMITS ON DARK MATTER

J. KOPP [a]
Theoretical Physics Department, Fermilab, PO Box 500, Batavia, IL 60510, USA

Dark matter pair production at high energy colliders may leave observable signatures in the energy and momentum spectra of the objects recoiling against the dark matter. We discuss signatures of Dark Matter in the jets + missing energy and photon + missing energy channels at the Tevatron and at LEP. Working in a largely model-independent effective theory framework, we can convert the collider bounds into constraints on the dark matter–nucleon scattering cross section and on the dark matter annihilation cross section. Our bounds are highly competitive with those from direct and indirect dark matter searches, especially for light WIMPs and for WIMPs with spin-dependent or leptophilic interactions. For example, we show that LEP rules out light ($\lesssim 10$ GeV) thermal relic dark matter if annihilation into electrons is among the dominant annihilation channels.

1 Introduction

Collider searches for dark matter are highly complementary to direct searches looking for dark matter–nucleon scattering and to indirect searches looking for signatures of dark matter annihilation or decay in stars or galaxies. The main advantage of collider searches is that they do not suffer from astrophysical uncertainties and that there is no lower limit to the dark matter masses to which they are sensitive.

In this talk, we discuss search strategies for dark matter at colliders and compare the obtained limits to those from direct and indirect searches. We work in a largely model-independent effective field theory framework, assuming the interactions between a dark matter Dirac fermion χ and standard model fermions f to be well described by contact operators of the form

$$\mathcal{O}_V = \frac{(\bar{\chi}\gamma_\mu\chi)(\bar{f}\gamma^\mu f)}{\Lambda^2}\,, \qquad \text{(vector, } s\text{-channel)} \tag{1}$$

[a] Based on work done in collaboration with Yang Bai, Patrick Fox, Roni Harnik and Yuhsin Tsai

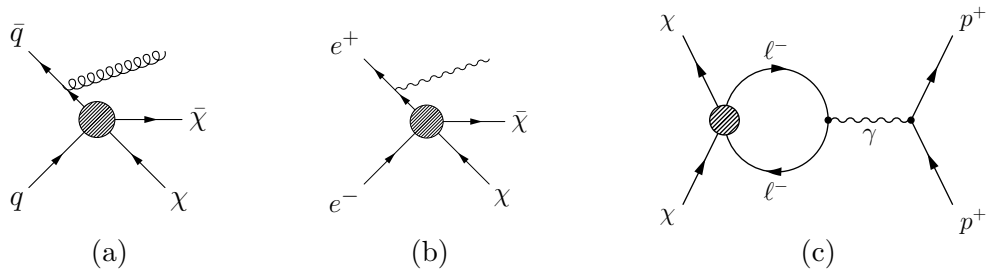

Figure 1: Dark matter production in association with (a) a mono-jet at a hadron colliders or with (b) a mono-photon at LEP. (c) Dark matter–nucleon scattering at one loop in models of leptophilic dark matter.

$$\mathcal{O}_S = \frac{(\bar{\chi}\chi)(\bar{f}f)}{\Lambda^2}\,, \qquad \text{(scalar, } s\text{-channel)} \tag{2}$$

$$\mathcal{O}_A = \frac{(\bar{\chi}\gamma_\mu\gamma_5\chi)(\bar{f}\gamma^\mu\gamma_5 f)}{\Lambda^2}\,, \qquad \text{(axial vector, } s\text{-channel)} \tag{3}$$

$$\mathcal{O}_t = \frac{(\bar{\chi}f)(\bar{f}\chi)}{\Lambda^2}\,. \qquad \text{(scalar, } t\text{-channel)} \tag{4}$$

While this set of operators is not exhaustive, it encompasses the essential phenomenologically distinct scenarios: spin dependent and spin independent dark matter–nucleus scattering, as well as s- and p-wave annihilation. The classification of the effective operators as s-channel or t-channel refers to the renormalizable model from which they typically arise: (1)–(3) are most straightforwardly obtained if dark matter pair production is mediated by a new neutral particle propagating in the s-channel, while eq. (4) arises naturally if the mediator is a charged scalar exchanged in the t-channel (for instance a squark or slepton). With such a UV completion in mind, the suppression scale Λ can be interpreted as the mass of the mediator M, divided by the geometric mean of its couplings to standard model fermions, g_f, and dark matter, g_χ: $\Lambda = M/\sqrt{g_f g_\chi}$. Note that there is some degree of redundancy in eqs. (1)–(4) because $\mathcal{O}_t$ can be rewritten as a linear combination of s-channel type operator using the Fierz identities.

The experimental signatures we will investigate include events with a single jet or a single photon and a large amount of missing energy (fig. 1 (a) and (b)). In sec. 2, we will focus on searches at the Tevatron[1–3], while in sec. 3, we will derive limits from a reanalysis of LEP data[4].

2 Mono-jets at the Tevatron

Events in which dark matter is pair-produced can contribute to mono-jet events at CDF[5] through diagrams like the one in fig. 1 (a). By comparing the number of observed mono-jet events to the number of events expected from dark matter production and from standard model backgrounds, one can derive limits on the suppression scale Λ of the effective dark matter couplings as a function of the dark matter mass m_χ. These limits can then be converted into constraints on the dark matter–nucleon scattering cross section.

In fig. 2, we compare these constraints to the ones obtained from direct dark matter searches. We find that the Tevatron limits are stronger than those from direct searches if dark matter is lighter than a few GeV or has predominantly spin-dependent interactions. At $m_\chi \sim$ few $\times$ 100 GeV, the Tevatron's sensitivity deteriorates due to kinematic limitations.

Note that the Tevatron mono-jet search is limited by systematic uncertainties, so more data alone will not be sufficient to improve the limits considerably. However, some improvement can be expected from an analysis taking into account not only the total number of mono-jet events, but also the transverse momentum spectrum of the jets. Such an analysis would require good understanding of the uncertainties associated with the prediction of QCD backgrounds. Performing an inclusive rather than exclusive search may help to reduce the these uncertainties.

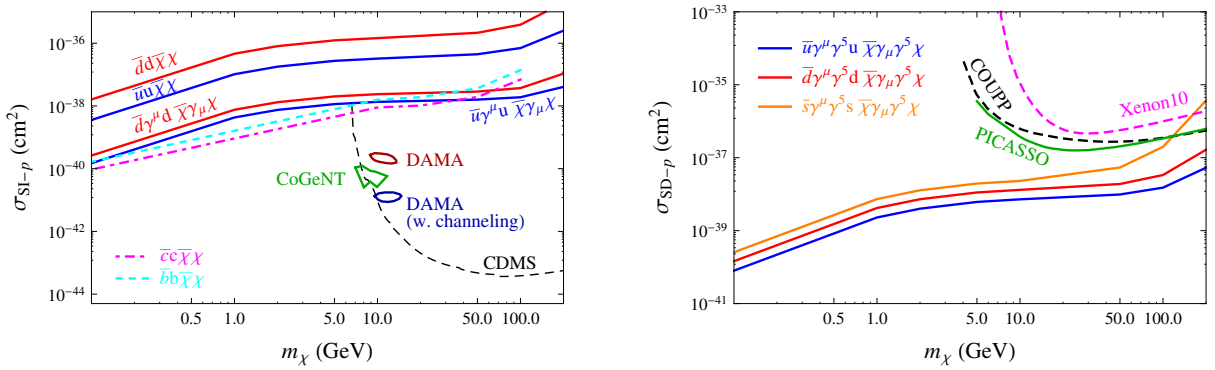

Figure 2: Limits on spin-independent (left) and spin-dependent (right) dark matter–proton interactions from a Tevatron mono-jet search[1;5]. We also show constraints from direct searches[6–8]. Plots taken from Bai et al.[1].

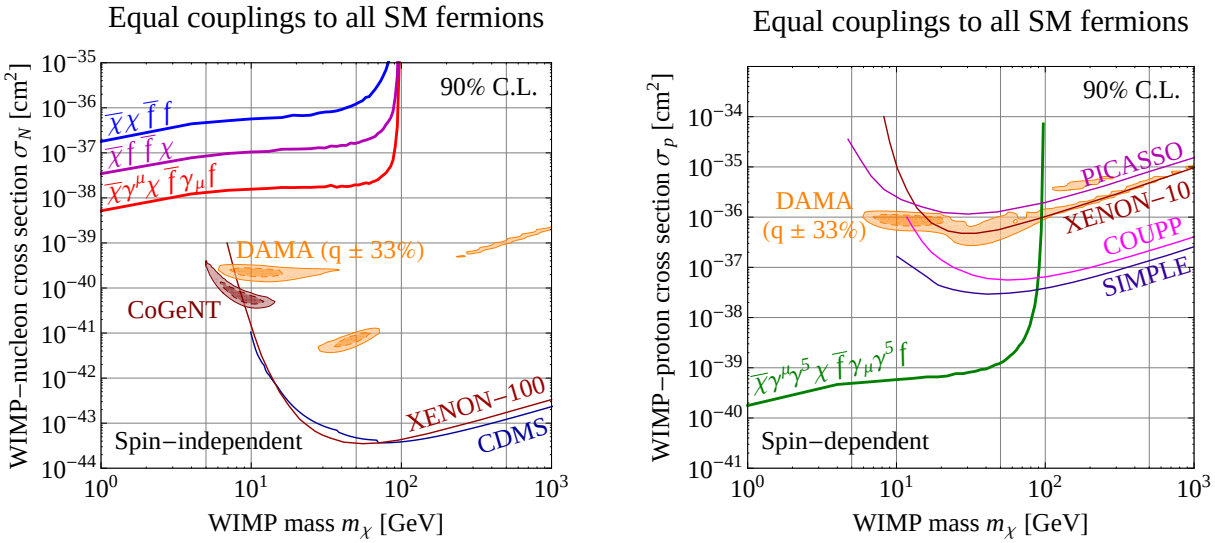

Figure 3: Limits on spin-independent (left) and spin-dependent (right) dark matter–nucleon interactions from a LEP mono-photon search[4;9]. Results are compared to constraints from various direct searches[6–8;10–15].

3 Mono-photons at LEP

Even though the total integrated luminosity of around 650 pb^{-1} recorded by the LEP experiments is smaller than the data set available at the Tevatron, we will now show that this data can still be used to set highly competitive limits on the properties of dark matter. Since initial state QCD radiation is absent at LEP, we will focus on final states with a single photon and a large amount of missing energy, *i.e.* we will study the process $e^+e^- \to \bar{\chi}\chi\gamma$ (fig. 1 (b)). Our analysis is based on the mono-photon spectrum observed by the DELPHI detector[9;16], which we will compare to predictions obtained using CompHEP[17], together with our own implementation of the DELPHI cuts, efficiencies, and energy resolutions in a modified version of the MadAnalysis framework[18]. Details on technical aspects of our analysis can be found in ref.[19]. We have verified our simulations by checking that we are able to reproduce the mono-photon distribution expected from the background process $e^+e^- \to Z\gamma$, with the Z decaying invisibly.

Like for the mono-jet channel, we first derive limits on the suppression scale Λ as a function of m_χ. While for mono-jets, a spectral analysis would have required detailed understanding of the systematic uncertainties in the background prediction, the mono-photon search at LEP is statistics-limited, and it is therefore straightforward to take into account the full mono-photon spectrum. This is advantageous because the distribution of signal events expected from dark

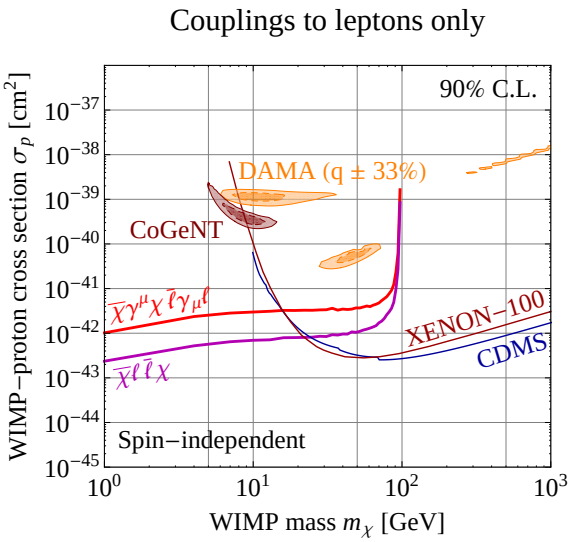

Figure 4: LEP constraints on dark matter with tree level couplings only to leptons[4], compared to limits from direct detection experiments[6–8;10;20;21].

matter pair production is different from the shape of the $e^+e^- \to \bar{\nu}\nu\gamma$ background.

To convert the LEP bounds on Λ into limits on the dark matter–nucleon scattering cross section, we need to make some assumption on the relative strength of dark matter–quark couplings compared to dark matter–electron couplings. If these couplings are identical, as assumed in fig. 3, we find that the collider limits are again highly competitive for very light dark matter ($m_\chi \lesssim 4$ GeV) and for spin-dependent scattering up to the kinematic cut-off of LEP.

LEP can do even better in models where dark matter is leptophilic, *i.e.* has tree level couplings predominantly to leptons. Such models are, for example, motivated by recent anomalies in cosmic ray spectra.[22;23] Even though dark matter–nucleon scattering may be absent or suppressed in such models at the tree level, it can still occur at the loop level, mediated for instance by the diagram shown in fig. 1 (c).[21] The expected signal in direct detection experiments in this case is suppressed by a loop factor, so that LEP, which is probing unsuppressed tree level interactions, has a relative advantage and is competitive with direct searches even for spin-independent scattering up to its kinematic limit around $m_\chi \sim 80$ GeV (see fig. 4).

Besides the dark matter–nucleon scattering cross section, LEP can also set limits on the dark matter annihilation cross section. *Per se*, only bounds on annihilation into e^+e^- pairs can be derived (fig. 5 (a)), but it is easy to generalize these bounds, though not in a model-independent way. In particular, if there are other annihilation channels besides $\bar{\chi}\chi \to e^+e^-$, the LEP limits on the annihilation cross section are weakened by the inverse of the branching ratio for $\bar{\chi}\chi \to e^+e^-$. Since the cross sections for some types of dark matter interactions (in particular scalar and axial vector) depend strongly on the relative velocity $v_{\rm rel}$ of the annihilating dark matter particles, we have to specify the value of this quantity. In fig. 5, we take the average squared velocity $\langle v_{\rm rel}^2 \rangle$ to have a value of 0.24, corresponding to the time of electron–proton recombination in the early universe. (At later times, $\langle v_{\rm rel}^2 \rangle$ is smaller and the limits on scalar and axial vector interactions improve dramatically.[4]) We see that, if dark matter annihilates exclusively into e^+e^- pairs, LEP is able to rule out the annihilation cross section required for thermal relic dark matter, $\langle \sigma v_{\rm rel} \rangle = 3 \times 10^{-26}$ cm^3/s, if $m_\chi \lesssim \mathcal{O}(10$ GeV).

In fig. 5 (b) we compare LEP limits on the dark matter annihilation cross section to various astrophysical constraints[24–26]. We assume dark matter to couple equally to all charged leptons, but it would again be straightforward to rescale our limits if this is not the case. We see that for low m_χ LEP limits are stronger than constraints from gamma ray and e^+e^- observations

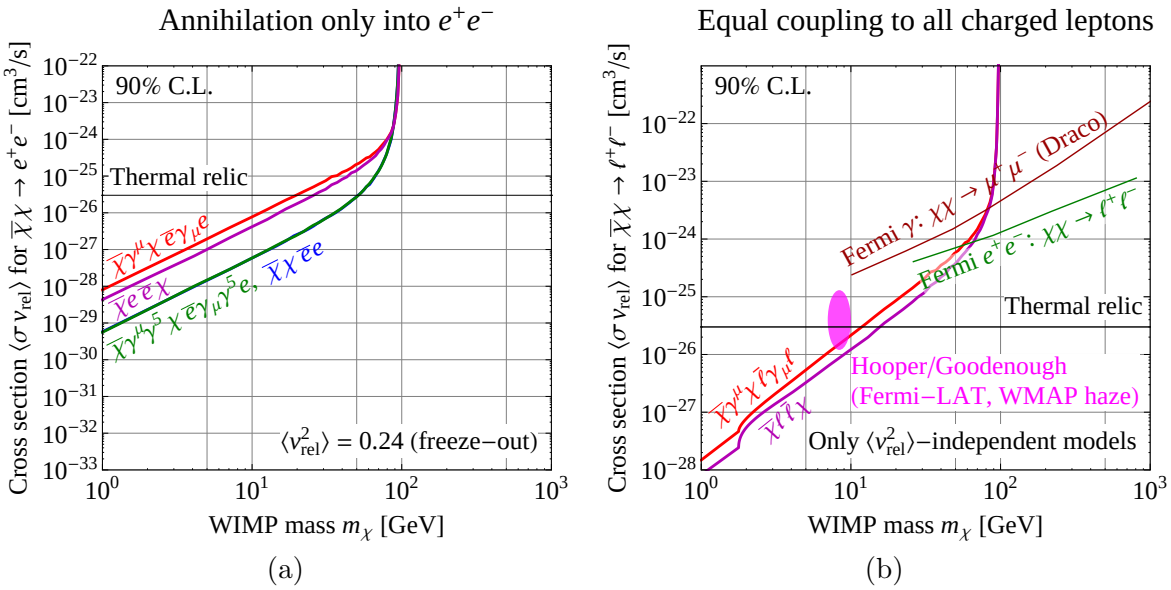

Figure 5: LEP constraints on the dark matter annihilation cross section for the case where the branching ratio for $\bar{\chi}\chi \to e^+e^-$ is 100% (left), and for the case where dark matter couples equally to all charged leptons (right)[4].

by the Fermi-LAT collaboration, and that LEP is also able to disfavor a large portion of the parameter region that could potentially explain gamma ray signals from the galactic center.[26]

In fig. 6, we depart from the effective theory formalism and consider the implications of dark matter interactions mediated by a particle whose mass M is comparable to or below the LEP center of mass energy $\sqrt{s} \sim 200$ GeV. For $M \sim \sqrt{s}$, there is a regime where dark matter production at LEP is resonantly enhanced, so that the limit on the dark matter–nucleon scattering cross section σ_N improves compared to the contact operator case. For smaller M, the LEP constraint becomes generally weaker because the production cross section at LEP is proportional to s^{-1}, whereas σ_N is proportional to μ_N^2/M^4 (with the dark matter–nucleon invariant mass μ_N), giving direct detection experiments a relative advantage at small M. A special situation arises when $2m_\chi < M$, so that the mediator can be produced on-shell at LEP and then decay into dark matter. In that case, the LEP limit on σ_N is very sensitive to the width Γ of the mediator, which is a measure for its branching ratio into $\bar{\chi}\chi$ (larger Γ implies smaller branching ratio). We also note that on-shell production of the mediator with subsequent decay into standard model particles may impose independent constraints on models of this type.

4 Conclusions

In conclusion, we have shown that a largely model-independent search for dark matter is possible at high-energy hadron and lepton colliders by looking for an excess of events with large missing energy and a single jet or photon from initial state radiation. Working in an effective field theory framework, we have shown that the limits that LEP and the Tevatron can set on the mass and couplings of dark matter are superior to direct detection constraints if dark matter is very light ($\lesssim 4$ GeV) or has predominantly spin-dependent or leptophilic interactions. Above masses of $\mathcal{O}(100$ GeV), collider limits deteriorate due to kinematic limitations. We have also used LEP data to set limits on the dark matter annihilation cross section. For example, we were able to rule out a thermal relic with a mass below $\lesssim 10$ GeV if the e^+e^- final state is among the dominant annihilation channels. Our limits on dark matter annihilation are highly complementary to those from astrophysical searches since they extend to very low dark matter masses, whereas astrophysical experiment are most sensitive for dark matter masses above ~ 50 GeV. Finally, we

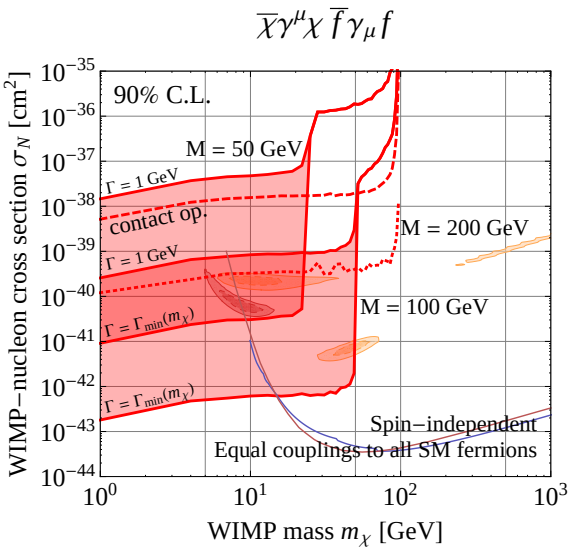

Figure 6: LEP constraints on the dark matter–nucleon scattering cross section in models where the interactions are mediated by a relatively light particle[4].

have also considered models in which dark matter interactions are mediated by a light particle and thus cannot be described in effective field theory. In this case, collider constraints can weaken, but depending on the details of the model may also become much stronger.

References

[1] Y. Bai, P. J. Fox, and R. Harnik, *JHEP* **12**, 048, (2010), arXiv:1005.3797.
[2] J. Goodman et al., *Phys. Rev.* **D82**, 116010, (2010), arXiv:1008.1783.
[3] J. Goodman et al., *Phys. Lett.* **B695**, 185–188, (2011), arXiv:1005.1286.
[4] P. J. Fox, R. Harnik, J. Kopp, and Y. Tsai, (2011), arXiv:1103.0240.
[5] T. Aaltonen et al., *Phys.Rev.Lett.* **101**, 181602, (2008), arXiv:0807.3132.
[6] R. Bernabei et al., *Eur. Phys. J.* **C56**, 333–355, (2008), arXiv:0804.2741.
[7] Z. Ahmed et al., *Science* **327**, 1619–1621, (2010), arXiv:0912.3592.
[8] C. Aalseth et al., *Phys.Rev.Lett.* **106**, 131301, (2011), arXiv:1002.4703.
[9] J. Abdallah et al., *Eur.Phys.J.* **C60**, 17–23, (2009), arXiv:0901.4486.
[10] E. Aprile et al., *Phys.Rev.Lett.* **105**, 131302, (2010), arXiv:1005.0380.
[11] M. Barnabe-Heider et al., *Phys. Lett.* **B624**, 186–194, (2005), arXiv:hep-ex/0502028.
[12] J. Angle et al., *Phys.Rev.Lett.* **101**, 091301, (2008), arXiv:0805.2939.
[13] E. Behnke et al., *Phys.Rev.Lett.* **106**, 021303, (2011), arXiv:1008.3518.
[14] T. Girard et al., (2011), arXiv:1101.1885.
[15] J. Kopp, T. Schwetz, and J. Zupan, *JCAP* **1002**, 014, (2010), arXiv:0912.4264.
[16] J. Abdallah et al., *Eur.Phys.J.* **C38**, 395–411, (2005), arXiv:hep-ex/0406019.
[17] E. Boos et al., *Nucl.Instrum.Meth.* **A534**, 250–259, (2004), arXiv:hep-ph/0403113.
[18] J. Alwall et al., *JHEP* **0709**, 028, (2007), arXiv:0706.2334, http://madgraph.hep.uiuc.edu.
[19] P. J. Fox and E. Poppitz, *Phys. Rev.* **D79**, 083528, (2009), arXiv:0811.0399.
[20] J. Kopp et al., *Phys. Rev.* **D80**, 083502, (2009), arXiv:0907.3159.
[21] J. Kopp, V. Niro, T. Schwetz, and J. Zupan, (2010), arXiv:1011.1398.
[22] O. Adriani et al., *Nature* **458**, 607–609, (2009), arXiv:0810.4995.
[23] A. A. Abdo et al., *Phys.Rev.Lett.* **102**, 181101, (2009), arXiv:0905.0025.
[24] A. A. Abdo et al., *Astrophys. J.* **712**, 147–158, (2010), arXiv:1001.4531.
[25] D. Grasso et al., *Astropart.Phys.* **32**, 140–151, (2009), arXiv:0905.0636.
[26] D. Hooper and L. Goodenough, *Phys.Lett.* **B697**, 412–428, (2011), arXiv:1010.2752.

RECENT RESULTS IN THE SEARCH FOR DARK MATTER WITH NOBLE LIQUID DETECTORS [a]

A. Manalaysay
Physics Institute, University of Zurich, Winterthurerstrasse 190, CH-8057 Zürich, Switzerland

The field of dark matter direct detection has seen important contributions in recent years from experiments involving liquid noble gases, specifically liquid argon and liquid xenon. These detection media offer many properties deemed useful in this search, including fast scintillation response, charge readout, 3-D position reconstruction, and nuclear recoil discrimination. Part of the very rapid emergence and dominance of noble liquids is due to the fact that these technologies are easily scalable to nearly arbitrary size and mass. However, the physics impact of recent results has called into question our understanding of the low-energy response of these detection media, in light of apparent contradictions with a possible low-mass WIMP signal observed in the DAMA/LIBRA and CoGeNT experiments. I discuss recent results and examine the details of this inconsistency.

1 Introduction

Stable, Weakly Interacting Massive Particles (WIMPs) naturally arise in a number of theories beyond the Standard Model of particle physics [1]. If nature allows for the existence of such a particle, it could have been produced thermally in the early Universe, resulting in a relic population persisting through to the present day, constituting what we observe as dark matter in astronomical observations [2,3,4]. Under this scenario, the Earth is embedded within a gas of WIMPs having a characteristic local energy density of $\sim 0.3\,\mathrm{GeV/cm^3}$, a roughly Maxwell-Boltzman velocity distribution with characteristic velocities of $\mathcal{O}(10^{-3}\,\mathrm{c})$, and a weak interaction cross section. Interactions between galactic WIMPs and atomic nuclei would produce roughly exponentially-falling differential energy spectra in terrestrial particle detectors, with energy depositions up to several—to several tens—of keV. The exact details of the expected recoil spectra depend on the target nucleus and type of particles exchanged in the interaction, in addition to specific details of the astrophysical properties of the dark matter halo. Typical interaction rates are expected to be low, ranging from a few counts/kg/day to a few counts/kg/year or fewer. These low rates are in stark contrast to background rates in most particle detectors of $\mathcal{O}(\mathrm{Hz})$ (from natural radioactivity and cosmic rays, for example), and therefore low-background techniques must be used to either reduce these backgrounds or otherwise distinguish signal from background. To drastically reduce the effect of cosmic rays, WIMP dark matter searches universally utilize underground laboratories, which provide factors of 10^{-5} to 10^{-8} reduction in the atmospheric muon flux.

Liquid argon (LAr) and liquid xenon (LXe), as particle detection media, have many properties that are beneficial from the standpoint of a low-background WIMP search. Among the

[a] Presented at Rencontres de Moriond 2011 (Electroweak Session), La Thuile, Italy.

most important properties of these materials is the ability to design such a detector of almost arbitrary size. A large detector has the ability to *self shield* itself from backgrounds due to radioactive isotopes present in other detector materials. This means that the outer regions of the detector can prevent much of these backgrounds from reaching the inner detector regions. This extremely simple property has been shown to be immensely effective at reducing the overall background rate, as compared with technologies utilizing other detector materials. Most background interactions arise from either gamma emitters in detector materials or beta emitters in the liquids themselves, whose energy deposition is characterized by recoiling electrons. This is in contrast to the expected WIMP signal which is highly dominated by nuclear recoils. Both LAr and LXe are able to reject electronic recoils ($\mathcal{O}(10^{-7})$ in LAr and $\mathcal{O}(10^{-3})$ in LXe).

Additional benefits of liquid noble detectors include a high scintillation yield, 3-D position reconstruction capabilities, fast response of $\mathcal{O}$(few ns), "easy" cryogenics (compared with semiconductor detectors), high sensitivity to scalar interactions in LXe ($A \sim 131$, scalar interaction rate $\propto A^2$), and sensitivity to axial vector interactions (48% odd isotopes in LXe).

Past, current, and future WIMP searches using noble liquids include DAMA/LXe[5], ZEPLIN-I[6], ZEPLIN-II[7], ZEPLIN-III[8], WArP 2.3l[9], WArP 100l[10], ArDM[11], DEAP/CLEAN[12], DarkSide[13], XENON10[14], XENON100[15], XENON1t[16], XMASS[17], LUX[18], LZ[19], PANDA-X[20], MAX[21], and DARWIN[22]. Of these, seven have released dark matter results[5,6,7,8,9,14,15]. I devote Section 2 to the four most-recent of these results (WArP 2.3l, ZEPLIN-III, XENON10, XENON100), describing the detectors, science runs, and main results. Later, in Section 3 I focus on low-mass WIMPs ($\sim$10 GeV/c^2) that have recently been a hot topic in the field, and describe what sensitivity noble liquids can provide to this type of dark matter candidate, in comparison with apparent detections in two non-noble-liquid experiments.

2 Recent Dark Matter Results with Noble Liquid Detectors

The four most-recent dark matter results from noble liquid detectors all use a detector design known as a dual-phase time projection chamber (TPC). These detectors detect both the scintillation photons and electrons emitted from an interaction site in the LAr or LXe. Photomultiplier tubes (PMTs), instrumented above and/or below the active liquid volume, detect a fraction of the scintillation photons. An applied static electric field drifts electrons away from the interaction site and up to the liquid surface, where a separate electric field extracts these electrons into the gas where they collide with gas atoms and stimulate further scintillation as they travel to the anode. This additional scintillation signal (caused by the electrons traveling through the gas) is known as *proportional scintillation light*, as its intensity is proportional to the number of extracted electrons, and is also detected by the PMTs. Therefore, the PMTs are responsible for detecting both scintillation ('S1') and charge ('S2'). The electrons drift through the liquid at a constant velocity, and therefore the z-position of the event is given by the delay time between S1 and S2. Additionally, because the S2 signal is emitted always directly below the top PMTs, the pattern of detected photons in this signal can be used to determine the x, y-position as well.

As the ionization density along a track from a nuclear recoil is generally much higher than that from an electronic recoil, the efficiency for electrons to recombine with parent ions is much higher in nuclear recoils. Therefore, the ratio of S2 to S1 is used as a parameter to distinguish the two types of recoils. This parameter by itself provides electromagnetic background rejection at the level of 99.0% to 99.9%. Additionally, the time structure of the scintillation emission can be characterized as a combination of a fast ($\sim$few ns) singlet de-excitation and a slow triplet de-excitation; the ratio of the intensity of scintillation from the fast and slow components can be used as an additional parameter to distinguish between electronic and nuclear recoils. The slow component in LXe is on the order of 10s of ns, and therefore does not provide a very good discrimination parameter, particularly at the low energies of interest in such a dark matter

search. However, in LAr the slow scintillation component is roughly three orders of magnitude slower than the fast component, and allows this additional discrimination parameter to reject electronic recoils at the level of ∼99.99999% efficiency.

2.1 WArP 2.3l

The WArP 2.3l experiment[9] operated a 2.3 l LAr dual-phase TPC at the underground Laboratori Nazionali del Gran Sasso (LNGS), in central Italy. This detector served as a prototype for the larger 100 l LAr TPC currently running in the same location. The active LAr volume was viewed from above by 12 PMTs, which (as described above) were responsible for measuring both the S1 and S2 signals. Nuclear recoil discrimination is performed based on two parameters. One parameter is $\log_{10}(\mathrm{S2/S1})$, and another parameter, F, quantifies the pulse shape.

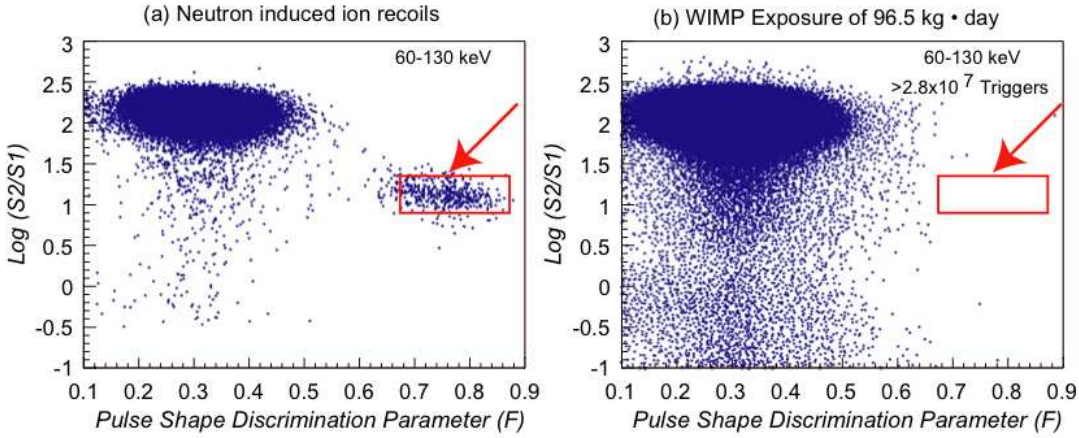

Figure 1: WArP 2.3 l events in one energy bin distributed according to the two discrimination parameters for neutron calibration data (*left*) and WIMP-search data (*right*). The red box, defined based on the neutron calibration, indicates the location in this parameter space where nuclear recoils are expected, and is therefore defined to be the signal region. Both figures taken from Ref. 9.

Data were collected from a central 3.2 kg region of the detector for a total effective exposure of 100 kg d. The two discrimination parameters are calculated for each event, with the WIMP signal window defined based on calibration with a neutron source. Figure 1 shows the distribution of these two discrimination parameters for one energy bin for a calibration with a neutron source (*left*) and from WIMP-search data (*right*). The signal from nuclear recoils, defined on the neutron calibration data, is indicated by the red box. In addition to this energy bin, no events were seen in the signal region for energies above 55 keV. This lack of events translates to an upper limit on the WIMP-nucleon scalar cross-section of $\sim 10^{-42}\,\mathrm{cm}^2$ for 100 GeV/c^2 WIMPs. The full exclusion curve is shown in Figure 4.

2.2 ZEPLIN-III

The ZEPLIN-III experiment[8] uses a dual-phase LXe TPC, operated at the Palmer Underground Laboratory in Boulby, UK. The detector is designed for high electric drift field (to improve nuclear recoil discrimination) and precise x, y-position reconstruction. Thirty-one 2-inch PMTs view the active LXe volume from below, which is 19 cm in diameter and 3.5 cm in thickness. As mentioned in Section 1, the singlet and triplet de-excitation time scales are too close together in LXe to be much use as a discrimination parameter, and therefore only the ratio of scintillation to charge can be used.

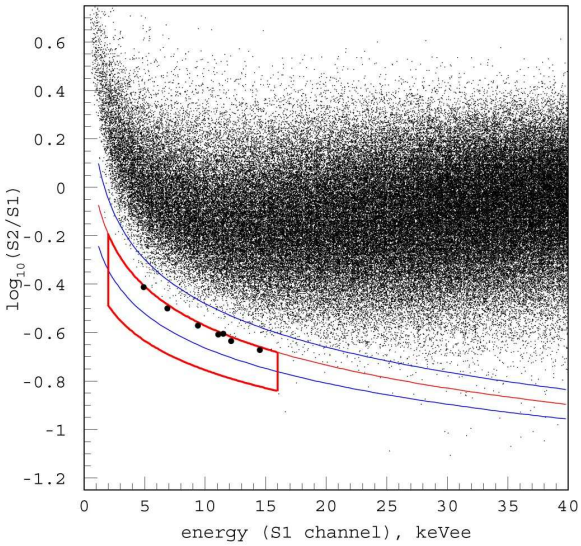

Figure 2: The ZEPLIN-III nuclear recoil discrimination parameter, $\log_{10}$(S2/S1), versus energy for the WIMP search data. The thin red line indicates the centroid of the nuclear recoil distribution, its 1σ spread shown by the thin blue lines. The signal acceptance region, defined as the space between the centroid and the -2σ contours, is indicated by the thick red box.

Figure 2 shows the LXe discrimination parameter, $\log_{10}$(S2/S1), as a function of energy. The units of the horizontal scale are given as "keVee", to indicate that these energies are reconstructed using the "electronic-equivalent" energy scale. The relation between S1 and the deposited energy differs for electronic and nuclear recoils. Seven events are seen in the signal acceptance region, following an effective exposure of 128 kg d, with expected background of 11.6 ± 3.0 events from electronic recoils, and 1.2 ± 0.6 events from neutrons. This leads to an upper limit on the WIMP-nucleon scalar interaction cross-section of $8.1 \times 10^{-44}\,\mathrm{cm}^2$ at $60\,\mathrm{GeV/c}^2$. The ZEPLIN-III detector is currently running with new PMTs and an overall electromagnetic background level $\sim$10 times lower than the data shown here.

2.3 XENON10

The XENON10 experiment[14] operated at the same underground facility as WArP in central Italy. Like the ZEPLIN-III experiment, it used a dual-phase LXe TPC. The active region was 20 cm diameter by 15 cm height, and viewed from above and below by 88 PMTs. Event position reconstruction featured resolution at the level of mm for all three spatial dimensions.

Figure 3 shows the main WIMP search data of the XENON10 experiment in the same parameter spaced used in ZEPLIN-III, after an effective exposure of 136 kg d. Ten events appear in the signal acceptance region, lying between the two blue lines. The expected background due to statistical leakage of the electronic recoils (black points) into the signal region was $7.0^{+1.4}_{-1.0}$, and is believed the be the origin of the five events labeled with blue numbers (3, 4, 5, 7, 9). Event 1 is a noise event, and events 2, 6, 8, and 10 are consistent with a separate class of background; see Ref([14]) for a description. Nevertheless, all ten events were treated in the analysis as signal (without background subtraction), which leads to an upper limit on the scalar WIMP-nucleon cross-section of $5.5 \times 10^{-44}\,\mathrm{cm}^2$ at $35\,\mathrm{GeV/c}^2$.

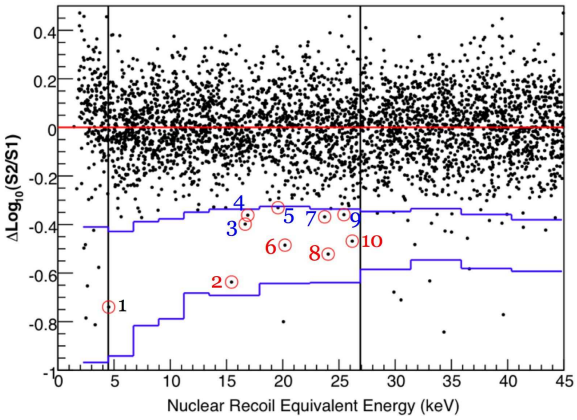

Figure 3: WIMP search data from the XENON10 experiment. Ten events are observed in the signal region, indicated by the blue lines.

2.4 XENON100

The XENON100 experiment[15] operates a very similar detector to XENON10 (and is located in the same shield where XENON10 operated), but with a detection volume larger by an order of magnitude. The active LXe volume, 30 cm in diameter and 30 cm in height, is viewed from the top and bottom by 178 PMTs. In addition to its larger size as compared with XENON10, additional steps were taken during construction to choose detector materials that are low in common radioactive contaminants (U, Th, K). Similar to ZEPLIN-III and XENON10, the WIMP search data in XENON100 was treated by constructing a plot of the nuclear recoil discrimination parameter versus energy. A blind analysis was performed on an effective exposure of ∼1.5 tonne d, after which 6 events were observed in the signal acceptance region. After unblinding, it was seen that a population of background events, arising from electronic noise, was contaminating the data. An additional, pos-unblinding cut was constructed to target these events specifically, which resulted in 3 remaining events in the signal region, shown in Figure 4 (*left*). The resulting upper limit on WIMP-nucleon scalar cross-section is $7 \times 10^{-45}\,\mathrm{cm}^2$ at $50\,\mathrm{GeV/c}^2$.

The full exclusion curves (90% C.L.) of the four experiments discussed in this section, for the WIMP-nucleon scalar cross-section, are shown in Figure 4 (*right*), as a function of WIMP mass. Also shown is a recent calculation of a favored region of this parameter space by CMSSM[23]. Figure 4 (*right*) was made using DM Tools[24].

3 Light WIMPs

Recently, considerable attention has been placed on the possible existence of low-mass WIMPs, of order $\sim 10\,\mathrm{GeV/c}^2$. The source of this excitement comes from two experimental results that point to such a particle. There is the long-standing observation of an annual modulation in the low-energy background rate of the DAMA/NaI and DAMA/LIBRA experiments[25]. Operating NaI scintillating crystals at LNGS, DAMA/LIBRA is unable to distinguish nuclear recoils from electronic recoils, and instead uses the observed annual modulation as a dark matter identification feature. This signal can be interpreted as being the result of WIMPs scattering off of sodium nuclei, which would imply the existence of a WIMP with mass in the range $\sim$8–$12\,\mathrm{GeV/c}^2$, with a WIMP-nucleon scalar cross-section of $\sim$few$\times 10^{-40}\,\mathrm{cm}^2$. However, it should be noted that the observed annual modulation is correlated with both the observed modulation in the cosmic muon rate[26] and the rate of ambient fast neutrons[27] in LNGS.

The second source of excitement over low-mass WIMPs comes from the observed exponentially-

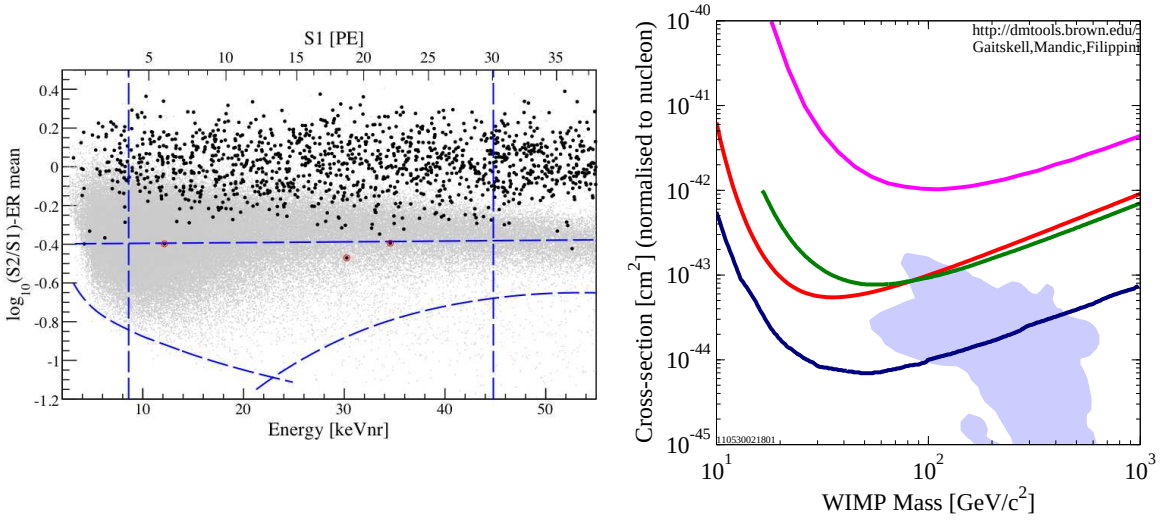

Figure 4: (*Left*) WIMP search data for the XENON100 experiment (black points); the nuclear recoil band, defined by a neutron calibration, is indicated by the gray points. The signal window is the region enclosed by the blue dashed curves. Six events existed in the signal region after unblinding, three of which were removed by an additional post-unblinding cut. The remaining three signal events are highlighted by red circles. (*Right*) Exclusion limits on the WIMP-nucleon scalar interaction cross-section as a function of WIMP mass for the four experiments discussed in the text: WArP 2.3 l (magenta), ZEPLIN-III (dark green), XENON10 (red), XENON100 (dark blue). Also shown is a region of parameter space favorable for the neutralino from SUSY in one calculation of CMSSM. Plot made using DM Tools. See text for citations.

falling spectrum in the background data of the CoGeNT experiment[28] below the normal threshold used for previous analyses. This detector also features no discrimination between electronic and nuclear recoils, but offers the ability to reject surface events with energies above ∼2 keV. The exponential fall in the differential spectrum, extending from roughly 0.5 keV to 1 keV, can be fit by the expected recoil spectrum of low-mass WIMP, with mass and cross-section similar to the interpretation of the DAMA signal mentioned in the previous paragraph. However, as many experiments should be sensitive to these regions of parameter space, the low-mass WIMP interpretation of these two signals is treated with varying degrees of skepticism and optimism within the field.

The exclusion curves shown in Figure 4 (*right*) are all calculated by using the scintillation signal (S1) to reconstruct the energy of each event. The nonlinear relationship between the average scintillation signal and the energy of the recoiling nucleus is quantified by the parameter $\mathcal{L}_{\rm eff}$ (the "effective Lindhard parameter"). For energies of interest to the WArP result, the LAr $\mathcal{L}_{\rm eff}$ measured values show little energy dependence, and are in agreement. However, this is very much not the case for $\mathcal{L}_{\rm eff}$ in LXe[29]. As a result, the exclusion curves for LXe contain a degree of uncertainty, and this uncertainty has lead some to question the robustness of these upper limits with respect to the possible signal detection by DAMA and CoGeNT.

Recently, however, it was pointed out that the charge signal (S2) can be used (instead of S1) to reconstruct the recoil energy of events with much greater sensitivity that what is possible with using S1 alone[30]. Measurements of the charge yield, unlike $\mathcal{L}_{\rm eff}$, have shown remarkable consistency, and are additionally well matched to theoretical expectations[31]. Using this insight, additional WIMP search data collected by XENON10 has been analyzed, specifically targeting low-mass WIMPs[32]. These data, not used in previous XENON10 publications, featured a reduced trigger threshold at the level of a single electron. Using a conservative analysis threshold of 5 electrons, corresponding to 1.4 keV, along with tight fiducial cuts, results in the exclusion curve shown in Figure 5.

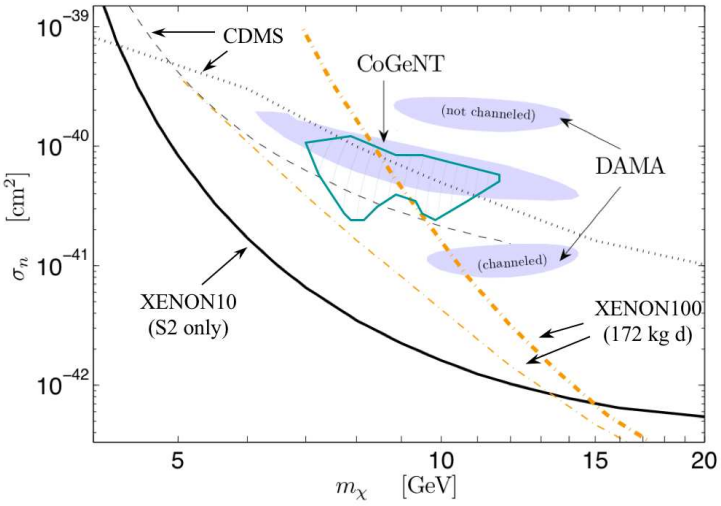

Figure 5: The typical WIMP parameter space, in WIMP-nucleon scalar cross-section versus WIMP mass, focusing on the regions around 10 GeV/c^2. Regions consistent with a light WIMP interpretation of DAMA and CoGeNT are indicated by the blue regions. Exclusion limits from several experiments are also shown (see text for explanation).

The 90% C.L. exclusion curves in Figure 5 include the low-threshold analyses of CDMS-I[33] and CDMS-II[34] experiments, XENON100 exclusions (based on 172 kg d)[15] using two choices of $\mathcal{L}_{\rm eff}$, and the new limit from the XENON10 S2-only analysis[32]. Regions consistent with CoGeNT (blue-green contour[28]) and CoGeNT and DAMA (light-blue shaded regions[35]) are also indicated. These constraints are not weakened if one considers scattering mediated by axial vector coupling ("spin dependent") in the case of CoGeNT. This is because germanium and xenon both have their main spin-dependent sensitivity on couplings to neutrons, and natural Xe contains more odd isotopes than natural germanium. Given the magnitude of this new XENON10 null result, it becomes difficult to understand the CoGeNT and DAMA signals with a light WIMP interpretation.

References

1. Gianfranco Bertone, Dan Hooper, and Joseph Silk. Particle dark matter: Evidence, candidates and constraints. *Phys. Rept.*, 405:279–390, 2005.
2. K. G. Begeman, A. H. Broeils, and R. H. Sanders. Extended rotation curves of spiral galaxies: Dark haloes and modified dynamics. *Mon. Not. Roy. Astron. Soc.*, 249:523, 1991.
3. J. Dunkley et al. Five-Year Wilkinson Microwave Anisotropy Probe (WMAP) Observations: Likelihoods and Parameters from the WMAP data. *Astrophys. J. Suppl.*, 180:306–329, 2009.
4. Douglas Clowe et al. A direct empirical proof of the existence of dark matter. *Astrophys. J.*, 648:L109–L113, 2006.
5. R. Bernabei et al. New limits on particle dark matter search with a liquid Xenon target-scintillator. *Phys. Lett.*, B436:379–388, 1998.
6. G. J. Alner et al. First limits on nuclear recoil events from the ZEPLIN I galactic dark matter detector. *Astropart. Phys.*, 23:444–462, 2005.
7. G. J. Alner et al. First limits on WIMP nuclear recoil signals in ZEPLIN-II: A two phase xenon detector for dark matter detection. *Astropart. Phys.*, 28:287–302, 2007.
8. V. N. Lebedenko et al. Result from the First Science Run of the ZEPLIN-III Dark Matter Search Experiment. *Phys. Rev.*, D80:052010, 2009.

9. P. Benetti et al. First results from a dark matter search with liquid argon at 87-K in the Gran Sasso underground laboratory. *Astropart. Phys.*, 28:495–507, 2008.
10. R. Acciarri et al. The WArP experiment. *J. Phys. Conf. Ser.*, 203:012006, 2010.
11. M. Haranczyk et al. The ArDM experiment. *Acta Phys. Polon.*, B41:1441–1446, 2010.
12. DEAP/CLEAN Collaboration. http://deapclean.org.
13. DarkSide Collaboration. http://lartpc-docdb.fnal.gov/0005/000581/001/-DarkSide50_DOE_Project_Narrative_FNAL.pdf.
14. J. Angle et al. First Results from the XENON10 Dark Matter Experiment at the Gran Sasso National Laboratory. *Phys. Rev. Lett.*, 100:021303, 2008.
15. E. Aprile et al. First Dark Matter Results from the XENON100 Experiment. *Phys. Rev. Lett.*, 105:131302, 2010.
16. XENON1T Collaboration. http://xenon.astro.columbia.edu/talks/-aprile_ucla_dm2010.pdf.
17. Hiroyuki Sekiya et al. XMASS. 2010.
18. C. Hall et al. A search for weakly interacting dark matter with the LUX experiment. *PoS*, ICHEP2010:431, 2010.
19. LZ Collaboration. http://odessa.phy.sdsmt.edu/ bai/dusel/talks-pdf/008.pdf.
20. PANDA-X Collaboration. http://rd.kek.jp/slides/20110203/KGiboniKEK1.pdf.
21. Ricardo Alarcon et al. MAX: Multi-Ton Argon and Xenon. FERMILAB-PROPOSAL-1001.
22. Laura Baudis. DARWIN: dark matter WIMP search with noble liquids. *arXiv:1012.4764 [astro-ph.IM]*, 2010.
23. Leszek Roszkowski, Roberto Ruiz de Austri, and Roberto Trotta. Implications for the Constrained MSSM from a new prediction for $b \to s\gamma$. *JHEP*, 07:075, 2007.
24. DM Tools. http://dmtools.brown.edu.
25. R. Bernabei et al. New results from DAMA/LIBRA. *Eur. Phys. J.*, C67:39–49, 2010.
26. M Selvi et al. Analysis of the seasonal modulation of the cosmic muon flux in the LVD dtector during 2001-2008. *Proceedings of ICRC*, 31:1, 2009.
27. John P. Ralston. One Model Explains DAMA/LIBRA, CoGENT, CDMS, and XENON. *arXiv:1006.5255 [hep-ph]*, 2010.
28. C. E. Aalseth et al. Results from a Search for Light-Mass Dark Matter with a P- type Point Contact Germanium Detector. *Phys. Rev. Lett.*, 106:131301, 2011.
29. A. Manalaysay. Towards an improved understanding of the relative scintillation efficiency of nuclear recoils in liquid xenon. *arXiv:1007.3746 [astro-ph.IM]*, 2010.
30. P. Sorensen et al. Lowering the low-energy threshold of xenon detectors. *arXiv:1011.6439 [astro-ph.IM]*, 2010.
31. Peter Sorensen and Carl Eric Dahl. Nuclear recoil energy scale in liquid xenon with application to the direct detection of dark matter. *Phys. Rev.*, D83:063501, 2011.
32. J. Angle et al. A search for light dark matter in XENON10 data. *arXiv:1104.3088 [astro-ph.CO]*, 2011.
33. D. S. Akerib et al. Low-threshold analysis of CDMS shallow-site data. *Phys. Rev.*, D82:122004, 2010.
34. Z. Ahmed et al. Results from a Low-Energy Analysis of the CDMS II Germanium Data. *Phys. Rev. Lett.*, 106:131302, 2011.
35. Spencer Chang, Jia Liu, Aaron Pierce, Neal Weiner, and Itay Yavin. CoGeNT Interpretations. *JCAP*, 1008:018, 2010.

LATEST RESULTS OF THE EDELWEISS-II EXPERIMENT

A.S. TORRENTÓ-COELLO
IRFU/SPP, CEA-Saclay, 91191 Gif-sur-Yvette, France

The EDELWEISS-II collaboration has performed a direct search for WIMP dark matter with an array of ten 400-g heat-and-ionization cryogenic detectors equipped with Inter-Digit electrodes for the rejection of near-surface events. Results from one year of continuous operation at the Laboratoire Souterrain de Modane will be presented. A sensitivity to the spin-independent WIMP-nucleon elastic cross-section of 4.4×10^{-8} pb was achieved using a 384 kg·d effective exposure. We also interpret the results in the inelastic scattering scenario, excluding the DAMA allowed region for WIMP masses greater than 90 GeV for a mass splitting of 120 keV. The results obtained demonstrate the excellent background rejection capabilities of these simple and robust detectors in an actual WIMP search experiment. Some first results with 800-g detectors will be also presented together with the prospects for this experiment and the ton-scale EURECA project.

1 The WIMP search and the EDELWEISS-II setup

The existence of Weakly Interacting Massive Particles (WIMPs) is a likely explanation for the various observations of a non-luminous, non-baryonic matter component from the largest scales of the Universe to galactic scales [1]. The WIMP search tests the hypothesis of the Milky Way being surrounded by a dark matter halo constituted by these particles. WIMPs would scatter off ordinary target nuclei on Earth yielding a low-energy deposit of the order of 10–100 keV. The expected interaction rate is very low, and it is currently constrained at the level of <1 event/kg/year. The detection of such small signals is technically difficult, requiring an ultralow radioactivity environment and detectors with a low energy threshold which could actively reject the residual backgrounds.

EDELWEISS is an experiment aimed at the direct detection of dark matter with ultrapure Ge bolometers. The EDELWEISS-II setup is installed in the Laboratoire Souterrain de Modane (LSM), the deepest underground laboratory in Europe. The 4800 m water-equivalent of rock above the experimental cavity reduces the cosmic muon flux to 4 $\mu/\mathrm{m}^2/\mathrm{day}$. The fast neutron flux from the rock has been measured to be 10^{-6} $\mathrm{n/cm}^2/\mathrm{s}$.

The 400-g Ge bolometers are operated at 20 mK in a dilution refrigerator which can be controlled remotely. The bolometers are protected against the relevant background contributions, i.e. gamma and beta radioactivity, cosmic muons and neutrons, by means of passive shields and active rejection. A 20-cm thick lead shield, with an inner part made up with roman lead, surrounds the detectors to attenuate the external γ radioactivity. It follows a 50-cm polyethylene shield which attenuates the fast neutron flux. An active muon veto system made of plastic scintillators covers the whole setup with a 98% geometrical efficiency. The setup is installed in

a clean room with deradonised air to minimise the beta contamination from Rn. Additional background monitoring is achieved by a Rn detector near the cryostat, a ^{3}He-gas detector inside the shielding (thermal neutron flux), and a Gd-loaded liquid scintillator outside the shielding (muon-induced neutrons). Radioactive sources are available for gamma (^{133}Ba), beta (Rn), and neutron (AmBe) calibration of the detectors.

The bolometers are instrumented to perform a dual heat and ionisation measurement of the signals arising from particle interactions in order to discriminate γ-induced electronic recoils from potential WIMP-induced nuclear recoils. The heat is measured with NTD [a] sensors glued on the surface of each detector. The ionisation signal is measured with a set of Al electrodes deposited on the bolometer surface, which are polarised at a few V/cm. The electronic/nuclear recoil discrimination is performed through the quantity called "ionisation yield" (Q) which is the ratio between the ionisation and recoil energies. By definition, Q=1 for electronic recoils and it is a factor $\sim$3 lower for nuclear recoils in Ge in the energy region of interest. This method allows to perform an event-by-event rejection of the bulk of γ radioactivity. However, when the interaction takes place near the detector surface the charge collection is incomplete, and the value of Q for electronic recoils can be at the level of that for nuclear recoils, leading to a mis-identification of these events. These surface events are mainly generated by local β radioactivity from ^{210}Pb, a daughter of Rn present in air which is deposited on all material surfaces.

To get rid of this intrinsic background, a new generation of detectors so-called "ID" (Inter-Digit) has been developped. The functioning principle of these detectors is shown in figure 1. The electrodes are concentric circles connected alternatively, forming 2 interleaved sets: one for ionisation charge collection and one for electric field shaping ("veto"). The electric field created is vertical in the bulk of the bolometer and near-horizontal next to the top and bottom surfaces. Two more electrodes covering the lateral surfaces ("guard") limit the detection volume to the bulk.

An interaction in the fiducial volume reaches both collecting electrodes with a perfect charge balance, leaving no signal in any of the veto or guard electrodes. An interaction on the surface is seen by the veto or guard electrodes, and the signal is asymmetrically collected by the collecting electrodes. This redundance on the identification of surface events provides a very high rejection efficiency ($\sim 10^{-5}$) for gammas and betas [2].

2 WIMP-search analysis and results

A WIMP search was carried out using ten 400-g ID detectors installed in the EDELWEISS-II setup from April 2009 to May 2010. Here we present the analysis of the full data set, which also includes the data from the validation run of the ID technology in 2008. The overall exposure doubles the one in the 6-month WIMP-search published in [3].

During the whole acquisition period, the cryogenic conditions were maintained stable at $\sim$18 mK without any major interruption. Most of the time was devoted to WIMP search (325 days), and a small fraction to gamma and neutron calibrations (10.1 and 6.4 days, respectively). All heat sensors and 90% of the ionisation channels were operational. The redundancy in the background rejection allowed to use all the detectors for WIMP search. An online trigger kept the trigger rate below a fraction of Hz.

[a] Neutron Transmutation Doped.

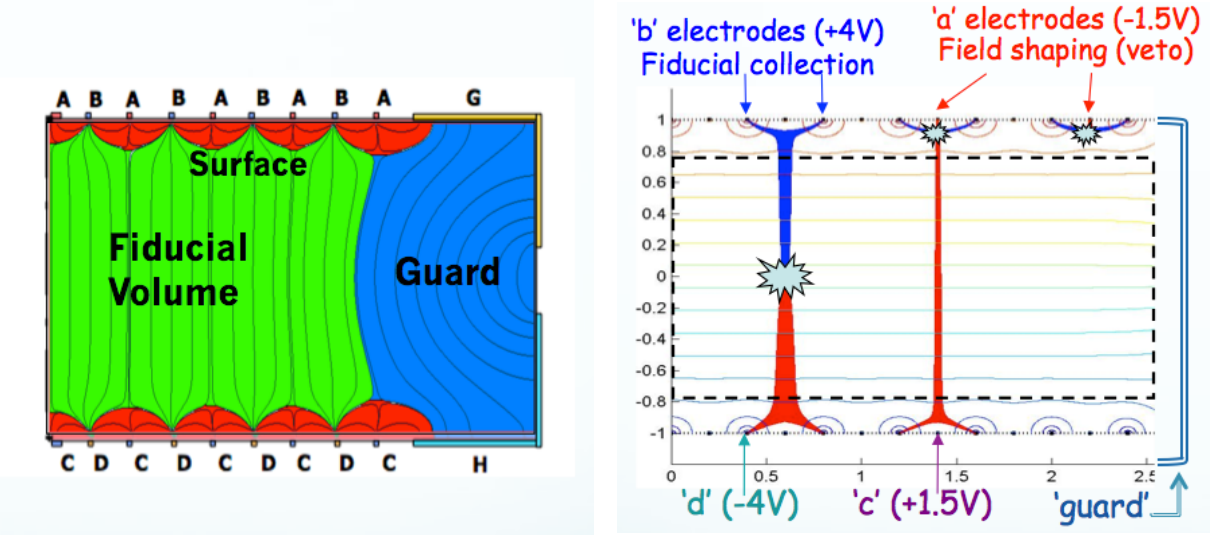

Figure 1: Left: Topology of the electric field created by interleaved electrodes. Right: Functioning principle of Inter-Digit detectors for a fiducial event (left) and two surface events (center, right). The lines represent the electrostatic equipotentials.

The data was analysed using two independent pipelines which yield consistent results. An optimal filtering algorithm allowed processing the signals accordingly to the changing noise conditions. The average baseline resolutions of heat and fiducial ionisation channels were of ∼1.2 keV FWMH and ∼0.9 keV FWHM, respectively. Noisy periods were automatically discarded on a baseline-measurement basis with 80% efficiency. A χ^2 cut was used to reject misreconstructed events. The WIMPs were searched among the fiducial events, using the ionisation yield to discriminate gamma-rays with a 99.99% rejection efficiency. Tagging of coincident events in bolometers and the muon veto allowed to reject neutron-induced recoils. Finally, a WIMP-search energy threshold was set a priori to 20 keV, so that the search efficiency is independent of the energy. After all cuts, the effective exposure obtained is 384 kg·d. This analysis procedure is identical to the one previously used in [3].

In figure 2 we show the ionisation yield vs. recoil energy obtained in the neutron and gamma calibrations. In the neutron calibration, the region with 90% acceptance for nuclear recoils, which is the one used in the WIMP search, is well described by the parametrisation of [4] using the measured resolutions of the heat and ionisation signals. From the γ-ray calibration we obtain a γ rejection factor of $\sim 3 \times 10^{-5}$. The origin of the six events leaking into the nuclear recoil band is being investigated. It has already been verified that they are not related to a specific time period, bolometers with missing electrodes or electrodes with bad resolution.

The ionisation yield plot obtained in the WIMP search after fiducial cuts is shown in figure 3 (left). Five events are found in the nuclear recoil band: four of them have energies between 20 and 23 keV, and one has 172 keV. All of them are well-reconstructed events which lie well above the noise level of the detectors. Background studies are ongoing to fully understand their origin. Upper limits may be derived from the known residual gamma, beta and neutron backgrounds, using calibration data, material radioactivity measurements and Monte Carlo simulation of the detectors. Overall, less than 3 events (90% CL) from known origin are expected in this WIMP search.

The spin-independent cross-section upper limit for WIMP-nucleon elastic scattering is cal-

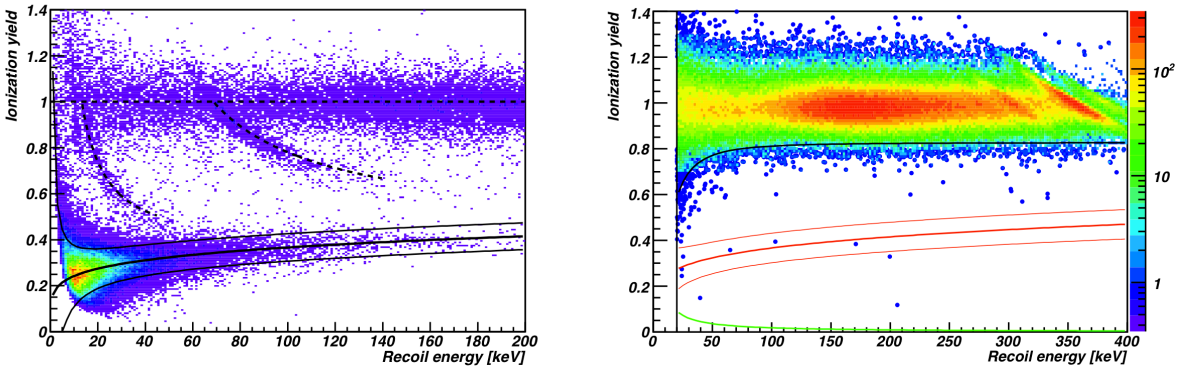

Figure 2: Ionisation yield vs. recoil energy. Left: Neutron calibration with an AmBe source. The electronic recoil nominal value Q=1, the 90%-acceptance nuclear recoil band (bottom) and the lines arising from inelastic neutron scattering at 13.26 keV and 68.75 keV (dashed) are highlighted. Right: Gamma calibration with a ^{133}Ba source. The lines superimposed represent the average 99.99% rejection line for electron recoils (black), the 90%-acceptance nuclear recoil band (red) and the typical ionisation threshold (green).

culated from the presented data following the optimum interval method described in [5]. A standard halo model is considered, and the calculation of the differential event rate is performed according to the analytical solution proposed by [6], with the following values for the relevant parameters: ρ_χ=0.3 GeVc^{-2}cm^{-3} (local dark matter density), v_0=220 km s^{-1}(dark matter Maxwellian velocity dispersion), $v_{\rm earth}$=235 km s^{-1} (average Earth velocity) and a recent estimation of the galactic escape velocity, $v_{\rm esc}$=544 km s^{-1} [7]. We include the effect of a detector finite recoil energy resolution of 1.5 keV. The 90% CL limit obtained vs. the WIMP mass is shown in figure 3 (right). The best sensitivity obtained by EDELWEISS-II is 4.4×10^{-8} pb at M_χ=85 GeV, which is more than twice as constraining than the one obtained with six months of data [3].

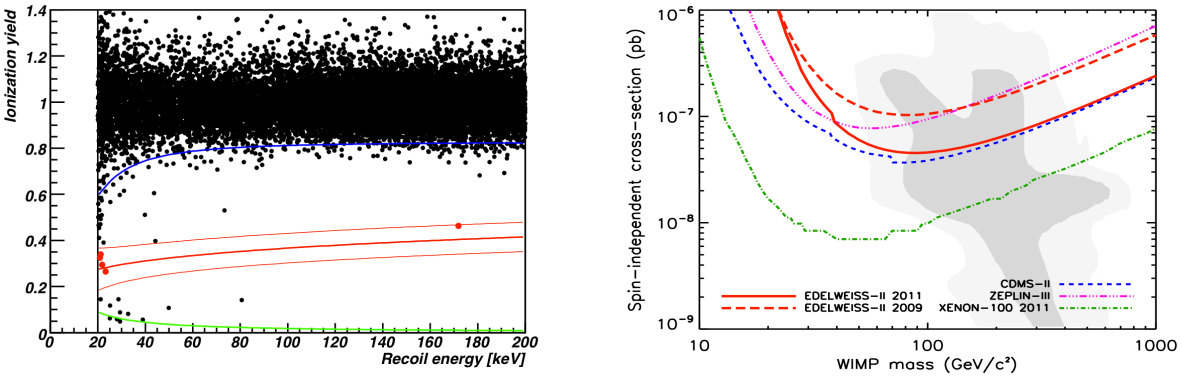

Figure 3: Left: Ionisation yield vs. recoil energy obtained in the WIMP search after fiducial cuts. Highlighted in red, the five events found in the nuclear recoil band which are retained as WIMP candidates. Right: WIMP-nucleon spin-independent elastic cross-section upper limit at 90% CL vs. WIMP mass obtained in this analysis (solid red) and recent results from other experiments. The shaded area corresponds to the 68% and 98% probability regions of the cMSSM scan from [8].

3 Inelastic scattering scenario

The inelastic dark matter scenario has been proposed to reconcile the dark matter modulation signal claimed by DAMA/LIBRA and the null detection in all the other direct detection experiments [9].

In this scenario, the WIMP has a ground state and an excited state $\delta\sim$100 keV heavier than the previous one. The WIMP-nucleus scattering would occur through a transition to the excited state ($\chi + \mathcal{N} \rightarrow \chi^* + \mathcal{N}$), with the elastic scattering being highly suppressed.

The kinematics of the scattering process in the inelastic scenario differs from the elastic one, as the kinetic energy needed for a WIMP to scatter off nuclei is higher in the former case. For the direct detection experiments this translates into a higher minimum velocity to deposit a recoil energy E_{R} in the detector

$$v_{\mathrm{min}} = \frac{1}{c^2}\sqrt{\frac{1}{2mE_{\mathrm{R}}}}\left(\frac{mE_{\mathrm{R}}}{\mu} + \delta\right) \tag{1}$$

where m is the mass of the target nucleus and μ is the reduced mass of the WIMP-target nucleus system. The increase of v_{min} results in a dramatic modification of the expected WIMP spectrum, as only the high end of the WIMP halo velocity distribution will contribute to the signal: the event rate is globally reduced and suppressed at low recoil energies, and the modulation signal is enhanced. Moreover, for a given E_{R} and δ, heavier targets will be more sensitive than lighter ones.

In both elastic and inelastic scenarios, the differential event rate can be calculated from

$$\frac{dR}{dE} = \frac{\rho_\chi}{2M_\chi\mu^2}\sigma_0 F^2(q)\int_{v_{\mathrm{min}}}^{v_{\mathrm{max}}}\frac{f(\mathbf{v})}{v}d^3v \tag{2}$$

where ρ_χ is the local WIMP density, M_χ is the WIMP mass, σ_0 is the zero-momentum WIMP-nucleus cross-section and $F^2(q)$ is the Helm nuclear form factor for momentum transfer $q = \sqrt{2mE_R}$, which is described in [10]. We consider a standard WIMP halo model with a Maxwellian velocity distribution characterised by a velocity dispersion $\sigma_v = \sqrt{2/3}v_0$ which is truncated at a galactic escape velocity v_{esc}. The integral of the inverse mean of the velocity distribution is done from v_{min} to v_{max}=v_{esc}+v_{earth}, the maximum velocity a WIMP can have to interact with a target nucleus (otherwise it would escape the Galaxy).

We have computed the differential event rate using the analytical solution of equation (2) proposed in [6] and considering the same values as in the elastic case describe above. In figure 4 we show the effect of the the mass splitting δ in the event rate for different targets in the case of a WIMP mass of 100 GeV, a cross-section of 10^{-8} pb, and v_{max}=774 km s^{-1}. We observe that an increase in the mass splitting globally reduces the signal, even suppresses it at low recoil energies. Given the same δ, heavier targets would be more sensitive to the signal. For instance an iodine target (which is the case of DAMA) could still detect a WIMP signal whereas a Ge detector would not be sensitive anymore.

We have interpreted the EDELWEISS-II results presented above in the inelastic scattering scenario. Following the same procedure as in the previous section, the WIMP-nucleon spin-independent cross-section upper limit has been computed for δ=120 keV with the optimum interval method [5]. The result is shown in figure 5 together with limits recently published by other direct detection experiments. The EDELWEISS-II limit excludes the DAMA region for

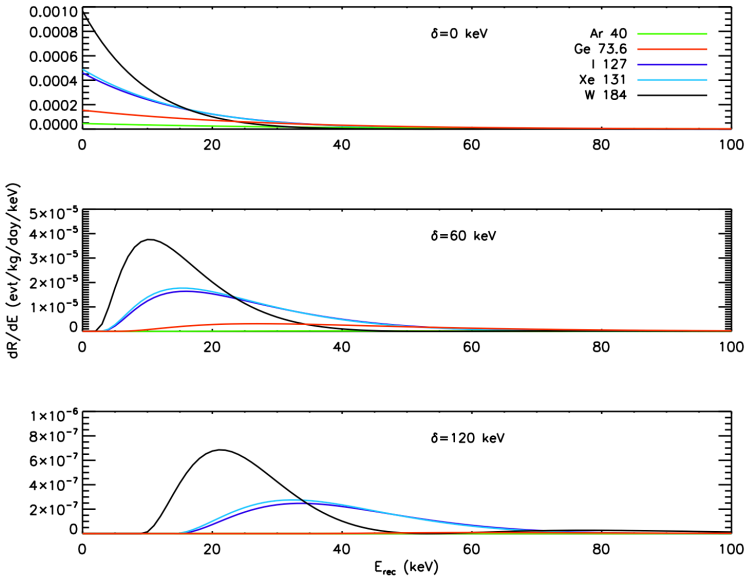

Figure 4: Differential event rate for a WIMP scattering off different target nuclei: Ar (green), Ge (red), I (dark blue), Xe (fair blue) and W (black). The mass splitting values considered are: δ=0 keV (top), 60 keV (middle) and 120 keV (bottom).

WIMP masses greater than 90 GeV. The lack of events between 23 and 172 keV provides a very good sensitivity at large WIMP masses.

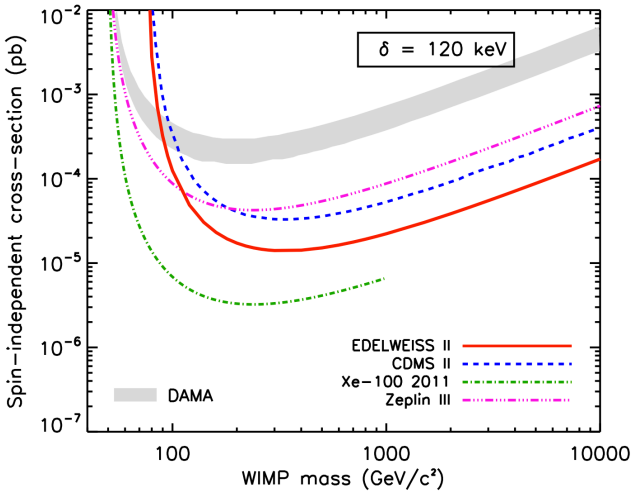

Figure 5: WIMP-nucleon spin-independent cross-section upper limit at 90% CL vs. WIMP mass for inelastic scattering with δ=120 keV. This analysis (solid red) together with the latest results from several direct detection experiments, and DAMA allowed region at 90% CL.

4 Current status and prospects

The EDELWEISS-II experiment has carried out a direct WIMP search with an array of ten 400-g Inter-Digit detectors, achieving an effective exposure of 384 kg·d. Five WIMP candidates

in the energy range [20,200] keV have been reported. The best sensitivity achieved in the elastic spin-independent WIMP-nucleon cross-section is 4.4×10^{-8} pb for a WIMP mass of 85 GeV. An interpretation of these results in the inelastic scattering scenario excludes the allowed DAMA region for WIMP masses greater than 90 GeV. The results are detailed in [11].

The Inter-Digit detector technology has proven to be reliable and robust enough to perform direct detection of WIMPs at a competitive level. To go beyond the present performance, a new generation of detectors has been conceived: the Full Inter-Digit (FID). In this new design, the interleaved electrodes cover also the lateral surfaces of the bolometers and they are connected such that surface event rejection is possible in both fiducial and guard volumes. A first series of two 400-g and four 800-g FID detectors has been built and tested (see picture in figure 6 (left)). The combination of an unprecedented mass of 800 g and the FID technology will significantly increase the fiducial mass of the detectors. In addition to this, the FID800 series will have two NTD sensors to have redundancy also in the heat measurement. Moreover, several surface treatments are under study to increase the surface event rejection.

Extensive γ calibrations of FID800 detectors have already been performed at LSM. The ionisation yield vs. recoil energy plot obtained is shown in figure 6 (right). The lack of events in the nuclear recoil band with a statistics equivalent to that shown for ID detectors in figure 2 (right) is proof of the improvement achieved.

Regarding the EDELWEISS-II setup, new upgrades in several parts (cryostat, shieldings, cabling, electronics) are foreseen to reduce the background and lower the energy threshold. The goal is to install 40 FID800 bolometers to reach a 3000 kg·d exposure in 2012 and a potential WIMP-nucleon cross-section sensitivity at the level of 5×10^{-9} pb.

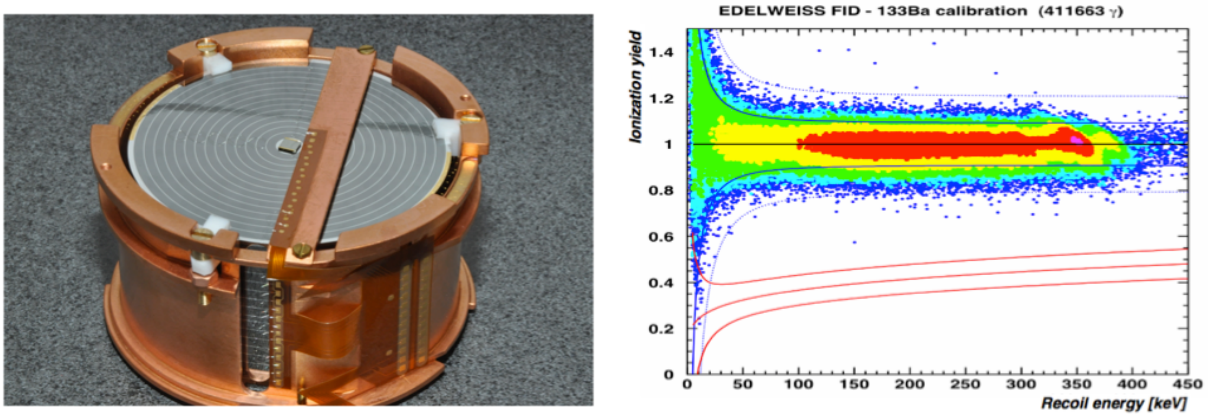

Figure 6: Left: FID800 detector. Right: Gamma calibration of a FID800. The lines superimposed represent the 90% (resp. 99.99%) rejection line for electron recoils in solid (resp. dashed) blue, and the 90%-acceptance nuclear recoil band (red).

The future European cryogenic experiment for direct detection of dark matter is the EURECA project, which intends to build an ultra-low background, ton-scale experiment combining different types of targets to reach cross-section values beyond 10^{-9} pb. The installation site would be an extension of the present Laboratoire Souterrain de Modane.

References

1. G. Bertone, D. Hooper and J. Silk, *Phys. Rep.* **405**, 279 (2005).

2. A. Broniatowski *et al*, *Phys. Lett.* B **681**, 305 (2009).
3. E. Armengaud *et al* (EDELWEISS collaboration), *Phys. Lett.* B **681**, 294 (2010).
4. O. Martineau *et al*, *Nucl. Instrum. Methods* A **530**, 426 (2004).
5. S. Yellin, *Phys. Rev.* D **664**, 032005 (2002).
6. C. Savage, K. Freese and P. Gondolo, *Phys. Rev.* D **74**, 043531 (2006).
7. M. C. Smith *et al*, *Mon. Not. Roy. Astron. Soc.* **379**, 755 (2007).
8. L. Roszkowsky, R. Ruiz de Autri and R. Trotta. JHEP **07**, 075 (2007).
9. J.D. Smith and N. Weiner, *Phys. Rev.* D **64**, 043502 (2001).
10. J. D. Lewin and P. F. Smith, *Astroparticle Physics* **6**, 87 (1996).
11. E. Armengaud *et al* (EDELWEISS collaboration), arXiv: **1103.4070**, (2011).

ASYMMETRIC DARK MATTER VIA LEPTOGENESIS AND DARK SPHALERONS

E. FERNANDEZ MARTINEZ
CERN Physics Department, Theory Division, CH-1211 Geneva 23, Switzerland

We discuss the generation of a dark matter asymmetry, via new sphaleron processes associated to an extra non-abelian gauge symmetry common to both the visible and the dark sectors. Such a theory can naturally produce an abundance of asymmetric dark matter which is of the same size as the lepton and baryon asymmetries, as suggested by the similar sizes of the observed baryonic and dark matter energy content, and provide a definite prediction for the mass of the dark matter particle. We discuss in detail a minimal realization in which the Standard Model is only extended by dark matter fermions which form "dark baryons" through an $SU(3)$ interaction, and a (broken) horizontal symmetry that induces the new sphalerons. The dark matter mass is predicted to be ~ 6 GeV, close to the region favored by DAMA and CoGeNT. Furthermore, a remnant of the horizontal symmetry should be broken at a lower scale and can also explain the Tevatron dimuon anomaly.

1 Introduction

We now know that about 73 % of the energy density of the Universe is in the form of dark energy and causes the accelerated expansion of the Universe while the remaining 27 % is composed of matter. Baryonic matter makes up only 5 %, while about five times as much is in the form of a non-luminous weakly interacting species, dubbed "Dark Matter" (DM). While this cosmological book-keeping is well developed [1], the particle nature of DM continues to be one of the most important open questions of particle physics. The most popular candidates for DM are weakly interacting massive particles (WIMPs). WIMPs arise naturally in theories, such as supersymmetry, which provide a solution to the hierarchy problem and include a "natural" DM candidate [2] once a discrete symmetry, *e.g.*, R-parity, is introduced, so that the least massive particle charged under the new symmetry is stable or very long lived [3]. This kind of DM comes with the WIMP miracle, *i.e.*, the correct interaction cross-section to thermally produce the density of DM in the early Universe [4]. The same is true for extra-dimensional models where KK parity ensures the stability of the DM candidates [5,6]. In this scenario, the closeness of the dark matter and baryonic energy densities is merely a coincidence, since they are produced by unrelated mechanisms. However, their similarity suggests that they originated from the same source. This is the case in models of asymmetric dark matter (ADM), a relatively old idea [7,8,9,10] which has recently received a rising interest. In ADM models, the DM is made up of charge-neutral Dirac fermions, just like baryonic matter and unlike the SUSY neutralino which is a Majorana fermion. Thus, the DM we see today is not generated thermally in the early Universe, but through a particle-antiparticle asymmetry in its production mechanism tied to the production of ordinary matter, giving rise to similar number densities for ordinary matter and DM. Therefore, models of ADM often predict DM masses of $\mathcal{O}(1)$ GeV. The phenomenology

of ADM is therefore quite different from that of a thermal DM relic. In particular, the prospects of indirect detection of DM in these models are suppressed, since the DM does not annihilate if only an asymmetric component is present. Nevertheless, there could still be some indirect effects, such as the effect of accreting ADM in the core of stars [11,12].

Here we will summarize the study presented in Ref. [13], where the asymmetries in both baryons and DM are created simultaneously by the same processes, as suggested by their similar abundances. First, a lepton asymmetry from the decay of heavy right-handed neutrinos, as in leptogenesis [14], is induced and then this lepton number is partially converted into both baryon and DM numbers through new sphaleron processes which we will dub dark sphalerons. In order to achieve this, we will assume that there is an additional non-abelian gauge symmetry group G, under which both the DM sector and the SM fermions are charged. For definiteness, we will consider an additional $SU(2)$ symmetry, but other symmetry groups could also fulfill our purposes. This extra gauge symmetry could arise from some unified theory at higher scales, although this is not required. Apart from the right-handed neutrinos and the extra gauge symmetry (spontaneously broken by scalar SM singlets), we only need to introduce new fermion fields X, that are singlets under the SM gauge group but couple to the new gauge symmetry, and will provide the DM candidates.

We include a QCD-like gauge interaction for the DM fermions that prevents their mixing with neutrinos, ensuring their stability without any ad hoc discrete symmetry. The similarity with the SM QCD interaction is also suggestive, given the similar masses of baryons and DM required to fit the observed energy densities. As the DM is essentially composed of dark baryons, it scatters with itself through the QCD-like gauge interaction. This self-interaction can be quite large and leads to almost spherical DM halos in galaxies, in somewhat better agreement with data, compared to WIMPs [15]. The current best limit on the interaction strength comes from observed ellipticities of DM halos of galaxies [16]. However, limits from colliding galaxy clusters, though slightly weaker, are thought to be more robust. These observations tell us that the QCD-like gauge interaction cannot be much stronger than that between baryons.

2 The Model

We extend the SM gauge group with an additional $SU(2)_H \times SU(3)_{DC}$, where the $SU(2)_H$ is a gauged flavour symmetry (horizontal symmetry) introduced to provide the dark sphalerons. We have chosen an $SU(2)_H$ for the simplicity of the discussion but, in principle, other non-abelian gauge symmetries encompassing all three fermion generations could be considered as well to address the flavor puzzle. The additional dark color (DC) group $SU(3)_{DC}$ is a color-like gauge interaction in the dark sector. The DM candidate in this model is a charge neutral $SU(3)_{DC}$ baryon.

The fermionic field content in the model is given in Tab. 1 with the corresponding charges. Notice that the choice of which fermion generations form the $SU(2)_H$ doublets is arbitrary and only affects the constraints that can be set with present data on flavour changing neutral current (FCNC) processes on the scale at which the symmetry is broken, but not the generation of the baryon and DM asymmetries. In Tab. 1 the $SU(2)_H$ doublets are composed from the fermions of the first two generations, for which the present bounds are strongest, but other possibilities will be briefly discussed in Sec. 3. Notice that the only fermion singlet is the right-handed neutrino, for which a Majorana mass is allowed and will be assumed in order to have a see-saw mechanism [17,18,19] for neutrino masses and a lepton number asymmetry in their decay that can seed baryon and DM asymmetry generation. Moreover, since the DM fermions are Dirac, we can define a global DM number X, that will be conserved at the Lagrangian level just as the baryon number B.

We further assume that the scalar sector is such that it can provide the required mass terms

Field	Y	L	H	C	DC
$L_{L\alpha}$ $(\nu_{\alpha L}, \ell_{\alpha L})$	$-1/2$	**2**	1	1	1
L_H (e_R, μ_R)	-1	1	**2**	1	1
τ_R	-1	1	1	1	1
$\nu_{\alpha R}$	0	1	1	1	1
$Q_{\alpha L}$ $(u_{\alpha L}, d_{\alpha L})$	1/6	**2**	1	**3**	1
Q_H^u (u_R, c_R)	2/3	1	**2**	**3**	1
Q_H^d (d_R, s_R)	$-1/3$	1	**2**	**3**	1
t_R	2/3	1	1	**3**	1
b_R	$-1/3$	1	1	**3**	1
X_H (x_R^1, x_R^2)	0	1	**2**	1	**3**
x_R^3, x_L^α	0	1	1	1	**3**

Table 1: Fermion field content for our illustrative model and the corresponding charge assignments. Whenever a field has an index α, the model contains three copies of this field. Note that the assignment of putting particular generations in the $SU(2)_H$ doublets is arbitrary.

for the fermions, either directly or through higher-dimensional operators, after the breaking of both, the electroweak and the $SU(2)_H$ symmetries. For instance, a minimal realization consists of an extra $SU(2)_H$ doublet, besides the SM Higgs, with Yukawa couplings given in terms of effective $d = 5$ operators such as

$$O_{d=5} = c_\alpha \overline{L_H} \Phi_H \Phi_L^\dagger L_{L\alpha}, \tag{1}$$

where $\Phi_{H,L}$ is the $SU(2)_{H,L}$ Higgs. After breaking of the $SU(2)_H$ symmetry, this reproduces the SM Yukawa terms. Just like the $d = 5$ Weinberg operator for neutrino masses, such operators can be generated in several different ways. The relevant phenomenological aspects of the model are independent of the scalar sector, so we shall not discuss it in more detail.

In this model, which is free of gauge anomalies, dark sphalerons satisfy $\Delta B/2 = \Delta X = \Delta L$, while the SM sphalerons satisfy $\Delta B = \Delta L$ as usual, resulting in an overall conservation of $B - X - L$ at scales where both sphalerons are active and conservation of both $B - L$ and X separately in the intermediate regime, where only the dark sphalerons are turned off. Thus, if an initial L asymmetry is produced in the decay of the heavy Majorana right-handed neutrinos, both kinds of sphalerons will try to erase it. However, since $B - X - L$ is exactly conserved by the combination of both sphalerons, net B and X asymmetries will be induced. In order to obtain the precise ratios between the final B, L and X asymmetries the equilibrium equations for the chemical potentials have to be written down. For the final DM to baryon ratio, we obtain

$$\frac{X}{B} \longrightarrow -\frac{11}{14}. \tag{2}$$

Therefore, in order to accommodate the observed values of Ω_X and Ω_B, we must have

$$m_{DM} \simeq m_B \frac{14\Omega_X}{11\Omega_B} = 5.94 \pm 0.42 \text{ GeV}, \tag{3}$$

including the errors of the WMAP7 measurements[1]. This value is in the low mass regime between 5 and 10 GeV favored by the claimed DM signals of the DAMA/LIBRA [20] and CoGeNT [21] collaborations. In particular it is strikingly close to the $\sim$ 7 GeV required to consistently describe both signals and is within the 99 % confidence level for the mass obtained in Ref. [22].

3 Constraints and phenomenological prospects

The first requisite that has to be met for successful generation of the baryon and dark matter asymmetries via leptogenesis, is that the $SU(2)_H$ sphalerons reach thermal equilibrium before the phase transition occurs and suppresses their rate. Thus, the sphaleron rate should be greater than the Hubble rate, leading to a lower bound on the $SU(2)_H$ coupling constant as a function of the temperature above which equilibrium should be achieved:

$$\alpha_H^4 = \left(\frac{g_H^2}{4\pi}\right)^4 \gtrsim 10\frac{T}{M_{Pl}}. \tag{4}$$

On the other hand, a lower bound on the strength of the $SU(2)_H$ interaction at lower energies can be derived from the requirement that the thermally produced symmetric component of dark matter is transfered to the SM fast enough. Indeed, as with any field which is kept in thermal equilibrium, the ADM candidate will have a thermal abundance of both particles and anti-particles in the early Universe. In order for the DM to become asymmetric, there must exist interactions through which this symmetric thermal abundance can be effectively annihilated once the ADM falls out of thermal equilibrium. In our example model, this is achieved by the strong $SU(3)_{DC}$ interactions connecting the symmetric part of the DM fields into dark $SU(3)_{DC}$ mesons which can decay to SM particles via $SU(2)_H$ gauge bosons. Analogously to pion decays in the SM, the dark meson decays will require a chirality flip of the SM fermions they decay into. To estimate the decay rate of the dark mesons we will assume that the dominant decay channel is either to two muons or a tau and a lighter lepton and thus proportional to the muon or tau mass.

In order not to disturb the standard history of the Universe, the $SU(3)_{DC}$ mesons (which constitute a large matter component) must decay sufficiently fast into SM fermions so that they are no longer present during big bang nucleosynthesis (BBN). Thus, the lifetime of the mesons must be significantly less than one second. Since the horizontal gauge bosons could also induce FCNC processes in the SM sector, bounds can be derived on the related effective $SU(2)_H$ Fermi constant $G_F^H = \sqrt{2}g_H^2/8M_H^2$. Naturally, such bounds are stronger if the two SM generations involved contain the lightest fermions of each type (*e.g.*, e and μ rather than μ and τ), since these FCNC have stronger experimental constraints. In Fig. 1 we show contours for the lower bound on G_F^H such that the lifetime of the dark mesons is smaller than 10^{-2} s as a function of the dark meson mass m_H and decay constant f_H. Notice that the values of these two quantities will depend on the strength of the $SU(3)_{DC}$ interaction as well as the masses of the dark matter fermions. In any case the "dark meson" masses should be heavier than ~ 100 MeV so that they decay before BBN but lighter than the "dark baryon" mass so that the symmetric component is stored mainly in mesons and not baryons and antibaryons, this corresponds to the maximum value of m_H depicted in Fig. 1. If the dominant decay channel is to a muon pair (left panel), then the bound is typically of $\mathcal{O}(10^{-10})$ GeV^{-2}, while the bounds are about an order of magnitude weaker for decays into a tau and a lighter lepton (right panel). In this last case the decay can only happen if $m_H > m_\tau$ which corresponds to the horizontal asymptote.

On the other hand, the strongest constraint on G_F^H from FCNC stems from the bound on the decay $K \to e\mu$ and implies that $G_F^H < 3.6 \cdot 10^{-12}$ GeV^{-2}, which would cause tension with the lower bounds derived in Fig. 1. However, this constraint does not apply if the horizontal symmetry is broken in stages. For example, this may be achieved by first breaking the $SU(2)_H$ to $U(1)_H$ by a real scalar triplet acquiring a vacuum expectation value along the σ_3 direction and giving large masses to the flavor changing gauge bosons while leaving the flavor conserving one massless. This procedure is similar to Georgi and Glashow's model of electroweak interactions, which did not include neutral currents [23]. The remaining flavor diagonal $U(1)_H$ can be subsequently broken at a scale low enough to obtain interactions of the strength required for

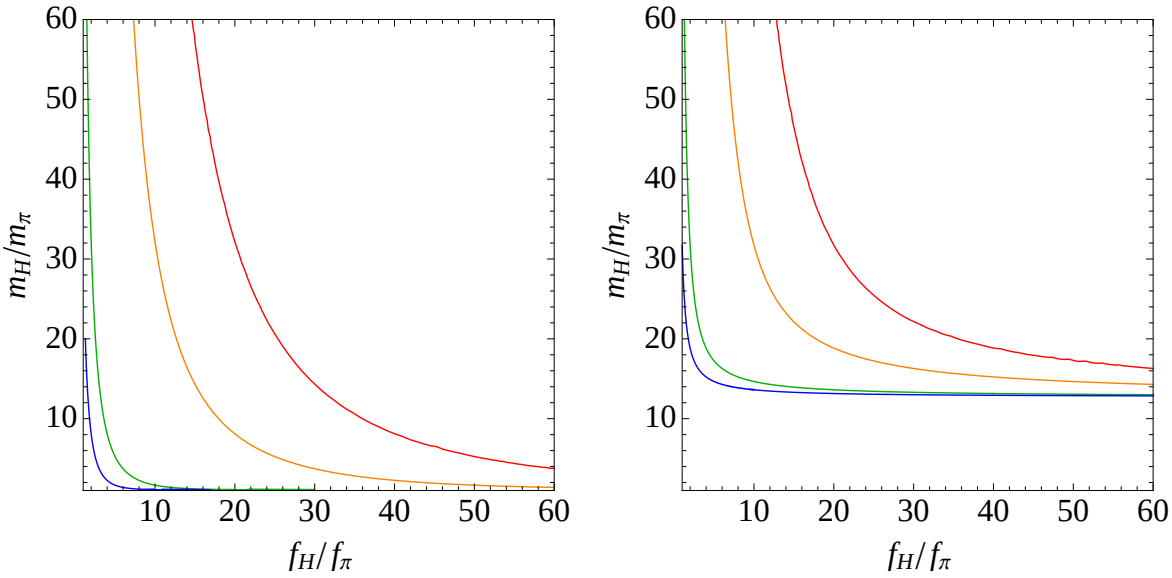

Figure 1: Contours for the lower bound on G_F^H such that the lifetime of the dark mesons is smaller than 10^{-2} s as a function of the dark meson mass m_H and decay constant f_H. Left panel for a dominant decay into muons depicts the contours for $G_F^H > 10^{-9}$, $5 \cdot 10^{-10}$, 10^{-10} GeV^{-2} and $5 \cdot 10^{-11}$ from the bottom of the plot to the top. Right panel for a dominant decay into a tau and a lighter lepton depicts the contours for $G_F^H > 10^{-10}$, $5 \cdot 10^{-11}$, 10^{-11} and $5 \cdot 10^{-12}$ GeV^{-2} from the bottom of the plot to the top.

the dark mesons to decay into two muons. In this case the dominant decay channel of the dark mesons could be to two muons and the constraints on the left-handed panel of Fig. 1 would apply. Reconciling this scenario with the lower bound on g_H from Eq. (4) is easy since the scale of the $SU(2)_H$ symmetry breaking is unrelated to the mass of the flavour-conserving Z', for instance with $g_H = 0.5$ the sphalerons would reach thermal equilibrium at $T \lesssim 10^{11}$ GeV and the first stage of symmetry breaking, which would freeze out the sphalerons, should occur above $\Lambda \gtrsim 10^5$ GeV. In this scenario, which would be mainly flavour conserving at low energies, sizable interactions between the visible and dark sectors via a relatively light Z' are allowed. Thus, a positive signal could be induced in direct DM detection searches and the extra Z' boson can be searched for at the LHC. In principle the interaction between DM and the visible sector can be large enough so as to accommodate the DAMA and CoGeNT, that require $G_F^H \sim 10^{-7}$GeV^{-2} [22]. The results from LEP-II suggest that, if the Z' at low energies couples with full strength to electrons and other charged leptons then $G_F^H < 5.14 \cdot 10^{-8}$ GeV^{-2} [24], therefore, the coupling to electrons via the $SU(2)_H$ has to be subleading in order to evade this tension.

An interesting alternative would be to couple the two heaviest SM fermion generations to the $SU(2)_H$ and having the scalar triplet acquire its vev along the σ_1 direction. In this case the residual $U(1)_H$ would still induce FCNC in the $t-c$, $b-s$ and $\tau-\mu$ sectors but the constraints are in this case weaker and allow for sufficiently fast dark meson decays. Indeed, such a $U(1)_H$ with strength $G_F^H = 7 \cdot 10^{-11}$ GeV^{-2} is allowed by present data and would contribute to CP violation in the B_s system, accommodating the observed dimuon anomaly at Tevatron [25]. In this case the dark mesons would decay into a tau and a muon and the constraints depicted in the right panel of Fig. 1 would apply. In this scenario, it is also possible to identify the scale of the $SU(2)_H$ symmetry breaking with the mass of the flavour-changing Z' contributing to B_s mixing. In combination with Eq. (4) this would imply that $g_H \gtrsim 0.06$ and $\Lambda \gtrsim 2.7$ TeV, for the dark sphalerons to enter in thermal equilibrium at $T \gtrsim \Lambda$. In this case, direct detection experiments and production at colliders would be much more challenging, given the suppressed interaction between the dark and visible sectors. On the other hand, observable new contributions to FCNC in B physics would be expected.

References

1. E. Komatsu *et al.* [WMAP Collaboration], Astrophys. J. Suppl. **192** (2011) 18 [arXiv:1001.4538 []].
2. G. Jungman, M. Kamionkowski and K. Griest, Phys. Rept. **267** (1996) 195 [arXiv:hep-ph/9506380].
3. R. Barbier *et al.*, Phys. Rept. **420** (2005) 1 [arXiv:hep-ph/0406039].
4. E. W. Kolb and M. S. Turner, Front. Phys. **69**, 1 (1990).
5. G. Servant and T. M. P. Tait, Nucl. Phys. B **650**, 391 (2003) [arXiv:hep-ph/0206071].
6. H. C. Cheng, J. L. Feng and K. T. Matchev, Phys. Rev. Lett. **89**, 211301 (2002) [arXiv:hep-ph/0207125].
7. S. Nussinov, Phys. Lett. B **165**, 55 (1985).
8. S. M. Barr, R. S. Chivukula and E. Farhi, Phys. Lett. B **241**, 387 (1990).
9. S. M. Barr, Phys. Rev. D **44**, 3062 (1991).
10. D. B. Kaplan, Phys. Rev. Lett. **68**, 741 (1992).
11. M. T. Frandsen and S. Sarkar, Phys. Rev. Lett. **105**, 011301 (2010) [arXiv:1003.4505 []].
12. M. Taoso, F. Iocco, G. Meynet, G. Bertone and P. Eggenberger, Phys. Rev. D **82**, 083509 (2010) [arXiv:1005.5711 []].
13. M. Blennow, B. Dasgupta, E. Fernandez-Martinez and N. Rius, JHEP **1103** (2011) 014 [arXiv:1009.3159 [hep-ph]].
14. M. Fukugita and T. Yanagida, Phys. Lett. B **174**, 45 (1986).
15. D. N. Spergel and P. J. Steinhardt, Phys. Rev. Lett. **84**, 3760 (2000) [arXiv:astro-ph/9909386].
16. M. Taoso, G. Bertone and A. Masiero, JCAP **0803**, 022 (2008) [arXiv:0711.4996 []].
17. P. Minkowski, Phys. Lett. B **67**, 421 (1977).
18. M. Gell-Mann, P. Ramond and R. Slansky,
19. R. N. Mohapatra and G. Senjanovic, Phys. Rev. Lett. **44**, 912 (1980).
20. R. Bernabei *et al.*, Eur. Phys. J. C **67**, 39 (2010) [arXiv:1002.1028 []].
21. C. E. Aalseth *et al.* [CoGeNT collaboration], Phys. Rev. Lett. **106**, 131301 (2011) [arXiv:1002.4703 []].
22. D. Hooper, J. I. Collar, J. Hall and D. McKinsey, Phys. Rev. D **82**, 123509 (2010) [arXiv:1007.1005 []].
23. H. Georgi and S. L. Glashow, Phys. Rev. Lett. **28**, 1494 (1972).
24. [LEP Collaboration and ALEPH Collaboration and DELPHI Collaboration and], arXiv:hep-ex/0312023.
25. S. C. Park, J. Shu, K. Wang and T. T. Yanagida, Phys. Rev. D **82**, 114003 (2010) [arXiv:1008.4445 []].

Probing the dark energy nature with type Ia supernovae : cosmological constraints from the Supernova Legacy Survey first 3-years

D. Hardin
(on behalf of the SNLS experiment)
LPNHE, Université Pierre et Marie Curie, Université Paris Diderot, CNRS-IN2P3, 4 place Jussieu, 75252 Paris Cedex 05, France

We present the recent cosmology results from the Supernova Legacy Survey (SNLS). Complementing the 242 high redshift type Ia supernovae sample from the first 3 years of the Supernova Legacy Survey with other mostly nearby supernovae samples, we measure a dark energy equation of state parameter w parameter consistent with a cosmological constant. The sytematic uncertainties we fully take into account are approximately equal to the statistical uncertainties. Combining the supernovae data with WMAP7 CMB and SDSS BAO measurements, we obtain a most precise measurement of the dark energy equation of state $w = -1.068$ with a precision of 0.08.

1 Introduction

The first evidence for the universe expansion acceleration was provided at the very end of last century [1,2a]. By using a few dozens of type Ia supernovae as standardized candles, discovered and monitored with CCDs camera on 4-m class telescope, the Supernova Cosmology Project and the High Z Team found that the universe expansion had stop decelerating 5 Gyr ago.

Since then, other cosmological probes — the cosmic microwave background (CMB) temperature fluctuations, the baryon acoustic oscillations (BAO) imprinted in the galaxies spatial distribution, weak gravitational lensing mapping dark matter clustering etc. — have provided new evidence for the presence of a dark energy component opposing gravity and accounting for 75% of the total universe energy density. The physical origin of cosmic acceleration remains though a deep mystery.

In the last decade, new generation supernova surveys have brought improvements in the quantity and the homogeneity of the supernova sample. The supernovae evidence for acceleration has been strengthed. Combining the different cosmological probes, it is now possible to adress the question of the dark energy nature, by measuring its equation of state parameter : $w = p_X/\rho_X$.

With the substantial increase up to ~ 1000 SNeIa distance measurements and the consequent reduction of statistical errors, sytematics errors have become the limiting factor and as such the key issue.

The Supernovae Legacy Survey is a 5 year program which goal is to measure the dark energy equation equation of state w in combination with other measurements to better than 0.10, paying special attention to include and limit thoroughly any systematics effects.

[a] See e.g. (Frieman, 2009)[3] for a review.

2 Expansion history and the universe content

In an expanding isotropic and homogeneous universe, distances between galaxies at rest scale as $d \propto a(t)$. In such an expanding universe, light emitted by one observer at time t and observed by another at later time t_0 is observed to be redshifted, by a factor $1 + z = \lambda(t_0)/\lambda(t) = a(t_0)/a(t)$, directly related to the scale factor $a(t)$. The expansion dynamics is governed through the Einstein equations by the universe energy content. Matter, with a present day reduced density $\Omega_M = \rho_M(t_0)/\rho_{crit}(t_0)$ – the critical density corresponds to a flat geometry for the universe — decelerates the universe expansion. If the expansion is accelerating, one of the simplest explanation is the existence of a second energy component, a perfect fluid X, with a repulsive equation of state $w = p_X/\rho_X < -1/3$ and a corresponding reduced density Ω_X : the dark energy. Mapping the expansion history $a(t)$ thus yields measurements of the cosmological parameters Ω_M, Ω_X, and w.

The nature of the dark energy remains enigmatic. It could be a constant energy component, such as the cosmological constant Λ originally postulated by Einstein, or, formally equivalent, the vacuum energy of particle physics, in these cases $w = -1$. Another possibility is that the dark energy be a dynamical fluid, whith a time variating equation of state $w(z)$ – or $w(a)$. An alternative explanation would require to modify the General Relativity at cosmologically large scales, or invoke inhomogeneities inducing apparent acceleration (the "back-reaction").

3 Type Ia supernovae : standard candles as cosmological probes

For an object of intrinsic luminosity L, the flux f measured by the observer defines the luminosity distance in term of the usual inverse square law : $f = L/(4\pi d_L^2)$. The dependency of d_L on the redshift z (the Hubble diagram) is related to the integrated expansion history, and as such to the energy content of the universe and the aforementionned cosmological parameters :

$$d_L \equiv \sqrt{f/4\pi L} = cz/H_0 \times \mathcal{D}(z; \Omega_M, \Omega_X, w) \tag{1}$$

As one measure fluxes and not luminosities, the use of standard candles is of particular importance. With these objects of fixed luminosity L, one can measure relative distances. and thus be able to constrain the cosmological parameters without having to know the luminosity L, nor the Hubble constant H_0 values.

Type Ia supernovae (SNe) are cosmic explosions that display an impressive homogeneity. These rare (1 per galaxy per millenium) and bright events, observable at cosmological distances, are thought to arise from the explosion of a white dwarf accreting matter from a companion and reaching the stability Chandrasekhar mass limit. The companion could be an evolved main sequence star, a red giant or a white dwarf. They are easily identified using spectroscopy, as they exhibit strong absorption features at the time of their peak luminosity.

With a 40% dispersion of their peak luminosity measured in the Johnson B band, they qualify as standard candles. But they do however exhibit a correlation bewteen their peak luminosity and the time evolution behaviour of their lightcurve and also with their restframe colors. By taking into account these empirical relations — acknowledged as the brighter-slower and the brighter-bluer relations —, the observed dispersion is reduced to ∼10%. This results in a dispersion of ∼5% for the estimated distance : they are standardized candles.

In order to estimate the cosmological parameters, we will be comparing the restframe peak fluxes (e.g. in the restframe Johnson B band) of SNe Ia exploding at different redshifts (Eq. 1). This requires to observe them in different filters, which intercalibration must then be precisely known. To evaluate the restframe Johnson B band value at peak, one needs to interpolate the fluxes measurement between several different filters and also at different dates : for this we

use a time dependent spectrophometric model of the SN Ia emission, $\phi(\lambda, t)$, that we construct empirically using spectrophometric data of nearby and distant SNe Ia.

The relationship between distance d, flux f and luminosity L translates simply in the logarithmic scales of the magnitudes, involving the corresponding quantities of distance modulus μ, apparent magnitude m and absolute magnitude $\mathcal{M}$:

$$\mu = m_B^\star - \mathcal{M}, \quad \mathcal{M} = M_B - \alpha \times shape + \beta \times color \tag{2}$$

For each SN are estimated the three quantities $m_B^\star$, corresponding to the peak B flux, the *shape* of its lightcurve, and its *color* at peak. The absolute magnitude of the SN is parametrized so that M_B (fully degenerated with H_0[b]) corresponds to the luminosity of the (*shape*=0, *color*=0) standard SN Ia, and α and β empirically account for the linear corrections corresponding respectively to the brighter-slower and the brighter-bluer relations. The cosmological parameters are evaluated through a χ^2 fit where μ is compared to its predicted value $\mu_{\rm cosmo}(z; \vec{\theta})$, $\vec{\theta}$ beeing the parameters describing the cosmological model. M_B, α and β are fitted on the Hubble diagram along with the cosmological parameters.

4 The Supernova Legacy Survey

The Supernova Legacy Survey experimental setup and strategy have been designed so as to obtain sufficient quality data and to meet the necessary requirements to control the systematics.

Using the 1 square degree imager Megacam[4] mounted on the 3.6-m Canadian-France-Hawai Telescope at Mauna Kea (Hawaii), we obtain a survey deep enough to reduce the Malmquist bias that affects all flux limited surveys[6].

Both supernovae discovery and photometry are carried out with one instrument. We can thus devoid all the necessary time to the thorough understanding and the calibration of the instrument[5].

SNLS is a rolling search i.e. we repeat observations of the same 4 fields, enabling the follow-up of the already discovered SN and the detection of newly exploded SN at the same time. It is thus possible to go back in our image data base to recover early, pre-discovery SN photometry. This strategy permits to obtain well sampled lightcurve so as to measure precisely of $m_B^\star$ and the lightcurve *shape*.

The four g r i z filters make it possible to measure the B restframe flux from z=0.1 to z=1., and also estimate precisely the restframe U-B and B-V colors of the SNe.

By observing 40 nights a year during 5 years (the survey ended in August, 2008), we obtained $\sim$ 450 SNe Ia. All were spectroscopically identified on 10-m class telescopes[7,9,10,11], which allows to limit the non Ia contamination of the sample.

Finally, deep SN-free images stacks were built, to estimate the SNe host galaxy colors, enabling to caracterize the SN environment.

5 SNLS-3 years data Analysis

The constraints and systematic uncertainties from the SNLS-3 data are fully detailed in Conley et al.[12]. We present here the SN sample, and some of the different steps involved in the data analysis.

SNLS is mainly a European and Canadian project : all the analysis steps were performed with independent pipelines on each side of the atlantic ocean. Calibration, the spectro-photometric model have been improved since the SNLS-1 year results. We also reckon with the host galaxy nature influence.

[b] We fix $H_0 = 70$ km/s/Mpc.

Finally, when estimating the cosmological parameters, we fully take into account the sytematics uncertainties as well as the statistical ones by incorporating them in the covariance matrix that enter the χ^2 minimization procedure. Publishing this full covariance matrix makes it possible to other authors to exploit the SN data without loss of information.

5.1 The supernovae sample

To obtain precise cosmological measurement requires a long enough lever-arm in redshift in the Hubble diagram (Eq. 1). We must then add to the SNLS sample complementary supernovae sample coming from external surveys.

The supernovae sample consists of 472 SNe Ia : 123 nearby supernovae, 93 at intermediate redshift form the Sloan Digitized Sky Survey (SDSS) supernovae search, 242 from SNLS and 14 Hubble Space Telescope (HST) supernovae.

The nearby sample at $z \sim 0$ are gathered from various sources, mainly the Calan/Tololo[13], the CfAI-II-III[14] and the CSP[15] searches. The photometry of one third of this sample is expressed in the Landolt system, to which the Megacam magnitude system must be tied : this cross-calibration requirement induces the main systematic effect in this analysis.

At $z > 1$, ground observations are difficult, and the HST sample of 14 SNe Ia at z=0.7-1.4 complements the high redshift part of the Hubble diagram.

Finally, we add 146 SNe Ia at intermediate redshift $z < 0.4$ from the SDSS Supernova Survey. This component of the SDSS-II survey carried out repeat imaging of a 300 square degree southern equatorial stripe using a dedicated 2.5-meter telescope in drifts scan mode at Apache Point Observatory, New Mexico. They discovered and measured about 500 spectroscopically confirmed SNe Ia. The SDSS filter system has been thouroughly studied and is very similar to the Megacam system : as a consequence the intercalibration is not as problematic as with the nearby sample.

5.2 Calibration

The calibration procedure of the SNLS data achieved an accuracy of a 1% precision[5]. It consists in two steps : the observations are first standardized onto some magnitude system, using a catalog of standard stars of known magnitudes. Then the standard system magnitudes are converted into absolute fluxes : for this we rely on a reference star, of known magnitudes and spectral energy density (SED). Both SNLS and SDSS survey selected a red reference star measured by the HST CALSPEC[16] calibration program.

To achieve the required precision, the spatial non-uniformities of the imager were mapped using dithered observation of dense stellar fields. Because part of the external low-z SNe sample is calibrated against the Landolt UBVRI system, the Megacam griz system has to be anchored to the Landolt system. The uncertainties in the Landolt magnitudes of our reference star BD 17° 4708 are the largest single identified sytematic uncertainty in our current analysis.

5.3 The spectro-photometric model : SALT2 & SIFTO

To obtain for each SN the peak restframe B band magnitude and its lightcurve *shape* and *color*, we make use of two independent lightcurve fitters, SIFTO[17] and SALT2[18]. The SALT2 model for the rest-frame flux parametrization may be written as :

$$\phi(\lambda, t) = X_0 \times [M_0(\lambda, t) + X_1 \times M_1(\lambda, t)] \exp(C\, CL(\lambda))$$

M_0 is the mean spectrum and the corresponding parameter X_0 is the flux normalisation. M_1 describes the main variability of the SNe Ia and happens to naturally reproduce a brighter-slower

relation : X_1 is thus equivallent to a lightcurve shape parameter. C corresponds by construction to a color, and the color law CL encodes the corresponding variation of the model.

M_0, M_1 and CL are computed using a training sample of nearby and SNLS SNe Ia lightcurves and spectra. The SNe distances are not used, which makes it possible to use nearby as well as distant SNe for the training. As the U band data from nearby SNe turned out to be problematic, we used u' measurement of nearby data when available, and we especially rely on distant SNe g optical data, which sample the UV restframe at a redshift of $z \sim 0.4$.

No assumption were made on the color law CL wavelength dependency nor its cause — wether it be due to intrinsic SNe Ia variation or to the reddening by dust somewhere along the line of sight : in the intergalactic medium, the host galaxy or a dust shell around the SN. As there is no a-priori knowledge of the dust properties, or its putative evolution with environment and/or redshift, no prior was set on the distribution of the SNe Ia C (*color*) parameter.

The color law is mathematically equivalent to an extinction law, but it does differ in the UV part from the dust extinction law as measured in the Milky Way Galaxy[19], and also the selective ratio corresponding to $\beta \sim 2.5-3$ in Eq. 2 is smaller than the MW value $R_B \sim 4$. This differences can be interpreted either as an unusual extinction occuring in the SN environnement, or an intrinsic color variation dominating the extinction effects.

In a nutshell, we make no assumption and let the SNe Ia data decide : on the range of their *color* value, on the selective ratio β value, and on the color law CL wavelength dependency.

SIFTO model consists of a SED sequence, which is time dilated by a stretch factor depending on the wavelentgh. It does not contain an explicit color variation law but a linear color relation tailing the *color*=B-V to the U-B color, and the lightcurve *shape*.

Comparing the two fitters results permits to evaluate the uncertainties associated with the different choices involved in their design. As they perform equally well, we use the average of the two, and propagate the differences as systematic uncertainties.

5.4 Host galaxy nature influence

To address the question whether M_B, α and β in Eq. 2 are universal parameters, and whether there is any dependence on the SN environnement, we undertook a photometric study of the SN host galaxies. Their ugriz fluxes were measured on deep stacked images free of SN light, and supplementary data from the WIRDS survey[20] in the IR part was added. The photometric data are fitted by templates spectral energy densities, using the redshift information from the SN : this permits to derive the restframe colors of the galaxy, and its intrinsic luminosity. Using SEDs computed with the population synthesis model PEGASE.2[21], one can recover the caracteristics of the synthetic model galaxy, such as its present star formation rate (SFR), and its stellar mass content.

The host galaxies properties are known[22,23] to correlate with the SNe *shape* parameter : SNe Ia in red/high SFR/ low mass/faint galaxies are slower, and as a consequence, brighter. This could result from different evolutionary pathes leading to the explosion of the parent white dwarf[24,25].

Although in massive galaxies the mean SN Ia is fainter, it has been recently brought to evidence[26,27,28] that the standard (*shape*=0, *color*=0) SN Ia is in fact there slightly brighter, at a $4-\sigma$ significance : this is a subtle effect - 0.08 mag, or 8% - smaller than the *shape* or *color* corrections.

We take this dependency into account by splitting the sample at $M = 10^{10} M_\odot$ between low and high mass galaxies, and using two different M_B values for each sub-sample. This leads to a significative improvement in the cosmological fits (at a $\sim 4\sigma$ level) and also to a shift in the measured cosmology : for a flat universe, Ω_M value is shifted by an amount comparable to the statistical precision.

5.5 *Including the systematics*

The χ^2 minimization procedure involves the residuals computed for each SN i : $r_i = \mu_i - \mu_{\rm cosmology}(z_i;\vec{\theta})$ and the associated covariance matrix $\mathbf{C}$: $\chi^2 = {}^t r \mathbf{C}^{-1} r$. The covariance matrix $\mathbf{C}$ can be splitted in 3 terms : $\mathbf{C} = \mathbf{D}_{\rm stat} + \mathbf{C}_{\rm stat} + \mathbf{C}_{\rm sys}$.

$\mathbf{D}_{\rm stat}$ is a diagonal part dealing with purely statistical uncertainties, which includes the errors on the light curve parameters of each SN and on its redshift value, plus several additional terms: $\sigma_{\rm int}$ to account for the intrinsic scatter of SNe Ia — $\sigma_{\rm int} = 0.07$ mag (or equivalently 7%) for the SNLS sample; $\sigma_{\rm lensing} = 0.055 \times z$ to account for the gravitational lensing by foreground galaxies[29] ; $\sigma_{\rm host}$ to account for the mis-classification of the SN host due to the host colors statistical errors.

As all the SNe shares the same spectro-photometric model used to estimate ($m_B^\star$, *shape*,*color*), the statistical covariance is not diagonal and $\mathbf{C}_{\rm stat} \neq 0$.

Finally, the $\mathbf{C}_{\rm syst}$ part accounts for the systematic errors affecting the SN measurements i.e. the uncertainties that will not be reduced by increasing the sample size. For example, the uncertainty on one of the calibration zero point will affect for each SN the estimation of ($m_B^\star$, *color*), not only through the value of this SN photometric points, but also through the model, which is trained on many other SNe photometry. The most important term entering $\mathbf{C}_{\rm syst}$, in terms of consequence on the cosmological parameters systematic uncertainties, is by far the calibration, especially the intercalibration of the different SNe sample.

6 SNLS-3 years cosmological results

The SNLS-3 cosmological results are presented in Conley et al.[12] and Sullivan et al.[30]. Including all identified systematic effects in the $\Omega_M - w$ plane assuming a flat universe is shown on Fig.1 as the blue contours. They are consistent with a cosmological constant. Including the systematic nearly double the size of the uncertainty-"ellipse". Excluding the calibration sytematic reduces this increase down to $\sim$10 %.

The degeneracy along the Ω_M axis is lifted when constraints from other cosmological probes are added. The measurements of the CMB temperature fluctuation yields estimation for[31] : the acoustic scale $l_A = \pi(1+z_*)D_A(z_*)/r_s(z_*)$; the shift parameter R ; the redshift at decoupling z_* ; The imprint of the Baryon Acoustic Oscillation (BAO) in the galaxies correlation function at a given redshift z yields a measurement of $r_s(z_d)/D_V(z)$ where $r_s(z_d)$ is the comoving sound horizon at the baryon drag epoch and $D_V(z)$ is the spherical average of the angular-diameter distance and the radial proper distance[32,33].

Combining results from the Wilkinson Microwave Anisotropy Probe 7-years (WMAP7)[34] and from the SDSSS Data Release 7 BAO measurement[35] yield the "green" contours shown on Fig.1. Combining both contours which are almost orthogonal yields $w = -1.068^{+0.080}_{-0.082}$ — this result is nearly equivalent to fix $\Omega_M = 0.27$ for the SNe Ia only contour.

7 Conclusion

Combining the SNLS-3 SNe Ia sample with measurements from observations of the CMB and of large scale structures, we obtain a most precise measurement of the dark energy equation of state consistent whith a cosmological constant.

The statistical uncertainties on the cosmological parameters are now exceeded by the systematics, although the situation could change were the major contribution of the calibration to the systematics to be reduced.

As the SDSS filter system is similar to the Megacam system, and as low redshift sample observed in a very similar way become available, we will in the future take full advantage of the

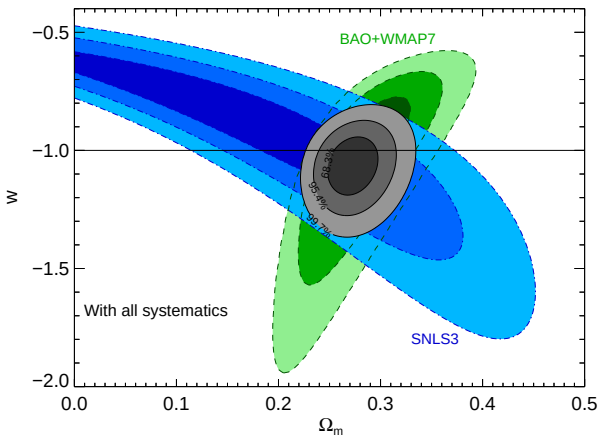

Figure 1: Confidence contours in the plane $\Omega_M - w$ obtained when fitting with the SNe Ia -only fit (in blue). A flat cosmology is assumed. Taking into account the systematics nearly double the size of the contour. The degeneracy along the Ω_M axis is lifted when adding the SDSS BAO and WMAP7 CMB constraints (in green).

inter-calibration improvements possibilities.

In the near future, the SkyMapper[36] project will provide nearby SNe Ia at $z \sim 0.05$ discovered and observed with a similar technique than SNLS. Next generation surveys either ground-based such as the Large Synodic Survey Telescope (LSST) project or space-born such as the Wide Field Infrared Survey Telescope (WFIRST) or the EUCLID mission could bring thousands of distant SNe Ia up to $z \sim 1.5$. Providing an adapted strategy , they could adress the question of a time variating equation of state for the dark energy, $w(a) = w_0 + (1-a)w_a$[37].

References

1. A. G. Riess et al., *Astronomical Journal* **116**, 1009 (1998)
2. S. Perlmutter et al., *Astrophysical Journal* **517**, 565 (1999)
3. J. Frieman, "Lectures on Dark Energy and Cosmic Acceleration", *arXiv:0904.1832*
4. O. Boulade et al., *Instrument Design and Performance for Optical/Infrared Ground-based Telescopes, ed M.Iye & A.F.M. Moorwood, Proc SPIE, 4841, 72*
5. N. Regnault et al., *Astronomy and Astrophysics* **506**, 999 (2009)
6. C. Perrett et al., *Astronomical Journal* **140**, 518 (2010)
7. D.A. Howell, et al., *Astrophysical Journal* **634**, 1190 (2005)
8. T.J. Bronder, et al., *Astronomy and Astrophysics* **477**, 717 (2008)
9. R.S. Ellis, et al., *Astrophysical Journal* **674**, 51 (2008)
10. C. Balland et al., *Astrophysical Journal* **507**, 85 (2009)
11. E. Walker et al., *Monthly Notices of the Royal Atronomical Society* **410**, 1262 (2011)
12. A. Conley et al., *The Astrophysical Journal Supplement* **192**, 1 (2011)
13. M. Hamuy et al., *Astronomical Journal* **112**, 2408 (1996)
14. M. Hicken et al., *Astrophysical Journal* **700**, 331 (2009)
15. C. Contreras et al., *Astronomical Journal* **139**, 519 (2010)
16. Bohlin, R.C. *Astronomical Journal* **111**, 1743 (1996)
17. A. Conley et al., *Astronomical Journal* **681**, 482 (2008)
18. J. Guy et al., *Astronomy and Astrophysics* **466**, 11 (2007)
19. J.A. Cardelli et al., *Astrophysical Journal* **345**, 245 (1989)
20. R. Bielby et al., *in preparation*
21. D. Le Borgne et al., *Astronomy and Astrophysics* **386**, 446 (2002)

22. M. Hamuy et al., *Astronomical Journal* **120**, 1479 (2000)
23. M. Sullivan et al., *Astrophysical Journal* **648**, 868 (2006)
24. E. Scannapieco et al., *Astronomical Journal* **629**, L85 (2005)
25. F. Manucci et al., *Monthly Notices of the Royal Atronomical Society* **370**, 773 (2006)
26. P.L. Kelly et al., *Astrophysical Journal* **715**, 743 (2010)
27. H. Lampeitl et al., *Astrophysical Journal* **722**, 766 (2010)
28. M. Sullivan et al., *Monthly Notices of the Royal Atronomical Society* **406**, 782 (2010)
29. M. Jönsson et al., *Monthly Notices of the Royal Atronomical Society* **405**, 535 (2010)
30. M. Sullivan et al., submitted
31. E. Komatsu et al., *The Astrophysical Journal Supplement* **180**, 330 (2009)
32. D. Eisentein et al., *Astrophysical Journal* **633**, 560 (2005)
33. C. Blake et al., *arXiv:1105.2862*
34. E. Komatsu et al., *The Astrophysical Journal Supplement* **192**, 18 (2011)
35. W.J. Percival et al., *Monthly Notices of the Royal Atronomical Society* **401**, 2148 (2010)
36. S.C. Keller et al., *Publications of the Astronomical Society of Australia* **24**, 1 (2007).
37. P. Astier et al., *Astronomy and Astrophysics* **525**, 7 (2011)

SEARCH FOR B-MODES IN CMB POLARIZATION – QUIET AND OTHER EXPERIMENTS

O. TAJIMA for the QUIET collaboration
High Energy Accelerator Research Organization (KEK), Institute for Particle and Nuclear Science, 1-1 Oho, Tsukuba, Ibaraki 305-0811, Japan

The inflationary universe is a very interesting subject for particle physics as well as for cosmology since its energy scale corresponds to the GUT scale. It is possible to reveal aspects of this early time with precise measurements of Cosmic Microwave Background (CMB) polarization. Degree-scale asymmetric (odd-parity) patterns in the CMB polarization map, or "B-modes", are considered a "smoking gun" signature of inflation. Many experiments are ongoing or planned towards the detection of B-modes. We review the experimental approach and status of B-mode searches, focusing on the QUIET experiment, which has observed CMB polarization from the ground.

1 Introduction

How did our Universe begin? This is a fundamental question for human beings. Cosmological observations have provided compelling evidence for the Big Bang; however, a very rapid expansion at the earliest times was proposed in order to account for the apparent fine-tuning of the matter-energy density. In this inflationary scenario, the rapid expansion occurred around 10^{-36} sec after the Big Bang.

Primordial gravitational waves are a generic prediction of inflation. The most promising method for detecting the primordial gravitational waves is the detection of "B-modes" in the CMB polarization [1]. The CMB is polarized because it was scattered by electrons until the electrons were captured by protons, i.e. at recombination, some 380,000 years after the Big Bang. After that period, most of the CMB photons have not been scattered. Therefore, the measured CMB map on the sky today contains information about the last scattering surface. The CMB scalar perturbation ($\sim$0.001%) only creates symmetric (even-parity) patterns in the CMB polarization map which are called E-modes. Asymmetric (odd-parity) pattern, B-modes, in the CMB polarization due to primordial gravitational waves are expected to peak at angular scales of around a few degrees. Detection of a B-mode component of the CMB polarization on these scales would be a strong signature of inflation.

The B-mode intensity is represented by a parameter called the tensor(T)-to-scalar(S) ratio "$r \equiv T/S$", which is the intensity of the primordial gravitational waves compared with the intensity of the scalar perturbations. Therefore, it is related to the energy scale of inflation approximately by $(r/0.01)^{1/4} \times 10^{16}$ GeV (with the slow-roll model approximation). The simplest models predict $r = 0.01 \sim 0.1$, which corresponds to GUT scale, i.e. $\approx 10^{16}$ GeV. Therefore, inflation is very important to ultra high-energy physics in addition to cosmology. At present, many B-mode experiments are ongoing or planned; QUIET [2] is one of the experiments searching for B-modes from the ground.

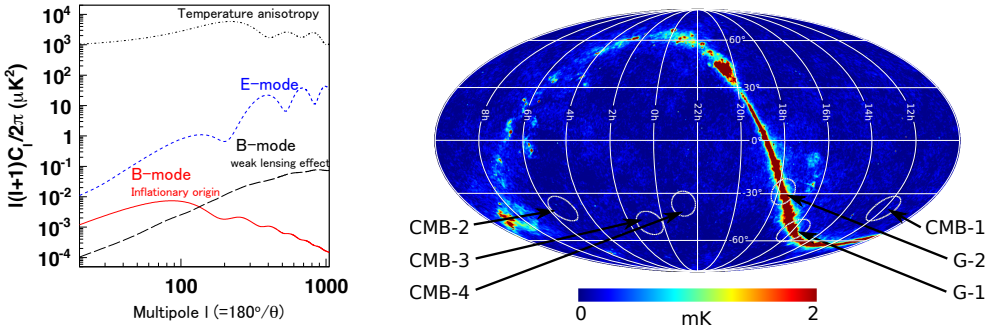

Figure 1: [Left panel] Simulated CMB polarization power spectra for B-modes and E-modes, We assume $r = 0.1$ for the B-modes of inflationary origin. The power spectrum of the temperature anisotropy, which is the non-polarized component, is also plotted for comparison. [Right panel] Observing regions of QUIET in equatorial coordinates, superimposed on a WMAP 7-year temperature map at Q-band. The diameter of each region is $\approx 20^\circ$ which is large enough for the B-mode detection because the B-mode power is maximized around an angular scale of 2 degrees.

2 Experimental Approach towards B-mode Detection

The most stringent indirect limit to date for the B-modes is $r < 0.20$ at the 95% confidence level set by combination of CMB temperature anisotropy measurements, baryon acoustic oscillations, and supernova observations [3]. However, cosmic variance prohibits further significant improvements using only these measurements. Therefore, we are trying to detect the B-modes directly with precision measurements of the CMB polarization. The experimental approach to detect the B-modes can be simply described; (1) measure the CMB polarization intensity map on the sky, then, (2) extract the B-modes from the measured polarization map. However this approach represents a major experimental challenge. The intensity of the CMB polarization is very small, $\lesssim \mu$K, [a], which is several hundred times smaller than the white noise level of the detector in the case of 1 sec integration time. We accumulate data for a few years of observation to improve the signal-to-noise ratio with higher number statistics. However, another strategy is needed to achieve a few orders of magnitude better sensitivity than past experiments. One approach is to use a larger number of detectors, e.g. having 10 detectors provides 10 times better B-mode sensitivity than the case of a single detector [b]. This is the general approach of the experiment [c]. Once a precise CMB polarization map is obtained, E- and B-modes can be transferred to power spectra in spherical harmonic space as shown in Fig. 1. Whereas the CMB polarization map is dominated by E-modes which have already been observed, we can evaluate B-mode (odd-parity) and E-mode (even-parity) power spectra separately. The E-mode spectrum is well estimated with the ΛCDM model, which is the standard model in cosmology. The ΛCDM model is described by cosmological parameters based on past measurements. Therefore, the measurement of E-modes is a good demonstration of experimental sensitivity.

Weak gravitational lensing also induces B-modes in addition to those of inflationary origin. However, the primordial B-modes are a degree-scale pattern whereas the B-modes from lensing are greatest on scales around one order of magnitude smaller. In these proceedings, the term "B-modes" refers to those from primordial gravitational waves only. Because of the scale of

[a] We measure the CMB intensity with temperature units, i.e. Kelvin, since it is black body radiation.

[b] The statistical error of power spectra proportionally improves with number of detectors as well as the observing time because the power spectrum is the angular correlation of the measured CMB polarization on the map.

[c] Since the improvement of a single detector sensitivity is limited by photon noise induced by the CMB itself as well as atmospheric emission, there is no prospect to have a detector which has more than 10 times better sensitivity than today's one. Future observations in space, on the other hand, require detectors with better sensitivities as there is no atmospheric emission.

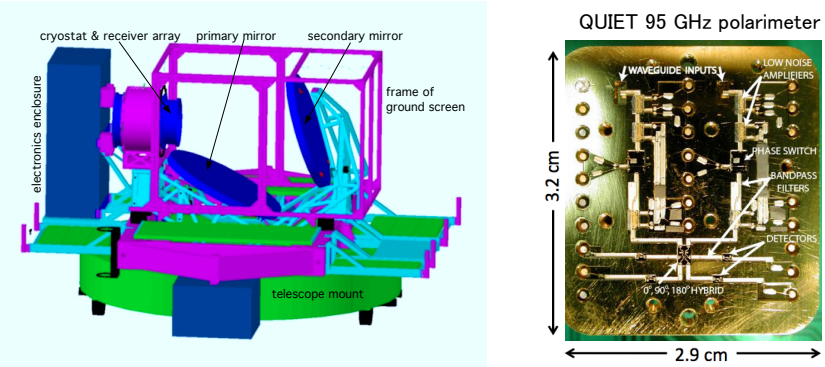

Figure 2: [Left panel] Overview of the QUIET intrument. The cryostat and 1.4-m telescope mirrors are enclosed in a rectangular co-moving absorbing ground screen (in this figure its walls are transparent). [Right panel] Photograph of the QUIET 95 GHz polarimeter module.

the B-modes, $\approx 20^\circ$ of diameter for the observing regions is sufficient for its detection and so ground-based searches are possible.

In order to claim a detection of the B-modes, control of systematic errors and foreground contamination (radiation mainly from the Galaxy) is particularly critical in addition to the statistics. For example, the temperature anisotropy, i.e. the non-polarized component of the CMB, is roughly a million times higher than the B-modes. Immunity against spurious polarization, which is induced by instrumental imperfection or instability is very important. Many experiments are making an effort to establish such systematic error control in addition to increasing the number of detectors.

3 QUIET Experiment

Table 1: Instrumental parameters of QUIET

Detector type	Coherent detector with HEMT amplifiers
Frequency (GHz)	95 / 43
Angular resolutions (arcmin)	12 / 27 in full-width-half-maximum
Number of detector elements	90 / 19
Array Sensitivity (μK$\sqrt{\text{s}}$)	$\sim$ 70 / 69
Knee of $1/f$ noise (mHz)	$\lesssim$ 10 / 5.5 median of all detectors
Polarization modulation	Phase switch (4 kHz and 50 Hz), sky & boresight rotations
Telescope optics	Mizuguchi-Dragone
Field centers (J2000 RA, DEC)	(181°, −39°), (78°, −39°), (12°, −48°), (341°, −36°)
Observation	August 2009 $\sim$ December 2010 with 95 GHz receiver / October 2008 $\sim$ June 2009 with 43 GHz receiver

An Instrumental overview of the QUIET is shown in Fig. 2 and Table 1. Incident CMB photons are first reflected, i.e. focused, with two mirrors, then come into the cryostat through an ultra-high molecular-weight polyethylene window. The CMB photons are detected with polarimeter (polarization sensitive detector) arrays in the cryostat. Miniaturization of the polarimeter into a highly integrated module (Fig. 2-right) allows us to have large focal plane arrays. The dimension of a single polarimeter is roughly ten times smaller than in the previous generation experiment [4].

The QUIET polarimeter also has excellent immunity to systematic errors. The CMB polarization properties can be expressed by the two linear polarization Stokes parameters, Q and U, which are defined by the following formula;

$$Q \equiv E_x^2 - E_y^2, \quad (1)$$
$$U \equiv E_a^2 - E_b^2, \quad (2)$$

where E_x, E_y are electric field components along $x-y$ coordinates on the sky, and $a-b$ coordinates are 45° rotated from the $x-y$ coordinates. In general, the simplest detection method is to use antenna coupled detectors for each axis, whereby the detected signals S_Q and S_U are described as follows;

$$S_Q = E_x^2 G_x - E_y^2 G_y, \quad (3)$$
$$S_U = E_a^2 G_a - E_b^2 G_b, \quad (4)$$

where $G_k (k = x, y, a, b)$ are the responses of the detectors for each antenna. A challenging aspect of this simple approach is to keep the detector responses very stable in order to minimize the systematic errors. Instability of the responses, especially the pair detector responses, causes spurious polarization even if the input photons are non-polarized, i.e. $E_x^2 = E_y^2$ ($E_a^2 = E_b^2$). In contrast to this approach, the QUIET polarimeter employs a coherent detection technique, with pseudo-correlation of incoming photons using HEMT (High Electron-Mobility Transistor) amplifiers in two parallel lines. The amplification factors are represented by G_L and G_R. Both Q and U are measured simultaneously by a single QUIET polarimeter [d]. Each response can be described as;

$$S_Q = (E_x^2 - E_y^2) G_L G_R, \quad (5)$$
$$S_U = (E_a^2 - E_b^2) G_L G_R. \quad (6)$$

It is obvious that instability of the polarimeter does not create any spurious polarization when the input photons are non-polarized: $E_x^2 - E_y^2 = 0$ ($E_a^2 - E_b^2 = 0$). Further details can be found in [5].

The CMB polarization was measured using QUIET at two different frequency bands around 43 GHz and 95 GHz. The dominant foreground below 100 GHz comes from Galactic synchrotron emission. The 43 GHz receiver is used for addressing synchrotron contamination since the synchrotron emission intensity decreases according to a power law as a function of frequency. So far, our sensitivity is not limited by foregrounds, however it is important to have such foreground receivers for the future.

Over two years of observations were obtained using QUIET. We recently published analysis results for our initial observations at 43 GHz (7.5 months of observing time) [6]. Figure 3 shows the measured power spectra for the E-modes and B-modes, in comparison with the most relevant experiments [7,8,9] [e]. We confirm the E-mode power with high significance in the region of the first acoustic peak ($\ell = 76 - 175$); we also agree with past experiments as well as with the ΛCDM model. With a χ^2 test, we find that the "probability to exceed" of the data is 14% for the ΛCDM model. We find no significant power in the B-modes, $r = 0.35^{+1.06}_{-0.87}$; the corresponding upper limit is $r < 2.2$ at 95% confidence level. These are the results based on 1/3 of our full data set. However, we have the potential to achieve the best limits from CMB polarization alone, $r \approx 0.5$, with the full data set.

[d] The name of QUIET: Q/U Imaging ExperimenT derives from this simultaneous detection technique.

[e] Since the WMAP results [9] do not provide an upper limit on the B-mode power, we use the diagonal elements of the Fisher matrix and show the points that are 1.65σ above their central values as 95% confidence limits.

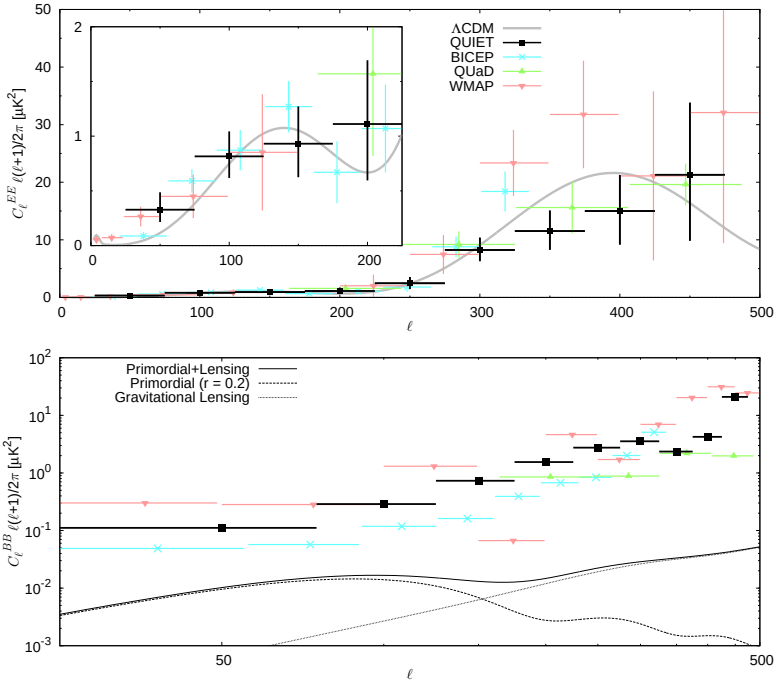

Figure 3: The top panel shows E-modes results; the bottom panel shows 95% confidence level upper limits for B-modes power. The inset of the top panel shows the low-ℓ region in detail. In addition to the results from QUIET, we also plot results previous experiments and the ΛCDM model (assuming $r = 0.2$) for comparison.

The smallest systematic errors in any B-mode experiment to date are another important result from the QUIET as shown in Fig. 4; below the level of $r < 0.1$. This was achieved with a combination of detector technology (as described in Eq. 5, 6) and carefully-chosen observation and calibration strategies.

4 Future Prospects

Since the simplest inflationary models favor $r = 0.01 \sim 0.1$, we are planning to increase our sensitivity by increasing the number of polarimeters to be 500. This upgrade, called QUIET-II, will allow us to search for the B-modes down to the level of $r \sim 0.01$. Many other experiments, BICEP2 [10], Keck Array [11], ABS [13], POLARBEAR [12], ACTpol [14], SPTpol [15], are also aiming

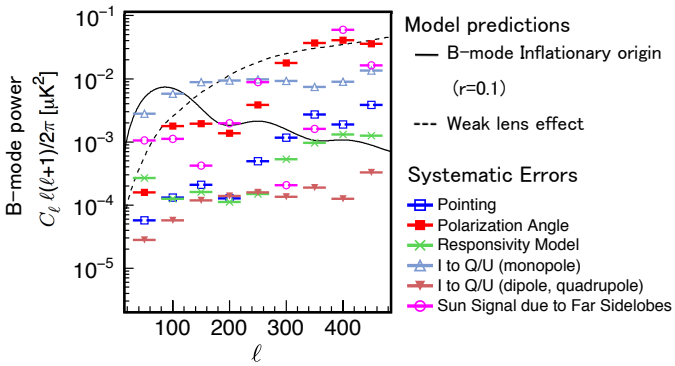

Figure 4: Systematic errors for the initial results from QUIET, the lowest systematic errors of any B-mode experiment to-date.

to achieve such sensitivity. In particular, observations have already begun with the $\sim 1,500$ TES (Transition Edge Sensor) bolometers of the Keck Array [11]. Nevertheless, QUIET leads the competition in achieving low systematic errors and has a good chance of discovery if a sufficient number of detectors is deployed in a timely manner.

The community of CMB polarization experiments is also planning to search for B-modes with balloon-borne experiments [16,17] and satellite experiments [18,19,20,21] in which they can observe a large area of the sky. This allows the B-modes from reionization at low-ℓ to be measured, where the contamination by the weak lensing signal is much reduced.

The coming years are definitely exciting for the search for primordial B-modes; we are looking forward to seeing a big discovery.

Acknowledgments

We thank the conference organizers who gave us a chance to present our first results from the QUIET. Support for the QUIET instrument and operation comes through the NSF cooperative agreement AST-0506648. Support was also provided by NSF awards PHY-0355328, AST-0448909, AST-1010016, and PHY-0551142; KAKENHI 20244041, 20740158, and 21111002; PRODEX C90284; a KIPAC Enterprise grant; and by the Strategic Alliance for the Implementation of New Technologies (SAINT).

References

1. M. Zaldarriaga and U. Seljak, *Phys. Rev.* D **55**, 1830-1840 (1997).
2. http://quiet.uchicago.edu/ .
3. E. Komatsu *et al.*, *Astrophys. J. Suppl.* **192**, 18 (2011).
4. C. Bischoff *et al.*, *Astrophys. J.* **684**, 711-789 (2008).
5. K. A. Cleary, Proc. SPIE, **7741**, 77412N (2010).
6. QUIET Collaboration, arXiv:1012.3191 [astro-ph.CO] (2010).
7. M. L. Brown *et al.*, *Astrophys. J.* **705**, 978-999 (2009).
8. H. C. Chiang *et al.*, *Astrophys. J.* **711**, 1123-1140 (2010).
9. D. Larson *et al.*, *Astrophys. J. Suppl.* **192**, 16 (2011).
10. http://www.astro.caltech.edu/~lgg/bicep2/bicep2_front.htm.
11. http://www.astro.caltech.edu/~lgg/keck/keck_front.
12. http://bolo.berkeley.edu/polarbear/ .
13. http://www.princeton.edu/physics/research/cosmology-experiment/abs-experiment/, T. Essinger-Hileman, *et al.*, arXiv:1008.3915v1 [astro-ph.IM] (2010).
14. http://www.physics.princeton.edu/act/ .
15. http://kicp.uchicago.edu/research/projects/spt.html.
16. http://groups.physics.umn.edu/cosmology/ebex/.
17. http://www.astro.caltech.edu/ lgg/spider/spider_front.htm.
18. J. Bock *et al.*, arXiv:0906.1188v1 [astro-ph.CO] (2009).
19. C. Armitage-Caplan, *et al.*, arXiv:1102.2181v2 [astro-ph.CO] (2011).
20. A. Kogut *et al.*, arXiv:1105.2044v1 [astro-ph.CO] (2011).
21. http://cmb.kek.jp/litebird/.

8.
Young Scientists Forum

THE SUPERSYMMETRIC HIGGS BOUNDS AT THE TEVATRON AND THE LHC

Julien Baglio
Laboratoire de Physique Théorique
Université Paris-Sud 11 and CNRS,
Bat. 210, 91405 Orsay Cedex, France

MSSM Higgs bosons are the most promising way to discover Higgs physics at hadronic colliders since their cross section is enhanced compared to that of the Standard Model. We will present theoretical predictions for their production and decay in the Higgs$\to \tau\tau$ channel at the Tevatron and the LHC, focusing on the theoretical uncertainties that affect them. The inferred SUSY Higgs bounds on the $[\tan\beta; M_A]$ plane and the impact of these uncertainties will also be discussed.

1 Introduction

The search for the Higgs bosons which are a trace of the electroweak symmetry breaking[1,2] is the main goal for current high–energy colliders. In the minimal supersymmetric extension of the Standard Model (SM), one of the most attractive solutions of the hierarchy problem in the SM[3], two Higgs doublets are required to cancel anomalies, which then lead to five Higgs states: the CP–even h, H, the CP–odd A and the two charged Higgs bosons $H^\pm$.

At tree–level two parameters in the Minimal Supersymmetric Standard Model (MSSM) describe the Higgs sector: the vacuum expectation values (vev) ratio between the two Higgs doublets $\tan\beta = \dfrac{v_1}{v_2}$ and the CP–odd Higgs mass M_A.

At high $\tan\beta$ values, $\tan\beta \gtrsim 10$, either h or H is SM–like and its couplings to other particles are the same as those of the SM Higgs boson, while the other CP–even state behaves as the CP–odd A: same couplings and almost same mass. We will denote these two states as Φ in the next sections. This behaviour occurs in current MSSM Higgs benchmarks scenarios[4] which are considered at the Fermilab Tevatron[5] and the CERN LHC[6,7] colliders.

b–processes are dominant as they are proportionnal to $\tan\beta$ contrary to that of the top–loop. We will thus consider the gluon–gluon fusion Higgs production through bottom quark loop[8,9] and the $b\bar{b}$ fusion channel[10,11,12,13], followed by the Higgs$\to \tau^+\tau^-$ desintegration. Squark loops can be safely neglected while SUSY Δ_b corrections to the $\Phi b\bar{b}$ coupling nearly cancel out in the production cross section times branching ratio calculation[14].

We will present numerical results at the Tevatron and the lHC (LHC at 7 TeV) for $\tan\beta = 1$, which means that we have to multiply by $2\tan^2\beta$ for actual values. Theoretical uncertainties will also be presented and their implications on the MSSM parameter space limits will be discussed. A more detailed discussion can be found in Refs.[14,15,16]

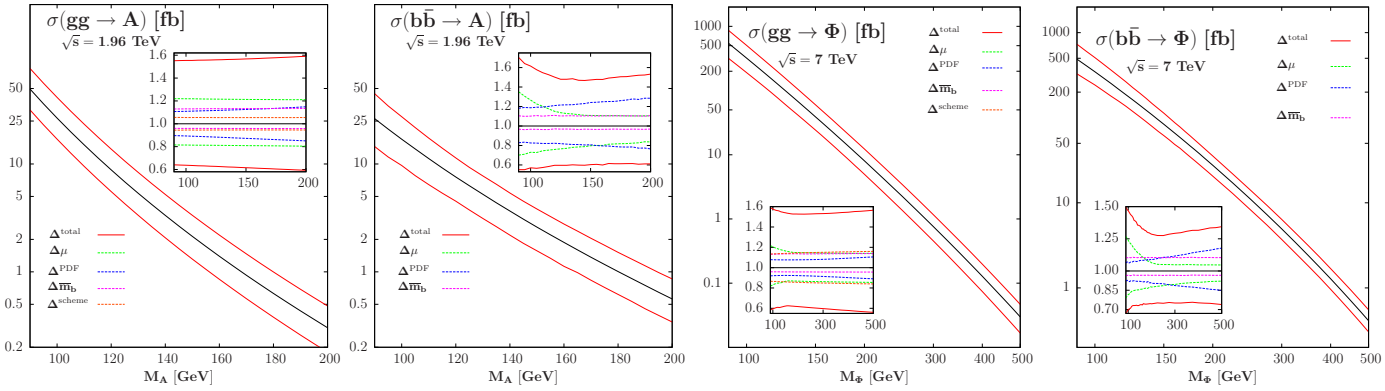

Figure 1: $\sigma^{\rm NLO}_{gg\to\Phi}$ and $\sigma^{\rm NNLO}_{b\bar{b}\to\Phi}$ central cross sections using MSTW 2008 PDFs and $\Phi b\bar{b}$ unit couplings together with total uncertainties at the Tevatron (left) and at the lHC (right). In the insert are shown the individual sources of uncertainties normalised to the central cross section.

2 SUSY Neutral Higgs production at the Tevatron and the lHC

2.1 $gg \to \Phi$ channel

The Higgs bosons in the gluon–gluon fusion channel is produced through top and bottom quarks loops. At $\tan\beta \gtrsim 10$ values the top loop is strongly suppressed because $\Phi t\bar{t}$ is inversely proportionnal to $\tan\beta$ contrary to the $\Phi b\bar{b}$ coupling. Although the top loop is known up to next–to-next–to–leading order (NNLO) in QCD, the b–loop is known up to next–to–leading order (NLO) only[9]. We will use NLO MSTW 2008 parton distribution functions (PDF) set[17]. We consider the standard QCD theoretical uncertainties that have been discussed in Refs.[14,15,16].

It is customary to estimate the uncertainty due to the missing higher order terms in a perturbative calculation by varying the renormalisation scale μ_R and the factorisation scale μ_F around a central scale μ_0: $\frac{\mu_0}{\kappa} \leq \mu_R, \mu_F \leq \kappa\mu_0$. We take $\mu_0 = \frac{1}{2}M_\Phi$ as the central scale in order to be consistent with the SM calculation[18], as one of the CP–even Higgs is SM–like. We use $\kappa = 2$ in the gluon–gluon fusion channel and obtain $\Delta\sigma/\sigma \simeq \pm 20\%$ at the Tevatron ($\pm 15\%$ at the lHC).

The next source of uncertainties is due to the combined uncertainty from the PDF and α_S coupling. We use MSTW collaboration scheme[19] and calculate the PDF+$\Delta^{\rm exp+th}\alpha_S$ 90% CL uncertainty which is equivalent to the MSTW PDF4LHC recommandation[20] and we obtain $\Delta\sigma/\sigma \simeq \pm 10\%$ both at the Tevatron and the lHC.

The last important uncertainty is specific to the MSSM case, and deals with the m_b mass. There are two types of uncertainties: the experimental errors on the $\overline{\rm MS}$ $\bar{m}_b(\bar{m}_b)$ value and the uncertainty due to the scheme choice for the renormalisation of the b–mass. The first uncertainty will cancel out in the production cross section times branching ratio (see below) but not the other one. We obtain $\Delta\sigma/\sigma \simeq \pm 15\%$ at both colliders due to these b–quark issues.

All these individual sources of uncertainties are shown in Fig.1 in the insert. We also display the total uncertainty on the cross section when combining the uncertainties according to the procedure developed in Ref.[15]. We obtain $\Delta\sigma/\sigma \simeq +58\%, -40\%$ at the Tevatron and $\Delta\sigma/\sigma \simeq +53\%, -38\%$ at the lHC.

2.2 $b\bar{b} \to \Phi$ channel

The bottom quark fusion channel is strongly enhanced because of the $\tan\beta$ effect in b–quark processes. This channel is known in the SM up to NNLO in QCD[13] and we rescale the predictions with the MSSM $\Phi b\bar{b}$ coupling to obtain a NNLO MSSM prediction. We use the same PDF set as for gluon–gluon fusion and consider the same set of theoretical uncertainties.

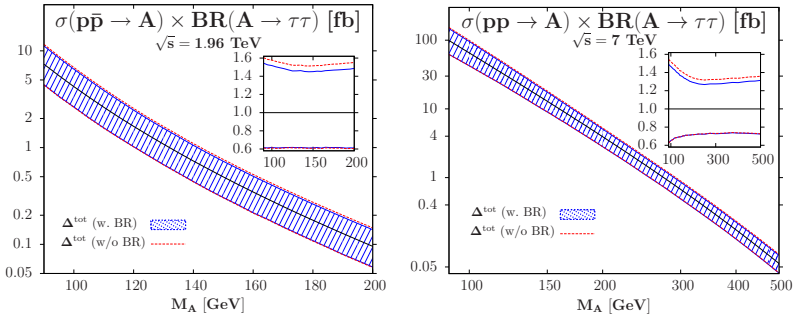

Figure 2: $\sigma(p\bar{p} \to A) \times \mathrm{BR}(A \to \tau^+\tau^-)$ as a function of M_A at the Tevatron (left) and at the lHC (right), together with the associated overall theoretical uncertainty; the uncertainty when excluding that on the branching ratio is also displayed. In the inserts, shown are the relative deviations from the central values.

For the scale uncertainties we consider here $\kappa = 3$ instead of $\kappa = 2$ in $gg \to \Phi$. Indeed this is well known that either four or five active flavours schemes can be used for the calculation. The two predictions differ significantly[21] and one way to reconcile them is to allow such a scale interval. Furthermore this also allows the inclusion of the b–mass scheme uncertainty that was obtained separately in the gluon–gluon fusion calculation. We obtain in the end $\Delta\sigma/\sigma \simeq 30\%$ for low masses at the Tevatron ($\pm 25\%$ at the lHC).

The combined PDF+α_S uncertainty is calculated exactly as in the gluon–gluon fusion case. We obtain in the bottom quark fusion $\Delta\sigma/\sigma \simeq \pm 20\%$ for low masses and $\simeq \pm 30\%$ for high masses at the Tevatron ($\simeq 10\%$ at low masses and $\simeq \pm 20\%$ at high masses at the lHC).

The last uncertainty involves only the experimental b–mass error. We obtain a $+10\%, -4\%$ uncertainty at the Tevatron (nearly the same at the lHC), which as discussed in the next section will cancel out in the cross section times branching ratio calculation.

All the uncertainties are displayed in Fig.1. The overall total uncertainty is $\Delta\sigma/\sigma \simeq +50\%, -40\%$ at the Tevatron ($+40\%, -30\%$ at the lHC).

2.3 Combinaison with the $\Phi \to \tau\tau$ branching ratio

We finally evaluate the combinaison of the two production channels together with the branching ratio $\Phi \to \tau^+\tau^-$. The issue is how to combine the uncertainties and we proceed as stated in Refs.[16,15]: the cross section uncertainties are weighted according to their importance and we add linearly the decay branching ratio uncertainty which is $\simeq +4\%, -9\%$ on $\mathrm{BR}(\Phi \to \tau^+\tau^- \simeq 10\%)$[16]. In this procedure, as the uncertainties due to the experimental errors on b–mass are anti-correlated in the production and decay, they cancel out.

We then obtain $\Delta(\sigma \times \mathrm{BR})/(\sigma \times \mathrm{BR}) \simeq +50\%, -39\%$ at the Tevatron and $\simeq +35\%, -30\%$ at the lHC, as shown in Fig.2.

3 Higgs bounds on the MSSM parameter space

We are left to evaluate the impact of the theoretical uncertainties calculated above on the 95% CL limits in the $[\tan\beta; M_A]$ plane using the experimental results at the Tevatron and the lHC. The results presented above are quite model independant as they do not depend on the details of the MSSM model as long as we have a degeneracy in the $h/H, A$ spectrum. We apply the limit on the minimal cross section times branching ratio instead of the central prediction in order to take into account the theoretical uncertainties.

The result is shown in Fig.3 and the theoretical uncertainties are extremely important. We obtain $\tan\beta > 45$ at the Tevatron, which thus reopens a large part of the parameter space excluded by CDF/D0[5]. The comparaison with CMS results at the lHC shows a slight reduction

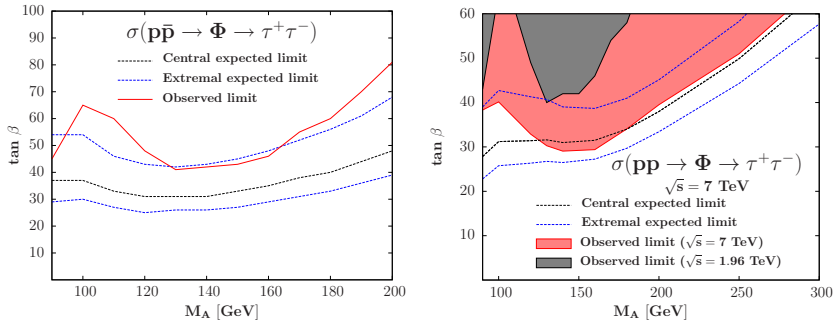

Figure 3: Contours for the expected $\sigma(p\bar{p} \to \Phi \to \tau^+\tau^-$ rate at the Tevatron (left) and at the lHC (right) in the $[M_A; \tan\beta]$ plane with the associated theory uncertainties, confronted to the 95% CL exclusion limit obtained by CDF/D0 and CMS.

of the exclusion limit as we obtain $\tan\beta > 29$ to be compared with $\tan\beta > 23$. The result is comparable to what can be obtained with the theory uncertainty quoted by CMS[7].

Acknowledgments

J.B. would like to thank the Moriond 2011 organisers for the very fruitful atmosphere and the organisation of the conference.

References

1. P. W. Higgs, *Phys. Lett.* **12**, 132 (1964).
2. F. Englert and R. Brout, *Phys. Rev. Lett.* **13**, 321 (1964).
3. A. Djouadi, *Phys. Rept.* **459**, 1 (2008).
4. M. S. Carena, S. Heinemeyer and C. E. M. Wagner and G. Weiglein, *Eur. Phys. J.* C **26**, 601 (2003).
5. D. Benjamin *et al*, TEVNPHWG, arXiv:1003.3363 [hep-ex] (2010).
6. ATLAS Collaboration, Conf. note ATLAS-CONF-2011-024 (2011).
7. CMS Collaboration, arXiv:1104.1619 [hep-ex] (2011).
8. H. M. Georgi and S. L. Glashow and M. E. Machacek and D. V. Nanopoulos, *Phys. Rev. Lett.* **40**, 692 (1978).
9. M. Spira and A. Djouadi and D. Graudenz and P. Zerwas, *Nucl. Phys.* B **453**, 17 (1995).
10. D. A. Dicus and S. Willenbrock, *Phys. Rev.* D **39**, 751 (1989).
11. J. M. Campbell and R. K. Ellis and F. Maltoni and S. Willenbrock, *Phys. Rev.* D **67**, 095002 (2003).
12. F. Maltoni and Z. Sullivan and S. Willenbrock, *Phys. Rev.* D **67**, 093005 (2003).
13. R. V. Harlander and W. B. Kilgore, *Phys. Rev.* D **68**, 013001 (2003).
14. J. Baglio and A. Djouadi, arXiv:1103.6247 [hep-ph] (2011).
15. J. Baglio and A. Djouadi, arXiv:1012.2748 (to appear in *Phys. Lett.* B) (2011).
16. J. Baglio and A. Djouadi, *JHEP* **03**, 055 (2011).
17. A. D. Martin and W. J. Stirling and R. S. Thorne and G. Watt, *Eur. Phys. J.* C **63**, 189 (2009).
18. J. Baglio and A. Djouadi, *JHEP* **10**, 064 (2010).
19. A. D. Martin and W. J. Stirling and R. S. Thorne and G. Watt, *Eur. Phys. J.* C **64**, 653 (2009).
20. see their website http://www.hep.ucl.ac.uk/pdf4lhc/PDF4LHCrecom.pdf.
21. J. Campbell in K. A. Assamagan *et al*, arXiv:hep-ph/0406152, p. 5 (2004).

SEARCH FOR SM HIGGS BOSON IN THE $\tau^+\tau^-$+ 2 JETS FINAL STATE

Kathryn Tschann-Grimm
Department of Physics and Astronomy, SUNY Stony Brook,
Stony Brook, NY 11794-3800, USA

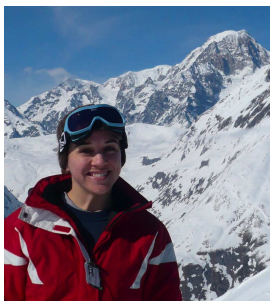

This note reviews the search for the Standard Model Higgs boson at the DØ experiment with the final state containing two τ's and at least two jets. Data from Run 2b of the DØ experiment are used with an integrated luminosity of 4.3 fb^{-1}. This final state is sensitive to the production mechanisms gluon gluon fusion, vector boson fusion, and associated Higgs production with a W or Z, for Higgs masses from 100 to 200 GeV. No evidence for the Higgs boson is yet observed, so upper limits are placed on the cross section of the SM Higgs production. Including a previous DØ measurement with 1.0 fb^{-1} of data, we set a 95% CL. limit on the measured H cross sections for $M_H = 110$, 130 and 160 GeV that are factors of 20, 24 and 11 larger than expectations from the standard model, respectively.

1 Introduction

We present a search for the standard model (SM) Higgs boson (H) in final states with a lepton (e or μ), a candidate for the decay of $\tau \to$ hadrons + ν_τ, and two jets. We refer these two final state signatures as the $e\tau jj$ or $\mu\tau jj$ channels, and analyze such events for contributions from $q\bar{q} \to H(\to b\bar{b})Z(\to \tau\tau)$(denoted HZ), or from $q\bar{q} \to ZH$(denoted ZH), or from $q\bar{q} \to WH$, or from $gg \to H + (\geq 2$ jets)(gluon gluon fusion, GGF), or from $q\overline{q'} \to q\overline{q'}H$(virtual vector boson fusion, VBF).

The ZH, WH, GGF and VBF production processes are sought both through the $H \to \tau\tau$ and $H \to W^+W^-$ decays, denoted with subscripts $X_{\tau\tau}$, or X_{WW}, respectively. For the VH_{WW} subprocesses ($V = W$ or Z), the lepton can be produced either directly from $W \to \ell\nu$ or $Z \to \ell\ell$ with one ℓ not detected, or through V decays to τ lepton states with subsequent decay $\tau \to \ell\nu\overline{\nu}$.

The backgrounds to the $\tau(\ell)$ τ(hadronic) jet jet signatures are from $t\bar{t}$, $W+$ jets, $Z+$ jets, multijets and diboson ($WW/WZ/ZZ$) production.

We use 4.3 fb^{-1} of data collected with the upgraded DØ detector [2].

2 Data and Monte Carlo event samples

2.1 Monte Carlo samples

Monte Carlo samples for the Higgs signals and for the backgrounds are generated using a combination of PYTHIA [3] and ALPGEN [4]. The signals and backgrounds are processed using the standard DØ GEANT3 [5] detector simulation, digitization and event-reconstruction programs.

2.2 Event preselection

A description of object identification is given in the longer conference note [6]. We select a sample of candidate events with the following requirements: One isolated lepton, e or μ; At least one $\tau \rightarrow$ hadrons candidate with opposite electric charge as the e / μ ; At least two jets. Leptons, taus and jets are required to be separated from each other by $\Delta\mathcal{R} > 0.5$, where $\mathcal{R} = \sqrt{(\Delta\phi)^2 + (\Delta\eta)^2}$. To assure orthogonality to other H searches, we require no additional electron and no additional muon for the $\mu\tau jj$ ($e\tau jj$) channels, respectively.

For the $e\tau jj$ analysis, there is a substantial background contribution from $Z(\rightarrow ee)+$ jets. Therefore we impose additional requirements on τ's in this channel including removal of τ candidates falling in regions of the detector with degraded EM energy response and use of a Neural Net trained to specifically distinguish τ's and electrons.

2.3 Estimation of background from multijet events

Multijet (MJ) events in which jets mimic electrons, muons or τ's are not reliably simulated in our MC, and are estimated with data-driven techniques. We select a baseline MJ background sample in which both the τ and lepton pass significantly relaxed selection cuts but also fail the tight selection criteria used for the signal sample.

The MJ background sample is normalized by comparing the ratio of the opposite-sign lepton-tau pairs to the same-sign pairs in the signal sample and the MJ background sample.

2.4 Yields

The estimated number of events from all background sources and the number of observed data in our signal selection are given in Table 1. For a Higgs boson mass of 160 the total number of expected signal events is 1.36 for $\mu\tau jj$ and 0.34 for $e\tau jj$.

Table 1: The number of background events expected from SM processes, MJ background, and observed data after preselection in the $\mu\tau jj$ and $e\tau jj$ analyses. "DB" stands for di-boson processes.

	$t\bar{t}$	W+jets	$Z_{\mu\mu}$+jets	$Z_{\tau\tau}$+jets	DB	MJ	ΣBkgd	Data
$\mu\tau jj$	82.0	64.8	22.3	154.5	11.3	70.0	404.9	414
$e\tau jj$	24.4	42.6	19.8	48.6	3.6	59.2	198.3	188

3 Multivariate analysis

As no single set of selections on kinematic variables suffices to discriminate signal from the background, we turn to multivariate techniques to attain better separation. We use stochastic gradient boosted decision trees (BDT) [7] as implemented in TMVA [8] for this purpose.

To train the BDT's we choose a set of 17 well-modelled kinematic variables, for which the distributions of at least some signal and some background are different.

There are three rather distinct regions of Higgs mass in this analysis, $M_H < 125$, $125 \leq M_H \leq 135$ GeV and $M_H > 135$ GeV, in which the dominant production and decay processes are different. The most dominant signals in the three regions are $\mathrm{GGF}_{\tau\tau}$, $VH_{\tau\tau}$, and $\mathrm{VBF}_{\tau\tau}$ in the low mass region, $\mathrm{GGF}_{\tau\tau}$, GGF_{WW}, $VH_{\tau\tau}$, and VH_{WW} in the intermediate mass region, and GGF_{WW}, VH_{WW}, and VBF_{WW} in the high mass region. The BDT's are trained separately in the three mass regions against the backgrounds $Z+$ jets, MJ, and $t\bar{t}$ plus $W+$ jets. This gives a total of 30 separate BDT's. The BDT's successfully separate the signals and backgrounds they are trained against, but sometimes the signals (backgrounds) that are not used for the training fall in the low (high) regions of BDT output where backgrounds (signals) are expected to dominate. We therefore construct a final combined BDT (cBDT) in each mass region, using the individual BDT outputs in that region as inputs into the cBDT. The task of the cBDT is to weigh conflicting information, *e.g.* whether a particular event is more like one of the signals than any of the backgrounds. The final cBDT distributions are shown in Fig. 1.

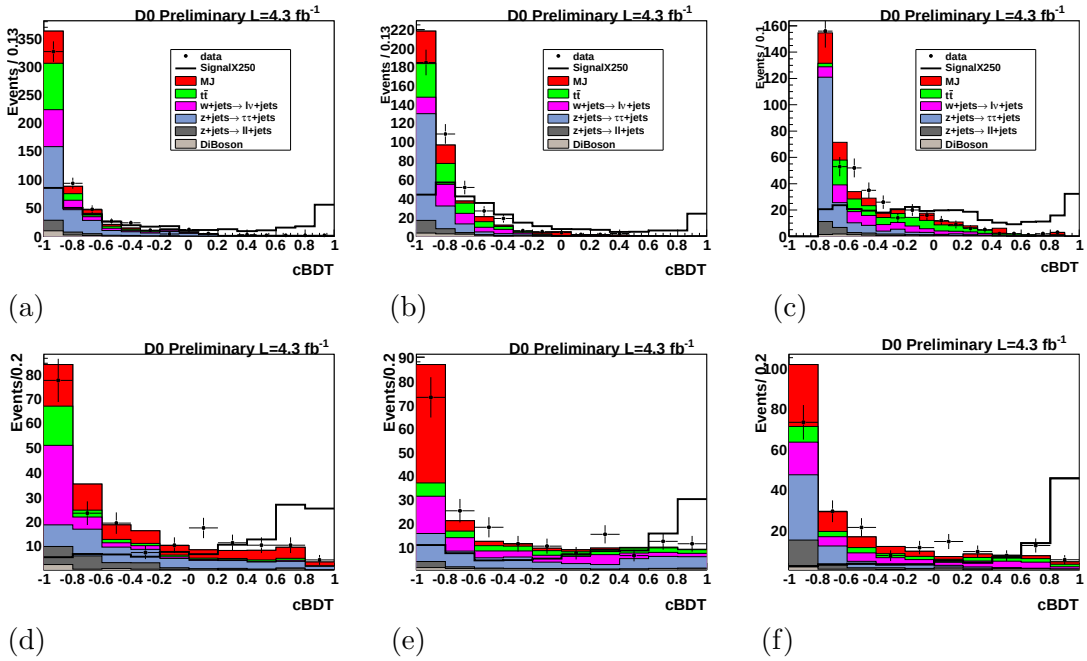

Figure 1: Combined BDTs for $\mu\tau jj$ (top) and $e\tau jj$ (bottom) for the: low M_H region (a), (d); intermediate M_H region (b), (e); high M_H region (c), (f) . Signals are multiplied by a factor of 250.

4 Systematic uncertainties

Systematic uncertainties for each factor that influences the final cBDT distributions are estimated by changing the relevant factor by $\pm$ 1 standard deviation from its nominal value and propagating the change to the cBDT distribution. The largest systematic uncertainties arise from jet identification and reconstruction (≈20%), from jet resolution (≈15%) and jet energy scale (≈15%) and from the estimation of the MJ background (≈15%).

5 Limit calculation

The upper limits on the production cross section of Higgs bosons assuming SM Higgs decay branching ratios are calculated using the modified frequentist method [9]. The test statistic is the negative of a binned Poisson log-likelihood ratio (LLR) computed at each of the assumed

Higgs mass values from 105 to 200 GeV in 5 GeV steps. The LLR for different hypotheses (*e.g.* background-only, LLR_b, or signal+background, LLR_{s+b}) are used to compute the confidence levels $\mathrm{CL_b}$ and $\mathrm{CL_{s+b}}$ that give the probability that the LLR value from a set of 50,000 simulated pseudo-experiments is less likely than that observed, at a given confidence level.

The cross sections of the hypothesized Higgs signal at a given M_H are then scaled up from their SM values until the value of $\mathrm{CL_s} = \mathrm{CL_{s+b}}/\mathrm{CL_b}$ reaches 0.05 which defines the limit cross sections at 95% CL. Figure 2 shows the expected and observed limits and the expected LLRs for the $\mu\tau jj$ and $e\tau jj$ channels combined (including the previous $\mu\tau jj$ limit [1]).

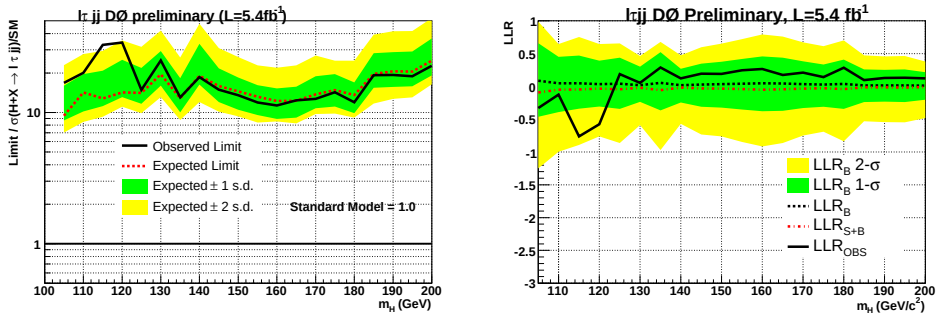

Figure 2: For the combined 4.3 fb^{-1} $\mu\tau jj$ and $e\tau jj$ analyses and the 1.0 fb^{-1} $\mu\tau jj$: the ratio of the 95% upper C.L. limits to the SM cross section (left) and the LLR as functions of Higgs boson mass (right).

6 Conclusion

We have searched for SM Higgs boson production in final states containing an electron or muon, a hadronically decaying τ plus two jets. Several different Higgs production processes contribute to this final state. At $M_H = 110$, 130 and 160 GeV, after combining the results in this analysis with that of a previous publication [1], we set a final combined limit on SM Higgs boson production that is a factor of 20, 24, and 11 times larger than the cross section predicted in the SM, to be compared to the expected ratios of 14, 20 and 12.

References

1. V.M. Abazov *et al.*, (DØ Collaboration), Phys. Rev. Lett **102**, 251801 (2009).
2. V.M. Abazov *et al.*, (DØ Collaboration), Nucl. Instrum. Methods Phys. Res A **565**, 463 (2006).
3. T. Sjöstrand *et al.*, Computer Phys. Commun. **135**, 238 (2001); T. Sjöstrand *et al.*, arXiv:(hep-ph) 0108264 (2001).
4. M. Mangano *et al.*, J. High Energy Physics **0307**, 001 (2003).
5. R. Brun and F. Carminati, CERN Program Library Long Writeup W5013, 1993 (unpublished), version V3.21.
6. The DØ Collaboration, "Search for the SM Higgs boson in the tau + tau + 2 jets final state" http://www-d0.fnal.gov/Run2Physics/www/results/prelim/HIGGS/H101/H101.pdf
7. L. Breiman *et al.*, *Classification and Regression Trees* (Wadsworth, Stamford CT, 1984); D. Bowser-Chao and D.L. Dzialo, Phys. Rev D **47**, 1900 (1993).
8. TMVA Users Guide, CERN-OPEN-2007-007 and arXiv:physics/0703039.
9. A. Read, J. Phys. G: Nucl. Part. Phys. **28**, 2693 (2002); T. Junk, Nucl. Instrum. Methods A **434**, 435 (1999).

Search for the Higgs Boson in Dilepton plus Missing Transverse Energy Final State with the DØ Detector at $\sqrt{s} = 1.96$ TeV

Ruchika Nayyar (for the DØ collaboration)
University of Delhi, India

We present a search for the standard model (SM) Higgs boson optimized in the decay channel $H \to W^+W^-$, where both W bosons decay leptonically. The final state considered contains dilepton and missing transverse energy from the neutrinos. A multivariate analysis is used to suppress the background. No significant excess above the SM background has been observed and limits on the Higgs boson production cross section times the branching ratio for $m_H = 115 - 200$ GeV are computed. Results using 8.1 fb^{-1}of data are presented.

1 Introduction

In this search channel, final states containing two leptons ($e^{\pm}\mu^{\mp}$, e^+e^- or $\mu^+\mu^-$) and missing transverse energy are considered. The production of Higgs boson by gluon fusion, vector boson fusion (VBF) and production in association with a vector boson (W/ZH) are considered. The preselection, based on the efficient reconstruction of the two leptons, is followed by additional requirements to suppress the large Drell Yan (DY) $Z/\gamma^* \to \ell\ell$ background. A final multivariate analysis based on a random forest of decision trees (DT) is used to separate the signal from the remaining background. The DT output is used to search for the Higgs signal. The analysis relies on efficient reconstruction of objects using all sub-detectors of the Run II DØ detector [1].

2 Data and Monte Carlo Samples

The data sample used in this analysis was collected between April 2002 and December 2010 by the DØ detector at the Fermilab Tevatron collider at $\sqrt{s} = 1.96$ TeV, and corresponds to an integrated luminosity of 8.1 fb^{-1} after imposing data quality requirements. Signal and SM background processes are simulated either with Pythia [2] or Alpgen [3] using the CTEQ6L1 [4] PDFs, followed by a Geant-based [5] detector simulation. The generated events are normalized to the highest-order cross-section calculation available. The transverse momentum of the Higgs boson generated in the gluon fusion process is weighted to reproduce the higher-order calculation by Hqt, at NNLL and NNLO accuracy [6].

The main backgrounds to the final state are diboson production, $Z/\gamma^* \to \ell\ell$ decays, W+jets/γ production, $t\bar{t}$ decays and multijet.

For the W+jets and Z+jets backgrounds we use the Alpgen [3] event generator. In the ee and $e\mu$ channels, the W+jets sample includes contributions from events where a jet or photon is misidentified as an electron. The size of each of these contributions is corrected to match the data in the W+jets enhanced control sample. For the WW production, the p_{T} of the diboson

system is modeled using the MC@NLO simulation [7] and the distribution of the opening angle of the two leptons is corrected to take into account the contribution from gluon fusion [8]. The background due to multijet production where jets are misidentified as leptons, is determined from data.

3 Preselection

All events are required to have two oppositely charged leptons originating from the same position (within 2 cm) along the beam-line. In the e^+e^- channel, the leading electron is required to have $p_{\mathrm{T}} > 15$ GeV and the second electron is required to have $p_{\mathrm{T}} > 10$ GeV. In the $e^{\pm}\mu^{\mp}$ channel, the muon must have $p_{\mathrm{T}} > 10$ GeV while the electron is required to have $p_{\mathrm{T}} > 15$ GeV. In the $\mu^+\mu^-$ channel the leading muon is required to have $p_{\mathrm{T}} > 15$ GeV and the second muon must have $p_{\mathrm{T}} > 10$ GeV. The e^+e^- and $\mu^+\mu^-$ channel also applied a cut on the $\mathrm{M}_{ll} > 15$ GeV. This stage of the analysis is referred to as "preselection". Figures 1 show some kinematic distributions at preselection.

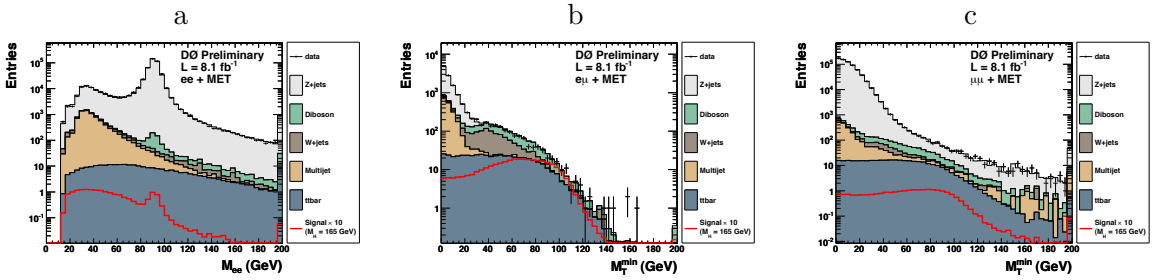

Figure 1: The (a) Dilepton mass, (b) $\not\!\!E_T$ and (c) minimum transverse mass between either lepton and the $\not\!\!E_T$.

To improve the sensitivity of the analysis, the preselection sample is further subdivided by the number of jets present in the event. Jets are required to have $p_{\mathrm{T}} > 20$ GeV, $|\eta| < 2.4$, pass quality requirements, and to have charged tracks associated with the primary $p\bar{p}$ vertex.

4 Final Selection

The Di-electron and Di-muon channel use a DT discriminant against the Z/γ^* background. The DT uses $\not\!\!E_T$ based variables to separate this dominant background. It is trained for each Higgs mass point considered in each jet bin. To reject most of this background, a cut is applied on this discriminant. The choice of the cut varies for each Higgs mass point in each jet bin. The electron-muon final state does not utilize such a discriminant and rather applies a cut on the minimum transverse mass, defined as:

$$M_T = \sqrt{2 \cdot \cdot \not\!\!E_T \cdot (1 - \cos\Delta\phi(\ell, \not\!\!E_T))}$$
$$M_T^{min} = min(\mathrm{M}_T^e, M_T^{\mu}) \quad (1)$$

The number of events at the final selection for the Dilepton states are shown in Table 1.

Table 1: Expected and observed number of events in each jet multiplicity after the final selection in all the final states. The signal assumes a Higgs boson mass of 165 GeV.

	Data	Total Background			Signal	$Z \to ee$	$Z \to \mu\mu$	$Z \to \tau\tau$	$t\bar{t}$	W+jets	Diboson	Multi-jet
$e\mu$:												
0 jets	1074	1163.5	±	145.4	16.0	16.9	74.7	89.9	14.1	462.8	473.2	31.9
1 jet	392	373.7	±	58.7	7.2	3.6	15.9	75.0	109.6	86.0	67.9	15.7
≥ 2 jets	280	285.7	±	41.4	3.2	1.1	3.9	21.8	220.6	24.2	10.2	3.9
ee:												
0 jets	676	715.8	±	89.9	7.2	108.5	-	9.1	6.1	376.8	205.3	10.0
1 jet	836	831.9	±	144.5	4.2	477.6	-	83.5	75.4	125.0	56.9	14.2
≥ 2 jets	477	442.6	±	73.9	2.4	201.7	-	42.9	160.8	13.9	17.1	6.2
$\mu\mu$:												
0 jets	612	689.7	±	60.7	9.3	-	201.8	2.7	3.8	136.6	240.6	104.2
1 jet	1420	1313.2	±	173.3	5.5	-	969.1	109.8	76.4	38.0	74.4	45.6
≥ 2 jets	888	890.8	±	135.4	3.7	-	579.6	46.8	209.4	7.2	28.2	19.5

5 Final Discriminant

After preselection, the signal is separated from the remaining background using an additional random forest decision tree (DT). Different discriminating variables such as b-tag information of the jets are employed to distinguish signal from background in various jet bins. The DT discriminant distributions for a Higgs boson mass of 165 GeV can be found in Fig.2.

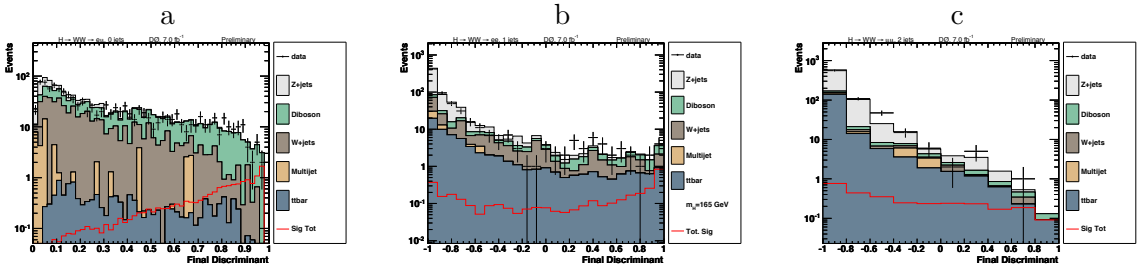

Figure 2: Final DT discriminant for (a)$e^+\mu^-$ in 0-jet bin, (b) e^+e^- in 1-jet bin and (c) $\mu^+\mu^-$ in $\geq$ 2-jet bin; The discriminant shown is trained for a Higgs mass of 165 GeV.

6 Systematic Uncertainties

The following sources of systematic uncertainty which affect only normalization are assessed: reconstruction efficiency for electrons (2.5% each) and muons (4% each); electron resolution (2% each); theoretical cross sections for Z+jets (6%), W+jets (6%), diboson (7%), and $t\bar{t}$(10%); multijet normalization (20%); W+jets overall normalization (20%); b-tagging in the heavy-flavor $t\bar{t}$ sample (5%) and remaining light-flavor samples (10%); and luminosity/normalization (6%). The signal $gg \to H$ cross-section has different cross-section and PDF uncertainties depending on the reconstructed jet bin: 0-jet (7% and 17.3%), 1-jet (23% and 29.7%) and 2-jet (33% and 30%). We also consider sources of systematic uncertainty which affect the shape of the final variable distribution (and quote here the average fractional change across bins of the final variable distribution for all backgrounds): jet energy scale (2.4%); jet resolution (3.8%); jet identification (2.1%); jet association to primary vertex (vertex confirmation) (1.7%).

Table 2: Expected and observed cross section $\sigma(p\overline{p} \to H + X)$ at 95 SM prediction for the Dilepton combination.

$M_H =$	115	120	125	130	135	140	145	150	155	160	165	170	175	180	185	190	195	200
Expected:	8.55	5.83	4.39	3.38	2.66	2.23	1.94	1.71	1.44	1.05	0.97	1.15	1.30	1.57	1.93	2.25	2.75	3.20
Observed:	9.95	9.12	8.06	4.97	4.25	3.45	3.83	2.85	2.73	1.61	0.91	1.55	1.65	1.91	2.56	2.93	3.55	4.15

7 Results and Conclusions

After the selection, the DT output distributions in data agree within the systematic uncertainties with the expected background prediction. Therefore the DT output distributions are used to set limits on the Higgs boson inclusive production cross section $\sigma(p\overline{p} \to H + X)$ assuming SM values for the branching ratios. Limits are calculated using a modified frequentist method (CLs), with a log-likelihood ratio (LLR) test statistic [9]. To minimize the degrading effects of systematics, the individual background contributions are fitted to the data observation by maximizing a profile likelihood function for each hypothesis [10].

Table 2 presents expected and observed upper limits at 95% CL. Figure 3a shows the expected and observed limits while Figure 3b shows the corresponding LLR distribution. At $M_H = 165$ GeV, the observed limit ratio is 0.91, with 0.97 expected, indicating that a standard model Higgs boson of this mass is excluded at the 95% CL.

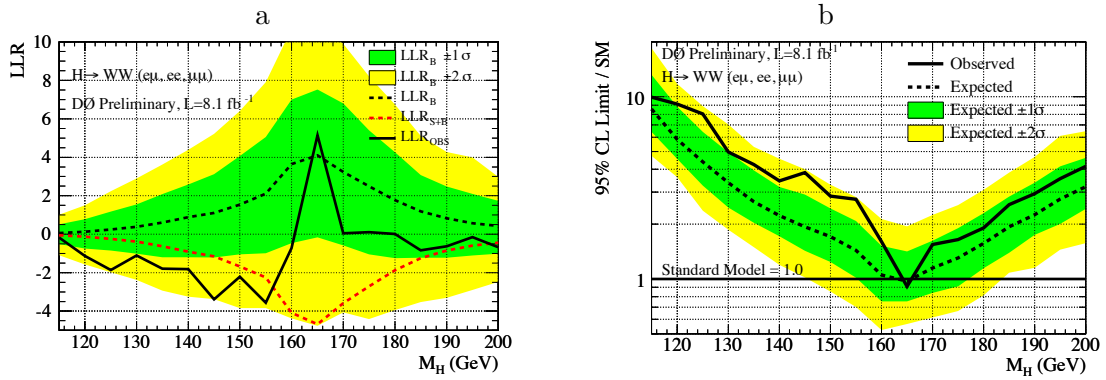

Figure 3: The observed LLR with the expected LLR for S and S+B hypothesis with green and yellow bands indicating one and two sigma bands is shown in (a) while (b) shows the excluded cross section ($\sigma(p\overline{p} \to H + X)$) at 95% CL in units of the SM cross section.

1. DØ Collaboration, V. Abazov *et al.*, Nucl. Instrum. Methods Phys. Res. A. **565**, 463 (2006).
2. T. Sjöstrand *et al.*, Comp. Phys. Comm. **135**, 238 (2001), we use version 6.323 or later.
3. M.L. Mangano, M. Moretti, F. Piccinini, R. Pittau, A. Polosa, JHEP **0307**, 001 (2003), we use version 2.11.
4. J. Pumplin et al., JHEP **07**, 012 (2002).
5. R. Brun and F. Carminati, CERN Program Library Long Writeup W5013, 1993 (unpublished).
6. G. Bozzi, S. Catani, D. de Florian, M. Grazzini, Phys. Lett.B 564 (2003) 65 [hep-ph/0302104]; Nucl. Phys. B 737 (2006) 73 [hep-ph/0508068].
7. S. Frixione and B.R. Webber, JHEP 0206 (2002) 029 [hep-ph/0204244].
8. T. Binoth, M. Ciccoli, N. Kauer, M. Krämer, JHEP **0503**, 065 (2005), JHEP **0612**, 046 (2006).
9. T. Junk, Nucl. Instrum. Methods Phys. Res. A. **434**, 435 (1999). A. Read, CERN 2000-005 (30 May 2000).
10. W. Fisher, FERMILAB-TM-2386-E.

Measurement of the $pp \to W \to \ell\nu$ Charge Asymmetry at $\sqrt{s} = 7$ TeV

Josh Bendavid for the CMS Collaboration

We present a measurement of the lepton charge asymmetry in $pp \to W \to \ell\nu$ decays at $\sqrt{s} = 7$ TeV with the CMS detector at the LHC. Results are presented corresponding to 36 pb^{-1} of integrated luminosity for both the electron and muon channels in 6 bins of lepton pseudorapidity up to $|\eta| = 2.4$ and $|\eta| = 2.1$ respectively. The measurements are compared to the theoretical predictions and the results are expected to provide additional constraints on the parton distribution functions of the proton.

1 Introduction

Production of W bosons in pp-collisions is expected to be charge-asymmetric, with more W^+ bosons being produced than W^-, due to the prevalence of u quarks over d quarks in the proton. The ratio of W^+ to W^- production is sensitive to the proton structure, and in particular the ratio of u to d quarks in the Parton Distribution Functions (PDF's). The inclusive cross section ratio has been measured previously in CMS [1] and found to be consistent with Standard Model expectations with several different PDF's [2] [3]. Measuring the charge asymmetry as a function of rapidity can provide additional information about the proton structure. The presence of the neutrino in $W \to \ell\nu$ prevents to directly reconstruct the rapidity of the W boson in hadron colliders, and leads instead to the lepton charge asymmetry as the experimentally accessible observable, defined as

$$\mathcal{A}(\eta) = \frac{\mathrm{d}\sigma/\mathrm{d}\eta_\ell(W^+ \to \ell^+\nu) - \mathrm{d}\sigma/\mathrm{d}\eta_\ell(W^- \to \ell^-\bar{\nu})}{\mathrm{d}\sigma/\mathrm{d}\eta_\ell(W^+ \to \ell^+\nu) + \mathrm{d}\sigma/\mathrm{d}\eta_\ell(W^- \to \ell^-\bar{\nu})}. \quad (1)$$

The lepton charge asymmetry is measured in both the electron and muon channels, in 6 bins of absolute pseudorapidity up to $|\eta| = 2.4$ and $|\eta| = 2.1$ respectively. Since the $V - A$ structure of the W decay introduces a dependence of the charge asymmetry on the lepton p_T, results are measured and compared to theory within two well-defined phase space regions corresponding to lepton p_T cuts of 25 and 30 GeV, with no cuts on the neutrino p_T or missing transverse energy.

2 Lepton Identification

Both electrons and muons are well-reconstructed in the CMS detector, a detailed description of which can be found elsewhere [4]. Electrons are reconstructed with the combination of a cluster in the Electromagnetic Calorimeter (ECal) and a track in the silicon tracker and pixel detector. Due to the large amount of material in the tracker, electron tracks are reconstructed using a Gaussian Sum Filter (GSF) algorithm[5] which takes into account non-Gaussian energy losses through Bremsstrahlung emission. The main sources of fake electrons from QCD are inelastic scattering of charged hadrons in the ECal, photons from neutral meson decays which convert in the beam-pipe or pixel detector, and electrons from heavy flavour decays. Electrons are required

to be isolated, with a cut on the total ECal + Hadronic Calorimeter (HCal) + Track transverse energy within a cone around the electron. There are also cuts on the shower shape as well as the geometric compatibility of the track with the ECal cluster. Finally in order to reject conversions, electrons are required to have no missing hits at the beginning of the track, and electrons with a nearby collinear oppositely-charged track are rejected. In order to suppress Drell-Yan background, events with a second loosely identified electron with $p_T > 15$ GeV are rejected. The large amount of material in the tracker poses a special challenge for the identification of the electron charge, which can be confused by the presence of a Bremsstrahlung photon which converts near to the prompt electron track. To minimize the charge mis-identification, three complementary measurements of the electron charge are required to agree. These are the charge of the GSF track, the charge of the corresponding standard Kalman Filter track, and the signed $\Delta\phi$ between the hits in the pixel detector and the ECal cluster. The level of charge confusion after this requirement is around 0.1% in the ECal barrel, and 0.4% in the endcaps.

Muons are reconstructed using the combination of the muon chambers with the silicon tracker and pixel detector. Since the level of muon fakes from QCD is lower than for electrons, fewer selection cuts are needed. Muons are required to have a good quality combined fit between the tracker and the muon detectors. A loose transverse impact parameter cut of 2 mm with respect to the beam-line is imposed in order to suppress background from cosmics. Isolation is not employed for the muon selection, since it is instead used as part of the signal extraction. As for the electron case, events with a second muon with $p_T > 15$ GeV are rejected to suppress Drell-Yan background.

3 Signal Extraction

After the lepton identification and kinematic selection, the Monte Carlo predicts that the electron sample is comprised of about 28% QCD, and 6.5% electroweak backgrounds (mainly remaining Drell-Yan as well as $W \to \tau\nu$ events). Similarly the expectation for the muon sample is about 13% QCD and 6.9% electroweak backgrounds. The final charge asymmetry is extracted using complementary methods for the two channels, with largely orthogonal systematic uncertainties. In the electron case, the signal is extracted using a binned likelihood fit to the missing transverse energy distribution, as reconstructed using the particle flow algorithm[6]. The signal template is obtained from simulation, with the missing transverse energy response and resolution modeled from hadronic recoil in $Z \to ee$ events. The background template is obtained from data using a QCD-enriched control region with inverted track-cluster matching cuts. In the muon channel, the signal is extracted fitting a modified isolation variable, where real isolated muons produce a peak consistent with a minimum ionizing particle. The signal shape is modeled from $Z \to \mu\mu$ events, and the parameterization for the QCD continuum is constrained from simulation and from a data control region. The remaining Drell-Yan background is subtracted from simulation, normalized to the $Z \to \mu\mu$ peak in data. Signal extraction fits for one pseudorapidity bin are shown in Figure 1.

4 Systematic Uncertainties

The main sources of systematic uncertainties are the charge-independence of the lepton reconstruction and identification efficiency, the electron energy scale and muon momentum scale, and the uncertainties associated with the signal extraction. The main signal extraction systematic in the electron channel is the uncertainty associated with the modeling of the hadronic recoil from $Z \to ee$. Instead for the muon case, the main systematic in the signal extraction is the normalization of the remaining Drell-Yan background. The systematics are largely independent, since the electron and muon reconstruction use in part different subdetectors, and largely dif-

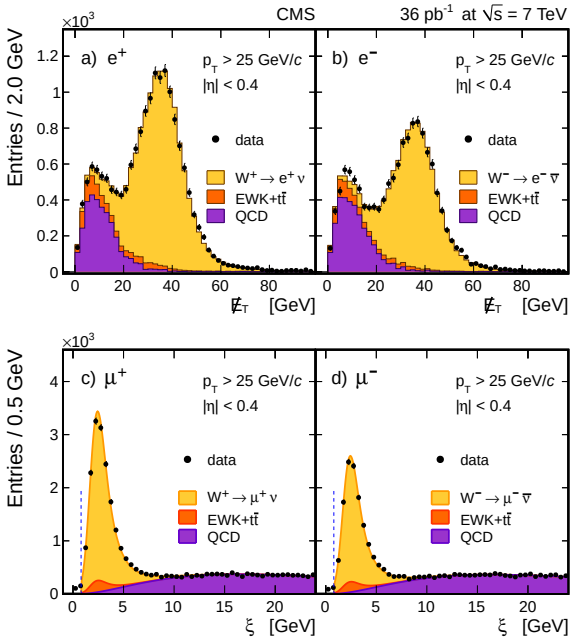

Figure 1: Signal extraction fits for the electron and muon channels in the $0.0 \leq |\eta| < 0.4$ pseudorapidity bin.

ferent cuts, and the electron energy measurement is dominated by the ECal, whereas the muon momentum measurement in this momentum range comes from the tracking detector.

5 Results

The measured lepton charge asymmetry in the electron and muon channels for the two different lepton p_T cuts are shown in Figure 2, with the results from the two channels in good agreement with each other. The measured asymmetry is compared with theoretical predictions using MCFM with the CT10W and MSTW2008NLO PDF's and the experimental uncertainties are comparable in size to the PDF uncertainties in the theory prediction. The data suggests a slightly flatter pseudorapidity dependence than the predictions considered here, and the measurement is precise enough to provide new inputs to the global PDF fits.

Acknowledgments

We wish to congratulate our colleagues in the CERN accelerator departments for the excellent performance of the LHC machine. We thank the technical and administrative staff at CERN and other CMS institutes, and acknowledge support from: FMSR (Austria); FNRS and FWO (Belgium); CNPq, CAPES, FAPERJ, and FAPESP (Brazil); MES (Bulgaria); CERN; CAS, MoST, and NSFC (China); COLCIENCIAS (Colombia); MSES (Croatia); RPF (Cyprus); Academy of Sciences and NICPB (Estonia); Academy of Finland, ME, and HIP (Finland); CEA and CNRS/IN2P3 (France); BMBF, DFG, and HGF (Germany); GSRT (Greece); OTKA and NKTH (Hungary); DAE and DST (India); IPM (Iran); SFI (Ireland); INFN (Italy); NRF and WCU (Korea); LAS (Lithuania); CINVESTAV, CONACYT, SEP, and UASLP-FAI (Mexico); PAEC (Pakistan); SCSR (Poland); FCT (Portugal); JINR (Armenia, Belarus, Georgia, Ukraine, Uzbekistan); MST and MAE (Russia); MSTD (Serbia); MICINN and CPAN (Spain); Swiss Funding Agencies (Switzerland); NSC (Taipei); TUBITAK and TAEK (Turkey); STFC (United Kingdom); DOE and NSF (USA).

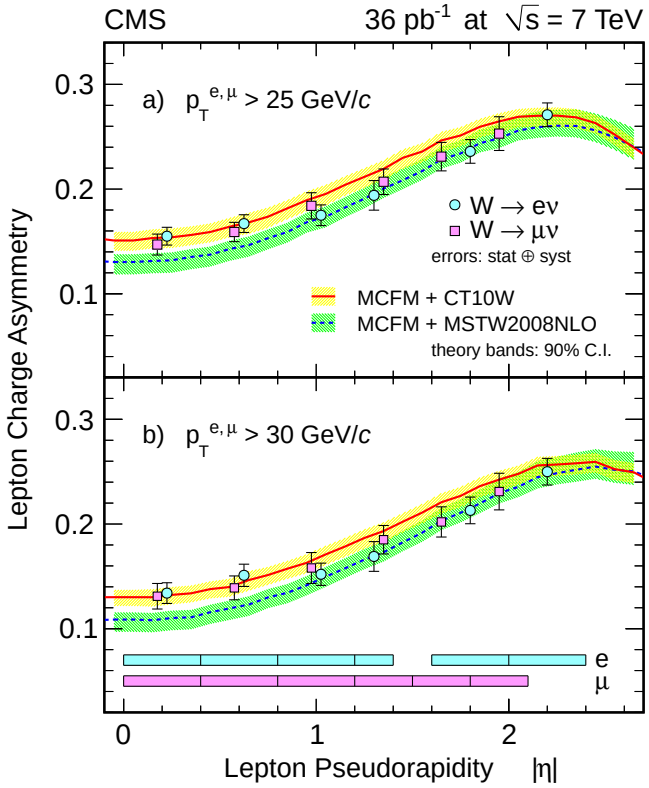

Figure 2: Lepton charge asymmetry in the electron and muon channels for $p_T^\ell > 25$ GeV (top) and $p_T^\ell > 30$ GeV (bottom). No explicit cut is applied on missing transverse energy.

References

1. Measurements of Inclusive W and Z Cross Sections in pp Collisions at $\sqrt{s} = 7$ TeV. *JHEP*, 2:2–40, 2011.
2. Hung-Liang Lai et al. New parton distributions for collider physics. *Phys. Rev.*, D82:074024, 2010.
3. A. D. Martin, W. J. Stirling, R. S. Thorne, and G. Watt. Parton distributions for the LHC. *Eur. Phys. J.*, C63:189–285, 2009.
4. The CMS experiment at the CERN LHC. *JINST*, 0803:S08004, 2008.
5. W. Adam et al. Reconstruction of Electrons with the Gaussian-Sum Filter in the CMS Tracker at the LHC. *CMS Note*, 2005/001, 2005.
6. Particle-flow commissioning with muons and electrons from j/psi, and w events at 7 tev. *CMS PAS*, PFT-2010-003, 2010.

Study of $W\gamma$ events at the CMS with 7 TeV LHC data

D. Majumder, on behalf of the CMS collaboration.
Tata Institute of Fundamental Research,
1 Homi Bhabha Road, Mumbai 400 005, India.

Abstract

The measurement of the inclusive cross section for $W\gamma$ production is presented based on 36 pb^{-1} of data acquired with the CMS detector from 7 TeV LHC collisions in 2010. Comparisons are made with the predictions of the standard model. The W bosons are identified through their leptonic decays to electrons and muons. The $W\gamma$ cross section is sensitive to anomalous triple-gauge couplings and hence this measurement probes physics beyond the standard model.

1 Introduction

Diboson productions ($W\gamma$, WW, WZ, $Z\gamma$, ZZ) are at the frontier of the standard model (SM) physics to be studied at the LHC before embarking on the search for physics beyond the standard model. In particular, the production rate of the $W\gamma$ process is large enough to be measured with data from the first year of the running of the LHC at a centre-of-mass energy of 7 TeV. The presence of anomalous $WW\gamma$ coupling (ATGC) modifies the cross section and the photon transverse momentum (p_T^γ) distribution and hence the measurement of the cross section is the first step towards the determination of the $WW\gamma$ coupling values. Here we present the first measurement of the cross section of $W\gamma$ production at $\sqrt{s} = 7$ TeV, using 36 pb^{-1} of data collected by the CMS detector in 2010. The measurement was done in the electron and muon decay modes of the W-boson.

2 $W\gamma$ event selection

The CMS detector and its trigger and data acquisition system [1] was used to record events from the LHC proton-proton collisions. The selection of potential $W\gamma$ events was done using single electron or single muon triggers, which require the presence of at least one electron or a muon with a transverse momentum above a given threshold, in the event. The $W\gamma$ events are studied in the final state $\ell\nu\gamma$, where ℓ represents either an electron or a muon.

The $W\gamma$ production cross section is measured within the phase space defined by $E_T^\gamma > 10$ GeV and $\Delta R(\ell,\gamma) > 0.7$ where E_T^γ is the transverse energy of the photon in the $W\gamma$ final state and $\Delta R(\ell,\gamma) \equiv \sqrt{(\eta_\ell - \eta_\gamma)^2 + (\phi_\ell - \phi_\gamma)^2}$. η_ℓ and η_γ are the pseudorapidities of the lepton and the photon respectively and ϕ_ℓ and ϕ_γ are their azimuthal angles.

The main background to the detection of $W\gamma$ events are W+jets, where the final state contains a W-boson and the photon is faked by the jet. This background is estimated from data using the methods described in Section 3. The lesser backgrounds are due to $t\bar{t}$ events, multijet QCD processes and other diboson events. These backgrounds are determined using event samples from Monte Carlo event generators. The W+jets, Z+jets and $t\bar{t}$ events were generated using a combination of the MADGRAPH [2] and PYTHIA [3] event generators while the rest were generated using only PYTHIA. Monte Carlo generated samples were processed using a GEANT4-based[4] simulation of the CMS detector and reconstructed in the same way as those from the collision data. For the background determination, all Monte Carlo samples are normalized to the integrated luminosity of the collision dataset and next-to-leading order cross section predictions were used.

The electrons are reconstructed in the electromagnetic calorimeter (ECAL) [5] and are identified using two sets of criteria, one based on the electron shower shape in the ECAL and the other based on the spatial matching of the charged track to the cluster of energy deposited in the ECAL. These selection criteria are designed to have a good rejection for jets from QCD multijet processes where the jet may be misidentified as an electron. The selection efficiency is about 80% for electrons from the decay of the W-boson. Electrons

originating from the pair production by photons interacting in the material of the detector are suppressed by the CMS electron reconstruction algorithm [6].

The muon reconstruction in CMS utilises information from both the muon chambers as well as the silicon tracker, to build up track segments which are finally matched to produce a muon candidate. For a well-reconstructed muon, its track should have at least 11 hits in the silicon tracker and should originate from the primary vertex in the event. The muon selection criteria has an efficiency of 95%.

The electrons and the muons are further required to be isolated, with energy deposits in the surrounding detector elements that are below required values. Both the electron and the muon selection criteria used in this analysis follow the standard selection used for the measurement of the W and Z boson cross section in CMS [7]. The W-boson candidates are reconstructed using a well-reconstructed charged lepton and the missing transverse energy ($\not\!\!E_T$), due to the neutrino from W-boson decay, in the event. Both the electrons and muons in the final states are required to have a transverse momentum above 20 GeV/c. The electrons' and the muons' pseudorapidities should be $|\eta_e| < 2.5$ and $|\eta_\mu| < 2.1$, respectively. The $\not\!\!E_T$ in the detector is reconstructed using the particle-flow (PF) method [8], which aims to reconstruct every particle in an event by combining the information from all CMS subdetector systems. The particles reconstructed are the electrons, the photons, the muons and the charged and neutral hadrons. The PF $\not\!\!E_T$ is then evaluated as the negative of the vector sum of the transverse momenta of all reconstructed particles in the event [9]. For an event to qualify as one containing a W-boson candidate, the value of PF $\not\!\!E_T$ should be above 25 GeV.

The photon candidates are reconstructed as clusters of energy deposited in the ECAL with the photon pseudorapidity in the range $|\eta_\gamma| < 1.44$ or $1.57 < |\eta_\gamma| < 2.5$. The photon selection criteria is aimed at reducing fakes due to electrons, by imposing the requirement that there should not be any hits in the pixel detector pointing at the ECAL energy deposit. The ratio of photon energy deposit in the hadron calorimeter (HCAL), which lies just behind the ECAL, to that in the ECAL should be less than 0.05. The photon is also required to be isolated in the tracker and the calorimeters. Further, the electromagnetic shower profile in pseudorapidity must be consistent with that of a photon [6]. The photon's selection criteria are mostly geared towards strongly suppressing misidentified jets and has an efficiency of 90%, while achieving a significant reduction in the number of the fake jets.

3 Determination of background

With the above selection criteria, 452 $W\gamma$ events are selected in the electron channel, while in the muon channel 520 events are selected. The background contamination in these events are evaluated using both the data as well as the Monte Carlo simulations. Two complementary approaches are used to determine the fake photon background.

The first approach, the *template or shape method* uses the photon shower shape profile in pseudorapidity, denoted by $\sigma_{\eta\eta}$, which describes the spread of the photon's electromagnetic shower in the pseudorapidity direction. Fake photons from jets have a different $\sigma_{\eta\eta}$ distribution from real photons and hence templates of $\sigma_{\eta\eta}$ for real and fake photons can be used to determine the background component in data. An extended maximum likelihood fit is used to obtain the signal component in the selected events, as shown in Fig. 1 (left) for the muon channel, with a particular E_T^γ range of 10 GeV$< E_T^\gamma <$20 GeV. The background yield using the shape method is 213.6$\pm$15.6 (stat.) $\pm$23.9 (syst.) for the muon channel and 213$\pm$ 16.1 (stat.) $\pm$24 (syst.) for the electron channel. The systematic uncertainty is mainly due to the variation of the signal template shapes in data and Monte Carlo and the contribution of real photons in the background templates obtained from the QCD multijet events.

The second method, the *ratio method*, is based on the assumption that the jets misidentified as photons in W+jets events have the same properties as the jets from QCD multijet events. The E_T^γ-dependent ratio of the number of fake photons being isolated to that being non-isolated is determined from an independent QCD multijet sample in data, which is then folded in with the number of events with a W-boson and a non-isolated fake photon, which yields the number of W+jets events according to the relation

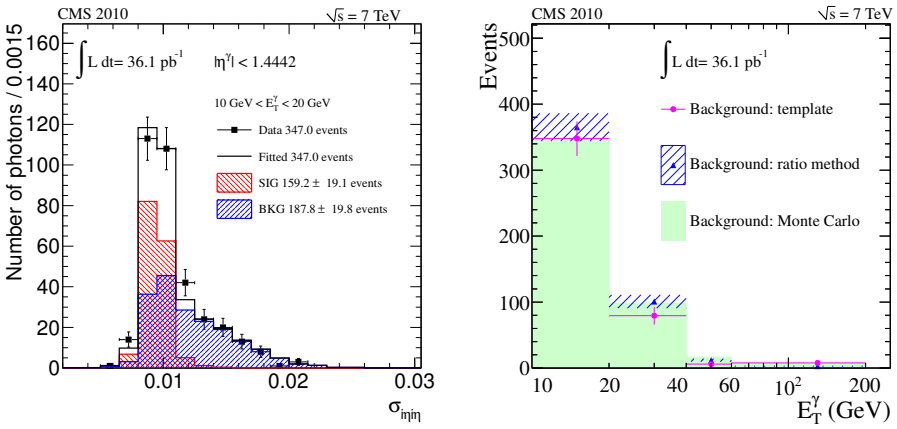

Figure 1: The fit of the signal (true photon) and the background (fake photon) $\sigma_{\eta\eta}$ shapes to the data to extract the signal component (left) and the comparison of the background yields from the shape method, the ratio method and Monte Carlo prediction for the electron and the muon channels combined (right). Both the statistical and systematic uncertainties are included.

$$N_{\text{W+jets}} = \left(\frac{N_{\text{isolated }\gamma}}{N_{\text{non-isolated }\gamma}}\right)_{\text{QCD multijet}} \cdot N_{\text{W+non-isolated }\gamma}$$

The non-isolated photon condition imposed is that the fake photon candidates should pass all the photon selection requirements listed in Section 2 but fails the tracker isolation requirement. The background estimated using the ratio method gives 260.5±18.7 (stat.) ±16.1 (syst.) events in the muon channel and 220.0±15.8 (stat.) ±13.9 (syst.) events in the electron channel. The systematic uncertainties involved are due to the modelling of the ratio distribution as well as due to the contamination of the real photons in the ratio obtained from the jet-triggered dataset.

The agreement between the shape and the ratio methods are shown in Fig. 1 (right). The two methods yield similar background estimates, which are also compared with the Monte Carlo prediction of the W+jets background. The ratio method has a smaller systematic uncertainty than the shape method and thus in the determination of the cross section, the background estimated using the ratio method is used.

The smaller backgrounds that are measured directly from the Monte Carlo simulated datasets have systematic uncertainties on them mostly due to the electron, photon and muon energy scale uncertainties.

4 Estimation of the cross section

The distribution of the photon transverse energy for the selected $W\gamma$ candidate events is shown in Fig. 2 (left) with the contribution from the signal and backgrounds shown separately. The E_T^γ distribution with a reference value of anomalous $WW\gamma$ coupling is also shown. The data is found to agree well with the SM signal and background prediction. The cross section is estimated using the formula

$$\sigma \times \mathcal{BR}(W\gamma \to \ell\nu_\ell\gamma) = \frac{N_{events} - N_{bkg}}{\mathcal{A}\cdot\epsilon\cdot\mathcal{L}}$$

where N_{events} and N_{bkg} are the number of selected $W\gamma$ candidate events and the number of estimated background events respectively. $\mathcal{A}$ and ϵ are the fiducial acceptance of the detector and the efficiencies of the various event selection criteria while $\mathcal{L}$ is the integrated luminosity of the dataset used in the measurement.

The cross section for the combined electron and the muon channels is estimated to be 56.3±5.0 (stat.) ±5.0 (syst.)±2.3(lumi.) pb which is in good agreement with the SM predicted value of 49.4±3.8 pb. The ratio method gives a systematic uncertainty of 6.3% and 6.4% for the electron and muon channels respectively. The photon energy scale uncertainty is 4.2%

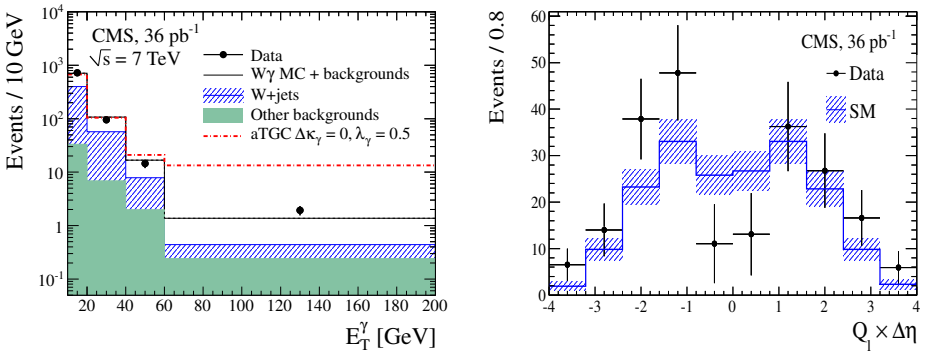

Figure 2: Left: The transverse energy distribution for photons in the selected $W\gamma$ events. The data are shown in black points with error bars while the expected SM $W\gamma$ signal is shown as a black solid histogram. The blue hatched histogram are the fake photons from jets as measured using the ratio method. The other backgrounds like QCD, $t\bar{t}$ and dibosons are shown in green. The red dot-and-line histogram shows the E_T^{γ} distribution in the presence of a reference value of anomalous $WW\gamma$ coupling. Right: The background-subtracted charge-signed rapidity difference between the photon and the charged lepton, for the combined electron and muon channels of $W\gamma$ production, is shown for data and SM simulation. The results of the Kolmogorov-Smirnov test of the agreement between data and MC prediction is 57%, which indicates a reasonable agreement.

for the electron channel and 4.5% for the muon channel. The uncertainty on the integrated luminosity is 4% [10].

5 The radiation amplitude zero

The radiation amplitude zero or *RAZ* is a unique feature of the $W\gamma$ production in the SM where the amplitude for the production of $W\gamma$ events vanish for certain angles that the W-boson makes with the incoming quark. A convenient variable at hadron colliders for studying the RAZ is $Q_\ell \cdot (\eta_\gamma - \eta_\ell)$ [11], where Q_ℓ is the charge of the lepton. This variable shows a dip at zero indicating the presence of the SM RAZ in the $W\gamma$ production. ATGC destroys the RAZ feature since is depends critically on the SM gauge nature of the $WW\gamma$ coupling. Further, next-to-leading order effects accompanying the $W\gamma$ production obscures the dip and makes the detection of the RAZ challenging at the LHC. The plot of $Q_\ell \cdot (\eta_\gamma - \eta_\ell)$ from data and the SM $W\gamma$ signal is shown in Fig. 2 (right) and show a reasonable agreement, within error estimates.

6 Summary

This paper presents the first study of the $W\gamma$ event production at the LHC at centre of mass energy of 7 TeV, made using the CMS detector. A measurement of the $W\gamma$ cross section is done using the electron and muon decay channels of the W-boson and the measured value is found to be in good agreement with the prediction of the standard model. An attempt has also been made to study the radiation amplitude zero feature of the SM $W\gamma$ production and with the limited data from the first year of the running of the LHC, the data is found to be consistent with the SM, though with a large uncertainty. The measurement of the cross section was one of the most important goals of this analysis and is the first step towards the determination of the $WW\gamma$ couplings.

References

1. R. Adolphi *et al.* [CMS Collaboration], JINST **3**, S08004 (2008).
2. F. Maltoni, T. Stelzer, JHEP **0302**, 027 (2003). [hep-ph/0208156].
3. T. Sjostrand, S. Mrenna, P. Z. Skands, JHEP **0605**, 026 (2006). [hep-ph/0603175].

4. S. Agostinelli *et al.* [GEANT4 Collaboration], Nucl. Instrum. Meth. **A506**, 250-303 (2003).
5. CMS Collaboration, CMS Physics Analysis Summary **CMS-PAS-EGM-10-004** (2010).
6. CMS Collaboration, CMS Physics Analysis Summary **CMS-PAS-EGM-10-005** (2010).
7. V. Khachatryan *et al.* [CMS Collaboration], JHEP **1101**, 080 (2011). [arXiv:1012.2466 [hep-ex]].
8. CMS Collaboration, CMS Physics Analysis Summary **CMS-PAS-PFT-09-001** (2009).
9. CMS Collaboration, CMS Physics Analysis Summary **CMS-PAS-JME-10-005** (2010).
10. S. Chatrchyan *et al.* [CMS Collaboration], [arXiv:1105.2758 [hep-ex]].
11. U. Baur, S. Errede, G. L. Landsberg, Phys. Rev. **D50**, 1917-1930 (1994). [hep-ph/9402282].

Analysis of $Z \to l^+l^-$ Polarization at CMS

Nhan Viet Tran on behalf of the CMS collaboration
Department of Physics and Astronomy, Johns Hopkins University,
3400 N. Charles St., Baltimore, MD 21218, USA

With approximately 35 pb^{-1} of LHC proton-proton collision data collected by CMS we study the Drell-Yan process $q\bar{q} \to Z \to l^+l^-$. Differential cross sections with respect to the invariant mass, rapidity, and transverse momentum are presented. The forward-backward asymmetry is measured as a function of the di-lepton invariant mass, and an analysis of the fully differential distribution leads to the measurement of the Weinberg weak-mixing angle.

1 Introduction

In the process $q\bar{q} \to Z/\gamma^* \to l^+l^-$, both the vector and axial vector couplings of electroweak bosons to fermions are present. In the Standard Model (SM), these couplings depend on the electroweak mixing angle, θ_W. This results in a forward-backward asymmetry, A_{FB}, in the number of Drell-Yan lepton pairs. In addition to being sensitive to the electroweak mixing angle, any deviation of the A_{FB} from the SM can be a sign of new physics from new gauge bosons, supersymmetry, or extra dimensions. The measurement of the A_{FB} can also improve QCD measurements and constrain Parton Distribution Functions (PDFs). The A_{FB} and $\sin^2\theta_W$ measurements by CDF[1] and D0[2] are given for reference. In addition to the traditional method of measuring $\sin^2\theta_W$ via the asymmetry, we also considering the measurement of the weak mixing angle via a multivariate likelihood analysis. Full information about the Drell-Yan process is parameterized as a function of the di-lepton rapidity Y, the di-lepton invariant mass m_{ll}, and the di-lepton decay angle θ^*_{CS} defined in the Collins-Soper frame[3] to reduce the effect of di-lepton transverse momentum.

The angular distribution for the Drell-Yan process is given in a simplified form as:

$$\frac{d\sigma}{d\cos\theta^*_{CS}} = A(1+\cos^2\theta^*_{CS}) + B\cos\theta^*_{CS} \tag{1}$$

Because the LHC is a pp collider, the quark direction is unknown and the definition of the Collins-Soper frame is defined using the boost direction of the di-lepton pair. This introduces a dilution of the asymmetric term since we can only determine the quark direction on a statistical basis. The forward-backward asymmetry is defined as

$$A_{FB} = \frac{N_F - N_B}{N_F + N_B} = \frac{3B}{8A} \tag{2}$$

where N_F (N_B) is the number of forward (backward) events. The A_{FB} is measured as a function of the di-lepton invariant mass where typically the slope of this quantity is sensitive to the electroweak mixing angle.

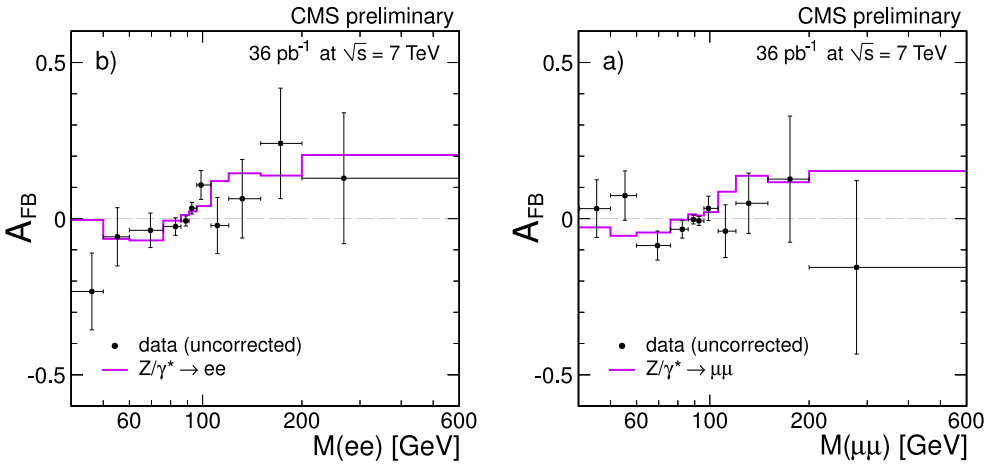

Figure 1: Uncorrected A_{FB} for the di-electron channel (left) and the di-muon channel (right).

Without applying any corrections, the uncorrected A_{FB} measurement is distorted from the original parton-level asymmetry because of bin-to-bin migration due to finite resolution of the detector and QED final state radiation (FSR). Moreover, the A_{FB} is further distorted by the detector acceptance and by the unknown quark direction at the LHC.

As an illustration of the multivariate analysis of the Drell-Yan process, we take the Standard Model description of electroweak interactions and PDFs in the proton as well-established and allow only the effective electroweak mixing angle θ_{eff} to be unconstrained, which is the same for both leptons and light quarks with the current precision of this analysis. We illustrate this method with analysis in the di-muon channel process. The choice of $\mu^+\mu^-$, as opposed to e^+e^- , is motivated by the simpler description of detector and background effects in this first study; however, we do not expect any limitation in the method for future application to other final states.

The formalism is built as an analytic description of the process at leading order where (next-to-)next-to-leading order effects are considered as corrections to the model. The description of the $pp \to Z/\gamma^* \to \mu^+\mu^-$ process is given by a probability distribution function of the triple differential cross-section in the observables , $P_{pp}(m_{ll}, Y, \cos\theta^*_{CS}; \sin^2\theta_{\text{eff}})$. This includes effects from PDFs, the partonic luminosity and the dilution, which requires an analytical parameterization of the PDFs. Then detector effects such as resolution and FSR, $R(m_{ll})$, and acceptance, $G(m_{ll}, Y, \cos\theta^*_{CS})$, are included such that we have the final description of the signal probability distribution function,

$$P_{sig}(m_{ll}, Y, \cos\theta^*_{CS}; \sin^2\theta_{\text{eff}}) = [P_{pp}(m_{ll}, Y, \cos\theta^*_{CS}; \sin^2\theta_{\text{eff}}) \times R(m_{ll})] \times G(m_{ll}, Y, \cos\theta^*_{CS}) \quad (3)$$

Information about the electroweak mixing angle is contained in the correlated three-dimensional shapes of the observables. The motivation for the introduction of the method is the improvement in statistical sensitivity; the increase in sensitivity is approximately 40% over traditional methods. Further details of the measurements of both A_{FB} and $\sin^2\theta_{\text{eff}}$ can be found in the public CMS results [4].

2 Measurement of A_{FB}

In these proceedings, we present the uncorrected A_{FB} vs. di-lepton mass and compare it to events generated with the POWHEG Next-to-Leading Order (NLO) generator and with detailed GEANT-based CMS simulation and reconstruction. Selection of both reconstructed electrons

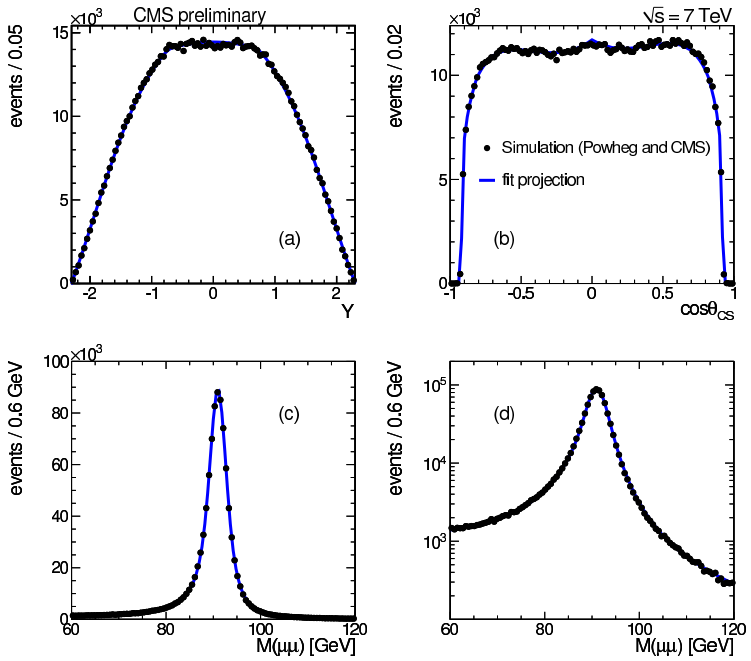

Figure 2: Projections of the fit model on simulation for the observables (a) rapidity, (b) $\cos\theta^*_{CS}$, and (c)/(d) di-lepton mass.

and muons require standard isolation and quality requirements which are detailed in the inclusive W and Z boson measurements at CMS [5]. The muons are required to have a $p_T > 20$ GeV and a pseudorapidity $|\eta| < 2.1$. The electrons are required to have an $E_T > 20$ GeV after energy scale corrections and $|\eta| < 2.5$ excluding the region from $1.442 < |\eta| < 1.560$. The uncorrected forward-backward asymmetry is given in Fig. 1 for the 2010 CMS dataset with an integrated luminosity of 36 pb^{-1}. The expectation from simulation is also given in Fig. 1; and for the given data sample, we observed agreement between the simulation and data.

3 Measurement of $\sin^2\theta_{\rm eff}$

For the measurement of $\sin^2\theta_{\rm eff}$, we perform a single parameter fit to extract the value of the electroweak mixing angle. The same isolation and quality requirements on the muons from the A_{FB} measurement are used. Looser phase space cuts are made in the Collins-Soper frame on the muons to increase sensitivity and accommodate the analytical acceptance, $p_T(CS) < 18$ and $|\eta|(CS) < 2.3$. In addition, there is a cut on the di-lepton transverse momentum to decrease contributions from next-to-leading order effects, $p_T(l^+l^-) < 25$ GeV. The fit value from simulation $\sin^2\theta_{\rm eff} = 0.2306 \pm 0.0004$ is in good agreement with the generated value $\sin^2\theta_{\rm eff}({\rm gen}) = 0.2311$. The fit result is shown in Fig. 2. In addition, we run 400 toy experiments and find the expected statistical error should be 0.0078. The pull distributions are found to be in good agreement with a unit Gaussian centered at zero.

The leading systematics come from the alignment and resolution model, the FSR modeling, and the PDF uncertainties. We also consider contributions from the LO model and initial state radiation, the fit model, and QCD background. The total systematic uncertainty is 0.0036 though these estimates are conservative and sometimes statistically limited. The total systematic uncertainty is less than the statistical errors.

With the CMS 2010 data sample of 40 pb^{-1}, we make a measurement of the weak mixing

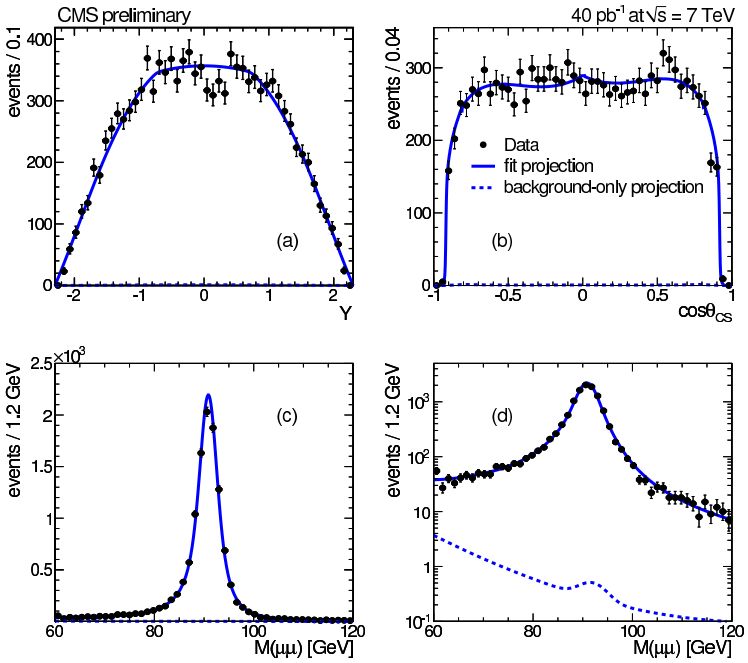

Figure 3: Projections of the fit model on CMS 2010 data for the observables (a) rapidity, (b) $\cos\theta^*_{CS}$, and (c)/(d) di-lepton mass.

angle. The fit value was kept blinded until evaluating all systematics and the final fit result is

$$\sin^2\theta_{\text{eff}} = 0.2287 \pm 0.0077(\text{stat.}) \pm 0.0036(\text{sys.}) \tag{4}$$

A final cross-check of the goodness-of-fit is found to be in agreement with simulation.

4 Summary

We have presented the measurement of the forward-backward asymmetry for the Drell-Yan process in pp collision at $\sqrt{s} = 7$ TeV. We have also presented the measurement of the effective electroweak mixing angle based on a multivariate likelihood fit which results in a value of $\sin^2\theta_{\text{eff}} = 0.2287 \pm 0.0077 \pm 0.0036$. We find both the A_{FB} distributions and the $\sin^2\theta_{\text{eff}}$ measurement to be consistent with the Standard Model predictions within uncertainties.

References

1. CDF Collaboration, Measurement of the forward-backward charge asymmetry of electron-positron pairs in $p\bar{p}$ collisions at $\sqrt{s} = 1.96$ TeV, Phys. Rev. D 71 (Mar, 2005) 052002. doi:10.1103/PhysRevD.71.052002.
2. The D0 Collaboration Collaboration, Measurement of the Forward-Backward Charge Asymmetry and Extraction of $\sin^2\theta^{\text{eff}}_W$ in $p\bar{p} \to Z\gamma^* \to e^+e^- + X$ Events produced at $\sqrt{s} = 1.96$ TeV, Phys. Rev. Lett. 101 (Nov, 2008) 191801. doi:10.1103/PhysRevLett.101.191801.
3. J. Collins and D. Soper, Angular Distribution of Dileptons in High-Energy Hadron Collisions, Phys. Rev. D 16 (1977) 2219. doi:10.1103/PhysRevD.16.2219.
4. CMS Collaboration, "Measurement of Forward-Backward Asymmetry of Lepton Pairs and the Weak-mixing angle at CMS", CMS PAS EWK-10-011 (2011).
5. CMS Collaboration, "Measurement of the W and Z inclusive production cross sections at $\sqrt{s} = 7$ TeV with the CMS experiment at the LHC", CMS PAS EWK-10-005 (2011).

Observation of $Z \to \tau_h\tau_\ell$ Decays with the ATLAS detector

Aimee Larner on behalf of the ATLAS Collaboration

A study of $Z \to \tau\tau$ decays has been performed with the ATLAS experiment at the Large Hadron Collider. The channel with one τ lepton decaying into an electron or muon and the second one into hadrons has been considered. The analysis is based on a data sample corresponding to an integrated luminosity of 8.3 pb^{-1} for the electron channel and 8.5 pb^{-1} for the muon channel, taken at a proton-proton centre-of-mass energy of 7 TeV. In the muon channel a total of 51 data events is selected, with a total estimated background of 9.9 ± 2.1 events. In the electron channel a total of 29 data events is selected, with an estimated background of 11.8 ± 1.7 events. The obtained number of events in data is compatible with the Standard Model expectation.

1 Introduction

Many new physics searches being undertaken by the ATLAS experiment [1], such as that for the Higgs boson, in particular in the $H \to \tau\tau$ channel, supersymmetric or exotic signatures include τ leptons in the final state. The $Z \to \tau\tau$ process is an important background and should be observed [2] and well measured. In this analysis final states were considered where one τ lepton decays leptonically and the other hadronically. It is possible to trigger on the single light leptons and obtain an unbiased sample of hadronically decaying τ leptons, which can be used for studies of reconstruction and identification of hadronically decaying τ leptons and τ triggers.

2 Object Selection

Following the requirement of a single light lepton trigger with a low p_{T} threshold, either a reconstructed electron or muon is selected together with a hadronically decaying τ lepton candidate. Electron identification uses calorimeter information, tracking information or a combination of both to define variables to accurately discriminate between real and fake electrons in particular from jets. Electrons are selected with $p_{\text{T}} > 15$ GeV and must pass "tight" level identification [3]. Muon identification uses Inner Detector tracks and Muon-Spectrometer tracks, combined using a chi-square (χ^2) matching procedure [4]. Selected muons must have $p_{\text{T}} > 15$ GeV.

Reconstruction of hadronically decaying τ leptons is seeded by jets reconstructed with the anti-k_{T} algorithm [5]. Tracks with $p_{\text{T}} > 1$ GeV which pass quality requirements are then associated to the τ candidates and various identification variables are calculated per candidate from the combined calorimeter and tracking information [6]. Selected τ candidates must pass "tight" cut-based identification [6].

Leptons from Z$\to \tau\tau$ decays are typically isolated, unlike those in the multijet background. Two isolation variables are defined, the first, $Iso_{PT}^{0.4}$, is a sum of transverse momenta of tracks in a cone of $\Delta R = 0.4$ [a] around the lepton, divided by its transverse momentum. For electrons and

[a] The distance ΔR in the $\eta - \phi$ space is defined as $\Delta R = \sqrt{\Delta\eta^2 + \Delta\phi^2}$.

muons the cut $Iso_{PT}^{0.4} < 0.06$ is applied. The second variable, $Iso_{ET}^{\Delta R}$, is a sum of the transverse energy of neutral and charged particles in the calorimeter, divided by the transverse momentum of the lepton. For electrons the cut $Iso_{ET}^{0.3} < 0.1$ is used, for muons $Iso_{ET}^{0.4} < 0.06$ is applied. For both variables the contribution to the sum of the track momenta or of the energies in the isolation cone from the light lepton itself is corrected for, using an inner cone of $\Delta R = 0.05$. Figure 1 shows the $Iso_{ET}^{0.4}$ and $Iso_{ET}^{0.3}$ variables for muons and electrons respectively.

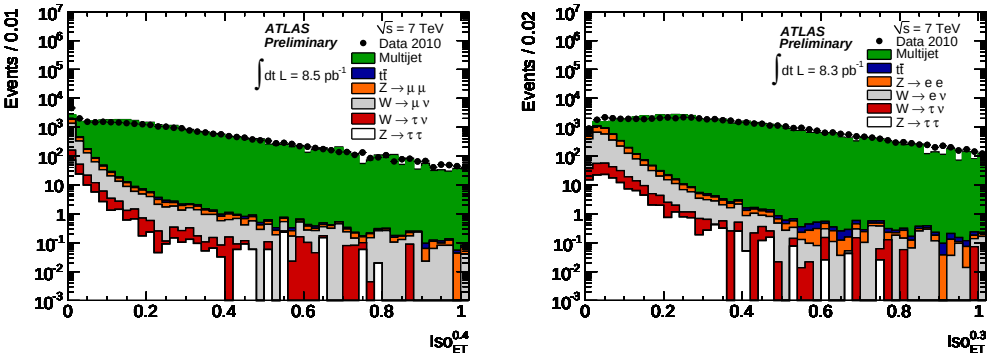

Figure 1: Isolation variables $Iso_{ET}^{0.4}$ and $Iso_{ET}^{0.3}$ for muons (left) and electrons (right) respectively, after selecting one τ candidate and one lepton. All backgrounds were obtained from Monte Carlo, weighted by cross-section and their sum normalized to data; they are represented by the shaded areas and the dots are the data.

3 Event selection

3.1 W + jets suppression cuts

W + jets is an important background, where the light lepton comes from the decay of the W, and one of the additional jets in the event is identified as the τ candidate. These events can be suppressed by requiring that the $E_{\mathrm{T}}^{\mathrm{miss}}$ vector be reconstructed inside of the region defined by the light lepton and the τ candidate. The following variable is defined:

$$\sum \cos\Delta\phi = \cos\left(\phi(\ell) - \phi(E_{\mathrm{T}}^{\mathrm{miss}})\right) + \cos\left(\phi(\tau_{\mathrm{h}}) - \phi(E_{\mathrm{T}}^{\mathrm{miss}})\right); \quad (1)$$

$\sum \cos\Delta\phi$ is zero when the two τ leptons are back to back, as is often the case in signal events. It is negative when the $E_{\mathrm{T}}^{\mathrm{miss}}$ lies outside of the azimuthal angle spanned by the decay products, as seen in Fig. 2. Cutting at $\sum \cos\Delta\phi > -0.15$ significantly reduces the W + jets contribution.

The transverse mass, calculated using the 4-vector of the light lepton and the $E_{\mathrm{T}}^{\mathrm{miss}}$ vector, defined as:

$$m_{\mathrm{T}}(\ell, E_{\mathrm{T}}^{\mathrm{miss}}) = \sqrt{2\, p_{\mathrm{T}}(\ell) \cdot E_{\mathrm{T}}^{\mathrm{miss}} \cdot (1 - \cos\Delta\phi(\ell, E_{\mathrm{T}}^{\mathrm{miss}}))} \quad (2)$$

also provides good separation. In Fig. 2 it is shown with all other cuts applied, further illustrating the strength of the $\sum \cos\Delta\phi$ cut.

3.2 Further cuts

To suppress contributions to the background from $Z \to \ell\ell$ + jets processes, a veto is placed on any event containing more than one light lepton and the visible mass, the invariant mass of the visible decay products, the light lepton and the τ candidate, is required to be in the window $35-75$ GeV. Additional requirements on the τ candidate ensure further multijet rejection. The τ candidate must have exactly one or three tracks, which is strongly characteristic of hadronic τ decays, and unit electric charge of opposite sign to the selected light lepton.

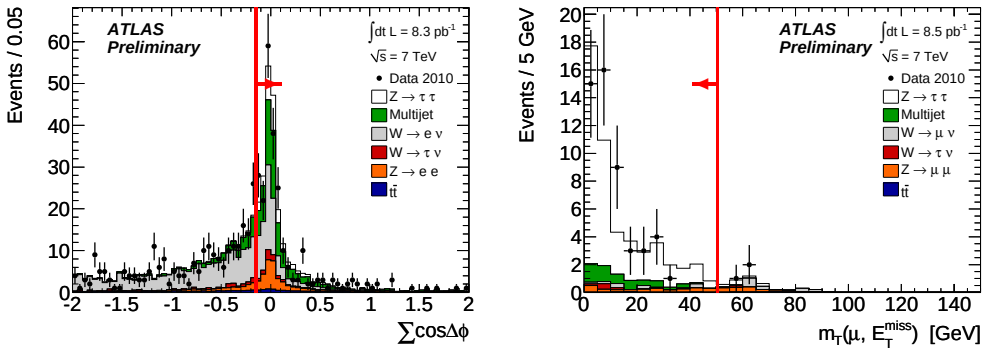

Figure 2: The distribution of $\sum \cos\Delta\phi$ (left) following the full object selections and dilepton veto, in the electron channel. The m_{T} distribution (right), with all other cuts applied, in the muon channel. The dots are the data and the contributions from background are indicated by the shaded areas.

4 Background estimation

The backgrounds from processes $Z \to \ell\ell$ and $t\bar{t}$ are estimated from Monte Carlo, normalized using a scale factor while $W \to \ell\nu$ and $W \to \tau\nu$ use Monte Carlo normalized to agree with data.

4.1 Data-driven multijet background estimation

The multijet background is estimated with a data-driven ABCD matrix method. The control samples are created by inverting the uncorrelated τ identification and lepton isolation requirements. The signal region A is defined as: isolated lepton and tight τ candidate, and the control regions are B: non-isolated lepton and tight τ candidate, C: isolated lepton and loose and not tight τ candidate and D: non-isolated lepton and loose and not tight τ candidate.

The multijet contribution to the signal region A can be calculated from Equation (3):

$$N^A = N^B \left(\frac{N^C}{N^D} \right), \tag{3}$$

where N^i is the number of multijet background events in region i. Since regions B, C, and D are not completely multijet-pure, corrections are applied for the expected contaminations from electroweak backgrounds from Monte Carlo in each region. Using these equations, the expected number of multijet events in the signal region A is:

$$N^A_{\mathrm{QCD}} = \begin{cases} 5.2 \pm 0.7\ (\mathrm{stat.}) \pm 0.7\ (\mathrm{syst.}) & \text{muon channel} \\ 6.8 \pm 0.6\ (\mathrm{stat.}) \pm 0.7\ (\mathrm{syst.}) & \text{electron channel}\,. \end{cases} \tag{4}$$

5 Observation of $Z \to \tau_h\tau_\ell$ candidates

After the visible mass cut there are 51 data events in the muon channel and 29 events in the electron channel. From the background estimates described for multijets, W, Z and $t\bar{t}$ decays, combined accounting for correlations between their uncertainties, there is a total estimated background of 9.9 ± 2.1 events in the muon channel and 11.8 ± 1.7 events in the electron channel. This is compatible with the Standard Model signal expectation of $39.9 \pm 1.8(\mathrm{stat.}) \pm 6.8(\mathrm{syst.})$ and $24.5 \pm 1.4(\mathrm{stat.}) \pm 5.9(\mathrm{syst.})$ events in the muon and electron channels respectively. The main contributions to the systematic uncertainties come from the τ fake rates from jets and electrons and the energy scale. The results for both channels are summarized in Table 1.

Figure 3 shows distributions of the visible mass of selected events, with the visible mass window marked by vertical red lines.

Table 1: Summary of observed numbers of events and a summary of the background estimations.

	Muon channel	Electron channel
Data (after all selections)	51	29
Total estimated background	9.9 ± 2.1	11.8 ± 1.7
Estimated multijet background	5.2 ± 0.7(stat.) ± 0.7 (syst.)	6.8 ± 0.6(stat.) ± 0.7 (syst.)
Estimated W, Z, $t\bar{t}$ background	4.7 ± 0.5(stat.) ± 1.5(syst.)	5.0 ± 0.6 (stat.) ± 1.4(syst.)
Data (after background subtraction)	41.1 ± 2.1	17.2 ± 1.7
SM signal expectation	39.9 ± 1.8(stat.) ± 6.7(syst.)	24.5 ± 1.4(stat.) ± 5.9(syst.))

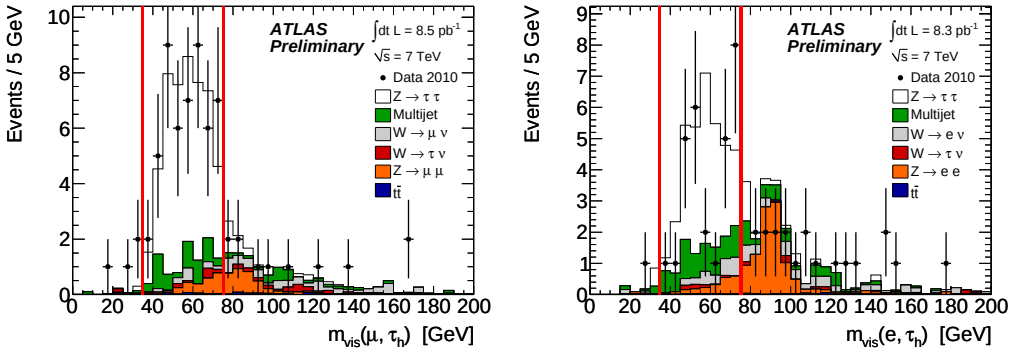

Figure 3: The distributions of the visible mass of the combination of the chosen τ candidate and the light lepton, for the muon (left) and electron (right) channels. The distributions are shown after the full event selection, except for the visible mass window. The dots are the data and the background contributions are the shaded areas.

6 Summary

An observation of $Z \to \tau_\ell \tau_h$ decays has been performed with the ATLAS experiment at the Large Hadron Collider at a proton-proton centre-of-mass energy of 7 TeV. The obtained number of events agrees with the Standard Model prediction.

References

1. The ATLAS Collaboration, *"The ATLAS Experiment at the CERN Large Hadron Collider"*, JINST **3** (2008) S08003.
2. The ATLAS Collaboration, *"Observation of $Z \to \tau_l \tau_h$ Decays with the ATLAS detector"*, ATLAS-CONF-2011-010: http://cdsweb.cern.ch/record/1331795, Feb, 2011.
3. The ATLAS Collaboration, *"Electron and photon reconstruction and identification in ATLAS: expected performance at high energy and results at $\sqrt{s} = 900$ GeV"*, ATLAS-CONF-2010-005: http://cdsweb.cern.ch/record/1273197, March, 2010.
4. The ATLAS Collaboration, *"Muon Performance in Minimum Bias pp Collision Data at $\sqrt{s} = 7$ TeV with ATLAS"*, ATLAS-CONF-2010-036: http://cdsweb.cern.ch/record/1277675, Jul, 2010.
5. M. Cacciari, G. P. Salam, and G. Soyez, *"The anti-k_T jet clustering algorithm"*, JHEP **04** (2008) 063.
6. The ATLAS Collaboration, *"Tau Reconstruction and Identification Performance in ATLAS"*, ATLAS-CONF-2010-086: http://cdsweb.cern.ch/record/1298857, Oct, 2010.

Observation of $W \to \tau\nu$ Production in pp Collisions at $\sqrt{s} = 7$ TeV

Abdollah Mohammadi on behalf of the CMS Collaboration
School of Particles and Accelerators, Institute for Studies in Theoretical Physics and Mathematics (IPM), Tehran, Iran; also at:
Shiraz University, Physics Department, 71454 Shiraz, Iran

The production of W bosons decaying into a tau lepton and a neutrino with the tau lepton decaying hadronically has been observed in LHC pp collisions at $\sqrt{s} = 7$ TeV with the CMS detector. The selection criteria provide a statistically significant signal on the top of QCD multi-jet and electroweak backgrounds. A data-driven method for the estimation of the QCD multi-jet background has been employed.

1 Introduction

Tau leptons serve as an important probe for many new physics processes at the LHC. Among others, experimental signatures that involve decays to tau leptons are crucial for searches of a light Higgs boson, Supersymmetry or extra dimensions.

Tau leptons can decay either leptonically via $\tau \to l\nu\bar{\nu}$ (l=e or mu, branching fraction is 36%) or into a hadronic jet and one tau-neutrino. Hadronic decay modes ($\tau_{\rm had}$) produce a highly collimated tau-jet signature, characterized by a low particle multiplicity that allows their separation from QCD-jets.

In the framework of the standard model, tau leptons are mostly produced in decays of electroweak vector bosons: $Z \to \tau^+\tau^-$ and $W^\pm \to \tau^\pm\nu$. These processes have relatively large cross sections and are among the largest sources of tau leptons at LHC. The $W \to \tau^\pm\nu$ channel benefits from a large production cross section, exceeding the production rate of $Z \to \tau^+\tau^-$ by nearly an order of magnitude. However, the experimental signature of a single tau-jet and undetected neutrino is challenging, requiring a good understanding of the tau identification and missing transverse energy (E_T^{miss}).

The study of $W \to \tau\nu$ production in the $\tau_{\rm had}\nu$ final state is an important calibration sample for understanding tau identification and reconstruction. Also, $W^\pm \to \tau^\pm\nu$ production has to be well understood as a test of the standard model and as a measure of important background process in several searches for new physics. In particular, it is the major background in the search for the charged Higgs boson in the $\tau\nu$ final state.

This study of $W \to \tau_{\rm had}\nu$ production has been conducted using 18.4 ± 0.7 pb^{-1} of collision data from the 2010 LHC run at $\sqrt{s} = 7$ TeV recorded with the CMS detector. See Ref. [1] for a measurement of the cross section for $Z \to \tau^+\tau^-$ production including tau-leptons reconstructed in the $\tau_{\rm had}$ final state.

2 Physics objects reconstruction

The particle flow (PF) reconstruction algorithm implemented at CMS [2] is used for identification of jets, muons, electrons, taus and E_T^{miss}. The PF technique utilizes the information from the whole event, aiming to provide a global event description at the level of individually reconstructed particles. Firstly, all tracks and energy clusters are reconstructed in each sub-detector. Next, all the candidates are associated in an optimal combination to one or more of these sub-detector signals, if they are compatible with the physics properties of each particle, and reconstructed in the event. The final set of particles (charged hadrons, neutral hadrons, photons, electrons and muons) is used to derive composite physics objects such as $\tau_{\rm had}$, jets and E_T^{miss}. The PF jets are clustered using the anti-k_T jet clustering algorithm [3] with distance parameter $R = 0.5$.

Typically, $\tau_{\rm had}$ is a highly-collimated jet comprising one or three charged mesons (predominantly $\pi^{\pm}$) and possibly one or two neutral pions always decaying via $\pi^0 \rightarrow \gamma\gamma$. The identification of $\tau_{\rm had}$ from W boson decays requires a robust algorithm and an efficient set of selection criteria, as it is one of the main discriminators against large QCD jet background.

The $\tau_{\rm had}$ identification algorithm used here is known as the Hadrons Plus Strips Algorithm (HPS) [4]. HPS starts from a high-p_T charged hadron and combines it with other nearby charged or neutral hadrons to reconstruct τ decay modes. The identification of π^0s is enhanced by clustering the PF electrons and photons in "strips" along the bending plane to take into account possible broadening of calorimeter signatures because of photon conversions.

3 Event selection

The following list of offline selection criteria is applied for the final event selection:

- There must be at least one HPS $\tau_{\rm had}$ candidate with $p_T > 30$ GeV and $|\eta| < 2.3$, and the leading track in the $\tau_{\rm had}$ candidate must have $p_T > 15$ GeV. Three different working points (Figure 1) for the isolation has been defined [5]. The definition of the medium, which has been used in this analyis follows as: there must be no PF charged hadron or photon candidates with $p_T > 0.8$ GeV within an isolation cone of size $\Delta R = 0.5$, (Those candidates which are associated to the tau decay signature are excluded.)

- Several cuts has been applied in order to rejects those electron and muons which fake taus. Furthermore we also veto the events which include good electron or muon. This cut supresses the W+Jet events where W decays either to muon or electron and jet fakes tau.

- We require $E_T^{miss} > 35$ GeV and we consider PF jets in an event with $p_T > 15$ GeV and $|\eta| < 3$, and compute the ratio, $R_{\rm HT}$, of the p_T of the $\tau_{\rm had}$ candidate to the sum of the p_T of the PF jets. We require $R_{\rm HT} > 0.65$.

  Further details about event selection can be found in elsewhere [6].

4 QCD Background Estimation

QCD events are the dominant background contribution to the final event sample. This background cannot be reliably estimated from simulation, so a data-driven method is used.

In the so-called "ABCD method," four regions are designated in a phase space defined by E_T^{miss} and $R_{\rm HT}$. We start with an event sample obtained with no cuts on E_T^{miss} and $R_{\rm HT}$, and then divide it into four subsamples as follows

- region A where $R_{\rm HT} > 0.65$ and $E_T^{miss} > 35$ GeV. This region is dominated by signal; we want to account for QCD background here.

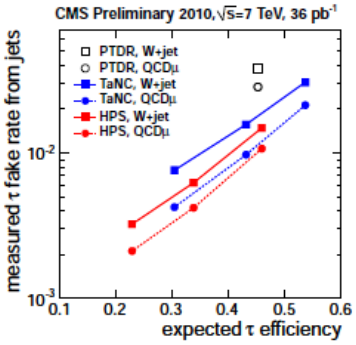

Figure 1: The measured fake rate as a function of efficiency evaluated using simulation for all working points for QCD m-enriched and W data samples. The PTDR points represent results of the fixed cone algorithm based on the PF taus

- region B where $R_{\mathrm{HT}} > 0.65$ and $E_T^{miss} < 35$ GeV
- region C where $R_{\mathrm{HT}} < 0.65$ and $E_T^{miss} < 35$ GeV
- region D where $R_{\mathrm{HT}} < 0.65$ and $E_T^{miss} > 35$ GeV.

In order to apply this method, we must assume that the event subsamples in regions B, C and D are dominated by QCD events, and there is a low statistical correlation between R_{HT} and E_T^{miss}. All other backgrounds have been neglected and no corrections have been applied due to the signal contribution in the B, C and D regions.

Figure 2 illustrates the transverse mass distributions of τ_{had} candidates and E_T^{miss} in regions B, C and D. One sees that indeed these regions are dominated by QCD background. The signal contribution is less than 1% in region C, and less than 5% and 10% in regions B and D, respectively. It has been shown [6] that the level of correlation between R_{HT} and E_T^{miss} is sufficiently low to yield accurate background estimation using the ABCD method

We estimate the yield of QCD background events in the signal region A from the numbers of events observed in the other regions. Specifically, we assume $N_A = (N_D \times N_B)/N_C$, and obtain $N_A = 109 \pm 6$ events, where the uncertainty is statistical only.

5 Results

After all selections, the expected yield of $W \rightarrow \tau\nu$ events as well as electroweak background contributions are estimated using simulation while the QCD multi-jet background is estimated from the ABCD method described above. With the selections used in this analysis, number of signal event is estimated to be 174 ± 3 (stat), the number of electroweak backgrounds (dominated by $W \rightarrow e\nu$) is estimated as 46 ± 2 (stat) and the QCD multijet contribution is 109 ± 6 (stat). The number of events observed in data is 372.

It should be mentioned that we have not yet assessed systematic uncertainties on the background predictions or on the signal efficiency.

The shape of the transverse mass distribution for QCD multi-jet events is estimated using a data-driven method. The strategy is to relax some cuts to move into a region where QCD is dominant, and normalize this shape to the number of QCD events estimated with the ABCD method. Figure 3 shows that when changing the isolation criterion or the R_{HT} cut (from 0.1 to 0.5), the QCD shape does not change drastically. We decided to use a working point where the contribution of electroweak processes and signal events under the mass peak is reduced to 15%, loosening the cut on R_{HT} from 0.65 to 0.3 and using a looser isolation requirement.

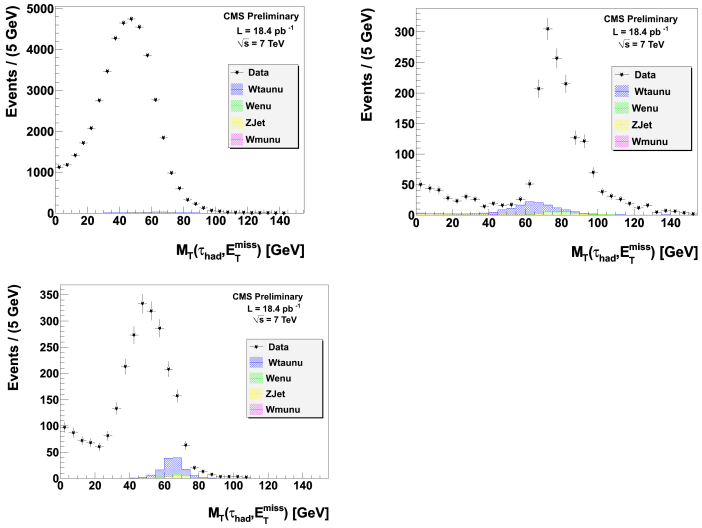

Figure 2: Transverse mass distributions of the $\tau_{\rm had}$ candidate and E_T^{miss} for the four designated regions in phase space: Region B (bottom left) where $R_{\rm HT} > 0.65$ and $E_T^{miss} < 35$ GeV, Region C (upper left) where $R_{\rm HT} < 0.65$ and $E_T^{miss} < 35$ GeV, and Region D (upper right) where $R_{\rm HT} < 0.65$ and $E_T^{miss} > 35$ GeV. The points represent the data. Simulated signal and electroweak backgrounds are represented by the filled histograms.

Figure 4 shows the transverse mass distribution for the final event sample, with the data-driven estimate of the QCD contamination.

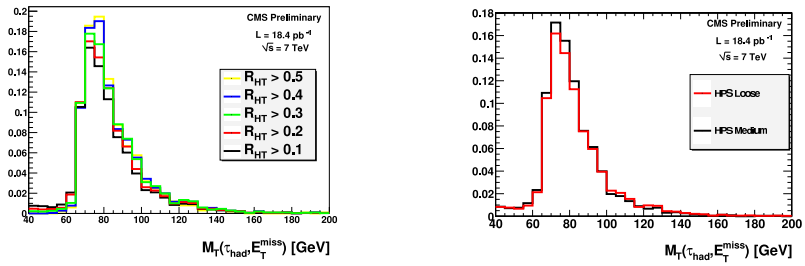

Figure 3: Effect of changing the $R_{\rm HT}$ and isolation criteria on the shape of Transverse Mass of $\tau_{\rm had}$ and E_T^{miss}.

6 Summary

We have statistically significant signal for $W \to \tau_{\rm had}\nu_\tau$ with the τ-lepton reconstructed in its hadronic decay modes, using 18.4 ± 0.7 pb^{-1} of data collected by the CMS Collaboration.

Acknowledgments

I would like to thank the CMS collaboration especially, L.Rebana, A.Nikitenko, M.Khakzad, M.V.Acosta, G.Bagliesi, M.Bachtis and A.N. Safonov for their helpful comments and cooperations.

References

1. CMS Collaboration , "Measurement of the Inclusive $Z \to \tau^+\tau^-$ Cross Section in pp Collisions at $\sqrt{s} = 7$ TeV",*CMS Physics Analysis Summary* **CMS PAS EWK-10-013**

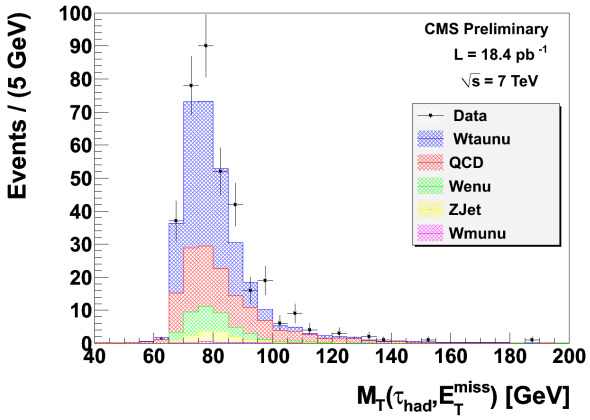

Figure 4: Transverse Mass of $\tau_{\rm had}$ and E_T^{miss} after all cuts

arXiv:1104.1617, submitted to JHEP

2. CMS Collaboration, "Particle-Flow Event Reconstruction in CMS", *CMS Physics Analysis Summary* **CMS PAS PFT-09-001** (2009)
3. Cacciari, M. and Salam, G. and Soyez, G, "The anti-k_T jet clustering algorithm", JHEP **04**, 063 (2008)
4. CMS Collaboration,"Tau Commissioning with 7-TeV data",*CMS Physics Analysis Summary* **CMS PAS PFT-10-004** (2010)
5. CMS Collaboration,"Performance of tau reconstruction algorithms in 2010 data collected with CMS", *CMS Physics Analysis Summary* **CMS PAS TAU-11-001** (2011)
6. CMS Collaboration,"Observation of $W \to \tau\nu$ Production in pp Collisions at $\sqrt{s} = 7$ TeV", *CMS Physics Analysis Summary* **CMS PAS EWK-11-002** (2011)

HIGGS PHYSICS IN WARPED EXTRA DIMENSIONS

FLORIAN GOERTZ
Institut für Physik (THEP), Johannes Gutenberg-Universität
D-55099 Mainz, Germany

In this talk, I present results for the most important Higgs-boson production cross sections at the LHC and the Tevatron as well as the branching fractions of the relevant decay channels in the custodial Randall-Sundrum model. The results are based on a complete one-loop calculation, taking into account all possible Kaluza-Klein particles in the loop. Due to the strong infrared localization of the top quark and the Kaluza-Klein excitations, the SM predictions receive sizable corrections in the model at hand. This could effect Higgs searches significantly.

1 Introduction

The Higgs boson represents the last missing ingredient of the Standard Model (SM) of Particle Physics. It offers the possibility to give masses to the weak gauge bosons and chiral fermions without breaking gauge invariance, which is important for a proper high energy behavior of the model. Electroweak precision measurements suggest that the SM Higgs boson is light, $m_h < 185\,\text{GeV}$ at 95% C.L.,[1] including the direct Limit $m_h > 114\,\text{GeV}$ from LEP2. Furthermore, theoretical arguments like unitarity, vacuum stability and triviality constrain the allowed range for the Higgs mass. In summary, we expect the SM Higgs boson to have a mass well below a TeV and to exhibit tree-level couplings to particles proportional to their mass. Imagine we do not discover the Higgs at the Large Hadron Collider (LHC) in the first years of running. Does this already mean that we have to abandon the corresponding mechanism of electroweak symmetry breaking? The answer is certainly no. Beyond the SM physics could feature a standard Higgs mechanism that could be much harder to detect, even for a Higgs mass easily accessible at the LHC. It is important to study Higgs physics in various models to be prepared for different possible scenarios. In this talk, I present results for Higgs production and decay within the custodial Randall-Sundrum (RS) model with gauge and fermion fields in the (5D) bulk and an infrared-brane Higgs sector. Here one expects big effects, due to the localization of the fields.

2 Aspects of the Randall-Sundrum Model

The RS model [2] provides an elegant possibility to address the large hierarchy between the electroweak scale M_{EW} and the Planck scale M_{PL} by means of a non-trivial geometry in a 5D Anti-de Sitter space. The fifth dimension is compactified on an S^1/Z_2 orbifold. The RS metric

$$ds^2 = e^{-2kr|\phi|}\eta_{\mu\nu}\,dx^\mu dx^\nu - r^2 d\phi^2\,, \tag{1}$$

with $\eta_{\mu\nu} = \text{diag}(1,\text{-}1,\text{-}1,\text{-}1)$ is such that length scales within the usual 4D space-time are rescaled by an exponential warp factor, depending on the position $\phi \in [-\pi, \pi]$ in the extra dimension. The curvature k and inverse radius r^{-1} of this dimension are of $\mathcal{O}(M_{\rm PL})$. The Z_2 fixed points at $\phi = 0, \pi$ correspond to boundaries: the ultraviolet (UV) and the infrared (IR) 3-branes. The model solves the gauge hierarchy problem by suppressing mass scales on the IR brane. One achieves

$$M_{\rm IR} \equiv e^{-L} M_{\rm Pl} \approx M_{\rm EW} \tag{2}$$

for $L \equiv kr\pi \approx 36$. The strong hierarchy between $M_{\rm PL}$ and $M_{\rm EW}$ is thus understood by gravitational red-shifting, if the Higgs field is localized on or close to the IR brane. The 5D gauge and fermion fields are decomposed into infinite towers of (massive) 4D fields, featuring profiles depending on ϕ, via a Kaluza-Klein (KK) decomposition. The massless zero modes can become massive via couplings to the Higgs sector and, given an appropriate setup of the model, they can be interpreted as the SM fields we observe in nature. The compactification of the fifth dimension leads to masses for the tower of KK excitations, which are set by the KK scale $M_{\rm KK} \equiv k\, e^{-L} \sim \mathcal{O}(\text{TeV})$. The warping of the fundamental Planck scale down to $M_{\rm IR} \sim \mathcal{O}(\text{TeV})$ on the IR brane results in a cutoff for the RS model at several TeV for amplitudes calculated on that brane. At this scale the model is assumed to be UV completed by a theory of quantum gravity. This is important for Higgs physics, because it means that just the exchange of the first KK excitations should be taken into account for the corresponding observables, while the effect of the higher modes is to be cut off. An attractive feature of RS models is the possibility to address the quark-mass hierarchies and the structure of the Cabibbo-Kobayashi-Maskawa (CKM) matrix by localizing the fermion zero modes differently in the extra dimension, without any hierarchies in the input parameters.[3] This anarchic approach to flavor improves the predictivity of the model, since the localizations of the quarks are now fixed to some extend by their masses and the CKM parameters. The top quark, being the heaviest quark of the SM, has to reside close to the IR brane, where also KK excitations tend to live. Due to the large overlap with these excitations, one expects interesting signatures of RS models in top and Higgs physics. A direct consequence of the different localizations of fermions are flavor changing neutral currents (FCNCs). The non-universal couplings to massive gauge bosons lead to offdiagonal transitions, after going to the mass basis. Furthermore, the KK masses (which are due to compactification) lead to a misalignment between the mass and the Yukawa matrix which results in modified Higgs couplings for RS models including FCNCs. Our SM assumption for Higgs searches, a coupling given by the mass of the corresponding particle, is spoiled in this model. The most optimistic RS predictions for $\mathcal{B}(t \to cZ)$ and $\mathcal{B}(t \to ch)$ are both around 10^{-5}.[4,5] Let me finally mention that in the *minimal* RS model a leading order analysis of the electroweak S and T parameters favors a heavy Higgs boson $m_h \sim 1$ TeV (which is not true for the custodial version) and that the theoretical Higgs-mass bounds can be altered. For more details and further references see [4]. The custodial RS model that provides the framework for the following analysis of Higgs physics, which is based on [5], features a protection for the T parameter [6] as well as for $Zb_L\bar{b}_L$ couplings.[7]

3 Higgs Production

The main production mechanism of the Higgs boson at hadron colliders is gluon-gluon fusion. In the SM, this process is dominated by a top-quark triangle loop. Within RS models, one has to consider additionally the KK tower of the top quark as well as of all other flavors present in the theory, which all contribute at the same order. The corresponding Feynman diagrams are given on the very left in the top row and bottom row in Figure 2. In order to obtain the $gg \to h$ production cross section in the custodial RS model, the SM prediction is rescaled according to

$$\sigma(gg \to h)_{\rm RS} = |\kappa_g|^2\, \sigma(gg \to h)_{\rm SM}\,, \tag{3}$$

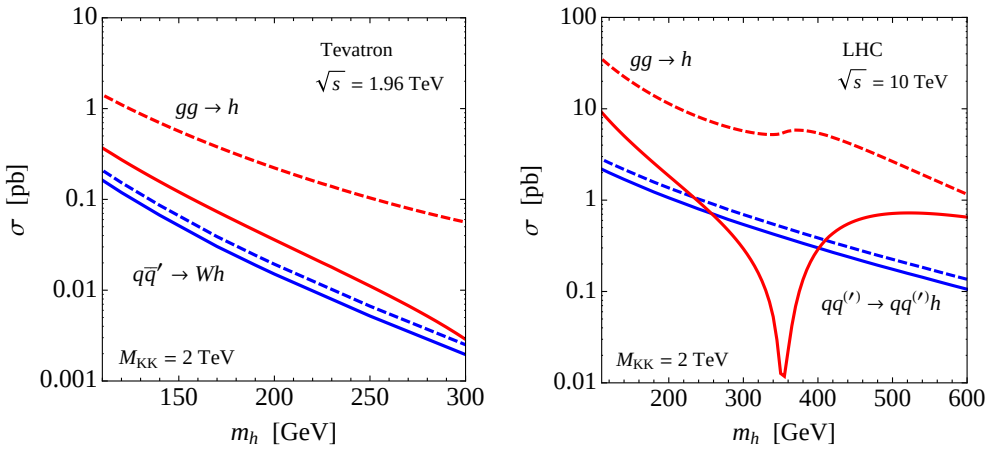

Figure 1: Main Higgs-boson production cross sections at the Tevatron (left) and the LHC (right). The dashed lines represent the SM predictions, while the solid lines correspond to the custodial RS model. See text for details.

where

$$\kappa_g = \frac{\sum_{i=t,b} \kappa_i A_q^h(\tau_i) + \sum_{j=u,d,\lambda} \nu_j}{\sum_{i=t,b} A_q^h(\tau_i)}\,, \tag{4}$$

with $\tau_i \equiv 4m_i^2/m_h^2$. The first sum in the numerator contains top and bottom quark zero modes running in the loop with Higgs couplings (normalized to the SM values) given by

$$\kappa_t = \mathrm{Re}[(g_h^u)_{33}]/\left(\frac{m_t}{v}\right)\,, \quad \kappa_b = \mathrm{Re}[(g_h^d)_{33}]/\left(\frac{m_b}{v}\right)\,. \tag{5}$$

Here, $v \approx 246$ GeV is the Higgs vacuum expectation value and m_t (m_b) is the top (bottom) quark mass. The Higgs couplings $(g_h^{u,d})_{33}$ in the custodial RS model as well as the form factor $A_q^h(\tau_i)$ can be found in [5]. It is easy to show that in the RS model $\kappa_{t,b} < 1$, independent of the input parameters,[5] where κ_t can become as small as 0.5 for $M_{KK} = 2$ TeV, which we will always employ in the following analysis. The second sum in (4) represents the contribution from the virtual exchange of KK excitations. The λ quarks, with electromagnetic charge 5/3, arise in the custodial RS model due to the more complicated fermion structure in order to protect the $Zb_L\bar{b}_L$ vertex. Details on the sums over KK excitations are given in [5]. Note that the contributions of the first KK levels (after summing the different same-charge flavors within a level) turn out to decrease quadratically. Thus the extrapolation from these levels to the whole tower, which actually should be cut off, does not change the results significantly. The predictions for the Higgs-boson production cross sections at Tevatron and the LHC for center-of-mass energies $\sqrt{s} = 1.96\,\mathrm{TeV}$ and $\sqrt{s} = 10\,\mathrm{TeV}$ are shown in Figure 1. The solid red lines correspond to the custodial RS expectations, whereas the SM predictions are indicated by dashed lines for comparison. In addition to gluon-gluon fusion, the plots show (in blue) the predictions for weak gauge-boson fusion, $qq^{(\prime)} \to qq^{(\prime)}V^*V^* \to qq^{(\prime)}h$ with $V = W, Z$, which is an important channel at the LHC, as well as for associated W-boson production, $q\bar{q}' \to W^* \to Wh$, for the Tevatron. The results have been obtained by an averaging procedure over 10000 sets of input parameters, fitting the quark masses, CKM mixing angles and the phase within 1σ. The plots show clearly that the Higgs-production cross sections in gluon-gluon fusion experience a strong reduction in the custodial RS model. This depletion remarkably survives even for $M_{KK} = 5$ TeV, which corresponds to a first KK-gauge boson mass of around 12 TeV, still reaching up to -40% for both colliders. The bump in the right plot is due to a destructive interference of the zero mode and KK contributions which becomes most effective for $m_h \approx 2m_t$.

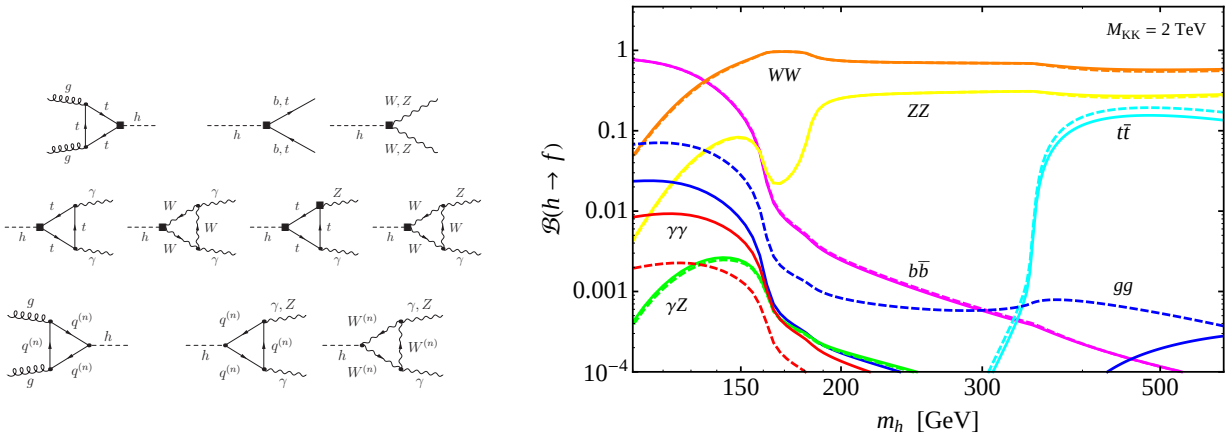

Figure 2: left: Feynman diagrams for Higgs production and decay, right: Branching ratios for $h \to f$ as functions of the Higgs-boson mass. The solid (dashed) lines indicate the custodial RS (SM) predictions. See text for details.

4 Higgs Decay

Concerning the decay of the Higgs boson, processes with heavy quarks and gauge bosons in the final state can experience significant RS corrections. The corresponding Feynman diagrams are depicted on the left of Figure 2, where vertices that receive non-negligible corrections are indicated by black squares. The analysis works in a similar way as that for Higgs production.[5] The results are shown on the right of Figure 2, where the solid (dashed) lines correspond to the RS (SM) predictions. All final states that can feature non-negligible RS corrections and have branching fractions above 10^{-4} are considered. While for Higgs masses below the WW threshold the enhanced branching fraction into two photons could compensate the lower production cross section in $gg \to h \to \gamma\gamma$, the discovery potential above this threshold is for all channels significantly worse than in the SM. Most important, the golden channel $gg \to h \to Z^{(*)}Z^{(*)} \to l^+l^-l^+l^-$ suffers from the strong reduction in the production cross section. The presented results suggest that a discovery of the Higgs boson, depending on its mass, could become more difficult in RS models. Existing SM bounds on the Higgs mass from the Tevatron and LEP are also altered if warped extra dimensions are realized in nature. Furthermore, the effects in Higgs physics should be notable at the LHC, even for KK scales which are by far not directly accessible.

Acknowledgments

I would like to thank the organizers of the *Rencontres de Moriond 2011 EW* for the wonderful atmosphere during the conference and the financial support. Furthermore, I want to thank Sandro Casagrande, Uli Haisch, Matthias Neubert, and Torsten Pfoh for the nice collaboration on the subject and Julia Seng for carefully proofreading the manuscript.

References

1. ALEPH Collaboration, *et al.*, arXiv:1012.2367 [hep-ex].
2. L. Randall and R. Sundrum, Phys. Rev. Lett. **83**, 3370 (1999)
3. S. J. Huber and Q. Shafi, Phys. Lett. B **498**, 256 (2001)
4. S. Casagrande, F. Goertz, U. Haisch, M. Neubert and T. Pfoh, JHEP **0810** (2008) 094
5. S. Casagrande, F. Goertz, U. Haisch, M. Neubert and T. Pfoh, JHEP **1009** (2010) 014
6. K. Agashe, A. Delgado, M. J. May and R. Sundrum, JHEP **0308**, 050 (2003)
7. K. Agashe, R. Contino, L. Da Rold and A. Pomarol, Phys. Lett. B **641**, 62 (2006)

Estimation of SM backgrounds to SUSY searches in the 1-lepton + jets + $E_{\mathrm{T}}^{\mathrm{miss}}$ channel

J. M. Lorenz
on behalf of the ATLAS Collaboration
Fakultät für Physik, Ludwig-Maximilians-Universität-München
Am Coulombwall 1, D-85748 Garching, Germany

The ATLAS Collaboration has reported the first results of the search for SUSY particles in 1-lepton + ≥ 3 jets + E_T^{miss} final states for $\int Ldt = 35$ pb^{-1}. An essential ingredient for these results is a reliable background estimation in the signal region, in particular of the $t\bar{t}$, W+jets and QCD backgrounds. The estimation of these three backgrounds is explained in this paper. The $t\bar{t}$ and W+jets backgrounds are obtained from a background dominated control region and extrapolated to the signal region, whereas for the estimation of the QCD background a matrix method is used.

1 Introduction

Supersymmetric extensions (SUSY) to the Standard Model (SM) predict the existence of supersymmetric particles which could be produced in the proton-proton collisions at a center-of-mass energy of 7 TeV at the LHC [1]. The search for SUSY is one of the main aims of the ATLAS experiment [2].
The main production channels of SUSY particles at the LHC are squark-(anti)squark, gluino-squark and gluino-gluino pairs if these sparticles are light enough. Typical squark and gluino decays contain isolated leptons, quarks and gluons (which result in jets) and end with the stable Lightest Supersymmetric Particle (LSP) if a R-parity conserving SUSY model is assumed. As the LSP escapes the detector undetected, missing transverse energy ($E_{\mathrm{T}}^{\mathrm{miss}}$) will be observed. Therefore, the typical experimental signature consists of multiple jets, isolated leptons and $E_{\mathrm{T}}^{\mathrm{miss}}$. Here only final states with one isolated muon or electron, at least three jets and $E_{\mathrm{T}}^{\mathrm{miss}}$ are considered (1-lepton + $\geq$ 3jets + $E_{\mathrm{T}}^{\mathrm{miss}}$ channel).
However, other physical processes can have similar experimental signatures, in particular:

- $t\bar{t}$ events with a semileptonic decay topology, where each top quark decays into a W-boson and a b-quark, with one of the W-bosons decaying into an isolated charged lepton and a neutrino ($E_{\mathrm{T}}^{\mathrm{miss}}$).
- W+jets events where the W-boson decays into a neutrino and the corresponding charged lepton.
- QCD events, like heavy flavor (b or c quarks) decays, events with photon conversions or jets which were reconstructed as isolated leptons.

A signal region rich in SUSY signal events but poor in background events (BG) which was motivated by studies on Monte Carlo event samples is defined as follows. Hereby, the channel

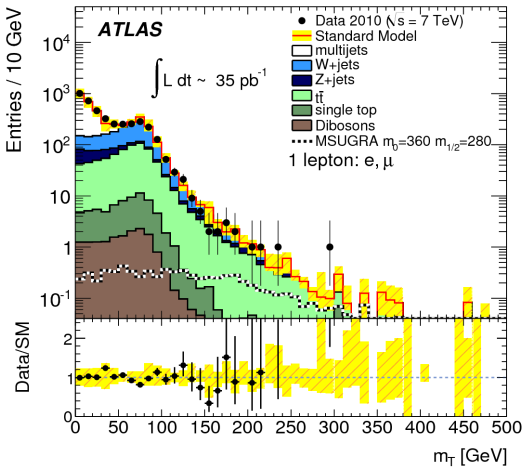

Figure 1: The m_{T} distribution after the lepton and the jets criteria. The ratio of data to SM expectations is given in the ratio plot below. The uncertainties on the MC predictions are indicated by the yellow bands.

itself is defined by asking for exactly one isolated lepton being in the event with a transverse momentum of $p_{\mathrm{T}} > 20$ GeV which already reduces the QCD BG. Furthermore, the event must contain at least three jets with $p_{\mathrm{T}}^{\text{leading jet}} > 60$ GeV and $p_{\mathrm{T}}^{\text{second,third jet}} > 30$ GeV. In addition to these cuts, various cuts are applied to reject background events: a further reduction of the QCD background is achieved by asking for the three leading jets and $E_{\mathrm{T}}^{\mathrm{miss}}$ not to point in the same direction [a]. Furthermore, only events with $E_{\mathrm{T}}^{\mathrm{miss}} > \max(125\ \mathrm{GeV}, 0.25 M_{\mathrm{eff}})$ [b] and a high transverse mass with $m_{\mathrm{T}} > 100$ GeV [c] are selected. The last cut reduces the W+jets and $t\bar{t}$ backgrounds considerably as illustrated in figure 1. Finally, a cut on the effective mass with $M_{\mathrm{eff}} > 500$ GeV is applied. After applying these cuts, $t\bar{t}$ events are the main background and QCD events are heavily suppressed.
The estimation of the three most important backgrounds in the signal region is discussed in the following.

2 *W* and top backgrounds

The magnitude of the backgrounds is estimated with the help of background dominated control regions. In figure 2, various control regions - one for each of the main backgrounds (QCD, $t\bar{t}$, W+jets) in the $E_{\mathrm{T}}^{\mathrm{miss}}$ - m_{T} plane are defined. All other cuts for these control regions correspond to the usual selection cuts presented above except the cut on M_{eff} which is not applied. For example, the QCD region (QR) which is defined by $E_{\mathrm{T}}^{\mathrm{miss}} < 40$ GeV and $m_{\mathrm{T}} < 40$ GeV is rich in QCD events. The control region with medium $E_{\mathrm{T}}^{\mathrm{miss}}$ and m_{T} values ($30 < E_{\mathrm{T}}^{\mathrm{miss}} < 80$ GeV and $40 < m_{\mathrm{T}} < 80$ GeV) is dominated by top and W+jets events. This control region is further divided into two control regions dominated by $t\bar{t}$ events (top region, TR) or W+jets events (W region, WR), respectively, by the requirement of finding at least one b-tagged jet (TR) or no b-tagged jet (WR) in the three leading jets. The QR is only used to estimate the QCD contamination in the TR or in the WR, whereas the QCD BG in the signal region itself is obtained with the method described in the next section. In contrast, the $t\bar{t}$ and W+jets BG in the signal region is obtained by extrapolating the number of measured W and top events in W and T control regions (other backgrounds were subtracted) into the signal region. For

[a] $\Delta\phi(\mathrm{jet_i}, \vec{\mathrm{E}}_{\mathrm{T}}^{\mathrm{miss}}) > 0.2$ (i = 1, 2, 3)
[b] the effective mass is defined as $M_{\mathrm{eff}} = p_{\mathrm{T}}^{l} + E_{\mathrm{T}}^{\mathrm{miss}} + \sum_{i=1}^{3} p_T^{\mathrm{jet_i}}$
[c] the transverse mass is defined as $m_{\mathrm{T}} = \sqrt{2 \cdot p_{\mathrm{T}}^{l} \cdot E_{\mathrm{T}}^{\mathrm{miss}} \cdot (1 - \cos(\Delta\phi(l, E_{\mathrm{T}}^{\mathrm{miss}})))}$

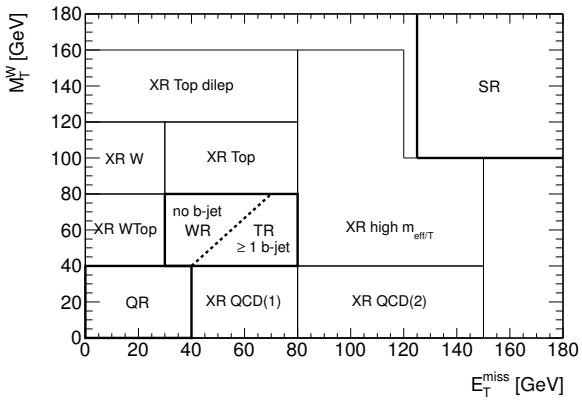

Figure 2: The positions of the signal region (SR) and of the main control regions (as QR, WR and TR, defined in the text) are indicated in the $E_{\mathrm{T}}^{\mathrm{miss}}$ - m_{T}-plane. Control regions which are not mentioned in the text (XR) are used to cross check the background estimation techniques presented in the text.

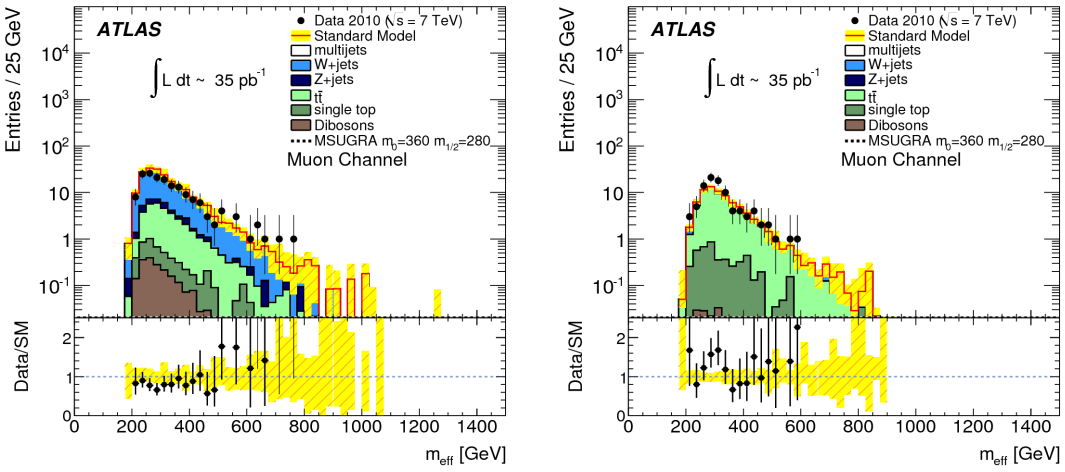

Figure 3: The M_{eff} distributions in the W region (left) and in the top region (right) in the muon channel. The yellow bands indicate the uncertainties on the MC predictions.

this an extrapolation factor which is obtained from Monte Carlo is used. The extrapolation is illustrated in equation 1 for the top background.

$$\underbrace{N(t\bar{t}\text{ pred., SR})}_{\text{predicted events in signal region}} = \underbrace{(N(t\bar{t}(\text{data}),\ \text{CR}))}_{\text{measured events in control region - other BG}} \times \underbrace{\frac{N(t\bar{t}(\text{MC}),\ \text{SR})}{N(t\bar{t}(\text{MC}),\ \text{CR})}}_{\text{extrapolation factor CR to SR}} \tag{1}$$

This method is validated by comparing data to MC in the relevant distributions for the extrapolation. Figure 3 shows for example the M_{eff} distributions in the TR and in the WR in the muon channel. The good agreement between data and MC gives confidence in the method.

3 QCD background

In contrast to the W and top backgrounds, the QCD background is estimated by a matrix method. As mentioned above, the signal selection cuts (tight selection cuts) choose only events with exactly one isolated lepton. By relaxing the isolation requirement for the lepton a loose control sample enriched with QCD events can be defined. The events passing the tight selection

Table 1: The number of observed events in $\int Ldt = 35$ pb^{-1} is compared to the total number of background events expected. The contribution of $t\bar{t}$, W and Z events and QCD events to the total number of background events is given.

channel	observed events	sum estimated BG events	estimated top	estimated WZ	estimated QCD
muon	1	2.25 ± 0.94	1.76 ± 0.67	0.49 ± 0.36	$0.0^{+0.5}_{-0.0}$
electron	1	1.81 ± 0.75	1.34 ± 0.52	0.47 ± 0.40	$0.0^{+0.3}_{-0.0}$

cuts can be expressed as the sum of QCD events ("fake") and non-QCD events ("real") as in equation 2.

$$N^{\text{obs}}_{\text{tight}} = N^{\text{real}}_{\text{tight}} + N^{\text{fake}}_{\text{tight}} \tag{2}$$

In the same way, the events passing the loose but not the tight selection cuts can be written as the sum of QCD and non-QCD events. By defining two efficiencies by $\epsilon^{\text{real/fake}} = \frac{N^{\text{real/fake}}_{\text{tight}}}{N^{\text{real/fake}}_{\text{loose}}}$ this sum can be written as:

$$N^{\text{obs}}_{\text{loose not tight}} = (1/\epsilon^{\text{real}} - 1)N^{\text{real}}_{\text{tight}} + (1/\epsilon^{\text{fake}} - 1)N^{\text{fake}}_{\text{tight}} \tag{3}$$

Both equations 2 and 3 are solved for the QCD events passing the tight selection cuts in equation 4. The result gives the QCD events in the SUSY signal region.

$$N^{\text{fake}}_{\text{tight}} = \frac{N^{\text{obs}}_{\text{loose not tight}} - (1/\epsilon^{\text{real}} - 1)N^{\text{obs}}_{\text{tight}}}{1/\epsilon^{\text{fake}} - 1/\epsilon^{\text{real}}} \tag{4}$$

This method was applied to the whole dataset of 2010 of 35 pb^{-1} in the electron and in the muon channel, respectively. Thus, $\epsilon^{\text{fake}} \sim 0.2 - 0.3$ was obtained in a QCD dominated control region with $E^{\text{miss}}_{\text{T}} < 40$ GeV and $M_{\text{T}} < 40$ GeV, whereas $\epsilon^{\text{real}} \sim 0.9 - 1.0$ was taken from Monte Carlo. Only an upper limit on the QCD background in the signal region could be derived with < 0.5 events in the muon channel and < 0.3 events in the electron channel due to low statistics in the loose-but-not-tight events.

4 Outlook

The QCD, $t\bar{t}$ and W+jets backgrounds in the signal region are estimated with the methods presented. Other backgrounds are taken from simulation. The final results are detailed in table 1. The top background is with 1.76 ± 0.67 (muon channel) and 1.34 ± 0.52 (electron channel) the most dominant background in the signal region. In total, 2.25 ± 0.94 background events are expected in the muon channel and 1.81 ± 0.75 background events in the electron channel, but only 1 event passes all the signal selection cuts presented above in each of the electron and the muon channels. An interpretation of the results in terms of limits is given elsewhere [3].

References

1. Lyndon Evans and Philip Bryant (editors). LHC Machine. JINST 3 S08001 (2008).
2. The ATLAS Collaboration. The ATLAS Experiment at the CERN Large Hadron Collider. JINST 3 S08003 (2008).
3. The ATLAS Collaboration. Search for supersymmetry using final states with one lepton, jets, and missing transverse momentum with the ATLAS detector in $\sqrt{s} = 7$ TeV pp collisions. Phys. Rev. Lett. 106, 131802 (2011)

YUKAWA UNIFICATION IN SUSY SO(10) FOR $\mu < 0$ CONSISTENT WITH MUON g − 2 AND b → sγ

MARCIN BADZIAK[1,2]
[1]*DAMTP, University of Cambridge, Wilberforce Road, Cambridge CB3 0WA, UK*
[2]*Cavendish Laboratory, University of Cambridge, J.J. Thomson Avenue, Cambridge CB3 0HE, UK*

It is shown that top-bottom-tau Yukawa unification for $\mu < 0$ can be consistent with $(g-2)_\mu$ and $b \to s\gamma$. This happens for non-universal gaugino masses which are assumed to be generated by the F-term vev in a 54-dimensional representation of SO(10). The requirement of $(g-2)_\mu$ and $b \to s\gamma$ being within 2σ from the experimental central values, together with the correct relic abundance of neutralinos, leads to rather definite predictions for sparticle spectrum. In particular, the gluino mass is predicted to be between 500 and 700 GeV or between 900 GeV and 1.6 TeV.

1 Introduction

Apparent gauge coupling unification in the Minimal Supersymmetric Standard Model (MSSM) is regarded as the one of the best motivations for supersymmetry (SUSY). Among the candidates for the unified gauge group SO(10) seems to be the most attractive. All Standard Model (SM) matter fields, as well as right-handed neutrino, of each generation fit into one irreducible 16-dimensional representation of SO(10). On the other hand, two MSSM Higgs doublets, H_u and H_d, sit in the 10-dimensional representation. Moreover, in the simplest version of SUSY SO(10) Yukawa couplings of top, bottom and tau unify at the same scale as the gauge couplings do.

One of the generic predictions of Yukawa unification is a large value of $\tan\beta \sim m_t/m_b$. For such values of $\tan\beta$ there are sizable threshold corrections to the bottom mass which are of major importance from the point of view of bottom-tau Yukawa unification. The main finite corrections, originating from gluino-sbottom and chargino-stop loops, are given by [1,2,3]:

$$\left(\frac{\delta m_b}{m_b}\right)^{\text{finite}} \approx \frac{g_3^2}{12\pi^2}\mu m_{\tilde{g}} \tan\beta\, I(m^2_{\tilde{b}_1}, m^2_{\tilde{b}_2}, m^2_{\tilde{g}}) + \frac{h_t^2}{32\pi^2}\mu A_t \tan\beta\, I(m^2_{\tilde{t}_1}, m^2_{\tilde{t}_2}, \mu^2)\,, \qquad (1)$$

where the loop integral $I(x,y,z)$ is well approximated by $a/\max(x,y,z)$ with a between 0.5 and 1. Bottom-tau Yukawa unification requires the above correction to be negative with the magnitude about 10% to 20% [4]. The gluino-sbottom correction dominates over the most of the parameter space so Yukawa unification generically prefers $\mu < 0$.

The sign of μ has also crucial impact on the muon anomalous magnetic moment, $(g-2)_\mu$, which experimental value is more than 3σ below the Standard Model prediction. The sign of the dominant SUSY contribution to $(g-2)_\mu$ is the same as the sign of the product μM_2. So, in phenomenologically acceptable models with negative μ gaugino masses with $M_2 < 0$ are required.

In GUT theories gaugino masses are usually assumed to be equal at the GUT scale. Under this assumption $(g-2)_\mu$ calls for $\mu > 0$ which makes top-bottom-tau Yukawa unification very

problematic. However, gaugino masses are universal only if the SUSY breaking F-term which gets a VEV is a singlet of the GUT gauge symmetry group. In general, the gaugino masses in supergravity can arise from the following dimension five operator:

$$\mathcal{L} \supset -\frac{F^{ab}}{2M_{\rm Planck}}\lambda^a\lambda^b + \text{c.c.}\,, \tag{2}$$

where λ^a are the gaugino fields. The vacuum expectation value of the relevant F-term, $\langle F^{ab}\rangle$, must transform as the singlet of the SM gauge group but it can be a non-singlet of the full GUT group. Since the gauginos belong to the adjoint representation, non-zero gaugino masses may arise from VEVs of the F-terms transforming as any of the representations present in the symmetric part of the direct product of the two adjoints, which for SO(10) is $(\mathbf{45}\times\mathbf{45})_S = \mathbf{1}+\mathbf{54}+\mathbf{210}+\mathbf{770}$.

In this work we consider $\mu < 0$ and assume that gaugino masses are generated by the F-term VEV transforming as **54** representation. In such a case gaugino masses are given by [5]:

$$(M_1, M_2, M_3) = \left(-\frac{1}{2}, -\frac{3}{2}, 1\right) m_{1/2}\,. \tag{3}$$

Tob-bottom-tau Yukawa unification requires also non-universal scalar masses to be compatible with radiative electroweak symmetry breaking [6]. We assume the following pattern of scalar masses:

$$\begin{aligned} m^2_{H_d} &= m^2_{10} + 2D\,, \\ m^2_{H_u} &= m^2_{10} - 2D\,, \\ m^2_{Q,U,E} &= m^2_{16} + D\,, \\ m^2_{D,L} &= m^2_{16} - 3D\,. \end{aligned} \tag{4}$$

D-term contribution which splits masses of scalars belonging to the same representation of SO(10) is a generic feature of models in which the GUT gauge group has larger rank than the SM gauge group [7]. The remaining free parameters in our model are the universal trilinear term A_0 and $\tan\beta$.

In these proceedings we show that in the above setup top-bottom-tau Yukawa unification can be realized. Moreover, we present Yukawa-unified solutions which predict the values of $\text{BR}(b\to s\gamma)$ and $(g-2)_\mu$ consistent with the experimental data at 2σ level. Combination of these constraints, together with the WMAP bound for the relic density of neutralinos, imply that the model predicts light SUSY spectrum with no sparticles with masses above 2 TeV.

2 Necessary conditions for Yukawa unification

Assuming that the finite threshold correction to the bottom mass is fully determined by the gluino-sbottom contribution (which is a good approximation over the most of the parameter space) the condition of top-bottom-tau leads to the upper bound for the parameter $|\mu|$ [8]:

$$|\mu| \lesssim 0.4 m_{\tilde{g}} \approx m_{1/2}\,. \tag{5}$$

In principle, the above bound for $|\mu|$ could be relaxed if $m_{1/2} \ll m_{16}$. However, Yukawa-unified solutions respecting the hierarchy $m_{1/2} \ll m_{16}$ which are compatible with all experimental constraints cannot exist for large values of $|\mu/m_{1/2}|$ for the reason that we explain later on.

At large $\tan\beta$, the condition of proper REWSB implies $\mu^2 \approx -\left(m^2_{H_u} + M_Z^2/2\right)$. Using this relation and the renormalization group equations one can estimate electroweak scale value of μ^2

in terms of the input parameters at the GUT scale:

$$\mu^2 \approx -m_{H_u}^2 \approx m_{1/2}^2 \left[1.2 + 0.65x^2 \left(0.97 - \frac{m_{10}^2}{m_{16}^2} + 1.9\frac{D}{m_{16}^2} + 0.1\frac{A_0^2}{m_{16}^2} - \frac{0.2}{x}\frac{A_0}{m_{16}}\right)\right], \qquad (6)$$

where $x \equiv m_{16}/m_{1/2}$. In order to satisfy the bound (5) the contribution from gaugino masses to μ^2 has to be (partially) cancelled by other terms in (6). Yukawa unification requires also $D > 0$ [9]. So, the cancellations in (6) may occur only for $m_{10} > m_{16}$. Since μ^2 cannot be negative, Yukawa unification consistent with REWSB requires correlation between m_{10}, D and A_0. This correlation is especially strong when $m_{1/2} \ll m_{16}$ because in such a case the value of μ^2 is very sensitive to the value of the expression in the round bracket in eq. (6).

3 Interplay between BR($b \to s\gamma$) and $(g-2)_\mu$

The main MSSM contribution to $(g-2)_\mu$ originates from the one-loop diagrams involving charginos accompanied by the muon sneutrino. Therefore, charginos and muon sneutrino have to be relatively light in order to explain $(g-2)_\mu$ anomaly. However, at large $\tan\beta$ light charginos give also significant contribution to BR($b \to s\gamma$) through the loops in which they are accompanied by up-type squarks. In order to avoid too large BR($b \to s\gamma$), the chargino contribution has to be necessarily negative, relative to the SM contribution.

At large $\tan\beta$, there are two types of chargino contributions that may affect significantly the prediction for BR($b \to s\gamma$). The first one is proportional to stop-mixing angle and its sign is given by $\mathrm{sgn}\,(\mu A_t)$. The RG running gives negative A_t with the absolute value of order $m_{1/2}$ unless A_0 is positive and few times larger than $m_{1/2}$ at the GUT scale. This implies that for $\mu < 0$ stop-mixing part of chargino contribution is typically positive. Fortunately, the sign of the second type of chargino contribution is given by $(-\mu M_2)$ which is always negative in our model. We call it gaugino contribution. This contribution is suppressed by squark GIM mechanism and vanishes for degenerate squark masses. In order to make chargino contribution to BR($b \to s\gamma$) negative, the gaugino contribution has to dominate over stop-mixing one. This is more likely when $m_{1/2} \ll m_{16}$ because in such a case intergenerational squark splitting may be large due to domination of RGEs by the terms proportional to Yukawa couplings. Moreover, $m_{1/2} \ll m_{16}$ typically suppresses stop-mixing angle. If there is no significant hierarchy between $m_{1/2}$ and m_{16} chargino contribution is typically positive excluding the possibility of sizable SUSY contribution to $(g-2)_\mu$ unless A_0 is relatively large and positive.

4 Yukawa-unified solutions consistent with $(g-2)_\mu$ and $b \to s\gamma$

We performed numerical analysis using SOFTSUSY [10] which solves 2-loop renormalization group equations implementing proper REWSB and calculate sparticle spectrum. We also used MicrOmegas [11] for calculating the relic density of dark matter, as well as, BR($b \to s\gamma$), $(g-2)_\mu$ and BR($B_s \to \mu^+\mu^-$).

Besides BR($b \to s\gamma$) and $(g-2)_\mu$, another important constraint for the model comes from the WMAP bound on the relic density of neutralinos. The requirement that these three constraints are satisfied leads to rather definite predictions for sparticle spectrum. In the following we discuss two types of Yukawa-unified solutions consistent with BR($b \to s\gamma$) and $(g-2)_\mu$ at 2σ level.

In the first class of solutions there is no large hierarchy between $m_{1/2}$ and m_{16} and $b \to s\gamma$ constraint is satisfied due to large positive A_0 at the GUT scale which allows for negative chargino contribution to BR($b \to s\gamma$). In this class of solutions $m_{1/2}$ is found to be between about 400 and 650 GeV, while m_{16} between 700 and 1200 GeV. In consequence, gluino mass is predicted to be between 900 GeV and 1.6 TeV. Squarks of the first and second generation are typically a

bit heavier than the gluino. On the other hand, squarks of the third generation are typically a bit lighter than the gluino except $\tilde{b}_R$ which is much lighter due to negative D-term contribution at the GUT scale and strong renormalization by large A_0. In some cases $m_{\tilde{b}_R}$ is even below 200 GeV which make annihilations of neutralinos through t-channel sbottom exchange efficient enough to satisfy the bound on $\Omega_{DM}h^2$. For larger values of $m_{\tilde{b}_R}$ this channel is less efficient and WMAP bound is satisfied due to neutralino co-annihilations with stau.

We found also Yukawa-unified solutions which respect the hierarchy $m_{1/2} \ll m_{16}$. In this case correct relic abundance of neutralinos requires resonant annihilations through Z boson or the lightest CP-even Higgs. This has a great impact on the allowed parameter space. First of all, these kind of annihilation channels are allowed only if the LSP has non-negligible higgsino component. This condition can be translated to the upper bound for $|\mu/M_1|$ which results also in the upper bound for $|\mu/m_{1/2}|$. We found numerically that in order to satisfy dark matter constraint $|\mu/m_{1/2}|$ has to be smaller than about 1.8 and 1.5 for $m_{\tilde{\chi}_1^0} \approx 45$ GeV and $m_{\tilde{\chi}_1^0} \approx 55$, respectively. For the LSP masses further away from the Z or h^0 resonances $|\mu/m_{1/2}|$ has to be even smaller. This class of solutions predict gluino masses in the range between about 500 and 700 GeV. The squarks of the first and second generation have masses between 1.1 and 1.5 TeV, while the masses of third generation squarks are found to be between 800 and 1000 GeV except $\tilde{b}_R$ which has a mass between 400 and 800 GeV.

In summary: We have shown that top-bottom-tau Yukawa unification in SO(10) can be realized for $\mu < 0$ in a way which is consistent with the experimental constraints from $(g-2)_\mu$ and $b \to s\gamma$ if gaugino mases are generated by F-term VEV transfoming as 54-dimensional representation of SO(10). Moreover, for $\mu < 0$ D-term splitting of scalar masses is compatible with Yukawa unification, in contrast to the case with positive μ. This is the first SO(10) model which predicts light SUSY spectrum with all sparticle masses below 2 TeV without violating any experimental constraints. The prediction of light gluinos make this model testable at the LHC in the very near future. More detailed analysis can be found in ref. [8].

Acknowledgments

M.B. would like to thank M. Olechowski and S. Pokorski for fruitful collaboration. This work has been partially supported by MNiSzW scientific research grant N N202 103838 (2010 - 2012) and by the European Research and Training Network (RTN) grant Unification in the LHC era (PITN-GA-2009-237920).

References

1. L. J. Hall, R. Rattazzi, U. Sarid, Phys. Rev. **D50** (1994) 7048-7065. [hep-ph/9306309].
2. M. S. Carena, M. Olechowski, S. Pokorski, C. E. M. Wagner, Nucl. Phys. **B426** (1994) 269-300. [hep-ph/9402253];
3. D. M. Pierce *et al.*, Nucl. Phys. **B491** (1997) 3-67. [hep-ph/9606211].
4. K. Tobe, J. D. Wells, Nucl. Phys. **B663** (2003) 123-140. [hep-ph/0301015].
5. S. P. Martin, Phys. Rev. **D79** (2009) 095019. [arXiv:0903.3568 [hep-ph]].
6. M. Olechowski, S. Pokorski, Phys. Lett. **B344** (1995) 201-210. [hep-ph/9407404].
7. Y. Kawamura, H. Murayama, M. Yamaguchi, Phys. Rev. **D51** (1995) 1337-1352. [hep-ph/9406245].
8. M. Badziak, M. Olechowski, S. Pokorski, in preparation.
9. H. Murayama, M. Olechowski, S. Pokorski, Phys. Lett. **B371** (1996) 57-64. [hep-ph/9510327].
10. B. C. Allanach, Comput. Phys. Commun. **143** (2002) 305-331. [hep-ph/0104145].
11. G. Belanger *et al.*, Comput. Phys. Commun. **176** (2007) 367-382. [hep-ph/0607059].

JET PRODUCTION CROSS SECTION MEASUREMENT WITH ATLAS

S.J. BAKER
Department of Physics and Astronomy, University College London, Gower Street, London WC1E 6BT, England.

The inclusive single jet and di-jet cross sections were measured for proton - proton collisions at the Large Hadron Collider (LHC), using the ATLAS detector. The initial measurement used a total integrated luminosity of 17 nb^{-1} of data collected at a centre-of-mass energy of 7 TeV. Jets are reconstructed using the anti-kt algorithm with the two jet resolution parameters 0.4 and 0.6. A jet energy scale correction is then applied to these jets. The uncertainty on this correction dominates the total uncertainty on the measurement, and is calculated to be 7% for central jets above 60 GeV. The final cross sections agree with the predictions of next to leading order perturbative QCD, providing comparisons with theory for a previously unmeasured energy regime.

1 Introduction

ATLAS has published an initial measurement of the inclusive single jet and di-jet cross sections at 7 TeV, for the data period spanning from 30th March to 5th June 2010. This data taking period corresponds to a total integrated luminosity of 17 nb^{-1}. The jet cross section allows precise measurements of the strong coupling constant and provides information on the structure of the proton. Moreover, a solid understanding of the physics of jets provides a firm basis for the search for physics beyond the Standard Model. Inclusive jet cross sections are sensitive to the combination of the QCD matrix element and parton densities within the proton. Di-jet measurements were made in a region with reduced sensitivity to the parton distributions, thus providing detailed information on the structure of the QCD matrix element.

2 Jet Selection

The ATLAS detector is constructed of from inner tracking detectors, calorimeters and outer muon chambers. These are described in detail elsewhere [1]. Jets are reconstructed using the anti-kt jet algorithm [2], implemented via the FASTJET package [3]. The jets are built from all stable particles, including neutrinos and muons. An uncorrected electromagnetic (EM) scale jet is defined as the sum of the uncorrected four momenta of its constituent calorimeter energy clusters. The ATLAS detector is non-compensating (the response to hadrons is lower than the response to electrons of the same energy). The EM energy scale is established from test beam measurements using electrons and muons. A jet energy scale (JES) correction is applied to calibrate each jet to the hadronic scale. This correction also accounts for energy losses due to dead material, and for particles where the shower is not contained within the calorimeter.

The jet energy scale is established by matching reconstructed calorimeter jets to Monte Carlo (MC) particle truth jets (excluding muons and neutrinos). The distribution of the response

between calorimeter and particle jets is used to determine an average jet energy response via a Gaussian fit. The correction is then obtained by determining a transfer matrix between the energy of particle level and EM scale jets, inverting it and refitting the distribution in bins of jet transverse jet momentum (p_T). For 0.6 anti-kt jets, the overall correction is less than 75%, and for central jets with p_T greater than 60GeV it is less than 50%.

2.1 Uncertainties on the Jet Energy Scale

The dominant systematic uncertainty on the overall measurement comes from the jet energy scale. The uncertainties on the JES were added in quadrature, except those of closure test (described below). These are treated as fully correlated and added linearly. The effect of dead material was estimated using test beam measurements and comparisons between MC simulations and the 900 GeV run. It contributes a total of 2% of the uncertainty of the jet energy scale. The uncertainty from discrepancies between noise descriptions in Monte Carlo and for data was estimated by lowing and raising the signal to noise thresholds for clusters from the nominal value by 10%. For low p_T jets this value reaches up to 3% of the jet energy. Jets are reconstructed with respect to the origin (x, y, z) = (0,0,0). If the shift in beamspot with respect to this position is not correctly modelled by Monte Carlo, the jet p_T will be biased. Differences in JES from discrepancies between data and Monte Carlo were evaluated using a sample generated with a beamspot shift. This effect was found to be less than 1%. Uncertainties on the EM scale were combined from the uncertainties on the electromagnetic and hadronic calorimeters, 4% and 3% respectively, in accordance to the relative average energy deposition between the two. This was done for each jet, as a function of p_T. Further uncertainties come from non-closure (deviation from unity) in the jet p_T and energy response. Two MC samples with differing hadronic shower models were compared to single pion test beam studies ranging from 2 GeV to 180 GeV, and found to contribute 4%. The effect of using differing event generators was determined to less than 4%. The contribution from pileup was estimated for each event by studying the dependence of the average energy density deposited as a function of the number of reconstructed vertices. No correction is applied, but the effect is accounted for in the JES uncertainty. The maximum JES uncertainty was found to be 9% for jets with 30 GeV $< p_T <$ 60 GeV, and 7% for $p_T >$ 60 GeV for the central region. Corrections for trigger and detector efficiencies and resolutions (other than the JES) were performed in a single step using a bin-by-bin unfolding from true (including muons and neutrinos) to reconstructed jets from Monte Carlo. The uncertainties were established by estimating the spread of the correction for different generators, and by changing shape of the simulated distributions. The total systematic uncertainty was 40% and was dominated by the jet energy response of the calorimeter.

3 Single Jet and Di-Jet Cross Section

The inclusive jet cross section was measured as as a function of p_T and rapidity y in the region $p_T > 60$ and $| y | < 2.8$. This is well within the trigger high efficiency plateau and the JES is well understood in this region. The data was compared with leading-logarithmic parton shower Monte Carlo generators. PYTHIA 6.421 calculates leading order (LO) pQCD matrix elements $2 \rightarrow 2$ processes and applies a p_T ordered parton shower [4]. Hadronisation is performed using the Lund String model. Systematics were assessed using HERWIG, which uses an angular ordered parton shower and cluster hadronisation model. [5] Monte Carlo is then run through a full simulation of ATLAS trigger and detector systems based on GEANT4 [8]. Data was compared to theoretical predictions for next to leading order (NLO) pQCD via NLOJET++ 4.1.2 [6]. CTEQ 6.6 parton densities were used for central values and uncertainties [7]. The renormalisation and refactorisation scales were set to the p_T of leading jet of the event and the uncertainty deter-

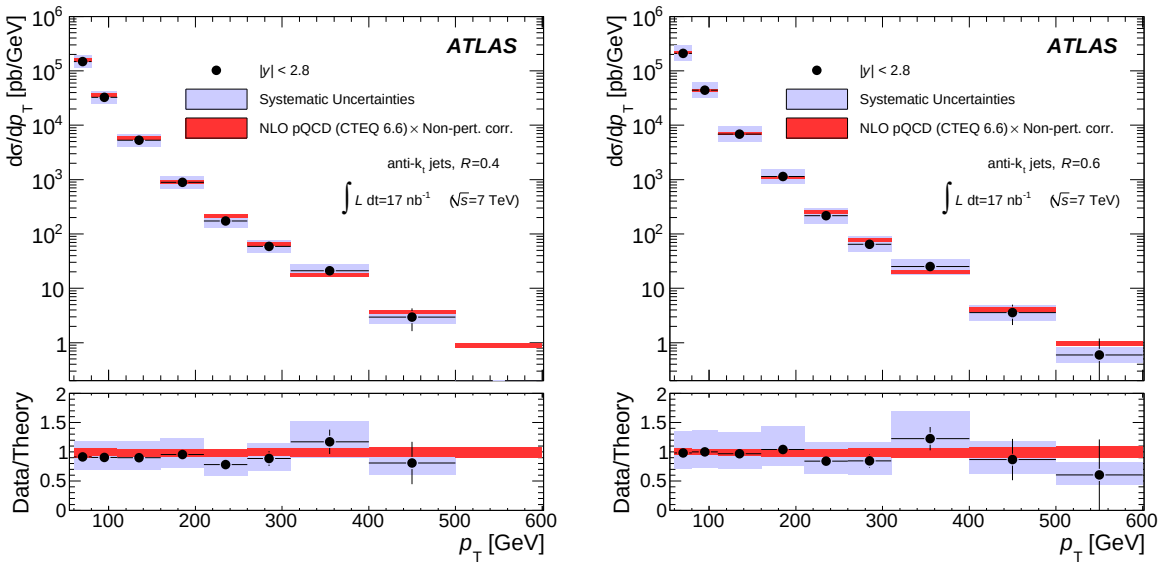

Figure 1: Inclusive jet differential cross section as a function of jet p_T integrated over the full region $| y | 2.8$ for jets identified using the anti-kt algorithm with R = 0.4 (left) and R = 0.6 (right). The data is compared to NLO pQCD calculations to which soft QCD corrections have been applied. The error bars indicate the statistical uncertainty on the measurement, and the grey shaded bands indicate the quadratic sum of the systematic uncertainties. There is an additional overall uncertainty of 11% due to the luminosity measurement that is not shown.

mined by varying the renormalisation scale from half, to double this value. The NLO calculations predict partonic cross sections, however these are unmeasurable in practice. NLO pQCD calculations were corrected for non-perturbative effects by applying soft corrections using leading logarithmic parton shower Monte Carlo. The NLO theory was divided by a factor obtained by calculating the ratio of the cross sections before and after the application hadronisation and underlying event. The soft QCD corrections depend on the size of the jets, since wide jets are more affected by underlying event and narrow jets lose particles through hadronisation. These effects become more significant with decreasing p_T, however the uncertainty is within 5% for the region of interest. The cross section extends from p_T = 60 GeV up to p_T = 600 GeV, and falls by more than four orders of magnitude over this range. The differential cross sections are described by theory within systematic uncertainties.

The di-jet cross section is measured as a function of the di-jet mass and the maximum rapidity of the two leading jets, $| y |$ max = max($| y_1 |$, $| y_2 |$) and of the variable χ. The measurement was undertaken in the region $| y | < 2.8$ and leading jet $p_T > 60$ GeV and sub-leading jet $p_T >$ 30 GeV. This ensures that the jet reconstruction efficiency and purity > 99%.

$$\chi = (| y_1 - y_2) \approx \frac{1 + \cos\theta}{1 - \cos\theta} \tag{1}$$

Where θ is the polar scattering angle of outgoing jets in the di-jet centre-of-mass frame. Similarly the data was found to be well described by theoretical predictions.

3.1 Summary

The inclusive and di-jet cross sections were measured at the LHC at a centre of mass energy of 7 TeV using 17 nb^{-1} of integrated luminosity. This is the first time such a measurement has been made at these energy scale. Work continues on a direct extension of this using all the 2010 dataset, extending the p_T range from 20 GeV to 1.5 TeV, and $| y |$ to out to 4.4. Work continues into other areas of jet physics, including using the sub-structure of reconstructed jets as a means

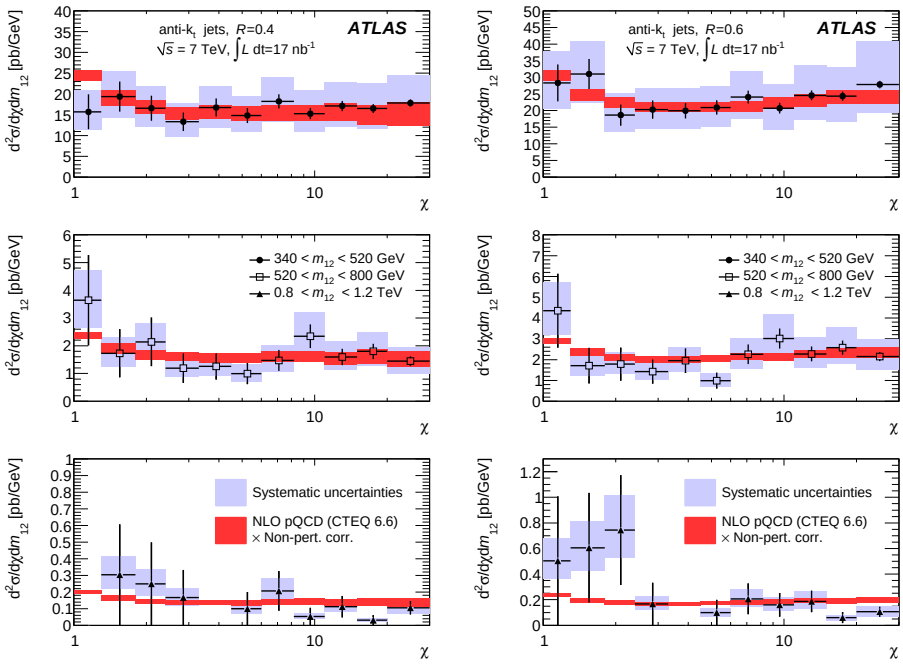

Figure 2: Dijet double-differential cross section as a function of angular variable chi in different bins of dijet mass m_{12}, for jets identified using the anti-kt algorithm with R = 0.4 (left) and R = 0.6 (right).

of identifying high p_T particle decays. This technique has multiple applications, including direct searches for the Higgs Boson.

Acknowledgments

With thanks to the ATLAS collaboration.

References

1. Atlas Collaboration, *The ATLAS EXPERIMENT at the CERN Large Hadron Collider*, JINST **3** (2008) S08003
2. M. Cacciari, G. Salam, and G Soyez, *The anti-kt jet clustering algorithm*, JHEP **0804** (2008) 063, arXiv:080.1189
3. G. P. Salam, M. Cacciari, and G. Soyez http':://www.lpthe.jussieu.fr/ salam/fastjet/
4. T. Sjostrand, S. Mrenna, and P. Skands, *PHYTHIA 6.4 physics and manual*, JHEP **05** (2006) 026 hep-ph/0603175
5. G. Corcell et al. *HERWIG 6: An event generator for hadron emmision reactions with interfering gluons (including super symmetric processes)*, JHEP **01** (001) 010, hep-ph/0011363
6. Z. Nagy, *Next-to-leading order calculation of three jet observables in hadron hadron collisions*, Phys. Rev. **D68**(2003) 094002 arXiv:he[-ph/0307268
7. P.M. Nadolsky et al *Implications of CTEQ global analysis for collider observables*, Phys. Rev. **D78** (2008) 013004, arXiv:0802.0007 [hep-ph]
8. GEANT4 Collaboration, S. Agostinelli et al. *GEANT4: A simulation toolkit*, Nucl. Instrum. Meth. A506 (2003) 250-303
9. G. Aad *et al.* [Atlas Collaboration], Eur Phys. J. C. **71** (2011) 1512 [arXiv:1009.5908]

Search for rare SM processes in the $\not\!\!E_T$+b-jets signature at CDF

K. Potamianos
Purdue University, West Lafayette, IN, USA

The missing transverse energy ($\not\!\!E_T$) plus b-jets signature is very promising for searches for the Higgs boson or new physics. Indeed, $\not\!\!E_T$ naturally arises from unidentified particles such as neutrinos, neutralinos, gravitons, etc., and b-quarks are the main decay products of a low mass Higgs boson as well as of several exotic particles. The main challenge is to identify and reject the numerous standard model (SM) backgrounds that mimic this signature. This is especially so for QCD multi-jet production, a large background due to mis-measurement (rather than undetectable particles). We present state-of-the-art data-driven and multivariate techniques to characterize and reject this instrumental background. These techniques make analyses in this signature as sensitive as those using lepton identification and allow probing for rare SM processes. We describe searches for electroweak single top production, a part of the observation of single top by CDF, and for a low mass SM Higgs boson, one of the most sensitive among low mass Higgs searches at CDF. We also present a measurement of the top pair cross-section in this signature, and discuss other analyses and future prospects.

1 Introduction

The standard model of particle physics (SM) accurately describes most physical observables not involving gravity. All of its particles have been observed and characterized, save to the Higgs boson [1], whose role is to provide mass to the elementary particles. Direct searches and precise electroweak fits constrain its mass, and favor a low mass ($m_H < 158$ GeV/c^2 at 95 % C.L.) [2].

At the Tevatron, the low mass range is best investigated through the associated production of a Higgs boson and a W or Z boson, whose leptonic decay products are triggered on [3]. At low mass, the Higgs predominantly decays to a $b\bar{b}$ pair. In the following, we focus on $ZH \to \nu\nu b\bar{b}$ events. These yield a large transverse energy imbalance ($\not\!\!E_T$), two high-p_T b-jets, and no identified lepton. Due to the difficulty to identify and reconstruct leptons, we are also sensitive to $WH \to \ell\nu b\bar{b}$. This is true especially when the W boson decays to a τ that is not reconstructed ($\sim 50\%$ of the times). Finally, we accept a tiny fraction of $ZH \to \ell\ell b\bar{b}$ events.

In addition to Higgs physics, this signature is also sensitive to the electroweak production of a single top quark, diboson production, and top pair production. These SM processes are either categorized as signal or background, while events from QCD multi-jet production and from the production of a vector boson in association with jets are part of the background.

Next to events from SM processes, many models of new physics also predict this signature: SUSY ($\tilde{b}\bar{\tilde{b}} \to b\tilde{\chi}^0\bar{b}\tilde{\chi}^0$), technicolor ($\rho_T^{\pm} \to Z\pi_T^{\pm} \to \nu\nu b\bar{q}$ and $\rho_T^{\pm} \to W^{\pm}\pi_T^0 \to \ell\nu b\bar{b}$), extra-dimension, etc. In this proceeding, we focus only on SM physics.

In the $\not\!\!E_T$+b-jets signature, the signal is very small when compared to the large backgrounds, especially from QCD production. In the following, we present a innovative technique to isolate and reject the large QCD background.

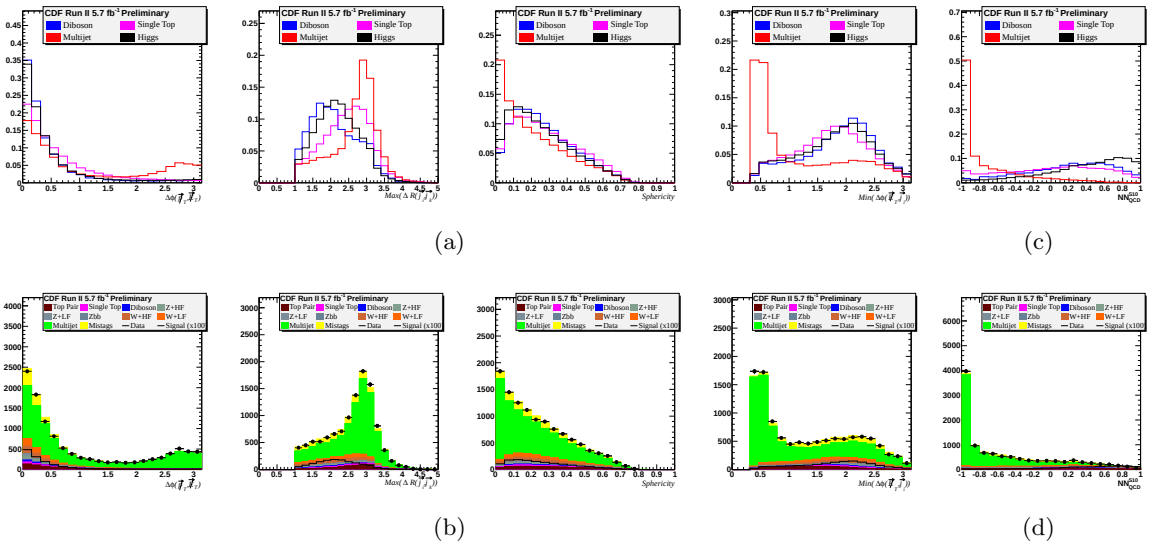

Figure 1: Some of the input variables to the neural network used to reject the QCD multi-jet background: (a) shape comparison, and (b) model validation. (c), (d): Neural network output.

2 Background modeling

The $\not\!\!E_T$+b-jets signature accepts events from every SM process. We use a combination Monte Carlo and data-driven techniques to provide a proper model for each of them. The electroweak processes yield *real* $\not\!\!E_T$ coming from the neutrino(s) in the event. We use Monte Carlo to model these [4]. Additionally, we use data to predict the rate at which light flavor events from these processes can be wrongly identified as originating from a b-quark (i.e. b-tagged). On the contrary, QCD multi-jet production (MJ) yields *instrumental* $\not\!\!E_T$, due to the mis-measurement of the energy of the jets. Because of a large cross-section and of the presence of non-negligible high order effects, it is impractical and not advised to use Monte Carlo to model MJ, especially with large datasets. We therefore use a data-driven model that defines a four-dimensional matrix to predict the probability for a data event to be b-tagged: the *Tag-Rate-Matrix* [4].

3 Tools for background rejection

We select events with $\not\!\!E_T > 50$ GeV/c^2, two or three jets (> 15 GeV/c^2, $|\eta| < 2$), and no identified lepton. We further require the leading (second) jet to have an energy of at least 35 (25) GeV/c^2 and either one to be central ($|\eta| < 0.9$). We remove mis-measured QCD events requiring $\Delta\phi(\not\!\!E_T, j_{(2,3)}) > 0.4$ and $\Delta\phi(\not\!\!E_T, j_1) > 1.5$. We then further improve the S/B ratio.

3.1 Signature of missing particles

A common technique to identify a particle such a neutrino is to measure the transverse energy imbalance in the calorimeter ($\not\!\!E_T$). Here, we also rely on an *independent* sub-detector, the spectrometer, to determine the transverse momentum flow imbalance ($\not\!\!p_T$). In the case of a particle escaping the detector, the $\not\!\!E_T$ and the $\not\!\!p_T$ are aligned. However, for a mis-measured QCD di-jet event, the $\not\!\!E_T$ and is either aligned or anti-aligned to the $\not\!\!p_T$ (Figure 1a, left).

3.2 A neural network to reject the QCD multi-jet background

Next to comparing $\not\!\!p_T$ to $\not\!\!E_T$, we identify kinematic quantities discriminating the signal from the QCD background.Instead of cutting on each variable, we feed a neural network that exploits their correlations, and then cut on its output, reducing the background more efficiently.

We train our network using the *pre-tag* data sample weighted by the *Tag-Rate-Matrix* to model MJ events. This choice is preferred over the use of a Monte Carlo QCD background because it allows not only to reject QCD but also a part of the other electroweak backgrounds. With this technique, it is possible to reject about 90% (70%) of the MJ (overall) background while only loosing 10% of the signal. The signal sample is composed of Monte Carlo events in proportion to the relative size of each signal component.

Figure 1a shows the difference in shape for some of the network input variables. Each of the variables is validated against data, as shown in Figure 1b. In addition to the region where the network is derived, we use five other control regions in which we check both the inputs to the network and its output. This makes us confident in using multivariate analysis to find a signal.

4 Analyses using this neural network background rejection technique

The technique we present is very generic and can be trained with different signals. We briefly describe several analyses that owe their significance to this technique. After rejecting the QCD background, we train another neural network to discriminate the signal from the background.

4.1 Measurement of the top pair production cross-section

First observed in 1995 [5], the top quark has been extensively studied at the Tevatron, mostly in the (semi-)leptonic and all-hadronic signatures. In 2010, we measured for the first time the top pair production cross-section in the $\not\!\!E_T$+b-jets signature [6]. This measurement is complementary to those preceding and contributes to improving the world average. Much importantly, probing a well known signal is a stringent test of the analysis technique. Analyzing 5.7fb^{-1} of CDF data, we measure a cross-section of $7.12^{+1.20}_{-1.12}$ pb, assuming $m_t = 172.5$ GeV/c^2. This measurement is as sensitive as the dilepton and all-hadronic signatures (Figure 2a).

4.2 Measurement of the single top production cross-section

In 2009, CDF and DZero observed the electroweak production of a single top quark [7]. The single top production cross-section is directly proportional to the square of the $|V_{tb}|$ element of the CKM matrix [8] and a measurement thus constrains fourth-generation models. Our analysis in the $\not\!\!E_T$+b-jets signature [4] contributed to the result by adding 30% orthogonal signal into the combination [7,9]. Analyzing 2.1fb^{-1} of CDF data, we measure a cross-section of $4.9^{+2.5}_{-2.2}$ pb (observed sensitivity of 2.1σ) and a $|V_{tb}|$ value of $1.24^{+0.34}_{-0.29} \pm 0.07$ (theory), assuming $m_t = 175$ GeV/c^2 (Figure 2b).

4.3 Search for the SM Higgs boson

The $\not\!\!E_T$+b-jets signature is one of the most sensitive for probing a low mass SM Higgs boson, and an important component of the CDF and Tevatron combination [3]. This search is challenging due to the tiny signal. We tune the analysis to $ZH \to \nu\nu b\bar{b}$ and $WH \to \ell\nu b\bar{b}$ [10,11]. Analyzing 5.7fb^{-1} of CDF data, we set a limit below 5 times the standard model prediction for a Higgs mass up to 135 GeV/c^2, and at 3 times for $m_H = 115$ GeV/c^2 (Figure 2b).

5 Summary and future prospects

The background rejection technique presented here yields similar performance to lepton identification and allows to exploit the large acceptance of the $\not\!\!E_T$+b-jets signature. We have presented several analyses using this innovative technique to isolate small signals. Further steps include relaxing the pre-selection requirements (lower $\not\!\!E_T$ and jet energy cuts) to gain in acceptance while still rejecting the large backgrounds. We then plan to measure the diboson production cross-section in this signature.

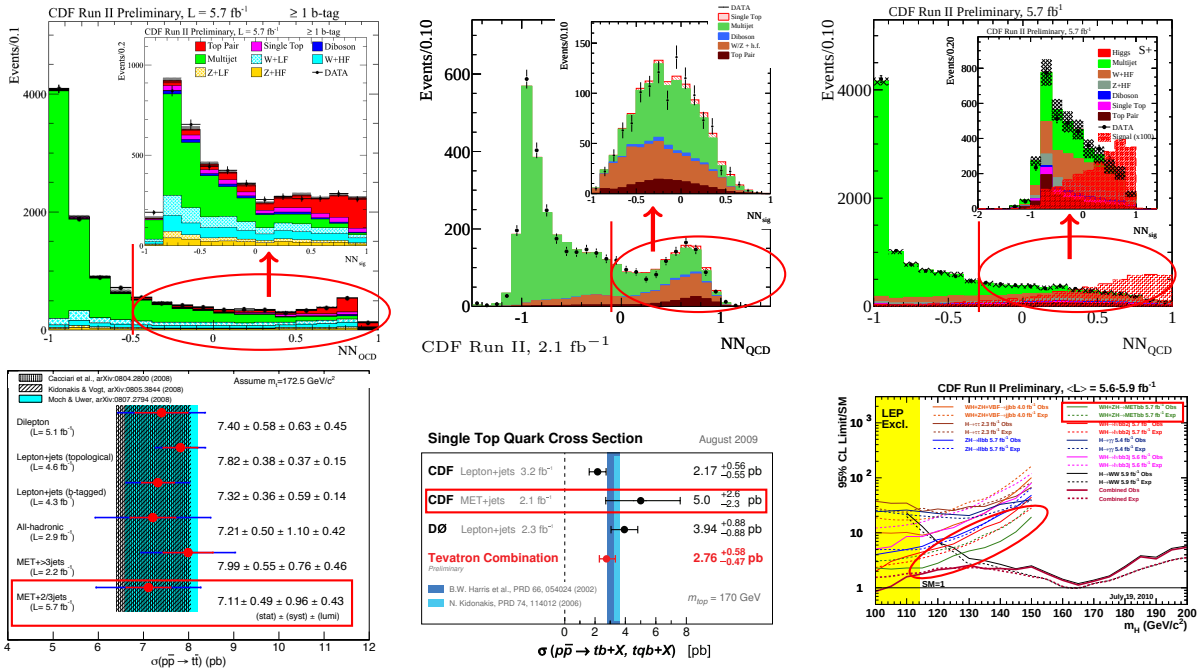

(a) Top pair production (b) EW single top (c) SM Higgs

Figure 2: Three analyses using a neural network to efficiently reject the QCD multi-jet background and another one to discriminate the signal from the remaining background: (a) Top pair cross-section, (b) EW single top cross-section, and (c) limit on SM Higgs.

Acknowledgments

We would like to thank the organizers of the XLVI Rencontres de Moriond for an excellent conference and the CDF collaboration for making these results possible.

References

1. Englert, F. and Brout, R. (1964), *Phys. Rev. Lett.* **13** 321–323 ; Higgs, P.W. (1964), *Phys. Rev. Lett.* **13** 508–509 ; Guralnik, G.S. and Hagen, C.R. and Kibble, T.W.B, (1964). *Phys. Rev. Lett.* **13** 585–587.
2. Barate, R. *et al.*, LEP Higgs Working Group (2003), *Phys. Lett. B* **565** 61–75
3. K. Potamianos [CDF], PoS **ICHEP2010** (2010) 073, [arXiv:1012.1365] ; Tevatron New Phenomena & Higgs Working Group (July 2010), [arXiv:1007.4587].
4. T. Aaltonen *et al.* [CDF], Phys. Rev. **D81** (2010) 072003, [arXiv:1001.4577].
5. F. Abe *et al.* [CDF], Phys. Rev. Lett. **74** (1995) 2626-2631. [arXiv:9503002] ; S. Abachi *et al.* [D0], Phys. Rev. Lett. **74** (1995) 2632-2637. [arXiv:9503003].
6. T. Aaltonen *et al.* [CDF], CDF Conference Note 10237.
7. T. Aaltonen *et al.* [CDF], Phys. Rev. Lett. **103** (2009) 092002, [arXiv:0903.0885] ; V. M. Abazov *et al.* [D0], Phys. Rev. Lett. **103** (2009) 092001. [arXiv:0903.0850].
8. N. Cabibbo, Phys. Rev. Lett. **10** (1963) 531 ; M. Kobayashi and T. Maskawa, Prog. Theor. Phys. **49**, 652 (1973).
9. T. Aaltonen *et al.* [CDF], Phys. Rev. **D82** (2010) 112005, [arXiv:1004.1181].
10. T. Aaltonen *et al.* [CDF], Phys. Rev. Lett. **104** (2010) 141801, [arXiv:0911.3935 [hep-ex]].
11. T. Aaltonen *et al.* [CDF], CDF Conference Note 10212.

Top-quark pair cross-section measurement in the lepton+jets channel

M. Pinamonti
on behalf of the ATLAS collaboration
INFN Udine & University of Trieste,
Strada Costiera 11, 34151 Trieste, Italy

A measurement of the production cross-section for top quark pairs in pp collisions at $\sqrt{s}$ =7 TeV is presented using data recorded with the ATLAS detector at the Large Hadron Collider (LHC). Events are selected in the lepton+jets topology by requiring a single lepton (electron or muon), large missing transverse energy and at least three jets. No explicit identification of secondary vertices inside jets (b-tagging) is performed. In a data sample of 35.3 pb^{-1}, 2009 and 1181 candidate events are observed in the μ+jets and e+jets topology, respectively. A simple multivariate method using three kinematic variables is employed to extract a cross-section measurement of $171\pm17(\text{stat.})^{+20}_{-17}(\text{syst.})\pm5(\text{lumi.})$ pb.

1 Introduction

A precise measurement of the top-pair ($t\bar{t}$) inclusive cross-section at this early stage of the LHC data taking is of central importance for several reasons.

First of all it allows a direct comparison with theoretical calculations providing a precision test of the predictions of perturbative QCD. Additionally $t\bar{t}$ production is an important background in many searches for physics beyond the Standard Model, and new physics may also give rise to additional $t\bar{t}$ production mechanisms or modifications of the top quark decay channels. Finally, this is one of the first precision measurements implying the reconstruction of final states including jets, electrons (e), muons (μ) and missing transverse energy (E_T^{miss}), and since many models of physics beyond the Standard Model predict events with similar signatures it provides an essential stepping stone toward the identification of new physics.

2 Top-pair production and decay

In the Standard Model (SM) the $t\bar{t}$ production cross-section in pp collisions is calculated to be 165^{+11}_{-16} pb at a centre of mass energy of $\sqrt{s}$ =7 TeV assuming a top mass of 172.5 GeV [1]. Top quarks are predicted to decay into a W boson and a b-quark ($t \to Wb$) nearly 100% of the time. Depending on the decays of the two W bosons into a pair of quarks ($W \to q\bar{q}'$) or a lepton-neutrino pair ($W \to \ell\nu$), events with a $t\bar{t}$ pair can be classified as:

- dilepton: when both Ws decay leptonically;
- single-lepton: when one of the W decays leptonically and the second one hadronically;
- all-hadronic: when both Ws decay into quarks.

For the analysis reported here single-lepton $t\bar{t}$ events are selected, considering only events with exactly one electron (e+jets channel) and exactly one muon (μ+jets channel) and without using any b-tagging information. A more detailed description of the analysis can be found in [2].

Other complementary analyses are performed in ATLAS to extract the $t\bar{t}$ production cross-section in dilepton [3] and all-hadronic [4] channels as well as in the single-lepton channel making use of the b-tagging information [5].

3 Event Selection

To select $t\bar{t}$ events in the single lepton final state, the following event selections are applied:

- the appropriate single-electron or single-muon trigger has fired;
- the event contains exactly one reconstructed lepton (electron or muon) with p_T >20 GeV, matching the corresponding high-level trigger object;
- if a muon is reconstructed, E_T^{miss} >20 GeV and $E_T^{miss} + m_T(W)$ >60 GeV is required [a];
- if an electron is reconstructed, E_T^{miss} >35 GeV and $mT(W)$ >25 GeV are required;
- the event is required to have $\geq$ 3 jets with p_T >25 GeV and $|\eta|$ <2.5.

Depending on the flavour of the lepton (e or μ) and on the number of reconstructed jets (exactly three or at least four) the events are classified as e+3-jets, μ+3-jets, e+$\geq$4-jets or μ+$\geq$4-jets, giving rise to four statistically independent channels.

4 Background treatment

The most important backgrounds after the event selections described above are:

- the production of a W boson in association with jets (W+jets),
- the production of QCD multi-jet events in which a fake or non-prompt lepton is reconstructed as a real prompt electron or muon,
- other minor backgrounds including single top electro-weak production, Z+jets and diboson (WW,WZ and ZZ) events.

The number of events observed in data and predicted by simulation or by data-driven estimates in each of the four channels are given in Table 1.

The different backgrounds are treated in different ways to determine the shape and the normalization of the kinematical distributions used to build the likelihood discriminant to extract the cross-section measurement. For the W+jets background the shapes are taken from Monte Carlo (MC) simulation, while the normalization is extracted from the fit (see Section 5). For the QCD multi-jet background both the shapes and the normalization are extracted with data-driven methods. For the other backgrounds, both the shapes and the normalization are taken from MC simulation.

[a] Here $m_T(W)$ is the W-boson transverse mass, defined as $\sqrt{2p_T^{\ell}p_T^{\nu}(1-cos(\phi_\ell-\phi_\nu))}$ where the measured missing E_T vector provides the neutrino information.

events	e +3-jets	e +$\geq$4-jets	μ +3-jets	μ +$\geq$4-jets
$t\bar{t}$	116	194	161	273
QCD	62	22	120	51
W+jets	580	180	1100	310
Z+jets	32	18	70	25
single t	22	11	32	15
diboson	9	3	16	4
Data	781	400	1356	653

Table 1: Numbers of events in the four selection channels. The observed data events are shown, together with the MC simulation estimates for $t\bar{t}$, W+jets, Z+jets and single-top and diboson events, normalised to the data integrated luminosity of 35 pb^{-1}. The data-driven estimates for QCD multi-jet background are also shown.

Source	$\Delta\sigma/\sigma$[%]
Statistical uncertainty	$\pm$9.7
ℓ reco., id. and trigger	-1.9 / +2.6
Jet energy scale, resolution and reco.	-6.1 / +5.7
QCD normalization	$\pm$3.9
QCD shape	$\pm$3.4
W+jets shape	$\pm$1.2
Other backgrounds	$\pm$0.5
ISR/FSR	-2.1 / +6.1
PDFs	-3.0 / +2.8
Parton shower generator	$\pm$3.3
Monte Carlo generator	$\pm$2.1
Limited MC statistics	$\pm$1.8
Pile-up	$\pm$1.2
Total systematics	-10.2 / +11.6
Luminosity	$\pm$3.4

Table 2: List of the main sources of uncertainty affecting the final measurement. For each of the listed sources the relative effect on the measured $t\bar{t}$ cross-section expressed as relative uncertainty is reported.

5 Cross-Section Measurement

The $t\bar{t}$ production cross-section is extracted by exploiting the different properties of $t\bar{t}$ events with respect to the dominant W+jets background. Three variables were selected for their discriminant power, for the small correlation between them and by considering the effect of the jet energy scale uncertainty.

These variables are:

- the pseudorapidity of the lepton η_{lepton}, which exploits the fact that $t\bar{t}$ events produce more central leptons than W+jet events;
- the charge of the lepton q_{lepton}, which uses the fact that $t\bar{t}$ events produce charge-symmetric leptons while W+jet events produce an excess of positively charged leptons;
- the exponential of the aplanarity $(exp(8 \times A))$,[b] which exploits the fact that $t\bar{t}$ events are more isotropic than W+jets.

A likelihood discriminant is built from these input variables following the projective likelihood approach defined in the TMVA package [6]. The distributions of the three input variables and of the likelihood discriminant in data and simulated events are shown in Fig. 1, for the μ+jets channel only.

A binned maximum likelihood fit is applied to the discriminant shapes to extract the $t\bar{t}$ cross-section. Likelihood functions are defined for each of the four channels (e and μ, 3-jets and $\geq$ 4-jets) and are multiplied together in a combined fit to extract the total number of $t\bar{t}$ events.

The performance of the likelihood fit (including statistical and systematic uncertainties) is estimated by performing pseudo-experiments. The systematic uncertainties associated with the simulation, object definitions and the QCD multi-jet estimate, as well as the statistical uncertainty and the uncertainty on the luminosity are summarized in Table 2.

The result coming from the combined fit (including systematic uncertainties) is:

$$\sigma_{t\bar{t}} = 171 \pm 17(stat.)^{+20}_{-17}(syst.) \pm 6(lumi.)pb, \quad (1)$$

for a total relative uncertainty of $-14.5/+15.5\%$. The measured cross-section is in good agreement with the theoretical predictions.

[b] Here $A = \frac{3}{2}\lambda_3$, where λ_3 is the smallest eigenvalue of the normalized momentum tensor calculated using the selected jets and lepton in the event.

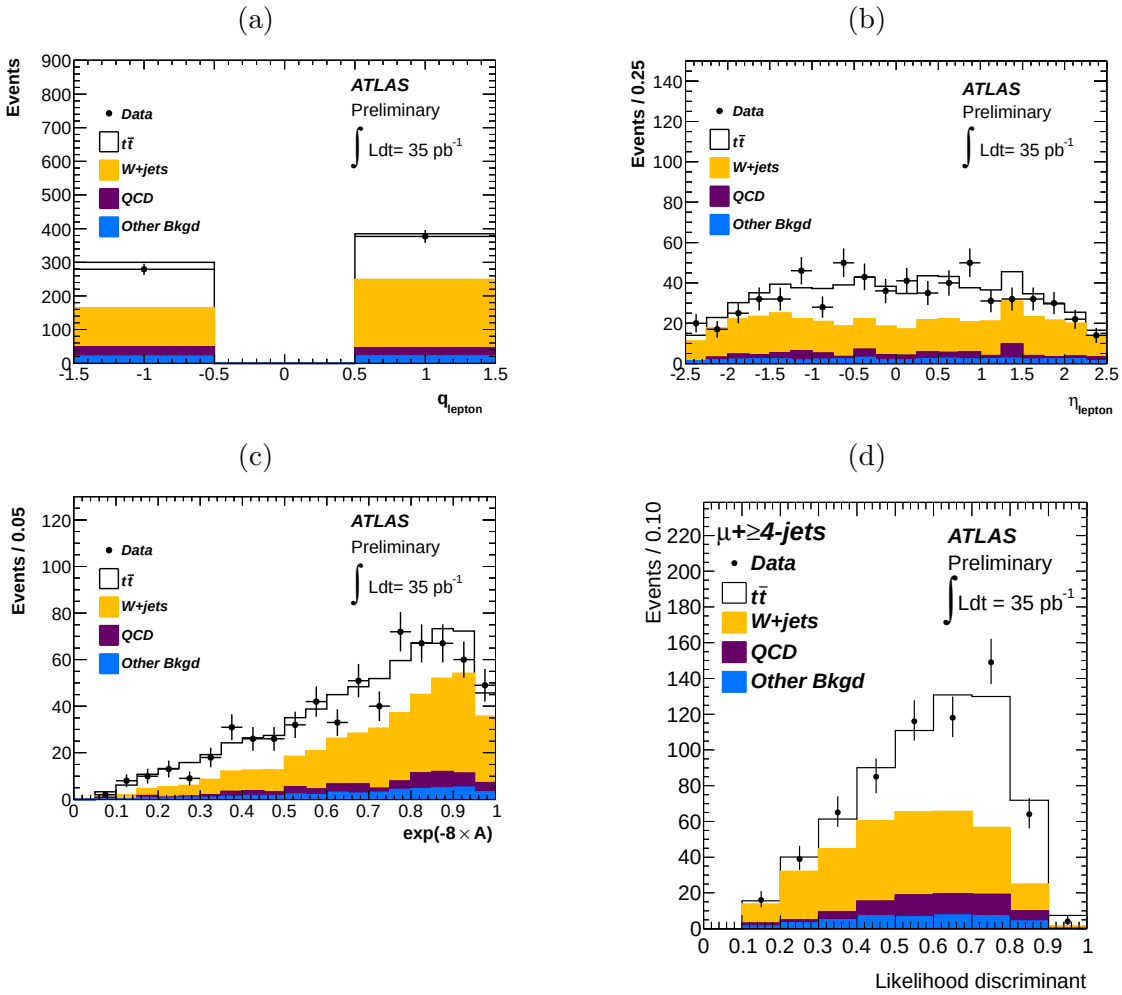

Figure 1: Distributions of the input variables to the likelihood discriminant (a, b and c) and of the likelihood discriminant itself (d) for the μ+$\geq$4-jets channel. In (a), (b) and (c) the normalizations for $t\bar{t}$ and W+jets are fixed to the theoretical predictions, while in (d) they are rescaled according to the result of the fit. The "Other Bkgd" (including Z+jets, single top and diboson) contribution is taken from theoretical predictions. For QCD multi-jet the data-driven estimate is used.

References

1. S. Moch and P. Uwer, Theoretical status and prospects for top-quark pair production at hadron colliders, Phys. Rev. D78 (2008) 034003.
2. The ATLAS Collaboration, Top Quark Pair Production Cross-section Measurements in ATLAS in the Single Lepton+Jets Channel without b-tagging, ATLAS-CONF-2011-023.
3. The ATLAS Collaboration, Measurement of the top quark pair production cross-section with ATLAS in pp collisions at $\sqrt{s}$ =7 TeV in dilepton final states ATLAS-CONF-2011-034.
4. The ATLAS Collaboration, Search for ttbar production in the all-hadronic channel in ATLAS with $\sqrt{s}$ =7 TeV data, ATLAS-CONF-2011-066.
5. The ATLAS Collaboration, Measurement of the top quark-pair cross-section with ATLAS in pp collisions at $\sqrt{s}$ =7 TeV in the single-lepton channel using b-tagging, ATLAS-CONF-2011-035.
6. A. Hoecker, P. Speckmayer, J. Stelzer, J. Therhaag, E. von Toerne, H. Voss, Toolkit forMultivariate Data Analysis with ROOT, arXiv:physics/0703039 (2007).

THE SUSY FLAVOR PROBLEM IN 5D GUTS

S. FICHET
Laboratoire de Physique Subatomique et Cosmologie,
53, rue des Martyrs, Grenoble, France

In 5D SUSY GUTs, wave-function localization permits to reproduce flavour hierarchy. As this mechanism also acts on SUSY breaking parameters, it can potentially solve the SUSY flavour problem. We carry out an analysis of the Holographic Grand Unification framework, where we take properly into account effects of matrix anarchy. In this contribution, we focus on brane-localized SUSY breaking and its consequences.

1 Flavour hierarchies in 5 dimensions

In the Standard Model (SM), the three generations of quarks and leptons follow a peculiar pattern of hierarchical masses and mixings. On the other hand, models with TeV-scale supersymmetry (SUSY) generically induce large, unobserved flavour violating neutral currents (FCNCs) through their scalar SUSY breaking soft terms. It is temptating to assume that the mechanism solving the Standard Model flavour puzzle also gives a peculiar structure to scalar soft terms, such that large FCNCs are suppressed.

An attractive mechanism permitting to realize this idea is wave-function localization [1]. Indeed, localising the Standard Model matter fields in the bulk of a compact extra dimension, for instance on a slice of AdS_5 [2], naturally leads to such flavour hierarchies. Depending on localization of Higgs fields and supersymmetry breaking, this localization can also alleviate the SUSY flavour problem (see, for example, [3,4,5]). Supersymmetry breaking can take place on a brane, or in the gravitational background. We will here consider the former possibility, for a more general analysis, see [6]. In that case, by localizing the Higgs fields and SUSY breaking on the same brane, the soft terms follow a similar hierarchy structure as the Yukawa couplings.

1.1 A 5D realization

Most of our analysis is sufficiently broad to cover, at least quantitavely, any 5D SUSY GUT with the Higgs and SUSY breaking sectors localised on the same brane. However, when we do need to work with a concrete model for definiteness, we choose the "holographic GUT" model of Nomura, Poland and Tweedie (NPT) [7]. A basic picture is given on Figure 1. In the NPT model, there is a warped extra dimension, and the bulk gauge group is $SU(6)$. It is broken by boundary conditions to $SU(5) \times U(1)$ on the UV brane, and by the VEV of an adjoint brane field Σ to $SU(4) \times SU(2) \times U(1)$ on the IR brane. This gives essentially the Standard Model gauge group in the 4D effective field theory. Matter fields are localised in the bulk, and boundary conditions are chosen such that their zero modes furnish precisely the matter content of the MSSM.

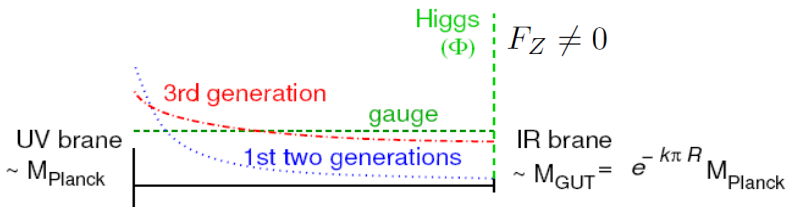

Figure 1: The 5D framework considered. Higgs and the SUSY breaking fields are localized on the IR brane. Matter fields propagate in the bulk, with different exponential profiles generating flavour hierarchy.

Within this 5D framework, the 4D effective Yukawa couplings generated by the overlap of matter fields with Higgs fields are :

$$Y_u = \begin{pmatrix} \varepsilon^4 & \varepsilon^3 & \varepsilon^2 \\ \varepsilon^3 & \varepsilon^2 & \varepsilon \\ \varepsilon^2 & \varepsilon & 1 \end{pmatrix} , \qquad Y_d = Y_l^t = \varepsilon \begin{pmatrix} \varepsilon^2 & \varepsilon^2 & \varepsilon^2 \\ \varepsilon & \varepsilon & \varepsilon \\ 1 & 1 & 1 \end{pmatrix} . \tag{1}$$

The scalar supersymmetry breaking parameters are

$$A_{u,d,l} \sim \frac{F_Z}{M_*} Y_{u,d,l} , \quad m^2_{Q,U,E} \sim \left|\frac{F_Z}{M_*}\right|^2 \begin{pmatrix} \varepsilon^4 & \varepsilon^3 & \varepsilon^2 \\ \varepsilon^3 & \varepsilon^2 & \varepsilon \\ \varepsilon^2 & \varepsilon & 1 \end{pmatrix} , \quad m^2_{D,L} \sim \left|\frac{F_Z}{M_*}\right|^2 \varepsilon^2 \begin{pmatrix} 1 & 1 & 1 \\ 1 & 1 & 1 \\ 1 & 1 & 1 \end{pmatrix} . \tag{2}$$

M^* is the 5D cutoff scale, and F^Z/M^* is the SUSY scale. Note that this SUSY GUT is $SU(5)$-like, Yukawa couplings and soft masses thus satisfy $SU(5)$ relations. These relations are however only approximate due to $SU(5)$ breaking operators residing on the IR brane.

To work out the phenomenology, we also need to specify the gaugino masses. We assume universality : $M_a = M_{1/2}$, and choose a generic parametrization :

$$M_{1/2} = \alpha_{1/2} \frac{F^Z}{M^*} . \tag{3}$$

1.2 Quantifying matrix anarchy

The above mechanism permits to elegantly explain flavour hierarchy. More precisely, it permits to transform anarchical matrices, whose elements are all of same order of magnitude, into hierarchical matrices, though multiplication by powers of ε. The same situation also appears in the Frogatt-Nielsen mechanism.

Even if anarchy of the original flavour matrices is overwhelmed by ε factors, it is necessary to parametrize and quantify it properly. Indeed, on one hand, some amount of matrix anarchy is still necessary to reproduce precisely the SM masses and CKM matrix. On the other hand, this anarchy can introduce uncertainty in the SUSY spectrum, and in flavour observables.

We call the elements of the original anarchical flavour matrices $\lambda_{ij}^{u,d,e}$, such that $Y_{ij}^{u,d,e} \propto \lambda_{ij}^{u,d,e} \varepsilon^{n_{ij}}$, where n_{ij} corresponds to the appropriate power of ε. These λ's are complex, $\mathcal{O}(1)$ coefficients. Other λ's also appear in the scalar soft terms. Since we do not study CP violation, we take them to be real without loss of generality. But there is still a freedom on their $\pm$ signs. Just taking all λ's positive would be a very unnatural choice, as in that case two eigenvalues of each Yukawa matrices are exactly zero. We do not restrict ourselves to an arbitrary choice of sign combinations, but instead scan over all physical, inequivalent combinations. Regarding the magnitude of the λ's, as they are multiplicative coefficients, it is natural to let them vary within a range $[\mathscr{L}^{-1}, \mathscr{L}]$, $\mathscr{L}$ being $\mathcal{O}(1)$. The logarithm of this range is symmetric, and it is in fact more intuitive to consider $\log|\lambda|$. The most natural probability density function associated

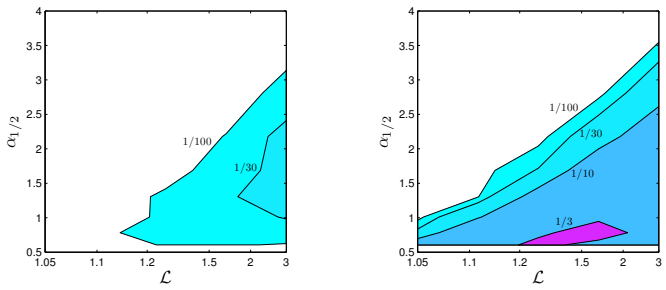

Figure 2: Probability of getting a neutralino LSP as a function of $\alpha_{1/2}$ and $\mathscr{L}$. On both plots, isolines of $\mathrm{P}(\tilde{\chi}_1^0\mathrm{LSP})$ are indicated The dependence on $\tan\beta$ and F^Z/M^* is marginal, they are fixed to $\tan\beta = 5$, $F^Z/M^* = 200$ GeV. *Left* : All sign combinations are taken into account with same weight. *Right* : A favorable sign combination.

to $\log|\lambda|$ (i.e. the prior) should be also symmetric, and we choose the simplest possible : the uniform distribution. We thus have

$$p(|\Lambda| = |\lambda|) = U(-\log\mathscr{L}, \log\mathscr{L}) \ , \tag{4}$$

$U(a,b)$ being the uniform distribution on the interval $[a,b]$. $\mathscr{L} = 1$ corresponds to setting all the $|\lambda|$'s to one, i.e to suppress matrix anarchy in magnitude.

The zero eigenvalues which can appear in Yukawa matrices for certain sign combinations are no longer zero once $\mathscr{L} \neq 1$. They have instead a widespread $\mathscr{L}$-dependent distribution. The predictivity being lost in that case, we consider only sign combinations leading to three non zero eigenvalues.

2 Phenomenological aspects

In the framework described above, we are left with four parameters : the SUSY scale F^Z/M^*, the gaugino mass parameter $\alpha_{1/2}$, the ratio of the two Higgs vevs $\tan\beta = v_u/v_d$, and the magnitude of flavour matrix anarchy $\mathscr{L}$. We emphasize that $\mathscr{L}$ should be considered as a parameter of the model.

2.1 The lightest supersymmetric particle

A crucial aspect of the SUSY spectrum is the nature of the lightest supersymmetric particle (LSP). In our framework, for $\mathscr{L} = 1$, the LSP is a charged slepton, mostly right selectron. However, with $\mathscr{L} > 1$, the probability $\mathrm{P}(\tilde{\chi}_1^0\mathrm{LSP})$ to have a neutralino LSP becomes non zero. This can be understood by considering one-loop RGEs. Indeed, for $\mathscr{L} = 1$, the RG invariant $S = m_{H_u}^2 - m_{H_d}^2 + \mathrm{Tr}(m_Q^2 - m_L^2 - 2m_U^2 + m_D^2 + m_E^2)$ is exactly zero due to $SU(5)$ relations between soft masses. But when $\mathscr{L} > 1$, the cancellations are not exact anymore, and S modifies the running of the selectron mass.

We therefore compute numerically $\mathrm{P}(\tilde{\chi}_1^0\mathrm{LSP})$, for all physical sign combinations of the λ's appearing in the soft masses. This probability depends of course on the weights given to the different sign combinations (i.e. the prior). In Figure 2, we show $\mathrm{P}(\tilde{\chi}_1^0\mathrm{LSP})$ in the $(\alpha_{1/2}, \mathscr{L})$ plane. Taking into account all sign combinations, even the one giving tachyons, $\mathrm{P}(\tilde{\chi}_1^0\mathrm{LSP})$ is at most of few percent. If one consider, however, a favorable sign combination, it can reach 30%.

2.2 Flavour constraints

Let us finally discuss flavour constraints. This time, not only the mass eigenstates, but also mixings are important. Our strategy is to scan over all physical sign combinations, keeping $\mathscr{L} = 1$, then select representative sign combinations and let vary $\mathscr{L}$. We focus on lepton

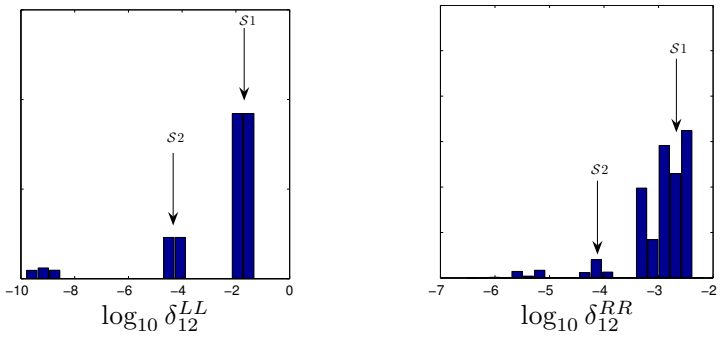

Figure 3: Distribution of mass insertions δ_{12}^{LL} and δ_{12}^{RR} for all sign combinations of λ's. The model parameters are fixed to $F^Z/M^* = 500$ GeV, $\tan\beta = 10$, $\alpha_{1/2} = 2$, $\mathscr{L} = 1$. The values for the two sign combinations $\mathcal{S}1$ and $\mathcal{S}2$ are indicated by arrows.

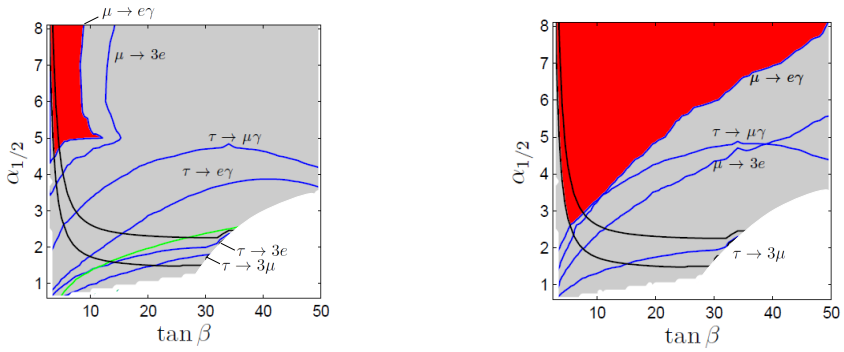

Figure 4: Constraints in the $(\alpha_{1/2}, \tan\beta)$ plane, with $\mathcal{L} = 1$. The red regions pass all constraints. Blue lines correspond to LFV constraints. The dark lines correspond to $m_h = 111$ GeV and $m_h = 114$ GeV. The green line is a conservative bound on $\Delta a_\mu^{BSM} = 450 \times 10^{-11}$. *Left* : Sign combination $\mathcal{S}1$. *Right* : Sign combination $\mathcal{S}2$.

flavour violation (LFV). As an example, we show in Figure 3 distributions of mass insertions $\delta_{XY} = \frac{\mathcal{M}_{XY}}{\sqrt{\mathcal{M}_{XX}\mathcal{M}_{YY}}}$, for given values of parameters. Different clusters appear, with more or less suppressed values of δ's. The origin of these clusters relies on "accidental" supressions. One then has to study how these clusters evolve when $\mathscr{L} > 1$, to check how the accidental supressions survives.

Here, we simply show in Figure 4 two slices of the parameter space for $F^Z/M^* \sim 200$ GeV, corresponding to a conservative sign combination $\mathcal{S}1$ and a more favorable sign combination $\mathcal{S}2$. The most stringent constraints are $\mathrm{BR}(\mu \to e\gamma) < 1.2 \times 10^{-11}$ and the Higgs mass bound. The red regions pass all constraints. The flavor constraints weaken if one increases the overall scale F^Z/M, as this is the decoupling limit. Moreover, depending on $\mathscr{L}$, different mass orderings can appear. In particular, at this scale, getting a neutralino LSP is highly unlikely. This can be seen by comparing Figure 4 to Figure 2. Details will be discussed in [6].

References

1. Y. Grossman and M. Neubert, Phys. Lett. B **474** (2000) 361 [arXiv:hep-ph/9912408].
2. L. Randall and R. Sundrum, Phys. Rev. Lett. **83**, 3370 (1999) [arXiv:hep-ph/9905221].
3. K. w. Choi, D. Y. Kim, I. W. Kim and T. Kobayashi, arXiv:hep-ph/0301131;
4. Y. Nomura, M. Papucci and D. Stolarski, JHEP **0807** (2008) 055 [arXiv:0802.2582].
5. E. Dudas, G. von Gersdorff, J. Parmentier and S. Pokorski, arXiv:1007.5208 [hep-ph].
6. F. Bruemmer, S. Fichet and S. Kraml, in preparation.
7. Y. Nomura, D. Poland and B. Tweedie, JHEP **0612** (2006) 002 [arXiv:hep-ph/0605014].

Measurements of $A_{CP}(B^0 \to K^+\pi^-)$ and $A_{CP}(B_s \to \pi^+K^-)$ at LHCb

Stefano Perazzini
on behalf of the LHCb Collaboration
Dipartimento di Fisica, Via Irnerio 46,
40126 Bologna, Italy

The LHCb experiment is designed to perform flavour physics measurements at the Large Hadron Collider. Using data collected during the 2010 run, we reconstruct a sample of $H_b \to h^+h'^-$ decays, where H_b can be either a B^0 meson, a B_s^0 meson or a Λ_b baryon, while h and h' stand for π, K or p. We provide preliminary values of the direct $\mathcal{CP}$ asymmetries of the neutral B^0 and B_s^0 mesons $A_{CP}(B^0 \to K^+\pi^-) = -0.074 \pm 0.033(\text{stat.}) \pm 0.008(\text{syst.})$ and $A_{CP}(B_s^0 \to \pi^+K^-) = 0.15 \pm 0.19(\text{stat.}) \pm 0.02(\text{syst.})$.

1 Introduction

The family of $H_b \to h^+h'^-$ comprises a large set of decays, namely: $B^0 \to \pi^+\pi^-$, $B^0 \to K^+\pi^-$, $B_s^0 \to K^+K^-$, $B_s^0 \to \pi^+K^-$, $\Lambda_b \to pK^-$, $\Lambda_b \to p\pi^-$, $B^0 \to K^+K^-$, $B_s^0 \to \pi^+\pi^-$ plus their $\mathcal{CP}$-conjugate states. Such decays are matter of great interest, as they are sensitive probes of the Cabibbo-Kobayashi-Maskawa [1,2] matrix and have the potential to reveal the presence of New Physics (NP) [3,4]. NP may alter in a subtle but sizeable way the Standard Model (SM) prediction of the $\mathcal{CP}$ asymmetries in these decays. In the following, we will present the preliminary measurements of the direct $\mathcal{CP}$ asymmetries in the $B^0 \to K^+\pi^-$ and $B_s^0 \to \pi^+K^-$ decays, obtained using the data collected by LHCb during the 2010 at a centre of mass energy of 7 TeV, corresponding to an integrated luminosity of $\int \mathcal{L}\mathrm{d}t \simeq 37\ \text{pb}^{-1}$. Such direct $\mathcal{CP}$ asymmetries are defined in terms of decay rates of B-hadrons as $A_{CP} = \left[\Gamma\left(\bar{B} \to \bar{f}\right) - \Gamma\left(B \to f\right)\right] / \left[\Gamma\left(\bar{B} \to \bar{f}\right) + \Gamma\left(B \to f\right)\right]$.

2 The LHCb detector

The LHCb detector [5] is a single arm spectrometer in the forward direction. It is composed of a vertex detector around the interaction region, a set of tracking stations in front of and behind a dipole magnet that provides a field integral of 4 Tm, two Ring-Imaging Cherenkov (RICH) detectors, electromagnetic and hadronic calorimeters complemented with pre-shower and scintillating pad detectors, and a set of muon chambers. The two RICH detectors are of particular importance for this analysis, as they provide the particle identification (PID) information needed to disentangle the various $H_b \to h^+h'^-$ final states. They are able to efficiently separate π, K and protons in a momentum range from 2 GeV/c up to and beyond 100 GeV/c. RICH-1 is installed in front of the magnet and uses Areogel and C_4F_{10} as radiators, while RICH-2 is installed behind the magnet and employs CF_4.

3 Events selection

The $H_b \to h^+h'^-$ decays are principally selected by the two-level hadronic trigger of LHCb. The first level (Level 0) is based on custom electronic boards, selecting events with high transverse energy clusters in the hadronic calorimeter. The second level, so called High Level Trigger (HLT), is software-based and selects events with at least one track with high transverse momentum and large impact parameter with respect to all reconstructed primary vertices.
The events used in this analysis are extracted from the triggered data using two different offline selections, each one targeted to achieve the best sensitivity on $A_{CP}(B^0 \to K^+\pi^-)$ and $A_{CP}(B_s^0 \to \pi^+K^-)$. The strategy used to optimise the cuts is divided into two steps. In the first step we define the kinematic cuts against the combinatorial background, selecting in an inclusive way the $H_b \to h^+h'^-$ candidates, without using any PID information and assigning by default the pion-mass hypothesis to all charged tracks. The two kinematic selections use the same set of cuts, but with different thresholds. They select pairs of oppositely charged tracks with high transverse momentum and large impact parameter with respect to all reconstructed primary vertices, fitted in a common vertex displaced from the related primary vertex.
In the second step, exploiting the capabilities of the two RICH detectors, two sets of PID cuts are defined (one for each set of optimised kinematic cuts) in order to separate the data into eight mutually exclusive sub-samples corresponding to distinct final state hypothesis ($K^+\pi^-$, $K^-\pi^+$, $\pi^+\pi^-$, K^+K^-, $p\pi^-$, $\bar{p}\pi^+$, pK^- and $\bar{p}K^+$). The guiding principle to identify the PID selection criteria is to limit the total amount of cross-feed backgrounds under the $B^0 \to K^+\pi^-$ and $B_s^0 \to \pi^+K^-$ mass peaks to the same level as the corresponding combinatorial background. Such cross-feed backgrounds are due to the other $H_b \to h^+h'^-$ where we mis-identified one or both final state particles.

4 Calibration of particle indentification

The calibration of the PID observables is a crucial aspect of this analysis, as it is the only variable allowing us to discriminate between the various decay modes. Hence, in order to determine the amount of cross-feed backgrounds for a given channel, the relative efficiencies of the PID selection cuts, employed to identify the specific final state of interest, play a key role.
Thanks to the high production rate of D^* mesons at LHC and to the kinematic characteristics of $D^{*+} \to D^0(K^-\pi^+)\pi^+$ decay chain (and its charge conjugate), samples of large statistcs and high purity of π and K can be extracted from these events without any use of PID information. The same consideration holds for protons obtained from $\Lambda \to p\pi^-$ decays.
Since production and decay kinematics of $D^0 \to K^-\pi^+$ and $\Lambda \to p\pi^-$ channels differ from those of $H_b \to h^+h'^-$, the distributions of PID observables are reweighted in momentum p and transverse momentum p_T, in order to match the corresponding distributions of particles from two-body B-hadron decays. The efficiencies for each set of PID cuts are evaluated from the reweighted distributions.

5 Fits to the $H_b \to h^+h'^-$ mass spectra

We perform unbinned maximum likelihood fits to the mass spectra of events passing the optimised offline selections for the measurements of $A_{CP}(B^0 \to K^+\pi^-)$ or $A_{CP}(B_s^0 \to K^-\pi^+)$. The fits are performed simultaneously on all the eight categories defined by means of the PID selection criteria. The signals, identified as the channels where both tracks are identified with the right mass hypothesis, are parameterized with a single Gaussian function convolved with a component accounting for final state QED radiation [6]. The combinatorial background is mod-

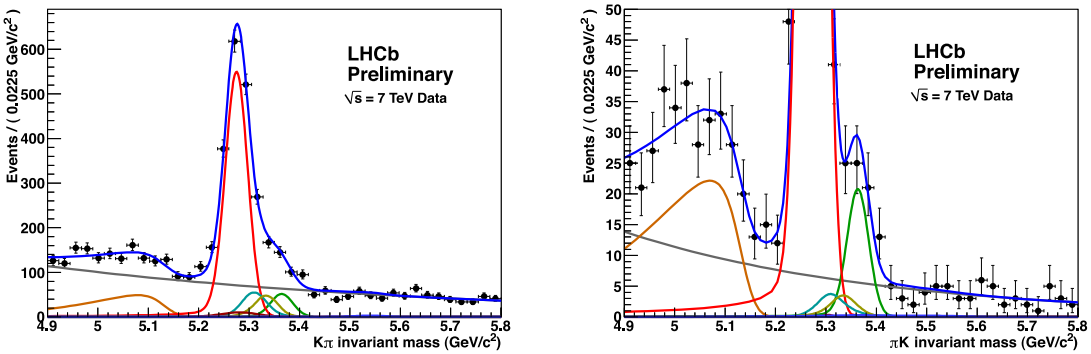

Figure 1: $K^+\pi^-$ (plus charge conjugate) invariant mass spectrum for events surviving the event selection optimised for the best sensitivity on $A_{CP}(B^0 \to K^+\pi^-)$ (left) and $A_{CP}(B^0 \to K^+\pi^-)$ (right). The result of the unbinned maximum likelihood fit is superimposed. The main components contributing to the fit model explained in the text are also visible: $B^0 \to K\pi$ (red), wrong sign $B^0 \to K\pi$ combination (dark red), $B^0 \to \pi^+\pi^-$ (light blue), $B_s^0 \to K^+K^-$ (dark yellow), $B_s^0 \to \pi K$ (green), combinatorial background (grey), 3-body partially reconstructed decays (orange).

eled with an exponential function. The invariant mass shapes of cross-feed backgrounds are parameterized by means of full simulated events, while the normalization of each mis-identified channel is determined multiplying the yield obtained from the right mass hypothesis fit by the ratio between PID efficiencies for the wrong and right final state hypothesis. For the $K^\pm\pi^\mp$ and $\pi^+\pi^-$ categories it is necessary to model also a component due to partially reconstructed 3-body B-hadron decays, while in the other final state categories such a contribution is found to be negligible.

The results of the fits superimposed to the $K^\pm\pi^\mp$ mass spectra (seperately for the samples obtained using the two optimised selections) are shown in Fig. 1. The asymmetries obtained from the fits are respectively: $A_{CP}^{RAW}(B^0 \to K^+\pi^-) = 0.086 \pm 0.033(\text{stat.})$ and $A_{CP}^{RAW}(B_s^0 \to K^-\pi^+) = 0.15 \pm 0.19(\text{stat.})$. The systematic errors due to the fit model and PID calibration are estimated to be respectively 0.002 and 0.004 for $A_{CP}(B^0 \to K^+\pi^-)$ and 0.021 and 0.001 for $A_{CP}(B_s^0 \to K^+\pi^-)$.

6 Correction to the A_{CP}^{RAW}

The physical $\mathcal{CP}$ asymmetries we want to measure are related to the raw asymmetries obtained from the invariant mass fit by:

$$A_{CP} = A_{CP}^{RAW} - A_D(K\pi) - \kappa A_P \tag{1}$$

where $A_D(K\pi)$ is the detector induced asymmetry in reconstructing $K^+\pi^-$ and $K^-\pi^+$ final states, A_P is the production asymmetry of B mesons and κ is a factor that takes into account the $B-\bar{B}$ oscillation. The production asymmetry is defined in terms of the B and $\bar{B}$ production rates $A_P = (R_{\bar{B}} - R_B)/(R_{\bar{B}} + R_B)$. The κ factor is given by

$$\kappa = \frac{\int (e^{-\Gamma t'} \cos \Delta m t') \varepsilon(t) dt}{\int (e^{-\Gamma t'} \cosh \frac{\Delta\Gamma}{2} t') \varepsilon(t) dt}, \tag{2}$$

where $\varepsilon(t)$ is the acceptance for the decay of interest, as function of the proper decay time t.

The detector induced asymmetry $A_D(K\pi)$ is determined using high statistics samples of tagged $D^{*+} \to D^0(K^-\pi^+)\pi^+$, $D^{*+} \to D^0(K^+K^-)\pi^+$ and $D^{*+} \to D^0(\pi^+\pi^-)\pi^+$, and untagged $D^0 \to$

$K^-\pi^+$ decays (plus their charge conjugates). Combining the integrated raw asymmetries obtained from the invariant mass fit of all these decay modes and employing the current world average of the integrated $\mathcal{CP}$ asymmetries for the two modes $D^0 \to K^+K^-$ and $D^0 \to \pi^+\pi^-$ [8], we determine $A_D(K\pi) = -0.004 \pm 0.004$ (the direct $\mathcal{CP}$ asymmetry of $D^0 \to K^-\pi^+$ is considered negligible).
The production asymmetry A_P is determined by means of a reconstructed sample of $B^\pm \to J/\psi(\mu^+\mu^-)K^\pm$ decays. Correcting the raw asymmetry measured from data by the current world average of the direct $\mathcal{CP}$ asymmetry $A_{CP}(B^+ \to J/\psi K^+) = 0.009 \pm 0.008$ [10], and taking into account the reconstruction asymmetry between K^+ and K^- we measure $A_P(B^+) = -0.024 \pm 0.013$. We assume $A_P(B^+)$ equal to $A_P(B^0)$, but introducing a systematic error of 0.01 to account for possible differences, obtaining $A_P(B^0) = -0.024 \pm 0.013 \pm 0.010$. Such a systematic uncertainty has been determined by studying the predictions of different fragmentation models [7].
For the evaluation of the κ factors, $\varepsilon(t)$ is determined from full simulated events using the selections optimised for the respective $A_{CP}(B^0 \to K^+\pi^-)$ and $A_{CP}(B_s^0 \to K^+\pi^-)$ measurements. The values of the parameters controlling the time evolution of neutral B mesons, namely Γ_d, Γ_s, Δm_d, Δm_s and $\Delta\Gamma_s$, are taken from the current world averages [10], but assuming $\Delta\Gamma_d = 0$. The κ factors, computed respectively for the B^0 and B_s^0, are $\kappa_d = 0.33$ and $\kappa_s = 0.015$. For the case of the $B_s^0 \to K^-\pi^+$ decay, even assuming conservatively $A_P(B_s^0) = A_P(B^0)$, the correction to the $A_{CP}^{RAW}(B_s^0 \to K^-\pi^+)$ results to be negligible.
Using Eq. (1) the central values of the direct $\mathcal{CP}$ asymmetries are $A_{CP}(B^0 \to K^+\pi^-) = -0.074$ and $A_{CP}(B_s^0 \to K^+\pi^-) = 0.15$. The statistical errors of $A_D(K\pi)$ and κA_P are considered as systematic uncertainties contributing to $A_{CP}(B^0 \to K^+\pi^-)$ and $A_{CP}(B_s^0 \to K^+\pi^-)$.

7 Final result

Using data collected by the LHCb detector during the 2010 run we provide preliminary values of the direct CP asymmetries:

$$A_{CP}(B^0 \to K^+\pi^-) = -0.074 \pm 0.033(\text{stat.}) \pm 0.008(\text{syst.}) \quad (3)$$

$$A_{CP}(B_s^0 \to \pi^+K^-) = 0.15 \pm 0.19(\text{stat.}) \pm 0.02(\text{syst.}). \quad (4)$$

The current HFAG average [9] $A_{CP}(B^0 \to K^+\pi^-) = -0.098^{+0.012}_{-0.11}$ and the CDF measurement [11] $A_{CP}(B_s^0 \to K^-\pi^+) = 0.39 \pm 0.15(\text{stat.}) \pm 0.08(\text{syst.})$ are in agreement with our values.

References

1. N. Cabibbo *Phys. Rev. Lett.* **10**, 531 (1963).
2. M. Kobayashi and T. Maskawa, *Prog. Theor. Phys.* **49**, 652 (1973).
3. R. Fleischer, *Eur. Phys. J.* C **52**, 267 (2007).
4. R. Fleischer, *Phys. Lett.* B **459**, 306 (1999).
5. A. A. Alves *et al.* [LHCb Collaboration], *JINST* **3**, S08005 (2008).
6. E. Baracchini and G. Isidori, *Phys. Lett.* B **633**, 309 (2006).
7. R. W. Lambert, CERN-THESIS-2009-001.
8. E. Barberio et al. [Heavy Flavor Averaging Group], *CP asymmetries in D0 decay modes: March 2010 update*, http://www.slac.stanford.edu/xorg/hfag/charm/cp_asym/charm_asymcp_10mar10.html.
9. E. Barberio et al. [Heavy Flavor Averaging Group], *CP Asymmetries in Charmless B Decays: ICHEP 2010 update*, http://www.slac.stanford.edu/xorg/hfag/rare/ichep10/acp/.
10. K. Nakamura *et al.* [Particle Data Group], *J.Phys.* G **37**, 075021 (2010).
11. T. Aaltonen *et al.* [CDF Collaboration], arXiv:1103.5762 [hep-ex].

RS MODEL EFFECTS ON B_s^0 CP-VIOLATION

TORSTEN PFOH
Institut für Physik (THEP), Johannes Gutenberg-Universität,
D-55099 Mainz, Germany

We study the impact of the Randall-Sundrum setup on the width difference $\Delta\Gamma_s$ and the CP-violating phase ϕ_s in the $\bar{B}_s^0$-B_s^0 system. We find that the correction to the magnitude of the decay amplitude Γ_{12}^s is below 4% for a realistic choice of input parameters. The main modification in the $\Delta\Gamma_s/\beta_s$-plane is caused by a new CP-violating phase in the mixing amplitude, which allows for a better agreement with the experimental results of CDF and DØ from $B_s^0 \to J/\psi\phi$ decays. The best-fit value of the CP asymmetry $S_{\psi\phi}$ can be reproduced, while simultaneously the theoretical prediction for the semileptonic CP asymmetry $A_{\rm SL}^s$ can enter the 1σ range.

1 Introduction

Within the search for new physics (NP) in the decay of B_s^0-mesons, an important observable is the width difference $\Delta\Gamma_s \equiv \Gamma_L^s - \Gamma_H^s$ between the light and the heavy meson state. According to the above definition, $\Delta\Gamma_s$ happens to be positive in the Standard Model (SM). It can be computed from the dispersive and absorptive part of the $\bar{B}_s^0$-B_s^0 mixing amplitude, M_{12}^s and Γ_{12}^s. To leading order in $|\Gamma_{12}^s|/|M_{12}^s|$ one finds the simple relation

$$\Delta\Gamma_s = -\frac{2\,\mathrm{Re}(M_{12}^s\Gamma_{12}^{s*})}{|M_{12}^s|} = 2\,|\Gamma_{12}^s|\,\cos\phi_s\,. \tag{1}$$

We define the relative phase ϕ_s between the mixing and the decay amplitude according to the convention

$$\frac{M_{12}^s}{\Gamma_{12}^s} = -\frac{|M_{12}^s|}{|\Gamma_{12}^s|}\,e^{i\phi_s}\,, \qquad \phi_s = \arg(-M_{12}^s\Gamma_{12}^{s\,*})\,, \tag{2}$$

for which the SM value is positive and explicitly given by [1] $\phi_s^{\rm SM} = (4.2\pm1.4)\cdot10^{-3}$. The combined experimental results of CDF and DØ [2] differ from the SM prediction in the $(\beta_s^{J/\psi\phi}, \Delta\Gamma_s)$-plane by about 2σ, whereas the latest CDF results disagree by 1σ only [3]. Here, $\beta_s^{J/\psi\phi} \in [-\pi/2, \pi/2]$ is the CP-violating phase in the interference of mixing and decay, obtained from the time-dependent angular analysis of flavor-tagged $B_s^0 \to J/\psi\phi$ decays. In the SM it is given by [1] $\beta_s^{J/\psi\phi} = -\arg\left(-\lambda_t^{bs}/\lambda_c^{bs}\right) = 0.020 \pm 0.005$, with $\lambda_q^{bs} = V_{qb}V_{qs}^*$. In the presence of NP, $\Delta\Gamma_s$ will be modified [4,5]. We adopt the notation of ref.[6] and extend the SM relations according to

$$M_{12}^s = M_{12}^{s\,\rm SM} + M_{12}^{s\,\rm NP} = M_{12}^{s\,\rm SM} R_M\, e^{i\phi_M}\,, \qquad \Gamma_{12}^s = \Gamma_{12}^{s\,\rm SM} + \Gamma_{12}^{s\,\rm NP} = \Gamma_{12}^{s\,\rm SM} R_\Gamma\, e^{i\phi_\Gamma}\,. \tag{3}$$

From (1) it follows that

$$\Delta\Gamma_s = 2\,|\Gamma_{12}^{s\,\rm SM}|\,R_\Gamma\,\cos(\phi_s^{\rm SM} + \phi_M - \phi_\Gamma)\,, \tag{4}$$

where [7] $\Delta\Gamma_s^{\rm SM} = (0.087 \pm 0.021)\,{\rm ps}^{-1}$. A further important observable is the semileptonic CP asymmetry $A_{\rm SL}^s = {\rm Im}(\Gamma_{12}^s/M_{12}^s)$. Including NP corrections, we find

$$A_{\rm SL}^s = \frac{|\Gamma_{12}^{s\,\rm SM}|}{|M_{12}^{s\,\rm SM}|}\,\frac{R_\Gamma}{R_M}\,\sin(\phi_s^{\rm SM} + \phi_M - \phi_\Gamma)\,. \tag{5}$$

Within the SM, the leading contribution to the dispersive part of the $\bar{B}_s^0$-B_s^0 mixing amplitude appears at the one loop level. If NP involves flavor-changing neutral currents (FCNCs) at tree level, these give rise to sizable corrections to the mass difference $\Delta m_{B_s} \equiv M_H^s - M_L^s = 2\,|M_{12}^s|$. Moreover, the presence of tree FCNCs and right-handed charged-current interactions give rise to new decay diagrams. However, the NP corrections to the absorptive part of the amplitude are suppressed by m_W^2/Λ^2 with respect to the SM contribution, where Λ is the NP mass scale. Thus, they are neglected in many NP studies.

2 RS corrections to the $\bar{B}_s^0$-B_s^0 system

The Randall-Sundrum (RS) model[8] is a five-dimensional (5D) quantum field theory (QFT) with an compactified extra-dimension of the order of the Planck length. A "warped metric" is used to generate hierarchies, which are non-understood in the SM. The theory is decomposed into an effective four-dimensional QFT by means of a Kaluza-Klein (KK) decomposition. This gives rise to an infinite tower of heavy copies of the SM particles. The mass scale of the first KK excitations $M_{\rm KK}$ is taken to be a few TeV.

We consider two different scenarios. The first one consists of the SM gauge and matter fields living in the bulk of the 5D space-time, and a Higgs doublet, which is confined to the so-called infra-red boundary of the extra dimension[9]. The second scenario features an extended symmetry group $SU(2)_L \times SU(2)_R \times U(1)_X$ of the electroweak (EW) sector, which is broken down $SU(2)_L \times U(1)_Y$ by the choice of boundary conditions of the respective gauge fields[10,12,13]. An appropriate embedding of the fermions allows for a protection of $Z^0 b_L \bar{b}_L$ couplings[11].

A numerical scan accross the "RS landscape" is performed by evaluating M_{12}^s and Γ_{12}^s for appropriate random sets of input parameters, that reproduce the quark masses, mixing angles, and CKM phase. Furthermore, bounds from the $Z^0 b_L \bar{b}_L$ coupling, the oscillation frequency Δm_{B_s}, and the observable ϵ_K, are taken into account. Details of the calculations are given in ref.[15].

3 Numerical analysis

In the first panel of Figure 1 we show the RS corrections to the magnitude and CP-violating phase of the $\bar{B}_s^0$-B_s^0 decay width, R_Γ and ϕ_Γ, for a set of 10000 parameter points at $M_{\rm KK} = 2\,{\rm TeV}$. The blue (dark gray) points correspond to the minimal RS model, where we plot only those that are in agreement with the $Z^0 \to b\bar{b}$ "pseudo observables". The orange (light gray) points correspond to the custodial extension, where the latter bound vanishes. As expected, the RS corrections to $|\Gamma_{12}^s|$ are rather small, typically not exceeding $\pm 4\%$. The corrections to the magnitude and phase of the dispersive part of the mixing amplitude, R_M and ϕ_M, are plotted in the second panel of Figure 1. Here, one should keep in mind the experimental result from the time-dependent measurement of the $\bar{B}_s^0$-B_s^0 oscillation frequency[16]

$$\Delta m_{B_s}^{\rm exp} = (17.77 \pm 0.10\,({\rm stat}) \pm 0.07\,({\rm syst}))\,{\rm ps}^{-1}\,, \tag{6}$$

which is in good agreement with the SM prediction[7] $(17.3 \pm 2.6)\,{\rm ps}^{-1}$. As a consequence, all points with $R_M \notin [0.718, 1.336]$ are excluded at 95% confidence level, as indicated by the dashed lines. Compared to ϕ_M, the new phase ϕ_Γ can be neglected (what we will do from now on).

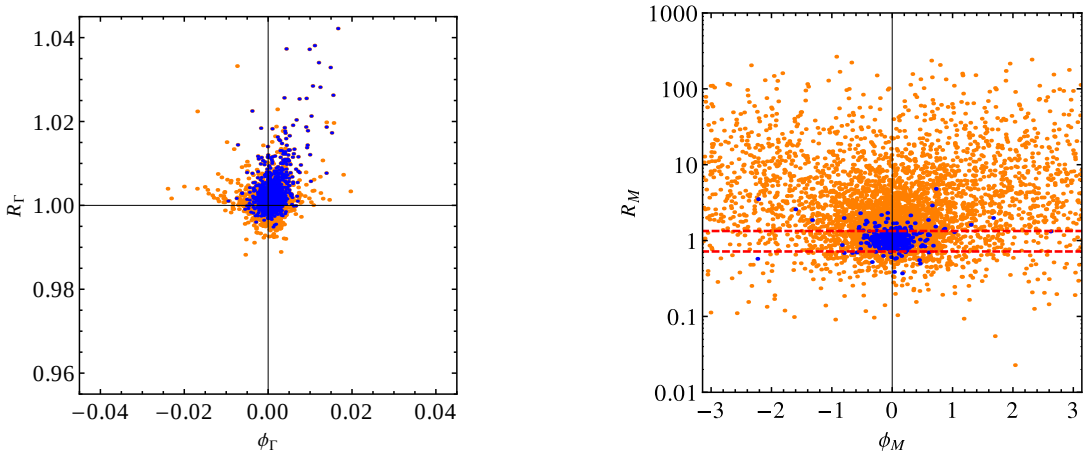

Figure 1: RS corrections to the magnitude and CP-violating phase of the $\bar{B}_s^0$-B_s^0 decay amplitude, R_Γ and ϕ_Γ, as well as for the mixing amplitude, R_M an ϕ_M. Blue points correspond to the minimal, orange to the custodial RS model. The red dashed lines mark the 99% confidence region with respect to the measurement of Δm_{B_s}.

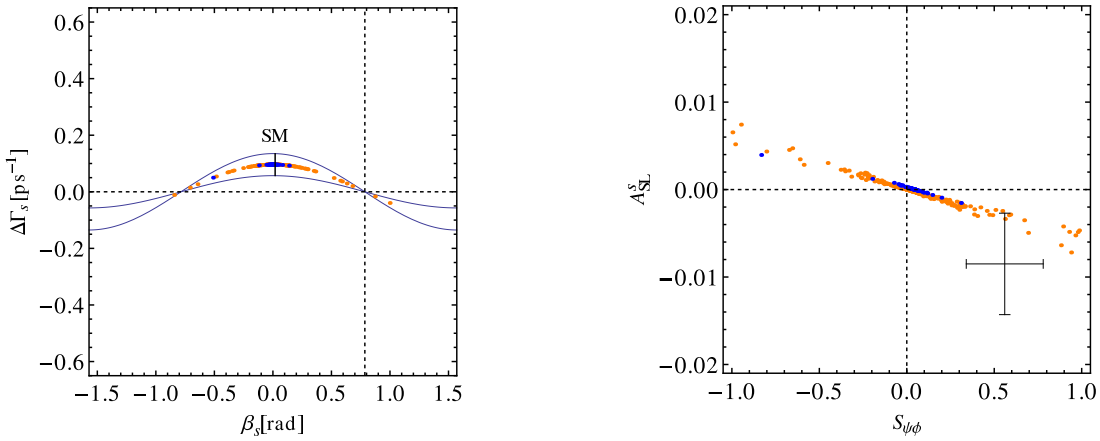

Figure 2: Left panel: Corrections within the $\Delta\Gamma_s^{\rm SM}/\beta_s$-plane for the minimal (blue/dark gray) and custodial (orange/light gray) RS model. Bounds from $Z^0 b\bar{b}$, Δm_{B_s}, and ϵ_K are satisfied. LRight panel: Corrections within the $A_{\rm SL}^s/S_{\psi\phi}$-plane for the minimal and custodial RS model.

Neglecting the small SM phases, the width difference (4) can be written as

$$\Delta\Gamma_s = \Delta\Gamma_s^{\rm SM}\, R_\Gamma\, \cos 2\beta_s\,, \tag{7}$$

where $2\beta_s \approx -\phi_M^{\rm RS}$. The preliminary CDF analysis [3] uses the older SM prediction [1] $\Delta\Gamma_s^{\rm SM} = (0.096 \pm 0.039)\text{ps}^{-1}$, which we will take as central value for our calculation. Taking the more recent value will not change our conclusions. The resulting RS predictions for $\Delta\Gamma_s$ are plotted against β_s in the left panel of Figure 2. Comparing to the latest preliminary CDF results [3], we conclude that the RS model can enter the 68% confidence region and come close to the best fit value. It stays below the desired value for $\Delta\Gamma_s$, as there are no sizable positive corrections to $|\Gamma_{12}^s|$.

The SM prediction [7] $(A_{\rm SL}^s)_{\rm SM} = (1.9 \pm 0.3)\cdot 10^{-5}$, which is often named $a_{\rm sl}^s$ or $a_{\rm fs}^s$ in the literature, agrees with the direct measurement [17] $(A_{\rm SL}^s)_{\rm exp} = -0.0017 \pm 0.0092$ within the (large) error. However, recent measurements of the like-sign dimuon charge asymmetry [18] $A_{\rm SL}^b$, which

connect $A_{\rm SL}^s$ to its counterpart $A_{\rm SL}^d$ of the B_d^0-meson sector [20], imply a deviation of almost 2σ. If one neglects the tiny SM phases and the NP phase corrections related to decay, $A_{\rm SL}^s$ is proportional to the quantity [19] $S_{\psi\phi}$, which is given by the amplitude of the time-dependent asymmetry in $B_s^0 \to J/\psi\phi$ decays, $A_{\rm CP}^s(t) = S_{\psi\phi}\sin(\Delta m_{B_s} t)$. Setting just the NP phase in the decay to zero, one obtains the well known expression [21] $S_{\psi\phi} = \sin(2\beta_s^{J/\psi\phi} - \phi_M)$, and thus

$$A_{\rm SL}^s \approx -\frac{|\Gamma_{12}^{s\,\rm SM}|}{|M_{12}^{s\,\rm SM}|}\,\frac{R_\Gamma}{R_M}\,S_{\psi\phi}\,. \tag{8}$$

The RS result is shown in the right panel of Figure 2, where we have sketched the experimental favored values $S_{\psi\phi} = 0.56 \pm 0.22$ [22] and $A_{\rm SL}^s = -0.0085 \pm 0.0058$ [17]. The latter number combines the direct measurement with the results derived from the measurement of $A_{\rm SL}^b$ in semileptonic B-decays together with the average $A_{\rm SL}^d = -0.0047 \pm 0.0046$ from B-factories. It is evident from the plot that the best fit value of $S_{\psi\phi}$ can be reproduced (with some tuning in the minimal RS variant), which has already been noted in ref.[14]. Furthermore, the custodial RS model can enter the 1σ range of the measured value of $A_{\rm SL}^s$. The necessary choice of input parameters is similar to that one, which is suggested by the $\Delta\Gamma_s/\beta_s$-confidence region.

Acknowledgments

I would like to thank the organizers of the Moriond conference for giving me the opportunity to speak about my research, and for granting me financial support. I further thank Martin Bauer, Sandro Casagrande, Uli Haisch, Tobias Hurth, Matthias Neubert, and Uli Nierste for useful discussions and remarks. Many thanks of course are devoted to my collaborator Florian Goertz.

References

1. A. Lenz and U. Nierste, JHEP **0706** (2007) 072 [arXiv:hep-ph/0612167].
2. CDF public note CDF/PHYS/BOTTOM/CDFR/9787, June, 2009.
3. CDF public note CDF/ANAL/BOTTOM/PUBLIC/10206, November, 2010.
4. Y. Grossman, Phys. Lett. B **380** (1996) 99 [arXiv:hep-ph/9603244].
5. I. Dunietz *et al.* Phys. Rev. D **63**, 114015 (2001) [arXiv:hep-ph/0012219].
6. A. Dighe *et al.* Phys. Rev. D **82** (2010) 031502 [arXiv:1005.4051].
7. A. Lenz and U. Nierste, arXiv:1102.4274 [hep-ph].
8. L. Randall and R. Sundrum, Phys. Rev. Lett. **83**, 3370 (1999) [arXiv:hep-ph/9905221].
9. S. Casagrande *et al.* JHEP **0810** (2008) 094 [arXiv:0807.4937 [hep-ph]].
10. K. Agashe *et al.* JHEP **0308**, 050 (2003) [arXiv:hep-ph/0308036].
11. K. Agashe *et al.* Phys. Lett. B **641**, 62 (2006) [arXiv:hep-ph/0605341].
12. M. Blanke *et al.* JHEP **0903** (2009) 001 [arXiv:0809.1073 [hep-ph]].
13. S. Casagrande *et al.* JHEP **1009** (2010) 014 [arXiv:1005.4315 [hep-ph]].
14. M. Bauer *et al.* JHEP **1009** (2010) 017 [arXiv:0912.1625 [hep-ph]].
15. F. Goertz and T. Pfoh, arXiv:1105.1507 [hep-ph].
16. A. Abulencia *et al.* [CDF Collaboration], Phys. Rev. Lett. **97** (2006) 242003 [arXiv:hep-ex/0609040].
17. D. Asner *et al.* [Heavy Flavor Averaging Group], arXiv:1010.1589 [hep-ex].
18. V. M. Abazov *et al.* Phys. Rev. D **82** (2010) 032001 [arXiv:1005.2757 [hep-ex]].
19. Z. Ligeti *et al.* Phys. Rev. Lett. **97** (2006) 101801 [arXiv:hep-ph/0604112].
20. Y. Grossman *et al.* Phys. Rev. Lett. **97** (2006) 151801 [arXiv:hep-ph/0605028].
21. M. Blanke *et al.* JHEP **0610** (2006) 003 [arXiv:hep-ph/0604057].
22. M. Bona *et al.* [UTfit Collaboration], PMC Phys. A **3** (2009) 6 [arXiv:0803.0659 [hep-ph]].

M_h in MSSM with HEAVY MAJORANA NEUTRINOS

S. HEINEMEYER[1],M.J. HERRERO[2], S. PEÑARANDA[3], A.M. RODRÍGUEZ-SÁNCHEZ[2*]

[1] *Instituto de Física de Cantabria (CSIC-UC), Santander, Spain*

[2] *Departamento de Física Teórica and Instituto de Física Teórica, UAM/CSIC Universidad Autónoma de Madrid, Cantoblanco, Madrid, Spain*

[3] *Departamento de Física Teórica, Universidad de Zaragoza, Zaragoza, Spain*

** Talk given by A.M. Rodriguez-Sanchez at Moriond EW 2011*

We review the main results of the one-loop radiative corrections from the neutrino/sneutrino sector to the lightest Higgs boson mass, M_h, within the context of the so-called MSSM-seesaw scenario where right handed neutrinos and their supersymmetric partners are included in order to explain neutrino masses. For simplicity, we have restricted ourselves to the one generation case. We find sizable corrections to M_h, which are negative in the region where the Majorana scale is large ($10^{13} - 10^{15}$ GeV) and the lightest neutrino mass is within a range inspired by data ($0.1 - 1$ eV). For some regions of the MSSM-seesaw parameter space, the corrections to M_h are substantially larger than the anticipated LHC precision.

Introduction

The current experimental data on neutrino mass differences and neutrino mixing angles clearly indicate new physics beyond the so far successful Standard Model of Particle Physics (SM). In particular, neutrino oscillations imply that at least two generations of neutrinos must be massive. Therefore, one needs to extend the SM to incorporate neutrino mass terms.

We have explored the simplest version of a SUSY extension of the SM, the well known Minimal Supersymmetric Standard Model (MSSM), extended by right-handed Majorana neutrinos and where the seesaw mechanism of type I [1] is implemented to generate the small neutrino masses. We focus here in the one generation case. The main advantage of working in a SUSY extension of the SM-seesaw is to avoid the huge hierarchy problem induced by the heavy Majorana scale.

On the other hand, it is well known that heavy Majorana neutrinos, with $m_M \sim 10^{13} - 10^{15}$ GeV, induce large LFV rates [2], due to their potentially large Yukawas to the Higgs sector. For the same reason, radiative corrections to Higgs boson masses due to such heavy Majorana neutrinos could also be relevant. Consequently, our study has been focused on the radiative corrections to the lightest MSSM $\mathcal{CP}$-even h boson mass, M_h, due to the one-loop contributions from the neutrino/sneutrino sector within the MSSM-seesaw framework.

In the following we briefly review the main relevant aspects of the calculation of the mass corrections and the numerical results. For further details we address the reader to the full version of our work [3], where also an extensive list with references to previous works can be found.

Calculation

The neutrino/sneutrino sector

The MSSM-seesaw model with one neutrino/sneutrino generation is described in terms of the well known MSSM superpotential plus the new relevant terms contained in:

$$W = \epsilon_{ij} \left[Y_\nu \hat{H}_2^i \hat{L}^j \hat{N} - Y_l \hat{H}_1^i \hat{L}^j \hat{R} \right] + \frac{1}{2} \hat{N} m_M \hat{N} , \tag{1}$$

where m_M is the Majorana mass and $\hat{N} = (\tilde{\nu}_R^*, (\nu_R)^c)$ is the additional superfield that contains the right-handed neutrino ν_R and its scalar partner $\tilde{\nu}_R$.

There are also new relevant terms in the soft SUSY breaking potential:

$$V_{\rm soft}^{\tilde{\nu}} = m_{\tilde{L}}^2 \tilde{\nu}_L^* \tilde{\nu}_L + m_{\tilde{R}}^2 \tilde{\nu}_R^* \tilde{\nu}_R + (Y_\nu A_\nu H_2^2 \tilde{\nu}_L \tilde{\nu}_R^* + m_M B_\nu \tilde{\nu}_R \tilde{\nu}_R + \text{h.c.}) \ . \tag{2}$$

After electro-weak (EW) symmetry breaking, the charged lepton and Dirac neutrino masses can be written as

$$m_l \ = \ Y_l \ v_1 \, , \qquad m_D \ = \ Y_\nu \, v_2 \, , \tag{3}$$

where v_i are the vacuum expectation values (VEVs) of the neutral Higgs scalars, with $v_{1(2)} = v \cos(\sin)\beta$ and $v = 174$ GeV.

The 2×2 neutrino mass matrix is given in terms of m_D and m_M by:

$$M^\nu \ = \ \begin{pmatrix} 0 & m_D \\ m_D & m_M \end{pmatrix} . \tag{4}$$

Diagonalization of M^ν leads to two mass eigenstates, $n_i \, (i = 1, 2)$, which are Majorana fermions with the respective mass eigenvalues given by:

$$m_{\nu,\, N} = \frac{1}{2} \left(m_M \mp \sqrt{m_M^2 + 4 m_D^2} \right) \ . \tag{5}$$

In the seesaw limit, i.e. when $\xi \equiv \frac{m_D}{m_M} \ll 1$

$$m_\nu = -m_D \xi + \mathcal{O}(m_D \xi^3) \simeq -\frac{m_D^2}{m_M} \ , \qquad m_N = m_M + \mathcal{O}(m_D \xi) \simeq m_M \ . \tag{6}$$

Regarding the sneutrino sector, the sneutrino mass matrices for the $\mathcal{CP}$-even, $\tilde{M}_+$, and the $\mathcal{CP}$-odd, $\tilde{M}_-$, subsectors are given respectively by

$$\tilde{M}_\pm^2 = \begin{pmatrix} m_{\tilde{L}}^2 + m_D^2 + \frac{1}{2} M_Z^2 \cos 2\beta & m_D (A_\nu - \mu \cot\beta \pm m_M) \\ m_D (A_\nu - \mu \cot\beta \pm m_M) & m_{\tilde{R}}^2 + m_D^2 + m_M^2 \pm 2 B_\nu m_M \end{pmatrix} . \tag{7}$$

The diagonalization of these two matrices, $\tilde{M}_\pm^2$, leads to four sneutrino mass eigenstates, $\tilde{n}_i \, (i = 1, 2, 3, 4)$. In the seesaw limit, where m_M is much bigger than all the other scales the corresponding sneutrino masses are given by:

$$\begin{aligned} m_{\tilde{\nu}_+, \tilde{\nu}_-}^2 &= m_{\tilde{L}}^2 + \frac{1}{2} M_Z^2 \cos 2\beta \mp 2 m_D (A_\nu - \mu \cot\beta - B_\nu) \xi \ , \\ m_{\tilde{N}_+, \tilde{N}_-}^2 &= m_M^2 \pm 2 B_\nu m_M + m_{\tilde{R}}^2 + 2 m_D^2 \ . \end{aligned} \tag{8}$$

In the Feynman diagrammatic (FD) approach the higher-order corrected $\mathcal{CP}$-even Higgs boson masses in the MSSM, denoted here as M_h and M_H, are derived by finding the poles of the (h, H)-propagator matrix, which is equivalent to solving the following equation [4]:

$$\left[p^2 - m_h^2 + \hat{\Sigma}_{hh}(p^2) \right] \left[p^2 - m_H^2 + \hat{\Sigma}_{HH}(p^2) \right] - \left[\hat{\Sigma}_{hH}(p^2) \right]^2 = 0 \, . \tag{9}$$

where $m_{h,H}$ are the tree level masses. The one loop renormalized self-energies, $\hat{\Sigma}_{\phi\phi}(p^2)$, in (9) can be expressed in terms of the bare self-energies, $\Sigma_{\phi\phi}(p^2)$, the field renormalization constants $\delta Z_{\phi\phi}$ and the mass counter terms δm_ϕ^2, where ϕ stands for h, H. For example, the lightest Higgs boson renormalized self energy reads:

$$\hat{\Sigma}_{hh}(p^2) = \Sigma_{hh}(p^2) + \delta Z_{hh}(p^2 - m_h^2) - \delta m_h^2, \tag{10}$$

Renormalization prescription

We have used an on-shell renormalization scheme for M_Z, M_W and M_A mass counterterms and T_h, T_H tadpole counterterms. On the other hand, we have used a modified $\overline{\rm DR}$ scheme $\left(\overline{\rm mDR}\right)$ for the renormalization of the wave function and $\tan\beta$. The $\overline{\rm mDR}$ scheme is very similar to the well known $\overline{\rm DR}$ scheme but instead of subtracting the usual $\Delta = \frac{2}{\epsilon} - \gamma_E + \log(4\pi)$ one subtracts $\Delta_m = \Delta - \log(m_M^2/\mu^2_{\overline{\rm DR}})$, hence, avoiding large logarithms of the large scale m_M. As studied in other works [5], this scheme minimizes higher order corrections when two very different scales are involved in a calculation of radiative corrections.

Analytical and Numerical Results

In order to understand in simple terms the analytical behavior of our full numerical results we have expanded the renormalized self-energies in powers of the seesaw parameter $\xi = m_D/m_M$:

$$\hat{\Sigma}(p^2) = \left(\hat{\Sigma}(p^2)\right)_{m_D^0} + \left(\hat{\Sigma}(p^2)\right)_{m_D^2} + \left(\hat{\Sigma}(p^2)\right)_{m_D^4} + \dots \ . \tag{11}$$

The zeroth order of this expansion corresponds to the gauge contribution and it does not depend on m_D or m_M. The rest of the terms of the expansion corresponds to the Yukawa contribution. The leading term of this Yukawa contribution is the $\mathcal{O}(m_D^2)$ term, because it is the only one not suppressed by the Majorana scale. In fact it goes as $Y_\nu^2 M_{\rm EW}^2$, where $M_{\rm EW}^2$ denotes generically the electroweak scales involved, concretely, p^2, M_Z^2 and M_A^2. In particular, the $\mathcal{O}(p^2 m_D^2)$ terms of the renormalized self-energy, which turn out to be among the most relevant leading contributions, separated into the neutrino and sneutrino contributions, are the following:

$\hat{\Sigma}_{hh}^{\rm m\overline{DR}}\Big|_{m_D^2 p^2} \sim$ 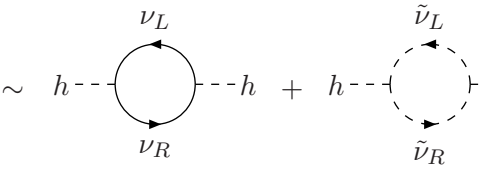

$\Big|_{m_D^2 p^2} \sim \dfrac{g^2 p^2 m_D^2 c_\alpha^2}{64\pi^2 M_W^2 s_\beta^2} + \dfrac{g^2 p^2 m_D^2 c_\alpha^2}{64\pi^2 M_W^2 s_\beta^2}$ (12)

Notice that the above neutrino contributions come from the Yukawa interaction $g_{h\nu_L\nu_R} = -\frac{igm_D\cos\alpha}{2M_W\sin\beta}$, which is extremely suppressed in the Dirac case but can be large in the present Majorana case. On the other hand, the above sneutrino contributions come from the new couplings $g'_{h\tilde{\nu}_L\tilde{\nu}_R} = -\frac{igm_D m_M\cos\alpha}{2M_W\sin\beta}$, which are not present in the Dirac case. It is also interesting to remark that these terms, being $\sim p^2$ are absent in both the effective potential and the RGE approaches.

With respect to the numerical results, figure 1 exemplifies the main features of the extra Higgs mass corrections $\Delta m_h^{\rm m\overline{DR}}$ due to neutrinos and sneutrino loops in terms of the two physical Majorana neutrino masses, m_N and m_ν. For values of $m_N < 3\times 10^{13}$ GeV and $|m_\nu| < 0.1 - 0.3$ eV the corrections to M_h are positive and smaller than 0.1 GeV. In this region, the gauge contribution dominates. In fact, the wider black contour line with fixed $\Delta m_h^{\rm m\overline{DR}} = 0.09$ coincides with the prediction for the case where just the gauge part in the self-energies have been included. This means that 'the distance' of any other contour-line respect to this one represents the difference in the radiative corrections respect to the MSSM prediction.

However, for larger values of m_N and/or $|m_\nu|$ the Yukawa part dominates, and the radiative corrections become negative and larger in absolute value, up to values of -5 GeV in the right upper corner of Fig 1. These corrections grow in modulus proportionally to m_M and m_ν, due to the fact that the seesaw mechanism impose a relation between the three masses involved, $m_D^2 = |m_\nu| m_N$.

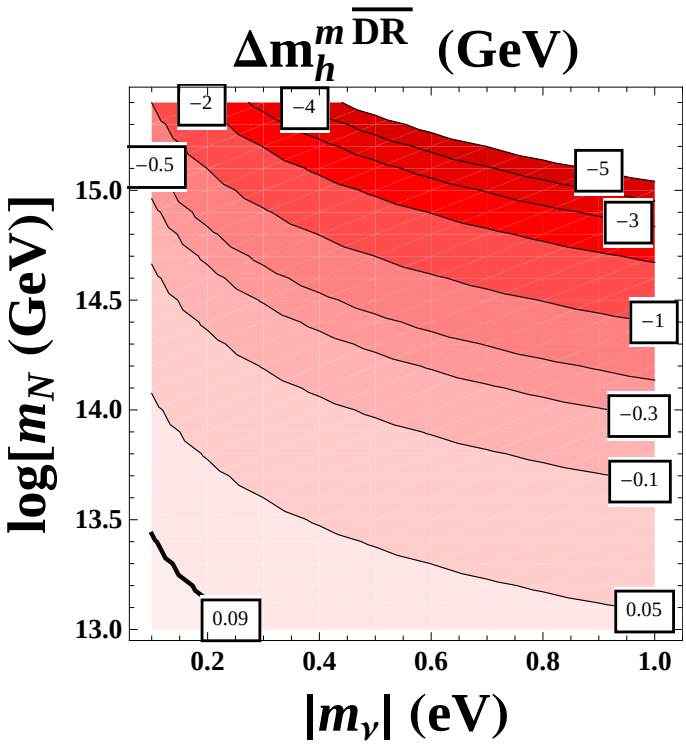

Figure 1: Contour-lines for the Higgs mass corrections from the neutrino/sneutrino sector as a function of the physical Majorana neutrino masses, light $|m_\nu|$ and heavy m_N. The other parameters are fixed to: $A_\nu = B_\nu = m_{\tilde{L}} = m_{\tilde{R}} = 10^3$ GeV, $\tan\beta = 5$, $M_A = 200$ GeV and $\mu = 200$ GeV.

Conclusions

We have used the Feynman diagrammatic approach for the calculation of the radiative corrections to the lightest Higgs boson mass of the MSSM-seesaw. This method does not neglect the external momentum of the incoming and outgoing particles as it happens in the effective potential approach. We have performed a full calculation, obtaining not only the leading logarithmic terms as it would be the case in a RGE computation but also the finite terms, that we have seen that can be sizable for heavy Majorana neutrinos ($10^{13} - 10^{15}$ GeV) and the lightest neutrino mass within a range inspired by data ($0.1 - 1$ eV). For some regions of the MSSM-seesaw parameter space, the corrections to M_h are substantially larger (up to -5 GeV) than the anticipated LHC precision (~ 200 MeV) [6].

References

1. P. Minkowski, *Phys. Lett.* **B 67** (1977) 421;
2. F. Borzumati and A. Masiero, *Phys. Rev. Lett.* **57** (1986) 961;
   M. Raidal *et al.*, Eur. Phys. J. C **57**, 13 (2008) [arXiv:0801.1826 [hep-ph]].
3. S. Heinemeyer, M. J. Herrero, S. Penaranda and A. M. Rodriguez-Sanchez, JHEP **1105** (2011) 063 [arXiv:1007.5512 [hep-ph]].
4. M. Frank, T. Hahn, S. Heinemeyer, W. Hollik, H. Rzehak and G. Weiglein, *JHEP* **0702** (2007) 047 [arXiv:0611326 [hep-ph]].
5. J. Collins, F. Wilczek and A. Zee, *Phys. Rev.* **D 18** (1978) 242.
6. G. Aad et al. [The ATLAS Collaboration], arXiv:0901.0512;
   G. Bayatian et al. [CMS Collaboration], *J. Phys.* **G 34** (2007) 995.

The Shadow of the Moon in IceCube

L. Gladstone, for the IceCube Collaboration [a]
University of Wisconsin-Madison, 1150 University Avenue, Madison, WI 53706, USA

IceCube is the world's largest neutrino telescope, recently completed at the South Pole. As a proof of pointing accuracy, we look for the image of the Moon as a deficit in down-going cosmic ray muons, using techniques similar to those used in IceCube's astronomical point-source searches.

1 Introduction

One of the main goals of the the IceCube detector[1] at the South Pole is to look for astrophysical point sources of neutrinos: essentially, IceCube is a telescope using neutrinos instead of light. Other telescopes can calibrate their signals with known standard candles (the Crab nebula is a traditional standard candle in gamma ray astronomy, for example). In the absence of known high-energy neutrino source, IceCube can use the deficit of cosmic ray muons from the direction of the Moon for calibration. This "Moon Shadow" is valuable because of its well-known position. While a muon calibration is not as directly applicable to neutrino astronomy as a Crab gamma calibration would be to gamma astronomy, it does provide valuable information about the pointing accuracy and resolution of the detector.

The 86-string IceCube detector was built modularly, with strings deployed during 7 consecutive austral summers. The changing detector size thus creates an annual discreteness in the data. A Moon shadow analysis was developed for several of the detector setups; this work focuses on a 40-string setup analysis [2] and a 59-string setup analysis [3,5].

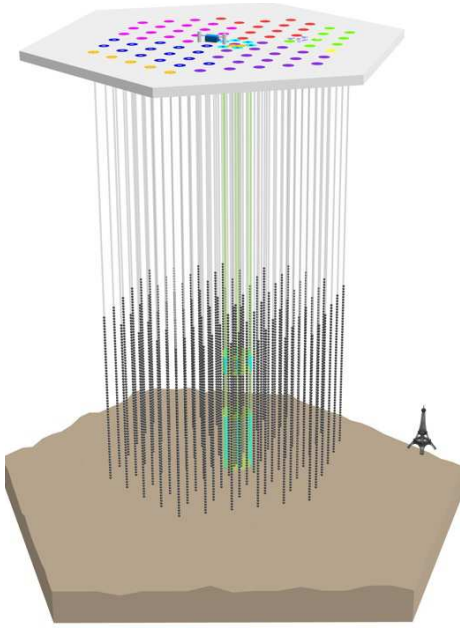

Figure 1: A schematic view of the IceCube detector, with the Eiffel Tower added for scale. There are 86 strings of detector modules deployed within the glacier; where each string connects to the surface, there is a dot. The color of the dot represents the year which that string was deployed.

[a] For a complete author list, see http://www.icecube.wisc.edu/collaboration/authorlists/2010/4.html

2 Data Sample

Because of bandwidth restrictions on the satellite transporting data from the South Pole to the North for analysis, a subset of available IceCube data is used. For these analyses, the data were collected in the following way: tracks were reconstructed quickly, and their direction of origin was compared to the current position of the Moon. If an event came from a position within 40° in azimuth or 10° in zenith, it was sent north. These data were collected only when the Moon was 15° or more above the horizon at the South Pole, which neatly splits the data into lunar months. This sample was used for both a Moon measurement and an off-source background estimate.

The estimated angular resolution of the reconstructions used here is of order 1°, similar to the 0.5°-diameter Moon, so for this analysis the Moon was considered point-like.

3 Binned 40-string analysis

One analysis of the Moon Shadow was performed on the data set from the 40-string detector setup. This dataset contained 13 lunar months. Cuts were applied to the data sample to optimize the expected signal (balancing passing rate with the expected improvement to the point spread function). Using simulation, the search bin size was optimized, and a band 1.25° tall at constant zenith with respect to the Moon was used. Figure 2 shows the number of events in this zenith band, using the same optimized bin size of 1.25° in azimuth as in zenith. Taking the mean of all the bins excluding the central 4 as a comparison, and using simple statistical $\sqrt{N}$ errors, we see a deficit of 7.6σ in the central bin at the position of the Moon.

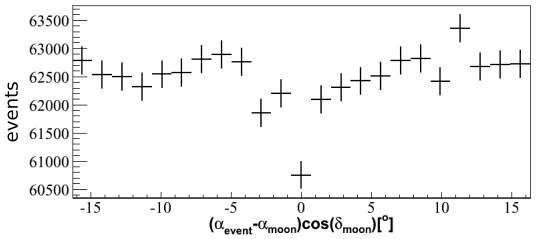

Figure 2: PRELIMINARY: Events in a 1.25° zenith band around the Moon, using the 40-string detector setup. A deficit from the direction of the Moon can be clearly seen at 0.

4 Likelihood 59-string analysis

A subsequent analysis[3] used data from the 59-string setup of the detector. The approach for this analysis was similar to the likelihood approach taken for the IceCube point source searches: an expected signal shape and background shape were developed, and then a likelihood was maximized at every point in the sky, allowing the number of signal events to vary. The likelihood formula used is:

$$L(\vec{x_s}, n_s) = \sum_i^N \log\left(\frac{n_s}{N} S_i + (1 - \frac{n_s}{N}) B_i\right)$$

where $\vec{x_s}$ is the position being considered (relative to the Moon), n_s is the number of signal events, N is the total number of events, S_i is the expected signal shape, and B_i is the expected background shape. Note that this has no explicit energy term; this a major difference between the IceCube Moon analysis and the IceCube point source searches[4]. For the Moon shadow, we expect the number of signal events to be negative, as the Moon produces a deficit.

Each event's contribution to the signal shape was assumed to be gaussian, with a width given by the estimated error on the reconstructed position.

The background shape was estimated using two off-source regions: to the right and left of the moon in azimuth, at the same zenith. For each region, the event rate was assumed constant in azimuth, and an 80 bin histogram (with interpolation between bins) was used to describe the zenith distribution.

One can test the quality of this background model by assuming it as the background truth, and examining the size of fluctuations in the background region (calling the background region data "signal" for the purposes of this test). For a perfect background model, this should result in only random fluctuations around zero. The result is shown in Figure 3a. The fluctuations of the background show up in the figure as indicated by the color axis. To test that these fluctuations are random, the value of each bin from Figure 3a is plotted in Figure 3b. The distribution of these values is consistent with a Gaussian fit centered at 0. The rms width of this distribution is about 680 signal events, which we take as the definition of 1σ. A similar analysis was performed on the other background sample, resulting in a width of 560 events. As the two rms values were slightly different, the significance reported here should be taken only approximately. We consider the wider fluctuation value of 680, to be conservative.

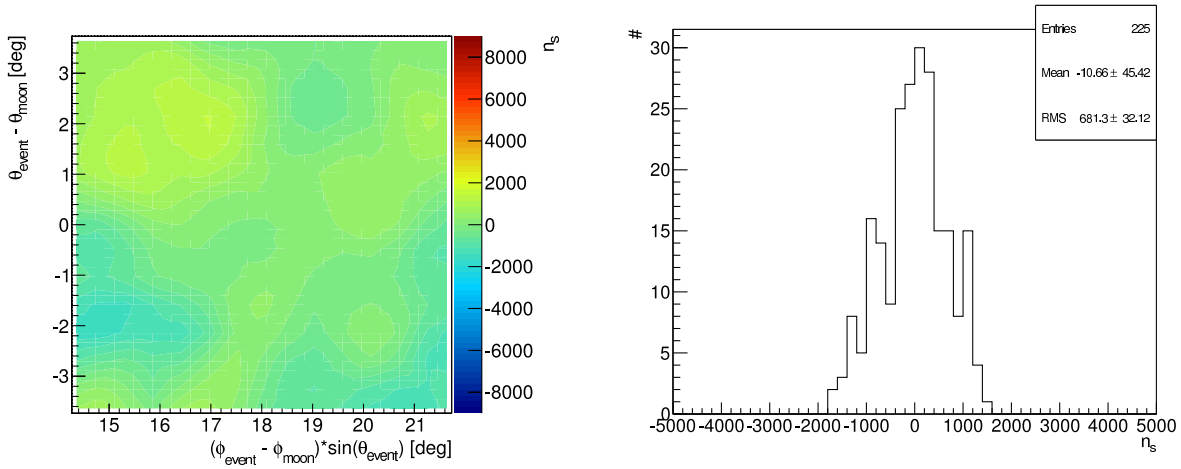

(a) Fluctuations around the background model of an off-source region, defined in relation to the position of the Moon. The color axis is the best-fit number of total "signal" events given the response at that point.

(b) The distribution of bins from Fig. 3a, which can be fit to a gaussian curve, confirming that the background is fluctuating randomly around 0.

Figure 3: PRELIMINARY: from [3]

This procedure is then applied to the signal region around the known Moon position: the binned and interpolated zenith model as a background description, and the sum of the observed data as the signal. The resulting plot is shown as Figure 4. Each point represents the number of events shadowed if the Moon were at that point; the maximum of these is at the expected position of the Moon, with 8660 events shadowed. Taking $1\sigma = 680$ events as discussed above, this is a 12.7σ observation.

The expected number of shadowed events, based on the background rate and the size of the Moon, was 8192 ± 91. The observation of a 8660 event deficit at the central grid position is within 1σ of the expectation.

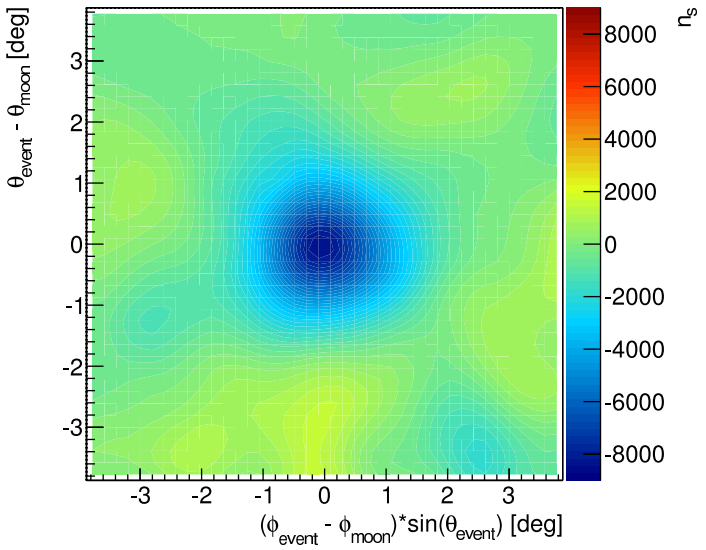

Figure 4: PRELIMINARY: The Moon Shadow from the 59-string detector setup, using a likelihood analysis approach. The position is given relative to the Moon position, and the color represents the number of total shadowed events for each point, assuming the Moon is at that point. From [3].

5 Conclusions

In each of two years of data during the construction of the IceCube detector, a shadowing effect was observed in cosmic rays from the direction of the Moon. In the 40-string setup, this deficit was observed with 7.6σ using a binned analysis. In the 59-string setup, this deficit was observed with 12.7σ using a likelihood analysis. The results confirms the pointing resolution of IceCube to within order 1°. Further studies of this shadowing effect are forthcoming.

Acknowledgments

We gratefully acknowledge support from the National Science Foundation, and LG acknowledges that this research was made with Government support under and awarded by DoD, Air Force Office of Scientific Research, National Defense Science and Engineering Graduate (NDSEG) Fellowship, 32 CFR 168a.

References

1. IceCube Collaboration, Astroparticle Physics, **26** 3 (2006) 155-173, arXiv:0604450
2. D.J. Boersma, L. Gladstone, A. Karle, for the IceCube Collaboration, Proceedings of the 31^{st} ICRC, LODZ, POLAND, 2009, arXiv:1002.4900.
3. J. Blumenthal, Diplomarbeit in Physik, 2011, Rheinisch-Westfälischen Technischen Hochschule Aachen, IceCube internal report 201103001, also available at `http://www.physik.rwth-aachen.de/fileadmin/user_upload/www_physik/Institute/Inst_3B/Forschung/IceCube/publications/thesis_JB.pdf`
4. R. Abbasi et al, Astrophysical Journal **732** (2011) 18
5. H. Stiebel, Master Thesis, 2011, Stockholm University, available upon request from IceCube internal documents, collection 8819.

CAN NEW GENERATIONS EXPLAIN NEUTRINO MASSES?

A. APARICI, J. HERRERO-GARCIA, N. RIUS and A. SANTAMARIA
Depto.de Fisica Teorica, and IFIC, Universidad de Valencia-CSIC
Edificio de Institutos de Paterna, Apt. 22085, 46071 Valencia, Spain

In this talk we explore the possibility that the smallness of the observed neutrino masses is naturally understood in a modified version of the standard model with N extra generations of fermions and N right-handed neutrinos, in which light neutrino masses are generated at two loops. We find that with $N = 1$ it is not possible to fit the observed spectrum of masses and mixings while with $N = 2$ it is. Within this extension, we analyse the parameters which are allowed and the possible phenomenological signals of the model in future experiments.

1 Introduction

Neutrino oscillations require at least two massive neutrinos with large mixing, providing one of the strongest evidences of physics beyond the Standard Model (SM). On the other hand, one of the most natural extensions of the SM is the addition of extra sequential generations [1].

LEP II limits on new generation leptons are: $m_{\ell'} > 100.8$ GeV and $m_{\nu'} > 80.5\,(90.3)$ GeV for pure Majorana (Dirac) particles. When neutrinos have both Dirac and Majorana masses, the bound on the lightest neutrino is 63 GeV. For stable neutrinos LEP I measurement of the invisible Z width, $\Gamma_{\rm inv}$, implies $m_{\nu'} > 39.5\,(45)$ GeV for pure Majorana (Dirac) particles.

The new heavy fermions contribute to the electroweak parameters and might spoil the agreement of the SM with experiment. Global fits of models with additional generations to the electroweak data have been performed and they favour no more than five generations. It should be kept in mind that most of the fits make some simplifying assumptions on the mass spectrum of the new generations and do not consider Majorana neutrino masses for the new generations or the possibility of breaking dynamically the gauge symmetry via the condensation of the new generations' fermions; all these would give additional contributions to the oblique parameters and will modify the fits. Therefore, in view that we will soon see or exclude new generations thanks to the LHC, it is wise to approach this possibility with an open mind.

In this talk (see [2] for further details and a complete list of references) we focus on how neutrino masses can be naturally generated at two loops by adding extra families and singlets. Recall that right-handed neutrinos do not have gauge charges and are not needed to cancel anomalies, therefore their number is not linked to the number of generations.

2 Four generations

We extend the SM by adding a complete fourth generation and one right-handed neutrino ν_R with a Majorana mass term [3]. We denote the new charged lepton E and the new neutrino ν_E. The relevant part of the Lagrangian is

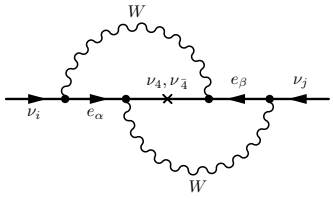

Figure 1: Two-loop diagram contributing to neutrino masses in the four-generation model.

$$\mathcal{L}_Y = -\bar{\ell} Y_e e_R \phi - \bar{\ell} Y_\nu \nu_R \tilde{\phi} - \frac{1}{2}\overline{\nu_R^c} m_R \nu_R + \text{H.c.}\ , \tag{1}$$

where ℓ are the left-handed lepton SU(2) doublets, e_R the right-handed charged leptons and ν_R the right-handed neutrino. In generation space ℓ and e_R are organized as four-component column vectors. Thus, Y_e is a general, 4×4 matrix, Y_ν is a general four-component column vector with elements y_α with $\alpha = e, \mu, \tau, E$, and m_R is a Majorana mass term.

After spontaneous symmetry breaking (SSB) the mass matrix for the neutral leptons at tree level is a 5×5 Majorana symmetric matrix which has only one right-handed neutrino Majorana mass term. Therefore, it leads to two massive Majorana and three massless Weyl neutrinos. Then it is clear that only the linear combination of left-handed neutrinos $\nu_4' \propto y_e \nu_e + y_\mu \nu_\mu + y_\tau \nu_\tau + y_E \nu_E$ will pair up with ν_R to acquire a Dirac mass term. Thus, it is convenient to pass from the flavour basis $(\nu_e, \nu_\mu, \nu_\tau, \nu_E)$ to a new one $\nu_1', \nu_2', \nu_3', \nu_4'$ where the first three states will be massless at tree level and only ν_4' mixes with ν_R.

After this change of basis, $\nu_\alpha = \sum_i V_{\alpha i} \nu_i'$ $(i = 1, \cdots, 4,\ \alpha = e, \mu, \tau, E)$ with $V_{\alpha 4} = y_\alpha / \sqrt{\sum_\beta y_\beta^2}$, we are left with a 2×2 mass matrix for ν_4' and ν_R which leads to two Majorana neutrinos ν_4 and $\nu_{\bar{4}}$ of masses $m_{4,\bar{4}} = \frac{1}{2}\left(\sqrt{{m_R}^2 + 4 m_D^2} \mp m_R\right)$,where $m_D = v\sqrt{\sum_i y_i^2}$, with $v = \langle \phi^{(0)} \rangle$, and $\tan^2\theta = m_4 / m_{\bar{4}}$. If $m_R \ll m_D$, we have $m_4 \approx m_{\bar{4}}$ and $\tan\theta \approx 1$ (pseudo-Dirac limit) while when $m_R \gg m_D$, $m_4 \approx m_D^2 / m_R$, $m_{\bar{4}} \approx m_R$ and $\tan\theta \approx m_D / m_R$ (see-saw limit).

Since lepton number is broken by the ν_R Majorana mass term, there is no symmetry which prevents the tree-level massless neutrinos ν_1', ν_2', ν_3' from gaining Majorana masses; they are generated at two loops by the diagram of Figure 1, and are given by

$$M_{ij} = -\frac{g^4}{m_W^4} m_R m_D^2 \sum_\alpha V_{\alpha i} V_{\alpha 4} m_\alpha^2 \sum_\beta V_{\beta j} V_{\beta 4} m_\beta^2 I_{\alpha\beta} \tag{2}$$

where the sums run over the charged leptons $\alpha, \beta = e, \mu, \tau, E$ while $i, j = 1, 2, 3$, and the loop integral $I_{\alpha\beta}$ can be found in [2]. It is easy to show that the eigenvalues of the light neutrino mass matrix are proportional to m_μ^4, m_τ^4, m_E^4 which gives a huge hierarchy between neutrino masses:

$$\frac{m_2}{m_3} \leq \frac{1}{4N_E^2}\left(\frac{m_\tau}{m_E}\right)^2 \left(\frac{m_\tau}{m_{\bar{4}}}\right)^2 \leq \frac{10^{-7}}{N_E^2}\ , \tag{3}$$

where we have taken $\ln(m_{\bar{4}}/m_4) \approx \ln(m_E/m_{\bar{4}}) \approx 1$ and in the last step we used that $m_E, m_{\bar{4}} \geq 100\,\text{GeV}$. To overcome this huge hierarchy very small values of N_E are needed, which would imply that the heavy neutrinos are not mainly ν_E but some combination of the three known ones ν_e, ν_μ, ν_τ; however this is not possible since it would yield observable effects in a variety of processes, like $\pi \to \mu\nu$, $\pi \to e\nu$, $\tau \to e\nu\nu$... This requires that $y_{e,\mu,\tau} \approx 10^{-2} y_E$, so $N_E \approx 1$.

Therefore, the simplest version of the model is unable to accommodate the observed spectrum of neutrino masses and mixings. However, notice that whenever a new generation and a right-handed neutrino with Majorana mass at (or below) the TeV scale are added to the SM, the

two-loop contribution to neutrino masses is always present and provides an important constraint for this kind of SM extensions.

3 The five-generation model

We add two generations to the SM and two right-handed neutrinos. We denote the two charged leptons by E and F and the two right-handed singlets by ν_{4R} and ν_{5R}. The Lagrangian is exactly the same we used for four generations but now ℓ and e are organized as five-component column vectors while ν_R is a two-component column vector containing ν_{4R} and ν_{5R}. Thus, Y_e is a general, 5×5 matrix, Y_ν is a general 5×2 matrix and m_R is now a general symmetric 2×2 matrix. The model, contrary to the four-generation case, has additional sources of CP violation in the leptonic sector, however, for simplicity we take all y_α and y'_α real.

As in the four-generation case, the linear combination $\nu'_4 \propto \sum_\alpha y_\alpha \nu_\alpha$ only couples to ν_{4R} and the combination $\nu'_5 \propto \sum_\alpha y'_\alpha \nu_\alpha$ only couples to ν_{5R}. Therefore, the tree-level spectrum will contain three massless neutrinos (the linear combinations orthogonal to ν'_4 and ν'_5) and four heavy Majorana neutrinos. For simplicity, we choose ν'_4 and ν'_5 orthogonal to each other, i.e., $\sum_\alpha y_\alpha y'_\alpha = 0$. We change from the flavour fields $\nu_e, \nu_\mu, \nu_\tau, \nu_E, \nu_F$ to a new basis $\nu'_1, \nu'_2, \nu'_3, \nu'_4, \nu'_5$ where ν'_1, ν'_2, ν'_3 are massless at tree level, so we are free to choose them in any combination of the flavour states as long as they are orthogonal to ν'_4 and ν'_5.

The model should be compatible with the observed universality of fermion couplings and have small rates of lepton flavour violation in the charged sector, which requires $y_e, y_\mu, y_\tau, y'_e, y'_\mu, y'_\tau \ll y_E, y_F, y'_E, y'_F$. In addition, it should fit the observed pattern of masses and mixings, for instance, reproducing the tribimaximal (TBM) mixing structure. A successful choice of the Yukawas to obtain normal hierarchy (see [2] for an analysis of inverted hierarchy and more details), i.e, $m_3 \approx \sqrt{|\triangle m^2_{31}|} \approx 0.05$ eV, $m_2 \approx \sqrt{\triangle m^2_{21}} \approx 0.01$ eV, will be $y_\alpha = y_E(\epsilon, \epsilon, -\epsilon, 1, 0)$ and $y'_\alpha = y'_F(0, \epsilon', \epsilon', 0, 1)$ which, keeping only terms up to order ϵ^2, leads to the 5×5 unitary matrix V that passes from one basis to the other, $\nu_\alpha = \sum_i V_{\alpha i}\nu'_i$ ($i = 1, \cdots, 5$, $\alpha = e, \mu, \tau, E, F$):

$$V \approx \begin{pmatrix} \sqrt{\frac{2}{3}} & \frac{1}{\sqrt{3}} - \frac{\sqrt{3}}{2}\epsilon^2 & 0 & \epsilon & 0 \\ -\frac{1}{\sqrt{6}} & \frac{1}{\sqrt{3}} - \frac{\sqrt{3}}{2}\epsilon^2 & \frac{1}{\sqrt{2}} - \frac{1}{\sqrt{2}}\epsilon'^2 & \epsilon & \epsilon' \\ \frac{1}{\sqrt{6}} & -\frac{1}{\sqrt{3}} + \frac{\sqrt{3}}{2}\epsilon^2 & \frac{1}{\sqrt{2}} - \frac{1}{\sqrt{2}}\epsilon'^2 & -\epsilon & \epsilon' \\ 0 & -\epsilon\sqrt{3} & 0 & 1 - \frac{3}{2}\epsilon^2 & 0 \\ 0 & 0 & -\epsilon'\sqrt{2} & 0 & 1 - \epsilon'^2 \end{pmatrix} \quad (4)$$

Assuming that $m_{E,F} \gg m_{4,\bar{4},5,\bar{5}} \gg m_W$, we find:

$$m_2 \approx \frac{3g^4}{2(4\pi)^4 m_W^4}\epsilon^2 m_{4D}^2 m_{4R} m_E^2 \ln\frac{m_E}{m_{\bar{4}}} \quad (5)$$

$$m_3 \approx \frac{g^4}{(4\pi)^4 m_W^4}\epsilon'^2 m_{5D}^2 m_{5R} m_F^2 \ln\frac{m_F}{m_{\bar{5}}}\ , \quad (6)$$

and the required ratio $m_3/m_2 \approx 5$ can be easily accommodated for different combinations of masses and mixing parameters ϵ, ϵ'.

4 Phenomenological analysis of the model

In general, the most restrictive experimental bound comes from $B(\mu \to e\gamma) < 1.2\times 10^{-11}$, and it is translated into $\epsilon < 0.03$. From $B(\tau \to \mu\gamma) < 4.4\times 10^{-8}$, we obtain $|\epsilon'^2 - \epsilon^2| < 0.09$. We display in Figure 2 a) $B(\mu \to e\gamma)$ versus the mass of the heavy neutrino m_4 in the NH case. We

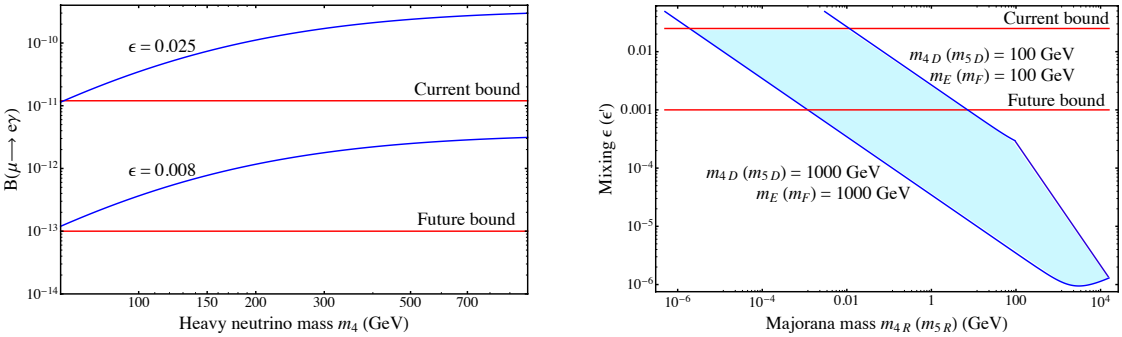

Figure 2: a) Left: $B(\mu \to e\gamma)$ against m_4 for different values of ϵ. We also display present and future limits. b) Right: Parameter space that predicts the right scale for heavy and light neutrinos (the region between the curves). We also present the current $\mu \to e\gamma$ bound and the expected μ–e conversion limit.

also display present and near future limits. Also, μ–e conversion in nuclei gives information on ϵ. We expect it to set much stronger bounds in the future.

Violations of universality constrain the model in both hierarchies. For example, from pion decay, we obtain $\epsilon' < 0.04$. Regarding neutrinoless double beta decay, there are contributions of the new heavy neutrinos, however, we obtain the same combination of parameters as in the light neutrino masses expressions, $m_{4R}\epsilon^2$, leading to unobservable effects in $0\nu\beta\beta$ when the former are fitted (of course the light neutrino contribution can be observed (in IH) in the future).

Also, a very striking effect of new generations is the enhancement of the Higgs-gluon-gluon vertex which arises from a triangle diagram with all quarks running in the loop, by a factor of 9 (25) in the presence of a fourth (fifth) generation. We estimate roughly that $m_H > 300\,\text{GeV}$ in the case of five generations. However, these limits may be softened in some cases.

To summarize the phenomenology of the model we present in figure 2 the allowed regions in the $\epsilon - m_{4R}$ plane which lead to $m_3 \sim 0.05\,\text{eV}$ varying the charged lepton masses $m_E\,(m_F)$ and the Dirac neutrino masses $m_{4D}\,(m_{5D})$ between 100 GeV–1 TeV, and imposing the bound on the neutrino mass, $m_4 > 63\,\text{GeV}$. We also plot the present bounds on the mixings $\epsilon\,(\epsilon')$ from $\mu \to e\gamma$ and future limits from μ–e conversion if expectations are attained.

So our conclusion is that with four generations and one singlet the correct spectrum of light neutrino masses cannot be generated. However, with five generations and two singlets all current data can be accomodated in the region of the parameter space between the curves of Figure 2 b), which will be probed in the near future.

Acknowledgments

This work has been partially supported by the grants FPA-2007-60323, FPA-2008-03373, CSD2007-00060, CSD2007- 00042, PROMETEO/2009/116, PROMETEO/2009/128 and MRTN-CT-2006-035482 (FLAVIAnet). A.A. and J.H.-G. are supported by the MICINN under the FPU program.

References

1. B. Holdom *et. al.*, *PMC Phys.* **A3** (2009) 4, [arXiv:0904.4698]. V. A. Novikov *et. al.*, *Phys. Atom. Nucl.* **73** (2010) 636–642, [arXiv:0904.4570]. L. M. Carpenter *et. al.*, *Phys. Rev.* **D82** (2010) 114019, [arXiv:1005.0628]. G. D. Kribs *et. al.*, *Phys. Rev.* **D76** (2007) 075016, [arXiv:0706.3718]. **PDG** Coll., *J. Phys.* **G37** (2010) 075021.
2. A. Aparici, J. Herrero-Garcia, N. Rius, and A. Santamaria, [arXiv:1104.4068].
3. S. T. Petcov *et. al.*, *Phys. Lett.* **B143** (1984) 175. K. S. Babu *et. al.*, *Phys. Rev. Lett.* **61** (1988) 674, *Phys. Lett.* **B218** (1989) 233–237.

K^+ Production from 8 GeV Protons using Neutrino Interactions in SciBooNE

Gary Cheng for the SciBooNE Collaboration
Department of Physics, Columbia University, New York, New York 10027, USA

The SciBooNE Collaboration reports K^+ production cross section measurement using high energy daughter muon neutrino scattering data off the SciBar polystyrene (C_8H_8) target in the SciBooNE detector. The K^+ mesons are produced by 8 GeV protons striking a beryllium target in Fermilab Booster Neutrino Beam (BNB) line. Compared to Monte Carlo predictions using previous higher energy K+ production measurements, this measurement, which uses the NEUT neutrino interaction generator, is consistent with a normalization factor of 0.87±0.12. This agreement is evidence that the extrapolation of the higher energy K^+ measurements to an 8 GeV beam energy using a Feynman scaling parametrization is valid. This measurement reduces the error on the K^+ production cross section from the 40% currently used in MiniBooNE and SciBooNE to 14%, which can be applied to reduce uncertainty in the beam MC simulation for future neutrino measurements.

1 Introduction

Inclusive kaon production by low-energy protons (1 to 15 GeV) is of interest both theoretically and experimentally. In this low-energy region, kaon production is dominated by exclusive processes. Since exclusive channel threshold effects are important, theoretical models such as Feynman scaling [1] may be good in describing low-energy production cross sections. Experimentally, kaon production is also relevant for neutrino experiments since important components of the incident neutrino flux come from kaon decays, such as ν_e from K^+.

Since measurements of K^+ production does not exist at the 8 GeV incident proton energy, a Feynman scaling parametrization is used to predict the double-differential K^+ production cross-section from higher incident proton energies [2]. The Feynman scaling parametrization show that while the shape of the K^+ production cross-section as functions of momentum and angle are in good agreement for the higher incident energy K^+ production measurements, the overall production normalization is not. A conservative 40% uncertainty is applied to the K^+ production, mostly coming from the discrepancy in the production normalization from different higher energy K^+ measurements.

2 Detector Description and MC Simulation

The Fermilab BNB uses 8 GeV kinetic energy protons striking a beryllium target. Secondary mesons, including K^+ measured in this analysis, are produced and focused by a magnetic horn into a downstream beam decay pipe. The polarity of the horn can be changed on based whether a neutrino or antineutrino beam is desired. In the beam decay pipe, the secondary mesons are allow to decay into neutrinos. At the end of the beam decay pipe, a stop removes all charged particles from the beam, creating an intense neutrino beam. The SciBooNE detector

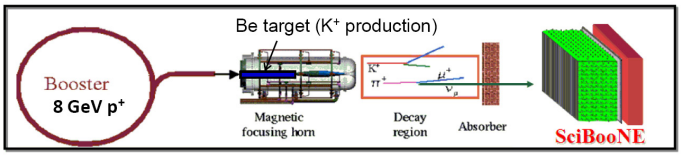

Figure 1: Schematic overview of the BNB line and location of SciBooNE.

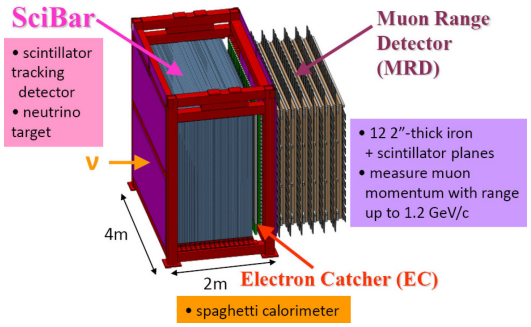

Figure 2: The different components of the SciBooNE detector.

was located 100 m downstream from the beryllium target on the axis of the beam. The BNB line with SciBooNE is shown in Fig. 1. The detector was comprised of three sub-detectors: a fully active and finely segmented scintillator tracker (SciBar), an electromagnetic calorimeter (EC), and a muon range detector (MRD) (shown in Fig. 2). Neutrino events in this analysis were required to interact in the SciBar detector.

In neutrino mode running (antineutrino mode running), defined as whether the polarity of magnetic horn is set to produce a neutrino (antineutrino) beam, the neutrino flux corresponding to 0.99×10^{20} (1.51×10^{20}) protons on target (POT) is collected and used for this analysis.

The MC simulation of the neutrino beam was modeled by the MiniBooNE collaboration using a Sanford Wang parametrization of HARP data for π^+ and π^- production and Feynman scaling for K^+ production[2]. The neutrino beam prediction is then propagated to the SciBooNE detector location where NEUT [3,4], a neutrino interaction library, models the initial neutrino interaction and subsequent nuclear modeling in SciBar. The particles that emerge from the nuclei are then propagated through GEANT4 and SciBooNE reconstruction algorithms to obtain hit and track based information.

3 Event Selection

While the neutrino flux at SciBooNE is predominantly due to π^+ decay in neutrino mode running and π^- decay in antineutrino mode running, K^+ decay is the dominant source of neutrinos above neutrino energy of 2 GeV for both running modes. The aim is to search for events where the high energy ν_μ from K^+ interacts within the volume of the SciBar detector through a charged current interaction, producing a high energy muon that penetrates though the SciBar, EC, and MRD detectors. Backgrounds include high energy ν_μ from π^+ and high energy $\bar{\nu}_\mu$ from π^-, which also produce a muon track that is indistinguishable from our signal. Fig. 3 shows a typical K^+ candidate event in the selected events. Tab. 1 shows the selected events in data and MC for neutrino and antineutrino mode. Separate samples are extracted for neutrino mode running and antineutrino mode due to different backgrounds. The selected events are further separated into three sub-samples based on the number of reconstructed SciBar tracks in each event: 1, 2, or 3-Track. The 1-Track sample has the largest statistics but contains mostly background events

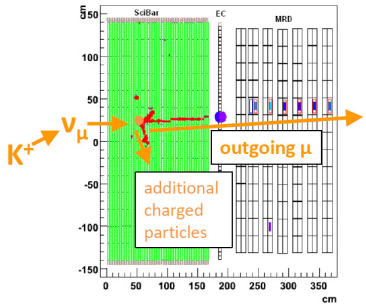

Figure 3: Event display of a K^+ candidate event.

Table 1: Number of selected events for data and MC in neutrino and antineutrino mode. The rightmost column shows the predicted contribution from K^+.

	Data	MC	K^+
Neutrino Mode	3,090	3,527	1398
Antineutrino Mode	1,699	1,604	285

(π^+ and π^-). The 2-Track sample contains a split between K^+ and background. The 3-Track sample contains mostly K^+ but has the smallest statistics.

The high energy muons penetrate through the entire SciBooNE detector so the reconstruction of the total muon energy, and thus the neutrino energy, cannot be done. The reconstructed muon angle relative to beam axis will be used as the primary kinematic variable for the analysis. Neutrinos produced from K^+ decay have a higher energy on average than neutrinos from π^+ and π^- decay. Therefore, the angular distribution of the resulting muon from the neutrino interaction of a neutrino from K^+ will be more forward peaked than those from neutrinos from π^+ and π^- and can help separate the signal from background.

4 Covariance Fit

The muon angle distributions are fitted to isolate the neutrinos from K^+ decay and determine the K^+ production normalization relative to the Feynman scaling predicted K^+ production currently implemented the beam MC. The following χ^2 function is minimized:

$$\chi^2 = \chi^2_\nu + \chi^2_{\bar{\nu}} = \sum_{i,j}^{N}(N_i^{obs} - N_i^{pred})(V^\nu_{stat} + V^\nu_{sys})^{-1}_{ij}(N_j^{obs} - N_j^{pred}) + \sum_{p,q}^{M}(M_p^{obs} - M_p^{pred})(V^{\bar{\nu}}_{stat} + V^{\bar{\nu}}_{sys})^{-1}_{pq}(M_q^{obs} - M_q^{pred}). \quad (1)$$

The χ^2 function in Eq. 1 contains two terms: the former χ^2_ν term is associated with events for neutrino mode running and the latter $\chi^2_{\bar{\nu}}$ term is associated with events for antineutrino mode running. $N^{obs}_{i(j)}$ and $N^{pred}_{i(j)}$ are the numbers of observed and predicted events in the $i(j)$-th angle bin for the neutrino mode analysis. $M^{obs}_{p(q)}$ and $M^{pred}_{p(q)}$ are the same quantities in the $p(q)$-th angle bin for the antineutrino mode analysis. The functions that describe the number of predicted events $N^{pred}_{i(j)}$ and $M^{pred}_{p(q)}$ are functions of the K^+ production normalization.

$(V^\nu_{sys})_{ij}$ and $(V^{\bar{\nu}}_{sys})_{pq}$ are the elements of the covariance matrix for systematic uncertainties in neutrino and antineutrino mode running, respectively. The systematic uncertainties consid-

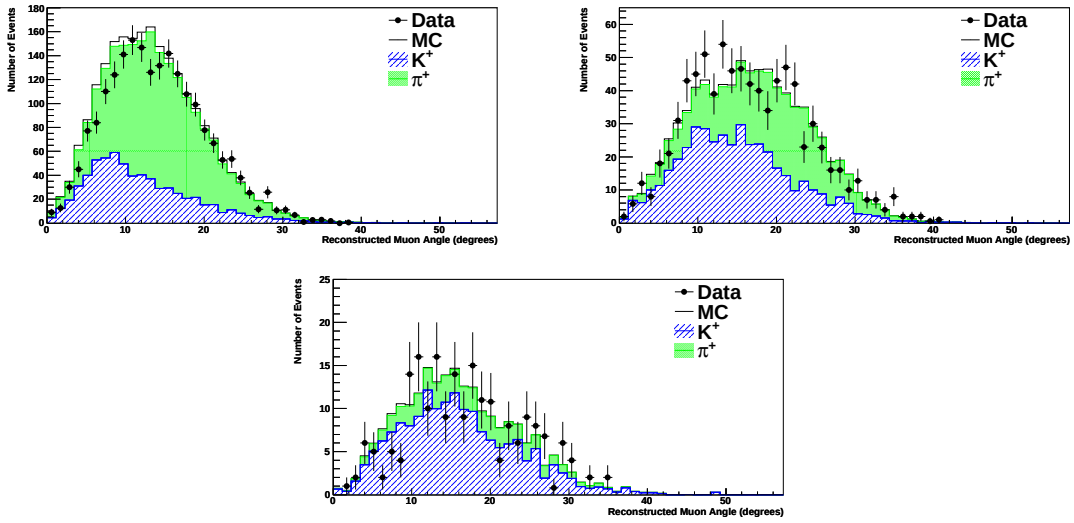

Figure 4: The reconstructed muon angle relative to beam axis for the SciBar 1-Track (upper left), 2-Track (upper right), and 3-Track (lower center) samples in neutrino mode running after the application of the K^+ production normalization of 0.87.

ered fall into three broad categories: the neutrino flux production uncertainties (initial meson production at target, magnetic horn current,etc.), neutrino cross-section and nuclear modeling uncertainties, and detector uncertainties (uncertainties associated with the instrumentation of the various detector components). V^{ν}_{stat} ($V^{\bar{\nu}}_{stat}$) represents the statistical error in neutrino mode running (antineutrino mode running).

After the χ^2 minimization, a K^+ production normalization of 0.87±0.12 is obtained. The reconstructed muon angle for the SciBar 1,2,3-Track samples in neutrino mode after the application of the K^+ production normalization are shown in Fig. 4. To ensure that the lack of the exact neutrino cross-section knowledge does not influence the final K^+ production result, this analysis was also performed using NUANCE [5], an alternate neutrino interaction library to NEUT. The result from NUANCE is in good agreement with the result stated here.

5 Conclusion

The K^+ production normalization relative to beam MC is obtained by fitting the muon angle relative to beam axis for a K^+ rich sample obtained by selecting ν_μ induced high energy muons that penetrate the entire SciBooNE detector. The K^+ production normalization of 0.87±0.12 shows that Feynman scaling is valid down to the 8 GeV incident proton energy. The measurement reduces the uncertainty on the K^+ production cross section from 40% (currently used in MiniBooNE and SciBooNE) to 14%, since most of the uncertainty is concentrated in the overall normalization. The measurement will also reduce uncertainty in neutrino backgrounds from K^+, which is essential for future precision neutrino measurements.

References

1. R.P. Feynman, *Phys. Rev. Lett.* **23**, 1415 (1969).
2. Aguilar-Arevalo et al., *Phys. Rev.* D **79**, 072002 (2009).
3. Y. Hayato, *Nucl. Phys. Proc. Suppl.* **112**, 171-176 (2002).
4. G. Mitsuka, *AIP Conf. Proc.* **981**, 262-264 (2008).
5. D. Casper, *Nucl. Phys. Proc. Suppl.* **112**, 161-170 (2002).

ON THE POTENTIAL OF MINIMAL FLAVOUR VIOLATION

Rodrigo Alonso
Departamento de Física Teórica, Universidad Autónoma de Madrid &
Instituto de Física Teórica IFT-UAM/CSIC, Cantoblanco, 28049 Madrid, Spain

Within the scheme of Minimal Flavour Violation, the possibility of spontaneous flavour symmetry breaking is explored by analyzing the scalar potential compatible with the symmetries. In this setup the Yukawa couplings arise from the vacuum expectation value (vev) of fields that transform under the flavour group. The outcome of the analysis of the potential depends much, especially for the mixing angles, on the field content.

1 Minimal Flavour Violation

The hypothesis of Minimal Flavour Violation [1] (MFV) accounts for the suppression of flavour changing neutral currents as well as for CP violating processes in any theory beyond the Standard Model. The reason for the flavour alignment of all processes is, in this hypothesis, assumed to stem in an underlying symmetry. In the limit of vanishing Yukawa couplings the quark sector of the Standard Model presents and extended symmetry group that is, aside from $U(1)$ factors:

$$\mathcal{G}_F \equiv SU(3)_{Q_L} \times SU(3)_{U_R} \times SU(3)_{D_R} \,. \tag{1}$$

Under this group the left-handed quark doublet Q_L would transform as $(3,1,1)$, the right-handed up-type quarks U_R as $(1,3,1)$ and the right-handed down type quarks D_R as $(1,1,3)$. This symmetry is assumed to be an exact symmetry at some high scale ($\Lambda_{fl} \gg v$). The introduction of the Yukawa couplings must then be accompanied by the assignment of transformation properties under $\mathcal{G}_F$, such that the Yukawa interaction is made invariant,

$$\mathscr{L}_Y = \overline{Q}_L Y_D D_R H + \overline{Q}_L Y_U U_R \tilde{H} + h.c. \,, \qquad Y_U \sim (3,\overline{3},1) \,, \qquad Y_D \sim (3,1,\overline{3}) \,. \tag{2}$$

Besides the flavour symmetry proposed, the other assumption of MFV is that these are the only flavour carrying structures. With this hypothesis, any operator arising from new physics in an effective Lagrangian formalism with the Standard Model fields has it's flavour structure determined by the imposition of invariance under $\mathcal{G}_F$, which is achieved by the proper insertion of Yukawa couplings.

2 The dynamical origin of MFV

Through all this reasoning there is the implicit assumption of a dynamical origin of these Yukawa couplings. The first consequence of exploring this assumption seriously is regarding the Yukawa interaction as an effective one [4] involving flavons, that is, the fields whose vevs will fix the

Yukawa couplings. The immediate extension is a dimension 5 *Yukawa operator*:

$$\mathscr{L}_Y = \overline{Q}_L \frac{\Sigma_d}{\Lambda_{fl}} D_R H + \overline{Q}_L \frac{\Sigma_u}{\Lambda_{fl}} U_R \tilde{H} + h.c. \,, \qquad \Sigma_u \sim (3, \overline{3}, 1) \,, \qquad \Sigma_d \sim (3, 1, \overline{3}) \,. \tag{3}$$

The transformation properties are fixed by the imposition of invariance under $\mathcal{G}_F$, and therefore the Σ scalar fields transform as *bi-fundamental* representations. From an effective Lagrangian point of view the next possibility is a dimension 6 *Yukawa operator*,

$$\begin{aligned} \mathscr{L}_{Y_D} &= \overline{Q}_L \frac{\chi_d^L \chi_d^{R\dagger}}{\Lambda_{fl}^2} D_R H + h.c. \,, & \chi_d^L &\sim (3,1,1) \,, \qquad \chi_d^R \sim (1,1,3) \,, \\ \mathscr{L}_{Y_U} &= \overline{Q}_L \frac{\chi_u^L \chi_u^{R\dagger}}{\Lambda_{fl}^2} U_R \tilde{H} + h.c. \,, & \chi_u^L &\sim (3,1,1) \,, \qquad \chi_u^R \sim (1,3,1) \,. \end{aligned} \tag{4}$$

The scalar fields χ transform as *fundamental* representations. The dimension 7 operator could contain a fermion condensate as Georgi and Chivukula suggested [2] but here only the two first cases will be discussed.

The scalar fields must acquire a vev through a scalar potential, and such potential must be invariant under $\mathcal{G}_F$ transformations. The discussion is now turned to whether a general scalar potential invariant under $\mathcal{G}_F$ will naturally fix the actual masses and mixing angles.

2.1 Dimension 5 Yukawa Operator

The construction of an invariant scalar potential for the fields Σ requires first the identification of the invariant magnitudes that can be constructed with the fields. Such a list was first made by Feldmann *et al.* [3], here we use a different notation:

$$\begin{aligned} A_u &= \mathrm{tr}\left(\Sigma_u \Sigma_u^\dagger\right) \,, & B_u &= \det\left(\Sigma_u\right) \,, \\ A_d &= \mathrm{tr}\left(\Sigma_d \Sigma_d^\dagger\right) \,, & B_d &= \det\left(\Sigma_d\right) \,, \\ A_{uu} &= \mathrm{tr}\left(\Sigma_u \Sigma_u^\dagger \Sigma_u \Sigma_u^\dagger\right) \,, & A_{dd} &= \mathrm{tr}\left(\Sigma_d \Sigma_d^\dagger \Sigma_d \Sigma_d^\dagger\right) \,, \\ A_{ud} &= \mathrm{tr}\left(\Sigma_u \Sigma_u^\dagger \Sigma_d \Sigma_d^\dagger\right) \,. \end{aligned} \tag{5}$$

The potential then has the form, for the three family case and to the renormalizable level,

$$V^{(4)}\left(\Sigma\right) = \sum_{i=u,d} \left(-\mu_i^2 A_i + \tilde{\mu}_i B_i + \lambda_i A_i^2 + \lambda_i' A_{ii}\right) + g_{ud} A_u A_d + \lambda_{ud} A_{ud} \,. \tag{6}$$

As the vevs of the Σ fields are related to quark masses and mixing through Eq. 3 ,

$$\frac{\langle \Sigma_u \rangle}{\Lambda_{fl}} = Y_U = V_{CKM}^\dagger \cdot Diag\left(y_u, y_c, y_t\right) \,, \qquad \frac{\langle \Sigma_d \rangle}{\Lambda_{fl}} = Y_D = Diag\left(y_d, y_s, y_b\right) \,, \tag{7}$$

substitution of these relations in Eq. 5 allows for the analysis of the potential as a function of quark masses and mixing parameters.

The study of the potential in Eq. 6 reveals that the complete pattern of masses and mixing angles cannot arise for any value of the potential parameters; one massive quark per sector and no mixing is the closest to the actual values achievable at this level. For the two family case a renormalizable potential can yield the hierarchy $y_u - y_c$ and $y_d - y_s$ for a certain set of fine-tuned parameters but again no non-zero angle is obtained. To obtain nonzero angles one can go to the non-renormalizable level, as, after all, ours is an effective Lagrangian with cut-off

Λ_{fl}. To illustrate how to fix the Cabibbo angle to it's actual value through a non-renormalizable potential, let's examine the angle dependence of the potential at the renormalizable level for two families:

$$V^{(4)}_{\theta_c} \equiv \lambda_{ud} A_{ud} = \lambda_{ud} \Lambda^4_{fl} \left(\cos 2\theta_c \left(y_c^2 - y_u^2 \right) \left(y_s^2 - y_d^2 \right) + \left(y_c^2 + y_u^2 \right) \left(y_s^2 + y_d^2 \right) \right) / 2 \,, \tag{8}$$

This term, regarded as a potential for θ_c, will have it's minimum at either $\theta_c = 0$ or $\theta_c = \pi/2$, so some different dependence on θ_c must be added for nonzero angle. The next relevant term appearing in the series of increasing dimension invariants depending on θ_c is A^2_{ud}. With these two terms one can construct a 'mexican hat' , $V^{(8)} \supset \lambda_{ud} A_{ud} + \lambda_{udud} A^2_{ud} / \Lambda^4_{fl} \sim \lambda_{udud} (A_{ud} - \alpha)^2 / \Lambda^4_{fl}$ that will fix the Cabibbo angle to the experimental value provided the fine tunned ratio $\lambda_{ud} / \lambda_{udud} \sim 10^{-10}$. This type of fine-tuning illustrates the difficulty within this approach for obtaining the actual masses and mixing parameters.

2.2 Dimension 6 Yukawa Operator

This case requires careful connection of the vev of the fields with the Yukawa couplings,

$$\frac{\left\langle \chi^L_u \right\rangle \left\langle \chi^{R\dagger}_u \right\rangle}{\Lambda^2_{fl}} = Y_U \,, \qquad \frac{\left\langle \chi^L_d \right\rangle \left\langle \chi^{R\dagger}_d \right\rangle}{\Lambda^2_{fl}} = Y_D \,. \tag{9}$$

The structure on the left of each term is not a general mass matrix but one composed of two 'vectors'. One finds the result of this fact by looking at the eigenvalues and eigenvectors of the matrix

$$Y_U Y_U^\dagger = \frac{\left\langle \chi^{R\dagger}_u \chi^R_u \right\rangle}{\Lambda^4_{fl}} \left\langle \chi^L_u \right\rangle \left\langle \chi^{L\dagger}_u \right\rangle \,. \tag{10}$$

The matrix structure is given only by the flavon χ^L_u, and has an immediate diagonalization; χ^L_u is the only eigenvector with non-zero eigenvalue, such eigenvalue being

$$y^2_{u_i} \equiv \left\langle \chi^{L\dagger}_u \chi^L_u \right\rangle \left\langle \chi^{R\dagger}_u \chi^R_u \right\rangle / \Lambda^4_{fl} \,, \tag{11}$$

where y_{u_i} is the only nonzero up-type Yukawa entry in this approach. The mixing then arises as the misalignment when diagonalizing both $Y_U Y_U^\dagger$ and $Y_D Y_D^\dagger$. Such misalignment is just the relative direction between χ^L_u and χ^L_d, but as we are talking of two 'vectors' this magnitude is described by one relative angle, which means there is one physical angle only in this scheme;

$$\cos\theta = \frac{\left\langle \chi^{L\dagger}_u \chi^L_d \right\rangle}{\left| \chi^L_u \right| \left| \chi^L_d \right|} \,, \tag{12}$$

where $\left| \chi^L_u \right|^2 \equiv \left\langle \chi^{L\dagger}_u \chi^L_u \right\rangle$. Once made the connection with masses and mixing angles we turn to constructing the potential. All the magnitudes related to masses and mixing angles have expressions in terms of the vevs of the only five possible $\mathcal{G}_F$ invariants:

$$X^2 \equiv \left(\chi^{L\dagger}_u \chi^L_u \,,\, \chi^{L\dagger}_d \chi^L_d \,,\, \chi^{R\dagger}_u \chi^R_u \,,\, \chi^{R\dagger}_d \chi^R_d \,,\, \chi^{L\dagger}_d \chi^L_u \right)^T \,. \tag{13}$$

The potential to the renormalizable level will be the sum of a linear combination of these invariants and products of two of these invariants. This can be formally written:

$$V^{(4)}(\chi) = -\mu^2 \cdot X^2 + \left(X^2 \right)^\dagger \lambda \, X^2 \,. \tag{14}$$

In a first approach we neglect any CP violation effect and chose real parameters, μ^2 is an array of 5 real components and λ a symmetric matrix [a]. The minimum of this potential is then:

$$\langle X^2 \rangle = \frac{1}{2}\lambda^{-1}\mu^2 \,, \tag{15}$$

provided that λ is invertible. This approach naturally accommodates the angle as it's expression in terms of the potential parameters involves the ratio of linear combinations of the entries of μ^2 given by λ^{-1}, which is naturally of $\mathcal{O}(1)$. For definiteness let us take the two family case, although the discussion this far is independent of the number of generations, and write explicitly:

$$\begin{gathered} y_c^2 = \frac{1}{4\Lambda_{fl}^4}\left(\lambda^{-1}\mu^2\right)_{uL}\left(\lambda^{-1}\mu^2\right)_{uR} \,, \qquad y_s^2 = \frac{1}{4\Lambda_{fl}^4}\left(\lambda^{-1}\mu^2\right)_{dL}\left(\lambda^{-1}\mu^2\right)_{dR} \,, \\ \cos\theta_c = \frac{\left(\lambda^{-1}\mu^2\right)_{ud}}{\sqrt{\left(\lambda^{-1}\mu^2\right)_{dL}\left(\lambda^{-1}\mu^2\right)_{uL}}} \,. \end{gathered} \tag{16}$$

3 Conclusions

Here the possibility of spontaneous breaking of the flavour symmetry regarded in MFV was considered. In such framework, the Yukawa couplings are fixed by the vev of flavour-carrying fields. The analysis of the potential leading to spontaneous flavour symmetry breaking differs for the field content and therefore the group representation on which the scalar fields are placed. The choice of a dimension 5 Yukawa operator, that is, the introduction of scalar fields transforming in bi-fundamental representations, does not allow for mixing among quarks at the renormalizable and classical level, it can accommodate the actual hierarchy of masses in the two family case and only a partial hierarchy for the three family case. The introduction of fundamental fields through a dimension 6 Yukawa operator allows for natural mixing among quarks and imposes the strong hierarchy of one massive quark only per up and down sector at the classical and renormalizable level. Although a dimension 6 Yukawa operator is better suited to accommodate the experimental data, none of the approaches gives the complete picture of masses and mixing angles. Such complete landscape could arise from the simultaneous consideration of both operators or addition of more scalar fields. Overall, it is remarkable that the requirement of invariance under the flavour symmetry strongly constrains the scalar potential of MFV, up to the point that the obtention of quark mass hierarchies and mixing angles is far from trivial.

Acknowledgments

R. Alonso acknowledges M. B. Gavela, L. Merlo and S. Rigolin with whom this study was carried. R. Alonso acknowledges CICYT through the project FPA2009-09017, CAM through the project HEPHACOS, P-ESP-00346 and financial support from the MICINN grant BES-2010-037869.

References

1. G. D'Ambrosio, G. Giudice, G. Isidori, and A. Strumia, Nucl. Phys. **B645** (2002) 155–187 [arXiv:hep-ph/0207036].
2. R. S. Chivukula and H. Georgi, Phys. Lett. **B188** (1987) 99.
3. T. Feldmann, M. Jung, T. Mannel, Phys. Rev. **D80** (2009) 033003. [arXiv:0906.1523 [hep-ph]].
4. R. Alonso, M. B. Gavela, L. Merlo, S. Rigolin, *On The Potential of Minimal Flavour Violation*, [arXiv:1103.2915 [hep-ph]].

[a] The indices of λ and μ^2 run over the five values $\{uL,dL,uR,dR,ud\}$.

Results of charged pions cross-section in proton carbon interaction at 31 GeV/c measured with the NA61/SHINE detector.

Sebastien Murphy
on behalf of the NA61/SHINE collaboration http://na61.web.cern.ch/
University of Geneva, DPNC, 24 Quai E. Ansermet, 1201 Geneva, Switzerland

Among other goals, the NA61/SHINE (SHINE ≡ SPS Heavy Ion and Neutrino Experiment) detector at CERN SPS aims at precision hadro-production measurements to characterise the neutrino beam of the T2K experiment at J-PARC. These measurements are performed using a 31 GeV/c proton beam produced at the SPS with a thin carbon target and a full T2K replica target. Spectra of π^- and π^+ inclusive inelastic cross section were obtained from pilot data collected in 2007 [1] with a 2 cm thick target (4% of the interaction length). The SHINE detector and its particle identification capabilities are described and the analysis techniques are briefly discussed.

1 Physics motivation

In T2K, neutrinos are produced by a high intensity proton beam of 31 GeV/c impinging on a carbon target and producing mesons (π and K) from the decay of which the neutrinos are produced. There exist so far no measurements of hadron inclusive spectra from p+C at 31 GeV/c. Thus the NA61/SHINE experiment provides a precise measurement of meson yield production in carbon at the proton beam energy of interest for T2K. These measurements are used for the T2K neutrino beam simulation and consequently reduce the systematic uncertainties of the neutrino energy distribution at the needed level for the physics goals of T2K [2].

2 The SHINE detector and combined particle identification

The set-up of the NA61/SHINE is shown in Fig. 1. The main components of the NA61 detector were constructed and used by the NA49 experiment [3]. The tracking apparatus consists in four large volume Time Projection Chambers (TPCs). Two of them, the vertex TPCs (VTPC-1 and VTPC-2), are located in the magnetic field of two super-conducting dipole magnets and, two TPCs (MTPC-L and MTCP-R) are positioned downstream of the magnets, symmetrically on the left and right of the beam line. The TPCs provide a measurement of charged particle momenta p with a high resolution. For the 2007 run a new forward time of flight detector (ToF-F) was constructed in order to extend the acceptance of the NA61/SHINE set-up for pion and kaon identification as required for the T2K measurements [4]. The ToF-F detector consists of 64 scintillator bars, vertically orientated, and read out on both sides with Hamamatsu R1828 photo-multipliers. The resolution of the ToF-F wall is < 120 ps [4] which provides a 5 σ π/K separation at 3 GeV/c. It is installed downstream of the MTPC-L and MTPC-R, closing the gap between the ToF-R and ToF-L walls. The ToF-F provides full acceptance coverage of the T2K phase-space (parent particles generating a neutrino which hit the far detector).

As demonstrated in Fig. 2, high purity particle identification can be performed by combining the tof and dE/dx information over the whole momentum range needed for T2K. Moreover, in the momentum range 1–4 GeV/c, where dE/dx bands for different particle species overlap, particle identification is in general only possible using the tof method. In each (p, θ) bin the bin-by-bin maximum likelihood method was applied to fit yields of π^+ and π^- mesons. The pion yields were calculated summing all particles within 2σ around the fitted pion peak.

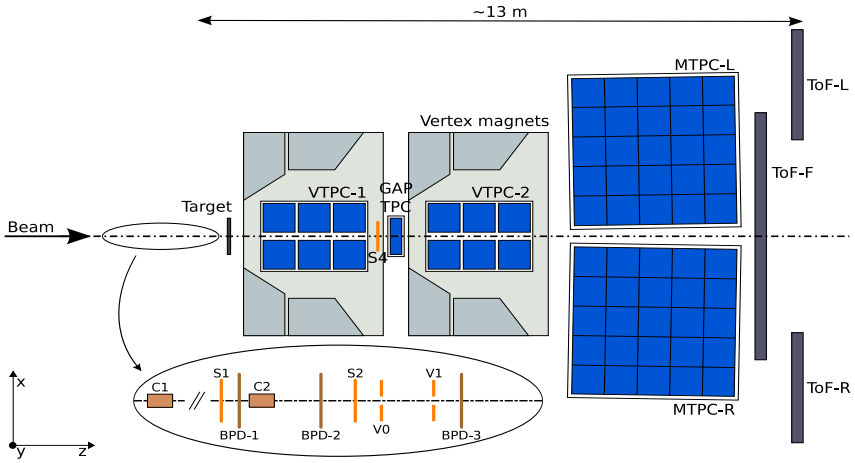

Figure 1: The layout of the NA61/SHINE set-up in the 2007 data taking.

3 Charged pion cross sections

The differential inclusive inelastic cross section $\frac{d\sigma_{inel}}{dp}$ are extracted using three independent analysis:

- π^+ and π^- spectra identified with dE/dx below 800 MeV/c [7].
- π^- spectra from a so called h-minus analysis in which all negative tracks were selected and yields were extracted from a global Monte Carlo factor [6].
- π^+ and π^- yields identified with the combined $tof - dE/dx$ method [8].

All pion yields were corrected with the help of the NA61 Geant3 based Monte-Carlo. The following effects have been accounted for: geometrical acceptance of the detector; efficiency of the reconstruction chain; decays and secondary interactions; ToF detection efficiency; pions coming from Lambda and K0s decays (called feed-down correction). The inverse corrections applied to the spectra for one angular bin in the tof+dE/dx analysis are shown in Fig. 3 as an example. The Systematic error associated with each correction and with the particle identification are also shown. The dominant systematic come from the uncertainty in the correction for weak decays and secondary interactions (30% of the correction value). In addition to several track quality cuts, maximum acceptance regions were selected by applying a cut on the azimuthal angle, thereby assuring tracks have a large number of measured points, and a very high reconstruction efficiency. This minimizes the systematical errors arising from possible differences in geometry between data and Monte-Carlo.

The spectra normalized to the inclusive cross section [5] are shown in Fig. 4 for positively charged pions. The spectra are presented as a function of particle momentum in ten intervals of the polar angle. The chosen binning takes into account the available statistics of the 2007 data sample, detector acceptance and particle production kinematics. The negatively charged pion cross sections are given in [1] along with details on all three analysis.

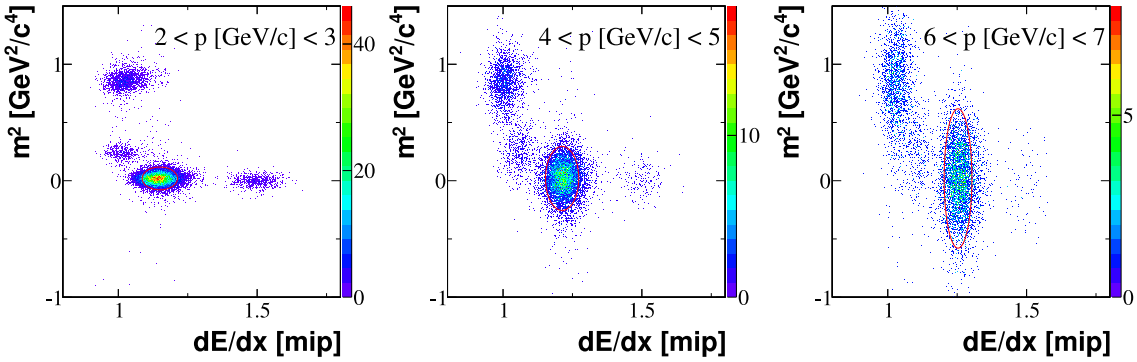

Figure 2: Examples of two-dimensional m^2–dE/dx plots for positively charged particles in three momentum intervals indicated in the panels. 2σ contours around fitted pion peaks are shown. The left and middle plots correspond to the dE/dx cross-over region while the right plot is at such a high momentum that the ToF-F resolution becomes a limiting factor. The combination of both measurements provides close to 100% purity in the pion selection over the whole momentum range.

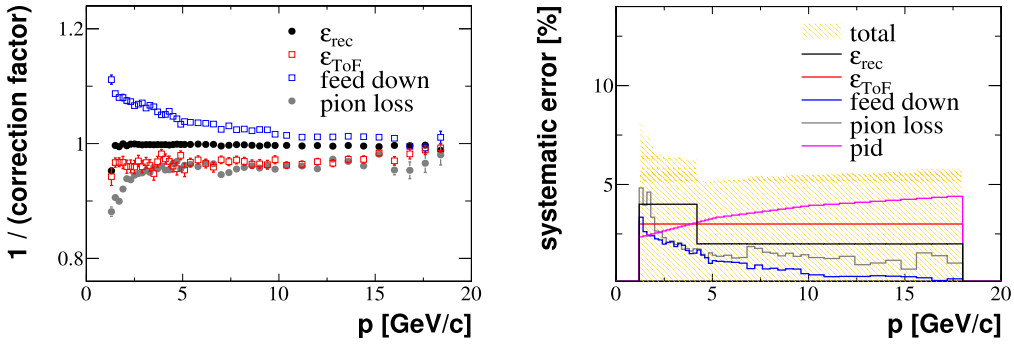

Figure 3: Example of momentum dependence of the inverse correction factor (left) and systematic errors (right) for the $tof - dE/dx$ analysis for positively charged pions in the polar angle interval [40,60] mrad. ϵ_{rec} and ϵ_{tof} are the efficiencies of the reconstruction and of the ToF-F, respectively. The feed-down correction accounts for pions from weak decays which are reconstructed as primary particles, while the pion loss accounts for pions lost due to decays or secondary interactions.

4 Conclusion

The presented results are essential for precise predictions of the neutrino flux in T2K and are currently used as input to the neutrino beam simulation. In 2009 and 2010 another much larger set of data has been collected with both the thin and a T2K replica carbon target and is presently being analysed. For both these data sets the ToF-F was extented yielding a higher detector acceptance, the TPC readouts were upgraded and a new trigger system was implemented. This new data will provide results of charged pion cross-section with a higher precision and will allow the measurements of other hadron species such as charged kaons, protons or K^0_s. Knowledge of kaon production is crucial for T2K to predict the intrinsic ν_e contamination of the neutrino beam.

5 References

1. NA61 Collaboration, Measurements of Cross Sections and Charged Pion Spectra in Proton-Carbon Interactions at 31 GeV/c arXiv:1102.0983v2 [hep-ex], submitted to Phys. Rev. C.
2. N. Abgrall [NA61 Collaboration], XLVth Rencontres de Moriond, Electroweak interactions

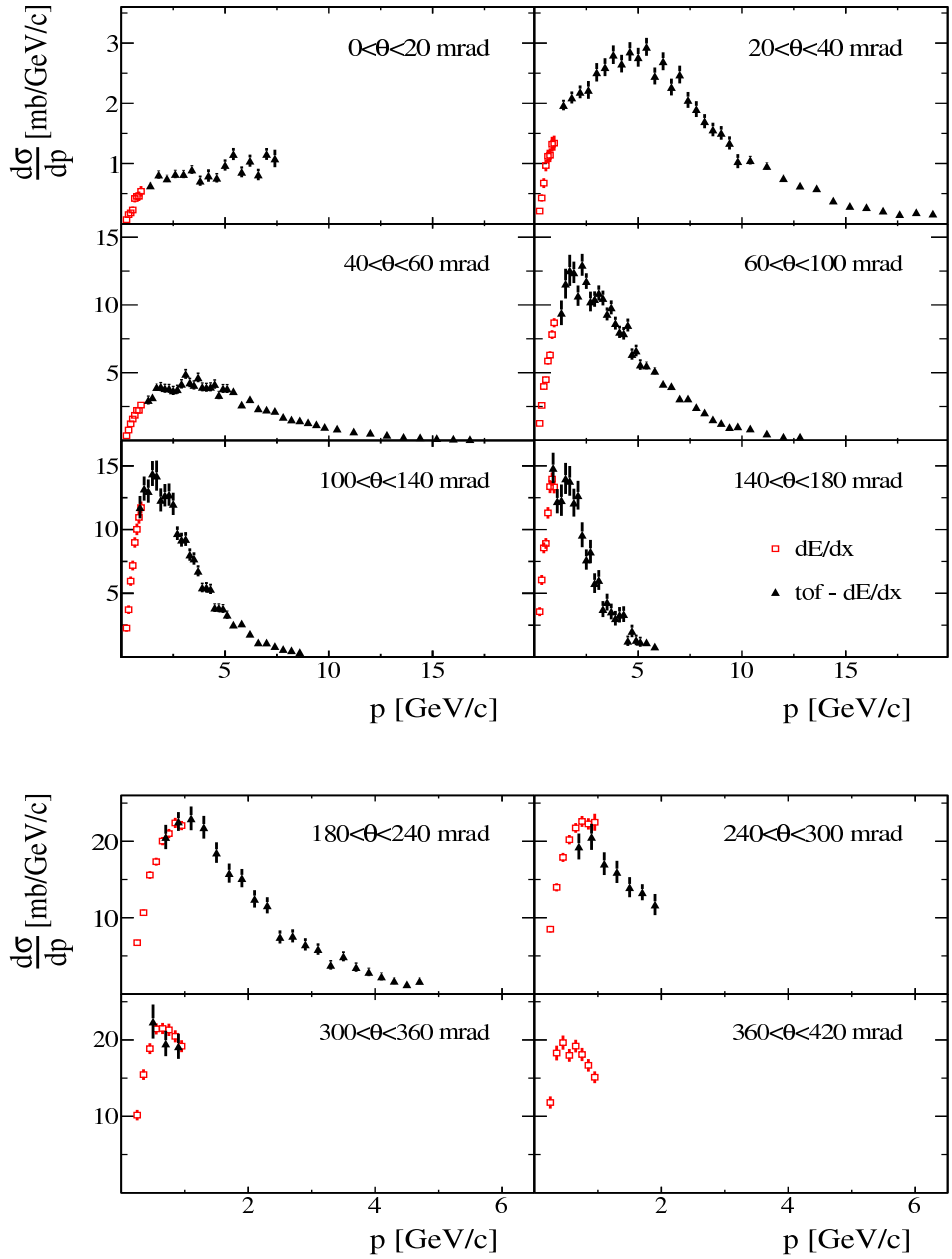

Figure 4: Differential cross sections for π^+ meson production in p+C interactions at 31 GeV/c. The spectra are presented as a function of laboratory momentum (p) in different intervals of polar angle (θ). Results obtained using two analysis methods are presented by different symbols: red open squares - dE/dx analysis and black full triangles - $tof - dE/dx$ analysis. Error bars indicate only statistical uncertainties.

and unified theories, La Thuile (March 2010).

3. S. Afanasev *et al.* [NA49 Collaboration], Nucl. Instrum. Meth. A 430, 210 (1999).
4. N. Abgrall *et al.* [NA61 Collaboration], CERN-SPSC-2008-018.
5. C. Strabel Ph.D. Thesis, ETH Zurich, 2011, Zurich Switzerland.
6. T. Palczewski, Ph.D. Thesis in preparation, Soltan Institute for Nuclear Studies, 2011, Warsaw Poland.
7. M. Posiadala, Ph.D. Thesis in preparation, University of Warsaw, 2011, Warsaw Poland.
8. S. Murphy, Ph.D. Thesis in preparation, University of Geneva, 2011, Geneva Switzerland.

List of Participants

XLVIth Rencontres de Moriond

Electroweak Interactions & Unified Theories

List of Participants

Family name	First name	Institution	Country	Email address
Abada	Asmaa	CNRS - Laboratoire de Physique Theorique	France	abada@th.u-psud.fr
Agarwalla	Sanjib Kumar	IFIC - Instituto de Física Corpuscular / CSIC	Spain	Sanjib.Agarwalla@ific.uv.es
Alison	John	University of Pennsylvania	USA	johnda@sas.upenn.edu
Alonso de Pablo	Rodrigo	Universidad Autónoma de Madrid	Spain	alonsodepablo.rodrigo@gmail.com
Altmannshofer	Wolfgang	Fermilab	USA	waltmann@fnal.gov
Anastasiou	Charalampos	ETH	Switzerland	babis@phys.ethz.ch
Augé	Etienne	CNRS / IN2P3	France	eauge@admin.in2p3.fr
Azzi	Patrizia	INFN	Italy	patrizia.azzi@pd.infn.it
Baak	Max	CERN	Switzerland	mbaak@cern.ch
Badziak	Marcin	University of Warsaw - ITP	Poland	Marcin.Badziak@fuw.edu.pl
Baglio	Julien	Laboratoire de Physique Théorique	France	Julien.Baglio@th.u-psud.fr
Baker	Sarah	University College	UK	christine.johnston@ucl.ac.uk
Bashir Butt	Jamila	University of Nebraska	USA	jbutt@cern.ch
Bechtle	Philip	DESY	Germany	philip.bechtle@desy.de
Bendavid	Josh	MIT	USA	jbendavid@mit.edu
Bernet	Colin	CERN	Switzerland	colin.bernet@cern.ch
Blennow	Mattias	Max-Planck-Institut für Physik	Germany	blennow@mppmu.mpg.de
Borzumati	Francesca	Tohoku University	Japan	borzumat@ictp.it
Boumediene	Djamel	LPC	France	djamel.boumediene@cern.ch
Bruemmer	Felix	Deutsches Elektronen-Synchrotron DESY	Germany	felix.bruemmer@desy.de
Caron	Sascha	University of Freiburg	Germany	scaron@physik.uni-freiburg.de
Cheng	Gary	Nevis Laboratories	USA	gcc2113@columbia.edu
Cinca	Diane	LPC	France	diane.cinca@cern.ch
Cossavella	Fabiana	Max-Planck-Institut für Physik	Germany	cossavel@mppmu.mpg.de
Covi	Laura	Georg-August Universitaet	Germany	Laura.Covi@theorie.physik.uni-goettingen.de
Dahl	Eric	The University of Chicago	USA	cdahl@kicp.uchicago.edu
Danilov	Mikhail	ITEP	Russia	danilov@itep.ru
De Rujula	Alvaro	CERN/IFT	Switzerland	alvaro.derujula@cern.ch
Delahaye	Timur	Instituto de Física Teórica	Spain	timur.delahaye@uam.es
Dissertori	Guenther	ETH Zurich Institute for Particle Physics	Switzerland	guenther.dissertori@cern.ch
Duperrin	Arnaud	CPPM	France	duperrin@cppm.in2p3.fr
Endo	Motoi	University of Tokyo	Japan	endo@hep-th.phys.s.u-tokyo.ac.jp
Falkowski	Adam	LPTO	France	adam.falkowski@th.u-psud.fr
Fernandez Martinez	Enrique	CERN	Switzerland	enfmarti@cern.ch
Fichet	Sylvain	LPSC	France	sylvain.fichet@lpsc.in2p3.fr
Frère	Jean-Marie	ULB - Physique Théorique	Belgium	frere@ulb.ac.be
Gersdorff	Gero	CPhT	France	gero.gersdorff@cpth.polytechnique.fr
Gingrich	Doug	University of Alberta	Canada	gingrich@ualberta.ca
Gladstone	Laura	University of Wisconsin	USA	gladstone@icecube.wisc.edu
Goertz	Florian	THEP Johannes Gutenberg-Universität	Germany	goertz@thep.physik.uni-mainz.de
Gomez Gonzalez	Luis Fernando	APC	France	lfgomez@gmail.com
Goudelis	Andreas	DESY	Germany	andreas.goudelis@desy.de
Goudzovski	Evgueni	Université Catholique de Louvain	Belgium	goudzovs@mail.cern.ch
Grajek	Phillip	Vrije Universiteit Brussel	Belgium	pgrajek@vub.ac.be
Grigoriev	Alexander	Skobeltsyn Institute of Nuclear Physics - MSU	Russia	ax.grigoriev@mail.ru
Grivaz	Jean-Francois	LAL	France	grivaz@lal.in2p3.fr
Grojean	Christophe	CERN	Switzerland	christophe.grojean@cern.ch
Guimarães da Costa	João	Harvard University	USA	guimaraes@physics.harvard.edu
Hardin	Delphine	LPNHE - UPMC	France	hardin@in2p3.fr
Harris	Philip	MIT	USA	pcharris@mit.edu
Hartz	Mark	University of Toronto / York University	Canada	mhartz@physics.utoronto.ca
Helbing	Klaus	Wuppertal University	Germany	helbing@uni-wuppertal.de
Herrero García	Juan	Universidad de Valencia	Spain	juan.a.herrero@uv.es

Family name	First name	Institution	Country	Email address
Hiller	Gudrun	TU Dortmund	Germany	gudrun.hiller@udo.edu
Hurwitz	Martina	LBNL	USA	mhurwitz@lbl.gov
Iconomidou-Fayard	Lydia	LAL	France	lyfayard@in2p3.fr
Indelicato	Paul	Laboratoire Kastler Brossel	France	paul.indelicato@lkb.ens.fr
Inoue	Yoshizumi	ICEPP - University of Tokyo	Japan	berota@icepp.s.u-tokyo.ac.jp
Ioannisian	Ara	Yerevan Physics Institute	Armenia	ara@cern.ch
Izubuchi	Taku	Brookhaven National Laboratory	USA	izubuchi@bnl.gov
Jaffré	Michel	LAL	France	jaffre@lal.in2p3.fr
Janot	Patrick	CERN	Switzerland	Patrick.Janot@cern.ch
Jayatilaka	Bodhitha	Duke University	USA	boj@phy.duke.edu
Jones	David	University of Southampton	UK	daj1g08@soton.ac.uk
Jones	Roger	Lancaster University	UK	Roger.Jones@cern.ch
Jüttner	Andreas	CERN	Switzerland	juettner@mail.cern.ch
Kachelriess	Michael	NTNU	Norway	Michael.Kachelriess@ntnu.no
Kadastik	Mario	NICPB	Estonia	mario.kadastik@cern.ch
Kado	Marumi	LAL	France	kado@lal.in2p3.fr
Kamenik	Jernej	Institut Jozef Stefan	Slovenia	jernej.kamenik@ijs.si
Kannike	Kristjan	Scuola Normale Superiore di Pisa	Italy	kannike@cern.ch
Kersten	Joern	University of Hamburg II	Germany	joern.kersten@desy.de
Kim	Yeong Gyun	Gwangju National University of Education	South Korea	ygkim@gnue.ac.kr
Kopp	Joachim	Fermilab	USA	jkopp@fnal.gov
Koshio	Yusuke	Gran Sasso National Laboratory	Italy	koshio@lngs.infn.it
Larner	Aimee	University of Oxford	UK	a.larner1@physics.ox.ac.uk
Lazopoulos	Achilleas	Institute of Theoretical Physics, ETH	Switzerland	lazopoli@phys.ethz.ch
Lees	Jean-Pierre	LAPP	France	lees@lapp.in2p3.fr
Leman	Steven	MIT	USA	swleman@mit.edu
Lhenry-Yvon	Isabelle	IPNO	France	lhenry@ipno.in2p3.fr
Li	Liang	Fermilab	USA	liangli@fnal.gov
Libanov	Maxim	Institute for nuclear research of RAS	Russia	ml@ms2.inr.ac.ru
Litim	Daniel	University of Sussex	UK	d.litim@sussex.ac.uk
Lorenz	Jeanette	LMU Muenchen	Germany	Jeanette.Lorenz@physik.uni-muenchen.de
Loucatos	Sotiris	Irfu, CEA - Saclay	France	s.loucatos@cea.fr
Majumder	Devdatta	Tata Institute of Fundamental Research	India	devdatta.majumder@cern.ch
Manalaysay	Aaron	Physik-Institut, Universität Zürich	Switzerland	aaronm@physik.uzh.ch
Margaroli	Fabrizio	Fermilab	USA	margarol@fnal.gov
Martinez Santos	Diego	CERN	Switzerland	diegomartinezsantos@hotmail.com
Mawatari	Kentarou	Vrije Universiteit Brussel	Belgium	kentarou.mawatari@vub.ac.be
Mention	Guillaume	CEA Saclay	France	guillaume.mention@cea.fr
Mertens	Susanne	Karlsruher Institut für Technologie	Germany	susanne.mertens@kit.edu
Mohammadi	Abdollah	IPM & Shiraz University	Iran	abdollah.mohammadi@cern.ch
Montanet	François	LPSC	France	montanet@in2p3.fr
Mori	Toshinori	ICEPP, The University of Tokyo	Japan	mori@icepp.s.u-tokyo.ac.jp
Moroi	Takeo	University of Tokyo	Japan	moroi@phys.s.u-tokyo.ac.jp
Muentel	Mait	NICPB	Estonia	maitm@cern.ch
Murphy	Sébastien	University of Geneva	Switzerland	sebastien.murphy@cern.ch
Nardini	Germano	Université Libre de Bruxelles	Belgium	germano@ifae.es
Nayyar	Ruchika	University of Delhi	India	ruchika.work@gmail.com
Nierste	Ulrich	TTP - Karlsruhe Institute of Technology	Germany	ulrich.nierste@kit.edu
Nonaka	Toshiyuki	University of Tokyo	Japan	nonaka@icrr.u-tokyo.ac.jp
Novella	Pau	CIEMAT	Spain	pau.novella@ciemat.es
Okumura	Ken-ichi	Kyushu University	Japan	okumura@phys.kyushu-u.ac.jp
Orloff	Jean	LPC Clermont	France	orloff@in2p3.fr
Palazzo	Antonio	Technische Universitat Munchen	Germany	antonio.palazzo@tum.de
Papucci	Michele	CERN	Switzerland	michele.papucci@cern.ch
Pavlovic	Zarko	Los Alamos National Laboratory	USA	zarko@fnal.gov
Perazzini	Stefano	Universitá di Bologna - INFN	Italy	stefano.perazzini@bo.infn.it
Perdue	Gabriel	Fermilab	USA	perdue@fnal.gov
Perez-Victoria	Manuel	Universidad de Granada	Spain	mpv@ugr.es
Petridis	Konstantinos	University of Manchester	UK	kap01@fnal.gov

Family name	First name	Institution	Country	Email address
Pfoh	Torsten	Institut für Physik	Germany	pfoh@thep.physik.uni-mainz.de
Pierini	Maurizio	CERN	Switzerland	maurizio.pierini@cern.ch
Pinamonti	Michele	Universtitá degli Studi di Trieste	Italy	michele.pinamonti@gmail.com
Poluektov	Anton	Budker Institute of Nuclear Physics	Russia	A.O.Poluektov@inp.nsk.su
Ponce	Laurette	CERN BE - OP/LHC	Switzerland	laurette.ponce@cern.ch
Potamianos	Karolos	Purdue University	USA	kpotamia@purdue.edu
Pozzato	Michele	Bologna University - INFN	Italy	michele.pozzato@bo.infn.it
Quigg	Chris	Fermilab	USA	quigg@fnal.gov
Remoto	Alberto	APC	France	remoto@in2p3.fr
Resende	Bernardo	CEA Saclay, DSM/IRFU/SPP	France	bernardo.resende@cea.fr
Rodriguez Sanchez	Ana Maria	UAM	Spain	anam.uam@gmail.com
Rogan	Christopher	California Institute of Technology	USA	crogan@caltech.edu
Rolandi	Luigi	CERN	Switzerland	gigi.rolandi@cern.ch
Romão	Jorge C.	Instituto Superior Técnico	Portugal	jorge.romao@ist.utl.pt
Roser	Robert	Fermilab	USA	roser@fnal.gov
Santanastasio	Francesco	University of Maryland	USA	francesco.santanastasio@cern.ch
Scanlon	Tim	Fermilab	USA	ts297@fnal.gov
Schaarschmidt	Jana	LAL	France	schaarsc@lal.in2p3.fr
Schaffer	Arthur	LAL	France	R.D.Schaffer@cern.ch
Schumacher	Markus	Albert-Ludwigs-University	Germany	markus.schumacher@physik.uni-freiburg.de
Schüssler	Fabian	CEA/Irfu	France	fabian.schussler@cea.fr
Sharma	Vivek	University Of California - San Diego	USA	vsharma@ucsd.edu
Simard	Olivier	CEA-Saclay, IRFU/SPP	France	olivier.simard@cea.fr
Soderberg	Mitchell	Syracuse University	USA	msoderbe@syr.edu
Soldner-Rembold	Stefan	University of Manchester	UK	soldner@fnal.gov
Soni	Amarjit	Brookhaven National Laboratory	USA	adlersoni@gmail.com
Strumia	Alessandro	Universitá di Pisa - INFN / NICPB	Italy	astrumia@mail.df.unipi.it
Tajima	Osamu	KEK	Japan	osamu.tajima@kek.jp
Tarrade	Fabien	Brookhaven National Laboratory	USA	Fabien.Tarrade@cern.ch
Teixeira	Ana M.	LPC	France	Ana.Teixeira@clermont.in2p3.fr
Theveneaux-Pelzer	Timothée	LPNHE	France	tpelzer@lpnhe.in2p3.fr
Thom-Levy	Julia	Cornell University	USA	jt297@cornell.edu
Thomas	Laurent	Université Libre de Bruxelles	Belgium	lathomas@ulb.ac.be
Torrento Coello	Ana Sofia	CEA - Saclay. DSM/IRFU/SPP	France	ana.torrento@cea.fr
Totaro	Pierluigi	University of Padova / INFN	Italy	pierluigi.totaro@pd.infn.it
Tran	Nhan	Johns Hopkins University	USA	ntran@pha.jhu.edu
Tran Thanh Van	Jean	LPT Orsay	France	jtrantv@gmail.com
Tschann-Grimm	Kathryn	Stony Brook University	USA	kgrimm@grad.physics.sunysb.edu
Tytgat	Michel	Université Libre de Bruxelles	Belgium	mtytgat@ulb.ac.be
Van Hove	Pierre	Institut Pluridisciplinaire Hubert Curien	France	vanhove@in2p3.fr
Vecchi	Manuela	CPPM	France	vecchi@cppm.in2p3.fr
Veelken	Christian	University of California	USA	christian.veelken@cern.ch
Velasco-Sevilla	Liliana	CINVESTAV - IPN	Mexico	lvelasco@fis.cinvestav.mx
Vesterinen	Mika	University of Manchester	UK	mikav@fnal.gov
Walsh	John	INFN	Italy	john.walsh@pi.infn.it
Weiler	Andreas	CERN	Switzerland	andreas.weiler@gmail.com
Westhoff	Susanne	Institut fuer Physik (WA THEP)	Germany	westhoff@uni-mainz.de
Wingerter	Akin	LPSC	France	akin@lpsc.in2p3.fr
Wingerter-Seez	Isabelle	LAPP	France	isabelle.wingerter@lapp.in2p3.fr
Xie	Yuehong	University of Edinburgh	UK	Yuehong.Xie@cern.ch
Yamamoto	Yasuhiro	KEK	Japan	yamayasu@post.kek.jp
Zabi	Alexandre	LLR - École Polytechnique	France	Alexandre.Zabi@cern.ch
Zheng	Bo	IHEP	China	zhengb@ihep.ac.cn